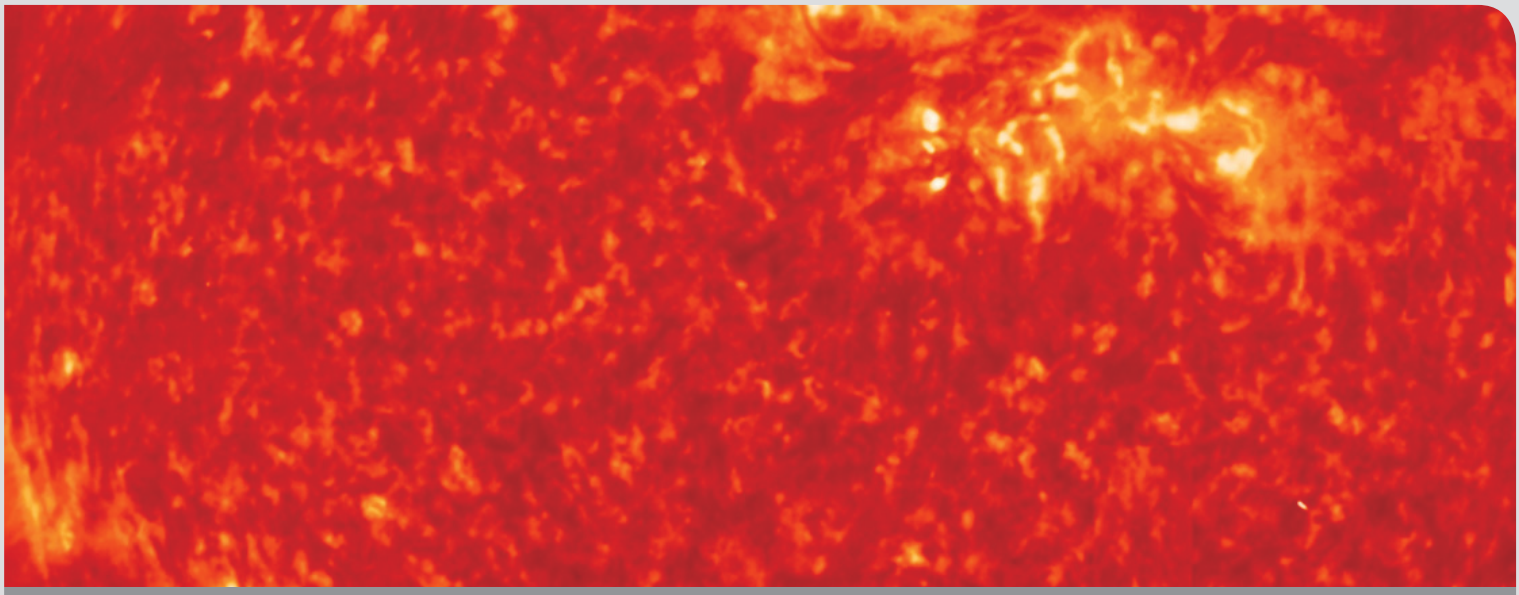

KIT SCIENTIFIC REPORTS 7671

Nuclear Fusion Programme

Annual Report of the Association
Karlsruhe Institute of Technology/EURATOM

January 2013 – December 2013

KIT Scientific Publishing

I. Pleli (ed.)

Nuclear Fusion Programme

Annual Report of the Association Karlsruhe Institute of Technology / EURATOM
January 2013 – December 2013

Karlsruhe Institute of Technology
KIT SCIENTIFIC REPORTS 7671

Nuclear Fusion Programme

Annual Report of the Association
Karlsruhe Institute of Technology/EURATOM

January 2013 – December 2013

I. Pleli (ed.)

KIT Scientific Publishing

Report-Nr. KIT-SR 7671

Impressum

Scientific Publishing

Karlsruher Institut für Technologie (KIT)
KIT Scientific Publishing
Straße am Forum 2
D-76131 Karlsruhe

www.ksp.kit.edu

Print on Demand 2015

ISSN 1869-9669
DOI: 10.5445/KSP/1000045307

Overview

Preface

The environmental impact of fossil fuels consumption, together with increasing concerns about the use of nuclear fission, is calling for new sources of energy supply. While in Germany, the “Energiewende” is targeting 2050 for accomplishing the change towards renewables, on the world level, which will determine the success of this change, the transition will be on an extended time scale.

Nuclear fusion offers an option of an environmental benign energy source with favourable safety features and almost unlimited fuel resources. Nuclear fusion research is aiming to generate the physical and technical basis of a fusion power station which, similar to the sun, gains energy from the fusion of light atoms.

The European fusion programme is determined to demonstrate fusion power supply by 2050, with subsequent deployment of power plants. It now has its major focus on the realisation of the experimental reactor ITER in Cadarache/France in the framework of a worldwide cooperation project. For the first time fusion power will be generated by a long-burning plasma, and the applied technologies will undergo extended tests. In parallel to the ITER construction, the “Accompanying Programme” is preparing the operation and use of ITER, as well as technical solutions and overall design for a fusion demonstration power plant.

With its total of about 220 scientists, engineers and support staff, the KIT Fusion Programme is completely integrated within the European programme, and is contributing to both, the construction of ITER and the Accompanying Programme – with a strong focus on fusion technologies. We are developing neutron radiation resistant, reduced-activation materials for in-vessel components of a fusion power plant, as well as engineering solutions for such components (i.e., breeding blanket and divertor), for heating systems (i.e., gyrotrons and microwave antennas), for the deuterium-tritium fuel cycle and for remote handling / remote maintenance systems, including irradiation / neutronics as well as system integration aspects. We are working on the next generation of fusion magnets, based upon high temperature superconductors, and characterize and qualify magnet materials for ITER. Furthermore, we develop numerical models for the plasma-wall interface. This Annual Report is giving a detailed account of all our work in these different areas.

We have extended our contributions to ITER, many of them in consortia with other European Fusion Laboratories. I.e., we have signed, in 2013, 16 new contracts with F4E, the European Domestic Agency for ITER, or directly with the ITER Organisation, with an overall budget of about 3.5 million Euros for our part. On the international level, we have intensified our contacts with the US, Korea and India, leading to two new framework cooperation agreements.

The year 2013 has seen the preparation for the next 5-annual Helmholtz evaluation of the German nuclear fusion programme. A new work programme, covering the years 2015 – 2019, was defined in close interaction with the other German fusion centres, IPP and FZJ, of course reflecting the work planning on the European level.

We have further increased our training efforts; e.g., the number of PhD students in the KIT fusion programme has increased to 40 at the end of 2013, and the KIT Summer School on Fusion Technologies has reached a new record level of 60 participants.

In 2013, the European Fusion Programme prepared for the transition from the system of EFDA and the Contracts of Association with EURATOM to the project-oriented work within

the EUROfusion consortium, to be implemented at the beginning of 2014. KIT has contributed to this transition by providing significant input to the EUROfusion work planning in particular in the area of Power Plant Physics and Technology, and by providing three of the nine Project Leaders in this area. Thus, we are well prepared to move ahead along the European Roadmap to Fusion Power.

Klaus Hesch, August 2014

Plasma Wall Interaction

In the big tokamaks (JET, ITER, DEMO) the most serious damage to plasma facing components (PFC) would be caused by disruptions and unstable edge localized mode (ELM). The PFC erosion is due to surface melt motion and violent vaporization of tungsten (W) divertor and beryllium (Be) or W first wall (FW) under the impacts of plasma, runaway electrons (RE) and photonic radiation from the plasma. The erosion estimation activity in KIT includes both ELM and disruption effects including the disruption mitigation by preventive massive gas injection (MGI). Dedicated computer codes are under development: MEMOS for melting/vaporization, ENDEP for RE stopping in W and Be, and TOKES for MGI thermal quench (TQ). The codes were earlier validated against a number of experiments at several tokamaks and plasma guns as well as the electron beam facility JUDITH. Many dedicated calculations applying these KIT codes for JET and QSPA Kh-50 are performed. Below the simulations for ITER and DEMO are exemplified.

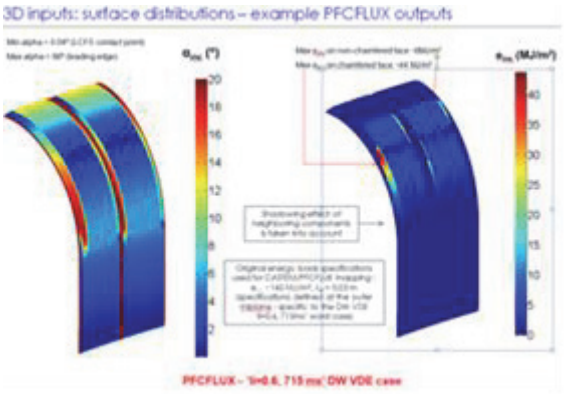

Typical geometry of MEMOS simulations.

To give an example, MEMOS simulations for ITER divertor baffle showed that in case of a mitigated disruption with an energy influx of Q = 45 MJ/m^2 perpendicular to the magnetic field and 5° incidence angle the surface temperature T_w remains below tungsten melting threshold for disruption durations τ from 3 to 10 ms; with Q = 70 MJ/m^2, T_w exceeds the melting threshold at τ < 9 ms. Maximum depth of melt pool h_m is about 70 μm. The plasma pressure causes melted material to move along the PFC surface with the velocity V_m of 0.1 - 0.5 m/s. The critical velocity of Rayleigh-Taylor instability is obtained of 1 m/s thus the melt splashing on the PFC edges shouldn't occur. The melt motion produces mountains at the castellation edges up to h_+ ~ 25 μm and craters of depth h_- ~ 10 μm per event. For small number of disruptions n the surface damage magnitude ($h_+ + h_-$) linearly increases with n; at n > 30 the surface profile becomes complex and the magnitude doesn't exceed a few mm. A moderate influence of halo current on the melt motion is obtained e.g. V_m increases by ~0.15 m/s and the changes of h_+ and h_- don't exceed 3 μm per event. The evaporation erosion is low (~0.1 μm) and the vapor shielding does not form. Only for non-mitigated major disruptions (Q > 300 MJ/m^2) significant evaporation (up to 6 μm) and the shielding occur.

Furthermore, RE and radiation impact consequences for stainless steel (St-St) and beryllium FW PFC are estimated with the code MEMOS. For MGI caused radiation wall load, T_w of St-St PFC is obtained to be higher than T_w of Be. Above the melting thresholds on the injected neon inflow magnitude J_m, the melt pool in St-St is deeper than that of Be by approximately a factor of 2. The melted St-St phase exists much longer than the melted Be phase. However, the thresholds for St-St and Be are approximately equal to each other: $J_{m,thr} \approx 2.2\times10^{26}$/s. For RE caused load with e.g. τ ~ 0.1 ms onto e.g. Be PFC the Be melting threshold on the RE current $J_{RE,Be}$ of 0.25 to 0.5 MA/m^2 is obtained, the melt layer thickness (when $J_{RE} > J_{RE,Be}$) up to 0.7 mm and the resolidification time longer than 30 ms.

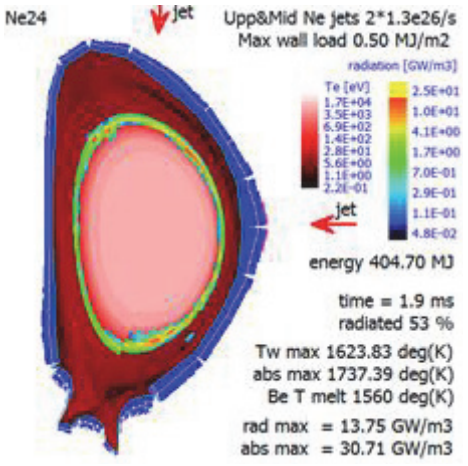

The ITER plasma and wall layout and the neon jet injection locations.

In MGI a heavy puff of noble impurity is injected rapidly into confined plasma to dissipate the plasma heat through the radiation. The TOKES simulations of plasma cooling due to the in-

jected neon are focused upon the following cases: upper-port injector, mid-plane injector and also two injectors used simultaneously and located at the upper-port and the mid-plane of ITER FW. The radiation loads of photonic losses from the plasma onto the wall surface are calculated varying J_m in order to obtain $J_{m,thr}$ for Be FW and different injector configurations under consideration. Each scenario starts at the gas valve opening moment (time t=0). Typical maximal radiation load onto the wall is of 0.5 MJ/m^2.

Two-dimensional TOKES simulations with assumed toroidal symmetry of injected gas showed that the melting threshold $J_{m,thr}$ of the mid-plane injector case is substantially smaller (by the factor ≈0.6) and the cooling time is also smaller (by ≈20%) in comparison with the upper port injector case. Small $J_{m,thr}$ is an advantage of the mid-plane location. The mid-and-upper injector configuration has the maximal melting threshold among the considered three cases (factor ≈2 compared to the upper port injector); however, it is an advantage that the cooling time τ_c is smaller (by ~20-30%) than τ_c in both other cases.

Also 3D TOKES simulations have been carried out for the first time. Compared to 2D simulations, the peaking of radiation load in vicinity of toroidally discrete upper-port injector resulted in significantly smaller value of Be FW melting threshold: $J_{m,thr}$ decreased by 4 times. At the 3D melting threshold the wall surface is substantially heated only in vicinity of injector. 3D cooling time τ_c ~9 ms for $J_m = J_{m,thr} = 0.65\times10^{26}$/s exceeds the 2D τ_c for ~1.5 times.

Addressing future applications of the mentioned KIT codes for the fusion reactor DEMO, an analytical transport model for the edge tokamak plasma and divertor transport is developed. The model is suitable for implementation into the integrated code TOKES and, in perspective, for applying to new system integrated code under development in KIT for predictive modeling of DEMO. The tokamak edge plasma configurations is assumed to be rather thin over inmost and outmost areas adjacent to the separatrix, the scrape-off layer (SOL) magnetic field lines terminate at either divertor plates or limiters. The region beyond the separatrix serves as a shield protecting the wall from the hot plasma and bulk plasma from the penetration of impurities. The model provides plasma density, temperature and velocity distribution along and across the magnetic field lines, and the dependence of temperature and density at the separatrix on the plasma conditions at the plate and the efficiency of the divertor operation. The model calculations give the power and particle loads on the divertor and FW.

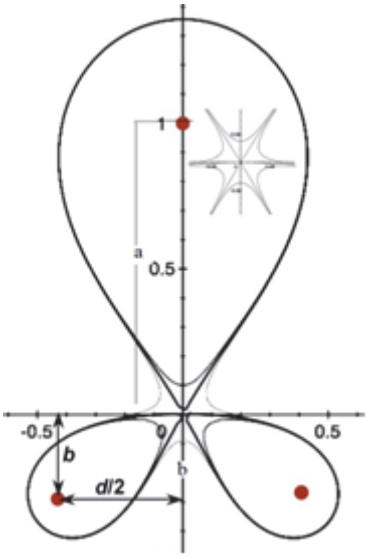

The SF configuration created by three straight wires (D. Ryutov, 2007, Phys. Plasmas 14, 064502).

Besides, analytic theoretical analyses and estimations for novel conceptual design of DEMO have been undertaken aiming eventual implementations of important processes and geometrical features in TOKES and the system code. They concern the snowflake (SF) x-point configuration being focused on an enhanced effect of poloidal magnetic flux expansion and the plasma stability of impurity radiation in SF configuration (MARFE) and the coupling of MARFE with the ballooning type MHD instability in the edge plasma. In particular, it is concluded that the SF configuration is more vulnerable to the onset of MARFE compared to the standard x-point configuration, because the MARFE can be triggered at lower impurity concentration.

Physics: Heating and Current Drive - ECRH

Electron Cyclotron Heating & Current Drive (ECRH & CD) will play a major role in forthcoming long pulse or continuous fusion devices like ITER, W7-X and DEMO. Due to their excellent coupling to the plasma and well localized power deposition in the plasma, microwaves in the range of 100 – 200 GHz are already being applied in existing fusion machines to heat and stabilize the plasma and to drive a toroidal current, which would be of particular importance for a continuous tokamak. Since many years, KIT has been developing high power gyrotrons as microwave sources, diamond window units, and launchers to inject the power into the fusion plasma.

Together with several European institutions and with a commercial partner, KIT developed the gyrotrons for the W7-X ECRH heating system. Continuous progress is being reported on the tests of the series gyrotrons and the assembling of the complete ECRH system at IPP Greifswald.

The development of a European 170 GHz gyrotron for ITER has been pursued within the European Gyrotron Consortium (EGYC), acting as a single scientific partner for F4E. The goal of this development is the supply of sources for 170 GHz ECH & CD to ITER, providing 6 MW CW power.

KIT is actively promoting the development of gyrotrons for application in a DEMO reactor and is investigating several basic phenomena of high power gyrotrons.

In the European ECHUL-CA consortium, KIT coordinates the ITER ECRH Upper Launcher development including ultra-low loss diamond torus windows. The main purpose of these launchers is plasma stabilization; an additional equatorial launcher will provide central plasma heating.

For DEMO, next after ITER on the fusion step ladder towards power generation, new concepts of ECRH heating like frequency tunable systems are under development, including ECRH RF sources, launcher components and broadband windows.

Microwave Heating for Wendelstein 7-X

The ECRH system for W7-X (10 MW, 140 GHz, CW) will be provided under the responsibility of KIT together with national and European partners. Most of the components of the transmission system, HV-systems and in-vessel-systems have been installed at IPP Greifswald, and have been already used for testing new concepts and components for ECRH. Progress has been made w.r.t. performance improvements of the series gyrotrons.

Due to delays and technical issues during manufacturing of the series tubes the final acceptance tests of series gyrotrons was not achieved. However, at the end of 2013 the series gyrotron SN2i has been delivered to KIT, tests starting in early 2014.

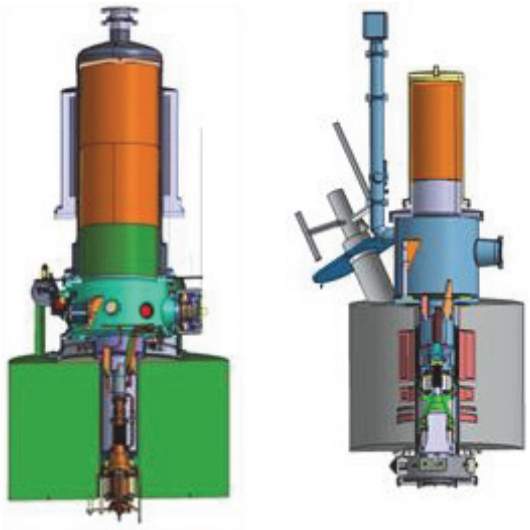

Three-dimensional cut-views of CW (left) and SP (right) prototype.

The manufacturing and installation of the components of the basic transmission system has been completed, except for the beam-matching optics units and the “towers” containing the mirrors in front of W7-X.

Development of the European 170 GHz Gyrotron for ITER

The development of the European 170 GHz 1 MW gyrotron for ITER is pursued within the European Gyrotron Consortium (EGYC, consisting of CRPP, Switzerland; KIT, Germany; HELLAS, Greece; CNR; Italy). EGYC acts as the scientific partner for Fusion for Energy (F4E).

The scientific design of the $TE_{32,9}$ mode gyrotron has been completed in 2013. The basis of the design of the components such as magnetron injection gun, beam tunnel, quasi-optical mode converter and mirror system and the single-stage depressed collector is very similar to the successful 140 GHz, 1 MW design. In particular the technological design of the tube, performed by THALES (France), is based on the experience with the 140 GHz gyrotron. As a risk mitigation action to the first industrial prototype, F4E decided to order a short pulse gyrotron (~ 10 ms) at KIT. This gyrotron will offer several advantages including the verification of the basic design prior to delivery of the industrial prototype. First tests will start in the second half of 2014.

Other Developments on Gyrotrons

The development of a 2 MW 170 GHz short-pulse coaxial-cavity gyrotron prototype is in progress at KIT. Coaxial-cavity gyrotrons (with inner rod) offer advantages in comparison to conventional-cavity gyrotrons, namely reduced voltage depression and mode competition, resulting in higher output powers and operating frequencies. Gyrotrons for future fusion devices, operating at multi-megawatt power levels and frequencies above 200 GHz, most probably will be of coaxial-cavity type. Stable gyrotron operation up to the nominal operating parameters (UC < 90 kV and Ib < 75 A) has been achieved with an output power of 2.0 MW at an efficiency of 28% (without depressed collector operation). The dependence of the generated RF output power on the accelerating voltage at the beam current of 75 A is shown in the above figure. At the limit of the magnetic field of the superconducting magnet, the coaxial gyrotron has been operated with an accelerating voltage of ~92 kV and an electron beam current of up to 84 A. At these conditions a new world record in the generated RF output power (per single tube), namely 2.3 MW at 30% efficiency, has been achieved.

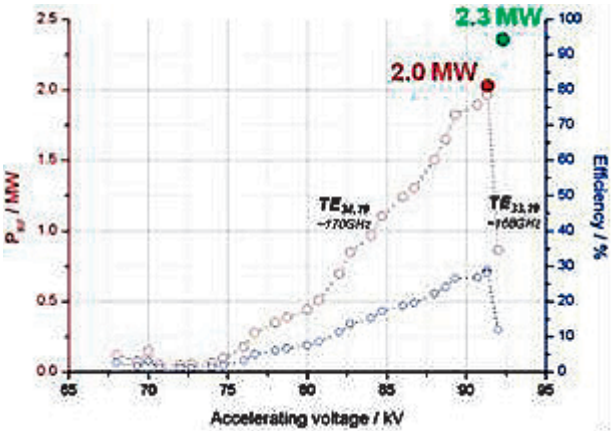

Measured RF output power of the coaxial cavity gyrotron as a function of accelerating voltage (obtained at B_{cav} = 6.87 T and I_b ~ 75 A).

Port and Plant Engineering

In fusion devices the ports of the vacuum chambers serve as an access for heating systems, in-vessel cooling lines, diagnostics and vacuum related services as pumping. The plant design further includes the vacuum chamber and magnets as well as the first wall, and the structures behind which form the interlink between the heat generated by the fusion reaction in the plasma and the power conversion system to the electrical grid. In this section “Port and Plant Engineering” specific developments around the ports and the installed port plugs, especially the ECRH heating antennas are presented together with plant engineering studies covering heat exchange, balance of plant, energy storage and maintenance.

Design, Analysis and Documentation to Produce the ITER EC H&CD Upper Launcher Final Design (F4E-GRT-161-01)

The four ITER ECRH Upper Launchers for plasma heating and instability control are developed in the European ECHUL-CA consortium (KIT, CNR/Italy, EPFL/CRPP-Switzerland, FOM-DIFFER/Netherlands, and IPP Garching/Germany) lead by KIT. Main purpose of these launchers is to couple the millimeter waves generated by gyrotrons (see also the heating & current drive section) into the plasma. The upper launchers provide plasma instability control while an additional equatorial launcher (developed by JAEA/Japan) provides central plasma heating.

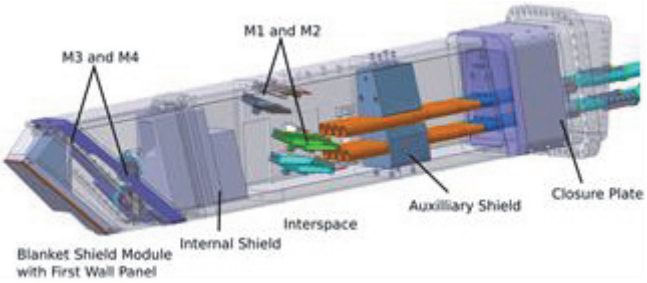

ITER ECRH Upper Launcher.

In the year 2013, ITER announced a revision of all geometrical interfaces of the ECRH antennas (except the first wall panel location, which was recessed in 2012). As a consequence, the ECHUL-CA team substantially focused on work on components either not or only to a low extent affected by this capital change of the port plug definition, e.g. definition of the ex-vessel first confinement system, optimization of launcher internal components and studies on the interaction with different plasma scenarios and beam overlapping. Furthermore, a significant effort was put in assessing the impact of the modified launcher geometry w.r.t. performance and launcher design.

Manufacturing of ITER ECH Upper Port Plug Structural System Prototypes (BMBF Reference No. 03FUS0010)

A double wall main frame prototype was defined and developed at KIT in intense collaboration with the German industry. Main goal of this development was to close the gap between the component design and a suitable and working manufacturing route. The development and prototype manufacturing of a Blanket Shield Module (BSM) is part of this study. Both components are thermally highly loaded and extensive prototyping and testing of these components at the KIT Launcher Handling Facility (LHT) is in progress.

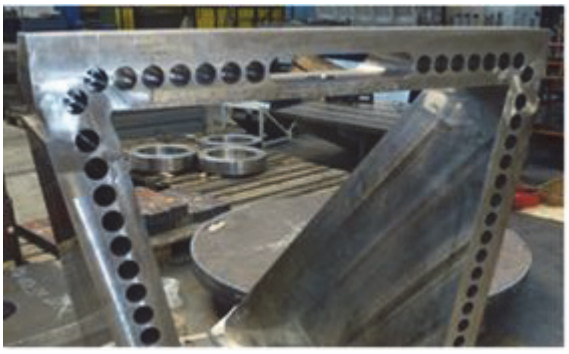

Double wall prototype.

DEMO System Integration Study of a Vertical Port Plug (VPP) for ECRH Launcher (WP13-SYS-03-T05-01)

For plasma stabilization and especially the suppression of neoclassical tearing modes, high requirements have to be met on beam focussing and injected power. As the ideal injection angles are located close to the vertical port, an assessment of vertical antenna integration was performed. A vertical port plug was drafted which occupies a relatively small volume in the vertical port. Candidate optical systems are a frequency tuneable (FT) one and a remote steering (RS) concept. The RS concept has the disadvantage of requiring a higher space occupation outside the port for the RS optics. The FT concept on the other hand seems attractive, but basic R&D is still required on the areas of broadband diamond windows and transmission line components. As plasma scenarios and beam focussing requirements are still not mature enough, it is too early to exclude one of the two solutions. The situation might change, if an additional upper port, similar to the ITER geometry, could be introduced with less space constraints.

Feasibility and Performance of Broadband Windows (WP13-DAS-03-HCD-EC-T07-02)

A key component of the ECRH&CD system is the low loss transmission diamond window as a first tritium and vacuum barrier in each waveguide transmission line as well as at the gyrotron. The development of broadband window concepts for the use of frequency-tuneable gyrotrons is a key activity of KIT in the PPPT program. Consequently, the status of three window concepts has been assessed: Brewster windows, tunable double disk windows and grooved disk windows.

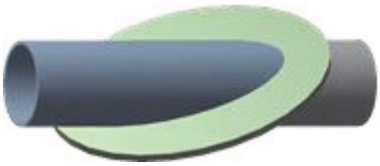

Brewster window.

Remote Maintenance Studies (WP13-DAS-07)

A logistics simulation model was developed for the ex-vessel operations during DEMO maintenance phase as well as a software tool for coupling the 3D radiation map to the radiation hardness assessment of the Remote Handling Equipment (RHE).

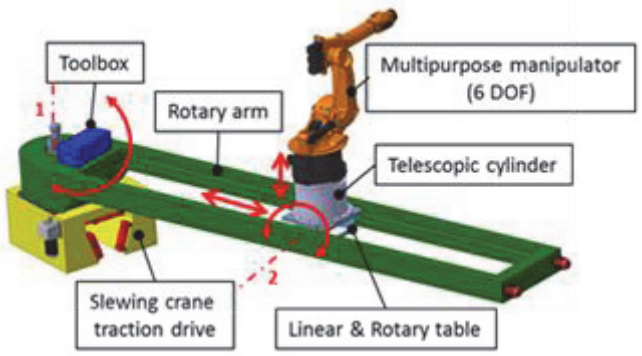

Multi-functional slewing crane.

In the area of ex-vessel remote maintenance systems a multifunctional slewing crane (mfc) was developed for assisting work on port covers and in the nearby area. Several transport options considering the bio shield plug, cask design and the linkage to the active maintenance facilities were elaborated. In addition different transport cooling options were developed taking into account the decay heat inside the casks. Due to contamination tightness and the limited available space inside the casks, investigations about possible storing solutions for the double-seal door were carried out. Furthermore solutions for mechanical pipe connections have been provided and a preliminary mechanical analysis of the connector has been performed. Studies on a generic equatorial port plug on the example of an ECRH antenna complemented the 2013 work.

Design, Modelling and Analysis of Primary Heat Transfer and Balance-of-Plant Options for Integration with a DEMO Fusion Power Plant (WP13-DAS-08-T02-01)

The static analysis indicated that the most efficient configuration is the one with molten salt in the Primary Heat Transfer System (which includes the heat buffer) and with water/steam in the Power Conversion System (PCS). The static cycle was estimated to be 25.6 %. However when tested in the pulsed DEMO operation mode, the overall cycle efficiency drops down to 19.7%, as heat storage equipment has to be included in the Balance of Plant scheme in order to compensate shut-down periods, with the steam turbine at constant speed. In all cases however, use of the divertor and vessel heat sources, coupled to the PCS, in pulsed DEMO operation results in fluctuations of the generated electrical power of ~ (47÷58) MW. A DEMO energy flow map is needed to define demands of the different plant systems and to identify optimization potentials.

Magnets and Affiliated Components

Cryomechanical Tests in the TOSKA-MTL CryoMaK (Cryogenic Material Testing Karlsruhe)

As a result of the increasing worldwide production for ITER, an increasing number of cryogenic components and structural materials are studied for qualification purposes at the CryoMaK Laboratory.

Beside standard tests performed for ITER and JT-60SA, the focus was on fatigue tests of the Toroidal-Field coil Helium-Inlet prototype. After qualification of the European prototype design, samples of the present Japanese design were provided. Full size samples were subjected up to 600,000 cycles of axial load. All samples reached the specified number of cycles exhibiting no failure. With these results the production of the winding and the subsequent heat treatment can carry on.

Japanese He-inlet prototype sample with fixture on both ends for machine installation.

Current Leads for Wendelstein 7-X and JT-60SA

The stellarator W7-X presently under commissioning in Greifswald needed 14 HTS current leads plus 2 prototypes as spares to supply the current to the magnet system. All current leads were fabricated and successfully tested at KIT and delivered to Greifswald. By now the current leads have been integrated by the IPP team into the machine and W7-X is under commissioning.

For the Japanese Tokamak JT-60SA that is co-funded by the EU under the Broader Approach Agreement KIT will deliver 6 HTS current leads for 26 kA and 20 HTS current leads for 20 kA. After agreement of interfaces with the JT-60SA project, KIT has started in 2013 to assemble the first 26 kA HTS current leads. The fabrication of first HTS modules, cold contacts and heat exchangers were performed. The following pressure safety test of insulated heat exchanger in presence of TÜV was successful, which was testified by guests from JAEA and F4E.

Half pieces (left) and completed heat exchangers (right) of 26 kA current leads.

High Temperature Superconductors for Fusion Magnets

In 2013, the upgraded 12 T split coil magnet of the FBI facility was commissioned. The magnetic field homogeneity is 97 % in a cylindrical volume of 92.2 mm in diameter and an axial length of 20 mm in z-direction. Subsequent to the upgrading work a variable temperature insert is under construction to standardize measurements in the FBI facility. The goal is that all cable measurements will have the same boundary conditions and are only limited to the maximum output current of the 10 kA power supply.

View to the split coil magnet of FBI.

A 40 cm long Roebel cable (4 mm width) has been fabricated and embedded in a stainless steel U-frame as a preparation of a 1.2 m long sample to be measured in 2014. It could be shown that due to the clamping the sample could be stabilized but due to the high forces slight degradation is observed.

Modelling of a high current HTS conductor for use in a DEMO TF Coil

In a conceptual design analysis, it is shown that HTS conductor is a potential candidate superconductor for pulsed DEMO. A HTS winding pack principally fits in the winding pack area given by the PROCESS code and can produce the required magnetic field at the plasma axis. The peak magnetic field at the superconductor is 13.27 T. The use of HTS can increase the temperature margin to more than 11.9 K. Compared to the parameter given in the PROCESS code, an increase of the discharge time constant from 17.78 s to 30 s is possible which helps limiting the discharge voltage.

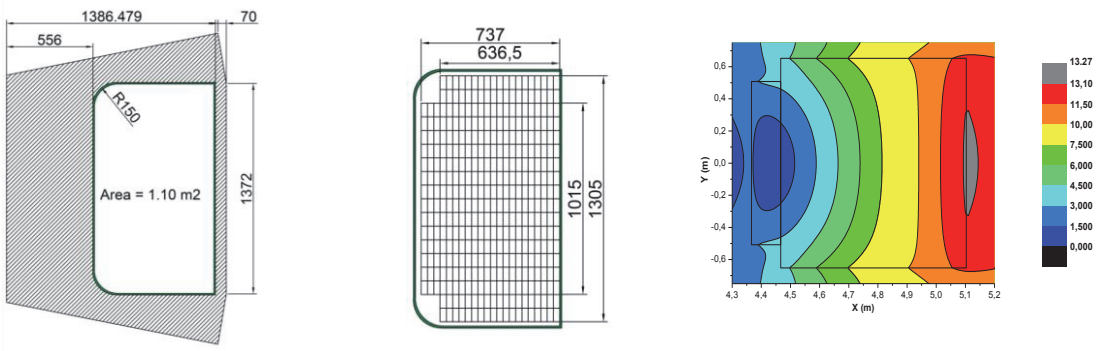

Proposed winding pack cross section with casing (left and center). Magnetic field plotted at winding pack cross section of the mid plane of the inner leg of TFC (right). X is radial dimension and Y is axial dimension.

Breeding Blanket

The design activity for the development of the KIT solid breeder blanket in EFDA/PPPT continued in 2013 with the completion of a new lay-out of the equatorial box (**WP13-DAS-02-T04, -T05, -T07**). The new design is illustrated in the figure; it has dimensions of about 1 m x 2 m in the toroidal-poloidal plane with a thickness of about 1 m.

The main innovation introduced in this design is the cooling of each box using two independent external helium loops able to remove each 50% of the heat generated in the blanket. Despite the more complex manifold plate arrangement, the double cooling system allows reduction of the internal pressure drops and better safety and reliability performances of the concept. In addition the report describes the new concept of connection of the box to the back supporting structure and an attachment system of the whole blanket segment to the Vacuum Vessel compatible with the vertical maintenance system.

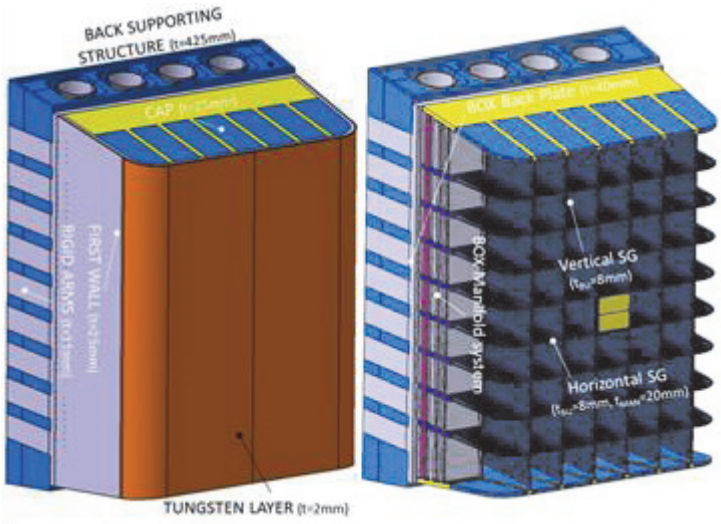

Outboard Equatorial Blanket Box (with and without FW).

In (WP13-DAS-02-T11) several CFD calculations have been performed to assess the cooling performances of helium systems used for FW application. The studies showed that the heat transfer coefficient could be significantly augmented by using structured surfaces, thus allowing much larger heat loads from the plasma. Different geometries of these turbulence enhancers have been investigated and the most promising selected.

In WP13-DAS-02-T13-01 numerical simulations have been performed to investigate MHD flows in model geometries of a liquid metal manifold for dual coolant lead lithium (DCLL) blankets. The geometry considered consists of a manifold feeding an array of three parallel poloidal first-wall ducts. The flow partitioning in poloidal ducts is affected by the length of the internal separating walls, by the 3D MHD pressure drop in the expanding zone and by the velocity distribution after the cross-section enlargement.

Liquid metal flows in helium cooled (HCLL) blankets are expected to be mainly driven by buoyancy forces caused by non-isothermal operating conditions due to neutron volumetric heating and cooling of walls. In **WP13-DAS-02-T04-02** magneto-convective flows in horizontal ducts having electrically and thermally conducting walls have been analyzed numerically for intense magnetic fields.

Loss of Coolant Accident (LOCA) caused by a pipe break of Helium Coolant System (HCS) is considered as one of the most critical accident for the Helium Cooled Pebble Beds Blanket system (HCPB); under certain accident assumptions the blanket segments are cooled only by radiation to the ultimate heat seek that is the Vacuum Vessel. For these conditions in **WP13-DAS-02-T09** several ANSYS analyses have been performed to calculate the maximum temperatures reached in that blanket structures. The thermal results show that the Ex-vessel LOCA accident with PFCs at 500 °C is the most challenging in terms of blanket temperature increase and temperature difference along the blanket and back supporting structure. A maximum temperature of 842 °C was calculated within the breeding zone in proximity of the first wall.

Electromagnetic Analyses of DEMO Blanket Loads (**WP13-SYS-02-T03-01**) have been performed for the Helium Cooled Pebble Bed (HCPB) and Helium Cooled Lithium Lead (HCLL). Plasma disruptions and vertical displacement events (VDEs) in tokamak reactors are design drivers for the in-vessel components' attachments as the induced loads constitute a severe issue for the mechanical structure. The Eddy currents, electromagnetic forces and moments were computed using the commercial ANSYS© code. On figure below, results of the total moment are reported for HCLL and HSPB in two configurations (S) with single and (C) with continuous electrical attachment between modules and manifold.

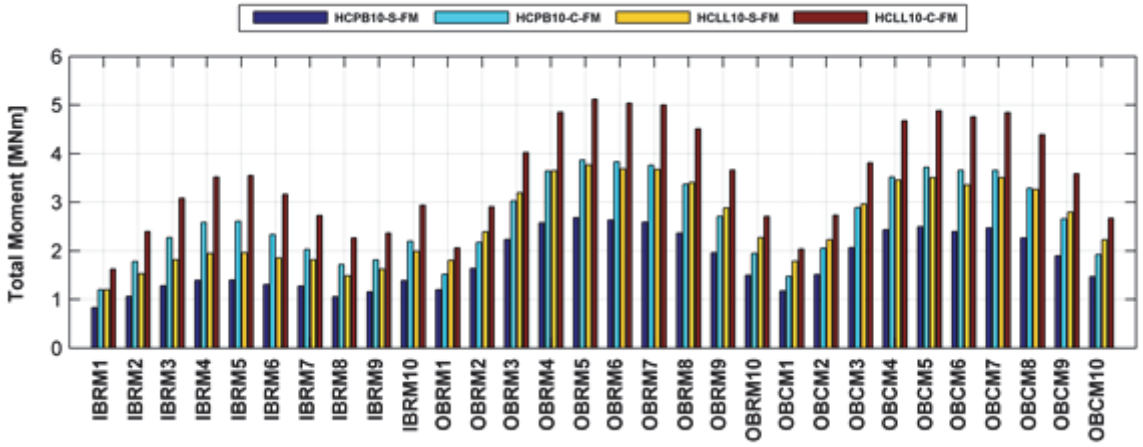

IB and OB modules´ total moment.

The activities within task **WP13-SYS-04-T03-01** aim to estimate DEMO source terms for the HCPB blanket concept, to identify initiating events in DEMO, to identify and describe critical accident sequences to be considered in the safety assessment of DEMO, and to summarize qualitatively the consequences of the event sequences. In addition a confinement strategy and a definition of safety functions are preliminary defined.

In the framework of the procurement contract **F4E-OPE-305-03**, KIT is completing the supply of Preliminary Fabrication & Welding Procedure Specifications for the breeding unit of the HCPB TBM. The construction of a Feasibility Mock-up in EUROFER and its examination with NDE and DE is part of the task. The fabrication strategy proposed by KIT for the realization of the Mockup is based on machining a cooling channel structure into a plane plate by Wire Spark Erosion; after the fabrication of the channels the plate will be bent. In 2013 the reports related to the "fabrication development plan" and to the "intermediate fabrication development and demonstration" have been completed and will be finalized at the beginning on 2014.

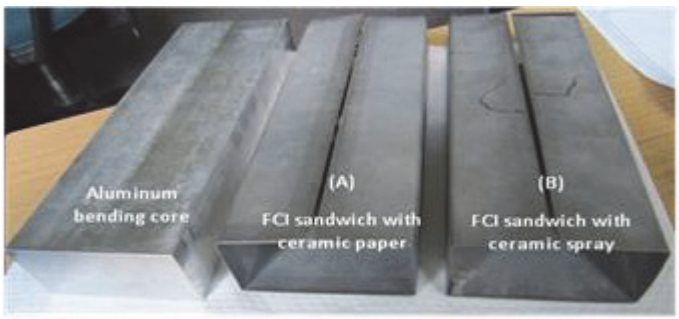

FCI bending experiment using sandwich composite with equally thick steel cover plates of 0.5 mm without groove, using an Al bending core (left). Two variants of the ceramic insert, ceramic paper (A) and ceramic spray (B), were investigated.

A Peculiarity of the dual coolant lithium lead (DCLL) blanket is the use of flow channel insert (FCI) for MHD pressure loss reduction. The feasibility of manufacturing technology for this component is investigated in **WP13-DAS-02-T13-03.** In this manufacturing feasibility study, a prototype in the scale of 1:4 of the original dimension of an equatorial DCLL-SiCf/SiC flow channel insert (~ 345 mm x 220 mm) was chosen. A flow channel insert consists of an outer steel casing as the carrier, an alumina intermediate layer as an electrical insulation, and a - as thin as possible - inner steel plate wall to protect against liquid metal leakage in the ceramic. Two different manufacturing tech-

niques for the production of a bent tube FCI or FCI with nested pipe-in-pipe were adopted as shown in Figure above.

Sensitivity Studies of DEMO Design have been carried out in **WP13-SYS-01-A-T02-01** with the system code PROCESS (CCFE) using a blanket model developed in KIT and implemented in 2013 for these analyses. The results show that the requirements on tritium breeding do not have a deep impact on the radial build since the optimization can be performed by varying the outboard breeding zone thickness and the lithium 6 enrichment. On the contrary, the shielding requirements on the inboard TFC might have a significant impact on the radial build of the reactor, because of the space to be allocated to the inboard shield and thus, of the potential increase of the major radius.

The completion of the EU TBS conceptual design in view of CDR (in 2014) and the preparation of the preliminary design for PDR (end 2015) in ITER require the support of more specialized and detailed engineering activities for the design of the TBM Ancillary Systems and their Integration in ITER. The related contract has been awarded to an ENEA-KIT Joint Team. The first specific task order (**F4E-OMF-331-02-01)** is focused on the design and integration in the ITER buildings of the seven ancillary systems of HCLL and HCPB-TBS. Within this task order KIT has been responsible for the design of Helium Cooling System (HCS) of HCLL/HCPB-TBS as well as the integration of the ancillary systems in the Port Cell. KIT provided also technical support in the design of other ancillary systems, the Cooling Purification System, Tritium Extraction system and Tritium Removal system.

As part of the Broader Approach DEMO activities (BMBF Reference No. 03FUS0012), the long-term stability of solid breeder ceramics was investigated in a long-term annealing (LTA) experiment. Three different compositions of two-phase tritium breeder pebbles, consisting of lithium orthosilicate and lithium metatitanate, produced by a melt-based fabrication (KALOS) at KIT, as well as two batches of lithium excessive lithium metatitanate pebbles, produced either by a sol-gel method or an emulsion method by JAEA were investigated. Before employing the pebbles in a breeder blanket, a significant annealing step is probably necessary as large amounts of water vapor were released from all samples during the first days of annealing, although the samples were carefully dried in advance at 300 °C in a vacuum furnace. The microstructure, porosity (open and closed), and crush loads of the pebbles were investigated as-received and during the annealing process. The properties of the pebble samples change significantly as a function of annealing duration. Most changes happen during the first 4 days of annealing with a subsequent stabilization of most properties at a certain level. In general, the properties of all pebble samples are still acceptable after 128 days of annealing for an application in a breeder blanket.

Hot-extruded Be-Ti rod inside of a steel jacket.

Titanium beryllide $Be_{12}Ti$ is considered to be one of the candidate materials for neutron multiplier of TBM in future fusion power plants. In the frame of Broader Approach activities **(**BMBF Reference No. 03FUS0012**)**, Be-Ti rods have to be produced for their further use for fabrication of titanium beryllide pebbles by melting in inert gas atmosphere. In KIT this goal was achieved by hot extrusion of blended beryllium and titanium powders; a process that is very attractive from the point of view of production of long and high-dense rods. The rod (shown in the figure of 32 mm diameter) was cut into discs for further density measurements and investigations of microstructure. In addition Several Be-Ti rods were obtained by sintering of blended Be and Ti powders at 1000 and 1100°C in vacuum (10^{-5}…10^{-4} mbar). Although this process is not as time-

consuming and expensive as the process of hot extrusion, Be-Ti rods having a density which does not exceed 80% T.D. were fabricated. Nevertheless, test at 4000 rpm using milling machine inside of a glove-box proved that the Be-Ti rod withstands rotation speed which could be used by production of titanium beryllide pebbles.

The aim of the ITER contract **(ITER/CT/13/4300000787)** was to provide the technical basis for Acceptance Criteria and Tests for ITER Test Blanket Systems. For each type of components, the acceptance criteria have been listed, firstly qualitatively according to the best engineering practices, and in a second phase quantitatively expressed and justified with regards to codes, standards, and requirements coming from several, relevant ITER handbooks. In particular, on component level, the clear distinction between actions required on the factory side, and those needed to be repeated on ITER side has been clearly indicated. On the system level, extension of criteria and test were also systematically described.

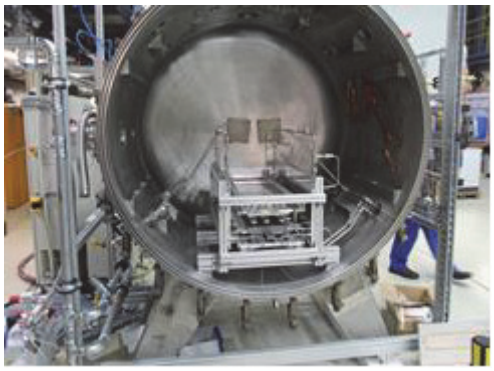

Partly assembled radiation heater test set-up inside vacuum vessel.

Finally, two activities were carried out in the framework of EFDA Goal Oriented Training Programme (GOTP). In the first (**EFDA-WP08-GOT-PSE**) the focus is on training power supply engineers needed for ITER. The specific training offered by KIT includes practical work experience at the HELOKA-HP experimental facility, whose object is to test the HCPB-blanket concept and to gain experience in operating such kind of helium facilities. The main work in 2013 was the management of the planning and construction of an experiment to test the feasibility of using an infrared radiation heater for high heat flux experiments up to 500 kW/m².(see figure right). Several industrial partners, like Kraftanlagen Heidelberg GmbH, SIEMENS AG Karlsruhe and Stapp GmbH were involved in the work. In 2013 the training programme was successfully completed.

The aim of the **"WP12-GOT-BeFirst (FU07-CT-2012-00066)**" is the education and training of early stage researchers in the field of “Plasma Facing Components”. It will be achieved by performing cooperative research and training programs in the area “Beryllium for the ITER First Wall”. The program is practically oriented and is realized through performing a set of practical exercises which include courses providing a theoretical background to the practical experience for extending the range of vision of young researchers. The Kick-off meeting which initiated the "BeFirst" Training Program was held at KIT on the 5th of March, 2013.

Divertor

The major goal of the KIT divertor programme is the investigation, development, and optimization of all fabrication processes required for helium and water cooled divertors (HCDs and WCDs) to provide an engineering basis for DEMO design. Based on present knowledge on neutron-induced embrittlement of tungsten, an operating temperature of at least 800°C is strongly recommended to reduce the risk of embrittlement. But for such elevated temperatures, helium loop solutions by any standard technology are not available today. That is, embrittlement of the structural subcomponents, which are made of tungsten in the well-known modular finger reference concept (HEMJ), may have to be accepted. Thus, design rules for brittle materials have to be developed, verified, and validated for the HEMJ multi-component design, which is a time-consuming long-term issue without guaranty of success.

Therefore, two possible HCD concepts to circumvent this problem are studied at KIT. One uses the HEMJ design but replaces the tungsten by a tantalum alloy for the cooling finger (see figure below). This could allow for a lower application temperature (<800°C) without embrittlement of the structure.

Design and fabrication of square finger mock-ups. (Left) Individual component parts as machined. The main difference to the standard HEMJ concept consists in the use of Ta-10%W for the finger (part 2) and in a square armor tile instead of a hexagonally shaped. (Right) Tile and finger (thimble) are diffusion bonded with a Ti interlayer. The thimble is brazed to a steel transition tube with PdCu filler.

The other HCD divertor concept is similar to the ITER design. It consists of a tungsten laminate pipe, which is cooled by jet impingement. The pipe is embedded in a row of monoblocks. Preliminary conceptual studies were already assessed and demonstration mock-ups are ready to be tested.

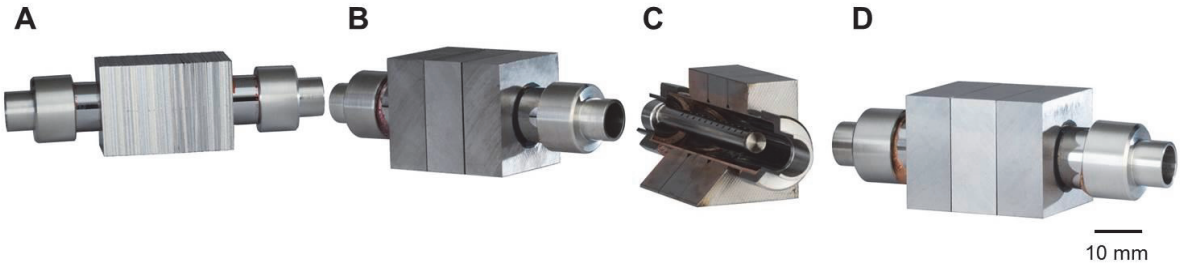

Highly cold rolled W semi-finished products like W-foils are the starting point of the synthesis of a W laminate pipe that appears to be an interesting candidate for structural divertor applications. In this figure, W laminate pipes are joined on both ends to austenitic steel plugs and they are surrounded by monoblocks of W or W alloys. (A) Monoblocks made of W foils. (B), (C), (D) Monoblocks made of W rods. (C) reveals an inside look of a test component for a helium-cooled divertor. Here, the helium jet impingement is realized by a steel cartridge positioned inside the W laminate pipe.

For the development of a WCD the starting point is to reach a heat flux higher than 5 MW/m² by the use of a reinforced CuCrZr heat sink with PIM-generated W monoblocks or tiles. The necessary reduction of thermal stresses due to the differing thermal expansion coefficients (CTE) will be achieved by W laminate, graded Cu-W or W fiber reinforcements. In a worst-case feasibility study, the effectivity of a W-Cu laminate to balance different CTE (stainless steel vs. tungsten) was assessed in cooperation with IPP. Tungsten armor parts (saddle type) were brazed on a stainless-steel (316) tube with a W-Cu laminate interlayer (see figure below).High-heat-flux tests in the GLADIS facility demonstrated that the interlayer could survive more than 100 pulses with a heat flux of 6 MW/m^2. As a conclusion, the performance of the ITER divertor concept could be significantly improved by the use of laminated pipes. Further studies focus on the adaptation to DEMO conditions.

In the KIT WCD concept, an inner layer of austenitic steel acts as corrosion protection for the Cu-W laminate pipe.
(Left) In this “worst-case scenario”, a 1 mm thick stainless steel tube is used to provide a big mismatch in thermal expansion (compared to tungsten). (Middle) High heat flux test in the GLADIS facility at 6 MW/m². (Right) In-situ thermography to record the temperature distribution during the test.

Structural Materials - Steels

Reduced Activation Ferritic/Martensitic steels are reference structural materials for in-vessel components of a fusion power plant because of their better irradiation resistance and improved radiological properties compared to commercial martensitic steels. EUROFER is the European development foreseen as material for structural parts of ITER-TBM and DEMO blanket and divertor. One of the most crucial items for steel applications in a fusion power plant are H/He embrittlement effects, which exceed even the operation window of EUROFER. Therefore, the focus of the 2013 activities of KIT was laid on the final analysis of irradiated EUROFER samples as well as on the further development and fabrication of ferritic oxide dispersion-strengthened (ODS) steels, which have a good chance to meet the power plant requirements.

Production of ferritic ODS alloys at KIT have been successfully demonstrated in the last years. These studies focused mainly on lab scale batches and were dedicated to basic mechanical and microstructural characterization. The optimization was performed under the objective of improving the Charpy impact properties and the examination of the evolution of crystallographic textures during thermo-mechanical treatments like hot rolling or hot extrusion. These studies were successful and led to an optimized ferritic ODS alloy. A further success was the adaption of the current production process for lab-scale batches to meet the requirements for large-scale industrial processes.

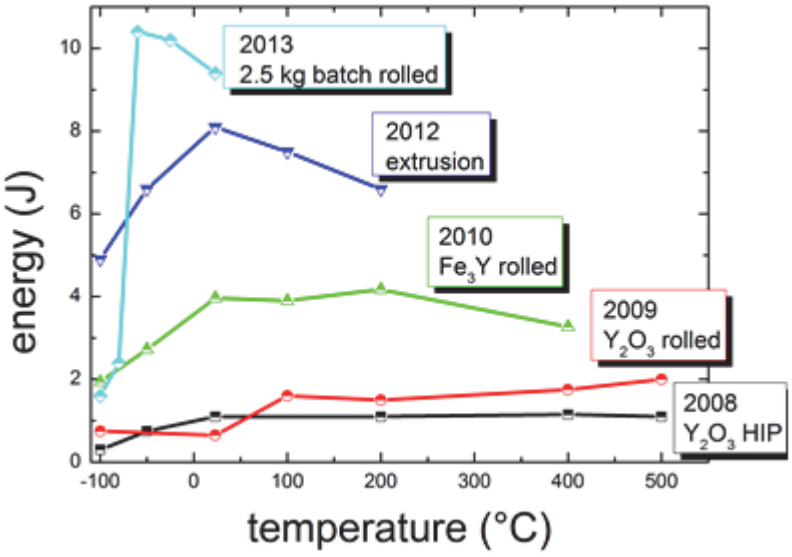

Progress in ODS steels development at KIT, which is demonstrated by increasing toughness levels (energy) and by reduced ductile-to-brittle transition temperatures in Charpy tests.

To assess the influence of helium transmutation on microstructure and swelling of EUROFER during neutron irradiation, several boron-doped EUROFER alloys (boron transmutes into helium and is used to simulate the fusion specific transmutation rates) were irradiated. Extensive TEM studies in hot-cells provided a comprising statics on helium bubble size and distribution, which in turn enabled a calculated prediction of the swelling rate. In literature on past studies with 9%-Cr-steels maximum swelling was reported to be around 420°C. These new results, however, show a tendency that the swelling peak appears already in the range of 350-380°C. In this case, the consequence would be that swelling of EUROFER in a fusion reactor might not be linear with the irradiation dose.

In addition, the microstructure of irradiated EUROFER was examined. After irradiation large $M_{23}C_6$ precipitates consisting of Cr, Fe, W, and C are observed, which in most cases are located at grain boundaries. A VN precipitate can also be seen at a grain boundary, while small spherical precipitates of TaC are distributed within the matrix. In summary, there is no fundamental difference in precipitate development between unirradiated and irradiated condition. An irradiation induced phase formation, in particular Cr rich α', could not be observed.

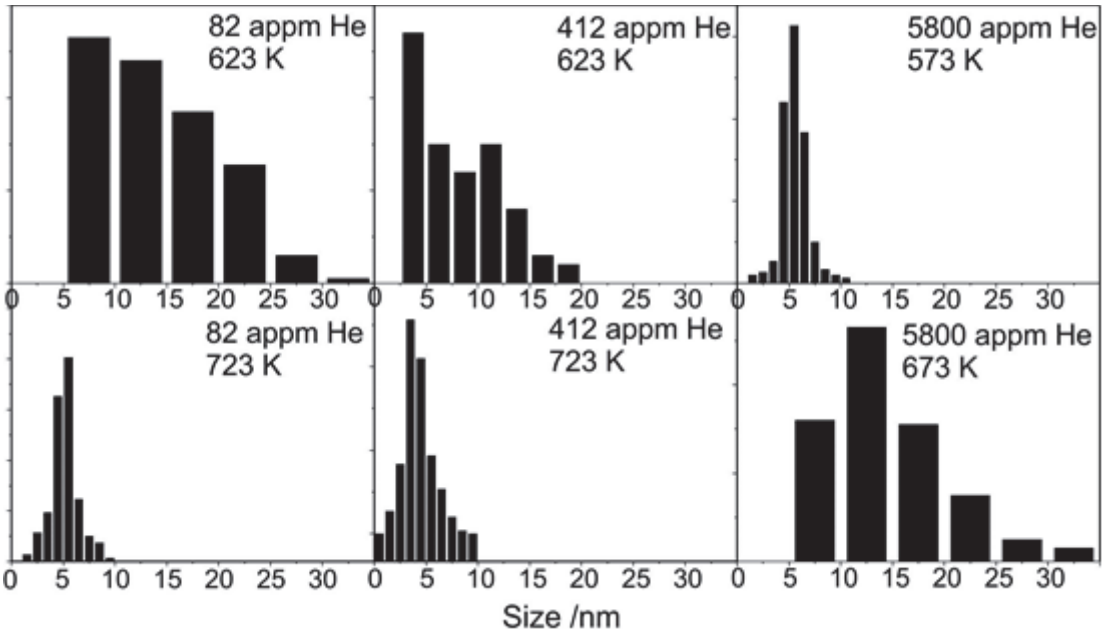

Size distribution histograms of helium bubbles or cavities as observed in numerous TEM studies of irradiated boron-doped EUROFER specimens.

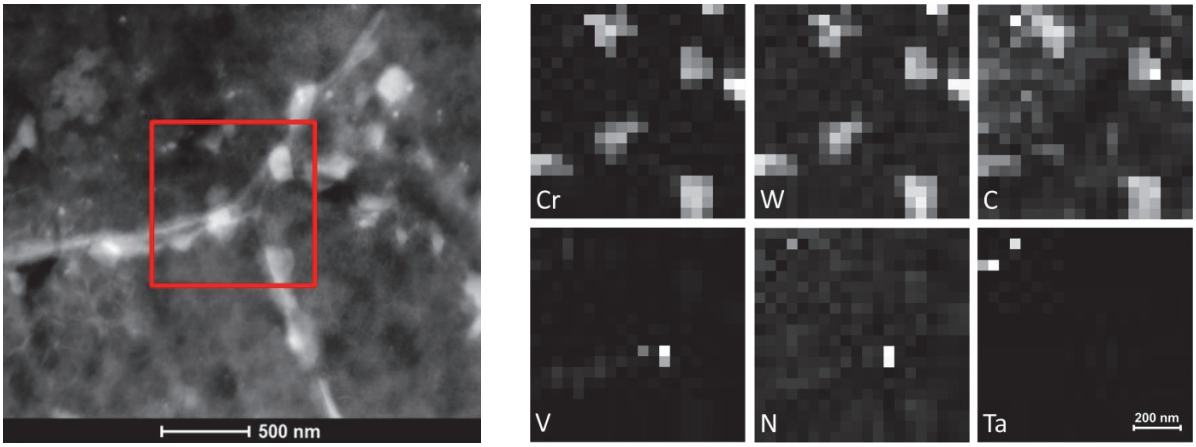

TEM study on EUROFER irradiated to 32 dpa at 330 °C.
The red square in the left image marks a grain boundary area, for which elemental maps (images on the right side) are produced to analyze the chemical composition of the precipitates. In EUROFER $M_{23}C_6$, TaC and VN can be identified.

Structural Materials – Refractory Alloys

The development of a divertor for DEMO or a power plant is very challenging since heat fluxes of up to 10-15 MW/m² have to be removed under high neutron loads. KIT is pursuing two concepts. One is a helium cooled (HCD), the other a water cooled divertor (WCD) where both are based on the use of pipes, which are protected by armour parts from plasma interactions. For armour materials, high temperature strength, good thermal conductivity, low sputter rates, and high crack resistance under extreme thermal operation condition is required, while for the pipe (structural) materials, sufficient fatigue strength and ductility within the operation temperature range is mandatory. Since none of the available standard materials (like for example those, which are foreseen for ITER) can sustain DEMO or power plant requirements, KIT follows several specific development lines: (1) Tungsten armour materials, produced by powder injection moulding, (2) tungsten laminate materials (pipes) for HCDs, (3) tungsten-copper laminates as functional interlayer between CuCrZr pipes and tungsten armour parts, and (4) tungsten reinforced CuCrZr composite materials (pipes) for WCDs. Of

course, these materials development routes require demanding testing, fabrication, and analysis tools, which are also part of the KIT programme.

Armour Materials

Powder Injection Moulding (PIM) is a near net-shape mass fabrication process for parts that require tight tolerances and good surface quality. During the past, at KIT PIM was adapted and optimized for tungsten part production. In the meantime, it also proofed as a perfect tool for rapid tungsten alloy development. In 2013, new tungsten materials (W-La_2O_3, W-Y_2O_3, W-TiC and W-TaC) were produced and assessed. The images in the figure below demonstrate that PIM fabricated particle reinforced tungsten materials show qualities, which are not possible by any other production route. Moreover, fracture mechanics and high-heat-flux tests indicated better ductile-brittle transition temperatures and higher crack resistance. Both properties are required for armour applications.

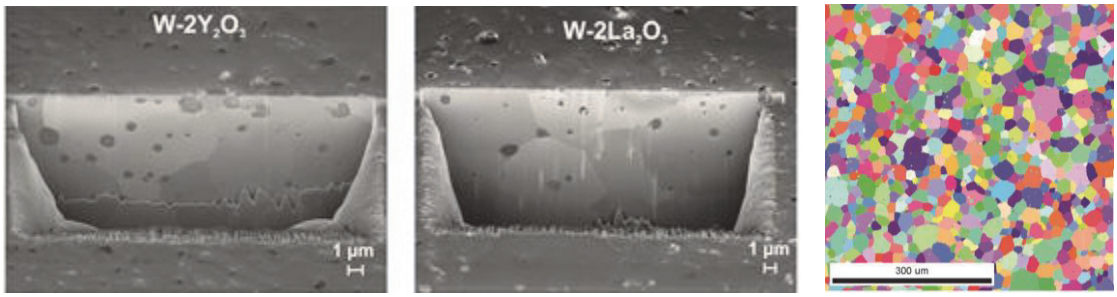

Typical advantages of powder injection moulding. Left & middle: Fine and homogeneous distribution of oxide particles. Right: Poly-crystalline, equally-axed grain structure.

Tungsten Laminates

Tungsten foil with a thickness of 100 µm has a ductile-brittle-transition temperature (DBTT) of -120 °C (strain rate: $3 \cdot 10^{-2}$ 1/s) and a fracture toughness of 70 MPa $m^{1/2}$ at room temperature. These extraordinary properties can be related to the ultra-fine grained (UFG) microstructure of the W foil in its as-received condition. Through the assembly and joining of several of these UFG W foils the extraordinary properties of a foil can be transferred to the bulk. It is obvious, that the applicability strongly depends on the right choice of interlayer (material, thickness, etc.) and joining technology.

In 2013, electroplating of W foils by Cu layers has been developed for possible large-scale production of W-Cu laminates, which could then be used to produce pipes for WCDs or as compliance layer between CuCrZr pipes and armor parts. It was shown that W foils have to be activated by etching to obtain good adherence of deposited Cu and that sulfuric based electrolytes lead to more homogeneous and stable Cu layers. With electroplating the Cu layer thickness can be easily varied by current strength and deposition time.

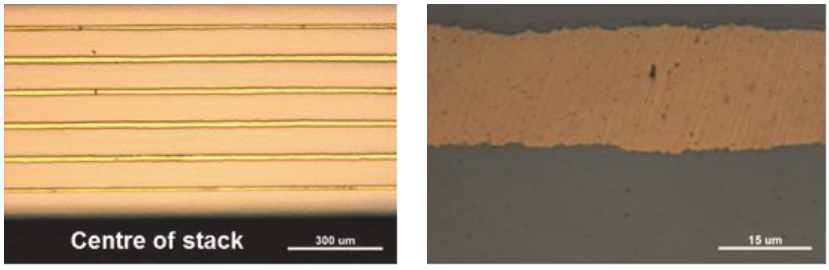

Microstructure of W-Cu laminates fabricated by electrochemically deposited Cu on W foils. Left: Cross-section of the laminate. Right: W-Cu interface.

For high-temperature applications, like for example in HCDs, the interlayer material requires a much higher melting point than copper. Therefore, a study using titanium (Ti, melting tem-

perature 1668 °C) was performed. W-Ti laminates were produced by diffusion bonding at temperatures well below the recrystallization temperature of the W foil. Thermal stability was investigated by ageing the W-Ti interface for 10 h, 100 h, and 1000 h at 1000 °C in vacuum. The assessment of the interface was done by mechanical tests and microstructure analysis. In conclusion, for the production of high-temperature W laminates, titanium cannot be used as thick interlayer (100 µm). However, it is a promising material for the use as bond activation layer in the order of a few microns.

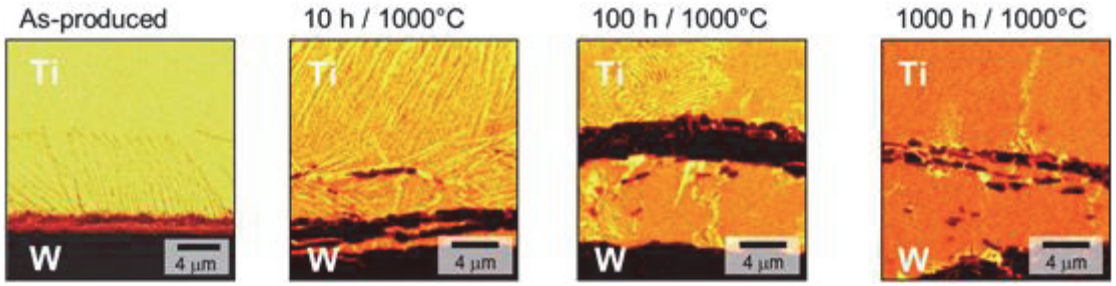

Ageing of W-Ti laminates for 10 h, 100 h and 1000 h at 1000 °C.

Copper Tungsten Composites

Under neutron irradiation, copper transmutes into medium-level radioactive waste. Nevertheless, WCDs based on CuCrZr pipes might be an intermediate solution - restricted to DEMO - towards a power plant. The operating window of CuCrZr in nuclear environments is limited to >180°C (irradiation hardening and embrittlement) and <280°C (irradiation enhanced softening effects). Since all well-known solution and oxide dispersion strengthening procedures would significantly increase activation or decrease thermal conductivity, the most promising solution seems to be the production of copper composite materials.

The KIT R&D activities target on industrial-scale production of composite pipes. This requires massive cylindrical CuCrZr blocks reinforced by particles or fibers. These could be fabricated easiest by sintering (melt-metallurgical processes are considered as back-up solutions). Therefore, in 2013 a sinter study has been completed using W, Ta, and stainless steel (316) fibers, which have been embedded in copper powder. The results after cold pressing and sintering are shown in the figure below. Nearly perfect interfaces have been produced immediately with tungsten. The Cu-Ta and Cu-SS composites improved only after cold working (rolling). However, tungsten-copper composites (particle as well as fiber reinforced) are identified as primary candidates and will be further developed at KIT.

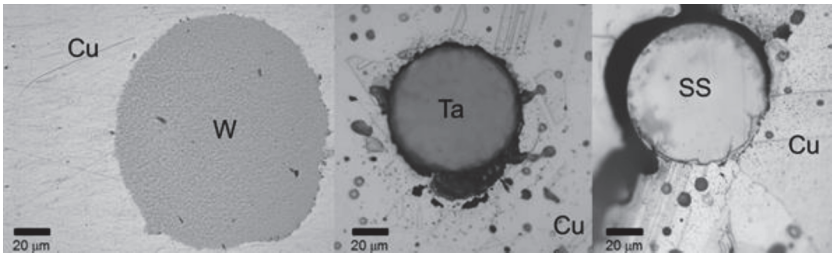

Interfaces of Cu-W, Cu-Ta, and Cu-316-Stainless-Steel (SS) composites produced by sintering.

Characterisation Tools

In materials development, characterisation is indispensable. In the case of tungsten armour and composite materials, however, this requires testing conditions, which exceed the usual range. Very high testing temperatures (sometimes up to 1600 °C), vacuum environment, miniaturized specimens, and even hot-cell applications are needed. Therefore, at KIT the equipment for the basic mechanical characterization (tensile, Charpy, fracture mechanics) was consequently adapted. Future developments include low-cycle and thermo-mechanical fatigue tests.

To progress on the database on irradiated tungsten materials, a high-temperature nano-indentation system will be used in a Hot Cell environment for that purpose. This technique requires only small testing volumes and offers the possibility to reuse already tested specimens. The figure below (left image) shows first results on the fracture behavior of tungsten. In addition, fracture mechanical characterization of tungsten alloys has been fully optimized and is now ready to use for all new refractory materials. As an example, the determination of the design space for a brittle fracture safe operation of tungsten components is shown in the figure (right image). It is a compilation of the fracture toughness data on polycrystalline tungsten including the results on disk and rod shaped materials. This fracture safe design space analysis is a first-of-its-kind which will be further validated.

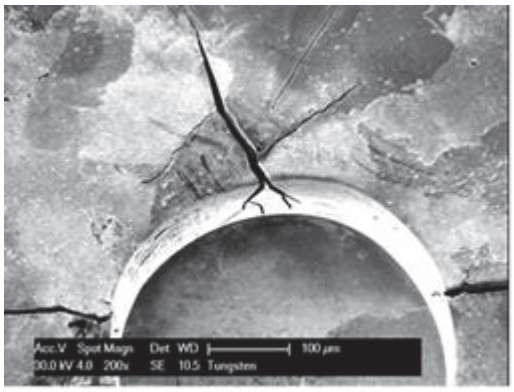

Left: Macro indentation on poly-crystalline tungsten by flat punch indentation for prediction of crack generation and propagation.

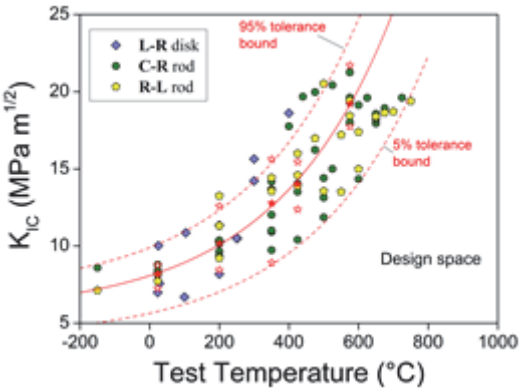

Right: Fracture toughness of polycrystalline tungsten vs. test temperature.

Neutronics and Nuclear Data

Neutronic Analyses of ITER Diagnostic Components

The crucial issue in the development of optimal shield design solutions for the ITER Diagnostic Port Plugs is the shutdown dose radiation level in the interspace behind the ports which needs to be minimized. The analyses performed over the reporting period 2013 focused on design solutions for the Diagnostic Equatorial and Upper Port Plugs (EPP and UPP) as major ITER Diagnostics Components. KIT's R2Smesh approach is applied for the assessment of the shut-down dose rate (SDDR) distribution. The dominant contribution to the SDDR inside the EPP port interspaces is due to the radiation streaming through the gaps surrounding the plugs. The proposed EPP shielding design solutions therefore include means to mitigate the gap streaming by using several types of labyrinths and horizontal rails inside the gaps. As a major result of the performed analyses an optimized double labyrinth was recommended and accepted by ITER for the current EPP design. A series of neutronics analyses was performed in support of the design development of the Generic Upper Port Plug (GUPP). Three diagnostics systems (Vacuum Ultra-Violet spectrometer - VUV, Vertical Neutron Camera - VNC, and Neutron Activation System - NAS) were integrated into the UPP with the optimal shielding performance.

Nuclear Analysis at Neutral Beam Injector (NBI) Ports

A suitable MCNP analysis model was developed on the basis of engineering CAD models provided by ITER for the heating and diagnostic NBI ports and the available 80° MCNP torus sector model ("A-lite"). The detailed engineering models were simplified on the CATIA platform, adapted to the needs for neutronics calculations, and then converted into the MCNP geometry representation using KIT's conversion software McCad. An entire vertical segment of the 80° A-lite model was replaced with the NBI port segment shown in the figure below (right side).

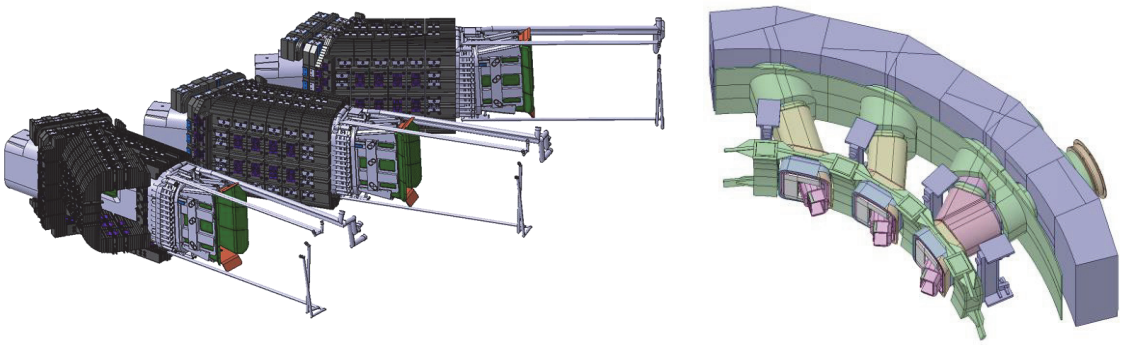

Engineering CAD models of the ITER NBI ports (left) and simplified CAD model for the nuclear analysis after integration into the vacuum vessel shell and the bio-shield (right).

A series of MCNP calculations was performed to provide distributions of the neutron flux density, the nuclear heating, the displacement damage and the gas production damage in the vacuum vessel, and the total dose to the TFC magnets and insulator. Distributions of the shutdown dose rates were calculated at 10^6s after irradiation with KIT's R2Smesh approach on a high resolution mesh spanning the entire region of the NBI port see figure below.

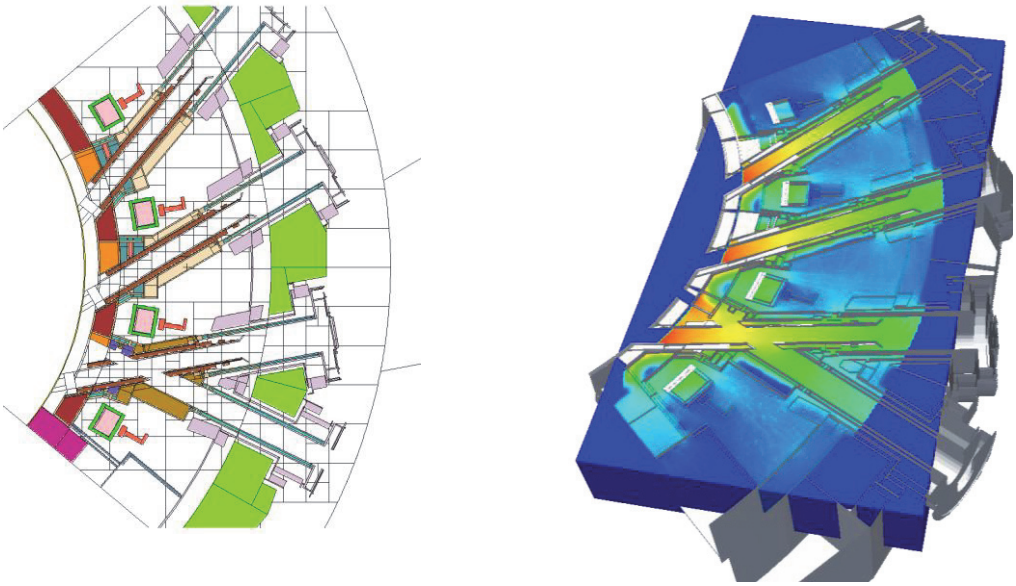

2D cut of the MCNP torus sector model showing the NBI port section (left) and the Shut-down Dose Rate distribution calculated at 10^6 s after irradiation (right).

Nuclear Analyses for Contact Dose on Transfer Cask and Dose outside Tokamak Building/Hot Cell Tunnel

This work, aimed at providing a reliable assessment of the biological dose rate fields around an automated ITER transfer cask loaded with activated in-vessel components. KIT's R2Smesh approach was utilized to determine the activation of the considered components in ITER and provide the photon radiation dose fields around the transfer cask loaded with the activated components. Various in-vessel components were assumed to be irradiated in ITER and then removed and integrated into a transfer cask model. The associated decay gamma source distributions were likewise transferred to the cask and overlaid to the geometry models of the activated components.

The figure below show maps of the biological dose rates as calculated across the transfer cask (interior and exterior) and at the surface of the transfer cask. The maximum dose level at the surface of the transfer cask amount to 56.6, 83.6, 18.5, and 54.2 Sv/h for the activated blanket first wall module (BFWM), the generic diagnostic equipment port plug (GEPP), divertor and TBM, respectively. The activated GEPP module will thus produce the maximal

biological radiation dose load around the transfer cask. The resulting maximal value on the surface of the cask is significantly lower than the limit of 430 Sv/h that was assumed by the French safety authorities.

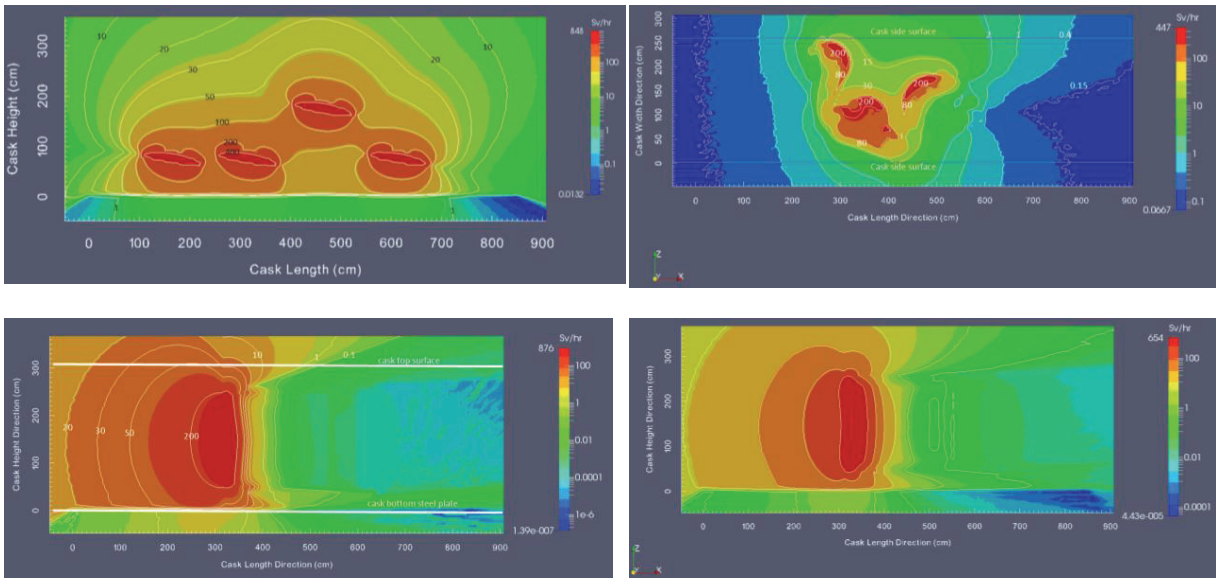

2D maps of the biological dose rates around the transfer cask loaded with four BFWM (top left), the divertor cassette (top right), the GEPP (bottom left), and the TBM assembly.

Nuclear Data Improvements and Development of Tools – Nuclear Data Evaluation (F4E-FPA-GRT-168.01)

The development of nuclear data and tools is performed within the Framework Partnership Agreement F4E-FPA-168 on “Development of Nuclear Data Files“ between F4E and the “Consortium on Nuclear Data Development and Analysis“.

KIT is leading the Consortium and is co-ordinator of the FPA-168 and the associated grants. It has contributed to the first specific grant, FPA-168.01, with the following activities. (i) evaluation of general purpose nuclear data files for n + ^{63,65}Cu including covariance data up to 200 MeV, (ii) benchmark analyses of Pb neutron cross-section data to assess their quality for design analyses of the HCLL breeder blanket concept, (iii) upgrading of the MCSEN sensitivity software to comply with the current standard of the MCNP-5 Monte Carlo code, and (iv) evaluation of advanced damage energy and displacement cross-sections for the major EUROFER constituents based on an atomistic modelling approach.

The figure below shows, as an example, the displacement cross-section prepared on the basis of Molecular Dynamics (MD) and Binary Collision Approximation (BCA) simulation methods for the EUROFER steel. This approach shows a better agreement with available experimental data of point-defect production in materials as compare to the standard Norgett-Robinson-Torrens (NRT) approximation used e. g. by the NJOY code.

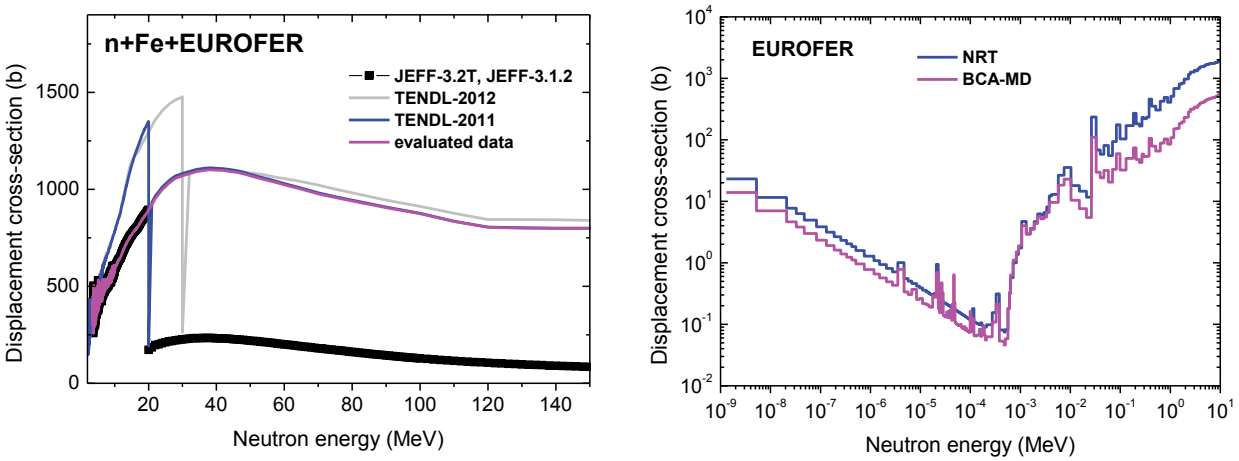

Displacement damage cross-section evaluated for the EUROFER steel (right) and the main constituent Fe based on the BCA/MD approach (left).

Cu Experiment and TBM Nuclear Instrumentation (F4E-FPA-395-01)

The first Specific Grant of the Framework Partnership Agreement FPA-395 concerns the development of the experimental data base required for the validation of the nuclear data libraries and measurement techniques of nuclear responses relevant to ITER, the ITER Test Blanket Systems, IFMIF and DEMO. KIT is involved in the design of the Cu assembly, the pre-analysis and the post-analysis of the experiment and it will perform neutron and gamma ray spectra measurements. A pre-analysis was performed for the optimization of the experimental set-up including sensitivity/uncertainty assessments of the responses to be measured in the experiment.

KIT is further involved in the development and qualification of nuclear instrumentation for the TBM in ITER. In a first Interim Report a mapping of the environmental conditions for the TBM was presented. The second Interim Report focussed on functional requirements and specifications of candidate sensors, and the evaluation of current detector designs. The candidate detectors considered are diamond and SiC detectors, self-powered neutron detectors and a neutron activation system.

System Level Analysis - Neutronics (WP13-SYS-02)

The objectives of the 2013 neutronics tasks within the EFDA PPPT Work Programme have been (i) to develop a suitable DEMO MCNP model, (ii) to conduct critical neutronic design assessments e. g. of the tritium breeding performance, and (iii) to develop and improve neutronic analysis tools and their integration in the design and analysis process of tokamak components. KIT co-ordinated the activities and conducted tasks on the “Development of a generic DEMO MCNP model”, the “Tritium Breeding Ratio (TBR) assessment of the HCPB DEMO”, the “Activation and rate map calculation of the HCPB DEMO”, the “Development of European Tool for the CAD import in MC code” and contributed to the “Development of a single European tool for coupled radiation transport and activation calculations”.

MCNP models were developed for the HCPB, HCLL, and WCLL blanket concepts consistent with the updated DEMO tokamak design by KIT, ENEA and CIEMAT, respectively. The TBR results for the currently assumed conceptual designs are very similar and show the need to improve the breeding blanket design and configuration, e.g. by decreasing the number of blanket modules (i. e. larger module size) and minimizing the amount of steel structure in the breeding modules. The neutron shielding calculations corresponding to each blanket concept showed that the currently assumed radial build is sufficient to shield the TF coils provided that an efficient shielding material like WC can be used in the radiation shield. Otherwise the assumed radial dimensions need to be increased.

International Fusion Materials Irradiation Facility (IFMIF)

In the Engineering Validation and Engineering Design Activities (EVEDA) for the International Fusion Material Irradiation Facility IFMIF, which is an element of the Broader Approach activities launched jointly by several European countries and Japan, the German contribution (executed by KIT) includes engineering tasks for the IFMIF Test cell and the IFMIF irradiation experiments. In accordance to the planning for EVEDA, the engineering design tasks were completed in the timeframe up to 12/2013, while the validation tasks will be continued in 2014.

System overview

The IFMIF facility is dedicated to fusion-relevant irradiation of structural and functional materials, with the objective to create an experimentally validated material properties database for design and licensing of future fusion power plants. The facility is composed of the deuteron accelerator, the lithium target and the test facilities. The target- and test cell (TTC, part of the test facilities), contains the lithium target and the test modules. It has the primary function to shield the environment against the intense radiation generated by the target, and to safely contain all hazardous materials. Inside the TTC, the target and test modules are arranged, as shown in the figure above. The irradiation modules are dedicated to specialized irradiation experiments, such as the irradiation of structural materials up to 50dpa in the High Flux Test Module (HFTM) or the irradiation of breeder and neutron multiplier materials in the Tritium Release Test Module TRTM).

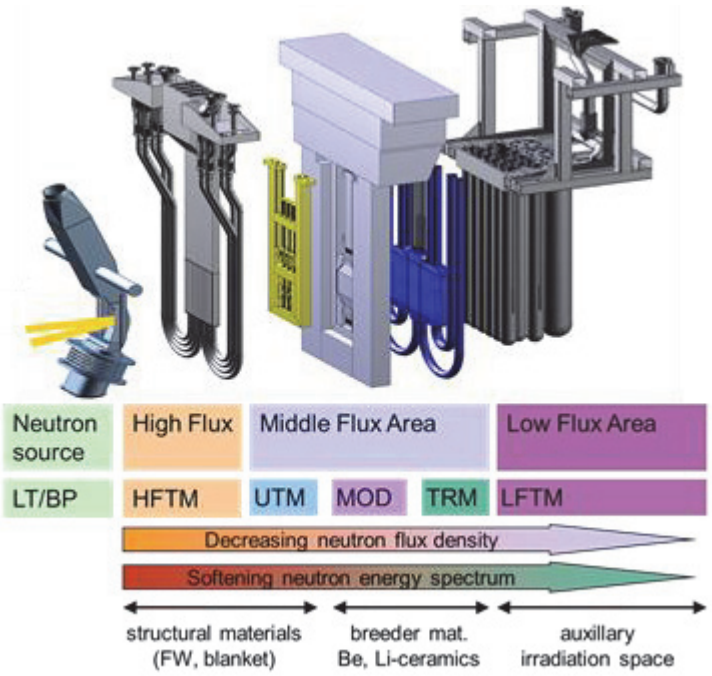

Overview on the irradiation experiments inside the IFMIF Target- and Test Cell (TTC).

Engineering Design and Validation of the HFTM and TRTM test modules

The designs of the HFTM and TRTM were consolidated. Based on the latest CAD models and operation conditions, finalizing neutronic and thermal hydraulic (CFD) analyses were performed, and the derived design was documented in the TF01 and TF04 DDD-III design reports. The written DDD-III reports define in detail the system functions, interfaces, requirements and design features. The design is characterized in terms of

- Component description including technical drawings, assembly (in hot cells) and quality control procedures,
- Operation scenarios including control procedures and interfaces to the ancillary systems, as well as requirements on nuclear waste evacuation,
- Design analyses, describing nuclear thermal and mechanical results. Nuclear responses include DPA and gas (He, H, T) production, activation and decay heat. Thermal analyses prove that the required irradiation temperature distributions can be reached.

The validation activities progressed with the test of single rigs in a helium loop, production, QA and delivery of three specimen-filled capsules for irradiation in the BR2 reactor, the handling of small scale specimens in a hot-cell simulator, and progress in manufacturing of the HFTM prototype.

Mounting of SSTT specimens into the assembly tray of an IFMIF capsule
using a vacuum gripper operated by a standard manipulator in a hot cell simulator.

Engineering Design of the Target- and Test cell and other cells

The design of the test cell, adjacent handling cells and the ancillary systems was documented in the ED04 DDD-III document.

The written DDD-III report defines in detail the system functions, interfaces, requirements and design features. The design is characterized in terms of:

- Radiation protection analyses, dimensioning of shielding walls according to the calculated radiation loads,
- Logistic flow of components during maintenance schemes, based on the plant requirements and optimizations using Event driven Process Chains. According physical layout was chosen and implemented in the global facility CAD model ,
- Detail solutions for critical components, such as penetrations to the radiation protection areas, remote handled signal, and energy and media connections, sealing, and cooling of nuclear heated components,
- Integration of requirements by client systems (i.e., test modules) in the definition of ancillary systems (helium or water cooling circuits, control units) and handling cells, basic dimensioning of the equipment and layout in the global facility CAD model.

Conclusions

The Engineering Design Activities for the IFMIF systems under responsibility of KIT have been successfully finished by preparation, review and approval of the according system design documents. The Validation activities for the High Flux Test Module, aiming at production and test of a prototype are ongoing, while results with single rigs already proved the fitness of the design.

Fuel Cycle – Vacuum Pumping

Since more than two decades now, KIT is developing vacuum pumping systems for fusion reactors. In recent years, the focus has been switched from ITER to DEMO, and new aspects, especially in the integration of plasma physics aspects in the modelling and optimisation of the divertor pumping system, have been included.

In view of ITER, the concept of cryogenic pumping based on cryosorption at activated charcoal has been successfully demonstrated at KIT in the past and has become the common technology used for all primary vacuum pumping systems at ITER. Europe has accepted the obligation to supply all primary cryopumps to ITER. These cryopumps are of two principle designs, i.e. cylindrical pumps for the ITER torus chamber and cryostat and very large rectangular pumps for the vacuum vessels of the ITER neutral beam injectors (NBI). To minimise the risks for ITER, both pump types will be tested on the 1:1 prototype scale. Manufacture of the prototype torus cryopump started in 2013 and will be completed presumably in mid-2015. A major task of pump manufacturing, namely, **coating of the ITER cryopanels that** are the main components of every cryopump, has started this year for the torus cryopump prototype.

Similar to the torus cryopumps, the NBI cryopumps are also planned to be tested on the original scale. This test will be performed in the specially constructed MITICA NBI test bed in Padova / Italy. The pump design was delivered in the past year. In this year, engineers and physicists worked on the **thermomechanical analysis of the NBI components** in the beam path. Work concentrated on the residual ion dump (RID). This component removes the charged particles remaining in the beam downstream of the main neutraliser by electromagnetic deflection to baffle plates. Detailed design studies covered the cooling system of the plates and the support structure of the RID under seismic loading. In addition, a feasible detailed design of a cooling channel was developed and studied. Development work relating to MITICA will be continued in 2014.

Under EFDA and its Power Plant Physics and Technology programme, we are charged to develop the vacuum systems for DEMO. Contrary to the cryogenic vacuum pumps of ITER, the new concept proposed for DEMO is operated continuously without a cryogen. An integrated system for the separation of the divertor exhaust gas directly recycles most of the unburnt fuel, as a result of which the tritium inventories and processing times can be reduced considerably. This is especially important to ensure a sufficiently high availability of the DEMO plant to the electricity grid. This so-called DIR concept (Direct Internal Recycling) consists of three pumping stages. For separation, metal foils are used. They are permeable for atomic hydrogen only and, hence, provide for a certain compression. For high-vacuum pumping, a diffusion pump is used. To make it tritium-compatible, it will be operated with liquid metal (mercury). A liquid ring pump that is also operated with mercury is used as a mechanical pump for compression to ambient pressure.

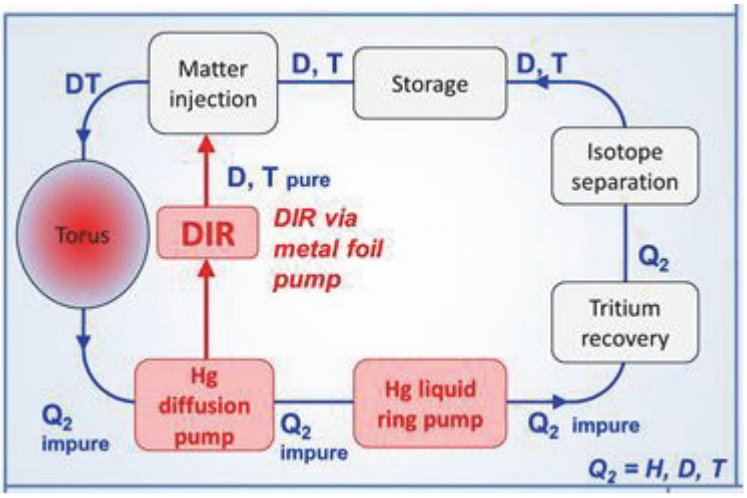

The new DEMO fuel cycle concept (KALPUREX Process).

Meanwhile, this concept has been established as **DEMO fuel cycle reference concept**. In 2013, a complete process, the KALPUREX process (Karlsruhe Liquid Metal Based Pumping

Process for Reactor Exhaust Gases), was developed to realise this concept in practice; the patent was filed in September. The mercury diffusion pump was proved to be suitable for DEMO in 2012 already. This year, proof-of-principle tests to demonstrate the functioning of the mercury-driven liquid ring pump and a metal foil were the clear technical highlights and were demonstrated successfully. Hence, use of cryopumps for DEMO will be considered only, if problems occurring during the further development of KALPUREX cannot be solved otherwise.

Further development of the new pumps will be one of the main KIT tasks in the next five-year plan of the European Fusion Programme within the EURO*fusion* Consortium. Here, KIT provides the project leader in the **EURO*fusion* work package Tritium-Fuelling-Vacuum** that will integrate the three systems most closely and develop a conceptual design of the complete inner fuel cycle for DEMO.

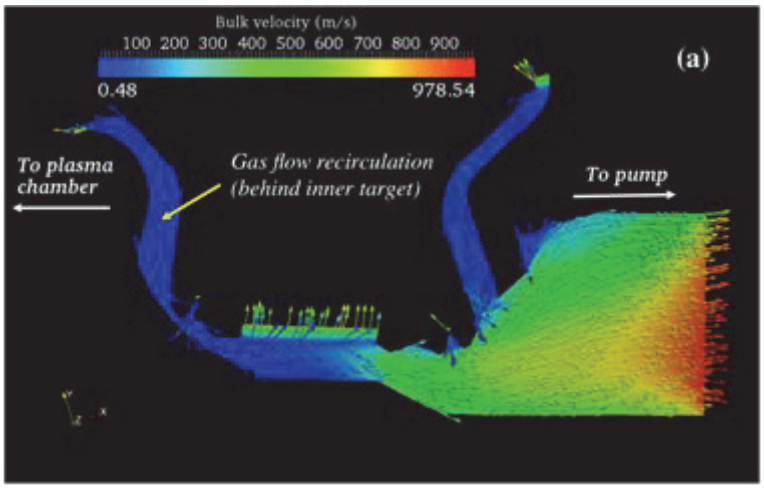

Typical calculation result of the subdivertor flow domain (ITER case).

The area of numerical simulation of vacuum flows in a wide range of gas rarefaction (i.e. from the viscous regime over the transition range to free molecular flow) was advanced significantly. In 2013, activities focused on the description of **neutral particle flow in the sub-divertor region**. In the divertor, high temperature gradients exist, as a result of which the plasma on the inner side is reconverted into neutral gas at the bottom. The divertor is one of the most important components, as it ensures stability of the selected plasma mode and reliably removes the helium produced by the fusion reaction. The divertor is a structure open to all sides (also towards the plasma). This gives rise to the problem that the pumping speed of the connected vacuum pumps competes with the black hole pumping speed of the plasma. The resulting neutral particle density in the divertor is a very sensitive parameter that might also be used for plasma control, if flow processes would be understood better. Development of an own code is a first step in this direction. In 2013, KIT succeeded in including the complex divertor geometry (2D) into a flow code (DSMC) and considering the plasma contour such that the distribution of macroscopic properties (density, velocity, pressure) in the sub-divertor can be predicted in a physically consistent manner.

In the **vacuum instrumentation activity**, the new OMA facility was used to measure outgassing rates of stainless steel subjected to various surface treatment methods. The main result obtained was that defined heating (100 h, 400°C) is sufficient to reduce the outgassing rate by one order of magnitude. It was found to be of no importance whether heating took place under vacuum or under air. The newly commercialised mass spectrometer (ART-MS) was analysed for its capacity to resolve the fusion relevant gases of D_2 and He that are located very closely to each other in the spectrum. It was found that the new instrument is not suited for this purpose. This work was done under the VACU-TEC Goal-oriented Training Programme, co-ordinated by KIT.

Fuel Cycle – Tritium Processing

The work performed by TLK on tritium processing for the fuel cycle covered a large variety of activities (experimental campaigns and design studies) tackling major tritium issues for ITER and DEMO.

For the **inner fuel cycle of ITER**, the **Water Detritiation System (WDS)** combined with the isotope separation system (ISS) is a European procurement package for which TLK is strongly involved especially for carrying out experiments in dedicated pilot plants. The TRENTA3 facility comprises mainly i) the Electrolyser unit, ii) the Liquid Phase Catalytic Exchange Column (LPCE) and iii) the preparation unit that allows studying the **Combined Electrolysis and Catalytic Exchange (CECE)** process selected for the ITER WDS. Several experimental campaigns have been conducted in order to evaluate the deuterium impact on the separation performances of the 8 m LPCE column. The tritium activity and the deuterium concentrations have been measured at various locations (highlighted in red on the figure below) allowing the isotopic profile to be measured along the column. The sampling and analytical measurement procedures have been especially improved for this experimental campaign. The TRIMO++ software has been used to analyse the data and extract key parameters such as mass transfer coefficients that are necessary for designing the future ITER systems. These experiments showed that the decontamination factor along the LPCE columns is significantly influenced by the amount of deuterium in the feeding gas and by the ratio gas to liquid along the column. WDS detritiation performances along the LPCE column are dramatically reduced when high deuterium concentration is being processed.

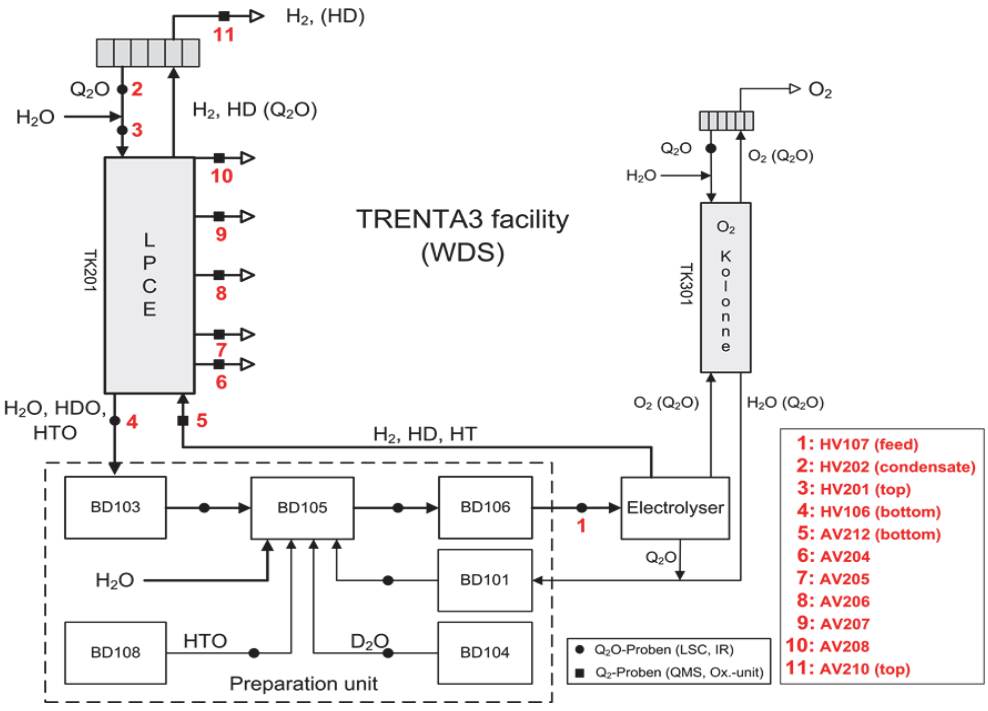

The schematic configuration of the TRENTA3 facility (in red are the several measuring locations).

For the **inner fuel cycle of ITER**, the **Highly Tritiated Water (HTW)** handling and processing issue has been tackled with experimental work carried out on the **Capture and Exchange (C&E)** method. After the selection of the most promising material candidate through screening tests, two kinds of experiments have been carried out in parallel to validate the C&E technique under relevant conditions. Small scale experiments (20 g bed) with relevant tritium levels (DTO up to 300 kCi/kg) have been successfully performed in the CAPER facility that has been upgraded integrating into the already existing system new components, especially (1) a micro-channel catalytic reactor (μ-CCR) producing the necessary HTW, (2) a

small Pt-zeolite bed. After having loaded the Pt-MSB with HTW, it was detritiated in-situ using fresh D_2 liberating the tritium from the water via isotope exchange reactions; the released tritium was monitored on-line and in real-time with two different ionisation chambers. Finally the detritiated water was de-loaded and collected for measuring the residual tritium with calorimetry. The experiments have highlighted that the C&E process is simple, robust and efficient for reaching moderately high decontamination factors. Increasing and controlling the temperature during isotope exchange showed to be the most effective way for enhancing the detritiation performances, as showed along the full scale inactive experiments performed in the ZICKE II facility on a 20 kg Pt-zeolite bed.

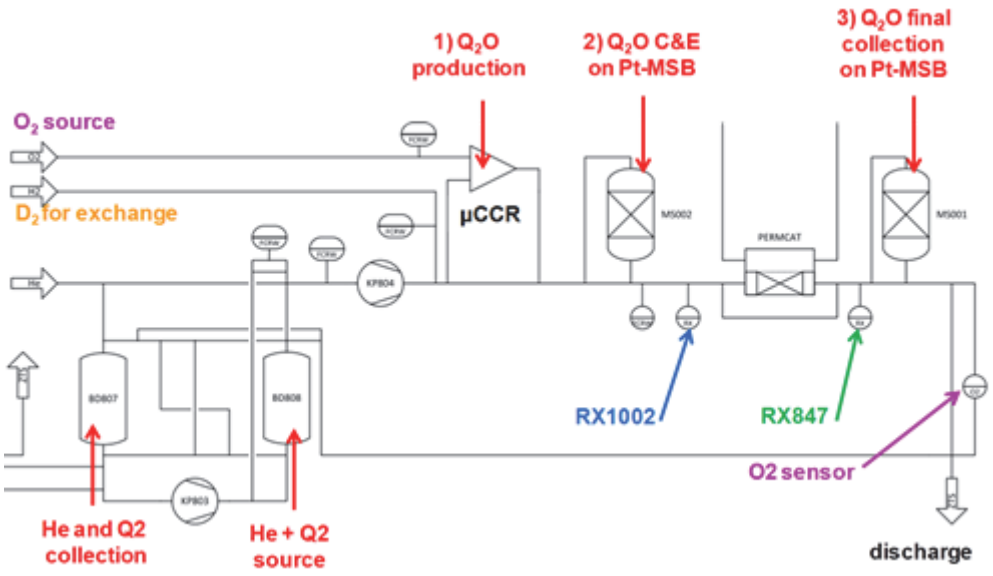

New arrangement inside the CAPER facility for testing the C&E technique at small scale with tritium.

For the **outer fuel cycle of ITER**, the TLK contributed to elaborate the strategy for the acceptance criteria and related test to be systematically applied by ITER for the 6 **Test Blanket Modules (TBM)** and associated ancillary systems (TBS). Even if only low amounts of tritium shall be produced and handled, the study confirmed that high quality standards required from the ITER tritium classification shall apply especially for ensuring clean surfaces and very high leak tightness all along the different circuits. In parallel, several contracts launched by F4E and awarded to the TBM - Consortium of Associates are coordinated by TLK. Under this frame, experimental R&D is being performed in several facilities of KIT and other European partners to support the conceptual and preliminary design the two EU-TBSs.

Concerning the **outer fuel cycle of DEMO,** TLK has coordinated (and contributed to) the **tritium extraction and permeation study** along the design assessment of the EFDA-PPPT project. The main objective of this work was to consolidate the different strategies for optimising the tritium management in the breeding blanket and mitigating the permeation issue. The numerical code for analysing the tritium transport from the production (breeding blanket) up to the environment has been upgraded implementing a new unified permeation model enabling to cover the full range of operational conditions. In addition, a roadmap for developing and qualifying tritium permeation barriers has been elaborated. Also advanced, simple and attractive techniques for tritium extraction from both solid and liquid breeding blanket concepts have been assessed as alternative to the baseline ITER-TBS approaches. All this work has served as basis to define and organise the future R&D work to be carried along the Eurofusion project.

Fusion Programme Management Staff

Head of the Research Unit	Dr. K. Hesch	ext. 25460 e-mail: klaus.hesch@kit.edu
Programme Assistant:	Ms. DP. A. Wagner	ext. 26461 e-mail: aleksandra.wagner@kit.edu
Secretary:	Ms. M. Spies	ext. 25461 e-mail: michelle.spies@kit.edu
Deputy Head; Program Budget, Administration, Reports, EU-Affairs	BW. M. Henn	ext. 25547 e-mail: michael.henn@kit.edu
	Ms. I. Pleli	ext. 28292 e-mail: ingrid.pleli@kit.edu
Blanket and Divertor Development, HELOKA, IFMIF, Materials Development, Fusion Materials Laboratory, CAD-Office, Public Relations	Dr. D. Radloff	ext. 28750 e-mail: dirk.radloff@kit.edu
Fuel Cycle, Superconducting Magnets, Plasma Heating Technology, Safety Studies, Neutronics, Summer School Fusion Technology	Ms. Dr. M. Ionescu-Bujor	ext. 28325 e-mail: mihaela.ionescu-bujor@kit.edu
Power Plant Integration, Gyrotron Development, Port and Plant Engineering	Dr. K. Hesch	ext. 25460 e-mail: klaus.hesch@kit.edu
Quality Management	Dr. J. Gafert	ext. 22923 e-mail: juergen.gafert@kit.edu
	Ms. Dr. M. Oron-Carl	ext. 25468 e-mail: matti.oron-carl@kit.edu
	Ms. DI. Ch. Schweier	ext. 28325 e-mail: christine.schweier@kit.edu

Address: **Karlsruhe Institute of Technology**
Nuclear Fusion Programme Management

Post Office Box 3640, D - 76021 Karlsruhe / Germany

Telephone No: **0721-608-Extensions .....**

Telefax No: **0721-608-25467**

world wide web: **http://www.fusion.kit.edu/**

Contents

Page

Page

Page

Page

Plasma Wall Interaction

Melting Damage and Erosion Analysis of the ITER Tungsten Divertor (ITER/CT/12/4300000720)

In the frame of this ITER contract, MEMOS simulations on the consequences of mitigated major disruptions (MD), mitigated vertical displacement events (VDE) and major disruptions expected in ITER have been performed for several scenarios of impact conditions specified by IO. With the 2D version of the code, damages to the castellated armour in the tungsten tile of ITER divertor dome under runaway electron impact are calculated. 3D simulations for the W-tile of ITER divertor baffle (Fig. 1) are carried out for the downward VDE impact. In addition W droplet splashing in the magnetic field **B** at the edges of divertor baffle monoblock is estimated based on melt layer instabilities under the **J**x**B** force, with the current density **J** determined by eddy currents in the plasma face component (PFC).

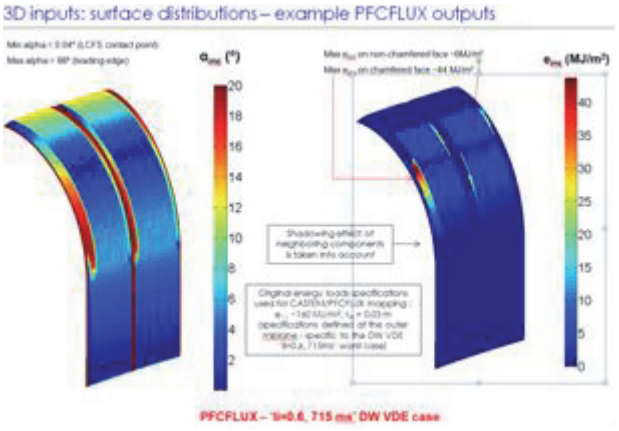

Fig. 1: Baffle geometry for 3D MEMOS simulations.

In the simulated ~20 scenarios in question the heat loads Q are expected to be so high that they cause severe surface melting of PFC. Simulations of MD and mitigated VDE are performed for as single as multiple events of different durations τ, they include melt layer motion and the vapour shield in front of the target.

To give examples, the simulations demonstrated that in case of mitigated MDs with Q = 45 MJ/m^2 surface temperature T_w remains below melting threshold for all given τ from 3 to 10 ms. With Q = 70 MJ/m^2 the temperature exceeds the melting threshold for τ < 9 ms, maximum depth of melt pool h_m is about 70 μm. Tangential friction pressure p_t of the impacting plasma causes a motion of melted material with the velocity along the surface about 0.1-0.5 m/s. The melt motion produces mountains at PFC edges up to h_+ ~ 25 μm height (per event) and craters depth h_- ~ 10 μm. For relatively low number of events (n < ~30) the surface damage magnitude $h_+ - h_-$ linearly increases with n. At n > 30 the profile of surface roughness becomes complex and the magnitude cannot exceed few mm. Estimated critical velocity of melt splashing on the PFC edges due to the Rayleigh-Taylor instability is above 1 m/s thus p_t is low enough to neglect the melt layer instability. Same nearly melt velocity is necessary for bridging of castellated PFC. The influence of halo current on the melt motion for given magnitudes of **J** is low e.g. the melt velocity increases for ~0.15 m/s and the changes of h_+ and h_- don't exceed 3 μm per event.

For all scenarios of mitigated MDs and mitigated VDE the evaporation erosion is low (below 0.1 μm) and the shielding does not form. Only in case of major disruptions (Q > 300 MJ/m^2) significant evaporation occurs and the shielding layer in front of the irradiated surface appears. For such cases h_m can be about 0.1-0.2 mm. The main erosion mechanism is surface evaporation of few μm of removed material per event, up to 6 μm at baffle edges. After 10 events the total baffle edge erosion increases up to 70 μm.

To compare advantage of chamfered baffle against cliff edge baffle simulation of damage of cliff edge baffle under DW VDE was performed for geometry and heat load parameters given by IO. Simulations demonstrated significant erosion of the cliff edge exceeding 300 μm per event. In case of the chamfered baffle the maximum erosion concentrated in the baffle edges and is about 8 - 14 μm per event.

Staff:

B.N. Bazylev

Acknowledgement

This work was supported by ITER Organization under the service contract No. IT-ER/IO/12/4300000687. The views and opinions expressed herein reflect only the author's views. The ITER Organization is not liable for any use that may be made of the information contained therein.

Simulation of ITER First Wall Energy Loading during Mitigated Disruptions and Runaway Electrons (F4E-GRT-315 (PMS-PE))

Introduction

This Fusion for Energy grant for numerical prediction of melt free margin of neon massive gas injection (MGI) mitigated disruptions and runaway (RE) impact damage to the first wall (FW) is now finished. The below described results are obtained in 2013 with 2D version of the integrated tokamak code TOKES and with the melt motion code MEMOS. These TOKES simulations of plasma cooling due to the injected neon focussed upon the mid-plane injector and two equal simultaneously acting injectors located at the upper-port and the mid-plane of ITER FW (see Fig.1). The radiation loads of photonic losses from the plasma onto the wall surface are calculated. The last MEMOS simulations concern diverse cases of RE impacts and also possible melting of stainless steel (St-St) inserts into FW under the radiation loads produced by TOKES. To calculate RE energy deposition in FW bulk the Monte-Carlo code ENDEP was applied.

TOKES simulations

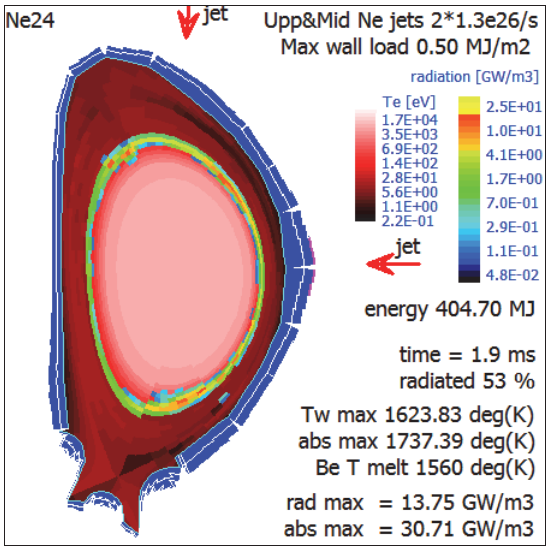

Fig. 1: The poloidal plane distribution of radiation losses (rainbow colour scale, the radiating wave is mainly green), electron temperature Te (red tints from both sides of the wave) and wall surface load (in blue) are shown for the case Jm = 2□1.3□1026/s at t=1.9 ms. At this moment halve of thermal energy (~2□102 MJ) is transformed into the radiation. In front of mid-plane injector the melting is indicated (in pink).

Varying the gas inflow magnitude J_m, we calculated with TOKES six scenarios of neon MGI: three cases for the mid-plane injector and three cases with two injectors, for the regimes with the maximum wall temperature $T_{w,max}$ about the beryllium melting point temperature $T_{melt,Be}$. In other words, the MGI regimes near the melting threshold $J_{m,thr}$ on J_m are calculated. Each scenario starts at the gas valve opening moment (time t=0). Typical maximal radiation load onto the wall is of 0.5 MJ/m^2 (Fig. 1).

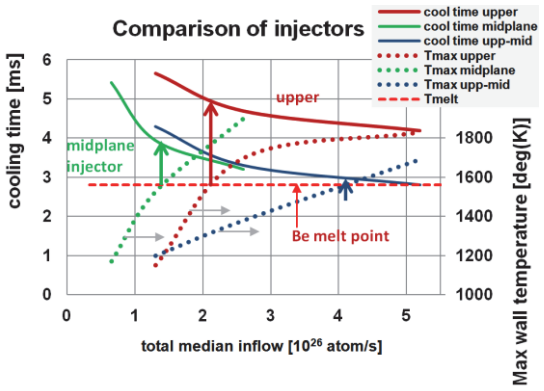

Fig. 2: The comparison of three injector configurations: upper port injector, mid-plane injector, and two injectors ('upper-mid'). The melting threshold is indicated e.g. with green vertical arrow for the mid-plane injector case.

By adding the earlier investigated case of single upper port injector, three injector configurations are compared (Fig. 2). The linear extrapolations of calculated cooling time $\tau_c(J_m)$ give the τ_c at the melting threshold on J_m. (At the melting threshold the curve of calculated maximum wall surface temperature T_w is crossing the constant of Be melting point.) The conclusion is drawn that the melting threshold $J_{m,thr}$ of the mid-plane injector case is substantially smaller (by the factor ≈0.6) and the cooling time is also smaller (by ≈20%) in comparison with the upper port injector case. Small $J_{m,thr}$ is an advantage of the mid-plane location. The mid-and-upper injector configuration has the maximal melting threshold among the considered three cases (factor ≈2 compared to the upper port injector); however, it is an advantage that the cooling time τ_c is smaller (by ~20-30%) than τ_c in both other cases.

MEMOS and ENDEP simulations

The MEMOS calculations for the stainless steel (St-St) plasma facing components (PFC) demonstrated that for equal loads the temperature of St-St PFC is higher than that of Be (which was calculated earlier). Above the melting thresholds on the median inflow J_m, the melt pool in St-St is deeper than that of Be by approximately a factor of 2. The melted St-St phase exists much longer than the melted Be phase. However, the thresholds for St-St and Be are approximately equal to each other: $J_{m,thr} \approx 2.2 \times 10^{26}$/s.

In the runaway impact damage simulations, geometric peculiarities of ITER upper FW modules in "single roof" and "double roof" configurations provided by IO and F4E (Fig. 3 and Fig. 4) are implemented into MEMOS and ENDEP. Predictive simulations for beryllium and tungsten PFC are performed in order to estimate after effects of "fast" and "slow" RE impacts (see below) as well as the melting threshold $J_{RE,Be}$ on RE beam current density J_{RE}.

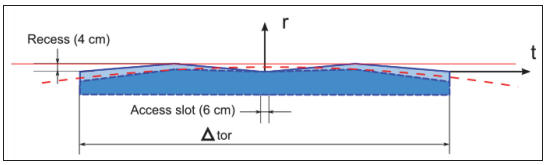

Fig. 3: The cross-section through the double roof ITER first wall panel is shown. The axis t means toroidal direction.

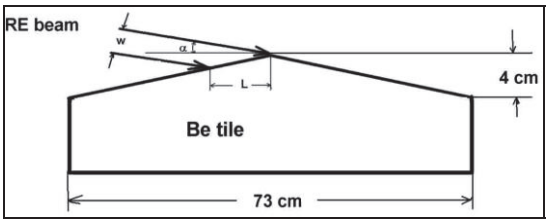

Fig. 4: The implemented single roof Be tile of the first wall module is shown.

The fast impact corresponds to load duration τ_{RE} ~0.1 ms. The Be threshold $J_{RE,Be}$ is in the range 0.25 - 0.48 MA/m^2, which depends on RE spectrum. A small increase of J_{RE} by 10-20% above $J_{RE,Be}$ results in surface melting up to 0.7 mm with the re-solidification time longer than 30 ms. For tungsten PFC, $J_{RE,W}$ of the fast impact is of ~0.2 MA/m^2. The small increase of J_{RE} above $J_{RE,W}$ results in the W melting up to 0.3 mm with the re-solidification time smaller than 4 ms.

For all slow impact cases (IO specified them in terms of τ_{RE} from 10 ms to 0.2 s) the heat loads Q (specified from 0.34 to 46 MW/m^2) are obtained to significantly exceed the melting threshold and, therefore, severe melting damage to the Be and W FW tiles is expected (Fig. 5), especially for the long pulse durations. The melt pool depth can achieve several mm and the molten phase lasts up to several second, so that even the Cu-Cr-Zr tubes of the cooling system beneath the PFC can be damaged (the tubes locate at the deepness 1.3 cm from the PFC surface). The large re-solidification time permits us to anticipate some pronounced splashing of melt layer.

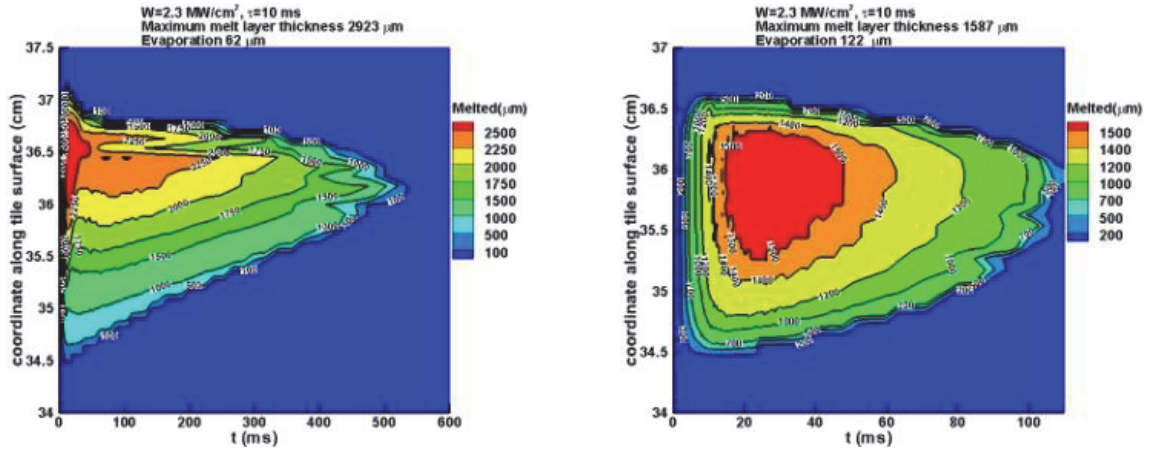

Fig. 5: Be (left) and W(right) melt pool depth against time t for Q = 2.3 MW/cm2 is shown.

Staff:

B. Bazylev
I. Landman

[1] I. Landman et al., “Radiation loads on the ITER first wall during massive gas injection”, Fusion Engineering and design 88 (2013) 1682-1685

[2] I.S. Landman et al. ‘Modelling of first wall photonic heat loads during disruption mitigation by massive gas injection on ITER’, Paper presented at the ICFRM-16 conference, Beijing, Oct 2013.

[3] B. Bazylev et al, Modeling of the impact of runaway electrons on the ITER first wall. submitted to the conference. Poster presented at the ICFRM-16 conference, Beijing, Oct 2013.

Acknowledgement

This work was supported by Fusion for Energy under the grant contract No. F4E-GRT-315 (PMS-PE). The views and opinions expressed herein reflect only the author’s views. Fusion for Energy is not liable for any use that may be made of the information contained therein.

Analysis and Computer Simulation of Disruption Mitigation Schemes of Massive Gas Injection (MGI) (WP13-IPH-A07-P1-01)

Introduction

The major disruptions expected in future tokamaks would produce plasma losses of high power which locally damage the plasma facing components (PFC). In ITER, to reduce the plasma impact a massive gas injection (MGI) of a noble gas into the confined plasma at the disruption onset is going to be applied. During MGI the confined thermal energy transforms into photonic radiation which loads the surface more evenly than the plasma fluxes do. The disruption development lasts for a small fraction of second so that the cooling time τ_c of MGI thermal quench (TQ) less than ~10 ms is required. The plasma cooling occurs due to ionization of injected atoms ('G-atoms') and following formation of radiating cooling wave which moves into plasma bulk.

The KIT activity for this task concerns further development and the applications of the numerical integrated tokamak code TOKES for 2D- and 3D-simulation of MGI radiation impact up to surface melting of beryllium first wall (FW) (Fig.1). A number of validation and scoping calculation scenarios have been performed for JET and ITER aiming at optimization of the amount of injected gas within the τ_c and melt free limits.

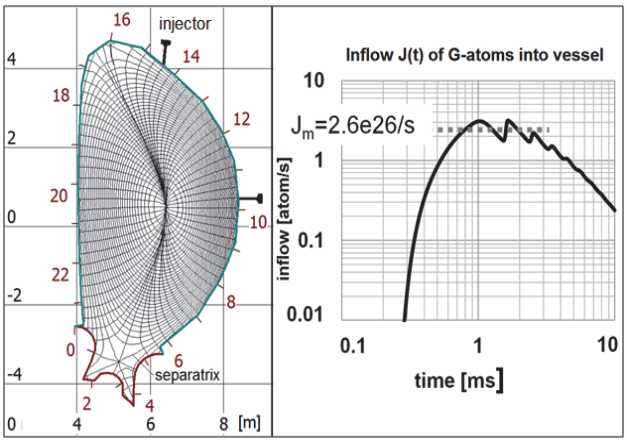

Fig. 1: Left: ITER vacuum vessel, magnetic flux coordinates of TOKES, wall surface coordinate X [m] and available injector locations are shown. Right: The maximum inflow J_m determines the MGI process. The gas inflow J(t) is calculated with TOKES.

Radiation energy transport during MGI: TOKES simulations

The main current TOKES development is the implementation of 3D model for the plasma and radiation emission in order to obtain toroidal peaking of radiation load in a vicinity of injector as a function of time and the gas inflow magnitude J_m (see Fig. 1). This work is in the stage of simplified plasma modelling being focussed mainly for 3D radiation load distribution near injector orifice in first wall surface.

The plasma is subdivided into many magnetic tubes along the magnetic lines which correspond to x_{max} = 30 nested magnetic layers in the confining region inside the separatrix (see Fig. 1). The wall surface is subdivided into numerical cells by the toroidal sectors $\Delta\zeta = 2\pi/N$ with the number of toroidal segments N = 18, and by the poloidal segments Δ_w (centred at some radiuses r_w) with w wall index coordinate. At fixed w the cell areas $s_w = \Delta_w r_w \Delta\zeta$ don't depend on ζ_n. Currently $0 \le w \le w_{max}$=105 thus the number of wall cells $K = (w_{max}-1)N$ = 1872 is available. The simulations show that for correct radiation load one emitting point per plasma layer per toroidal sector of magnetic tube is sufficient. Thus $I = x_{max}N$ = 522 emitters from all magnetic tubes are available per one toroidal turn of magnetic field lines.

Visualization tools for 3D magnetic field configuration are developed and for pre-TQ phase 3D results for single toroidally discrete upper port neon injector achieved. Fig. 2 exemplifies 3D distribution of radiation load over wall surface at the time moment t = 3.2 ms of MGI start (opening the valve of gas plenum) for a calculated scenario near obtained melting threshold on the gas inflow $J_{m,thr} \approx 0.6\times10^{26}$/s. A sharp maxi-mum of deposited energy density is in front of injector. $T_{w,max}$ is seen. Compared to earlier 2D simula-tions in which the gas injection assumed uniform on toroidal angle was used, the discrete injector positions decreased the value of $J_{m,thr}$ by 4 times. The wall surface is substantially heated only in vicinity of injector. 3D

calculations were carried out until the full plasma cooling. The obtained cooling time ~9 ms for $J_m = J_{m,thr}$ exceeds ~1.5 times the 2D τ_c ~5 ms.

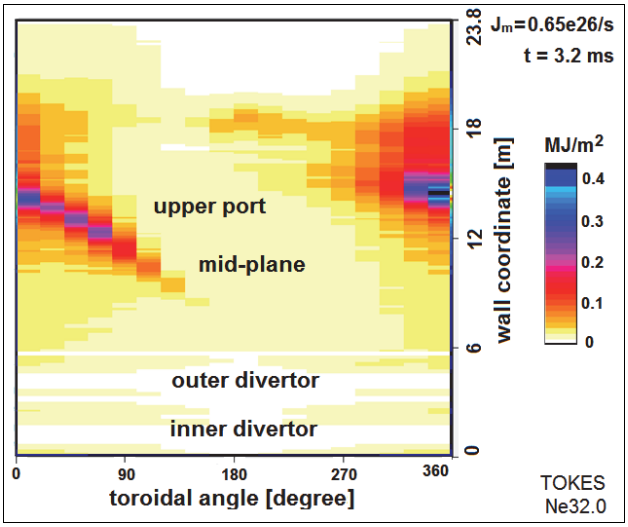

Fig. 2: Toroidal-poloidal distribution of radiation load over the wall surface is shown at the time 3.2 ms after opening the valve of single upper port neon injector, which is the moment of maximum wall temperature T_w, with $T_{w,max} = T_{melt,Be}$ = 1560 K.

Latest TOKES validations against JET

TOKES MGI simulations have been validated against JET experiments: for the discharges #76314 (neon MGI) and #77806, #77808 (argon MGI). Line integrated plasma densities obtained with 2D version of TOKES during MGI are compared with corresponding experimental data. A reasonable fitting of experimental and simulated time dependences is obtained for electron densities in the time interval when the experimental data is valid (Fig. 3). The difference of 30% can be attributed to 2D nature of simulations and 3D experimental conditions. For the discharge #77806 a parametric study for τ_c by decreasing argon amount has been performed with TOKES. We found that the discharge interruption can be provided until the amount of injected gas reduces by 40 times from the experimental value 5.6×10^{22} atoms. As MGI with small gas amounts increases the probability of generation of runaway electrons (RE), for ITER special sacrificing diaphragm for mitigation of RE damage to FW is proposed.

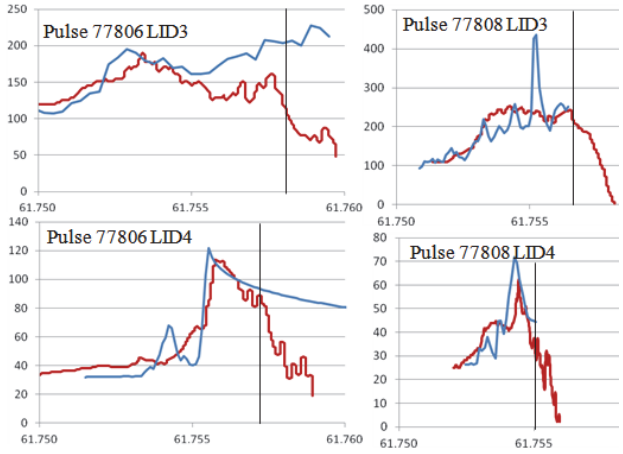

Fig. 3: Comparison of line integrated density [10^{18} m^{-2}] for 77806 and 77808 JET deuterium discharges (in red) with the validated TOKES simulations (in blue). The vertical line indicates maximum time [s] after which the diagnostics fail.

Evolution of magnetic field behind the MGI cooling front

In addition, the change of magnetic field before and behind the cooling wave was analysed in cylinder geometry, as first stage of addressing magnetic energy contribution in tokamaks to the radiative wall load. The magnetic energy releases in the cooling front as the Joule heat and then transfers there into the radiation. The estimated magnetic energy can be the factor of 3.5 larger than that of plasma thermal energy. Negligibly small cross-motion of magnetically frozen plasma before the cooling front was obtained.

Conclusions

The maximal possible surface temperature of ITER Be first wall after neon massive gas injection is numerically simulated with newly developed 3D version TOKES in the tokamak configuration with single discrete upper port injector. The wall surface is substantially heated only in vicinity of the injector. The obtained cooling time ~9 ms for the melt threshold scenario is still appropriate of using MGI for the disruption mitigation.

The analysis of available JET data with the described simulations allowed a qualitative description of energy and particles transport processes in the course of MGI thermal quench (TQ) which consists of the pre-TQ phase in which the thermal cross transport is rather small and the TQ itself with the development of anomalous plasma transport. The pre-TQ occurs at the plasma edge, with ionization of injected atoms and radiation losses as the main contributors to plasma cooling. During TQ the plasma current is contracted by the cooling front, and the corresponding change of magnetic energy can result in substantial increase of wall load. Sufficient understanding of physics of these processes would allow proper extrapolations of the JET results upon ITER.

Staff:

I.S. Landman
S.E. Pestchanyi

Literature:

[1] I.S. Landman et al. 'Modelling of first wall photonic heat loads during disruption mitigation by massive gas injection on ITER', Paper presented at the ICFRM-16 conference, Beijing, Oct 2013.

[2] S. Pestchanyi et al. 'Analysis of energy cross-transport during MGI: JET experiments and TOKES simulations', Fusion Engineering and Design, 88 (2013) 1127

Acknowledgement

This work, supported by the European Communities under the contract of Association between EURATOM and Karlsruhe Institute of Technology, was carried out within the framework of the European Fusion Development Agreement. The views and opinions expressed herein do not necessarily reflect those of the European Commission.

Modelling of Plasma Wall Interaction Applying the Melt Motion Code MEMOS (WP13-IPH-A11-P1-01)

Introduction

The ITER Organization has recently decided to install a full-tungsten (W) divertor from the start of operations. One of the key issues of this strategy is the possibility of W melting and melt splashing during the transient events such as giant edge localized modes (ELMs) and the disruptions, which can lead to deterioration of vessel wall surface and higher disruption frequency, thus compromising the tokamak operation. Although every effort will be made to avoid leading edges, ITER plasma stored energies are sufficient that transients can drive shallow melting on the top surfaces of components.

Experiments designed to investigate plasma transient heat load damage of ITER-like W targets have traditionally been performed at plasma gun facilities, in which the transient plasma pulse pressure significantly exceeds the values attainable in tokamaks, including ITER, and the melt motion dynamics is determined by the tangential friction force of the impacting plasma. These experiments at the QSPA-Kh50 plasma gun facility (IPP Kharkov, Ukraine) are continued, in cooperation with KIT. A new experiment has now also been performed on JET in the ITER-Like Wall (ILW) environment, in which a deliberately misaligned W element (lamella) in the outer divertor has been used to perform controlled ELM transient melting experiments for the first time in a tokamak.

Simulations of plasma impact on a lamella tile of JET ILW

In the frame of the programs M13-01 and M13-02, 3D MEMOS calculations have been performed and compared with JET experiments for the ITER-like wall, in which tungsten PFC surface melt motions under ELM impacts is under investigation. The 3D MEMOS simulations allowed prompt estimations of the time intervals and heat loads needed for melting of the special lamella (Fig. 1). Simulation results allowed reproducing of involved surface processes and the melt damage for the surface temperature measured at the lamella leading edge.

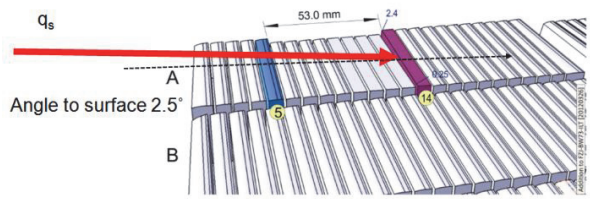

Fig. 1: The design of JET divertor lamellas used in MEMOS. The height of exposed edge of the special lamella (in magenta) is 2.4 mm.

Simulations are performed at first for L-mode plasma loads (i.e. without ELMs) both for the reference well aligned lamella and a misaligned one (reference discharge #84514). The input heat loads are obtained from experimental data, for which a high resolution infrared thermograph (IR) camera was used. Then the ELMing H-mode was simulated (reference discharge #84779, ELM frequency 30 Hz). The time dependent 3D temperature distribution in the special lamella was calculated. The ELM loads lead to extremely high temperature gradients at the leading edge (~10^6 K/m) and noticeable W evaporation.

3D MEMOS simulations discovered that a consistency of numerical results with the IR measured temperatures is only possible if the impinging heat flux would about a factor 3 lower than that expected from the geometrical considerations of MEMOS model. Importantly, the code indicates that that the shielding by the evaporated tungsten in front of the target prevents bulk melting between ELMs.

The simulations are also able to quantitatively reproduce the dimensions of the damaged area observed by high resolution photography after the first pulse in which melting was achieved. The principle mechanism responsible for the melting is identified as the **JxB** force due to the thermo-emission currents from the hot surface. This force generates velocities up to 0.7 m/s in the calculated direction observed also experimentally. No melt splashing is ob-

served experimentally, nor is it expected on the basis of the MEMOS simulations of melt depth and melt velocity. The pressure of the ELM transients is also too low to generate melt layer instability and melt motion damage.

Cooperation with plasma gun experiments and ITER. Brittle destruction activity

The cooperation with the team of plasma gun QSPA-Kh50 has continued. The theoretical model for W melt splashing earlier developed in KIT based on the Kelvin-Helmholtz (KH) instability was confirmed in the last QSPA experiments with pulse duration $\tau \approx 0.25$ ms and the wall load $Q \approx 0.75$ MJ/m^2. The W droplet sizes, inverse proportionality of droplet velocity on Q and the re-solidification wave profile correspond to the KH model. The droplets fly mainly the upstream direction of plasma stream. The W splashing during the plasma exposure is followed at the end of pulse by W dust emission.

After validation of the code 3D MEMOS against experiments on JET-ILW, the code was applied for the simulations of the transients interactions with the W divertor and Be first wall expected in ITER. The codes ENDEP and MEMOS were applied for the simulations of expected damages of PFCs under expected runaway electrons heat loads in ITER. Also similar scenarios for DEMO were addressed.

In the frame of this task also a comprehensive investigation of divertor armor erosion under action of ELM-like surface heat loads using the PEGASUS-3D code has been performed. Different erosion mechanisms for tungsten and CFC armor materials have been revealed. This difference explains almost 3 orders of the magnitude difference in erosion rates of CFC and W. Investigations of the crack pattern evolution under repetitive ELM-like surface heat load have been done. Special treatment for tungsten armor tiles has been proposed for reduction of dust production in operation regime.

Conclusions

The results of MEMOS modelling are generally in good agreement with the experimental data of the tokamak JET and the plasma gun QSPA-Kh50. Both plasma and run away electron loads onto the wall surfaces of JET and ITER and the following wall damages have been simulated for diverse conditions such as the heat flux and pulse durations.

Staff:

B. Bazylev
S. Pestchanyi

Literature:

[1] B. Bazylev et al., MEMOS code validation on JET transient tungsten melting experiments,. submitted to the conference - PSI 2014

[2] J.W.Coenen, et al., ELM induced tungsten melting and its impact on tokamak operation, submitted to the conference - PSI 2014

[3] G. Arnoux et al., Thermal analysis of an exposed tungsten edge in the JET divertor, submitted to the conference - PSI 2014.

[4] V.A. Makhlaj, et al., Tungsten damage and melt losses induced by plasma accelerators exposures at ITER ELM conditions. 14th PFMC, May 2013, Jülich, Germany, accepted for publication

[5] S. Pestchanyi et al, Simulation of dust production from tungsten armour using PEGASUS-3D code. Paper presented at the ICFRM-16 conference, Beijing, Oct 2013.

Acknowledgement

This work, supported by the European Communities under the contract of Association between EURATOM and Karlsruhe Institute of Technology, was carried out within the framework of the European Fusion Development Agreement. The views and opinions expressed herein do not necessarily reflect those of the European Commission.

Novel PFC Material Solutions / Liquid Metals (WP13-PEX-03b-T05-02)

Introduction

The main objective of this task is the modelling of Li surface erosion under ITER and DEMO Type I ELM high power loading. This includes 1) melting and evaporation of the Li surface, 2) molten layer flow and deformation caused by the magnetic fields and thermo emission current, 3) effect of shielding owing to the Li evaporation. The 3D version of the predictive code MEMOS has been employed. The behaviour of liquid metal both in a Capillary Porous System (CPS) structure and as free flowing films is considered. The influence of porous substrate (W) on the melt motion damage is investigated for heat loads accounting for the melt layer and Li vapour shielding effect. MEMOS has been modified (and consequently validated against experimental results) in order to simulate heat removal under DEMO conditions by using the CPS. Modelling of the flow of liquid metals under the influence of strong magnetic fields and the associated heat transport under high power loads is the main objective.

The expected damage of plasma facing components (PFC) made from refractory materials as well as from the liquid metals in CPS under tokamak transient energy loads is simulated numerically in the wide region of heat loads using 2D and 3D versions of the code MEMOS [1]. The code was successfully validated for the short pulses against experiments at QSPA-T (Troitsk, Russia) [2] and QSPA-kh50 (Kharkov, Ukraine) [3] facilities and for the long-time plasma loads against experiments at TEXTOR. Now 3D MEMOS is validated against melt motion experiments in JET-ILW(ITER-like wall) and in its 3D version describes a macro brush structure of PF surface.

Target heating by plasma and electron-beam impact takes into account the effect of plasma shielding by vapour cloud due the armour material evaporation. The Stefan problem including a surface evaporation, melting and re-solidification are described. Motion of the melted material is simulated by 2D/3D Navier-Stocks equation in the „shallow water“ approximation. On the armour surfaces thermo-emission current and the temperature dependent thermophysical properties of materials are taken into account. The simulation of the molten layer motion includes the driving forces like a gradient of plasma pressure (in the case of developed plasma shielding), the surface tension and JxB force caused by current flowing into the armour (hallo current or by thermo-emission current).

Recently we use in MEMOS calculation new specifications of Type I ELM power loads, envisaged for DEMO reactor plasmas [4]. The power load of unmitigated ELMs on the DEMO I case is estimated as 3MW/m^2 and for the mitigated ELMs with about 33 times reduced amplitude like in ITER. The case of DEMO1 was considered, were the uncontrolled ELM peak deposition energy/deposition time to the divertor plate are 10MJ/m^2/1.2ms. In the case of DEMO II peak deposition energy/deposition time to the divertor plate is 20MJ/m^2/1.2ms. Pressurized water reactor (PWR) cooling conditions with about 150°C inlet water temperatures and pressure about 15,5MPa are used for the calculations.

Modelling of Li layer behaviour under ITER like ELM loads

The behaviour of Li layer on various porous substrates is investigated by using MEMOS code, which takes into account capillary porous system and Li layer recovery under transients (ELM) impact. Calculations were performed for the following conditions: the melt motion and the evaporation of Li film on impermeable tungsten substrate, the Li coating of 5-50 μm thickness on W bulk material and W capillary porous system. Previously the following reference parameters where assumed heat load, Q = 0.1 MJ/m^2, the ELM pulse load time τ = 0.5 ms, the magnetic field B = 5 T and the tangential pressure in the range of 2×10^{-4} to 2×10^{-3} bar. The electric current component normal to the target surface is varied in the range 5-50 A/cm^2 and that the initial surface temperature is T_0 = 30°C (assuming that Li melts during the transient). The thickness of evaporation layer is investigated for the reference pulse duration and heat load ranged between 0.1 and 0.4 MJ/m^2. The applied force and the energy flux cor-

respond to the rectangular pulse shape. The time shape of the pulse was simulated similar to that of a real ELM.

Significant evaporation starts at heat loads ≥ 0.2 MJ/m^2 (see Fig. 1). Strong plasma shielding forms above the Li layer thus preventing Li from intensive evaporation. For the reference heat load, the vaporization is negligible, and the melt motion only causes the melt layer damage. In calculations the effects of tangential plasma pressure and the JxB force on liquid Li motion were investigated as well as the dependence of the surface damage on the pulse shape. The effect of different Li thickness on the formation of crater was investigated. It is shown that surface craters are caused by the tangential pressure for different thickness of Li layer and after 3 ms from pulse trail (see Fig. 1 and 2). The capillary porous system is taken into account. In scenarios with Δ_{Li} = 5 μm removed melted materials from the crater bottom is recovered by the capillary forces from the W porous matrix and the thickness of liquid Li at the crater bottom remains about 0.4 μm.

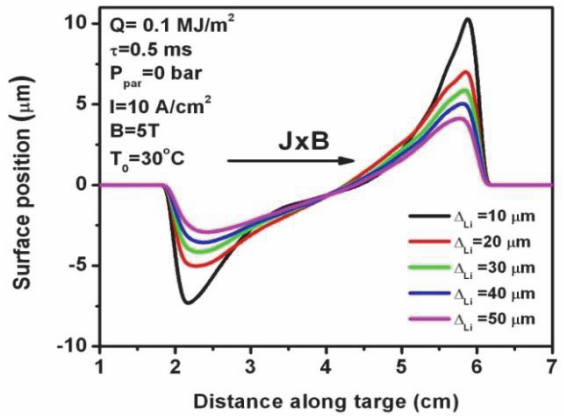

Fig. 1: Crater shape caused by JxB force on Li layer for different thickness of Li layer after 3 ms.

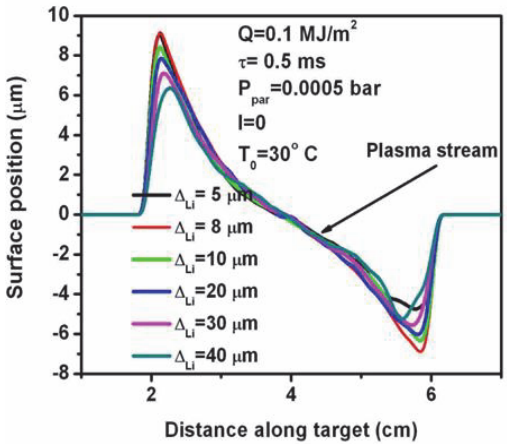

Fig. 2: Crater shape caused by tangential pressure on Li layer for different thickness of Li layer after 3 ms. Capillary porous system is taken into account.

The capillary porous system is taken into account. In scenarios with Δ_{Li} = 5 μm removed melted materials from the crater bottom is recovered by the capillary forces from the W porous matrix and the thickness of liquid Li at the crater bottom remains about 0.4 μm.

Calculations show that even small ELMs can completely remove Li away from W subtract.

Damage by JxB (volumetric) force strongly depends on layer thickness (due to effect of melt layer viscosity). Damage caused by tangential pressure (surface force) weakly depends on layer thickness. Under these conditions the vapour shield does not develop for investigated heat loads.

The first 3D MEMOS results of Li characteristics on the W sample with CPS after irradiation with plasma energy are presented here. In the Fig. 3 plasma heat loads in MW/cm^2 on the Li surface is shown. 3 μm of Li is coated on tungsten CPS. Target initial temperature was taken as 300 K. Impact energy Q = 0.1 MJ/m^2 in maximum and pulse duration about 0.5ms. The pulse shape was taken as rectangular. The effect of vapour shielding is taken into account. A spatial energy pulse profile in Y direction (see Fig. 1) was taken as half Gaussian with half width of 2 cm (similar to the typical ELM shape). In Z direction energy pulse has Gaussian profile with half width of 7 cm. Two plasma pressure values in maximum 0.1 bar and 0.15 bar have been chosen.

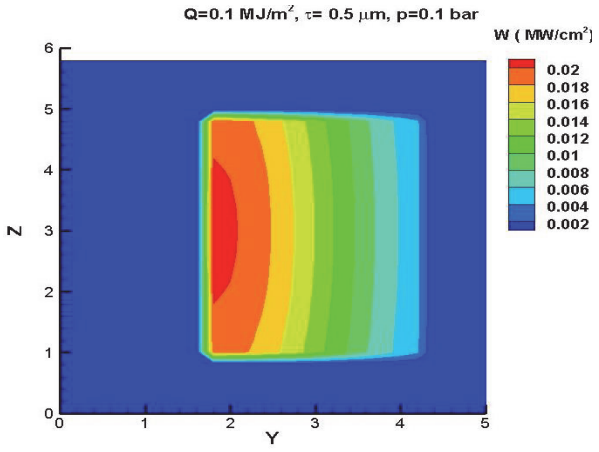

Fig. 3: Contour plot of plasma heat loads (in MW/cm^2) on the Li surface, Q=0.1MJ/m^2, t=0.5msec, vapour pressure p=0.1bar. ITER like conditions.

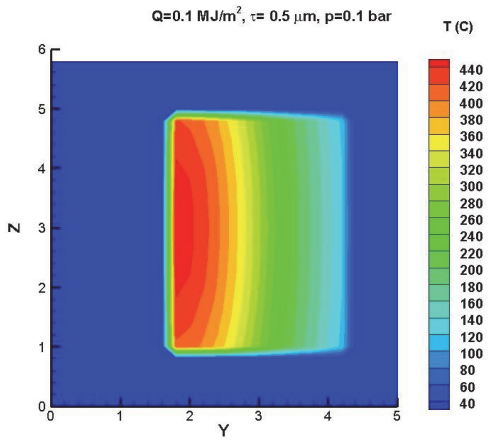

Fig. 4: Contour plot of temperatures (in ºC) on the irradiated surface for 0.1MJ/m^2 of energy load, evaporation depth 0.5μm, maximum pressure 0.1bar; low evaporation. ITER like conditions.

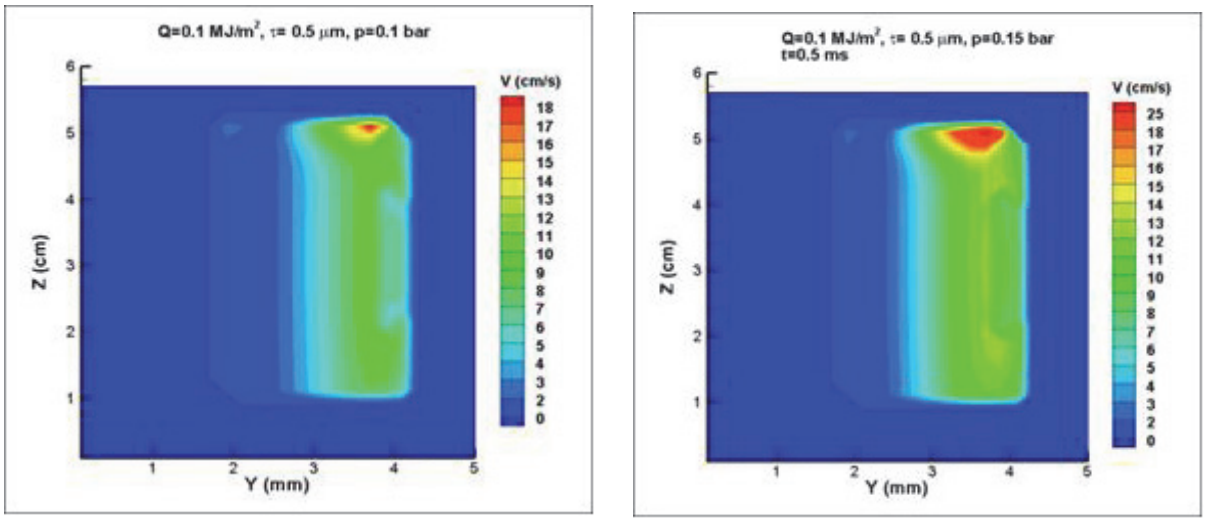

Fig. 5: Contour plots of melt layer velocity along the irradiated surface for of energy load of 0.1MJ/m^2, evaporation depth 0.5μm and the maximum pressures 0.1bar on the left figure and 0.15bar on the right figure. Evaporation level is low. Gradient of plasma pressure generates the melt motion. ITER like conditions.

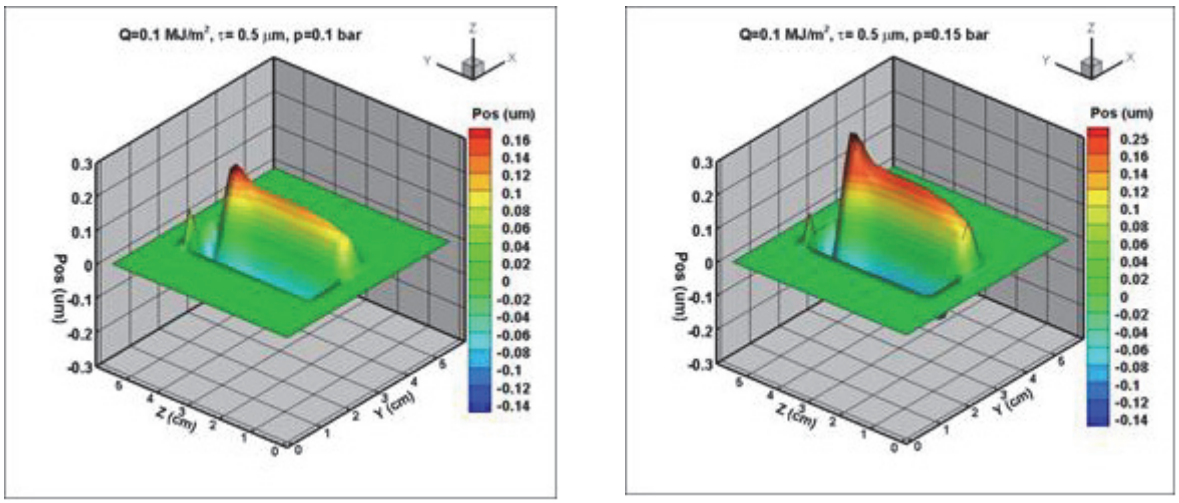

Fig. 6: Final surface profile for two plasma pressure scenarios 0.1 bar (left) and 0.15 bar; (right) evaporation is at low level. Position in ?m is plotted along the target surface.

Results of MEMOS calculation of Li melting under DEMO like ELM impact

Recently we use in MEMOS calculation new specifications of Type I ELM power loads, envisaged for DEMO reactor plasmas [4]. The power load of unmitigated ELMs on the DEMO I case is estimated as 3MW/m^2 and for the mitigated ELMs with about 33 times reduced amplitude like in ITER. The case of DEMO1 was considered, were the uncontrolled ELM peak deposition energy/deposition time to the divertor plate are 10MJ/m^2/1.2ms. In the case of DEMO II peak deposition energy/deposition time to the divertor plate is 20MJ/m^2/1.2ms. Pressurized water reactor (PWR) cooling conditions with about 150°C inlet water temperatures and pressure about 15,5MPa are used for the calculations. In the case of mitigated like in ITER the ELMs power loads to the DEMO divertor have been taken in the range of 0.01-0.025MW/cm^2. Fig. 7 shows the contour plot of evaporated Li for mitigated ELMs impact for ELM heat flux Q=0.3MJ/m^2, τ=1.2msec, and incoming plasma and vapour pressure p=0.25bar, which correspond to DEMO1 conditions with Type 1 mitigated ELMs with reduced about 33 times amplitude. Fig. shows the final surface profile after the mitigated ELMs impact on the Li surface. Position in μm is plotted along the target surface. Erosion forms the hell and hill shape due to molten layer motion under pressure impact. Fig. 9 shows the contour lines of evaporated Li depth for mitigated ELMs impact (in μm) for the ELM load Q=0.24MJ/m^2 and deposition time τ=1.2msec, The vapour pressure *p*=0.2bar is assumed. The corresponding surface deformation after the ELM impact is shown in Fig. 10. With decreasing of ELM size, the Li erosion becomes smaller (see Figs. 11-12). Impact of unmitigated ELMs on Li layer is shown in Fig.13, where Q=1.2MJ/m^2, τ=1.2msec and plasma pressure *p*=0.4bar are considered. It is shown, that evaporation of Li reaches almost 0.14mm even in the case of capillary porous Li supplies. This depth of erosion could even exceed the molten layer thickness. The resulting evaporation depth as a function of the DEMO ELM heat loads is summarized in Fig. 14. The evaporation of Li dramatically increases with impact power and for heat loads above 1.2MJ/m^2 per ELM exceeds 0.1mm. Under those conditions the CP system does not work.

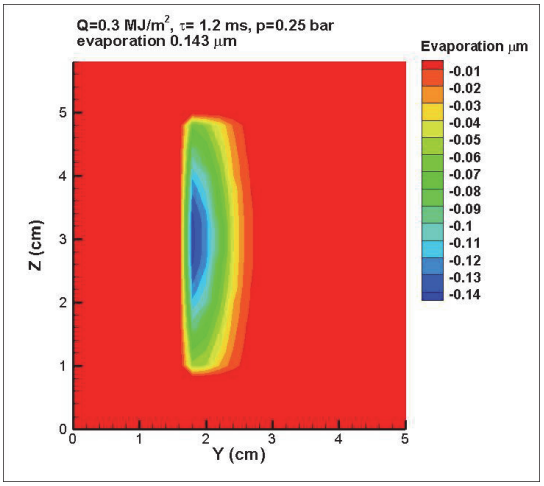

Fig. 7: Contour plot of evaporated Li for mitigated ELMs impact (in μm), Q=0.3MJ/m^2, τ=1.2msec, vapour pressure p=0.25bar. DEMO like conditions.

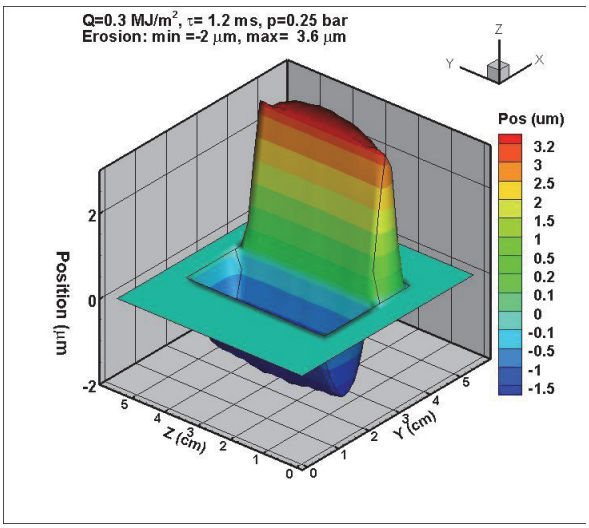

Fig. 8: Final surface profile after DEMO mitigated ELMs impact. Position in μm is plotted along the target surface.Erosion level:min=-2μm, max=3.6μm.

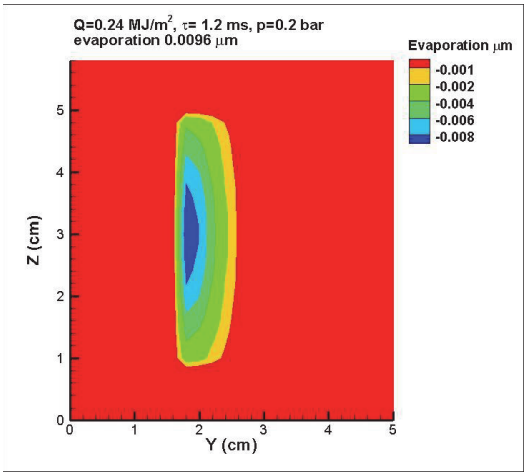

Fig. 9: Contour plot of evaporated Li for mitigated ELMs impact (in μm), Q=0.24MJ/m^2, τ=1.2msec, vapour pressure p=0.2bar. DEMO like conditions. The mitigated ELMs.

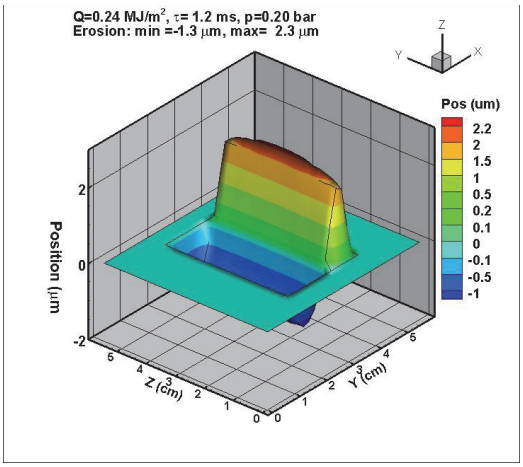

Fig. 10: Final surface profile after DEMO mitigated ELMs impact. Position in μm is plotted along the target surface. Q=0.24MJ/m^2, τ=1.2msec, vapour pressure p=0.2bar.

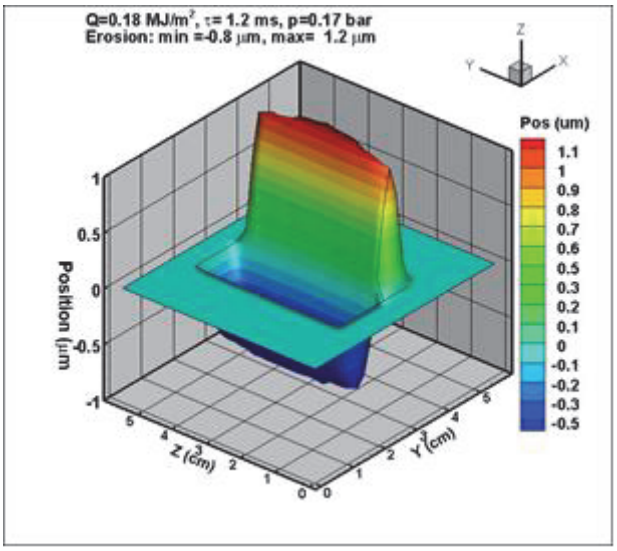

Fig. 11: Final surface profile after DEMO mitigated ELMs impact. Position in μm is plotted along the target surface. Q=0.18MJ/m^2, τ=1.2msec, vapour pressure p=0.17bar.

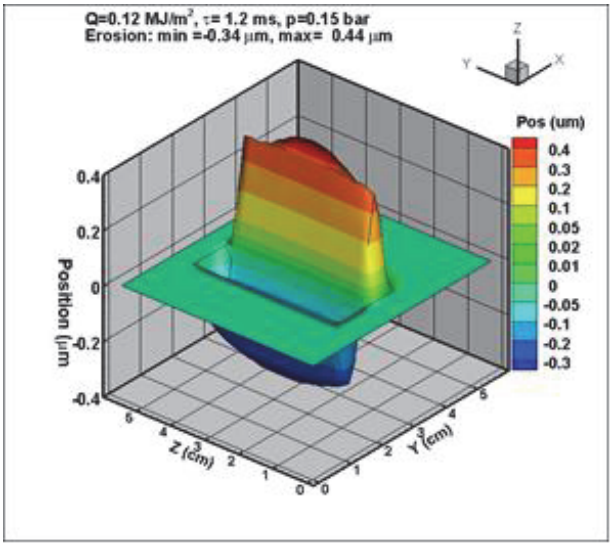

Fig.12: Final surface profile after DEMO mitigated ELMs impact. Position in μm is plotted along the target surface. Q=0.12MJ/m^2, τ=1.2msec, vapour pressure p=0.15bar.

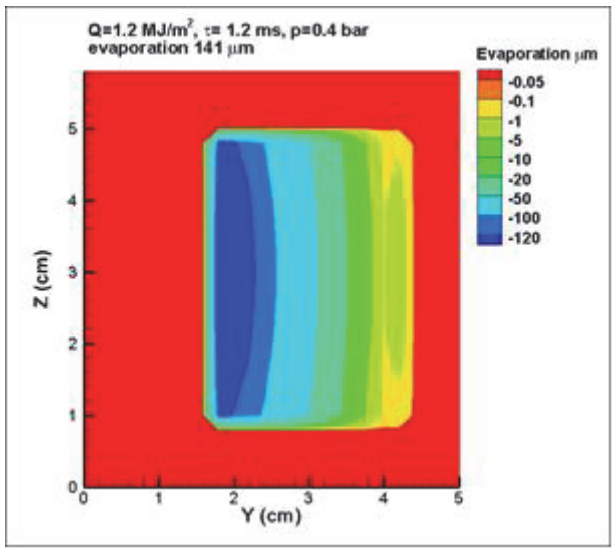

Fig. 13: Contour plot of evaporated Li for mitigated ELMs impact (in μm), Q=1.2MJ/m2, τ=1.2msec, vapour pressure p=0.4bar. DEMO like conditions. Conditions for unmitigated ELMs.

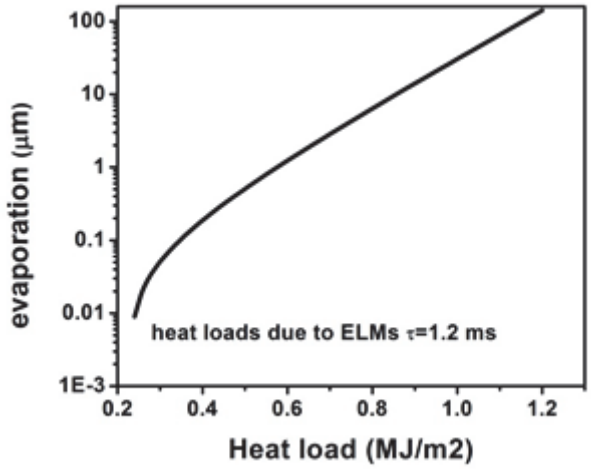

Fig. 14: Li Evaporation depth vs the ELM heat loads. The evaporation of Li dramatically increases with impact power and for heat loads above 1.2MJ/m2 per ELM exceeds 0.1mm. Under those conditions the CPS does not work.

Conclusions

The lithium surfaces divertor concept allows one to increase the heat-flux exhaust capability by flowing the heated material to a cooling region and eventually out of the machine, and/or by being able to withstand a higher peak heat flux. In our calculation we investigate the impact of Type I ELM heat loads expected in ITER or in DEMO on erosion of Li divertor target. We investigate a molten layer distortion under different forces, acting on the molten layer. The 3-D version of MEMOS code is employed. The effect of porous substrate (W) on the melt motion damage is investigated for various heat loads, expected for transients. Calculations are taking into account the formation of Li vapour shielding. It is shown, that the CPS could not effectively compensate of molten layer evaporation or removal under ITER or DEMO ELMs impact.

In the case of ITER envisaged Type I ELMs heat loads the remaining liquid Li layer is estimated to be below 0.4 μm which could easily evaporate under high heat loads. Damage caused by JxB (volumetric) force impact strongly depends on layer thickness (due to effect of melt layer viscosity). Damage caused by tangential pressure (surface force) weakly depends on layer thickness. Under these conditions the vapour shield does not develop for investigated heat loads. The same is correct for the DEMO case. However, under reactor conditions erosion, splashing and stability of liquid flow remains an issue and requires further investigation.

In the case of DEMO1 envisaged unmitigated Type I ELMs heat loads that evaporation of Li reaches almost 0.14mm even in the case of capillary porous Li supplies. This depth of erosion could even exceed the molten layer thickness and results in intolerable erosion (see Fig 13 and 14).

In the case of DEMO1 mitigated ELMs (with 33 times reduced amplitude, like in ITER) impact the evaporation of Li per ELM is small ≤ 0.15μm and effect of molten layer deformation due to pressure gradient effect does not exceed 10 μm, e.g. after one ELM impact the crater depth is about 2 μm and the hill height about 3.6 μm.

Up to now the impact of a single ELM is considered. Modelling of the surface erosion under multiple ELM impact has been completed for the JET case (see Bazylev et al., paper submitted to PSI 2014 conference). Similar calculation can be done in future for DEMO conditions. We would like also to point out, that a further benchmarking of MEMOS code with experimental results (e.g. JET) will help to increase the confidence of numerical predictions.

Staff:

B. Bazylev
Yu. Igitkhanov

Literature:

[1] B. Bazylev and J.W. Coenen, Problems of Atom. Sci. and Techn. 1, Series: Plasma Phys.19 (2013) 3

[2] N.I. Arkhipov, et al.// J. Nucl Mater. 1996, v. 233-237, p.686.

[3] I. Garkusha, et al.,"The latest results from ELM-simulation experiments in plasma accelerators ",Physica Scripta, Volume 138, Issue , article id. 014054, 6 pp. (2009).

[4] Yu. Igitkhanov and B. Bazylev "Modeling of DEMO PFC Erosion due to ELM Impact", submitted to the IEEE Transactions on Plasma Science, SOFE 2013.

Acknowledgement

This work, supported by the European Communities under the contract of Association between EURATOM and Karlsruhe Institute of Technology, was carried out within the framework of the European Fusion Development Agreement. The views and opinions expressed herein do not necessarily reflect those of the European Commission.

Plasma Boundary Modelling - Model of the SOL and Divertor Transport (WP13-PEX-01-T01-02)

Introduction

The main purpose of this report is the development of analytical transport models of the edge tokamak plasma, suitable for implementation into the integrated code TOKES and in perspectives for implementation into System integrated Code for predictive modelling of the fusion reactor DEMO. The tokamak edge plasma in reactor configurations is expected to be rather thin inmost and outmost areas (adjacent to the last closed magnetic surface) with strong radial plasma gradients inside the separatrix and the area outside the separatrix, a scrape-off layer (SOL), with open magnetic field lines, terminated at the divertor plates and limiters. The region beyond the separatrix plays an important role because it serves as a shield, protecting the wall from the hot plasma and bulk plasma from the penetration of impurities and because it is mostly affected by transients. The transport model, proposed here, provides plasma density, temperature and velocity distribution along and across the magnetic field lines in bulk and the edge plasma region. It describes the dependence of temperature and density at the separatrix on the plasma conditions at the plate and the efficiency of the divertor operation, depending on power and particle sources. The calculation gives eventually the power and particle loads on the divertor plates and side walls.

2D fluid equations for SOL and divertor plasma in TOKES

We are considering a 2D orthogonal coordinate system in the rectangular SOL domain with the *x*-axes across and the *y*-axes along the magnetic field lines (See Fig. 1). In tokamak configuration plasma near the wall has in general a complex curvilinear configuration. The magnetization of the plasma and relatively narrow boundary region, however, makes it possible to “straighten out” the separatrix and, in some approximation, to treat the problem in a rectangular geometry (Fig.1). If there is substantial uncertainty regarding the transport in radial direction, the effects of the curvature and of the variation of the poloidal magnetic field along B can be simply ignored. The SOL width, Δ_{sol}, is specified as a distance from the first wall to the separatrix and is much less than a minor radius, a.The plasma is assumed to be in steady state quite dense and cold (excluding transients), and is described by the system of hydrodynamic equations. The following hydrodynamic equations for density, n, momentum, and energy in the SOL plasma are employed [1]:

$$\frac{\partial n}{\partial t}+\frac{\partial}{\partial x}nV_x=-\frac{\partial}{\partial y}\left(nV_y\right)+n\left(\left\langle\sigma V\right\rangle_{ion}N_0-\alpha_{rec}n-\alpha_3 n^2\right) \tag{1}$$

$$nV_x=-D_B(T)\frac{\partial n}{\partial x} \tag{2}$$

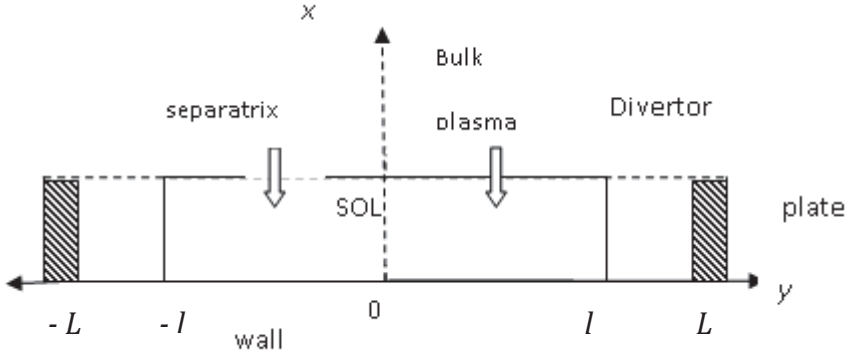

Fig. 1: The computational domain for the SOL and divertor region.

where N_0 is the neutral gas density, $D_B(T)$ is the Bohm diffusion coefficient, $\langle \sigma V_{ion} \rangle$ is the ionisation rate, The recombination rate α has the form $\alpha = \alpha_{rec} + n\alpha_3$, where α_{rec} and α_3 are the radiative and three-body recombination rates, respectively. The momentum and energy equations read:

$$m_i \frac{\partial n V_y}{\partial t} + \frac{\partial}{\partial y} n\left(m_i V_y V_y + 2T\right) + \frac{\partial}{\partial x}\left(m_i n V_y V_x\right) = \frac{\partial}{\partial y}\left(\eta_{yy} \frac{\partial V_y}{\partial y}\right) + Q_p \tag{3}$$

$$\begin{aligned} &\frac{\partial}{\partial t}\left(3nT + \frac{m_i n\left(V_x^2 + V_y^2\right)}{2}\right) + \frac{\partial}{\partial x}\left(5nT + \frac{m_i n\left(V_x^2 + V_y^2\right)}{2}\right) V_x + \\ &+ \frac{\partial}{\partial y}\left(5nT + \frac{m_i n\left(V_x^2 + V_y^2\right)}{2}\right) V_y + \frac{\partial}{\partial y} \chi^0 T^{5/2} \frac{\partial T}{\partial y} + \frac{\partial}{\partial x} n D_B(T) \frac{\partial T}{\partial x} = Q_\varepsilon \end{aligned} \tag{4}$$

Where

$$Q_p = -m_i n V_y \left[(\alpha_{rec} + \alpha_3 n^2) + \nu_{cx}\right] \text{ (The velocity of neutrals is neglected)} \tag{5}$$

$$Q_\varepsilon = -Q_{rad} - \left(I_i + \varepsilon_*\right) n N_0 \langle \sigma V \rangle_{ion} - \left(\varepsilon_{tot} \alpha_{rec} + \left(\varepsilon_{ion} - I\right) n \alpha_3\right) n^2 \tag{6}$$

Here $T \equiv T_e = T_i$, η_{yy} is the viscosity and χ^0 is the Spitzer-Harm conductivity coefficient along B (for one *eV*), D_B is the radial diffusion coefficient (in calculation is taken as 1m^2/sec. though, generalization to functional Bohm coefficient is straightforward). Particle source, nN_0S_0 is due to ionization of neutrals, $S_0 = \langle \sigma V \rangle_{ion}$. The momentum sink, Q_p, is due to charge exchange with cold neutrals, N_0, and the recombination. The energy sink, Q_ε, is due to radiation, ionization and recombination of neutrals., Neutrals are currently given arbitrary by specifying a distribution of atoms in divertor.

Here $\tau_{cx} = 1/N_0 \langle \sigma_{cx} V_i \rangle$ is the charge exchange collision time and Q_{rad} are the radiation losses for cold neutrals. In the energy loss term ε^* is the average excitation energy, $\varepsilon_{tot} = \varepsilon_i + \varepsilon_e$, where:

$$\varepsilon_i = \left(\frac{3}{2} T_i + \frac{m_i\left(V_y^2 + V_x^2\right)}{2}\right) n_i, \; \varepsilon_e = \left(\frac{3}{2} T_e\right) n_i, \; Q_{rad} = N_0 n L_H \tag{7}$$

and L_H is the cooling rate for hydrogen radiation, I .is the ionization potential.

The following improvements are foreseen in near future:

1) separation of electron and ion temperatures, $T_e \neq T_i$,
2) appropriate model of the neutral atoms (self-consistent calculation),
3) equations for realistic curvilinear geometry.
4) the terms with parallel current along the magnetic field lines will be added
5) to include terms associated with impurities.

Boundary conditions

The 2D fluid equations are required initial and boundary conditions at the computation boundaries. As initial conditions, density, temperature and velocities are taken from the 1D analytical profiles along the B and exponential across the SOL. Since we are looking for stationary solution, this choice is unimportant. The kinetic effects in boundary conditions are neglected and all transmission coefficients derived assuming a half Maxwellian function for

the incident particles. We also neglect here the influence of impurities on the boundary parameters. One can distinguish five boundaries: at the separatrix, in private zone region, at the divertor plates and at the first wall.

Input particles, Γ and heat, $Q_e = Q_i = Q$ fluxes are specified at the separatrix:

Separatrix between the SOL and core: $x = 1 \;\; (r = \Delta_{sol}), \quad -l \le y \le l$

$$q_x = -nD_B \left.\frac{\partial T}{\partial x}\right|_{x=1;-d\le y\le d} + 5nTV_x = Q / S_{sep} \tag{8}$$

$$nV_x = -D_B \left.\frac{\partial n}{\partial x}\right|_{x=1;-d\le y\le d} = \Gamma / S_{sep} \tag{9}$$

Divertor & private zone boundary: $x = 1 \;\; (r = \Delta_{sol}), \quad \left|-L\right| \le y \le \left|L\right|)$

$$q_x = -nD_B \left.\frac{\partial T}{\partial x}\right|_{x=1;|-L|\le y\le|L|} = 2(1-\alpha)nV_T T \tag{10}$$

$$\Gamma_x = -D_B \left.\frac{\partial n}{\partial x}\right|_{x=1;|-L|\le y\le|L|_y} = \frac{1}{4}(1-\alpha)V_T n \tag{11}$$

Divertor plates: $y = \pm L \quad 0 \le x \le 1$

$$-\chi_0 T^{5/2} \frac{\partial T}{\partial y} = 2T\Gamma_y \tag{12}$$

$$\Gamma_y \equiv nV_y = \frac{1}{4}(1-R)nc_s(T) \tag{13}$$

$$V_y = c_s(T), \quad T = T_w \tag{14}$$

where T_w is the wall temperature, $c_s(T)$ is the sound speed.

Private region: $x = 1 \quad -L \le y \le -l; \;\; l \le y \le L$

$$q_x \equiv -TD_{Bohm} \frac{\partial n}{\partial x} = 2(1-\alpha)nT \cdot c_s(T) \tag{15}$$

$$\Gamma_x \equiv -D_{Bohm} \frac{\partial n}{\partial x} = \frac{1}{4}(1-\alpha)n \cdot c_s(T) \tag{16}$$

where α is some reflexion coefficient ≤ 1, which describes the ratio of reflected back from private region particles.

Wall: $x = 0, \;\; -L \le y \le +L$

We assume $n = 0 \quad T = 0$ (17)

The boundary conditions at the divertor plate can be generalized by assuming that the distribution function at the boundary is a one-directed and somewhat shifted Maxwellian function for ions (due to the acceleration in the electric pre-sheath, $e\varphi$) and truncated at some velocity double side Maxwellian function for electrons (because of a cut-off in the retarding electric

field). The boundary conditions at the plate then can be obtained by equating the fluid particle and energy fluxes to kinetic ones:

$$(\frac{5}{2}nV_sT_e + q_e) = f_eT_enV_{Te} \tag{18}$$

$$(\frac{m_iV_i^2}{2} + \frac{5}{2}T_i)nV_i + q_e = f_iT_inV_{Ti} \tag{19}$$

$$(m_inV_i^2 + nT_i + nT_e - \eta_i\frac{\partial V_i}{\partial y}) = f_{pe}T_en + f_{pi}T_in \tag{20}$$

where

$$f_e = 2 + \varepsilon \tag{21}$$

$$f_i = \frac{e^{-M_1^2}(2+M_1^2) - \sqrt{\pi}M_1\left(M_1^2 + \frac{1}{2}\right)Erf(-M_1)}{G(M_1)}\cdot \tag{22}$$

$$f_{pi} = \frac{2\sqrt{\pi}M}{G(M_1)}\cdot\left\{\frac{M_1}{\sqrt{\pi}}e^{-M_1^2} + (M_1^2 + \frac{1}{2})Erf(-M_1)\right\} \tag{23}$$

$$f_{pe} = \frac{2\sqrt{\pi}M}{G(M_1)}\cdot\left\{-\sqrt{\frac{\varepsilon}{\pi}}e^{-\varepsilon} + \frac{1}{2}Erf(-\varepsilon)\right\} \tag{24}$$

Here $M = V_i / V_{Ti}$ where V_i is the fluid velocity along B at the plate and V_{Ti} is the ion thermal velocity; $Erf(x) = \frac{2}{\sqrt{\pi}}\int_{-\infty}^{x} e^{-t^2}dt$. The parameter M_1 is equal to M if $V_i \geq C_s$, while at $V_i \leq C_s$, it is found from the condition $\int_0^\infty F_i(M_1)VdV / \int_0^\infty F_i(M_1)dV = C_s$, where F_i is boundary distribution function for ions, $F(M_1)_i = \frac{c_i\vartheta(u)}{\sqrt{\pi V_{Ti}}}\exp\left\{-(u-M_1)^2\right\}$, $u \equiv V / V_{Ti}$, $\vartheta(x)$ is the Heaviside function and $C_s = \sqrt{5(T_e+T_i)/3m_i}$ is the sound velocity. The dimensional potential of the sheath $\varepsilon = e\varphi / T_e$ is found from quasineutrality condition [2]:

$$\varepsilon = \frac{\ln\sqrt{\frac{m_i}{m_e}\frac{T_e}{T_i}}Erf(-M_1)}{G(M_1)Erf\left(-\sqrt{\varepsilon}\right)} \tag{25}$$

where $G(M_1) \equiv e^{-M_1^2} + \sqrt{\pi}M_1Erf(-M_1)$ (26)

Note that the plasma parameters may have a discontinuity at the boundary, but the fluxes remain continuous.

The value of the electric potential in pure plasma at the plate is about $e\varphi \propto 3.5\cdot T_e$ in absence of current flow to the plate and electron emission. But this potential could considerable increase in non-stationary case, when the material surface becomes due to erosion not even.

Kinetic effects in the SOL plasma

One of the factors limiting the applicability of the hydrodynamic approach is the effect of the suprathermal particles upon the parallel heat conductivity and viscosity. Even when the conditions of hydrodynamics are strongly satisfied (e.g. the mean free path of particles are small compare with the SOL length), the expressions for the parallel heat conduction and viscosity coefficients turn out to be wrong. This is related to the fact that hydrodynamic fluxes are higher order moments and are determined mainly by suprathermal particles for which the hydrodynamic approximation turns out to be violated. When this occurs, the heat and momentum fluxes become non-local in their nature. It is shown [19] that the non-local representation for fluxes naturally follows from the equations for higher order moments of the distribution function, provided that the spatial derivatives of these moments with respect to coordinates are retained. This allows one to use differential equations for moments and their derivatives instead of complicated integral expressions for the flux in numerical calculations. In simulation of kinetic effects a simplified approach is often used, assuming the heat flux to be constrained from above by the quantity

$$q_e = \frac{q_{SH} \cdot q_{kin}}{q_{SH} + q_{kin}}, \qquad (27)$$

where $q_{kin} = FLF \cdot 2nTV_{Te}$

Here FLF = 0.1-0.3 is a flux limiting factor which is found either from experiments or from the results of numerical solution of a kinetic equation [20-22]. Unfortunately, the great uncertainty found in the experimental data does not allow one to make a quantitative conclusion about the value of FLF. As a non-local approach, FLF increases the upstream plasma temperature and reduces the density, whilst not changing significantly the plasma parameters in the vicinity of the plate. However, with the introduction of the FLF the transport remains local. Such an approach does not represent all the features related to the nature of the non-local transport. Furthermore, the applicability of the integral expression is limited to cases with low parallel plasma gradient, where a strong anisotropy in the particle distribution function can be neglected. In cases of large temperature gradient the main contribution to transport is supplied by the “tail” particles. These hot electrons can reach the divertor plate and, essentially produces an increase in the sheath potential (see Fig. 2) that can result in increased plate erosion. For a higher sheath potential, however, the energy transfer ability of each electron-ion pair on the plate is increased. The implication is that the plasma temperature near the plate may be less than that predicted by fluid modelling, thus reducing sputtering by hot ions to some extent. In summary of the above arguments, one can say that the non-local transport redistributes the fluxes over the thermal layer, reducing the peak power load. Therefore existing hydrodynamic models probably give pessimistic values of heat loading and local plasma temperature at the divertor plate. The kinetic effects can noticeably affect the transport of impurities in the divertor, in particular that of helium. The localisation of impurities is determined by the competition of many forces, including the ion thermal force. Under ITER divertor plasma conditions one can expect a reduction in the ion thermal force in comparison with the hydrodynamic limit [16, 17]. In the case of helium ions this reduction is approximately equivalent to a reduction of the thermal force coefficient by a factor of two to three.

To summarize, we are suggesting the following kinetic correction in fluid equation. Since electrons are predominantly deviate from hydrodynamic limit the local expression for parallel heat conductivity in energy equation, $q_{e,SH}(y) = -\chi_{SH}\partial T_e / \partial y$ can be replaced by:

$$q_e(y) = \int_{-L}^{+L} G(y - y') \cdot q_{e,SH}(y')dy', \qquad (28)$$

where

$$G(y-y') \approx \frac{1}{2\lambda(y')} \exp\left(-\left| \int_{y}^{y'} \frac{d\eta}{\lambda(\eta)} \right| \right) \tag{29}$$

Here

$\lambda(y) = V_{Te}(T_e^*) \cdot \tau_{ei}(n, T_e^*)$ and $T_e^* \approx 3.8 \cdot T_e$

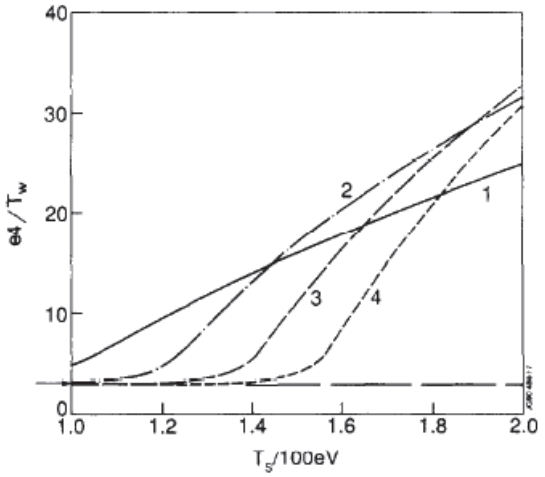

Fig. 2: The influence of hot particles on the sheath potential $e\varphi / T_w$ versus temperature T_s, and density n_s at the separatrix:
(1) $n_s = 1 \cdot 10^{13} cm^{-3}$, (2) $n_s = 2 \cdot 10^{13} cm^{-3}$,
(3) $n_s = 3 \cdot 10^{13} cm^{-3}$, (4) $n_s = 4 \cdot 10^{13} cm^{-3}$
and T_w is, the temperature at the plate.

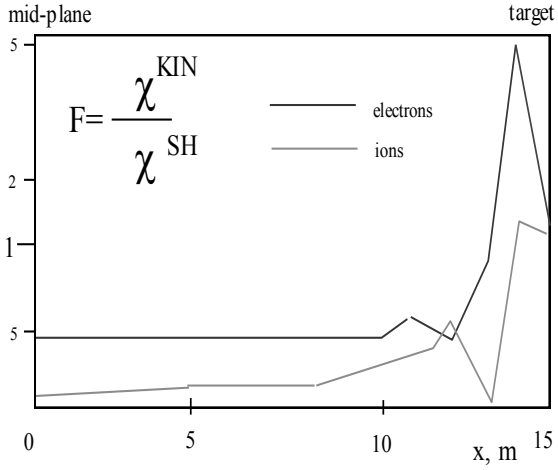

Fig. 3: Kinetic correction to heat conductivity vs. distance along B; here $F = 1/FLF$; Heat flux near the plate increases several times due to the contribution of supra thermal particles.

Analyse of kinetic correction of fluid equations shows, that the supra thermal particles are largely responsible for the parallel transport in boundary plasma. Non-locality produces two kinds of effect on the heat flow: reduction in the hot region of the SOL and enhancement in the cool region near the plate. Reduction of the heat conductivity results in stronger temperature gradients and, this, in combination with pressure balance along B reduces upstream plasma densities. Supra thermal particles can considerable enhance the sheath potential and increase neutral ionization and excitation rates. An efficient numerical procedure for kinetic correction to 2D fluid includes the following corrections:

1) the flux limit factors for electron and ion heat flux along B or
2) the introduction of non-local heat flux expression (which changes energy equation to integer-differential and requires another numerical solver).

Model for H-Mode Pedestal formation

During the L to H-mode transition, when input power, Q .exceeds some critical value, Q_{LH} [3]:

$$Q_{LH} = 0.084 \cdot \bar{n}^{0.73} B_T^{\ 0.74} S^{0.98} M^{-1} \tag{30}$$

a strong pressure gradient forms at the edge because of the turbulent transport suppression outwards beyond some radial position. This pressure gradient separates the anomalous core and the neoclassical pedestal region, which spreads from the top of the pedestal up to separatrix and is marginally stable. There are two suppression factors: 1) proportional to $1/\left(1 + k \cdot \left(\omega_{ExB} / \gamma\right)^2\right)$, where γ is an increment of the ion temperature gradient (ITG) instability and ω_{ExB} is ExB shearing rate, and 2) due to increase of edge (e.g. bootstrap) current and, consequently, the magnetic shear at the edge. Since $\gamma \sim 1/s$, increase of shear sup-

presses the turbulence. We assume here, that the turbulent transport is mainly suppressed by $\boldsymbol{E_r \times B}$ velocity shear at the plasma edge. This means, that the radial transport coefficients for thermal conductivity and particle diffusion drop down to subdominant (neoclassical) value:

$$\chi_{e,i} = \chi_{e,i}^{an} \cdot \left\{ 1 + k \cdot \left(\frac{\omega_{ExB}}{\gamma(s)} \right)^2 \right\}^{-1} + \chi_{e,i}^{neo} \tag{31}$$

$$D_{e,i} = \chi_{e.i} \cdot n \tag{32}$$

Here $\chi_{e,i}^{an}$ is the anomalous conductivity, which dominates in the core region, where $\gamma > \omega_{ExB} \sim 0$. Within pedestal region, where $\gamma < \omega_{ExB}$, anomalous transport is suppressed by the magnetic shear *s* and ExB shear. In this region the dominate transport is neoclassical (second term in (4)). Here *k* is some fitting factor~1. The anomalous conductivity is

$$\chi_{e,i}^{an} = \chi_{GB} \approx \rho_{tor}^2 C_s / s^{\varepsilon} \Delta_{ped} \tag{33}$$

and

$$\gamma_s = \chi_{GB} k_\perp^2 \approx \rho_{tor}^2 C_s k_\perp^2 / s^{\varepsilon} \Delta_{ped} \qquad k_\perp^2 \rho_{tor}^2 \approx 0.03 \tag{34}$$

where γ is the growth rate of a gyro-Bohm type instability. Expression for shearing rate ω_{ExB} reads as:

$$\omega_{ExB} = \frac{\partial}{\partial r}\left(\frac{E_r}{B} \right) \approx \frac{\partial}{\partial r}\left(\frac{\nabla p}{n \cdot B} \right) \approx \rho_{tor} C_s / \Delta_{ped}^2 \tag{35}$$

Here we assume, that $E_r \approx en\nabla p$ and $\nabla p \approx nT / \Delta_{ped}$ .The width of the pedestal region, Δ_{ped}, can be defined as a radial position inside the separatrix , where turbulence is suppressed by the combined effect of the magnetic and $\boldsymbol{E \times B}$ shear (see Fig. 4). The pedestal width depends on the toroidal Larmor radius ρ_{tor} and the magnetic shear $s(r)$, and can be expressed as:

$$\Delta_{ped} = \rho_{tor} \cdot s^2 \qquad \rho_{tor} = 3.23 \cdot 10^{-3} \cdot B_T^{-1} Z^{-1} \sqrt{A \cdot T_{i,}} \tag{36}$$

Here B_T is the toroidal magnetic field in Tesla, A is the mass number, Z is the charge state, T_i is the ion temperature in keV, ρ is in m. The shear depends on radial position, but for simplicity sake it can be arbitrarily chosen at 95% flux surface.

The pedestal width, Δ_{ped} be define as a radial position where:

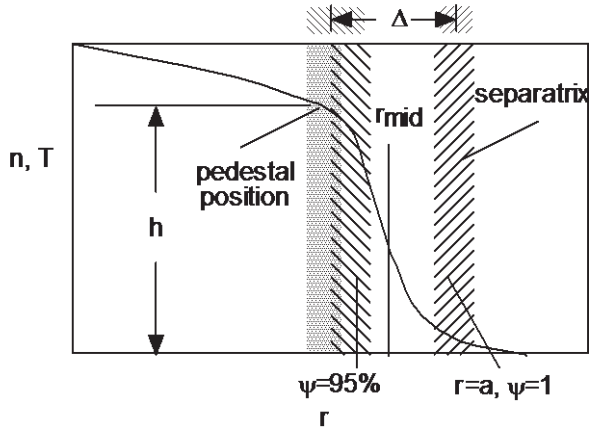

Fig. 4: Definition of pedestal width.

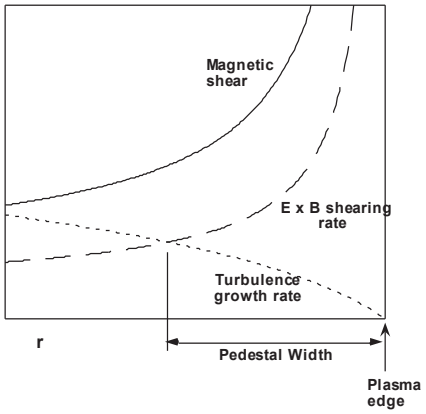

Fig. 5: Pedestal width is defined at radial position where turbulence is suppressed by magnetic and electric shear.

The radial transport suppression in TOKES, which describes the L to H transition is implemented (taking into account threshold dependence of the H-mode onset on input power) as

$$\chi = \frac{\chi_{an}}{1 + \mu\theta(Q - Q_{LH})(s^2 \rho_i / k_{ped})^2} + \chi_{neo} \qquad (37)$$

where $\Delta_{ped} \propto \mu\rho_{tor} s^{\varepsilon}$ and $k_{ped} \approx p / \nabla p$

For ITER Q_{LH} value is estimated about 60MW.

Conclusions

The main purpose of this report is the development of analytical and numerical transport models of the tokamak plasma, suitable for implementation into the integrated transport code. The tokamak edge plasma in reactor configurations is expected to be rather thin outmost area with strong radial plasma gradients inside the separatrix and the area outside the separatrix, a scrape-off layer (SOL), with open magnetic field surfaces, terminated at the divertor plates. The region beyond the separatrix plays an important role because it serves as a shield, protecting the wall from the hot plasma and bulk plasma from the penetration of impurities and because it is mostly affected by transients. The transport model, proposed here, provides plasma density, temperature and velocity distribution along and across the magnetic field lines in bulk and the edge plasma region. It describes the dependence of temperature and density at the separatrix on the plasma conditions at the plate and the efficiency of the divertor operations, depending on power and particle sources. The calculation gives eventually the power and particle loads on the divertor plates and side walls. The following tasks have been completed:

- The 2D transport model for the SOL have been prepared and implemented into the TOKES code. This model is suitable for description of stationary plasma processes in the edge tokamak region.
- The model of pedestal formation at the plasma edge in H-mode operation was implemented in TOKES. The model based on power scaling for L to H transition and includes the mitigation of turbulence at the edge once the flowing power exceeds the H-mode onset threshold.
- The boundary conditions for fluid equations at the divertor plates and at the main chamber wall are formulated and implemented into the integrated code.
- Analyses of available experiments and benchmarking with simple analytical solutions in respect to SOL transport phenomena will be provided.

Staff:

Yu. L. Igitkhanov

Literature:

[1] Braginski S.I., Reviews of plasma physics (ed. Leontovich, M.A.),Vol. 1, Consaltants Bureau, New York (1965).

[2] Igitkhanov Yu., Kukushkin A., Pigarov Yu., Pistunovich V., Sov. J. Plasma Physics12(1) January 1986

[3] ITER Physis Bases; Nucl. Fusion 39, (1999)

Acknowledgement

This work, supported by the European Communities under the EFDA contract of Association between EURATOM and Karlsruhe Institute of Technology, was carried out within the framework of the European Fusion Development Agreement. The views and opinions expressed herein do not necessarily reflect those of the European Commission.

Extend Physics Assessment of Novel Configurations (WP13-PEX-02-T02-01)

Introduction

In this report we assess some important physics issues related to the snowflake (SF) configuration, namely effect of flux expansion/connection length/poloidal length on stability of impurity radiation in SF configuration and the coupling of MARFE with the ballooning type MHD instability.

Effect of flux expansion/connection length/poloidal length on stability of radiation

In the snowflake (SF) configuration the poloidal magnetic flux becomes strongly broadened well above the second-order null point, making the geometrical connectivity of the divertor with the main SOL easier than in the standard divertor. This may lead to the increased impurities flow to the vicinity of the null point and an increase of plasma radiation from that region. The plasma radiation locally decrease the temperature in circumstances where the cooling itself leads to an increase of radiation and hence the further cooling. Below we will consider a 2D stability analysis of the MARFE-type perturbation inside the last magnetic surface in a toroidal geometry with a separatrix and will show that the broadening of the null point region facilitates the onset of thermal instability. The impurity radiation loss is proportional to the electron density, n, the impurity fraction f_z, the local emissivity, L, and the volume of the radiative region, dV:

$$W = \int f_Z n^2 L(T,n) dV \approx \overline{f_Z n^2 L \cdot V}_{rad} \qquad (1)$$

The radiative volume V_{rad} is determined by the peak of either f_z , L , or n^2 . Each of those parameters can strongly affect the magnitude of impurity radiation. Experimental observations show that for some cases (MARFE [1], and radiative divertor [2]) a significant amount of radiation (approximately a half) is coming from relatively small volume of rather cold plasma. It is possible that this effect may be explained by the local increase of the emissivity and impurity fraction f_z. However, even for f_z = const., and L = const. these features of the MARFE and radiative divertor can be explained by high value of n^2V in the low temperature region caused by the perpendicular plasma energy transport. Impurity radiation in simple 1D approximation can be easily expressed as

$$W \approx 4\pi R \cdot \Delta_0 \cdot \sqrt{2\int^{T} f_z \cdot n^2 \cdot \chi_{//}(T) \cdot L(T) \cdot dT} \qquad (2)$$

Here $\chi_{//} = \chi_0 T^{5/2}$ is the electron conductivity along B and Δ_0 denotes the SOL width at the mid-plane. However, the radiation is localized in the vicinity to null point, where the SOL width Δ is broader than at the mid-plane because of the contribution of heat transport across the field lines and the magnetic geometry of the SF configuration:

$$\Delta \propto \Delta_0 \cdot \sqrt{\chi_{//} / \chi_{\perp}} \cdot \left(\frac{b}{\Delta_0} \right)^{2/3} \qquad (3)$$

Substitution of this estimate in Eq. (2) gives $W \approx \sqrt{\chi / \chi_{\perp}} \cdot (..\chi.)^{1/2} \propto \sqrt{\chi_{\perp}}$ or

$$W \approx S_{rad} \cdot \sqrt{2\int^{\infty} f_z \cdot n_2 \cdot \chi_{\perp}(T) L(T) dT} \,, \qquad (4)$$

Therefore, a strong impurity radiation occurs in the low temperature region, where the perpendicular plasma heat transport dominates. Here S_{rad} is the surface of the radiating flame enveloping the area near the null point. The upper limit of the integral in Eq. (4) can be taken

infinity, because the integral converges unless $\chi_\perp$, f_z or L increase very rapidly with the temperature increase.

The radiation losses can be roughly estimated from the energy balance equation on the close magnetic surfaces close to separatrix by retaining only radial derivatives in the energy balance equations and considering the parallel heat transport as a sink:

$$\chi_\perp \nabla_\perp \cdot T \approx f_z n^2 L - \chi_0 \frac{T^{5/2}}{l^2} \tag{5}$$

The connection length l between the equatorial plane and the vicinity of the null point for the standard divertor is $l = (qR)ln(b/\Delta_0)$, where q, R and Δ_0 (the SOL thickness) are taken at the equatorial plane. For the SF case $l_{sf} = (qR)\,(a^2/b\Delta_0)^{1/3} = l\cdot(a/b)^{1/3}(a/\Delta_0)^{1/3}/\,ln(b/\Delta_0)$ that considerably exceeds l [3]. Linearizing Eq. (5) and assuming adiabatic type of perturbation one gets the condition for the instability onset:

$$f_z \cdot n \cdot T^2 \frac{d}{dT}\left(\frac{L(T)}{T^2}\right) > \left(\frac{\pi}{\Delta}\right)^2 \cdot \chi_\perp + \chi_0 \frac{T^{7/2}}{n \cdot l^2} \tag{6}$$

In the vicinity to null point $l \to \infty$ and the last term in (6) can be omitted. Therefore, the increase of connection length reduces a stabilizing effect of parallel heat flux. The heat flux due to the perpendicular thermal conduction varies as $1/\Delta^2$. Δ being determined in part by the width of a radiative cloud above the null point and this in turn depending on the radial temperature gradient. Simple assessment can be made without solving Eq.(6) by assuming that temperature in the cloud is about T~20eV, density ~ 10^{20}m^{-3}, the anomalous value of $\chi_\perp \sim 3\mathrm{m}^2\mathrm{s}^{-1}$ and $\chi_{//} \sim 1.3\cdot 10^{22}\cdot T^{5/2}$. Compering two terms on the r.h.s. of Eq. 6 it is seen that perpendicular thermal conduction is dominant for $\Delta \le 23/T^{5/4}\,(eV) \sim 50\mathrm{cm}$. Using the coronal emissivity for carbon impurities to estimate the radiation term in Eq. (6) for considered density and temperature a typical value might be ~ 10^{26} f_z m^{-3} s^{-1}. This term should be compared with the first term in the r.h.s. of Eq. 6, which gives $f_z \ge 0.25/\Delta^2$, where Δ is in cm. For our estimations we will take $\Delta \sim$ 15cm. Therefore, for example, a 0.1% impurity level would sustain a MARFE with the width greater than 15cm. Fig. 1 shows the marginal impurity level in the case of the SF configurations and for the conventional x-point case.

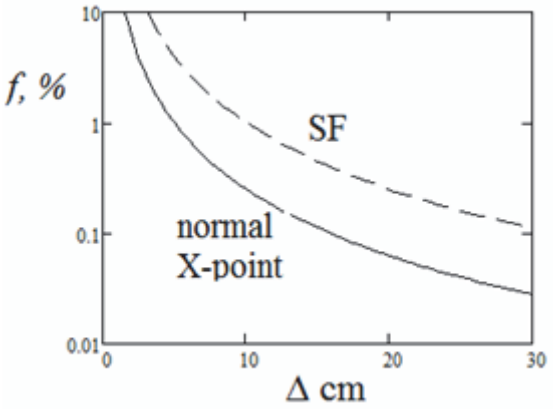

Fig. 1: Impurity concentration (carbon) required for onset of the temperature instability in the case of the SF (dashed) and conventional x-point divertor.

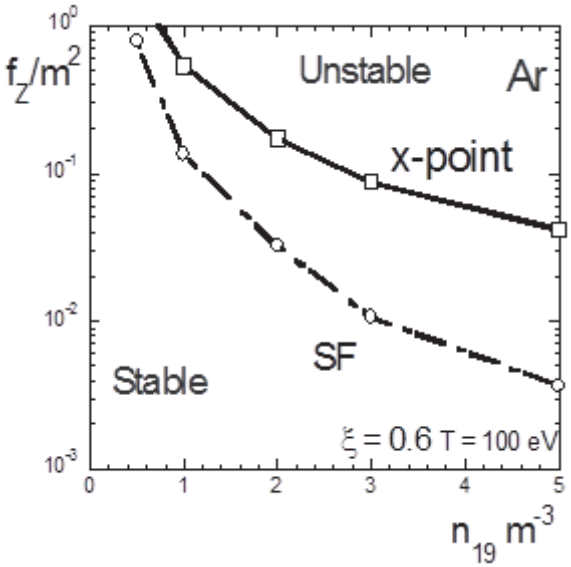

Fig. 2: Ar concentration vs. plasma density at given toroidal mode number m, boundary temperatures T = 100eV, $\xi = 0.6$; above the curves the configuration is unstable for both cases (see details in appendix).

It is important to note additionally that in the case of SF configuration Δ substantially exceeds that for the conventional x-point configuration. The smaller temperature gradient length the weaker the stabilizing effect is and, a smaller impurity concentration could trigger the instability. This simple assessment shows that the SF configuration is more vulnerable to the onset of MARFE type instability. The main reason eventually is the higher concentration of plasma/impurity density expected in the broader region above the null-point on the closed magnetic surfaces in the SF configuration.

The detailed analysis of thermal instability onset has been carried out for the x-point configuration (see the attachment below). In the Fig. 2 the critical impurity concentration (in this case of Ar) required for MARFE onset as a function of the plasma density for the SF and the normal x-point configurations is shown. The perturbation mode number *m* is localized at the radial ξ=0.6 position. It is seen that the SF configuration is more vulnerable to the onset of MARFE. It can be triggered at lower impurity concentration. For higher densities above the null-point the difference in marginal impurity concentration f_z is more pronounced. Excitation of high toroidal mode numbers occurs for smaller concentration

Coupling of ballooning instability with thermal (MARFE) instability under DEMO conditions

Here we analyze a snow flake (SF) alternative divertor magnetic configuration with respect to coupling of ballooning instability with thermal (MARFE) instability under DEMO conditions [4]. We also consider of ballooning instability in specific snow-flake topology of magnetic field in the vicinity to X-point. The separatrix and x-point region is immediate affected by boundary plasma and as a result could trigger MHD instability. However the features of MHD perturbation near the expanded SF region is not well known .Ballooning modes appear to be the most unstable in this region due to increase of potential magnetic well. The ballooning equation for the marginal stability reads as:

$$\left(\vec{B}\nabla\right)\left[\frac{k_\perp^2}{B^2}\left(\vec{B}\nabla\right)\xi\right]+2(1-\gamma)\left(\left[\vec{B}\times\vec{k}_\perp\right]\nabla p\right)\left(\frac{\left[\vec{B}\times\vec{k}_\perp\right]\vec{k}}{B^4}\right)\xi=0 \qquad (1)$$

Metrics for SF geometry is simplified and is taken as magnetic topology of the straight current strings combine with the toroidal angle ϕ (see Fig. 3).

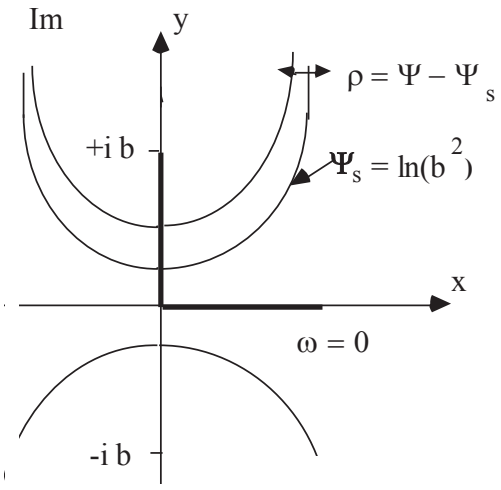

Fig. 3: Magnetic topology of the straight current strings.

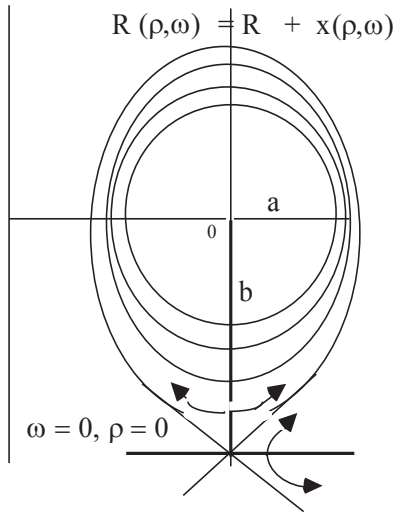

Fig. 4: Magnetic topology of SF used for ballooning stability analysis.

$$ds^2 = h_\rho^2 d\rho^2 + h_\omega^2 d\omega^2 + R^2 d\phi^2$$

And near the SF region, were ρ,ω <<1

$$h \equiv h_\rho = h_\omega = \frac{b}{2\sqrt{1-\cos\omega+\rho^2/2}}$$

The flux expantion at the SF-region:

$$\Delta_{X-point} \approx \sqrt{\Delta_{mid-pl.} b}$$

Criterion of ballooning stability near the separatrix and SF area can be derived as follows. Using the magnetic topology shown in Fig: 4 the criterion for ballooning stability can be written as [5]:

$$\left.\frac{dP}{d\rho}\right|_{X-point} < Const \frac{B^2 R}{q^2} \frac{b}{\sqrt{\rho}}, \qquad (2)$$

or as:

$$\frac{4\pi q_\pi{}^2 R}{B^2}\left(\frac{dP}{dr}\right)\Big|_{mid-plane} > \sqrt{\frac{b}{\Delta}} \quad or \quad \left(\frac{dP}{dr}\right)\Big|_{mid-plane} > \frac{b}{P_0}\left(\frac{B^2}{4\pi q^2 R}\right)^2 \qquad (3)$$

Where

$$\alpha \equiv \frac{4\pi q_\pi{}^2 R}{B^2}\left(\frac{dP}{dr}\right)\Big|_{mid-plane} > \frac{b}{P_0}\left(\frac{B^2}{4\pi q^2 R}\right)$$

Here the safety factor q was taken as: $q_\pi(\rho) \equiv q_\pi(0.1) = q_{95}/3$

Neglecting the dependence on shear and assuming that P_0 is the pedestal pressure, one can find that:

$$\left.\frac{\partial P}{\partial r}\right|_{x-point} \approx \frac{P}{\sqrt{\Delta_{mid.-pl.} b}} < Const. \frac{B^2}{4\pi R q_s^2} s(q,k,\varepsilon,\delta), \quad where\ q_s = q_{95}\frac{\pi}{6}\ln(4\pi/\rho),$$

The difference in magnetic potential well for the SF case and normal X-point configurations are shown in Fig. 5.

One can conclude that due to different magnetic well inside and outside in the case of SF configuration the critical pressure gradient inside is less than outside. From Ballooning MHD mode stability ($\Delta_{mid.-plane} \sim \lambda\ \rho_\theta$) follows the edge density limitation:

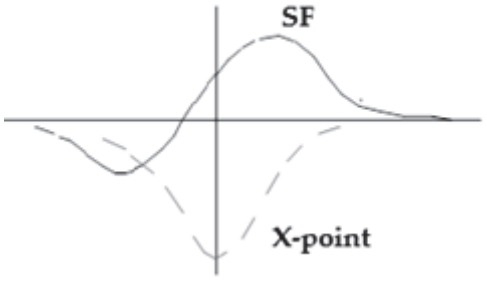

Fig. 5: Magnetic well in case of SF and normal X-point configurations (dashed line).

$$n_{[10^{20}m^{-3}]} < 1.15\left(\frac{I_{MA}}{\pi a^2}\right)^{3/2}\left(\frac{1}{T_{100}^{3/4}}\right)\left(\frac{R}{a}\right)^{3/4}\frac{A^{1/4}\sqrt{k}}{(1+k^2)^{3/4}}\lambda a\ s(k,\delta,\varepsilon q)$$

From the other side, the requirements to avoid thermal (MARFE) stability

$$\chi_{//}^{0}T^{5/2}/Z_{eff}R^2q^2 \quad > \quad n^2C_Z\overline{L_Z}, \qquad where\ \overline{L_Z}=(2L-TdL/dT)$$

electron density at the separatrix mid-plane has to be

$$n_{[10^{20}m^{-3}]}=\frac{45\left(T_{100}\right)^{7/4}}{qR}\frac{1}{\sqrt{\overline{L_Z}C_Z Zeff}}$$

Thermal - Ballooning stability diagram is shown in Fig. 6.

Thermal instability (MARFE) is suppressed for higher temperature range, whereas the ballooning modes are unstable for higher pressure. Critical density can for perturbation in inner region (see Fig. 6) reads:

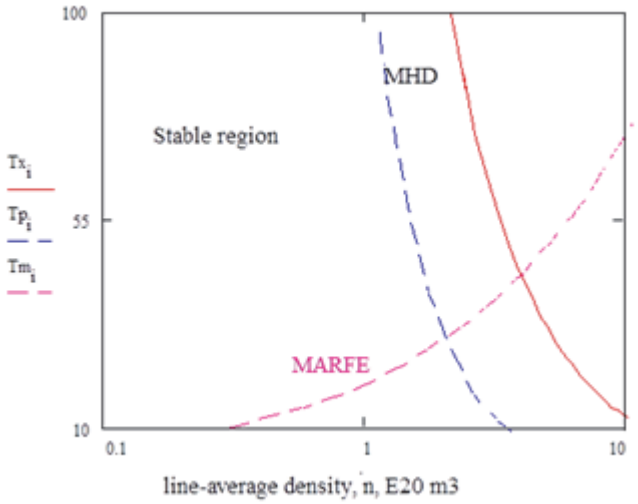

Fig. 6: Stability diagram for DEMO. For expecting densities at the edge (>10^{20} m^{-3}) and temperatures above several keV the SF divertor will be unstable against the coupled ballooning-thermal modes.

$$n_{[10^{20}m^{-3}]}=1.15\left(\frac{I}{\pi a_m^2}\right)\frac{a_m^{0.175}R^{-0.3}}{\left(\sqrt{Z_{eff}\,\alpha\overline{L_{33}}C_Z q_{95}^2}\right)^{3/10}}\left(\frac{A^{1/4}\left(s\sqrt{k\lambda}\right)}{(1+k^2)^{3/4}}\right)^{7/10}$$

and for outer region

$$n_{[10^{20}m^{-3}]}=0.67\left(\frac{I}{\pi a_m^2}\right)^{7/9}\frac{1}{\left(Z_{eff}\,\alpha\overline{L_{33}}C_Z q_{95}^2\right)^{1/9}}\left(\frac{A(s\lambda)^2}{\sqrt{\frac{R}{a}}(1+k^2)}\right)^{7/18}$$

In conclusion one can state that:

The analysis of a density limit in tokamaks for DEMO configuration is done for up-down symmetric equilibrium of SF configuration. It is shown that the ideal ballooning mode significantly change their feature. The ballooning perturbation inside the configuration is much weaker, than outside, due to the stabilizing effect of a favorable magnetic curvature in inner side. The upper attainable density exhibits almost linear dependence on the plasma current similar to the Greenwald limit. However it differs from the Greenwald value: at low temperatures (<100eV) this limit is less restrictive. A weak dependence on impurity content was ob-

tained. However the influence of impurities can emerge through the resistive modes, which in turn can trigger the ideal modes.

Staff:

Yu. L. Igitkhanov

Literature:

[1] Lipshultz B., J. Nucl. Mater. 1458~147, (1987) 15.

[2] Porter G., Bulletin of the American Physical Society, 40 (1995) 1693.

[3] Ryutov D.D. Phys. Plasmas 14, 064502 (2007); doi: 10.1063/1.2738399

[4] Zohm H.: On the minimum size of DEMO, Fusion Science and Technology 58

[5] Pogutse O. et al., EPS, 1995

Acknowledgement

This work, supported by the European Communities under the EFDA contract of Association between EURATOM and Karlsruhe Institute of Technology, was carried out within the framework of the European Fusion Development Agreement. The views and opinions expressed herein do not necessarily reflect those of the European Commission.

Attachment

A MARFE–type thermal-radiation instability on closed magnetic field lines

Introduction

The thermal-radiation instability develops when a local decrease of temperature re-enforces the impurity radiation, causing a further cooling of the plasma, and when thermal conduction enables the compensation of this energy loss. The experimental observations indicate that the MARFE tends to locate itself near to the x-point, where it can be almost in quasi-steady state condition [1,2]. The linear stability analyses of the plasma edge parameters which provides the onset of the x-point MARFE should be carried out in a 2-D toroidal magnetic geometry with an x-point. The main problem of solving such a problem in the toroidal geometry is that the variables (usually they are the flux co-ordinates) are not separable, thus one is unable to apply the usual representation involving the ordinary Fourier expansion without having a mixture of the eigenmodes. The problem arises due to the poloidal variation of the metric coefficients and the equilibrium quantities. A number of investigations have been performed in this direction, reducing the 2-D problem to a 1-D problem by simply excluding the radial or poloidal heat flux in the heat equation or by considering the cylindrical approximation, thus ignoring the toroidal and x-point effects [3]. In some consideration the perpendicular heat fluxes were excluded because of the high classical electron heat conduction along the field lines, enforcing nearly constant temperature on magnetic flux surfaces. However, because of the strong temperature dependence of the classical parallel conduction and the electron heat flux limit at low densities, noticeable gradients along field lines are to be expected at typical tokamak edge parameters if there are sufficiently strong, localized energy sinks. These can be caused by, for example, impurity radiation. It is obvious that this simplification does not work close to the x-point, where the radial fluxes are expected to be strong. For the same reason the toroidal effects must be fully employed in the stability analyses of the MARFE-type perturbation in a realistic tokamak configuration [4]. Here we consider a 2D

linear stability analysis of the MARFE-type perturbation inside the last magnetic surface in a toroidal geometry with a separatrix. Based on the special type of perturbation which allows one to resolve the separability problem of the heat equation in toroidal geometry, we will prove that both the radial and parallel heat fluxes should be taken into account and cannot be omitted without change of the spectral properties of the anisotropic heat conduction equation. The separation of variables can be strictly performed in case of the 2D toroidal geometry including the x-point by employing a so-called "ballooning type" of perturbation. The ballooning representation has been first invented to overcome the same difficulty in the ballooning equation of the MHD perturbation in the toroidal geometry [5].

Below we will show that this type of perturbation, being applied to the heat equation can resolve the problem of the separability of the variables and to provide the analyses of the onset conditions without any "simplified" suggestions, corrupting the operator of the 2D differential equation.

Equation and topology for the standard divertor configuration

We begin the linear stability analyses by considering the heat equation in orthogonal flux coordinate system and assuming the constant pressure along the magnetic field lines:

$$\dot{\varepsilon} + \frac{1}{\sqrt{g}} \frac{\partial}{\partial x^i} \left(\sqrt{g} q^i \right) = S_\varepsilon, \quad \text{and} \qquad \left(\vec{B} \nabla p \right) = 0, \tag{1A}$$

where:

$$q^i \equiv - \chi_\perp g^{ik} \frac{\partial T}{\partial x^k} - (\chi_{//} - \chi_\perp) b^i (b^k \frac{\partial T}{\partial x^k}), \qquad \left| \vec{b}^2 \right| = 1 \tag{2A}$$

Here b^i and q^i are the covariant components of a unit vector in the direction of the magnetic field, $\vec{b} = \vec{B} / \left| \vec{B} \right|$, and the heat flux components, respectively. $\varepsilon = 3nT$. In (2A) we took into account the different heat conduction coefficients along *B*, $\chi_{//}$ and across the magnetic surfaces, $\chi_\perp$. The source term in (1A) arises from impurity radiation $S_\varepsilon = -n^2 c_z L(T)$, where n is a plasma density $L(T)$ is a cooling rate function and c_z is an impurity concentration. The rest of the definitions are obvious. We aim to consider the linear stability of the equations (1A) in toroidal geometry close to the separatrix area. For this purpose we choose the orthogonal flux co-ordinate system allowing for a plasma shape with x-point. For simplicity we choose the topology created by a pair of parallel wires carrying equal currents [6]. The model possesses a separatrix, with an x-point midway between the wires and allows one to investigate thermal stability at various distances from the separatrix and to examine the effect on marginal stability when changing the location (in poloidal angle) of the x-point. The metric coefficients can be expressed analytically. The line element in this case reads as: $ds^2 = h^2 (d\rho^2 + d\theta^2) + R^2 d\varphi^2$, where ρ is marking the magnetic surfaces, and θ and φ are the poloidal and toroidal angular variables. Here $g_{\psi\psi} = g_{\theta\theta} \equiv h^2, g_{\varphi\varphi} = R^2$, $\sqrt{g} = h^2 R(\theta, \varphi)$ and $h^2 = e^{2\rho} / 4 y_0^2 \mathrm{b}^2$. The major radius for the current point position at the surface is $R(\theta, \rho) = \frac{R_0}{y_0} \pm \sqrt{\frac{\mathrm{a} + \mathrm{b}}{2}}$. Here R_0 is the distance from the azimuthal axes to the current position at the mid-plane, y_0 is the distance of the current wire from the x-point position (see Fig.1A). Here $\mathrm{a} \equiv e^\rho \cos\theta - 1$ and $\mathrm{b}^2 \equiv (1 - 2e^\rho \cos\theta + e^{2\rho})$. We shall consider the surfaces lying inside the separatrix and they are labeled by a parameter ρ, such that when $\rho \to -\infty$ the surfaces become circular. As $\rho \to 0$, the shape of the surfaces approaches that of a separatrix and $h \propto 1/\rho$. For numerical convenience we will use below another parame-

ter for labeling the surfaces, ξ, which is linearly shifted relative to ρ, $\xi \equiv k\rho + const.$ Here $k \approx 7.9.$ ξ ranges from $-\infty$ at the core area to some positive value $\xi = \xi_{sep}$ ($\xi_{sep} \approx 0.58$) at the separatrix. The ψ_{95} distance corresponds to about $\xi_{95} \approx 0.6$. The poloidal magnetic field caused by straight currents and the toroidal magnetic field can be chosen as $b_\theta = \gamma / \sqrt{h^2 + \gamma^2}$, $b_\varphi = \sqrt{1 - b_\theta^2}$, $b_\rho = 0$, where $b_\theta \equiv B_\theta / B$, $b_\varphi \equiv B_\varphi / B$ are the physical components and $\gamma \approx const.$ is taken to match the ITER magnetic field. The heat equation in the orthogonal co-ordinates reads:

$$\frac{\partial}{\partial\theta}\left\{h^2 R q^\theta\right\} + k\frac{\partial}{\partial\xi}\left\{h^2 R q^\xi\right\} + \frac{\partial}{\partial\varphi}\left\{h^2 R q^\varphi\right\} = -n^2 c_z L(T) h^2 R \qquad (3A)$$

where $p \approx const.$ on the magnetic surfaces. Here

$$q^\theta \equiv -\frac{\chi_\theta}{h_\theta^2}\frac{\partial T}{\partial\theta} - (\chi_{//} - \chi_\perp)\frac{b_\theta}{h_\theta}\frac{b_\varphi}{R}\frac{\partial T}{\partial\varphi}; \qquad (4A)$$

$$q^\xi \equiv -\frac{\chi_\perp}{h_\rho^2}\frac{\partial T}{\partial\xi}; \qquad (5A)$$

$$q^\varphi \equiv -\frac{\chi_\varphi}{R^2}\frac{\partial T}{\partial\varphi} - (\chi_{//} - \chi_\perp)\frac{b_\theta}{h_\theta}\frac{b_\varphi}{R}\frac{\partial T}{\partial\theta}; \qquad (6A)$$

and $\chi_\theta \equiv \chi_\perp + (\chi_{//} - \chi_\perp) b_\theta^2$, $\chi_\varphi \equiv \chi_\perp + (\chi_{//} - \chi_\perp) b_\varphi^2$.

In equilibrium, due to the toroidal symmetry of the problem we can omit the third term in Eq.(4A). The equation reveals several equilibrium solutions which may be classified as those which have a constant temperature along the field line (MARFE-free, radial equilibrium) and to a MARFE equilibrium when the temperature varies along the field line, i.e. exhibit a MARFE-like character. The first case can also be considered as a poloidally symmetric radiating region on closed flux surfaces (detached MARFE) and its linear stability against the most unstable poloidal mode has been treated in [3] as an eigenvalue problem, ignoring the dependence of the metric coefficients on θ. In the geometry adopted here a poloidally symmetric equilibrium reads as a balance of the radial heat fluxes incoming to and outgoing from the poloidal layer:

$$\left\{Rq_\xi \frac{h}{k}\right\}_\xi^2 = \left\{Rq_\xi \frac{h}{k}\right\}_\infty^2 - \int_\infty^T 2n^2 c_z L(T)\left(\frac{hR}{k}\right)^2 \chi_\perp dT, \text{ where } q_\xi \frac{h}{k} d\xi = -\chi_\perp dT \qquad (7A)$$

Since the coefficients in this equation are the functions of ρ and θ, the equilibrium differs from that in [3]. In equilibrium the temperature gradient along the magnetic field lines from the midplane to the x-point caused by a strong radiative cooling due to impurity accumulation in the vicinity of the x-point. The stability analyses of equation (1A), with the periodic boundary conditions in poloidal direction on the closed magnetic field lines must be treated as an eigenvalue problem for the parabolic partial differential equation (3A). In this equation the thermal coefficients are functions of temperature and density: $\chi_{//} = \chi_{//,0} T^{5/2}$, $\chi_\perp = \chi_{\perp,0} nT$. The eigenfunction must be periodic in θ, φ space and zero in infinity with respect to ξ. Obviously the operator in (3A) is not separable as it stands. Following [5] we consider equation (3A) in "ballooning space"- which is the extended infinite θ domain and try the temperature perturbation of the form

$$T(\theta,\xi,\varphi) = W(y)e^{im\left(\varphi-\int_0^y q(\xi,t))dt\right.} \tag{8A}$$

where $y \equiv \theta - \theta_0$, m is a toroidal mode number and $q(\xi,y) \equiv \frac{h_\theta}{R}\frac{b_\varphi}{b_\theta}$. The trial function (8A) corresponds to a perturbation with a long parallel wavelength and short perpendicular wavelength with a large harmonic number $mq >> 1$. θ_0 is a free parameter in the ballooning presentation. The perturbation (8A) enables us to separate variables and brings us to the following 1D Schrodinger-type equation for $\Phi(y)$:

$$\Phi_y'' = \mathbf{U}(y,\xi,m,\gamma)\ \Phi\ , \tag{10A}$$

where $\Phi \equiv \frac{W}{b_\theta\sqrt{R}}$ and for the potential well we have:

$$\mathbf{U}(y,\xi,m,\gamma) \equiv \mathbf{U_m}(y,\xi,m) + \mathbf{U_Z}(y,\xi,\gamma) + \mathbf{U}_\theta(y,\xi,\nabla T_0) \tag{11A}$$

$$\mathbf{U_m}(y,\xi,m) \equiv m^2\frac{\chi_\perp}{\chi_{//}b_\theta^2}\left(\frac{h_\theta^2}{R^2b_\theta^2} + I_\xi^2\right) \tag{12A}$$

$$\mathbf{U_Z}(y,\xi,\gamma) = \gamma\frac{h^2}{\chi_{//}b_\theta^2}\frac{\partial}{\partial T}\left(\frac{L(T)}{T^2}\right) \tag{13A}$$

$$\mathbf{U}_\theta(y,\xi,\nabla T_0) = \frac{1}{4}\left(\left(\frac{\partial\ln(R\chi_\theta)}{\partial y} + \frac{\partial\ln\chi_\theta}{\partial T}\left(\frac{\partial T}{\partial y}\right)_0\right)\right)^2 + \frac{1}{2}\frac{\partial}{\partial y}\left(\left(\frac{\partial\ln(R\chi_\theta)}{\partial y} + \frac{\partial\ln\chi_\theta}{\partial T}\left(\frac{\partial T}{\partial y}\right)_0\right)\right) \tag{14A}$$

$$-\frac{1}{R\chi_\theta}\left[\frac{\partial}{\partial y}\left(R\left(\frac{\partial\chi_\theta}{\partial T}\right)\frac{\partial T}{\partial y}\right)\right]_0$$

Here $\gamma \equiv p^2c_z$ is the eigenvalue and we denote the equilibrium terms in (11A) by prescribing index 0. Equation (10A) is an ordinary 1D differential equation, which can be easily analyzed and solved numerically, assuming that a new independent variable y varies in the infinite domain. The boundary conditions are now: $\Phi(\pm\infty) = 0,\ \ y \in (-\infty,\ \infty)$. The basic idea of the chosen transformation is that the spectrum of this eigenvalue problem in the infinite θ range is the same as in the original equation (3) in the periodic poloidal domain [5]. Following the property of the ballooning modes only terms of the order of m^2 remained in equation (10A). Further we are solving the eigenvalue problem (10A-14A) numerically. The domain of integration of 5π in poloidal angle was found to be adequate. As a reference we took the DEMO - parameters (R=7.5 m, B =6T etc.). Argon has been taken as an impurity sample and the cooling rate L(T) was employed from [7], assuming a non-coronal radiative equilibrium. The second equation in (1A) for pressure balance along the magnetic field suggests that the pressure perturbation equals to zero and that impurity density variation follows the perturbation of the plasma ions. The first term U_m in the expression for the potential well (11A) is always positive. It represents the toroidal part of the perturbation and is attributed to a stabilizing role of the perpendicular (to the magnetic field lines) heat fluxes both along the magnetic surfaces ($\propto \frac{h_\theta^2}{R^2b_\theta^2}$) and across the surfaces ($I_\xi \equiv k\int_0^y \frac{\partial q}{\partial\xi}dy'$). The second term $\mathbf{U_Z}$ is a destabilizing term and is attributed to the thermal instability. This term creates a negative potential due to a negative slope of the cooling rate function in the corresponding tempera-

ture domain. The rest of the terms in $\mathbf{U}_\theta$ are associated both with the poloidal variation of the magnetic topology (volume element and the parallel heat flux) and with the equilibrium temperature gradient along the field lines. The stabilizing effect of the parallel heat flow reveals itself in denominators of all terms, which contain the value $\chi_\theta \approx \chi_{//} b_\theta^2$, so that the contribution of all terms (stabilizing or destabilizing) in the potential well is normalized to that of the parallel heat conductivity. In the vicinity of the x-point the flux expansion and the vanishing of the poloidal projection of the parallel heat flux should diminish the stabilising effect as $\frac{b_\theta^2}{h^2} \to \rho^{-4} (\rho \to 0)$ and $\mathbf{U}_m \to 0$ at the separatrix.

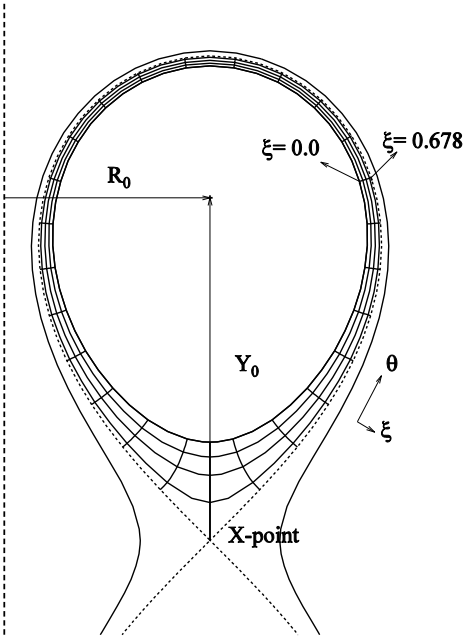

Fig. 1: Co-ordinate system allowing for the x-point.

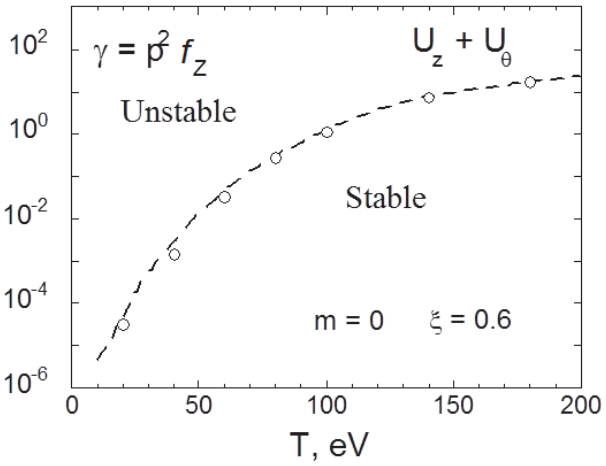

Fig. 2: Stability diagram for toroidally symmetric temperature perturbation on the magnetic surface at ξ =0.6 (95%); toroidally mode number m=0; At high temperatures modes become more stable.

First we consider the toroidally symmetric temperature perturbations (*m=0*). Fig. 2 shows the stability diagram for such perturbations at the magnetic surface position $\xi = 0.6$, which corresponds roughly to ψ_{95}. The stability diagram has two regions, the region above the marginal value of $\gamma = p^2 f_z$ which is unstable to MARFE and the region below this value where the temperature perturbations become stable. The marginal γ increases as expected for higher temperatures. Fig. 3 and 4 show the corresponding eigenfunction and potential behaviour vs. poloidal angle for T=100eV. Numbers on figures indicate: 1 for Um terms, 2 for Uz, 3 for the terms in U_θ proportional to the equilibrium temperature gradient, 4 and 5 represent the first terms in U_θ. The dashed line shows the resulting potential. It is interesting to note, that at θ = 0 the potential has a maximum (the eigenfunction passes through the minimum (see Fig. 3)) and the negative part of the well is shifted symmetrically away from the x-point. This indicates that the perturbations are more stable at the x-point, than expected. This result is attributed to the poloidal variation of the coefficient in U_θ, namely: $\frac{1}{2}\frac{\partial}{\partial\theta}\left(\frac{\partial \ln\left(Rb_\theta^2\right)}{\partial\theta}\right)$ which overcomes the negative contribution from U_z at the x-point and creates two negative wells in neighbouring positions to the x-point. The closer to the separatrix the well is located the deeper it becomes, however, in reality its shape and deepness do not change much, because they are limited by a similar term as the one in U_θ: $\frac{1}{4}\left(\frac{\partial \ln\left(Rb_\theta^2\right)}{\partial\theta}\right)^2$ which gives a positive

contribution. This is the reason, why the perturbations become almost insensible to the radial position from the separatrix (see Fig. 5), except in the very vicinity to x-point.

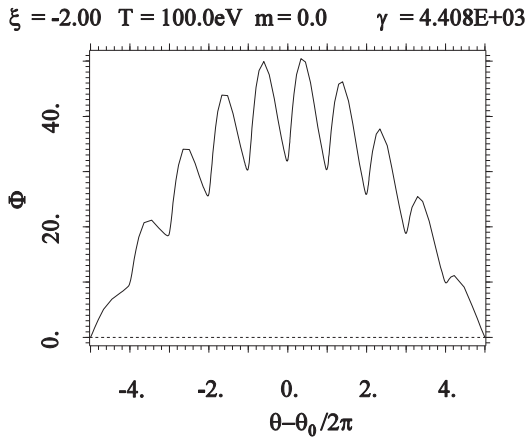

Fig. 3: The eigenfunction for m=0; T=100eV . It passes through the minimum at the x-point position.

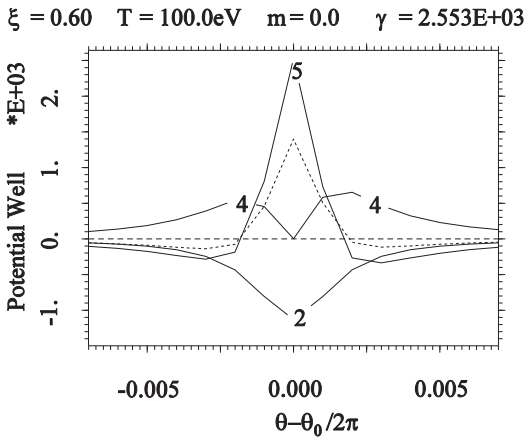

Fig. 4: Potential U vs. poloidal angle; toroidally symmetric perturbation, m=0; T=100eV . Dashed line is a sum of all terms; Um = 0. Potential has a maximum at the x-point.

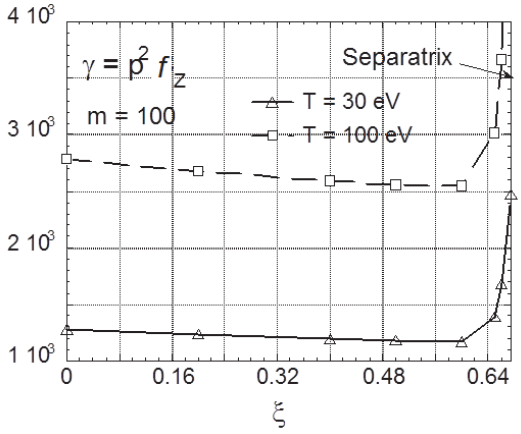

Fig. 5: Marginal value $p^2 f_z$ on the different magnetic surfaces, m=100; for T=30eV and T=100eV.
The perturbations are almost insensible to the radial position except to the very vicinity to the x-point.

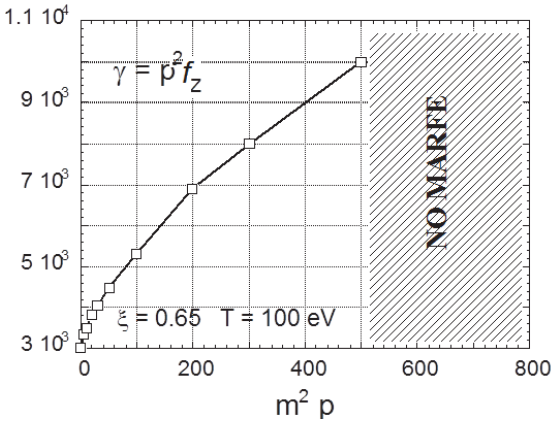

Fig. 6: Stability diagram for toroidal temperature perturbation on the magnetic surface, m>1; ξ =0.65 . Above some critical $m^2 p$ the perturbation does not exist anymore.

The stability of the toroidal perturbations ($m \neq 0$) is shown in the Fig. 6, 7. The critical impurity concentration f_z triggering a MARFE onset can be estimated for each toroidal mode number *m* (for given plasma density or pressure). The perturbations of this type become more stable due to the stabilizing role of the perpendicular heat fluxes. They are strongly stabilized especially near the x-point, where the perturbations on each magnetic field line approach each other, resulting in strong gradients both across and along the surfaces. This increases the fluxes and brings about the stabilization. Far from the x-point position, the shape of the potential well becomes more shallow (see Fig. 8) due to the positive contribution of U_m. We also investigated how sensitive is stability against the poloidal variation of the temperature. We chose the equilibrium temperature profile along the field line as $T(\theta) = T_1 - T_2 \cos\theta$, where T_1 is some average temperature. By varying T_2 we find that the potential well (being mostly affected by U_z) becomes negative and centered at the x-point, whereas the contribution of the rest terms in U_θ is negligible. This effect of destabilization (the increasing of U_z) is mainly due to the lowering of $\chi_\theta(T, \theta)$ at low temperatures.

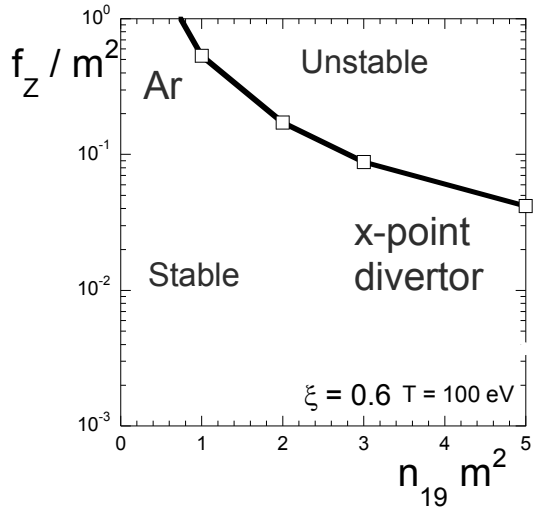

Fig. 7: Ar concentration f_z vs. plasma density for arbitrary toroidal mode number **m** and at the radial position ξ=0.6. The boundary temperature T=100eV.

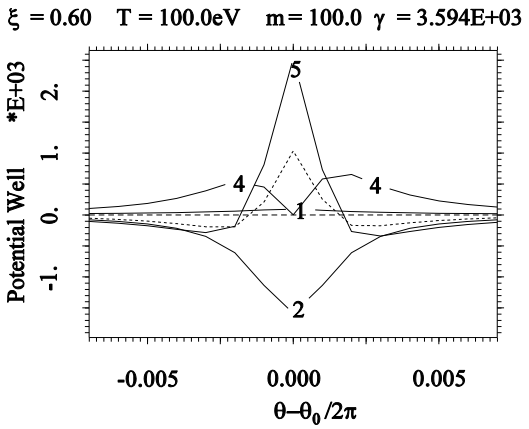

Fig. 8: Potential U vs. poloidal angle; toroidally non-symmetric perturbation, m=100; T=100eV.

Topology of the 2nd order null point configuration in the SF divertor

The snowflake divertor (Ryutov 2007, Phys. Plasmas 14, 064502) uses a 2nd order null of the poloidal magnetic field instead of the 1st order null used in the standard divertor. This leads to a number of interesting geometric properties such as stronger fanning of the poloidal flux, stronger magnetic shear in the edge region, larger radiating volume, and larger connection length in the scrape-off layer. These can potentially lead to new ways for alleviating heat loads on the divertor target plates. For our purpose important is that a strong flaring of the scrape-off layer near the null-point compare with the x-point configuration. The model the SF configuration employed here is created by three straight wires as it shown in the Fig. 11. Although this configuration is unstable, we use it just for illustrative purposes. Because of a larger poloidal flux expansion the connection length between the equatorial plane and the vicinity of the null is higher for the SF configuration. The connection length between the equatorial plane and the vicinity of the null point for the standard divertor is $L = (qR)ln(b/\Delta_0)$, where q, R and Δ_0 (the SOL thickness) are taken at the equatorial plane (see Fig. 1and Fig. 10).

For the SF case the SOL connection length, $L_{sf} = (qR)\,(a^2/b\Delta_0)^{1/3} = L\bullet(a/b)^{1/3}(a/\Delta_0)^{1/3}/\,ln(b/\Delta_0)$ (see Fig. 11). In this configuration the magnetic flux becomes strongly broadened well above the second-order null point, making the geometrical connectivity of the snowflake divertor with the main SOL easier than in the standard divertor (see Fig. 12). This may lead to the increased impurities flow to the vicinity of the null point and increase the plasma radiation. The plasma radiation from the null point region could locally decrease the temperature in circumstances where the cooling itself leads to increase radiation and hence the further cooling. It was shown that the broadening of the null-point region facilitates the onset of thermal instability. The longer connection length the stronger plasma cooling by radiative losses is expected. We skip here all numerical details of stability analysis (which is similar to the previous consideration apart from the metric coefficients, which are different). In Fig. 2 in the main text the critical impurity concentration (Ar) required for MARFE onset is shown as a function of the plasma density for the cases of SF and normal x-point configurations.

Conclusive remarks

The main results are the following. The 2D linear stability problem of a MARFE-like temperature perturbation on closed magnetic surfaces has been reduced to a 1D eigenvalue problem using the ballooning representation for the perturbation. This type of a perturbation has a long parallel wavelength and short perpendicular wavelength typical for ballooning modes. The toroidally inhomogeneous temperature perturbations with non-zero mode toroidal num-

bers, m, having a weak variation along the magnetic field lines have been analysed and compared with toroidally symmetric temperature perturbations (*m*=0). The trial functions for the temperature perturbations for both (*m*=0) and (*m* >1) cases are localized on the closed magnetic surfaces near the x-point. The toroidal mode numbers *m* of marginally stable perturbations were found as a function of impurity concentration (at given plasma density or pressure).The geometry effects (variation of the metric coefficients with poloidal angle) have a strong influence on stability, ensuring localization of the MARFE-type perturbation slightly above the x-point.

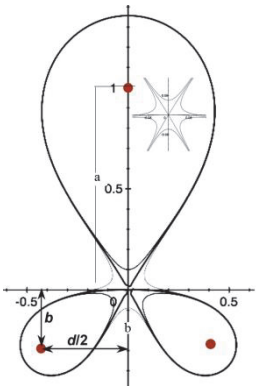

Fig. 9: The SF configuration created by three straight wires (D.Ryutov 2007, Phys. Plasmas 14, 064502).

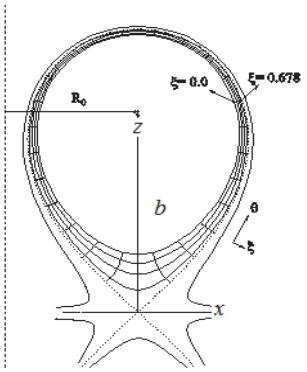

Fig. 10: The SF configuration in poloidal cross section. The region above the null-point is expanded.

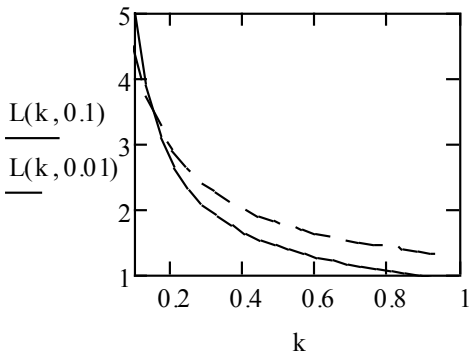

Fig. 11: The connection length in the SOL for the SF L_{SF} (dashed line) and for the normal x-point configuration. a=5m, k=b/a, Δ_0 = 0.1m is the SOL width at the mid-plane. L_{SF}= (qR) $(a^2/b\Delta_0)^{1/3}$ = L•(a/b)$^{1/3}$(a/Δ_0)$^{1/3}$/ ln(b/Δ_0).

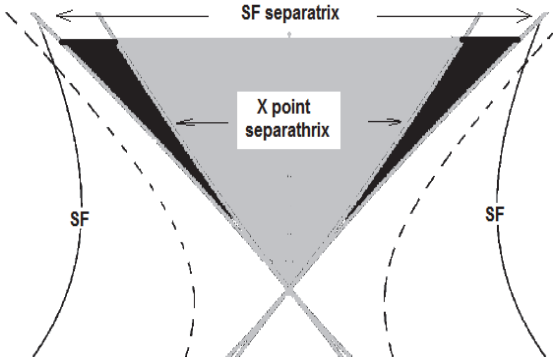

Fig. 12: The expansion of the region above the null-point in the case of the SF configuration. Because the null of the poloidal field is now of a higher order than in a standard X-point configuration, the magnetic flux threading the scrape-off layer SOL expands near the null point stronger than in a standard situation.

Staff:

Yu. L. Igitkhanov

Literature:

[1] B. Kadomtzev " Tokamak plasma: A Complex Physical System", plasma physics series, Editor: Prof. E. Laing, Institute of Physics Publishing, Bristol & Philadelphia, 1992

[2] V. Mertens et al.16th IAEA Fusion Energy Conference, IAEA-CN-64/A, Montreal, 1995.

[3] J. Wesson, T. Hender, Nuclear Fusion 33, 1019 (1993)

[4] A. De Ploey et al, MARFEs: A magnetohydrodynamic Stability Study of Two-dimensional Tokamak Equilibria, JET-P(96)49

[5] J. W. Connor, R. J. Hastie and J.B. Taylor, Phys. Rev. Letts. 40, p.396, (1978)

[6] G. Hobbs, J. Taylor, The properties of Linear Filamentary Multipole Magnetic Fields, UKAEA, Culham Lab., Rep. CLM-R-95 (1968);

[7] D. Post et. al. Atomic Data and Nuclear Data Tables 20,397, (1977)

Physics: Heating and Current Drive – ECRH

Microwave Heating for Wendelstein 7-X (CoA)

Introduction

Electron cyclotron resonance heating (ECRH) and current drive (ECCD) are the standard methods for localized heating and current drive in future fusion experiments. Thus, ECRH will be the basic day-one heating system for the stellarator W7-X which is currently under final construction at IPP Greifswald. It is expected that the ECRH system for W7-X will be finalized in 2014. In its first stage W7-X will be equipped with an 10 MW ECRH system operating at 140 GHz in continuous wave (CW).

The complete ECRH system is coordinated by the project “Projekt Mikrowellenheizung für W7-X (PMW)”. PMW has been established by KIT together with IPP and several EU partners in 1998. The responsibility of PMW covers the design, development, construction, installation and system tests of all components required for stationary plasma heating on site at IPP Greifswald. PMW coordinates the contribution from Institut für Plasmaforschung (IPF) of the University of Stuttgart too. IPF is responsible for the microwave transmission system and part of the power supply (HV-system). IPP Greifswald is responsible for the in-vessel components and for the in-house auxiliary systems. PMW benefits from the collaboration with Centre de Recherche de Physique des Plasmas (CRPP) Lausanne, Commissariat à l´Energie Atomique (CEA), Cadarache and Thales Electron Devices (TED), Vélizy.

A contract between CRPP Lausanne, FZK Karlsruhe and TED, Vélizy, had been settled to develop and build the series gyrotrons. First step in this collaboration was the development of a prototype gyrotron for W7-X with an output power of 1 MW CW at 140 GHz.

Seven series gyrotrons have been ordered from industrial partner Thales Electron Devices (TED), Vélizy. First operation and long pulse conditioning of these gyrotrons is being performed at the test stand at KIT. Pulses up to 180 s duration at full power are possible (factory acceptance test, FAT) whereas 30 minutes shots at full power are possible at IPP (necessary for site acceptance test, SAT). Including the pre-prototype tube, the prototype tube and the 140 GHz CPI-tube, in total 10 gyrotrons will be available for W7-X in final state. To operate these gyrotrons, in addition to the Oxford Instruments and Accel magnets, eight superconducting magnet systems have been manufactured at Cryomagnetics Inc., Oak Ridge, USA.

Most of the components of the transmission system, HV-systems and in-vessel-components have been ordered, manufactured, delivered and are ready for operation at IPP Greifswald. A part of the existing ECRH system has been already used to test new concepts and components for ECRH. A significant delay arose in the project due to unexpected difficulties in the production of the series gyrotrons.

Series Gyrotrons

In 2005, the first TED series gyrotron SN1 had been tested successfully at FZK and IPP (920 kW/1800 s). It met all specifications during the acceptance test, no specific limitations were observed. In order to keep the warranty SN1 has been sealed, one prototype gyrotron is routinely used for experiments.

Series gyrotrons following SN1 did show a more or less different behavior with respect to parasitic oscillations excited in the beam tunnel region. These oscillations resulted in an excessive heating of the beam tunnel components, in particular of the absorbing ceramic rings. The gyrotrons re-opened after operation showed significant damages due to overheating at the ceramic rings and the brazing of the rings. A possible solution was proposed and successfully tested by KIT. As the main difference to the usual beam tunnel this design features corrugations in the copper rings which handicap the excitation of parasitic modes.

The thermal loading of the collector depends on the interaction efficiency between the electromagnetic field and the electron beam. And, of course, it depends on the pulse length. For high power operation at continuous wave (CW) thermal loading is close to what is feasible in terms of cooling and lifetime of the collector. For the series tubes a patented sweeping procedure has been introduced which combines a vertical and radial displacement of the electron beam at the collector. This results in an almost constant power deposition at the inner wall along the axis and removes the particularly dangerous temperature peaks at the lower and upper reversal points of the electron beam. Already in 2012 complete sweeping systems for the series gyrotrons have been procured.

Additional to the innovative collector sweeping, modifications have been realized and already tested in order to reduce the absorption of the internal stray radiation by covering stainless steel components with copper.

A possible corrosion in the water cooling circuit of the diamond window at the brazing structure is prevented by replacing the water by inert Silicon oil.

In 2013, the plan has been to achieve Factory acceptance (FAT) and Site Acceptance (SAT) of the series gyrotrons SN7 and SN5R2. SN7 has been delivered in January 2013 already. Short pulse operation showed 1 MW output power with an expected efficiency of 30 % without energy recovery at the collector. However, the measurement of the output beam quality showed a clear deviation from the specification which prevents the tube from long pulse operation. Low power RF measurements on a similar device and mechanical measurements confirmed a manufacturing failure of the internal surface of the quasi-optical mode transformer (launcher). The failure happened at the manufacturer of the launcher. Based on this, the complete gyrotron was taken back to the TED for repair.

As planned, the gyrotron SN5R2 has been repaired at TED (correction of the position of the mirror 3). Additionally, the tube has been updated according to all improvements done for SN6. The tube has been taken into operation at KIT in October 2013. During short pulse tests, the tube SN5R2 showed very promising results comparable to the measurements done on SN6. The output beam quality has been in good agreement with the specification. During conditioning of the tube long pulse experiments with more than 500 kW output power and a pulse length of up to 30 min has been performed. Full power operation (1 MW) of the gyrotron has been stopped due to a defect in the CVD diamond window. The disassembling of the window unit and a failure analysis is ongoing.

At the end of 2013 the gyrotron SN2i has been delivered to KIT, operation of this tube will start in early 2014.

Transmission Line System

The transmission of the gyrotron output power to the plasma is performed via an quasi-optical system, which consists of single-beam and multi-beam waveguide (MBWG) elements, in total more than 150 reflectors. For each gyrotron, a beam conditioning assembly of four mirrors is used to match the gyrotron output to a Gaussian beam with the correct beam parameters, and to set the appropriate polarization needed for optimum absorption in the plasma. A fifth mirror directs the beam to the beam combining optics, which is situated at the input plane of a multi-beam wave guide. This MBWG is designed to transmit up to seven beams (five 140 GHz beams, one 70 GHz beam, and one channel connected to the N-port remote-steering launchers via switches) from the gyrotron area (entrance plane) to the stellarator hall (exit plane). To transmit the power of all gyrotrons, two symmetrically arranged MBWGs are used. At the output planes of the MBWGs, two mirror arrays separate the beams again and distribute them via two other mirrors and CVD-diamond vacuum barrier windows to individually movable antennas (launchers) in the torus.

The manufacturing and installation of the components of the basic transmission system has been completed, except for the beam-matching optics units and the “towers” which contain the mirrors in front of W7-X. In autumn 2013, access to the W7-X torus hall was given, and the mounting of the towers could be performed. Both towers are in place with the required high positioning accuracy of a few Millimeters. The towers are equipped with the control units for remote control of the front steering launchers, the vacuum shutters, arc detectors and beam monitoring diagnostics. Data acquisition modules for slow and fast recording of W7-X relevant signals are installed. The installation and connection of cooling tubes to supply the mirrors and stray radiation absorbers in the towers is underway.

Work for beam diagnostics and power measurement of the gyrotron beams continued. Concepts for 2-frequency sensors were followed, and linearization amplifiers for the detectors were built. For the receivers attributed to the directional couplers on the mirrors M14, the conical scan mechanics and electronics for the alignment control were further developed.

For the THALES gyrotrons SN7 and S5R2, which had been delivered to KIT for acceptance tests, beam characterization and phase retrieval were performed. Both gyrotrons finally were not accepted. SN7 had a strongly structured output beam with low Gaussian content as seen from the figure below (left) and high stray radiation, which prevented long pulse operation. Nevertheless, the time until rejection of the tube was used to upgrade the PROFUSION program package, and to design phase-correcting surfaces for matching mirrors. As can be seen from the figure 1, surfaces for the matching mirrors could be designed, which in principle – for perfect alignment and without aberration due to curved mirrors – allow a conversion of the gyrotron beam with a TEM00 contents as low as 80% to a good Gaussian beam with a mode purity of 97.7%.

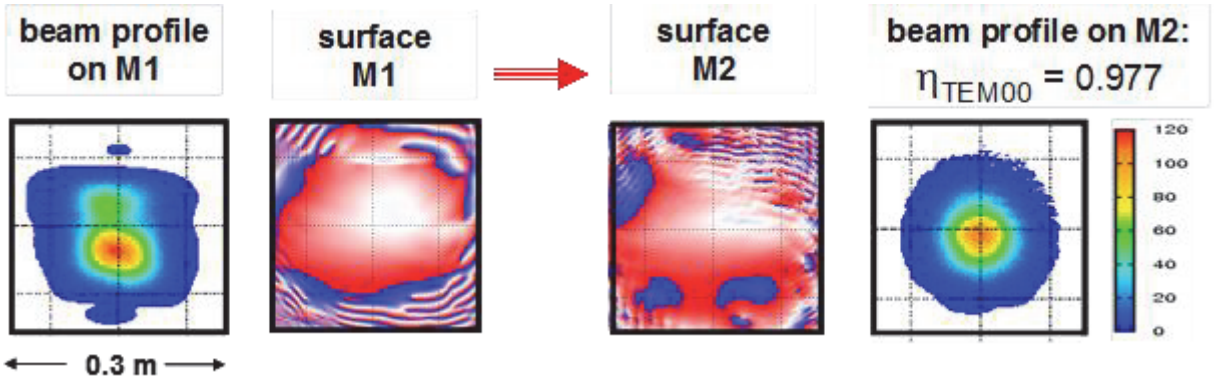

Fig. 1: From left to right: Gyrotron SN7 output beam profile at position of mirror M1; Phase profile for surface of M1; Phase profile for surface of M2; Beam profile on M2, with 97.7 % TEM00 contents.

For investigations on trapped particles in W7-X as well as a demonstration for a reactor-compatible antenna for ECRH, two N-ports of W7-X will be equipped with remote-steering (RS) launchers. This is due to the fact, that front steering launchers as used in the A and E ports will not fit into these narrow ports. The remote-steering properties are based on multi-mode interference in a square waveguide leading to imaging effects. For a proper length of the waveguide, a microwave beam at the input of the waveguide (with a defined direction set by a mirror system outside of the plasma vacuum) will exit the waveguide (near the plasma) in the same direction. All R&D activities regarding the design, optimization, and production of the RSLs are being done within the frame of the Verbundprojekt "FORMIK3", with preferential funding by the BMBF. The project is running under leadership of IPP-Greifswald and coordinates the contributions of the research laboratories IGVP Stuttgart and IPP-Garching, and two industrial partners, Neue Technologien GmbH, Gelnhausen (NTG), and Galvano-T (G-T) electroforming-electroplating GmbH, Windeck.

In-vessel components

The four ECRH-plug-in launchers have been equipped with silicon oil manifolds for the cooling of the diamond disc vacuum barrier windows.

The vacuum measurement and pumping valves for each shutter, which is in front of each window, were also installed. The thermal isolation and the electric flange heating for the vacuum bake-out have been defined.

Cabling and pressured air connections have been completed.

The electron cyclotron absorption (ECA) diagnostics (128 waveguides), which measures the transmitted ECRH power, the beam position and polarization was assembled inside the plasma vessel. Eight compact amplifier boxes with 16 channels each have been manufactured at the IGVP Stuttgart University. These boxes have been mounted on the protection housing of the ECA-diagnostic outside the vacuum vessel.

The design of the immersion tubes for the video diagnostic has been finished and fabrication has started. Several cameras have been tested in the 3T magnetic field of a gyrotron magnet. A compact near infrared C-mos video camera was chosen to be installed in the immersion tubes.

The design of the microwave stray radiation monitors, so called sniffer probes, was finished. The manufacturing drawings are produced presently.

The required wide angle antenna sensitivity could be achieved by inserting a transmitting random phase plate (Schroeder diffuser) into the microwave optic system.

Staff:

KIT/IHM

K. Baumann
B. Bazylev
G. Dammertz
J. Franck
M. Fuchs
G. Gantenbein
H. Hunger
Yu. Igitkhanov
S. Illy
J. Jelonnek
J. Jin
Th. Kobarg
I. Landman
R. Lang
W. Leonhardt
M. Losert
A. Malygin
D. Mellein
A. Meier
S. Miksch
I. Pagonakis
A. Papenfuß
K. Parth
S. Peschanyi
B. Piosczyk
T. Rzesnicki
A. Samartsev
A. Schlaich
Th. Scherer
A. Schlaich
M. Schmid
W. Spiess
Dr. D. Strauss
J. Szczesny
M. Thumm
J. Weggen
J. Zhang

(Diploma/Master students)
M. Cordova
F. Kahl
V. Kamra
M. Hruszowiecz
V. Ramopoulos
S. Ruess
C. Wu

IPF (University of Stuttgart)

W. Kasparek
C. Lechte
R. Munk
B. Plaum
H. Röhlinger
F. Remppel
P. Salzmann
K.H. Schlüter
S. Wolf
A. Zeitler

(Diploma/Master students)
Z. Popovic
P. Rohmann
D. Tretiak

IPP (Greifswald/Garching)

B. Berndt
H. Braune
V. Erckmann (PMW)
F. Hollmann
L. Jonitz
Dr. H. Laqua
G. Michel
F. Noke
M. Preynas
F. Purps
T. Schulz
T. Stange
P. Uhren
M. Weißgerber

1 MW Short Pulse Gyrotron for the Development of the European RF Sources for ITER (F4E-OPE-458)
Design and Development of the European Gyrotron (F4E-GRT-432)

Introduction

EU is presently developing the 1MW, 170GHz conventional cavity gyrotron for ITER. The development of the 1 MW gyrotron was initiated in 2008 as a risk mitigation measure during the development of the 2 MW coaxial-cavity gyrotron. In the last year the scientific design of the 1 MW gyrotron components, such as the gun, beam tunnel, cavity, quasi-optical output coupler and single-stage depressed collector has been finalized. The EU gyrotron development plan is based on a single 1 MW, CW prototype. This prototype shall fulfill the main ITER requirements in terms of output power, beam quality and pulse length. In parallel a short pulse prototype gyrotron is under development in order to validate the design of the components of the 1 MW CW prototype. Main test campaigns on the short pulse gyrotron are going to take place in the KIT test facility (using an existing superconducting magnet -SCM-).

Gyrotron Design

The mode TE32, 9 has been selected as the nominal mode of the new gyrotron cavity operation using criteria related to similarity with the 140 GHz 1 MW CW W7-X gyrotron, mode competition and stability. Three independent EU numerical interaction codes (SELFT, EURIDICE and COAXIAL) have been used for the cavity geometry optimization and the performance verification. Some of the operating parameters and the numerically calculated performance are presented in Table 1.

Table 1: Basic operation and calculated performance parameters of the ITER EU-1 MW gyrotron.

Cavity magnetic field B_o	6.78 T
Accelerating voltage V_c	79.5 kV
Beam current I_b	40.0 (45.0) A
Beam radius R_b	9.44 mm
Electron velocity ratio α	1.3
Output power at RF window	1.0 (1.14) MW
Operating frequency (cold cavity)	170.23 GHz
Overall efficiency (w/o SDC)	31.4 %
Peak ohmic wall loading ($\sigma = 1.7\times10^7$ S/m)	2.2 (2.5) kW/cm^2

The magnetron injection gun has been designed using a parametric technique in order to optimize the beam quality in the cavity. In addition, some additional criteria have been implemented for the suppression of the electron trapping mechanisms in the gun region. The codes Ariadne and ESRAY have been used for the optimization and verification of the design.

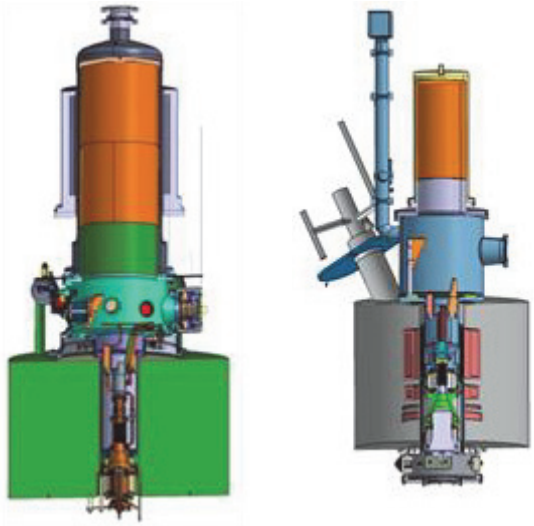

Fig. 1: Three-dimensional cut-views of CW (left) and SP (right) prototype-

A beam-tunnel similar to that of the gyrotron for W7-X has been designed. It consists of a stack of alternating copper and lossy ceramic rings. While the ceramics should attenuate possible RF fields, thereby lowering the quality factor in order to increase the starting currents of possible parasitic oscillations, the indented copper rings suppress low loss circular symmetric modes, define the electric potential and prevent static charges on the insulators.

A quasi-optical mode converter is employed in the gyrotron to transform the high order cavity mode to a fundamental Gaussian wave beam. It contains a launcher and three mirrors. The simulation results show that the fundamental Gaussian mode content of the wave beam is

98.6% in the window plane and the stray radiation inside the tube is estimated to 1.75%. The synthesis and analysis of the quasi-optical mode converter have been verified by comparison with the calculation results using the commercial 3-D full-wave vector analysis SURF3D code.

The single-stage depressed collector of the new tube will be identical to that of the W7-X gyrotron. The specific design with a transversal sweeping system is adequate for an efficient operation of the collector system. This has been shown by numerical simulations with the 3D collector code COLLSIM.

Finally, the design of the technological parts of the new gyrotron, such as the assembly, the cooling system, the positions of the isolation ceramic, etc., is based on the W7-X gyrotron technology.

Short Pulse Prototype

The short pulse prototype is a risk mitigation action for the development of the CW prototype. The geometry of all critical components of the short pulse gyrotron ought to be identical to the CW prototype. However, the structure of the components is significantly simpler, due to the fact that no cooling is required for all components except the collector and gun (see Figure 2). For the collector no sophisticated cooling system is required, since the pulse length will be limited to 10 ms. A simple water cooling will be applied in order to keep the duty cycle as high as possible. On the other hand oil cooling similar to CW gun is used for the gun in order to dissipate the heat for the cathode structure generated by the emitter ring. Vacuum tight flanges will be used for the connection of the components. This gives the flexibility to exchange parts of the tube in case of further improvement of the design, if necessary.

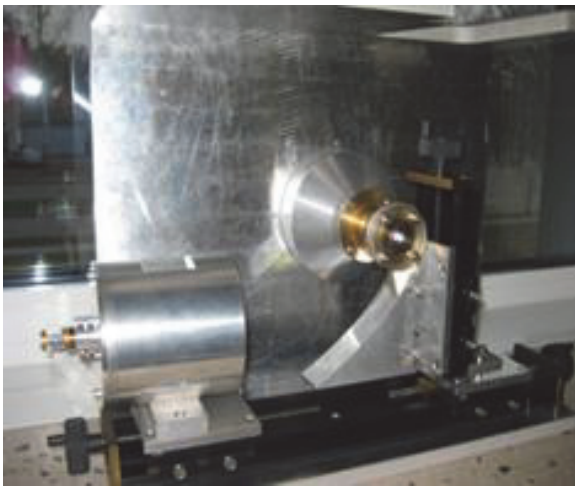

Fig. 2: $TE_{32,9}$ mode generator.

The manufacturing of the SP prototype has been started since October in the context of the contract OPE-458 which has been signed between F4E and KIT. The detailed industrial drawings of subcomponents and auxiliaries have been completed. The manufacturing of the most of the components will take place in the IHM and TID workshops of KIT, while some of them will be externally ordered. In the SP contract, TED has been nominated as subcontractor and it will be responsible for the manufacturing of the electron gun.

The assembly of the gyrotron and the first test at KIT are expected at the end of the next year. The manufacturing of several subcomponents have been completed while some first tests have been performed. In particular, the following subcomponents have been manufactured:

- beam tunnel copper rings
- oil tank
- body ceramic insulator
- launcher

In addition, for the cold test of the Q.O. System, a $TE_{32,9}$ mode generator has been manufactured at KIT. The output pattern of the mode generator consists of 9 rings in radial direction and the azimuthal index is 32. The unwanted counter rotating mode content has been deter-

mined to be less than 5%. This is sufficient to perform measurements of quasi-optical components to be integrated into the gyrotron.

Preliminary cold test of the launcher has been performed using the mode generator. The output pattern is in a good agreement with the calculated one.

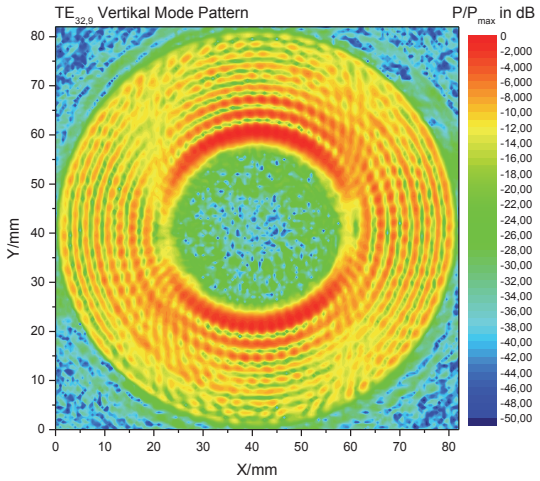

Fig. 3: (a)Output pattern of the $TE_{32,9}$ mode generator.

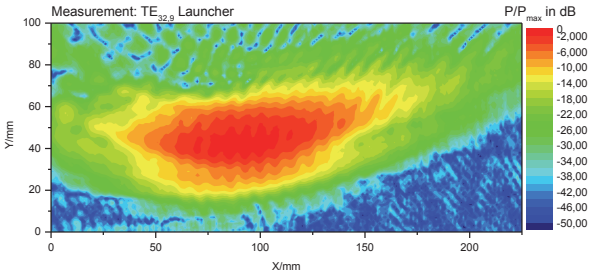

(b) Output pattern of the mode converter.

Lifetime Estimation for the Collector of the ITER EU-1 MW, 170 GHz Gyrotron

In the case of the ITER EU 1 MW, 170 GHz CW prototype gyrotron, an efficiency of 50 % is expected. Based on that, one can expect roughly 1 MW of electron beam power on the collector wall during normal operation at nominal parameters. To avoid local overheating of the collector structure, it is planned to sweep the electron beam across the inner surface with low sweeping frequencies between 5 Hz and 50 Hz. This will lead to localized cyclic thermal loads, which will induce thermo-mechanical fatigue of the collector material. To estimate the lifetime of the collector transient finite element (FE)-analyses were performed for vertical magnetic field sweeping (VMFS) and transverse magnetic field sweeping (TMFS). In the simulation a modified, strain based Manson-Coffin Basquin law was used.

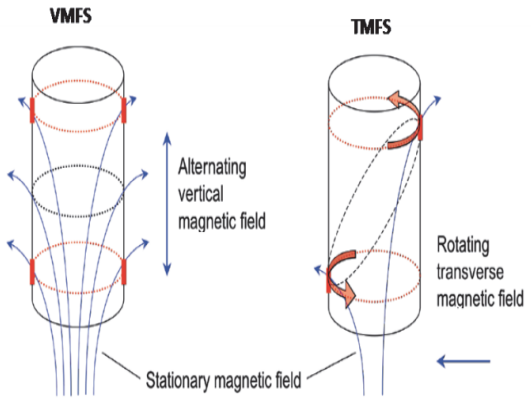

Fig. 4: The vertical magnetic field sweeping (VMFS) and the transverse magnetic field sweeping (TMFS) for gyrotron collectors. The strike area is shown as the black dotted line. The electrons follow the field lines of the stationary magnetic field created by the main magnet system of the gyrotron.

In case of VMFS, the electron beam forms a circular strike area on the collector wall with an instantaneous heat load of up to 35 MW/m^2. Transient load profiles obtained from ESRAY electron beam trajectory calculations have been used as input for the ABAQUS time-dependent thermo-mechanical FEM simulations that were performed for different sweeping frequencies, collector wall materials and collector wall thicknesses. After obtaining the maximum strain range in the most critical point on the collector wall, one could estimate the collector lifetime according to the so-called design curve for the material under consideration. Table 2 shows a small excerpt of all obtained results. As input, oxygen-free high thermal conductivity copper (Cu-OFHC-) material and a typical VMFS sweeping frequency of 7 Hz have been assumed. The simulation results indicate that for a wall thickness of 10 mm the calculated lifetime N_f will be only 1.14 h. Although pessimistic assumptions have been used, this indicates a risk connected to only using the VMFS sweeping concept together with a sweeping frequency of only 7 Hz. Even a reduction of the wall thickness to 7.5 mm and 5 mm

will not improve the situation. Even the use of advanced materials like CuCrZr will not help much – the calculations indicate that the use of this material will increase the lifetime N_f to values which are still below 200 h. Nevertheless, ABAQUS simulations show that a sweeping frequency of 50 Hz would increase the lifetime to values above 50000 h (in the case of a 10 mm Cu-OFHC wall). Moreover, a sweeping frequency of 50 Hz is not applicable in a VMFS system due to strong eddy currents induced in the collector wall.

TMFS accepts sweeping frequencies of above 50 Hz, transient 3D ABAQUS simulations have been performed to show the main advantages of this concept in the case of Cu-OFHC material, a 10 mm wall thickness and a 50 Hz sweeping frequency. Table 3 lists the simulation results for nominal loading of the collector wall and an additional 150 % loading which may occur during power modulation of the gyrotron. In the first case (100 % loading) the resulting lifetime is 550.000 h and therefore more than acceptable. By increasing the loading to 150 %, the lifetime will be reduced to a value close to 800 h. To reduce the risk of a collector failure a combination of TMFS and VMFS could be used. This concept has been already proven experimentally with the 140 GHz, 1 MW CW gyrotron for W7-X.

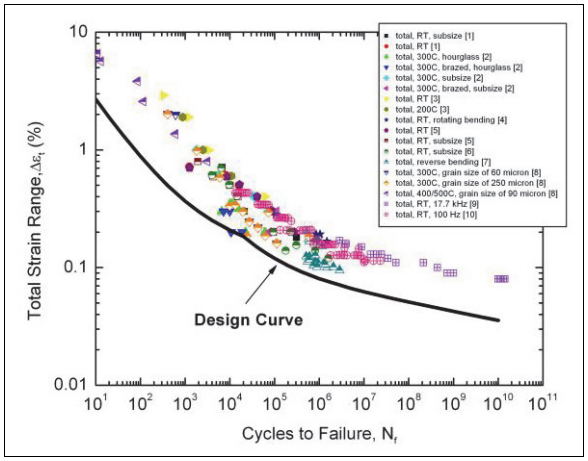

Fig. 5: Design curve for Cu-OFHC and experimental fatigue data. The design curve is generated from the Manson-Coffin Basquin law which describes the experimental data.

Table 2: Lifetime estimation for the wall thickness analysis for VMFS (in the case of Cu-OFHC and 7 Hz sweeping)

Wall thickness	mm	*10*	*7.5*	*5*
T_{max}	°C	*359*	*349*	*335*
ΔT	K	*113*	*117*	*119*
$\Delta\varepsilon_{tot}$	%	*0.17*	*0.171*	*0.1652*
N_f	h	***1.14***	***1.09***	***1.23***

Table 3: Lifetime estimation for the increased heat load analysis for TMFS

at load	%	*100*	*150*
T_{max}	°C	*315*	*468*
ΔT	K	*17.7*	*28.3*
$\Delta\varepsilon_{tot}$	%	*0.0291*	*0.0488*
N_f	h	***550000***	***811.1***

Thermo-mechanical modelling of the gyrotron cavity

It is well known that the ohmic loading of the gyrotron cavity walls is one of the major limiting factors for high-power, continuous-wave (CW) operation. The present cooling technology is able to evacuate no more than 2-3 kW/cm^2 of heat flux on the cavity wall. The first result of the heat flux is the thermal expansion (deformation) of the cavity, which leads to a decrease in operating frequency (frequency shift) during the gyrotron pulse. Experimental measurements with the 140 GHz gyrotron series for W7-X show that this frequency shift is in the order of 200-300 MHz. Excessive heat flux can result in unacceptable frequency shifts in terms of reflections at the gyrotron window, which reflection coefficient is acceptably low in a small frequency range only. Moreover, the frequency specification itself may not be met. If excessive heating causes cavity expansion beyond the limit of plastic deformation, the device will be unusable.

It is understood that accurate modelling of the thermo-mechanical behaviour requires a multi-physics simulation. To this end, a numerical tool to simulate and analyse the thermal stresses in the gyrotron cavity was developed using the multi-physics, finite element software COMSOL. Input for the COMSOL simulations was delivered from the in-house code-package EURIDICE. Final target of the multi-physics tool has been to understand the behavior of the

cavity, especially the deformations, and the consequences on the physical interactions generating the RF signal. The modelling focused on the 1 MW, 140 GHz gyrotron for W7-X. That is the gyrotron series for which the most experimental results on CW operation exist. However, even more important in future, will be the use of this tool in support of the forthcoming gyrotron developments for ITER and DEMO, for which the ohmic loading of the cavity wall is expected to be noticeably increased.

The developed model takes following into account: (i) An input heat flux with a specific profile, (ii) a complex coaxial cooling system (porous media and highly turbulent flows), and (iii) the mechanical interaction with surrounding components (fixed constraints and heat transfer). For such a tool, all the influential parameters in real conditions have to be considered. A major part of the work was devoted to the identification of these parameters. This included a preliminary study of the material properties, the architecture of the gyrotron, and the beam-wave interaction physics. The material used for the cavity is GlidCop® Al-15, which is a copper-based metal matrix composite (MMC) alloy containing a small amount of aluminium oxide ceramic particles. The relevant parameters are: Thermal conductivity [W/(m.K)], thermal expansion [K^{-1}], specific heat [W/(kg.°C)], density [kg/m^3], Young's modulus [GPa], and electrical conductivity σ [S/m]. An additional parameter is the heat transfer coefficient h [W/(m^2.K)] of the cooling system. After extensive research and discussions with specialists at TED, the proper range of the values for most of the parameters was identified. From simulations, it was seen that the most influential parameters are the heat transfer coefficient h and the electrical conductivity σ. Consequently, the investigations focused on improving the estimations for the values of these two parameters.

Typical results of the simulations are shown in the Figures 6 (a) and (b). The model is iterative: First, the beam-wave interaction is calculated by EURIDICE for the cold, undeformed cavity and the hear flux on the wall is obtained (see Figure 6(a)). This heat flux is then introduced to COMSOL and the cavity deformation is calculated. Next, EURIDICE calculates the updated interaction and heat flux in the deformed cavity. This is repeated until convergence of the results is reached (see Figure 6(b)). We note that both steady-state (estimating the final frequency shift) and time-dependent simulations (estimating the time constant for the deformation) were performed.

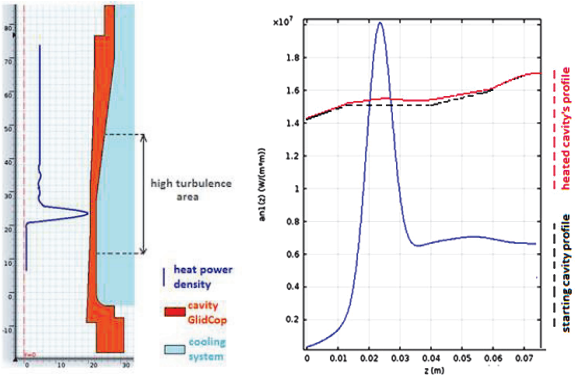

Fig. 6: (a) Cavity, cooling system, and heat flux profile.

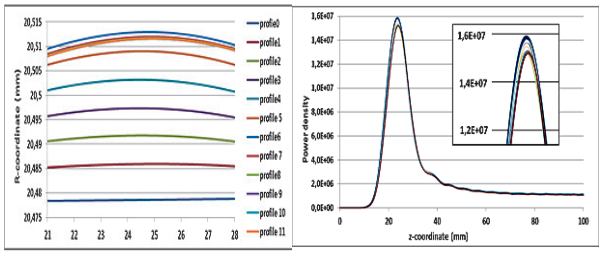

(b) Convergence of iterative scheme: Cavity profile (top) and heat flux profile (bottom) at each step.

Following the development of the model, comparisons with experimental results were initiated. This step pointed out some discrepancies, which indicate that the estimations of the model parameters, and in particular of h and σ, should be improved. This, together with enriching the experimental database with more measurements from dedicated experiments, is foreseen for the next research period. In conclusion, the developed tool, although in need of further calibration, is suitable for giving a much more detailed understanding of the thermo-mechanical behaviour of the cavity in operating conditions. The adaptability and simplicity of the model are very advantageous for studies dedicated to the design of forthcoming gyrotrons.

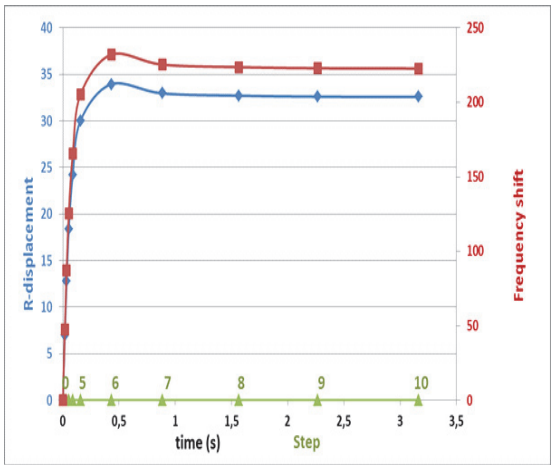

Fig. 7: Deformation and frequency shift as functions of time.

Beam-wave interaction modelling and code improvements

Extensive, highly realistic multi-mode interaction simulations for the updated design of the 170 GHz, 1 MW cylindrical gyrotron for ITER have been performed (also in collaboration with HELLAS). The following issues were addressed: Validation of the final gun design with emitter thickness of 5 mm, validation of the final cavity geometry with 19.24 mm outer radius, identification of appropriate operating point for highly efficient 1 MW short-pulse operation, and parametric studies for operation with electron beam of reduced quality. The simulations of the cavity and the non-linear uptaper took into account the start-up and beam neutralisation phase, as well as a realistic magnetic field profile and the spread in electron velocity. The final design was validated. An appropriate operating point for short pulse was also verified. The parameter studies at reduced beam quality (low pitch factor- high velocity spread) showed that the design is robust. Typical simulation results for the output power and the efficiency in the nominal CW operation scenario are shown in the following graphs:

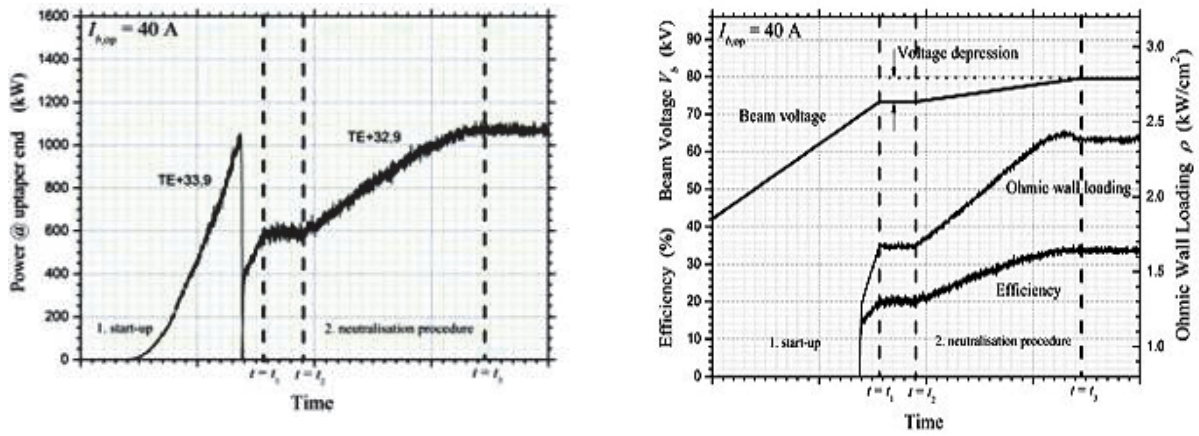

Fig. 8: Typical simulation results of mode sequence and output power (top) and voltage, Ohmic wall loading and efficiency dependence (bottom) during start-up.

Numerical studies on parasitic dynamic After-Cavity Interaction (ACI) generated a multitude of results and code upgrades in the last 3 years. To clarify the situation, a direct comparison between different codes and approaches has been performed for the first time, encompassing all the known (in simulation) ACI cases, namely (i) the 140 GHz, 1 MW gyrotron for W7-X, (ii) the step-tunable gyrotron, (iii) the 170 GHz, 1 MW gyrotron design for ITER with the ASG magnetic field, and (iv) the 118 GHz, 0.5 MW gyrotron for TCV, EPFL, Switzerland with uniform magnetic field. The following codes and approaches were compared:

1. SELFT and EURIDICE (trajectory approach)
2. EURIDICE quasi-PIC (filled-cavity approach)
3. GyroDyne (1-D PIC approach)

The result is that ACI appears in all four cases using the trajectory approach, whereas it clearly appears only in case (iv) with the PIC approach. Taking into account that the PIC approaches are more valid for ACI modelling, we could conclude that the trajectory codes exaggerate on their results on ACI and there is a considerable possibility that dynamic ACI can sometimes be an artefact of the trajectory approach. However, in contrast to the trajectory codes, EURIDICE quasi-PIC and GyroDyne are newly developed codes and their verification cannot be considered complete. At the same time, the ACI cases studied up to now cannot be investigated with commercial full-wave PIC codes because of the extreme computational resources needed due to the high-order modes involved. Thus, to verify the newly developed codes and their results on ACI, an artificial scaled-down ACI case with the low-order TE03 mode at 140 GHz in an appropriate cavity & uptaper was found and simulated with CST Studio Suite. The studies, done in collaboration with HELLAS, are ongoing, but up to now no ACI is predicted. More definitive conclusions are expected in the near future, after additional simulations and code upgrades towards the PIC approach.

For dynamic ACI studies, as well as for studies of gyrotron operation for which sidebands around the operating frequency appear, the usual single-frequency boundary condition for the RF field profile is not appropriate. It introduces additional artificial numerical reflections in the simulation. A more suitable, broadband, totally adsorbing boundary condition is available in EURIDICE. However, it requires a very short simulation time-step to work properly. Significant efforts were made on improving this matched condition and also, going a step further, on formulating a more general boundary condition for which a frequency-dependent reflection can be externally defined. By doing this, the reflection from the components following the gyrotron cavity can be modelled more realistically. The reasoning and first results of the extended model are described below.

The boundary condition for a single mode in frequency domain can be formulated as

$$\left[A(z,\omega) = s\,\frac{Z(\omega)}{i\,k(\omega)}\,\frac{\partial A(z,\omega)}{\partial z}\right]_{\text{for } z \text{ at boundaries}},$$

where $A(z,\omega)$ is the envelope for the field, $s = 1$ at the emitter side and $s = -1$ at the launcher side, $Z(\omega)$ is the normalised wave impedance, which can be expanded in Taylor series

$$Z(\omega) = \frac{1+\Gamma(\omega)}{1-\Gamma(\omega)} = \sum_n a_n\,\omega^n,$$

$\Gamma(\omega)$ is the frequency dependent reflection coefficient, and $k(\omega)$ is the axial wave number

$\frac{1}{k(\omega)} = \frac{c_0}{\sqrt{\omega^2-\omega_{cut}^2}}$, which can be written as $\frac{1}{k(\omega)} = \frac{c_0}{\sqrt{\omega_0+\omega_{cut}}}\frac{P(\omega)}{\sqrt[*]{\omega-\omega_0+\omega_{cut}}}$,

Here, ω_0 is the mode carrier frequency, ω_{cut} is the cut-off frequency, c_0 is the velocity of light, $\sqrt{x}$ stands for the square root with a zero or negative imaginary part, and $P(\omega)$ is the Taylor series

$$P(\omega) = \sum_{n=0}\frac{1\cdot3\cdot5\cdots(2n-1)}{2^n\,n!}\left(\frac{\omega_0-\omega}{\omega_0+\omega_{cut}}\right)^n$$

The existing matched broadband boundary condition is improved with the introduction of the Taylor series. The two series can be merged into one polynomial and can be handled together.

The Figures 9(a) and (b) demonstrate two test cases for a boundary configuration relevant to the W7-X gyrotron (cut-off frequency ≈130 GHz, carrier frequency at 140 GHz). In both cases a Gaussian pulse from 120 GHz to 160 GHz is used as a source term. The Figure 9(a) shows the improved matched boundary condition. In the Figure 9(b) an externally defined reflection is taken, which is assumed to be 0 at 150 GHz and 5% at 140 GHz. It can be observed, that the simulated reflection follows the theoretical (dashed) curve inside the defined frequency range.

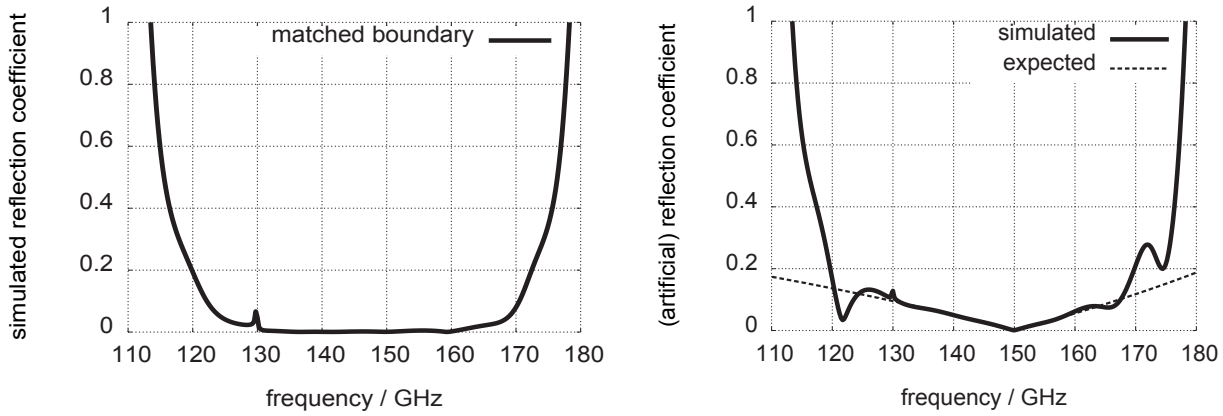

Fig. 9: Simulated reflection coefficient versus frequency for imposed reflection at the boundary equal to zero (a - left) and for linear dependence (b - right). Note: the physical region is above 130 GHz (cut-off).

Quasi-optical mode converter and Matching Optics Unit for $TE_{32,9}$-mode gyrotron

KIT is leading the theoretical design of mirror-line type launchers. As the surface contours of mirror-line launchers are more complicated compared to helically deformed launchers, it is very important to investigate a tolerance analysis of mirror-line launchers. A mirror-line launcher has been designed for the $TE_{32,9}$-mode gyrotron developed for the ITER tokamak. The tolerance of the mirror-line launcher has been investigated. An important result is that if deviations of the surface of the real device and the design are less than 10 micrometer, the stray radiation from the launcher will be smaller than 3%.

A Matching Optics Unit (MOU) has been designed for the $TE_{32,9}$-mode ITER gyrotron in order to match the free space Gaussian output beam of the gyrotron to the corrugated HE_{11} waveguide transmission line. The structure of the MOU vessel has been designed according to the technical requirements. The beam-shaping mirrors have been optimized to provide a conversion efficiency of 95.57% for the RF beam to the HE_{11} mode which can satisfy the requirement of the conversion efficiency to be larger than 95%. The field distribution of the RF beam radiated from the MOU is shown in the Figure 10. It has been found that the current design of the MOU vessel is not big enough for the possible displacement of the gyrotron mirrors.

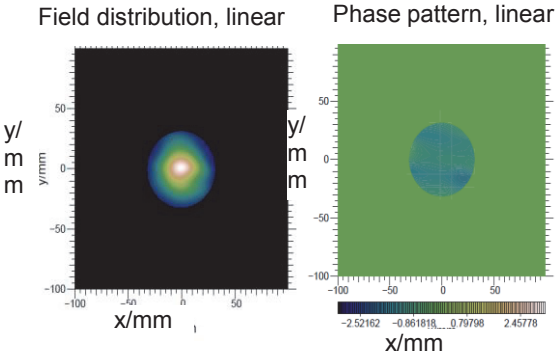

Fig. 10: Field distribution at the output of MOU.

A parallelized version of TWLDO code has been developed which reduces the CPU run time by 20%.

A computer code for the vector analysis of RF fields in launchers is under development at KIT. Curved triangle meshes will be used to match the circular waveguide wall surface. A formula for the calculation of the field at the neighbor mesh points has been derived. In order to improve the conversion efficiency of cavity modes to a Gaussian distribution, the combination of helically deformed launcher

and mirror-line launcher has been tested. However, the simulation results show no enhancement of the conversion efficiency.

Other Activities

Emitter surface roughness model for gyrotron calculation

The velocity spread of the electron beam from the Magnetic Injection Gun (MIG) is assumed to be one of the most important factors that decreases the efficiency of a gyrotron and facilitates mode selection in the cavity. The microstructures on the emitter surface which will decrease the uniformity of the local electric field on the emitter surface are one of the most important reasons for that velocity spread. In order to investigate the effect a new surface roughness model has been build. The surface roughness is modeled with several kinds of microstructures in a modified version of the electrostatic beam optics code ESRAY, as is shown in the Figure 11. The new emission model can reproduce the effect of the microstructure even under the influence of a tilted magnetic field.

Calculations done with the gyrotron interaction code EURIDICE show that in the gyrotron the transverse velocity spread $\delta\beta_\perp$ of the electron beam and the gyrotron efficiency are affected by the microstructure, as is shown in the Figure 12.

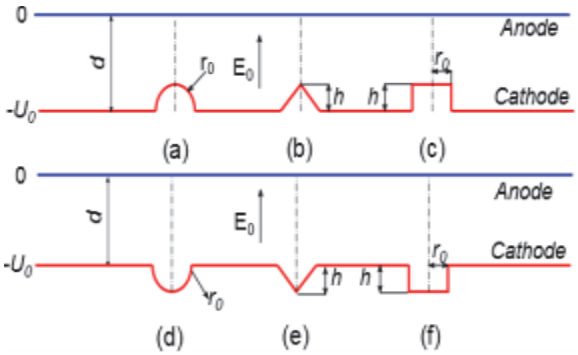

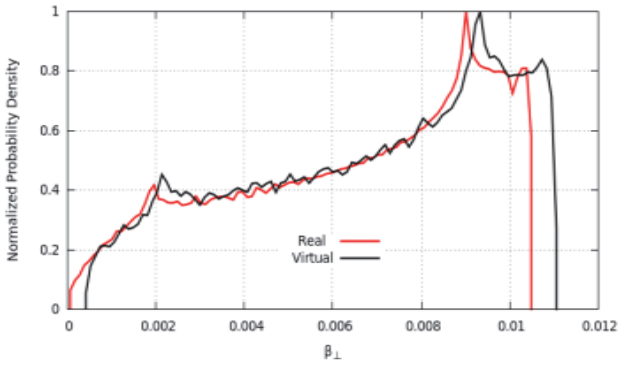

Fig. 11: (a)The six microstructures used in the ESRAY. (b) Comparison of the velocity spread caused by the real and virtual bump.

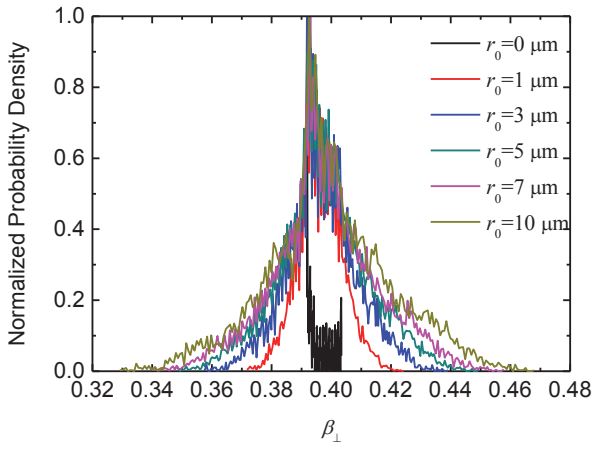

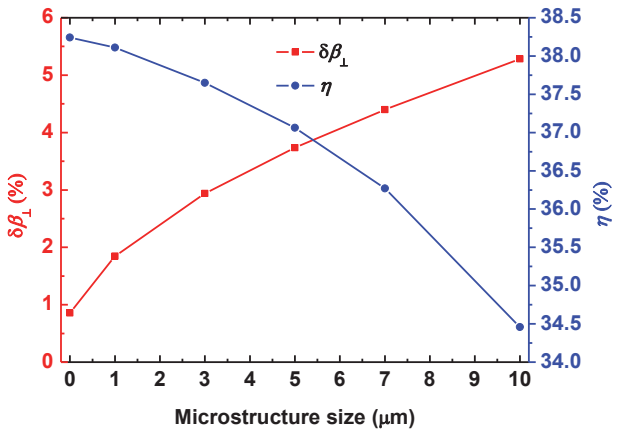

Fig. 12: Relation between microstructure size, final $\beta\perp$ distribution (left), $\delta\,\beta\perp$ and gyrotron efficiency η (right) in the case of the 1 MW, 170 GHz EU gyrotron for ITER.

From the Figure 12 one can see that with the increase of the microstructure size from 0 μm to 10 μm the perpendicular velocity spread $\delta\beta_\perp$ increases from 0.86% to 5.3% and the gyrotron efficiency η decreases from 38.2 % to 34.5%, respectively. Multimode calculations show that the working mode will start later due to the increase of the microstructure size.

Emission uniformity test device

The emission uniformity of the emitter is another factor which will increase the velocity spread of the electron beam of the MIG. A new emission uniformity test device has been developed at KIT and is in use since 2013. In the emission uniformity test device the distance between the anode and the cathode is designed to be 2 mm, so that it can work at a lower voltage with the same electric field strength compared to the gyrotron.

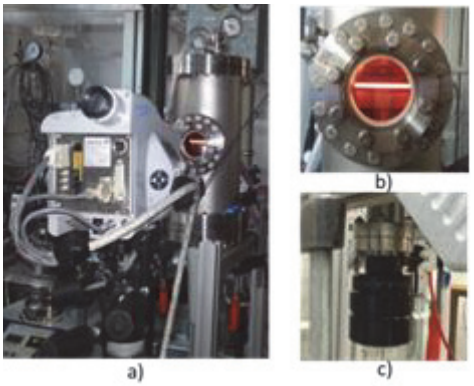

Fig. 13: Emission test device.

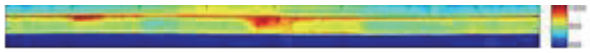

Fig. 14: Relative temperature distribution alone the emitter surface (middle part of the picture).

The temperature information of the emitter is measured by an infrared camera which is put in front of an infrared window, as is shown in the Figure 13(a). The emitter is heated up to its nominal temperature about 900ºC, as is shown in the Figure 13(b). In order to receive the information about the angular temperature and emission uniformity the emitter is designed to be rotable, as is shown in the Figure 13(c). Relative temperature distribution along the whole emitter surface is shown in the Figure 14. The Figure 14 shows significant temperature differences. One possible reason for that temperature increase on some places of the emitter is that the emissivity of those areas is different from that of the rest.

The next step is to get the absolute temperature on the emitter surface with the correction of a pyrometer and test of the angular emission uniformity.

Staff:

G. Gantenbein
K. Pagonakis

Acknowledgement

This work was supported by Fusion for Energy under the grant contract F4E-GRT-432 with collaboration by EPFL, Switzerland; HELLAS, Greece; and CNR, Italy and the Service Contract F4E-OPE-458. The views and opinions expressed herein reflect only the author's views. Fusion for Energy is not liable for any use that may be made of the information contained therein.

Analyse Development Requirements of Gyrotrons up to 250 GHz and Investigate Possible Alternative Generators (WP13-DAS-03-HCD-EC-T03)

Introduction

Overview

Electron Cyclotron Resonance Heating (ECRH) and Current Drive (ECCD) have been employed for many years in magnetic confinement devices. It is being used for bulk heating as well as for spatially localised current drive. With growing RF power, pulse length, efficiency and reliability of gyrotrons, ECRH has become one of the first choices for heating and plasma stabilisation in existing and planned fusion devices.

With its small RF wave length, ECRH offers the advantage of small antenna structures and torus openings together with a well-controlled localized heating, which is particularly useful for plasma stabilisation and shaping current drive profiles. Localised heating has been used to alter the q-profile in a tokamak near the q=1 surface and has been used to control the frequency of sawteeth and modulated ECRH can be used to control sawteeth and recent experiments have shown real-time control of the sawtooth instability.

Current drive is of fundamental importance to tokamak operation as it is with highly spatially localised current drive that deleterious MHD modes can be stabilised and/or destabilised according to the requirement. Neo-classical tearing modes (NTMs), which are a major worry for ITER and, one supposes for DEMO too, can be detected and stabilised before their effects are too damaging. In addition to good spatial localisation, high current drive efficiency is required. One of the potential weaknesses of ECCD is its relatively poor current drive efficiency compared to other current drive methods.

In order to overcome this for a DEMO reactor the frequency has been optimized in numerical simulations [1] to values much higher than what is state-of-the-art. Therefore we started an initial conceptual design work of such a high frequency gyrotron.

In this report we will also give an assessment of alternative generators for ECH applications.

Initial conceptual design work of a high frequency gyrotron

Overview

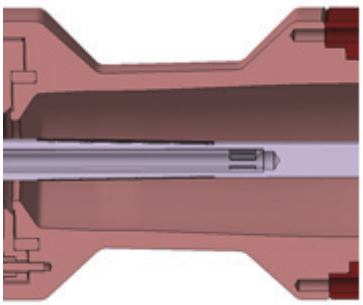

Fig. 1: Typical cavity and inner conductor of a coaxial gyrotron.

The centrepiece of gyrotrons is the resonator (alternatively denoted as cavity; see Fig. 1), an open waveguide where millimetre waves are produced by weakly relativistic electrons (relativistic factor γ~1.15) moving on helical trajectories in a strong magnetic field and interact with a transverse electrical field with azimuthal mode number m, radial mode number p and longitudinal mode number l ($TE_{m,p,l)}$. The field can be rotating in the same direction as the electrons (co-rotating, $TE_{-m,p,l}$) or in the opposite direction (counter-rotating, $TE_{+m,p,l}$); usually, the excitation of a co-rotating field is more efficient. The hollow electron beam stems from a frustum-shaped emitting cathode within the magnetron injection gun (MIG, see Fig. 2). Between MIG and resonator the beam tunnel is located and the beam undergoes a process called magnetic compression in an increasing magnetic field, where its radius decreases and the exploitable transverse energy of the electrons grows.

The resonator consists of a cylindrical middle section which is placed between tapered sections towards the beam tunnel (down-taper section) and towards the RF launcher (up-taper section), see Fig. 3. The narrowing down-taper section shall reflect the emerging wave as completely as possible, cumbering backward waves to enter the beam tunnel. The widening up-taper section shall lead to reflection and to transmission of the wave resulting in resonance conditions inside the cavity. As in all oscillations, the oscillation in a resonator can be described by a diffractive quality factor Q (or, alternatively, a damping factor δ), where a high Q indicates that the transmitted energy relative to the stored energy is small. For gyrotrons for fusion applications, Q-factors of approximately 1000 to 2500 are typical, which means the frequency of such modes is approximately the same as in resonance condition of the unloaded case.

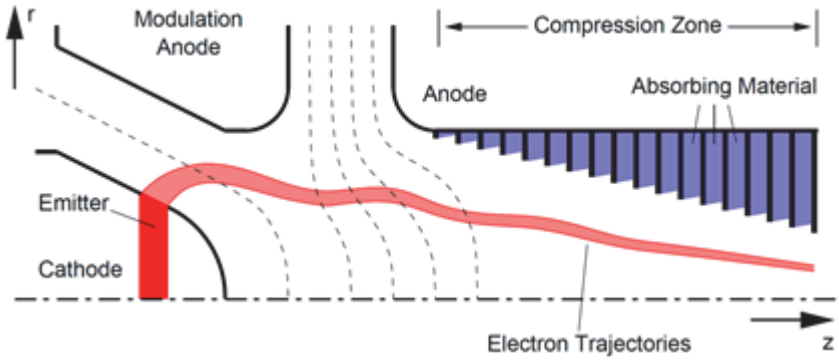

Fig. 2: Cross-section of a typical triode Magnetron Injection Gun [3].

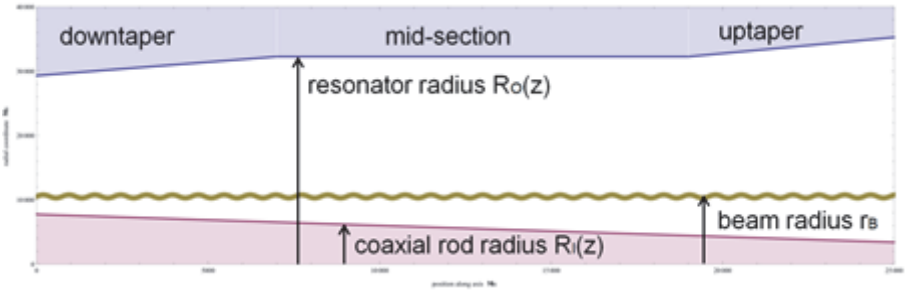

Fig. 3: Cross-section of a typical coaxial resonator. In conventional resonators, the coaxial rod is not present.

Stable, continuous radiation of a single frequency can only result from such an approximately standing wave, having a distinct mode profile (in both longitudinal and transversal directions, see Fig. 4), high quality factor and being near cutoff. For a given axial index l, e. g. l=1, each mode can be characterized by an eigenvalue χm,p, which is in turn proportional to the ratio of resonator radius RO and design (cutoff) wavelength λD. The eigenvalue χm,p is the p-th root of a characteristic equation of m-th degree Πm(x)=0, which, for conventional gyrotrons, is the derivative of the Bessel function: Πm(χm,p)=Jm'(χm,p)=0.

In gyrotrons operating at the fundamental frequency s=1, the gyrating frequency of the electrons is approximately equal to the frequency of the outgoing electromagnetic wave. For megawatt gyrotrons, a radiation frequency of f=240 GHz (λD ≈ 1.25 mm) corresponds to a magnetic field of approximately 9.6 T (f[GHz] ~ 28·B[T] / γ), γ is the relativistic factor. A preselection of the desired mode (main mode, design mode) can be undertaken by proper choice of resonator radius and beam radius, and by the beam parameters e.g. voltage, current and pitch factor (ratio between longitudinal and transversal velocity components of the electrons at the resonator entrance).

Coaxial gyrotrons, which have a longitudinally corrugated conducting rod (coaxial insert) from the MIG along the axis to the resonator, have been under investigation in the past (see e. g. [1]) Compared to conventional (hollow-resonator) gyrotrons, they can produce more output power due to several effects, most prominently better frequency separation (through reduction of the quality of some modes, see below) of the modes and reduced voltage depression. Coaxial resonators also have another (analytically more complicated) characteristic function which generally leads to shifts in the eigenvalues, dependent on the mode and on the ratio between wall radius and rod radius.

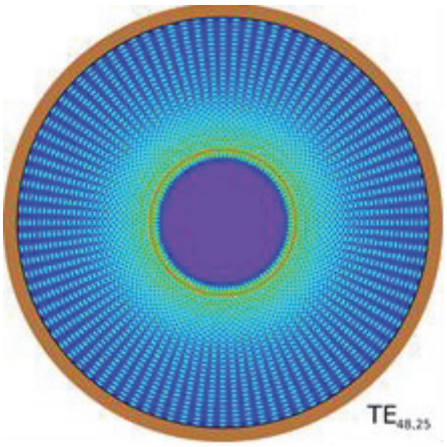

Fig. 4: Transversal mode profile of the high-order mode TE48,25. The colour scheme indicates the strength (absolute square) of the transversal electric field. In the centre, the field is small (purple), then rises from the caustic radius (dark blue) of the mode to its maximum (red), then decreases moderately until the resonator wall. In radial direction, the field has p maxima; in azimuthal direction it has 2m maxima.

All this makes coaxial gyrotrons favourable, if not even the only feasible solution, for high frequency (>200 GHz) CW megawatt gyrotrons. However, manufacturing of these gyrotrons is more complicated since the inner rod – as another conducting surface in the microwave tube – has to be shaped and aligned very precisely.

There are two important technical constraints on the design of a resonator of a gyrotron which will be mentioned in the following chapters.

Magnetic field strength and bore hole diameter

The required magnetic field can only be produced in CW operation by a superconducting coil system. The gyrotron has to fit into the bore hole of the magnet. The transverse dimensions of the gyrotron are mainly defined by the MIG and the resonator diameter, including housing, cooling systems and possible diagnostics systems. Magnets with bore-hole diameters of up to ~270 mm and fields of up to ~7 T are used for high power gyrotron development. The increase of the magnetic field up to ~10 T is certainly a technical challenge in this field.

Thermal loading of resonator and consequences

The oscillating field of the wave imposes a certain fraction of its power on the surface of the resonator as ohmic loading, leading to thermal and mechanical stresses on the resonator wall. For a given wavelength and well-defined modes, a larger resonator radius generally reduces the ohmic loading due to the geometric structure of modes in cylinder-symmetric structures (cf. Fig. 4). Thus, so-called over-sized resonators are favourable for high-power gyrotrons. Corresponding eigenvalues are about 50 to 60 for conventional (1 MW, 140/170 GHz with about 500 non-evanescent TE_{mn} modes) and 85 to 95 for coaxial (2 MW, 170 GHz with about 1200 non-evanescent TE_{mn} modes) gyrotrons. On the other side, modes with higher eigenvalues have a denser spectrum – in a certain frequency band, more modes can be excited – and are therefore less likely to be excited purely, resulting in a diminished efficiency. See Fig. 5:

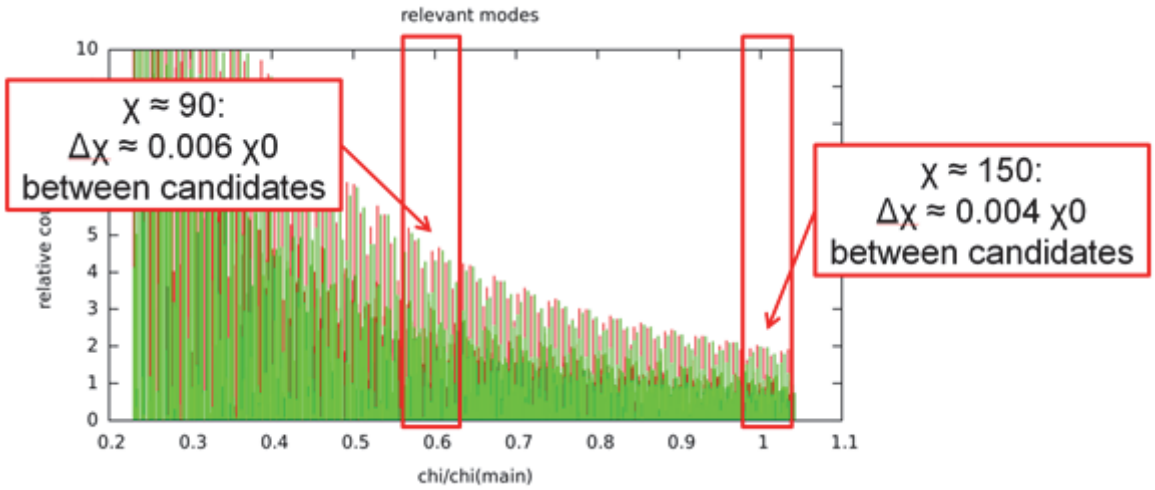

Fig. 5: Spectrum (relative coupling to a broad electron beam vs. eigenvalue) of all modes with eigenvalues up to 160 (co-rotating modes in red, counter-rotating modes in green). The potential main modes (candidates) are equidistant in χ, so the normalized distance Δχ/χ0, which is proportional to the relative frequency distance, decreases with increasing eigenvalue.

By selecting a suitable start-up scenario, i.e. definition of the time-dependence of the beam parameters, pure excitation of the main mode can usually be achieved, but this scenario might be hard to implement practically. Usage of a triode MIG basically allows separate control of beam voltage and pitch factor. Another practical problem is voltage stability of the power source. The denser the mode spectrum, the smaller is the voltage range where the main mode does not break down in favour of another, competing mode. Since the stability of oscillating modes which supress other modes depend on the time-evolution of the beam parameters; a break-down of the main mode cannot, due to hysteresis effects, be compensated by simply re-adjusting the voltage to the nominal value.

These issues are reduced, at least for moderately high frequencies, in coaxial resonators by selective decrease of the quality factor of some modes. Furthermore, the electron beam needs to have a minimum radius, e. g. 10 mm, to keep the intra-beam interactions (space-charge effects of the beam electrons on each other) low and therefore ensure good beam quality and – for coaxial gyrotrons – a sufficient spacing from the coaxial rod. If one now assumes a fixed ratio between the radii of beam and outer wall (see below), the resonator radius has a minimum value too.

Description of conducted studies

In order to obtain a physical design for a coaxial megawatt CW gyrotron at a frequency of 240 GHz, the following activities have been undertaken:

General approach

During preliminary design parameter studies, it has been investigated which area in the design parameter space is physically and technically reachable. To do this, conservative values for parameters like ohmic loading (20 MW/m^2), specific conductance of the resonator material (ideal copper at room temperature with $5.7 \cdot 10^7\ \Omega^{-1}\ m^{-1}$), emitter radius (60 mm), magnetic compression (40) and beam voltage (<90 kV) were used (see [2]), together with formulas found in the literature and in textbooks ([3]-[10]). Since the number of different formulas and constraints is rather large and difficult to take them all into account simultaneously, a simple, interactive design code (named Design-o-mat) has been written based on these data, giving the user full design flexibility within the given constraints. With respect to quasi-optical launcher and single-disk window considerations, the code also informs the user on possible multi-frequency options, such as operation of the gyrotron in multiple frequencies having a typical separation of 30 to 40 GHz. The code has been proven to give good results for existing high-power, high-frequency gyrotron designs, especially with coaxial inserts.

Usage of CAVITY

The outcome of Design-o-mat was used for finer studies using CAVITY, an in-house gyrotron design package at IHM [11]. CAVITY consists of twelve interconnected modules; each calculates necessary data for gyrotron design. The modules used during the DEMO study are:

- MAXPO estimates the maximum output power for given frequency, efficiency and other basic parameters.
- GEOMT handles the resonator geometry.
- SCNCHI scans for possible modes in the given resonator.
- CHIMP calculates mode eigenvalue shifts in coaxial resonators.
- GYMOT helps finding optimum operating parameters, e. g. beam voltage and current.
- SELFC determines the self-consistent solution of the field profile in the resonator.
- MCONV calculates possible mode-conversion in the resonator.
- SELFT is a self-consistent, time-dependent code for mode-excitation in the resonator. It simulates even multi-mode scenarios very fast and has been proven reliable in previous

projects. Nevertheless, since it is based on fixed mode content, it is not capable to simulate all events which might occur in a real resonator.

Cross-checks between Design-o-mat and MAXPO have been done. Several studies have been conducted for conventional and coaxial resonators, azimuthal indexes from 34 to 63 and frequencies between 200 and 300 GHz, resulting also in improvements of the Design-o-mat code.

Simultaneously, the CAVITY package was tested for accuracy and limitations during high-mode and high-frequency calculations. One severe problem which occurred were the large oscillations of the characteristic function of modes in coaxial gyrotrons in radial direction, exceeding a factor of 10^{34} (limits of 128 bit precision) within reasonable steps in χ. This led to incorrect calculation, counting and assignment of the eigenvalues to the respective modes. Inconsistent predictions of the SELFC code for the ohmic loading on the coaxial insert are under investigation. Overall, a thoroughly revision of the CAVITY codes seems necessary to ensure that the package retains its reliability in the future and to fully use the present-day software capabilities.

Currently these irregularities must be corrected manually.

Mode selection strategy

The characteristic functions $\Pi_m(x)$ are quite irregular for small arguments, but show a more regular behaviour for large arguments. Therefore, for low-order modes, the eigenvalues, and thus the spectral neighbourhood, differ much from mode to mode, while for high-order modes, spectral neighbourhoods are similar for modes with similar indexes. This is also true for e. g. starting currents, achievable efficiency and tunability. Due to this, the high-order mode selection may focus more on other aspects than the spectral neighbourhood of the main mode, if this is analysed once.

The mode selection strategy pursued at the moment is the following:

- An area in the mode index space is searched for modes $TE_{-m,p}$ which
  a) are well separated from their main competitors $TE_{+(m-4),p+1}$, $TE_{+(m-3),p+1}$, $TE_{+(m-2),p+1}$, $TE_{-(m-1),p}$, $TE_{-(m+1),p}$ (which are close in eigenvalue and radius of the field maximum). For high-order modes, this is the case if the ratio between radial index p and azimuthal index m is between 0.56 and 0.58, also leading to fixed ratios of rod, caustic, beam and resonator wall radii,
  b) are an element of a series of modes which
     A. do not differ too much in their caustic radius, that is the radius below which the field amplitude is insignificantly low (this increases the possible quality of a quasi-optical launcher), and
     B. have a good frequency proportionality (for multi-frequency operation, this describes the possibility of using one single-disc window for the several frequencies, i.e. that has a thickness corresponding to small multiples of each half wavelength).

  Based on (b.1) and (b.2), modes which fulfil (a) are rated on a scale from 0 to 5 points. Only modes with at least 4 points are considered for further investigation. By this strategy, basic spectral, multi-frequency and launcher requirements are already considered.

- Based on validated designs, a suitable initial resonator profile, including corrugated coaxial rod and electron beam radius is set up, using Design-o-mat and GEOMT. Spectral properties are verified with SCNCHI and CHIMP.
- The resonator profile is optimized using COLDC, SELFC and MCONV. A first estimation for the maximum output power and optimum beam parameters is obtained using Design-o-mat, MAXPO and GYMOT.

- Start-up calculations are then being performed with the self-consistent, time-dependent code SELFT.

Results

In high-order mode regime, the dependence of key parameters like output power and efficiency on the mode index is less important compared to the dependence on geometry of the cavity, quality of the electron beam and magnetic field profile.

At a constant resonator radius, the width of the mode maximum decreases for high frequencies (above 200 GHz) and therefore, coaxial insert and beam have to be closer to each other than at lower frequencies.

Furthermore, the beam needs to be thinner for high frequencies (inversely proportional to the frequency) which in turn, considering otherwise constant design parameters, requires a larger emitter radius to obtain enough beam current sufficient for the desired output power. This might be a more severe design challenge than the restricted ohmic loading on the resonator wall mentioned in section 2.3.

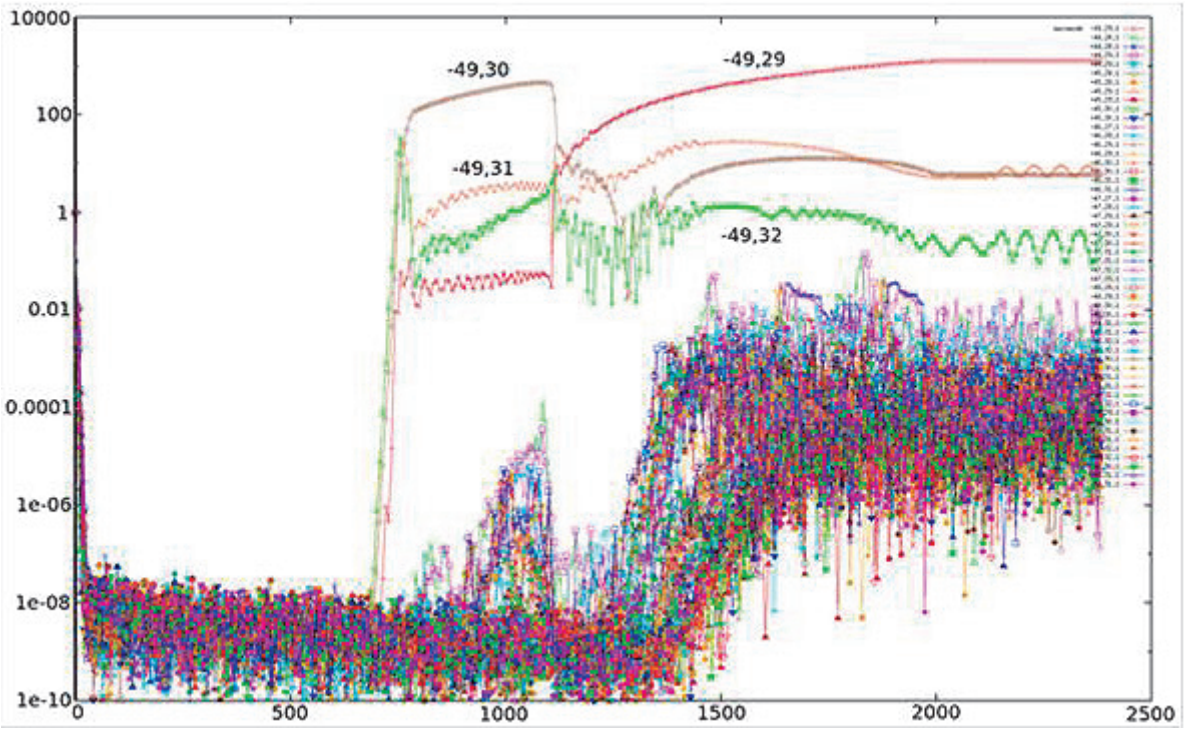

Fig. 6: Start-up scenario considering 52 modes, output power in W (logarithmic scale) vs. time in ns. Only four modes rise above 0.2 W. The radial competitor $TE_{-49,30}$ (brown lozenges) is excited from 800 ns to 1100 ns, then suppressed by the design mode $TE_{-49,29}$ (red plus signs). At design conditions, the main mode is stable, but the oscillations of $TE_{-49,31}$ (orange plus signs) lead to fluctuations of the total output power, which needs further investigation.

At present, a set of modes is chosen for which the resonator geometry is optimized and for which more intense investigations are planned. These include quasi-particle-in-cell (quasi-PIC) verification of the processes in the resonator using the EURIDICE code [12] which employs a different simulation approach. Another property to be investigated is fast frequency-tunability of the gyrotron, e. g. 2 GHz steps (in a few seconds) by fast change of the magnetic field and by variation of the azimuthal index at constant radial index. Additional investigations on possible smaller frequency steps by variation of both azimuthal and radial indexes are planned. Such a gyrotron needs a broadband or a tunable CVD diamond window.

The co-rotating mode $TE_{49,29}$ is a very promising candidate as main operating mode: The frequency ratios with $TE_{35,21}$, $TE_{42,25}$, $TE_{56,33}$ and $TE_{63,37}$ are very close to 5:6:7:8:9, making them very suitable for slowly tunable multi-frequency operation with a conventional CVD win-

dow which is transparent for this frequency sequence. Such a multi-purpose gyrotron would have various applications, e.g. use in an upgraded ITER ECH&CD system, ECH&CD in DEMO and with the highest frequency for optimum ECCD in DEMO. The mode can be excited in a SELFT scenario where 50 other modes, including its five main competitors, are also present (see Fig. 6). First investigations suggest that it is possible to achieve more than 1.2 MW output power at the resonator at 34% electronic efficiency (not taking into account energy recovery by operation of the tube with depressed collector and with operating parameters: U_{beam} = 79.00 kV, I_{beam} = 46.50 A, α= 1.35, B_z= 9.60 T, r_{beam}= 10.04 mm). Preliminary simulations for a 2 MW operating point are being performed and show promising results.

Outlook

The next step after verification of the resonator calculations will be the physical design of other major gyrotron components: MIG, quasi-optical launcher, mirror system and collector. Also, thermo-mechanical and tolerance studies have to be undertaken to verify the practical feasibility of the design.

Assessment of alternative generators

In this chapter we follow the presentation given in [13].

Classification of Fast-Wave Microwave Sources

Fast-wave devices, in which the phase velocity v_{ph} of the electromagnetic wave is greater than the speed of light c, generate or amplify coherent electromagnetic radiation by stimulated emission of bremsstrahlung from a beam of relativistic electrons. The electrons radiate because they undergo oscillations transverse to the direction of beam motion by the action of an external force (field). For such waves the electric field is mainly transverse to the propagation direction.

The condition for coherent radiation is that the contribution from the electrons reinforces the original emitted radiation in the oscillator or the incident electromagnetic wave in the amplifier. This condition is satisfied if a bunching mechanism exists to create electron density variations of a size comparable to the wavelength of the imposed electromagnetic wave. To achieve such a mechanism, a resonance condition must be satisfied between the periodic motion of the electrons and the electromagnetic wave in the interaction region

$$\omega - k_z v_z \cong s\Omega \quad , \quad s = 1,2,... \quad (k_z v_z = \text{Doppler term}) \qquad (1)$$

here ω and k_z are the wave angular frequency and characteristic axial wavenumber, respectively, v_z is the translational electron drift velocity, Ω is an effective frequency, which is associated with macroscopic oscillatory motion of the electrons, and s is the harmonic number.

In the electron cyclotron maser (ECM), electromagnetic energy is radiated by relativistic electrons gyrating in an external longitudinal magnetic field. In this case, the effective frequency Ω corresponds to the relativistic electron cyclotron frequency:

$$\Omega_c = \Omega_{co}/\gamma \quad \text{with} \quad \Omega_{co} = eB_o/m_o \quad \text{and} \quad \gamma = [1 - (v/c)^2]^{-1/2} \approx 1 + eV_o / m_o c^2 = 1 + eV_o/511 \qquad (2)$$

where e and m_o are the charge and rest mass of an electron, γ is the relativistic factor, B_o is the magnitude of the guide magnetic field and V_o is the acceleration voltage in kV. The non-relativistic electron cyclotron frequency is f_{co} / GHz = 28 B_o / T. A group of relativistic electrons gyrating in a strong magnetic field will radiate coherently due to bunching caused by the relativistic mass dependence of their gyration frequency. Bunching is achieved because, as an electron loses energy, its relativistic mass decreases and it thus gyrates faster. The consequence is that a small amplitude wave's electric field, while extracting energy from the

particles, causes them to become bunched in gyration phase and reinforces the existing wave electric field. The strength of the magnetic field determines the radiation frequency.

In the case of a spatially periodic magnetic or electric field (undulator/wiggler), the transverse oscillation frequency Ω_b (bounce frequency) of the moving charges is proportional to the ratio of the electron beam velocity v_z to the wiggler field spatial period λ_w. Thus,

$$\Omega_b = k_w v_z \quad , \quad k_w = 2\pi/\lambda_w \tag{3}$$

The operating frequency of such devices, an example of which is the free electron maser (FEM), is determined by the condition that an electron in its rest frame "observes" both the radiation and the periodic external force at the same frequency. If the electron beam is highly relativistic, ($v_{ph} \cong v_z \cong c$) the radiation will have a much shorter wavelength than the external force in the laboratory frame ($\lambda \cong \lambda_w/2\gamma^2$ so that $\omega \cong 2\gamma^2 \Omega_b$). Therefore, FEMs are capable of generating electromagnetic waves of very short wavelength determined by the relativistic Doppler effect. The bunching of the electrons in FEMs is due to the perturbation of the beam electrons by the ponderomotive potential well which is caused by "beating" of the electromagnetic wave with the spatially periodic wiggler field. It is this bunching that enforces the coherence of the emitted radiation.

In the case of the ECMs and FEMs, unlike most conventional microwave sources and lasers, the radiation wavelength is not determined by the characteristic size of the interaction region. Such fast-wave devices require no periodically rippled walls or dielectric loading and can instead use a simple hollow-pipe oversized waveguide as a circuit. These devices are capable of producing very high power radiation at cm-, mm-, and submillimeter wavelengths since the use of large waveguide or cavity cross sections reduces wall losses and breakdown restrictions, as well as permitting the passage of larger, higher power electron beams. It also relaxes the constraint that the electron beam in a single cavity can only remain in a favourable RF phase for half of a RF period (as in klystrons and other devices employing transition radiation). In contrast with klystrons, the reference phase for the waves in fast wave devices is the phase of the electron oscillations. Therefore, the departure from the synchronous condition, which is given by the transit angle $\theta = (\omega - k_z v_z - s\Omega)L/v_z$, can now be of order 2π or less, even in cavities or waveguides that are many wavelengths long.

Dispersion Diagrams of Fast Cyclotron Mode Interaction

Many configurations can be used to produce coherent radiation based on the ECM instability. The departure point for designs based on a particular concept is the wave-particle interaction. Dispersion diagrams, also called ω-k_z plots or Brillouin diagrams, show the region of cyclotron interaction (maximum gain of the instability) between an electromagnetic mode and a fast electron cyclotron mode (fundamental or harmonic) as an intersection of the waveguide mode dispersion curve (hyperbola):

$$\omega^2 = k_z^2 c^2 + k_\perp^2 c^2 \tag{4}$$

with the beam-wave resonance line (straight) given by eq. (1). In the case of a device with cylindrical resonator the perpendicular wavenumber is given by $k_\perp = X_{mn} / R_o$ where X_{mn} is the nth root of the corresponding Bessel function (TM_{mn} modes) or derivative (TE_{mn} modes) and R_o is the waveguide radius. Phase velocity synchronism of the two waves is given in the intersection region. The interaction can result in a device that is either an oscillator or an amplifier. In the following subsections, the different ECM devices are classified according to their dispersion diagrams.

Gyrotron Oscillator and Gyroklystron Amplifier

Gyrotron oscillators (gyrotrons) were the first ECMs to undergo major development. In September 1964 scientists at IAP Nizhny Novgorod operated the first gyrotron (mode: TE_{101} rectangular cavity, power: 6 W, CW). In 1966 the term “gyrotron” was coined by Arcady Goldenberg at IAP. Increases in device power were the result of Russian developments from the early 1970s in magnetron injection guns, which produce electron beams with the necessary transverse energy (while minimizing the spread in transverse energies) and in tapered, open-ended waveguide cavities that maximize efficiency by tailoring the electric field distribution in the resonator. In 1967 Igor Antakov performed at IAP first gyroklystron experiments.

Gyrotrons and gyroklystrons are devices which usually utilize only weakly relativistic electron beams (V_o < 100 kV, γ < 1.2) with high transverse momentum (pitch angle $\alpha = v_\perp/v_z > 1$). The wavevector of the radiation in the cavity is almost transverse to the direction of the external magnetic field ($k_\perp >> k_z$, and the Doppler shift is small) resulting, according to eqs. (1) and (2), in radiation near the electron cyclotron frequency or one of its harmonics:

$$\omega \cong s\Omega_c \ , \qquad s = 1,2, \tag{5}$$

In the case of cylindrical cavity tubes the operating mode is close to cutoff ($v_{ph} = \omega/k_z >> c$) and the frequency mismatch $\omega - s\Omega_c$ is small but positive in order to achieve correct phasing, i.e. keeping the electron bunches in the retarding phase. The Doppler term $k_z v_z$ is of the order of the gain width and is small compared with the radiation frequency. The dispersion diagrams of fundamental and harmonic gyrotrons are illustrated in Figs. 7 and 8, respectively. The velocity of light line is determined by $\omega = ck_z$. For given values of γ and R_o, a mode represented by X_{mn} and oscillating at frequency ω is only excited over a narrow range of B_o. Quasi-optical gyrotrons employ a Fabry-Pérot mirror resonator perpendicular to the electron beam, also providing $k_\perp >> k_z$ (Fig. 7). By variation of the magnetic field, a sequence of discrete modes can be excited. The frequency scaling is determined by the value of B_o/γ. Modern high-power high-order volume mode CW gyrotron oscillators for fusion plasma applications employ an internal quasi-optical mode converter with lateral microwave output and a single-stage depressed collector (SDC) for energy recovery. Cavity expansion due to ohmic wall heating and electron beam space charge neutralization reduce the operating frequency by a few hundred MHz. Cyclotron harmonic operation reduces the required magnetic field for a given frequency by the factor s. However, the measured efficiencies for gyrotrons operating at higher harmonics (s = 2 and 3) are lower than those operating at the fundamental frequency.

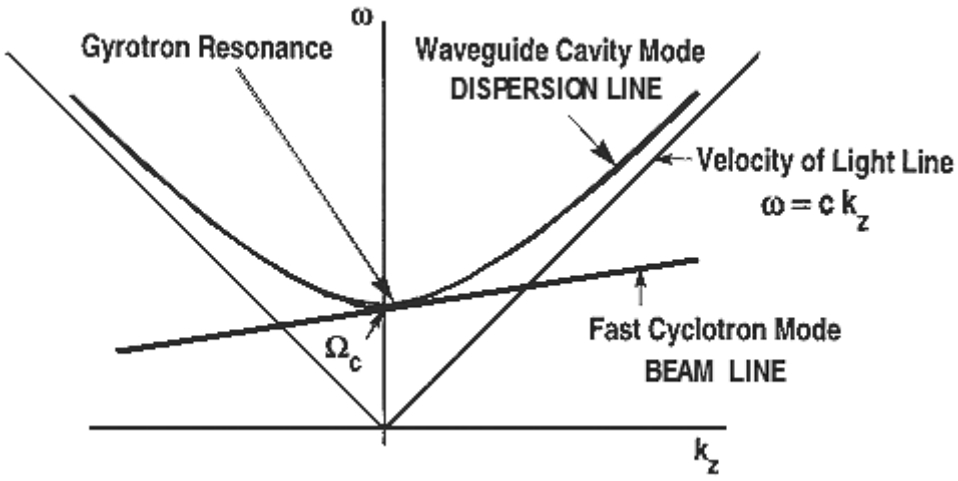

Fig. 7: Dispersion diagram of gyrotron oscillator (fundamental resonance).

At low voltages, the number of electron orbits required for efficient bunching and deceleration of electrons can be large, which means that the resonant interaction has a narrow bandwidth, and that the RF field may have moderate amplitudes. In contrast with this, at high voltages, electrons should execute only about one orbit. This requires correspondingly strong RF fields, possibly leading to RF breakdown, and greatly broadens the cyclotron resonance band, thus making possible an interaction with many parasitic modes.

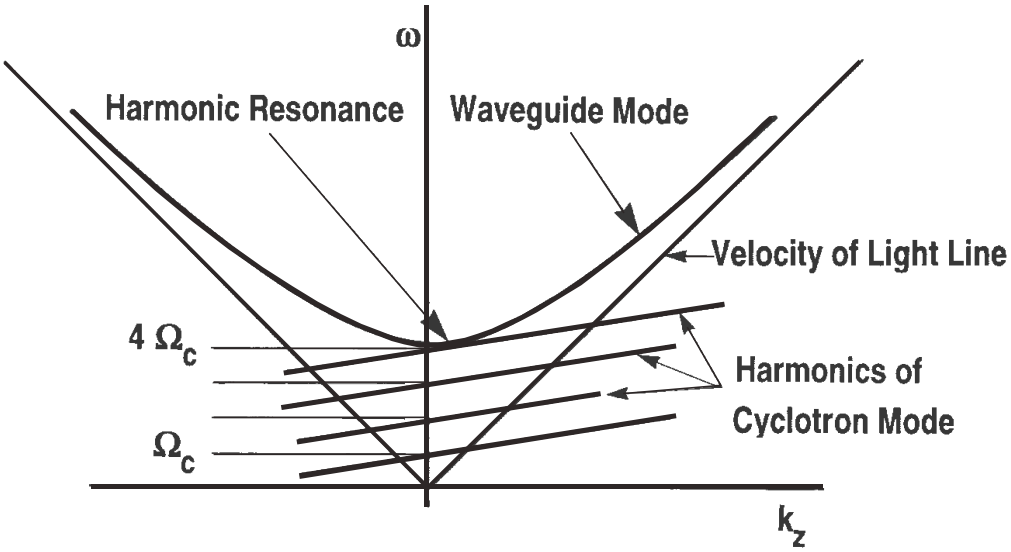

Fig. 8: Dispersion diagram of harmonic frequency gyrotron oscillator.

Cyclotron Autoresonance Maser (CARM)

In a gyrotron with a highly relativistic beam ($\geq$ 1MeV), an efficient interaction will lead to an average energy loss in the order of the initial electron energy. As a result, the change in the gyrofrequency is much greater than in the mildly relativistic case. It is therefore desirable to identify the condition under which such a highly relativistic electron beam remains in synchronism with the RF field. A possibility for achieving synchronism is to utilize the interaction of electrons with electromagnetic waves propagating with a phase velocity close to the speed of light in the direction of the magnetic field. In this case, the Doppler shift term $k_z v_z$ is large, and the appropriate resonance condition is [14]

$$\omega \cong k_z v_z + s\Omega_c \qquad (6)$$

If $v_{ph} \cong c$, the increase in cyclotron frequency due to extraction of beam energy (decrease of γ) nearly compensates the decrease in the Doppler-shift term. Therefore, if the resonance condition is initially fulfilled, it will continue to be satisfied during the interaction. This phenomenon is called autoresonance, and the cyclotron maser devices operating in the relativistic Doppler-shifted regime are called cyclotron autoresonance masers. Fig. 9 shows how the Brillouin diagram of the fast cyclotron wave changes during the autoresonance interaction such that the working frequency ω remains constant even though both Ω_c and v_z are changing. The CARM interaction corresponds to the upper intersection and is based on the same instability mechanism as that of the gyrotron but operated far above cutoff. The instability is convective, so feedback, e.g. by a Bragg resonator (see Fig. 10) [15] is required for an oscillator and it is necessary to carefully discriminate against the other interactions corresponding to the lower frequency intersection in the dispersion diagram Fig. 9.

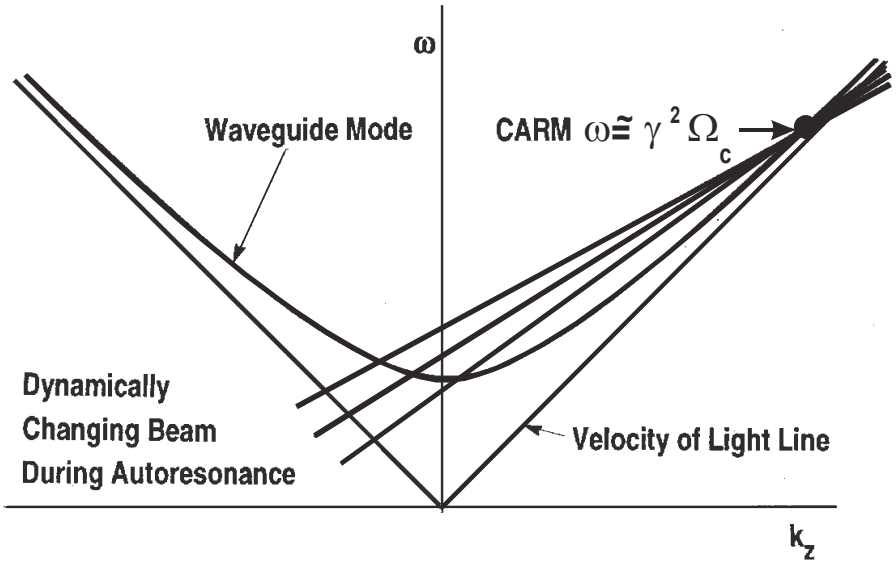

Fig. 9: Dispersion diagram of the cyclotron autoresonance maser (CARM).

The problem can be alleviated by employing the fundamental TE11 or (HE11 hybrid mode) and properly choosing system parameters to be within the stability limit. Compared to a gyrotron, there is a large Doppler frequency upshift of the output ($\omega \cong \gamma^2\Omega_c$) permitting a considerably reduced magnetic field Bo. Since the axial bunching mechanism can substantially offset the azimuthal bunching the total energy of the beam and not only the transverse component is available for RF conversion.

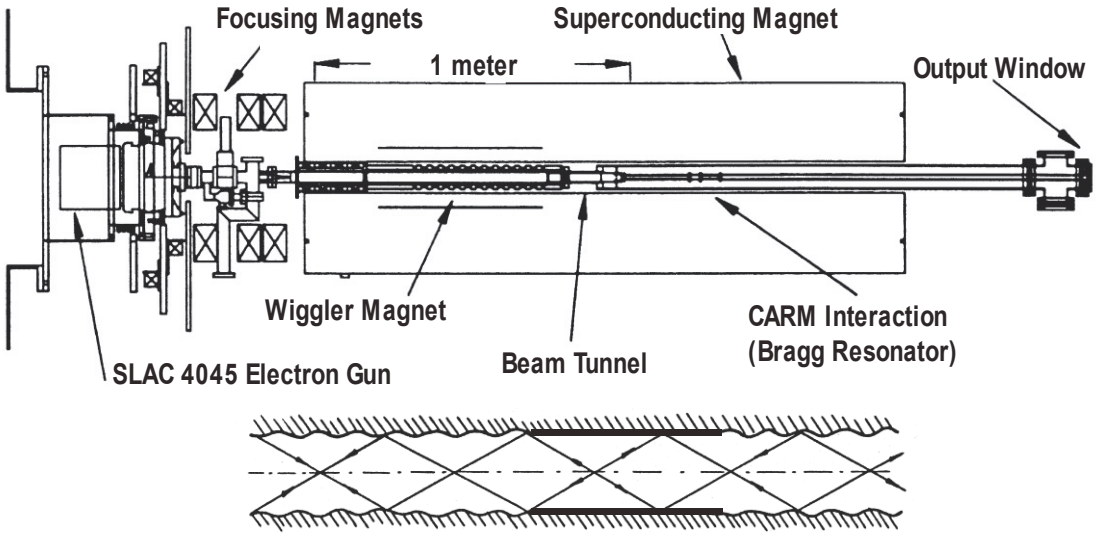

Fig. 10: Schematic of the “long-pulse” (800 ns) MIT CARM oscillator experiment [16] and scheme of a Bragg resonator [17].

In contrast to the gyrotron the CARM has an electron beam with low to moderate pitch angle ($\alpha < 0.7$). The efficiency of CARMs is extremely sensitive to spread in the parallel beam velocity. The velocity spread $\Delta v_z/v_z$ must be lower than 1% to achieve the full theoretically expected efficiency of 40%.

Table 1: State-of-the-art of fast-wave CARM experiments (short pulse: 0.5 ns – 1 μs). The MIT experiment with about 800 ns pulse duration is called "long-pulse experiment" ([16], [28], [29]). Efficiencies in the brackets are relative to the total generated and accelerated electron beam. The experimental efficiency at frequencies higher than 100 GHz are 2 - 2.5 %. There is no research activity in this field of CARMs since 2001.

Institution	Freq. [GHz]	Mode	Power [MW]	Eff. [%]	Gain [dB]	B-Field [T]	Voltage [MV]	Current [kA]	Type
IAP	31.5-34.5	TE_{11}^{*}/TE_{21} ($2\Omega_c$)	3.4	17 (0.21)	-	1.05-1.2	0.40	0.05 (4)	CARM-BWO
IAP	35.7	TE_{51}	30	10	-	1.12	0.4	0.6	oscillator
IAP	36.5	TE_{11}	9	18 (0.45)	-	1.15	0.4	0.6	oscillator
IAP, IHCE	37.5	TE_{11}	10	4	30	0.5	0.5	0.5	amplifier
IAP, U. Strath., HERC	37.5	TE_{21}	0.2	0.5 (0.25)			0.15	0.25 (0.5)	Super-radiance
IAP	38	TE_{11}^{*}/TE_{21} ($2\Omega_c$)	13	26 (0.65)	-	1.24	0.5	0.1 (4)	CARM-gyrotron
	40	TE_{11}	6	22 (0.44)	-		0.46	0.06 (0.3)	oscillator
IAP, IHCE, JINR	50	TE_{11}	30	10	-	0.7	1.0	0.3	oscillator
IAP	66.7	TE_{21}	15	3	-	0.6	0.5	1.0	oscillator
IAP, IHCE, JINR	68	TE_{11}	50	8	-	1.0	1.2	0.5	oscillator
IAP	69.8	TE_{11}	6	4	-	0.6	0.35	0.4	oscillator
IAP [15], [17] – [26]	125	TE_{41}	10	2	-	0.9	0.5	1.0	oscillator
LLNL Livermore (27)	220	TE_{11}	50	2.5	-	3.0	2.0	1.0	oscillator
MIT Cambridge [16], [28], [29]	27.8 30 32 35	TE_{11} TE_{11} TE_{11} TE_{11}	1.9 0.1 0.11 12	5.3 3 2.3 6.3 (0.04)	- - - 30	0.6 0.64 0.63 0.7	0.45 0.3 0.32 1.5	0.080 0.012 0.015 0.13 (20)	oscillator oscillator oscillator amplifier
UNIV. Michigan [30], [31]	15	TE_{11}	7	1.5	-	0.45	0.4	1.2	oscillator
UNIV. Strathclyde [32] – [34]	13 14.3 ($2\Omega_c$)	TE_{11} TE_{21}	0.18	4 (0.4)	- -	0.3 0.2	0.4 0.3	0.04 0.015 (0.15)	oscillator oscillator

* output

HERC Moscow, IAP Nizhny Novgorod, IHCE Tomsk, JINR Dubna

Conclusions

The concept of the CARM shows a strong dependence of the interaction on velocity spread of the electrons. Thus, several experiments show a very low efficiency.

Up to now only TEm_1 modes with m = 1 – 5 have been used in the interaction circuit.

The power limitations (in MW) for those modes in CW or high-duty cycle pulsed operation (average power) at cutoff (in gyrotron cavity) are summarized in the following table.

Mode	Power limitation [MW]	
	170 GHz	240 GHz
TE_{11}	0,018	0,0075
TE_{21}	0,018	0,0075
TE_{31}	0,018	0,0075
TE_{41}	0,022	0,009

However, for CW or high-duty pulsed operation much higher order operating mode must be utilized which will result in severe competition due to higher axial modes as well as gyro-TWT, gyrotron, harmonic gyrotron, gyro-BWO and harmonic gyro-BWO interactions with other modes (see. e.g.[35], here TE_{61} was the design interaction mode).

It is important to note that the development of high-order mode CARMs is in an early stage with respect to physics and technological issues and is up to now not successful. Therefore, there is no research activity in the field of CARM development since more than one decade!

We conclude that the CARM concept is not suitable for application in high-power long-pulse regime.

Staff:

Avramidis, K.
Franck, J.
Jelonnek, J.
G. Gantenbein
Thumm, M.

Literature:

[1] E. Poli et al., “Electron-cyclotron-current-drive efficiency in DEMO plasmas”, Nuclear Fusion, 53, 2013.

[2] Piosczyk et al. “156 GHz, 1.5 MW-Coaxial Cavity Gyrotron with Depressed Collector”, IEEE Transactions on plasma science, 27, No. 2, 1999

[3] K. A. Avramidis et al. “Mode selection for a 170 GHz, 1 MW Gyrotron”, 5th EPS 2008

[4] M. V. Kartikeyan, E. Borie, M. Thumm “Gyrotrons”, Springer 2004

[5] C. J. Edgcombe (Ed.) “Gyrotron Oscillators”, Taylor & Francis, London 1993

[6] K. A. Avramidis “Design and Simulation of Coaxial Gyrotrons” (in Greek), NTU Athens, 2006

[7] O. Dumbrajs, G. S. Nusinovich, T. M. Antonsen Jr. “Regions of azimuthal instability in gyrotrons”, Physics of Plasmas 19, 063103, 2012

[8] K. E. Kreischer et al. “The Design of Megawatt Gyrotrons”, IEEE Transactions on plasma science, PS-13, No. 6, 1985

[9] M. I. Airila, O. Dumbrajs “Spatio-Temporal Chaos in the Transverse Section of Gyrotron Resonators”, IEEE Transactions on plasma education, 30, No. 3, 2002

[10] A. T. Drobot, K. Kim “Space charge efffects on the equilibrium of guided electron flow with gyromotion”, Intl. Journal of Electronics, 51:4, pp 351-367, 1981

[11] A. S. Gilmour “Principles of traveling wave tubes”, Artech House Inc., 1994

[12] S. Kern “Numerische Simulation der Gyrotron-Wechselwirkung in koaxialen Resonatoren”, FZKA5837, Karlsruhe, 1996

[13] K. A. Avramidis, I. G. Pagonakis, C. T. Iatrou, J. L. Vomvoridis “EURIDICE: A code-package for gyrotron interaction simulations and cavity design”, proceedings 17th Joint Workshop on ECE and ECRH, Deurne (NL), 2012

[14] M. Thumm, “State-of-the-art of high power gyro-devices and free electron masers”, KIT scientific reports, 7641, 2012.

[15] Bratman, V.L., Denisov, G.G., Ginzburg, N.S., and Petelin, M.I., 1983, FEL's with Bragg reflection resonators. Cyclotron autoresonance masers versus ubitrons. I.E.E.E. Journal Quantum Electronics, QE-19, 282-296.

[16] Pendergast, K.D., Danly, B.G., Menninger, W.L., Temkin, R.J.,1992, A long-pulse CARM oscillator experiment. Int. J. Electronics, 72, 983-1004.

[17] Bratman, V.L., Denisov, G.G., 1992, Cyclotron autoresonance masers - recent experiments and prospects. Int. J. Electronics, 72, 969-981.

[18] Bratman, V.L., Denisov, G.G., Ofitserov, M.M., Samsonov, S.V., Arkhipov, O.V., Kazacha, V.I., Krasnykh, A.K., Perelstein, E.A., Zamrij, A.V., 1992, Cyclotron autoresonance maser with high Doppler frequency upconversion. Int. J. Infrared and Millimeter Waves, 13, 1857-1873.

[19] Bratman, V.L., Denisov, G.G., Samsonov, S.V., 1993, Cyclotron autoresonance masers: achievements and prospects of advance to the submillimeter wavelength range. Proc. 2nd Int. Workshop on Strong Microwaves in Plasmas, Moscow - Nizhny Novgorod -Moscow, Inst. of Applied Physics, Nizhny Novgorod, 1994, Vol. 2, 690-711.

[20] Bratman, V.L., Denisov, G.G., Kol'chugin, B.D., Samsonov, S.V., Volkov, A.B., 1995, Experimental demonstration of high-efficiency cyclotron-autoresonance-maser operation. Phys. Rev. Lett., 75, 3102-3105.

[21] Ginzburg, N.S., Zotova, I.V., Sergeev, A.S., Konoplev, I.V., 1997, Experimental observation of cyclotron superradiance under group synchronism conditions. Phys. Rev. Letters, 78, 2365-2368.

[22] Ginzburg, N.S., Zotova, I.V., Sergeev, A.S., Phelps, A.D.R., Cross, A.W., Shapk, V.G., Yaladin, M.I., Tarakanov, V.P., 1999, Generation of ultrashort microwave pulses based on cyclotron superradiance. IEEE Trans. on Plasma Science, PS-27, 462-469.

[23] Bratman, V.L., Denisov, G.G., Kalynov, Yu.K., Samsonov, S.V., Savilov, A.V., Cross, A.W., He, W., Phelps, A.D.R., Ronald, K., Whyte, C.G., Young, A.R., 1999, Novel types of cyclotron resonance devices. Proc. 4th Int. Workshop on Strong Microwaves in Plasmas, Nizhny Novgorod, ed. A.G. Litvak, Inst. of Applied Physics, Russian Academy of Sciences, Nizhny Novgorod, 2000, Vol. 2, 683-702.

[24] Bratman, V.L., Fedotov, A.E., Kolganov, N.G., Samsonov, S.V., Savilov, A.V., 2000, Effective co-generation of opposite and forward waves in cyclotron-resonance masers. Phys. Rev. Lett., 85, 3424-3427.

[25] Bratman, V.L., Fedotov, A.E., Savilov, A.V., 2000, A gyrodevice based on simultaneous excitation of opposite and forward waves (Gyrotron BWO-TWT). IEEE Trans. on Plasma Science, PS-28, 1742-1746.

[26] Bratman, V.L., Fedotov, A.E., Kolganov, N.G., Samsonov, S.V., Savilov, A.V., 2001, Experimental study of CRM with simultaneous excitation of traveling and near-cutoff waves (CARM-Gyrotron). IEEE Trans. on Plasma Science, PS-29, 609-612.

[27] Caplan, M., Kulke, B., Westenskow, G.A.; McDermott, D.B., Luhmann, Jr.,N.C., 1992, Induction-linac-driven, millimeter-wave CARM oscillator. Laboratory Report UCRL-53689-80, Lawrence Livermore National Laboratory, Livermore, California.

[28] Danly, B.G., Hartemann, F.V., Chu, T.S., Legorburn, P., Menninger, W.L, Temkin, R.J., 1992, Long-pulse millimeter-wave free-electron laser and cyclotron autoresonance maser experiments. Phys. Fluids, B4, 2307-2314.

[29] Alberti, S., Danly, B.G., Gulotta, G., Giguet, E., Kimura, T., Menninger, W.L., Rullier, J.L., Temkin, R.J., 1993, Experimental study of a 28 GHz high-power long-pulse cyclotron autoresonance maser oscillator. Phys. Rev. Lett., 71, 2018-2021.

[30] Wang, J.G., Gilgenbach, R.M., Choi, J.J., Outten, C.A., Spencer, T.A., 1989, Frequency-tunable, high-power microwave emission from cyclotron autoresonance maser oscillation and gyrotron interactions. IEEE Trans. Plasma Science, 17, 906-908.

[31] Choi, J.J., Gilgenbach, R.M., Spencer, T.A., 1992, Mode competition in Bragg resonator cyclotron resonance maser experiments driven by a microsecond intense electron beam. Int. J. Electronics, 72, 1045-1066.

[32] Cooke, S.J., Cross, A.W., He, W., Phelps, A.D.R., 1995, The operation of a second harmonic CARM oscillator. Conf. Digest 20th Int. Conf. on Infrared and Millimeter Waves, Lake Buena Vista (Orlando), Florida, 427-428.

[33] Cooke, S.J., Cross, A.W., He, W., Phelps, A.D.R, 1996, Experimental operation of a cyclotron autoresonance maser oscillator at the second harmonic. Phys. Rev. Lett., 77, 4836-4839.

[34] Young, A.R., He, W. Ronald, K., Cross, A.W., Whyte, C.G., Phelps, A.D.R., 1998, Cold and thermionic cathode CARM experiments. Conf. Digest 23rd Int. Conf. on Infrared and Millimeter Waves, Colchester, UK, 448-449.

[35] R.B. McCowen et al., Observation of harmonic gyro-backward-wave oscillation in a 100 GHz CARM oscillator experiment, Int. J. Electronics, Vol 72, Nos. 5 and 6, 1033-1043 (1992)

Acknowledgement

This work, supported by the European Communities under the contract of Association between EURATOM and Karlsruhe Institute of Technology, was carried out within the framework of the European Fusion Development Agreement. The views and opinions expressed herein do not necessarily reflect those of the European Commission.

ITER ECRF Advanced Source Development (CoA)

Coaxial-cavity Gyrotron

The development of a 2 MW 170 GHz short-pulse coaxial-cavity gyrotron prototype is in progress at KIT. Coaxial-cavity gyrotrons (with inner rod) offer advantages in comparison to conventional-cavity gyrotrons, namely reduced voltage depression and mode competition, resulting in higher output powers and operating frequencies. The coaxial arrangement has a potential to provide higher RF output power per unit, compared with conventional hollow-cavity gyrotrons, for reduced cost and space requirements. Gyrotrons for future fusion devices, operating at multi-megawatt power levels and frequencies above 200 GHz, most probably will be of coaxial-cavity type. Since the coaxial-cavity technology has the potential of considerably higher output power KIT is continuously pushing forward this development, as very attractive alternative solution for the ECRH systems of future fusion experimental reactors and demonstration power plants (particularly DEMO).

Preliminary experimental results

In the first experiments, stable operation of the KIT short-pulse coaxial-cavity prototype was limited to a cathode voltage below 80 kV and a beam current of maximum 60 A. Instabilities limited the pulse length to below 0.5 ms. Nevertheless, an RF output power of 1.9 MW with an overall efficiency of 28% (without depressed collector) has been obtained in single $TE_{34,19}$-mode operation at 170 GHz. The following parasitic effects limited the gyrotron operation:

1. Electron beam instabilities: The clearance between the electron beam and the anode wall has been ~0.2 mm only, which is not in line with the 2.3 mm which has been obtained from numerical calculations. The clearance has been observed by measuring the body current at the halo shield. The significant increase of the beam thickness confirmed an existence of an electron halo consisting of electrons trapped between the cathode and the magnetic mirror. It is assumed that those trapped electrons were also responsible for a rise of body/coaxial-insert currents observed during the gyrotron operation.
2. Parasitic oscillations: Low frequency (LF) oscillations at two different frequencies, 112 MHz and 453 MHz, were found for beam currents Ib > 60 A. The observed spectrum of LF-parasites was depending on the gyrotron operating parameters. But, surprisingly, no dependence of the frequency values on the accelerating voltage was observed. The excitation of another type of unwanted oscillations in the higher GHz-range is usually related to the beamtunnel region. In order to suppress such oscillations, the patented KIT-standard design of the beam tunnel (absorption ceramic-copper rings “sandwich” structure) was equipped with additional slots on the copper rings. Recently, a different concept of the beam tunnel (fully out of absorbing semiconductor ceramics SiC) has been manufactured and successfully tested. In the experiments with that new ceramic beam tunnel no parasitic oscillations have been found.

Theoretical investigations on the electron beam instabilities

The beam halo current as observed in the recent experiment could have been a reason for the reduction of the gyrotron performance. The beam halo (travelling electrons outside the regular electron beam) is thought to be caused by electrons trapped between the cathode and the magnetic mirror. In particular, secondary electrons emitted from the cathode surface near the emitter are assumed to contribute significantly to the halo current. Thus, the properties of electrons emitted from that surfaces may be of big importance for the halo generation. Therefore, the trajectories of electrons emitted from the cathode surface around the emitter have been calculated. The calculations have been done for electrons leaving the cathode surface with zero velocity. The results shown in the figure below and the second figure below confirm the existence of magnetically trapped electrons between the electron gun and the cavity region. The next figure shows the maximum value of the pitch angle of the electrons as obtained for the nominal operating gyrotron parameters (U_C = 90 kV, I_b = 75 A).

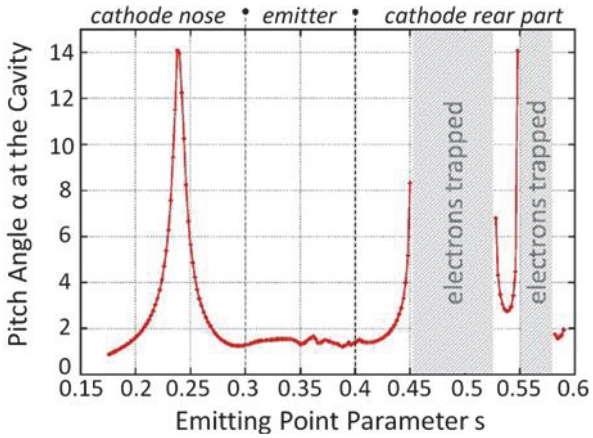

Fig. 1a: Pitch angle at the cavity of electrons emitted from different positions of the cathode surface.

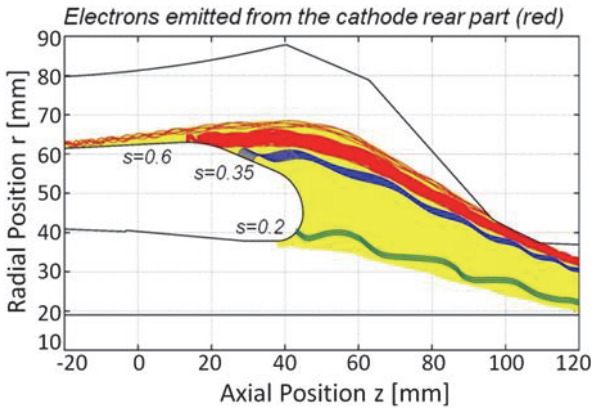

Fig. 1b: Calculated trajectories of electrons emitted from the cathode surface. Magnetically trapped electrons are indicated in red.

The parameter *s* represents the emitted position of the electrons along the cathode surface, starting from the inner side of the cathode nose (s < 0.3), passing through the emitter region (0.3 < s < 0.4) and ending at the rear part of the cathode (0.4 < s < 0.6). As shown in the Figure 1a, the electrons emitted from the emitter surface have a maximum pitch angle $\alpha \sim 1.5$, a value far away from being trapped. On the other hand, electrons emitted above the emitter ring (s > 0.45) and around the cathode nose (s ~ 0.24) have very high pitch angle values. Electrons emitted from these areas could be trapped with very high probability. The trajectories of the electrons emitted along the cathode surface are presented in the Figure1b. The yellow lines represent not magnetically trapped electron trajectories, the blue lines show the trajectories of electrons emitted from the emitter ring. The red lines define the electron trajectories that are magnetically trapped. The number of the trapped electrons could increase very rapidly (catastrophic event) if the emitted electrons are secondary electrons with a non-zero starting velocity. A secondary electron emission can be caused due to the bombardment of the cathode by the already existing trapped electrons. From the recent experiments the beam halo current can be estimated to be nearly as high as the beam current, which results in a significantly increased space charge level. A high level of trapped electrons might explain the rise of the currents to the body/coaxial insert and the discharges/arcing observed inside the tube during the experiments resulting in a reduction of the stable operation of the gyrotron.

Fig. 2: Surface damages observed on of the anode (left) and coaxial insert (right) created due to the activity of trapped electrons.

Further inspection of the gyrotron components confirmed the existence of trapped electrons. In the region of anode (very close to the halo shield) and in the middle part of the coaxial insert, characteristic surface damages and melted spots have been found (see Figure 2)

Results of the experimental investigation on LF- parasitic oscillations

As mentioned before, two different parasitic LF-oscillations in the MHz range (at 112 MHz and 453 MHz) were found in the experiments. The fact, that the frequency of both oscillations was totally independent on the accelerating voltage, indicated an unwanted resonant behavior of the geometrical structure. In that case, the oscillation is generated due to the interaction of the pre-bunched electron beam with the existing field excited in the resonant regions of the gyrotron construction. In order to find the spectrum of resonances of the gyrotron construction, the tube has been modeled and analyzed using the CST Microwave Studio. The simulation results show that the first oscillation at 112 MHz is related to the resonance of the coaxial insert. However, because of the relatively low intensity of the resonating

field the oscillation has been classified as uncritical for the stable gyrotron operation and therefore was not investigated in particular. Another, much stronger resonance was found at 453.4 MHz in the mirror-box and collector section of the gyrotron. The theoretically predicted frequency was in a very good agreement with the frequency of the strong LF-oscillation obtained experimentally. The calculated distribution of the longitudinal component of the resonant electric field is presented in the Figure 3a. Numerical simulations at ~453 MHz confirm that the travelling electrons can interact with the field which is excited in the mirror-box and the collector region. As observed experimentally, the amplitude of the resonant field was constant in time, which indicated a closed feedback loop in the interaction between the field and the travelling electrons. An inspection of the gyrotron assembly show a problem with the RF isolation of the internal gyrotron connector: the shielding of the feed-through connector placed at the mirror-box wall connected via coaxial cable to the cavity probe was not correctly installed (see Figure 3b). Due to missing RF-isolation a part of the resonating field was coupled back from the mirror-box directly into the gyrotron cavity. It resulted in an additional modulation of the electron velocity in the cavity region. In effect the bunched electrons, passing through the mirror-box region, interacted again with the resonating field and leaded to increase of the intensity of parasitic oscillation.

Due to the improved shielding the problem with the previously observed limitations in the gyrotron operation has been solved. It results finally in a much better performance of the gyrotron.

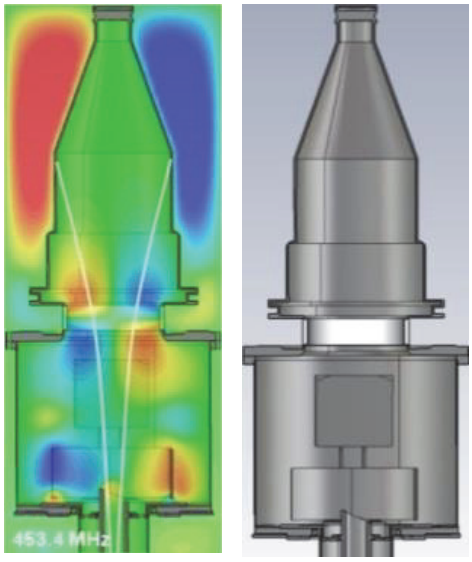

Fig. 3a: Calculated distribution of the resonating field at 453.4 MHz (mirror-box and collector region)

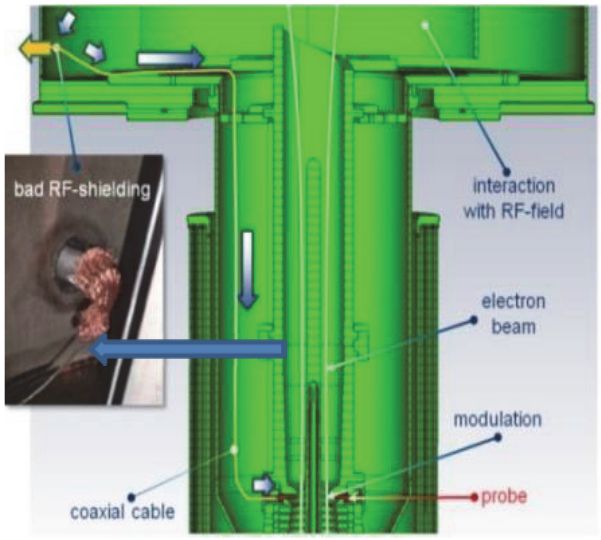

Fig. 3b: Excitation mechanism of the parasitic LF-oscillation at 453 MHz.

Stable gyrotron operation – final results

The removal of the LF-oscillations resulted in a significantly more stable gyrotron operation up to the nominal operating parameters (U_C < 90 kV and I_b < 75 A). Finally, close to the nominal operating point an output power of 2.0 MW at an efficiency of 28% (without depressed collector) has been successfully achieved. The dependence of the generated RF output power on the accelerating voltage at the beam current of 75 A is shown in Figure 4. Additionally, in order to increase the generated output power, the magnetic field in the gyrotron cavity has been slightly risen up. It allowed shifting the excitation region of the nominal mode to ~92 kV. In parallel the electron beam current has been set to be 84 A. At these conditions a new world record in the generated RF output power (per single tube), namely 2.3 MW at 30% efficiency, has been set.

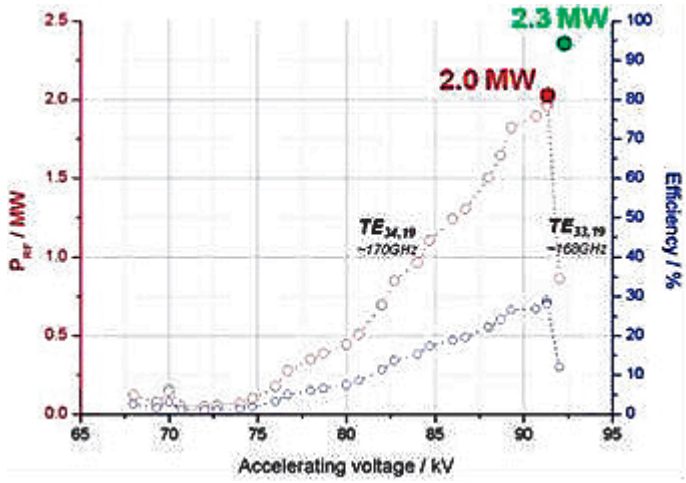

Fig. 4: Measured RF output power as a function of accelerating voltage (obtained at B_{cav} = 6.87 T and I_b ~ 75 A)

Furthermore, in the very preliminary gyrotron experiments with depressed collector an output power of 1.9 MW at an efficiency of ~43% has been demonstrated. The optimization of the operating point with the depressed collector is planned for begin of 2014.

Alternative method for the electron beam alignment with respect to the mechanical axis of the gyrotron

The position of the electron beam axis relative to the axis of the cavity can be obtained, under operating conditions with high accuracy, by measuring of the region of single mode oscillation in dependence of a transverse shift of the electron beam. The transverse displacement of the electron beam around the position of the cavity is obtained by applying independently a current to two sets of dipole coils of the OI SC-magnet. Doing that, the electron beam can be displaced independently in two radial directions (x- and y-direction) which are perpendicular to each other. In order to determine the area of single mode oscillation in the xy-plane, the electron beam is radially displaced and the oscillating mode is observed. In general, the boundary of single mode oscillation in dependence of the shift is very well defined. It has been detected with a frequency filter bank together with a frequency measurements device. Based on the measured points in the xy-plane an oscillating range in form of a circle is found (see Figure 5). From the center of the circle the information about the displacement of the electron beam relative to the cavity can be obtained.

Firstly, the position of the electron beam relative to the cavity has been determined by measuring the area of the single-mode operation. Then, the solenoid coils of the SC-magnet, respectively, the axial B-field B(z) has been shifted radially. The related displacement of the electron beam has been determined from the single-mode oscillation area. After doing that, the measured shift of the electron beam has been compared with the values expected from the mechanical parameters of the SC-magnet, and, in addition, it has been compare with the values obtained from the position of the electron beam relative to the coaxial insert.

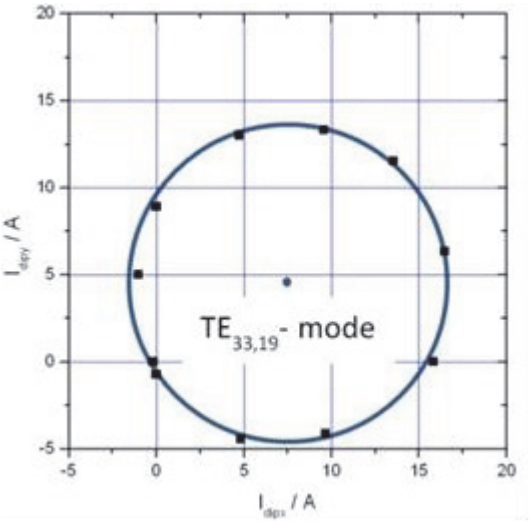

Fig. 5: Example: Oscillating range for the $TE_{33,19}$, 167.9 GHz; U_c = 72 kV; I_b = 24 A.

The Table 1 shows an example of the results obtained from the measurement of the single-mode operating area. The results are consistent with the positions of the electron beam obtained from the measurements of the electron beam relative to the insert and from the mechanical data. The experiments have also shown that it is not necessary to use the nominal 170 GHz $TE_{34,19}$-mode for the definition of the area of mode operation. The measurements with the $TE_{33,19}$-mode (next neighbour of the nominal mode) have provided identical results compared to the measurements using the $TE_{34,19}$-mode.

Table 1: Measurement example;
* values estimated from the shift of the e-beam relative to the insert.
** values estimated from the mechanical shift of the displacement.

action	e-beam to center of cavity	e-beam to the insert	shift of the electron beam obtained from: [a] insert position, [b] oscillating area, [c] mechanical shift [a]	[b]	[c]
Insert aligned	——	**0.12 / 0.07**	——	——	——
SC-coils shift ~0.15	**0.26 / 0.16**	**0.12 / -0.13**	**0.0 / -0.2**	**-0.03 / -0.2*** **-0.07 / -0.17 ****	**0 /-0.15**

ECR Heating and Current Drive: Step-Tunable Gyrotron Development

Energy spectra of spent electron beam recovered from x-ray spectrometry

In 2013, the proof-of-the-principle testing and facilitation of the x-ray based technique of definition of energy distributions in electron beams in the conditions of high-power gyrotrons were performed. In previous sessions (October 2012) the problem with excessive photon flux density was determined, deteriorating the performance of x-ray spectrometer. It was decided to solve the problem by the use of Compton scattering in the materials.

The schematics of layout are shown in the Figure 6a. The spectrometer was placed at the collector and protected with a thick-walled pipe from the direct x-rays generated by the electron beam. It collected only photons scattered in the 2 mm thick Al window irradiated with the direct x-rays. For the energy band of interest (20-100 keV) and scattering angles below 30 degrees the relative energy loss (due to inelastic scattering) cannot exceed 2%. The energy distribution can be corrected to take this into account.

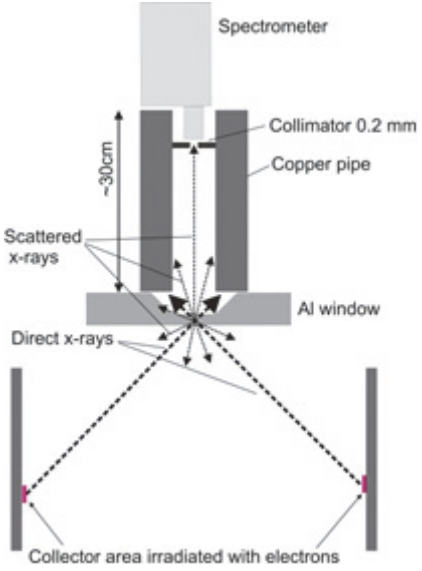

Fig. 6a: Experimental layout.

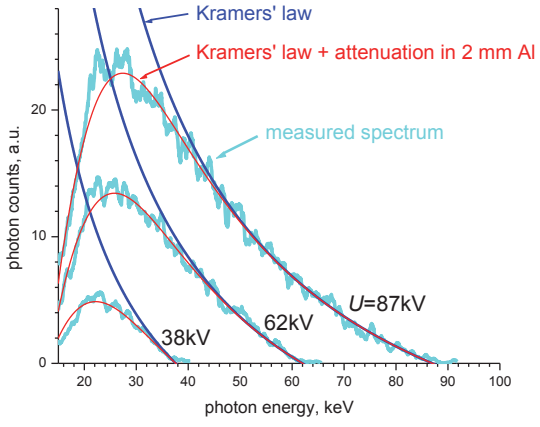

Fig. 6b: Bremsstrahlung spectra for low current (without RF).

To calibrate the data acquisition system and compare experimental data with theoretical predictions, we measured bremsstrahlung spectra in low-current regimes of the gyrotron without interaction in the cavity. This should ensure that all electrons have the same energy corresponding to the gun voltage *U*. The measured bremsstrahlung spectra demonstrated a very good agreement with predictions of the basic theory: Kramers' law and exponential attenuation of low-energy photons in the aluminum window (see Figure 6b).

If we divide the bremsstrahlung spectra to the corresponding Kramer's law, the fit may be interpreted as full attenuation coefficient for photons of energy E on their way to the spectrometer. Therefore, this ratio must be independent on the parameters of the electron beam, which is demonstrated in the Figure 7a.

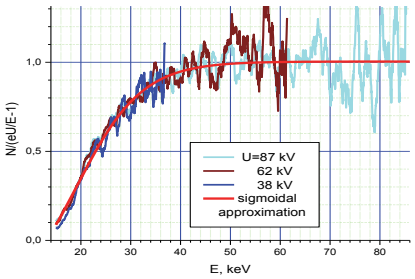

Fig. 7a: Ratio of X-ray spectra for low-current regimes measured with 200 μm collimator, divided by the Kramers' factor $N_{Kram}(E)=Const\cdot(eU/E-1)$.

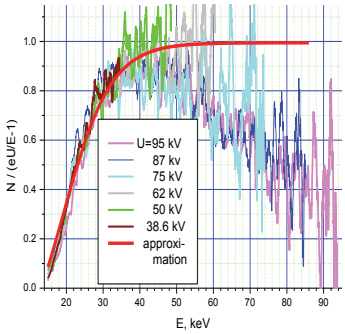

Fig. 7b: X-ray spectra for low-current regimes with 400 μm x-ray collimator.

The measurements of the spectra were performed for different aperture of the spectrometer in order to check the independence of the energy spectra on the photon flux. It is shown that by a higher spectrometer input flux (400 μm collimator) it gives a lower number of photons in the high-energy part of the spectrum. For instance, in the Figure 7b one can find a plot where the normalized spectra were divided by the Cramer's distribution. In this case, no saturation above 50 keV takes place and discrimination of photon signal with higher energy occurs. The observed errors may originate from incorrect performance of so-called "Baseline restoration system" (BLR).

The appearance of a baseline shift leads to incorrect definition of these energies. Even though the BLR system of the spectrometer was "ON" during our experiments, it may be inefficient (or insufficiently efficient) when the photon flux represents a series of ms-length pulses with high intensity separated by long (a few seconds) intervals. In the regimes when the flux intensity was the highest (large collimator hole, high gyrotron gun voltage), the baseline of the spectrometer measurement circuit might had shifted during a gyrotron pulse. As a result, photon energies were determined correctly only at the beginning of each gyrotron pulse (and gave us correct high-energy cut-offs in the measured spectra), while most part of photons were ascribed to lower energies in comparison to their correct values.

During the reported experimental session, we measured x-ray bremsstrahlung spectra for 8 regimes of the gyrotron. The regimes were different in generated mm-wave power, gun voltage, beam current and magnetic compression. For all these regimes the electron energy distributions were reconstructed. All distributions are wide and include electrons with energies between 32.5-35 keV and 80-90 keV (the latter corresponds to the gun voltage). In the most cases a correlation with the output power value (though not very pronounced) may be noted: the distribution for the regime with the lowest mm-wave output obviously has the highest energy "cut-off".

The discrepancy between the measured value of efficiency and obtained from reconstructed electronic spectra may achieve up to 15-20 percentage points (in the best case). The disagreement between experimental values of RF efficiency of the gyrotron and electronic efficiency calculated from experimental data originates from incorrect spectrometer performance in pulsed regime with high peak x-ray flux as noted above. The spectrum which was measured with the 400 μm collimator demonstrates the highest discrepancy predicting an efficiency of 0.6, while the largest value of RF efficiency measured experimentally is 0.27. Usually the "dead time" parameter of spectrometer substantially exceeds the 0.5-0.6 value which was set to ensure correct performance of the spectrometer. The smallest difference between val-

ues of calculated electron efficiency and RF efficiency corresponds to measurements which were performed at low beam current and short “dead time” value.

Numerical study of the influence of the axial electron beam misalignment effect on the performance of the 1MW gyrotron and comparison with experiment

In 2012 the results of numerical simulation using the recently developed self-consistent multimode non-stationary code “Gyrodyne” were reported. In both cases, experimental and numerical simulation predict a similar type of dependence – quadratic decay of the output power with the shifting of the beam axis relative the center of the resonator (see Figure 8a).

The properties of the beam used in the simulation are obtained from an ESRAY static self-consistent code. From ESRAY calculation it follows that the pitch factor of the electron beam is more than 1.4, the electron beam radius is 7.9 mm. The spread of the pitch factor is taken to 20%. These simulations show that the output power is more than 1300 kW, while in the experiment the measured value is around 1000 kW. In addition, the experimentally measured curve demonstrates less steep decay in comparison to numerical simulation, and both curves cross at 0.9 mm beam shift.

It is also interesting to note that in the measurement the excitation of the main mode is observed at relatively large beam misalignments, up to 1.1 mm, while in the numerical simulation at this beam shifting the counter rotating mode is excited with power less than 200 kW (in experiment such a power would be even less at the output due to counter rotation of the mode and a mismatch with the quasi optical system).

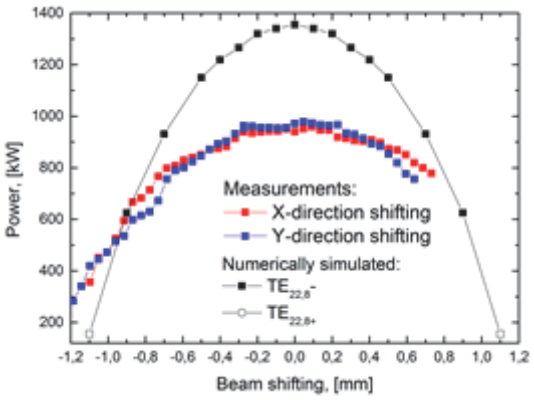

Fig. 8a: Numerical simulation and measurement of the output power as the function of beam shifting.

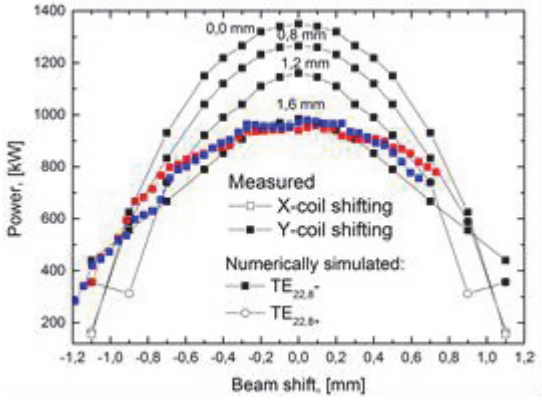

Fig. 8b: Numerical simulation for electron beams with different thickness.

In both cases, in the measurement and in the numerical simulation with large beam shifting (> 0.6 mm) with the increase of the beam energy the excitation of the main mode is terminated by the appearance of the spurious $TE_{19,9}$ mode instead of $TE_{21,8}$- mode as it takes place in the normal, aligned condition. The result can be interpreted considering the averaged structural factor corresponding to the coupling of the beam and the mode.

Since the discrepancy between the measurement and numerical simulation can always occur because the real electron beam properties can be different from the assumed ones, it was interesting to try to perform the numerical simulation taking imperfections of the beam into account. Deterioration of the energy spread of the electron beam, but remaining the coupling of the beam and the mode, would not change the relative sensitivity of the output power in dependence of the beam axial misalignment, while reducing overall performance. Therefore, the thickness of the beam was varied. In the Figure 8b the numerical simulation performed for a number of “thick” electron beams presented by quasi particles with an introduced spread of guiding centers is shown. The current density of the electron beam within the cross section of thick beam is kept constant.

Better quantitative agreement is obtained for thicker electron beams. The results suggest that the performance of the gyrotron can be improved by improving the quality of the electron beam inside the cavity (e.g. “thickness” and shape of electron beam).

Detailed diagnosis of undesired transient effects

The continuous development of more elaborate means for gyrotron spectrum analysis has yielded in a sophisticated measurement system which allows the time-dependent investigation of the spectral mode evolution over time. Apart from a high dynamic range of 50-60 dB, frequency unambiguity is a key feature of the measurement system.

As an example, in the Figure 9 a measurement containing highly transient effects is depicted. It shows the direct observation of mode competition and switching during an external arc, which occurred during the operation of a W7-X gyrotron close to the edge of the stability area of the nominal mode $TE_{28,8}$.

Along the time axis (bottom to top), first the slow starting of oscillations over the high voltage power supply (HVPS) parameter ramp (right part of figure) of the cathode voltage V_c and the beam current I_b is visible. After the HVPS reaching flat-top, stable operation of the nominal cavity mode at 140.25 GHz is established.

Around pulse time 300µs, a destabilization of the mode occurs, which is followed by the start of a competing cavity mode at 137.45 GHz. The prolonged competition between the two modes is directly visible in the spectrogram through strong symmetrical modulation patterns. After ~50 µs of mode competition, the nominal cavity mode is suppressed, which allows the competitor to oscillate undisturbed till pulse end.

During the measurement, an arc at the gyrotron’s microwave output window was detected, which is very likely the cause of the perturbations: being essentially a plasma, an arc at the window can absorb, but also reflect significant amounts of power back into the tube. This can disturb the oscillation (load pull effect) and hence lead to changes in behaviour. Since such events are to be avoided because of their damage potential, detailed information on their properties and behaviour is scarce and valuable. The availability of this data enables closer linkage between experiments and general gyrotron simulation, and after parameter studies more information on the arcing phenomena can be gathered by comparison with the measurement data.The fundamental effect of the arc with respect to the gyrotron interaction lies in the back-reflected power. The intermediate result of a parameter study of complex reflection factors at the gyrotron output is shown. While for many reflection factors stable operation at relatively constant power is maintained, in a significant area of the reflection factor plane stationary oscillations (auto-modulation) is observed.

In a small convex area, the reflection causes a mode switch to the azimuthal neighbour mode $TE_{27,8}$ at 137.45 GHz after a short interval of auto-modulation, matching the effects documented in the Figure 10 surprisingly well. Such investigations still are subject to many degrees of freedom and physical uncertainties; however, this example demonstrates the new opportunities not only for basic gyrotron physics investigation, but also for the assessment and benchmarking of the available simulation tools.

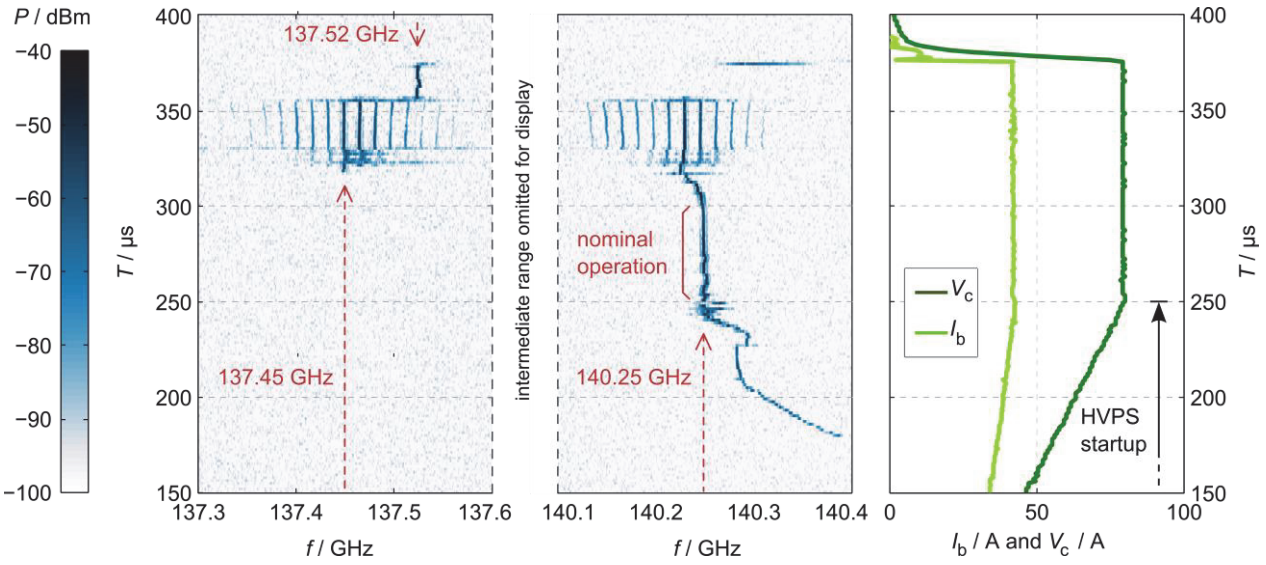

Fig. 9: Excerpt from spectral measurement during RF window arc. The measurement system allows the detailed investigation of the mode spectrum and its evolution over time with a high dynamic range and microsecond time resolution.

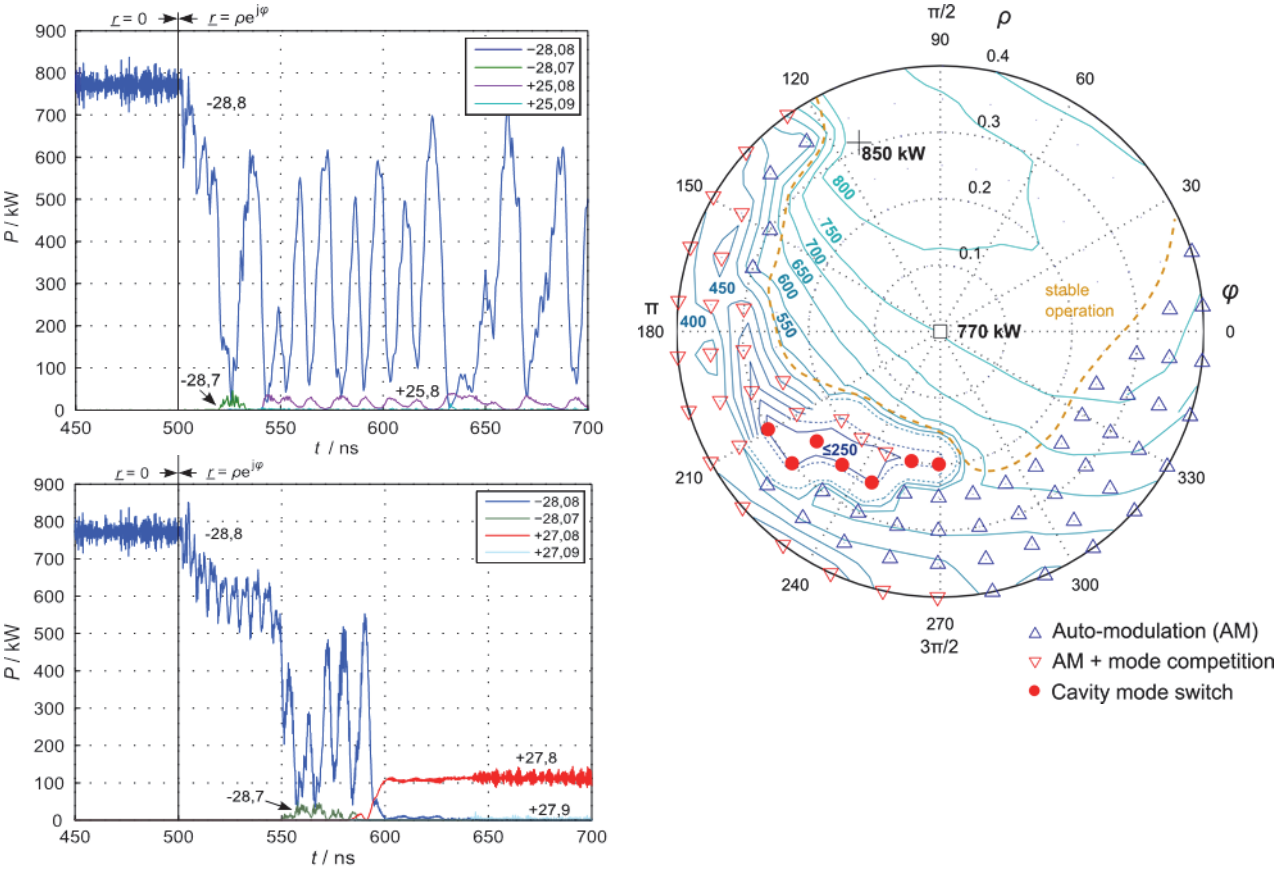

Fig. 10: right: simulated Rieke diagram
Left: sample mode evolutions from simulation parameter study

Development of a low power gyrotron for the test of a new emitter concept

A 10kW/28GHz gyrotron has been designed and manufactured to evaluate the use of controlled porosity reservoir (CPR) emitters for gyrotron applications. CPR cathodes allow operation with higher current density (up to 50 A/cm^2) and provide much longer lifetime (~100000 h) compared to conventional emitter materials (LaB6, conventional dispenser cathodes, etc.). In addition, the azimuthally segmented emitter ring provides the possibility to

generate controlled non-uniform electron beams in order to study the effect of non-uniform emission on the gyrotron output power and efficiency.

All parts for a 10kW/28GHz gyrotron with conventional M-type emitter have been manufactured and assembled. The designed drawing and a photography of the 10kW/28GHz gyrotron are shown in the Figure 11 a. For verification of the gyrotron parameters first experiments will be performed with a conventional M-type emitter. Cathode with this emitter is shown in the Figure 11b a test of the cathode has been performed in a vacuum bell jar. There the emitter has been heated up to nominal temperature and showed uniform temperature distribution along the azimuth as well as good thermal isolation of the emitter from its adjacent parts like cathode nose and back focus electrode.

The manufacturing of the gyrotron test stand is almost finished, including water cooling, data acquisition, interlock and power supply systems. Start of experimental investigation is planned for first quarter of 2014. The segmented emitter is in the final manufacturing phase and has to be assembled at the beginning of 2014. The design drawing for the segmented cathode and a photography of a single manufactured segment are shown in the Figure 11c.

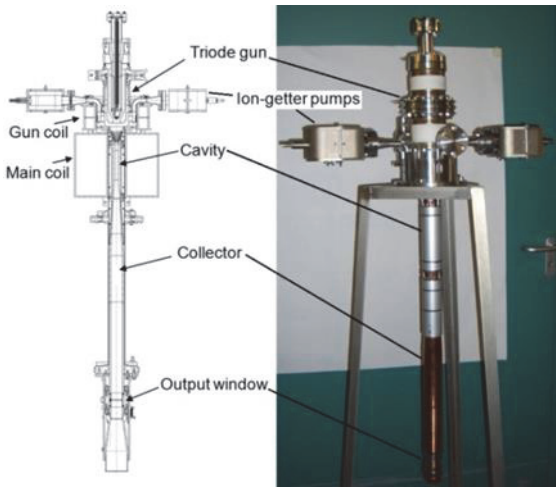

Fig. 11a: Design drawing (left) and assembled 10kW/28GHz gyrotron (right).

Fig. 11b: Design drawing of the segmented emitter (top left), manufactured segment (top middle and bottom right).

Fig. 11c: Design drawing of the conventional emitter (left), manufactured cathode (middle) and heated emitter (right).

Staff:

G. Gantenbein	I. Pagonakis
S. Illy	A. Papenfus
J. Jelonnek	B. Piosczyk
J. Jin	T. Rzesnicki
R. Lang	A. Samartsev
W. Leonhardt	A. Schlaich
A. Malygin	M. Schmid
D. Mellein	W. Spiess

Step-tunable Gyrotrons (WP13-DAS-03-HCD-EC-T05)

Introduction

In recent years electron cyclotron resonance heating and current drive (ECRH and ECCD) have been established as successful instruments for magnetically confined fusion plasmas. Gyrotrons are the unique sources which meet the extraordinary requirements of those applications: RF output power in the MW range, operating frequencies at about 100 – 200 GHz, and pulse lengths of several seconds up to continuous wave (CW). Due to its excellent coupling to the plasma and the very good localization of the absorbed RF power, ECRH is applied in present day machines and is also foreseen in all large forthcoming fusion projects: it will be the main heating system for the W7-X stellarator and it will also be employed at the tokamaks ITER and JT-60SA which are currently under construction and it will play a major role in a future DEMO power plant.

In particular advanced tokamaks are operated in a plasma regime where magneto-hydrodynamic instabilities, occurring at different locations in the plasma, may limit the performance. To a large extent the stability in a tokamak is influenced by the distribution of the internal plasma currents which can be manipulated by the injection of RF waves. These effects call for very localized current drive. The location of the absorption of RF waves with the angular frequency w is dependent on the resonance condition w-kzvz=wc (kz: z-component of the wave number, vz: electron velocity along z-axis). The cyclotron frequency wc of electrons is proportional to the magnetic induction B. Since in a tokamak the magnetic field B(R) is monotonically decreasing with increasing major radius R, the deposition center is a unique function of the wave frequency for radial injection. Thus, by changing the RF frequency w the absorption can be moved to any radial position where the local cyclotron frequency of the electrons wc holds for the expression above [1]. This concept avoids any mechanically moveable components close to the plasma in a harsh environment.

Today, high power gyrotrons for fusion applications in the relevant frequency range with an output power of about 1 MW operate at a fixed frequency. In some cases gyrotrons are designed for two or more discrete frequencies with a separation of a few tens of GHz taking benefit of a minimum of reflection at the single disk output window if the thickness of the disk correspond to an integer multiple of half of the wavelength of the RF radiation in the material (see e.g. [2], [3], [4]). Frequency step-tunable gyrotrons (beyond the dual frequency range) are not standard products since these broadband tubes require additional optimization of the key components, namely the electron beam forming optics, interaction cavity, quasi-optical mode converter and output window [5], [6].

The design of the output window of a frequency step-tunable gyrotron is a particular challenge since it has to provide operation of the gyrotron at different frequencies with minimum reflection of the RF waves. From a technological point of view the design and material must support reliable CW operation with low RF losses in and adequate cooling of the disk. Due to its very good mechanical and electrical properties chemical vapor deposition (CVD) diamond has been established in recent years as a standard material for output window disks of high power CW tubes [7]. In the literature several different approaches of broadband window types such as circularly brazed Brewster diamond window with specific beam optics [3], double disk windows [8] and “travelling wave” windows [9] are reported. From a physics point of view a Brewster angle window with straight transmission without additional beam optics is the most elegant solution since it needs only one diamond disk. It is characterized by a simple and compact unit. For the geometry of Ref. [3] the metallic reflector close to the air side of the diamond disk may lead to arcing induced by the strongly focused RF beam.

Experimental set-up

The experimental investigations were performed with the modular step-frequency tunable short pulse (~ms) D-band gyrotron at KIT [10] which is schematically shown in Figure 1. Originally this device has been designed for the TE22,6 mode operation at 140 GHz [11]. It was the first high power gyrotron operated with a Brewster angle window which in the early phase consisted of a fused silica quartz glass or SiN disk. A combination of the super conducting magnet system and a normal conducting coil system has been used to demonstrate fast (~ 1 s) step-frequency tuning in the frequency range from 132 GHz up to 147 GHz [12]. In 2002 the operating cavity mode of the tube has been modified [13] in order to be compatible with a parallel development in cooperation with the Institute of Applied Physics, Nizhny Novgorod, Russia.

This gyrotron has the advantage of being modular and allows the relative simple replacement of all key components. Furthermore, it is designed for broadband operation with regard to all components such that experiments over a wide parameter range can be performed.

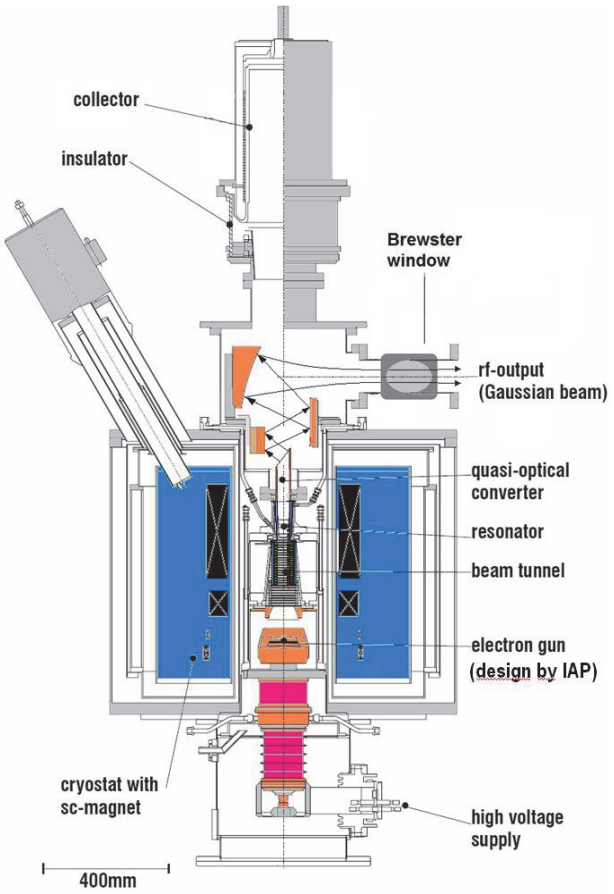

Fig. 1: Modular design of the step-frequency tunable D-band gyrotron with quasi-optical mode converter and lateral RF output with a Brewster angle window.

Table 1: Design parameters of step-frequency tunable gyrotron.

Cavity mode at 140 GHz	$TE_{22,8}$
Output power [MW]	1
Accelerating voltage [kV]	80
Beam current [A]	40
Velocity ratio at cavity, $v_\perp/v_\parallel$	1.4
Magnetic induction at cavity [T]	5.54
Frequency range [GHz]	105 - 143
Pulse length [ms]	< 10

The step-frequency tunable gyrotron was designed for operation in the frequency range 105 – 143 GHz in different operating modes (e.g. TE17,6 at 105 GHz, TE20,7 at 124 GHz, TE22,7 at 131 GHz and TE22,8 at 140 GHz) [13]. Frequency-step tuning is performed by changing the magnetic field and exciting corresponding TE modes in the cavity, while at a fixed magnetic field mainly the acceleration voltage is changed, yielding different RF output power levels. Typical high power operating parameters of the gyrotron are an accelerating voltage of 80 kV and a beam current of 40 A. However, beam currents up to 50 A have been used in the experiments. Details of the gyrotron can be found in [14]. The electron gun is a diode type magnetron injection gun which was designed and manufactured by the Institute of Applied Physics (IAP), Nizhny Novgorod, Russia [15]. Some of the most important design parameters are given in Table 1.

Design of Brewster angle window

In order to minimize reflection of a linearly polarized beam at any frequency at the interface of a material with refractive index n_1 and a material with refractive index n_2 the input angle must be $\Theta_B = \arctan(n_2/n_1)$ (Brewster angle) and the polarization vector must be in the reflection plane. Taking a dielectric constant $\varepsilon_r = 5.67$ for diamond results in a Brewster angle of

67.2°. Simple calculations using analytic formulae predict reflections below -30dB for a variation of QB in the order of ±1.5°. The dimensions of the elliptically shaped diamond disk which was laser cut from a circular disk are: 139 x 95 x 1.7 mm (see Fig. 2).

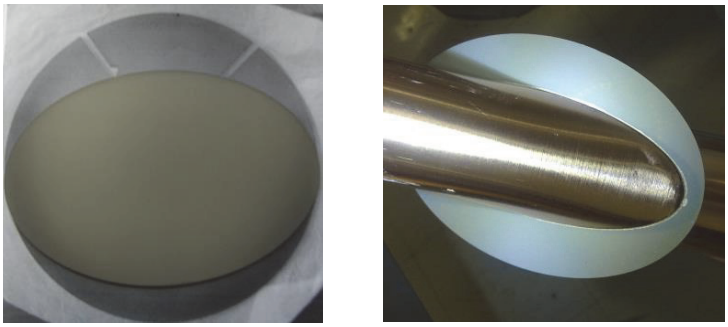

Fig. 2: Diamond disk laser cut from circular disk (left) and brazed to copper cuffs (right).

The brazing of the disk was performed in cooperation with the company Thales Electron Devices, Velizy-Villacoublay, France. Several brazing tests have been performed with dummy ceramic disks in order to optimize the brazing tool. Finally, the diamond disk is brazed with an Ag based brazing material to cylindrical copper cuffs which have an outer diameter of 50 mm, the inner diameter of the system is 49 mm and the total length of the unit is 206 mm. This system is integrated into a housing which is flanged to the gyrotron. Since the pulse length of the gyrotron is limited to a few ms no cooling of the window unit is foreseen.

Structural analyses based on static finite element (FEM) simulations have been performed in order to check the stresses in the device after the cool down phase of the brazing process (see Fig. 3). In fact, the process is carried out in vacuum at 800°C and, since copper and diamond have very different thermal expansion coefficients (ratio of 16 to 1 at 20°C, respectively), the cool down phase to room temperature results in high stresses that might lead to failure of the disk. Stresses and deformations were calculated by decreasing the temperature from 800°C down to 20°C. For the analysis of stresses in the brittle diamond the first principal stress was used while for the ductile copper the equivalent (von Mises) stress was calculated. The first principal stress is in the range of 30 MPa - 75 MPa along the contact region between the disk and the cuffs and reaches a maximum level of 137.4 MPa at the tip of the disk in the contact region with the longer side of the cuffs. This corresponds to an increase factor of 1.4 compared to a circular disk.

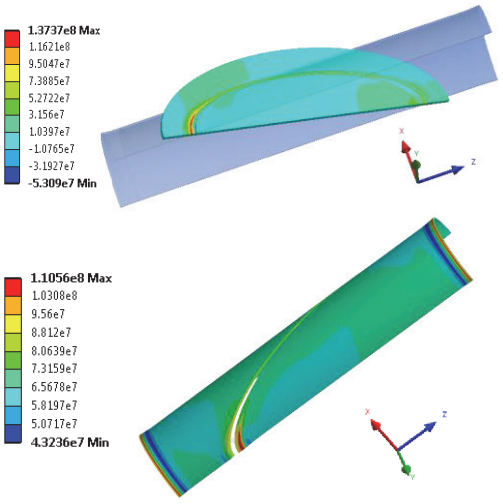

Fig. 3: First principal stress distribution on the top side of the diamond disk (top) and averaged von Mises stress for the copper cuffs (values are in Pa).

The cuffs experience plastic behaviour, in fact the equivalent stress varies between 50 and 75 MPa (yield strength of OFHC copper is 45 MPa at 20°C) in the most part of the cuffs and has maximum values in the range 103.1-110.6 MPa, located close to the area of maximum principal stress and to the support. However, the maximum first principal stress is below the permissible stress of diamond which is 150 MPa (ultimate strength is approximately 450MPa [16]) and the maximum equivalent stress is below the ultimate strength of OFHC copper (250 MPa at 20°C).

Low power measurements with diamond Brewster angle window

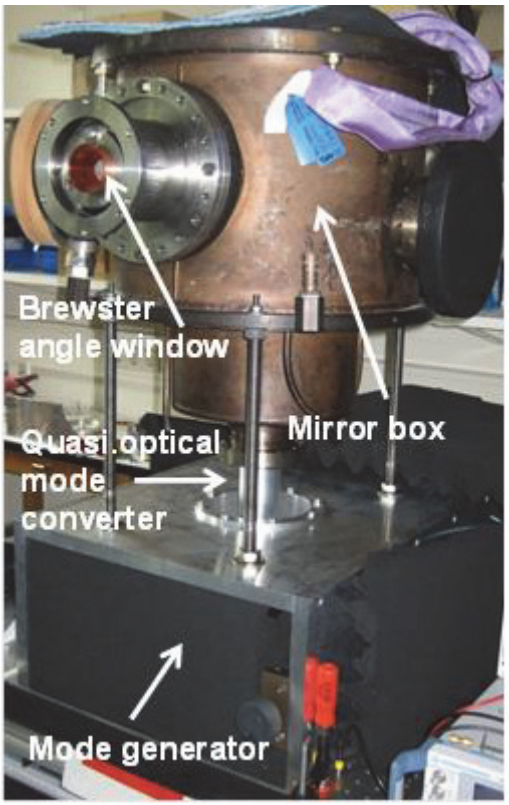

Fig. 4: Experimental setup for low power measurements and built-in quasi-optical mode converter.

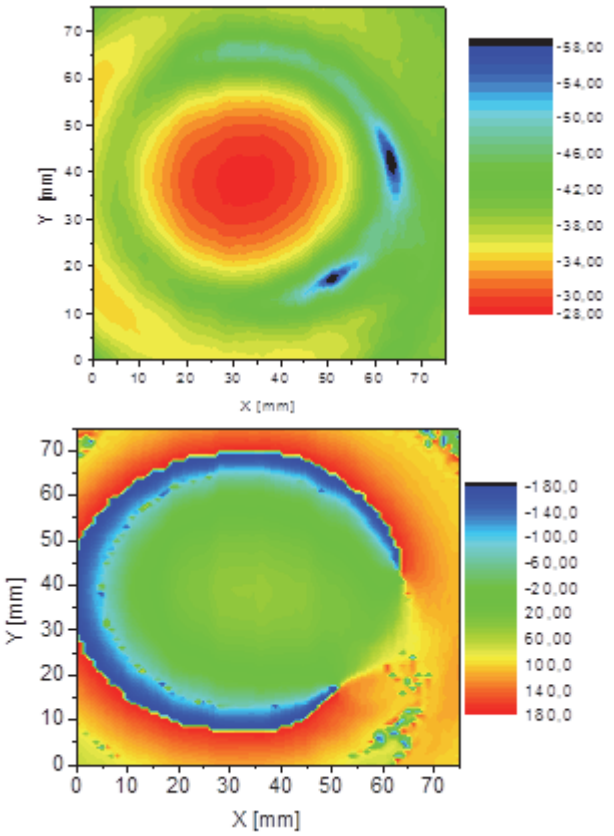

Fig. 5: Low power RF measurement of amplitude (top, values in dB) and phase (bottom, values in deg) of Gaussian output beam at 140 GHz (518 mm from center of window).

In order to verify the RF performance of the complete quasi-optical system including the window, low power RF measurements have been performed prior to installation into the gyrotron. A mode generator, optimized for the TE22,8 mode at 140 GHz, has been used to test the quasi-optical mode converter and the 3-mirror system. The mode generator and the measurement technique are discussed in more detail in [17]. The experimental set-up for the low power RF measurements is shown in Fig. 4.

According to the design the beam waist w0 of the Gaussian output beam is targeted for w0 ~12 mm, centred at the position of the disk with a small variation for the different modes and frequencies. Fig. 5 shows the measured output wave beam of the generated TE22,8 mode at a distance of about 518 mm from the centre of the window.

It is assumed that small distortions from a perfect Gaussian beam which are visible in the amplitude and phase are caused by a non-ideal generation of the TE22,8 mode, non-perfect quasi-optical launcher or diffraction (e.g. at the limited aperture of the window unit). A numerical analysis is applied to the complex field pattern. It maximizes the overlap of a TEM00 mode with the measured profile and analyses the remaining field in terms of higher TEMmn mode contributions taking 13 x 13 modes into account. The analysis of the profile at 518 mm and a profile measured at about 203 mm from the centre of the window in terms of Gaussian mode content shows consistently a TEM00 mode content of 95%. The RF power transmission through the window aperture is estimated to be higher than 99.5%.

Step tunable operation of gyrotron with Brewster angle window

During the experimental investigations reported here the gyrotron has been operated in up to 10 different modes covering the frequency range from 111.6 GHz up to 165.7 GHz (see Table 2). The output beam of each mode has been recorded using infrared measurements of the thermal beam pattern on a suitable target at different positions along beam propagation. Thus it is possible to reconstruct the complex field structure using appropriate algorithms (see e.g. [18]). As an illustration of the beam profile Fig. 6 shows the measured beam pattern of the modes TE20,7 (124.1 GHz), TE22,8 (140.0 GHz), and TE23,8 (143.3 GHz). The pictures have been taken at 760 mm distance from the centre of the window disk, showing an area with a cross section of 80 x 80 mm. With respect to the position of the TE22,8 mode the centre of the mode TE20,7 is shifted approximately by -5.9/-1.3 mm and the mode $TE_{23,8}$ by -0.6/1.0 mm which is much less than the aforementioned 1.5°.

Table 2: Gaussian mode content according to experiment and simulation.

Mode	Frequency [GHz]	TEM_{00} [%] Experiment	TEM_{00} [%] Simulation
$TE_{19,6}$	111.6	89.5	90.4
$TE_{20,7}$	124.1	92.1	93.4
$TE_{21,7}$	127.5	93.5	91.7
$TE_{21,8}$	137.0	92.8	93.0
$TE_{22,8}$	140.0	94.0	93.3
$TE_{23,8}$	143.3	92.4	91.5
$TE_{24,9}$	155.8	85.0	Not investigated
$TE_{25,9}$	159.2	91.0	
$TE_{26,9}$	162.4	92.4	
$TE_{27,9}$	165.7	92.8	

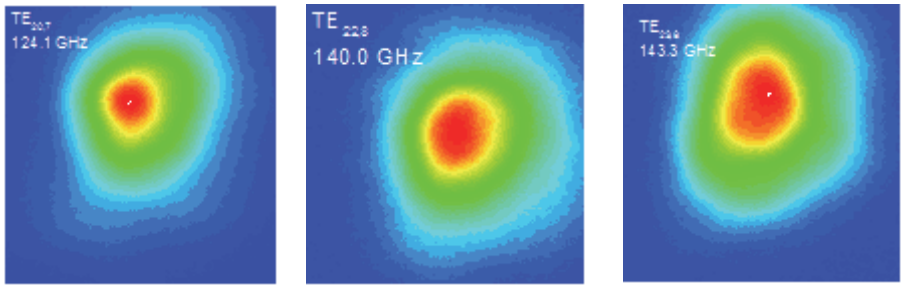

Fig. 6: Output beam profiles measured with an IR system at several frequencies.

The experimental results and a comparison with simulations are given in Table 2. Note that the launcher has been designed according to [19] which is a broadband design taking modes into account up to the TE23,8 at 143.3 GHz. In general there is a very good agreement of the results (low power RF measurements, high power measurements and simulations), small deviations arise from the limited accuracy of the measurement technique and the numerical stability of the analysis procedure. Nevertheless, it should be mentioned that the design shows in the experiment also a high fundamental Gaussian mode content for higher order operating modes which have not been considered initially in the design phase. In order to reduce stray radiation and minimize thermal loading of the transmission components the TEM00 mode content should be as high as possible, for single frequency gyrotrons this part is usually > 95 %.

Optimization and high power experiments have been performed for modes in the frequency range from 124.1 GHz up to 162.5 GHz. The gyrotron has been operated in the 1 MW power regime for all operating modes. A maximum peak power of 1.3 MW in short-pulse operation has been achieved at 143.3 GHz and at a beam current of 52 A. Fig. 7 shows the achieved output power versus the beam current for the TE23,8 mode and an optimized magnetic field. That measurement demonstrates that the operation of the TE23,8 mode is stable over a broad beam current range from 10 A to 52 A with a corresponding output power from 100 kW up to 1.3 MW. The gyrotron has been operated in the short pulse regime (~ 3 ms) without depressed collec-

Table 3: Output power of the different modes.

Mode	Frequency [GHz]	U_{cath} [kV]	I_{beam} [A]	Power [kW]	Efficiency [%]
$TE_{20,7}$	124.1	91.7	42	900	23.4
$TE_{21,7}$	127.4	90.0	42	920	24.3
$TE_{22,8}$	140.0	91.0	50	1250	27.5
$TE_{23,8}$	143.3	92.9	52	1300	26.9
$TE_{25,9}$	159.2	92.3	40	975	26.4
$TE_{26,9}$	162.5	92.3	41	950	25.1

tor. The output power has been measured with a precise short pulse calorimeter which was directly placed at the output window flange. A summary of the results for other operating modes in terms of output power and efficiency is given in Table 3. Note that the efficiency is calculated using the cathode voltage. This does not take into account voltage depression due to the electron beam and thus a reduced electron energy during the start-up phase.

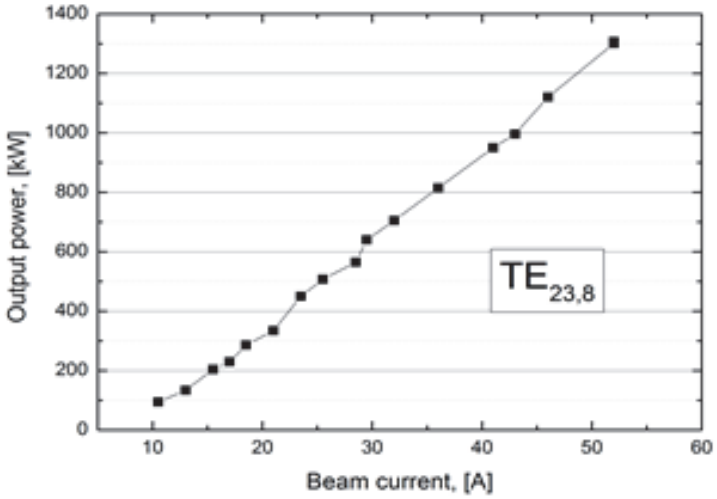

Fig. 7: Gyrotron output power versus beam current for the $TE_{23,8}$ mode.

Conclusions

For the first time an elliptically brazed Brewster angle window of diamond material obtained by chemical vapour deposition (CVD) technique has been used in a MW class high power gyrotron. A frequency step-tunable gyrotron has been used for these experiments. Although after brazing the stress profile of the elliptic geometry of the Brewster angle window is more critical than a standard circular geometry the maximum thermal stress is still well below the ultimate strength. A gyrotron operation in the short-pulse regime without additional cooling of the window unit has been achieved. The high power experiments using the frequency step-tunable gyrotron showed an excellent agreement of the output beam with the simulations for several cavity modes in the frequency range from 111.6 GHz up to 165.7 GHz. Those promising results will be the base for the future design of a Brewster window for long pulse operation including an appropriate cooling technique.

Description of the multi-frequency system at ASDEX-Upgrade and latest results with a broadband travelling wave window

The multi-frequency project on ASDEX Upgrade originates from a collaboration between the Max-Planck-Institute for Plasma Physics (IPP), Garching (Germany), the Institute of Applied Physics (IAP) and GYCOM, both Nizhny Novgorod (Russia), the “Institut für Plasmaforschung” (IPF) at the University of Stuttgart1 (Germany) and the Karlsruhe Institute of Technology (KIT), Karlsruhe (Germany) with the “Institut für Angewandte Materialien” (IAM) and.the Institute for pulsed power and Microwave Technology (IHM). It started in 2000 and was partially funded by the German Helmholtz society and the EU via preferential support (Grant number FU06-CT-2005-00143). A major success is the routine fabrication of two-frequency gyrotrons (1.0 MW/140 GHz, 0.8 MW/105 GHz, 10s) and their standard usage at ASDEX Upgrade ([20], [21]). This success has meanwhile triggered several follow-ups (JAERI, W7-X ([22], [23], [24]). The concept is based on the usage of two neighbouring Fabry-Pérot resonances of the output window together with a gyrotron design capable to oscillate within a few 100 MHz close to the respective Fabry-Pérot frequencies. This concept can

[1] The Institute has recently been reorganised and is now part of the “Institut für Grenzflächenverfahrenstechnik und Plasmatechnologie” (IGVP).

be considered as technologically mature. A recent improvement has been added by JAERI where as additional design feature it could be realized that the caustic radii of both frequencies where so close that the output beams leave the gyrotron in almost identical direction minimizing the effort on mirror adjustment after a change of frequency [23].

As discussed in previous sections, a major goal for technological development is the step-tuneable gyrotron for which all natural resonances of the gyrotron spaced typically by a few GHz should be used for power generation such that the deposition radius in the plasma can be varied quasi-continuously. The excitation of these oscillations over a range $\Delta f/f \approx \pm 0.25$ with respect to the optimum f has been demonstrated by IAP/GYCOM [25] and KIT (IHM) (see section 5) with significant power (> 0.6 Pmax) but only for short pulses. The major issue is the development of broadband vacuum windows for the gyrotron (linear polarisation) and the torus (any polarization) for long pulses.

Gyrotron Windows

Four options for multi-frequency (mf-) windows for GYCOM gyrotrons were pursued by IPP, IAP and GYCOM in parallel to the activities at KIT described in earlier sections:

1. *Double Disk (DD) Window*

   A second diamond disk parallel to the main window allows extending the Fabry-Pérot principle to intermediate frequencies. Frequency tuning requires an adjustable distance between the disks. Technological difficulties: parallelity and adjustability, evacuation of the volume between the disks (approx. 4mm), space limitations leading to cooling issues. Physical problem: usage of DD-windows at gyrotron and Torus sharpens the Fabry-Pérot minima such that the band with is reduced well below the frequency chirp of the gyrotron. Technical drawings were completed but no window was built.

2. *Brewster-Angle Window*

   The concept is similar to the KIT project described in section 3, except for the geometry of the window. In order to minimize the stress on the diamond due to brazing, the disk was manufactured as circular window, but the beam was focussed in one direction and two small mirrors on both sides of the window made this beam crossing the disk at the Brewster angle. The concept was realized, but the disk was destroyed during an arc when conditioning an intermediate frequency [26]. A fault analysis revealed that the free diameter of 106 mm of the diamond disk could only withstand a pressure difference of 2 bar. Since the gyrotron was operated against air, 1 bar was inevitable and the other bar may have been generated during the arc. It was concluded that the concept should only be followed-up when operating with vacuum on both sides of the window, i.e. without one bar pressure difference and without shock waves due to arcs. Since this was not compatible with the AUG system, this window concept was given up for AUG.

3. *Grooved Diamond Disk Window*

   An elegant solution to get the reflection between two specific Fabry-Pérot resonances below 1% is the usage of an anti-reflective coating as for example known from glasses in optics. Obviously the layers must be thicker for microwave radiation and the coating must withstand the high power flux. Grooves on both sides of the diamond disk could in principle be used to provide the necessary optical properties [27]. Element-6 has produced small samples of grooved diamond according to specifications by IAP using LASER-etching. These samples were analysed by IAM. The grooves were rather sharp with rough edges raising concern that stress will accumulate in these areas. Since the rigidness of the disks was anyway reduced due to the grooves [28] also this concept was abandoned for a gyrotron operating in air.

4. *Ring-Resonator Based Window*

   In the context of frequency dependent switches [29] a simplified concept was proposed as mf-window. Here two parallel diamond disks are the entrance and exit to a ring resonator. The beam crosses the disks with an angle of 15° degrees with respect to the disk normal. The disk thickness is chosen such that, in the specific case of AUG, the disks are resonant at 105 and 140 GHz. So at these frequencies the beam simply passes both disks without reflection. At intermediate frequencies 30% to 40% of the power is reflected at both disks. The reflection at the first disk is directed towards the relief load of the gyrotron. The reflection of the second disk is led via to mirrors back to the first disk such that it overlays with the beam initially reflected at the first disk. Part of this beam will now pass the first disk and go to the relief load, the other part will be reflected on the outer side of the first disk and do another round through the resonator. If one can manage to overlay the phases on the first disk and adjust the mirrors such that the phase difference is 180° degrees, the resonator will load up until the reflection from the first disk is exactly cancelled and all the power leaves through the second disk. Due to the field enhancement in the resonator this box with the two mirrors has to be evacuated. See [30] for details. In the AUG ECRH-system one of the 2f-gyrotrons has been built with a beam leaving the output window by an angle of 15° and a relief load at the corresponding position to catch reflections. The gyrotron has been tested with a BN window to deliver power at 105, 117, 127, and 140 GHz. The gyrotron, now equipped with a diamond window, is already routinely used for 2f-operation with AUG. The ring resonator for 4f-operation can be attached to the output window via a CF-flange. First tests with short pulses (< 10ms) have been made in December 2013. The gyrotron oscillation could be easily excited even with strong reflection. Transmitted and reflected powers were measured calorimetrically. It turned out that the range of adjustability of the resonator mirrors was too small to reproduce the resonant behaviour observed in low power experiments. Therefore the reflectivity at intermediate frequencies could not be reduced significantly and no long pulse operation was possible. Still the periodicity of the absorption maxima with respect to the mirror position had the expected period and could be tuned reproducibly. In the coming months the adjustability of the resonator will be improved and a next test is foreseen after the next campaign of AUG, i.e. end of 2014.

Torus Windows

Although not directly related to the gyrotron, the broad band torus window relies on the same concepts as developed for the gyrotron. Note that Brewster–angle based windows require polarizers inside the torus since only one polarization may pass the window. On ASDEX Upgrade two concepts are envisaged.

1. *Double-Disk Window*

   A prototype has been developed by KIT (IAP) [8] and was mounted with an inclination of 2° (in order to prevent reflected low order modes to travel back to the gyrotron [31]) at AUG. Unfortunately the outer disk broke already when operating at 140 GHz after 5 sec and 600 kW of power. Some speculation exists about the reason, but full wave modelling seems the appropriate choice to understand this unexpected behaviour. If this is understood a second window of this kind may be modified and tested carefully before starting long pulse operation.

2. *Ring-Resonator Window*

   We note here that the ring resonator window discussed above is not polarisation dependant and the principle can also be used as torus window. No detailed design has been made yet. Progress will depend on the outcome of the experiments with the respective gyrotron window and the double-disk torus window.

Staff:

G. Gantenbein
J. Stober (IPP Garching)

Literature:

[1] H. Zohm, M. Thumm, “On the use of step-tuneable gyrotrons in ITER”, Journal of Physics: Conference Series, 25, 274-282, 2005.

[2] X. Yang, G. Dammertz, R. Heidinger, K. Koppenburg, F. Leuterer, A. Meier, B. Piosczyk, D. Wagner, M. Thumm, “Design of an ultra-broadband single-disk output window for a frequency step-tunable 1 MW gyrotron”, Fusion Eng. and Design, 74, 489-493, 2005.

[3] G.G. Denisov, A.G. Litvak, V.E. Myasnikov, E.M. Tai, V.E. Zapevalov, "Development in Russia of high-power gyrotrons for fusion," Nucl. Fusion, 48, 054007, 2008.

[4] K. Sakamoto, A. Kasugai, K. Kajiwara, K. Takahashi, Y. Oda, K. Hayashi, N. Kobayashi, “Progress of high power 170 GHz gyrotron in JAEA”, Nucl. Fusion, 49, 095019, 2009.

[5] K.E. Kreischer, R.J. Temkin, “Single-mode operation of a high-power, step-tunable gyrotron”, Phys. Rev. Letters, 59, 547-550, 1987.

[6] M. Thumm, A. Arnold, R. Heidinger, M. Rohde, R. Schwab, R. Spoerl, “Status report on CVD-diamond window development for high power ECRH”, Fusion Engineering and Design, 53, 517-524, 2001.

[7] M. Thumm, “MPACVD-diamond windows for high-power and long-pulse millimeter wave transmission”, Diamond and Related Materials, 10, 1692-1699, 2001.

[8] R. Heidinger, I. Danilov, A. Meier, B. Piosczyk, P. Späh, M. Thumm, W. Bongers, M. Graswinckel, M. Henderson, F. Leuterer, A.G.A. Verhoeven, D. Wagner, “Development of high power window prototypes for ECH&CD launchers”, Fusion Engineering and Design, 82, 693-699, 2007.

[9] A.G. Litvak, G.G. Denisov, V.E. Myasnikov, E.M. Tai, E.V. Sokolov, V .I. Ilin, "Recent development results in Russia of megawatt power gyrotrons for plasma fusion installations", EPJ Web of Conferences, 32, 04003, 2012.

[10] O. Braz, G. Dammertz, M. Kuntze, M. Thumm, “D-band frequency step-tuning of a 1 MW gyrotron using a Brewster output window”, Int. J. Infrared and Millimeter Waves, 18, 1465-1477, 1997.

[11] G. Dammertz, O. Braz, A.K. Chopra, K. Koppenburg, M. Kuntze, B. Piosczyk, M. Thumm, “Recent results of the 1 MW, 140 GHz, TE22,6-mode gyrotron”, IEEE Trans. on Plasma Science, 27, 330-339, 1999.

[12] K. Koppenburg, G. Dammertz, M. Kuntze, B. Piosczyk, M. Thumm, “Fast frequency-step-tunable high-power gyrotron with hybrid-magnet-system”, IEEE Trans. on Electron Devices, 48, 101-107, 2001.

[13] E. Borie, O. Drumm, S. Illy, K. Koppenburg, M.V. Kartikeyan, B. Piosczyk, D. Wagner, X. Yang, G. Dammertz, M.K. Thumm, “Possibilities for multifrequency operation of a gyrotron at FZK”, IEEE Trans. on Plasma Science, 30, 828-834, 2002.

[14] G. Gantenbein, G. Dammertz, J. Flamm, S. Illy, S. Kern, G. Latsas, B. Piosczyk, T. Rzesnicki, A. Samartsev, A. Schlaich, M. Thumm, I. Tigelis, “Experimental Investigations and Analysis of Parasitic RF Oscillations in High-Power Gyrotrons”, IEEE Trans. on Plasma Science, 38, 1168-1177, 2010.

[15] V.K. Lygin, B. Piosczyk, G. Dammertz, A.N. Kuftin, V.E. Zapevalov, “A diode electron gun for a 1 MW 140 GHz gyrotron”, Int. J. Electronics, 82, 193-201, 1997.

[16] M. Thumm, “State of the Art of High Power Gyro-Devices and Free Electron Masers”, KIT Scientific Reports 7575, Update 2010.

[17] M. Losert, J. Jin, T. Rzesnicki, “RF Beam Parameter Measurements of Quasi-Optical Mode Converters in the mW Range”, IEEE Trans. on Plasma Science, 41, 628-632, 2013.

[18] A. V. Chirkov, “Analysis and synthesis of the structure of the field in high-power microwave beams”, Radiophys. and Quantum Electronics, 50, 209-215, 2007.

[19] O. Prinz, A. Arnold, G. Gantenbein, Y. Liu, M. Thumm, D. Wagner, “Highly efficient quasi-optical mode converter for a multifrequency high-power gyrotron”, IEEE Transactions on Electron Devices, 56, 828-834, 2009.

[20] F. Leuterer et al., Fusion Engineering and Design, 74, 199, 2005.

[21] D.H. Wagner et al., IEEE Trans. Plasma Sci., 37, 395, 2009

[22] K. Kajiwara et al., Appl. Phys. Express., 4, 126001, 2011

[23] Y. Oda et al., Rev. Sci. Instr., 84, 013501, 2013

[24] V. Erckmann et al., AIP Conf. Proc., 933, 421, 2007

[25] G. Denisov et al., “Multi-frequency gyrotron with BN Brewster window” in Conference Digest of the Joint 31th International Conference on Infrared and Millimeter Waves and 14th International Conference on Terahertz Electronics, Shanghai, China, 2006, page 75

[26] J. Stober et al., ”ECRH on ASDEX Upgrade – System extension, new modes of operation, plasma physics results” in Electron Cyclotron Emission and Electron Cyclotron Resonance Heating (EC-16): Proceedings of the 16th joint Workshop, edited by R. Prater (World Scientific Publishing Co, Singapore, 2011), pp. 28-41, ISBN 978-981-4340-26-7

[27] V. Belousov et al., “Broad band matched windows for gyrotrons” in Conference Digest of the Joint 34th International Conference on Infrared and Millimeter Waves and Terahertz Waves, Busan, Korea, 2009

[28] A. Vaccaro et al., “Grooved CVD Diamond windows: Grooves’ profiles and structural simulations” in IEEE Conference Publications: Joint 36th International Conference on Infrared and Millimeter Waves and Terahertz Waves, Houston, USA, 2011

[29] W. Kasparek et al., ”Status of Resonant Diplexer Development for high-power ECRH Applications” in Electron Cyclotron Emission and Electron Cyclotron Resonance Heating (EC-17): Proceedings of the 17th joint Workshop, edited by E. Westerhof and P.W.J.M. Nuij (EPJ Web of Conferences, 32, 2012), 04008, DOI: http://dx.doi.org/10.1051/epjconf/20123204008, ISBN 978-90-386-3241-4

[30] A.G. Litvak et al., ”Recent Development Results in Russia of Megawatt Power Gyrotrons for Plasma Fusion Installations” in Electron Cyclotron Emission and Electron Cyclotron Resonance Heating (EC-76): Proceedings of the 17th joint Workshop, edited by E. Westerhof and P.W.J.M. Nuij (EPJ Web of Conferences, 32, 2012), 04003, DOI: http://dx.doi.org/10.1051/epjconf/20123204003, ISBN 978-90-386-3241-4

[31] G. Dammertz et al., IEEE Trans. Plasma Sci., 28, 561, 2000

Acknowledgement

This work, supported by the European Communities under the contract of Association between EURATOM and Karlsruhe Institute of Technology, was carried out within the framework of the European Fusion Development Agreement. The views and opinions expressed herein do not necessarily reflect those of the European Commission.

Port and Plant Engineering

Design, Modelling and Analysis of Primary Heat Transfer and BoP Options for Integration with a DEMO Fusion Power Plant (WP13-DAS-08-T02-01)

Objectives of the work that was performed in the frame of WP13-DAS-08-T02-01/KIT/PS "Design, modelling and analysis of primary heat transfer and BoP options for integration with a DEMO fusion power plant" were as follows: 1) Evaluate potential design options for the DEMO PHTS including the primary heat exchangers and BoP system in terms of efficiency & performance; 2) To assess the impact of pulsed DEMO operation on the PHTS and the need of an Energy Storage Systems (ESS) for the continuous operation of the PCS.

Based on the available data regarding the usable heat sources from the DEMO fusion reactor, an initial study of BoP for DEMO was conducted using EBSILON® Professional software package. The three usable heat sources from the DEMO fusion reactor were identified as being: 1) hot Helium gas coming from the blanket - inlet temperature 500°C, outlet temperature 300°C, pressure 80 bar; 2) hot water/steam coming from the divertor - inlet temperature 250°C, outlet temperature 150°C, pressure 65 bar; 3) hot water coming from the vessel cooling circuit - inlet temperature 105°C, outlet temperature 95°C, pressure 11 bar. The results of this initial study of BoP for DEMO are presented in Table 1.

Table 1: Results of the initial BoP simulations for DEMO steady state operation.

Steam pressure at turbine inlet, bar	Condenser pressure, bar	Steam flowrate, kg/s	Water pressure (from divertor), bar	Water flowrate (from divertor), kg/s	Water pressure (from vessel cooling), bar	Water flowrate (from vessel cooling), kg/s	Total Thermal Power Input , MW	Gross electrical power generated, MW	Cycle efficiency, %
78	0.056	631.308	65	330.669	11	819.835	2018.07	701.682	27.0
75	0.056	630.469	65	330.668	11	819.865	2018.07	699.195	26.9
65	0.056	627.720	65	330.670	11	819.808	2018.07	689.994	26.5

Note: The values of different DEMO BoP parameters in the above table are valid only for steady state conditions and for BoP without a heat storage system.

In the next step of the project, stationary calculations of the three proposed DEMO BoP configurations, that included also a heat storage system, for DEMO pulsed operation were performed: 1) The first DEMO BoP system proposal consists of a water cooling loop (PHTS) that receives heat from the blanket cooling system. Then this heat is being transferred to the intermediate cooling loop where the coolant is molten salt and has cold and hot storage tanks, representing a heat buffer that will be used during the pulsed operation of DEMO. In the PCS steam is generated and directed to the steam turbine to produce electricity. This water cooling circuit (PCS) receives also heat coming from divertor and vessel cooling loops, thus preheating the condensate before it arrives at the molten salt/water HX, where heat is being obtained from the intermediate cooling loop (heat storage loop); 2) In the second DEMO BoP system proposal the PHTS uses molten salt. Then this heat is being transferred to the intermediate cooling loop where the coolant is again molten salt and has cold and hot storage tanks, representing a heat buffer (storage) that will be used during the pulsed operation of DEMO. The PCS, receiving heat from the intermediate cooling loop, is a water loop, where the steam is generated, directed to the steam turbine and electricity is produced. This water cooling circuit (PCS) receives also heat coming from divertor and vessel cooling loops, thus preheating the condensate before it arrives at the molten salt/water HX, where heat is being obtained from the intermediate cooling loop (heat storage loop); 3) The third DEMO BoP system proposal is very similar to the second DEMO BoP proposal, however the PHTS is directly connected to the buffer tanks (heat storage). So, this proposal consists of molten salt cool-

ing loop (PHTS) that receives heat from the blanket cooling system, transports the hot coolant to the hot storage tank of the heat buffer, then hot salt from the hot storage tank arrives at the molten salt/water heat exchanger where it transfers heat to the water of the water cooling loop (PCS), thus generating steam for the steam turbine. From the molten salt/water heat exchanger cooled down molten salt arrives into the cold storage tank of the heat buffer, from which it is pumped again to cool down the blanket. The PCS, receiving heat from the hot molten salt in the molten salt/water heat exchanger, is a water loop, where the steam is generated, directed to the steam turbine and electricity is produced. This water cooling circuit (PCS) receives also heat coming from divertor and vessel cooling loops, thus preheating the condensate before it arrives at the molten salt/water HX.

The results from the above mentioned stationary calculations for DEMO pulsed operation are presented below in Table 2.

Table 2: Results of the stationary BoP simulations for DEMO pulsed operation.

Steam pressure at turbine inlet, bar	Condenser pressure, bar	Steam flowrate, kg/s	Water pressure (from divertor), bar	Water flowrate (from divertor), kg/s	Water pressure (from vessel cooling), bar	Water flowrate (from vessel cooling), kg/s	Total Thermal Power Input, MW	Gross electrical power generated, MW	Cycle efficiency, %
15.5	0.056	709.083	65	330.668	11	819.805	2018.07	543.990	19.4
33.5	0.056	671.936	65	330.670	11	819.851	2018.07	619.876	23.0
58.5	0.056	645.796	65	330.668	11	819.797	2018.07	675.011	25.6

Note: The values of different DEMO BoP parameters in the above table are valid for DEMO pulsed operation conditions, but just for that part (~2 h) of its operation where plasma is being generated.

Later into the project, transient calculations of the three proposed DEMO BoP configurations were conducted using EBSILON® Professional software package. As related to the pulsed operation of the DEMO, it was assumed that it consists of the repeated ~2.5 h cycles: where during ~2 h plasma is being generated, then during the following ~0.5 h the DEMO is being prepared for the next plasma generation (in that time period plasma is not generated). Besides, it was assumed in our calculations (as a very conservative case), that during the ~0.5 h shutdown period of DEMO, all coolant flowrates from the three existing heat sources (blanket, divertor and vessel) are being reduced down to zero, and correspondingly all the temperatures of the coolants drop down: to 300 °C for the blanket, to 150 °C for the divertor and to 95°C for the vessel. During that ~0.5 h time period, decay heat is the only heat source keeping all these temperatures at the above specified values.

While investigating the possible operation of DEMO during its pulsed operation, the following assumptions were made: 1) as related to the three heat sources (blanket, divertor and vessel), coolant flow rates are 100 % during the ~2 h time period and 0 % during the ~0.5 h shutdown time period. Coolant temperatures during the ~ 2 h time period are: blanket - 500 °C in the inlet line and 300 °C in the return line, divertor - 250 °C in the inlet line and 150 °C in the return line, vessel - 105 °C in the inlet line and 95 °C in the return line. Coolant temperatures during the ~0.5 h shutdown time period drop down: to 300 °C for the blanket, to 150 °C for the divertor and to 95°C for the vessel; 2) as related to the PHTS, coolant flow rate is 100 % during the ~2 h time period and 0 % during the ~0.5 h shutdown time period; 3) as related to the intermediate heat storage loop, coolant flow rate from the cold storage tank to the hot storage tank is 100 % during the ~2 h time period and 0 % during the ~0.5 h shutdown time period, while coolant flow rate from the hot storage tank to the cold storage tank is always ~81.77 % nominal flow; 4) as related to the PCS, coolant flow is varying between

~74 % and ~85 % nominal flow, depending on the availability of the heat sources from divertor and vessel (related to ~2 h and ~0.5 h time periods).

The results from the above mentioned transient calculations of the three proposed DEMO BoP configurations are presented below in Table 3.

Table 3: Results of the transient BoP simulations for DEMO pulsed operation.

Total Thermal Power Input, MW	Gross electrical power generated (static), MW	Max. gross electrical power generated (dynamic), MW	Fluctuation of gross electrical power generated (dynamic), MW	Cycle efficiency (static), %	Cycle efficiency (dynamic), %
2018.07	543.990	452.303	~46.6	19.4	14.8
2018.07	619.876	510.684	~50.9	23.0	17.6
2018.07	675.011	556.854	~58.4	25.6	19.7

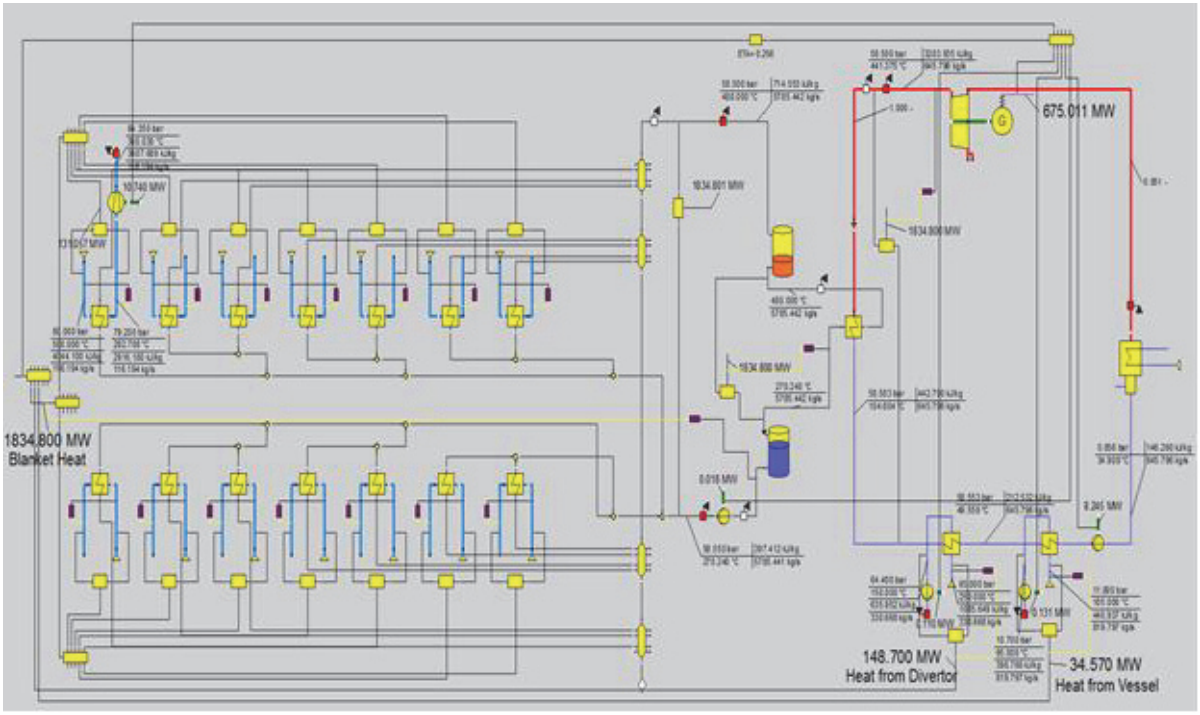

Fig. 1: BoP scheme for DEMO pulsed operation (case 3: PHTS (including heat buffer) – molten salt; PCS - water).

In the conclusion of this work one should state that, static analysis indicated that the most effective configuration is the one with molten salt in the PHTS (which includes also the heat buffer) and with water/steam in the PCS - 3rd BoP configuration (see Fig. 1). The static cycle efficiency of such a BoP configuration was estimated to be 25.6 %. However when this BoP configuration is tested in the pulsed DEMO operation mode, the cycle efficiency drops down to 19.7%. This is mainly due to the pulsed mode of DEMO operation, where we need to include heat storage equipment into the BoP scheme in order to be able to compensate for these ~0.5 h DEMO shut-down periods and still manage to run steam turbine at a constant speed, thus constantly producing electricity. In all cases however, usage of the divertor and vessel heat sources, coupled to the PCS, during the pulsed DEMO operation results in the generated electrical power fluctuations of ~ (47÷58) MW. If this will not be acceptable from the electrical grid operations point of view (taking into account the requirements for the electrical grid stability), then in order to have a stable electricity generation without fluctuations,

usage of the heat sources from divertor and vessel should be organized in a different manner or should be simply discarded.

Staff:

E. Bubelis
W. Hering

Acknowledgement

This work, supported by the European Communities under the contract of Association between EURATOM and Karlsruhe Institute of Technology, was carried out within the framework of the European Fusion Development Agreement. The views and opinions expressed herein do not necessarily reflect those of the European Commission.

Remote Maintenance Studies (WP13-DAS-07)

This report presents the activities assigned to KIT-IFL within EFDA-DEMO-WP13 remote maintenance activities. The contributions are allocated into individual tasks of the work package on which KIT-IFL has cooperated and are summarized as follows:

Task 03: Assessment of operations logistics

- Development of a model for ex-vessel operations
- Input models into combined simulation
- Combine output into single report

The logistics simulation model from 2012 for the operations during DEMO-maintenance phase was adapted to the actual design and further detailed descriptions of operations were done. Furthermore the layout and the processes inside the AMF (Active maintenance facility) were integrated. All changes were made in a way that easy adaptions to alternative solutions that have been discussed in the last years and will appear within the next years of development are possible. The ex-vessel operations concern mainly the time-critical operation of the polar crane above the vacuum vessel. The polar crane per-forms all the movements of the individual casks between the AMF and its position on top of the bio shield. For this crane the logistics model has been developed. With this logistics it is possible to run different maintenance scenarios considering the number of identical casks, the cask sequence or the number of entrances and exits to the AMF, and etc.

Task 04: Assessment of radiation, activation and decay heating implications on remote maintenance system

- Development of a zonal applicability tool
- Radiation hardness report

The work performed by KIT-IFL under Task 04 Remote Maintenance activities was to develop a tool (using Excel VBA) for assessment of zonal applicability for coupling a 3D radiation map to the radiation hardness assessment of RHE. The zonal applicability tool allows deciding about the applicability of RHE for certain locations and durations (expected lifetime) in the vacuum vessel and the ports.

Task 05: Communication, knowledge and design development exchange with the WP13-DAS02-T07

The objectives of the activities conducted by KIT-IFL are to provide communication, to exchange knowledge and design development ideas between the DAS02-MMS attachment (which is mainly performed at KIT) and the DAS07-Remote Maintenance working groups. The main goal from this communication is to bring together the component designers with the RHE designers, in order to achieve an optimal solution regarding the MMS attachment concept.

Task 07: Ex-vessel remote maintenance system

- Development RHE for work on port covers and in the nearby area
- Cask independent slewing cranes
- VR of work on port cover
- Determine duration of work on port cover
- Develop transport cooling options
- Develop cask and cask transport options
- Access mounting and structural arrangement studies

- Determine cask transfer solutions
- Propose conceptual solutions for storing double lidded door
- Report on ex-vessel RM system

Development of RHE operating in DEMO focuses on speed, redundancy and modularity to ensure high availability. KIT-IFL activities included investigations on transport options for the casks. Considering the bio shield plug, cask design and the connection to the maintenance facilities were developed and weighted against the overall plant requirements. Specific transport concepts for each reactor level were elaborated. It was pointed out, that further RHE for preparation before, during and after placement of the up-per casks is needed. Therefore cask independent multi-functional slewing cranes (MSC) were introduced and concepts were given. Due to contamination tightness and the limited available space inside the casks, investigations about possible storing solutions for the double-seal door were carried out.

The decay heat was assessed with a tool developed in 2012. As an exact neutronic model of the new reactor design (2013) is still missing, the calculation of a similar plant was adapted to the planned DEMO reactor. From the current state of design, it seems reasonable to have a central cooling system to cool the casks while they are settled on top of the reactor and use the passive cooling for the transport from the vessel to the AMF.

Task 09: Services joining technologies

- Mechanical connections
- Develop purex connection
- Develop alternative solutions
- Consider load handling and tritium permeation
- Prepare R&D plan for mock-up work
- Report on connection solutions

An up scaled CAD model of the Purex Connector was created and FEM analyses with the loads and forces the connection has to withstand has been successfully completed on a conceptual level. To meet all requirements for a sophisticated solution, investigation of commercial available connectors like Camerons Deepwater High Capacity Collet Connector and the Purex Connector has been performed. Building a test stand to simulate forces from ongoing operations and building a mock-up of the connection to ensure leak tightness and others by ongoing operations are the next steps to work on. Industry may be involved in the development.

Staff:

D. Eilert
M. Kubaschewski
C. Lang
V. Madzharov
M. Mittwollen

Acknowledgement

This work, supported by the European Communities under the contract of Association between EURATOM and Karlsruhe Institute of Technology, was carried out within the framework of the European Fusion Development Agreement. The views and opinions expressed herein do not necessarily reflect those of the European Commission.

DEMO: Ex-Vessel Remote Maintenance System Pre-concept Study (WP13-DAS-07-T07-01)

Introduction

Overview

In DEMO due to the neutron activation, the repair, inspection and/or maintenance of the in-vessel (ex-vessel) components must be carried out using Remote Handling Equipment (RHE). Due to reduce the downtime costs of the plant, minimization of maintenance time is a major requirement. Sophisticated principles for work on the reactor are required. The facility transport system specifically considering the casks and the according cask design, the optimisation of the transport system and the continuous adjustment following the steps of the development process are from major importance to lead to a reliable and economic plant design.

The Work Programme 2013 in Power Plant Physics and Technology (PPPT) aims at completing the selection of the key physics/technology prerequisites for DEMO, the definition of a set of technical characteristics for DEMO and the assessment of the R&D needs to establish its conceptual design. Within WP13-DAS07 it has been partially continued the work started during the EFDA WP12, particularly in the following areas:

- RMS Requirements analysis, investigating the full context of the RMS within its operating environment
- Establishing top-level requirements and goals
- Establishing the main functions that the RMS must perform when the plant is in various operational states (e.g. assembly; commissioning; operational; planned maintenance shutdown; unplanned maintenance shutdown; upgrade; decommissioning; etc.)
- Performing trade-off studies between the optimization of plant maintainability and other tradable factors such as system performance, cost, structural efficiency, performance / configuration of other systems
- Radiation Dose mapping to understand the implications and constraints on remote maintenance operations and technology
- Services joining technology, assessing the feasibility of various RH pipe connection technologies within the different zone of the plant
- Pre-concept for ex-vessel RH equipment (e.g. RH movers and manipulators in line with overall maintenance concepts)
- Decay heat and maintenance cooling systems

Development of Cask concepts and Cask transport concepts

Ex-vessel operation concepts are based on the VMS (Vertical Maintenance System) with multi module segments which is the most promising maintenance concept for a fusion power plant. With this respect, the activity carried out in 2013 included:

1) The development of the upper port cask design to account sufficient cooling structures, cooperation with the chosen transport concept, adequate devices to be mounted to the port and considering interfaces for electricity, data and cooling media.
2) Cask Transport Options are introduced, considering the requirements for different levels of the reactor building (upper, equatorial and lower) and the connected active maintenance facility, also considering the cask transfer solutions in there.
3) Mounting and structural arrangement studies based on twist locks.

Cask independent multi-functional slewing cranes (MSC)

The following concept is related to the upper ports (vertical ports) located on top of the vacuum vessel (VV). These ports allow - after removal of the bioshield plug and opening, the vertically extraction of the blanket segments and the additional piping system.

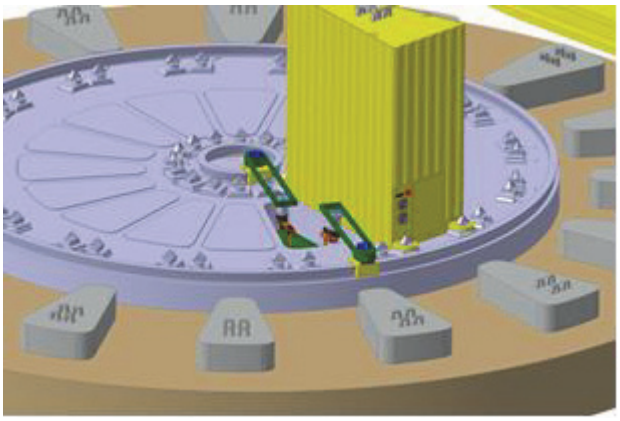

Fig. 1: Overview.

A cask independent multi-functional slewing crane (MSC) can perform several RH operations around the upper port and the casks. The slewing crane is running on circular rails on the top of the bio-shield (see Fig. 1) and consists of the following basic components (see Fig. 2):

- Slewing crane traction drive, which allows the circular motion on the top of the bio-shield
- rotary arm attached on the top of the slewing crane traction drive, which can rotate on axis 1 (see Fig. 2)
- linear & rotary table integrated in the rotary arm. The linear table, as the name indicates, can move linearly along the rotary arm by the means of spindle drive. The rotary table is pivoted to the linear one and can rotate (360°) on axis 2
- telescopic cylinder responsible for the vertical movements (up to 3m) installed on the linear & rotary table
- a commercial multipurpose manipulator with 6 rotating DOF attached on the top of the telescopic cylinder
- toolbox with tools for diverse RH operations manageable by the multipurpose manipulator (cutting, welding, gripping etc.)

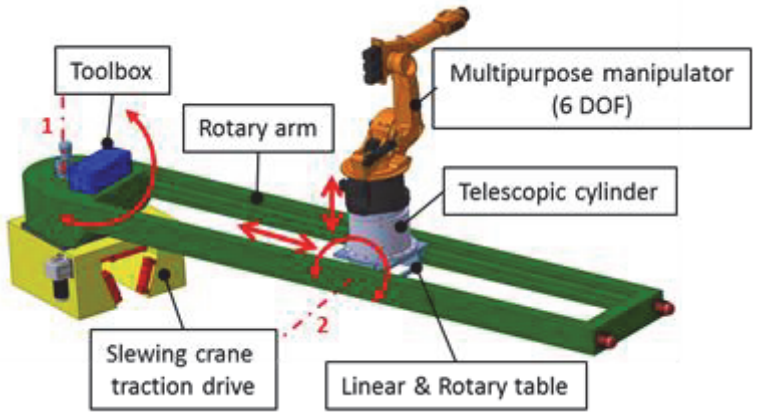

Fig. 2: Multi-functional slewing crane (MSC).

Propose conceptual solutions for storing double lidded door

The opening of the vacuum vessel sets contamination free from the inside of the VV to the environment, therefore release of activated dust from the VV has to be prohibited as far as possible. Investigations showed that there is a feasible looking solution used in ITER and it may be possible to use the ITER principle for having contamination – controlled conditions also for DEMO. The double-seal door system (see Fig. 3), which is composed of a cask door and a port door, installed to the front end of the cask allows the transportation of in-vessel components inside and outside the cask under contamination controlled conditions. The

double seal door system is designed to minimize the risk of a spread of activation dust during maintenance and transport operations. The double seal door is made of two separable doors: the cask door, which is fixed to the cask and the port door, which is connected to the upper port. After docking the cask to the upper port, the two parts are connected tight to each other and opened as one part for allowing transfer of in-vessel components to the cask (and vice versa).

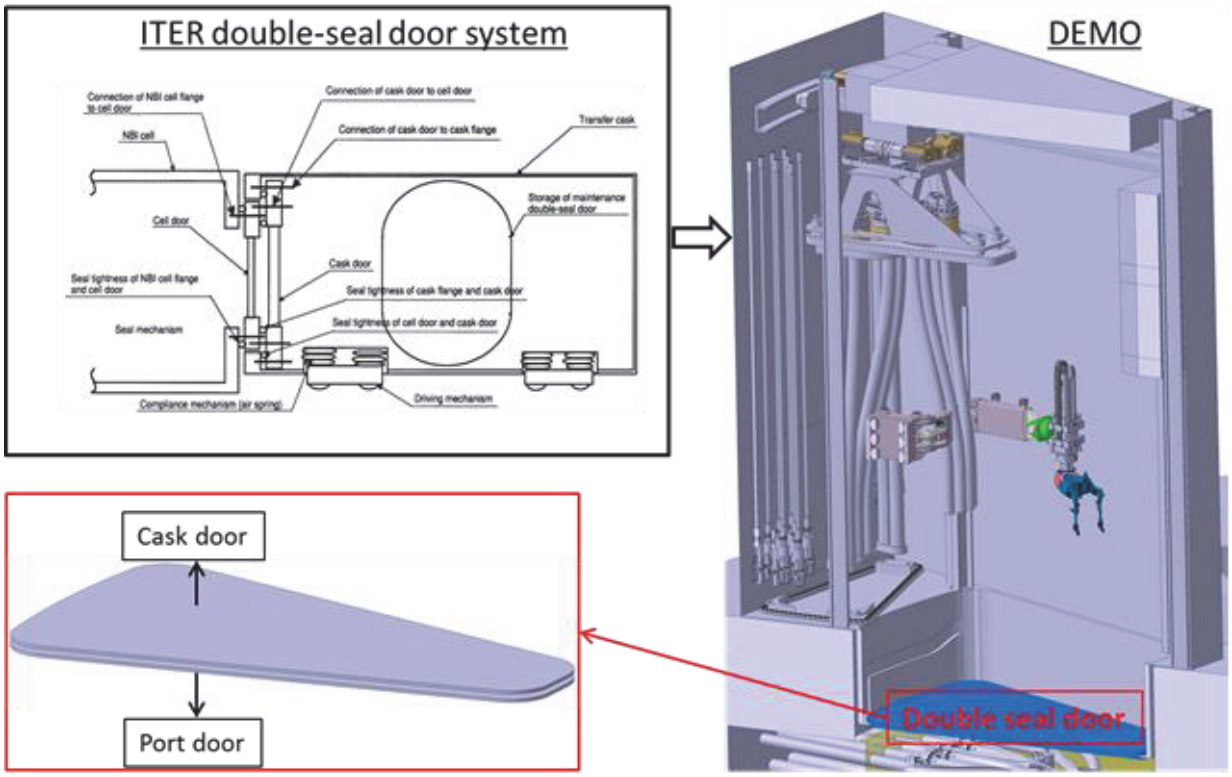

Fig. 3: Conceptual design of the double-seal door system.

Assess cooling requirements during transport

The decay heat was assessed with the tool developed last year. As an exact neutronic calculation of the new reactor design (2013) is still missing, the calculation of a similar plant had to be adapted to the planned DEMO reactor.

Currently, it is assumed that approximately 30 days will pass, before the maintenance begins. Under this assumption, the decay heat has already reduced to about 6% of the initial decay heat, respectively 0.1% of the fusion power of DEMO. Assuming a fusion power of 1.5GW, the segments of the outboard blanket will have the highest heat flux with about 19kW. A segment of the divertor has with 8 kW the lowest heat flux. Although the divertor has the lowest heat flux, it has with about 5.5K/h the highest temperature increase in uncooled and adiabatic conditions. The reason is the lower mass of the divertor segments, which have a much higher activation level than the blanket. The temperature increase for the inboard and outboard segment will be in the range of 1 to 1.5 K/h.

For the development of different cooling options, two different phases have to be considered. At first the cask is placed on top of the reactor and the double lidded door is opened. Additionally, the passive cooling by the cask walls is limited due to neighboured casks. Beside the decay heat of one segment, it is possible that an additional heat flux comes from the vessel. This should in general be avoided by the vessel cooling and is not taken into account for the calculation.

The transport of the cask from the vessel to the AMF is seen as the second phase. In this case, all walls of the cask are free and can be used for natural convection.

The decay heat production within the segments is much lower compared with nuclear fission power plants. The expected decay heat corresponds to about 0.4 kW/t. This is roughly the amount of decay heat of nuclear fuel, after 100 years (~0.5kW/t). After this time span the decay heat is reduced so far, that active cooling is not necessary and the material can be stored in Deep geological repository. Therefore it is absolutley unlikely that the segments in the cask can heat up so far, that severe safety problems arise or the material melts. However it is necessary to keep the temperature low enough to avoid any damage of the remote handling equipment in the cask. A limit of 328K is assumed for the calculations.

In prinicipal the cooling can be done in two ways. The first possibility is active cooling by an additional cooling circuit, the second is passive cooling via the cask walls. As it cannot fail, passive cooling is desirable from the safety point view, although the removable heat is limited depending on the design. Of cause, a much higher heat transfer can be achieved by an active cooling system. However, the cask should be designed in a way to support passive cooling, to avoid a quick temperature rise if the cooling system fails. For the same reasons, transport and storage containers for hot material from nuclear power plants (dry cask storage) are not equipped with an active cooling system and can remove up to 60 kW by passive cooling. The stored material heats up to about 670 K.

Generic Equatorial Port Plug: Preliminary Maintenance Concepts

In this chapter a description of the Generic Equatorial Port Plug (GEPP) is given.

ECH&CD systems, and possible diagnostic systems, are foreseen to be accommodated in the equatorial ports. For this reason, a preliminary assessment on a Generic Equatorial Port Plug has been started in WP13-DAS07. The main goals of the activity have been:

- To start the conceptual design of the GEPP with respect maintainability
- To assess on RH procedure for insertion and removal of the GEPP into the VV
- To start the conceptual design of RHE tools

In Fig. 4 a sketch of the GEPP is shown. In blue the pipes for cooling are shown, while in yellow the waveguides are shown. Both are inserted into the plug as placeholder, as during the activity no assessment on plug internals has been performed. The whole assembly is inserted into the port duct and attached via captive bolts at the launcher back end, the Closure Plate which ensures the vacuum compatibility and Tritium Compatibility of the system, to the torus vacuum vessel. The whole structure is therefore in a cantilevered configuration, which is free floating from the Front Shield to the launcher back-end.

Table 1: Key parameters for the Generic Equatorial Port Plug.

Physical Properties:	
Mass [tons]	ca. 50 – 60
Size [m]:	4.8L x 1.84H x 1.84W (to Flange: 4.6L) Flange Dimension: 2.4H x 2.4W
Material(s)	Support Structure: SS 316 LN

The port plug structure has to be a rigid system that can support the weight of launcher internals (e.g. waveguide or other kind of transmission lines, cooling pipes, shielding blocks, etc…) and its own weight all from the connection to the vacuum vessel at the back end. Its external structure is composed by a Front Shield and a Main Frame. An Additional Shield is inserted in the central part of the launcher to damp the neutron streaming and to create a labyrinth with the Front Shield.

In table 1 are reported the values of the key parameters of the GEPP.

On the closure plate flange, two openings are included to allow the insertion of the rails with which installation/removal of the plug into/from the VV can take place. During Tokamak operations, the two openings will be closed by proper flanges vacuum and tritium compatible.

Moreover, on the closure plates are integrated feedthroughs for pipes for the cooling circuits and for waveguides. As already previously mentioned, these are placeholder. The clearly early stage of the design did not allow a more advance design of plug internals. Therefore, the assessment of the feedthroughs is a preliminary stage and a more detail development is scheduled in the forthcoming Work Programmes.

The launcher internals include (see Fig. 4):

- Cooling pipes (represented in blue). During the design development, we have foreseen a double wall structure in the front part of the plug, which can be used to drive water towards different components and to cool the main itself.
- Shielding Blocks: two blocs were integrated. Their thickness do not take into account the neutron streaming ratio, therefore they still act as placeholder and they provide weight to the overall structure so that RH operations can be better assessed
- Waveguides (shown in yellow). So far, no study on an mm-wave system for ECH application has been carried on and also in the case of the transmission lines, they act as placeholder.

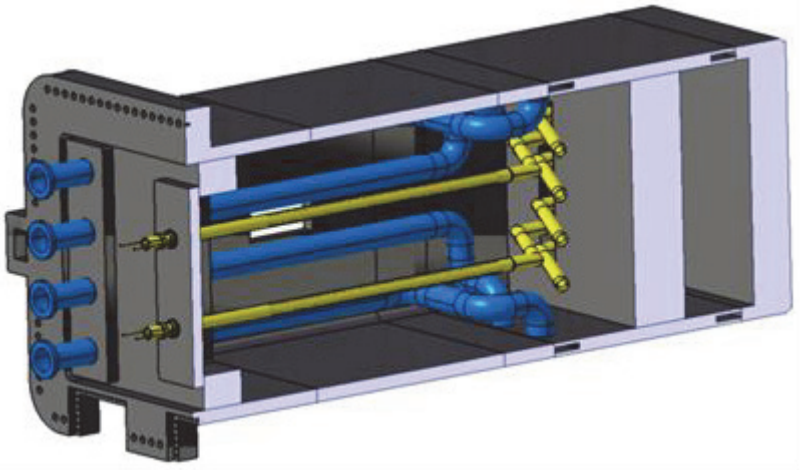

Fig. 4: Cut-out of the Generic Equatorial Port Plug.

The front shield has been provided with two openings. In the current design, there is no interaction between the GEPP and the OB-MMS. This choice is motivated, in order to minimize the impact on blanket segments maintenance. Obviously, openings into the blankets with similar aperture to the ones included into the front shield are assumed to be made.

Rail system for the insertion/removal of the GEPP

Within WP13-DAS07-T07, two concepts for a rail system aiming to aid the installation removal of the GEPP into/from the VV have been considered:

- Ceramic wheel Rails
- Magnetic Rails

The former has been more extensively assessed due to commercial availability of its components, while the latter is, for the moment, at pre-conceptual development level and will be further exploited in the near future. The equipment that will be used to aid the extraction/insertion of the GEPP consists in two rails. Two different concepts have been, during

WP13-DAS07 considered: rails that use ceramic wheels (see Fig. 5) and rails that use magnetic loops.

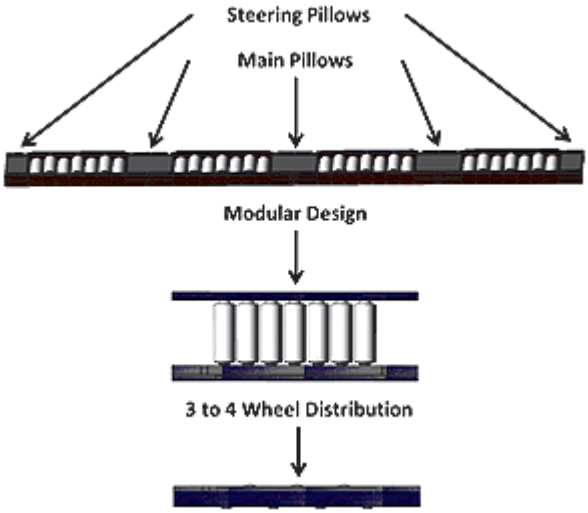

Fig. 5: Sketch of the Generic Equatorial Port Plug – Front Shield.

In Table 2 the advantages and disadvantages of two different systems are compared. For WP13 the concept using ceramic wheels and air cushions has been more deeply developed, with respect to the one using magnetic loops (for which only the principle has been assessed). Further development is planned to be carried on in 2014.

Table 2: Trade-off comparing the two concepts for the rails.

Ceramic wheels & cushions	Magnetic Loops
Pros Simple Easy to handle **Allows to cover huge gaps between port plugs and ports** ...	**Pros** **No contact between parts (i.e. no dust)** Easy to handle Reliability ...
Cons Dust due to friction Reliability (composed of several components)	**Cons** Smaller displacement w.r.t. wheels Dimension of the system might weaken the port structural integrity

Conclusion

Taking the current state of design under consideration, the upper cask has been conceptually designed to be fully functional for the use on the upper port plug and the transport system. Cooling structures, transport attachment and interfaces for electricity, cooling liquid and data are foreseen.

The further elaboration regarding the multi-functional slewing crane consists of several important issues: being in the preliminary concept studies the concept with the slewing crane shall be further investigated. Major advantage of this concepts is the possible saving of one RHE cask operation (and with that, also a lot of time can be saved – keeping overall downtime short) and the capability for doing various supporting RH work outside the cask and around the upper port plugs.

From the current state of design, it seems reasonable to have a central cooling system to cool the casks while they are settled on top of the reactor and use the passive cooling for the transport from the vessel to the AMF. Further, a rescue solution for an unexpected heat production could be reasonable but not absolutely necessary. The passive cooling has the main advantage that it cannot fail by design. The cooling capacity is limited, but is sufficient with the current data. Design changes regarding the cask wall thickness and shape were suggested.

A preliminary assessment on a Generic Equatorial Port Plug has been presented, including a concept for a rail system aiming to be used during insertion and extraction of the GEPP from the port duct.

Further investigation, including prototyping, shall be made in particular to evaluate the dust that might be produced during maintenance operation.

Staff:

D. Eilert
R. Geßner
G. Grossetti
C. Lang
M. Kubaschewski
V. Madzharov
M. Mittwollen
D. Strauß

Literature:

[1] Tesini, A; Honda, T.; Palmer, J.; et al.: ITER in-vessel components transfer using remotely controlled casks; FusEngDes 58-59(2001) 469-474

[2] Oka, K., Tada, E., Design of remote handling equipment for the ITER NBI, Jaeri-Tech 99-055

Acknowledgement

This work, supported by the European Communities under the contract of Association between EURATOM and Karlsruhe Institute of Technology, was carried out within the framework of the European Fusion Development Agreement. The views and opinions expressed herein do not necessarily reflect those of the European Commission.

Goal Oriented Training Programme on Remote Handling (WP10-GOT-GOTRH (FU07-CT-2010-00065))

Overview / Introduction

The EFDA European Goal Oriented Training programme on Remote Handling (RH) "GOT RH " aim is to train engineers for activities to support the ITER project and the long-term fusion programme in European Associations, associates, Fusion for Energy, the ITER organization, Industry and activities beyond ITER (DEMO). The GOT RH serves as practical level project for increasing the coherence within RH context of collaborative training between 5 participating European Associations: TEKES - Finland; coordination, CEA - France, CIEMAT - Spain, DIFFER - Netherland, KIT - Germany. The official start of the program was the October 1st 2010 at its original duration 4 years (depending on the recruitment time for trainees). KIT Trainee started on 01.09.2011.

The major objective is to implement a structured remote handling system design and development oriented training task that is carried out in a multidisciplinary Systems Engineering (SE) framework by using ITER/F4E task and QA processes and available documents, and ITER-relevant software products. The approach is on top-down engineering with multidisciplinary design requirements considerations on reliability, availability, maintainability and inspectability (cf. RAMI).

The training program is divided into 3 Work Packages and the KIT trainee is mainly involved in WP 1 on **"**Mentored case studies on the ITER RH system requirements, concepts and designs." An additional WP 3 is on common annual RH Summer and Winter Schools, Workshops and Scientific Events with contribution from all participating associations**.**

A special aim of the KIT WP 1.1 is the "Identification of main requirements and elaboration of RH procedures for providing a high availability of the ECH Upper Port Plug system.", but also general studies on maintenance studies for future power plants are part of the work.

Status of the activity

The 2013 activities (2nd year of training) dealt with two main projects:

- Design and analyses for the ITER EC H&CD Upper Launcher Final Design development.
- Pre-concept study on the Ex- Vessel Remote Maintenance System for DEMO.

<u>Design and analyses for the ITER EC H&CD Upper Launcher Final Design development</u>

On ITER, due to the high neutron fluxes generated during plasma operations, material activation of the in-vessel components occur. Therefore, maintenance can only be performed by robust RH operations. These have to be developed through a RAMI analysis.

Assessments on maintenance concepts for the Mid-Optics assembly (a set of Quasi-Optical mirrors) and the Waveguide Assembly have been carried on. Following what has been done in 2012, the core of the process consisted in the formalization of a set of assumptions to be applied on the Baseline CAD model (structural and mm-wave component designs). Trade-Off documents that aim to compare different possible designs, which have to meet different requirements, have been developed.

The Assessment has been used to drive the design of both the Mid-Optics and the Waveguide assembly through the requirements dictated by maintenance necessities. The result is shown in Fig. 1.

A "living" document (Technical Report), collecting the results has been written and will be constantly updated as the project moves on towards the Final Design Review.

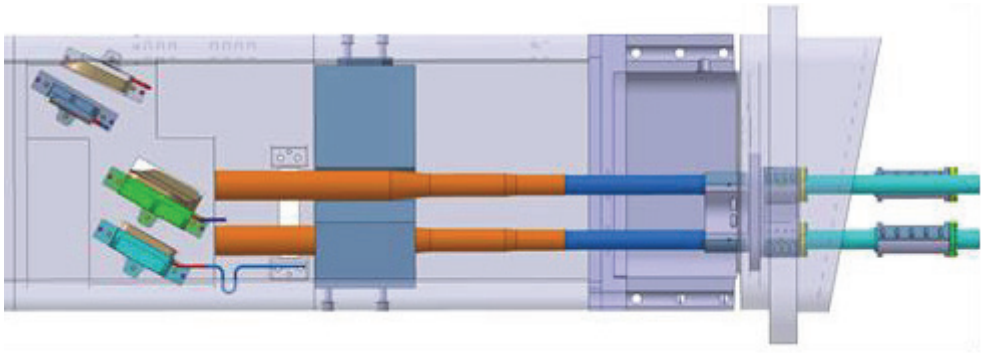

Fig. 1: Sketch of the EC H&CD Upper launcher: on left part it is shown the Mid-Optics.

Pre-concept study on the Ex- Vessel Remote Maintenance System for DEMO

Related to the Power Plant Physics and technology activity (DEMO power plant development), concepts for the remote maintenance of Heating & Current Drive Systems, Vacuum Pumping Systems and Diagnostic Systems have been developed.

The development is driven by the following key requirements:

Feasibility and reliability of the plant maintenance system

High overall plant availability, and therefore, minimization of plant down time for the foreseen maintenance operations

The main result consisted in a preliminary design for Port Plug integration and maintenance (Generic Equatorial Port Plug, GEPP). Coarse requirements for the GEPP have been defined with respect maintainability. In particular, in order to exploit the extraction of the GEPP from the port duct, a preliminary design of rails given by ceramic wheels and air cushions has been developed and the proper maintenance sequence actions has been assessed.

In fig. 2 the concept of the rails is shown.

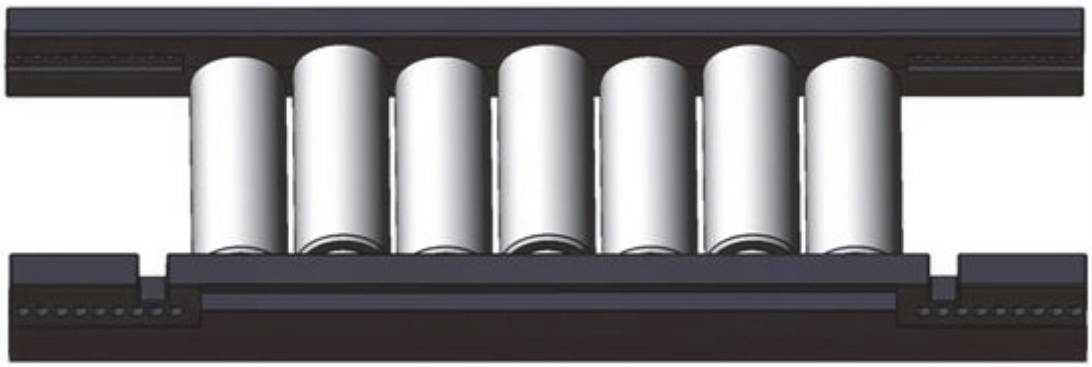

Fig. 2: Sketch of a rail module containing 7 ceramic wheels.

During the EFDA GOT project development, several internal milestones have been reached and different deliverables have been produced (details are available in the respective Annual Report for the EFDA-WP10-GOT-GOTRH).

Staff:

G. Grossetti (trainee)
S. Schreck (mentor)

Literature:

[1] G. Grossetti et al., ITER EC H&CD Upper Launcher: Design Options and Remote Handling Issues of the Waveguide Assembly, accepted for publication on Fusion Engineering and Design (December 2013)

[2] G. Grossetti et al., The ITER EC H&CD Upper Launcher: Analysis of Vertical Remote Handling applied to the BSM maintenance, Fusion Engineering and Design, Volume 88, Issues 9–10, October 2013, Pages 1929-1933

Acknowledgement

This work, supported by the European Communities under the contract of Association between EURATOM and Karlsruhe Institute of Technology, was carried out within the framework of the European Fusion Development Agreement. The views and opinions expressed herein do not necessarily reflect those of the European Commission.

Design, Analysis and Documentation to Produce the ITER EC H&CD Upper Launcher Final Design (F4E-GRT-161-01)

The design of the ITER ECRH system provides 20MW millimeter wave power for central plasma heating and MHD stabilization. The system consists of an array of 24 gyrotrons with power supplies coupled to a set of transmission lines guiding the beams to the four upper launchers and one equatorial launcher. The front steering upper launcher design described herein has passed successfully the preliminary design review, and it is presently in the final design stage. The launcher consists of a millimeter wave system and steering mechanism with neutron shielding integrated into an upper port plug with the plasma facing blanket shield module (in-vessel) and a set of ex-vessel waveguides connecting the launcher to the transmission lines.

Part of the transmission lines are the ultra-low loss CVD torus diamond windows and a shutter valve, a mitre bend section and the feedthroughs integrated in the plug closure plate. These components are connected by corrugated waveguides and form together the first confinement system (FCS) to which a high safety requirement fulfilling nuclear codes and standards applies as confinement and stability against loads including emergency cases (e.g. seismic events, disruptions). In-vessel, the mm-wave system includes a quasi-optical beam propagation system including four mirror sets and a front steering mirror. The millimeter wave system is integrated into a specifically optimized upper port plug providing structural stability to withstand plasma disruptions forces and the high heat load from the plasma side with a dedicated blanket shield module. A recent update in the ITER interface definition has resulted in the recession of the upper port plug first wall panels, which is now integrated into the design. Apart from the millimeter wave system the upper port plug houses also a set of shield blocks which provide neutron shielding. An overview of the actual ITER ECRH upper launcher is given together with some highlights of the design.

Introduction

The four ITER ECRH Upper Launchers (UL, see figure 1 and [1]) are plasma facing port plugs located in the ITER upper ports, their development is driven by ITER with European support by F4E. The Upper Launcher design is developed by the European ECH Upper Launcher Consortium of Associations ECHUL-CA (KIT/Germany, CNR/Italy, CRPP/Switzerland, Differ/Netherlands, IPP and IPF/Germany). The upper launchers are connected via transmission lines [2] to a set of gyrotrons providing up to 20 MW millimeter wave power at a fixed frequency of 170 GHz [3].

The main purpose of the upper launchers is to drive local current with the aim to suppress neoclassical tearing modes which on one side can trigger plasma disruptions generating loads on the components close to the plasma and on the other side lead to confinement degradation. The coupling of the fixed frequency millimeter waves to the plasma via electron cyclotron requires beam steering realized by front steering mechanisms to match resonance and local heating (electron cyclotron resonant heating, ECRH). The upper launcher millimeter wave power injection system is complemented by an equatorial launcher (JAEA [4]) for central plasma heating and off-axis current drive. This publication gives an overview of the developments towards final design since the preliminary design review of the ITER ERCH Upper Launchers [1]. The technical requirements describe criteria which should be fulfilled to obtain a working design. Their fulfillment however is not yet a guarantee to reach the ideal of a good design. The selected design updates show improvements of the design towards this ideal based on simple reliability, availability, maintainability and inspectability (RAMI) considerations. The design validation finally provides criteria to prove the design by means of numerical simulations, prototyping and testing.

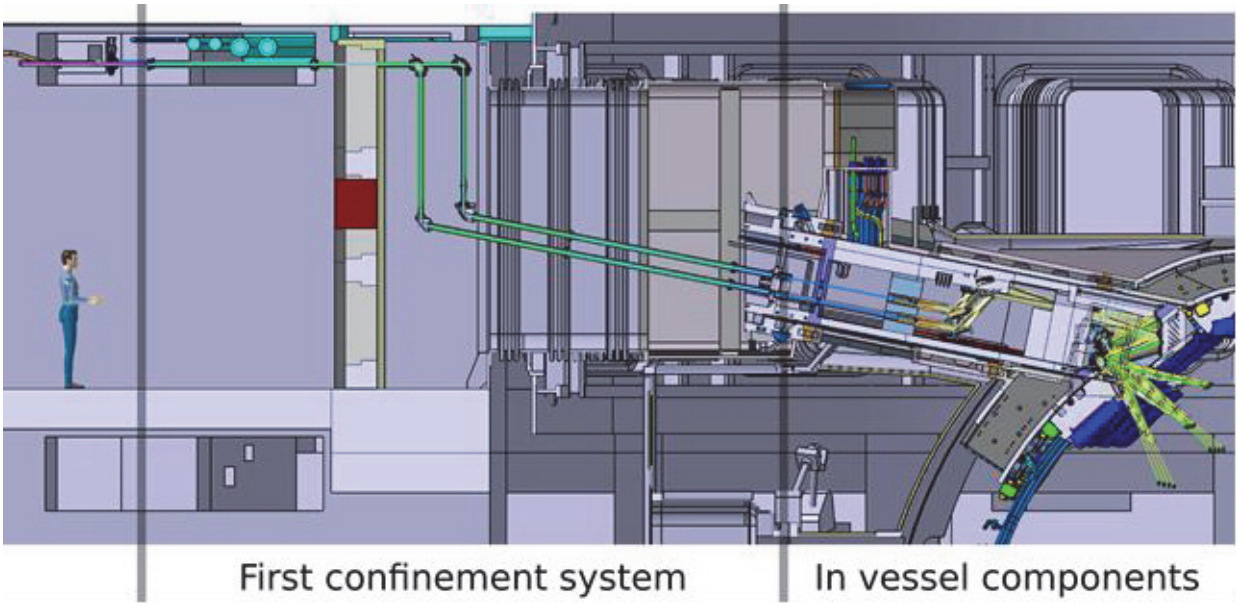

Fig. 1: The ITER ECRH Upper Launcher: overview of in and ex-vessel parts.

Requirements

Two requirement categories for the UL design can be defined: on one side the operational ones shall guarantee the component integrity withstanding operational loads fulfilling reliability and maintainability criteria. On the other side functional requirements must be fulfilled which are in the case of the ITER ECRH upper launchers MHD instability stabilization of the neoclassical tearing modes (NTMs) avoiding confinement degradation. Compared to other components the two requirement categories are coupled for the upper launchers: if the NTM can't be stabilized, which is the main functional purpose of the ULs, a disruption might be triggered with severe loads an all in-vessel components; quality and quantity of disruptions might affect their operational integrity. It can be concluded that the functional requirements on the ULs are entangled with operational requirement not only for the UL itself, but also for the other in-vessel components. In the following a brief description of the main functional requirements and an overview of the operational ones are given.

The NTM evolution is usually calculated using the generalized Rutherford equation. Two criteria [5], derived from this equation, have been proposed to describe the requirements for local current drive and hence the UL performance. First the locally driven current density should exceed the unperturbed bootstrap current density by a factor of 1.2 at the flux surface where the mode develops. Second the driven current density multiplied by the full width of the deposition profile and divided by the bootstrap current density should be larger than 5 cm. These two criteria impose geometrical requirements on the optical system of the UL as focal points size and depth of focus as well as poloidal and toroidal injection angles. They directly affect the design of the plasma facing components, the ECRH port plug blanket shield module with its first wall panel as well as neighboring blankets which need to have specific cut-outs to allow a line of sight access of the beam to the location of the instability in the plasma. Cut outs in the ITER first wall have to be designed preserving the shielding function of the blankets. Only a matching intersection between functional and operational requirements can fulfill the ideal of the UL design and it is very challenging to find such a working intersection. It can be concluded that here physics and tokamak design constraints give the lowest degree of design freedom and the design of the entire upper launchers is based on the fulfillment of these criteria defining also key requirements for transmission lines and gyrotrons. The optical and structural design close to the first wall can therefore be identified as the major challenge on the ITER ECRH Upper Launcher design.

First wall cut outs and the plasma injection angles determine the design of the optical system in order to access the location of the q=2/1 and 3/2 rational surfaces. The beam paths are constrained by the interfaces to the neighbouring components in the port and the corresponding wall thickness needed for the structural system. Specific design requirements arise e.g. for the velocity of the steering mirror mechanism to access the instability in time or for ultra-low loss CVD diamond windows to assure tritium confinement for which applicable nuclear codes and standards are not available. Additionally, active cooling of structural and optical systems has to be foreseen as well as sufficient neutron shielding and the component maintainability. The design has further to fulfill load requirements during normal operation and during off-normal events such as plasma disruptions, earth quakes etc. A large number of these events, defined by the ITER load specifications and the EC-UL specific loads, have to be considered as well as combined loads during the design validation process. High requirements have to be fulfilled as ITER is a nuclear facility including the demonstration of the tritium confinement of the ex-vessel components, and this is a further huge challenge for the launcher design.

The interfaces to neighbouring components determine the geometrical constraints of the launcher design including the cut outs at neighbouring blankets. An update of these beam paths might require an interface change for the affected blankets. A clear definition of these interfaces and their validity ideally over the time of the final design development is a key requirement in the hands of the ITER team and the design teams for an effective design progress allowing a proper definition of the constraints, based on which the designers develop a matching intersection between operational and functional requirements.

Design status

The design development is based on the preliminary design of the four upper launchers [1] and the actual intermediate design is shown in figure 2.

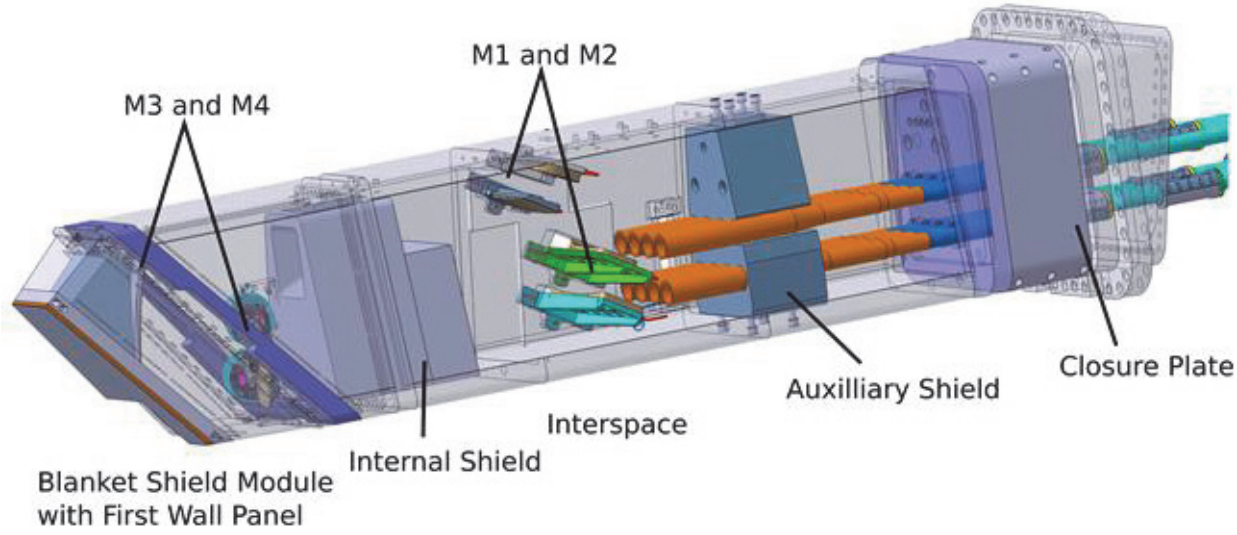

Fig. 2: In-vessel part of the ECRH Upper Launcher.

Eight transmission lines transport the beam into each launcher with diamond windows as the first tritium barrier, after a transition to a quasi-optical system two front steering mirror units give access to the resonance location on the targeted magnetic flux surface.

The final procedure for a generic maintenance solution, namely the removal of ECRH and diagnostics upper port plugs with the help of a port plug cask system is still under work and therefore interface changes, e.g. by the introduction of rails in the plug-port interspace with a potential impact on both the optical and structural design, are probable. This uncertainty led to the decision to continue the design with an emphasis on the first confinement system

(FCS), which has its criticality due to tritium confinement and nuclear codes and standards fulfillment, accompanied by a design update of the in-vessel part. As a consequence, the upper launcher final design review was split into two parts: first the final design of the FCS is planned, and after a second design iteration of the in-vessel components the remaining second final design review is foreseen. This means a compromise between the urge of finalizing the first wall design, not yet fixed interfaces to the upper launcher and resolving the high requirements on tritium confinement.

First confinement system

The first confinement system of the UL starts with the CVD torus diamond windows [6] forming the interface to the transmission line section developed by the US Domestic Agency. The waveguide section includes shutter valves protecting the transmission lines in the case of a window failure. Mitre bends form a dogleg beam path followed by a waveguide section ending at the UL closure plate. The connection to the closure plate is formed by a double helicoflex sealed sub-plate. It allows the removal of the entire set of eight waveguides and their connected counter pieces including tapers placed inside the launcher.

The actual design has been validated for different aspects including seismic loads [7] and thermal expansion from room temperature to operating temperature and vacuum vessel bake out conditions. The analysis showed that the waveguide couplings initially foreseen are too stiff to compensate for the thermal expansion. With the aim to avoid bellows in the transmission lined it was decided to develop more flexible waveguide components in the planned next design iteration. As a further design progress, the formerly individual mitre bends placed in each waveguide section are to be replaced by mitre bend blocks. They have the further advantage of stabilizing the ex-vessel ensemble against seismic events.

CVD diamond windows [8] are a key component of the ITER ECRH system. In today's knowledge only diamond provides the required material properties as transparency, mechanical strength and thermal conductivity for the use in the high power millimeter-wave system. For the four upper launchers and the equatorial launcher a set of 56 CVD torus diamond windows for tritium confinement are used. Additional 24 diamond windows are foreseen for the protection of the gyrotron vacuum. Each diamond disk is optimized for the fixed frequency of 170 GHz, the torus window disks have a thickness of 1.11 mm, a beam aperture of 63.5 mm and a weight of 86 karat. The actual torus diamond window design is considered mature and the final prototyping and testing is being initiated. A new development has been started with the integration of a detector array, which can be integrated into the torus window. The aim is to detect coupling of higher order modes through the cylindrical side face of the diamond disk for beam profile reconstruction and to detect a potential crack in the diamond disk.

For the sub-plate waveguide feedthroughs several options as welded solutions with or without individual maintenance, helicoflex sealed waveguide feedthroughs have been checked. The favorite solution is a monoblock with geometrically staged helicoflex sealed connectors to the waveguides. The minimization of SIC-1 welds has been a major design driver for this development with the limited space as a major design constraint.

The closure plate was retracted close to the port plug seal compared to the PDR design [9]; with this simple modification a number of SIC-1 welds is now located in the in-vessel part no longer forming a first confinement barrier. Further the maintenance access to the closure plate feedthroughs is now significantly simplified.

In vessel part of the upper launcher

In parallel to the progress on the final design of the first confinement system also the in-vessel components are being developed. The UL has a trapezoidal shape with the blanket shield module (BSM) connected via a bolted flange. The UL is connected with a flange on its

back end to the port with lip seals and a closure plate for tritium confinement. The closure plate has feedthroughs for cooling lines, the waveguides and the Helium supply lines driving the front steering mirror mechanism. An actively cooled auxiliary shield in the rear part serves for neutron shielding and fixes the waveguide tapers at their transition to the quasi-optical propagation. To minimize neutron streaming, two mirror sets form a dogleg beam path through the internal shield, which is located in the front section of the trapezoidal main frame. The side wall of the main frame serves as an optical bench, on which the mirror sets M1, M2 and M3 are fixed. The focusing mirror unit M3 is integrated into the BSM.

Availability considerations lead to the need for efficient maintenance solutions, usually by remote handling [10]. Two mainly independent approaches can be defined; on one side the general reliability of tools and processes can be optimized, on the other side the reduction of amount and complexity of the required remote handling tasks leads to faster and more reliable maintenance operations. If a subcomponent is deeply nested in a subcomponent tree requiring a serial remote handling approach, then the ideal is to break up the nested subcomponent tree by design to independently maintained subcomponents. These can be ideally accessed directly converting the serial RH operations approach to parallel ones, strongly reducing the complexity of the maintenance process.

In the preliminary upper launcher design the maintenance of the mirror sets M1 and M2 required the removal of a bottom hatch in the plug main frame, a cutting of a number of water and He pipes for the BSM, the front mirrors and the internal shield directly above the hatch for obtaining access to the mirrors in a blocked geometrical configuration requiring several remote handling steps. This serial process could be broken up by design; the new solution [11] is to insert and remove the mirror sets fixed with captive bolts in small slits within the main frame wall directly from the outside including access for cutting and re-welding of only the attached cooling lines, resembling to minimally invasive surgery.

Another approach to reduce complexity and risks of maintenance operations is to carefully assess the need for remote handling for specific components. It is actually under investigation if it is sensible to suggest a downgrade of the auxiliary shield block in its remote handling class to a fixed installation for lifetime. The benefits would not only be a significant reduction of RH operations, also the bottom hatch for maintenance access might be revised or even become obsolete reducing design complexity and manufacturing costs.

The need for maintenance arises either from planned service intervals with an exchange of critical components reaching their lifetime or when a component fault or failure is assumed. The ideal component inspectability provides fault detection during operation before a failure occurs; the ideal robust design has sufficient fault to failure intervals allowing an early mitigation before a failure affects the system integrity. With the given boundary conditions such as an environment with significant neutron fluxes, ionizing radiation and very limited space for inspection tools it is very difficult and challenging, often out of the actual technical reach, to develop designs and inspection solutions close to this ideal. One compromise is to refrain from an on-line inspection and to use off-line inspection tools instead, during planned downtimes.

A specific failure mode for ECRH launchers is arcing caused by the millimeter wave beams, which can lead to high local thermal loads and melting of component parts. In the interspace between the auxiliary and the internal shield blocks, where the mirror sets M1 and M2 are located, the beams are no longer guided by waveguides. They enter via tapers to an quasi-optical (vacuum) beam propagation. Due to the local magnetic field strength in this interspace a resonance might trigger arcing. An early detection of such arcing as a fault condition would be highly beneficial; the time to failure interval could be used to mitigate the problem e.g. switching off the relevant beam lines relying on the other ULs. Two tubes running from a closure plate feedthrough to the M1/M2 interspace, passing through the auxiliary shield block, are being studied in the present design phase. The use of fibre optics is investigated with the ideal of having the on line inspection of arcing in the critical interspace. The system

could be further explored as an off-line inspection tool if the fibre optics system is removed and instead a camera system is introduced for interspace and mirror set inspection. Without such a system only a complicated and very time consuming port plug removal with associated hot cell operations for the interspace fault inspection could provide similar information. This however is not foreseen for practical reasons such as availability and costs.

Design validation

Two categories of design validation are used for the ITER ECRH Upper Launcher design. Models derived from the CATIA design are used for a set of numerical design analyses and its validation against codes & standards. The simulations however have their limits in modeling assumptions such as the validity of material properties, especially after irradiation, or idealized joining techniques as well as load assumptions. Prototyping and testing are the complementing method for further validation covering manufacturing issues as costs, tolerances and weld qualities. Prototype test facilities have been set up; the Launcher Handling and Testing facility LHT at KIT provides water flows with fast temperature transients up to the bake out conditions with 240 °C at 4.4 MPa [15]. The facility has recently been extended with a large vacuum chamber able to house large launcher structural components. Another prototype testing facility has been built up at CRPP for the test of highly loaded millimeter wave components as the mirrors.

The quality of the numerical analyses has been significantly improved since the preliminary design review. Higher resolved MCNP analyses [12] and a direct interpolation of nodal results directly to the mesh of the FEM models give a better representation of volumetric neutron heat loads. In combination with CFD and thermal analyses the generated stresses are calculated now with higher accuracy [13]. The same approach has been successfully introduced for EM analyses [14]. Further the seismic analysis approach could be improved using response spectrum analysis with spatial combinations based on Newmark's rule [7]. Thermal expansion simulations of the ex-vessel system accompany the millimeter-wave system design. The ITER load specifications define a huge set of possible load combinations; a subset of UL relevant load combinations for specific components is being developed and suggested to ITER.

Conclusions

Since the preliminary design review significant progress has been made for the upper launcher design and the validation tools. The experience and knowledge base to develop well detailed RAMI criteria is very sparse, especially regarding load conditions, material properties and component reliability. Simple deductions of design criteria from basic RAMI considerations turned out to be a valuable guideline for design improvements. Therefore, apart from the goal of fulfilling the system requirements, also RAMI considerations could be successfully used for design optimizations. Finally as the design approaches its final status, the importance of stable interface and technical requirement definitions is raising and becomes a key necessity for an efficient design progress.

Staff:

G. Aiello
R. Geßner
G. Grossetti
A. Meier
T. Scherer
S. Schreck
A. Serikov
P. Späh
D. Strauss
A. Vaccaro
B. Weinhorst

Literature:

[1] D. Strauss et al., Preliminary design of the ITER ECH Upper Launcher, In Press, Fusion Engineering and Design, Available online 11 May 2013

[2] Gandini, F. et al., The EC H&CD transmission line for ITER, Fusion Science and Technology 59 (4) , pp. 709-717, 2011

[3] T. Omori et al., Overview of the ITER EC H&CD system and its capabilities, Fusion Engineering and Design 86 (6–8), 951-954, 2011

[4] Takahashi, K. et al., Progress of ITER equatorial electron cyclotron launcher design for physics optimization and toward final design, Fusion Engineering and Design 86 (6-8) , pp. 982-986, 2011

[5] Sauter, O. et al., Plasma Physics and Controlled Fusion 52 (2010) 025002

[6] T. A. Scherer et al., Experimental analysis of the inserted waveguide CVD diamond window prototype for the ITER ECRH upper launcher, 36th IRMMW-THz Conf., Houston, Texas (USA), IEEE-Proc., 2011

[7] G. Aiello et al., The ITER EC H&CD Upper Launcher: Seismic Analysis, ISFNT 11, to be published, 2013

[8] Theo A. Scherer et al., Investigations of dielectric RF properties of ultra low loss CVD diamond disks for fusion applications, Proc. 34th Int. Conf. on IRMMW-THz Wave 2009, IEEE CFP09IMM-CDR, ISBN 978-1-4244-5417-4, Busan, Korea, 2009

[9] P. Spaeh, The ITER ECH & CD Upper Launcher: Steps towards final design of the First Confinement System, Proc. SOFE 2013

[10] J. F. Koning, Analysis of ITER upper port plug remote handling maintenance scenarios, Fusion Engineering and Design 87(5-6), 2012

[11] D. Ronden, The ITER EC H&CD Upper Launcher: Maintenance concepts, In Press, Fusion Engineering and Design, Available online 11 May 2013

[12] B. Weinhorst et al., Neutronic Analyses for the ITER electron cyclotron-heating upper launcher, ISFNT 11, to be published, 2013.

[13] A. Vaccaro et al., The ITER EC-H&CD Upper Launcher: FEM Analyses of the Blanket Shield Module with respect to Surface and Nuclear Heat Loads, Proc. SOFE2013 Conference, San Francisco, 2013.

[14] A. Vaccaro et al., The ITER EC H&CD upper launcher: EM disruption analyses, Fusion Engineering and Design, Available online 20 February 2013.

[15] D. Strauss et al, “Objectives and design of the launcher handling test facility at FZK,” US-EU-JPN RF Heating Technology Workshop, Nara, J, September 26-30, 2006

Acknowledgement

This work was supported by Fusion for Energy under the grant contract No. F4E-GRT-161-01 (part of ITA C52TD39FE between IO and F4E in support of the final design of the launcher) with collaboration by CRPP Switzerland, DIFFER Netherlands, CNR Italy and IPP Germany. The views and opinions expressed herein reflect only the author’s views. Fusion for Energy is not liable for any use that may be made of the information contained therein.

Manufacturing of ITER ECH Upper Port Plug Structural System Prototypes (BMBF Reference No. 03FUS0010)

Introduction

The ITER Tokamak will be equipped with five ECRH (Electron Cyclotron Resonance Heating) launchers, of which four will be located in the upper region of the machine. These upper launchers main purpose will be to provide up to 24 MW microwave power in order to counteract plasma instabilities during ITER operation [1].

The Microwave power will be generated far outside the Tokamak vessel and will be transmitted by circular waveguides into the launchers, where they propagate quasi-optically through a system of mirrors and actuators into dedicated positions at nearly any location across the plasma cross section. The microwave systems will be mounted into casks, which will be installed into four of the 18 upper ports. These upper port-plugs must fulfill a number of technical requirements, of which mechanical integrity, removal of substantial heat loads, nuclear shielding, and maintainability are the principal ones.

The port plugs are designed as hollow elements with a trapezoidal profile, which will be mounted into the port as a cantilever. The front element of the port plug, which faces the plasma, has to resist much higher heat loads than the main body of the plug, why it must be equipped with a high-performance cooling system, avoiding areas of un-cooled material accumulation.

Due to the tremendous mechanical loads that can be applied during plasma disruptions the structure must be as rigid as possible. To access the internal space of the port plug for maintenance reasons, the front element must be removable. As the port plug will be activated after D-T-operation this service procedure must be capable to be performed by Remote Handling (RH) tools in the Hot Cell Facility (HCF). As this front element will be placed at similar radial position as the regular blankets for ITER it is called Blanket Shield Module (BSM). Fig. 1 shows an upper launcher, mounted in one of the upper ports of the ITER Tokamak.

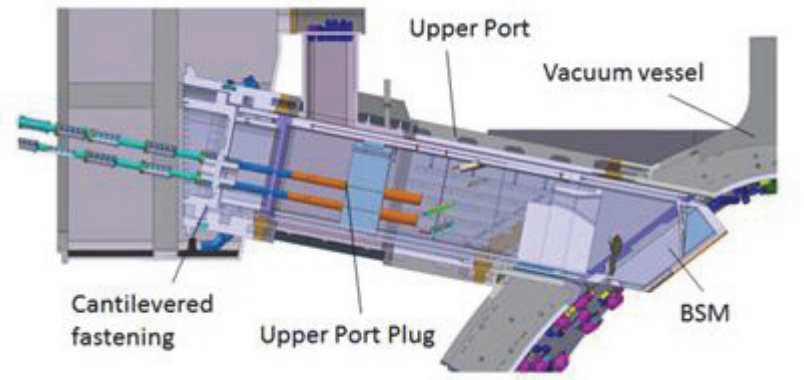

Fig. 1: Outline of the ECRH Upper launcher.

Preliminary design of an EC H&CD port plug

The outer structure of the launcher consists of two main components, the plasma-facing Blanket Shield Module (BSM) and the launcher main frame and is designed as a cantilevered beam, bolted at the port extension of the vacuum vessel [2]. The launcher has to withstand very high moments during plasma disruptions [3], which causes strong bending of the launcher [4]. In the front area of the launcher very high nuclear heat loads will occur. These heat loads decrease by more radial distance from the plasma. For the specific part of the launcher structure straight rear of the BSM, a double-wall frame was designed, consisting of two shells of stainless steel with ribs in between, forming meandering cooling channels. Fig. 2 gives an outline of the present launcher design.

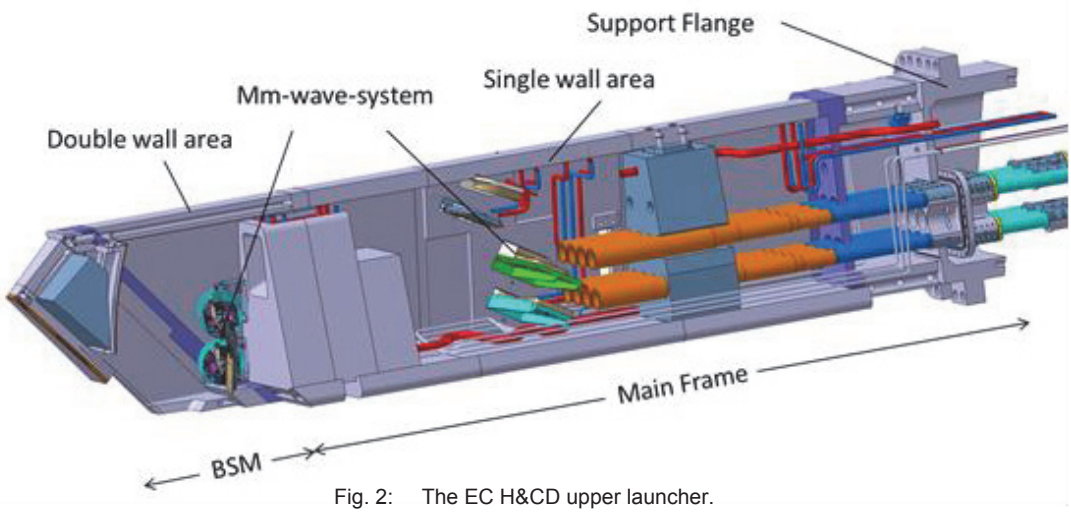

Fig. 2: The EC H&CD upper launcher.

Motivation for double wall prototyping

The mechanical design of the ECRH port plug structure raises high demands on potential manufacturing procedures. The very high mechanical loads during plasma disruptions require a rigid structure to comply with the maximum allowable limits of deflection of the plug. The welding of such strong joints usually causes shrinkage and distortion of the welded structure, while the installation of precisely performing mm-wave-components requires high dimensional accuracy. Therefore prototyping with focus on manufacturing strategies is mandatory to gain experience on the behavior of the component during manufacturing.

Furthermore the detailed design of the cooling passages inside double wall structures must be supported by prototype studies. As no electrical control systems are permitted in the In-vessel area, all branches, manifolds and cooling channels must be designed in a way that guarantees correct flow of the coolant by an optimum geometrical layout. This will be achieved by computational analysis and must be approved by prototypes.

To benefit optimally from the results of prototype manufacturing, full-size mock-ups of the Double Wall Main Frame (DWMF) and the BSM were envisaged to gain maximum experience on the influence of the welding parameters, shrinking effects and dimensional accuracy. Both prototypes are also foreseen to be tested at the Launcher Handling Test facility (LHT) at KIT, where structural components can be tested under ITER operating conditions [5] to verify simulations on heat removal and flow characteristics of coolant.

Design of the Double Wall Main Frame (DWMF) prototype

The design of the prototype was basically derived from the preliminary design of the double wall area of the launcher. It consists of two shells, forming the trapezoidal contour of the component and two cover plates at the front and the rear side of the prototype. The gap between the shells is used as cooling passage. Fig. 3 shows the design concept.

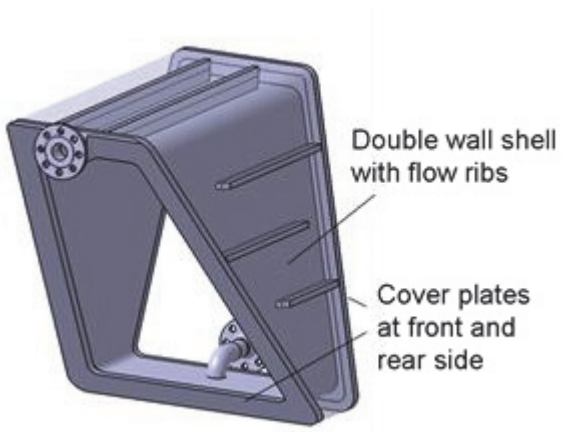

Fig. 3: Double Wall Main Frame design concept.

As pre-prototype studies have shown that a design that relies on deep-drilled cooling structures will be more reliable, easier to manufacture and also cost saving, the double-shell concept was abandoned and a new design with machined structures has been established.

Another issue that was resolved by analysis of the pre-prototypes is the non-uniform flow characteristics of parallel cooling channels. Especially at the manifolds where the flow direction changes, a substantial discrepancy of the flow rate in particular channels can be observed. A good solution for this problem was the installation of throttles with individual aperture on each circular channel in order to distribute the coolant mass-flow equally. Moreover, to avoid dead recirculation of the coolant in corner areas, small leakage gaps were designed. CFD analyses of the flow characteristics have established the design.

Based on the experience from these pre-prototypes the design for a full-size DWMF prototype was made. The trapezoidal body shell is assembled from four forged plates (two side walls, one bottom- and one top-plate), joint by EB-welding and provided with substantial oversize to enable correction of distortions from welding by subsequent machining. The cooling paths are machined by deep-drilling and milling. The shell with its internal cooling paths is enclosed by cover plates on both face sides. These covers are welded onto the shell by a combination of TIG- and manual electronic arc welding.

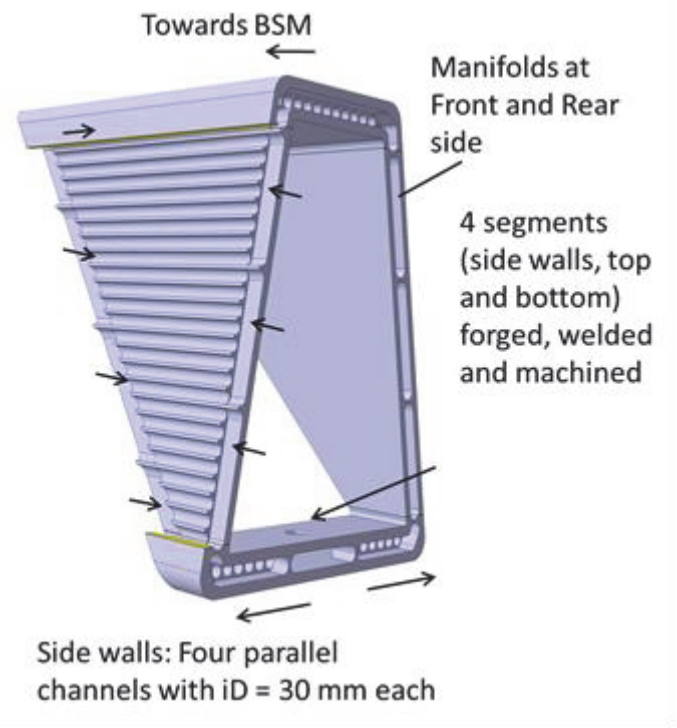

Fig. 4: Double wall prototype design.

To achieve sufficient coolant mass flow as well as an optimum ratio between steel and water for proper shielding capability, it is necessary to arrange parallel cooling channels inside the walls of the structural launcher components. For the DWMF this ratio shall be of 80:20 [6]. Thus a cooling system was designed, which routes the coolant in two symmetrically branched off cooling paths from bottom to top of the DWMF. The path´s layouts feature meandering sections, which comprise four circular parallel channels each. The parallel channels with an inner diameter of 30 mm each are terminated at their ends by machined manifolds. Fig. 4 shows the design and the basic flow scheme of the DWMF prototype.

The DWMF prototype has been manufactured then by MAN Diesel und Turbo SE in Deggendorf (Germany). All parameters determined for EB-beam welding, TIG welding and the machining processes have turned out to be applicable for manufacturing. Fig. 5 shows the DWMF prototype during the manufacturing process.

Since the EB-welds have statistically a higher risk of being not 100 percent qualified, also a weld-repair-test for defective EB-welds was tested to be prepared for such events during production of real port plugs. A defective EB-weld was created and a strategy for removal and refurbishment of the defective zones has been investigated and successfully tested.

After assembly of the prototypes shell a dimensional survey by means of laser tracking has been performed. The angular deviation from the reference dimensions was determined to be less than 0.1° after successful welding while the linear mismatch of the profile was maximum 1.9mm. After simulated repair of one EB-weld the angular deviation was maximum 0.4° and the linear mismatch was up to 4.9mm, which can be compensated by subsequent machining of the oversized surfaces.

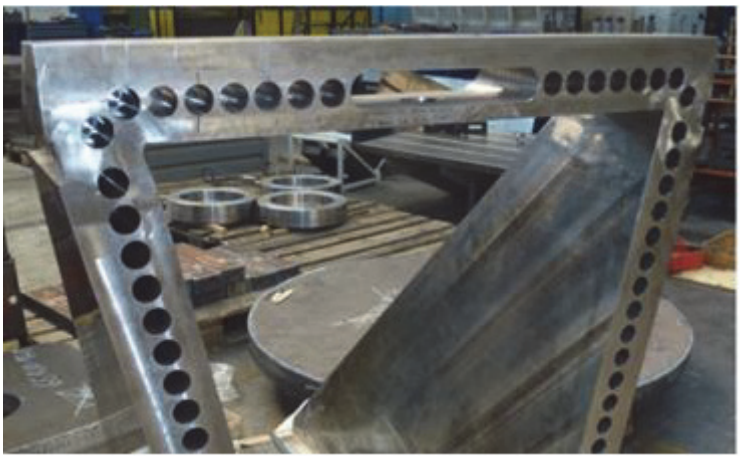

Fig. 5: DWMF prototype during manufacturing.

Fluid-dynamical analysis of the Double Wall Main Frame Prototype

Beside the identification of potential manufacturing problems, the main purpose of doing Double Wall Prototyping is to demonstrate the efficiency of the internal cooling channels, which depends strongly on a uniform coolant flow in parallel channels. This can be achieved by installation of individual throttles either at the end or the beginning of the channels.

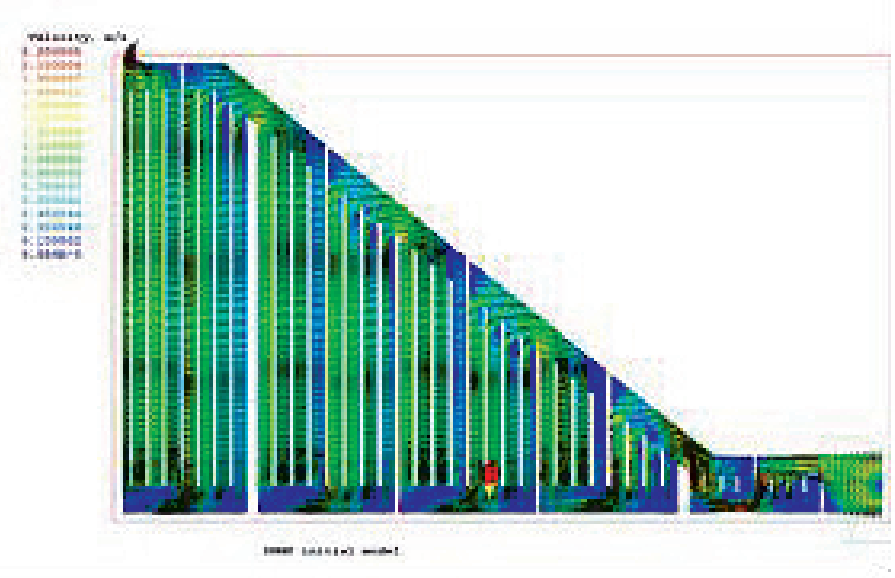

Fig. 6: Flow characteristics of the initial DWMF model.

To determine the optimum aperture of those throttles, a CFD-model of the DWMF has been created and the cooling flow was simulated and optimized on an iterative basis. To start the iteration, an initial model was made where the cooling path did not feature any throttles, thus the “natural” flow of the coolant was simulated.

It turned out that the average flow velocity of parallel channels showed a wide range from 1.5 m/s down to less than zero which means that for particular channels even reverse flow was simulated (cf. Fig. 6). This means, that local cooling water circuits have been created, which might lead to critical thermal hot spots in the structure.

In order to harmonize flow velocity, throttles in the channels have been simulated (cf. Fig. 7). Hereby the diameter of the throttle´s aperture has been varied and the simulation has been repeated until the discrepancy of the flow velocity between all parallel bunches of cooling pipes was below five percent. As a result from this iteration, the need for installation of 30 throttles in total with diameters from 18 to 29 mm was determined.

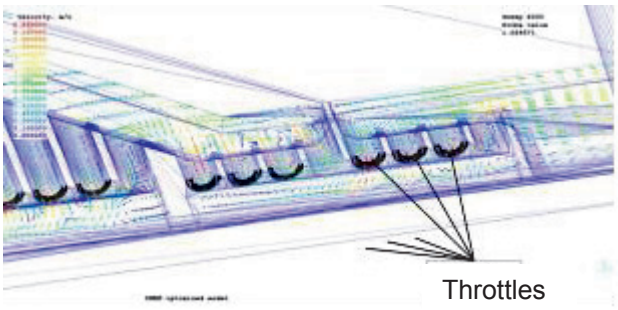

Fig. 7: CFD-simulation of throttles in parallel cooling channels.

For the final arrangement the CFD-simulation calculated average flow velocities in the channels of 0.67 to 0.77 m/s, which means an average velocity of 0.71 to 0.74 for all the bunches of parallel channels. Fig. 8 shows the flow velocity of the optimized model. The overall pressure drop for the entire model (without the supply lines) was determined to be 0.128 bar for the initial model and to 0.172 bar for the final model with throttles. These values show good accordance with analytical calculations of pressure drop.

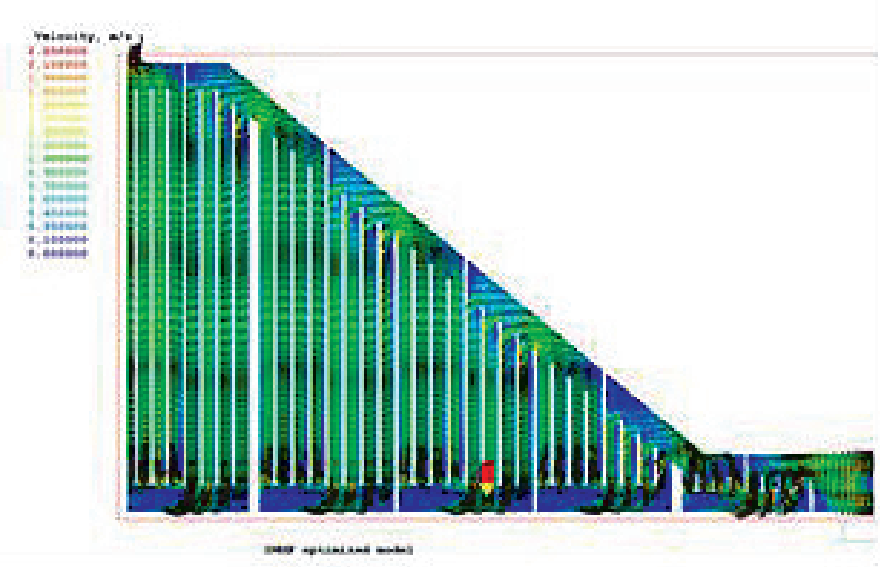

Fig. 8: Flow characteristics of the optimized DWMF model.

To simplify manufacturing the throttles will be designed as a single sheet metal element with eight individual apertures according to the CFD-simulations. They will be installed at the bottom of the manifolds on the vertical face side of the DWMF-prototype to avoid elliptical machining.

Conclusion and next steps

For ITER In-vessel double wall structures an optimum manufacturing route with respect to processing time, thermo-hydraulic performance and cost has been identified and a full scale prototype of a typical double wall structure was designed. The manufacturing design allows inspection of all welds in accordance with the safety requirements as well as machining of complex cooling layouts for In-vessel structural components. The flow characteristics of the cooling layout were investigated and optimized by CFD calculations. Individual throttles to be installed into the cooling channels were used to apply the results of the simulations. The compliance of the manufacturing route with dimensional tolerances after manufacturing was shown. The manufacturing of the DWMF prototype will be finished early 2014. It will be followed by a full size prototype of the BSM, which is under construction and its delivery is expected end of 2014.

Industry cooperation

MAN Diesel & Turbo SE, D-94452 Deggendorf, Germany

Staff:

G. Aiello
G. Grossetti
A. Meier
T. Scherer
S. Schreck
A. Serikov
P. Späh
D. Strauss
A. Vaccaro

Literature:

[1] D. Strauss et al., Progress of the ITER EC H&CD Upper Launcher, 2013, Proceedings of the 11th ISFNT conference, Barcelona, Spain, 2013

[2] P. Spaeh et al., The ITER EC H&CD upper launcher: Structural design, Proceedings of the 25th SOFE conference, San Francisco, US, 2013

[3] A. Vaccaro et al., The ITER EC H&CD upper launcher: Transient mechanical analysis, Proceedings of the 26th SOFT conference, Porto, Portugal, 2010

[4] D. Strauss, Deflections and Vibrations of the ITER ECRH Upper Launcher, EC-16 meeting, 12-15 Apr. 2010, Sanya, China

[5] S. Schreck et al., Prototype manufacturing and testing of components of the ECH upper launcher for ITER, 23rd IAEA Fusion Energy Conference, Daejeon, Korea, October 11-16, 2010

[6] A. Serikov et al., Overview of recent nuclear analyses for the Upper ECH launcher in ITER, Proceedings of the ISFNT-9 conference, 2009, Dalian (CN), http://dx.doi.org/10.1016/j.fusengdes.2010.06.016

Acknowledgement

This work was financially supported by the Ministry of Research and Education (BMBF) under the grant No. 03FUS0010. The views and opinions expressed herein do not reflect necessarily those of the BMBF or the European Commission.

Report on Feasibility and Performance of Broadband Windows (WP13-DAS-03-HCD-EC-T07-02)

Executive Summary

CVD diamond windows act as confinement barriers in H&CD applications allowing transmission of high power mm-wave beams at the same time. For example, diamond windows in the ITER electron cyclotron H&CD system are used to send mm-wave beams between 1 and 2 MW for plasma heating and mode stabilization. To meet several plasma requirements, the beams must be deployed at different positions inside the plasma. It can be achieved by sending a fixed frequency beam via moveable mirrors or a beam at different frequencies. In the first case, a conventional single disc window is used and thus the disc thickness must be in resonance condition in order to minimize the power reflection. Moveable mirrors are then used to deploy the beam at different locations in the plasma, as in the ITER electron cyclotron H&CD system [1]. However looking at DEMO, moveable parts close to the plasma have to be avoided because of the higher heat loads and neutron fluxes. A promising alternative might be the use of gyrotrons able to tune the beam frequency to the desired resonance in a given range (e.g. 105-140 GHz) [2], so that the beam is directly sent to the correspondent resonant magnetic flux surface. Broadband window solutions are thus required. There are three concepts of such a window and they are reported in Figures 1-3.

Figure 1 shows the tuneable double disc window which is composed of two window structures and a housing. Each window structure consists of one diamond disc to which two copper cuffs are brazed at one face and then in a second step these cuffs are brazed into a steel flange containing the cooling pipes and connections to the housing. The housing ensures fine-tuneable adjustment of the distance between the two discs allowing transmission of beams at different frequencies with minimum reflection conditions. The power absorbed by the disc is partially removed by direct contact between the diamond and the water and partially diffuses in the copper cuffs. The manufacturing of such a window is a bit hard because very small tolerances are required and a high number of brazing has to be performed. Direct contact with water ensures thermal stresses during the beam power absorption in the disc which are far from the ultimate strength of the materials. Finally, it has to be considered that the double disc window is relatively expensive because two discs have to be fabricated for one window and its frequency bandwidth is rather limited.

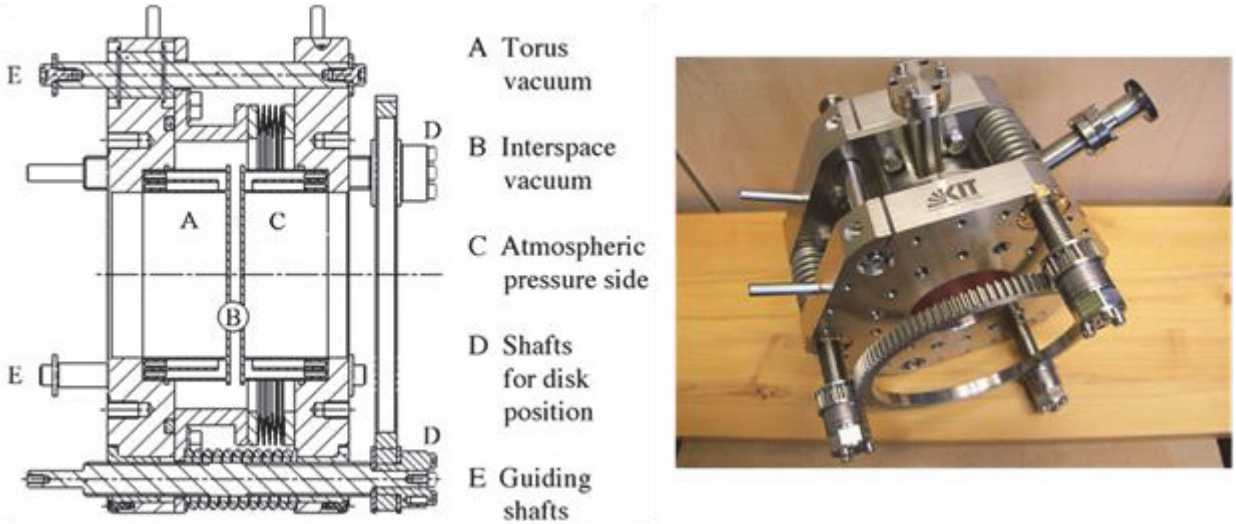

Fig. 1: Tuneable double disc window.

Figure 2 reports the Brewster window which consists of an elliptical CVD diamond disc brazed to two copper cuffs at the Brewster angle. This angle for diamond is 67.2°. With respect to the double disc option, this window offers a larger frequency bandwidth, but the main challenge here is the asymmetric brazing between diamond and copper. The brazing

process is already hard because it is carried out at about 800°C and since copper and diamond have very different thermal expansion coefficients (ratio of 16 to 1 at 20°C, respectively), the cool down phase to room temperature results in high stresses that might lead to failure of the disc. In addition, the complex geometry of the Brewster window with the skewed position of the disc makes the stress profile worse than the one obtained in a conventional circular window. However, FEM structural analyses have shown the CVD diamond Brewster window is a feasible broadband window solution for H&CD applications [3]. High stresses are located on the major axis of the brazing ellipse, but they are anyway far from the ultimate strength of the diamond. Values of the cuff thickness greater than 1.2 mm and of the disc thickness less than 1.7 mm are not recommended. Finally, it is also important to note that because of its skewed position, a large diamond disc is required for the Brewster window. For instance, being 50 mm the diameter of the cuffs, the possible minimum major axis of the disc has to be 140 mm. The manufacturing of a disc with major axis higher than 140 mm is very hard and therefore this imposes an upper boundary on the diameter of the waveguides to be used for the transmission of the mm-wave beams.

Fig. 2: Brewster window.

Figure 3 shows the last concept of diamond window where the frequency band is expanded by modifying the surface finish of the diamond disc [4]. Grooves on the surfaces of the disc can be achieved by laser processing and so they were formed on a small rectangular diamond sample (Element6, The Netherlands). Results have shown that well defined grooves cannot be obtained because of irregularities at the corners of the grooves and moreover the manufacturing process of such corrugated surfaces would be too expensive. In addition, the grooves lead to local stress accumulation beyond tolerable limits for the diamond [5]. This window concept cannot be thus considered as a feasible broadband window solution.

Tables 1-3 summarize advantages, disadvantages and issues to be still solved for the different concepts of broadband window. In the past different concepts have been studied.

1. An asymmetrically brazed Brewster window prototype has been manufactured and it performs well in short pulse tests at 1.3MW. It is considered as a quite promising straight forward approach to a broadband window. For the future the brazing has to be optimized for tightness and the transmission losses of the diamond disk should be lowered to reduce cyclic stresses during operation for lifetime optimization (although cyclic failures did not occur up to now). As a next step the development of a cooling strategy to allow long pulse operation is considered.

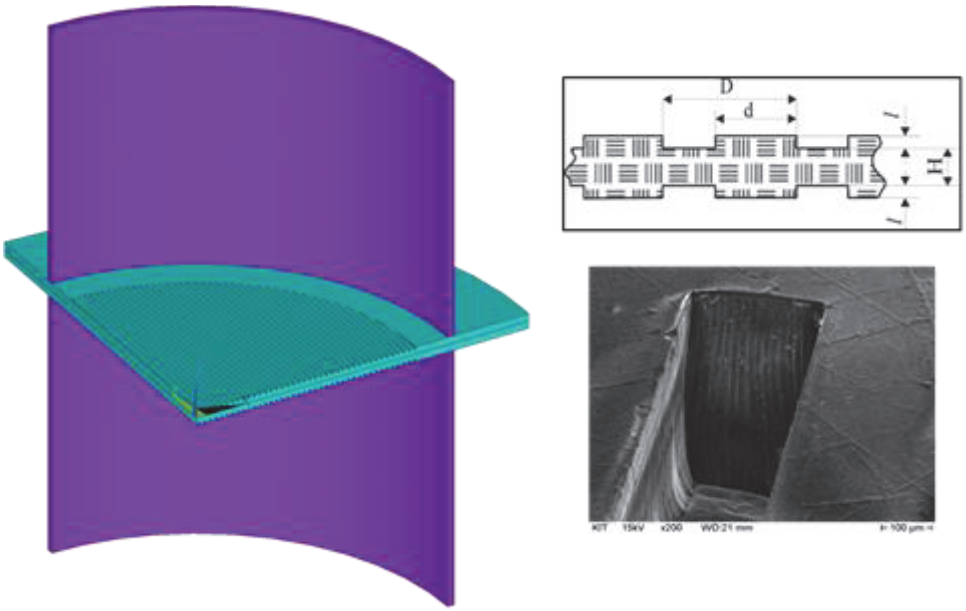

Fig. 3: Antireflection window by surface modification.

2. Two tuneable double disk windows have been manufactured successfully, while the first shot was successful a disk failure occurred during the next experiment. The assessment is still ongoing, the reason for the failure was most probably local heat generation in the cooling water channel resulting in steam formation and a cavitation like process generating excess loads on the diamond. Here the next step should be to coat the diamond disk surface forming part of the cooling channel.
3. Surface modification of diamond by laser has proven to be possible; it leads however to high stress concentrations at groove edges. With further simulations the feasibility of this concept should be checked – if the disk is thick enough, the excess stress might be controlled.
4. The ring resonator is prototyped and being installed as ASDEX-UG. Here the reflected power fraction is dumped to a load, experiments are expected in the near future.

Table 1: Advantages of the different concepts of broadband window.

Description	Brewster Window	Double Disk Window	Grooved Disc Window	Ring resonator (Russia)
Advantages	■ fast tuning ■ no reflection ■ loss intrinsic ■ simple structure ■ short pulse operation already tested @ 1.3 MW ■ minimal influence of brazing on WG ■ minimal space for implementation	■ symm. brazing in comparison to Brewster concept ■ prototype already manufactured ■ tunable, narrow bandwidth ■ robust housing ■ pol independent	■ symm. brazing in comparison to Brewster concept ■ large apertures possible	■ pol independent ■ implementation in AUG ongoing – waiting on results from the experiments!

In the past a further Brewster window with a symmetrical disk brazing has been tested. In this concept two mirrors direct the beam through the window in the Brewster angle. Here arcing led to a disk failure, the concept is actually not followed anymore.

Summarizing it has to be stated, that there is still significant and challenging progress required to obtain a working broadband window solution. First the asymmetrically brazed Brewster window seems to be quite attractive; additional development work is required for the disk cooling, the challenging brazing process and finally the loss tangent optimization of the diamond to reduce the thermal cyclic loading during operation. Secondly, a prototype of the tuneable diamond window is available; with a relatively minor effort the disks could be coated in the cooling channel area to avoid millimetre wave absorption in the cooling water. The grooved disks have weak mechanical properties causing problems during pressure exposure. The concept could be further studied with respect to an optimization of the groove geometry (avoid sharp edges) and an increased diamond disk thickness. Finally the ring resonator concept will be studied in the near future by experiment, its outcome will allow to better assess this option.

Table 2: Disadvantages of the different concepts of broadband window.

Description	Brewster Window	Double Disk Window	Grooved Disc Window	Ring resonator (Russia)
Disadvantages	■ asymm. brazing ■ pol dependent ■ stress accumulation on large half axis of elliptic disc ■ deformation during cool down of the brazing process of the WG structure ■ max. aperture limited by ellipse ■ expensive wrt. elliptic geometry	■ tuning needs positioning time ■ backlash ■ weight ■ size (installation space large) ■ stray radiation ■ expensive (2 disks and high precision housing)	■ pol dependent ■ grooves weaken the disk → large thickness ■ laser patterning produces sharp kink-like bottom profile ■ laser patterning causes sp2-phase transformation at the surface	■ load ■ size ■ weight ■ expensive

Staff.

G. Aiello
T. A. Scherer
D. Strauss

Table 3: Issues to be still solved of the different concepts of broadband window.

Description	Brewster Window	Double Disk Window	Grooved Disc Window	Ring resonator (Russia)
To be solved (challenges)	■ implementation of water cooling ■ optimization of brazing process: e.g. 700°C annealing during braze cool down ■ inserted WGs ■ corrugated WGs ■ optimization of diamond losses (surface and bulk) wrt. low cyclic stress during MW operation	■ coating of optical components open to radiate with Ag or Cu to reduce the stray radiation in the FABRY-PEROT resonator	■ improve laser process due to groove profile improvement ■ development of a chemical process to remove Laser induced sp2-carbon phases on the surface of the diamond structure	

Literature:

[1] D. Strauss et al., Preliminary Design of the ITER ECH Upper Launcher, conf. proc. 38th ICOPS, Chicago, USA, 2011.

[2] D. Wagner et al., J. Infrared Milli Terahz Waves 32, 274-282 (2011).

[3] G. Aiello et al., CVD diamond Brewster window: feasibility study by FEM analyses, conf. proc. EC-17, EPJ Web of Conferences 32, 04014 (2012), http://dx.doi.org/10.1051/epjconf/20123204014.

[4] V.I. Belousov et al., Broad band matched windows for gyrotrons, conf. proc. 34th IRMMW, Busan, Korea, 2009.

[5] A. Vaccaro et al., Grooved CVD diamond windows: grooves' profiles and structural simulations, conf. proc. 36th IRMMW, Houston, USA, 2011.

Acknowledgement

This work, supported by the European Communities under the contract of Association between EURATOM and Karlsruhe Institute of Technology, was carried out within the framework of the European Fusion Development Agreement. The views and opinions expressed herein do not necessarily reflect those of the European Commission.

DEMO System Integration Study of a Vertical Port Plug (VPP) for ECRH Launcher (WP13-SYS-03-T05-01)

Introduction

Overview

In this report is shown the activity carried out within the EFDA Work Programme 2013, System Integration Study on a preliminary assessment for the integration into DEMO of an ECH Upper Port Plug.

Preliminary conceptual design of a vertical ECRH launcher

In this chapter we briefly show which input and assumptions have been taken into account in order to assess the preliminary conceptual study on the Vertical Port Plug for DEMO.

Input and assumptions used in the conceptual design

The justification for requiring an ECRH Upper Launcher, lies in the higher efficiency in mitigating plasma instabilities, like Neo-classical Tearing Modes[1], reached when injecting high power mm-wave beams from a top position of the Tokamak.

Due to the current maintenance scheme of the MMS, that foresees extraction from the Vertical Port, integrating an Upper Port Plug into the Vertical duct is a challenging study.

In this early phase the distribution and space allocation of the pipes (whose number is still uncertain) for the cooling of the blanket system is not taken into account.

As primary input for the design of the Vertical Port Plug has been used the outcome of the study on the Electron-cyclotron-current-drive efficiency in DEMO plasmas [1]. The structure of the launcher has been developed taking the injection point, localized at (R, Z) = (11, 2.5) m, that maximizes the CD efficiency as a function of the poloidal injection angle α and the toroidal injection angle β, for a wave frequency of 270 GHz. As shown in Fig. 1 the maximum CD efficiency is obtained is obtained for α = 47 deg and β = 41 deg.

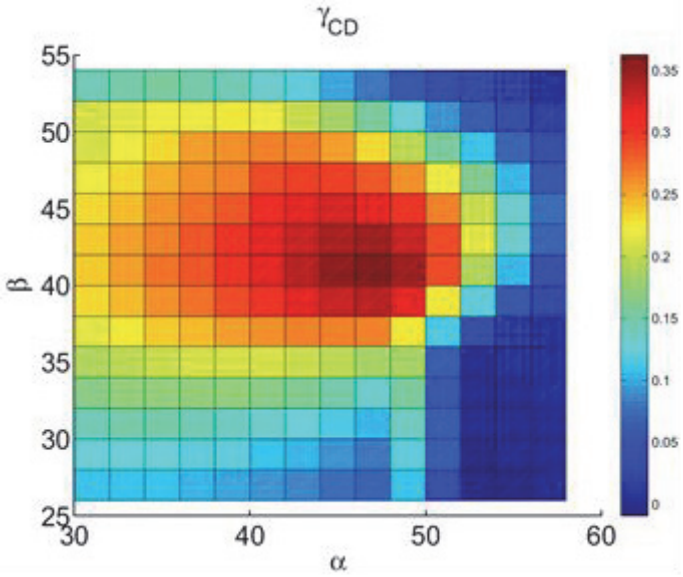

Fig. 1: CD efficiency for injection from the upper part of the vessel (from [1]).

The second step has been to include in the assessment a set of assumptions to provide the constraints for the development of the design, taking however into account that, since we are in a pre-conceptual phase, the different components act more like a place holder than real design features of the VPP.

With this respect, considering the development for a DEMO-1 tokamak (early DEMO), we assumed:

[1] That represent a potential threat for plasma operation and Tokamak safety, since NTM can increase in size leading to a disruption

- No front-steering mechanism due to the extremely harsh environment. If steering is then required, then must be remote.
- 5 waveguide per launcher (with 1MW per beam line). This number might increase if higher local current drive is necessary.
- 2 shielding blocks (acting for the moment as place holder)

Design of the Upper Port Plug for DEMO

With the assumption mentioned in the previous paragraph, we developed a preliminary concept for the Vertical Port Plug where the dimension in the radial direction is kept shorter than the one in the toroidal direction, in order to compensate more easily to the momenta induced by the eddy currents resulting after a disruption.

A sketch of the Vertical Port Plug inserted into the vertical duct is shown in Fig. 2. It is worth to mention that we do not foresee any penetration of the Vertical Port Plug into the MMS. In fact, as already discussed in the EFDA WP12-DAS06-T05 final report, the ECH system needs relatively small openings for allowing the beam to be injected into the plasma.

In Fig. 3 are reported the cut outs of the Port Plug, where are clearly the waveguide, bended to provide a labyrinth structure for the neutron streaming. An internal frame is provided as support system for the waveguide.

A preliminary maintenance scheme foresees the possibility to extract the plug internals, all attached at the internal frame. In the next chapter the EM analysis will be discussed in details.

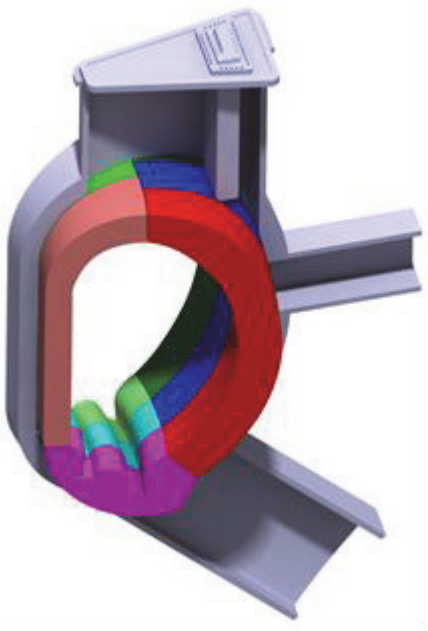

Fig. 2: DEMO sectors in which is visible, inserted into the vertical duct, the VPP.

Fig. 3: DEMO sectors in which is visible, inserted into the vertical duct, the VPP.

Electromagnetic analysis

FEM Model

Geometry

The FEM model consists of a 22.5-degree sector model of DEMO based on the same CATIA drawings that have been used for the current design of the VPP. The WP13 CATIA model here used is up to date, consistent with the status of the DEMO development and, most important, already contains the modifications of the upper port that are necessary to accommodate the VPP.

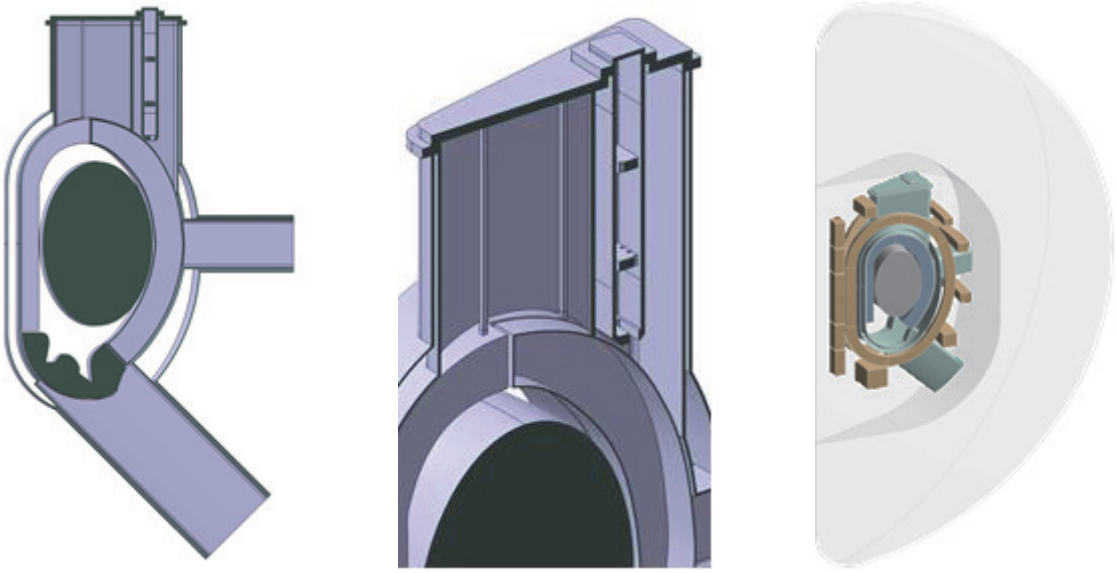

Fig. 4: Section view of the modified CATIA drawing (left); detail of the Vertical Port Plug (centre); geometry implemented in the FEM model (right).

Material properties

The vacuum vessel and the upper port plug are considered as made of pure SS316. For these parts, the resistivity was calculated at a temperature of 100 °C.

The blanket segments, on the other hand, consist of a mixture of several materials, thus the electrical properties are calculated as volume-weighted averages, summarized in table 1.

Table 1: Calculation of the equivalent resistivity for the two partitions of the blanket segments.

Component	Eq. Resistivity (Ω m)	Vol (m^3)	Volumes Fractions	
			Blanket Shell	Blanket Vol
BMS	8.42620E-07	4.258	0	1
BMC	8.42620E-06	9.7742	0.145	0.855
FW	1.53030E-06	3.4302	1	0
MMS	1.24691E-06	2.5649	0	1
MMC	4.80951E-06	6.1131	0	1
BZ (HCPB)	7.76922E-06	15.506	0	1
Equivalent resistivities (Ω m)			3.54703E-06	6.17063E-06

Additional pure materials, directly obtained from the ANSYS standard materials library and used in the model are:

5. Air, to model the boundary. Equivalent to vacuum.
6. Copper alloy, used to just distinguish the coils from the rest of the structure.

All the materials in the FEM model have relative magnetic permeability set to 1, that is, no ferromagnetic properties of the EUROFER were modelled, which leads to a linear solution of the problem.

Mesh and element types

The mesh consists of about 700k/470k nodes/elements (SOLID236, [3]). This is a rather low number, considering the size of the model. For reference, the same disruption analysis with detailed blanket modules, carried out in the frame of the EFDA-WP12-DAS02-T09 activity, needed a 4-million-nodes mesh [1].

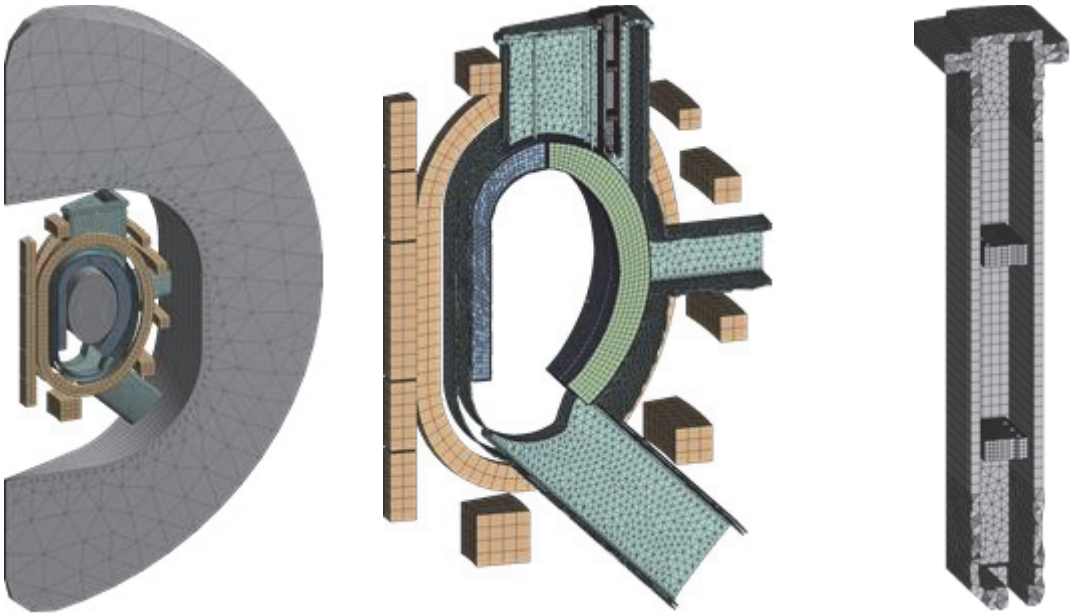

Fig. 5: Overview of the meshed model (left), section of the conductive region and coils (middle) and section of the Vertical Port Plug structure (right).

Boundary conditions and loads

Periodicity is defined at the two cut planes at ϑ=−11.25° and ϑ=11.25°, by coupling the DOFs of periodic couples of nodes (match control is used to have identical meshes at the two sides of the model).

The total current applied to PF and CS coils is referred to the set of SOF (betapol = 1.2). The toroidal field is defined as B_{tor} = 7.1 T at r = 9 m [4], which is obtained by applying a 20 MA current. The coils are modelled as stranded conductors and therefore a homogeneous current density is actually applied to their elements. As a consequence, a complete definition of each coil also requires the cross-sectional area of the coil itself. In Table 2the cross section and total current applied to the CS, PF and TF coils are reported. The currents are imposed as constant during the plasma disruption.

Table 2: Total current applied to the coils in the EM models.

Coil	CS3_U	CS2_U	CS1	CS2_L	CS3_L	PF1	PF2	PF3	PF4	PF5	PF6	TF
Area (m²)	2.6543	2.6543	5.3087	2.6543	2.6543	1.44	0.64	1	1	1.96	4	0.45
Current (MA)	2.7436	26.543	−10.2712	20.7079	2.5303	10.7779	−3.17	−2.7415	−1.0377	−14.8739	36	10

Finally, as far as the plasma current quench is concerned, the same definition made in [1] is used in the present work, that is a central disruption with a linear quench, the current quench time being 35 ms·A_{DEMO}/A_{ITER}, where A_{DEMO}/A_{ITER} = 1.2 is the ratio of the plasma cross sections of the systems as indicated in the subscript (details to be found in [4] and [5]). This assumption sums up to a quench time of 42 ms.

The plasma is represented by the current density j_{Plasma} defined as a quadratic distribution with elliptical cross-section:

$$j_{Plasma}(t,r,z) = j_{peak}(t)\left[1-\frac{(r-r_0)^2}{a^2}-\frac{(z-z_0)^2}{b^2}\right]$$

where j_{peak} (0) = 1.71·10^6 A, r_0 = 9 m, z_0 = 0, a = 2 m, and b = 3 m. The value of j_{peak} (0) has been calculated on the assumption that the total current has to be 16 MA.

To apply this current density to the elements in the plasma region, an array table has been used. This method allows a simple definition of the current density and it has been proved to be very fast and reliable since it does depend neither on the specific scenario nor on the mesh that was chosen for the plasma region in the EM model.

Results

Static load step

The contour plot on a plane at $\vartheta = 0$ of the vector sum of the magnetic field is shown in Fig. 6(left). In the inner volume of the tokamak, the 1/r distribution of the toroidal field (which is the dominant component, in that region) is clearly visible. This is also shown in Fig. 6 (centre), which shows a very good agreement between the toroidal magnetic field (sampled at $\vartheta = 0$ and z = 0) and its analytical approximation ($B_{tor} = 9 \cdot 7.1/r$). Finally, a contour plot of the total static magnetic field (vector sum) on the conductive structure is shown in Fig. 6 (right). The effect of the discrete nature of the toroidal excitation (discrete number of TF coils) is clearly visible (toroidal ripple and perturbation of the poloidal field).

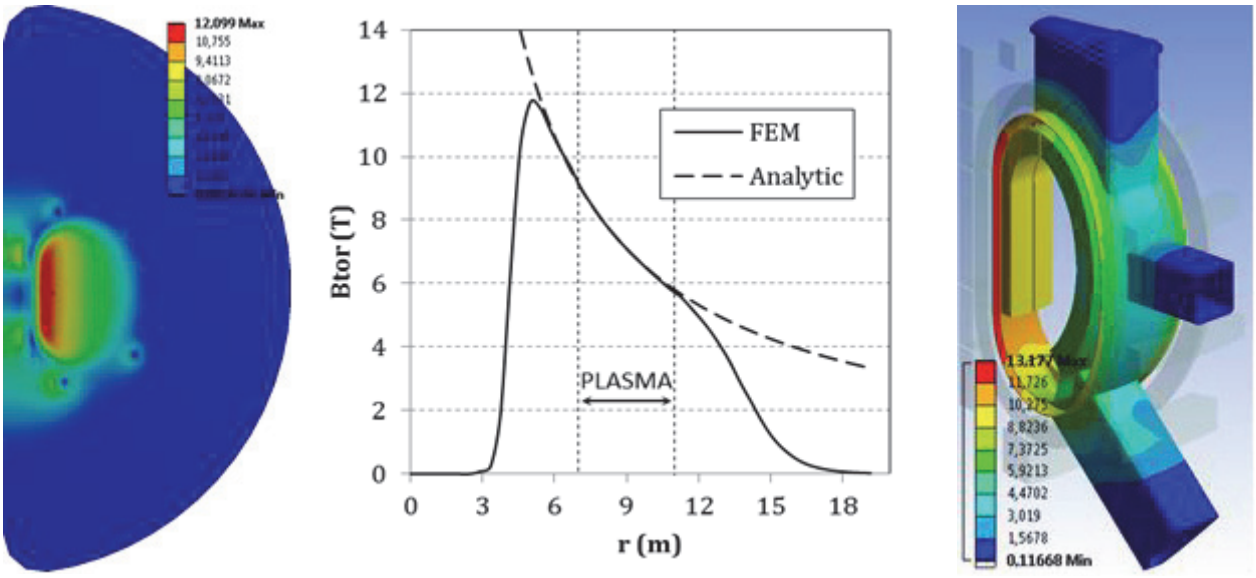

Fig. 6: Magnetic field (vector sum) on a plane at $\vartheta = 0$ (left); comparison between toroidal field on a radial path at $\vartheta = z = 0$ and the $1/r$ distribution (centre); magnetic field (vector sum) on the conductive structure (right).

Transient analysis

The auto time stepping option was used for the solution of the analysis and resulted in a subdivision of the transient load step in 86 substeps. This results in a rather high time resolution with a very smooth description of the loads.

Fig. 7 shows a vector plot of the eddy currents at $t = 42$ ms and $z = 0$. The picture shows a typical result for this type of simulation: as the quench is central, without any vertical movement and/or resizing of the plasma distribution — the peak of the distribution decreases to zero, but its size and shape does not change — the eddy currents are mostly rotating around the poloidal axis. This result leads to high radial moments on the structures. This is also shown in Fig. 8 (left and centre): the toroidal component of the moment acting on the outboard blanket segment is negligible with respect to the other components. Depending on the blanket's symmetry grade with respect to the plane $z = 0$, different behaviours of the total forces are found (Fig. 8, right): since the OBC blanket has higher symmetry, the forces tend to cancel, resulting in a non-monotonic curve. For the same reason, a moment in the vertical direction is also acting on the (non-symmetric) IBR blanket.

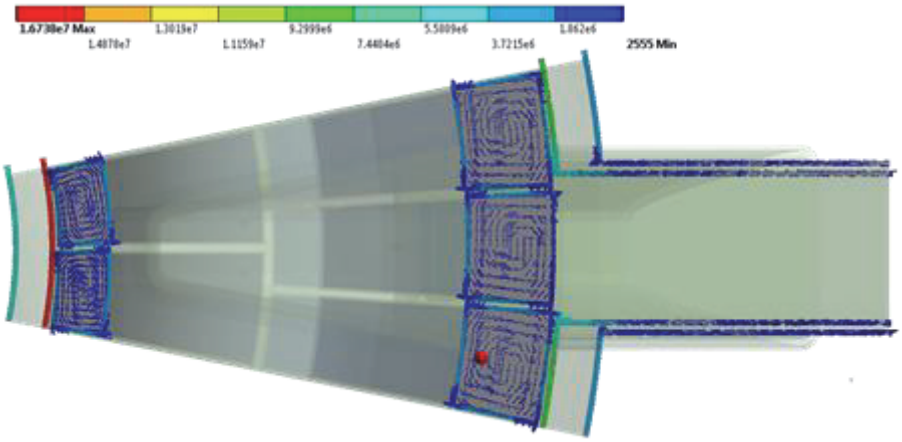

Fig. 7: Eddy currents (in A/m²) induced in the vessel and the blankets at t = 42 ms and z = 0.

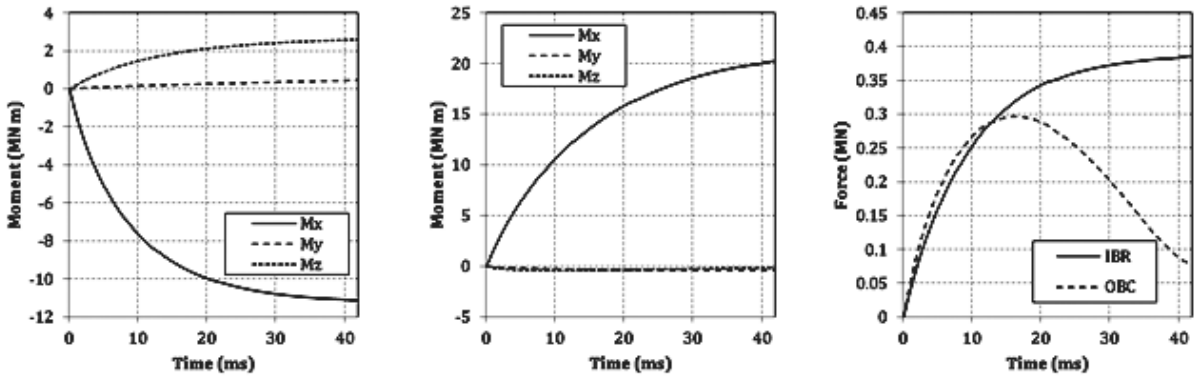

Fig. 8: Moments acting on the IBR blanket (left); moments acting on the OBC blanket (centre); comparison of the total forces on the IBR and OBC blankets (right).

Finally, the forces and moments acting on the structure of the Vertical Port Plug are reported in Fig. 9 (left and centre). Similar considerations as for the blanket segments apply to the VPP, the toroidal moment being much lower than the radial and poloidal components. As far as the internal components are concerned, the loads on the front shield block are significantly higher than the loads on the rear one (Fig. 9, right), the natural consequence of the front block being closer to the plasma.

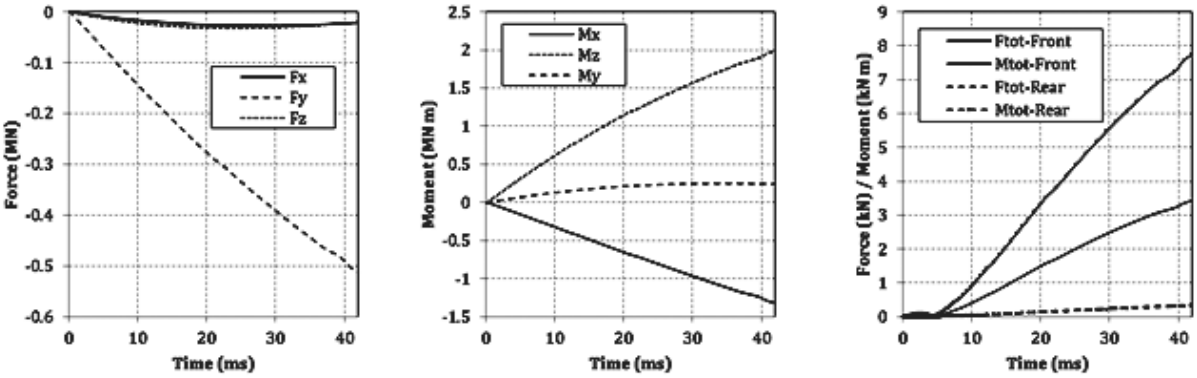

Fig. 9: Lorentz's forces (left) and moments (centre) acting on the structure of the VPP; forces and moments acting on the front and rear shielding blocks (right).

A number of assumptions are limiting the peak values found in the present calculation:

First, the launcher is located behind the blanket, which in turn provides EM shielding.

Secondarily, a detailed description of the plasma disruption is so far not available.

Finally, the EUROFER ferromagnetic properties are not taken into account.

A simple quick estimation of all these factors would be too uncertain, a new set of analyses with more accurate assumptions are necessary for a more realistic assessment.

Conclusions

A pre-conceptual Vertical Port Plug with 5 beam lines à 1MW has been designed. The Launcher internals as optical system and shield blocks are only of exemplary nature, also the integration of the front beamlines into the blankets still has to be developed with the aim for high Tritium breeding space as well as the sufficient MHD control. The design shows that a relatively small volume occupation in the port still allows substantial space for supply line routing for the blankets. The Port Plug assembly has been integrated into a vertical port and an EM analysis has been performed. The major acting moments are radial and poloidal and the absolute calculated numbers are roughly in the range of the ITER ECRH Upper Launcher. The simulations can be considered only as a starting point for further analysis, as the plug integration into the blanket as well as EUROFER ferromagnetic material parameters could not be considered here.

Staff:

R. Geßner
G. Grossetti
P. Späh
D. Strauss
A. Vaccaro

Literature:

[1] E. Poli et al, 2013 Nucl. Fusion 53 013011

[2] WP12-DAS02-T09: EM analysis of the DEMO1 blankets, EFDA_D_2LJB6G

[3] ANSYS 14.0 APDL manual.

[4] DEMO design summary, EFDA_D_2L2F7V.

[5] Annex–A - PROCESS paper draft_rk_16_8_11b

Acknowledgement

This work, supported by the European Communities under the contract of Association between EURATOM and Karlsruhe Institute of Technology, was carried out within the framework of the European Fusion Development Agreement. The views and opinions expressed herein do not necessarily reflect those of the European Commission.

Goal Oriented Training Programme “Diagnostic Systems for Upper Port Plug Structures” (WP12-GOT-4-DIAG (FU07-CT-2012-00067))

Introduction

One of the subsystems ITER will adopt to heat up the plasma is the Electron Cyclotron Resonance Heating. Consisting of 4 upper launchers and an equatorial launcher capable together of injecting roughly 20 MW of power via microwaves at 170 GHz, it will require the implementation of a broad spectrum of diagnostic systems in order to guarantee optimal and safe operation. This work is mainly focused on the development of such diagnostics systems for the waveguides CVD diamond windows, located in the First Confinement System of the Upper Port Plug, behind the bio shield.

Status of Activities

The first months of this project schedule were spent gaining knowledge on various topics and starting a first assessment of the diagnostics required for such purpose, while also producing conceptual drawings (with the use of CATIA) of the windows copper cuff with the added diagnostics mock ups.

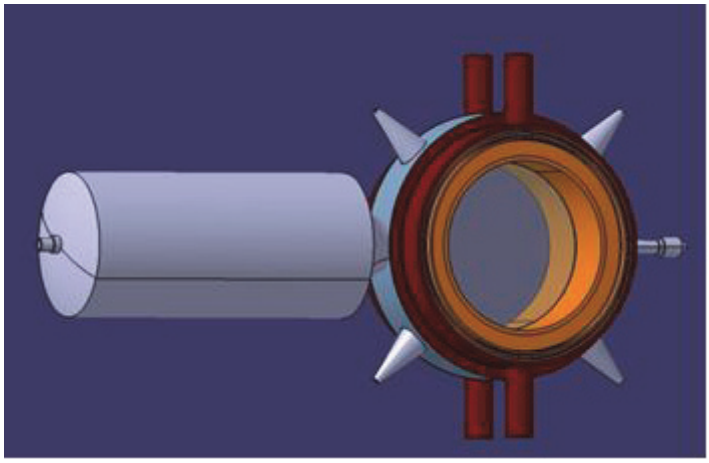

Fig. 1: Window copper cuff, with added diagnostics mockups.

The investigated topics include microwave antenna theory, plasma heating by ECRH, radiation detectors. Attendance to Erice International School of Fusion Reactors Technology added considerable knowledge on neutronics topics.

The diagnostic in development consist of four main kinds, some of them with different possible candidates. They are, in order of importance: arc detection, tritium detection, MW transmitted / reflected power measurements and diamond disk temperature.

Arc detection is the most critical diagnostic, since these electric disruptions are capable of delivering extensive high damage to the waveguides and to the diamond windows, impairing transmissivity performances and neglecting the correct operation of the whole ECRH system. The initial design is based on a fiber optic + detector concept, implementing a fiber optic vacuum feedthrough on the outer ring of the copper cuff, in order to detach the detector itself (composed by a photomultiplier and photodiode) from the CVD windows assembly. This aspect is of primary importance, given the small space at our disposal in the position of the copper cuff. Arc detection will be directly interlocked to the gyrotrons, in order to stop immediately mw generation in the case of a discharge.

Tritium is the second most important diagnostic of the bunch, given the biological and chemical hazard that this gas poses to the human beings. Being tritium a low energy beta emitter, we can exploit this feature in order to detect the presence of the hydrogen isotope in regions where it shouldn’t be, like in the proximity of the diamond windows.

There are various kind of beta detectors, but the operational environment in which the detector will operate strongly suggest the adoption of solid state detectors, more rugged and with better performances per unit volume if confronted with gas detectors. The two main options are silicon detectors and diamond ones, with a preference for the latter, given the superb hardness and radiation resistance of the diamond. Another option consist in adopting a total-

ly passive device, using phosphorescent crystals coupled to a PMT, in order to avoid bias voltages and obtaining a simpler device.

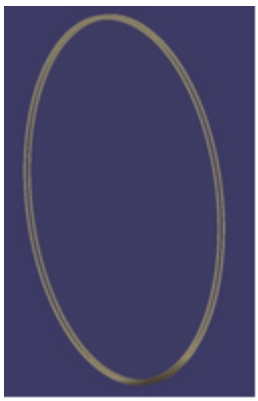

Fig. 2 Metallized diamond window, for direct implementation of tritium detection.

Fig. 3: Third party diamond detectors.

Assessment about the possibility of using part of the window as a detector is also on its way, although it seems that the problems arising from such a solution overcome the benefits.

Microwave power transmission / reflection should allow a general evaluation of the windows performance and of the beam profiling, monitoring the operation of the gyrotrons. Detection of the leaked microwave beam will be performed by Direct Conversion Homodynes, via four horn antennas installed on the outer ring of the copper cuff.

The final diagnostic is the disk temperature measurement, performed with thermocouples in direct contact with the outer part of the brazed disk. Paired with the mw data it will allow a more precise beam profiling.

Staff:

G. Grossetti
F. Mazzocchi (Trainee)
T. Scherer (Coordinator of the GOT-4-DIAG trainee programme)
A. Vaccaro

Acknowledgement

This work, supported by the European Communities under the contract of Association between EURATOM and Karlsruhe Institute of Technology, was carried out within the framework of the European Fusion Development Agreement. The views and opinions expressed herein do not necessarily reflect those of the European Commission.

Magnets and
Affiliated Components

Current Leads for Wendelstein 7-X and JT-60SA (CoA; BMBF Reference No. 03FUS0013)

Current Leads for Wendelstein 7-X

The stellarator W7-X presently under construction at the Greifswald branch of the Max-Planck-Institute for Plasma Physics consists of 50 non-planar and 20 planar coils with a maximum conductor current of 17.6 kA. KIT has delivered the current leads for the magnet system. In total 16 current leads were required (maximum design current I_{max} = 18.2 kA, nominal current I_{nom} = 14 kA): 14 current leads are used for the W7-X machine and 2 prototype current leads are used as spares.

Series current lead manufacturing

Due to the tight schedule it was decided to manufacture and assemble the series current leads for W7-X in KIT. All 14 series current leads have been fabricated and 12 of them successfully tested. After the completion of the series production in house in 2012 two series tests were performed, one in December 2012 and one in March 2013. All current leads behave very similar and confirm the results of the prototype current lead tests in 2010 (examples see in Fig. 1). Due to problems with the current lead bus bar connection which was not caused by the current lead the tests were delayed. All current leads were accepted by IPP Greifswald and the project “Current Leads for Wendelstein 7-X” was finished in June 2013 with a colloquium taken place at KIT.

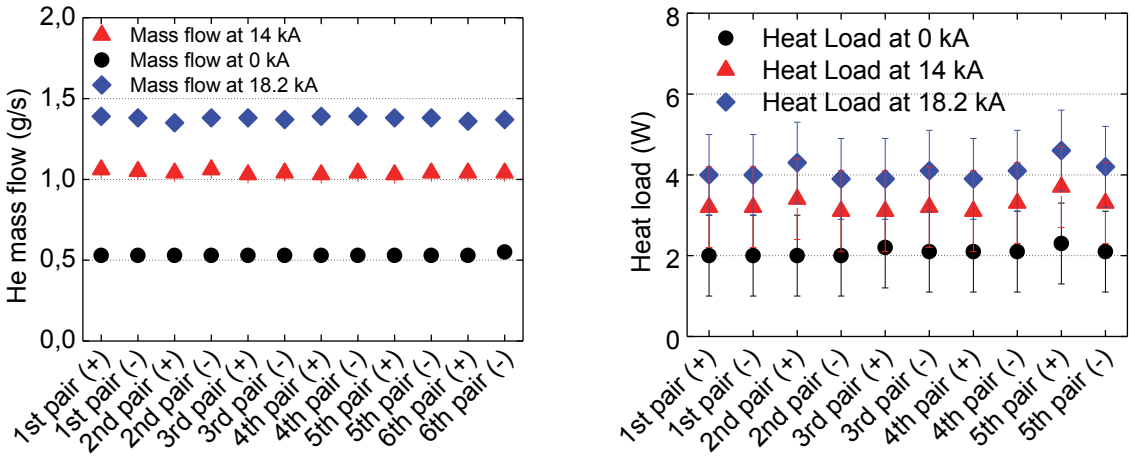

Fig. 1: 50 K He mass flow rate (left) and heat load at 4.5 K level (right) at 0, 14 and 18.2 kA for the current lead pairs 1 to 6.

Fig. 2: Handover of the acceptance certificates of the last current lead pair delivered to IPP at the concluding colloquium at KIT.

Current Leads for JT-60SA

In the frame of the Broader Approach Agreement between Japan and the EU and concomitantly to the ITER project, a satellite tokamak project called JT-60SA has been agreed. The magnet system of JT-60SA consists of 18 toroidal field coils (25.7 kA), 4 central solenoid modules (20 kA) and 7 poloidal field coils (20 kA). Following the commitment of the German Government to the EU, KIT shall design, construct and test the current leads. In total 6 leads for a maximum current of 26 kA and 20 leads with a maximum current of 20 kA, mounted in vertical, upright position are required.

In 2013 the project funding by the German Government was approved. The work for manufacturing and testing of the current leads started and it is expected to complete in 2017.

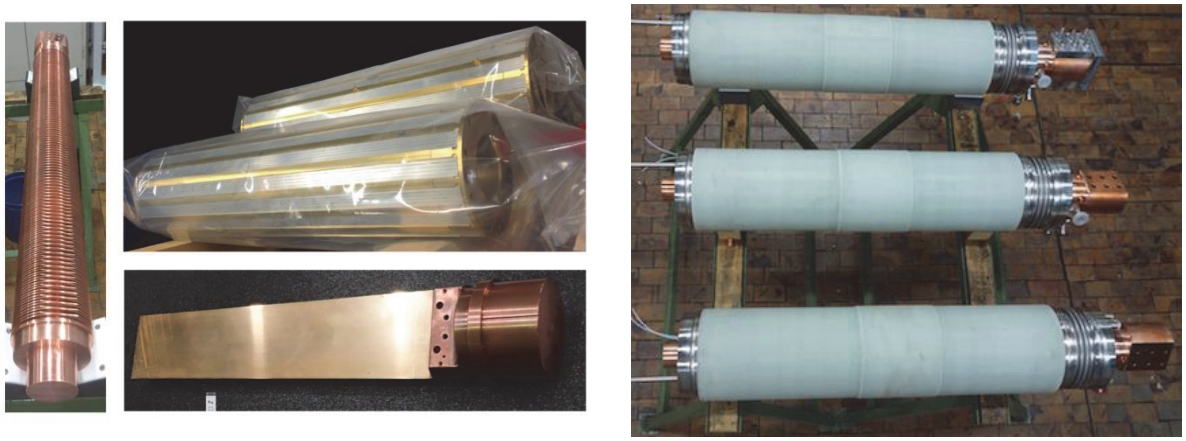

Fig. 3: Half pieces (left) and completed heat exchangers (right) of 26 kA current leads.

Fig. 4: Acceptance test of first heat exchanger for 26 kA current leads at presence of TÜV and witnessed by a JAEA representative.

Status

The status is as follows:

- A new configuration model was prepared, uploaded in IDM, and approved by the project management.
- The test programme was prepared, uploaded in IDM, and approved by the project management.

- The quality plan was prepared, uploaded in IDM, and approved by the project management.
- All half pieces for the 6 current leads for 26 kA have been manufactured in the central workshop at KIT. 6 heat exchangers have been assembled and tested with presence of TÜV. All copper cold end bars and 4 of 6 HTS modules have been fabricated. The final assembly of the first current lead pair has started.
- The fabrication of half pieces for the 20 current leads for 20 kA is underway.

Staff.

W7-X CL:

M.S. Darweschsad
G. Dittrich
S. Drotziger
S. Eckerle
W.H. Fietz
U. Fuhrmann
M. Gehrlein
F. Gröner
R. Heger
M. Heiduk
R. Heller
M. Hollik
A. Kienzler
C. Lange
R. Lietzow
I. Meyer
C. Molnar
T. Richter
R. Rotondo
U. Saller
E. Specht
E. Urbach
T. Vogel
P. Wagner-Nagy

JT-60SA:

M.S. Darweschsad
S. Drotziger
S. Eckerle
W.H. Fietz
U. Fuhrmann
M. Gehrlein
F. Gröner
R. Heger
M. Heiduk
R. Heller
M. Hollik
A. Kienzler
C. Lange
R. Lietzow
I. Meyer
C. Molnar
R. Müller
T. Richter
R. Rotondo
U. Saller
E. Specht
E. Urbach
T. Vogel
P. Wagner-Nagy
T. Wahl (since 11/2013)

Literature:

[1] E. RIZZO, R. HELLER, L. SAVOLDI RICHARD, R. ZANINO, CtFD-based correlations for the thermal-hydraulics of an HTS current lead meander-flow heat exchanger in turbulent flow. Cryogenics 53, (2013) 51-60

[2] S. DROTZIGER, W. H. FIETZ, M. HEIDUK, R. HELLER, M. HOLLIK, C. LANGE, R. LIETZOW, T. RICHTER, K.-P. BUSCHER, T. MOENNICH, T. RUMMEL, Overview of results from Wendelstein 7-X HTS current lead testing. Fusion Engineering and Design 88, (2013) 1585– 1588

[3] Y. KAMADA, P. BARABASCHI, S. ISHIDA, The JT-60SA Team and JTt-60SA Research Plan Contributors, Progress of the JT-60SA project. Nucl. Fusion 53, (2013) 104010

[4] R. HELLER, S. DROTZIGER, W. H. FIETZ, A. KIENZLER, R. LIETZOW, T. RICHTER, E. WEISS, K.-P. BUSCHER, T. MOENNICH, T. RUMMEL, Status of series production and test of the HTS current leads for Wendelstein 7-X. Fusion Engineering and Design 88, (2013) 1482– 1485

[5] M. HOLLIK, W. H. FIETZ, S. FINK, M. GEHRLEIN, R. HELLER, C. LANGE, T. MÖHRING, Design of electronic measurement and quench detection equipment for the Current Lead Test facility Karlsruhe (CuLTKa). Fusion Engineering and Design 88, (2013) 1445– 1448

[6] E. RIZZO, R. HELLER, L. SAVOLDI-RICHARD, R. ZANINO, Computational thermal-Fluid Dynamics analysis of the laminar regime in the meander flow geometry characterizing the heat exchanger used in the High Temperature Superconducting current leads. Fusion Engineering and Design 88(11), (2013) 2749–2756

[7] K. YOSHIDA, H. MURAKAMI, K. KIZU, K. TSUCHIYA, K. KAMIYA, Y. KOIDE, G. PHILLIPS, L. ZANI, M. WANNER, P. BARABASCHI, P. DECOOL, A. CUCCHIARO, R. HELLER, F. MICHEL, L. GENINI, Mass Production of Superconducting Magnet Components for JT-60SA. IEEE Transactions on Applied Superconductivity 24(3) (2014) 4200806

[8] T. RICHTER and R. LIETZOW, Cryogenic experiences during W7-X HTS-current lead tests. accepted for publication to Advances in Cryogenic Engineering: Transactions of the Cryogenic Engineering Conference – CEC2013

Acknowledgement

This work was financially supported by the Ministry of Research and Education (BMBF) under the grant No. 03FUS0013 and is done in the Project JT-60SA under the Broader Approach Agreement between Europe and Japan. The views and opinions expressed herein do not reflect necessarily those of the BMBF or the European Commission.

Provision of Material Characterization at Cryogenic Temperatures (F4E-OPE-084-01 (ES-MF))

Background and Objectives

Fusion for Energy has launched an open tender for the provision of cryogenic material characterization via a Framework Contract (F4E-OPE-084 (ES-MF)). This framework contract concerns the mechanical characterization of materials at cryogenic temperatures, which are present in the Magnet System and Cryoplant of ITER and JT-60SA. The materials to be characterized will originate from manufacturing processes, qualification and R&D activities.

Scope of Work

Within Task Order 3, tensile tests on jacket material are to be performed:

- mechanical characterization at 4K of the base material of the ITER TF-Conductor's jacket including extended cleaning, SEM inspection and heat treatment processes

and

- mechanical characterization at 4K of the base material of the ITER TF Dummy Conductor's jacket (only compacted empty jacket cold worked as well as heat treated conductor jacket).

Material is provided by F4E and specimens are prepared by KIT.

Influence of Cleaning Procedure

The material of the jacket will be 316LN and will be delivered in form of tubes, which are "as compacted". The "as compacted" tube will have outside diameter 43.7 ± 0.2 mm and wall thickness 2.0± 0.1 mm. The workflow is described in the following list:

1. KIT will receive 2 pieces of 1.5-2 m long tubes from supplier.
2. KIT shall perform stretching of the jackets, so that a 2.5% plastic deformation is induced to the specific length where the test specimens are extracted (specific length 1.2m).
3. KIT shall cut the stretched length into 30cm long sections, clean them and send the "middle 4" pieces to CRPP (Zurich, Switzerland) for cleaning and heat treatment process.

a. CRPP will perform the vacuum heat treatment process according to a specification agreed between IO, CRPP and F4E.

4. KIT will receive the 4 cleaned and heat treated sections back from CRPP. KIT shall order the transport.
5. KIT shall fabricate 3 tensile test specimens per section (12 in total).
6. KIT shall perform tensile tests as indicated in the table 3.1.
7. KIT shall report the results according to the quality requirements of the task order and the framework contract.
8. Additionally a Scanning Electron Microscope (SEM) inspection shall be conducted on the fracture surfaces if the resulting total elongation of the tensile test is between 15% and 20%.

In figure 1 the tubes and machined specimens are shown. The results are summarized in table 1. The results indicate that the extended cleaning procedure has no significant impact on the performance, namely the total elongation of the jacket material.

To investigate the failure surfaces, SEM pictures were taken from 3A1 and 3A2 and given in figure 2, showing a mixture of brittle, inter granular and partly ductile fracture.

Fig. 1: On the left jacket sections after 2.5% stretching at room temperature and sectioned returned from CRPP after heat treatment (in the middle the specimen of 21EP002P002A after cutting, on the right specimen taken from 21EP003P003A).

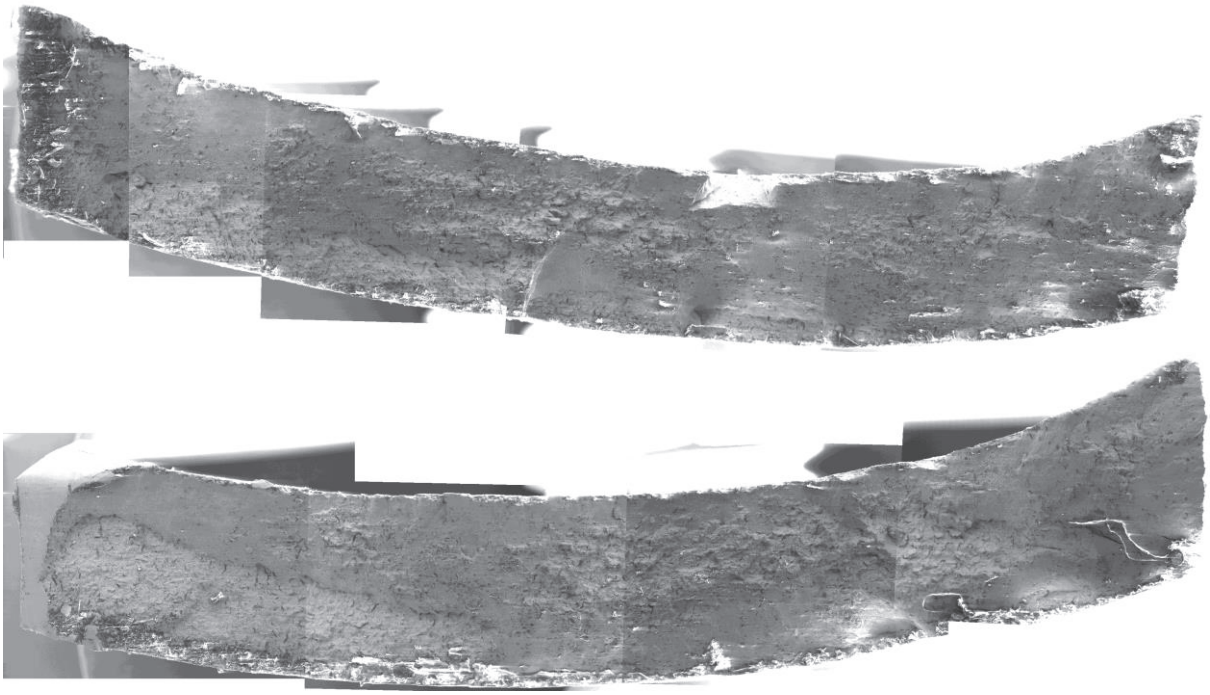

Fig. 2: SEM pictures taken from the failure surface of 3A1(top) and 3A2(bottom).

Characterization of TF Jacket

ITER Dummy TF-Conductor has been heat treated and the mechanical characterization of the jacket base material is measured. The material of the dummy jacket is 316LN and it comes in form of tubes, which are “as compacted” and heat treated. Both have outside diameter 43.7 ± 0.2 mm and wall thickness 2.0± 0.1 mm. KIT performed the machining of the specimens including removal of the conductor inside. In figure 3 the two jackets are shown, here the black appearance of the heat treated section is visible. The test results are shown in table 2 indicating the typical reduction in total elongation of this material after heat treatment. Still the mean value of the total elongation is within the range of 20%.

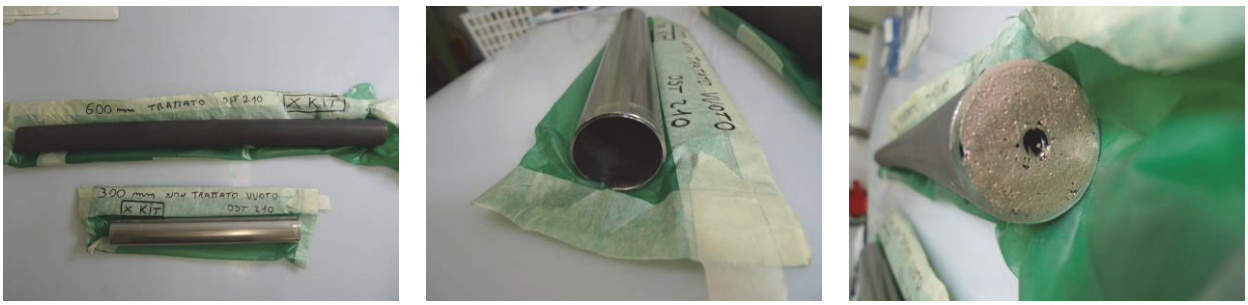

Fig. 3: Jacket material received from ASG (only compacted and heat treated conductor section).

Summary

Several TF jacket sections were investigated. First, a possible impact on mechanical properties of an extended cleaning procedure prior to the heat treatment was examined. Here no significant influence could be seen. SEM pictures also show no difference to material tested without this special cleaning procedure.

Second, jacket sectioned from “not heat treated” and “heat treated” material was characterized. The material was provided by ASG, Italy coming from a first trial heat treatment of the TF winding furnace. The typical reduction of total elongation was seen.

After completion of task order 3 within this framework contract the following task order 4 is now conducted, testing JT60SA casing material. Task order 5 is under preparation and should start until mid 2014.

Table 1

Filename	Temperature	Young's Modulus	Yield Strength	Ultimate Tensile Strength	Uniform Elongation	Total Elongation
-	K	GPa	MPa	MPa	%	%
Jacket from supplier 2A						
2A1	4.2	209,7	1300	1553	16,1	17,7
2A2	4.2	211,3	1285	1570	15,8	22,1
2A3	4.2	218,8	1284	1544	20,7	20,7
2A4	4.2	208,1	1270	1542	17,5	18,7
2A5	4.2	206,4	1250	1583	16,0	20,6
2A6	4.2	206,7	1268	1537	18,5	18,9
Jacket from supplier 3A						
3A1	4.2	203,5	1267	1514	18,4	21,5
3A2	4.2	209,3	1307	1538	14,2	16,7
3A3	4.2	211,6	1307	1538	14,2	16,7
3A4	4.2	217,1	1310	1565	15,9	20,8
3A5	4.2	203,0	1229	1491	13,6	17,9
3A6	4.2	204,2	1260	1533	13,4	15,7

Staff:

N. Bagrets
A. Jung
B. Purr
V. Tschan
E. Urbach
K.-P. Weiss
S. Westenfelder

Table 2

Filename	Temperature	Young's Modulus	Yield Strength	Ultimate Tensile Strength	Uniform Elongation	Total Elongation
-	K	GPa	MPa	MPa	%	%
Only cold worked (OST210)						
NotHT1	4.2	194.6	1328	1595	24.6	31.7
NotHT2	4.2	206.1	1310	1638	27.2	27.4
NotHT3	4.2	201.8	1281	1595	23.5	32.3
NotHT4	4.2	196.9	1297	1634	34.4	34.4
Heat treated (OST210)						
HT1	4.2	206.4	1289	1585	15.2	18.5
HT2	4.2	201.6	1228	1496	11.1	15.0
HT3	4.2	203.1	1201	1519	17.5	22.2
HT4	4.2	202.7	1297	1589	23.0	23.4

Acknowledgement

This work was supported by Fusion for Energy under the service contract No. F4E-OPE-084 (ES-MF) The views and opinions expressed herein reflect only the author’s views. Fusion for Energy is not liable for any use that may be made of the information contained therein.

Conductor Jacket Mechanical Testing Reference Laboratory (ITER/IO/10/4300000292)

Background and Objectives

The helium inlet of the TF coil was tested under fatigue in 2005 following ASME criteria for fatigue qualification which indicates one among two options:

1) service life at x2 calculated strains or
2) calculated strains at x2 service life.

FE analysis performed in CEA resulted in tests conditions of 11 x 10^{-4} static strain +/-3 x 10^{-4} cyclic strains. Though the cyclic loads are transversal to the He inlet axis, the tests were performed axially since the stresses developed are mostly in this direction and the approach was conservative. Tests carried on helium inlets at that time at 4 K failed at 80% of the 20 x 30000 = 600000 cycles. However the breaking region seemed to indicate that an annealing of the HAZ took place during the welding process weakening the metal, possibly due to a poorly controlled weld.

The objective of this work is to qualify the new design that implements different alternatives aiming to extend the fatigue life beyond the qualifying threshold cycles. The tests will be performed until a maximum cycle number of 261.000 or 600.000 (as given below) or rupture at 4 K with a static strain of 10.2 x 10^{-4} +/- 2.3 x 10^{-4} ε The cycles shall present a maximum frequency of 2 Hz.

Scope of Work

Fatigue tests on six TF inlet prototypes provided by ITER taken from the European production need to be performed. Here, dressed Tungsten Inert Gas (TIG) welded using DIN1.4453 filler material and following ITER standard heat-treatment of the cable in conduit conductor is applied. The re-melting of the weld toe by dressed TIG helps to reduce the size of or even remove flaws, therefore, improving the fatigue life behavior, as observed as possible weak part in the former inlet design.

Fig. 1: Helium inlets as received in KIT.

Further two helium inlets provided by JAEA using different filler JK2LB material were tested. With these tests a complete validation of the design should be accomplished.

Four of these TF helium inlets are shown in figure 1 after delivery. The overall length is about 1.5 m.

Fatigue Tests

According to statistical methods proposed by the fatigue experts of The Welding Institute (TWI) and FEM analysis a cycle number of 261,000 is a sufficient acceptance criterion. For the test following conditions apply (see also table 1):

Table 1

sample	strain level	envisaged cycle number	achieved cycle number	comments
S01	(10.2 +/- 2.3) x 10^{-4} ε	261,000	261,247	survived
S02	(10.2 +/- 2.3) x 10^{-4} ε	261,000	262,535	survived
S03	(10.2 +/- 2.3) x 10^{-4} ε	600,000	601,877	survived
S04	(10.2 +/- 2.3) x 10^{-4} ε	261,000	261,589	survived
S05	(10.2 +/- 2.3) x 10^{-4} ε	261,000	267,674	survived
S06	(11.7 +/- 2.3) x 10^{-4} ε	600,000	602,241	survived
S07 (JAEA3)	(10.2 +/- 2.3) x 10^{-4} ε	261,000	261,072	survived
S08 (JAEA2)	(10.2 +/- 2.3) x 10^{-4} ε	261,000	261,203	survived

- Fatigue cycle cut off condition
- four EU and two JA samples up to 261,000 cycles (8.7x service life) and
- two up to 600,000 cycles (20x service life) as additional test information
- boundary conditions as per TF operation mean strain and range (10.2 +/- 2.3) x 10^{-4} ε
- one 600.000 cycle sample with increased mean strain level (11.7 +/- 2.3) x 10^{-4} ε

Starting with installation and instrumentation at KIT customizing 3 extensometer systems (see figure 2):

- over the complete inlet (gage length can be adjusted from 60 to 270 mm),
- on lower weld (gage length approx. 20 mm),
- on base material (gage length approx. 20 mm),
- 3 temperature sensors are placed on the jacket on top, middle and bottom of helium inlet, and
- liquid helium level meter is adjusted to verify that the welded part is immersed in liquid helium during test.

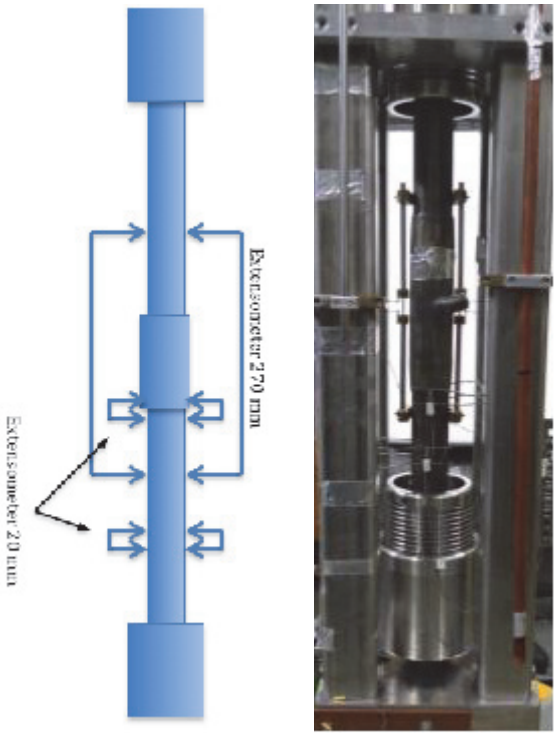

Fig. 2: Left: helium inlet structure schematically showing the used extensometer systems. Right: mounted in ATLAS facility for fatigue test.

The specified elongation is controlled by the 270 mm extensometer system monitoring both welds of the helium inlet. The fatigue test is done symmetrical to the previous test of the clamping system sample:

- first loading to strain level below maximum strain level for cycling to verify functionality of sensors after cool down,
- 3 times loading to maximum strain level for cycling,
- fatigue test according to criteria applied strain (10.2 +/- 2.3) x 10^{-4} ε and for sample S06 (11.7 +/- 2.3) x 10^{-4} ε at a frequency of approximately 2 Hz,
- during fatigue test only min/max strain values will be recorded, to observe slipping or failure of system,

- end of the test: according to sample cut off specification (261,000 cycles or 600,000 cycles),
- after reaching specified cycle number or failure warm up of system and opening of cryostat.

All helium inlets are successfully tested. As an example the load versus strain of the sample one (S01) is given in figure 3. The load lines follow the same paths of all 4 loadings and return to the same zero strain value. This behavior was visible for all samples tested.

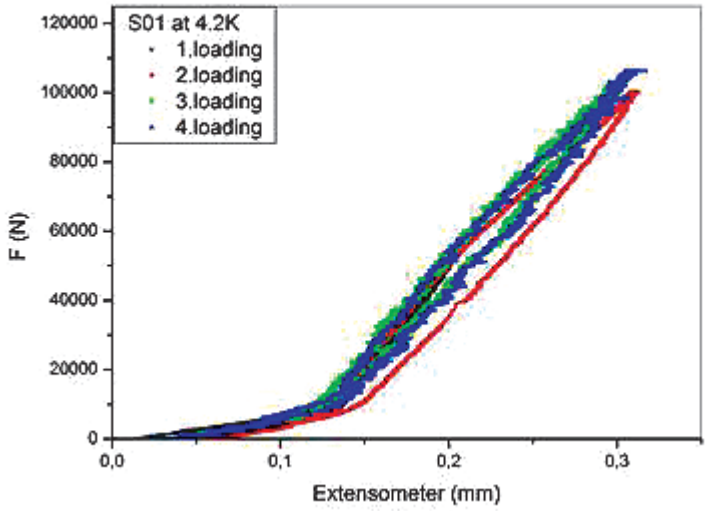

Fig. 3: Load versus strain (270 mm system) at 4.2 K of sample one (S01).

Additionally, only a very small hysteresis is visible, showing a good reproducibility of the performance.

The fatigue test was recorded fully for start, then somewhere in middle of cycle life of each test and end of test. In figure 4 load and displacement is depicted over time. The amplitudes of both are constant verifying the constant strain range and triangular fatigue mode. The given time is only relative time of each test day and not to be seen as continuous axis over the three graphs.

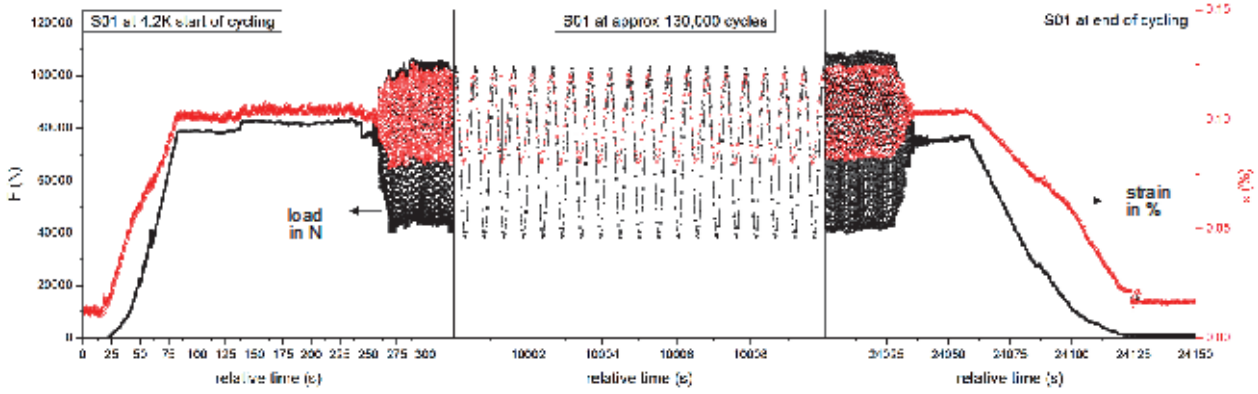

Fig. 4: Helium inlet structure S01 tested under fatigue loading at 4.2 K.

The conditions for the tests as strain amplitude and cycle number is given in the table 1. All of them reached the envisaged cycle number showing no failure, owing to the high structural integrity of the present design.

Summary

For all 8 samples it was verified, that the current helium inlet design is feasible. The clamping system allowed a constant load and strain range applied throughout the fatigue tests. Disassembly of the clamping system after test exhibited no slipping of the jacket or conductor inside. The next steps in winding and heat treatment of the TF coil can be taken.

Within a contract with JAEA it is planned to test further TF helium inlets from Japan in 2014.

Staff:

N. Bagrets
B. Purr
V. Tschan
E. Urbach
K.-P. Weiss
S. Westenfelder

Acknowledgement

This work was supported by ITER Organization under the service contract No. IT-ER/IO/10/4300000292. The views and opinions expressed herein reflect only the author's views. The ITER Organization is not liable for any use that may be made of the information contained therein.

Development of HTS Cables for Magnets (CoA)

The investigations in 2013 on HTS conductor solutions for fusion applications covered following topics:

- Investigation of a 2 m Roebel cable at low temperature
- Investigation of a solenoid winding of Roebel cables and modelling the coil properties
- Preparation of medium lengths of Roebel cables between 2 and 5 m.
- Revision of the Rutherford cabling concept for HTS ROEBEL strands avoiding current degradations and meeting technical features

In the following section these aspects are addressed and discussed in detail.

Low Temperature properties of a Roebel cable

Standard 12 mm wide Roebel cables of 2 m length were prepared for a current test in the FRESCA test facility at CERN. This facility provides at 4.2 K a background field of nearly up to 10 Tesla and a homogeneous field range of slightly above 0.5 m. Lorentz Forces are balanced by means of sophisticated mounting of the sample in the sample holder with controlled transverse precompression loaded by screws. KIT cables as well as samples from General Cable were analysed. The KIT cable was made with the standard design of 10 strands 12 mm wide, SuperPower coated conductor with 20 microns Copper coating and a 77K self-field current capacity of 1.1 kA. At low temperatures a strong enhancement of the currents was measured ending up at 14 kA s.f. at 4.2 K. The anisotropy of the current at 4.2 K is still strong reaching a factor of approximately 4 approaching 10 T.

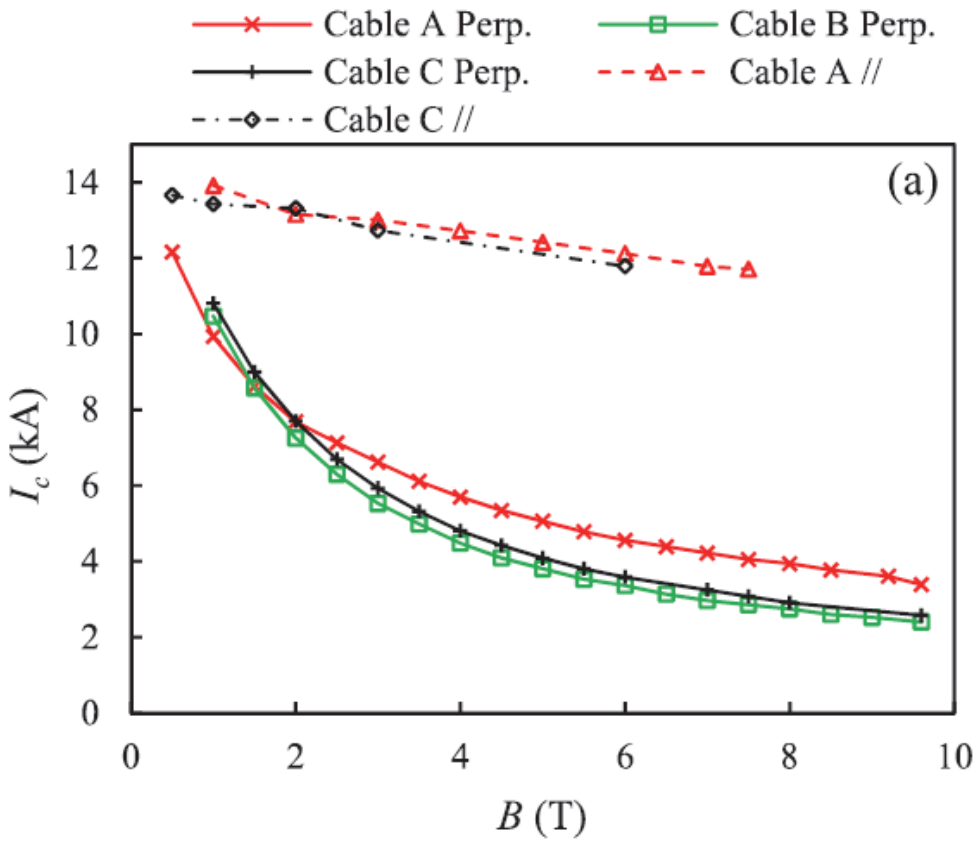

Fig. 1: Transport current measurement of Roebel cables at 4.2 K in the FRESCA Test facility at CERN Ref. [Fleiter 2013].

Investigation of Roebel solenoid by measurements and modelling

A 5 m piece Roebel cable was used for a systematic investigation of a solenoid winding with varied spacings between the turns. In contrast to the pancake coil made from the identical piece of cable, the solenoid winding showed less current degradation from the created field due to a smaller contribution of perpendicular components. The effect of the different spacings is also smaller. The current carrying capacity of the close packed coil was modeled with COMSOL codes including the current anisotropy of the coated conductors. The calculated fields and currents correlate very well with measured data taking into account the influence of conductor inhomogeneities, which cause a slight contribution to the degradation.

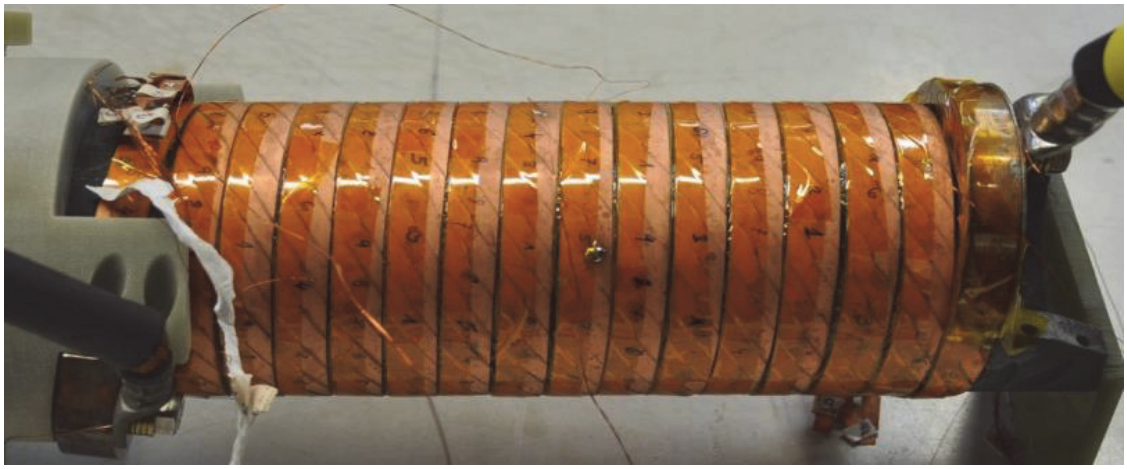

Fig. 2: Picture of the solenoid Roebel winding using 5 m cable length.

Fig. 3: Pancake coil of Roebel cable with spacings between turns.

Coated Conductor Rutherford Cable (CCRC) with HTS Roebel strands

The CCRC was already shown 2010 and the development of a sub-size CCRC demonstrator with Roebel cables as strands was started and was equipped with 3 strands on a stainless steel central former with grooves (Fig. 4). In accordance with bending tests performed on an Edge-bending-strain rig (see report 2012) a degradation of the transport currents of the strands was observed after applying the strands on the structure, showing that the cable design was too progressive leading to irreversible strain effects. The bending of the strands was already in the regime where overbending occurs with around 5% current degradation.

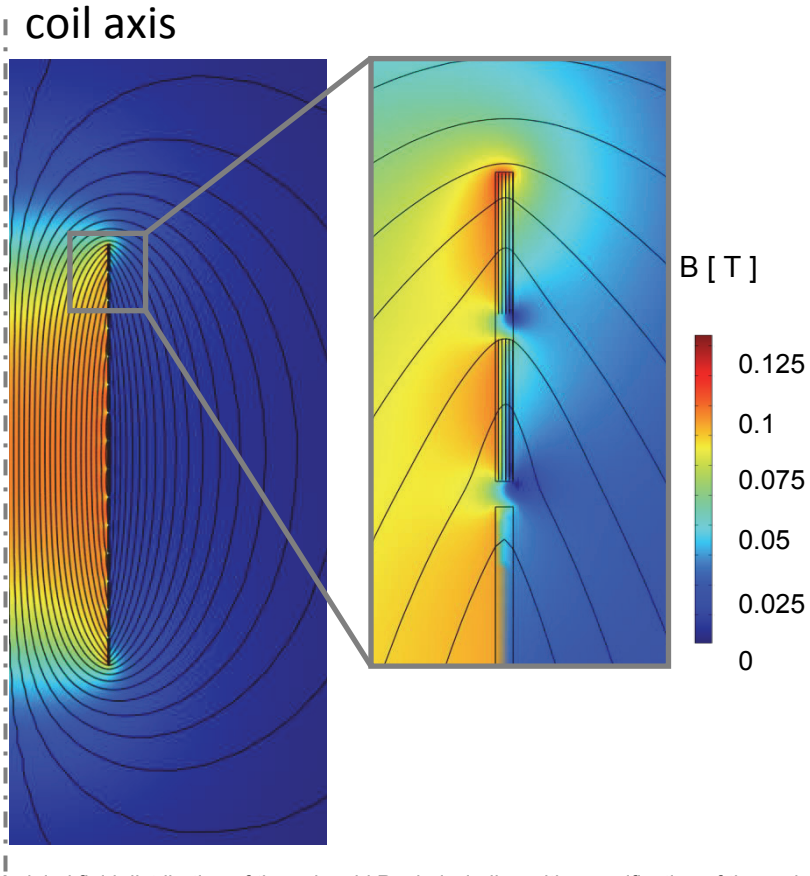

Fig. 4: Modeled field distribution of the solenoid Roebel winding with magnification of the end section.

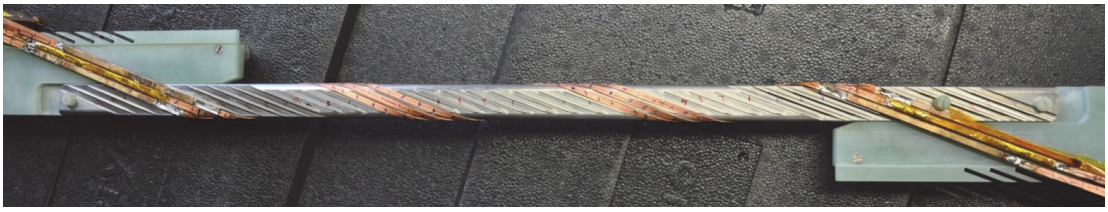

Fig. 5: Flat Rutherford cable (CCRC) with 3 Roebel strands of 4 mm width.

The consequence of the results was a revision of the design using a round former with longer transposition of 0.66 m which is equivalent to a transposition angle of approximately 4 degree for a central core of 15 mm diameter. Related to the former current vs. bending graph no degradation of the current is expected. The new cable with a length of 1.4 m was designed to finally match into the FBI test facility and should demonstrate several features:

- Proposal of an approach addressing all technical cable features, stabilization, mechanical reinforcement, full transposition of strands and cable, cooling channel and thermal match of the material contraction
- Cable processing approach suitable for long lengths
- Use of industrial material, Roebel strands from General Cable
- Replacement by KIT strands (scheduled for 2014)
- Testing joint technique and interaction with conductor stability
- Investigation of current homogeneity and redistribution
- Applying a conduit

Due to a delay of 6 months by General Cable (GC) only an intermediate result was achieved in 2013 testing one strand on the cable structure. The strand carried 425 A at 77 K in s.f., which was the expected value and equivalent to the straight sample. This already indicates the absence of bending effects. The critical current was determined on single coated conductors in the strands. The scattering of the currents expressed the inhomogeneity of the coated conductor material.

Fig. 6: Revised design of CCRC cable with 6 ROEBEL strands of 4 mm width.

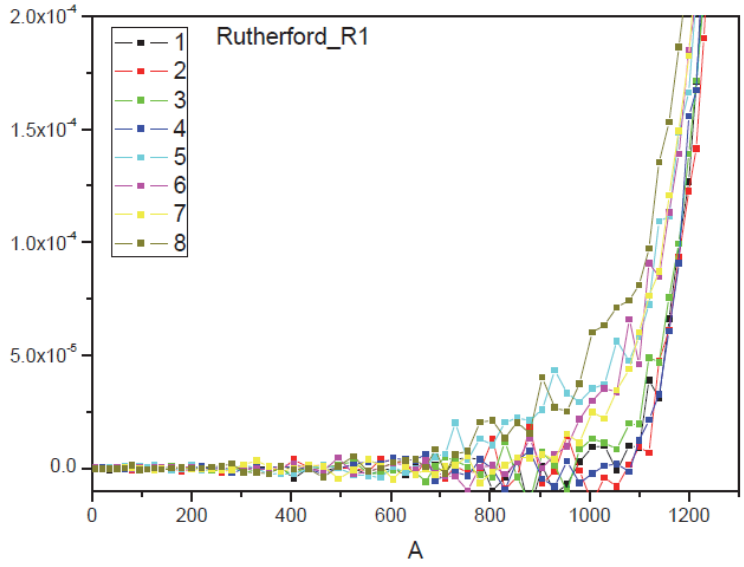

Fig. 7: Current measurements on 8 coated conductors of one Roebel strand on a round core Rutherford cable structure.

Future Work

Roebel cable provide with an elongated transposition length a way to increase the current capacity. A cable with 30 strands and 425 mm transposition should prove the approach and the method of extrapolation of the currents. From these results a reliable extrapolation to low temperature and high field values should be made.

With the achieved knowledge on the Rutherford cable's revised round core design the next steps via a functional sub-size cable will follow. After testing all strands on the cable, the conduit will be applied and the cable tested again. As a next step KIT strands will be applied increasing the current carrying capability. A systematic qualification of the joint technology and the stabilization issues should qualify the design for 3 m samples suitable for EDIPO test facility.

Staff:

A. Kario
H. Fillinger
W. Goldacker
F. Grilli
A. Kling
B. Ringsdorf
B. Runtsch
A. Jung
S. Schlachter

Literature:

[1] Kario A., Vojenciak M., Kling A., Jung A., Brand J., Walschburger U. Goldacker W.: Solenoid and pancake coils assembled from 5 m longroebel coated conductor cable. Cryogenic Engineering Conf.and Internat.Cryogenic Materials Conf. (CEC-ICMC), Anchorage, Alaska, June 17–21, 2013

[2] Kario A., Vojenciak, M., Grilli F., Kling A., Ringsdorf B., Walschburger U., Schlachter S.I., Goldacker W.: Investigation of a Rutherford cable using coated conductor Roebel cables as strands. Superconductor Science and Technology, 26(2013) S. 085019/1–6

[3] Fleiter J., Ballarino A., Bottura L., Tixador P., Supercond. Sci. Technol. 26 (2013) 065014

Studies, Testing and Development of HTS Cable Concepts (WP13-DAS-01-T06-01)

Following the testing of twisted stacked cables, CORC Cable and Roebel cable and the detailed work on bending properties of Roebel Cable and the demonstration of Roebel Strands in a Rutherford Cable concept during WP12, the following work has been performed:

- Investigation of resin or stainless steel reinforced Roebel Cables in FBI to determine limits of degradation
- Measurement of HTS cable produced from Versatile Round Strands in FBI (CRPP sample)
- Preparation of sub-cable tests in FBI with current, perpendicular field and defined strain (also CRPP sample)
- Improvement of existing Rutherford Cable concept with Roebel strands towards a Round Rutherford Cable

Upgrade of FBI facility

In 2013, the FBI facility has been upgraded. The former 12 T split coil magnet had been replaced by a new superconducting 12 T split coil magnet with a significantly enlarged gap. The magnetic field homogeneity is 97 % in a cylindrical volume of 92.2 mm in diameter and an axial length of 20 mm in z-direction.

Subsequent to the upgrading work a variable temperature insert is under construction to standardize measurements in the FBI facility. The goal is that all cable measurements will have the same boundary conditions and are only limited to the maximum output current of the 10 kA power supply.

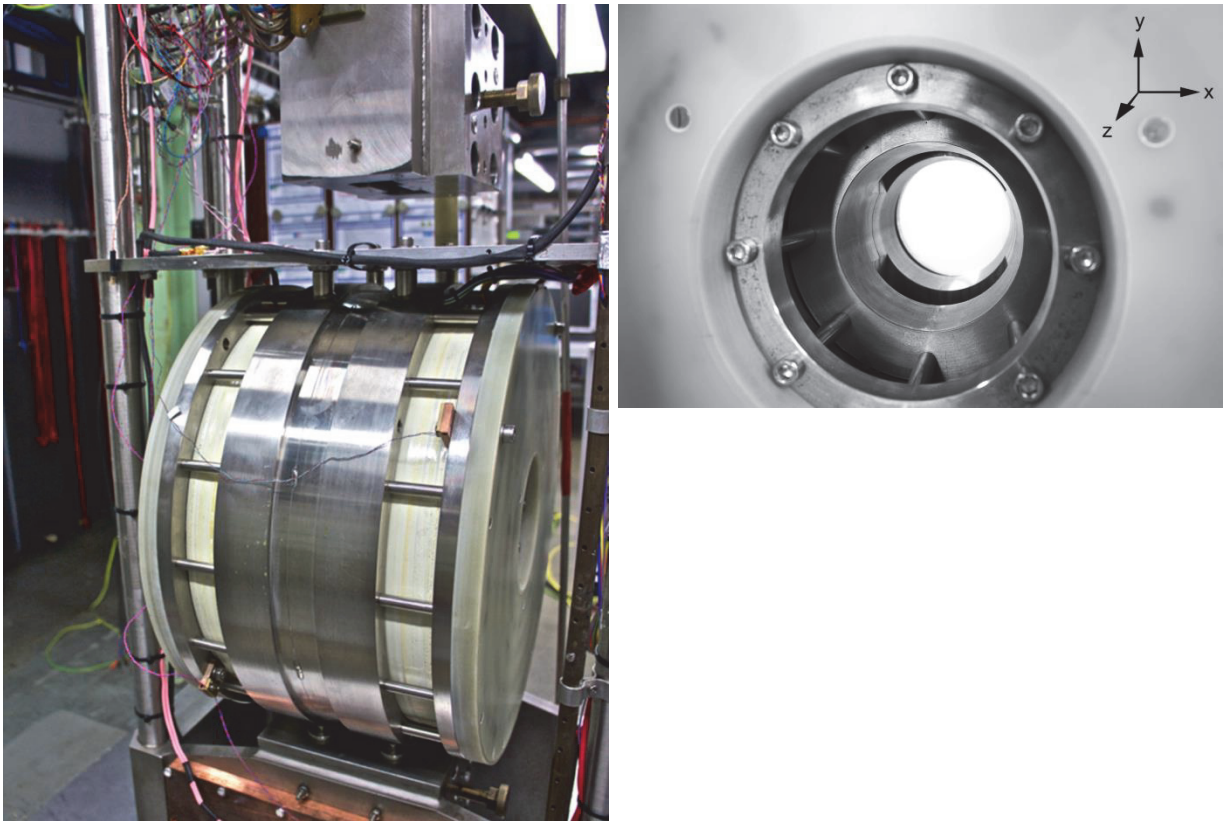

Fig. 1: View to the split coil (left) and close view of the magnet bore (right).

Stabilisation of Roebel Assembled Coated Conductors

The stabilisation of a RACC cable design against mechanical strain has been investigated. Two options have been studied.

Initially the RACC cable was impregnated with a mixture of Araldite epoxy resin and quartz powder. Measurements in liquid nitrogen proved a high mechanical stability and no degradation due to thermal contractions. However, we experienced a set-back during the measurement at 4.2 K. During a quench inside the RACC cable, the superconductor was destroyed before the quench protection system was triggered. The extraordinary low thermal conductivity of Araldite and quartz powder prevented the ohmic heat to flow out of the superconductor.

In the second option the mechanical stabilisation of the cable is provided by clamping the RACC cable inside a stainless-steel frame, preventing the single strands from moving under the influence of Lorentz forces. To investigate the maximum pressure of the stainless steel frame on the HTS strands a 40 cm long RACC sample (4 mm width) has been fabricated and embedded in a stainless steel U-frame. After cooling down in a LN2 bath a 120 mm long stainless steel bar with a central force transmitting section of 40 mm is pressed against the strands and the force is measured by a load cell. Fig. 2 shows the normalized critical current as a function of the average compressive load. At 6000 N the degradation is about 10%. At 6700 N the maximum load of the load cell used in the test was reached.

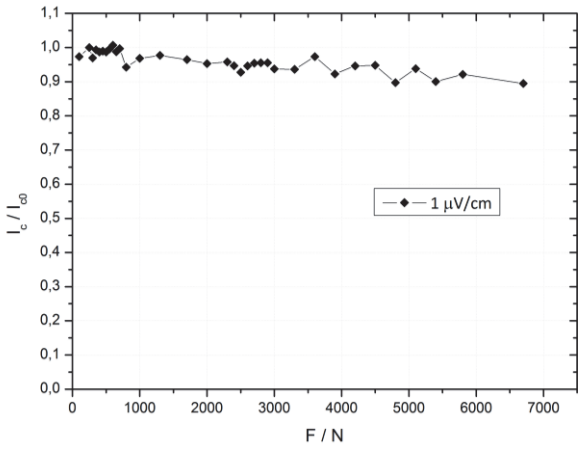

Fig. 2: Normalized critical current as a function of the average compressive load.

The results demonstrate that the applied pressure lowers the performance of the Roebel cable. With the arguments discussed above the real pressurized area is smaller, which gives a higher local load. Assuming an effective pressurized area of 33% the force of 6000 N, where the degradation is about 10%, would correspond to approx. 40 MPa. Similar results were obtained by CERN.

In 2014 this knowledge will be used to fabricate a clamped 4 mm wide and about 1.2 m long Roebel-cable to be measured in the FBI facility. The test will be conducted first at LN2 before and after clamping to verify that no damage occurred during clamping. Afterwards a test in LHe and at magnetic fields up to 12 T will be performed.

Development work on Roebel and Roebel-Rutherford cables

Two concepts are developed in parallel at KIT: the Roebel cable and the Rutherford cable with Roebel strands on basis of second generation HTS. Enhancement of the HTS-tape performance and the successful application of the necessary stabilization in the cable cross section determine the current carrying ability as well as the stability of the cable.

The first design of a CC-Rutherford cable (CCRC) with Roebel strands used a flat central former, which is favourable for windings. As was confirmed by parallel performed systematic investigations, the bending was clearly beyond the reversible bending regime, explaining the observed current degradation. Since a cable experiences further bending in a magnet structure which may cause further degradation, this performance is not acceptable.

To overcome this limitation as well as to increase engineering critical current density, a new cable design with round cross section was chosen. The investigations proved that the round CCRC design works and that strand bending is indeed in the reversible regime.

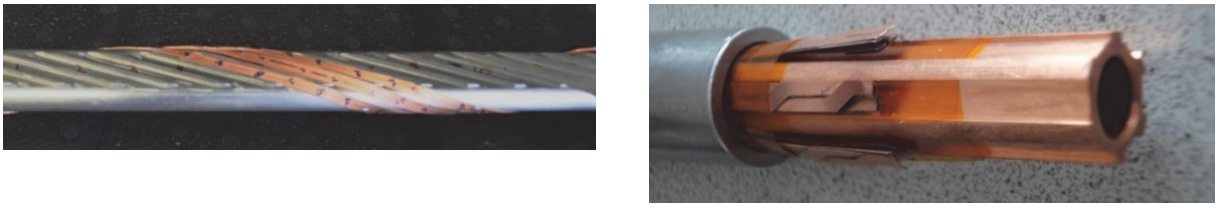

Fig. 3: Flat (left) and round CCRC cable design (right side).

Modelling of a high current HTS conductor for use in a DEMO TF Coil

In a conceptual design analysis, it is shown that HTS conductor is a potential candidate superconductor for pulsed DEMO. A HTS winding pack principally fits in the winding pack area given by the PROCESS code and can produce the required magnetic field at plasma axis. The peak magnetic field at the superconductor is 13.27 T. The use of HTS can increase the temperature margin to more than 11.9 K. Compared to the parameter given in the PROCESS code, an increase of the discharge time constant from 17.78 s to 30 s is possible which helps limiting the discharge voltage.

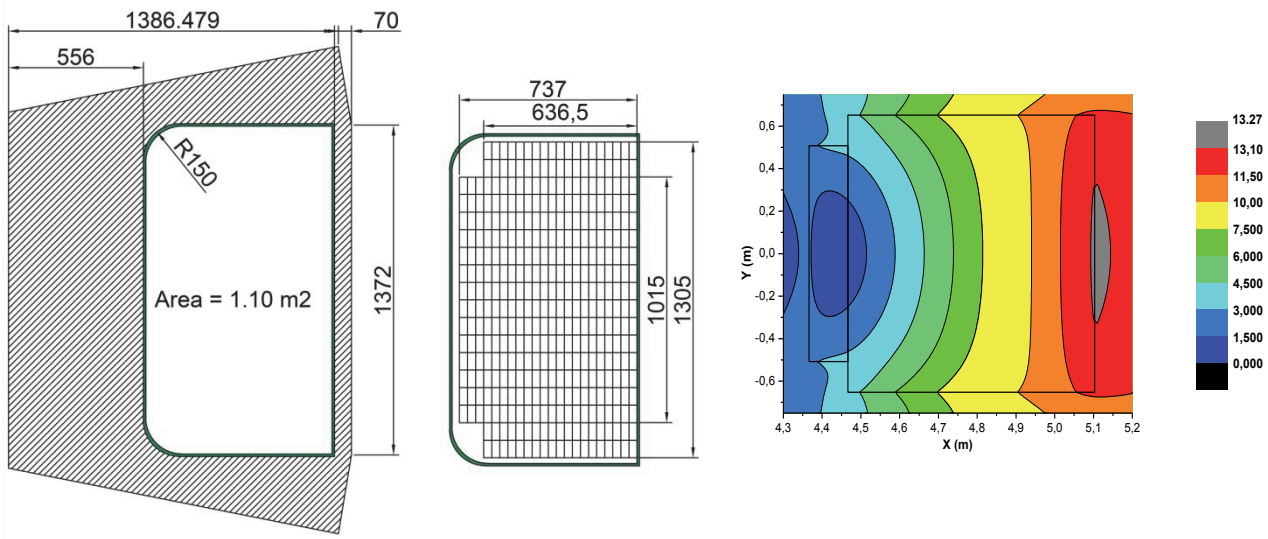

Fig. 4: Proposed winding pack cross section with casing (left and center). Magnetic field plotted at winding pack cross section of the mid plane of the inner leg of TFC (right). X is radial dimension and Y is axial dimension.

Staff:

C. Bayer
W.H. Fietz
V. Gade
W. Goldacker
R. Heller
A. Jung
A. Kario
A. Kling
B. Ringsdorf
B. Runtsch
K.P. Weiss

Literature:

[1] W. H. FIETZ, S. DROTZIGER, W. GOLDACKER, R. HELLER, K.-P. WEISS, C. BARTH, Prospects of High Temperature Superconductors for fusion magnets and power applications, Fusion Engineering and Design 88, (2013) 440– 445

[2] C. BAYER, C. BARTH, P. V. GADE, K.-P. WEISS, AND R. HELLER, FBI Measurement Facility for High Temperature Superconducting Cable Designs, IEEE Transactions on Applied Superconductivity 24(3) (2014) 9500604

[3] P. V. GADE, C. BAYER, F. FRANZA, R. HELLER, K.-P. WEISS, K. HESCH, W.H FIETZ, Conceptual Design of a Toroidal Field Coil for a Fusion Power Plant using High Temperature Superconductors, presented at 23rd Magnet Technology Conference, Boston, MA, USA, July 15-19, 2013, accepted for publication in IEEE Transactions on Applied Superconductivity

[4] C. BARTH, High Temperature Superconductor Cable Concepts for Fusion Magnets, PhD Thesis

Acknowledgement

This work, supported by the European Communities under the contract of Association between EURATOM and Karlsruhe Institute of Technology, was carried out within the framework of the European Fusion Development Agreement. The views and opinions expressed herein do not necessarily reflect those of the European Commission.

Superconducting Magnet (WP13-DAS-01)
HTS Activity Coordination (WP13-DAS-01-T05)

The WP13-DAS-01 Superconducting Magnet task was organized in subtasks with contributions from the associations for each subtask as indicated below in brackets:

T05: Coordination (KIT)

T06: Studies, testing and development of HTS cable concepts (KIT, CRPP, FOM)

T07: Development and testing of HTS jointing techniques (CIEMAT, ENEA)

T08: Determination of HTS properties after fast n-irradiation of HTS samples (ÖAW, IPP.CR)

T09: Preparation of the SULTAN facility (CRPP, IPP-LM)

Coordination Work

3 Meetings have been held in 2013:

Kick off Meeting
The Kick-off Meeting was held on March 26th, 2013 in Garching.

Interim Review Meeting
An Interim Review Meeting was held on October, 1st, 2013 in Garching

Final Review Meeting
Final Review Meeting was held on December, 5th 2013 in Garching. At this meeting the results and draft final reports of the associations were discussed.

In early 2014 the reports of the different subtasks have to be reviewed together with EFDA.

Staff:

W.H. Fietz

Acknowledgement

This work, supported by the European Communities under the contract of Association between EURATOM and Karlsruhe Institute of Technology, was carried out within the framework of the European Fusion Development Agreement. The views and opinions expressed herein do not necessarily reflect those of the European Commission.

Goal Oriented Training Programme “Cryogenic Training Programme for Fusion” (WP10-GOT-GIRO (FU07-CT-2010-00065))

Objectives

In this structured training program early-stage engineers are educated during 3 years in the technical know-how and the skills which are necessary for the engineering of components for ITER or similar programs and for the management of ITER relevant projects. It is intended to deepen the know-how of the trainees by involving the trainees in an engineering team of experts in various domains.

Status

In 2013 Benedikt Kuffner worked to derive characteristic curves of valves under cryogenic conditions. Several measurements of the characteristics of a test valve with two different valve plugs were performed and the obtained data was analysed. The characteristic curves were acquired and compared to theoretical curve progressions. Furthermore the measured mass flow for given boundary conditions was compared to the one predicted by established design equations. First results of the measurements were presented during the 2013 Cryogenic Engineering Conference and International Cryogenic Materials Conference.

Michael Schrank worked in 2013 mainly on safety equipment for pressure vessels. He investigated burst discs that burst at a specific pressure and release the entire inventory to avoid crossing the maximum design pressure. Some measurements were made with unused burst discs in stock at ITEP. The goal was to determine if the burst discs open at the specified pressure and if pressure and vacuum cycling has an influence on the opening pressure. In addition safety valves and the influence of pressure drops due to long pipes was investigated.

In March 2013 the "course on European directive on pressure vessels" was held at JET (Culham) with all trainees as participants. During this visit an advisory board and an acting board meeting was held and the trainees showed presentations about details of their work.

In June 2013 the “Control and Instrumentation School" was held at CEA (Saclay).

Both trainees visited the schools in March and June and gave a status report of their work.

From March 18th to May 3rd Benedikt Kuffner visited JET and was involved in the J1S Cryo Plant work.

Michael Schrank was at JET from January 28th to March 21st working on PLC programming and pipe tracing. In addition he visited CEA during April 29th to June 14th, working on the calibration of venturi tubes at cold temperatures.

Staff:

W.H. Fietz
B. Kuffner
R. Lietzow
M. Schrank
M. Süßer

Literature:

[1] Schrank M., Reiner A.: Auslegung eines Gasanwärmers für kryogenes Helium, DKV 2013 conference proceedings, Hannover Germany, 2013

Acknowledgement

This work, supported by the European Communities under the contract of Association between EURATOM and Karlsruhe Institute of Technology, was carried out within the framework of the European Fusion Development Agreement. The views and opinions expressed herein do not necessarily reflect those of the European Commission.

Cryogenic infrastructure (CoA)

Introduction

The cryogenic infrastructure of the ITEP supplies different experiments within the ITEP and other institutes of the Karlsruhe Institute of Technology (KIT), which are working for the Fusion Programme with refrigeration power or liquid helium. Such experiments in the ITEP are tests of superconductive components in the TOSKA facility, experiments for the ITER-cryopump in TIMO, and mechanical material tests in different cryostats equipped with traction engines.

Fig. 1: He-purifier with a continuous purification rate of 14 g/s at 200 bar.

Fig. 2: Cold box and valve box of the 2 kW-He-refrigerator.

For these experiments the cryogenic infrastructure comprises among other things:

- A 2 kW-refrigerator at 4.4 K with a liquefaction rate of 21 g/s (equivalent to 600 litres/h).
- A 300 W-refrigerator at 1.8 K with a liquefaction rate of 5 g/s (equivalent to 145 litres/h).
- A high pressure helium purifier working at 200 bar with a continuous purification mass flow of 14 g/s and a discontinuous purification mass flow of 28 g/s. The residual impurity content is lower than 1 ppm.
- Three recovery compressors with a pressure increase from one to 200 bar and a maximum mass flow of 26 g/s or 527 standard cubic meter respectively.
- A Helium storage system consisting of:
  - stationary liquid helium vessels with a capacity of 15,000 litres or 1,875 kg respectively
  - storage tanks for impure helium with a capacity of 1,075 kg
  - storage tanks for pure helium with a capacity of 1,275 kg

  The whole storage system has consequently a capacity of 4,225 kg or 23,985 standard cubic meter respectively, see Fig. 3.
- A liquid nitrogen storage vessel with a capacity of 32,650 litres for the supply of all experiments and a filling station to distribute liquid nitrogen in transport vessels.

Fig. 3: Remedial maintenance work at components of the 300 W He-refrigerator.

The cryogenic infrastructure is controlled by a state-of-the-art control system based on PCS7 and WinCC. The operation of the components can be done in two control rooms or via clients installed directly at the experiments.

A team of five operators, three engineers and one academic staff member is responsible for maintenance, repair, upgrading and extension of the cryogenic infrastructure for new or changed experiments.

Additional tasks are the supervision of peripheral installations such as

- energy distribution system
- re-cooling water unit
- compressed-air distribution system.

Also, maintenance, repair, upgrading and extension of the

- vacuum systems
- different safety devices like oxygen monitors

are tasks of this group.

Beyond these regularly routine works this report is focused on selected extension projects, as well as giving an overview of the cryogenic supply activities for fusion projects.

Selected maintenance and extension works

The following selected maintenance and extension works were done in 2013:

- repair of oil-pumps of compressors and turbine units
- revision of power switches
- change of measuring converter cabinets and analytical measuring techniques
- disassembly and revision of cryogenic valves
- structural alteration works at the He-purifier
- replacement of different He-lines
- 20,000 h service at He-recovery compressor V40
- replacement of high pressure pipes of recovery compressors

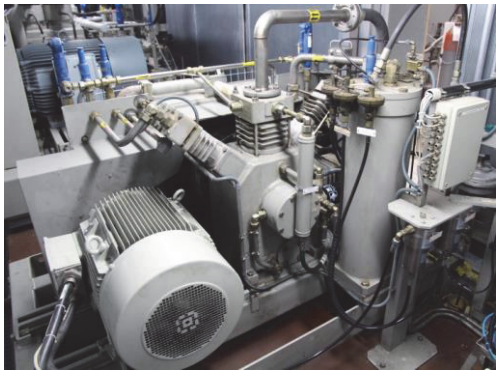

Fig. 4: Revision of the He-recovery compressor V40.

Miscellaneous

- work for the implementation of the CuLTKa control system in the cryogenic infrastructure

Cryogenic supply for the Fusion Programme

The different experiments for the Fusion programme in ITEP are supplied with circa 45,608 litres liquid helium. In addition the refrigerators ran nearly 301 hours in 2013 for the supply of refrigeration power.

For comparison, the average consumption for such experiments in the period between 2003 and 2012 is about 27,968 litres liquid Helium and 1,288 hours of refrigeration power. So in 2013 we had a higher liquefaction rate and a lower refrigeration power than the mean values of the years before.

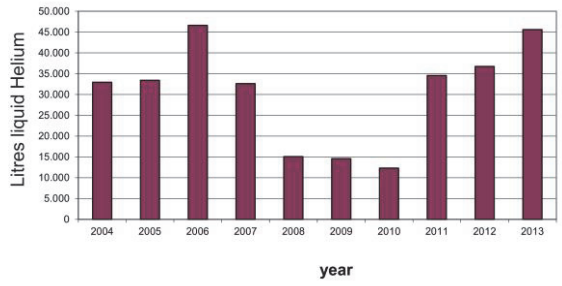

Fig. 5: Liquid Helium supply between 2004 and 2013.

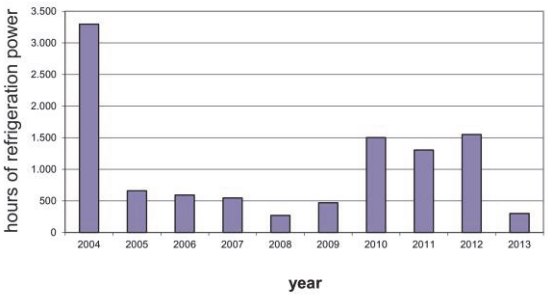

Fig. 6: Hours of refrigeration power between 2004 und 2013.

Staff:

A. Baumgärtner
S. Bobien
M. Duelli
U. Fuhrmann
H. Neumann
S. Holzmann
B. König
K. Metzger
D. Wetzel
H. Zimmermann

Breeding Blanket

Sensitivity Studies of DEMO Design to Key Assumptions (WP13-SYS-01-A-T02-01)

Objectives

As part of the PPPT 2013 programme, an activity on systems codes work for DEMO has been carried out. This has focused on two activities; the majority of the work concerns sensitivity studies looking at the impact on DEMO design of varying the main parameters around the starting reference cases, the second activity relates to a similar but smaller task to look at the way that the cost of electricity in a future power plant is expected to vary with key assumptions.

Results and discussions

In the 2013, KIT carried out a sensivity study with the PROCESS systems code concerning the key parameters included in a new blanket model proposed in the 2012 PPPT programme. The model was developed by KIT and it is based on HCPB blanket concept. It attempts to provide the overall blanket radial build consistently with breeding and shielding requirements, i.e. guaranteeing a minimum TBR (tritium breeding ratio) and a maximum fast neutron fluence and nuclear heating on the inner leg of the toroidal field coil. The model computes these parameters (including the energy multiplication factor) extrapolating from detailed 3D neutronics analysis.

During the 2013, the model has been implemented in PROCESS and, after some preliminary tests, it showed some imperfections which have been immediately corrected. Consequently, the sensivity study concerning the blanket-related parameters has been carried out and the main results are reported hereafter.

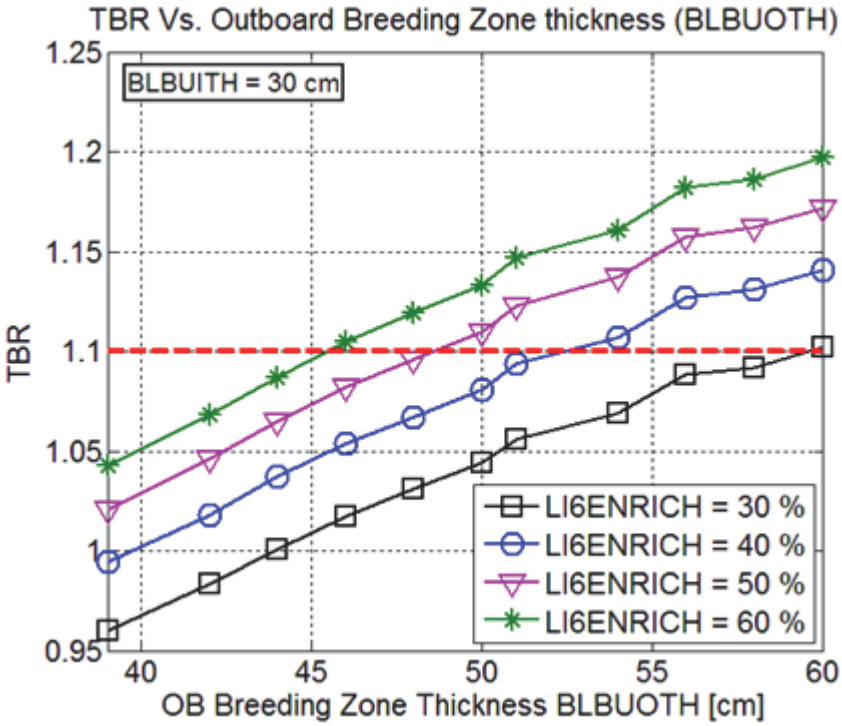

Fig. 1: Results from the blanket model, showing how increase in the outboard breeding zone.

Figures 1 and 2 show results from the model for TBR, and how it depends on breeding zone thickness and Li6 enrichment, Figure 3 shows the effect of shield thickness on reducing the fast neutron exposure of the TF coils.

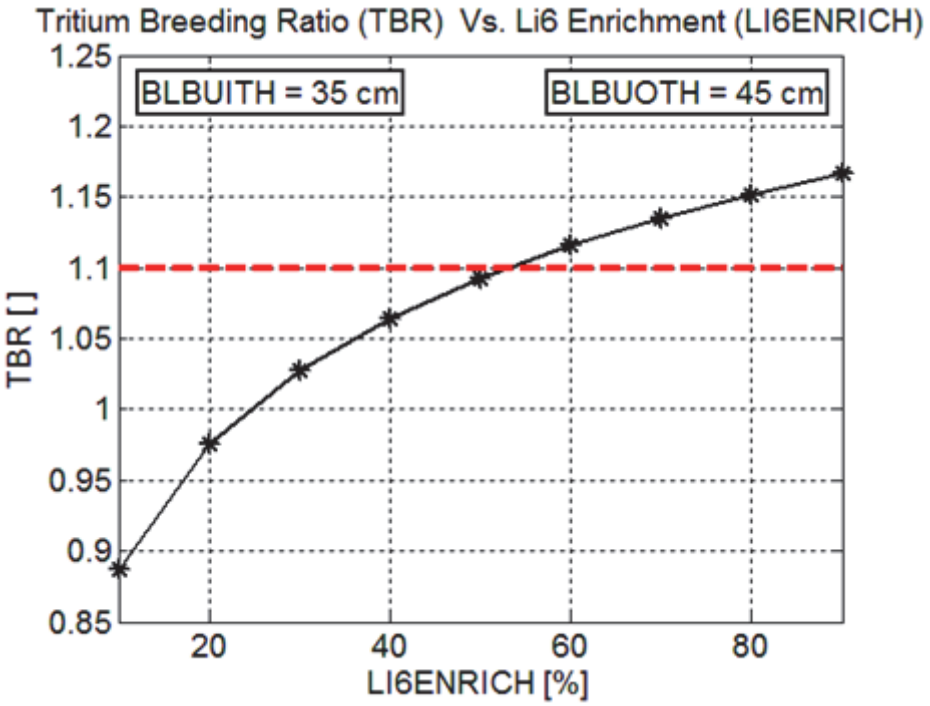

Fig. 2: Results from the blanket model showing how the tritium breeding ratio varies with the Li6 enrichment.

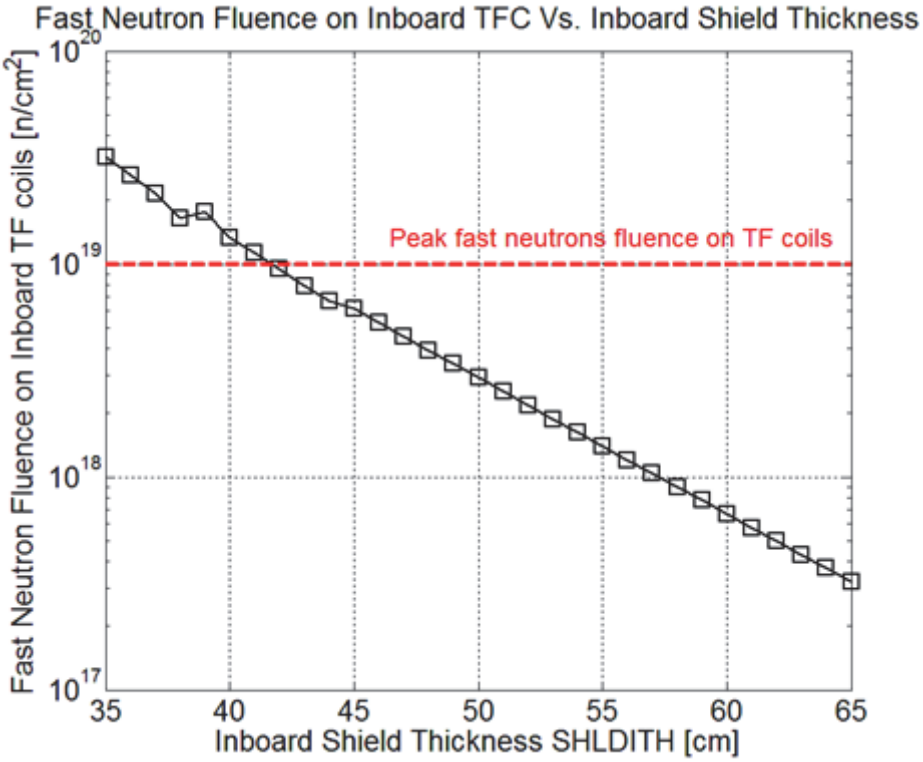

Fig. 3: Results from the blanket model illustrating the effect of increased shielding thickness, on the inboard of the device, in protecting the TF coils from fast neutrons.

Conclusions

A wide range of sensitivity studies have been carried out to look at how varying key parameters around reference DEMO designs leads to changes in design.

Concerning the blanket parameters, the requirements on tritium breeding do not have a deep impact on the radial build since the optimization can be performed by varying the outboard breeding zone thickness and the lithium 6 enrichment. On the contrary, the shielding requirements on the inboard TFC might have a significant impact on the radial build of the reactor, because of the space to be allocated to the inboard shield and thus, of the potential increase of the major radius.

Staff:

F. Franza
L.V. Boccaccini

Acknowledgement

This work, supported by the European Communities under the contract of Association between EURATOM and Karlsruhe Institute of Technology, was carried out within the framework of the European Fusion Development Agreement. The views and opinions expressed herein do not necessarily reflect those of the European Commission.

Electromagnetic Analysis of DEMO Blanket Loads (WP13-SYS-02-T03-01)

Plasma disruptions and vertical displacement events (VDEs) in tokamak reactors are design drivers for the in-vessel components' attachments as the induced loads constitute a severe issue for the mechanical structure. These off-normal operations result in the induction of eddy currents in the electrically conductive components that, coupled with the large magnetic field, impose strong electromagnetic forces (Lorentz's forces) to fusion reactor components. In addition the presence of ferromagnetic material in the blanket structures induces Maxwell's forces as interaction between the magnetized material and the external magnetic field. The related electromagnetic (EM) loads can have a significant impact on the design of the reactor's components, thus having an impact on the parameters related to the structural integrity of the reactor itself. In particular, in a DEMO reactor configuration based on Multi Module Segment (MMS) design, the magnitude of the EM loads both on the single module as well as on the complete blanket segment are expected to be a design driver in the definition of the number of modules per each blanket vertical segment. This definition is the basis of the blanket conceptual design development.

A DEMO reactor configuration (Fig. 1) based on a model elaborated by EFDA in 2013 on the basis of PROCESS system code optimization is here considered. The reactor has been designed to consolidate the present knowledge and technology into a reference design. The 3D model of the reactor is based on the assumption of a Multi Module Segment (MMS) structure with vertical ports for inserting and removing of the MMSs. The complete Blanket System is divided in 16 toroidal 22.5-degree sectors. Each sector is then divided into 5 segments: 2 inboard (IB) segments (11.25-degree) and 3 outboard (OB) segments (7.5-degree). Each segment consists of a number of modules that are connected to a strong manifold structure.

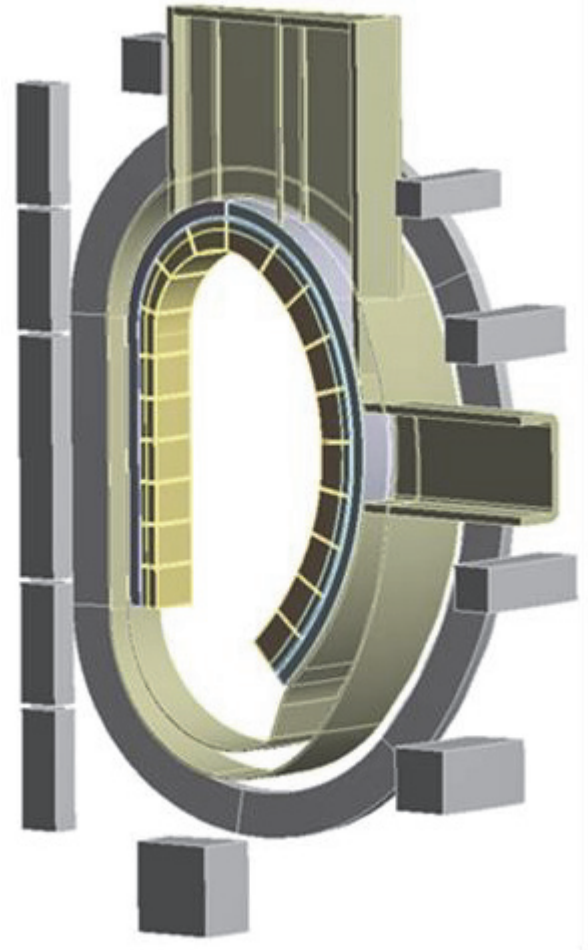

Fig. 1: Schematic of half DEMO sector.

The modules structure is based on the CAD model provided by the Test Blanket Module (TBM) group at INR-KIT. It has been developed on the basis of the EU-TBM to be tested in ITER and it features a common architecture in both the two European concepts: Helium Cooled Pebble Bed (HCPB) and Helium Cooled Lithium Lead (HCLL).

The blanket module is mainly divided into: 1) a U-shaped first wall (FW); 2) two side walls; 3) a Breeding zone (BZ) with an internal stiffening grid for the cooling of the breeding units (BU) and 4) a box manifold whose back plate (BP) is attached to the segment's manifold. Each sub-component presents a complex internal structure (pipes, holes and cooling channels) that would result in a too high level of detail for the model here considered. For this reason each module has been simplified and modelled as represented in Fig. 2.

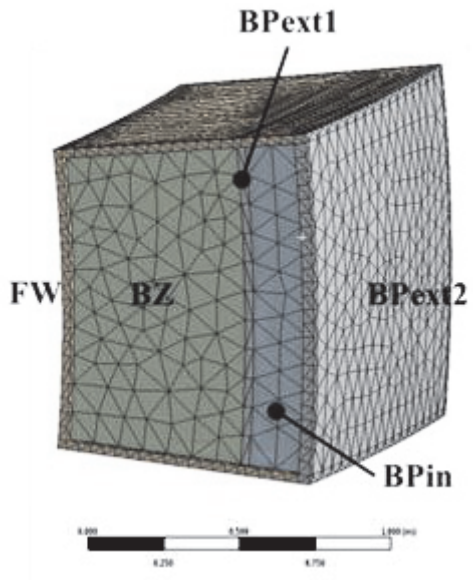

Fig. 2: Schematic of a module.

The structural materials used for blankets and VV are the Reduced Activation Ferritic Martensitic (RAFM) steel EUROFER97 and the Stainless Steel 316 (SS316) respectively. The complete static magnetic field is modelled (complete set of TF, PF and CS coils). Therefore saturation effects of the ferromagnetic materials are correctly taken into account in the analysis.

Three different models have been implemented to study the EM response of the system with different electrical contacts. All the models have the electrical contact between manifold and VV at the top, while differ as follow:

1. **Model S:** single electrical attachment between modules and manifold;
2. **Model C:** continuous electrical attachment between modules and manifold;
3. **Model CB:** continuous electrical attachment between modules and manifold **and** bottom electrical contact between manifold and VV.

The Eddy currents, electromagnetic forces and moments were computed using the commercial ANSYS© code. The study performed in this work is aimed to assess the EM loads acting on the single HCPB and HCLL module as well as on the complete blanket segment during a major central disruption scenario with a linear quench of 42 ms and a total plasma current of 16 MA.

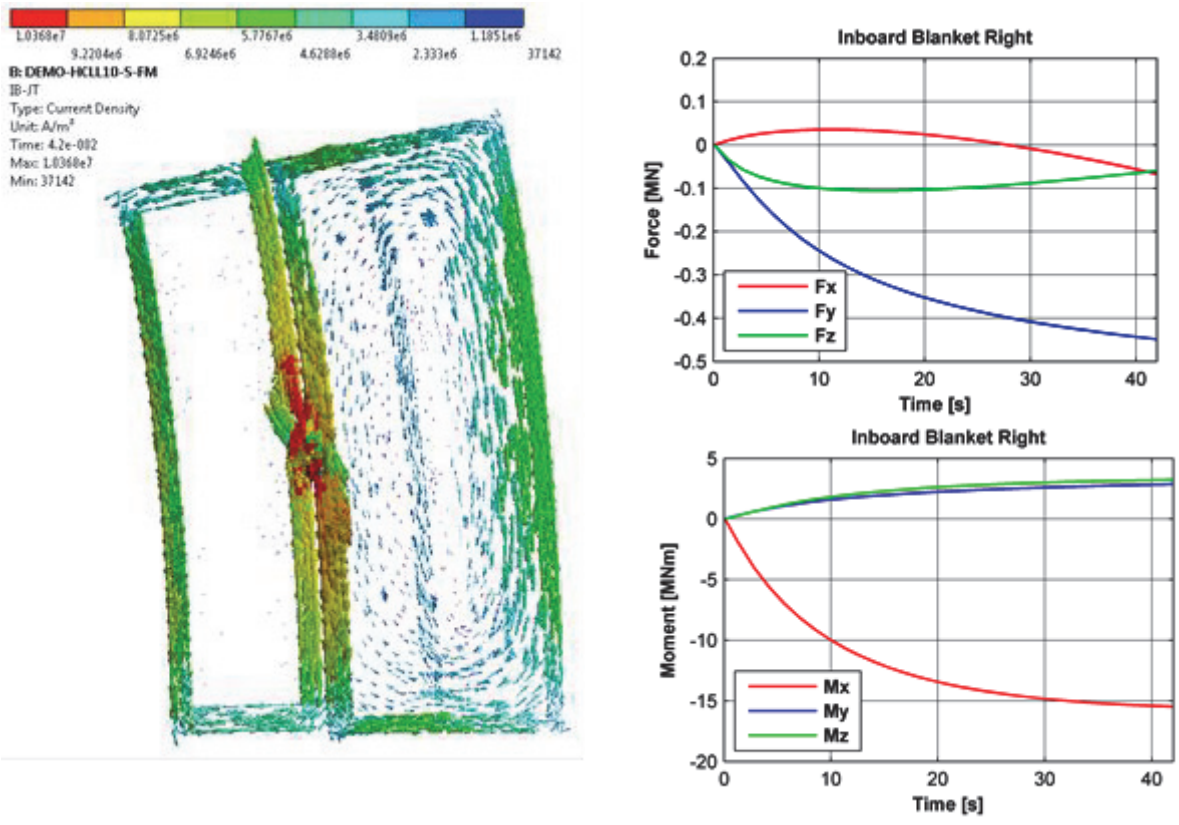

Fig. 3: Example of eddy currents (left) and forces and moments on the IB blanket.

The results show that the evolution of forces and moments on the whole blanket is not trivial and underlines the complexity of the system. In general, the forces do not reach significant magnitudes, due to cancellations that can even result in nonmonotonic curves. The radial moment (M_x) is predominant with respect to the other components because the magnetic field is predominant in toroidal direction (smaller M_y), while the current loops (Fig. 3) mainly turn around the poloidal direction (smaller M_z).

In general, higher loads are found for the HCLL configurations (Fig. 4), which is the obvious consequence of having more conductive material in the BZ. It is also very clear that the configurations with a continuous module−manifold attachment deliver higher loads: a continuous attachment, in fact, allows a single loop to go through the module and the blanket manifold, while a single−point attachment, instead, breaks such current loops in two smaller ones, thus resulting in lower loads.

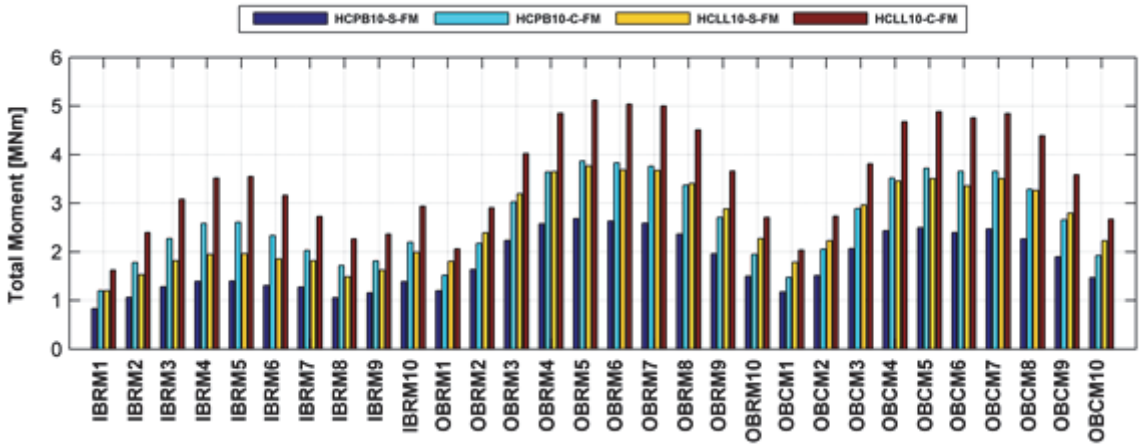

Fig. 4: IB and OB modules´ total moment.

Finally, since the eddy currents are mainly oriented in toroidal direction, the introduction of a bottom connection between the blankets and the vacuum vessel has shown no significant change in the total loads acting on the segments. This result is expected to change whenever moving plasma will be considered in the analysis, as it will enable the circulation of eddy currents in poloidal direction.

The implemented model is intended to be used as reference for future analysis in which EM loads are investigated under different plasma displacement events, modules segmentation and electrical connections between modules, manifold and VV.

Staff:

I.A. Maione
A. Vaccaro

Acknowledgement

This work, supported by the European Communities under the contract of Association between EURATOM and Karlsruhe Institute of Technology, was carried out within the framework of the European Fusion Development Agreement. The views and opinions expressed herein do not necessarily reflect those of the European Commission.

NAFEMS and CFD Benchmarks with ANSYS (Benchmarking Tests against Industrial Standard Cases and TBM-like Blanket Case) (WP13-DTM-01-T02)

Objectives

10 linear elastic, 4 thermal, 11 free vibration and 7 CFD test cases have been performed in ANSYS platform to compare ANSYS code with SIMULIA and COMSOL from the aspect of capability, accuracy, speed and usability.

NAFEMS Benchmarks test

The NAFEMS Standard Benchmarks consist of 10 linear elastic, 4 thermal, and 11 free vibration cases. The geometries for the test case are very simple, the boundary conditions are defined, and also the target output has been provided. The Moustron has been used to record the process of the pre-forming test. Figure 1 shows the record results of test LE1. The Moustron measurements include all the pre-processing, solution and post-processing operations to obtain the results in one representative case. The table 1 shows the summary of all NAFEMS Benchmarks case results.

Fig. 1: Moustron record for TEST LE1.

There are three test results significantly outside the 5% limit; these should be investigated (if they have not already been) to ensure that the source of the error is not in the test model setup. Anyway, ANSYS shows a higher reliability score.

CFD Benchmarks test

7 CFD test have been received, both quad and tetra mesh types have been applied on each case during the calculation. The Test No 1 is to test the mesh deformation capability and examine the extent of element deformation due to boundary displacement. The results show that Minimum face angle on quad face: 42.48o; Maximum face angle on quad face: 137.6o. Minimum face angle on tetra face: 16.85o; Maximum face angle on tetra face: 137.0o. No apparent output target provided to compare in No 1.

The results of Test No 2~6 have been put in Table 2.

Table 1: Summary of test results.

Test platform: ANSYS Hybrid								
Test ID	Title	speed	Duration [min]	Mouse [m]	Clicks	Usability	Accuracy	Reliability
LE1	Elliptic membrane	196	6.75	34.05	325	6.790	0.3%	1
LE2	Cylindrical shell bending patch test	196	37.78	157.32	1.388	171.309	1.1%	1
LE3	Hemisphere-point loads	140	18.28	213.50	1.918	113.116	1.3%	1
LE5	Axisymmetric hyperbolic shell under uniform internal pressure	112	10.35	36.62	372	11.430	0.8%	1
LE6	Skew plate normal pressure	112	5.67	28.17	304	4.918	1.7%	1
LE7	Axisymmetric cylinder/sphere - pressure	112	13.27	52.26	1.231	30.205	0.9%	1
LE8	Axisymmetric shell pressure	112	19.12	66.08	729	38.825	1.9%	1
LE9	Axisymmetric branched shell-pressure	112	22.57	107.45	2.916	114.317	7.3%	
LE10	Linear elastic solid	140	23.50	98.53	1.180	74.039	7.9%	
LE11	Linear elastic solid	308	37.45	1.125. 68	1.418	896.238	5.0%	1
T1	Membrane with hot-spot	168	16.83	63.12	591	31.192	0.5%	1

T2	One dimensional heat transfer with radiation	140	5.38	25.70	238	4.045	0.5%	1
T3	One Dimensional Transient Heat Transfer	140	9.30	37.60	359	10.332	0,0%	1
T4	Two Dimensional Heat Transfer With Convection	112	7.15	35.24	235	6.719	2.6%	1
FV2	Pin-ended double cross: In-plane vibration	140	9.35	49.06	498	13.830	0.3%	1
FV4	Cantilever with off-centre point masses	112	7.25	41.14	278	7.980	12.243%	
FV5	Deep simply-supported beam	112	5.33	26.53	181	3.792	3.688%	1
FV12	Free thin square plate	168	3.53	16.64	144	1.683	1.712%	1
FV15	Clamped thin rhombic plate	140	5.67	28.85	273	4.819	0.009%	1
FV16	Cantilevered thin square plate	140	35.85	133.02	1.248	140.116	5.303%	
FV22	Clamped thick rhombic plate	140	5.95	31.24	280	5.383	0.691%	1
FV32	Cantilevered tapered membrane	112	6.18	25.02	208	4.377	0.302%	1
FV41	Free cylinder: Axi-symmetric vibration	112	5.62	21.22	177	3.379	0.554%	1
FV42	Thick hollow sphere	140	14.58	67.74	538	27.597	0.631%	1
FV52	Simply-supported 'solid' square plate	112	4.73	22.03	209	3.072	4.883%	1

Table 2: Summary of CFD results.

Platform: ANSYS-CFX						
TEST-ID	Output Description			Target Value	Test Result	Error
CFD NO2	Oscillatory motion of viscous boundary layer	10S	0.1m	-0.147	-0.147	0.0%
			0.4m	-0.320	-0.319	0.3%
			0.8m	-0.239	-0.237	0.9%
			2.0m	0.011	0.016	40.7%
		100S	0.1m	-0.132	-0.134	1.1%
			0.4m	-0.313	-0.315	0.7%
			0.8m	-0.238	-0.241	0.8%
			2.0m	0.0108	0.0092	15.3%
		200S	0.1m	-0.101	-0.100	0.7%
			0.4m	-0.299	-0.298	0.2%
			0.8m	-0.237	-0.235	0.9%
			2.0m	0.0098	0.0124	27.0%
CFD NO3	Convective heat transfer from a plate	δ_{99}	1.5m	0.06	0.045	25.0%
			2.0m	0.07	0.055	21.4%
			3.0m	0.085	0.07	17.6%
			5.0m	0.11	0.094	14.5%
			10.0m	0.156	0.135	13.5%
		Nu	1.5m	121.35	132.33	9.1%
			2.0m	121.18	132.61	9.4%
			3.0m	133.16	147.31	10.6%
			5.0m	159.63	177.39	11.1%
			10.0m	214.06	242.89	13.5%
CFD NO4	Turbulent momentum and heat transfer	Yplus Pr=5		0.5	0.500002	0.0%
				5	5.00005	0.0%
				50	45.0011	10.0%
		Yplus Pr=0.71		0.5	0.501569	0.3%
				5	4.98608	0.3%
				50	48.2815	3.4%
CFD NO5	Turbulent momentum convection	Reattachment length	0^o case	6.26	5.92	5.4%
			6^o case	8.3	6.63	20.1%
CFD NO6	Transient simulation of multiphase flow	Time of onset		1.88	2.02	7.4%
		Wave number		197	60	69.5%

The predictions of the most flow parameters are quite good, although the values of some parameters are quite devious.

The test No. 7 is about wall boiling multiphase flow. The target output results are the radial distribution of water vapour volume fraction; the value is also not apparently readable. The figure 2 and 3 show respectively the experimental results and the calculation results. And it can be seen that test results of the water vapour volume fraction distribution along radial is coherent with the experiment results.

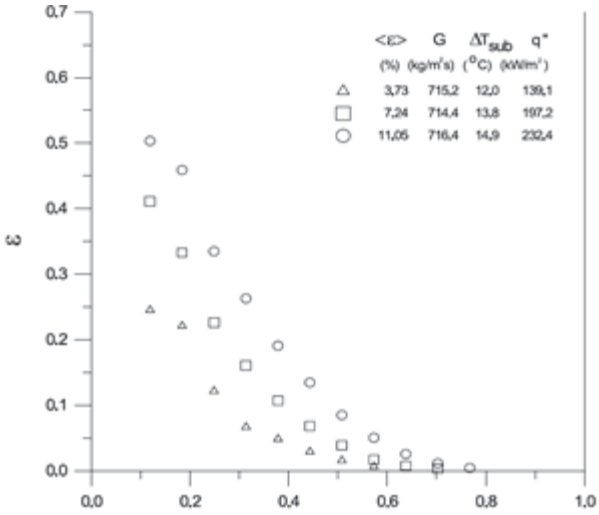

Fig. 2: Water vapour volume fraction distribution (experimental results).

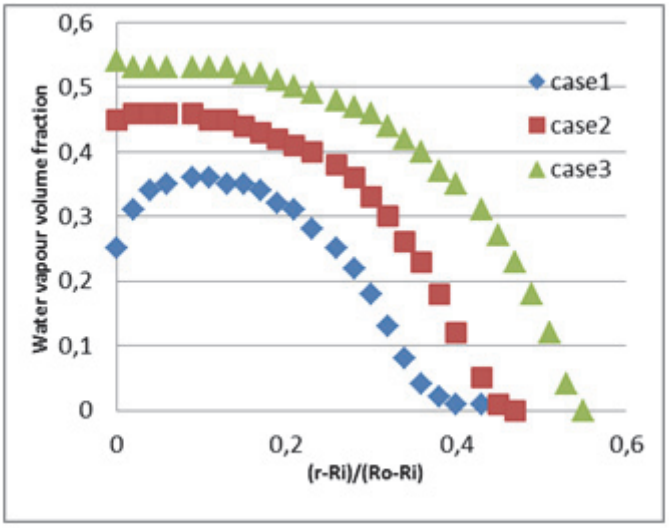

Fig. 3: Water vapour volume fraction distribution (test results).

Note that 2D models are not supported in CFX, thin models used when 2-D geometry found. In some cases, solution times for tetrahedral meshes are more than the hexahedral meshes due to increasing of mesh numbers. CFX supports multiphase flows. The integration of the pre-processing, solving and post-processing is very good, which results in simplicity and speed. Specifically, the change between different models and results files is fast, allowing an efficient comparison between results.

Staff:

Q. Kang
Sz. Kecskes
L.V. Boccaccini

Acknowledgement

This work, supported by the European Communities under the contract of Association between EURATOM and Karlsruhe Institute of Technology, was carried out within the framework of the European Fusion Development Agreement. The views and opinions expressed herein do not necessarily reflect those of the European Commission.

Helium Cooled First Wall Optimization Study (WP13-DAS-02-T11)

The design of the first wall calls for an efficient temperature control, limiting the maximum operation temperature of the structure to about 550°C or less, and reduce stresses induced by the temperature gradients inside the component. At the same time, a reasonable pumping power must be maintained for the helium to maximize the net power output of the plant.

In the frame of this task, several CFD simulations on heat transfer of cooling channels for the DEMO first wall, cooled with high pressure helium at a mass flow rate of 49g/s were performed. The assumed incident heat flux density from the plasma was 750kW/m² for all simulations. Several numerical approaches were used, especially the turbulence modelling was adapted to each geometry case.

The considered geometries were channels featuring different examples of surface structures (i.e., ribs), which were aimed at inducing turbulence and/or large scale mixing of the flow. In comparison, also a smooth walled channel was studied. Each option develops peculiar features, like recirculation vortices or jets, leading to individual wall temperature distributions. Engineering quantities like heat transfer coefficients and pressure drop coefficients were derived from each CFD solution. Representative results for several geometries are shown in-Figure 1.

The CFD studies showed that the heat transfer coefficient could be significantly augmented by using structured surfaces, thus allowing much larger heat loads from the plasma. The largest reduction of the Eurofer temperature on the plasma facing wall was obtained by the geometry termed “G2”, which is a downstream pointing “V” rib. At 49 g/s and 750 kW/m², this geometry would reduce the wall temperature by 150K compared to the smooth walled bass case “G0”.

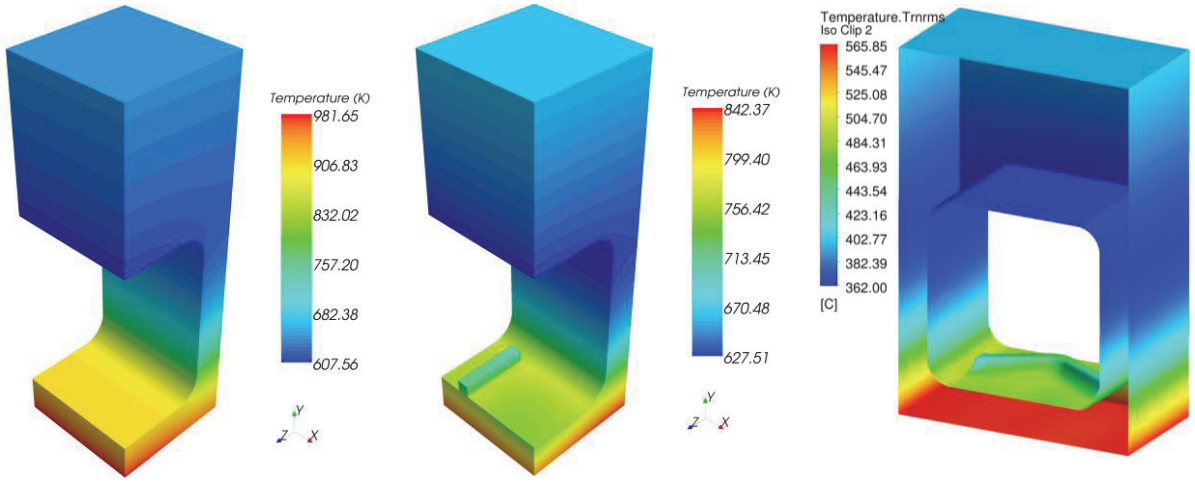

G0 (smooth walls)
ΔT(wall-fluid) : 368.2 K
Pressure drop: 4000 Pa/m

G5 (transversal rib)
ΔT(wall-fluid) : 228.6 K
Pressure drop: 11600 Pa/m

G2 (V-rib)
ΔT(wall-fluid) : 218.0 K
Pressure drop: 18200 Pa/m

Fig. 1: Representative CFD results showing the temperature distribution in the channel wall and engineering data for the smooth walled geometry G0 and the two ribbed geometries G2 and G5, all data for 49g/s Helium mass flow rate and 750kW/m² wall heat flux density from the plasma.

The reduction of wall temperature is however accompanied by an increase of pressure drop. For geometry G2, the pressure drop increases by a factor of nearly 4.6 relative to the smooth walled G0 at the same mass flow rate. Even though this seems a high penalty at first glance, further analysis showed that in fact the required pumping power for the cooling of the first wall at a specified plasma heat load is *less* for the structured surfaces, since a lower mass flow rate is required to obtain the same cooling.

The obtained results therefore indicate, that structured surfaces of the FW cooling channels can be very advantageous to balance optimization of the component lifetime (by the possibility to reduce the component temperature and therefore increase creep lifetime) and Balance-of-Plant aspects (by the possibility to reduce pumping power for a specified heat load).

It is planned to extend the optimization studies in the framework of EUROFUSION. Based on the results from this study, targeted optimization of the channel geometry can be further pursued by CFD. In order to validate the CFD results, an experimental campaign is also planned.

Staff:

F. Arbeiter
T. Böttcher
Y. Chen
M. Ilic
Ch. Klein
F. Schwab

Acknowledgement

This work, supported by the European Communities under the contract of Association between EURATOM and Karlsruhe Institute of Technology, was carried out within the framework of the European Fusion Development Agreement. The views and opinions expressed herein do not necessarily reflect those of the European Commission.

Goal Oriented Training Programme "Beryllium for the ITER First Wall" (WP12-GOT-BeFirst (FU07-CT-2012-00066))

The aim of the "BeFirst" training program is the education and training of early stage researchers in the field of “Plasma Facing Components”. It will be achieved by performing cooperative research and training programs in the area “Beryllium for the ITER First Wall”. The program is practically oriented and is realized through performing a set of practical exercises which include courses providing a theoretical background to the practical experience for extending the range of vision of young researchers.

To be able to procure material for the ITER first wall, one has to be acquainted with:

- Physical, chemical and mechanical properties of beryllium and main areas of its application in nuclear industry;
- Hazards associated with beryllium and overview of health and safety regulations applied for beryllium;
- Rules for beryllium handling and requirements for the design of beryllium handling facilities including requirements for protective equipment and health surveillance procedures;
- Waste management including storage, decontamination and disposal requirements;
- Analyses of beryllium using chemical and accelerator-based surface techniques.

The project is performed in close collaboration with six research institutions and coordinated by KIT. Project coordination is realized through regular bilateral e-mail exchange as well as by regular remote meetings involving representatives of all participating organizations and trainees.

The following research organizations take part in this project:

1. Karlsruhe Institute of Technology (**KIT, project coordination**)
2. Forschungszentrum Juelich (FZJ)
3. Royal Institute of Technology (KTH, Stockholm, Sweden)
4. Alternative Energies and Atomic Energy Commission (CEA, France)
5. University of Latvia (AEUL)
6. National Agency for new technologies, Energy and sustainable economic development (ENEA, Italy)

Four trainees have been employed by KIT, FZJ, KTH and CEA, accordingly. The duration of each training program is limited by three years. Each trainee should spend, besides hosting organization (employer), several months in other laboratories.

For example, KIT trainee has to work, besides KIT, three months at AEUL and three months at CEA.

Meetings in Year 2013

The Kick-off meeting which initiated the "BeFirst" Training Program was held at KIT on the 5th of March, 2013. Representatives of scientific organizations involved in this project showed the main tasks, aims and time schedules of training programs of their trainees.

Reports in Year 2013

Several reports were delivered by trainees during this year.

Staff:

P. Kurinskiy
D. Bachurin
P. Vladimirov

Acknowledgement

This work, supported by the European Communities under the contract of Association between EURATOM and Karlsruhe Institute of Technology, was carried out within the framework of the European Fusion Development Agreement. The views and opinions expressed herein do not necessarily reflect those of the European Commission.

DEMO Blanket Design (WP13-DAS-02-T09)

Objectives

Loss of Coolant Accident (LOCA) caused by a pipe break of Helium Coolant System (HCS) is considered as one of the most critical accident for the Helium Cooled Pebble Beds Blanket system (HCPB).

The DEMO HCPB Blanket temperature behaviour has been assessed, as well as stress and displacement within the Blanket structure, assuming the complete emptying of the cooling channel and heat coming from the irradiated structures.

Thermal Analysis of accidental Blanket temperature

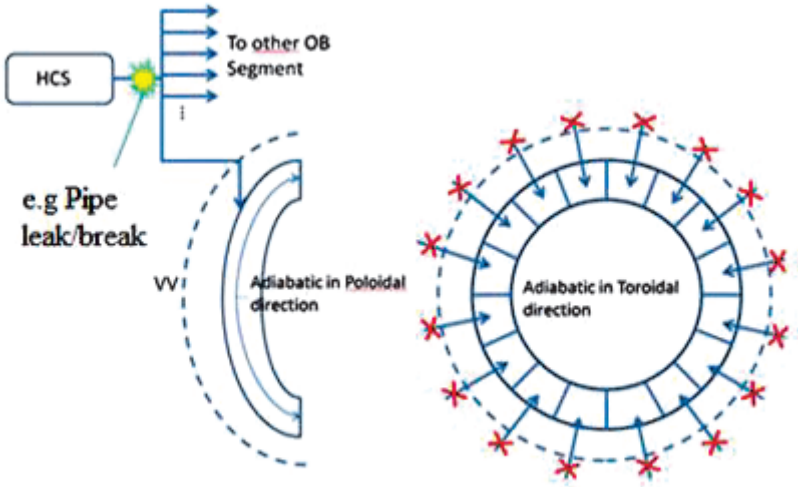

Fig. 1: Schematic of Ex-vessel LOCA.

In the selected ex-vessel LOCA scenario a complete loss of helium coolant is assumed and it is released in the reactor building (see figure 1). Hence, the vacuum vessel (VV) remains in vacuum condition (not affected by the helium blow-down), therefore no heat convection has been analyzed. The heat is transferred only by radiation from the modeled box towards the surrounding environment: the VV inner surface and the FW facing the surfaces of Inboard Blanket (IB) and divertor.

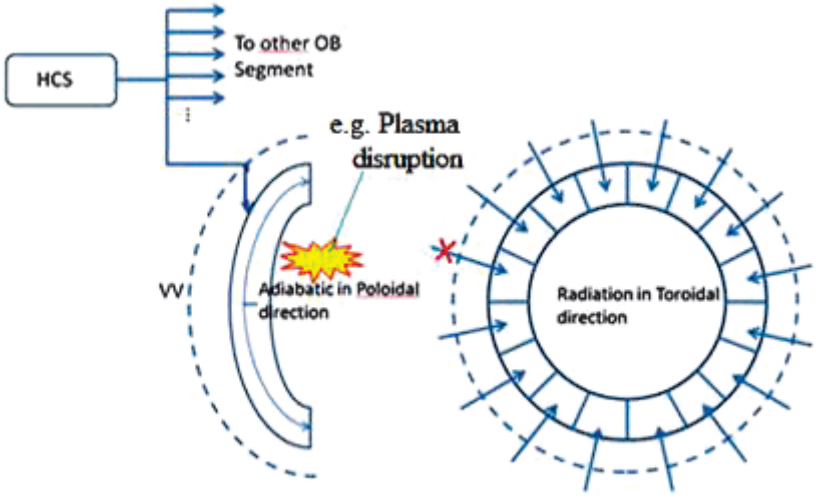

Fig. 2: Schematic of In-vessel LOCA.

In the in-vessel LOCA scenario First Wall (FW) break is assumed and helium ingresses into the VV (see figure 2). Therefore a portion of the decay heat is removed from the FW surface by the He coolant (heat transfer by convection), while the rest is transferred to the surrounding structures (heat transfer by radiation). A parametrical study on different heat transfer conditions regarding different helium temperatures and heat transfer coefficients has been performed.

The heat power distribution is estimated based on former neutronic analyses [1]. The decay heat power is a function of normal plasma operation heat power generated in the structures. The ratio between normal heat and decay heat immediately after shut down has been calculated based on previous neutronic analyses [2].

The radiation surface of vessel inner shell is considered at uniform temperature of 100°C and the emissivity of it is assumed to be 0.35. Two cases have been assessed regarding the FW temperature of the other blanket segments and divertor cassettes, the so called Plasma Facing Components (PFCs). In the first case the PFCs temperature is set to 300°C; in the second case the temperature is set to 500°C. For in-vessel LOCA, two additional different cases have been calculated regarding He heat transfer coefficient: 4W/m^{2}K at 300°C and 20W/m^{2}K at 200°C. The heat transfer assumptions have been described in schematic graph which can be found in figure 3 and figure 4.

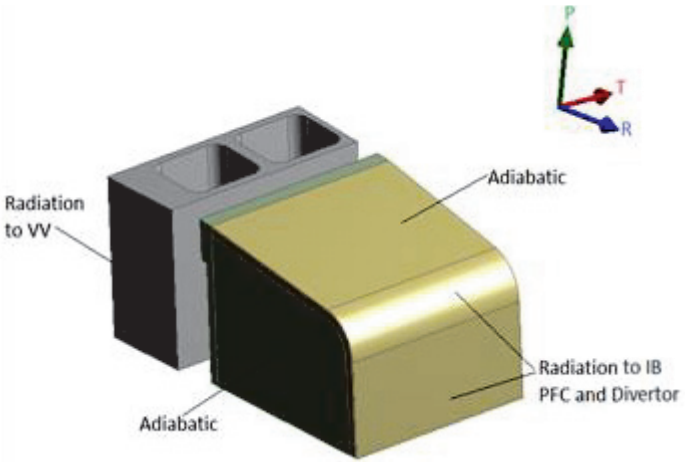

Fig. 3: Heat transfer in Ex-vessel LOCA.

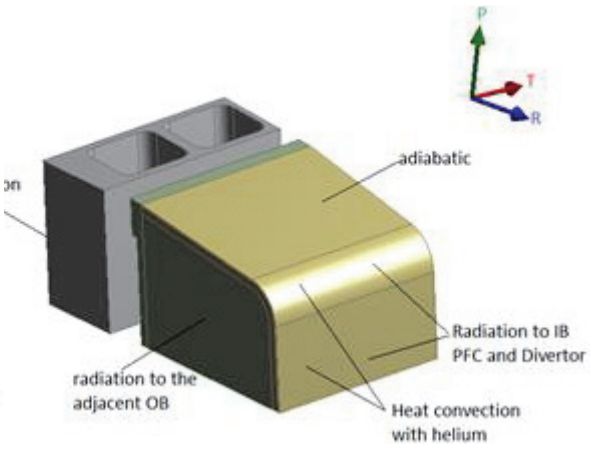

Fig. 4: Heat transfer in In-vessel LOCA.

The thermal results show that the Ex-vessel LOCA accident with PFCs at 500 °C is the most challenging in terms of blanket temperature increase and temperature difference along the blanket and back supporting structure (figure 5). The maximum temperature is 842 °C and occurs within the breeding zone in proximity of the first wall.

The worst case, Ex-vessel LOCA accident with PFCs at 500 °C has been selected to perform the thermal stress calculation. The temperature field obtained with the thermal analysis has been interpolated into mechanical analysis to study the thermal expansion and assess the secondary stress. The mechanical properties of Eurofer material at 800°C are not yet available, so engineering assumption has been used to perform the stress analysis. The figure 6 shows the Von Mises stress on the module in case of secondary stress. The damage modes considered are the following: taking into account the level D criteria low temperature rules and the monotonic type damages: the immediate plastic flow localization and immediate local fracture due to exhaustion of ductility (with and without peak stresses). According to the stress field hereafter are identified the segment for the stress linearization on the FW, the Back Supporting Structure and the body which has maximum stress. The behaviour is globally good since the stresses are well below the acceptable limits using above three criterions. Furthermore, the assumption of 500 °C as temperature for the PFCs is conservative; hence the blanket structure behaviour in terms of temperature and stress will be lower than the calculated one.

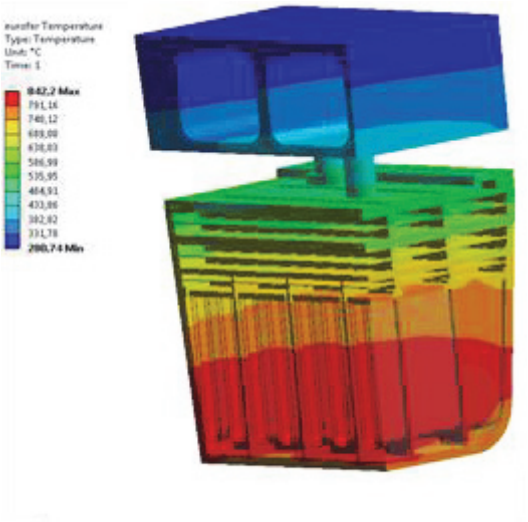

Fig. 5: Temperature contours in worst case.

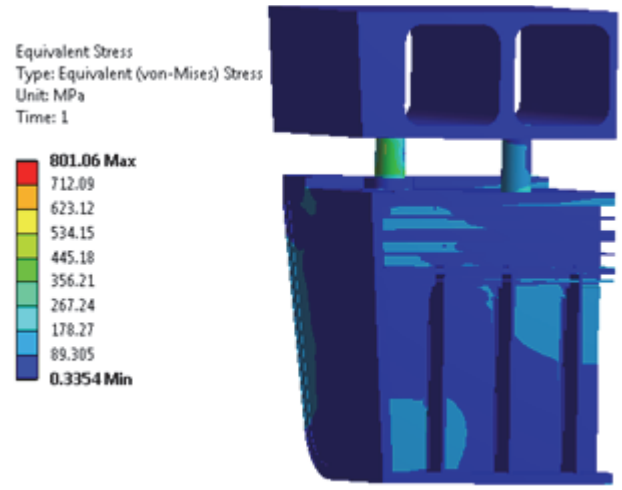

Fig. 6: Von Mises stress field in worst case.

Staff:

D. Carloni
Q. Kang
L.V. Boccaccini

Literature:

[1] U. Fischer et al., Neutronic design optimization of modular HCPB blankets for fusion power reactors.23rd Symposium on Fusion Technology (SOFT), Venice. September 20-24, 2004

[2] Fischer, U.; Leichtle, D.; Tsige-Tamirat, H. Neutronics characteristics of a solid breeder blanket for a fusion power demonstration reactor. Jahrestagung Kerntechnik '99, Karlsruhe, 18.-20.Mai 1999 Bonn: INFORUM GmbH, 1998 S.553-56

Acknowledgement

This work, supported by the European Communities under the contract of Association between EURATOM and Karlsruhe Institute of Technology, was carried out within the framework of the European Fusion Development Agreement. The views and opinions expressed herein do not necessarily reflect those of the European Commission.

FMEA for the DEMO HCPB Concept (WP13-SYS-04-T02-01)

Objectives

The Failure Mode and Effect Analysis (FMEA), has been used to ensure that a full range of potential faults and off-normal conditions have been considered.

The scope of the performed analysis is to identify representative accident initiators, whose sequences will be described in the WP13-SYS-04-T03.

Justification of the FMEA

The approach followed for the present work is based on a FMEA at component level with evaluation of loss of functions. In fact, the current status of the design of system analysed allows the identification of the various components, and hence of the associated functions.

Each component/subsystem has been identified with a PBS number and its associated functions. For each function, possible failures have been evaluated and listed, together with consequences and possible preventive and/or mitigating measures. Finally, for each failure an Initiating Event is identified. From the complete list of IEs, a set of Postulated Initiating Events (PIEs) can be identified as the most representative in terms of challenging conditions for the safety of the plant. Each elementary accident initiator is associated to the related PIE, according to the procedure explained below. In such a way, it is possible to concentrate safety studies on the most relevant accident sequences, avoiding studies related to the other minor and almost equivalent sequences.

Each important initiator could then be discussed in order to define the accident sequences that could stem from the initiator and the possibly required deterministic assessment.

The following steps have been pursued performing the work:

- Identification of the plant functional breakdown (since no FBS was available from designers);
- Assessment of possible loss of functions associated to the components by the FMEA;
- Identification of Postulated Initiating Events;
- Discussion of possible sequences arising from PIEs (in WP13-SYS04-T03).

Systems analysed in the FMEA

The systems analysed in the FMEA are:

- HCPB Blanket
- Primary Heat Transfer System (PHTS)
- Coolant Purification System (CPS)
- Pressure Control System (PCS)
- Secondary Cooling Water System (SCWS)

Applied Methodology

Firstly each system is subdivided in different component/subsystem following the structure of simplified process flow diagrams. For each component/subsystem, different functions are identified and listed. The loss of a function is categorized as failure and the possible causes investigated and listed. The individuation of the causes has to be handled carefully: this refers to the failure of components (e.g. piping, valves, I&C) of a subsystem (e.g. cold leg between steam generator and pump) that can induce the loss of the specific function. Some components were considered in the analysis (for example Valves and I&C) even though not

reported in the diagrams. This was justified using similar systems with higher level of design detail as reference.

The next step is the individuation of the consequences for the overall system associated to the loss of a function. Here it is possible to distinguish in consequences that occur immediately after the loss of the function and consequences that can occur in aggravating sequences. Then a set of mitigating actions is proposed to limit the consequences of the failure. Eventually the event is categorized as Initiating Event (IE).

Once all the IEs are identified, similar IEs are grouped in a unique PIE. The derived representative PIE must be the most challenging in terms of safety to encompass also the other IEs consequences. In WP13-SYS04-T03, for each PIE the accidental sequence is described considering aggravating events and possible mitigating actions.

The accidental scenarios, i.e. the accidental sequences most representative in terms of safety, are defined by grouping different PIEs with similar consequences, and the phenomenology of each scenario described. Finally a selection of accident sequences for which further deterministic accident transient analyses are recommended must be redacted.

Applicable failure modes

Applicable failure modes are those affecting the loss of function of a component. Generally these are

- Fail to operate
- Leakage
- Rupture
- Fails to start
- Fails to stop

These failure modes can arise from several causes and occur with different modalities. Among the possible causes of structural materials fails [J. Aktaa et al] we mention:

- Electromagnetic loads which causes stress in most parts of structures,
- Cycle thermo-mechanical loads due to temperature fields; nonhomogeneous temperature causes cycle peak stress at geometrical discontinuities,
- Radiological due to modification of materials properties because radiation (irradiation creep, swelling, embrittlement, hardening/softening, loss of elongation, thermal conductivity modification, etc.),
- Chemical damage due to corrosion,
- Physical damage due to physical sputtering and coolant erosion.

Among failure occurrence modalities (produced by damage mechanism that increases stress in a component) we mention:

- Immediate elastic collapse and instability: caused by too high primary stress (electromagnetic loads).
- Progressive inelastic deformation (Ratcheting): increase of inelastic strain under cyclic primary and secondary stress (cycle thermo-mechanical loads).
- Creep: occur in high temperature region>370ºC for EUROFER). Fatigue: it is relevant where appear high stress peaks (thermo mechanical loads) .
- Creep-fatigue: temperature peaks generate stress loads: failure is accelerated in discontinuities due to long pulsed operation. Lifetime limiting.
- Fatigue: relevant in notches and discontinuities in temperature regions < 370ºC.
- Fast fracture: occur in welds caused by defects.

Postulated Initiating Events

The total list of PIEs recognized by the FMEA on European HCPB Test Blanket Module systems is reported in the following Table 1. Furthermore it has been reported in the attachment B the list of identified PIEs and the related elementary failures that contribute to each PIE. In the tables, Operating phase, PIE code, code and description of components whose failure will induce the PIE and component failure mode are detailed.

Table 1: List of Postulated Initiating Event (PIEs).

PIE	Description
FB1	Loss of flow in all FW-BK cooling channels of one section (A,B,C or D) of the outboard or inboard segments (48 or 32) because stop of circulators for CCF
FB2	Reduction of flow in all FW-BK cooling channels of one section (A,B,C or D) of the outboard or inboard segments (48 or 32) because stop of circulator in one SG line
FB3	Reduction of flow in cooling channels of one FW-BK module because internal clogging
AOP1	Loss of Off Site Power <1h
AOP2	Loss of Off Site Power from 1h up to 32h
HB1	Loss of heat sink in all FW-BK primary cooling circuits because trip of both HP and LP turbines due to loss of condenser vacuum
HB2	Loss of heat sink in one FW-BK cooling train
LBB1	Loss of FW-BK cooling circuit inside breeder blanket box: Rupture of a sealing weld
LBB2	Loss of FW-BK cooling circuit inside breeder blanket box: Leak of a sealing weld
LBO1	LOCA Out-VV because large rupture of He Manifold feeder inside HCS Vault
LBO2	LOCA Out-VV because small rupture of He Manifold feeder inside HCS Vault
LBO3	LOCA Out-VV because rupture of tubes in a Steam Generator
LBV1[(1)]	Loss of FW-BK cooling circuit integrity inside VV: Rupture of FW-BK module
LBV2[(2)]	Loss of FW-BK cooling circuit integrity inside VV: Leak from FW-BK module
TBO2	Small rupture from HCS "Coolant purification system" process line inside the HCS Vault (Outside VV), i.e. significant amount of tritium released into building
N/S	Not Safety Relevant

[(1)]Since the design of the cooling circuits inside the box is currently not yet defined, the PIEs associated to the failure of the box have been taken from previous TBM FMEA [Pinn06] and reported here only for completeness purposes.

[(2)]See note 1

Staff:

D. Carloni
X. Jin
L.V. Boccaccini

External Contributors from ENEA Frascati
D. Dongiovanni
T. Pinna

Literature:

[1] W. Gulden: “Review technical information available in EU from previous fusion reactor studies relevant for safety”, Safety workshop, Garching, 5. December 2012.

Acknowledgement

This work, supported by the European Communities under the contract of Association between EURATOM and Karlsruhe Institute of Technology, was carried out within the framework of the European Fusion Development Agreement. The views and opinions expressed herein do not necessarily reflect those of the European Commission.

DEMO Blanket Design (WP13-DAS-02-T04, -T05, -T07)

Objectives

A HCPB DEMO blanket design study has been performed within the frame of the EFDA PPPT 2013 activities, in the subgroup IVCC DAS02. This task comprises the design of the blanket box and the attachments of the individual components with each other, such as the blanket box with the Back Supporting Structure (BSS) and the BSS to the Vacuum Vessel (VV).

Design of the Blanket Box (WP13-DAS-02-T04)

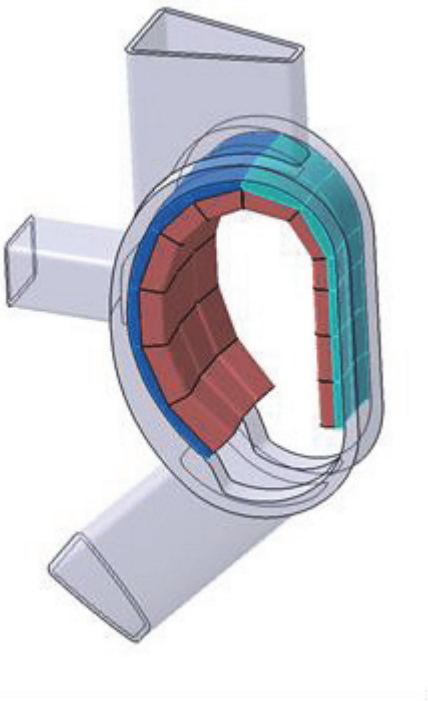

Fig. 1: Blanket sector within the VV.

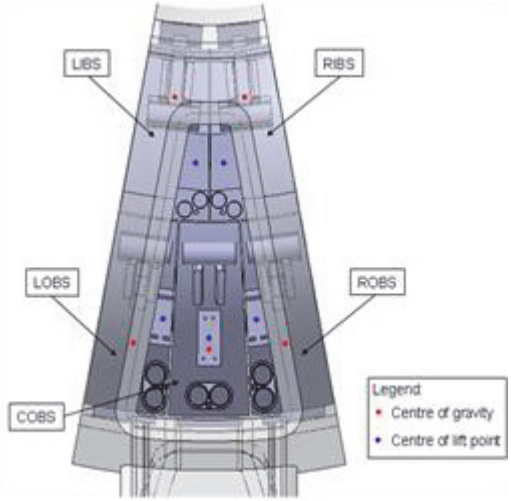

Fig. 2: Blanket sector top-view.

The current structural breakdown foresees 16 Blanket toroidal sectors, each including 3 outboard (OB) and 2 inboard (IB) blanket segments, having a poloidal height of about 12 m (Figures 1 and 2). Each OB and IB blanket segment consists of 6 blanket modules which are attached to the BSS along the poloidal direction. The largest radial x toroidal x poloidal module size at the torus equatorial plane is about 1 x 1 x 2 m, respectively. The BSS, having a structural function, provides for the blanket cooling through the helium manifolds, for the tritium purge in the breeding zone, and for the shielding of the VV against neutrons. The blanket modules consist of First Wall (FW), box manifold, caps, vertical and horizontal stiffening grids, and breeder units (BUs). A parametric CATIA model of the blanket box, the BUs and BSS has been realized to enhance the flexibility and, hence, the optimization of the design through compliance to different requirements, such as mechanical loads, Tritium Breeding Ratio (TBR), and safety. From the design point of view, the reduction of the module numbers per segment (from 10 in the previous design to 6) is driven from the considerations expressed in recent neutronic analyses [1]: i.e. the smaller the number of modules the smaller the neutronic captures within the structural material that surrounds the breeding zone. The design of stiffening grids and BUs has been modified as well to increase the TBR. On the other hand, the modularization of the blanket´s FW allows thermal expansion during plasma operation, and hence reduces the stresses on the box itself. The dual cooling of the FW and module internal represents the main innovation of the 2013 blanket box design (with respect to both the safety and the reliability), characterised by: two separate parallel cooling systems with mutual flow direction, each able to remove 50% of the heat generated in the blanket, are

routed through the BSS to the module and back[1]. Within the Box manifold, the dual coolant flow system is achieved by the collection and distribution of helium coolant to the various components by means of two parallel and independent flow paths: through a series of drilled plates the FW is cooled by the two cooling systems in counter current flow along the toroidal channel paths in order to achieve a uniform temperature distribution and thus to prevent unnecessarily high temperatures and at the same time high thermal stresses in the EUROFER steel (the structural material for the entire blanket system).

Despite the more complex manifold plate arrangement, the dual cooling system allows a parallel cooling of the modules internals, which desirably reduces the overall pressure drop of the Primary Heat Transfer System (PHTS) of the blanket. Also, the possibility to ensure cooling of the module even in case of failure in one of the two systems (e.g. due the circulator trip or pipe leakage), increases sensibly the reliability of the blanket box during plasma operation. At the outlet of the FW, one system is routed to the stiffening grids and caps, while the other provides cooling to the BUs cooling plates.

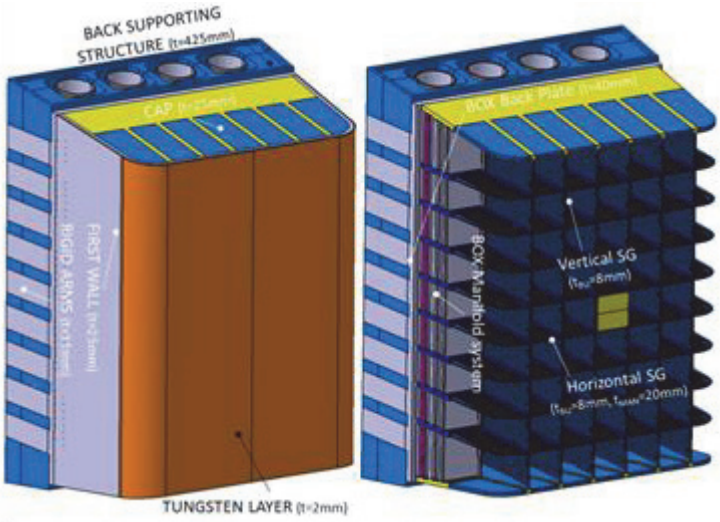

Fig. 3: Outboard Equatorial Blanket Box (with and without FW).

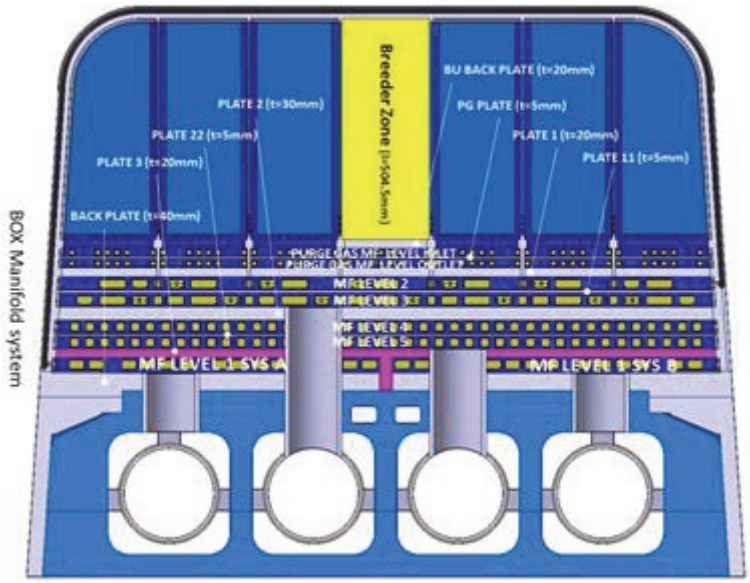

Fig. 4: Poloidal Cross section of The OB Segment (Equatorial Plane).

The high pressure (8 MPa) Manifolds distributing the helium coolant in the Blanket are created by several thick plates to separate the two independent cooling circuit. The Breeder Unit Back Plate is 20 mm thick, and the Closure Back Plate is 40 mm thick. The place between these two plates is further sub-divided by thinner separator plates (5 mm) in several to distribute and collect coolant for different in-box components. The temperature difference between inlet and outlet (respectively 300 °C and 500°C) could be a serious concern for the structural material. To avoid high thermal stress a thermal insulation system (Figure 4) has been integrated in the BSS to keep the structural material uniformly at 300°C. Coaxial pipes with insulating gaps on the outer surface have been introduced within the square channels of the BSS. The inlet flow goes in the square channels and then is distributed to the modules along the poloidal direction. After the pass through the modules, the outlet flow is collected inside the coaxial pipes and then routed again towards the upper part of the Blanket and then outside the Vacuum Vessel.

[1] Originally this solution was introduced by M. Dalle Donne in the Breeder Out of the Tube (BOT) Blanket concept [2], which foresees a unique large Blanket module for each poloidal segment.

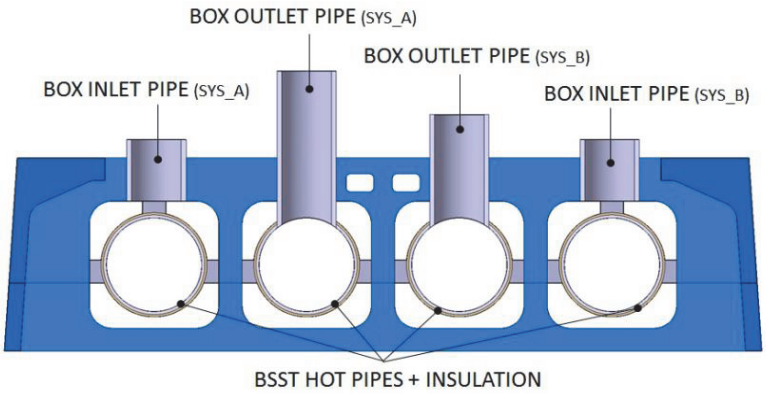

Fig. 5: BSS Manifolds System.

A Tritium Extraction System (TES) has been also integrated in the 2013 Blanket design. The purge function is accomplished by a relatively low pressure (0.1-0.4 MPa) low velocity helium circuit routed through the BSS and the box to the breeding zone. The purge gas manifolds are located in the inner part, in between the 20 mm thick plate (PLATE 1) and the BUs back plate (20 mm). The inlet and outlet purge gas pipes are routed through the Blanket back-plate and then through the high pressure region to connect with the BBS. The purge gas inlet is led to the purge gas distributor manifold located right behind the BUs back plate though a pipe. The purge gas feeds each BU through a grid path designed in the BU back plate. After sweeping the pebble beds, the purge gas is guided from each BU by individual pipes to the collector located between the purge gas distributor MF and the 30 mm thick manifold plate. The purge gas is then routed out of the Blanket by the outlet pipe crossing the high pressure manifold region as the inlet pipe.

Attachment to the BSS (WP13-DAS-02-T05)

A novel attachment concept has been developed based on “L” shaped steel components (so called “Stiffening Fingers”) welded on the prepared (welding island) surface of the Box Back plate and then to the BSS. The attachment system doesn’t have to bridge over high temperature difference thanks to the manifold arrangement of the dual cooling system: 1st level of box manifold is providing cooling to the FW; hence the 300 °C Helium is also directly cooling the Box Back Plate. Therefore no large temperature differences are expected to occur between the Back Plate, the fingers and the BSS, which is definitely desirable to avoid high thermal stresses in the contact regions. The longer side of the L-shaped SFs are connected by welding to the BSS structure to ensure mechanical support to the gravity and electromagnetic loads. The current status of the design doesn’t foresee the use of bolts to connect the box to the BSS, nonetheless bolted connection of the SFs to the BSS (along the toroidal plane) could simplify the assembly/disassembly sequence in hot cell.

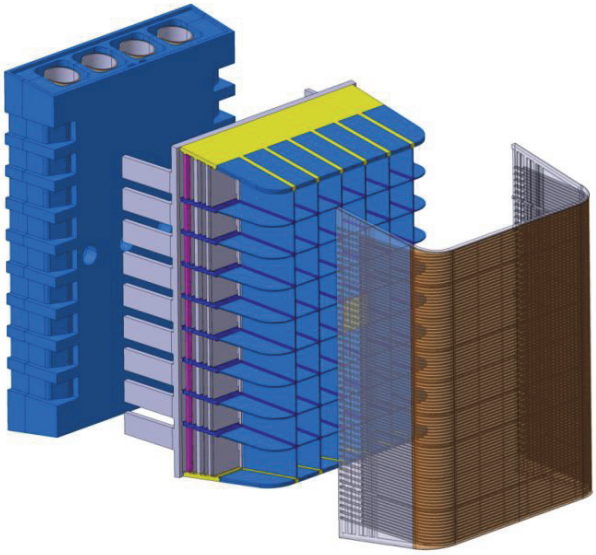

Fig. 6: Exploded view of the OB Equatorial Module.

The main advantages of this solution are:

- Low stresses for the piping connecting the BSS to the box
- Increase of the space available for the box’s internals (e.g. BUs and Box Manifold)

- Limited effects due the thermal expansion of the box
- No movable joints required (e.g.: keys, pins)
- Easy replacement of a failed module in hot cell (by welding cut)

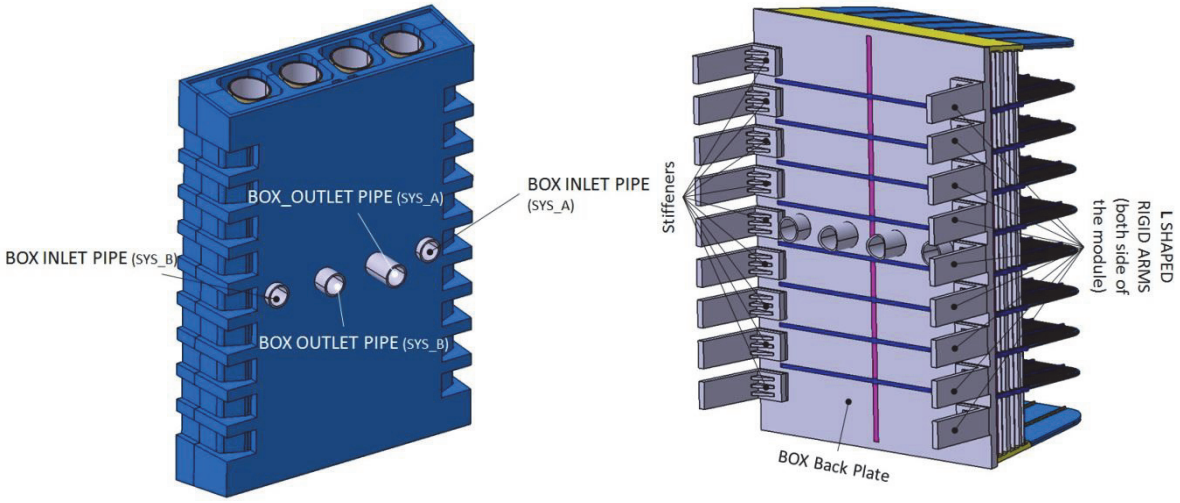

Fig. 7: OB Equatorial Module SFs system attachment.

Attachment to the VV (WP13-DAS-02-T07)

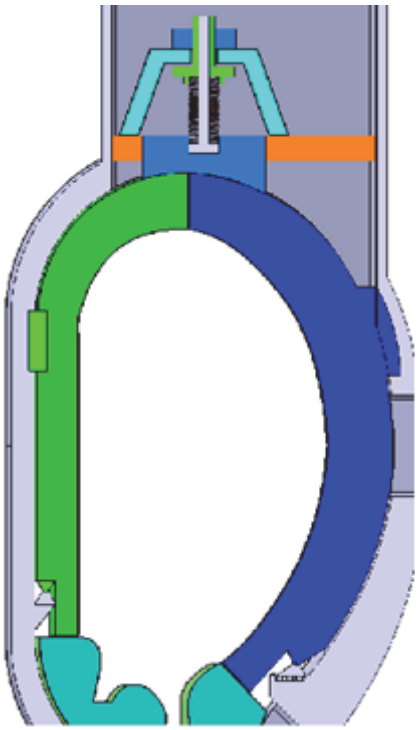

Fig. 8: Schematic of VV-BBS attachment system.

The attachment between Vacuum Vessel (VV) and Blanket drives very basic reactor design solutions since it impacts also the remote handling concept and sequences, hence the Tokamak architecture. The attachment system (Figure 8) has to cope with different loads: gravity, electromagnetic forces and thermal expansion of the Blanket. Electromagnetic loads coming from the Plasma Disruption (Eddy currents and Halo currents) are really challenging since they can generate the Blanket vertical displacement (VD): i.e. the Electromagnetic (EM) forces intensity is greater than Gravity force itself; such a “lift” of the Blanket could severely damage the Blanket and jeopardize the integrity of the VV, that in a fusion reactor is also providing the function of first confinement barrier. Hence four different solutions have been proposed and studied to limit the risk connected to the VD event, which are mainly deferring in the bottom part of the back supporting structure. The Blanket has to be mounted within the VV at room temperature (20 °C) and then heated up to 300 °C prior to the plasma operation, while the VV temperature varies from 20 °C (room temperature) to 100 °C (plasma operation) which increases up to 200 °C (Baking scenario). The thermal expansion of the Blanket shall be allowed in such a way that the mechanical stresses in the EUROFER material are not exceeding the design limit. Furthermore the FW surface shape has to be kept within narrow tolerances to avoid potentially dangerous plasma-wall interactions. Although reduced space availability in the VV upper port and component weights are challenging for the design, all the developed options are compliant with Remote Handling (RH) and space requirements. Two load combinations (thermal + gravity + EM) have been studied (sign of the EM forces) for each option. Option 1 (Figure 9) is hereafter reported as example

of a viable solution: the mechanical design consists of a thick actively He-cooled shelf integrated in the BSS inserted in a VV vane. Option 1 allows limited sliding of the BBS in radial and toroidal direction, while no displacement is allowed towards the vertical direction.

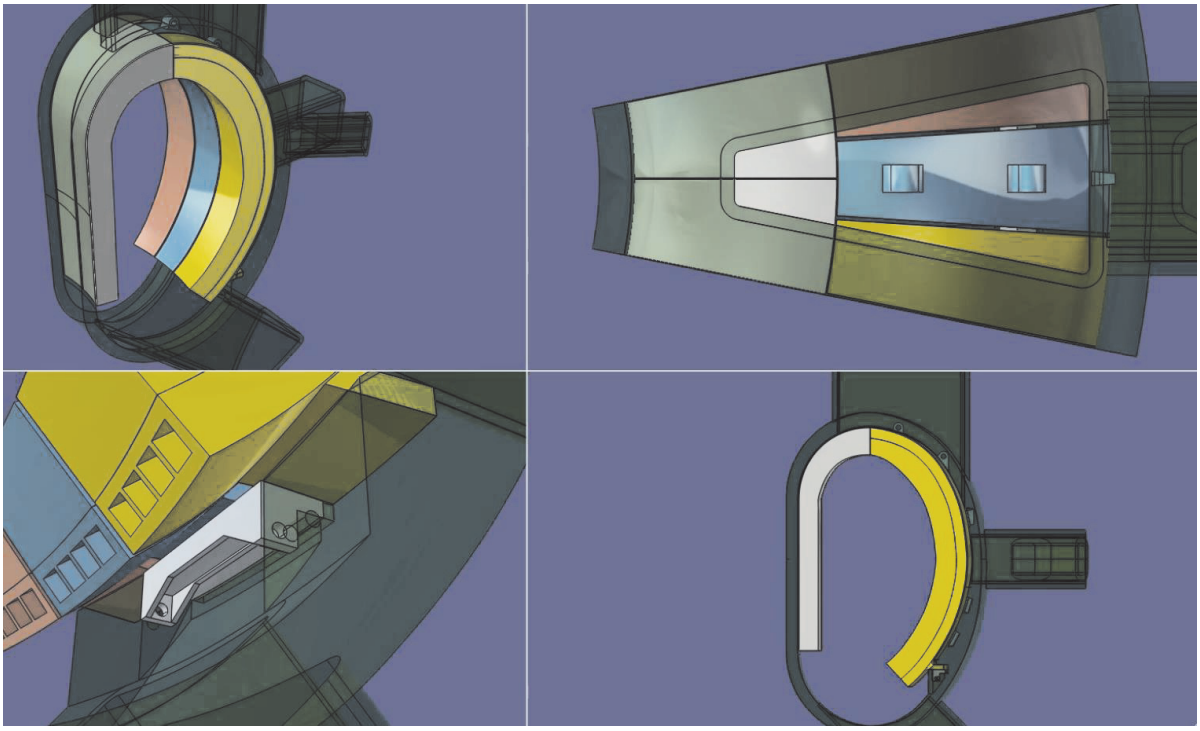

Fig. 9: Option 1 CAD model.

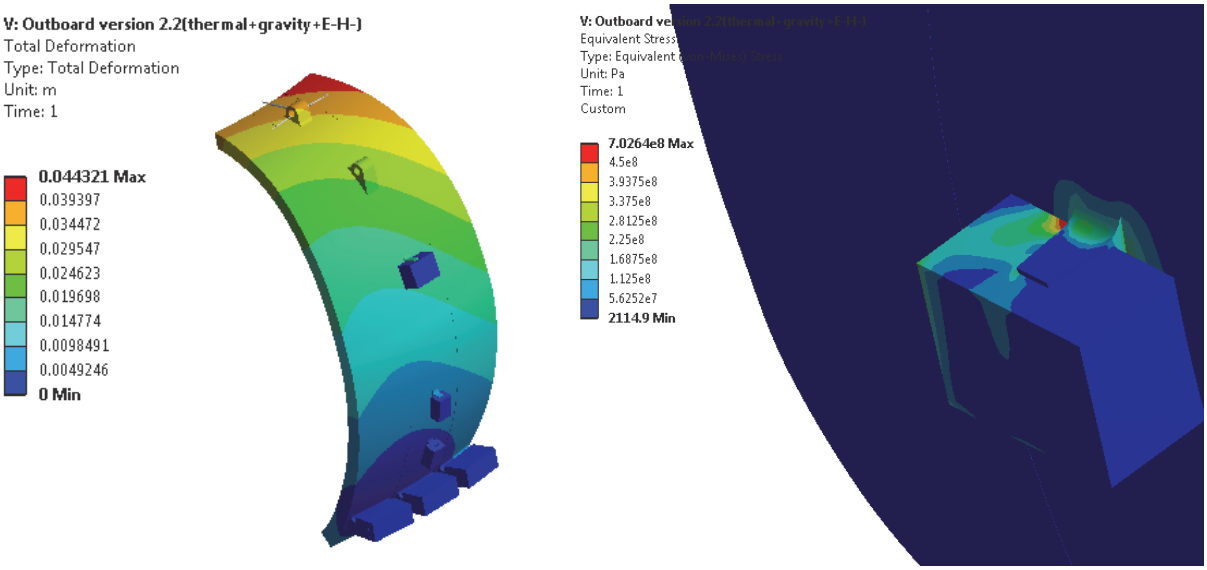

Fig. 10: Option 1 OB total deformation and localised high stress.

The relative displacement of the BSS with respect to the VV is about 40 mm, and it occurs mainly along the vertical and radial directions (Figure 10, left). The global stress results are below the admissible limits for the selected material; hence the soundness of the proposed conceptual design is demonstrated. Localised high stress (Figure 10, right) occurs in proximity of the upper vertical key: although the calculated stress is higher than the allowable limit, the adoption of rounded corners (compatible with manufacturing processes) in the next phases of the design should help reduce the stress value within the allowable limit.

Staff:

L.V. Boccaccini
O. Bitz
D. Carloni
F. Hernandez
Q. Kang
S. Kecskes
I. Maione
C. Zeile

Literature:

[1] P. Perelsavtsev et al., Neutronic analyses of the HCPB DEMO reactor using a consistent integral approach, Fusion Engineering and Design, 2014

[2] M. Dalle Donne et al., European Helium Cooled Pebble Bed blanket design of blanket test module to be tested in ITER, Fusion Engineering and Design 39-40 (1998) 825-833

Acknowledgement

This work, supported by the European Communities under the contract of Association between EURATOM and Karlsruhe Institute of Technology, was carried out within the framework of the European Fusion Development Agreement. The views and opinions expressed herein do not necessarily reflect those of the European Commission.

Source Terms and Critical Event Sequences for the Blanket Concept HCPB (WP13-SYS-04-T03-01)

Objectives

The activities within this task aim to estimate DEMO source terms for the HCPB blanket concept, to identify initiating events in DEMO, to identify and describe critical accident sequences to be considered in the safety assessment of DEMO, and to summarize qualitatively the consequences of the event sequences.

Systems and confinement strategy

The Nominal fusion power of DEMO HCPB blanket concept is 1.943 GW [1]. Concept dependent and safety related systems are mainly: blanket-PHTS including CPS and PCS, SWCS, HCPB blanket system, water cooled divertor and purge gas system. The design data for the HCPB blanket are: 2143 kg/s mass flow rate, 300 °C and 8 MPa at the blanket inlet and 500°C at the blanket outlet. The total neutron power is 1547 MW. EUROFER is used as structural material and Tungsten as PFC. Li_4SiO_4 is the breeding material and beryllium is the neutron multiplier. TBR target is designed to be 1.12. Multi Module Segments (MMS) are designed for the blanket arrangement.

Based on ITER, confinement strategies and safety functions have been proposed for DEMO (see Fig. 1). Confinement barriers and associated confinement systems are required to protect the personnel, public and environment against radioactive material releases. They are defined for the systems as follows:

- First barrier
  - VV and the PHTSs
- Second barrier
  - VVPSS and EV, and their connections to the VV
  - Glove boxes
  - Cryostat
  - Emergency cooling
- Third barrier
  - Active systems: HVAC, NDS, SDS
  - common release point
  - Tokamak and tritium building

The first and second barriers build the first confinement and the third barrier provides the second confinement function.

Fig. 1 contains the systems for major safety functions that can be applied to DEMO. They are reported with respect to the intended function of the system, logic to perform the safety function (active/passive), conditions for the system requirement, and consequence by system failure.

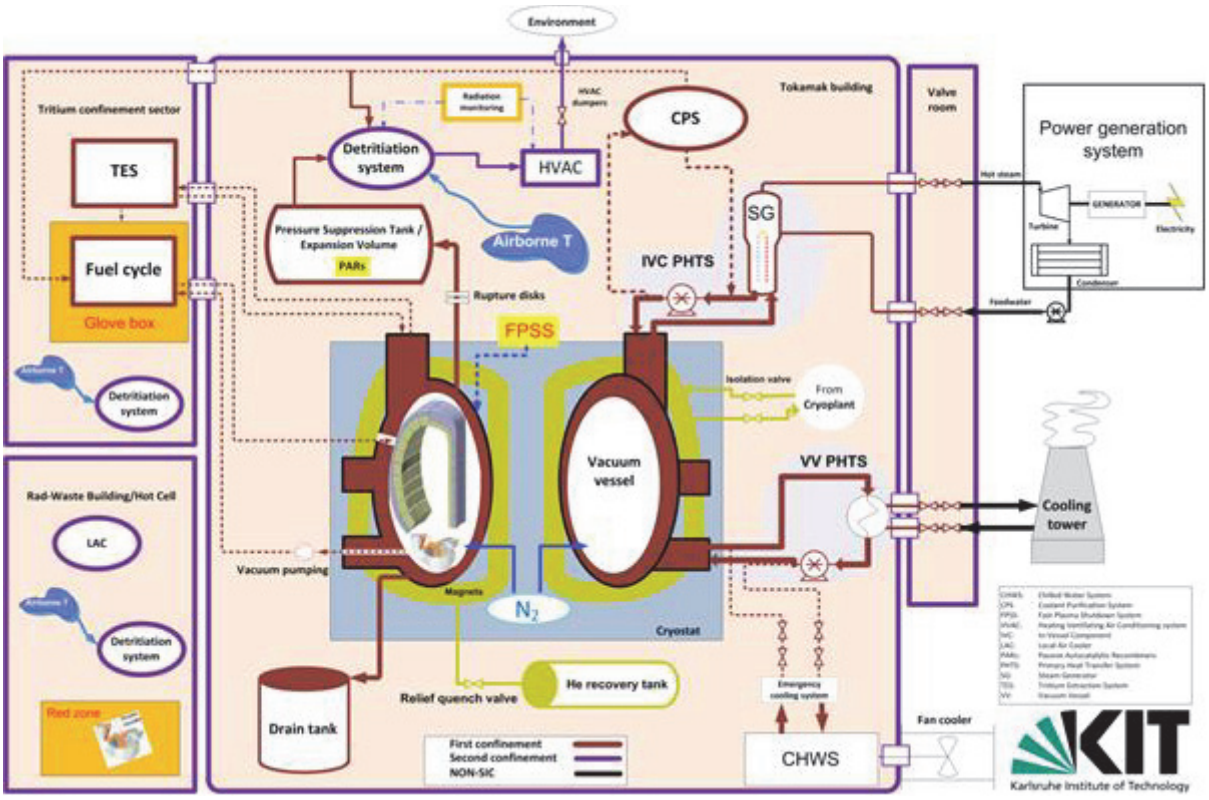

Fig. 1: Scheme of DEMO confinement.

Safety relevant sources and inventories

For the current DEMO HCPB concept source terms have been identified as energy, tritium, activation products, dust, ACPs and neutron sputtering products. Energy sources in system can be performed in kind of enthalpy in structure and coolant, plasma thermal energy and magnetic energy in operation; decay heat after the plasma shutdown; energy from exothermal chemical reactions between materials; and energy release due to postulated H_2 explosion. Source terms are described with respect to the generation, treatment and available inventories - mainly based on the previous studies. Missing inventories due to incomplete design and analysis are pointed out as well. The radioactive inventory assumed for the accident sequences are summarized in Table 1.

Table 1: Radioactive inventories.

Inventories	DEMO HCPB	Note
Tritium in VV	1.0 kg	Due to the mobility of tritium the total inventory is considered in accident sequences (mobilization fraction = 1)
Dust	100 kg	~ 1 kg tritium, mobilizable dust.
Tritium in the blanket-PHTS (He coolant)	1 g (per loop)	Calculated on the basis of 1 Pa limit of tritium in the He coolant. (mobilization fraction = 1)
Tritium in divertor-PHTSs (water coolant)	TBD	In principle no tritium should be present in this loop, but some maybe from the plasma.
ACPs	TBD (divertor, VV loop)	ACPs mobilization fraction is consider as 1% of the total inventory.
Sputtering products	TBD	In coolant

Critical event sequences selected for DEMO HCPB concept

It is necessary to identify representative accident initiators and related accident sequences in order to give indications for the selection of the accident analysis to be performed deterministically. Concerning the PIEs identified by the FFMEA analyses in WP13-SYS-04-T02-01/KIT/PS, the main initiators are related to loss of power, LOFA, in-vessel LOCA, ex-vessel LOCA, loss of heat sink and in-box LOCA for the blanket. The related accident sequences are described with respect to the causes, scenarios by failure assumptions, possible consequences and proper mitigating actions limiting the accident consequences. Failures are assumed for DBA (Design Basis Accidents) and for BDBA (Beyond Design Basis Accidents) by additional aggravating failures.

In order to understand the probability of DBA and BDBA, mitigation of accident and dose limit to the public, safety risk approach is shown in Fig. 2. It schematizes the behaviour of public dose vs. probability (i.e. occurrence rate or frequency) on a logarithmic scale. The red line in the figure separates dose rates in the acceptable risk zone (left) and the not acceptable risk zone (right) depending on the probability. Accidents events with frequency larger than 10^{-6} are classified as DBA; while Design Basis Extension with frequency lower than 10^{-6} is considerable as BDBA. The field of acceptable accident is further limited by a maximum admissible dose rate that is related to the so called “fusion bounding accident sequences” in green bar, which are the worst consequences of an accident driven by in-plant energies. This was assumed to be a total loss of cooling from all loops in the plant, with no active cooling, no active safety system operating, and no intervention whatever for a prolonged period. The decay heat is rejected by passive conduction and radiation only. For this kind of events a maximum limit of dose of 50 mSv was selected, which is recommended by the ICRP and is used as ITER dose criterion. Accidents in the not acceptable risk zone can be brought back to the acceptable risk zone taking proper countermeasures, e.g. improving the confinement reduces the dose rate and can move the accidental event down to the acceptable risk zone; adding certain safety system, even the dose rate is unchanged, it can reduce the probability of the event moving left to the acceptable risk zone.

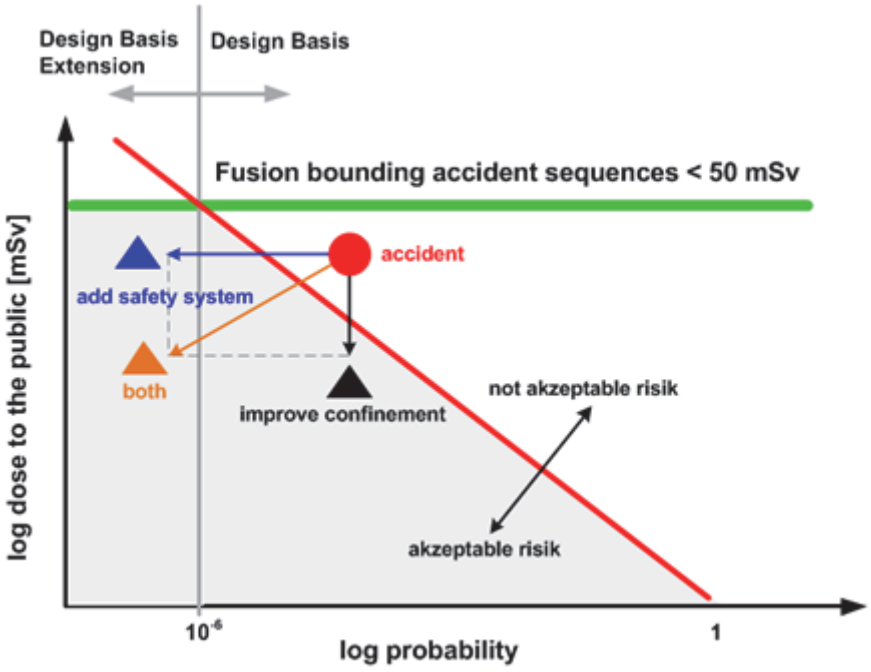

Fig. 2: Safety risk approach.

Concerning safety assessment in terms of containments challenging, mobilised radioactive products and radioactive releases towards the environment a priority list for the event sequences has been generated from the overall accident scenarios discussion to show which events have to be analysed deterministically:

- Loss of power
  - AOP2: Loss of off-site power for long duration
- LOFA inducing in-vessel LOCA
  - FB1: Loss of flow in all FW-BK cooling channels of one redundant section because of stop of circulators for common cause failure
- Ex-vessel LOCA inducing in-vessel LOCA
  - LBO1: LOCA out-VV because large rupture of He manifold feeder inside PHTS vault
  - LBO3: LOCA out-VV because rupture of tubes in a steam generator
- Loss of heat sink due to loss of condenser in the SWCS
  - HB1: Loss of heat sink in all FW-BK primary cooling circuits because trip of both HP and LP turbines due to loss of condenser vacuum
- In-box LOCA inducing in-vessel LOCA
  - LBB1: Loss of TBM cooling circuit inside breeder blanket box: rupture of a sealing weld

Finally, station blackout and bounding accident are proposed as well; even they are not identified by the current FFMEA. Because these are the most severe conceivable accidents driven by in-plant energy that can lead to the maximum radiological doses, thus the plant safety will be affected concerning evacuation criteria.

Staff:

X. Jin
D. Carloni
L.V. Boccaccini

Literature:

[1] W. Gulden: “Review technical information available in EU from previous fusion reactor studies relevant for safety”, Safety workshop, Garching, 5. December 2012.

Acknowledgement

This work, supported by the European Communities under the contract of Association between EURATOM and Karlsruhe Institute of Technology, was carried out within the framework of the European Fusion Development Agreement. The views and opinions expressed herein do not necessarily reflect those of the European Commission.

Long-term Stability of Ceramic Breeder Pebbles (BMBF Reference No. 03FUS0012)

As part of the BA DEMO activities, the long-term stability of solid breeder ceramics was investigated in a long-term annealing (LTA) experiment. Three different compositions of two-phase tritium breeder pebbles, consisting of lithium orthosilicate and lithium metatitanate, produced by a melt-based fabrication (KALOS) at KIT [1-3], as well as two batches of lithium excessive lithium metatitanate pebbles, produced either by a sol-gel method or an emulsion method by JAEA were investigated:

LTA1: KALOS, 80 mol% lithium orthosilicate + 20 mol% lithium metatitanate
LTA2: KALOS, 75 mol% lithium orthosilicate + 25 mol% lithium metatitanate
LTA3: KALOS, 70 mol% lithium orthosilicate + 30 mol% lithium metatitanate
LTA4: JAEA, emulsion method, lithium metatitanate, Li/Ti ratio of 2.16
LTA5: JAEA, sol-gel method, lithium metatitanate, Li/Ti ratio of 2.11

In order to examine their long-term stability, the pebbles were annealed under reference purge gas atmosphere at 900 °C [4,5]. The samples were placed in platinum or alumina crucibles and purged with 1200 ml/h He+0.1%H_2 inside a gas tight aluminum tube at a constant absolute pressure of 1200 mbar. During annealing, the oxygen and water contents were continuously monitored by an optical oxygen sensor and an alumina moisture sensor at the inlet and outlet of the tube. Samples were taken after 4, 32, 64, and 128 days of annealing. The microstructure and the phase content of the annealed pebbles were examined by scanning electron microscopy and X-ray diffractometry, respectively, and were compared to the as-received state. To complement the X-ray diffractometry analysis, the chemical composition of the five samples was analyzed by inductively coupled plasma optical emission spectrometry with respect to the main constituents, lithium, silicon and titanium, as well as the main impurity elements. Also the open and closed porosity were measured by He- and Hg-porosimetry. Additionally, the evolution of the pebbles' surface area was examined by multipoint BET nitrogen adsorption measurements. Crush load tests of single pebbles were used to study possible changes in the mechanical behavior of the pebbles.

The microstructure of the as-received LTA3 pebbles is dominated by lithium metatitanate dendrites (see figure 1), while it is dominated by lithium orthosilicate dendrites in the samples LTA1 and LTA2. The space between the dendrites is mainly filled with the respective other phase. In general the microstructure of the LTA1, LTA2 and LTA3 samples is very stable during the annealing, while the LTA4 and LTA5 samples exhibit considerable grain growth. In contrast to the other samples, the annealing does not notably change the microstructure of the LTA3 pebbles. Significant grain growth or coalescence of the lithium metatitanate dendrites does not occur. For the LTA1 and LTA2 pebbles, certain areas show a higher tendency for coalescence. Yet, the lithium metatitanate phase remains finely dispersed within lithium orthosilicate grains.

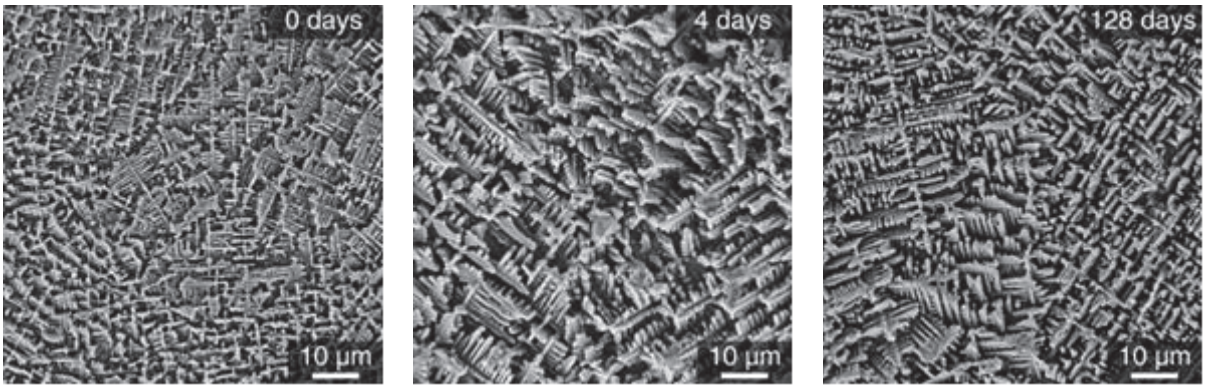

Fig. 1: Evolution of the microstructure of sample LTA3.

The high stability of the KALOS samples' microstructure is attributed to the negligible solubility of lithium orthosilicate and lithium metatitanate, which hampers diffusion-based processes significantly. There can, however, occur favorable circumstances that allow for coalescence of the lithium metatitanate grains to some extent. Probably the crystallographic orientation of the lithium orthosilicate with respect to the lithium metatitanate grains plays an important role in these cases.

The open porosity of the KALOS samples only changes slightly during the annealing, however, the samples show distinctly different porosity values. The mean open porosity decreases in the order LTA1, LTA2 and LTA3 from 4.1% to 3.5% and 2.4%. All samples show an increase in open porosity after annealing for 4 days. For the samples LTA2 and LTA3 the open porosity decreases again with continued annealing to reach slightly higher porosity values than as determined in the as-received state. This decrease is not observable for sample LTA1. The open porosity of the pebbles continues to increase and only slightly drops after 128 days of annealing to a value of 4.3%.

The developing of the total porosity (see figure 2) of the pebbles is dominated by the changes of the closed porosity for the KALOS samples. In terms of closed porosity, all samples behave in a similar way. The closed porosity increases significantly after 4 days of annealing over the as-received state. Annealing the pebbles for longer times reduces the closed porosity more or less distinctively. The closed porosity of the samples LTA1 and LTA3 exceeds the values of the as-received state after annealing for 128 days, whereas the closed porosity of the other samples reaches the as-received values or lie far below. Large drops in closed porosity, observed for the samples LTA4 and LTA5 with increasing annealing duration, offset the high closed porosity values to a certain degree. Yet, the total porosity of these samples is reduced with longer annealing times.

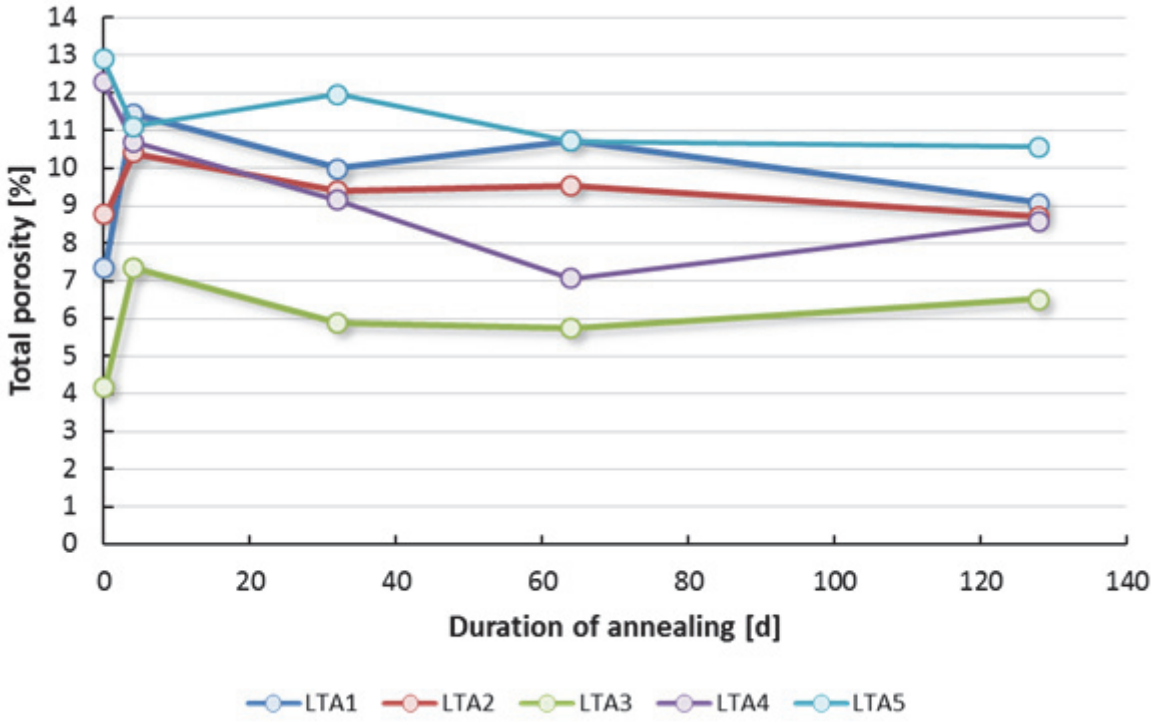

Fig. 2: Developing of the total porosity of the annealed samples.

With the exception of sample LTA3, the annealing in purge gas atmosphere reduces the mechanical rigidity of all other samples compared to the as-received state. The crush loads of the Ø1000 µm pebbles of sample LTA1 drop from a mean of 13.5 N to 6.9 N after 4 days of annealing and then stabilize at about 6.0 N for longer annealing durations (see figure 3). The loss of rigidity of the LTA2 pebbles seems to occur in two separate steps. Both, the 500 µm

pebbles as well as the Ø1000 µm pebbles, lose a significant portion of their strength after annealing for 4 days.

In contrast, the LTA3 pebbles do not show a significant degradation due to the annealing. The crush loads of the Ø500 µm and Ø1000 µm pebbles of this sample significantly increase after annealing for 4 days. While the crush loads of the Ø500 µm pebbles more or less reach a plateau at 9.5 N, the crush loads of the Ø1000 µm pebbles constantly decrease with increasing annealing time until a lower level, at slightly higher crush load values with respect to the as-received values, is reached for the pebbles annealed for 64 days and 128 days. The governing processes of the developing of the crush loads are currently not fully understood.

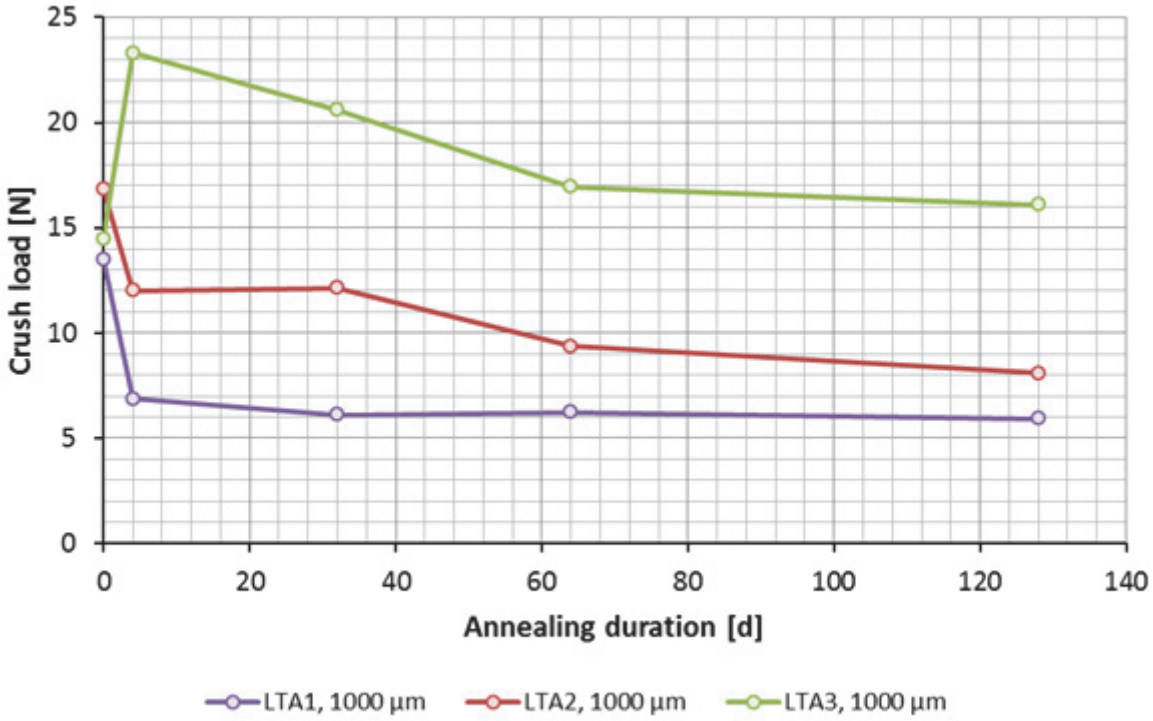

Fig. 3: Developing of the mean crush load of Ø1000 µm pebbles of the annealed KALOS samples.

Before employing the pebbles in a breeder blanket, a significant annealing step is probably necessary as large amounts of water vapor were released from all samples during the first days of annealing, although the samples were carefully dried in advance at 300 °C in a vacuum furnace.

The properties of the pebble samples change significantly as a function of annealing duration. Most changes happen during the first 4 days of annealing with a subsequent stabilization of most properties at a certain level. The processes that govern the changes are not understood completely and therefore have to be investigated in the future. However, the properties measured on as-received pebbles can only be used for process and materials development, as they are not indicative for the behavior of the material in a fusion relevant environment. In general, the properties of all pebble samples are still acceptable after 128 days of annealing for an application in a breeder blanket.

Cooperation with industry

The company Goraieb Versuchstechnik, Karlsruhe, Germany, is involved in the BMBF project to develop an alternative production route for advanced lithium orthosilicate pebbles. The company is responsible for the technical setup and the operation of the facility. The optimization of the facility and the material development is carried out in cooperation with KIT.

Staff:

R. Knitter
M. Kolb
O. Leys
U. Maciejewski
C. Odemer
M. Offermann

Literature:

[1] Knitter, R.; Kolb, M.H.H.; Kaufmann, U.; Goraieb, A.A., Fabrication of modified lithium orthosilicate pebbles by addition of titania. J. Nucl. Mater. 442 (2013) Suppl.1, S433-S436

[2] Leys, O.; Odemer, C.; Maciejewski, U.; Kolb, M.H.H.; Knitter, R., Microstructure analysis of melt-based lithium orthosilicate/metatitanate pebbles. Practical Metallography 50 (2013) 196-203

[3] Leys, O.; Kolb, M.; Goraieb, A.; Knitter, R., Recent developments of the melt-based production of lithium orthosilicate pebbles. 17th International Workshop on the Ceramic Breeder Blanket Interactions (CBBI- 17), Barcelona, E, September 12-14, 2013

[4] Kolb, M.; Leys, O.; Odemer, C.; Frey, C.; Knitter, R., Behavior of advanced ceramic breeder pebbles in long-term heat treatment. 17th International Workshop on the Ceramic Breeder Blanket Interactions (CBBI-17), Barcelona, E, September 12-14, 2013

[5] Kolb, M.H.H., Leys, O., Knitter, R., Long-term annealing of lithium orthosilicate based ceramic breeder pebbles. 11th International Symposium on Fusion Nuclear Technology (ISFNT 2013), Barcelona, E, September 16-20, 2013

[6] Annabattula, R.K.; Kolb, M.; Rolli, R.; Gan, Y.; Kamlah, M., Size dependent crush analysis of lithium orthosilicate pebbles for fusion reactors. 16th International Conference on Fusion Reactor Materials (ICFRM-16), Beijing, China, October 20-26, 2013

[7] Hernandez, F.; Kolb, M.; Annabattula, R.; Bitz, O.; Haefner, U.; Ilic, M.; Schmidt, R.; von der Weth, A., Construction of PREMUX and preliminary experimental results, as preparation for the HCPB breeder unit mock-up testing. 11th International Symposium on Fusion Nuclear Technology (ISFNT 2013), Barcelona, E, September 16-20, 2013

[8] Hernandez, F.; Kolb, M.; Ilic, M.; Kunze, A.; Nemeth, J.; von der Weth, A., Set-up of a pre-test mock-up experiment in preparation for the HCPB breeder unit mock-up experimental campaign. Fusion Eng. Design 88 (2013) 2378-2383

[9] Knitter, R.; Kolb, M.H.H.; Leys, O., Ba DEMO R&D activities on advanced tritium breeders in EU. Jahrestagung Kerntechnik, Berlin, 14.-16. Mai 2013

[10] Knitter, R.; Chaudhuri, P.; Feng, Y.J.; Hoshino, T.; Yu, I.K., Recent developments of solid breeder fabrication. J. Nucl. Mater. 442 (2013) Suppl.1, S420-S424

[11] Mukai, K.; Yasumoto, M.; Terai, T.; Hoshino, T.; Kolb, M.; Knitter, R.; Suzuki, A., Vaporization property of lithium metatitanate and orthosilicate pebbles by high temperature mass spectrometry. 17th International Workshop on the Ceramic Breeder Blanket Interactions (CBBI-17), Barcelona, E, September 12-14, 2013

[12] Munakata, K.; Wada, K.; Nakamura, A.; Kim, J.H.; Nakamichi, M.; Knitter, R., Basic studies on new neutron multiplier and breeder materials. 17th International Workshop on the Ceramic Breeder Blanket Interactions (CBBI-17), Barcelona, E, September 12-14, 2013

[13] Zarins, A., Kizane, G., Knitter, R., Supe, A., Influence of chemisoprtion products of carbon dioxide on radiolysis of tritium breeding ceramic. 11th International Symposium on Fusion Nuclear Technology (ISFNT 2013), Barcelona, E, September 16-20, 2013

[14] Zmitko, M.; Poitevin, Y.; Knitter, R.; Magielsen, L.; van Til, S., Development and qualification of ceramic breeder materials for the EU test blanket module: strategy and R&D achievements. 17th International Workshop on the Ceramic Breeder Blanket Interactions (CBBI-17), Barcelona, E, September 12-14, 2013

Acknowledgement

This work was financially supported by the Ministry of Research and Education (BMBF) under the grant No. 03FUS0012. The views and opinions expressed herein do not reflect necessarily those of the BMBF or the European Commission.

Breeder and Neutron Multiplier Materials: Development of Beryllium and Beryllium Alloy Pebble Beds with Improved Tritium Release Characteristics (BMBF Reference No. 03FUS0012)

Introduction

Titanium beryllide $Be_{12}Ti$ is considered to be one of the candidate materials for neutron multiplier of TBM in future fusion power plants. Attempts to fabricate titanium beryllide specimens using two methods – powder metallurgical fabrication and melting technologies were successfully implemented in Europe and Japan. In the frame of BA activities, Be-Ti rods have to be produced for their further use for fabrication of titanium beryllide pebbles by melting in inert gas atmosphere.

Fabrication of Be-Ti rods

Production of titanium beryllide rod by hot extrusion

The process of fabrication of Be-Ti rods by hot extrusion of blended beryllium and titanium powders is very attractive from the point of view of production of long and high-dense rods.

The powder mixture having the composition of Be-30.8 wt.% Ti which corresponds to stoichiometric content of Be12Ti intermetallic phase was milled down to few μm in size in decalin C10H18 and subsequently extruded at 900 0C in a double-walled container (outer jacket was made out of nickel-chromium steel and titanium inner jacket).

Fig. 1 depicts the cross-section of the extruded at 900 0C Be-Ti rod right after cutting by a disc saw in a glove-box. The diameter of fabricated rod (including steel jacket) is 32 mm.

Fig. 1: Hot-extruded Be-Ti rod inside of a steel jacket.

The Produced Be-Ti rod was cut into discs for further density measurements and investigations of microstructure both in "as-extruded" state and after high-temperature annealing in vacuum at 1000 and 1100 ^{0}C.

Fig. 2 shows XRD patterns corresponding to Be-Ti rod in "as-extruded" (initial) state and after high-temperature annealing tests at 1000 and 1100 0C.

One can observe the tendency of pure Be peaks to disappear after high-temperature heat treatments. While performing the annealing tests, diffusion rates of Be increase with increasing temperature. Thus, beryllium dissolves in complex Be-Ti matrix and forms Be-rich phases (Be17Ti2, Be12Ti). It should be emphasized that in spite of high signal-to-noise ratio observed during XRD measurements of specimen annealed at 1100 0C, pure Be12Ti phase was detected.

Production of Be-Ti rod by high-temperature sintering in vacuum

Several Be-Ti rods were obtained by sintering of blended Be and Ti powders at 1000 and 11000C in vacuum (10-5…10-4 mbar). Although this process is not as time-consuming and expensive as the process of hot extrusion, Be-Ti rods having a density which does not exceed 80% T.D. were fabricated.

Additionally, one of the Be-Ti rods was successfully tested at 4000 rpm using milling machine inside of a glove-box. Fig. 3 shows Be-Ti rod fixed in the machine's chuck after the rotation test. The performed test proved that, in spite of relatively low density, the Be-Ti rod withstands rotation speed which could be used by production of titanium beryllide pebbles.

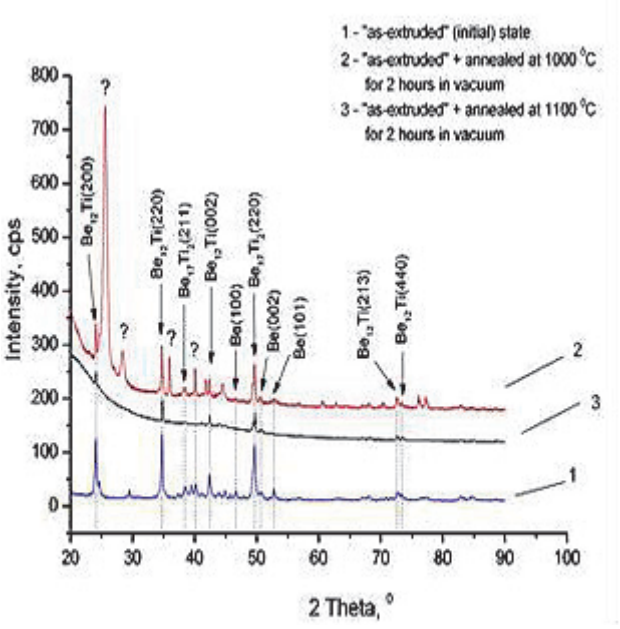

Fig. 2: XRD patterns of Be-Ti rod in initial and annealed states.

Fig. 3: Be-Ti rod right after testing at 4000 rpm.

Staff:

P. Kurinskiy
A. Möslang

Acknowledgement

This work was financially supported by the Ministry of Research and Education (BMBF) under the grant No. 03FUS0012. The views and opinions expressed herein do not reflect necessarily those of the BMBF or the European Commission.

Helium-cooled Blanket Design Development: Simulations performed on HPC-FF: Investigation of MHD Flows in Model Geometries for Liquid Metal Blankets for Fusion Reactors (WP13-DAS-02-T04-02)

Liquid metal flows in helium cooled (HCLL) blankets are expected to be mainly driven by buoyancy forces caused by non-isothermal operating conditions due to neutron volumetric heating and cooling of walls.

Magneto-convective flows in horizontal ducts having electrically and thermally conducting walls have been analyzed numerically for intense magnetic fields [1]. Two configurations are considered. In a first case the flow is studied in slender channels infinitely extended in axial direction, a heat source is distributed uniformly in the fluid and heat is homogeneously extracted from the walls. In a second case magneto-convective flows in a cavity are investigated, both uniform and spatially varying thermal loads are applied and the wall cooling depends on the difference between temperatures of wall and helium coolant. A model has been developed that uses an empirical correlation [2] to simulate the heat transfer from the hot structural material into the helium flow. For both cases isotherms, flow streamlines and electric potential iso-surfaces have been studied for different internal heat sources, i.e. various Grashof numbers Gr in a range between 10^6 and 10^8 corresponding to volumetric heating of about 0.04÷5 MW/m³.

The first simplified case has been selected since it allows getting an overview of the mechanism that determines the onset of convective motions in geometries related to HCLL blankets and the way in which convective instabilities develop from periodic patterns to irregular large time dependent flow structures. When considering a single infinitely long horizontal channel, it is found that if the internal heating is large enough ($Gr > Gr_{cr}$), the stable state, characterized by a parabolic vertical distribution of the temperature, loses its stability and convective motions set in as spatially periodic pairs of counter-rotating rolls with their axes aligned with the horizontal magnetic field. The number of cells depends on the intensity of the magnetic field and on the volumetric thermal load. By increasing the Grashof number instabilities extend towards the lower wall and flow structures become larger. Three main flow regimes have been identified: a 2D stable flow, where a weak convective motion driven by horizontal temperature gradients is present, a first 3D regime characterized by periodic convective rolls aligned with the magnetic field and a second 3D regime in which small structures combine to form larger cells.

In case of three electrically and thermally coupled parallel ducts, the vertical temperature distribution is strongly asymmetric resulting in a significant temperature difference between the two horizontal stiffening plates that depends on the magnitude of the magnetic field (Ha) and the heat source (Gr). Noticeably different flow conditions are present in the three coupled ducts and perturbations in the flow field first occur in the upper duct, then in the middle one and for sufficiently large heat sources in the lower channel. An example is shown in Fig. 1. In the upper duct large irregular structures are present while in the middle channel smaller periodic convective rolls develop. Instabilities start as periodic rolls along the upper stiffening plate where strong temperature gradients are present. The development of convective structures by increasing the volumetric heat source is analogous to the one in a single duct: periodic cells, elongated rolls, larger rotating structures and time dependent instabilities. The numerical results clearly show the importance of the thermal coupling when predicting magneto-convective flows in geometries relevant for liquid metal blanket applications. Fundamental is also the use of realistic electric and thermal conditions of fluid and wall materials.

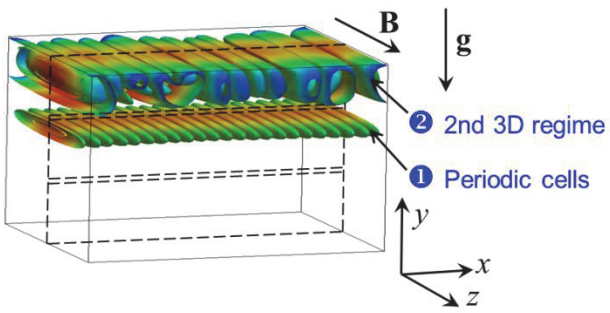

Fig. 1: Iso-surfaces of electric potential for the flow at Ha = 2000 and Gr = 2.2·10^7 in three coupled, infinitely extended ducts.

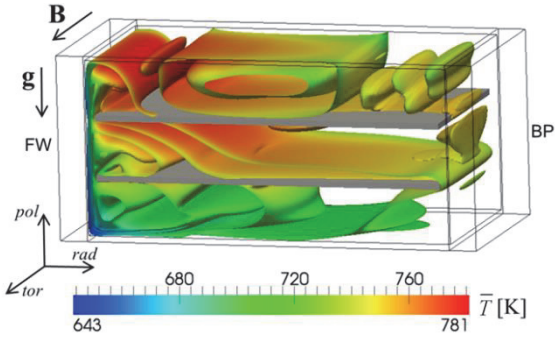

Fig. 2: Iso-surfaces of time averaged electric potential, colored by averaged temperature, for flow at Ha = 2000 and Gr = 1.2 10^8 in a cavity.

Three dimensional numerical simulations have been also performed for magneto-convective flows in a breeder unit of a HCLL TBM when a spatially varying power source is present. Realistic thermal and electrical properties of structural material and liquid breeder have been considered, as well as thermal operating conditions as expected in ITER [3]. The influence of the radial distribution of the neutron load in the lead lithium has been investigated for increasing strength of the applied magnetic field. The non-uniform thermal conditions, caused by the generated neutron power density and heat extraction through the walls, result in complex convective motions in the form of cells of different size with axes aligned with the toroidal magnetic field (Fig. 2). In all investigated cases a large convective stream is present that moves the fluid from the colder FW to the BP and to the upper stiffening plate.

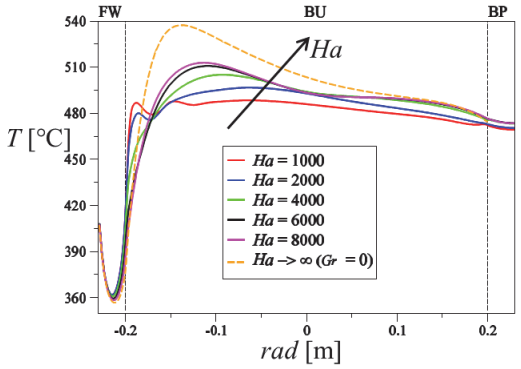

Fig. 3: Radial distribution of time-averaged temperature along the central line of the geometry at y=0, z=0.

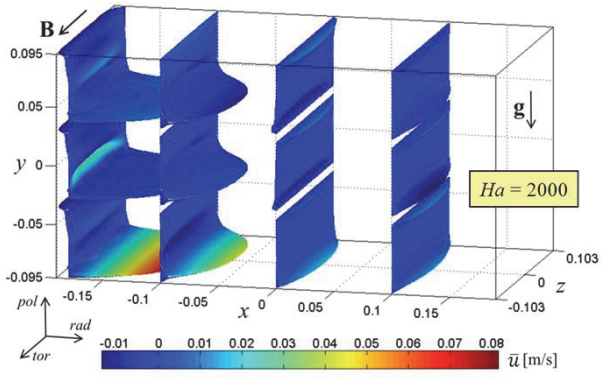

Fig. 4: Time averaged radial velocity distribution in a BU at four x locations for MHD-convective flows at Ha = 2000.

By increasing the magnitude of the magnetic field, i.e. Ha, the average convective motion and perturbations are significantly damped due to the braking action of the stronger electromagnetic Lorentz forces. As a result the velocity decreases and the average temperature becomes larger (Fig. 3 and Fig. 4). The increased mean temperature in the BU when increasing Ha indicates the degradation of the convective heat transfer in the liquid metal (Fig. 3). At the FW an intense downward flow is present due to the significant cooling of this wall leading to the formation of a high velocity jet that enters the lower channel (Fig. 4). As a consequence, a stable density stratification establishes between the lower stiffening plate and the first cooling plate. For flows at Ha = 2000 the temperature difference between these two plates can be of the order of 45-55 degrees. This strong temperature gradient is most likely reduced if the thermal coupling of adjacent breeder units in a column of a TBM is considered; as it will be analyzed in future work.

Staff:

L. Bühler
H. -J. Brinkmann
V. Chowdhury
S. Ehrhard
C. Mistrangelo

Literature:

[1] C. Mistrangelo, L. Bühler and G. Aiello, "Buoyant-MHD flows in HCLL blankets caused by spatially varying thermal loads," IEEE Transactions on Plasma Science, p. in print, 2014.

[2] V. Gnielinski, "Neue Gleichungen für den Wärme- und den Stoffübergang in turbulent durchströmten Rohren und Kanälen," Forschung im Ingenieurwesen A, vol. 41, pp. 8-16, 1975.

[3] R. Villari, L. Petrizzi and F. Moro, "Neutronic analysis for HCLL TBM Preliminary design phase," 2010.

Acknowledgement

This work, supported by the European Communities under the contract of Association between EURATOM and Karlsruhe Institute of Technology, was carried out within the framework of the European Fusion Development Agreement. The views and opinions expressed herein do not necessarily reflect those of the European Commission.

Study on DCLL Flow Channel Insert Fabrication (WP13-DAS-02-T13-03)

The dual-coolant (helium and lead-lithium) blanket (DCLL) is a candidate for DEMO and also possibly for fusion power plants. The original DCLL design version [1] uses SiC_f/SiC flow channel insert (FCI) for MHD pressure loss reduction and thermal insulation functions. The SiC_f/SiC FCI unfortunately has the disadvantage of difficult production and requires a relatively long technological development. Taking into account the tight time line for the DEMO foreseen in the EU Fusion Roadmap, a possible low-temperature design, which allows the use of a relatively low PbLi temperature < 500 °C, is investigated. This enables the use of an alternative, simpler Eurofer-Alumina-Eurofer sandwich FCI instead of the SiC_f/SiC version whose fabrication is more challenging. The focus of the 2013 task is therefore a technological study for the production of such sandwich FCIs.

In this manufacturing feasibility study, a prototype in the scale of 1:4 of the original dimension of an equatorial DCLLSiC_f/SiC flow channel insert (~ 345 mm x 220 mm) was chosen (Fig. 1, top). In principle, a flow channel insert consists of an outer steel casing as the carrier, an alumina intermediate layer as an electrical insulation, and a as thin as possible inner steel plate wall to protect against liquid metal leakage in the ceramic. Two different manufacturing techniques for the production of a bent tube FCI or FCI with nested pipe-in-pipe (Fig. 1, bottom) were first considered. The latter proves to be more complicated in the manufacture, so the bent channel was examined first.

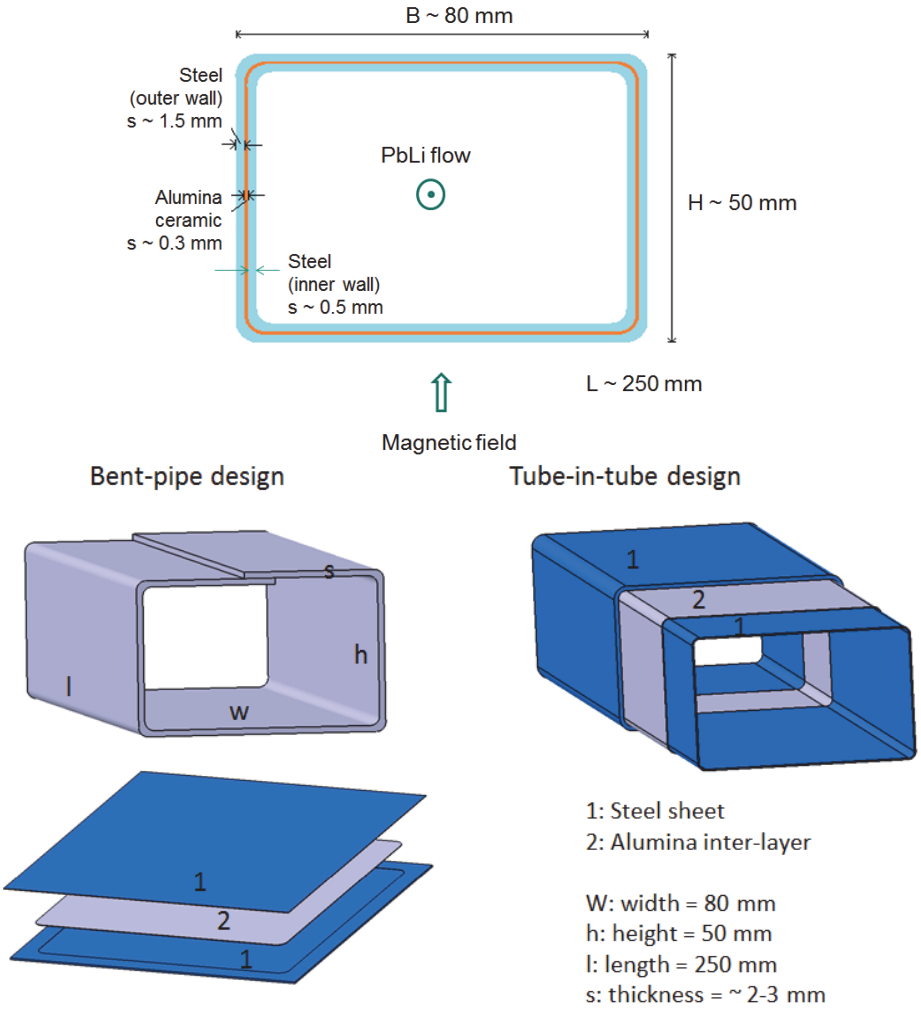

Fig. 1: Basic structure of a sandwich FCI prototype in a scale of ~ 1:4 (top), design of possible types of sandwich FCI (bottom).

Fabrication of a bent-pipe sandwich FCI: The first experiment was started with a 1.5 mm steel sheet as an outer wall (260 mm x 250 mm), a 0.5 mm thick ceramic paper layer (240 mm x 230 mm), and a 0.5 mm steel inner wall (260 mm x 250 mm). The thicker outer sheet metal was milled on the inner surface with a groove of 0.25 mm to accommodate the ceramic paper. Thereafter, the composite sandwich was diffusion-welded in a vacuum oven at a temperature of about 1100 °C, 10 MPa pressure, and 1 h hold time. After diffusion welding the steel plates were joined tightly at the edges. After bending of the diffusion pre-welded sandwich composite, in order to form a channel, wrinkles occurred on the inner wall of the FCI. It was assumed that the reason for this lies in the different thicknesses of the outer and inner cover plates of steel, which result in different degrees of deformation of the plates. Therefore two equally thick steel cover plates of 0.5 mm thickness were applied in a further step. A lower stiffness of the outer structure hereby was accepted, as it may later be remedied with reinforcing strips. In addition, two variants of the ceramic insert were examined, namely, the ceramic paper and ceramic spray. It was also dispensed with the groove of the outer steel plate for accommodating the ceramic interlayer due its smaller thickness.

Fig. 2 shows the results of recent tests with the described changes in the sandwich structure. A further improvement in bending of the sandwich structure has been the use of an aluminum bending core for even more precise dimensional accuracy. In the two experimental variants no wrinkles were observed, as can be clearly seen from the figure. A uniform thickness of the finished sandwiches was achieved. This suggests that the steel sheets and the deformable ceramic layer of paper or spray powder are pressed well together tightly and gap-free. Nevertheless, the so-fabricated flow channel inserts are to be post-examined in a further step. Summarizing it can be said that the so-produced flow channel inserts are a good basis for further qualifications which should ideally be carried out in a liquid metal loop for MHD study.

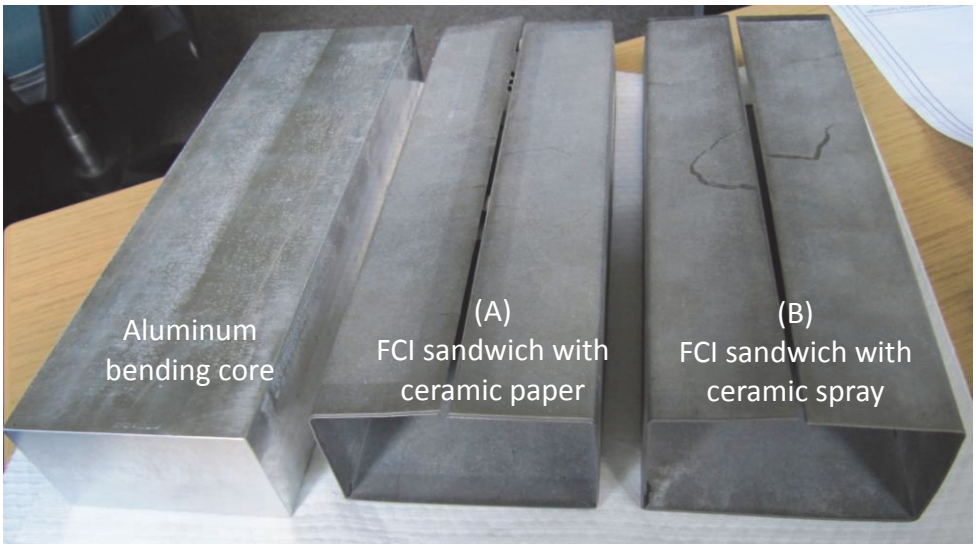

Fig. 2: FCI bending experiment using sandwich composite with equally thick steel cover plates of 0.5 mm without groove, using an Al bending core (left). Two variants of the ceramic insert, ceramic paper (A) and ceramic spray (B), were investigated.

Staff:

P. Norajitra
W. Basuki
A. Hüll
L. Spatafora
V. Toth

Literature:

[1] P. Norajitra, L. Bühler, A. Buenaventura, E. Diegele, U. Fischer, S. Gordeev, E. Hutter, R. Kruessmann, S. Malang, A. Orden, G. Reimann, J. Reimann, G. Vieider, D. Ward, F. Wasastjerna: Conceptual design of the dual-coolant blanket within the framework of the EU power plant conceptual study (TW2-TRP-PPCS12), Final Report, Forschungszentrum Karlsruhe, Wissenschaftliche Berichte, FZKA 6780, 2003.

Acknowledgement

This work, supported by the European Communities under the contract of Association between EURATOM and Karlsruhe Institute of Technology, was carried out within the framework of the European Fusion Development Agreement. The views and opinions expressed herein do not necessarily reflect those of the European Commission.

DCLL Blanket Design: Simulations performed on HPC-FF: Investigation of MHD Flows in Model Geometries for Liquid Metal Blankets for Fusion Reactors (WP13-DAS-02-T13-01)

Numerical simulations have been performed to investigate MHD flows in model geometries of a liquid metal manifold for dual coolant lead lithium (DCLL) blankets [1]. The geometry considered consists of a manifold feeding an array of three parallel poloidal first-wall ducts (Fig. 1). The liquid metal is supplied through an inlet horizontal rectangular channel that expands in toroidal direction into a larger distribution zone. The transition from radial to poloidal flow is achieved by a 90 degree elbow.

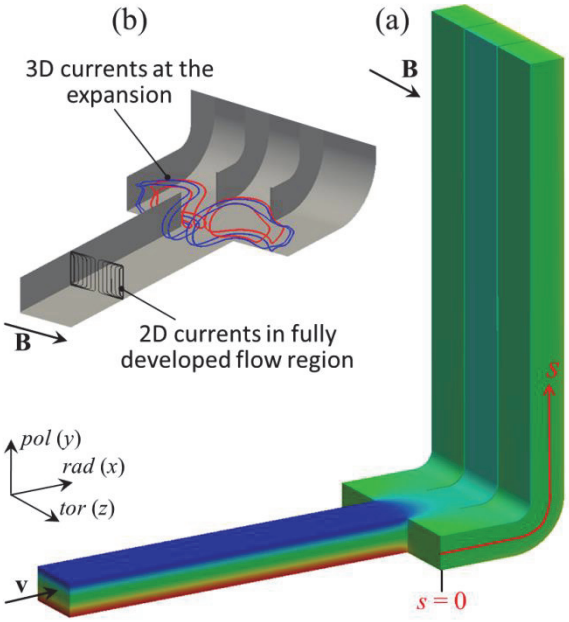

Fig. 1: Surface electric potential distribution: fully developed flow at inlet/outlet and strong 3D effects at the expansion and in the bend.

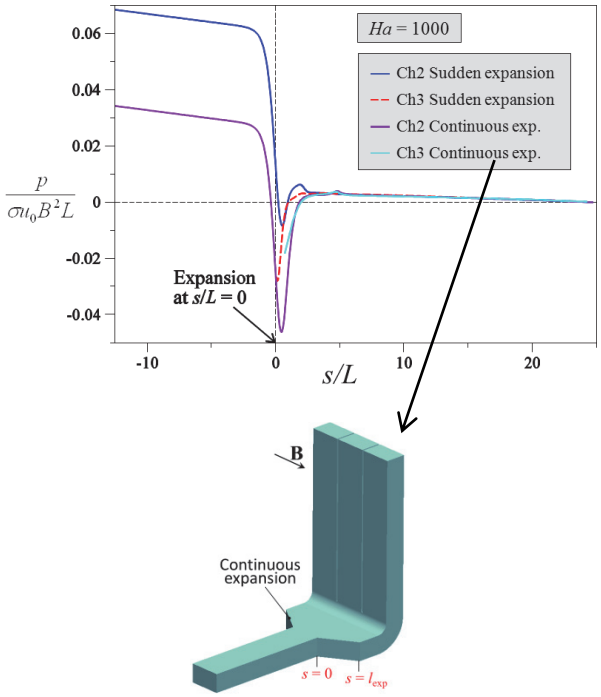

Fig. 2: Axial distribution of scaled pressure in the case of a sudden and a continuous expansion.

Different design options for the manifold are considered to identify geometric features that can affect flow distribution in parallel ducts. Same flow rate among parallel channels is required to ensure homogeneous heat transfer conditions and to minimize the occurrence of locally overheated ducts where larger thermal stresses could occur. Two possible expanding zones are compared, a sudden expansion and a continuous enlargement (Fig. 1 and Fig. 2). We discuss in the following numerical results for a reference MHD flow at Ha = 1000, with an inlet average velocity of about 0.05 m/s. For the description of the results the coordinate s is introduced, which varies along the central line of the geometry. The sudden expansion is located at s = 0 (Fig. 1). In Fig. 1(a) the electric potential distribution is shown on the surface of the manifold. In almost the entire inlet duct the electric potential does not vary in axial direction and electric current paths are contained in 2D cross-sectional planes (see Fig. 1(b)). Near the expansion a streamwise potential gradient occurs, which drives electric currents that close inside the fluid (Fig. 1(b)). The poloidal currents interact with the toroidal magnetic field resulting in streamwise Lorentz forces that brake the liquid metal in the middle of the channel. Electromagnetic forces created by radial currents push the PbLi towards the walls that are parallel to the magnetic field. In Fig. 2 the scaled pressure is plotted along the normalized coordinate s for a sudden and a continuous expansion. In both cases the pressure profiles in the outlet ducts almost coincide, while in the feeding channel the pressure in the case of a continuous expansion is reduced by a factor two. This is due to the fact that the influence of the viscous internal layer that forms at the expansion is less important for longer

expansion length. Moreover, in case of continuous expansion the 3D current loops are longer and the related resistance of the circuit is higher.

The flow partitioning in poloidal ducts is affected by the length of the internal separating walls, by the 3D MHD pressure drop in the expanding zone and by the velocity distribution after the cross-section enlargement. The latter one changes significantly when considering a continuous expansion rather than a sudden one.

Staff:

L. Bühler
H. -J. Brinkmann
V. Chowdhury
S. Ehrhard
C. Mistrangelo

Literature:

[1] C. Mistrangelo and L. Bühler, "Liquid metal magnetohydrodynamic flows in manifolds of dual coolant lead lithium blankets," *Fusion Engineering and Design,* p. in print, 2014.

Acknowledgement

This work, supported by the European Communities under the contract of Association between EURATOM and Karlsruhe Institute of Technology, was carried out within the framework of the European Fusion Development Agreement. The views and opinions expressed herein do not necessarily reflect those of the European Commission.

Definition of Test Blanket System (TBS) Acceptance Criteria and of Required TBS Acceptance Tests (ITER/CT/13/4300000787)

Objectives

The aim of this work was to provide the technical basis for Acceptance Criteria and Tests for ITER Test Blanket Systems.

The objectives of this activity were the following:

- Define the acceptance criteria for each TBS components (or family of components); this definition will give the type of criteria that can be associated to each family of components;
- Identify the acceptance tests that need to be performed on each TBS components (or type of components) in the factory (i.e., before the shipping to ITER Site);
- Identify the acceptance tests that need to be performed on each TBS components (or type of components) in the ITER Site prior to its installation;
- Identify the acceptance tests that can only be performed during TBS commissioning (i.e., after TBS installation);
- Identify possible needs of qualification.

Six different Test Blanket Module concepts will be installed in ITER reactor. Although their are differences in design solutions among the various concepts, a standard approach for the acceptance and test of the various components/subsystems was defined.

Work description

The work was performed in three different stages (phases):

- Phase A - Starting from the TBS Preliminary Safety reports, a list of all the components and their classifications have been prepared; the components have been grouped taking in account the similarities of the individual acceptance tests. In particular, the groups of components that could have a significant impact of ITER Safety and Availability have been clearly identified.
- Phase B - Starting from the list of components, the acceptance criteria that can be applied to each of them (or to each family) have been determined. The qualitative acceptance criteria have been firstly defined based on sound engineering practices. Secondly, proposals for quantitative acceptance criteria are expected.
- Phase C - For each group, the list of acceptance tests that needs to be performed have been identified, including the technical justification of these choices. For the tests a clear distinction has been made between acceptance tests that have to be performed in the factory, the acceptance tests that have to be performed in ITER Site after delivery, and the acceptance tests that can be performed only after installation or during TBS commissioning.

The present document focuses on the tests and the associated acceptance criteria that ITER will perform in order to establish if the component meets the same level of quality as required to ensure the safe operation of the ITER machine.

For the purpose of this document it is assumed that the TBS are designed and built by DAs under the supervision of IO. This means that the procurement of the components and the assembly work and the associated acceptance procedures are going to be mainly under the responsibility of DAs. Due to the complexity of the TBS and since, at the end of the manufacturing process, these systems will be transferred to IO for operation, it is considered as necessary that IO specific acceptance criteria need to be included already in the specifications.

Outcome of the work and remarks

It turned out that the identification of families with common acceptance criteria and tests was difficult to establish using the different classifications. Taking as example the tritium classification, since mostly all components and system have the function of confining radioactivity and are the first barrier, they fall under the highest classification with very high requirements in term of leak rate. The only practicable way to build families was to consider the types of component. The different fluids (He, PbLi, water) or operating conditions (pressures, temperatures) encountered along the different systems seem to a less extend relevant to establish criteria and acceptance tests.

For each type of components, the acceptance criteria have been listed, firstly qualitatively according to the best engineering practices, and in a second phase quantitatively expressed and justified with regards to codes, standards, and requirements coming from several, relevant ITER handbooks. In particular, on component level, the clear distinction between actions required on the factory side, and those needed to be repeated on ITER side has been clearly indicated. On the system level, extension of criteria and test were also systematically described.

As a particular outcome of this work, it should be noticed that

- The type of fluid has limited impact on the acceptance criteria, the sequence of tests, and the quantitative values for final acceptance; as a consequence, TBMs using liquid breeder and their associated PbLi loops have not been particularly detailed since the acceptance strategy should follow the one described in details for He circuits;
- The Tritium Classification imposes likely too demanding requirements for the systems that contains only traces of tritium like HCS and CPS, so that it is recommended to relax these among IO in order to avoid handling case by case deviation requests from DAs;
- The proof pressure tests should be carried out with gas for certain components, and for sure at systems level for most of the gas circuits;
- The time, efforts, and costs associated to the numerous and extensive acceptance tests will ask for a careful analysis to not endanger time schedule and budget (to minimize possible delays or difficulties coming from non-conformity of some of the components and/or system, it is recommended to perform the inspections and tests as early as possible during manufacturing and assembly, ideally on shop where the default part could be more easily replaced and/or repaired).

Staff:

L.V. Boccaccini
D. Carloni
D. Demange
B. Ghidersa

Acknowledgement

This work was supported by ITER Organization under the service contract No. ITER/CT/13/4300000787. The views and opinions expressed herein reflect only the author's views. The ITER Organization is not liable for any use that may be made of the information contained therein.

Supply of Preliminary Fabrication & Welding Procedure Specifications and Feasibility Mock-ups for TBMs EUROFER Subcomponents: Lot-3: HCPB CP FMU and pF/WPS (F4E-OPE-305-03 (TBM-MD))

The design of the cooling plate for the HCPB TBM concept bases on an arrangement with a 180° bending in the front part. The subcomponent fabrication strategy proposed by KIT for the realization of a Cooling Plate Feasibility Mockup bases on machining a cooling channel structure into a plane plate by Wire Spark Erosion. After the fabrication of the channels the plate will be bent. The scope of this task is to develop a set of preliminary fabrication procedure specifications. The fabrication parameters will be demonstrated by a relevant scale FMU which is estimated to be completed for demonstration of the present state of the art achieved by KIT in February 2014.

In 2013, one report related to the contract OPE-305 Lot 3 was concluded and accepted by F4E:

L3.2-D1: HCPB CP - Fabrication Development Plan

- Update of description of fabrication processes/ technologies for fabrication of the FMU
- Technical plan detailing the foreseen development activities (incl. duration and time sequence)
- Updated tentative usage plan of EUROFER semi-finish products up to the fabrication of the
- FMU in focus of last missed detailed process parameters.

Based on the results of these reports the intermediate fabrication experiments have been started and concluded. The definition, preparation and completion of additional fabrication experiments were necessary (e.g. in case of the start hole drilling and erosion procedure) in order to demonstrate the applicability of intermediate scale procedures to relevant scale.

For realization of post fabrication heat treatment a clamping tool turned out to be mandatory; the tool ensures to stay within the tolerance values specified for the front part of the components. The design and the procurement of the tool has been realized in July 2013. In parallel to the fabrication experiment also the destructive and non-destructive examination procedures have been defined and required technology and equipment had been developed and procured.

Presently (end of 2013) the draft version of two reports are almost concluded and will be issued to F4E in January 2014:

L3.2-D2: HCPB CP - Report on intermediate fabrication development and demonstration

- This document gives an overview on the complete fabrication strategy developed for the realization of the HCPB TBM Cooling Plate in the intermediate fabrication phase. It includes detailed documentations of the different fabrication steps developed in the intermediate fabrication experimental phase; also methodologies applied for non-destructive and destructive qualification of fabrication results are reported.

Several test components in relevant length of 850 mm have been fabricated in order to adjust machining parameters related to the start-hole drilling and cooling channel cutting.

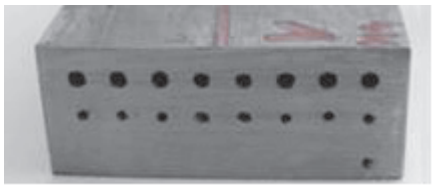

Fig. 1a: 39/S1/1: Intermediate Start-hole/ Wire Cutting MU.

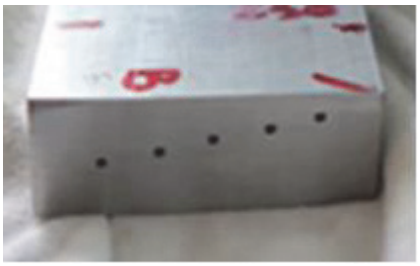

Fig. 1b: 39/A5/1: Start hole MU in production of geometry aspects.

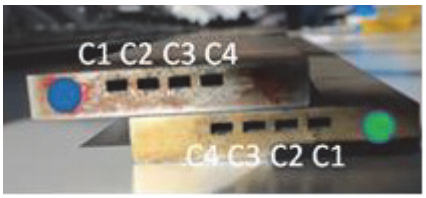

Fig. 1c: 39/A4/1: Final Start-hole/Wire Cutting MU.

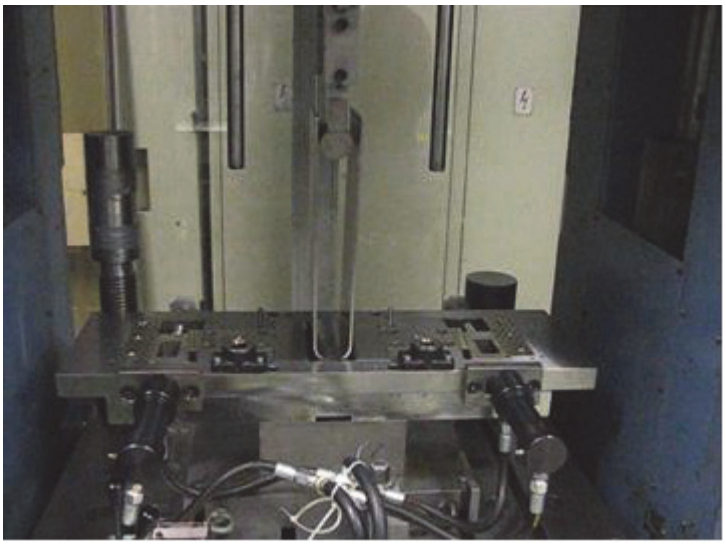

Fig. 2: Fabrication step: 3x point bending of FMU Breeder Unit Cooling Plate (internal radius R25).

L3.3-D2: HCPB CP Reference codes & standards to be used as basis for the development of pF/WPS

- Reference sets of codes & standards have been used as basis for the development of pF/WPS mainly focused to French nuclear code RCC-MR in version 2007

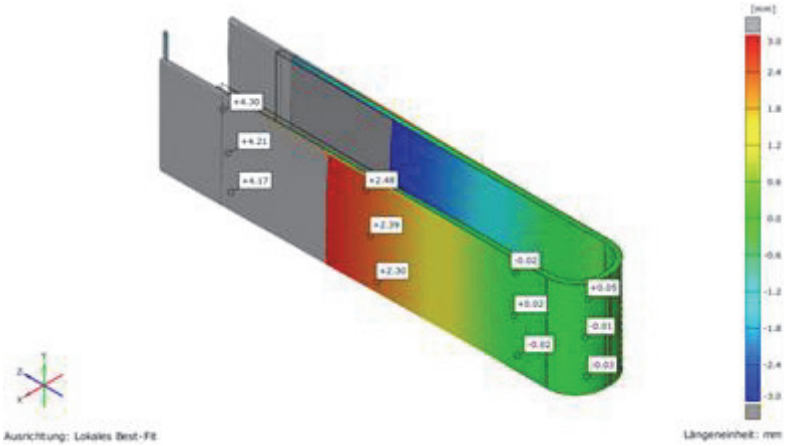

Fig. 3: Laser measurement of half scale mock up (with internal channels) after forming step.

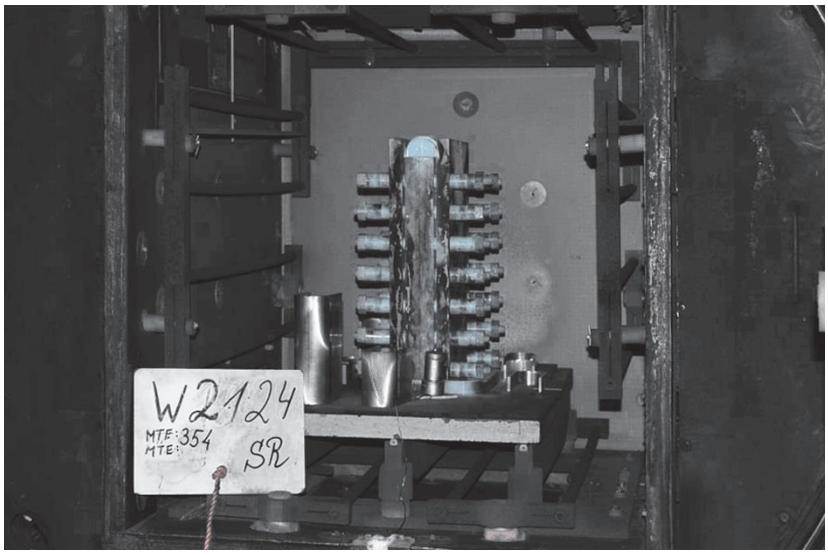

Fig. 4: Same component after forming step II installed in clamping tool.

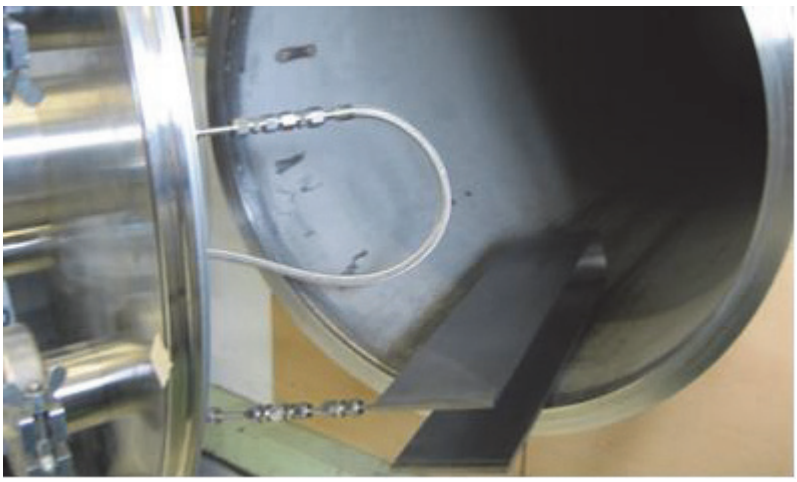

Fig. 5: Leak tightness test of half scale HCPB TBM CP (ITEP). Leak rate max. 1x10-9mbarl/s.

Staff:

P. Freiner
F. Hernandez
H. Neuberger
J. Rey
A. von der Weth

Acknowledgement

This work was supported by Fusion for Energy under the service contract No. F4E-OPE-305-03 (TBM-MD). The views and opinions expressed herein reflect only the author's views. Fusion for Energy is not liable for any use that may be made of the information contained therein.

Design of TBM Ancillary Systems and Integration in ITER (F4E-OMF-331-02-01)

An important step in the development of the conceptual design of the European HCLL/HCPB TBS was carried out in the period 2009-2011, mainly through the implementation of the activities foreseen in the Grant F4E-2008-GRT-09. These activities made available a first set of CAD models, DDDs and interface specifications for all hardware to be installed in ITER for testing the European TBS, namely the TBMs, their ancillary systems and the related maintenance equipment. The completion of the conceptual design in view of CDR (early 2014) and the preparation of the preliminary design for PDR (end 2015) require now the support of more specialized and detailed engineering activities. For instance, detailed technical interfaces with the ITER facility have to be consolidated, iterative design activities are needed to comply with design requirements/specifications requested by IO (e.g. external dimension of TBMs, components integration in buildings, etc.). In addition, the design of the two TBS has to be consolidated with respect to Codes & Standards in view of their future licensing.

The main objective of the Engineering Framework Contract OMF-331 is to provide engineering services related to the development of the European Helium-Cooled Lithium-Lead (HCLL) and Helium-Cooled Pebble-Bed (HCPB) Test Blanket Systems (TBS) for: the completion of the Conceptual Design and the Preliminary Design (CAD models, analyses reports, integration model in ITER, etc.); the preparation of design documents required by IO for the Design Reviews; the consolidation of technical interfaces with ITER; the update of engineering data (e.g. radiation protection, releases during maintenance, etc.), accident analyses and studies for the update of the TBS Preliminary Safety Report; the preparation of standardized procedures for TBM structures assembly by welding and the design of TBM prototypical mock-ups. Within this framework contract there are 5 lots; the second lot, Design of TBM Ancillary Systems and integration in ITER, has been awarded to an ENEA-KIT Joint Team.

The first specific task order (F4E-OMF-331-02-01: Engineering support in the area of Test Blanket Module (TBM) systems design and technological demonstration) is focused on the design and integration in the ITER buildings of the seven ancillary systems of HCLL and HCPB-TBS. Within this task order KIT has been responsible for the design of Helium Cooling System (HCS) of HCLL/HCPB-TBS (Subtask 1) as well as the integration of the ancillary systems in the Port Cell (Subtask 4). KIT provided also technical support in the design of other ancillary systems, the Cooling Purification System, Tritium Extraction system and Tritium Removal system. The work done by KIT under this contract has been focused mainly on a review of the previous HCS design followed by a selection of the technologies for the major components, including a preliminary sizing of the corresponding components. As part of these activities, a preliminary functional analysis of the system has been done and, an updated Process Flow Diagram (PFD) and a new Piping & Instrumentation Diagram (PID) have been produced.

This work has been summarized in a preliminary HCS Sub-system Technical Report (STR) which was delivered to F4E in July 2013. A final version of this document is under preparation and is due in January 2014. This document will include, besides the information included in the preliminary version, a stress analysis of the circuit and reviewed PED, ESPN and tritium classification of the HCS individual components for each of the two European blankets.

Staff:

D. Demange
B. Ghidersa
X. Jin
A. Kunze
M. Lux
A-L Muche
K. Tian

Acknowledgement

This work was supported by Fusion for Energy under the service contract No. F4E-OMF-02-01. The views and opinions expressed herein reflect only the author's views. Fusion for Energy is not liable for any use that may be made of the information contained therein.

Goal Oriented Training Programme “Power Supply Engineering” (WP08-GOT-PSE (FU07-CT-2009-00084)

The Power Supply Engineering plays an important role in the design, operation and exploitation of the fusion experimental devices and relevant test facilities. The role of the power supply engineers in this sense is a key role, as the power supplies are active devices which can be designed, optimized and upgraded to satisfy the requirement. These are the power supply engineers needed for ITER and to form them in this sense is the main objective of this training program.

The training activities are divided into two main areas:

- General engineering training and experience including personal development.
- Training and experience in specific technical areas to conclude with involvement in and/or management of one or more significant technical projects.

In 2013 the general training was finished. No more courses have been done since the work now was focussed on the specific training.

The specific training consists of practical work experience at the HELOKA-HP experimental facility (HELOKA-HP stands for “Helium Loop Karlsruhe – High Pressure”). The object of HELOKA is to test the HCPB-blanket concept and to gain experience in operating such kind of helium facilities. In this sense it also acts as a prototype for the ITER TBM helium cooling system.

In 2013 besides some work for the HELOKA control system most of the time was dedicated to the management of the planning and construction of an experiment to test the feasibility of using an infrared radiation heater for high heat flux experiments up to 500 kW/m². The scope of the work not only encompassed the power supply for the heater (50 kW) but the whole electrical installation of the experiment including instrumentation like temperature sensors, flow meters and pressure sensors, and including the set-up of the control system using LabVIEW. In addition, calculations for the design and layout of the water cooled target plate have been done with ANSYS. The construction is almost completed and the start of the experimental campaign is scheduled for early 2014. Based on the results of the experiment a bigger heater (150…200 kW) will be procured for testing of helium cooled First Wall samples in HELOKA.

With the work on the experiment the training programme has been completed successfully in 2013 after three years. As a result, the Trainee will continue the work on this and other experiments.

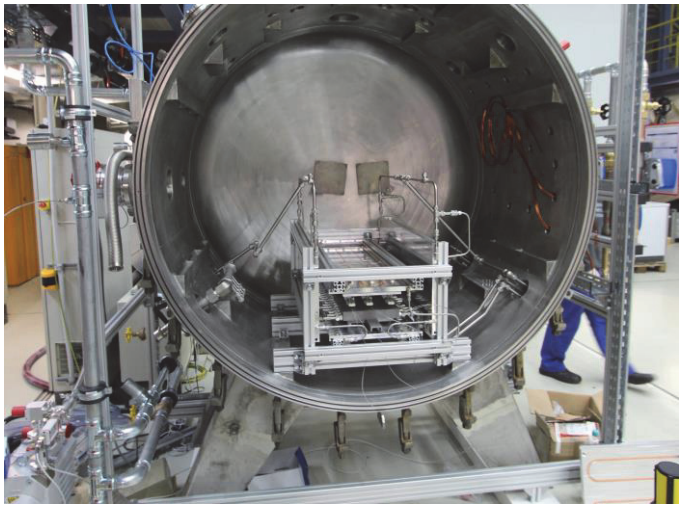

Fig. 1: Partly assembled radiation heater test set-up inside vacuum vessel.

Cooperation with industry

Kraftanlagen Heidelberg GmbH, Germany, contractor:
- installation of water cooling systems

SIEMENS AG Karlsruhe, Germany, contractor:
- implementation of hard- and software into control system

Stapp GmbH, Germany, contractor:
- vacuum brazing of thermocouples

Staff:

A. Kunze

Acknowledgement

This work, supported by the European Communities under the contract of Association between EURATOM and Karlsruhe Institute of Technology, was carried out within the framework of the European Fusion Development Agreement. The views and opinions expressed herein do not necessarily reflect those of the European Commission.

Goal Oriented Training Programme "Project & Quality Management Network for the European Fusion Programme" (WP12-GOT-PQM-NET (FU07-CT-2012-00067))

Introduction / Main Objectives

The aim of the Project & Quality Management Network for the European Fusion Programme (PQM-NET) is to develop in the European Fusion Associations the knowledge of project and quality management sufficiently to allow them to participate fully in the contracts proposed by F4E and in other activities in support of ITER. As a nuclear licensed facility the design, construction, and operation of ITER is subject to rigorous quality standards and detailed project management arrangements not normally required for experimental fusion devices. It is therefore necessary to raise quality awareness and project management expertise across the European Fusion community. To meet this aim the two main objectives of the Network are:

Objective 1 ("ESR Training"): To train four Early Stage Researchers (ESR; or: trainees) to a high level of knowledge regarding project and quality management in relation to ITER and fusion research generally such that they can contribute to ITER related activities within Europe.

Objective 2 ("Wider Scope"): To raise the general level of knowledge of project and quality management amongst the much wider body of engineers and scientists involved in ITER related activities within the European Fusion Associations.

The inclusion of the "Wider Scope" in PQM-NET recognises the special place of quality and project management in the effective and timely delivery of all ITER related activities. It is considered imperative that knowledge of quality and project management is spread to all levels of engineers and scientists across the fusion community and not confined to the limited number of Early Stage Researchers (trainees). The activities of the Network, including those of the parties who do not themselves have a trainee, are designed to deliver training and development opportunities to the staff from all Associations and F4E.

The experience and lessons learned by the PQM-NET partners, both in delivering training and in implementing F4E/ITER projects, is of great value to other Associations in avoiding unnecessary effort in establishing the systems necessary to successfully bid for and deliver ITER related projects.

The "Wider Scope" training programme also foresees the inclusion of project and quality management related events organised by F4E and ITER-IO (if considered beneficial), as well as the participation of staff from F4E and ITER-IO in PQM-NET's training events (e.g. through lectures).

Participants and Organizational Aspects

The seven PQM-NET partners are KIT (Germany; Coordinator), CCFE (United Kingdom), CRPP (Switzerland), ENEA (Italy), HAS (Hungary), IST (Portugal) and SCK-CEN (Belgium). Objective 1 ("ESR Training") is covered by four Associations (KIT, CRPP, ENEA, SCK-CEN) through recruiting and training one Early Stage Researcher each, whereas all seven contribute to Objective 2 ("Wider Scope").

The management of PQM-NET is based on a Work Breakdown Structure (WBS) with specific "Strands" assigned to each participant Association. Each Strand is broken down into Work Packages related to the "ESR Training" and to the work related to the "Wider Scope". KIT, as the lead Association, has an additional Work Package related to the coordination of the Network. Each participant provides the required input related to all their activities (e.g. for the respective deliverables, regular progress reports and monitoring meetings).

The PQM-NET Task Agreement has an overall duration of four years. While the first year was foreseen for the recruitment of all four trainees (with ESR contracts of three years' duration), the "Wider Scope" was decided to start immediately in order to benefit from it as early as possible; i.e. the "Wider Scope" covers all four years.

Status of Project / Achievements (in 2013)

The Entry-Into-Force of the PQM-NET Task Agreement on 01/01/2013 was the formal start of KIT's "Network Coordination & Project Management" activities. Those included, apart from the usual coordination tasks (organisation, meetings, reports, etc.), the setup, customization and maintenance of a "PQM-NET Team Site" which aims at facilitating (internal and external) communication and contains, as a main constituent, different libraries for formal and other relevant documentation.

After the Kick-Off-Meeting had been held at KIT on 29/01/2013, all partners' activities – for both objectives, "ESR Training" and "Wider Scope" – have started.

The four Trainees have been recruited in 2013 as foreseen, with the start dates of the respective ESR contracts as follows (in chronological order): 01/03/2013 (SCK-CEN), 01/06/2013 (CRPP), 09/09/2013 (ENEA), 15/09/2013 (KIT). The corresponding initial Personal Career Development Plans (PCDP) have been established afterwards together with the respective mentors.

With respect to KIT's trainee, the two mentors have started, during and after establishment of the PCDP, with the implementation of the coaching activities as foreseen. Those included thorough introductions to KIT's Fusion Programme, to its Quality Management System (QMS) established for ITER-related Contracts and to the set of customized project management tools in use. Furthermore, KIT's trainee has participated in a "Wider Scope" training course and has been involved in suitable activities of existing contracts (under close supervision of the mentors).

As the first important milestone within the "Wider Scope", the "1st Year (2013) Wider Scope Training Programme" was established (accepted by EFDA on 25/03/2013). This programme consisted of training courses organised by KIT ("KIT-1", "KIT-2"), and by CCFE ("CCF-1", CCF-2").

The two courses under KIT's responsibility, including contributions from various PQM-NET partners and from F4E, have been held at KIT as follows: "KIT-1" ("Existing Quality Management Systems for ITER-related Contracts: Implementation at KIT, CRPP, CCFE, ENEA, HAS, SCK•CEN") from 25/06/2013 – 27/06/2013); "KIT-2" ("Planning Tools & Documentation Management Systems in use for ITER-related Contracts") from 15/10/2013 – 17/10/2013). The corresponding deliverables (i.e. summary documentation of the courses) have been produced, and all presentations are available on the PQM-NET Team Site.

As last milestone within the "Wider Scope" in 2013, the "2nd Year (2014) Wider Scope Training Programme" was established (accepted by EFDA on 12/12/2013). This programme includes training courses to be organised by HAS ("HAS-1"), CCFE ("CCF-1", CCF-2"; repetition and updated as appropriate) and IST ("IST-1").

Conclusions & Outlook

In its first year (2013, PQM-NET was running as originally planned (see above).

In 2014, KIT's activities with respect to coordination of PQM-NET, "ESR Training" and "Wider Scope" are expected to continue as foreseen.

Staff:

J. Gafert (PQM-NET Coordinator; Mentor No.1 - shared)
Ch. Schweier (Mentor No.2 - shared)
M. Oron-Carl (KIT's trainee)

Acknowledgement

This work, supported by the European Communities under the Contract of Association between EURATOM and Karlsruhe Institute of Technology, was carried out within the framework of the European Fusion Development Agreement. The views and opinions expressed herein do not necessarily reflect those of the European Commission.

Divertor

Design and Fabrication of Square Finger Mock-ups (WP13-DAS-02-T12-02)

A study on the integration of the helium-cooled cooling fingers to the target plate has shown among other that the hexagonal shape of the tile despite the demonstrated feasibility of its integration and assembly to form a target plate offers a low degree of flexibility in adapting to any change in the geometry of the reactor. In addition, the jagged edges of the target plate with hexagonal honeycomb shape require a greater angle of inclination for sufficient shading. To facilitate the integration of helium-cooled divertor target plates, therefore, straight target edges would be preferable to jagged ones. Another concern was raised regarding the embrittlement of the structural tungsten alloy thimble below 700 °C. The dilemma of a divertor design is that the irradiated material data for the used tungsten and tungsten-based materials are unknown. The assumption for the lower operating temperature window of the refractory metals are based on conservative estimates under expectations of large increase in hardening at low neutron irradiation temperatures < 0.3·Tm.

Fig. 1: Design and fabrication of square finger mock-ups: Individual component parts machined (top); diffusion bonding of W tile and Ta-10W thimble with Ti interlayer (bottom left); brazing Ta-10W thimble with steel transition tube with PdCu filler (bottom right).

Another study on alternative design has additionally revealed that the use of a tantalum alloy, such as T-111 (Ta-8wt%W-2wt%Hf) or another commercially available substitute material with similar doping, for the thimble instead of WL10 may satisfy the requirements, when

working at a coolant temperature of 350 °C. This solution even offers the advantage to avoid the need for ODS steel (for ease of joining of components, since ODS steel is not fusion-weldable).

A new design of a square-shaped finger has been proposed which is based on 17.1 mm tile size and Ta alloy material for the thimble (Fig. 1, top). Its thermal-hydraulic performance and temperature loading on the structure materials is evaluated using the code ANSYS-CFX. The sensitivity analyses were performed for two different surface heat fluxes (10 MW/m^2 and 8.7 MW/m^2), two mass flow rates (6.8 g/s and 9 g/s) and two helium inlet temperatures (350 °C and 450 °C). The results were also compared with previous simulations for the 16.5 mm square finger. All in all, the performed CFD analyses have confirmed the 10 MW/m^2 performance of the new divertor cooling finger design. This forms the basis for the production of such cooling fingers for future HHF tests. In this fabrication task with the production focus for cooling fingers, the commercially available alloy Ta-10W (Plansee Company) was selected as a replacement for T-111. The production of the cooling fingers took place in several steps, starting with the mechanical production of the component parts (Fig. 1, top). In the first joining step, a tungsten tile and a Ta-10W thimble were diffusion-bonded using Ti interlayer at a material-friendly temperature of 900 °C (Fig. 1, bottom left), a joining technique which was newly developed. In the second joining step, the Ta-10W thimble was connected with the steel sleeve by means of brazing using Pd18Cu82 filler (Fig. 1, bottom right), a well-developed brazing technology for the production of the multi-finger divertor modules. No retroactive effect of the elevated brazing temperature on the diffusion-bonded joint was detected in a post-examination. Multiple follow-up examinations have also confirmed the perfection and applicability of the produced cooling finger made from combined materials W, Ta-10W, and steel, which mean that the so-produced divertor cooling fingers are in an optimal state.

Staff:

P. Norajitra
W. Basuki
L. Spatafora

Acknowledgement

This work, supported by the European Communities under the contract of Association between EURATOM and Karlsruhe Institute of Technology, was carried out within the framework of the European Fusion Development Agreement. The views and opinions expressed herein do not necessarily reflect those of the European Commission.

Prototype Cooling Structures (WP13-MAT-HHFM-05-01)

Introduction

Coarse grained tungsten (W) is known to be a brittle material with a low fracture toughness (e.g. 5 MPa $m^{1/2}$ at RT) and a high brittle-to-ductile transition temperature (BDTT). The situation appears different for tungsten in the shape of a thin foil. W foil with a thickness of 100 μm, has a BDTT of -120 °C (strain rate = $3*10^{-2}$ 1/s) and a fracture toughness of 70 MPa $m^{1/2}$ at RT (L-T orientation, source R. Pippan, Leoben). These extraordinary properties can be related to the ultra-fine grained (UFG) microstructure of the W foil in its as-received condition.

Through the assembly and joining of several of these UFG W foils the extraordinary properties of a foil can be transferred to the bulk.

By rolling up and joining W laminate pipes can be produced that show extraordinary Charpy impact properties and an excellent behaviour in burst test. Furthermore the joining of a W laminate pipe to a steel pipe is possible which allows fabricating testable mockups.

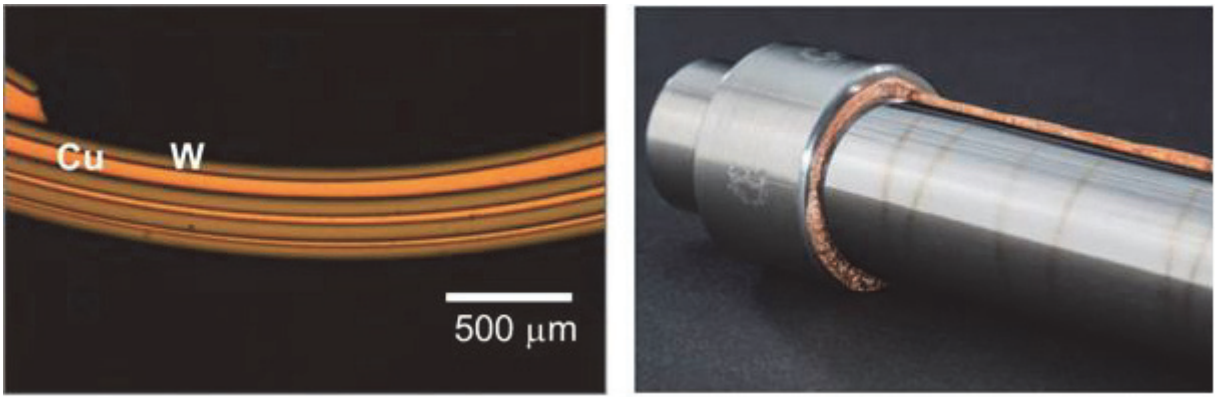

Fig. 1: Left: By rolling up and joining a W laminate pipe can be produced. These pipes have extraordinary mechanical properties. Right: A W-Cu laminate pipe is joined on both ends to a pipe made of austenitic steel. The joining of W laminate pipe to steel pipe works excellent.

Mockups based on a W laminate pipe and water coolant

The idea is to use a W laminate pipe with water coolant for a DMEO divertor. As it is very likely that W is getting brittle under neutron irradiation at low temperature it is aimed to user water in the pressurized water reactor (PWR) condition being T_{in} = 275 °C, T_{out} = 325 °C, 160 bar. At these water temperatures however corrosion of W becomes an issue. This is why a W corrosion protection layer made of an austenitic steel pipe (316Ti, 1.4571) is used as a water facing material. The setup of such a mockup can be seen in the figure below, left side.

HHF tests were performed at the IPP in Garching at GLADIS by H. Greuner. The test conditions were water, 20 °C, 10 bar, 1.13 l/s, 20 s beam on, 40 s beam of. The mockup during the HHF test can be seen in the figure below, middle right side.

The results show that at 6 MW/m^2 and 100 load cycles there is no change in the surface temperature showing that the mockup can bear at least this heat load. At 7 MW/m^2 however the surface temperature increases cycle by cycle indicating a change in the mockup. The test were stopped after several cycles and the post examination show that at 7 MW/m^2 the Cu interlayer between W laminate pipe and W saddle armour melted.

It can be concluded, at testable mockups using a W laminate pipe and an austenitic pipe corrosion protection layer works. Next steps might be to decrease the thickness of the steel pipe from 1 mm to 0.1 mm.

Fig. 2: For water in the PWR condition an austenitic steel pipe is used as a corrosion protection layer for the W laminate pipe. Successful tests were performed at the IPP in Garching (GLADIS, H. Greuner). Next steps might be to decrease the thickness of the steel pipe from 1 mm to 0.1 mm.

Mockups based on a W laminate pipe and helium coolant

Within this study we present a design and mockup for a He-cooled divertor based on a W laminate pipe. The design of the mockups is similar to that of an ITER inner or outer vertical target, meaning a pipe being surrounded by pure W armor material in a monoblock shape. The W monoblocks have the original ITER dimensions of 12 mm x 30 mm x 32 mm, 16 mm hole. Different to the ITER design the structural cooling pipe is made of a W-Cu laminate pipe that is joined on both ends on austenitic steel pipes. It is worth to mention that the joining of W-Cu laminate pipe to austenitic steel pipes works perfect. As known from the finger concept HEMJ, the heat transfer coefficient can be increased by jet impingement. In the mockup presented here the jet impingement is realized by a steel cartridge being positioned inside the W-Cu laminate pipe.

Objective of this study was to prove the feasibility of a proper fabrication process. This objective was successfully reached. In a next step the performance of the mockups will be assessed by HHF tests.

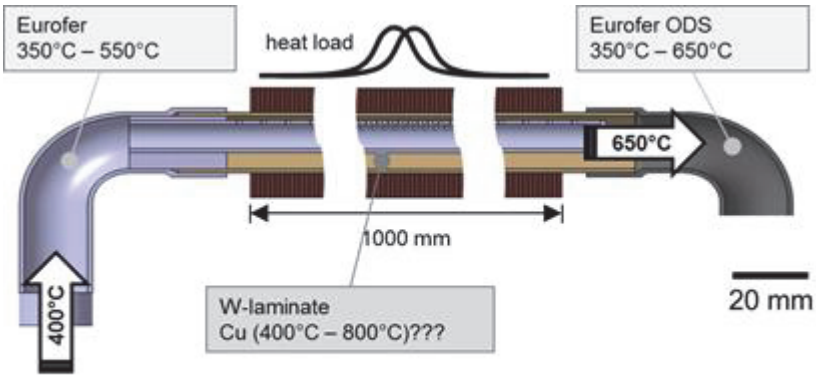

Fig. 3: Concept of a He-cooled divertor based on a W laminate pipe. The jet impingement to increase the heat transfer coefficient is realized by a cartridge positioned inside the W laminate pipe.

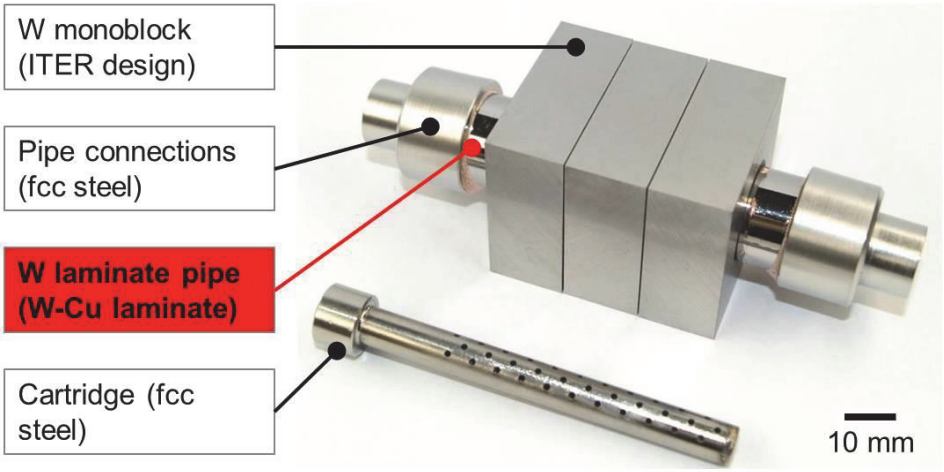

Fig. 4: Mockup for a He-cooled divertor. This picture shoes the result of a successful fabrication study of the concepts mentioned above. In a next step the performance of the mockups will be assessed by HHF tests.

Burst test / HRP device for W laminate pipes

The burst test device is of significant importance for the development of a divertor due to two reasons:

1. The answer whether or not W laminate pipes show leak-before-failure has to be answered and
2. W laminate pipes with high melting interlayer like Ti, V, or no interlayer at all have to be fabricated by hot radial pressing (HRP) at 900 °C, which will also be performed by this device.

The work is in progress. No significant news can be reported here.

Fig. 5: Setup of a burst test / HRP device. The performance planed is 900 bar and 1100 °C, Ar gas.

Spin of project: W laminate pipes for concentrated solar power (CSP)

In the field of concentrated solar power meaning for towers or dishes, there is a need for materials beyond Ni-base super alloys. A W laminate might be an option as W is the metal with the highest melting point of all metals (Tm = 3422 °C) and has excellent behavior towards liquid metals. In this context a proposal to test W laminate pipes at the Plataforma Solar de Almeriá (PSA) was successfully approved. Within last summer W laminates were tested at PSA showing that we are able to produce testable W laminate pipes.

Fig. 6: W laminate pipe tested at PSA. The laminate pipe is coated with a black surface (H. Leiste, KIT, IAM-AWP) for a high absorption and low reflection of the sun light. On both ends the laminate pipe is joined to steel pipes made of austenitic steel. The HHF tests at the PSA were performed with water as cooling media. The W laminate pipe has a diameter of 15 mm and a wall thickness of 1 mm.

Staff:

S. Baumgärtner
D. Bohlich
B. Dafferner
M. Hoffmann
U. Jäntsch
A. Möslang
A. Németh
J. Reiser
M. Rieth
R. Ziegler

Literature:

[1] J. Reiser, M. Rieth, A. Möslang, et al., 'Tungsten (W) foil laminate pipes for innovative high temperature energy conversions systems', under review.

Acknowledgement

This work, supported by the European Communities under the contract of Association between EURATOM and Karlsruhe Institute of Technology, was carried out within the framework of the European Fusion Development Agreement. The views and opinions expressed herein do not necessarily reflect those of the European Commission.

First Simulations Concerning Liquid Metals in Tokamaks Divertor - CPS and Free Flowing Liquids (WP13-PEX-03b-T05-01)

The aim of the present study is providing a first description of the behavior of a liquid metal in a capillary porous system (CPS) when an external uniform magnetic field is imposed in order to judge about the feasibility from the magnetohydrodynamic (MHD) point of view of the CPS technology for steady-state divertor applications [1] [2]. The final objective is estimating a permeability tensor $\mathbf{K}$, which relates the pressure gradient and the fluid velocity (volume flux), to be used for a macroscopic description of the problem. MHD liquid metal flows in a model porous structure have been analyzed for strong imposed magnetic fields. The permeability tensor $\mathbf{K}$ has been determined by means of numerical simulations of liquid metal flows in a microscopic representative fluid volume. Most of the discussed results are obtained for a magnetic field $\mathbf{B} \simeq 4.5$ T ($Ha = 50$, where the Hartmann number Ha is a non-dimensional measure for the magnetic field strength). The effects of the reciprocal orientation of the forcing pressure gradient and the magnetic field have been studied. Numerical results show that, independently of the orientation of $\mathbf{B}$, the permeability $\mathbf{K}$ strongly reduces in a MHD flow compared to the one in the corresponding hydrodynamic Darcy regime (Re<1). Due to the known fundamental role of the magnitude of the induced current density in determining electromagnetic Lorentz forces and hence the pressure heads that balance those forces, the impact of various electric boundary conditions on the permeability has been carefully investigated.

By progressively increasing the strength of the imposed magnetic field, i.e. the Hartmann number Ha, the dimensionless pressure gradient G_{ij} becomes larger and it varies as $G_{ij} = K_{ij}^{-1} \sim Ha$ for electrically insulating boundary conditions and as $G_{ij} = K_{ij}^{-1} \sim Ha^2$ in the case of a perfectly electrically conducting porous system. The most critical conditions in terms of pressure drop are those where wires and external domain are perfectly conducting.

Under these conditions it is found that for a flow at $Ha = 50$ the permeability is 50 times smaller than in the corresponding hydrodynamic flow. Additional studies should be performed to define the range of validity of Darcy's law for MHD flows, i.e. it is necessary to identify the maximum Reynolds number Re for which a linear relation between pressure gradient and velocity can be verified. When Re becomes too large the influence of inertial forces increases and this can cause deviations from Darcy's law.

The present study has been performed by considering lithium as model fluid, but the results are presented in terms of non-dimensional parameters and therefore they become independent of the selected working fluid.

A behavior analogous to the one described in the present work is expected when operating with another liquid metal in the same parameter range.

Staff:

L. Bühler
H. -J. Brinkmann
V. Chowdhury
S. Ehrhard
C. Mistrangelo

Literature:

[1] M. Ono, M. Bell, Y. Hirooka, R. Kaita, H. Kugel, G. Mazzitelli, J. Menard, S. Mirnov, M. Shimada, C. Skinner and F. Tabares, "Conference Report on the 2nd International Symposium on Lithium Applications for Fusion Devices," Nuclear Fusion, vol. 52, p. 037001, 2012.

[2] S. Mirnov, "Plasma-wall interactions and plasma behaviour in fusion devices with liquid lithium plasma facing components," Journal of Nuclear Materials, vol. 390, pp. 876-885, 2009.

Acknowledgement

This work, supported by the European Communities under the contract of Association between EURATOM and Karlsruhe Institute of Technology, was carried out within the framework of the European Fusion Development Agreement. The views and opinions expressed herein do not necessarily reflect those of the European Commission.

Structural Materials – Steels

Production and Characterization of Laboratory-scale Batches of Nano-structured ODSFS (WP13-MAT-ODSFS-01-02)

Introduction

Concepts for future generation fusion reactors have demanding requirements for the structural materials. The high neutron doses and elevated temperatures form a harsh environment in which present materials cannot be used. A new class of oxide dispersion strengthened (ODS-) materials which are currently being developed have a high chance of meeting these requirements.

Production of ferritic ODS alloys at KIT has been successfully demonstrated in the last years under the EFDA framework. These studies focused mainly on lab scale batches and were dedicated to mechanical and to microstructural characterization. The optimization were performed under the objective of improving Charpy impact properties and the examination of the evolution of crystallographic textures during thermo-mechanical treatments like hot rolling or hot extrusion. These studies were successful and led to optimized ferritic ODS alloys on a laboratory scale.

The application of ferritic ODS steels depends strongly on the availability of larger amounts of materials. This can only be achieved by up scaling current production processes or adapting new methods.

Materials and Methods

The objective of this work is the adaptation of the current production process for lab scale batches of ODS steels to meet the requirements for large scale and semi industrial production. This also includes considerations if each step of the production route can be up scaled. If this is not the case, alternatives need to be explored and examined. This objective is divided into several sub tasks:

Work on powder processing:

a. *Powder fabrication:* a large batch of 30 kg of pre-alloyed ferritic powder is ordered from Nanoval in Berlin. A suitable composition needs to be chosen for a low activation ODS steel
b. *Powder characterization (as-received condition):* The pre alloyed powder in the as-received state is going to be examined by chemical analysis.
c. *Powder preparation and blending:* In order to be mechanically alloyed, the powders need to be mixed with Yttrium. The objective is to add as less oxygen as possible.
d. *Mechanical alloying:* After successful production of lab scale batches in a small Attritor mill, the possibility of up scaling these techniques is examined. Larger batches of powders are sent to Zoz GmbH for mechanical alloying.
e. *Powder sieving:* To clarify the influence of the particle size on the resulting grain size after compacting, the powders need to be sieved into 2 fractions.
f. *Powder characterization (as-milled condition):* The powder in the as-milled state is going to be examined by chemical analysis and SEM images. Special attention is paid to the levels of impurities which were taken up during the mechanical alloying. Good materials properties can only be achieved by keeping these levels as low as possible.

Powder consolidation process:

a. Layout of container parts: The current container design is suitable for batches up to approx. 1 kg. The layout needs to be adapted to fit more powder and allow the degassing of the whole container. Preferably, a design with two suction pipes should be created to ensure complete evacuation of the capsule during the degassing process.

b. *Filling of the capsules:* The capsules are filled inside an Argon filled glove box. The current process needs only minor adaptations, since the filling process was already capable of handling larger amounts of powders. The two size fractions of powders are going to be canned each individually.

c. *Setup for degassing:* The filled capsules need to be heated up to 500°C for the degassing process. The furnace which has been used in earlier studies cannot fit the new capsule design due to the larger diameter. It is also not possible to degas from multiple ends of the cans. The whole setup needs to be changed to ensure homogeneous heating and degassing from both ends of the can.

d. *Sealing procedure:* For the HIPing process, the capsules need to be sealed after degassing. The sealed suction pipes have to withstand the high pressures during the compacting and ensure tightness during the whole process. Previous sealing techniques led to inconsistent results. Some capsules failed to compact during hot isostatic pressing. A new and more reliable method needs to be developed.

e. *HIP:* Consolidation of the materials by hot isostatic pressing. The process is well known and can be easily adapted to larger batches of material.

f. *Hot rolling:* Hot rolling at temperatures around 1100°C has been successfully performed on small batches of materials. During the multiple passes of the rolling, it needs be ensured that the temperature in the material is homogeneous. However, due to the larger volume of the material, keeping the temperature constant should be easier.

After production

a. *Removal of the capsule sheet:* Since all the thermo-mechanical treatments are performed with the capsule sheet still on, the outer material needs to be removed. This can be done by either mechanical milling or electro discharge machining.

b. *Specimen fabrication:* Specimens for standard mechanical characterization are fabricated by electro discharge machining.

Characterization

a. The produced materials need to be examined by electron microscopy (*Microstructural characterization)* to prove the existence of nano-clusters and a fine and uniform microstructure.

Results

The results corresponding to the task given above are described here:

1. Low-activation ferritic steel was chosen as a pre-alloyed composition. The alloy contents are described in the table below (table 1).

   Table 1 Composition of pre-alloyed powder.

Element	Fe	Cr	W	Ti	O	C
[%]	bal.	13	1	0.3	ALAP	ALAP

   The powder in the as-received condition was analysed by the chemical analytics department of the IAM-AWP institute. The results are given in the table below (table 2). They show that the powder was produced with the correct chemical composition and the quantities of the alloying elements were in the specified ranges. Especially carbon and oxygen levels, which are crucial for the mechanical properties, are low in this stage of the production route.

   After mechanical alloying, the particle size distribution was measured by a Laser Particle analyzer. The results are shown in Figure 1. The powder was separated into two size fractions by sieving. The shape of the powder particles in the two different size regimes were characterized by SEM (Figure 2 + 3).

Table 2: Chemical analysis of the powder in as-received condition (values in wt.%).

element	average value	SD
B	< 0,005	-
C	0.0078	0.0002
N	0.0039	0.0003
O	0.038	0.001
Al	0.0049	0.0001
Si	< 0,05	-
S	0.0037	0.00007
Ti	0.152	0.0150
Cr	13.3	0.05
Co	0.0019	0.0002
Ni	0.0193	0.0002
Cu	0.0095	0.0002
Y	< 0,005	-
Nb	< 0,001	-
Mo	0.0015	0.00003
W	1.17	0.020
S	**14.7125**	**-**

Table 3: Chemical analysis of the powder in as-milled condition (values in wt.%).

Size fraction	< 90 µm		> 90 µm	
element	**average value**	**SD**	**average value**	**SD**
B	< 0,005	-	< 0,005	-
C	0.0216	0.0004	0.0214	0.0001
N	0.0098	0.0004	0.0101	0.0001
O	0.087	0.002	0.081	0.001
Al	0.0061	0.0000	0.0061	0.0001
Si	< 0,05	-	< 0,05	-
S	0.0040	0.00005	0.0039	0.00005
Ti	0.152	0.0001	0.151	0.0002
Cr	13.1	0.01	13.1	0.01
Co	0.0071	0.0001	0.0072	0.0000
Ni	0.0876	0.0009	0.0894	0.0005
Cu	0.0118	0.0001	0.0118	0.0001
Y	0.199	0.02500	0.217	0.00040
Nb	< 0,001		< 0,001	-
Mo	0.0029	0.00010	0.0030	0.00010
W	1.13	0.002	1.11	0.003
S	**14.8189**		**14.8119**	

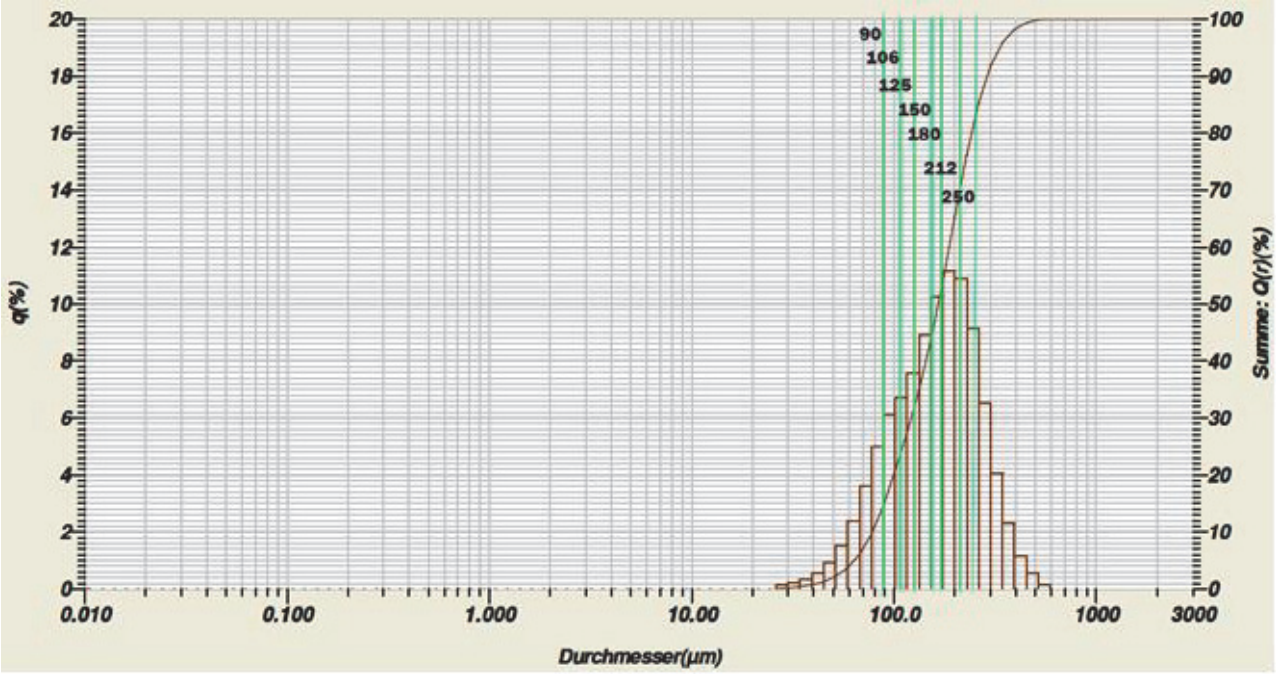

Fig. 1: particle size distribution in as-milled condition:

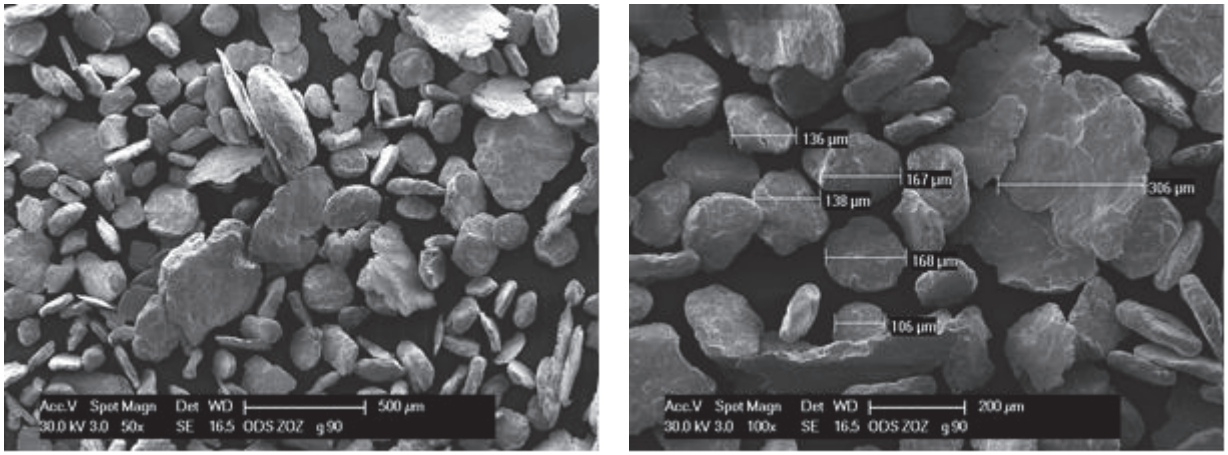

Fig: 2: SEM image of powder >90 µm.

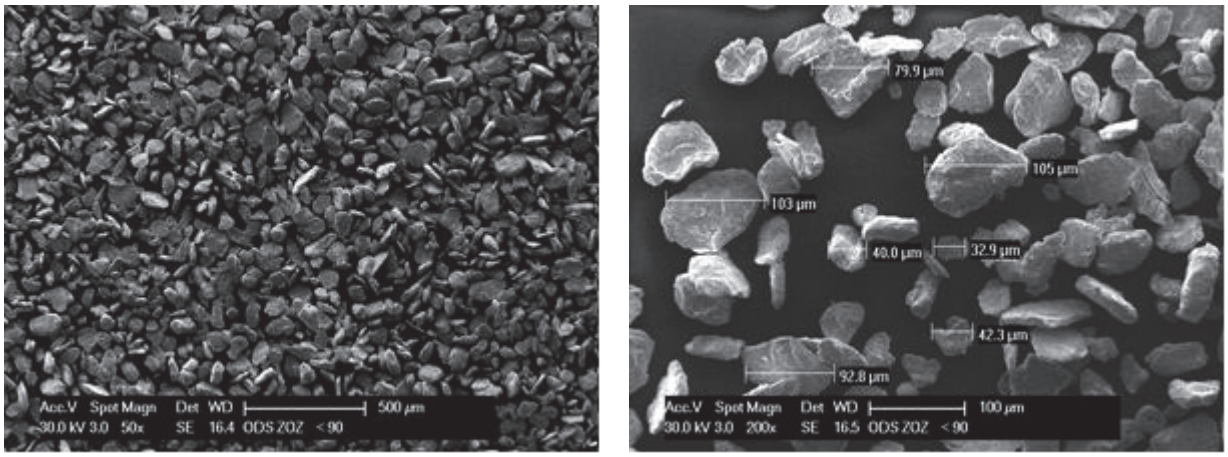

Fig. 3: SEM image of powder < 90 µm.

2. The layout of the container parts was modified. Earlier designs featured only one suction pipe at the top of the can. A second pipe on the bottom was added to ensure the complete degassing of the capsule. To fit the larger amount of powder, the size was increased but the height to diameter ratio was kept nearly constant. This ensures similar deformation behaviour during the hot isostatic pressing.

Figure 4 shows the new capsule design with all parts. This design features the two suction pipes attached to top and bottom lids and Swagelok components for the connection to the vacuum system. Two small filter pieces (seen in the middle right of the image) inside the suction pipes ensured that the filling could be performed without powder leaving through the bottom pipe.

Fig. 4: Stainless steel container.

The capsules were filled in an Argon-filled glove box. The powder was pre-compacted by hand to in-crease the density of the powders inside the can. A filling density of 54 % was achieved. The cans were sealed by TIG welding inside the box without exposing the powder to air.

Figure 5 Filling of the capsules inside an Argon-filled glove box.

The new setup for the degassing can be seen in Figure 6. A new furnace was bought, which could fit the larger capsule and allowed access to both bottom and top side. Swagelok adaptors with valves on both suction pipes were used to attach the can to the vacuum system. After evacuation of the capsule for more than 12 hours to a level of 10-5 mbar, the furnace was heated to approx. 600°C and held there for 4 hours. At the end of the degassing, the furnace was switched off and the capsule was left to cool inside. The vacuum pump was only switched off right before the capsules were sealed.

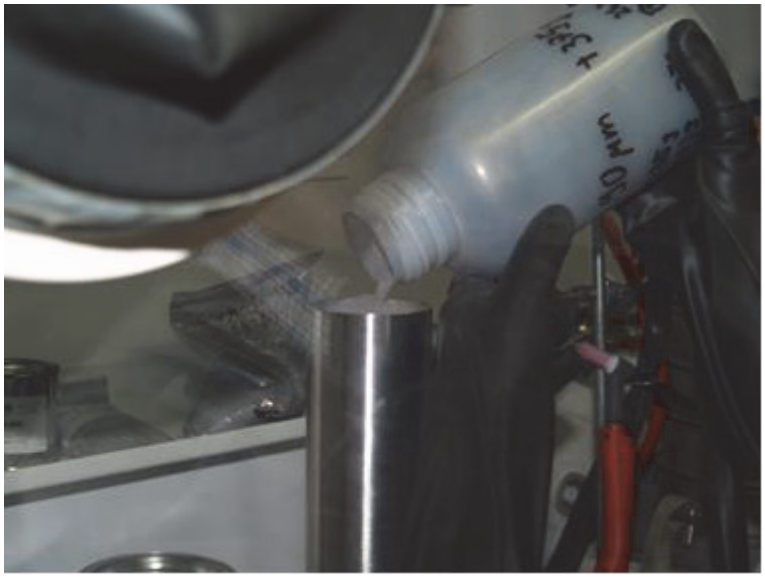

Fig. 5: Filling of the capsules inside an Argon-filled glove box.

The sealing in earlier works was done by mechanically crimping the suction pipe and closing it by a TIG weld. To improve the reproducibility and reliability, the procedure was modified. While still attached to the vacuum pump, the pipes on both ends where heated with a blowtorch and forged flat (Figure 7 (1)). The flat pipe is then heated again and folded twice to ensure tightness. (Figure 7 (2)). For the final step, the flat pressed ends of both pipes were sealed with a TIG weld (Figure 7 (3)).

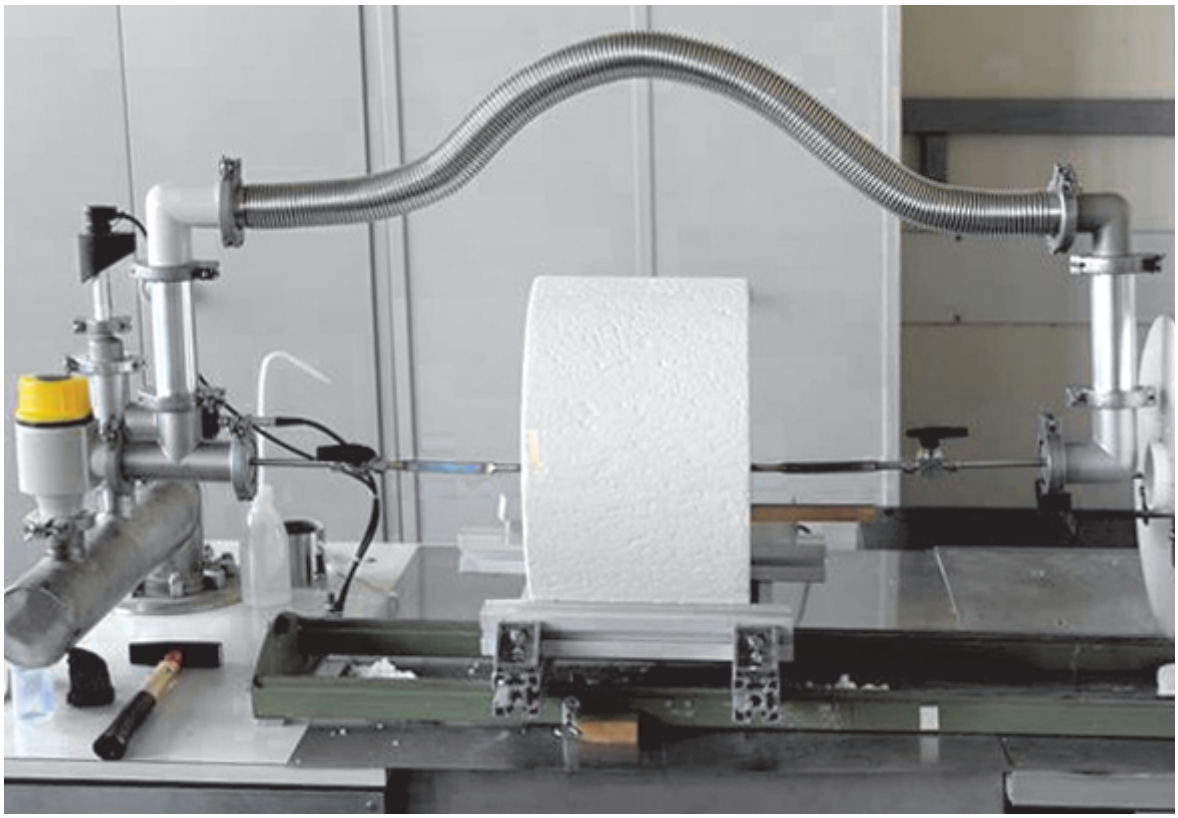

Fig. 6: Setup for degassing of the capsules.

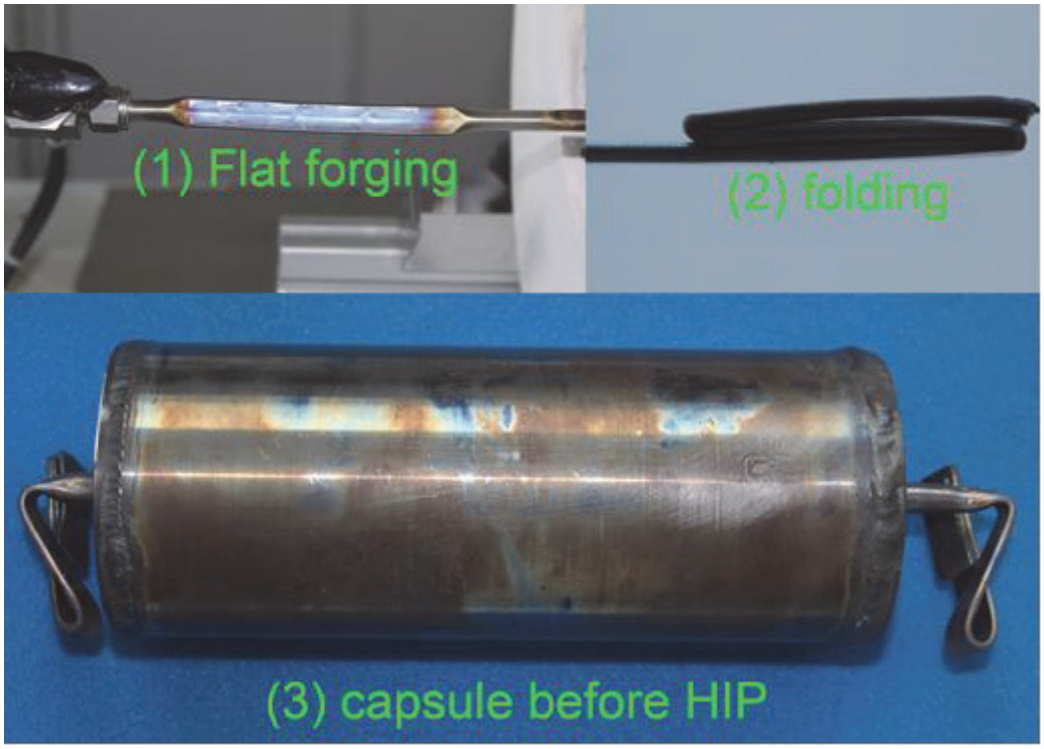

Fig. 7: sealing of pipes at top and bottom of the capsules.

Although more precautions were made to ensure tightness of the capsule, a wrong adjustment of the welding parameters caused a leakage of the pipe. This leak led to an exposure of the small fraction powder (< 90 µm) to air. The capsule was then moved back into to the glove box and refilled after re-pair.

The hot isostatic pressing was performed at the IAM-WPT institute at KIT. The capsules were consolidated on individual runs at 1100°C for 2 hours. The HIP of the larger fraction

(> 90 µm) was successful. However, the capsule with the small fraction powders did not consolidate. Although the conditions were kept the same as the earlier runs, a leakage in the capsule did not allow compaction. This capsule was considered a failure and was not processed any further.

The large fraction capsule in as-hipped condition can be seen in Figure 8. Both ends were cut away by EDM to allow microstructural characterizations by SEM and TEM at a later stage.

Fig. 8: Capsule after HIP (both ends removed by EDM).

Because of the failure during the sealing and HIP, the hot rolling could only be performed on the large fraction capsule (> 90 µm). The material after hot rolling is displayed in Figure 9. During the rolling, cracks appeared at both sides of the flat pressed sheet and the ends spread open and delaminated visibly. However, these damages only affected the stainless steel coating. The ODS material inside was still intact and unaffected.

Fig. 9: Capsule after hot rolling.

3. After thermo-mechanical treatments, the stainless steel capsule sheet was removed by EDM. Mechanical test samples were also cut out and fabricated. Since these processes are well established and have been successfully performed before, no problems occurred during this stage of the production.

4. The materials in as-hipped conditions were examined by conventional TEM BF images to show the existence of nano-clusters. The images in Figure 10 show these nano-clusters with a fine and homogeneous distribution across the whole microstructure.

   Grain sizes are slightly larger than one would expect from conventional ODS materials. This is due to the fact that only the larger fraction of powder particles was compacted. Although being an order of magnitude different, the power particle sizes can be correlated to the final resulting grain size distribution.

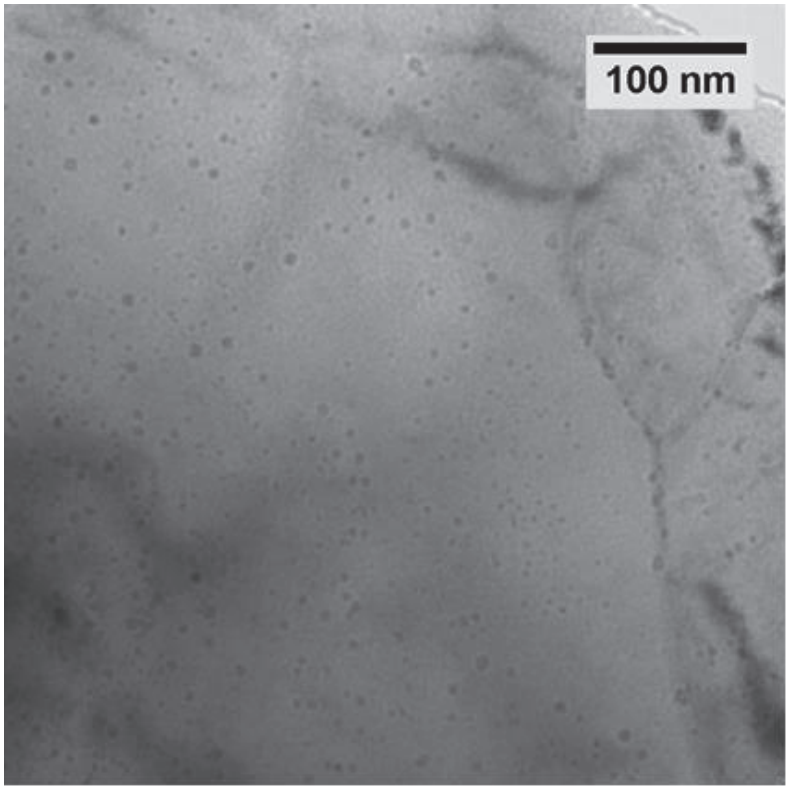

Fig. 10: Distribution of nanoclusters (TEM image).

Summary

The process with all the steps
presented here is capable and well established for production of larger scale batches of ferritic ODS steels. The findings and implications of the results are described below:

- The mechanical alloying process can be up scaled up to multiple kilograms per batch in a single attritor run. The milling in large attritor has the advantage of producing materials with lower levels of impurities. The speed of the attritor is reduced because of the larger diameter and leads to less wear of the rotor ends and milling container walls. Overall, this produces material with better mechanical properties.
- It was demonstrated that the capsules design can be adapted for hot isostatic pressing of larger quantities. The hot isostatic pressing itself is a standard industrial process and facilities are available up to a diameter of around 3 meters. Generally, non-cylindrical capsules should be avoided. It is essential to have a uniform pressure distribution across the whole capsule wall. This is not the case for square or cubic shaped cans.
- The results of the degassing and sealing of the capsules showed that this is a crucial step in the production of the materials. Leaks after sealing can easily occur and fail the whole production. From our experience, the failure rate is at approx. 10 %. Up to this point, no reliable sealing method with 100% success rate has been found or demonstrated.
- Results of previous EFDA tasks showed that hot extrusion and hot isostatic pressing are both capable of producing large quantities of ferritic ODS materials with good mechanical properties.
- Hot isostatic pressing is a flexible way to produce ODS materials, because nearly all shapes of cans and capsules can be processed. The mechanical behavior of the materials in as-hipped condition is also full isotropic. But one has to keep in mind that the density which is achieved after HIPing is only in the range of 98-99% theoretical density. For a full

densification hot rolling, hot forging or hot extrusion as a thermo-mechanical after-treatment afterwards are essential.

- The resulting grain size distribution can be correlated to the initial powder particle size after mechanical alloying. By sieving the powders before or after mechanical alloying, both of those values can be adjusted. This is an important lesson learned, since it opens up to possibility to produce tailored ODS materials with grain sizes optimized to the field of application.
- Our previous work on crystallographic texture and microstructural characterization in the framework of the EFDA programme ([2]) gives pathway to advanced ferritic ODS alloys. These materials are not only optimized in a general manner, but highly specialized on the desired application and boundary conditions.

Staff:

S. Antusch
S. Baumgärtner
T. Bergfeld
D. Bohlich
L. Commin
B. Dafferner
N. Denker
T. Gräning
S. Heger
J. Hoffmann
M. Hoffmann
U. Jäntsch
M. Klimenkov
A. Krüger
R. Lindau
J. Moch
A. Möslang
M. Müller
M. Offermann
J. Reiser
M. Rieth
V. Widak
R. Ziegler
H. Zimmermann

Literature:

[1] J. Hoffmann, M. Klimenkov, R. Lindau, M. Rieth, TEM study of mechanically alloyed ODS steel powder, Journal of Nuclear Materials, 428 (2012) 165-169.

[2] J. Hoffmann, M. Rieth, R. Lindau, M. Klimenkov, A. Möslang, H.R.Z. Sandim, Investigation on different oxides as candidates for nano-sized ODS particles in reduced-activation ferritic (RAF) steels, Journal of Nuclear Materials, 442 (2013) 444-448.

Acknowledgement

This work, supported by the European Communities under the contract of Association between EURATOM and Karlsruhe Institute of Technology, was carried out within the framework of the European Fusion Development Agreement. The views and opinions expressed herein do not necessarily reflect those of the European Commission.

Nano-structured ODS Ferritic Steels Development
Production and Characterization of Industrial Batches of Nano-structured ODS FS (WP13-MAT-ODSFS-02-01)

Abstract

This activity is focused on the fabrication of ODS FS using semi-industrial or industrial scale-methods. Therefore, the goal of this line of work is to probe the feasibility of production of ODS FS in large batches around 5-15 kg.

While laboratory scale production was successful, in the large scale production of 5kg slabs of an ODS steel unexpectedly cracks occurred during hot rolling. Metallographic examinations showed that high porosity can be regarded as main reason for this failure.

Chemical analyses of materials from the different production steps supported the assumption that leaking of the HIP containers during the consolidation process was the most likely reason.

Further experiments with a second hip step of the porous material and rolling tests afterwards were performed to find out whether the quality of the material could be improved.

Introduction

The work to develop nano-structured ODS steels in Europe is carried out in laboratories at universities and research centres at laboratory scale, i.e. small batches of a few grams to about 200 grams. The presently identified applications in future nuclear fusion reactors require instead amounts of material that are orders of magnitude larger and need therefore an industrial-scale fabrication. Among others, the transferability of the results gained in lab-scale to industrial scale production has also to be proven.

Since today no commercial producer is available in Europe like it was in the past, a development in cooperation with an industrial partner is no longer possible.

Such a close cooperation of KIT and PLANSEE finally lead to the development of a reduced activation ferritic martensitic 9Cr ODS-steel with good mechanical properties. These improvements would allow to increase the operational temperature compared to the non-ODS Eurofer 97 steel by about 100°C to 650-700°C making the material suitable for application in the blanket and divertor of a DEMO-type reactor.

Due to the α-γ phase transformation in these steels, the application temperature of this type of ODS-steels is limited to temperatures of about 800°C. Purely ODS ferritic steels (ODSFS) which do not show such a phase transformation would allow to further increase the operational temperature. This task is strongly intertwined with other tasks in which the influences of composition and production parameters on the properties of ODSFS are investigated.

Objectives

This activity is focused on the fabrication of ODS FS using semi-industrial or industrial scale-methods. Therefore, the goal of this line of work is to check the feasibility of production of ODSFS in large batches around 5-15 kg.

Following the identification of chemical composition and manufacturing conditions, production of one or several batches and preliminary characterization of the batch(es) in the unirradiated condition have to be carried out.

From preliminary productions of small 0.2 to 1kg laboratory the optimum composition for the semi-industrial batches of a ferritic ODS steels was assumed to be 13.5%Cr-2.0%W-0.3%Ti.

About 10 kg mechanically alloyed powder of this composition were produced in the last reporting period by an industrial partner according to the procedure developed at KIT in the lab scale.

As reported in the task report of 2012, problems with a large scale test production occurred due to crack formation in the rolling step of 5kg slabs.

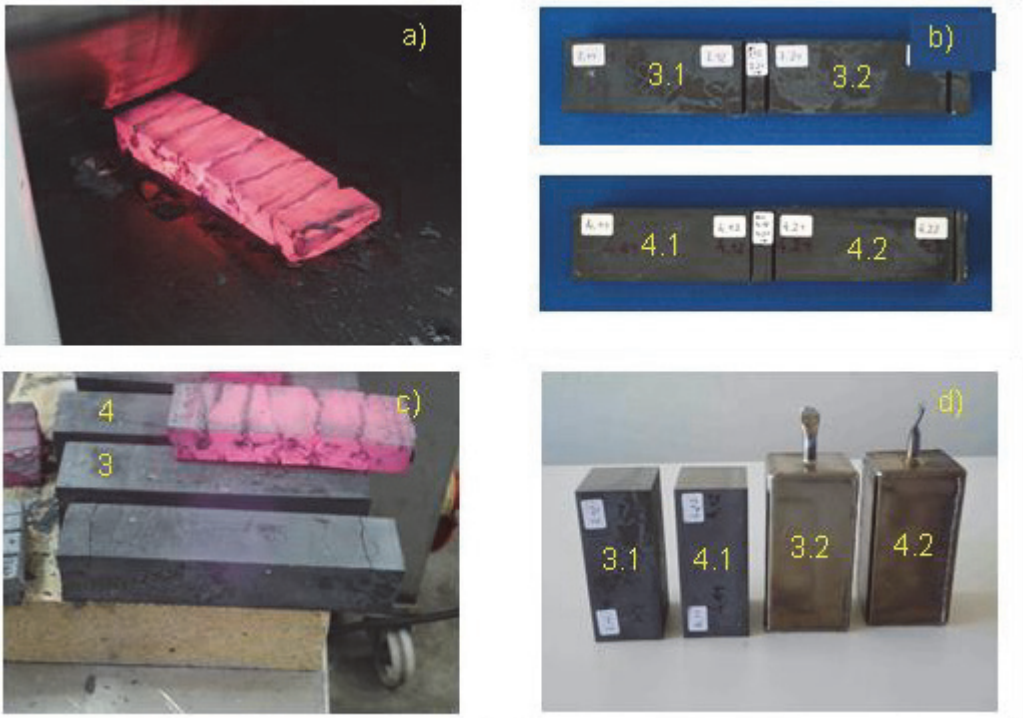

Fig. 1: Cracked slabs after rolling (a, c) and pieces from interrupted roll with no visible cracks (b, d) for further trials.

To understand the reasons for the failure two different approaches were used.

The first one used the pieces where the rolling was interrupted after very little deformation (3 and 4) in Figure 1c). The slabs of 45x50x220 mm were cut into two halves each (Fig.1 b). It was not sure whether a second HIP could improve the density of these pieces which showed large porosity and, whether these pieces would withstand the deformation during the rolling without any cracking. A second open issue was the role of a supporting sleeve around the pieces. So two pieces (3.1, 4.1) were hipped without sleeve and two pieces (3.2, 4.2) with stainless steel jacket (Fig. 1.d).

The second one was going back to successful procedures to prove repeatability and to learn more about the production process. Since the so far produced 1 kg batches did not show any failure during rolling, five capsules were filled with mechanically alloyed 9Cr ODS powder from which enough material was available. Two of these capsules showed large porosity after HIP, three of them had acceptable low porosity. The pieces were machined to rectangular blocks and put into sardine-can like containers where a lid was EB-welded. Degassing was performed in the EB-welding machine over night. They were hipped like all other pieces at 1100°C at 100 MPa pressure for 2.5 hours.

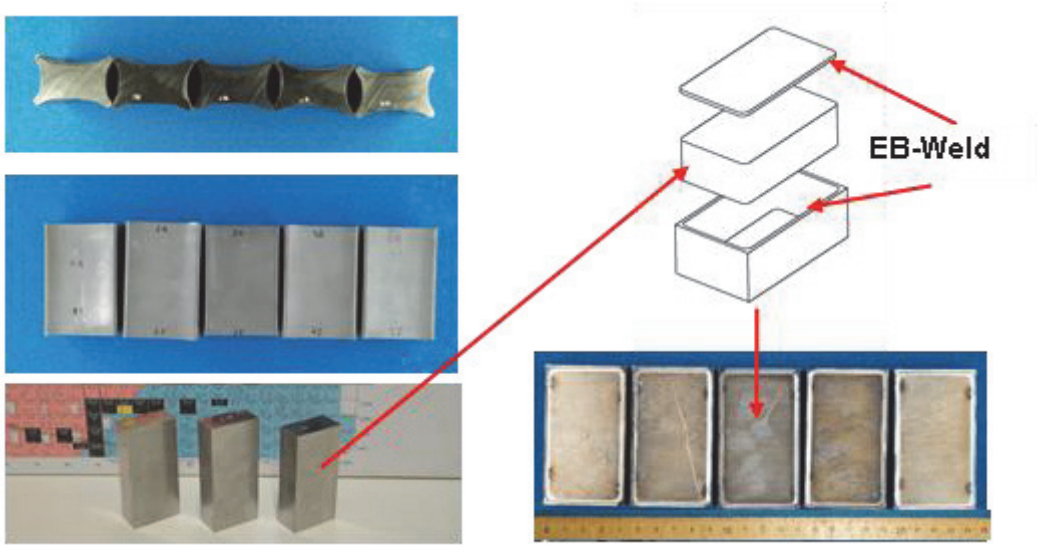

Fig. 2: 1 kg pieces after HIP, machining, boxing in a "sardine can" like canister, degassing and EB-welding of the lid.

Results

The rolling was performed in cooperation with the Technical University of Clausthal on a 12 inch Duo Mill (roll diameter 295 mm, roll width 360 mm, max. roll force 1,800 kN). The 45 mm bars were rolled down in 8 steps to a final thickness (incl. sleeve) of 9.5 mm, the 27 mm thick bars were rolled in 5 steps down to 9.5 mm. The last 5 steps for the 45 mm thick bars were identical to those of the 27 mm bars. During the rolling different parameters were recorded (rolling force, motor rotation speed, rolling gap size). Figure 3 shows all above described bars. Fig. 3a shows the first rolling step of a 45 mm thick bar. The start temperature was 1100°C. After each rolling step the slabs were reheated to 1100°C. Fig. 3b on the upper left side showed severe cracking of the bar without sleeve after the first rolling pass with 11% thickness reduction. The second piece in Fig. 3b was not rolled. All encapsulated and hipped large bars of 45 mm and 27 mm thickness in Fig 3c (lower left side) and Fig. 3d (lower right side) could be rolled to the final thickness without obvious cracking

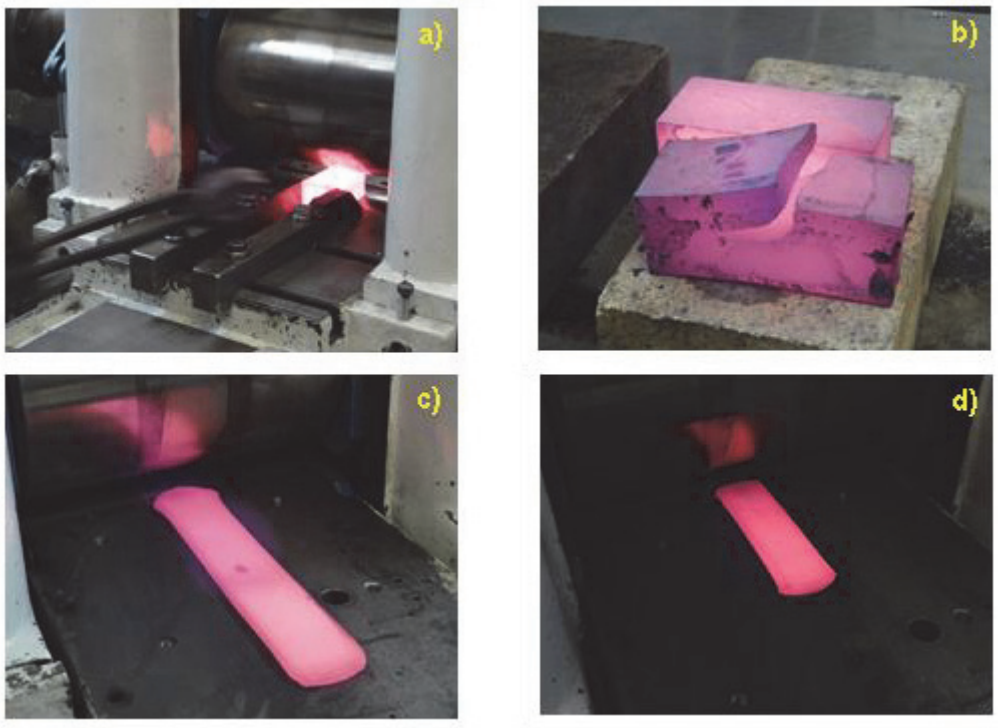

Fig. 3: Rolling of slabs of different size with (a, c, d) and without sleeve (b).

Figure 4 shows the shape of the plates after rolling of the different slabs to the same final thickness of 9.5 mm plate. During the rolling process some sleeves showed blisters which cracked in a later state. This is assumed to be caused by the different expansion and deformation behaviour of the austenitic steel can and the ferritic core. Nevertheless the sleeves prevented cracking like it happened in the sleeveless rolling. Samples were cut from the top and bottom of the rolled plates for metallographic

The metallographic examinations of the two larger plates showed that there is still a large amount of porosity is left. Although the material could be rolled down to 21% of the original thickness it was not possible to close the initial porosity. Besides porosity also little delamination cracks were observed.

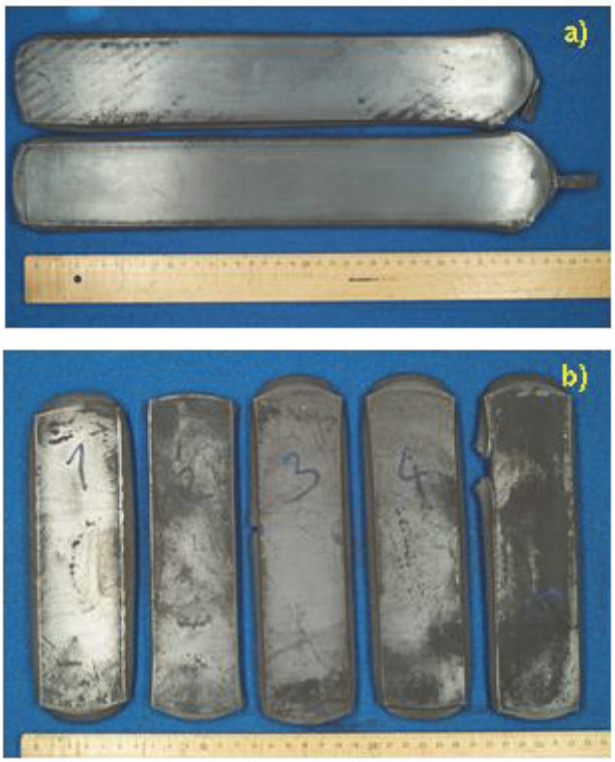

Fig. 4: Hipped slabs after rolling in 8 (a) and 5 steps (b) to 9.5 mm final thickness.

This behaviour will for sure not provide favourable mechanical properties of the material.

In the lower part of Fig.4 the 5 plates produced from the "sardine cans" are shown. As mentioned above the first two of them showed high porosity after hipping. In this case the same observation as for the larger plates was made. Although deformable to a large thickness reduction, the porosity could not be closed by the rolling process.

Further examinations will show whether the plates are totally porous or whether some good areas without porosity exist. At least three of the smaller plates can be used for further mechanical testing.

Summary and conclusions

The large scale production of ODS steels according to the so far successful production route developed for small scale production failed due to unexpected difficulties and cracking in the rolling step. New trials to improve the manufacturing process, including a second HIP with and without canister showed that rollability can be strongly improved in the case of using HIP canisters.

Nevertheless, if the basic material is porous before this procedure, rollability can be provided, but it is not possible to reduce the porosity to a large extent. Whether much higher degrees of deformation could provide this, must be proven.

A second HIP without canning showed the same disastrous cracking like in the very first rolling tests. Canning is inevitable to get good materials with satisfying properties. Special quality control shave to be performed to exclude failure.

Currently the fabrication of these containers is under way. It is foreseen to make a degassing in the EB-device prior to EB welding. These cans will then be hipped prior to hot rolling. Besides the supporting function of the can it would be interesting also to see whether this method with a second HIP before rolling would have an effect on the porous slabs. It cannot be excluded that the porosity can be closed to some extent.

Staff:

S. Baumgärtner
T. Bergfeldt
D. Bolich
B. Dafferner
P. He
M. Hoffmann
U. Jäntsch
T. Kaiser
M. Klimenkov
R. Lindau
A. Möslang
R. Ziegler
H. Zimmermann

Literature:

[1] Commin, L.; Rieth, M.; Widak, V.; Dafferner, B.; Heger, S.; Zimmermann, H.; Materna-Morris, E.; Lindau, R.; Characterization of ODS (Oxide Dispersion Strengthened) Eurofer/Eurofer dissimilar electron beam welds; J. Nucl. Mater. 442 (2013) S552-S556.

[2] Ryazanov, A.I.; Chugonov, O.K.; Latushkin, S.T.; Lindau, R.; Möslang, A.; Prikhodko, K.E.; Semenov, E.V.; Unezhev, V.N., Vladimirov, P.; Investigations of High Concentration of Helium Atoms Effects on Microstructure and Mechanical Property Changes in EUROFER ODS Materials; J. Nucl. Mater. 442 (2013) S153-S157.

[3] He, P.; Lindau, R.; Moeslang, A.; Sandim, H.R.Z.; The influence of thermomechanical processing on the microstructure and mechanical properties of 13.5Cr ODS steels; Fus. Eng. Des. 88 (2013) 2448–2452

[4] Malitckii, E.; Yagodzinskyy, Y.; , M.; Binyukova, S.; Hänninen, H.; Lindau, R.; Vladimirov, P.; Moeslang, A.; Comparative study of hydrogen uptake and diffusion in ODS steels; Fus. Eng. Des. 88 (2013) 2607– 2610.

Acknowledgement

This work, supported by the European Communities under the contract of Association between EURATOM and Karlsruhe Institute of Technology, was carried out within the framework of the European Fusion Development Agreement. The views and opinions expressed herein do not necessarily reflect those of the European Commission.

Handling and Storage Services for the EUROFER-97-HEAT 3 Semi Finished Products (F4E-OPE-412)

This task includes the documentation of the storage and handling of the boxes of EUROFER-97#3 semi-finished products in KIT, intended to be used for F4E-OPE-305 by KIT and other associations under F4E contract. According to the time schedule, in 2013 all relevant reports of work package WP1+2 where successfully concluded and accepted by F4E.

KIT is also responsible for the storage of all rest material up to 2 years from the starting date of the contract in July 2012. In order to provide adequate storage facilities, it was decided to procure and to install in the KIT central materials storage facility (responsible for material handling and dispatching) a new heavy duty rack system. This rack system facilitates the access to all OPE-412 related material inventories and is installed in a separated limited access area in the KIT central store. All racks of this system can be lifted / exchanged directly by use of a fork truck.

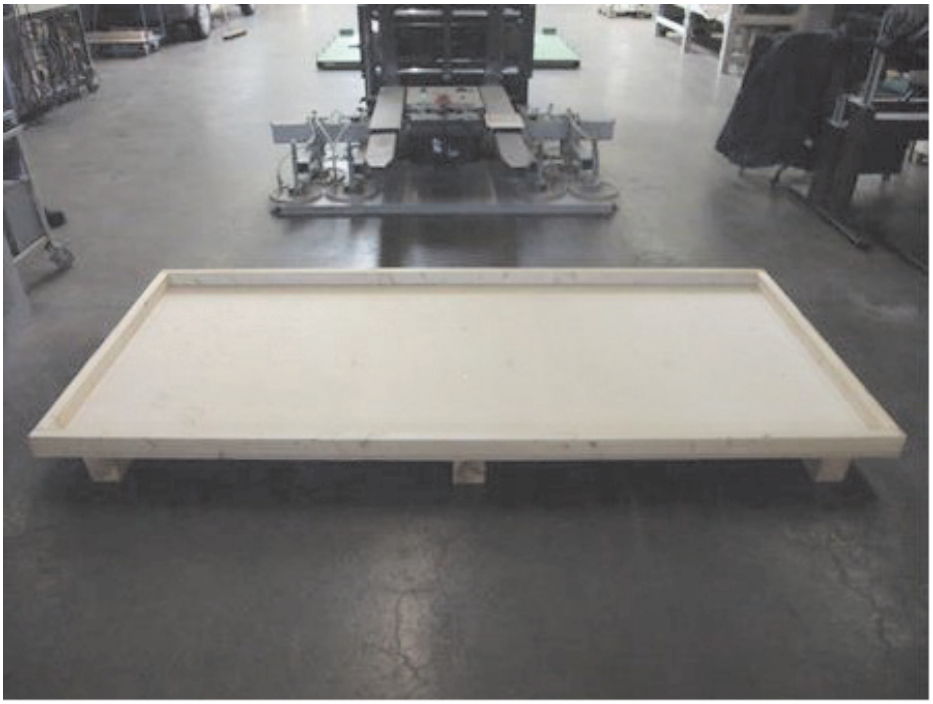

Fig. 1: New KIT boxes together with vacuum lifting system mounted directly on fork truck.

KIT decided also to replace the old box system from the steel producer Saarschmiede by making use of 3 point mounting boxes which provide an optimal mechanical support without sagging of the plates ensuring easy access for fork lifting device. Following pictures show briefly standard procedures of the contract.

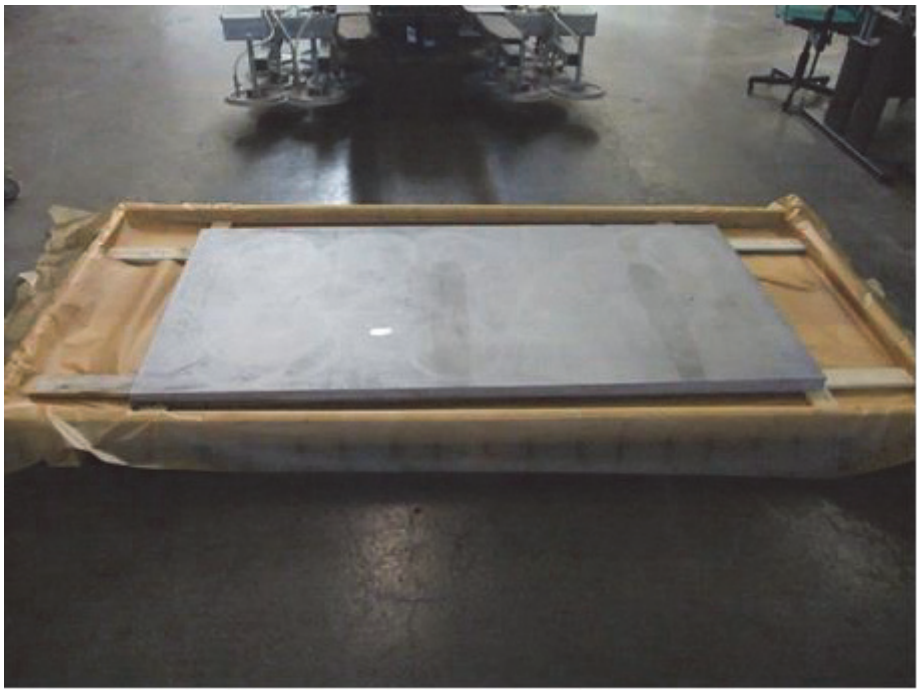

Fig. 2: Packing of plate ID 48mm covered by anticorrosive coating foil.

Fig. 3: New KIT heavy duty rack system for maximum plate dimensions of 4m x 2m.

Staff:

P. Brecht
St. Fischer
P. Freiner
K. Gross
M. Heilig
F. Hohmann
S. Linke
H. Neuberger
J. Rey
A. von der Weth

Acknowledgement

This work was supported by Fusion for Energy under the service contract No. F4E-OPE-412. The views and opinions expressed herein reflect only the author's views. Fusion for Energy is not liable for any use that may be made of the information contained therein.

Material Science Armour Materials and Joints (WP13-MAT-IREMEV-04-01)

The mechanical behavior of metallic materials for structural applications and as a substrate base for heat-protecting coatings is investigated in the present task by instrumented indentation at high temperatures.

A previous study had shown the ability of the instrumented indentation technique to both, determine at room temperature the irradiation damage in irradiated RAFM samples (15 dpa HFR-irradiation programme) and recovery effects after thermal annealing. Further characterization of irradiated material at high temperature by indentation at the macro- and microscale is required for a more complete description of the mechanical behavior.

Instrumented indentation here is of a special interest, as it allows the determination of mechanical properties not only of bulk materials, but also of coatings applied to a substrate, p. ex. of a tungsten layer on steel.

The newly developed machine, an instrumented indentation device operating at up to 650 °C and capable of testing up to 200 N, enables such investigations also on irradiated specimens and has been taken in service during the reported period.

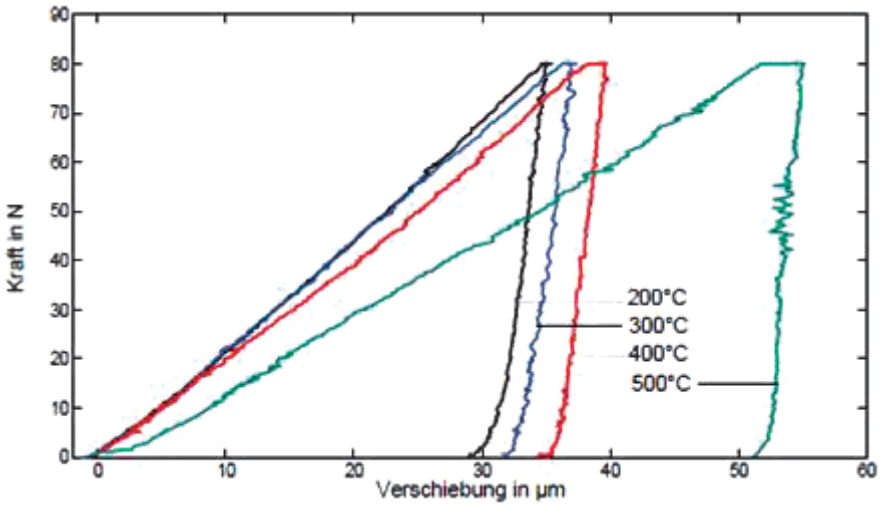

Fig. 1: Force-displacement recordings for ball indents (200µm radius) in EUROFER steel at (from left to right) 200, 300, 400, and 500 °C (B. Albinski).

Fig. 1 shows monocyclic indents on EUROFER steel, applied at different temperatures between 200 and 500 °C. Indentation depth is - at constant load - increasing with the temperature as the materials' resistance decreases and the tendency to creep increases. The unloading stiffness is unchanged, the change in plastic behavior seems not to affect the elastic behavior which is in good agreement with conventional testing methods; yield stress decreases with increasing testing temperature.

In Fig. 2, a specimen is displayed with indents between room temperature and 650 °C, the trend is as expected: with rising temperature the material gets softer and therefore, the indentation depth is increased. Indents' diameter is used for the determination of Brinell hardness.

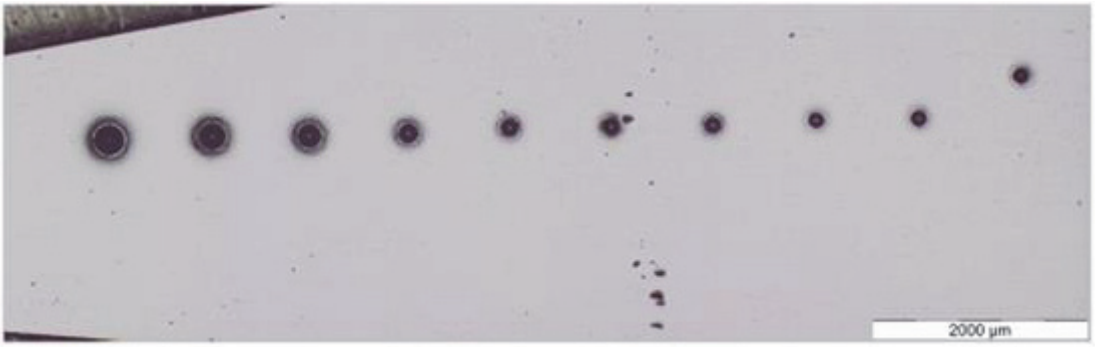

Fig. 2: Overview of indents at various temperatures in EUROFER: testing temperature between room temperature (right) and 650 °C left (B. Albinski).

Fig. 3 displays the temperature-depending Brinell hardness of the specimen from Fig. 2. The different columns represent hardness measured at different machines (red, black, green) The grey columns are hardness values calculated with a corrected contact area of the ball indenter - this was necessary as the geometry of the indenter was sinking in deeper then the pure ball shape in soft material state.

For comparison, the black dots show the tensile strength for the same material, as it was reported in: R. Lindau, M. Schirra: First results on the characterisation of the reduced activation-ferritic-martensitic steel EUROFER, Fus Eng Des 58-59 (0) (2001) 781 – 785.

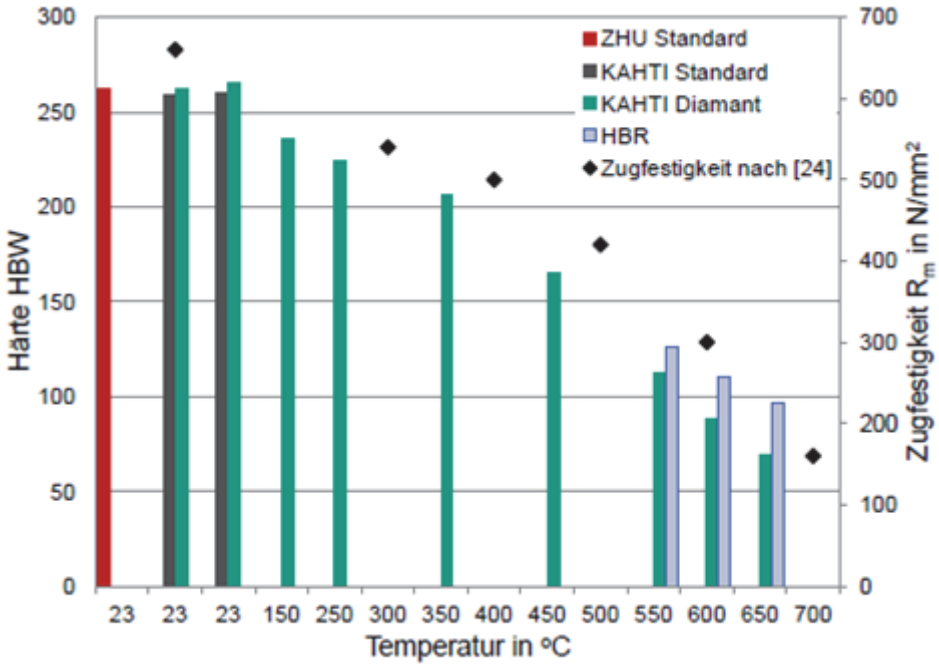

Fig. 3: Brinell hardness of EUROFER, tested in diefferent machines and at different temperatures (columns) and comparison with tensile strength (black dots) (B. Albinski).

Future activities:

- Continuation of the calibration work
- Comparison with conventional testing results
- Extension of the temperature- and force range to tungsten materials

Staff:

B. Albinski
I. Bernstein
J. Bredl
M. Dany
M. Holzer
W. Ibbe
S. Lautensack
I. Sacksteder
H.-C. Schneider

Literature:

[1] I. Sacksteder, S. Hostettler, G. Charbonneau, B. Albinski, H.-C. Schneider: Requirements for investigating the temperature-dependent fracture behavior of irradiated materials by indentation, Fus Eng Des, 88, 9–10, October 2013, 2577-2580

[2] B. Albinski, H.-C. Schneider, I. Sacksteder, O. Kraft: A new high-temperature indentation device for characterization of materials for fusion applications, J Nucl Mate, 442, 1–3, S1, November 2013, S865-S868

[3] B. Albinski: Instrumentierte Eindringprüfung bei Hochtemperatur für die Charakterisierung bestrahlter Materialien. Zur Erlangung des akademischen Grades Doktor der Ingenieurwissenschaften der Fakultät für Maschinenbau am Karlsruher Institut für Technologie (KIT) vorgelegte Dissertation. December 16th, 2013

Acknowledgement

This work, supported by the European Communities under the contract of Association between EURATOM and Karlsruhe Institute of Technology, was carried out within the framework of the European Fusion Development Agreement. The views and opinions expressed herein do not necessarily reflect those of the European Commission.

Quantitative TEM Analysis of Precipitation Evolution in Neutron irradiated EUROFER97 (WP13-MAT-IREMEV-05-01)

Objectives

The current task aims at continuation of analysing the neutron irradiation induced evolution of the microstructure in the RAFM steel EUROFER97 and its boron doped variants addressing (a) irradiation dose dependence of *sizes* and *volume densities* of radiation defects (e.g. defect clusters, dislocation loops, voids, helium bubbles, precipitates); (b) neutron flux dependence of *sizes* and *volume densities* of radiation defects. A long term goal is the correlation of the neutron irradiation induced changes in the microstructure to the changes in the mechanical properties, as well as verification of models for the evolution of radiation defects. The specimens to be studied in this task stem from SPICE (15 dpa/300 °C, HFR, NRG, Petten), WTZ (15 dpa/330 °C, Bor-60, JSC "SSC RIAR", Dimitrovgrad), ARBOR 1 (32 dpa/330 °C, Bor-60, JSC "SSC RIAR", Dimitrovgrad) and ARBOR 2 (70 dpa/330 °C, Bor-60, JSC "SSC RIAR", Dimitrovgrad) irradiation programmes. The neutron fluxes (>0.1 MeV) for Bor-60 and HFR irradiations were 1.8×10^{19} $m^{-2}s^{-1}$ and 4.0×10^{18} $m^{-2}s^{-1}$, respectively.

Task Current Status

The microstructure of EUROFER97 irradiated to 32 dpa in the ARBOR 1 irradiation programme was analysed with the high resolution FEI Tecnai G² F20 X-TWIN TEM installed in the hot cells of the FML. TEM specimens were prepared from the undeformed parts of impact tested KLST specimens by mechanical and electrolytic polishing in a solution of 20 % H_2SO_4 + 80 % CH_3OH at room temperature. The last reports focused on the dose dependence of size distributions of defect clusters and dislocation loops, quantitative analysis of voids and helium bubbles and irradiation induced grain boundary segregation. In the present work, the emphasis was put on determination of neutron irradiation induced precipitate evolution, i.e. types, volume densities and size distributions of precipitates. The TEM data was used for correlation of the irradiation induced changes in the microstructure to the changes in the yield stress.

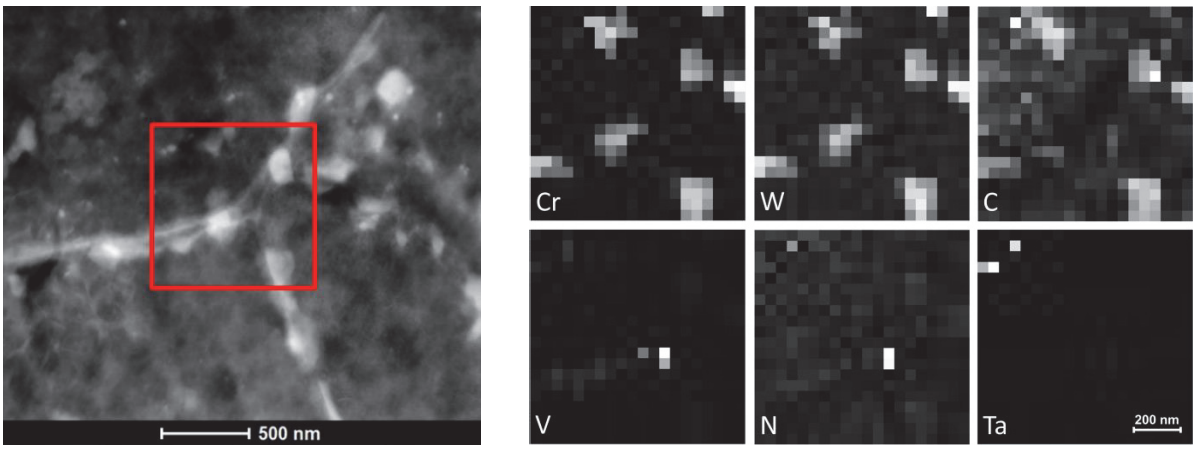

Fig. 1: STEM-HAADF micrograph of EUROFER97 irradiated to 32 dpa at 330 °C in ARBOR 1.
Red square marks grain boundary area analyzed by EDX providing elemental maps shown on the right. Precipitates of $M_{23}C_6$, TaC and VN are observable.

The microstructure of irradiated EUROFER97 is presented in Fig. 1. EDX elemental maps of the main alloying elements were obtained from the area marked with the red square. A detailed characterization of precipitates in unirradiated EUROFER97 has already been presented in our last year's report. Comparable to the unirradiated condition, after irradiation large $M_{23}C_6$ precipitates composed of Cr, Fe, W, C are observed, which for the most part are located at grain boundaries. A small VN precipitate is detected which also is located at the grain boundary, while small spherical precipitates of TaC are distributed in the matrix.

In summary, no fundamental difference in precipitate types and composition between unirradiated and irradiated EUROFER97 was found. The precipitation of a new phase induced by irradiation, in particular Cr rich α', could not be observed either by EDX or energy-filtered (EFTEM) mapping in irradiated EUROFER97 so far.

Quantification of precipitate sizes and density was performed on four different TEM specimens and corresponding areas (see Table 1). Reference measurements in the unirradiated state were performed on two samples A1 and A2 cut from the same impact testing specimen, whereof A2 was analyzed with the TEM at the common (cold) laboratory and A1 with the TEM in the Hot Cells. Both irradiated samples (32 dpa, 332 °C) were prepared out of an impact test specimen fractured at 138 °C.

Table 1: Specifications of investigated areas and results of quantitative precipitate analysis.

Sample	Irrad. Status	TEM location	Area (μm^2)	Mean foil thickness (nm)	Precipitate				
					total number (-)	mean diam. (nm)	density ($10^{19}/m^3$)	vol. fraction (%)	hardening σ_{prec} (MPa)
A2	unirr.	cold lab	75	140	949	50.1	9.9	0.7	128
A1	unirr.	hot cell	93	130	976	66.2	8.1	1.2	133
E105-3	irr.	hot cell	131	119	1517	67.6	9.7	1.6	147
E105-1	irr.	hot cell	106	167	817	81.5	4.6	1.3	111

Due to the high Z contrast of the HAADF detector precipitates appear bright in the STEM micrograph and show a good contrast to the surrounding ferritic matrix. This fact allows for a distinct identification of the precipitates and an accurate determination of their sizes without interference of diffraction contrasts or blooming. Precipitate size distributions for each analyzed area are presented by the histograms (bin size of 10 nm) in Fig. 2. In the unirradiated case a high fraction of small precipitates is observed which differs significantly in the two measured areas. While for sample A2 an amount of 26 % of the precipitates has a size between 10 and 20 nm, the fraction is only 14 % in sample A1. Apart from that the further curve progression is comparable. In the irradiated samples a slightly lower fraction of precipitates in the small size regime is detected. While a difference between both irradiated areas still exists (20 % for E105-3, 14 % for E105-1), it is not as pronounced as in the unirradiated case.

It is obvious that all histograms are a superposition of at least two different size distributions. Since the main types of precipitates were identified as MX and $M_{23}C_6$ according to analyses shown in Fig. 1, the histograms in Fig. 2 are fitted each by a sum of two standard log-normal distributions of type

$$f(x) = A/(\sqrt{2\pi}\sigma x)\exp[-\left(\ln(x/\bar{d})\right)^2/(2\sigma^2)]\,. \qquad (1)$$

Table 2 presents corresponding fitting parameters. As shown in Fig. 2 experimentally determined size histograms are well described by the two log-normal distributions. Slight irregularities at the MX peak shoulders exist, they should however show little influence on the evaluation. Based on the continuous fitting curves precipitate number fractions of all histograms are split for MX and $M_{23}C_6$ precipitates. Final results of the precipitate analysis shown in Table 1 and Table 3 reveal an irradiation induced growth which affects both MX and $M_{23}C_6$ precipitates. The mean diameter of precipitates grows for MX from 21.1 nm to 29.0 nm by 37 % and for $M_{23}C_6$ from 82.0 nm to 100.0 nm by 22 % when averaged each for the unirradiated and irradiated state, while the averaged mean diameter of all precipitates increased by 25 % from 58.2 nm to 72.5 nm as determined experimentally.

A comparison of the mean diameter including both precipitate types, e.g. 66.2 nm for A1 and 67.6 nm for E105-3, is however misleading, since the number fraction of MX varies significantly between 30 % and 43 % for the different areas.

Table 2: Parameters of log-normal distributed fitting curves from Fig. 2 with Eq. (1): mean diameter , standard deviation σ, curve integral A.

Sample	MX			$M_{23}C_6$		
	$\bar{d}$ (nm)	σ	A	$\bar{d}$ (nm)	σ	A
A2	17.0	0.43	4.1	61.9	0.60	5.9
A1	21.0	0.43	3.0	73.5	0.65	7.1
E105-3	26.0	0.35	4.2	85.5	0.50	5.6
E105-1	30.0	0.35	3.2	95.6	0.45	6.7

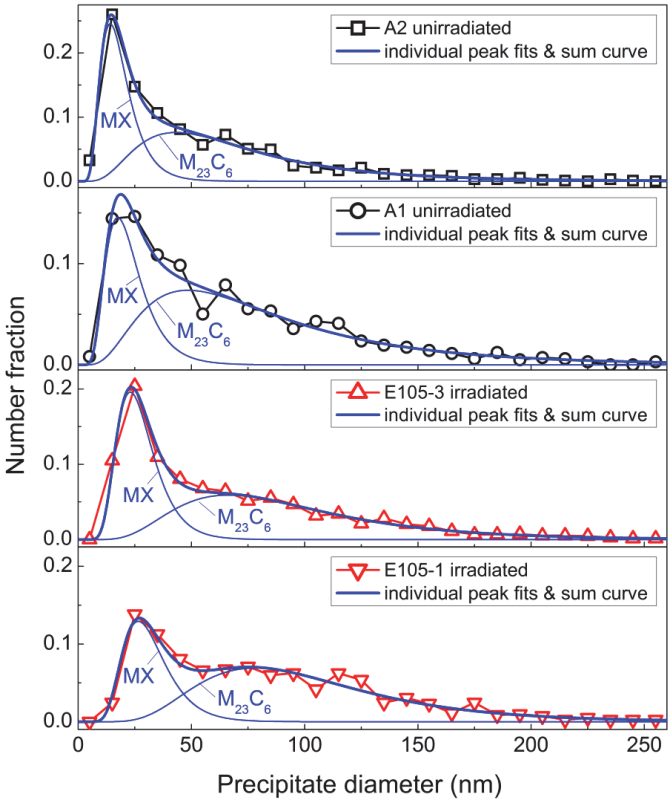

Fig. 2: Precipitate size distributions measured for all four samples (see Table 1) using a histogram bin size of 10 nm. Each histogram was fitted by a sum of two log-normal distributions according to expected MX and $M_{23}C_6$ precipitates. Fitting parameters are given in Table 2.

Furthermore, a consequence of the irradiation on the number fraction of MX precipitates is not observed. Therefore size distributions separated for both precipitate types with corresponding mean diameters are best to be compared, and they reveal a clear precipitate growth. Precipitate densities were evaluated through thickness measurements in all four areas. Three to five different grains were investigated yielding six to eighteen different CBED thickness analyses per area (see calculated mean foil thicknesses in Table 1).

In the unirradiated case precipitate densities show slight differences. When splitting the density for the distinct precipitate types according to the peak fitting curves, the density of $M_{23}C_6$ yields 5.9×10^{19} m^{-3} and 5.7×10^{19} m^{-3} for sample A2 and A1, respectively. Obviously, a lower density of MX in sample A1 of 2.4×10^{19} m^{-3}, which is only 60 % of the value for sample A2, is responsible for the difference in the total precipitate density. In the irradiated case, on the other hand, large differences in the detected density are observed. Sample E105-3 shows a precipitate density of 9.7×10^{19} m^{-3} with a high number fraction of MX (43 %), leading to a density for $M_{23}C_6$ of 5.5×10^{19} m^{-3}. Thus the precipitate structure in sample E105-3 is in agreement with sample A2 except for the irradiation induced precipitate growth in the former case. However in sample E105-1, where the largest mean precipitate diameters are observed, the total precipitate density is only half the value as in sample E105-3. The number fraction of MX (32 %) remains comparable to that of the unirradiated sample A1. Most probably, the precipitate density in the investigated area of sample E105-1 was lower already before irradiation.

Hardening caused by irradiation induced precipitation growth is evaluated by applying the Dispersed Barrier Hardening (DBH) model to above described TEM results. The DBH model assumes homogeneously distributed obstacles which impede dislocation movement, and is expressed by the equation

$$\sigma_{\mathrm{prec}} = M_{\mathrm{T}} \alpha_{\mathrm{prec}} \mu b_{\mathrm{disl}} \sqrt{N_{\mathrm{prec}} \bar{d}_{\mathrm{prec}}} \quad . \tag{2}$$

Therein, parameters are the shear modulus of the matrix μ, the Burgers vector of gliding dislocations b_{disl}, the barrier strength α_{prec}, and the density N_{prec} and mean size $\bar{d}_{\mathrm{prec}}$ of precipitates as determined in Table 1. The Taylor factor M_{T} relates the shear stress necessary for a dislocation to glide on a slip plane in a single crystal to the external tensile stress applied to a polycrystalline sample. Corresponding values based on parameters for a bcc Fe-10%Cr model alloy at 300 °C are (references given in [1]): M_{T} = 3.06, μ = 75.3 GPa, α_{prec} = 1, b_{disl} = 0.249 nm. Results for σ_{prec} determined in all for studied areas are given in Table 1. The comparison of sample A2 and E105-3, which showed similar precipitate densities and type fractions, demonstrates a hardening increase from 128 MPa to 147 MPa due to precipitate growth. σ_{prec} for the irradiated sample E105-1 was calculated to 111 MPa and presents the lowest value, but the microstructure in this sample is assumed to differ from the other three already before irradiation as discussed in the last section. Therefore, the yield strength increase $\Delta\sigma_{\mathrm{prec}}$ of 19 MPa between A2 and E105-1 can be taken as the maximum impact on hardening caused by radiation induced precipitation growth determined in this work.

Table 3: Individual mean diameters of MX and M23C6 and number fraction were determined by evaluation of the peak fitting curves from Fig. 2.

Sample	Irrad. Status	Mean diameter		Number fraction
		MX (nm)	$M_{23}C_6$ (nm)	of MX (-)
A2	unirr.	19.0	74.0	0.40
A1	unirr.	23.2	89.7	0.30
E105-3	irr.	27.5	96.9	0.43
E105-1	irr.	31.9	105.7	0.32

In our previous work hardening contributions of dislocation loops and voids were determined in EUROFER97 after irradiation to 32 dpa in ARBOR 1. Applying Eq.(1) we calculated a dislocation loop and void related hardening of $\Delta\sigma_{\mathrm{loops}} = 355\ \mathrm{MPa}$ and $\Delta\sigma_{\mathrm{voids}} = 110\ \mathrm{MPa}$, respectively. Contributions to hardening of different obstacle types are in general considered by a root sum square rule as described by

$$\Delta\sigma_{\mathrm{tot}} = \sqrt{\Delta\sigma_{\mathrm{loops}}^2 + \Delta\sigma_{\mathrm{voids}}^2 + \Delta\sigma_{\mathrm{prec}}^2 + \Delta\sigma_{\alpha'}^2 + \cdots} \quad . \tag{3}$$

Calculating the total hardening, it becomes obvious that radiation induced precipitation growth has only a minor influence and causes an increase of less than 1 MPa ($\Delta\sigma_{\mathrm{tot}} = 372\ \mathrm{MPa}$) after ARBOR 1 irradiation when compared to the other obstacle types. As shown in our previous work experimentally determined hardening ($\Delta\sigma_{\mathrm{exp}} = 492\ \mathrm{MPa}$) after 32 dpa could not be completely explained by dislocation loops and voids alone. As it was shown the contribution of further precipitation growth of MX and $M_{23}C_6$ induced by neutron irradiation can be neglected.

Conclusion and Outlook

In this work the precipitate structure and evolution under neutron irradiation in the irradiation experiment ARBOR 1 to 32 dpa at 330-340 °C in EUROFER97 was analyzed by TEM. After irradiation the dominant precipitate species remain $M_{23}C_6$ located preferentially at grain boundaries, followed by homogeneously distributed MX carbonitrides of TaC and VN. α' precipitates could not be detected so far. Neutron irradiation is responsible for a significant precipitate growth of both MX and $M_{23}C_6$, causing a mean diameter increase from 21.1 nm to 29.0 nm (+37 %) and from 82.0 nm to 100.0 nm (+22 %), respectively. The precipitate density of $M_{23}C_6$ is about 5.7×10^{19} m^{-3} in both the unirradiated and irradiated state, while the MX density varies between 2.4×10^{19} m^{-3} and 4.2×10^{19} m^{-3}. One irradiated area shows a low total density, which is probably unrelated to irradiation. Hardening due to irradiation induced precipi-

tate growth of MX and $M_{23}C_6$ was estimated by applying the DBH model and found to be insignificant (<0.2 %) when compared to dislocation loop hardening.

Further TEM investigations of irradiated EUROFER97 will provide quantitative analysis of dislocation loops (SPICE), precipitate size distributions and precipitate composition analysis (WTZ). The search for Cr-rich α' precipitates will be continued by means of STEM-EDX and EFTEM analysis, because they are expected to have a significant influence on hardening. Furthermore, TEM investigations will be conducted on irradiated EUROFER97 at high damage doses (ARBOR 2: 70 dpa, 330 °C) with respect to quantification of sizes and volume densities of radiation induced defects (e.g. defect clusters, dislocation loops, voids/bubbles, precipitates). The results of quantitative microstructure analysis will be used for verification of models for evolution of radiation defects in RAFM steels and for correlation of changes in the microstructure to the changes in the mechanical properties.

Staff:

C. Dethloff
E. Gaganidze

Literature:

[1] C. Dethloff, E. Gaganidze, J. Aktaa, Quantitative TEM analysis of precipitation and grain boundary segregation in neutron irradiated EUROFER97, to be submitted to JNM.

[2] C. Dethloff, E. Gaganidze, J. Aktaa, Quantitative TEM analysis of precipitation and grain boundary segregation in neutron irradiated EUROFER97, poster presentation at the ICFRM-16, Beijing, China, October 20-26, 2013.

[3] E. Gaganidze, J. Aktaa, Assessment of neutron irradiation effects on RAFM steels, Fus. Eng. Des. 88 (2013) 118-128.

Acknowledgement

This work, supported by the European Communities under the contract of Association between EURATOM and Karlsruhe Institute of Technology, was carried out within the framework of the European Fusion Development Agreement. The views and opinions expressed herein do not necessarily reflect those of the European Commission.

He Influence on the Microstructure and Swelling of 9%Cr Ferritic Steel after Neutron Irradiation up to 16.1 dpa (WP13-MAT-IREMEV-05-03)

Introduction

To provide quantitative microstructural information on helium bubble development under the influence of irradiation, 3 heats of EUROFER 97 composition with the addition of natural boron as well as pure ^{10}B isotope were fabricated. He concentrations after irradiation were ~81, ~415, and ~5800 appm for these three specimens, respectively. Neutron irradiation with a dose of up to 16 dpa was performed in the temperature range from 523K to 723K. This allowed for a detailed study of the influences of radiation parameters on the size, morphology, spatial distribution, and density of He bubbles. These investigations are necessary to correlate radiation-induced changes of the microstructure to the mechanical properties of this material.

The irradiated specimens of these materials were tested for tensile properties. It was found that higher He concentration resulted in higher strengthening of the material after irradiation at 523K-673K. Previous publications that were dedicated to the microstructural characterization of boron-alloyed EUROFER 97 do not present any statistical data of bubble distribution or general swelling, which are essential for understanding mechanical properties, such as tensile strength and hardness. In the work reported here, the influence of helium concentration and irradiation temperature on bubbles formation was determined. Correlation of the microstructure with radiation-induced hardening was studied.

Method

The irradiated, active specimens were prepared from undeformed parts of KLST specimens after testing and investigated in the fusion materials laboratory (FML) of Karlsruhe Institute of Technology. After complete ^{10}B transmutation (corresponding approximately to a displacement damage dose of 1 dpa), this amount of boron produces about 82 appm (alloy 1), 415 appm (alloy 2), and 5800 appm (alloy 3) He, respectively. After fabrication, the ferritic-martensitic alloy was heat-treated at 1313K for 30 min and normalized at 1023K for 90 min. The specimens for TEM investigations were prepared by electrochemical etching. The disks with a thickness of 0.2 to 0.3 mm were thinned by electropolishing in a TENUPOL device using H_2SO_4 + 80 % CH_3OH as electrolyte. From that material, disks of 1 mm in diameter were punched. TEM investigations were performed using an FEI Tecnai 20 FEG microscope with an accelerating voltage of 200 kV.

Results

The TEM investigations of alloys 1, 2, and 3 after irradiation at different temperatures are presented in Figs. 1-3, respectively. The statistical data of He bubbles such as average size and density obtained from TEM micrographs is listed in Tab. 1. Fig. 1 presents TEM micrographs of alloy 1 irradiated at 523K, 623K, and 723K. In the specimen irradiated at 523K, only the formation of dislocation loops and points defects was detected. No He bubbles were found. In the specimen irradiated at 623K, the formation of randomly distributed cavities and bubbles without any preferred location was observed (Fig. 1b). Some cavities show a faceted shape. Preferable nucleation of He bubbles with sizes around 5 nm was observed in the alloy 1 irradiated at 723K. The bubbles in this specimen are mainly located on the lath boundaries or dislocations.

The microstructure of alloy 2 is very similar to that of alloy 1 irradiated at the same temperature (Fig. 2). In the specimen irradiated at 523K, only the formation of dislocation loops and point defects was detected (Fig. 2a). The randomly distributed cavities and bubbles were detected in the specimen irradiated at 350° (Fig.2b), and in the specimen irradiated at 723K, a preferable location of bubbles on dislocations and grain boundaries was found (Fig. 2c). In

some cases, the bubbles formed two-dimensional arrays on the grain boundaries, which might be caused by a dislocation network (Fig. 2c).

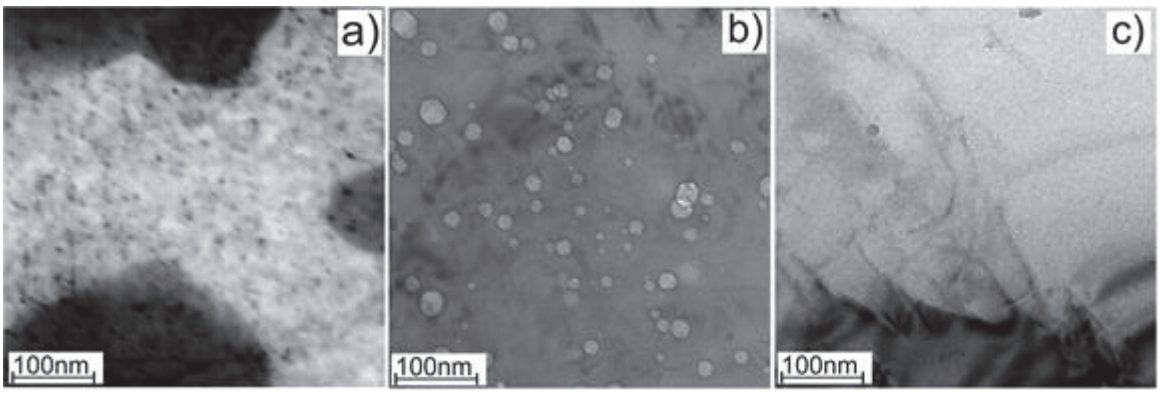

Fig. 1: TEM images of alloy 1 irradiated at 523K, 623K, and 723K are shown in parts a, b, and c, respectively.

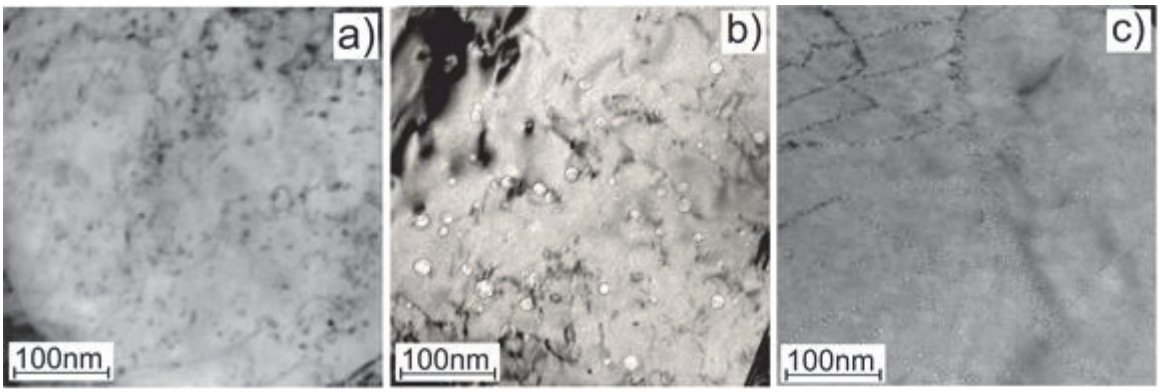

Fig. 2: TEM images of alloy 2 irradiated at 523K, 623K, and 723K are shown in parts a, b, and c, respectively.

Alloy 3 was irradiated at 573K and 673K – temperatures which differ from alloy 1 and 2. The investigation of alloy 3 revealed the formation of randomly distributed nano-sized He bubbles at both irradiation temperatures (Fig. 3). Preferential nucleation of He bubbles on structural defects was not detected.

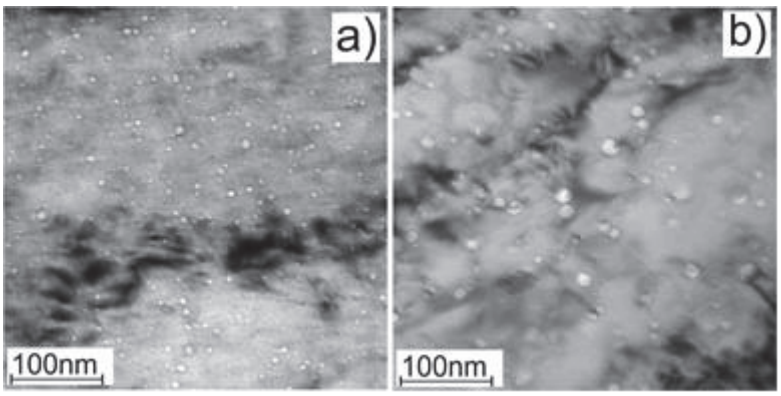

Fig. 3: TEM images of alloy 3 irradiated at 573K and 673K are shown in parts a and b, respectively.

Fig. 4 presents size distribution histograms for all specimens, in which bubbles and cavities were detected. This is the case for each specimen at 2 irradiation temperatures. The bubbles or cavities in alloys 1 and 2 irradiated at 623K and 723K show a very similar size distribution. The irradiation of these alloys at 623K leads to the formation of broad cavities with a broad size distribution – ranging from 2-3 to 25 nanometers.

A similar distribution can be observed in alloy 3 irradiated at 673K. The irradiation of alloys 1 and 2 at 723K and of alloy 3 at 573K leads to the formation of He bubbles with a sharp and narrow size distribution with the maximum at 5 nm.

Tab. 1 shows the statistical evaluation of the TEM results. The bubble density and material swelling were calculated from presented TEM analysis (Fig. 5). Additionally, the swelling was

calculated for EUROFER 97 without boron based on results published. The total density of dislocation loops/point defects for specimens irradiated at 523K was calculated based on the image with (110)g vector and then calculated as $N=2/3n_{110}$.

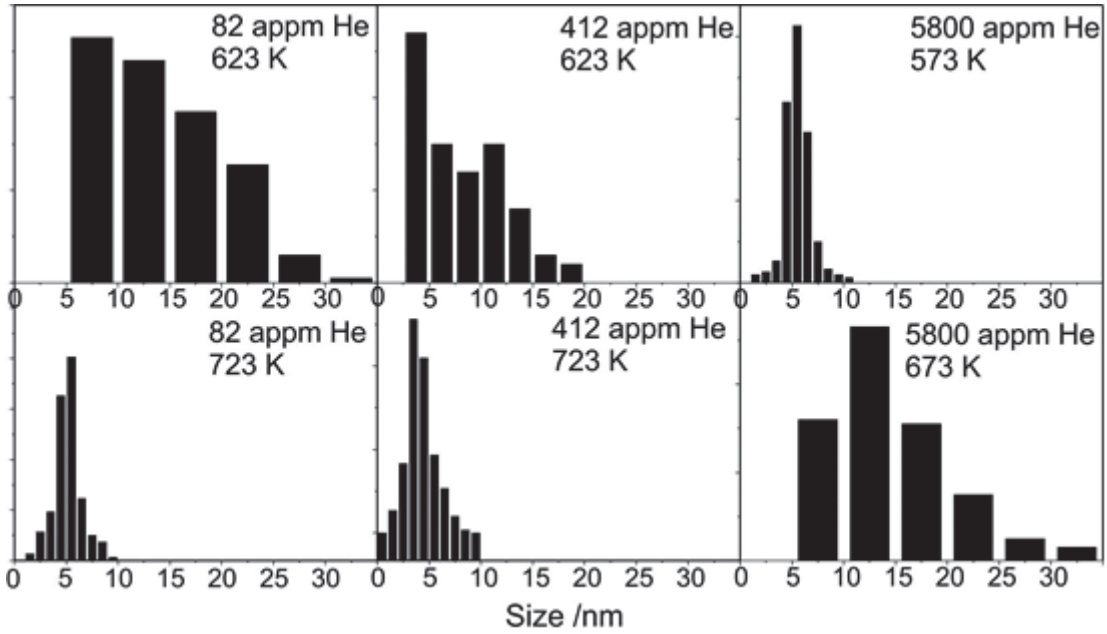

Fig. 4: Size distribution histograms of He bubbles or cavities evaluated for irradiated specimens.

Table 1: The density of bubbles or cavities and swelling for EUROFER 97 and alloys 1-3 irradiated at different temperatures. “n.o.” means “not observed”. ‘---‘means specimens were not irradiated at this temperature.

	Cavity density /m^{-3}				Swelling /%			
Temperature K	573	623	673	723	573	623	673	723
EUROFER 97	n.o.	$1.2*10^{20}$	$2*10^{18}$	n.o	n.o	0.12	0.002	n.o
Alloy 1	---	$3.2*10^{21}$	---	$2.4*10^{21}$	---	0.68	---	0.09
Alloy 2	---	$7.1*10^{21}$	---	$8.1*10^{21}$	---	0.54	---	0.15
Alloy 3	$16*10^{21}$	---	$6.6*10^{21}$	----	0.18	---	0.42	----

Mainly faceted cavities in EUROFER97 and alloys 1 and 2 were detected after irradiation at 623K. The swelling of 0.5-0.6% calculated for this temperature is the highest of all irradiation temperatures. Remarkably, swelling here is less dependent on the He content. Alloys 1 and 2 with 82 and 415 appm He, respectively, show similar swelling values within the error range. Presumably, the radiation dose which is equal for both materials plays a more important role for the formation of cavities than He concentration. Swelling of EUROFER 97 irradiated under the same conditions was measured to be 0.15% - 3-4 times lower than for specimens with He. This result is a clear indication of He promoting the formation of voids in the temperature range from 603K – to 703K. Swelling of 0.5% was detected in alloy 3 irradiated at 673K. This effect was already detected and described in literature.

Post-irradiation microstructural investigation of ferritic steels under neutron irradiation revealed increased void formation and swelling in the temperature range between 330° and 703K. Irradiation-induced swelling was first measured by TEM (the first voids of bubbles could be detected) at 593K, reached a maximum at 673K – 693K, and disappeared at 723K.

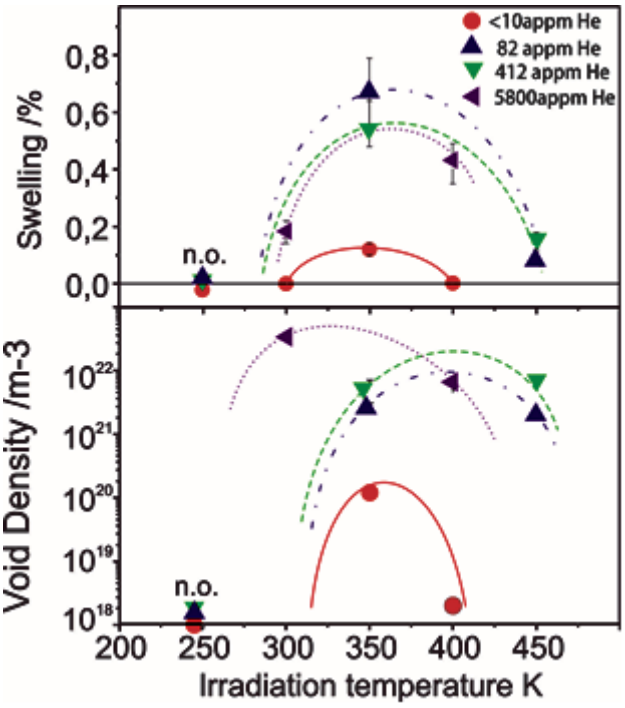

Fig. 5: The swelling and spatial density of cavities of alloys 1-3 and EUROFER 97 calculated for different temperatures.

This swelling depends on different parameters, for example on Cr concentration or the presence of transmutation-induced He inside the steel. The maximum swelling value was reached for the specimen irradiated at 693K. Our results suggest maximum swelling in the range of 623K-653K.

Discussion

Mainly faceted cavities in EUROFER97 and alloys 1 and 2 were detected after irradiation at 623K. The swelling of 0.5-0.6% calculated for this temperature is the highest of all irradiation temperatures. Remarkably, swelling here is less dependent on the He content. Alloys 1 and 2 with 82 and 415 appm He, respectively, show similar swelling values within the error range. Presumably, the radiation dose which is equal for both materials plays a more important role for the formation of cavities than He concentration. Swelling of EUROFER 97 irradiated under the same conditions was measured to be 0.15% - 3-4 times lower than for specimens with He. This result is a clear indication of He promoting the formation of voids in the temperature range from 603K – to 703K. Swelling of 0.5% was detected in alloy 3 irradiated at 673K. This effect was already detected and described in literature.

Post-irradiation microstructural investigation of ferritic steels under neutron irradiation revealed increased void formation and swelling in the temperature range between 330° and 703K. Irradiation-induced swelling was first measured by TEM (the first voids of bubbles could be detected) at 593K, reached a maximum at 673K – 693K, and disappeared at 723K. This swelling depends on different parameters, for example on Cr concentration or the presence of transmutation-induced He inside the steel. The results published in the literature reveal an increase of voids density and swelling by a factor of 3 when ~30 appm He is contained in 9% Cr steel with a chemical composition similar to that of EUROFER97. The maximum swelling value was reached for the specimen irradiated at 693K. Our results suggest maximum swelling in the range of 623K-653K. Such behavior has the consequence that EUROFER 97 swelling in the fusion reactor might not be linear with the irradiation dose.

The theoretical analysis of experimental swelling data in ferritic-martensitic steels show swelling rate can be conveniently expressed in terms of parameter Q, which demonstrate the relative importance (strength) of dislocation and cavities sink (Fig. 7). The maximal swelling rate of 0.04 %/dpa is expected where the sink ratio is near unity. The total swelling measured for the specimens with boron after irradiation up to 16 dpa is in the range of 0.6%. This value corresponds to 0.04% - the maximal value of swelling rate.

Conclusion

The microstructure and swelling of ^{10}B-alloyed EUROFER97 were investigated after neutron irradiation up to 16 dpa in the temperature range from 523K to 723K. TEM analysis reveals the formation of visible cavities and bubbles at temperatures higher than 573K. In the specimens irradiated at 523K, only the formation of dislocation loops and point defects was observed. The presence of He inside the material, even at a concentration of 83 appm, leads to an increase in the density of cavities and swelling by a factor of four compared to EU-

ROFER97 after irradiation at 623K. The high concentration of cavities and bubbles in material irradiated at 623K leads to the reduction of hardness despite the high swelling value. The small He bubbles which form on dislocations and grain boundaries do not have any influence on material hardness. The results show that boron alloying certainly is a good method to simulate He effects.

Staff:

M. Holzer
U. Jäntsch
M. Klimenkov
E. Materna-Morris
A. Möslang
M. Rietschel
R. Rolli
H.-C. Schneider

Acknowledgement

This work, supported by the European Communities under the contract of Association between EURATOM and Karlsruhe Institute of Technology, was carried out within the framework of the European Fusion Development Agreement. The views and opinions expressed herein do not necessarily reflect those of the European Commission.

Open Access to JANNuS: Synergetic Effects of Hydrogen and Helium Implantation in Fe-Cr Alloys (WP13-MAT-IREMEV-05-05)

Overview and project description

ODS steels are foreseen for the use in future advanced fission, spallation and fusion facilities. They should withstand high operation temperature and radiation loads without notable degradation of their properties. One of the key issues is high temperature helium embrittlement (HTHE) resulting in decreased fracture toughness of structural materials. Numerous experiments have shown that addition of hydrogen can drastically increase the size of helium bubbles, swelling and thus increase material susceptibility to HTHE. However, the mechanisms of interaction of radiation defects and, especially, transmutation gases like helium and hydrogen with radiation defects and ODS particles are not yet completely understood. Some of the recent experimental findings indicate that presently we can only guess what is really going on at the microstructural level during the steel operation in radiation environment. JANNuS facility is a unique and invaluable tool for experiments that can shed light on the mechanisms of microstructural kinetics at the nanoscale, which we are trying to understand using multiscale modeling approach.

The main project objective is the study of interaction of displacement damage, helium and hydrogen atoms with radiation defects and ODS particle-matrix interface. One of the particular objectives is to study material behavior under fusion relevant irradiation conditions which in the absence of dedicated neutron sources (as e.g. IFMIF) will be modeled by triple ion beam irradiation.

Experiment

Typical displacement damage curves after 24h of 24 MeV Fe^{8+} irradiation are shown in **Fehler! Verweisquelle konnte nicht gefunden werden.**. Energies of helium (2.2 MeV) and hydrogen (0.7 MeV) ions are selected so that the maximum of their stopping profiles is below the region with the maximum damage. This allows helium and hydrogen ions to interact with vacancies during their diffusion.

In addition to EUROFER and ODS-EUROFER several model alloys with varying Cr concentration are going to be irradiated (see Table 1).

Table 1: Materials

Pure Iron.	(EFDA batch)	EUROFER
Fe- 3%Cr	(EFDA batch)	ODS- EUROFER
Fe- 8%Cr	(EFDA batch)	
Fe- 14%Cr	(EFDA batch)	

It is proposed to irradiate these materials using Fe^{+3} with 10.5 MeV, He^{+} with 1.05 MeV and H^{+} with 0.38 MeV and the damage rate of 1.6 10-3 dpa/s up to 50 dpa at the half depth of the samples.

To evaluate the effect of temperature five temperatures are proposed: 320, 400, 450, 500 and 600°C. This produce a total of 30 samples irradiated in different conditions.

Future activities

This proposal was submitted in 2011 for the JANNuS Open Access through EFDA, was approved in 2012 and should have been executed in 2013. However, due to high occupancy of the JANNuS beam lines the proposal was not executed. Presently because of restructuration of EFDA into EUROFUSION it is unclear if the funds for the project could be transferred into the new structure.

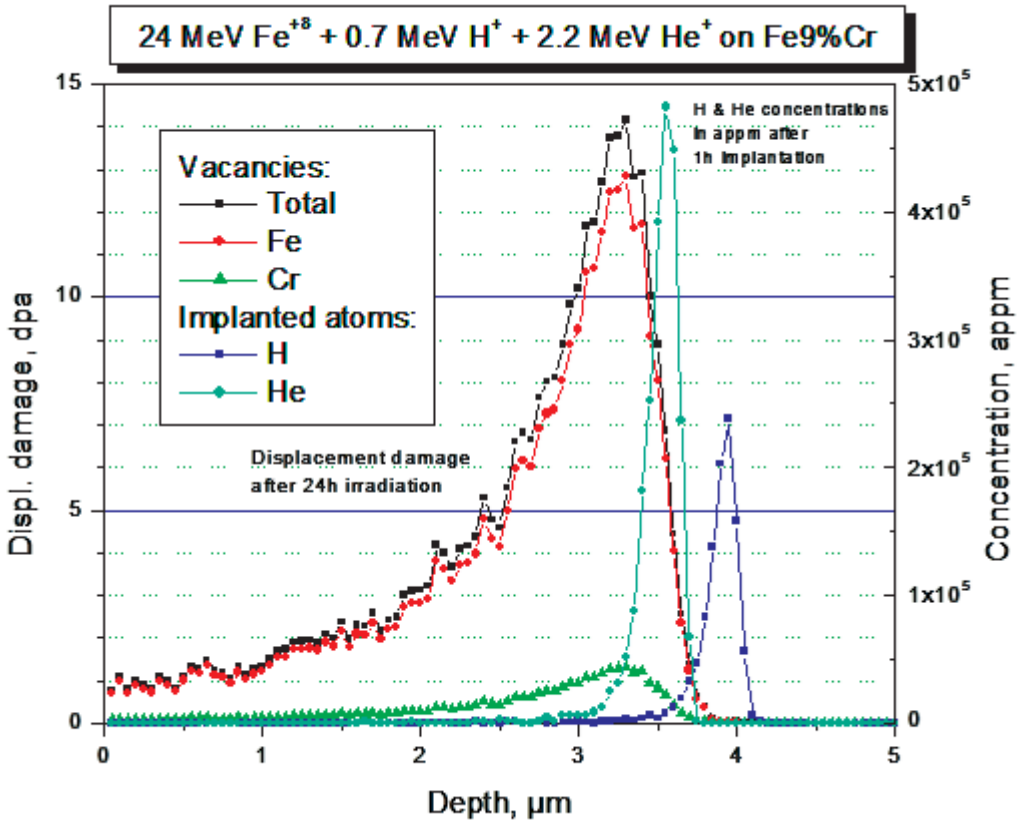

Fig. 1: Example of radiation damage profiles (left axis) and stopped ion profiles (right axis) for triple beam irradiation of Fe-9%Cr model alloy.

Staff:

KIT:
L. Commin
J. Hoffmann
M. Klimenkov
P. Vladimirov

CIEMAT:
F. Motta
Ch. Ortiz
R. Villa

Acknowledgement

This work, supported by the European Communities under the contract of Association between EURATOM and Karlsruhe Institute of Technology, was carried out within the framework of the European Fusion Development Agreement. The views and opinions expressed herein do not necessarily reflect those of the European Commission.

Goal Oriented Training Programme “Fabrication and Characterization of Materials” (WP10-GOT-FabriCharMe (FU07-CT-2010-00065))

The EFDA 2010 Work Programme covers a training activity in the field of Materials Science and Technology called FabriCharMe (Fabrication and Characterization of Materials). The general aim of the training programme is to prepare engineers and scientists for activities to support the ITER project and the long-term fusion programme within the Associations, Fusion for Energy and ITER Organization. The special aim of this training is to provide knowledge and to develop expertise of young engineers to fulfil future duties of structural materials foreseen for in-vessel components in DEMO and TBM of ITER. These materials include the low activation ferritic/martensitic steel EUROFER (foreseen to be used on the ITER TBM), nano-structured low activation Fe-Cr steels and tungsten and copper alloys as structural, heat sink or protective elements. Thus training is needed in the procurement of these materials, managing qualification programmes and guiding the development of the materials. To achieve this, the training includes practical and/or theoretical laboratory activities and educational tasks (formal courses and conferences).

The main activities according the priority area “Materials Science and Technology” are specific issues of structural materials in fusion, e.g. selection of materials, alloy compositions and tailoring of properties, properties and failure mechanism under radiation (hardening, fracture, creep) and the role of gaseous transmutations, especially helium. In addition, modern tools for modelling and simulation of radiation e.g. methods to simulate evaluation of microstructure, advanced characterization methods including electron microscopy, energy dispersive spectroscopy, diffraction methods, and micro-mechanical testing are covered as well as practice in materials technology, e.g. overview on different fabrication processes and joining techniques, qualification of base materials and welds according to nuclear standards, and non-destructive testing.

The whole network consists of 5 associations from 5 different European countries. KIT is hosting the two trainees working in this programme under WP1 and WP2, training topics are focussed on KIT’s activities in post-irradiation testing, determining of irradiation damages, appropriate advanced characterization and microstructural investigation techniques, continuum mechanics modelling and design rules including radiation damage, selection and fabrication of materials, and joining techniques. CEA provides the opportunity to work with the SYSWELD analysis software (WP2) and on the Jannus beam line (WP1). IPPLM-WUT is providing training on nanoscale microstructural characterization. CRPP qualified a trainee on small and ultra-small specimen test techniques. CCFE-Oxford gave a training unit on focused ion beam-machined micromechanical specimens.

In 2013, there was the yearly network meeting - with presentations by the trainees and by the mentors of the host associations - on July 15th and 16th, held at IPPLM-WUT. The next and final network meeting is scheduled for March, 24th and 25th 2014 at KIT.

Work package No. 1 (WP1)

Irradiation damage - advanced characterization and modelling
L. Commin, hosted at KIT since April 2011, supervised by A. Möslang
Associated Partners in this programme: CEA, IPPLM-WUT, CRPP
Secondments in 2013: IPPLM-WUT

In fusion reactors, due to pulsed operation, the combined creep and fatigue loading of structural materials will occur. Therefore, fatigue, creep and creep–fatigue analysis of the candidate structural materials was performed. Pure fatigue tests have been conducted on Eurofer97 base material and similar electron beam welds, and then fatigue pre-stressed samples at different number of cycles were produced. Microstructural analysis of the samples was done using optical microscopy and SEM. In a second step, creep analysis on these pre-

stressed samples will be performed until fracture occurs. Hence, the damage contributions of fatigue and creep were studied.

During the secondment to the host association IPPLM-WUT, ODS steel powder consolidation was performed using Pulse Plasma Sintering (PPS). In the PPS process, the powder is heated by the Joule heat evolved when the electric current pulses pass through the die and the powder to be consolidated. Processing parameters as temperature, pressure, holding time were varied and the resulting materials were studied using SEM and mechanical testing.

Fig. 1 shows the parameters' (temperature, pressure, and holding time) influence on the microstructure, Tab. 1 the change in density and Vickers hardness. The comparison to the base powder is established and a publication of the results is foreseen for 2014.

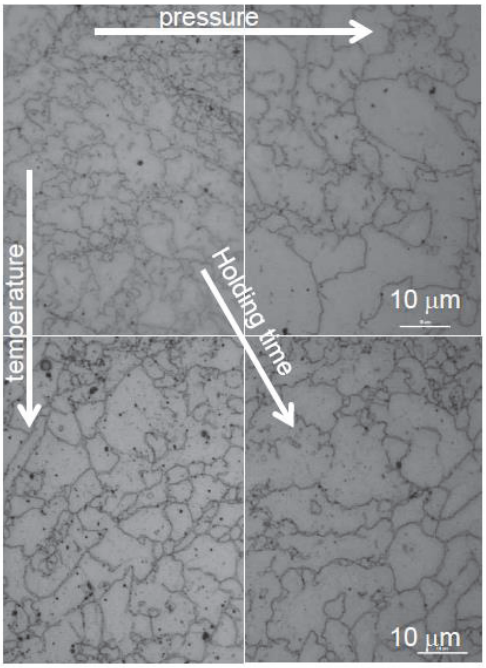

Fig. 1: Influence of processing parameters as temperature, pressure, holding time on the microstructure of powder steel.

Fig. 2: PPS facility at IPPLM-WUT.

Table 1: Influence of processing parameters temperature, pressure, and holding time on the density and Vickers hardness of powder steel.

Temperature [°C]	Pressure [MPa]	Holding time [min]	Density [%]	HV1 [-]
1100	1000	5	100.0	-
1000	1000	5	98.9	448
950	1000	5	99.4	445
1000	1200	5	98.9	425
1000	1200	10	94.0	403

A detailed description of the work on copper based materials for water cooling applications is given by L. Commin in the report on WP12-MAT-01-HHFM-02-01/KIT/BS, "Mid-term structural materials".

In brief: in nuclear fusion reactors, the copper grades currently used for ITER water-cooled divertor will no more be usable, because of their lack in irradiation resistance and thermal strength. Investigation of new copper-based material was then performed and small scale samples produced. The materials investigated are Cu-Mn alloys and Cu-Y_2O3 dispersed

material. Several processing routes (sintering, induction melting, HIP) were studied and the resulting microstructure, microhardness and thermal conductivity were determined.

Work package No. 2 (WP2)

Structure Materials and joining development
M. Scherwitz, hosted at KIT from October 2010 until September 2013, supervised by H.-C. Schneider
Associated Partners in this programme: CEA, CCFE-Oxford
No Secondments in 2013
Work Package No. 2 has been completed by end of September 2013.

The RAFM steel Eurofer97 is a potential candidate as structural material for in-vessel components of future fusion power plants. During operation it will be subjected to cyclic thermo-mechanical loading and therefore it is necessary to characterize its LCF behaviour. Beside lifetime investigations on the base material, it is also important to characterize the behaviour of its welding joints by considering the various bonding techniques.

In 2013, additional sub-sized TIG specimens of Eurofer97 were investigated. The weld was placed with a shift of 2 mm out of the specimen centre. Due to that the amount of base material was increased within the gauge length of the specimen. The semi-finished goods underwent PWHT (760 °C/2 h) before specimen fabrication. The tests were conducted in strain controlled mode with a strain rate of $3x10^{-3}$ s^{-1} and a total strain range of 0.6 %, and 1.0 %.

Results of the LCF experiments are illustrated in Fig. 3.The various tests under equal test conditions show, that lifetime of specimens, including diffusion- and EB welds, is almost as high as specimens of the base material. TIG specimens show lower lifetimes compared to the other welds. This can be traced back on clearly higher stress levels monitored during testing, since the controlled gauge length is mostly occupied by the TIG weld (including HAZ). Specimen with shifted TIG welds show much higher lifetimes compared to centred TIG welds. According to the different material sections and the respective different local stress-strain fields, TIG and EB welded samples failed within the transition regions of the HAZs and the base material.

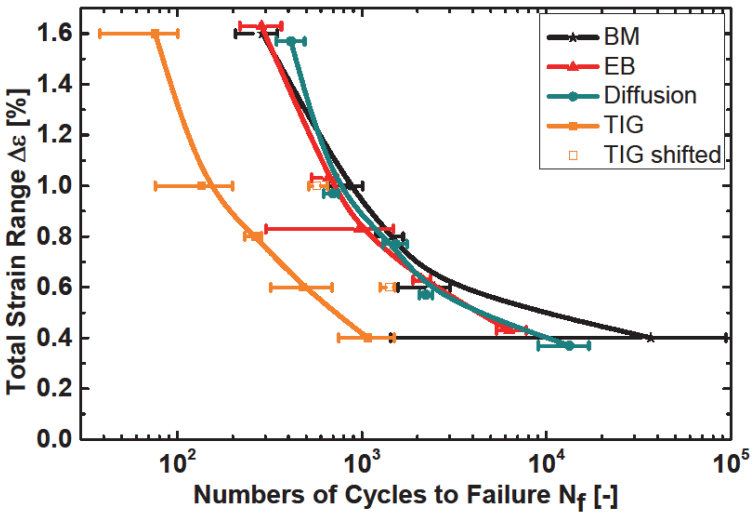

Fig. 3: Results of LCF tests on welded Eurofer97 specimens.

Further micromechanical experiments were performed by micro cantilever bending. Micro beams with triangular cross sections, a length of 30 µm and a width of 5 µm were fabricated. The beams were placed in Eurofer97 TIG- and EB welds in the BM, HAZ and WZ. A nanoindenter G200 was used for the bending experiments. All specimens were loaded elastic and afterwards elastic-plastic. Different lever arms were used for these experiments.

In Fig. 4, the cantilever of the EB weld in the base material is shown. This beam was fabricated by FIB at CFN (KIT) and exhibits a smooth surface. A load-displacement curves of the experiments are illustrated in Fig. 5. The continuous line shows the Load vs. Displacement of the EB base material. It can be seen, that no plastic deformation occurred. Second loading is

illustrated by the dashed line and show that the beam was elastic-plastic bended and plastic deformation remains after load removal.

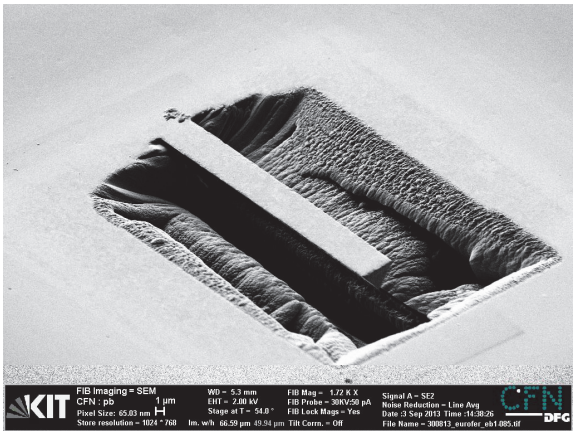

Fig. 4: Micro cantilever before testing is shown on the left.

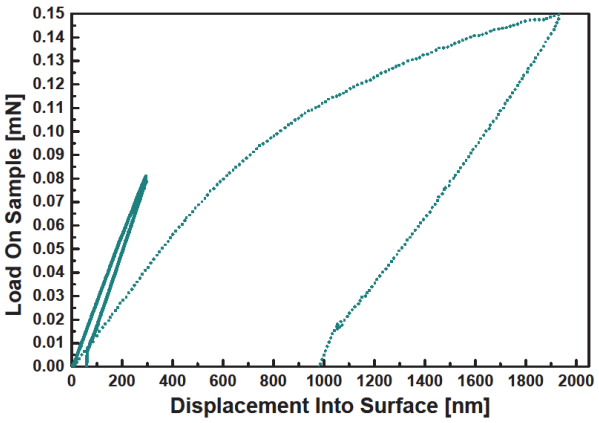

Fig. 5: Elastic and elastic-plastic bending of the cantilever in the base material of an EB weld.

Staff:

J. Aktaa
L. Commin
A. Möslang
M. Rieth
M. Scherwitz
H.-C. Schneider
P. Vladimirov
M. Walter

Literature:

[1] Schneider, H.-C.: EFDA WP10-GOT-FabriCharMe - Training programme annual report 2013

[2] Commin, L.: EFDA WP10-GOT-FabriCharMe - Trainee report, WP1, 2013

[3] Scherwitz, M.: EFDA WP10-GOT-FabriCharMe - Trainee report, WP2, 2013

[4] L. Commin, M. Rieth, V. Widak, B. Dafferner, S. Heger, H. Zimmermann, E. Materna-Morris, R. Lindau: Characterization of ODS (Oxide Dispersion Strengthened) Eurofer/Eurofer dissimilar electron beam welds, J Nucl Mat 442, 1–3, S1, November 2013, 552–556

[5] S. Antusch, L. Commin, M. Mueller, V. Piotter, T. Weingaertner: Two component tungsten powder injection molding – An effective mass production process, J Nucl Mat, in press, Corrected Proof, Available online November 2013

[6] L. Commin, M. Rieth, B. Dafferner, H. Zimmermann, D. Bolich, S. Baumgärtner, R. Ziegler, S. Dichiser, T. Fabry, S. Fischer, W. Hildebrand, O. Palussek, , H. Ritz, A. Sponda: Fail safe and cost effective fabrication of a first wall by diffusion welding: J Nuc Mat, 442, 1–3, November 2013, 538-541

[7] S. Antusch, L. Commin, J. Heneka, V. Piotter, K. Plewa, H. Walter: A new fully automatic PIM tool to replicate two component tungsten DEMO divertor parts, Fus Eng Des, 88, 9–10, October 2013, 2461-2465

[8] L. Commin, S. Antusch, S. Baumgärtner, W. Goldacker, P. Lukits, M. Rieth, D. Bolich, M. Hoffmann: Assesment of Copper Based Materials For the Water-cooled Divertor Concept of the Demo European Fusion Reactor, SOFE, San Francisco, USA, June 10-14, 2013, to be published in proceedings

[9] L. Commin, S. Baumgärtner, B. Dafferner, S. Heger, M. Rieth, A. Möslang: Creep-Fatigue interaction in Eurofer 3 Electron Beam Welds, to be published in proceedings

[10] M. Dumont, L. Commin, I. Morfin, F. DeGeuser, F. Legendre, P. Maugis: Chemical composition of nano-phases studied by anomalous small-angle X-ray scattering: application to oxide nano-particles in ODS steels, Materials Characterization, 2013 (accepted)

[11] EFDA Workprogramme 2010, Goal Oriented Training Programme, Task Agreement WP10-GOT-FabriCharMe between the EFDA Leader and the Associates KIT, CEA, IPPLM-WUT, CRPP, and CCFE-Oxford

Acknowledgement

This work, supported by the European Communities under the contract of Association between EURATOM and Karlsruhe Institute of Technology, was carried out within the framework of the European Fusion Development Agreement. The views and opinions expressed herein do not necessarily reflect those of the European Commission.

Goal Oriented Training Programme “Radiation Effects in RAFM Steels: Experiments & Modelling” (WP12-GOT-RadEff (FU07-CT-2012-00066))

Objectives

The general aim of the RadEff training programme is to prepare materials engineers and scientists to support the ITER project and the EU long-term fusion programme within Associations and F4E. The task activities within the current reporting period aimed at reviewing of failure mechanisms under neutron irradiation, training in selected post irradiation mechanical testing techniques at the FML of KIT, learning SEM and TEM techniques to investigate irradiated specimens and the calculation of experimental conditions for dual beam irradiation experiments at the JANNUS facility. In addition, one of the objectives was an identification of new approaches for the further development of the rate theory model for the description of nucleation and evolution of helium bubbles under neutron and dual beam irradiation experiments irradiation.

Task Current Status

After studying the helium effects in RAFM steels by reviewing the experimental data on formation and growth of helium bubbles in the irradiated boron doped EUROFER97 based steels, the PIE training was performed on base EUROFER97. Mechanical testing of steel specimens and the accompanying metallography were carried out in the hot cell laboratory, to examine the unirradiated sample and to get acquainted with the facilities. In addition to the optical microscopy the samples were examined under TEM and SEM. The Fortran code developed at KIT for simulation of nucleation and growth of helium bubbles inside the steel microstructure under neutron irradiation was analysed and on the basis of other literature works in the field further development approaches were identified. In order to validate the existing Fortran code the necessary dual beam irradiation experiments were prepared.

Two unirradiated KLST EUROFER97 specimens have been tested in the hot cell laboratory. The Charpy impact tests were performed at two different temperatures to examine the behaviour in the upper and lower shelves. Fig. 1 shows the results of the Charpy impact tests on the two KLST-Specimens. The specimen tested in the lower shelf at -118 °C had a much lower impact energy (0.4 J) but a higher Yield Stress (871 MPa) than the specimen tested in the upper shelf at ambient temperature (Yield Stress 648 MPa and an impact energy 9.9 J). The two samples were prepared metallographically to investigate with the microscope and

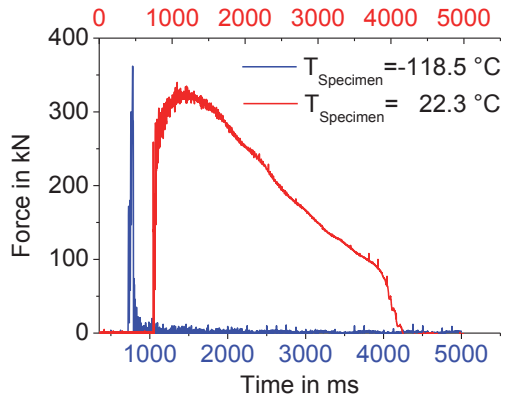

Fig. 2: Result of the Charpy impact tests on the two EUROFER specimens.

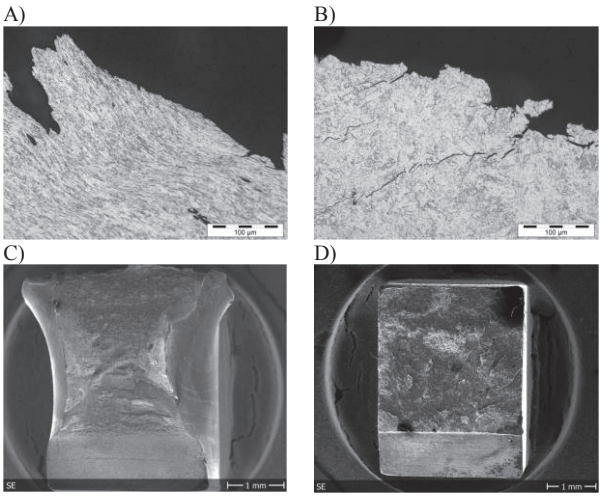

Fig. 3: A and B: optical images of EUROFER97 microstructure revealing ductile (A) and brittle (B) behaviour; C and D: SEM images of ductile (C) and brittle (D) fracture surfaces.

SEM. Fig. 2 A shows how the grains are deforming during a ductile fracture at ambient temperature. In contrast, the specimen tested in the lower shelf shows no deformed grains and rather cracks inside the sample in Fig. 2 B. The SEM pictures of the fracture surfaces in Fig. 2 C and D show that the brittle sample fractured near the notch without observable deformation of the specimen. The origin of the fracture initiation in the ductile sample is far away from the notch and the KLST specimen is severely deformed.

To analyze the microstructure of the irradiated steel specimens the knowledge of the transmission electron microscopy technique is required. Therefore the basic techniques of the TEM were taught and practiced with standard TEM samples (carbon mesh) and EUROFER97.

The existing master equations for the description of the evolution of helium bubble microstructure in the RAFM steel during fission reactor irradiation have been studied as well as the corresponding Fortran code built for solution of the system of the master equations has been analyzed. The model developed at KIT allows the description of the homogeneous nucleation and the time evolution of helium bubbles during neutron irradiation and was adapted to helium generation in boron doped neutron irradiated RAFM steel EUROFER97. After getting acquainted with the model the main parameters were varied to understand their influence on the helium bubble formation visible. For a further development of the model and to adapt it to the case of neutron irradiation under Fusion reactor condition several improvements of the model were planned. One improvement step should be the use of the real gas law which would be implemented into the model by EOS. Another important improvement aims at the use of analytic expressions of the bubble formation energies taking into account number of helium and vacancy atoms in the cluster/bubble with a varying radius of helium clusters in the vacancy. Another step aims at the consideration of the arbitrary helium to vacancy ratio instead of using the fixed one in the current model. The lateral (depth) dependence of helium concentration has also to be implemented in the model.

A review of the main scientific articles on dual beam irradiation experiments was necessary to find the appropriate experimental conditions and to avoid repeating a failed experiment. The experimental conditions including temperature, helium generation rate, concentration of implanted helium and depth of peak concentration of implanted helium should be varied to obtain a maximum of information.

Table 1: Conditions for Dual-Beam Irradiation Experiments.

Ions	Energy MeV	Flux min Ions/(cm²s)	Dose Ions/(cm²)	Temperature °C
Fe2+/He+	3 MeV/1.2MeV	$1.4*10^{12}/4.8*10^{11}$	$3.2*10^{16}/1.1*10^{16}$	330
Fe2+/He+	3 MeV/1.2MeV	$1.4*10^{12}/4.8*10^{11}$	$3.2*10^{16}$/1.1e16	400
Fe2+/He+	3 MeV/1.2MeV	$1.4*10^{12}/4.8*10^{11}$	$3.2*10^{16}/1.1*10^{16}$	550

In order to obtain a fusion like appm helium to dpa ratio the experimental conditions for dual beam irradiation were calculated in cooperation with the trainee from CEA. Particularly, the acceleration voltages, required degraders, displacement cascades, helium implantation rates have been calculated by the help of the software TRIM, which are shown in Table 1.

Conclusion and Outlook

The main work in the reporting period was the identification of failure mechanisms under neutron irradiation, getting acquainted with post irradiation mechanical testing and the investigation of the microstructure by SEM and TEM. The first both activities are nearly finished and the third one is started by investigating of unirradiated EUROFER97 under SEM and TEM. The development of the rate theory model for the description of nucleation and evolution of helium bubbles was also going on by familiarization with the model and looking for the further development of the existing code. Some preparation work of the dual beam irradiation

experiments is already done, particularly the first calculation and article review to obtain a homogeneous helium bubble formation in the microstructure of the RAFM steel.

Within the upcoming dual beam irradiations a large number of samples will be produced which will be prepared for TEM examination. The results of the microstructural investigations will be used for validation and further development of the existing rate theory model.

Staff:

O. Tröber
E. Gaganidze
C. Dethloff
H. C. Schneider
R. Rolli
M. Holzer
H. Ries

Literature:

[1] O. Tröber, C. Dethloff, E. Gaganidze and J. Aktaa, D. Brimbal, P. Trocellier and L. Beck; Experiments for Helium Bubble Formation in the Microstructure of EUROFER97 with Dual-Beam Injection; CIMTEC 2014 abstract

Acknowledgement

This work, supported by the European Communities under the contract of Association between EURATOM and Karlsruhe Institute of Technology, was carried out within the framework of the European Fusion Development Agreement. The views and opinions expressed herein do not necessarily reflect those of the European Commission.

Goal Oriented Training Programme “Radiation Induced Microstructural Evolution and Strengthening in High-Cr-Steels (WP12-GOT-RIMES (FU07-CT-2012-00066))

Overview and project description

The primary objective of this GOT-4 project in the area of 'Materials Technology for In-Vessel components' is to contribute to education and training of specialists for development of in-vessel structural materials for DEMO and ITER. This objective will be achieved through hands-on training on activities ranging from modeling to experiments, aimed at the understanding of the interrelation between radiation induced micro-structure and hardening in high-Cr steels, with and without oxide dispersion strengthening (ODS) inclusions. Various experimental and modeling tasks are distributed between the members of consortium which includes SCK-CEN, Belgium, KIT, Germany and CIEMAT, Spain.

The major goal of this project is to get insights into relation between irradiation induced microstructure and atomic scale mechanisms of irradiation hardening using model iron-chromium alloys and ferritic-martensitc steel EUROFER97 as well as its oxide dispersion strengthened (ODS) counterpart. The goal should be reached through extensive multiscale modeling, validation experiments and quantitative microstructure investigation of irradiated samples.

KIT contribution to the project consists in in-depth investigation of irradiation-induced microstructure changes relevant for mechanical properties. The main features expected to increase material’s hardness are interstitial loops, small precipitates of secondary phases and helium bubbles.

Specimens of EUROFER97 and EUROFER ODS irradiated within several irradiation campaigns (SPICE: 16 dpa, 250-450°C; WTZ: 15 dpa, 330-340°C; ARBOR: 15, 32 and 70 dpa, 330-340°C). Some specimens from SPICE were doped with boron isotopes to simulate various levels of helium production (80, 450 and 5800 appm He).

The characterizations of the mechanical properties of the samples and part of the microstructural investigations have been already performed. The trainee is expected to carry out a systematic study of dislocation network and dislocation loop size distribution and their number density, as functions of irradiation temperature, dose and He content, in EUROFER97, including the investigation of □′ precipitates and helium bubbles.

The following major accomplishments are expected as a result of project completion:

- Collection of experimental database for development of models of nanostructure evolution and hardening, for calibration and verification of their predictions.
- Report on the literature review and preliminary results of the investigation of specimens from SPICE program
- Report on the investigation of nondeformed specimens from ARBOR program
- Final report on the investigation of deformed and nondeformed specimens from SPICE and ARBOR programs

First year activities of KIT trainee

During the reporting period the main training activities were focused on training in electron microscopy and spectroscopy techniques.

In February 2013, the trainee attended a seminar “Texture in Materials”. The subject of this course was to learn about typical characterization methods for measuring texture, graphical representation and electron-backscatter diffraction.

In March 2013, the trainee attended a course on electron-backscatter diffraction (EBSD) in modern scanning electron microscopes. The focus of this course was the deeper understanding of EBSD techniques for the characterization of phases, orientation and deformation structures in materials.

In preparation of the work on the irradiated materials in the hot-cells of Fusion Materials Laboratory (FML) at KIT, the focus of the remaining year was on preparation and characterization of steel samples for transmission electron microscopy. The trainee prepared different classes of steels from conventional (low activation) materials to oxide dispersion strengthened steels for fusion applications. These materials were then characterized by the various characterization methods of the TEM. Special emphasis was on spectroscopy with combined energy-dispersive x-ray spectroscopy (EDS) and electron energy loss spectroscopy (EELS).

During the above tasks, access to the hot cells was requested. The final authorization and approval was granted in the last half of the year.

Future activities

In the second year the main focus of the work will be on the investigation of microstructure of nondeformed irradiated EUROFER 97 and EUROFER ODS samples from the ARBOR irradiation. In addition a three months visit is foreseen to CIEMAT, Madrid to get familiar with investigations of ferritic-martensitic steels there. This year will be concluded with a report on the investigation of nondeformed specimens from the ARBOR program.

During the third year the trainee will perform investigations of microstructure of deformed irradiated EUROFER 97 and EUROFER ODS. Here interaction of dislocation with irradiation induced obstacles is the main center of the studies. The training will be completed with a final report on the investigation of deformed and nondeformed specimens from SPICE and ARBOR programs.

Staff:

J. Hoffmann – trainee
M. Klimenkov
E. Materna-Morris
M. Rieth
P. Vladimirov

Acknowledgement

This work, supported by the European Communities under the contract of Association between EURATOM and Karlsruhe Institute of Technology, was carried out within the framework of the European Fusion Development Agreement. The views and opinions expressed herein do not necessarily reflect those of the European Commission.

Creep-fatigue Design Rules for EUROFER97 (WP13-DTM-03-T04-01)

Objectives

ASME-BPVC (Boiler Pressure Vessel Code) provides the design-by-analysis rules to prevent structural failures from load- and time-dependent damages at high temperature. For a reliable fusion reactor design the design rules in Section III of ASME-BPVC (subsection NH) should be checked for the creep-fatigue assessment when the metal temperature is subjected to elevated temperatures (for 2 1⁄4 Cr-1 Mo, above 370°C) [1]. Since blanket and diverter components in DEMO are subjected to high thermo-mechanical loading, evaluation of creep-fatigue interaction based on elastic stress analysis in ASME-BPVC is essential for the engineering design.

After review of ASME-BVPC rules for design of nuclear components, it was found that the evaluation procedures and rules for creep–fatigue damage are too complicated to apply to an actual reactor design with consideration of all the design transient conditions by hand calculations. In order to resolve this problem elastic creep-fatigue rules in ASME-BPVC are computerized and implemented into MAPDL (Mechanical Ansys Parametric Design Language) as a post processing. This effective design tool provides a huge investigation potential for the complex geometry of Eurofer97 components in DEMO with considering influence of different dwell time at local temperature whether the construction under given boundary conditions is acceptable to run.

Task current status

Creep-fatigue analysis of the components built from Eurofer97 in a test blanket module (TBM) was evaluated based on the elastic analysis approach in ASME-BPVC. Required allowable number of cycles design fatigue curve, and stress-to-rupture curve to estimate the creep-fatigue damage are used from literature. Local stress, strain and temperature inputs for the analysis of creep-fatigue damage were delivered from MAPDL. Developed extern FORTRAN code as a post processing was coupled with MAPDL. Influence of pulsed mode with different pulse durations (hold-times) and number of pulses on creep-fatigue damage for the preliminary design of the Helium Cooled Pebble Bed Test Blanket Module (HCPB-TBM) were discussed at critical regions. Investigation of critical regions in TBM shows that failure is inevitable for the investigated paths under typical ITER loading conditions [2]. Possible upgrades and solution suggestions to overcome the allowable limits in the structure are available in [3] for the next TBM design.

Staff:

J. Aktaa
F. Özkan

Literature:

[1] American Society of Mechanical Engineering Boiler&Pressure Vessel Code, Section III Subsection NH, NB, Division 1, 2004.

[2] F. ÖZKAN and J. AKTAA, Creep-Fatigue Design Rules for Eurofer97, Fusion Science and Technology, submitted.

[3] F. CISMONDI et. al, HCPB TBM thermo mechanical design: Assessment with respect codes and standards and DEMO relevancy, Fusion Engineering and Design, 86, 9–11, 2228 (2011).

[4] F. ÖZKAN and J. AKTAA, Creep-Fatigue Design Rules for Eurofer97, Fusion Science and Technology, submitted.

[5] F. ÖZKAN and J. AKTAA, Development of DEMO SDC-IC – Creep-Fatigue Rules for EUROFER97, EFDA_D_2M7GWF, 2013, submitted.

Acknowledgement

This work, supported by the European Communities under the contract of Association between EURATOM and Karlsruhe Institute of Technology, was carried out within the framework of the European Fusion Development Agreement. The views and opinions expressed herein do not necessarily reflect those of the European Commission.

Interaction of Hydrogen with Beryllium Surfaces (HCP-FF-HySuBe; WP13-MAT-IREMEV-01-01; WP13-MAT-IREMEV-01-02)

Introduction

After the end of life of the DEMO fusion reactor blanket about 7 kg of ß-radioactive tritium will be generated within the 310 tons of beryllium pebbles used in the helium-cooled pebble bed of fusion reactor blanket. Therefore prediction of tritium inventory retained in beryllium pebbles is very important both for safety during the fusion reactor operation and utilization of radioactive beryllium pebbles after the end of life of the reactor. Associative desorption of the accumulated tritium might occur at the external surface of pebble as well as on the internal surface of helium filled bubbles. This was a motivation for the study of hydrogen interaction on and with beryllium surface which was investigated in this work.

Calculation method

In this work static and dynamic first principles density functional theory (DFT) calculations were used. *Ab initio* calculations were performed using plane-wave VASP computer code [1]. Full geometry optimization is carried out using Generalized Gradient Approximation (GGA) with Perdew-Wang non-local exchange-correlation functional [2] and the scalar relativistic PAW [3]. The calculations involve typically 13x13x13 Monkhorst-Pack k-point mesh [4] and the cutoff energy of 450 eV. Migration barriers were estimated by means of the drag and/or nudged elastic band methods. Typically rhombohedral supercells with 64 and 96 lattice sites are applied.

Static ab-initio calculations were performed using VASP code. 128 CPUs (8 nodes) were found to be optimal for our calculations. In order to mimic the free surfaces a 17-23Å thick vacuum gap was introduced. The volume and the shape of the simulation cell were rigidly fixed during relaxation. No restrictions on the relaxation of atoms were imposed.

Results

<u>Determination of hydrogen adsorption/desorption barriers in dependence on hydrogen surface coverage</u>

It was found previously that being on Be(0001) surface hydrogen molecules dissociate immediately. Individual hydrogen atoms cannot desorb from the surface before they form a hydrogen molecule again. The barrier for dissociative adsorption for hydrogen molecule on virgin Be(0001) surface is about 0.75 eV, while that for associative desorption is about 1 eV. The first energy barrier implies that the energy of hydrogen molecule should be slightly higher than 0.75 eV. If the energy of hydrogen molecule is significantly higher than the barrier (but not so high that it can penetrate the surface), the molecule will be reflected by the surface without adsorption.

Access to one of the 25 most powerful supercomputers in the world (IFERC-Helios, Japan) allowed us to investigate how these barriers depend on the hydrogen surface coverage. Hydrogen molecule is impinging the surface in the direction opposite to the surface normal vector with various initial velocities while the number of hydrogen on the surface can be adjusted to mimic certain hydrogen surface coverage. Our ab initio molecular dynamics runs using 4x4 unit cell surface at 200K have shown that surface hydrogen coverage of 16/32=0.5 ML (half of the available adsorption positions are occupied with hydrogen) is sufficient to prevent adsorption of new hydrogen molecules. Our previous study has shown that this coverage is a maximum allowable coverage as any additional H atom will be a nearest neighbour of another one providing conditions for hydrogen molecule formation. In this case hydrogen associative desorption occurs without any energy barrier. Removing one of 16 hydrogen atoms (one H-vacancy on the surface corresponding to the surface coverage of 15/32≈0.47 ML) does not improve the situation: no molecule adsorption follows. We found that notably higher energy

of incident H_2 (2.28 eV) is required for adsorption if two H atoms are removed (two H-vacancies; coverage 14/32≈0.44 ML).

Surprisingly, higher kinetic energy of H_2 (4.1 eV) results in the molecule adsorption neither in the case of one nor two H-vacancies. In the second case, separation of H atoms occurs temporary, but then both H atoms are reflected back from the surface and, finally, form a molecule again.

Determination of hydrogen surface and subsurface adsorption sites and migration barriers between them

Soaking of metals in hydrogen atmosphere at high temperature and increased pressure is very useful for express estimation of hydrogen-metal affinity. However, the relation between hydrogen release curves obtained after soaking through the surface and after irradiation where hydrogen is produced in the bulk of material is still questionable. Many researchers assume that hydrogen is only adsorbed at the metal surface, but is not penetrating into the bulk (no hydrogen absorption). In the experiments performed in the KIT hot cells, tritium release peaks at similar temperatures are observed both on irradiated and tritium soaked samples, suggesting that trapping on defects (i.e. vacancies) in the bulk happened in both cases.

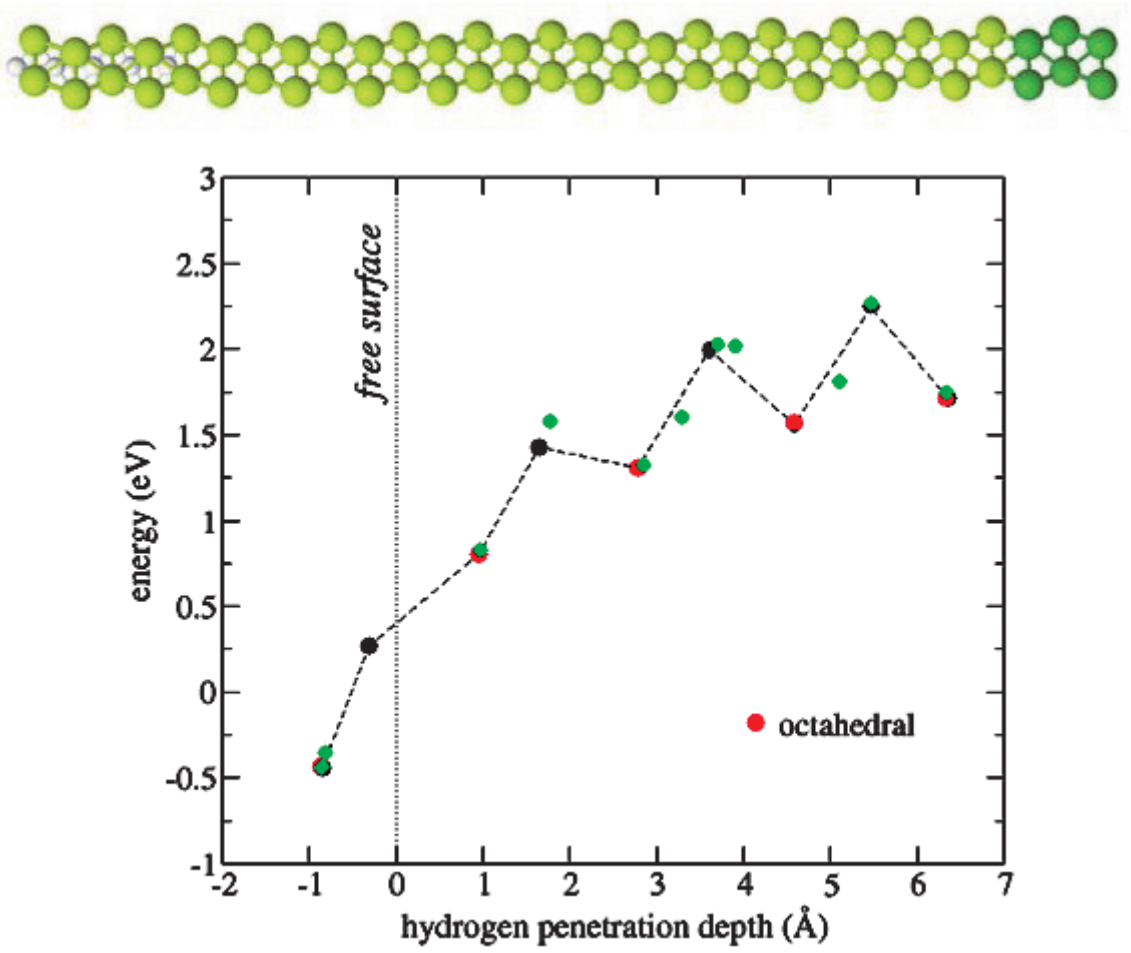

Fig. 1: Top: side view of the Be slab used for (0001) surface simulation. Regular beryllium atoms are coloured light green, while fixed Be atoms are coloured dark green. Hydrogen atoms are shown as white spheres.
Bottom: Energy profile for hydrogen diffusion from the surface (left) into bulk (right).

To study the process of H absorption, we performed ab initio nudged elastic band (NEB) simulations to estimate the energetic barriers for penetration of hydrogen from the Be(0001) surface into the material bulk. As was shown previously, interstitial hydrogen is stable both in basal tetrahedral (BT) and octahedral (O) positions, while BT is by 0.2 eV more favourable.

Straightforward H diffusion path from the (0001) surface is along c axis through O-BO-O positions forming octahedral channel.

Hence, we have prepared Be slab 2x2x15 consisting of 30 layers parallel to (0001) surface (see Figure 1/top) with a gap of four lattice parameter in the [0001] direction to mimic free surface and to avoid mutual interactions between the free surfaces. Three Be layers on the side opposite to hydrogen were fixed to the bulk interlayer distance. First, five configurations corresponding to one H surface adsorption site (fcc) and four octahedral subsurface positions were relaxed to provide initial and final configurations for NEB calculations.

The preliminary results of these simulations are compiled in Figure 1 (bottom). Red dots correspond to octahedral positions of hydrogen, except the leftmost one which is fcc hydrogen surface adsorption site. While black dots are energy barriers are matching the saddle points at basal octahedral positions. Forth migration barrier (0.75 eV) is already quite close to the migration barrier in the bulk of material (0.6 eV).

Conclusions and future prospects

Hydrogen molecule adsorption/desorption energy barriers on beryllium (0001) surface were investigated using ab initio molecular dynamics. It was found that the height these barriers have, changes with hydrogen surface coverage. After formation of 0.5 ML hydrogen layer (one hydrogen per surface unit cell) no hydrogen molecules can be adsorbed additionally. Two neighbouring vacant adsorption sites are sufficient for dissociative adsorption of H_2 molecule. However, in this case higher initial velocity of H_2 molecule than for virgin Be surface is required for adsorption.

To penetrate from the Be(0001) surface into the bulk a series of migration barriers should be overcome by an adsorbed H atom. Especially problematic seems to be the first jump from the surface as the octahedral position between first and second layer of Be atoms has only very shallow energy minimum, so that the reverse jump back to the surface is very probable. However, it seems that at high temperatures hydrogen can penetrate from the surface into the material bulk. The Diffusion barrier for other Be surfaces should be investigated to find the most favourable way of surface hydrogen absorption in the bulk.

Staff:

P. Vladimirov
D. Bachurin
Ch. Stihl

Literature:

[1] G. Kresse, J. Hafner, Abinitio Molecular-Dynamics for Liquid-Metals, Phys Rev B, 47 (1993) 558-561.

[2] J.P. Perdew, Y. Wang, E. Engel, Liquid-Drop Model for Crystalline Metals - Vacancy-Formation, Cohesive, and Face-Dependent Surface Energies, Phys Rev Lett, 66 (1991) 508-511.

[3] G. Kresse, D. Joubert, From ultrasoft pseudopotentials to the projector augmented-wave method, Phys Rev B, 59 (1999) 1758.

[4] H.J. Monkhorst, J.D. Pack, Special points for Brillouin-zone integrations, Phys Rev B, 13 (1976) 5188.

Acknowledgement

This work, supported by the European Communities under the contract of Association between EURATOM and Karlsruhe Institute of Technology, was carried out within the framework of the European Fusion Development Agreement. The views and opinions expressed herein do not necessarily reflect those of the European Commission.

Corrosion Testing of Bare Eurofer and Al-based Coatings in PICOLO Loop (CoA)

General Introduction

Liquid lead lithium is foreseen in several blanket designs, e.g., HCLL, WCLL and DCLL (**H**elium **C**ooled, **W**ater **C**ooled and **D**ual **C**oolant **L**ead **L**ithium) [1] as breeding material. All these blanket designs are common that the liquid breeder lead lithium is in direct contact with the structural material. Essential for the application of the developed Reduced Activation Ferritic-Martensitic steels (RAFM) as structural material is their compatibility with the liquid breeder and the permeation behavior of Tritium through the walls into the coolant to ensure safe and reliable system operation.

In the past most of the activity concerning the issue of corrosion behavior was spent to determine material loss during exposure to flowing Pb-15.7Li at high flow velocities. A lot of data were collected concerning corrosion behavior of early developed RAFM steels like Manet, F82H-mod. and Optifer or testing of Eurofer, e.g., [2,3,4] at low temperatures (480°C, 753K) and flow velocity of 0.22 m/s, Under these soft conditions material losses are moderate at about 90 µm/year [4] and steel dissolution is the main corrosion mechanism. Meanwhile higher testing temperatures (550°C, 823K) are included into test scenarios as envisaged as operation temperature in HCLL blankets and flow velocities are scaled down towards more representative conditions. The corrosion testing of Eurofer at 0.22 m/s and 550°C showed a dramatically increase of the corrosion attack to about 400 µm/year [5]. Such a corrosion attack will produce about 4 kg of dissolved and subsequently transported corrosion products per square meter and year of exposed blanket surface to lead lithium. In the last years beyond erosion modeling and other corrosion associated effects gathered attention in the field of compatibility testing. By the MATLIM code [6] which is based on physicochemical properties the corrosion attack could be simulated in the turbulent flow regime rather well and material losses for temperatures 480 and 550°C and flow velocity 0.22 m/s are comparable with measured values. However, validation at smaller flow velocities need more reliable experimental data at long term exposure of RAFM steels to flowing Pb-15.7Li. For continuation the model development and validation a new test series was initiated to be performed at the Pb15.7li corrosion testing loop PICOLO at KIT. Under this campaign a first data set was elaborated for corrosion attack of Eurofer at flow velocity of 0.1 m/s and 550°C testing temperature.

In general, by considering all corrosion data available, it is obvious fact that corrosion attack is always present in a system working with flowing Pb15.7Li at elevated temperatures. Wall thinning, transport of corrosion products and precipitate formation will be present and has to be considered as potential risk as discussed in [6]. A reduction may be seen and given by application of corrosion barriers, which may act simultaneously as T-permeation barrier, too. As known from earlier examinations Al-based scales [7] may fulfill such criteria and thus more industrial relevant electrochemical Al plating of Eurofer is under progress as well as qualification of processed scales. In this report both topics I) compatibility testing of bare Eurofer in Picolo and II) qualification of Al-based barriers in flowing Pb-15.7Li produced by the so named ECA process on Eurofer will be reported.

Compatibility testing of bare RAFM steels

Corrosion testing in Picolo

Picolo is a Pb-15.7Li testing loop with a total length of ca. 12 m and an inventory of roughly 20 kg Pb-15.7Li. The test section is designed to operate at 550°C and is fabricated from a ferritic-matensitic steel (DIN 1.4914) as well as the other parts in the hot sections. The cooler parts are machined from austenitic steels (e.g., 1.4571). The Pb-15.7Li flow is powered by an electromagnetic pump and is adjustable in the range of roughly 0.01 to 1 m/s. The lowest

temperature is about 350°C in the surrounding of the pump, the flow meter and the magnetic trap. The latter is installed to collect magnetic particles moving with the melt.

Cylindrical samples (diameter 8 mm) are exposed in the test section in an arrangement concentric with the Pb-15.7Li flow. The test section has an inner diameter of 16 mm and a length of roughly 450 mm. About 12 samples are screwed together to a testing stack.

The actual test campaign (0.1 m/s 550°C) reached the designed long term exposure times of 12,000 h and the post mortem analyses of the samples are finalized. The test program for this campaign was mainly focused on testing of Eurofer, however, other materials as the Chinese low activation steel CLAM, and Al-coated samples were also exposed to Pb-15.7Li flow at 0.1 m/s. The Al-coated samples were processed using the formerly developed ECA process (**E**lectro-**C**hemical plating by **Al** deposition applying an organic toluene based electrolyte).

Corrosion attack at 550°C testing temperature and high flow velocity of 0.22 m/s was evaluated to be near 400 µm/year of material loss. This corresponds to an amount of roughly 4 kg dissolved Fe/Cr from a square meter Eurofer plate in one year, which is dissolved and transported with the Pb-15.7Li flow. The new corrosion testing campaign was designed to be at lower flow velocity (0.1 m/s) to provide corrosion data towards conditions present in a TBM for system layout and modeling. The value of 0.1 m/s was chosen to provide a second corrosion attack value for Eurofer coming from long term exposure in Picolo loop in the turbulent flow regime but in close neighborhood to mixed flow conditions. Turbulent conditions should be present in Picolo loop in the range of roughly 0.1 to 0.02 m /s flow velocity.

Fig. 1 shows the schematic view of PICOLO and the samples manufactured for testing. A mayor revision of the PICOLO was done shortly before starting this test campaign with renewing the tubing channel of the magnetic pump due to plugging by precipitates which were formed in the cooler sections of the loop and not completely collected by the magnetic trap. This feature may indicate that beyond dissolved corrosion products also fine precipitates are circulating. PICOLO loop was filled with fresh Pb-15.7Li delivered by GMH Stachow-Metall GmbH, Germany. The impurity levels were monitored by extracting samples at position of Pb-15.7Li entry into the test section and from the expansion vessel. The fresh Pb-15.7Li showed Fe, Cr and Ni levels near 1, 1 and 6 wppm, respectively, after filling the loop. The Ni impurity stepped up within several 100 h to ca. 30 wppm with fluctuations around this number over the testing time from 500 to 12,000 h. This indicates that corrosion is also present in the cooler sections which are fabricated from austenitic steel. The Fe concentration increased slightly from the 1 wppm value to some wppm with fluctuations around 5 wppm. A significant or clearly evaluable tendency was not observed. In contrast to the other hot sections (e.g., the heater), where very small flow velocities are present, the testing section was fabricated from an aluminum-coated FM steel to reduce corrosion attack of this component.

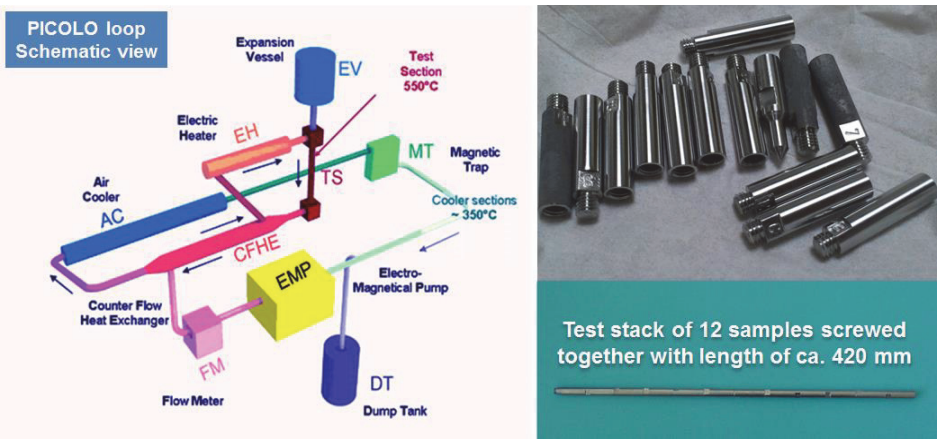

Fig. 1: Schematic view of PICOLO loop and test samples incl. assembled test stack.

Results

Corrosion behavior

The corrosion testing was performed in PICOLO loop at a flow velocity of 0.1 m/s and a testing temperature of 550°C. The temperature was kept rather stable with ± 2K and long term deviations from the projected flow velocity were controlled to be in a ± 5% range with short time deviations up to – 10% to obtain mostly constant test conditions. The samples designed for long term exposure (e.g., 12,000 h) were mounted at the top of stack i.e. at the Pb-15.7Li entrance into the test section. Samples for short time exposure were positioned at the end of the stack and removed samples were replaced by fresh ones.

The first sample was removed at 500 h testing time and showed first traces of corrosion attack. Still after 1000 h testing time some areas remained unattacked and the surfaces indicated clearly that the samples exhibit an incubation time before corrosion starts. The cross section given in Fig. 2 also point out that the breeder was wetting the sample, completely. This short term behavior is well known from tests performed earlier also at higher flow velocity [4,5]. For durations longer than 1500 h the metallographic pictures didn't show remaining unaffected surface fractions at any sample. All test pieces were covered by a Pb-15.7Li skin which was in good contact with the base alloy. SEM analyses showed that corrosion products (e.g., Fe, W) are present in the adherent Pb-15.7Li layer. In general the surface structure of the analysed samples did not change much in roughness and global appearance. No washing out of FM needles was seen and rather smooth surfaces are present as shown in Fig. 3. All these features indicate that the dominating corrosion mechanism is dissolution.

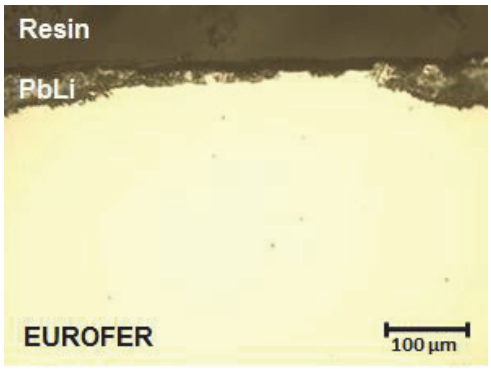

Fig. 2: (Left picture) Cross sections of EUROFER sample exposed for 1000 h with adherent Pb-15.7Li.

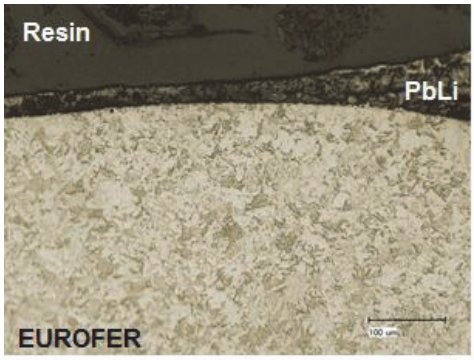

Fig. 3: Etched cross sections of EUROFER sample exposed for 12,000 h.

Corrosion attack

The corrosion attack was determined from diameter reduction. The diameter of the fresh test samples was measured by using a laser method with a resolution of ca. 1 µm. The samples were rotated to determine the diameter in dependence of radial positions and moved in axial position to measure diameter versus length of the sample. Two different measurement techniques were applied to evaluate the diameter of the corroded samples. Method one used the cross sections and the diameter was measured under a microscope by laterally moving the cut from one edge to the other by micrometer step controller. The second tech-

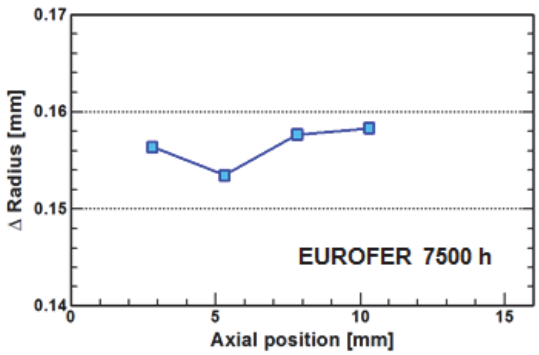

Fig. 4: Corrosion attack of an EUROFER sample in axial direction measured by laser scanning method as indicated in the picture in the left.

nique was the laser method and used the samples after removing the Pb-15.7Li by etching. Both methods determined the diameter in dependence of radial positions. The evaluated values for one special axial position are the arithmetic average of all measured radial values (step angle Δρ = 30°) at that position. Fig. 4 shows the behavior of an EUROFER sample removed after 7,500 h testing time from PICOLO loop. The reduction in radius is about 0.16 mm and the corrosion attack along the sample is rather constant as can be seen from Fig. 4. This indicates that homogeneous dissolution is present and that both steels undergo similar attack. The results of both measurement techniques for diameter determination are in good agreement with pictures taken from cross sections, e.g., as shown in Fig. 3.

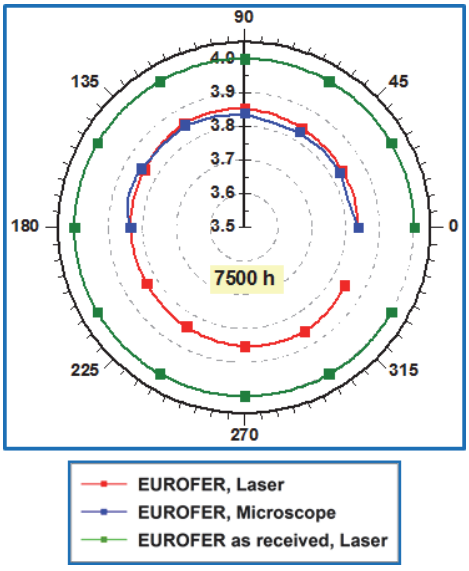

Fig. 5: Corrosion behavior of a cylindrical EUROFER sample in dependence on the radial position after 7500 h exposure to Pb-15.7Li.

The corrosion behavior in dependence on the radial position is shown in Fig. 5. Given are in this diagram the original radius of the fresh sample, radii determined by laser measurement and evaluated from metallographic cross section by microscope. The excellently visible information is that corrosion attack has significantly reduced the radius by material take off comparing the circles of fresh sample r (t=0) = 4 mm with radius of corroded sample r (7500 h) = 3.84 mm. The second extractable result is that the collected data points for radii by laser and microscope measurement are rather similar. This indicates that the sample surface was not attacked by removing the Pb-15.7Li skin i.e. no dissolution of the steel appeared and leads to misleading diameters. Both measurement techniques point out that the corrosion attack under the present conditions (local flow velocity, degree of turbulence) is rather homogeneous on the whole surface of the samples. No deep gaps are detected and the surface stays smooth. Small local deviations from cylindrical shape may come from, e.g., delayed surface attack during incubation time.

Corrosion rate

Long term corrosion behavior was analyzed for EUROFER in the PICOLO loop at flow velocity 0.1 m/s. The longest exposed samples remained for ca. 12,000 h in the PICOLO loop. The first sample was removed at 500 h test time and replaced by fresh ones. The evaluated corrosion attack is plotted in Fig. 6 vs. exposure time.

The 500 h sample showed clearly unattacked surface fractions due to incubation effects and the measurable diameter loss is small compared to the original diameter thus error bars may be larger for this samples. The Eurofer sample exposed 12,000 h shows a relatively high material loss compared to all other samples. This may be caused by local effects, e.g., mounted near to the upper end of the test section or by the coated sample in front causing higher turbulence. It has to be mentioned that flow velocity at 0.1 m/s is in the transition zone from turbulent to mixed flow regime. Considering such local and equipment specific details an average corrosion rate of 220 µm/year seems the most reliable one as indicated in the diagram.

The total number of test samples evaluated is small and no statistics exist at the moment for flow velocity of 0.1 m/s. Thus an assessment of the evaluated material loss should be done by comparison with other data collected at different flow velocities. Fig. 6 also shows the comparison of corrosion attack found at 0.22 and 0.1 m/s. This type of presentation confirms for both test velocities that a linear corrosion correlation is most reliable for the given test conditions. The corrosion attack at 0.1 m/s is clearly smaller than that evaluated at 0.22 m/s with about 400 µm/year. This corrosion rate of EUROFER is very reliable due to similar be-

havior of other earlier tested RAFM-steels [4]. The evaluated corrosion rate of 220 µm/year seems plausible for roughly half flow velocity of 0.1 compared to 0.22 m/s. There is also no disagreement with values expected by MATLIM modeling [8].

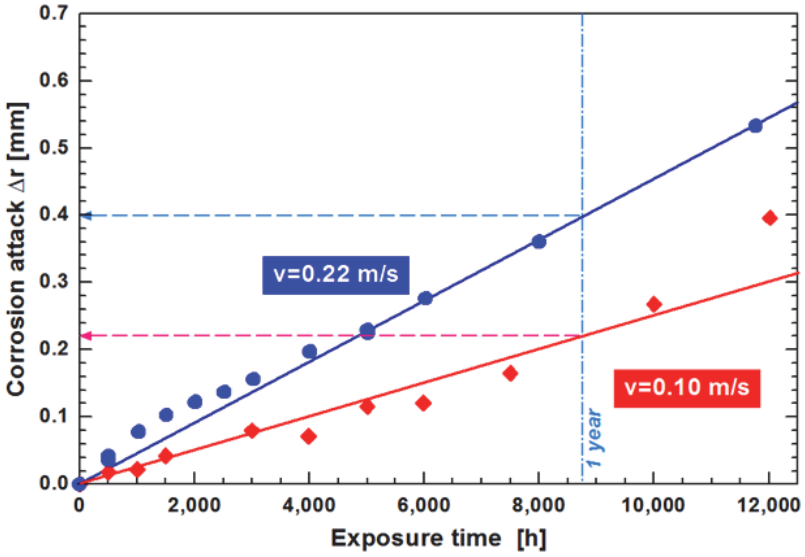

Fig. 6: Comparison of corrosion rates at flow velocities 0.22 and 0.1 m/s.

Conclusions

The corrosion testing campaign at 0.1 m/s was successfully performed up to ca. 12,000 h exposure time. A long term data base was elaborated and corrosion rate for 0.1 m/s flow velocity can be quoted with good reliability to be 220 µm/year. It was the first long term test campaign at reduced flow velocity in PICOLO loop under the test program of extending test scenarios towards TBM relevant conditions.

The corrosion attack was found to be rather homogeneous and shows less dependency on radial and axial positions of a test sample. However, it was seen that small steps (< 0.2 mm) can increase corrosion significantly due to additional turbulences. The dissolved amount of material (ca. 2 kg/m²year) is eminent and precipitates formed at cooler loop sections are still a serious risk for plugging compared to observations done at 0.22 m/s [6]. The evaluated corrosion rate at 0.1 m/s is in agreement with RAFM steels tested at higher flow velocity and with predictions coming from modeling. Looking towards blankets test conditions in a forced Pb-15.7Li loop have to be scaled down to the cm range to analyze laminar corrosion conditions and to provide data for model validation in this flow regime. However, it should be mentioned that smaller flow velocities will not solve the corrosion and precipitates issues and risks. A combination with corrosion barriers, which will also act as T permeation barriers, will be necessary to control precipitate risks.

Qualification of Al-based corrosion and T-permeation barriers

To keep corrosion rates in acceptable limits the application of coatings is required to ensure the long term application of RAFM steels under these challenging conditions in future blanket systems. Therefore, aluminum-based coatings are proposed to comply with these requirements. Besides the corrosion protection purpose they also provide tritium permeation reduction properties due to the formation of Al_2O_3 on the surface [9]. One of the first processes, which was under intensive investigation to apply such scales on RAFM steels, was the Hot-dip aluminizing process (HDA) with subsequent heat treating to form the desired ductile Fe-Al phases. Corrosion tests performed in the past revealed the corrosion protection properties of scales made by HDA process different RAFM steels (MANET, F82H-mod. and Eurofer) in flowing Pb-15.7Li [7,9].

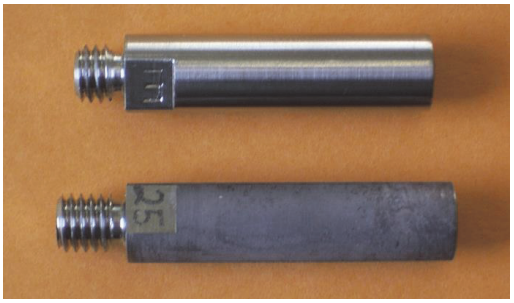

Fig. 7: Eurofer samples for corrosion testing in PICOLO loop: Bare steel sample (top) and ECA coated after HT (below).

In the last years, two different coating processes based on electrochemical methods to deposit Al on Eurofer steel were developed to overcome the drawbacks of the HDA process. These coating processes are both based on water-free electrolytes, but differ from each other in the type of solvents uses as electrolytes: The ECA process is based on volatile, organic solvents such as toluene, while the newer process, referred to as ECX process is based on the use of ionic liquids as electrolytes for the electro deposition of aluminum. Both electrochemical processes are able to provide controllability of layer thicknesses even in the micrometer range. Comparable to the HDA process a subsequent HT is also needed to form the actual protective scale on the steels. Fig. 7 shows a ECA processed sample after heat treatment in comparison to bare EUROFER as used in the compatibility testing in PICOLO loop.

Corrosion testing

Under this campaign mainly ECA coated samples were processed and exposed to Pb-15.7Li flow for determination of their corrosion resistance. The diameters of the samples were measured by a laser scanner at different positions (distance every 5 mm) and angles (0° to 330°, 30° step) before aluminum plating, after plating and after HT. In Fig. 8 the average diameters (12 values per position) are plotted against the position on the sample. Clearly visible is that the deposition of Al was very homogeneously with a layer thickness of about 15 µm. During the heat treatment the diameter of the test samples increased further due to the desired reactions of Eurofer and Al and formation of protective surface scales. These measured diameter values of the heat treated samples were used as initial values for the determination of corrosion rates after the exposure to the flowing Pb-Li melt. The specimens were then screwed together to a stack and were introduced into the test section of the PICOLO loop. After exposition times between 4000 hours and up to 12000 hours the electrochemically coated and heat treated samples were removed from the loop. From the middle of the sample, small disks were cut out for metallographic and SEM/EDX analyses. The lower parts of the samples were used for diameter determination by laser scanning method after removing the adherent Pb-15.7Li layer.

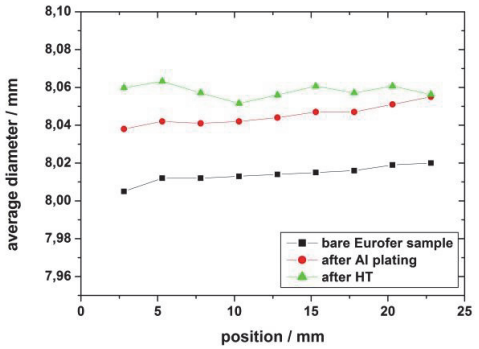

Fig. 8: Diameter measurements by Laser scanning system: Bare steel sample (green), after plating with Al (red) and after HT (blue).

Corrosion attack

All ECA coated samples had a grey colored surface as shown in Fig. 7 after the heat treatment. In the surface near area the diffusion correlated Kirkendall pores are clearly visible (Fig. 9). The general view shows that the surface is slightly rough, however, beneath the pores a well formed α-Fe(Al) zone was formed during the heat treatment. The complete structure implies that metallic Al were transformed to Fe-Al phases anticipation corrosion protectiveness.

Cross sections made from the middle part of ECA coated Eurofer samples after exposure to Pb-Li revealed, that for all exposition times under investigation the Eurofer steel was protected by the applied Fe-Al scale against corrosion and protective Fe-Al scales of a certain

thickness of above 30 µm were still observable for all exposure times. Fig. 9 (right) shows the microstructure of a sample removed from PICOLO loop after more than12,000 h.

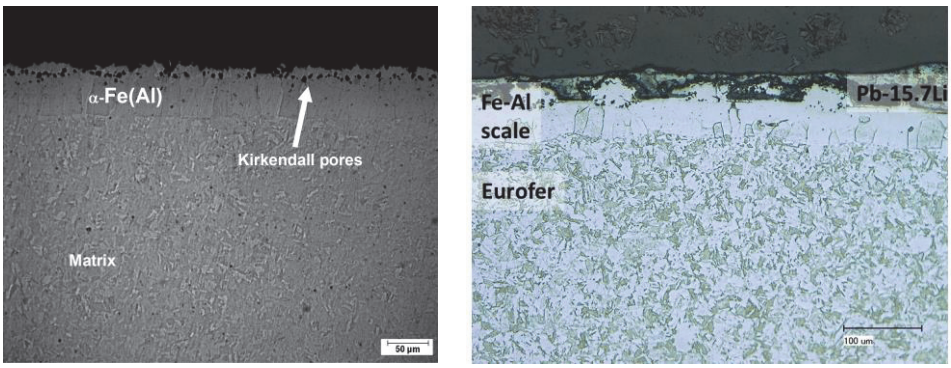

Fig. 9: Cross sections of ECA coated Eurofer samples before (left) and after exposition to flowing Pb-15.7Li for 12012h (right).

The cross cut of the exposed sample may probably show that the surface was affected by inhomogeneous attack leading to a more rough surface. However, it is still valid that the desired Fe-Al scales for corrosion protection did not disappear. Assuming an inhomogeneous attack may cause a scale structure of plateaus of different "heights", whereby the amount of remaining "low" plateaus seems to increase with exposure time. For this reason two diameters (D) were measured by microscopic investigations to estimate the corrosion attack by flowing Pb-Li. The first D_{min} is received by measuring from the low part on one side to the opposite low part. For the other, D_{max}, the distance between the high parts were measured. Afterwards the measurement was repeated for both diameters 12 times, while turning the sample in 15° steps (0° to 165°) under the microscope and an average diameter was calculated for each of them (D_{min} / D_{max}).

Fig. 10 shows the loss of diameter in dependence of the exposure time to Pb-Li in comparison to the initial diameter measured at the position of the micro cut by the laser scanner. Differences are calculated and plotted for D_{min} and D_{max} respectively.

The calculated material loss is below 35 µm for all exposure times. Corrosion rates were calculated by:

$$\Delta r_{min/max} = \frac{\frac{(\overline{D}_{inital} - \overline{D}_{min/max})}{2}}{t_{exposure}}$$

$$C_{r-min/max} = \frac{\Delta r_{min/max}}{t_{exposure}} \times 8760\ h$$

for both D_{min} and D_{max}. Thereby it was found, that corrosion rates decrease from 40 - 55 µm/a to values near 10 µm/a with ongoing exposure times. This is presumably due to the removal of partly adherent material caused by the roughened surface of the sample after HT in the start phase of the exposure to the flowing environment.

The corrosion resistance of ECA coated samples was shown for long term exposure in flowing Pb-15.7Li. A smoothing of surfaces together with a small material take off was found, however, these processes did not accelerate under long term testing. The corrosion testing campaign of ECA coated Eurofer confirmed the barrier function of the processed Al based surface layers and scales on top of the structural material. Improved processing of Al-based coatings by ECX process is under investigation. Metallurgical analyzes showed smoother surfaces and pretesting in flowing Pb-15.7Li indicated advanced stability.

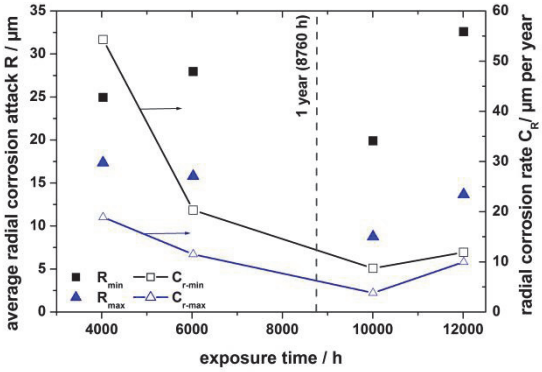

Fig. 10: Corrosion attack of ECA coated EUROFER in dependence of exposure time to flowing Pb-15.7Li in PICOLO loop. Labeling of the left axis gives the material loss and the right axis shows the corrosion rate per year.

Conclusion

The early development of Al-based barriers processed by HDA process lined out that such barriers poses capability to act as corrosion and T-permeation barriers. However, it was found that this process has drawbacks, e.g., restriction to plate like geometries or disadvantages in control of deposited layer thickness. Meanwhile advanced electrochemically based coating processes named ECA and ECX were developed and the formation of barriers was improved on top of RAFM steel Eurofer. Necessary deposition parameters for the Al coating and the heat treatment steps to form protective surface structures were optimized and parts were fabricated for characterization and corrosion testing in the Pb-15.7Li corrosion loop PICOLO. The microstructural analyzes of test samples clearly exhibited the advantages of the new coating processes. The main features are, e.g., the improved controllability of coating thickness and the ability to deposit thin Al coatings (micrometer range) on RAFM steels, what is preferable concerning low activation criteria and seems to facilitate subsequent heat treatment processes.

The corrosion testing showed for ECA samples with not optimized surface structure high corrosion resistance in fast flowing Pb-15.7Li. Compared to bare Eurofer a significant reduction in material attack was reached by a factor of at least 10. No accelerated attack was observed for long term testing up to 12,000 h. This underlines the excellent protective nature of the processed corrosion barriers and leads to significantly reduced corrosion products dissolved in the breeder compared to uncoated steel walls. This behavior has absolutely positive impact on transport of impurities in the breeder, repurification of the breeder and safety issues. The performed work on ECX coated samples showed that surface quality can be improved furthermore and that ECX scales withstand Pb-15.7Li attack. All facts shown highlight the potential of Al based barriers and their stability. However corrosion resistance is the first absolutely necessary condition to act as T permeation barriers, too. Further qualification and improvement of such barriers is needed and will be conducted in future to demonstrate DEMO relevancy.

Staff:

M. Heck
N. Holstein
J. Konys
W. Krauss
J. Lorenz
J. Novotny
O. Wedemeyer
S.-E. Wulf

Literature:

[1] S. Malang, A.R. Raffray, N.B. Morley, An example pathway to a fusion power plant system based on lead–lithium breeder: Comparison of the dual-coolant lead–lithium (DCLL) blanket with the helium-cooled lead–lithium (HCLL) concept as initial step, Fusion Engineering and Design 84 (2009) 2145–2157.

[2] H.U. Borgstedt, G. Frees, Z. Peric , Material compatibility tests with flowing Pb-17Li eutectic, Fusion Engineering and Design 17 (1991) 179-183.

[3] G. Benamati, C. Fazio, I. Ricapito, Mechanical and corrosion behavior of EUROFER 97 steel exposed to Pb-17Li, Journal of Nuclear Matateriales 307-311 (2002) 1391-1395.

[4] J. Konys, W. Krauss, Z. Voss, O. Wedemeyer , Corrosion behavior of EUROFER steel in flowing eutectic Pb–17Li alloy, Journal of Nuclear Materials 329-333 (2004) 1379-1383.

[5] J. Konys, W. Krauss, J. Novotny, H. Steiner, Z. Voss, O. Wedemeyer, Compatibility behavior of EUROFER steel in flowing Pb–17Li, Journal of Nuclear Materials 386-388 (2009) 678–681.

[6] W. Krauss, J. Konys, A. Li-Puma, TBM testing in ITER: Requirements for the development of predictive tools to describe corrosion-related phenomena in HCLL blankets towards DEMO, Fus. Eng. Design, 87 (2012) 403–406.

[7] J. Konys, W. Krauss, Z. Voss, O. Wedemeyer, Comparison of corrosion behavior of bare and hot-dip coated EUROFER steel in flowing Pb–17Li, J. Nucl. Mat. 367-370, (2007) 1144-1149.

[8] H. Steiner, W. Krauss, J. Konys, Journal of. Nuclear Materials 386-388 (2009) 675-677.

[9] T. Shikama, R. Knitter, J. Konys, T. Muroga, K. Tsuchiya et al., Status of development of functional materials with perspective on beyond-ITER, Fusion Engineering and Design, 83, (2008), 976-982

[10] J. Konys, W. Krauss, Corrosion and precipitation effects in a forced-convection Pb–15.7Li loop, Journal of Nuclear Materials 442, (2013), 576-579.

[11] S-E. Wulf, N. Holstein, W. Krauss, J. Konys, Influence of deposition conditions on the microstructure of Al-based coatings for applications as corrosion and anti-permeation barrier, Fusion Engineering and Design, 88, (2013), 2530-2534.

[12] Q. Huang, N. Baluc, Y. Dai, S. Jitsukawa, A. Kimura, J. Konys et al., Recent progress of R&D activities on reduced activation ferritic/martensitic steels, Journal of Nuclear Materials, 442, (2013) 2-8.

[13] L. Bühler, C. Mistrangelo, j. Konys, R. Bhattacharyay, Q. Huang et.al , Facilities, testing program and modeling needs for studying liquid metal magnetohydrodynamic flows in fusion blankets (invited talk), 11th International Symposium on Fusion Nuclear Technology (ISFNT 2013) Barcelona, Spain, September 16-20, 2013.

[14] W. Krauss, J. Konys, S-E. Wulf, Corrosion barriers processed by Al-electroplating and their resistance against flowing Pb-15.7Li, 16th International Conference on Fusion Reactor Materials (ICFRM-16), Beijing, China, October 20-26, 2013.

[15] J. Konys, W. Krauss, Z. Zhu, Q.; Huang, Comparison of corrosion behavior of EUROFER and CLAM steels in flowing Pb-15.7Li, 16th International Conference on Fusion Reactor Materials (ICFRM-16), Beijing, China, October 20-26, 2013.

[16] J. Konys, Advanced processes for T-permeation and corrosion barriers for the $DCLL_{mod.}$ Concepts, 1st EU-US DCLL Workshop, Karlsruhe, April 23-24, 2013.

[17] S-E. Wulf, W. Krauss, J. Konys, Comparison of coating processes in the development of aluminum-based barriers for blanket applications,11th International Symposium on Fusion Nuclear Technology (ISFNT 2013), Barcelona, Spain, September 16-20, 2013.

Operation of the KIT Fusion Materials Laboratory (CoA)

The Fusion Materials Laboratory provides the infrastructure for the performance of tasks defined in the EFDA and F4E work programmes related to the characterisation and testing of irradiated and non-irradiated materials. Methods such as optical and electron microscopy, tritium adsorption and desorption, crush load, micro hardness, creep, charpy impact, tensile, LCF and instrumented indentation tests as well as long-time annealing tests are applied. The work includes Post Irradiation Examinations (PIE) of Reduced Activation Ferritic Martensitic (RAFM) steels (reference material for DEMO and ITER-TBMs) and tungsten as well as investigations on materials relevant for the HCPB blanket (ceramic breeder materials, beryllium) and technical aspects (glasses).

Fig. 1: Operating the FML at Hot Cells and Glove Boxes (Photo by B. Ludewig).

PIE on selected samples from the HFR IIB, MEGAPIE, and BOR 60 experiments were performed. For this purpose, in 2013 mostly LCF tests were performed. Tested specimens' small cuts were prepared for LOM, SEM, and TEM and examined. Broken halves of charpy specimens were prepared for instrumented indentation and served for identifying material parameters and Vickers hardness. The aim of the investigations is to study the irradiation effects on the mechanical and structural properties of these materials and to investigate the possibilities of a post-irradiation heat-treatment in order to reduce irradiation defects.

The investigation of functional blanket materials was continued. Lithium orthosilicate pebbles were investigated by LOM and crush-lod tested.

Tritium adsorption / desorption tests and creep tests were done on irradiated and unirradiated beryllium, beryllium-vanadium, and beryllium-titanium alloys and on BeO-doped beryllium, both on single pebbles and on pebble beds.

Adsorption and desorption experiments were also done with unirradiated beryllium-titanium pebbles. Furthermore different beryllium-titanium alloys were characterized by LOM and SEM. Porosity measurements and creep tests were performed. Activated beryllium from the HIDOBE irradiation was investigated by LOM and SEM. For TEM investigations, a new preparation method for the extremely brittle irradiated beryllium was applied, producing thin fragments by crush-test and fixing them on ultra-fine meshes, furnishing images of a quality never reached before on irradiated beryllium.

The quadrupole mass spectrometer, able to identify the tritium release and retention of fusion-relevant materials, was used for quantitative analysis of a high number of tritium release

experiments (Be of HIDOBE). Detailed results and consecutive analysis of the measurements are reported in the respective chapters of this report.

Operation of the 200 kV high resolution TEM for investigation of radioactive material down to atomic scale was continued. Various results, identifying the damage mechanisms in highly irradiated steel and Beryllium, could be published.

Fig. 2: FEI „SCIOS“: brand new dual beam microscope type.

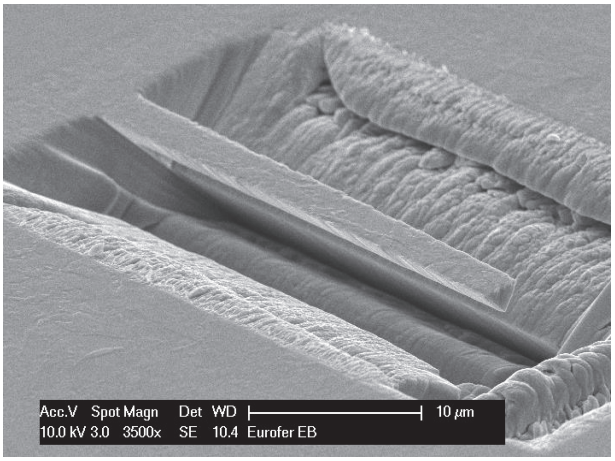

Fig. 3: FIB-cut micro-bar, prepared in the heat affected zone of an EB Eurofer weld (M. Scherwitz).

The procurement and installation of a newly developed type of dual beam Focused Ion Beam- and electron microscope was done in the laboratory, see Fig. 2. Its purpose is ion-cutting of radioactive specimens by a Ga-ion-source and the use of a FEG for imaging without damaging the specimens' surface. The microscope disposes of a micro-manipulator for extraction of TEM-lamellas; a heated nano-manipulator for in-situ-tests will be installed. The software equipment allows the 3D-reconstruction of cut microstructures.

Applications are on the one hand the preparation of thin TEM lamellas, on the other hand the preparation of micromechanical specimens like bending bars (Fig. 3) for characterization of small volumes to identify material parameters like Young‘s modulus or yield stress.

The microscope will be suitable to cut specimens out of the thin, surface-near damaged areas of ion-implanted specimens (penetration depth in the order of magnitude of 10 µm) and will allow comparison between ion- and neutron-irradiation damage.

PIE of irradiated Tungsten: First HFR-irradiated tungsten samples (origin: Extremat-project, CCFE-Oxford, specimens had been n-irradiated at HFR at 600 and 900 °C to 3 to 5 dpa) have been transported to FML. A dedicated testing device (Fig. 4) for application of four-point-bending tests an 1mm² cross section, 12mm long bars has been developed and manufactured for use in the vacuum high temperature testing machine in the Hot Cell.

A first series of un-irradiates reference samples, of irradiated poly-crystalline samples and of irradiated single-crystalline samples has successfully been tested at various temperatures up to 900°C in vacuum.

Fig. 4: Testing equipment for 4-point-bending-tests in universal testing machine.

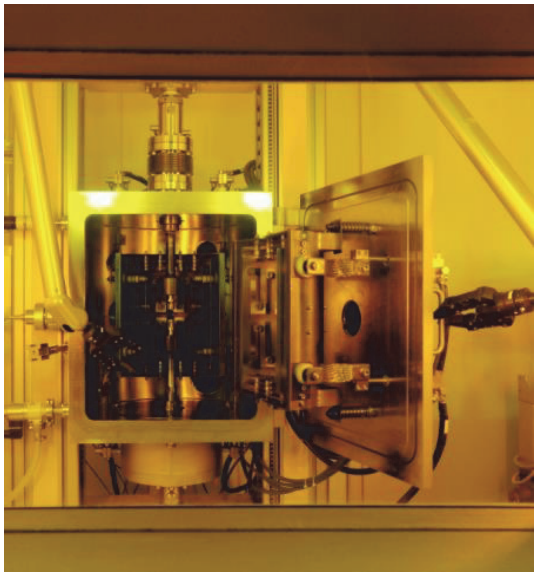

Fig. 5: Universal testing machine in Hot Cell.

Fig. 6 shows on the left the poly-crystalline sample tested at 230°C, the temperature identified to be the DBTT for 1mm² cross section bending bars. Trans- and intergranular fracture both occur. The photo on the right is the cross section of a single-crystalline specimen, tested at 600°C, still collapsing by cleavage fracture. In higher resolution (Fig. 7) small areas with very ductile behaviour can be seen. The DBTT is suspected to be not much higher than 600°C, tests at 900°C are completely ductile.

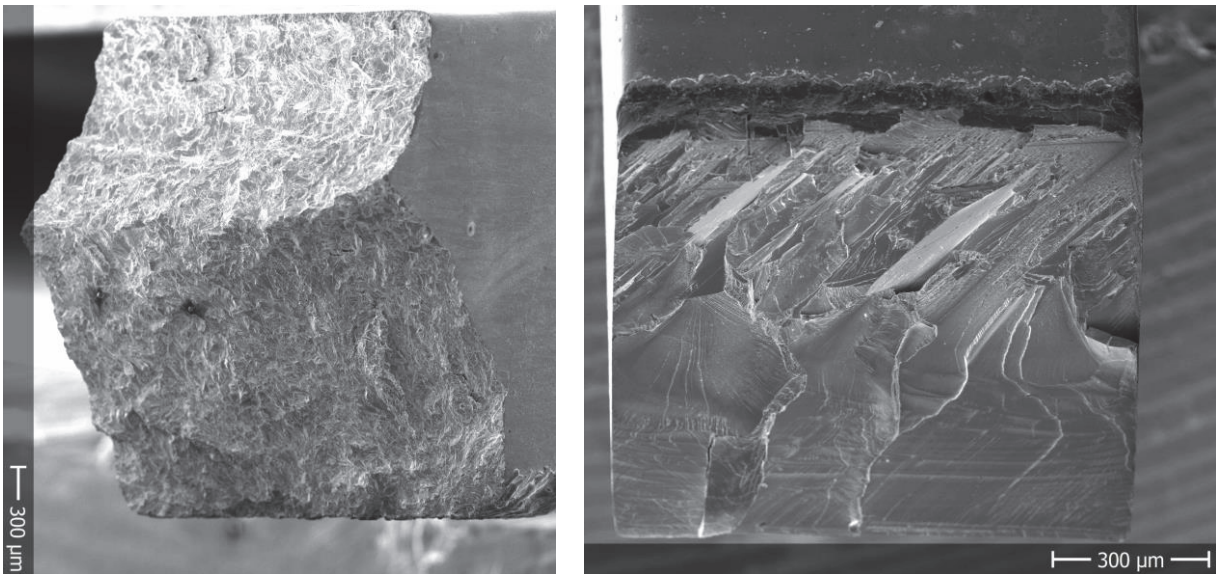

Fig. 6: Poly-crystalline Tungsten at DBTT (230°C, left) and single-crystalline Tungsten at 600°C (DBTT after irradiation > 600°C, right), pre-crack in the top.

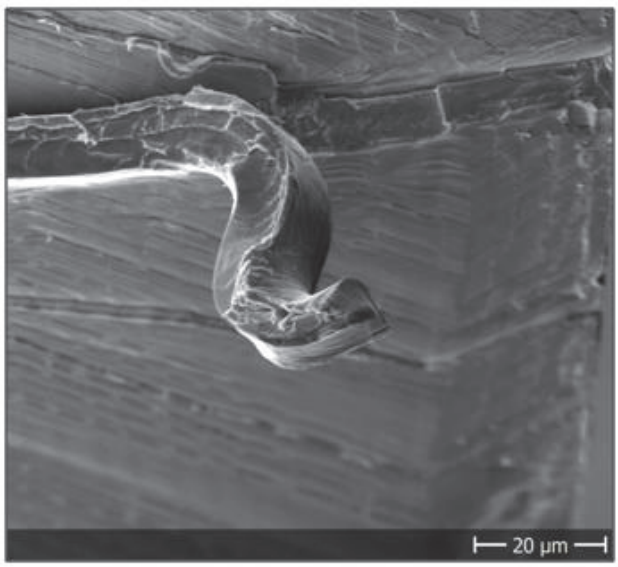

Fig. 7: Small area of fully ductile behaviour, magnification of single-crystalline Tungsten specimen (Fig. 6).

Another example for the specific work in the FML is given in Figs. 8 and 9, showing 15 dpa n-irradiated Eurofer with 0.0083 wt% 10B isotope instead of natural boron, tending to complete He-transmutation under irradiation:

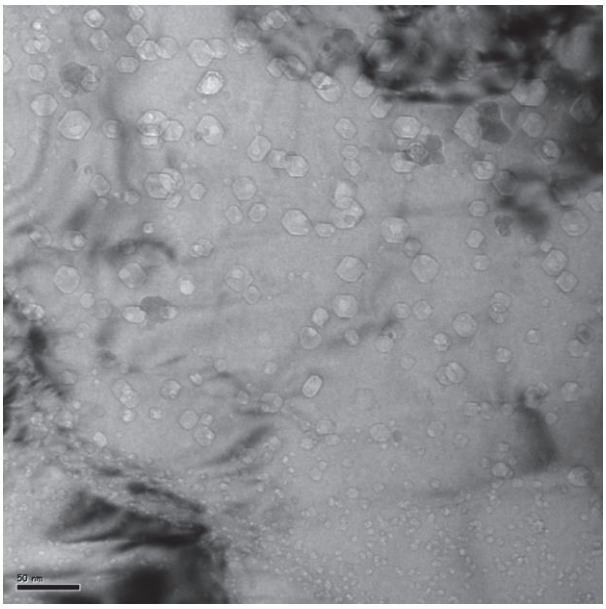

Fig. 8: Eurofer with 83 wppm 10B, irradiated at 350°C, forming big cavities.

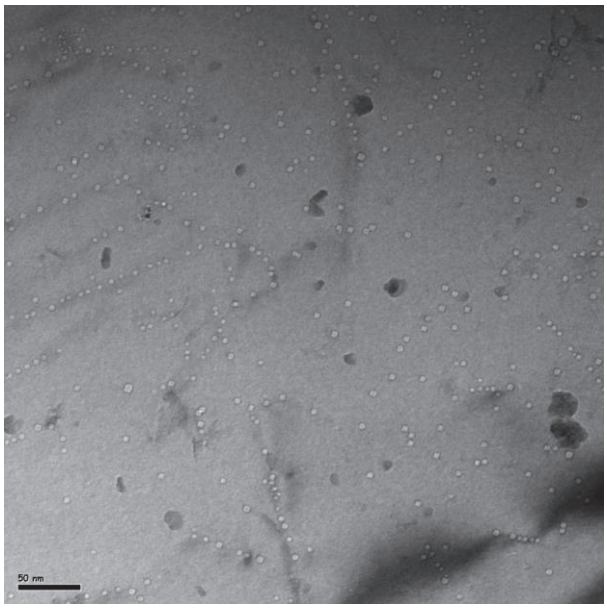

Fig. 9: The same material, irradiated at 450 °C, forming small cavities (TEM images by M. Klimenkov).

Staff:

B. Albinski
P. Barié
J. Bredl
I. Bernstein
M. Dany
J. Ehrmann
A. Erbe
M. Gilpert
M. Holzer
W. Ibbe
S. Lautensack
G.Mangei
U. Meyer
H. Ries
M. Rietschel
R. Rolli
I. Sacksteder
M. Scherwitz
R. Schmidt
H.-C. Schneider
M. Weber

Literature:

[1] I. Sacksteder, S. Hostettler, G. Charbonneau, B. Albinski, H.-C. Schneider: Requirements for investigating the temperature-dependent fracture behavior of irradiated materials by indentation, Fus Eng Des, 88, 9–10, October 2013, 2577-2580

[2] B. Albinski, H.-C. Schneider, I. Sacksteder, O. Kraft: A new high-temperature indentation device for characterization of materials for fusion applications, J Nucl Mate, 442, 1–3, S1, November 2013, S865-S868

[3] B. Albinski: Instrumentierte Eindringprüfung bei Hochtemperatur für die Charakterisierung bestrahlter Materialien. Zur Erlangung des akademischen Grades Doktor der Ingenieurwissenschaften der Fakultät für Maschinenbau am Karlsruher Institut für Technologie (KIT) vorgelegte Dissertation. December 16th, 2013

[4] P. Kurinskiy, A. Moeslang, V. Chakin, M. Klimenkov, R. Rolli, S. van Til, A.A. Goraieb: Characteristics of microstructure, swelling and mechanical behaviour of titanium beryllide samples after high-dose neutron irradiation at 740 and 873 K, Fus Eng Des, 88, 9–10, October 2013, 2198-2201

[5] V. Chakin, R. Rolli, A. Moeslang, M. Klimenkov, M. Kolb, P. Vladimirov, P. Kurinskiy, H.-C. Schneider, S. van Til, A.J. Magielsen, M. Zmitko: Tritium release and retention properties of highly neutron-irradiated beryllium pebbles from HIDOBE-01 experiment, J Nuc Mat, 442, 1–3, S1, November 2013, S483-S489

[6] M. Klimenkov, V. Chakin, A. Moeslang, R. Rolli: TEM study of beryllium pebbles after neutron irradiation up to 3000 appm helium production, J Nuc Mat, 443, 1–3, 2013, 409-416

[7] V. Chakin, R. Rolli, A. Moeslang, P. Vladimirov, P. Kurinskiy, S. van Til, A.J. Magielsen, M. Zmitko: Characterization of constrained beryllium pebble beds after neutron irradiation at HFR at high temperatures up to helium production of 3000 appm, Fus Eng Des, 88, 9–10, October 2013, 2309-2313

[8] Materna-Morris, E., Möslang, A., Schneider, H.C.: Tensile and low cycle fatigue properties of EUROFER97-steel after 16.3 dpa neutron irradiation at 523, 623 and 723 K, J Nuc Mat, 442, 1–3, S1, November 2013, S62-S66

[9] M. Klimenkov, A. Möslang, E. Materna-Morris: New method for detection of Li inside He bubbles formed in B10-alloyed steel after neutron irradiation, Micron, 46, March 2013, 51-56

[10] M. Klimenkov, A. Möslang, E. Materna-Morris, H.-C. Schneider: Helium bubble morphology of boron alloyed EUROFER97 after neutron irradiation, J Nuc Mat, 442, 1–3, S1, November 2013, S52-S57

[11] S. Zhao, Y. Gan, M. Kamlah, T. Kennerknecht, R. Rolli: Influence of plate material on the contact strength of Li4SiO4 pebbles in crush tests and evaluation of the contact strength in pebble–pebble contact, Eng Fract Mech, 100, March 2013, 28-37

Structural Materials - Refractory Alloys

Coordination for EFDA Fusion Materials Topical Group (WP13-MAT-HHFM-03-03)

During the reporting period the EFDA program 2013 on high heat flux materials development was compiled and evaluated. The according proposals were assessed. In several working and monitoring meetings the progress was monitored and discussed. The results of the Topical Group were published in a review article [1].

Staff:

M. Rieth

Literature:

[1] M. Rieth, S.L. Dudarev, S.M. Gonzalez de Vicente, et al., Recent progress in research on tungsten materials for nuclear fusion applications in Europe, Journal of Nuclear Materials 432 (2013) 482–500.

Acknowledgement

This work, supported by the European Communities under the contract of Association between EURATOM and Karlsruhe Institute of Technology, was carried out within the framework of the European Fusion Development Agreement. The views and opinions expressed herein do not necessarily reflect those of the European Commission.

Development of DEMO SDC-IC – Structural Design Criteria for W/W Alloys (WP13-DTM-03-T05-01)

Objectives

To develop reliable rules for considering the brittleness of W/W alloys as structural materials existing rules of ASME-BPV, KTA, and EN 13445 for design against non-ductile failure are reviewed within the work reported here. Thereby suitable rules shall be identified with which the design space of W/W alloys can be extended when possible towards temperatures lower than the DBTT.

In addition, the preparation of a DEMO Structural Design Criteria for In-vessel Components (SDC-IC) shall be initiated proposing a table of contents and identifying high priority rules to be developed.

Task current status

The deterministic rules of ASME-BPV, KTA, and EN 13445 for design against brittle failure were analyzed. Due to the probabilistic nature of brittle failure probabilistic assessment procedure mainly applied to ceramic components was considered in addition and its applicability to W/W alloys in the brittle and brittle-to-ductile temperature regimes was discussed. The main outcomes can be summarized with the following conclusions:

- All rules provide design space for operation at temperatures below the ductile-to-brittle transition temperature with however very limited loading capability.
- Considering the wall thickness effect on brittle failure helps in extending the design space towards lower temperatures.
- Utilization of probabilistic approaches which intrinsically consider size effects might also help in extending the design space.

In a first step towards a DEMO SDC-IC rough tables of contents have been proposed for “Volume A: Design Criteria (DC)” and “Volume B: Material Design Data (MDD)”. Thereby the base structure of ITER SDC-IC was adopted and modified taking into account DEMO relevant issues related to the failure modes already identified for DEMO in-vessel components and the gaps in ITER SDC-IC in considering them.

The identified gaps in already existing design codes have shown that due to the remarkable cyclic softening of the reduced activation ferritic martensitic steel EUROFER97 [1] new rules for ratcheting and creep-fatigue need to be developed for this type of material [2]. These rules have the highest priority as EUROFER97 is a primary candidate for in-vessel components, where it will also subjected to high dose irradiation which needs also to be taken into account.

For the application of W/W alloys as structural materials their brittleness in the low temperature regime has to be covered by the design criteria by developing proper rules on the base of existing rules for design against brittle failure considering the effect of high dose irradiation. The use of composite material to overcome the brittleness of W/W alloys will also require the development of proper design criteria for covering specific failure mechanisms.

Staff:

J. Aktaa

Acknowledgement

This work, supported by the European Communities under the contract of Association between EURATOM and Karlsruhe Institute of Technology, was carried out within the framework of the European Fusion Development Agreement. The views and opinions expressed herein do not necessarily reflect those of the European Commission.

Mechanical Characterisation of W-armour Materials (WP13-MAT-HHFM-01-01)

Background and Objectives

Tungsten and tungsten alloys are presently considered for helium cooled divertor and possibly for the protection of the helium cooled first wall in DEMO designs, mainly because of their high temperature strength, good thermal conductivity, and low sputter rates. There are two types of applications for these materials which require quite different properties: one is the use as plasma-facing armour or shield component, the other is for structural purposes. An armour material needs high crack resistance under extreme thermal operation condition while a structural material has to be ductile within the operation temperature range. Both material types have also to be stable with respect to high neutron irradiation doses and helium production rates.

The part protection materials development focussed on an optimisation of armour materials and high heat flux testing. Candidate materials have to be characterised by fatigue and shock tests for an assessment of their possible lifetimes. Additionally, basic mechanical characterisations have to be performed on new developed materials, to support the alloys optimisation processes.

Activity 1, Armour Materials, Characterisation of W-ODS alloys: The objective is a mechanical characterization of selected W-ODS materials, based on tensile tests, LCF tests and TMF tests in the interesting temperature region for fusion applications (up to 1600 °C).

Status

For validation, 3-point-bending tests on samples from a second charge from WCr12Ti2.5 were performed. It was found, that the second charge reveals a lower strength compared to the first charge. However, when analysing the results from both charges one may assume, that the ductile to brittle transition behaviour (DBTT: 900°-950°C) is not significantly affected by manufacturing depending fluctuations of the mechanical properties.

Additionally, 3-point-bending tests on samples from plasma spark sintered graded EUROFER-tungsten were conducted at 550°C. Based on the test performance it was found, that an increasing loading of the W-rich side in compression leads to a continuous hardening of the material after yielding without any damage, whereas an increasing loading of the W-rich side in tension leads to an onset of failure after low plastic deformation at a significantly low stress level, followed by a stepwise crack growth.

Since the group of Nadine Baluc from CRPP-EPFL PSI, Switzerland is in liquidation (Producer of W-2Y_2O_3 alloys) and the group of Carmen Garcia-Rosales from CEIT, Spain (Producer of W-Cr-Ti/Si alloys) had big problems to produce usable ingots during 2013, the mechanical tests on promising W-ODS alloys for armour applications could not be continued. However, within the frame of EFDA WP13 for the project materials, first 3-point-bending tests on different sintered EUROFER-ODS samples, produced and provided by Valentina Mihalache from NIMP Ilvov, Romania, were performed at room temperature (RT). Fig. 1 shows the material behaviour in dependence of the fabrication conditions (within the sinter process, sinter time, pressure and temperature were varied).

Compared to standard EUROFER (plate material), one can see that all samples show a clearly higher strength. However, only specimen P1 also exhibits a sufficient large ductility. Consequently, the related fabrication parameters will be used to produce more samples, particularly in order to investigate the material behaviour at application relevant temperatures.

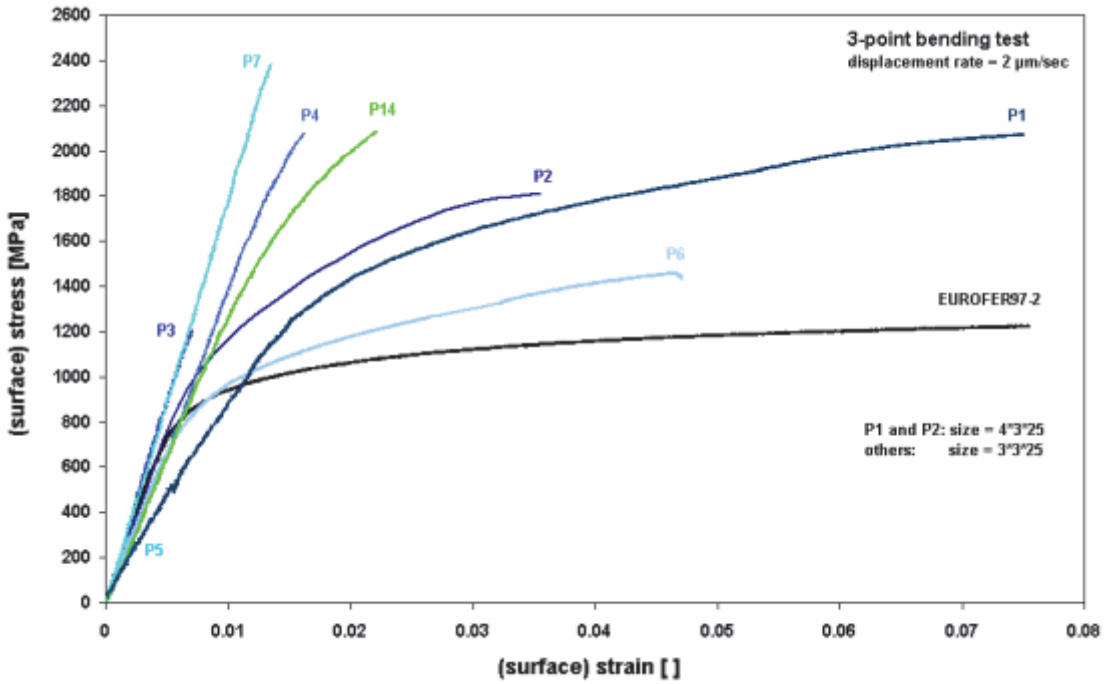

Fig. 1: Results of 3-point-bending tests at RT on EUROFER-ODS samples (the samples were produced under different pressure/temperature/time conditions during the sinter process).

Conclusion and Outlook

3-point-bending tests on samples from EUROFER-ODS, produced at NIMP Ilvov, Romania, were performed at room temperature. It was found, that for well selected sinter conditions the material exhibits sufficient large ductility and compared to standard EUROFER, a significant higher strength. The tests will be continued in 2014, particularly to study the material behaviour at application relevant temperatures. Additionally it is planned to continue the mechanical characterization of tungsten alloys provided by CEIT. Beside additional bending tests, in particular WCr12Ti2.5 will also be tested in tensile experiments. Therefore, CEIT still tries to manufacture some usable bigger ingots.

Staff:

M. Walter

Literature:

[1] M. Rieth et al., Recent progress in R&D on tungsten alloys for divertor structural and plasma facing materials, J. of Nucl. Mat. 432 (2013) 482 – 500

[2] S. Wurster et al., Recent progress in R&D on tungsten alloys for divertor structural and plasma facing materials, J. of Nucl. Mat. 442 (2013) 181 - 189

[3] M. Battabyal et al., Microstructure and mechanical properties of a W–2wt.%Y2O3 composite produced by sintering and hot forging, J. of Nucl. Mat. 442 (2013) 225 – 228

[4] P. Lopez-Ruiz et al., Powder metallurgical processing of self-passivating tungsten alloys for fusion first wall application, J. of Nucl. Mat. 442 (2013) 219 - 224

Acknowledgement

This work, supported by the European Communities under the contract of Association between EURATOM and Karlsruhe Institute of Technology, was carried out within the framework of the European Fusion Development Agreement. The views and opinions expressed herein do not necessarily reflect those of the European Commission.

Armour Materials - Fabrication and Optimization of Different Armour Materials by PIM (WP13-MAT-HHFM-01-02)

Objectives

At Karlsruhe Institute of Technology (KIT) manufacturing methods for the mass production of divertor parts for future nuclear fusion power plants beyond ITER are intensively investigated. The activities are focussed on the development of manufacturing methods in view of large-scale production. The Powder Injection Molding (PIM) technology is a promising manufacturing method of parts with high near-net-shape precision. This process was adapted and developed at KIT also as method for joining without brazing or welding for tungsten and doped tungsten alloys. Another application of the PIM process is the rapid development of new tungsten materials and their screening in terms of basic mechanical and HHF properties. This activity is closely connected to WP13-MAT-01-HHFM-04-04/KIT/PS, where PIM is used for mass production of divertor parts.

This report describes the investigations on different tungsten materials produced by powder injection molding. The new doped tungsten materials are produced by powder mixing (and not by mechanical alloying) to ensure an industrial scale production route. Furthermore, the different manufactured tungsten and doped tungsten alloy grades were characterized by mechanical tests and texture analyses.

State of the art PIM R&D

Powder Injection Molding is a powder metallurgy (PM) near net shape fabrication process for metals and ceramics with tight tolerances and good surface finishes. This process enables the mass production of low cost and high performance parts with complex geometries. Materials with high melting points such as tungsten or tungsten alloys can be effectively fabricated with this process. Furthermore is this method proper to join tungsten and doped tungsten alloys without additional brazing or welding [1-6].

The focus at KIT is now on the use of PIM technology to produce various tungsten alloys for scientific investigations. This process allows the creation of new materials and the investigation of the material properties [7-8]. The characterization and testing of the new materials are in close cooperation with colleagues from the University of Oxford.

Results

Different new tungsten and doped tungsten alloys are developed. All materials are produced only by mixing, without mechanical alloying and small prototype plates produced via PIM. Also a new heat-treatment process, consisting only of high temperature sintering was used. The characterization of the materials via mechanical tests and texture analyses are in close cooperation with the University of Oxford, Department of Materials.

<u>Microstructure</u>
The results of the microstructure, performed by using a Zeiss AURIGA FIB are shown in Figure 1. For all doped materials, the embedded particles (La_2O_3, Y_2O_3, TiC and TaC), are homogeneous around the tungsten grain boundaries and act as grain growth inhibitor.

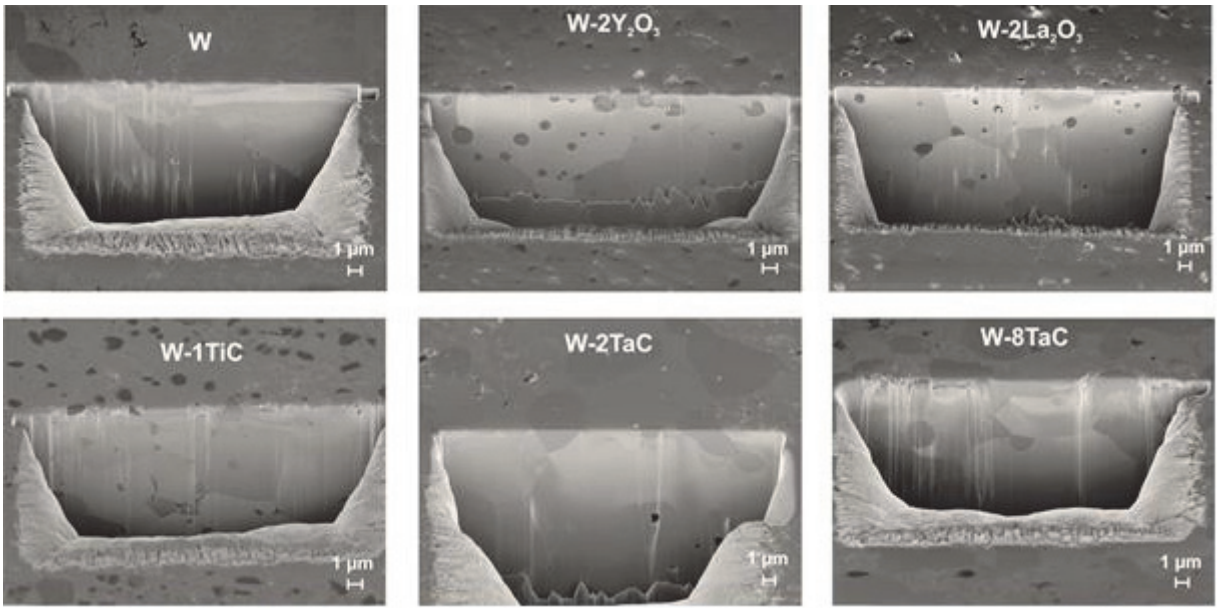

Fig. 1: SEM image of the microstructure for all samples performed via FIB.

Crystallographic texture

For analyses of the crystallographic texture a field emission scanning electron microscope JEOL JSM-6500F was used. Electron backscatter diffraction (EBSD) is a powerful microstructural characterization tool in combination with a SEM and allows analyses e.g. of the crystal type. All samples are finish polished with colloidal silica and tilted at 70°. The resulted images are rotated at 180° and clean up.

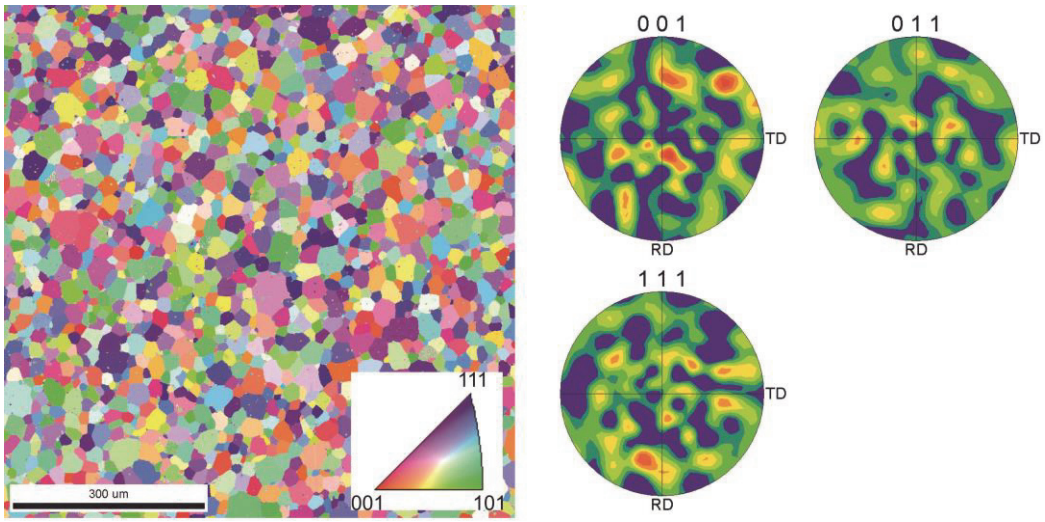

Fig. 2

Figure 2 shows the crystallographic texture in normal direction (ND) exemplarily for pure PIM tungsten. The texture is homogeneous and no preferred orientation (as expected) is visible.

Mechanical testing

To analyse the mechanical properties small samples of (12x1x1) mm are produced via electrical discharge machining (EDM). After polishing of all four sides of each sample, all samples are notched. The 4-Point bending tests were carried out on an INSTRON 3366 testing machine with a constant strain rate of 0.0330 mm/min, with the cross-head velocity adjusted for each test to account for the different dimensions of each beam, at temperatures from RT to 500 °C. The raw load displacement data were then converted into stress-strain data.

The results are shown in Fig. 3. The pure tungsten sample, W-2La_2O_3 and W-1TiC break until 350 °C, over 400 °C for all materials no break are observed. W-2Y_2O_3, W-2TaC and W-8TaC shown a very brittle manner and break until 500 °C.

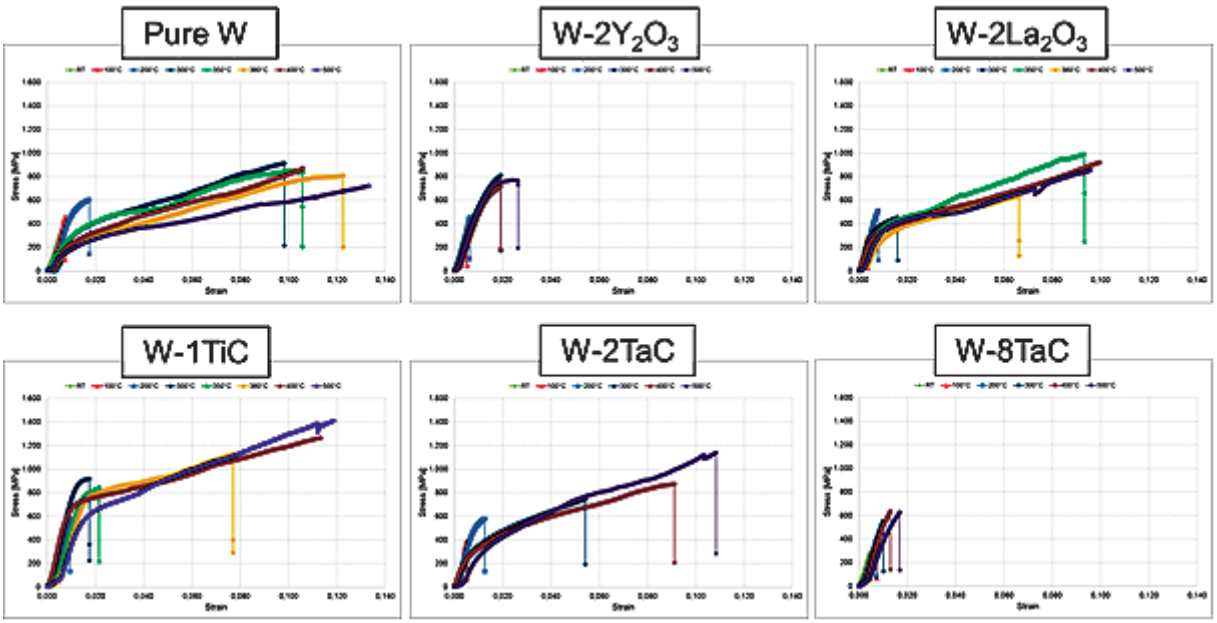

Fig. 3: Complete stress-strain curve for pure tungsten, tested from 20 °C to 500 °C.

Conclusions and outlook

The motivation for this work was the investigation of prototype materials produced by PIM. The microstructure of the finished doped tungsten materials shows a homogeneous allocation of the embedded particles. The result let conclude, that the producing of the materials only by mixing was successful. And that would save a lot of cost and time in the whole process chain. The mechanical tests show for pure tungsten the best results, also the microstructure looks homogeneous, and the density is high (99% T.D.). The crystallographic texture is homogeneous and no preferred orientation (as expected) is visible. Particularly the addition of 1wt-% TiC into the tungsten matrix shows a better stress-strain relationship. The tungsten grains are small, because the embedded particles acts as grain grow inhibitor.

The results of the tests are very important for continuation of this work. New materials for testing and a new heat-treatment process will be developed. Further investigations in 2014 will deliver more information about the properties of materials produced via PIM.

Collaborations

T. Barrett, S. Dudarev (CCFE),
D. Armstrong, S.G. Roberts (University of Oxford),
W. Knabl (PLANSEE SE)

Staff:

S. Antusch
N. Denker
M. Offermann
M. Rieth
H. Walter

Literature:

[1] S. Antusch, V. Piotter: KIT investigates the mass production and joining of divertor parts for nuclear fusion power plants via multicomponent tungsten PIM. Powder Injection Molding International 6 (2012).

[2] S. Antusch, L. Commin, M. Müller, V. Piotter, T. Weingärtner, Two component tungsten Powder Injection Molding – an effective mass production process. Journal of Nuclear Materials (2013), DOI:10.1016/j.jnucmat.2013.11.007.

[3] S. Antusch, V. Piotter: A new fully automatic Multicomponent PIM tool at KIT allows the replication and joining without brazing of components for future nuclear power plants. Powder Injection Molding International 7 (2013).

[4] S. Antusch, T. Hanemann, V. Piotter, M. Rieth: Mass production of components for future fusion power plants via one and two component Powder Injection Molding. 2nd International Conference on Materials for Energy EnMat II, Karlsruhe, Germany, May 12-16, (2013).

[5] S. Antusch, V. Piotter, M. Rieth: Mass production and joining via Multicomponent tungsten powder injection molding. In: Proceedings of the 18th Plansee Seminar, Reutte, Austria (2013).

[6] S. Antusch, L. Commin, J. Heneka, V. Piotter, K. Plewa, H. Walter: A new fully automatic PIM tool to replicate two component tungsten DEMO divertor parts. Journal of Fusion Engineering and Design 88 (2013) 2461-2465.

[7] S. Antusch, D.E.J. Armstrong, J.S.K.-L. Gibson, W. Knabl, M. Rieth, S.G. Roberts, T. Weingaertner: Processing of complex shaped tungsten parts by PIM. Workshop on Tungsten for Nuclear Applications, September 23-25, Oxford, UK (2013).

[8] S. Antusch, D.E.J. Armstrong, T. B. Britton, L. Commin, J.S.K.-L. Gibson, J. Hoffmann, W. Knabl, M. Müller, G. Pintsuk, V. Piotter, J. Reiser, M. Rieth, S.G. Roberts, T. Weingaertner: Multicomponent powder injection molding as method for mass production, joining and material development for tungsten armour materials. 16th ICFRM, Beijing, China (2013).

Acknowledgement

This work, supported by the European Communities under the contract of Association between EURATOM and Karlsruhe Institute of Technology, was carried out within the framework of the European Fusion Development Agreement. The views and opinions expressed herein do not necessarily reflect those of the European Commission.

Mid-term Structural Materials (WP13-MAT-HHFM-02-01)

Description

This activity is aimed at studying copper based materials for water cooling applications.

Introduction

For a future fusion reactor, the structural lifetime of pure copper is limited by:
- its high creep rate
- an anticipated high swelling rate
- helium embrittlement

Therefore, an improvement in strength and irradiation resistance of copper-based materials is required. At the same time, this should not be too detrimental to the thermal conductivity since copper alloys will be used as heat sink materials.

The copper alloys considered as candidates for fusion applications can be divided into two groups: precipitation hardened alloys and dispersion strengthened alloys. The high density of small particles is used to improve void swelling and mechanical strength and to provide a high sink density for the possible recombination of vacancies and interstitials produced during neutron irradiation.

Precipitation hardened alloys like Cu-Cr-Zr grades have been chosen for ITER and they can likely be used as a structural material in the temperature range of 180-280°C. However, under irradiation, the same problems will arise as with pure copper above 280°C due to radiation-enhanced precipitate over-aging and softening effects.

Dispersion strengthened alloys using Alumina particles (GlidCop types) were investigated and could present better properties such as a high stability under irradiation and under higher temperatures. The fine particles are hard and thermally stable even at temperatures approaching the melting point of the copper matrix. The fine dispersion of the alumina particles in the copper matrix also prevent recrystallization (depending on the particles size and distribution). However, it has been reported that the ductility and low cycle fatigue properties of GlidCop copper alloys are weak at elevated temperatures. And in addition, aluminum is a rather high activating element.

Therefore, this activity was aimed at investigating the capabilities of new copper alloys.

Materials, Study and Results

Precipitation hardened Mn-Copper alloys had been successfully produced in the previous period using induction melting for several Mn contents from 0.2 to 5 wt%. They had shown a good density (98%) and dissolution of Mn in the Cu matrix.

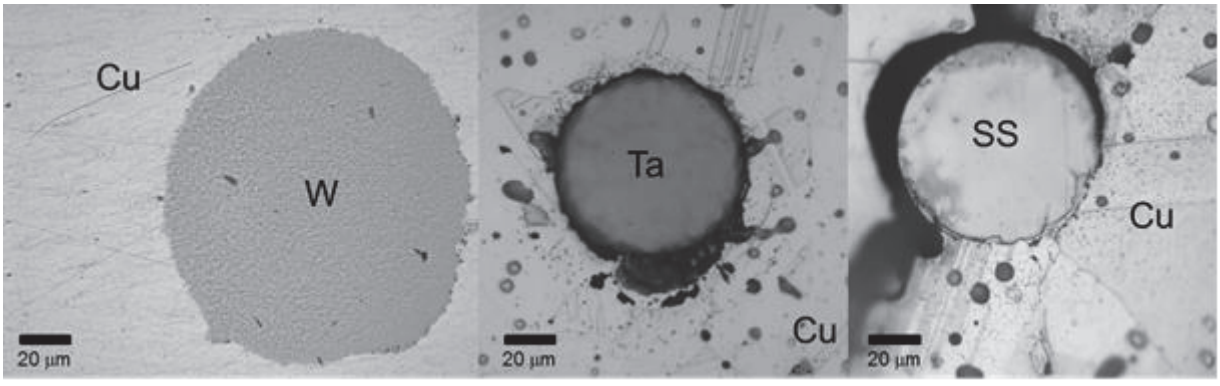

Fig. 1: Cu composites produced by sintering.

2wt% Y_2O_3 dispersion strengthened copper alloys had been successfully produced in the last period using mechanical alloying and HIP with a resulting density of 95% and a good dispersion of the nanoparticles.

During this period, composite copper alloys were produced using cold rolling and sintering (Figures 1-2).

Further examination of the materials produced had been done during this period: Thermal properties (thermal conductivity, coefficient of thermal expansion) and mechanical properties (micro hardness, tensile tests) were analyzed (Figures 3-4).

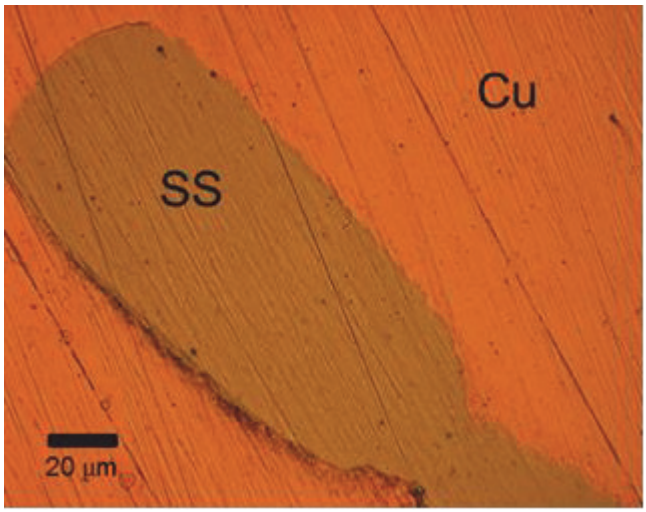

Fig. 2: Cu composites produced by rolling.

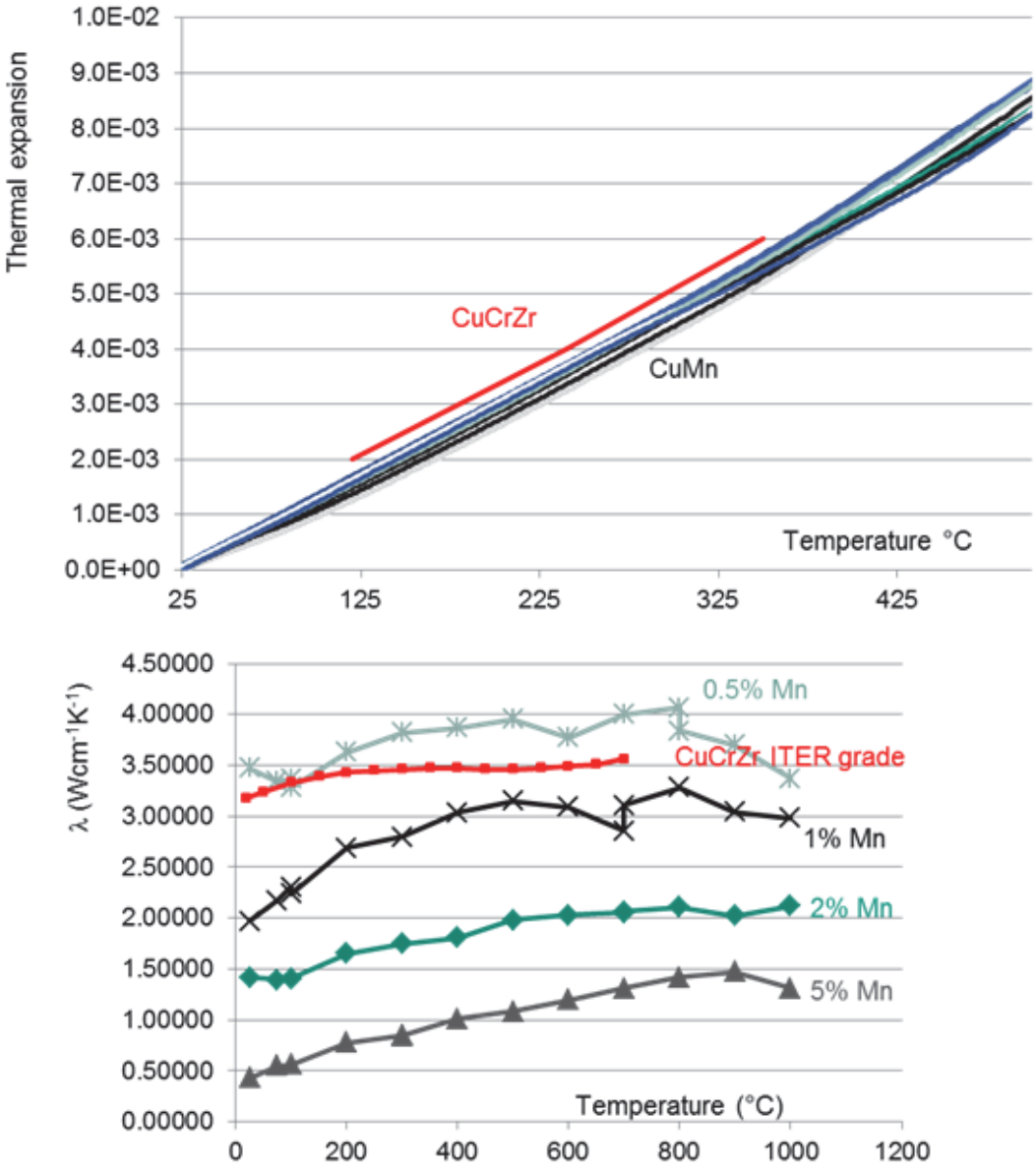

Fig. 3: Thermal properties.

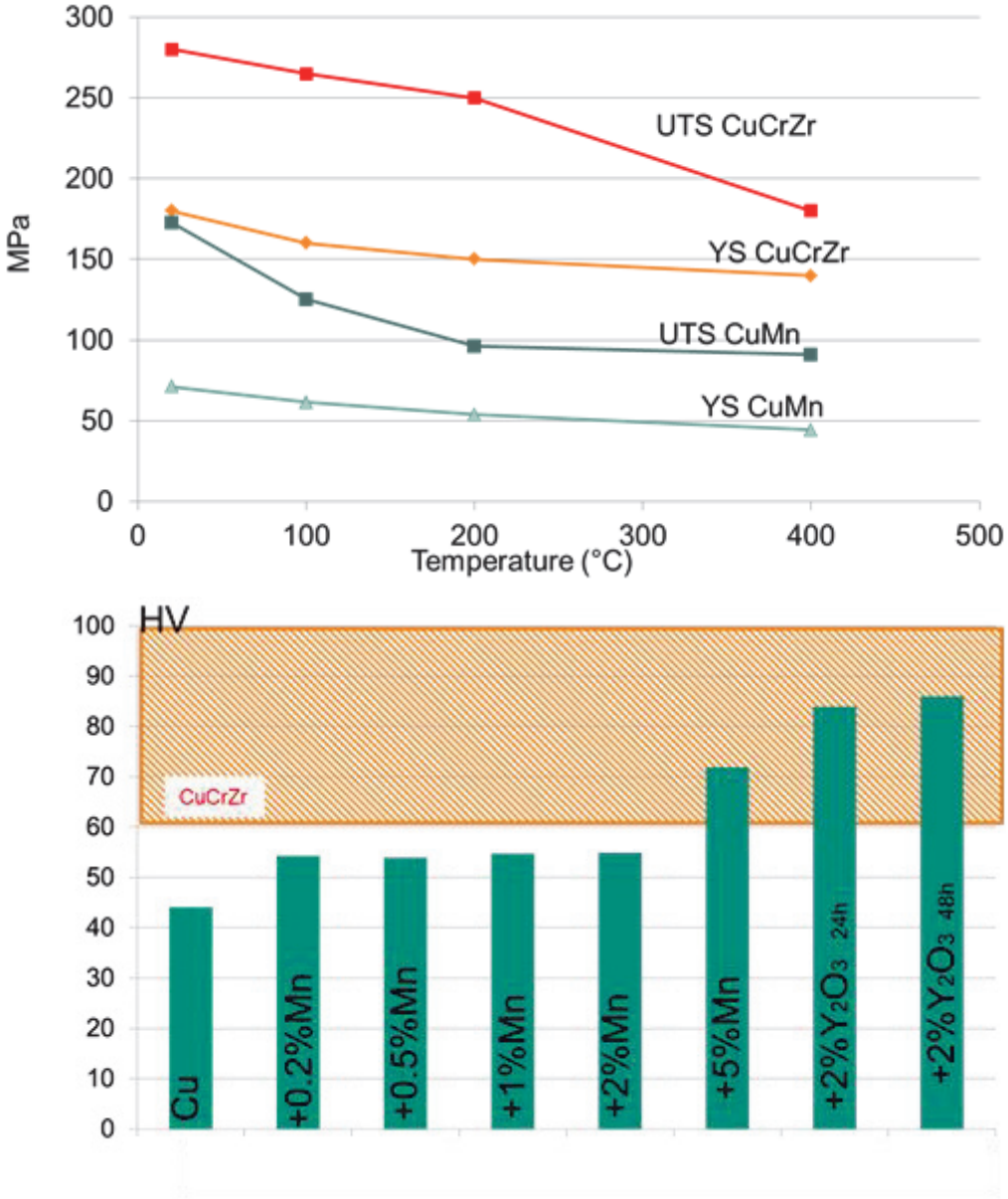

Fig. 4: Mechanical properties.

Conclusions

The processing of new copper based materials was completed. Precipitation hardened Mn-copper alloys, Y_2O_3 dispersion strengthened copper alloys and copper-based composites were successfully produced. Thermal and mechanical properties were analyzed. A further investigation on the irradiation resistance would be useful to completely assess these new material capabilities.

Staff:

S. Antusch
D. Bolich
L. Commin
B. Dafferner
W. Goldacker
M. Hoffmann
U. Jäntsch
P. Lukits
M. Rieth
H. Zimmermann

Literature:

[1] L. Commin, S. Antusch, S. Baumgärtner, W. Goldacker, P. Lukits, M.Rieth, D. Bolich, M. Hoffmann, Assessment of Copper based materials for the water-cooled Divertor Concept of the DEMO European fusion Reactor, SOFE, San Francisco, USA, June 10-14, 2013

Acknowledgement

This work, supported by the European Communities under the contract of Association between EURATOM and Karlsruhe Institute of Technology, was carried out within the framework of the European Fusion Development Agreement. The views and opinions expressed herein do not necessarily reflect those of the European Commission.

Fracture-Mechanical (FM) and Microstructural Characterization of Tungsten Alloys (WP13-MAT-HHFM-03-01)

Objectives

Inherent low Fracture Toughness of tungsten combined with the high Ductile-to-Brittle Transition Temperature (DBTT) are major drawbacks for structural application of tungsten alloys. Furthermore, Fracture Mechanical (FM) properties are expected to exhibit strong anisotropy due to (i) different grain shape/orientation with respect to the rolling direction and (ii) texture. The current task aimed at continuation of FM characterization of different laboratory and industry scale W-alloys in the interesting temperature window for fusion applications (RT-1300 °C). The emphasis was put on the investigation of the upper shelf fracture behaviour. The FM tests were accompanied by fractographic and microstructural investigations. A Master Curve approach is proposed to describe fracture toughness vs. test temperature data on polycrystalline tungsten. Fracture safe design space was identified by analysis of compiled fracture toughness data.

Performed Work

The investigation of Fracture Mechanical (FM) behaviour of tungsten has been continued. Miniaturized 3PB specimens of KLST geometry with dimensions of 27x4x3 mm^3 and with a V shaped notch of 1 mm depth have been used for fracture toughness tests. To increase the stress triaxiality at the notch sharp crack starter notches with a final radius of 20-25 µm have been introduced by a razor blade polishing of the notch tip. The initial crack lengths varied in the range of 1040-1200 µm. The quasi-static three-point bending was performed in a deformation controlled way at deformation rates between 0.2 and 20 µm/s which corresponded to a stress intensity factor rates between 0.06 and 18 $MPam^{1/2}$/s. The fracture surface morphology of the specimens has been investigated with a scanning electron microscopy (SEM).

The study of the upper shelf fracture behaviour of polycrystalline round blank tungsten fabricated by PLANSEE through the powder metallurgic process involving sintering into rods and subsequent forging into round blanks showed large plastic deformation of the specimens above 800 °C, see Fig. 1. The analysis of the unloading compliance up to deformation levels of 1 mm did not show any noticeable crack growth in the deformation rate range between 0.06 and 18 $MPam^{1/2}$/s.

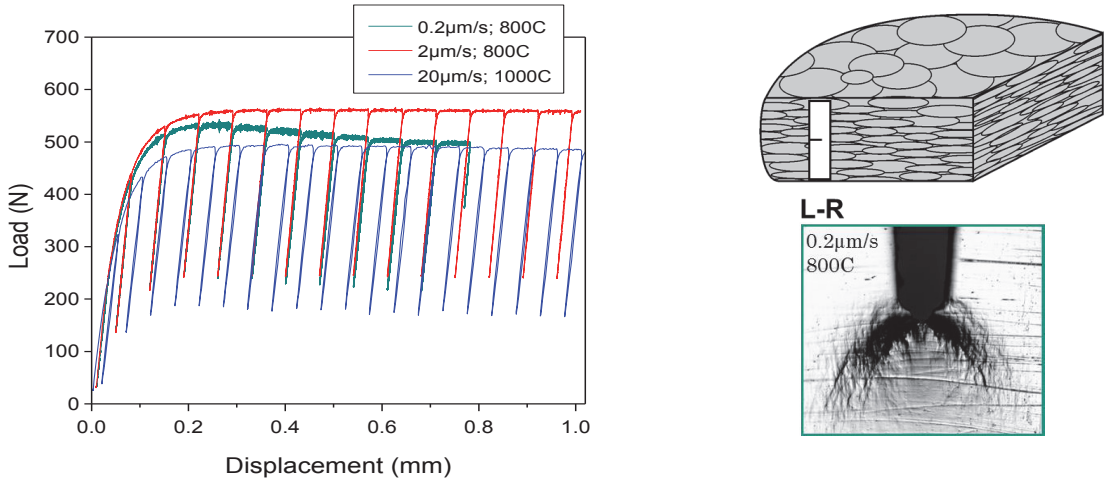

Fig. 1: Left: Load vs. displacement curves for round blank tungsten specimens extracted in L-R orientation. The tests are performed at different deformation rates between 0.2 and 20 µm/s; Right top: Schematic representation of grain structure in round blank tungsten and specimen extraction orientation; Right bottom: Formation of plastic zone near crack tip.

Similar behaviour was shown by commercial W-1%L_2O_3 (PLANSEE) at a test temperature of 800 °C. No crack advancement was observed up to deformation levels of 1 mm.

For further improvement of the constraint state near the main notch tip 0.33 mm deep side grooves have been machined in the specimens. Finally the main notch was again refined by razor blade polishing. The load vs. displacement diagrams recorded at elevated temperatures at a deformation level of 2 µm/s are shown in Fig. 2. Partial unloadings of the specimens have been performed periodically in order to monitor unloading compliance. Similar to the observations on specimens without side grooves no advancement of the crack could be monitored at a test temperature of 700 °C up to deformation level of nearly 1 mm. At about 1 mm deformation, however, in contrast to the specimens without side grooves a rapid load drop was recorder, see Fig. 2, which is related to initiation and unstable propagation of the crack.

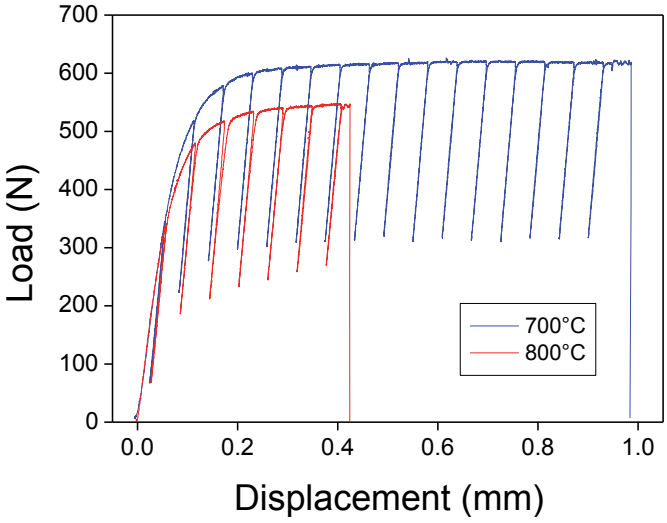

Fig. 2: Load vs. displacement curves for side grooved tungsten L-R specimens. Deformation rate 2 µm/s.

The fracture surface of the specimen tested at 700 °C was examined under SEM, see Fig. 3. A general view on the fracture surface, Fig. 3 left, indicates brittle fracture of the tested specimen without noticeable deformation. The closer look at the fracture surface reveals the dominant fracture mode to be an intergranular fracture, see Fig. 3 middle. Isolated areas indicating the transgranular cleavage were also identified, see Fig. 3 right.

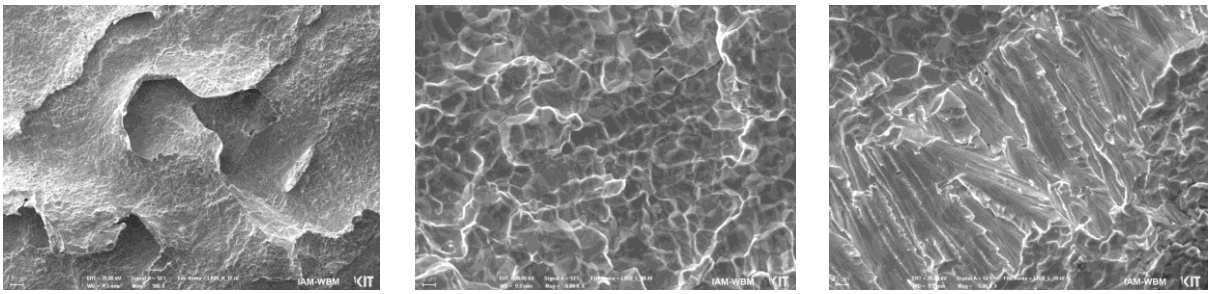

Fig. 3: Fracture surface of side grooved tungsten specimen tested at 700 °C. Left: overview; Middle: magnified area indicating intergranular fracture; Right: magnified area indicating mixture of transgranular cleavage and intergranular fracture.

Brittle fracture safe design space

Aiming at the determination of the design space for a brittle fracture safe operation of components made out of tungsten compilation of the fracture toughness data on polycrystalline tungsten including the results on disk and rod shaped materials were performed, see Fig. 4. For a conservative assessment of the design space only fracture toughness data satisfying the ASTM 399 validity criteria and obtained in the weak orientations for given product forms have been implied.

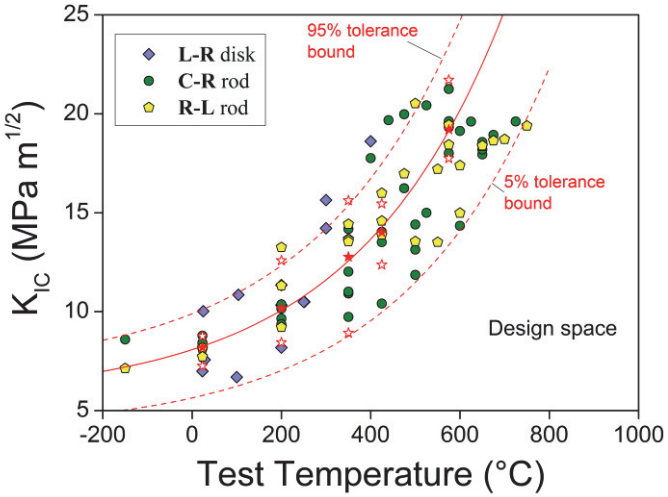

Fig. 4: Fracture toughness of polycrystalline tungsten vs. test temperature (E. Gaganidze, D. Rupp, J. Aktaa, J. Nucl. Mater 2013). The full stars show calculated median fracture toughness values corresponding to 50% cumulative failure probabilities. The open stars show calculated fracture toughness corresponding 95% and 5% failure probabilities. The solid line is the least square fit to median fracture toughness with Master Curve type function given by Eq. (2). The dashed lines represent calculated 95% and 5% tolerance bounds for fracture toughness.

The cumulative failure probability (P_f) of tungsten alloys was assumed to follow the three parameter Weibull model

$$P_f(T) = 1 - \exp\left\{-\left(\frac{K_{IC}(T) - K_{min}(T)}{K_o(T) - K_{min}(T)}\right)^{m(T)}\right\}, \quad (1)$$

where $K_o(T)$ is the fracture toughness corresponding to 63.2% cumulative failure probability, $K_{min}(T)$ is the lower bound fracture toughness and $m(T)$ is the Weibull exponent.

The Weibull model parameters $K_o(T)$, $K_{min}(T)$ and $m(T)$ have been assessed for weak specimen orientations at five selected temperatures of 23, 200, 350, 425 and 575 °C. The fracture toughness values corresponding to 5%, 50% and 95% cumulative failure probabilities were calculated according to Eq. (1) and included in Fig. 4.

In analogy with the Master Curve (MC) approach, see ASTM E1925-05, describing the behaviour of fracture toughness of ferritic steels in the transition range, the dependence of the calculated median fracture toughness values (corresponding to 50% failure probability) on the test temperature was described by the following equation

$$K_{IC} = A + B \cdot exp\big(C * (T - T_o)\big). \quad \textbf{(2)}$$

Within the MC approach the parameters A, B and C are fixed providing the best description of the common shape of fracture toughness vs. temperature curve for ferritic steels in the transition region and T_o is the reference temperature at which the median fracture toughness of ferritic steel specimens of a reference thickness equals to 100 MPa $m^{1/2}$. Due to absence of ASTM procedure for determination of the reference temperature T_o for tungsten alloys we applied a least square fitting to the median fracture toughness data in Fig.4 with Eq. (2). The best fit to the median fracture toughness was obtained with A =5.63 MPa $m^{1/2}$, B =8.93 MPa $m^{1/2}$, C =0.00297 1/°C and T_o =435.48 °C and is shown by a solid line in Fig. 4. In analogy with the ASTM E1925-05 Master Curve (MC) approach we calculated the upper and lower tolerance bounds corresponding to 95% and 5% cumulative failure probabilities which are shown in Fig. 4 by the dashed lines. The two lines confine the fracture toughness data set to a large extent. The area right to the lower tolerance bound is identified as brittle fracture safe design space for polycrystalline tungsten. For more conservative definition of the fracture safe design space the use of an even lower cumulative probability level (less than 5%) can be also considered. State of the art polycrystalline tungsten alloys fail by ductile tearing

above 800 °C so that the shape of design space shown in fig. 4 will be changed above 800 °C and expand to much higher stress intensity factors. The fracture safe design space analysis for tungsten alloys performed within the current work is the first attempt of this kind up to authors' knowledge and will require further validation for alternative fracture toughness dataset on tungsten alloys.

Conclusion and Outlook

Fracture mechanical and microstructural characterization of tungsten alloys provided within EFDA Task Agreement has been continued. The upper shelf fracture behaviour of W and W-1%L_2O_3 specimens has been investigated. When using the specimens without side grooving large deformation levels were achieved without any indication of the crack growth. Neither the specimens with machined side grooves did show any stable crack growth up to large deformation levels. Beyond some deformation levels, however, initiation and propagation of unstable crack was observed indicating the improvement of the constraint state by side grooving. It is noteworthy to note that in spite of large deformation levels preceding the crack initiation the crack propagation appeared to be fully brittle.

Compilation of fracture toughness data on polycrystalline tungsten has been performed for identification of the brittle fracture safe design space. Weibull analysis of the cumulative failure probability distributions were implied for calculation of fracture toughness values corresponding to specified confidence levels. Master Curve description is proposed for description of the temperature dependence of the median fracture toughness in the transition region. The upper and lower tolerance bounds constructed on the base of Master Curve were shown to fairly describe the scatter of the compiled fracture toughness data. The lower tolerance bound was used for identification of fracture safe design space.

Fracture-Mechanical characterization of different novel laboratory and industry scale W-based structural materials that are being developed under EFDA HHFM Task Agreement will be performed in the interesting temperature window for fusion applications (RT-1300 °C). The J-Integral and/or COD methods will be applied for the investigation of upper shelf fracture toughness. FM experiments will be accompanied by fractographic and microstructural investigations. The probabilistic analysis of the fracture behaviour of commercially available tungsten alloys will be performed for identification fracture safe design space.

Staff:

J. Aktaa
E. Gaganidze
S. Kohnle
D. Litvinov

Acknowledgement

This work, supported by the European Communities under the contract of Association between EURATOM and Karlsruhe Institute of Technology, was carried out within the framework of the European Fusion Development Agreement. The views and opinions expressed herein do not necessarily reflect those of the European Commission.

Structural Materials for High Temperature Cooling Concepts (WP13-MAT-HHFM-03-02)

The focus of the project is generation of knowledge on irradiated tungsten's mechanical behavior at high temperatures. The high temperature nanoindentation technique will be used in a Hot Cell environment for that purpose. This technique requires only small testing volumes and offers the possibility to reuse already tested specimens.

A preliminary task of this study consists in the choice of the indenter tip's material which has to withstand high heat loads, mechanical loads and diffusion and corrosion processes for comparably long time.

For that purpose, a comparison study of the mechanical properties obtained on a reference sample material was be made with different tip materials. The mechanical behavior resulting from indentation of unirradiated samples made of pure, single and polycrystalline tungsten was investigated from room temperature up to 1000 °C.

The ability of the indentation technique to generate cracks will be utilized to examine the temperature-dependant changes in the fracture mechanisms of tungsten and determine the ductile to brittle transition temperature based on the indentation method. The requirement for the choice of an adapted geometry of the indenter tip also was investigated for that purpose.

Different materials and shapes of indenters have been evaluated: Sapphire, CBN, and diamond, in the shape of ball, Rockwell cone, Vickers pyramid, Berkovich, flat punch, and cube corner, leading to the following results:

- CBN showed a high mechanical sensibility and can only be used for non-rounded tips.
- Diamond showed a good stability at lower temperatures, but tends at higher temperatures to diffusion processes (Figs. 1 and 2).
- Sapphire has a good thermal stability, but is not hard enough for brittle tungsten.
- Vickers shape is unable to produce cracks in brittle tungsten at room temperature (Figs. 3 and 4).
- Flat punch indenters are able to produce cracks in polycrystalline tungsten (Fig. 5). This leads to an adapted testing method for generation of high stress and fracture in tungsten, and thus prediction of indentation derived fracture toughness is possible.

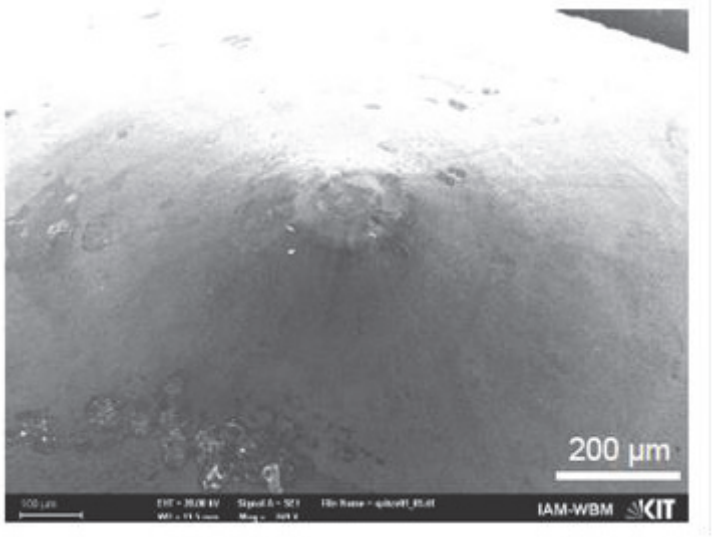

Fig. 1: Diamond tip, rounded after indent at temperatures > 500 °C due to diffusion processes (B. Albinski).

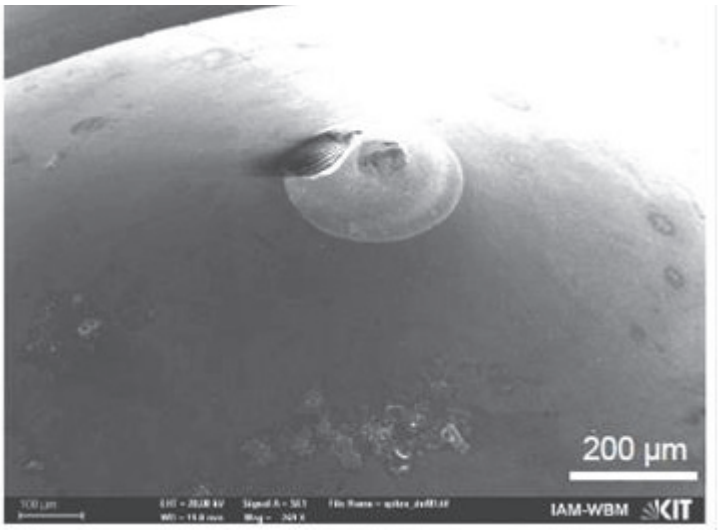

Fig. 2: Diamond tip. Missing part was connected to steel after indent at temperatures > 500 °C and broken during separation (B. Albinski).

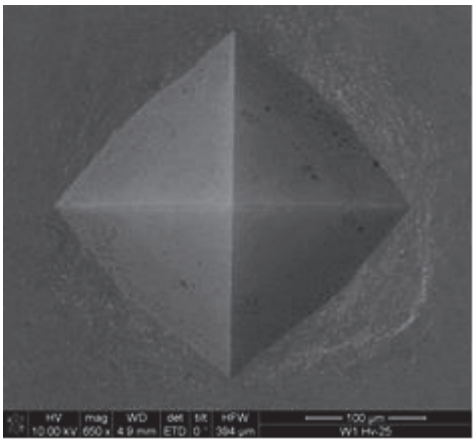

Fig. 3: Vickers imprint in poly-crystalline tungsten.

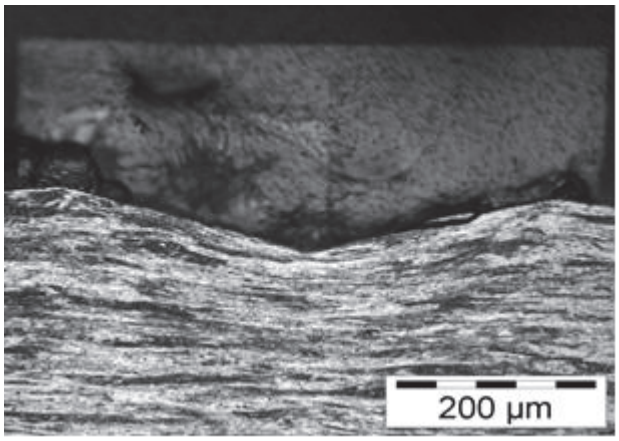

Fig. 4: Cross-section, etched surface of a Vickers imprint (method used for the detection of underlying cracks) (I. Sacksteder).

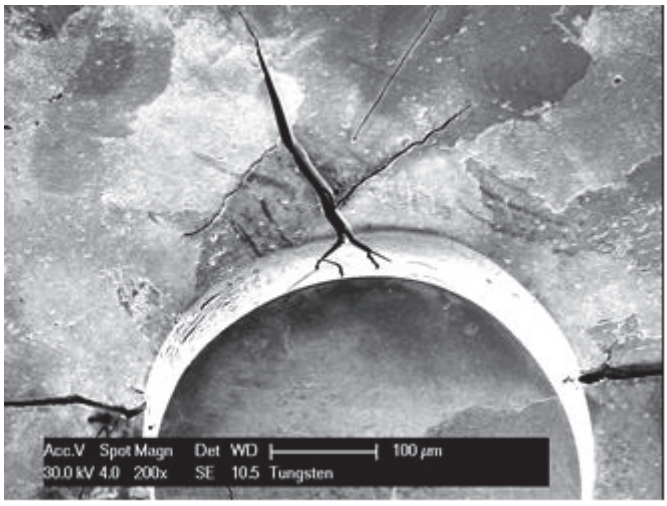

Fig. 5: Macro indentation on poly-crystalline tungsten by flat punch indentation for prediction of crack generation and propagation (I. Sacksteder).

Future Activities:

- Characterisation of unirradiated RAFM steels by instrumented indentation up to 650°C.
- Characterisation of unirradiated tungsten by instrumented indentation up to 1000°C.

Staff:

B. Albinski
I. Bernstein
J. Bredl
M. Dany
M. Holzer
W. Ibbe
S. Lautensack
I. Sacksteder
H.-C. Schneider

Literature:

[1] I. Sacksteder, S. Hostettler, G. Charbonneau, B. Albinski, H.-C. Schneider: Requirements for investigating the temperature-dependent fracture behavior of irradiated materials by indentation, Fus Eng Des, 88, 9–10, October 2013, 2577-2580

[2] B. Albinski, H.-C. Schneider, I. Sacksteder, O. Kraft: A new high-temperature indentation device for characterization of materials for fusion applications, J Nucl Mate, 442, 1–3, S1, November 2013, S865-S868

[3] B. Albinski: Instrumentierte Eindringprüfung bei Hochtemperatur für die Charakterisierung bestrahlter Materialien. Zur Erlangung des akademischen Grades Doktor der Ingenieurwissenschaften der Fakultät für Maschinenbau am Karlsruher Institut für Technologie (KIT) vorgelegte Dissertation. December 16th, 2013

Acknowledgement

This work, supported by the European Communities under the contract of Association between EURATOM and Karlsruhe Institute of Technology, was carried out within the framework of the European Fusion Development Agreement. The views and opinions expressed herein do not necessarily reflect those of the European Commission.

Material and Joining Process Development by Electro-chemical Plating (WP13-MAT-HHFM-04-02; WP13-MAT-HHFM-03-06)

Introduction

Tungsten will be used as armor material for blanket shielding and is designated as high heat flux material for divertors, beyond application of improved W composite alloys as structural material. Independent from the design (water- or helium-cooled), a successful development is inherently correlated with joining of tungsten with functional components and development of improved W composites.

Depending on the design variants, the fabricated joints have to guarantee specific functional or structural properties, e.g. good thermal conductivity or mechanical load transmission. Tungsten shows lacks in adapted joining due to its metallurgical behavior ranging from immiscibility over bad wetting to brittle intermetallic phase formation. Electroplating has shown to overcome such drawbacks and that homogeneous functional (e.g., Ni or Pd) and filler (e.g., Cu) layers can be deposited.

In this report the progress achieved in development of electroplating processes for joining W to W or steel to steel will be shown as well as the applicability to tungsten copper laminate processing.

Joining by electroplating

The He cooled divertor concept designed at KIT works with a finger like structure of cooling segments to manage heat loads near 10 MW/m² [1]. The armour material has to be joint to a structural, He pressure loaded, W-based part which has to be gas tight fitted to the steel structure beneath. Looking on water cooled designs the armour material will also be tungsten; however, the cooling tubing has to be fabricated from water resistant alloys as, e.g., copper, stainless steel or ferritic steel. All these design variants have in common, that tungsten has to be brazed to the cooling construction. For the He cooled divertor the joining types will be W to W or W to steel (Eurofer), whereas, in water based designs W will be brazed to copper or steel directly or with interlayers to reduce stresses. Essential is, that brittle phase formation can be avoided in the brazing zone and that good wetting is present. The interface temperature between structural component steel or Cu tubing and tungsten in water cooled option is below roughly 700°C. In the He cooled layout the W-steel joint will be also operated near 700°C and the W – W joint will be heated up to near 1200°C. This means, that only the higher melting elements can be used for filler composition or that the remelting temperature has to be increased by diffusion reaction with the base material. The first technological tests joining W to W were performed with STEMET alloy 1311 a Ni-based filler with additions of 16% Co, 5% Fe, 4% Si, 4% B and 0.4% Cr with remelting near 1200°C [2]. This alloy exhibits excellent wetting but forms brittle phases after short time at operation temperature which lead to failure, e.g., by detachment. Similar behavior was also present if tungsten was brazed to steel due to the large expansion mismatch between both materials. Steel-tungsten connections conducted by copper seemed to balance the expansion but showed bad wetting of tungsten which caused improper joints or leakages und cycling. Active interlayers deposited by electro-plating technology showed to be a solution for improved wetting and guided the path for development of filler systems to be applied in steel-steel, W-steel and W-W alloy joining. General coating tests showed that Pd or Ni, beyond some other transition elements; possess such ability of surface activation [3]. However, the technological application needs qualification in the field of mechanical behavior.

<u>Element selection for electroplating</u>

Wetting of tungsten by copper as pure filler is rather difficult due to the nearly completely missing miscibility of both elements as stated in phase diagrams [4]. Reactive interlayers can overcome this behavior if they have some miscibility with the parts to be joined and the filler

metal, e.g., copper. Some transition metals show wetting / miscibility with tungsten as, e.g., Pd, Ni, Fe, V or Ti and exhibit affinity to Cu. Thus, they may be excellent components in filler design. Additionally, they have not too high melting points but clearly above 1000°C to manage as Cu-based filler the temperature requirement of 1200°C.

Electroplating can work with water based electrolytes or if high temperature molten salts are neglected from organic solvents like ionic liquids. Elements with high oxygen affinity like Al or V [5] can only be electroplated from such electrolytes. In contrast, the elements Cu, Pd or Ni can be handled easily in aqueous systems and reduced to metallic layers in electroplating technology. This group of elements was selected for the first series in development of brazing by deposition of filler and interlayers and qualification of the fabricated joints.

Samples and electroplating

For fabricating the joints processed by electroplating cylindrical parts were cut from standard rod material with a diameter of 8 mm and length of 10 and 30 mm, respectively. The selection of the sample geometries was a contribution to the dimensions required for mechanical testing. Raw materials were tungsten delivered by Plansee Group, Austria and Eurofer steel (charge nr. E 83698) produced by Böhler Edelstahl GmbH, Austria. The end faces of the pieces to be joined were of fine turned quality as can be seen from Fig.1a. The surfaces of tungsten parts to be electroplated were cleaned and activated for improved adherence of coatings by currentless etching at about 50°C for 5 min. It is visible that turning traces disappeared and that a homogeneous slightly rough surface was produced by the etching with $K_3[Fe(CN)_6]$ * KOH solution (Fig. 1b).

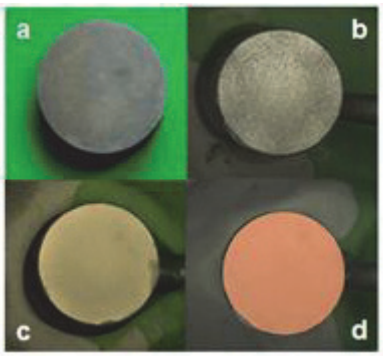

Fig. 1: Surface of W parts in the condition as turned (a), etched and conditioned for coating (b), deposited interlayer on W (c), and filler metal Cu deposited on top of the interlayer. Diameter is 8 mm.

As seen by earlier performed copper casting as bonding method [1] proper wetting of W is insufficient due to missing miscibility. Such fitted parts failed easily under load and thermal cycling. This lack can be overcome by interlayers, e.g., Ni [3] or Pd. These materials have the ability to react with both the matrix (tungsten) and the filler (copper). Deposition of Ni or Pd layers on tungsten can be performed by electroplating from aqueous electrolytes.

Best results for Ni deposition (Fig. 1c) were obtained applying an electrolyte consisting of a mixture of Nickelsulphamate with a Ni^{2+} amount of 76 g/l, boric acid and a fluorinated tensile. The layers exhibit good adherence and withstand stretching tests. They obey uniform color which is an indication for homogeneous thickness and missing voids between substrate and coating. As Ni reservoir was used a consumable Ni anode. The pH value was kept in the range 3.3 to 3.5. Deposition was performed at about 50°C with a current density near 10 mA/cm². Layer thickness can be adjusted by deposition time easily.

In contrast to Ni deposition of Pd interlayers were performed from an electrolyte working in the basic regime near pH = 7.5. This electrolyte was delivered by AMI DODUCO Company and is designed to deposit thicker scales in the µm range. Applied current densities were a little bit smaller (0.4 - 0.8 mA/cm²) and the anode was made of Pt coated Ti.

On such reactive interlayers copper was subsequently deposited as the main filler material (Fig. 1d). The thickness could be easily adjusted in the range 5 to 200 µm by variation of the deposition time. As electrolyte a mixture was used of 120 g/l $CuSO_4$ in 120 g/l H_2SO_4, 0.19 ml/l HCl and 10 ml tenside solution Primus CD KN 438021. The copper concentration was kept constant by working with a consumable copper anode. Temperature of the well stirred bath was near room temperature and deposition currents were applied of about 30 mA/cm². To keep processing simple only one piece of the parts to be joined were coated by

copper. Fig. 2 shows a cross cut of a tungsten piece coated by Ni and Cu. Clearly visible is that both layers are deposited homogenously and that wetting is always present without any voids.

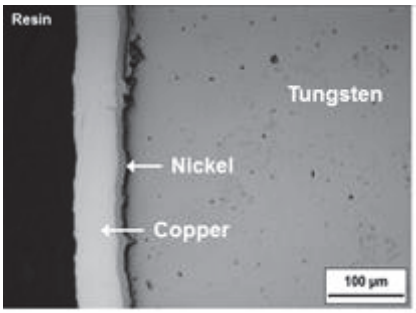

Fig. 2: Interlayer and filler deposited on tungsten.

In the He cooled divertor design tungsten is selected as armor and as structural material, whereas in other e.g. water cooled variants tungsten is considered as armor material and cooling pipes may be from steel as shown in Fig.1. Interface temperatures between structural component steel and tungsten may be for both designs similar, e.g., below roughly 700°C. In the He cooled layout the W – W joint will be operated near 1200°C. In all cases the filler alloy should not contain elements which form brittle intermetallic phases. The STEMET alloy 1311 is such Ni-based filler with additions of 16% Co, 5% Fe, 4% Si, 4% B and 0.4% Cr as used in first technological tests [1] due to the melting temperature near 1050°C and increasing re-melting temperature after joining. This alloy exhibits excellent wetting but forms brittle phases after short time at operation temperature which lead to failure, e.g., by detachment. Similar behavior was also present if tungsten was brazed to steel due to the large expansion mismatch between both materials. Steel-tungsten connections conducted by copper seemed to balance the expansion but showed bad wetting of tungsten. Active interlayers deposited by electro-chemical technology promised to be a solution and guided the path for development of filler systems to be applied in W-steel and W-W alloy joining or for development of W-composites with laminate structure.

Joint samples

The plated pieces were mounted for brazing in a support device to guarantee best axial arrangement for manufacturing reproducible joints. Always, one piece was only plated by a reactive interlayer, e.g., Ni and the other part was coated twice by interlayer and filler component copper. Brazing temperature was selected well above the melting of copper (T_M = 1084°C / 1357 K) at, e.g., 1150°C (1423 K). The brazing was performed in a tubular furnace under inert gas atmosphere and the support system was moved by a manipulator system into the warm brazing zone. The whole duration of brazing, consisting of heating up and dwell time, lasted 10 min and the temperature of the support system was monitored exceeding the desired brazing temperature. In a second batch a higher furnace temperature was chosen (1250°C), however the samples were removed after heated up to 1150°C without dwell time within approximately 5 min. Fig. 3 shows a sample brazed with dwell time of 5 min at 1150°C together with a detail section of the brazing zone. Visible is that some small traces of the filler were blown out from the brazing gap. This material formed droplets indicating that melting temperature of the filler was clearly crossed.

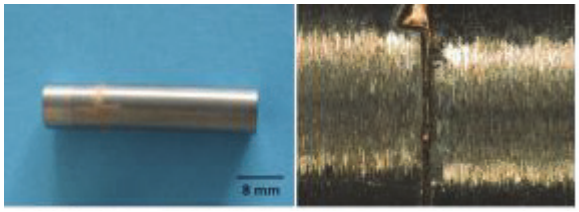

Fig. 3: Joint tungsten sample (8 mm diameter) fabricated for shear testing. Left: Detail view of brazing zone.

The performed metallographic examinations revealed that a homogeneous gap filling took place together with wetting of the tungsten surface by the filler. More detailed information concerning the reactions in the brazing gap was collected by performing SEM and EDX analyses. Fig. 4 shows a line scan across the brazing zone of a joint tungsten Eurofer part. The Ni interlayer reacts with both materials as can be seen by the rounded steps of the concentration curves for W or Fe plus Cr as Eurofer components in the contact zone joining parts – Ni interlayer and filler. Between interlayer and copper diffusion is also monitored which leads to a Ni-Cu solid solution. Metallography, SEM and EDX analyses confirmed that brazing by

electroplated Ni and Cu layers leads for both materials tungsten and Eurofer to good and reproducible wetting as main criteria for bonding.

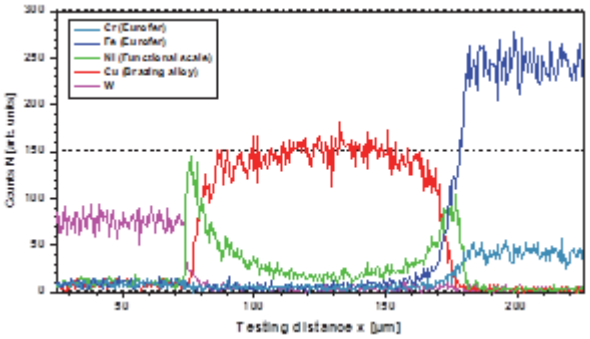

Fig. 4: EDX line scan of a W - Eurofer joint. Visible is that the functional layer Ni reacts with all other components and caused the wetting for the Cu filler.

Mechanical testing

The microstructural analyses pointed out, that interlayers (Ni, Pd) can be electroplated on tungsten and Eurofer in adjustable thickness and well adherent quality. Additionally was seen, that the filler copper can be deposited on the interlayers and that anticipated reactions occur to form joints during brazing treatment. Microcuts of brazing zones showed homogeneous gap filling an indication for good thermal and mechanical bonding which has to be separately proven in single effect tests, e.g., shear tests for qualification of their applicability.

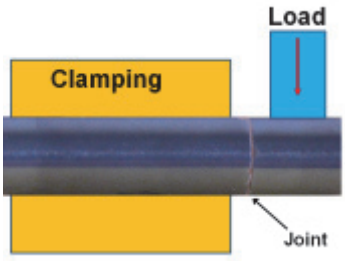

Fig. 5: Configuration of shear testing.

Shear testing was chosen as the first mechanical qualification step due to the simplest sample preparation and testing configuration. The tests were performed in an arrangement as shown in Fig. 5 with samples fabricated from electroplated end planes of rod segments with diameter 8 mm and length of 27 and 10 mm, respectively. The longer piece was clamped and the shorter part was loaded in a shear testing facility in a manner to avoid bending forces.

Shear testing of W joints

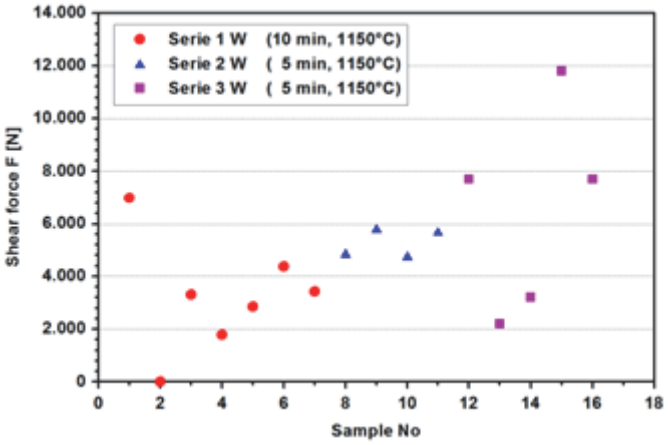

Fig. 6: Shear force of tested tungsten samples at RT.

The tungsten samples, fabricated in three separate batches, showed a not expected strong scattering in failure concerning the recorded shear force. Sample 2, which showed improper bonding, was disregarded; the shear force at failure of the others ranges from 1,800 to 11,800 N as shown in Fig. 6. There seems to be no correlation to fabrication. However, most surprising was that the failure appeared mostly in the bulk tungsten and only partly in the braze point. Some of the samples, e.g., No. 13 failed completely in the W bulk without affecting the brazing zone in any way. Also the 'strongest' joint (sample No. 15) showed no failure in brazing zone. The global resume of these tests is thus that the joints show high shear strength at RT of about L ≥ 235 N/mm². This value is in the range of technological joints fabricated with commercial Ni-based brazes of non-tungsten materials [6]. This underlines that the electroplating of interlayers and fillers

can compete in brazing technology as alternative technology with high flexibility in adjusting interlayer types.

Fig. 7 shows a typical cracking behavior of the joint samples if the failure did not only appear in the W bulk (in the top right corner is the overview). This cracking behavior indicates that the weak point is the tungsten at RT testing and not the braze. Some remaining sections of braze are visible in the brazing zone. The crack is there partly in the bulk of the braze. More detailed view to the crack position in the braze shows that the grains exhibit ductile behavior as can be seen from the enlarged part on the right side. This indicates that the combination of Ni interlayer and filler Cu produces ductile joints in contrast to the joints fabricated earlier in [2] by STEMET alloy at similar remelting temperature.

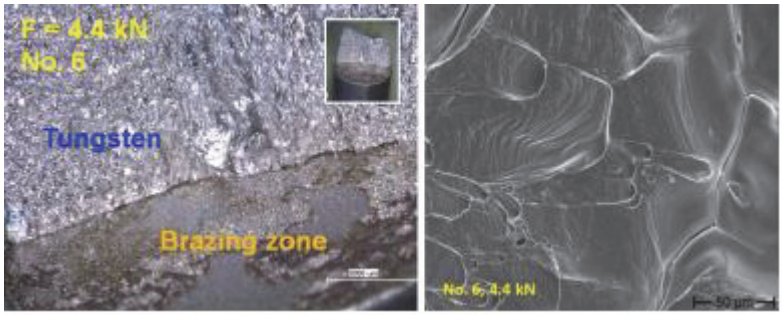

Fig. 7: Cracking zone of failed W joint at 4.4 kN with detailed view of the grains of the filler.

Shear testing of Eurofer joints

Beyond W-W also Eurofer-Eurofer and combined W-Eurofer joints will appear. This was the first reason to integrate the steel into the shear testing. During the W-W testing the relevance for steel tests increased due to the fact that Eurofer is ductile at RT. Thus no brittle cracks of the bulk should appear and affect the measured values as found for the W testing. The fabricated samples from Eurofer had the same dimensions as given for the tungsten pieces and were processed in the same equipment. Fig. 8 shows the force vs. shift of the load piston for a tested Eurofer sample. The force increases up to the peak value before cracking occurs in the brazing zone and the shape of curve indicates ductile behavior for the joint. The maximum load was roughly 11,500 kN similar to the value observed for the 'strongest' W-W joint. However, the view of cracking zone (Fig. 9) shows some spots of insufficient gap filling or of cracking not in the braze. Recalculating of the active surface = well joint areas with crack in the braze deliver a value of approx. 90 %. Thus, the observed shear strength of approx. 230 N/mm² has to be increased and will lie then above the values measured for failed W-W joints. Fig. 10 shows the corresponding X-Ray computer tomography (RCT) view of the cracked Eurofer-Eurofer joint before shear testing. The picture indicates that most of the surface is homogeneously brazed. Some darker small spots hints towards possible changes in braze composition or insufficient bonding. The macroscopic picture (Fig. 9) and the RCT view are comparable, thus RCT may be a tool for future qualification of joints which will be used for analyzing aging effects at elevated temperature.

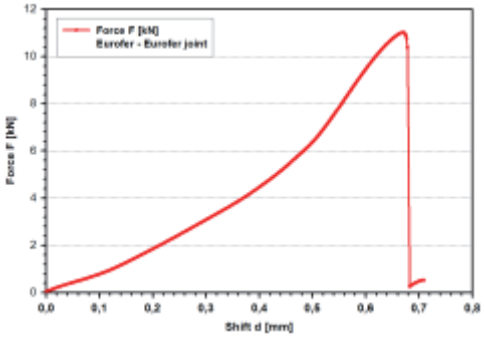

Fig. 8: Shear testing of brazed Eurofer sample with 8 mm diameter at RT.

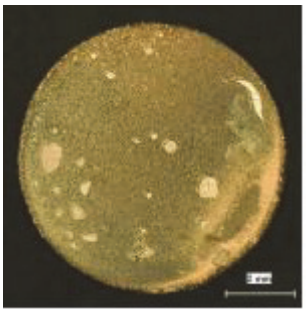

Fig. 9: View of cracking zone of Eurofer sample.

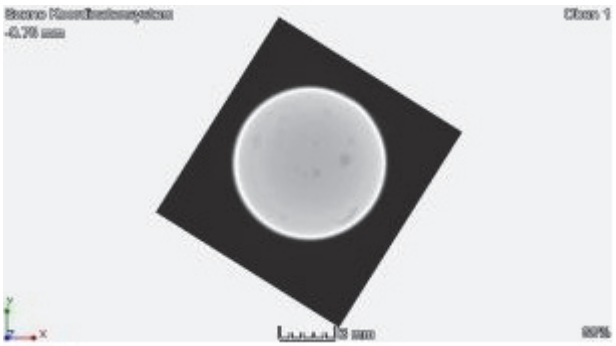

Fig. 10: RCT picture of brazing zone before shear testing.

Summary

Reliable and reproducible joining of divertor components is a challenging issue and the fabrication of parts for different kinds of testing have shown that surfaces especially of tungsten have to be pretreated and activated to achieve good wetting. Electrochemically based processes fulfill this requirement excellently and offer additionally a wide variety of elements to be electroplated as filler components. The preferentially examined interlayers Ni and Pd and copper as main filler component confirmed the applicability of electroplating in brazing technology to manufacture W-W and steel joints. The performed tests showed that the coating quality is defect free. However, brazing conditions, e.g., clamping during brazing or dwell times can influence the whole joint quality. The conditions for Ni-Cu based joints could be optimized for manufacturing of joints of rather homogeneous quality as can be seen from crack braze sections of Eurofer-Eurofer joints. The shear values at RT surely offer sufficient strength for W-Eurofer joints which can withstand adequate mechanical load. The W-W shear testing at RT was disappointing due to W cracking and claims additional tests in the ductile regime of W to measure shear values where both parts, braze and bulk, are ductile. More attention has to be paid to nondestructive joint qualification especially if aging behavior will be analyzed to obtain values for long term application.

W laminates by electroplating

Tungsten is also considered in fusion technology as structural material in the area of divertor for future application in DEMO. However, tungsten suffers by a high ductile to brittle transition temperature [9], which forecast operation temperatures at about 800°C as lower limit. This value is too high to be compatible with RAFM steels as structural material with operation temperatures up to about 700°C. Thus, the development of W composites was initiated to overcome the brittle behavior or shift it to acceptable boundary conditions. The development in the field of W composite materials by combination of thin W foils and interlayers of, e.g., Cu foils showed, that an improvement in properties seems to be possible [4]. However, several open issues are present in this development area, ranging from thinner interlayers up to industrial relevant processing. Electroplating of W foils seems to be a promising tool due to the ability of thickness control of layers during deposition by time or deposition current.

Electroplating as tool for W composite materials

Based on the experience in W coating for joining, a development program was set up to coat W foils. In the first stage surfaces were characterized in as delivered and etched conditions to evaluate suitable agents for electroplating. Alkaline hexacyanoferrate solution was used as etching agent to remove surface impurities as described in [3] and to achieve a surface roughening. The first tests showed, that deposition behavior of Cu on foils is different to plating of massive parts, e.g., cut from rods. Cyanidic electrolytes showed unfavorable behavior despite their better ability in micro scattering. In contrast, sulfatic electrolytes formed more bright and stable layers; however, the surfaces have to be activated by etching as shown in

Fig. 11. By this method W foils with thickness of 0.1 mm were coated by well adherent Cu layers and assembled to stacks for processing to W laminate structures.

Fig. 11: Cu coated W foils in the condition as delivered (left) and etched (right) in solution of K3[Fe(CN)6] * KOH.

Assembling of W laminates

The stacks of electrochemically coated W foils were axially hot pressed at 900°C and a load of 2 kbar to achieve bonding similarly to laminates fabricated by stacking W and Cu foils of 0.1 mm thickness. Fig. 12 shows the arrangement of the foils in the pressing equipment. Top and bottom foil were uncoated to avoid cu reactions with the pistons. The foils in the centre were all side coated by roughly 10 - 15 µm Cu. Fig. 13 shows the hot pressed stacks of conventionally assembled stacks and electrochemically processed foils. The electrochemically processed stack showed good bonding comparable with the behavior of the stack fabricated by conventional method. The deposited Cu layers reacted to dense interlayer without any visible inclusions, e.g. oxide particles. Compared to the foil stacking method the electrochemically deposited and reacted interlayers were much thinner (10 and 20 µm). Thus, the electrochemical Cu deposition showed that interlayers can be reduced to obtain W laminates with less Cu amount and that the Cu layer thickness can be varied easily by deposition time. Both, 20 and 10 µm interlayers reacted well and no gaps were formed between Cu and W foil as can be seen in Fig. 14.

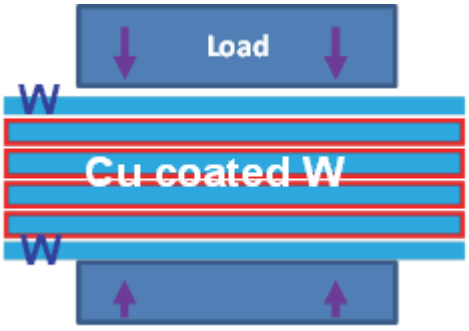

Fig. 12: Schematic illustration of the arrangement of electrochemically coated W foils in the hot pressing.

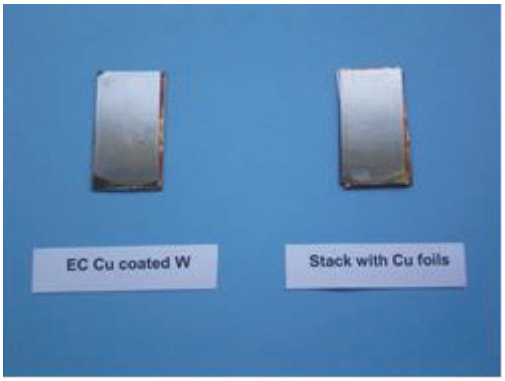

Fig. 13: W laminates fabricated from electrochemically coated W foils and conventionally stacked W and Cu foils.

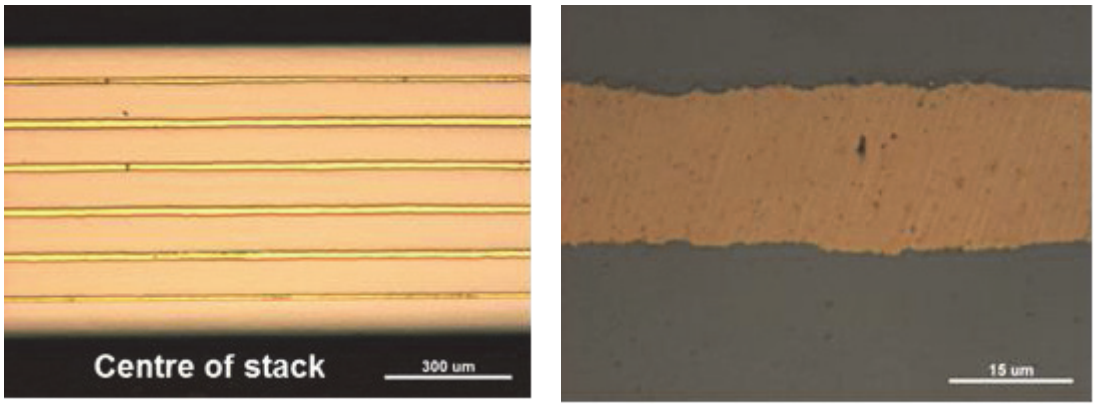

Fig. 14: Microstructure of W laminates fabricated by electrochemically deposited Cu on W foils. Left: Overview of stack. Right: Enlarged view Cu – W interface.

Summary

Reliable and reproducible assembling of W laminates was demonstrated applying electroplating of W foils by Cu layers. It was shown that W foils have to be activated by etching to obtain good adherence of deposited Cu. It was found that sulfatic based electrolytes lead to more homogeneous and better stable Cu layers compared to cyanidic electrolytes. The coating development of foils showed that the Cu layer thickness can be varied easily by current or deposition time and that thin homogenous layers can be processed also in the 10 µm range – a factor 10 lower that stacking W and Cu foils together. The metallurgical investigations indicated, that high purity Cu was present after hot pressing of the stack without any inclusions or cracks. The activation by etching lead additionally to a better interlinking of W and Cu compared to pure foil stacking as can be seen in Fig. 14 (right picture). The development conducted up to yet showed clearly the potential of applying electroplating for laminate technology. Extremely thin interlayers in laminate processing will not be accessible by foil stacking and claim improved technologies as, e.g., electroplating.

Conclusions

The performed high heat flux tests under development of He cooled divertor components showed clearly that improvement of brazing technology is absolutely necessary to manufacture reliable joints between armor material tungsten and structural cooling components beneath. This finding is independent of design or cooling variant helium or water. The defects analyzed in high heat flux testing guided the path towards development of joining technology based on electro plating, e.g., by observed strong deficits in homogeneous wetting of the components applying common technology and not adapted fillers.

The development of tools based on electro plating for brazing showed that deposition of metallic well adherent layers on tungsten is possible if surfaces are cleaned. Copper as main filler component can be used if reactive interlayers are first deposited on tungsten to allow metallurgical reactions. The application of electro plating eliminated here the main risk of inhomogeneous wetting and formation of defects, responsible for failure under load.

Ni has proven to be an excellent activator for brazing and possesses industrial relevance in common technology. Different types of joints, e.g., W to W and W to steel were successfully manufactured by Ni - Cu. The amount of Ni may underlie ‘neutron restrictions’ and has to be kept low. However, the performed tests showed that Ni-Cu is an excellent model system which defines quality for other filler compositions. Further development in joining by electro plating showed that Pd can successfully overtake the part of Ni in brazing with Cu. However, more stable Pd deposition under industrial view is required for transferring successfully performed lab tests to manufacturing.

First performed mechanical load tests indicated that joints fabricated by electro plating have high potential in joining fusion relevant components. Surely, additional development and qualification work is absolutely necessary in both fields mechanical tests and filler adjustment.

Activities in the field of W laminate processing indicated that W in the shape of foils show a more complex surface behavior which may be correlated to the high degree of deformation. Application of sulfatic electrolytes indicated that Cu layers can be deposited and that the layer thickness can be controlled by the deposition parameters current and time very well. The electroplating showed the ability to fabricate W laminates with thin ductile interlayers in the 10 µm range easily. It was well demonstrated that Cu interlayers deposited by electroplating form no gaps in the interface to the W foil. The whole work on laminates by electroplating needs of course additional development, e.g. mechanical testing and variation of interlayer element.

Staff:

M. Heck
N. Holstein
J. Konys
W. Krauss
J. Lorenz
J. Novotny
O. Wedemeyer
S.-E. Wulf

Literature:

[1] P. Norajitra, R. Giniyatulin, T. Hirai, W. Krauss, V. Kuznetsov, I. Mazul et al., Current status of He-cooled divertor development for DEMO, Fus. Eng. Design., 84 (2009) 1429-1433.

[2] P. Norajitra, L.V. Boccaccini, A. Gervash, R. Giniyatulin, N. Holstein, T. Ihli, Development of a helium-cooled divertor: Material choice and technological studies J. Nucl. Mater. 367–370 (2007) 1416–1421.

[3] W. Krauss, J. Lorenz, N. Holstein, J. Konys, Alternative electro-chemically based processing routes for joining of plasma facing components, Fus. Eng. Design, 86 (2011) 1607-1610.

[4] ASM Intern., Materials Park, OH, USA, 2006-2013, http://www1.asminternational.org/AsmEnterprise/APD/

[5] W. Krauss, J. Konys, N. Holstein, Development of advanced Al-coating processes for future application as anti-corrosion and T-permeation barriers, Fus. Eng. Design, 85 (2010) 2141-2262.

[6] Copper Development Association, Pub 139 Copper-Nickel Fabrication, http://www.cda.org.uk.

[7] P. Norajitra, R. Giniyatulin, T. Ihli, G. Janeschitz, W. Krauss, R. Kruessmann et al, He-cooled divertor development for DEMO, Fus. Eng. Design, 82 (2007) 2740-2744.

[8] W. Krauss, J. Lorenz, J. Konys, performance of electro-plated and joined components for divertor application, Fus. Eng. Design, In Press, (2013) http://ac.els-cdn.com/S0920379613004304/dx.doi.org/10.1016/j.fusengdes.2013.04.049

[9] M. Rieth, A. Hoffmann, Influence of microstructure and notch fabrication on impact bending properties of tungsten materials, Int.Journal of Refractory Metals and Hard Materials, 28, (2010) 679-686

[10] J. Reiser, M. Rieth, B. Dafferner, A. Hoffmann, Charpy impact properties of pure tungsten plate material in as-received and recrystallized condition (1 h at 2000°C (2273 K)), J. Nucl. Mater., 442, (2013) 204-207.

[11] J. Aktaa, W. Basuki, T. Weber, N.Norajitra, W. Krauss, J. Konys, Manufacturing and joining technologies for helium cooled divertors. (invited talk), 11th International Symposium on Fusion Nuclear Technology (ISFNT 2013), Barcelona, Spain, September 16-20, 2013.

[12] W. Krauss, J. Lorenz, J. Konys, Joining HHF components applying electroplating technology, 11th International Symposium on Fusion Nuclear Technology (ISFNT 2013), Barcelona, Spain, September 16-20, 2013.

[13] W. Krauss, J. Lorenz, J. Konys, Performance of electroplated and joined components for divertor applications Fusion Engineering and Design, 88, (2013), 1704-1708.

[14] M. Rieth et al., A brief summary of the progress on the EFDA tungsten materials program, Journal of Nuclear Materials, 442, (2013), 173-180.

[15] M. Rieth et al., Recent progress in research on tungsten materials for nuclear fusion applications in Europe, Journal of Nuclear Materials, 432, (2013), 482-500.

Acknowledgement

This work, supported by the European Communities under the contract of Association between EURATOM and Karlsruhe Institute of Technology, was carried out within the framework of the European Fusion Development Agreement. The views and opinions expressed herein do not necessarily reflect those of the European Commission.

Long-term Structural Material: W Laminate Materials (WP13-MAT-HHFM-03-04)

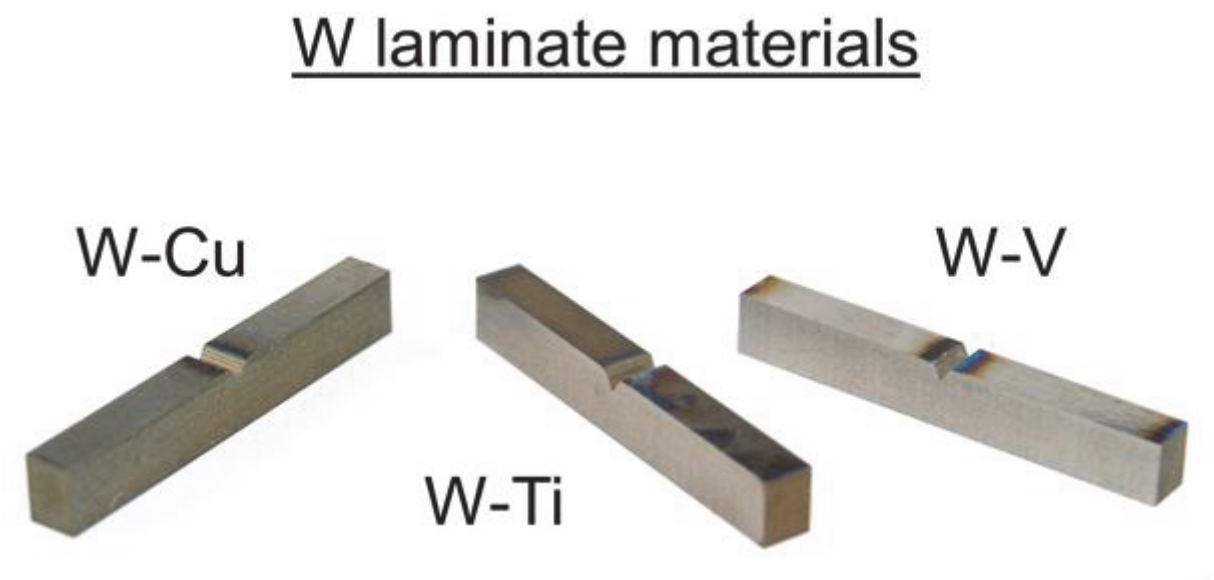

Introduction

Coarse grained tungsten (W) is known to be a brittle material with a low fracture toughness (e.g. 5 MPa $m^{1/2}$ at RT) and a high brittle-to-ductile transition temperature (BDTT). The situation appears different for tungsten in the shape of a thin foil. W foil with a thickness of 100 µm, has a BDTT of -120 °C (strain rate = $3*10^{-2}$ 1/s) and a fracture toughness of 70 MPa $m^{1/2}$ at RT (L-T orientation, source R. Pippan, Leoben). These extraordinary properties can be related to the ultra-fine grained (UFG) microstructure of the W foil in its as-received condition.

Through the assembly and joining of several of these UFG W foils the extraordinary properties of a foil can be transferred to the bulk.

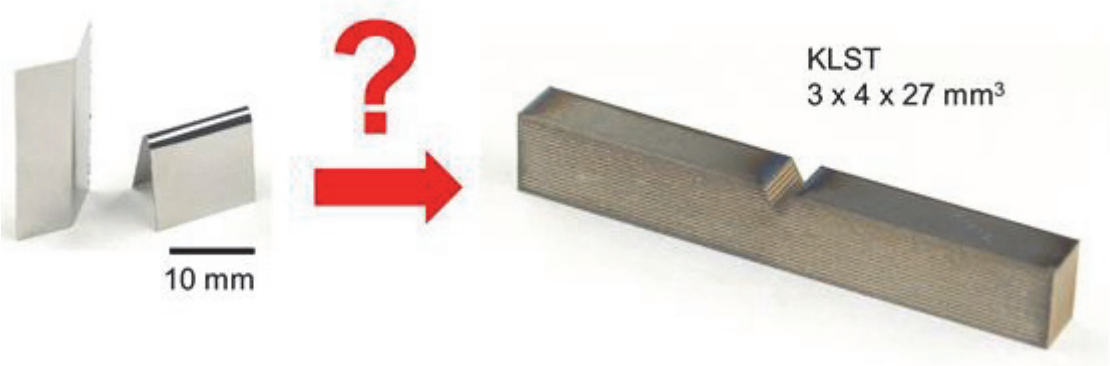

Fig. 1: W foil has extraordinary properties that can be related to its UFG microstructure. Through the synthesis of a W laminate the properties of a foil can be transferred to the bulk.

W foil and ductility: Identification of the mechanism of plastic deformation of UFG W foil (in cooperation with the University of Oxford, D.E.J. Armstrong, S. Roberts)

UFG materials are produced by severe plastic deformation (SPD) processes like high pressure torsion (HPT), equal channel angular pressing (ECAP), accumulative roll bonding (ARB) or other. According to VALIEV et al. UFG material combines high strength with sufficient ductility. However the deformation mechanism of this extraordinary material combination is not understood now.

The mechanism of plastic deformation can be determined in a direct way through tensile tests with subsequent TEM analyses, or in an indirect way through the determination of the strain rate sensitivity (SRS) and the activation volume, as the activation volume is the “finger print” of the kinematics of the plastic deformation.

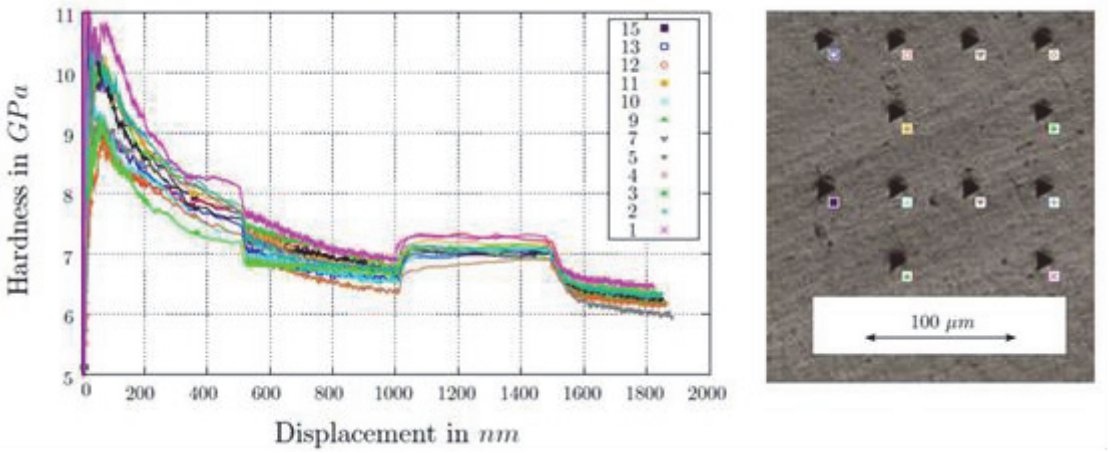

Fig. 2: Nanoindentation strain rate jump tests. In cooperation with D.E.J. Armstrong and S. Roberts (Department of Materials, University of Oxford) and V. Maier and R. Pippen (ESI, Leoben) we determined the SRS and the activation volume of W foil in as-received and recrystallized condition, showing a change in the dominating deformation mechanism.

In cooperation with D.E.J. Armstrong and S. Roberts (Department of Materials, University of Oxford) and V. Maier and R. Pippen (ESI, Leoben) the SRS and the activation volume of W foil in as-received and recrystallized condition by nano-indentation strain rate jump tests were determined. For the recrystallized W foil an activation volume of 6.8 b3 was determined whereas for the W foil in the as-received condition (UFG W foil) a value of only 5.3 b3 was measured. This change in the activation volume might be interpreted as a change of the dominant deformation process from the thermal activation of a kink-pair (recrystallized W foil) to thermal processes at the grain boundaries (UFG W foil).

W foil and fracture mechanics: Determination of the activation energy of the brittle-to-ductile transition, ΔH_{BDT}, of W foil in as-received and recrystallized condition
(in cooperation with the University of Oxford, D.E.J. Armstrong, S. Roberts)

The mechanism controlling the BDT is not identified yet. As the temperature at which the BDT occurs strongly depends on the strain rate, an activation energy for the BDT can be determined. As this activation energy is equal to that for dislocation motion the BDT might be controlled by the formation of a kink pair and the movement of the screw dislocations. “On the other hand, specimen size and the availability of dislocation sources have a pronounced influence on the fracture toughness to the degree that they may even switch the material’s behavior from brittle to ductile which supports a nucleation-controlled interpretation” (P. Gumbsch, JNM, 2003).

As W foil has extraordinary properties in terms of ductility and toughness we determined the activation energy of the BDT in order to correlate this value with a deformation mechanism. Material used was 100 μm tungsten foil in as-received and recrystallized condition (2 h / 1800 °C). The BDT was determined by 4PB tests. For each strain rate a BDTT was determined and by an ARRHENIUS plot the activation energy was calculated. For the coarse grained W foil (recrystallized foil) an activation energy of the BDT of 1.27 eV was determined. By comparing this result with the kink pair theory of SEEGER with experimental date from BRUNNER we calculated a value for the formation of a kink-pair of 1.25 eV. As both values are similar one can conclude that the BDT of recrystallized W foil is controlled by the formation of a kink-pair of a screw dislocation. This result fits well to results obtained from literature measured on notched W sinter parts, notched W single crystals, notched polycrystalline W material, and un-notched polycrystalline W material.

Now for the W foil in as-received condition the situation appears to be different as the brittle - semi-brittle transition is not strain rate dependent anymore resulting in an activation energy of 0 eV. So the controlling mechanism of the BDT is now for sure not the formation of a kink-pair but maybe twinning or the movement of edge dislocations. As twinning is only known to appear only at very low temperatures in α-Fe it is very likely that twinning can be excluded from the discussion. By considering small errors in the temperature measurements on can see an activation energy of 0.2 eV for the BDT of as-received W foil as feasible. In this case the BDT is than controlled by the movement of edge dislocations.

These edge dislocations might either be (i) stored in the thick grain boundaries (g.b.) of the W foil, be (ii) stored in the grains or (iii) the grains of a UFG W foil are that small that the screw parts of a dislocation loop are stuck in the grain boundaries whereas the edge parts are able to move.

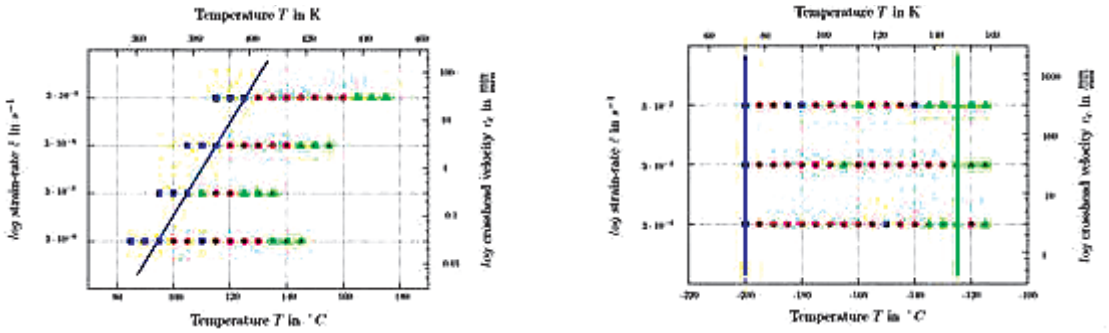

Fig. 2: Left: The activation energy of the BDT of W foil in the recrystallized condition (2 h / 1800 °C) was measured with 1.27 eV so the BDT might be controlled by the formation of a kink-pair of **screw** dislocation. Right: The situation appears different for W foil in the as-received condition (UFG W foil). Here the measured activation energy is zero, and the BDT controlling mechanism might be the movement of **edge** dislocations.

W laminates: Ageing of W-Ti laminates

It is obvious, that the success of expanding the excellent properties of a W foil to the bulk through the synthesis of a W foil laminate strongly depends on the right combination of interlayer and joining technology. The interlayer chosen in this study is titanium (Ti) with a melting temperature of 1668 °C, the bonding technology is diffusion bonding and the joining temperature is well below the recrystallization temperature of the foil.

Like this Charpy impact test samples with KLST dimension were produced and tested. As in operation the W laminates have to withstand long time at high temperatures an ageing campaign was started intending to assess the change of the W-Ti interface and the change of the mechanical properties after 10 h, 100 h, and 1000 h at 1000 °C in vacuum. The assessment of the interface was done by SEM and AES.

The AES shows that in the as-produced condition there is diffusion of W in Ti and nearly no diffusion of Ti in W. The Ti rich side shows the formation of cubic β-W needles in a hexagonal α -Ti matrix. After 10 h at 1000 °C the Ti rich side shows a lamellar structure being a sign of a mono eutectic reaction as it can also be seen in the phase diagram. On the W rich side whole W grains are detached from the W foil by grain boundary diffusion of Ti. The situation appears similar after 100 h at 1000 °C. Again on the W rich side whole grains are detached by grain boundary diffusions of Ti, whereas on the Ti rich side still same lamellar structures are visible coming along with a homogeneous Ti-W solid solution. After 1000 h at 1000 °C there is nearly only a Ti-W solid solution on the Ti rich side defining a metastable condition according to the phase diagram.

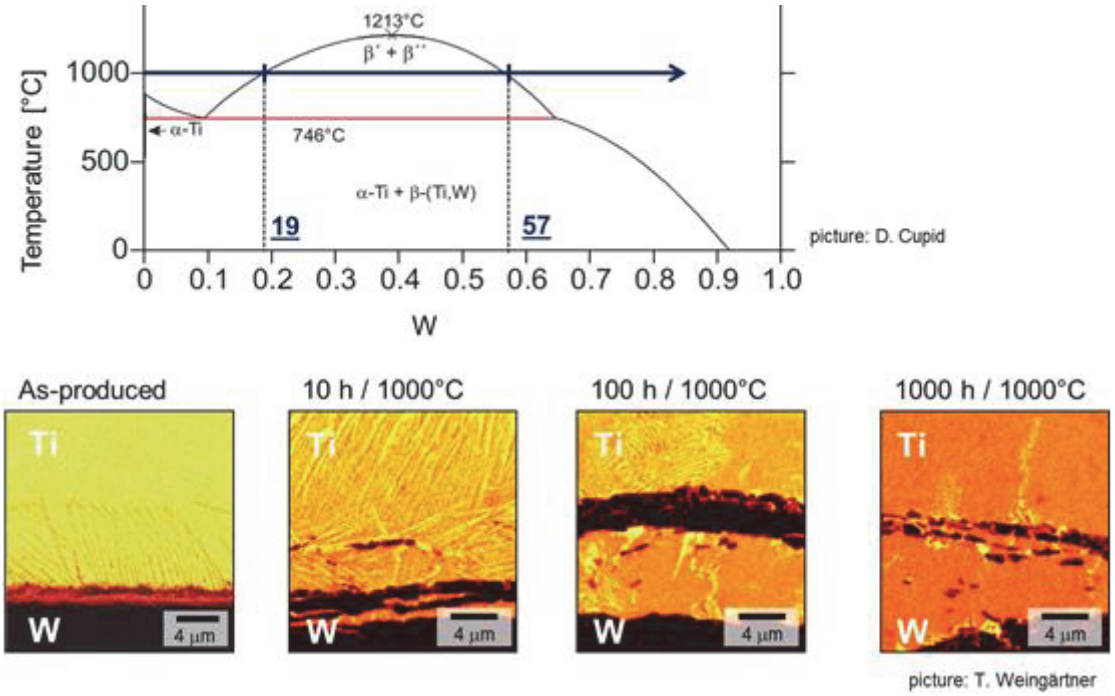

Fig. 3: Ageing of W-Ti laminates, 10 h, 100 h and 1000 h at 1000 °C. From the left to the right shows the change of the W-Ti interface at 1000 °C with increasing time. This change of the interface comes along with a change of the Charpy impact properties.

Staff:

S. Baumgärtner
D. Bohlich
B. Dafferner
M. Hoffmann
U. Jäntsch
A. Möslang
A. Németh
J. Reiser
M. Rieth
J. Scherbarth
T. Weingärtner
R. Ziegler

Literature:

[1] J. Reiser, M. Rieth, B. Dafferner, A. Hoffmann, Tungsten foil laminate for structural divertor applications – Basics and outlook, Journal of Nuclear Materials 423 (2012) 1–8.

[2] J. Reiser, M. Rieth, B. Dafferner, A. Hoffmann, X. Yi, D.E.J. Armstrong, Tungsten foil laminate for structural divertor applications – Analyses and characterisation of tungsten foil, Journal of Nuclear Materials 424 (2012) 197–203.

[3] J. Reiser, M. Rieth, A. Möslang, B. Dafferner, A. Hoffmann, X. Yi, D.E.J. Armstrong, Tungsten foil laminate for structural divertor applications - Tensile test properties of tungsten foil, Journal of Nuclear Materials 434 (2013) 357-366.

[4] J. Reiser, M. Rieth, A. Möslang, B. Dafferner, J. Hoffmann, T. Mrotzek, A. Hoffmann, D.E.J. Armstrong, X. Yi Tungsten foil laminate for structural divertor applications – Joining of tungsten foils, Journal of Nuclear Materials 436 (2013) 47-55.

Acknowledgement

This work, supported by the European Communities under the contract of Association between EURATOM and Karlsruhe Institute of Technology, was carried out within the framework of the European Fusion Development Agreement. The views and opinions expressed herein do not necessarily reflect those of the European Commission.

Production of Real-size Parts Consisting of Different W Materials using PIM as an Alternative Joining Process (WP13-MAT-HHFM-04-01)

Objectives

At Karlsruhe Institute of Technology (KIT) divertor design concepts for future nuclear fusion power plants beyond ITER are intensively investigated, which includes also the development of manufacturing methods for the mass production of divertor parts. Powder Injection Molding (PIM) is a powder metallurgy (PM) near net shape fabrication process for metals and ceramics with tight tolerances and good surface finishes. This process enables the mass production of parts with complex shaped geometries at low cost and high performance. Materials with high melting points such as tungsten or tungsten alloys can be effectively fabricated by this process. At KIT small tungsten parts were successfully produced in the past. The challenge and motivation for this work was the potential up-scaling to produce bigger parts as before. The PIM process was applied as a method for mass production. This activity is in closely connected to WP13-MAT-01-HHFM-01-01/KIT/PS, where PIM is used as method for the rapid development of new materials.

The present report describes the development of a new PIM tool to replicate parts with variable sizes and shapes, and the joining of tungsten and doped tungsten alloys. The technological fabrication process of Powder Injection Molding, including material and feedstock (powder and binder) development, injection molding, the new developed heat-treatment process and the characterization of the microstructure is shown exemplarily.

State of the art PIM R&D

At KIT various Powder Injection Molding processes for tungsten and tungsten alloys are intensively investigated. The fabrication route of pure W-PIM parts was developed in 2009 – 2010 [1-3]. In 2011 two new doped tungsten alloy feedstocks (W-2La_2O_3 and W-2Y_2O_3) were developed and the production route of two-component parts by a new insert PIM process was successfully demonstrated [4]. In 2012 a real 2C-PIM tool was developed, optimized by simulations, and fabricated. This new 2C-PIM tool allows the fully-automatic replication of fusion relevant components, such as the tungsten tile and the tungsten alloy thimble, in one single step and without additional brazing [5-7].

But the design and engineering of such PIM tools are very time and cost intensive. The motivation for this work was the modification of a common PIM tool and the development of insert plates with different sizes and shapes. This allows the use of only one PIM tool to replicate different parts. Furthermore, this is one more step on the route to produce bigger tungsten parts. The activity is also closely connected to WP13-MAT-01-HHFM-01-01/KIT/PS.

Results

Design ideas

Fig. 1 shows typical design ideas which could be realised by such a new so-called “multi-phase PIM tool”. Depending on the thickness and size of each insert plate, parts with variable shapes and geometries (Fig. 1, left) and also the joining of different materials as well as the integration of interlayers (Fig. 1, right) could be carried out.

Fig. 2 shows the insert of cores to replicate parts with holes, in the middle or on a surface (Fig. 2, top). After the final heat-treatment of the PIM parts tungsten laminate pipes could be integrated (Fig. 2, down).

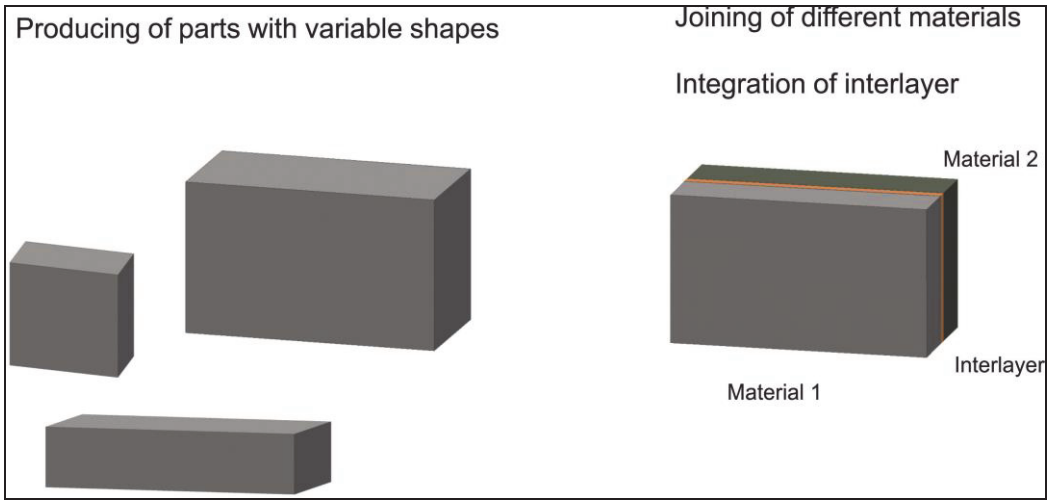

Fig. 1: Parts with different sizes and the integration of interlayers.

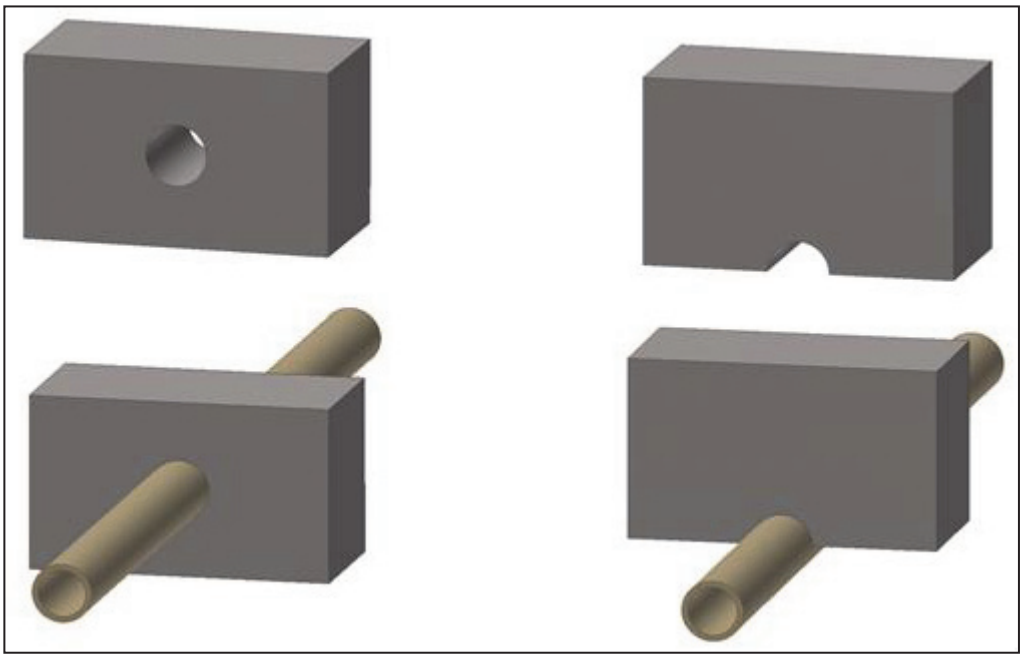

Fig. 2: Development of parts for new divertor designs.

The new “multiphase PIM tool”: running-in tests

A typical PIM tool has a mold cavity, a pathway for filling the cavity with ejectors for extracting the component from the cavity, and it is oversized to account for the sintering shrinkage. Fig. 3 shows the open new tool, left the ejection side with cavity and right the nozzle side. To replicate the parts, granulated, homogeneous and agglomeration-free tungsten and tungsten alloy feedstock is used. The particle size of the pure tungsten powder is in the range of 0.7 µm to 1.7 µm. The particle size of the powders for the preparation of the doped tungsten alloys was for the yttrium oxide (Y_2O_3) powder, 1.50 µm and for the titanium carbide powder, 50 nm. For the composition of W-2Y_2O_3, the tungsten was doped with 2wt.-% Y_2O_3 powder and for W-1TiC with 1wt.-% TiC powder. The doped powders are produced by mixing. This is just a blending process that can be up-scaled in any order. The most critical point of the feedstock preparation is the fabrication of a homogeneous distribution of agglomerate-free powder within the binder matrix. After heating the powders at 80 °C to remove moisture, a portion was mixed with a 50 vol.-% binder system in a kneader. After that, the feedstocks were then compounded and granulated.

The injection molding was carried out on an ARBURG ALLROUNDER 420C injection molding machine. Depending on the size and shape of each insert plate, different parts were produced.

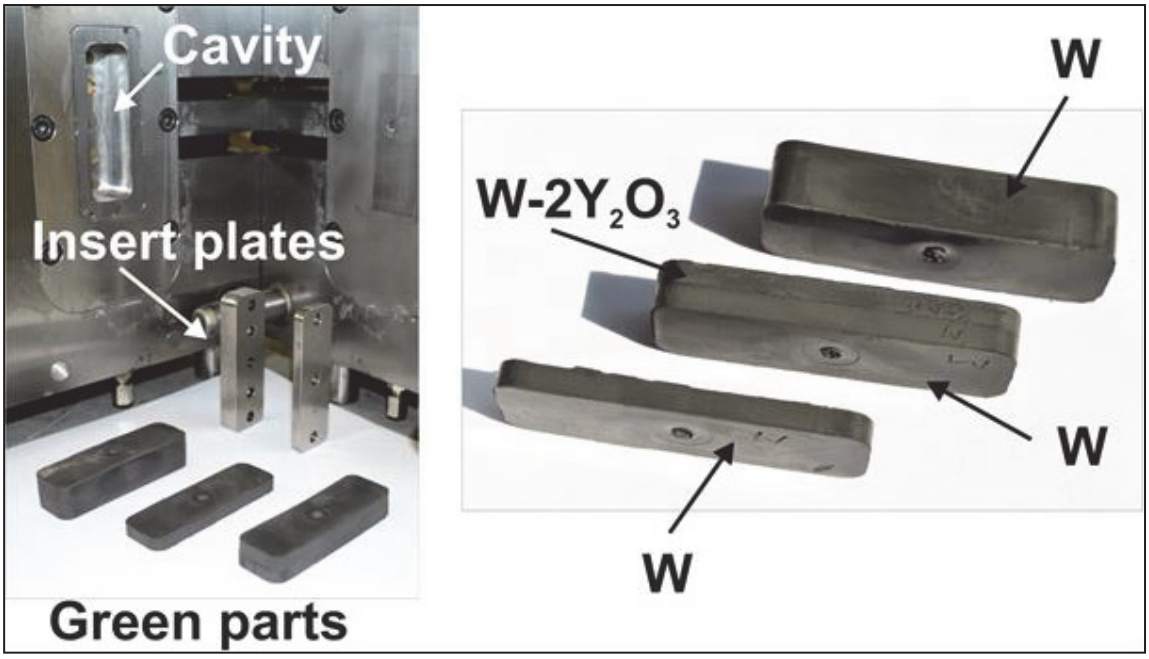

Fig. 3: Production of green parts with the new tool.

Debinding and heat-treatment process

After injection molding, but before heat-treatment, the green parts have undergone solvent debinding. The new developed heat-treatment process is a two-step procedure: (1) Pre-sintering in a sinter furnace (MUT, Germany) at 1800 °C in dry H_2 for 2 hours. After that, the parts have a density of 96%. (2) The samples are sintered at 2400 °C in dry H_2 also for 2 hours (carried out by PLANSEE). The density of the finished parts is 99% T.D., and the shrinkage of the finished parts after the heat-treatment process is at about 22% (see Fig. 4).

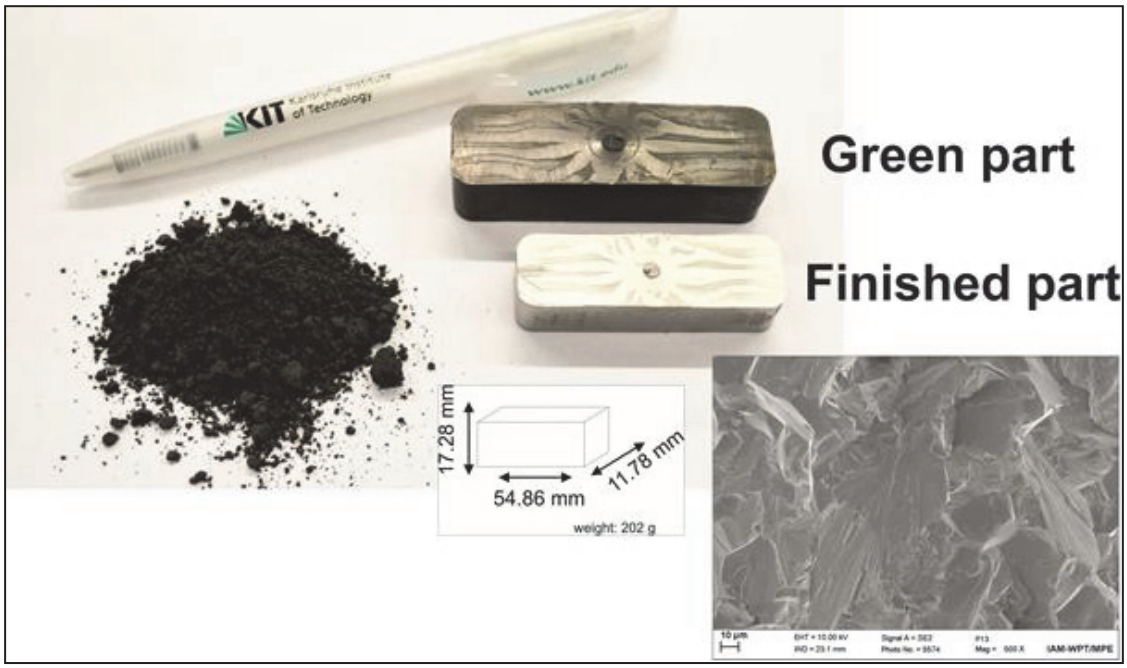

Fig. 4: Green part (top) and after heat-treatment (down). The size of the finished part consisting of pure tungsten after heat-treatment is (54x17x11) mm and the weight is 200 grams. The microstructure of the finished parts (fracture surface) is without cracks, gaps or pores.

Conclusions and outlook

The motivation for this work was the realization of parts with various sizes and shapes via PIM. Common PIM tools were modified and insert plates with different sizes and shapes developed. The production of tungsten parts with different sizes and the joining of tungsten with doped tungsten materials were successful. The microstructure of the finished tungsten samples after the new developed heat-treatment process were characterized and found to be remarkably fine.

However, in 2014 first prototype divertor studies, consisting of PIM tungsten and a laminate tungsten pipe, will be produced and tested via HHF-testing.

Collaborations

T. Barrett, S. Dudarev (CCFE),
S. G. Roberts, D. Armstrong (University of Oxford),
W. Knabl (PLANSEE SE)

Staff:

S. Antusch
N. Denker
J. Heneka
A. Klein
M. Offermann
M. Rieth
H. Walter

Literature:

[1] S. Antusch, P. Norajitra, V. Piotter, H.-J. Ritzhaupt-Kleissl, Powder Injection Molding for mass production of He-cooled divertor parts. Journal of Nuclear Materials 417 (2011), 533-535.

[2] S. Antusch, P. Norajitra, V. Piotter, H.-J. Ritzhaupt-Kleissl, L. Spatafora, Powder Injection Molding – an innovative manufacturing method for He-cooled DEMO divertor components. Fusion Engineering and Design 86 (2011), 1575-1578.

[3] S. Antusch, V. Piotter, KIT investigates the mass production and joining of divertor parts for nuclear fusion power plants via multicomponent tungsten PIM. Journal of Powder Injection Molding International 6 (2012).

[4] S. Antusch, M. Müller, P. Norajitra, G. Pintsuk, V. Piotter, H.-J. Ritzhaupt-Kleissl, T. Weingärtner, Two component tungsten Powder Injection Molding for mass production of He-cooled DEMO Divertor parts. Journal of Fusion Science and Technology 62 (2012), 110-115.

[5] S. Antusch, L. Commin, M. Müller, V. Piotter, T. Weingärtner, Two component tungsten Powder Injection Molding – an effective mass production process. Journal of Nuclear Materials (2013), 10.1016/j.jnucmat.2013.11.007.

[6] S. Antusch, L. Commin, J. Heneka, V. Piotter, K. Plewa, H. Walter, A new fully automatic PIM tool to replicate two component tungsten DEMO divertor parts. Journal of Fusion Engineering and Design 88 (2013) 2461-2465.

[7] S. Antusch, V. Piotter, M. Rieth, Mass production and joining via Multicomponent tungsten powder injection molding. In: Proceedings of the 18th Plansee Seminar, Reutte, Austria (2013).

Acknowledgement

This work, supported by the European Communities under the contract of Association between EURATOM and Karlsruhe Institute of Technology, was carried out within the framework of the European Fusion Development Agreement. The views and opinions expressed herein do not necessarily reflect those of the European Commission.

Fission Reactor Irradiation Programs Needed to Fill in Most Urgent Gaps in the Materials Database on Advanced Blanket RAFM Steels (WP13-MAT-02-02-01)

Objectives

The RAFM steels and their ODS variants are considered as primary candidate structural materials for the FW and HC BB of DEMO with operating temperatures between 350 and 650 °C. Although RAFM steels are primarily developed for structural application in HCBB concepts, their potential use in water cooled breeding blanket concepts under PWR condition with coolant inlet/outlet temperatures of 290/325 °C (at a pressure of ~15.5 MPa) can also be considered taking into account that neutron irradiation of EUROFER97 in the temperature range between 290 and 325 °C results strong degradation of the mechanical properties. Main goal of the current task was a definition of urgent fission reactor irradiation programmes needed to fill in most urgent gaps for the consolidation of the materials database on new EUROFER charges, advanced ODS-EUROFER and ODS FS steels as well as advanced technological specimens (diffusion welds, EB/TIG welds).

Task Current Status

The main objectives of the near to mid-term fission irradiation programs on novel EUROFER charges are identified as (i) generation of mechanical and physical properties data in a temperature range being relevant for the both helium and water cooled blanket concepts, (ii) investigation of helium effects and swelling by using isotopically/chemically tailored model steels, and (iii) investigation of evolution of the radiation defect microstructure. EUROFER97 and other reference RAFM steels exhibit strong irradiation induced hardening which is accompanied by embrittlement and loss of toughness and ductility at irradiation temperatures below 340 °C. Fission irradiation experiments at multiple temperatures in a temperature range between 250 and 400 °C will provide adequate information with respect to the most mechanical properties including tensile, low cycle fatigue, Charpy impact and fracture toughness properties. At higher irradiation temperatures the mentioned mechanical properties are practically not affected by neutron irradiation as the irradiation defects e.g. small defect clusters and dislocation loops are effectively annealed out. The fission irradiation experiments on isotopically or chemically tailored model steels at high irradiation temperatures of up to 450-550 °C will be however required for investigation of possible high temperature helium embrittlement and the swelling behavior with expected peak swelling temperature of 430 °C (E. Wakai, et al., Nucl. Mater. 356 (2006) 95-104). In addition for the study of the creep behavior under neutron irradiation a possibility of the performance of in-situ creep experiments at irradiation temperatures of up to 550 °C has to be examined.

The increase of the Yield Stress and the DBTT of RAFM steels is rather steep at doses below 10-15 dpa at T_{irr} ≤335 °C. At higher damage doses a clear reduction of the hardening and embrittlement per dose increment is observed. Due to these observations the irradiation experiments have to be performed at least up to 15 dpa to make a rough estimate of the magnitude of expected hardening and embrittlement. As the irradiation data is very rare at damage doses above 15 dpa, the irradiations up to 30 dpa is suggested and ideally multi-target dose of 5, 10, 15, 20, 25, 30 dpa irradiation experiments have to be performed. For the case of isotopically- and chemically tailored fission irradiation experiments for investigation of swelling and high temperature helium embrittlement the target damage dose will depend on the isotope type and neutron spectrum used. For example by using the 10B doping technique a 2 dpa will be already enough for complete boron-to-helium transmutation in the spectrum of HFR, Petten reactor, whereas damage doses well above 100 dpa will be required for experiments in the fast spectrum of BOR-60 fast breeder reactor.

For proper planning and preparation of the irradiation experiments the geometry and number of specimens to be used should be identified. Geometries of the specimens have to be chosen (i) by taking into account the mechanical properties under investigation and (ii) by considering available volume for specimen irradiation. Taking into account the high fission neutron costs and small available irradiation volumes the use of SSTT becomes mandatory. This approach is also justified with respect to following irradiation experiments in future fusion neutron spectrum irradiation facilities like IFMIF. The reliability of the results obtained with SSTT should be guaranteed and validated by performing experiments in the reference unirradiated state and by accompanying appropriate modelling activities. Special emphasis was put on the investigation of fracture mechanical and LCF properties by using SSTT.

The data quality criteria for the consideration of the testing results in Materials Properties Handbook of DEMO In-Vessel components were elaborated. In addition, on the base of the data acquisition templates developed by F. Tavassoli (CEA) the material handbook templates have been produced for the documentation of information on material product, material composition as well as the Charpy impact, fracture toughness, tensile, fatigue and creep testing results. The elaborated templates have been uploaded to the EFDA IDM system.

General recommendations based on the experience from previous irradiation programmes have been given.

The compilation of the existing mechanical data on EUROFER97 steel was launched. The data compilation aims at creation of baseline EUROFER database as well as Materials Properties Handbook for DEMO In-Vessel components. The tensile, impact fracture toughness and LCF data on EUROFER97 were collated in the reference unirradiated condition as well as after neutron irradiation in several European irradiation programmes.

Conclusions and outlook

The urgent fission reactor irradiation programmes needed to fill in most urgent gaps in the materials database on advanced blanket RAFM steels have been identified. An irradiation programme manual is elaborated including information on target irradiation temperatures, target damage doses, type and number of specimens, material needs and costs, specimen fabrication costs and time. The recommendations on the Post Irradiation Examinations indicating the applicable standards are elaborated. The accompanying irradiation experiments supporting the modelling activities for evaluation of fracture-mechanical experiments on miniaturized specimens as well as the experiments for validation of the results obtained on miniaturized fracture-mechanical and low cycle fatigue specimens are proposed.

The compilation of EUROFER existing data launched within the EFDA WP13 MAT-02 task will be continued aiming at creation of baseline EUROFER data base as well as Materials Properties Handbook for DEMO In-Vessel components. The analysis of the available mechanical and microstructural properties of fusion reactor materials before and after neutron irradiation will be proceeded. Special emphasis should be put on the compilation and analysis of the data on mechanical behavior of the technological specimens in the unirradiated and irradiated conditions.

Staff:

J. Aktaa
E. Gaganidze

Literature:

[1] E. Gaganidze and J. Aktaa, Assessment of neutron irradiation effects on RAFM steels, Fusion Engineering and Design 88 (2013) 118– 128.

Acknowledgement

This work, supported by the European Communities under the contract of Association between EURATOM and Karlsruhe Institute of Technology, was carried out within the framework of the European Fusion Development Agreement. The views and opinions expressed herein do not necessarily reflect those of the European Commission.

Neutronics and Nuclear Data

Neutronic Analysis of ITER Diagnostic Components (ITER/IO/12/4300000548 and ITER/IO/13/4300000896)

Objective

The objective of this work was to provide neutronics computational service for the ITER Organization (IO) Diagnostics Division in order to improve the shielding performance of the Diagnostic Equatorial and Upper Port Plugs (EPP and UPP) in ITER. The aim was to guide and assist the EPP and UPP design developers with optimal shielding solutions which are characterised by maintaining the primary diagnostics purposes and providing, at the same time, adequate radiation shielding performance. In this regard, the Shut-Down Dose Rate (SDDR) inside the Upper and Equatorial Port interspaces inside the ITER bio-shield is the crucial nuclear response which needs to be minimised.

Introduction

This year we have concentrated our efforts on the improvement and optimization of the design solutions for two types of Diagnostics Port Plugs as the major ITER Diagnostics Components. Radiation shielding of the ITER diagnostics ports should provide the possibility for personnel access for the port maintenance inside the interspace between the ITER bioshield and the Equatorial and Upper Port Plugs (EPP and UPP) shown in Figure 1. The port plugs are large structures which play the dual and conflicting roles of providing access for the diagnostic systems while ensuring that the vacuum vessel ports are adequately “plugged” against the leakage of neutron and gamma radiation and are vacuum leak tight. Shielding performance of the plugs should be effective not only against the neutron irradiation from the igniting D-T plasma and secondary gammas produced by neutron interaction with the ITER structures, but also against the decay gamma irradiation emitted from the radioactive materials of the ITER machine. Problem of materials activation caused the use of low-activated ITER grade materials. As the personnel access is planned in the port interspaces at 10^6 s (around 12 days) after shut-down with a limiting target value of 100 μSv/h, at that cooling time the Shut-Down Dose Rate (SDDR) calculations and activation analyses were performed using the state-of-the-art methodology. Neutronics parametric analysis has been performed by varying its geometrical configuration and material composition following the ALARA (As Low as Reasonably Achievable) principle taking into account the feasibility to implement the shielding options with the actual hardware.

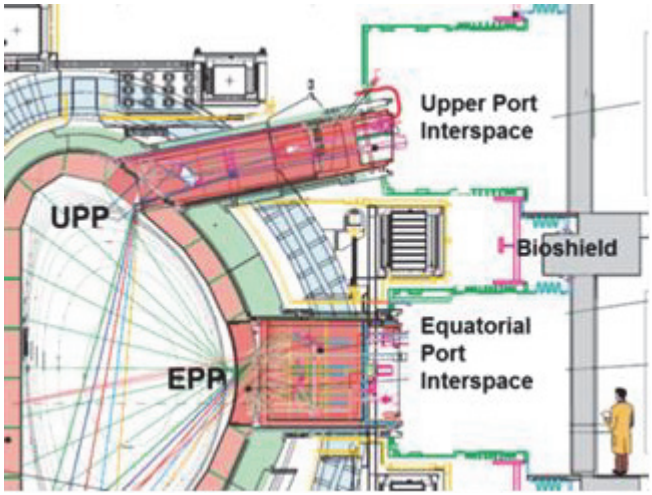

Fig. 1: Schematic view for the ITER Diagnostic Equatorial and Upper Port Plugs (EPP and UPP) and port interspaces for personnel access.

Methodological approach

This type of neutronic analysis is based on the long-term experience gained in the fusion neutronics group at KIT, with well-established methodological approach for solving the task of Shut-Down Dose Rate (SDDR) calculations in large tokamaks such as ITER or DEMO. The distinctive feature of SDDR calculations in ITER is the need to take into account gamma transport from decay gamma sources spatially distributed over the activated components of the ITER reactor with complicated toroidal geometry. Therefore we have solved two challenging methodological tasks: 1) modeling of the complex toroidal geometry; 2) radiation transport in large system such as ITER. The most suitable method of radiation transport in

complex geometries is Monte Carlo method, practically implemented in the MCNP5 code [1]. The problem of large size of ITER (30 m of height and diameter) is related with very strong attenuation of neutron and gamma fluxes and correspondingly, all flux-dependent nuclear responses. The attenuation factor for the total neutron flux was encountered ~8 orders of magnitude along the 6 m distance from the ITER plasma source to the bio-shield shown in Figure 1 of ITER scheme and in Figure 2 of the MCNP model. Following the principle of the Monte Carlo method of particle transport, for every 1e8 sampled source particles only one particle could reach bio-shield. And as the particle detector is located at the bio-shield, the number of detecting particles is very low, leading to high statistical errors in estimation of the fluxes and nuclear responses. To overcome this problem of high errors we have applied variance reduction techniques available in the Monte Carlo code MCNP5 with the purpose to preserve number of scoring events in the detecting region. Also to increase the number of sampled source particles with the MCNP5 code, we have used extreme computation power of the high performance supercomputers such as HPC-FF system at FZJ, Juelich [2] and Helios at CSC-IFERC in Rokkasho, Japan [3].

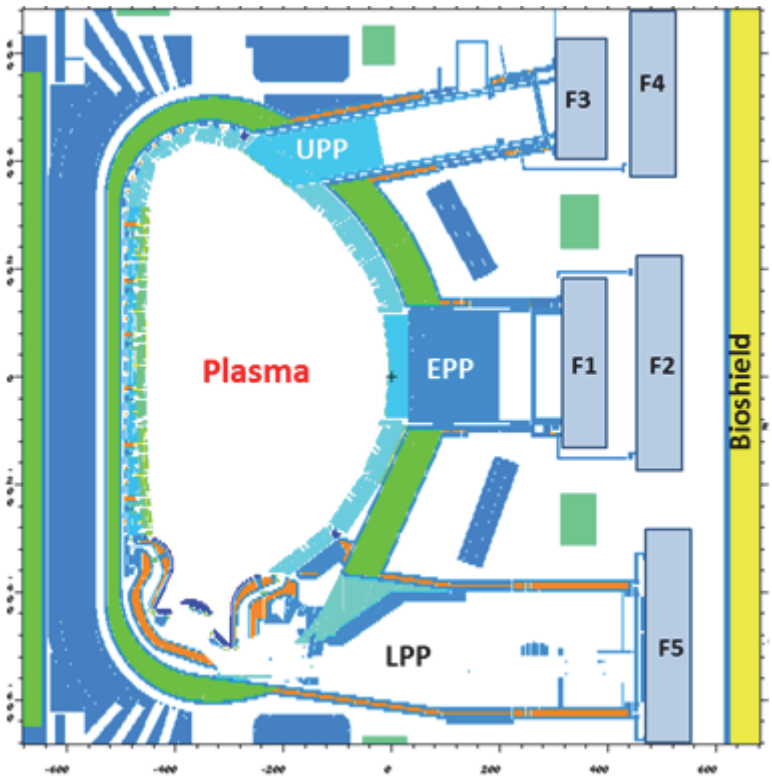

Fig. 2: Vertical cut of the MCNP global B-lite model of ITER with its three ports and five control volumes F1-F5 – so called “interspaces” inside these ports: Upper, Equatorial, and Lower (UPP, EPP, LPP) used for the Shut-Down Dose Rate (SDDR) calculations.

For this SDDR analysis, the R2Smesh interface system [4] has been applied, which couples the MCNP5 transport and FISPACT-2007 [5] activation calculations through the common use of mesh-tally distributions. In the R2Smesh scheme, the results of neutron fluxes, generated decay photon sources and the final results of shutdown dose rates are calculated on a 3D mesh, which can have a high spatial resolution. In this contract the effect of mutual dependence of three ITER ports (upper, equatorial, and lower) was quantified by presenting separate SDDR contributions inside each of the port interspace. The radiation leakage from one port volume to another port volume is called as “radiation cross-talk”. The computational scheme was devised to quantify the radiation cross-talk effect between the interspace volumes F1-F5 pinpointed in Figure 2. This annual report presents a brief overview of the neutronics results for the two ports of ITER (equatorial and upper ports) used for the diagnostics purposes.

Neutronics results for Diagnostics Equatorial Port Plug (EPP)

It was found that in the homogenized approximation of the port plugs, the dominant contribution to the SDDR inside the port interspaces is coming from the radiation streaming through the gaps surrounding the plugs, especially for the Diagnostics Equatorial Port Plug (EPP). Therefore, the EPP design shielding solutions include a means to mitigate the gap streaming. To this end, the labyrinths of several configurations and horizontal rails inside the gaps were proposed. The labyrinth configurations are discussed in parametric neutronic analysis [2] in application to the EPP. The SDDR results are extensively analysed in [6-9]. As a major result of the EPP analysis [6], an optimized double labyrinth was recommended and has been accepted for the current EPP design shown in Figure 3.

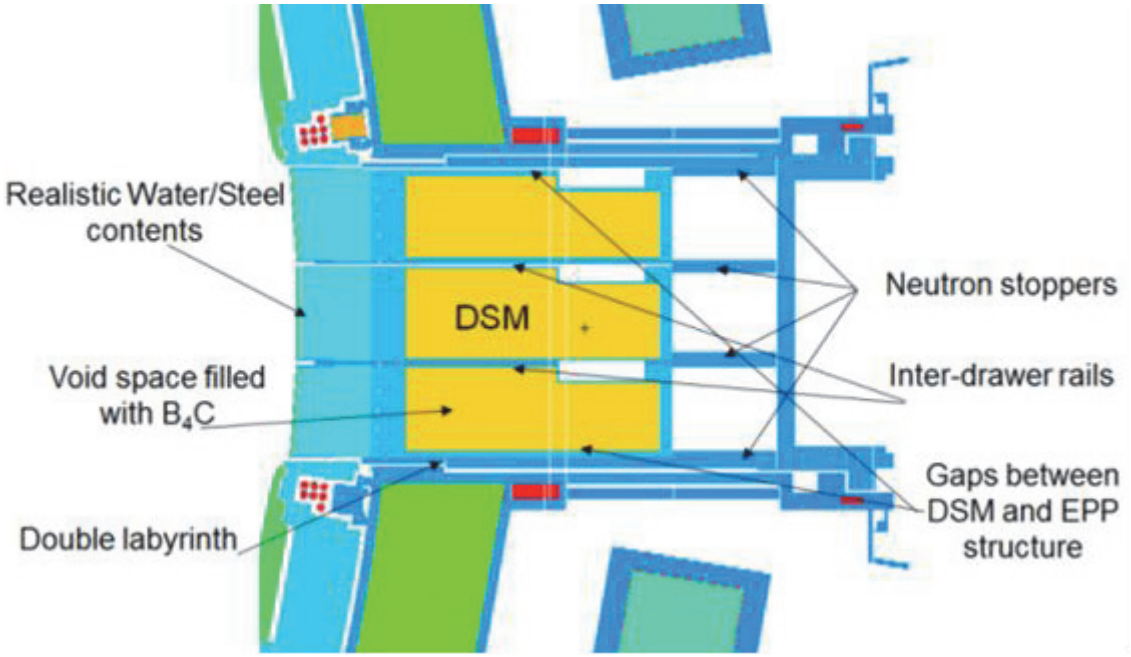

Fig. 3: Horizontal cut of the MCNP B-lite ITER model through the optimized Diagnostics EPP.

Neutronics analyses of the Diagnostic Upper Port Plug (UPP)

The SDDR for the interspace of the upper port have been evaluated in the control volume F3 shown in Figure 2, representing MCNP cell tallies (F3 cell). Case studies were done to figure out contribution from several design parameters such as gap, material, labyrinth, penetration through the adjacent gaps in the blanket and ELM/in-vessel coils, etc. A series of neutronics analyses were performed in support of the design development of the Generic Upper Port Plug (GUPP), the outcomes were presented at international conferences and published in peer-reviewed journals [6 - 9]. About the definitions of the objects of these analyses, the “Generic” port plug does not include any specific diagnostics system and the results obtained by its use are universal. The GUPP includes three major blocks shown in Figure 4: Diagnostics First Wall (DFW) panel, Diagnostics Shielding Module (DSM), and Generic UPP trapezoidal structure. We have considered two variants of homogenized steel-water composition of DSM: V1 (80% steel, 20% water) and V2 (90% steel, 10% water) The GUPP results include distributions of neutronics characteristics of radiation shielding the GUPP during the ITER operation on 500 MW of DT fusion power such as neutron and photon fluxes, nuclear heating, helium gas production, neutron damage, and activation parameters of the GUPP after the ITER operation, such as shut-down dose rate (SDDR) inside the GUPP interspace control volume F3 depicted in Figure 2. It is assumed to be accessible by the personnel for the post irradiation maintenance of the UPP Diagnostics systems. The strategy of radiation shielding development of the GUPP components followed the ALARA principle taking into account the feasibility to implement the shielding options with the actual hardware of the Diagnostics Upper Port to maintain the minimum SDDR. In relation to SDDR, five different op-

tions of the GUPP shielding design were investigated, and finally, three diagnostics systems (Vacuum Ultra-Violet spectrometer - VUV, Vertical Neutron Camera -VNC, and Neutron Activation System - NAS) have been integrated into the UPP#18 with the optimal shielding performance. The effect of these three diagnostics on the value of SDDR was estimated in work [6], its results indicated that the SDDR at 106 s after the ITER SA2 irradiation scenario increased on 9 μSv/h due to the diagnostics apertures of UPP#18.

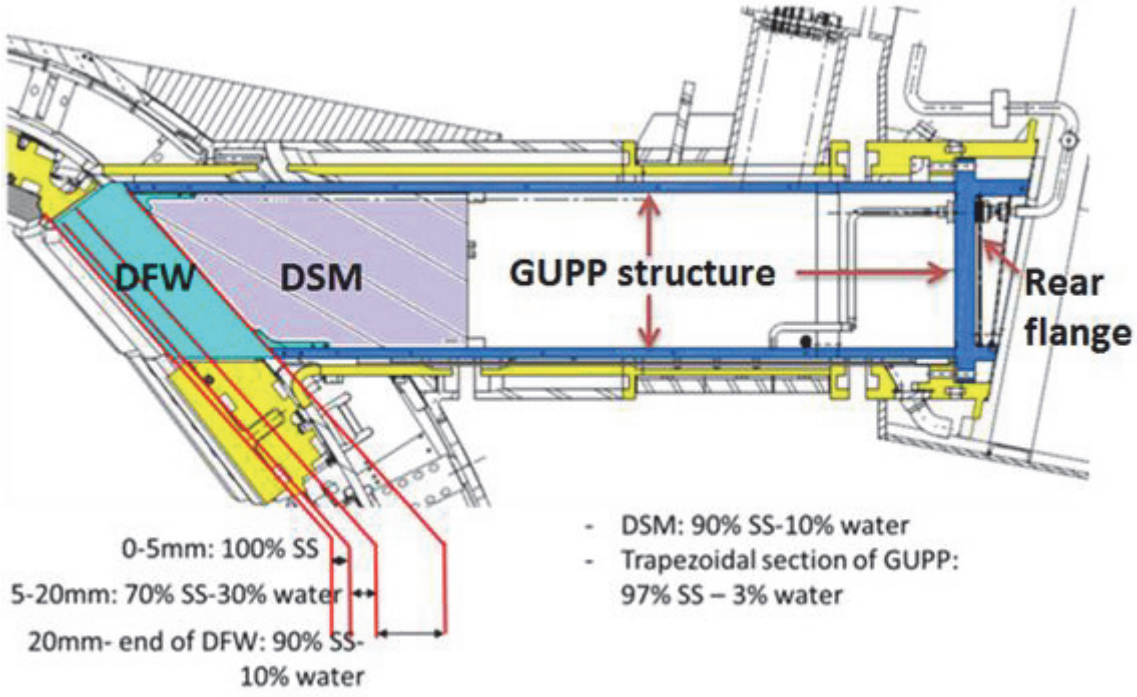

Fig. 4: Material and geometrical definitions of the Variant V2 of the GUPP with mixture of 90% steel and 10% water as constituent material of its DSM.

Based on the outcomes of this year works [6-9], in general we can conclude that the environmental features of UPP contribute 53 μSv/h, the UPP structure itself deposits only 19 μSv/h. Therefore, SDDR depends mainly on the environment, not on the UPP structure itself. By using feasible shielding improvements it is possible to reduce SDDR from 95 μSv/h (current UPP design) to 48 μSv/h (desired design of UPP and adjacent environment).

The following shielding improvements are proposed to decrease the baseline SDDR in the UPP interspace:

- Keeping nominal 25 mm gaps on the top and bottom sides of UPP, increased gap up to 45 mm gap results in surplus of 13 μSv/h in SDDR to the baseline value;
- A single labyrinth between DFW and blanket module #11 underneath the UPP results in decrease of SDDR on 20 μSv/h inside the UPP interspace;
- Shielding between the UPP and the VV port causes decrease of SDDR on 8 μSv/h inside the UPP interspace;
- Limit on Co and Ta contents in the Inconel-718 material or change it to SS660 of the bolts in the back flange causes decrease of SDDR on 19 μSv/h inside the UPP interspace.

Staff:

A. Serikov
U. Fischer

Literature:

[1] X-5 Monte Carlo Team, “MCNP—A general Monte Carlo N-particle Transport Code, Version 5, Vol. I: Overview and Theory,” LA-UR-03-1987, Los Alamos Nat. Lab. (2003).

[2] HPC-FF system at FZJ, Juelich: http://www.fz-juelich.de/ias/jsc/EN/Expertise/Supercomputers/JUROPA/JUROPA_node.html.

[3] Helios supercomputer at Computational Simulation Centre (CSC) of the International Fusion Energy Research Centre (IFERC): http://www.iferc.org

[4] M. Majerle, D. Leichtle, U. Fischer, A. Serikov, “Verification and validation of the R2Smesh approach for the calculation of high resolution shutdown dose rate distributions,” Fusion Engineering and Design 87, 443-447 (2012).

[5] R. A. Forrest et al., “FISPACT 2007 user manual,” UKAEA FUS 534 report, March 2007.

[6] A. Serikov, U. Fischer, C. S. Pitcher, A. Suarez, B. Weinhorst, “Computational Challenges of Fusion Neutronics for ITER Ports,” Proceedings of Joint Int. Conference on Supercomputing in Nuclear Application and Monte Carlo (SNA+MC 2013), Paris, France, Oct. 27-31, 2013.

[7] A. Serikov, U. Fischer, M. Henderson, D. Leichtle, C.S. Pitcher, P. Spaeh, “Neutronics for equatorial and upper ports in ITER,” Fusion Engineering and Design, 88 (2013) 1965–1968, http://dx.doi.org/10.1016/j.fusengdes.2013.03.037.

[8] A. Serikov, L. Bertalot, U. Fischer, S. Pak, A. Suarez, R. Villari, “Neutronic Challenges for the Estimation of Shut-Down Dose Rates in ITER Ports,” Transactions of the American Nuclear Society, 109 (2013) 1163-1166.

[9] A. Serikov, L. Bertalot, U. Fischer, C.S. Pitcher, A. Suarez, V.S. Udintsev, B. Weinhorst, “Shut-Down Dose Rate Analysis for the ITER Diagnostic Equatorial and Upper Ports,” 11th Int. Symposium on Fusion Nuclear Technology (ISFNT-11), Barcelona, Sept. 16-20, 2013, accepted in Fusion Engineering and Design, http://dx.doi.org/10.1016/j.fusengdes.2014.01.025.

Acknowledgment

This work has been funded by the ITER Organization under the ITER service contracts Nr. IO/12/4300000548 and Nr. IO/4300000896 using an adaptation of the B-lite MCNP models which were developed as a collaborative effort between the FDS team of ASIPP China, University of Wisconsin-Madison, ENEA Frascati, CCFE UK, JAEA Naka, and the ITER Organization. The views and opinions expressed herein do not necessarily reflect those of the ITER Organization.

Nuclear Analysis at Neutral Beam Injector (NBI) Ports (ITER/CT/12/4300000687)

Overall objective

The purpose of this work was to check whether the performance of the shielding of the NBI ports is adequate to meet the ITER safety requirements. To this end, a suitable MCNP model of the ITER NBI port needed to be developed and analysed. The nuclear heating and nuclear damage in the VV, the total dose to the TFC magnets and insulator as well as the shutdown dose rates in the space between the VV and the cryostat thus were to be calculated and compared with the design limits.

Task 1
Update the MCNP model of the ITER NBI sector out to the bio-shield, perform radiation transport calculations to determine the nuclear responses in the vacuum vessel, the NBI duct and the shielding inside the cryostat

Introduction

The ports for neutral beam injectors (NBI) have openings to the plasma chamber that leads to an intense irradiation of all attachments in this region. The vacuum vessel (VV) shell, vacuum vessel inter-wall shielding, the NBI ducts, NBI duct liners and the additional shield around NBI ports must reliably protect the toroidal field coil (TFC) magnets and the space between vacuum vessel and cryostat from intense neutron and gamma irradiation. The purpose of the present work was to check whether the performance of the shield in the NBI ports is adequate to meet the ITER safety requirements. The investigation must provide an updated MCNP geometry model extended up to a bio-shield making use of a new CAD design of the NBI ports. To this end new NBI ports detailed enough to enable a study of streaming effects between different details and shielding blocks must be included in an available 80^{o} MCNP model of an ITER sector. Using this updated model following nuclear responses must be provided: nuclear heating distribution in the vacuum vessel; nuclear heating in all NBI ducts; nuclear heating, neutron flux and total dose to insulator and TFC magnets; nuclear damage distribution (He-production and dpa) in the VV; biological shutdown dose rate outside ducts and inside cryostat.

Simplified model of the NBI ports

The simplification of the original CAD models is a prerequisite procedure necessary for their use in the MCNP particle transport calculations. The small details available in the CAD engineering models are usually not essential for Monte Carlo particle transport simulations if the mean free path of the particles is much bigger than the size of the fine details. Additionally a too detailed geometry model leads to 1) the significant expansion of the computer code virtual memory up to physical limits and 2) redundant complexity of the geometry model and, as a result, increasing of the computational time. In a practice the small details such as chamfers, bolts etc. are homogenized keeping the proper material fraction in a final homogenized material composition. From other side the level of the details retained in the model must be sufficient to resolve, for instance, localized nuclear heating. It means that channels potentially important for a particle streaming must be kept in the model and other small details should be homogenized. Shown in Fig.1 are the results of the simplifications done on the CATIA platform for CAD duct liner model. The cooling pipes were removed from the model because they are not important for neutron streaming compared to the interior duct liner channel.

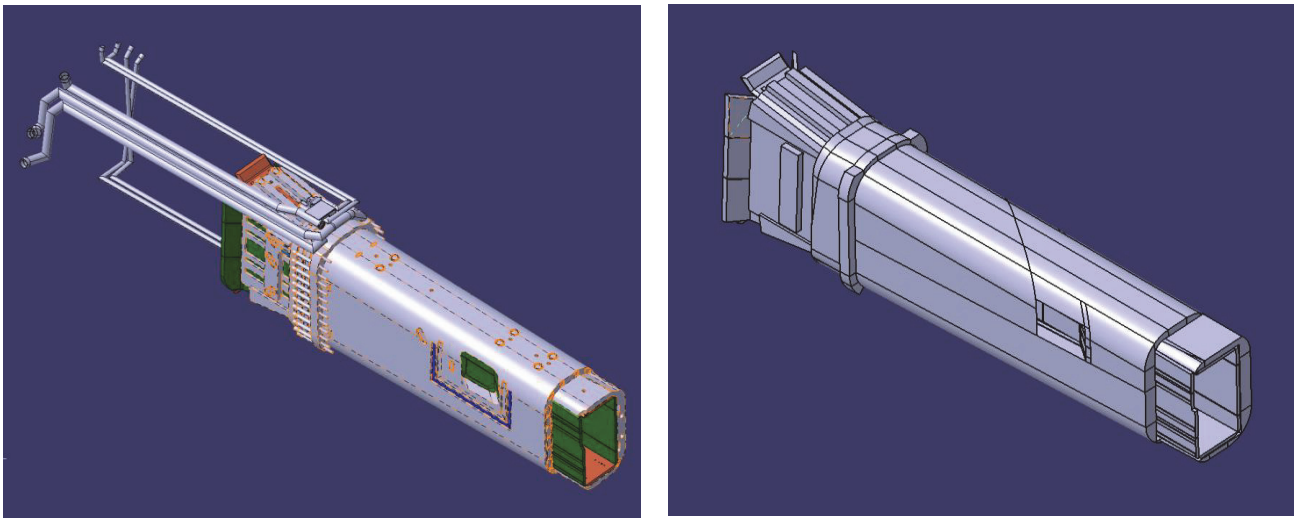

Fig. 1: Simplification of the Duct liner: original CAD model (left) and simplified CAD model (right).

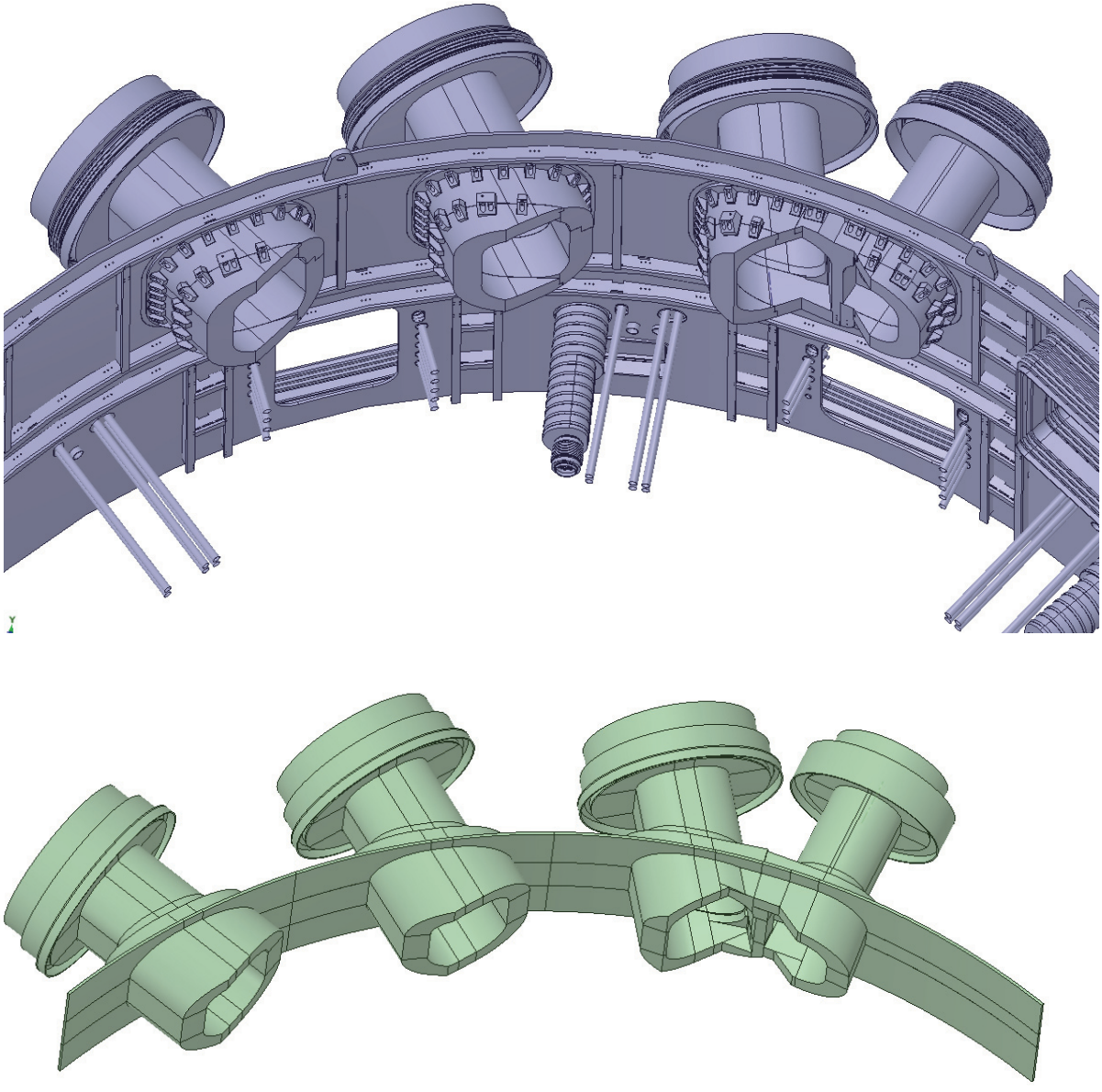

Fig. 2: Original (top) and simplified (bottom) CAD models for cryostat and attached shield.

The CAD models produced by CATIA can in general have small geometry errors such as intersections of details appearing in the complex models. Such errors, which are very difficult to detect using CATIA platform, result in fatal errors in MCNP geometry models. These problems can be quickly corrected using SpaceClaim software.

Shown in Fig. 2 are the results of engineering CAD model simplifications using SpaceClaim. The original model for cryostat with attached NBI shell and shield were simplified to be included in the CAD model of the new NBI ports. Small details were removed because they are not important for particle transport simulations.

CAD to MCNP model conversion

The approach applied in this work is based on a close agreement of the engineering design of the NBI ports and the model used in the neutronic calculations. The main element in this approach is the McCad [1] code for the automated generation of the geometry model from CAD data for use in the subsequent neutronics calculations.

The CAD model for NBI ports, even after simplification, is very big and complicated for the processing with McCad. Therefore the whole CAD model was divided into 3 parts: 1) part in the vacuum vessel, 2) between vacuum vessel and bio-shield and 3) inside and outside of the bio-shield. The boundaries of each part are shown in Fig. 3. Presented in Fig. 4 is the final simplified CAD model of the NBI ports that was used for the CAD to MCNP model conversion with McCad tool.

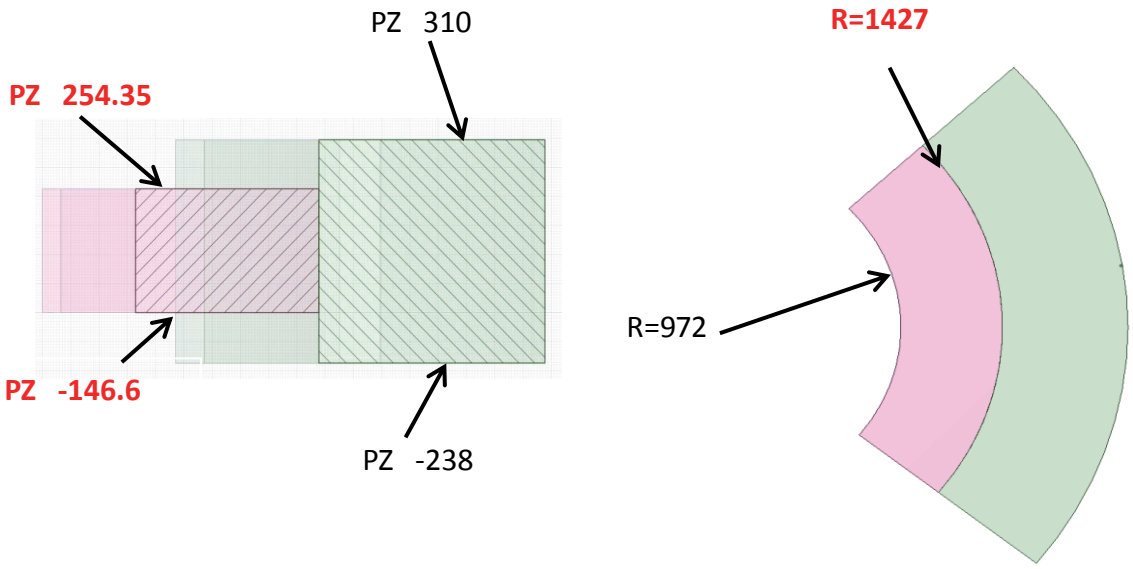

Fig. 3: Definition of the geometry layer for updating.

Before conversion of each composed part of NBI ports the separate conversions for each assembled NBI port was performed with McCad to check the geometry. If the output MCNP file has geometry errors (intersections, unclosed bodies, etc.) additional fine corrections are applied to the simplified CAD model. In some places McCad was not able to decompose complex geometry parts. In such cases the problematic geometry parts were decomposed manually using SpaceClaim software to enable further processing with McCad. Prepared in this way separate small MCNP input files were additionally checked invoking MCNP stochastic cells volume calculations. If MCNP results show lost particles, the position of the geometry error is examined and the CAD geometry is corrected accordingly. By finishing these additional tests each composed geometry part of 3 NBI ports was processed with McCad. The McCad geometry model conversion performed demonstrate a very high performance of the algorithm implemented in this software. The number of material cell for such complex construction as a duct liner is quite low and the number of void cells appeared to be very low.

The same separate MCNP voided geometry models were generated also for the parts 1 and 3.

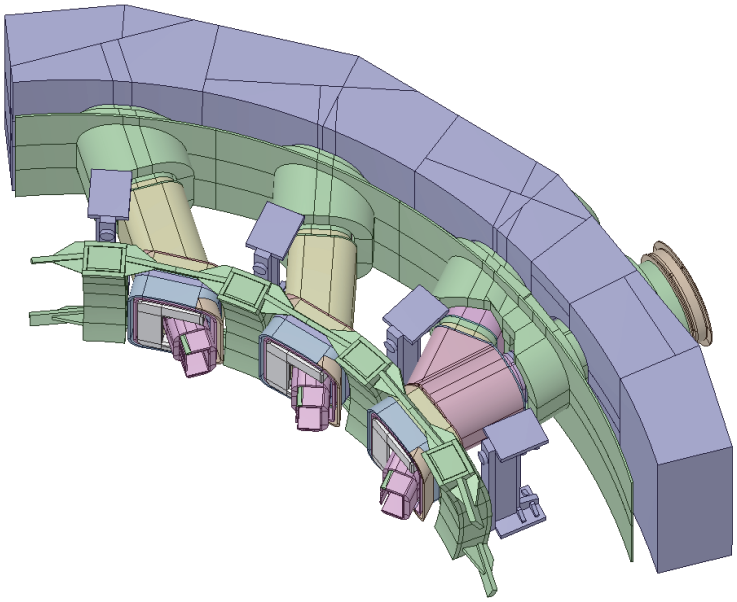

Fig. 4: Entire vertical segment (MCNP model) including the NBI ports and all components from the vacuum vessel port down to the bio shield for integration into the 80° ITER A-lite model.

Generation of the MCNP model for the nuclear analysis

MCNP geometry model for the nuclear analysis of the NBI ports is based on the already available 80° MCNP ITER A-lite model, Fig. 5 (left). It was decided to modify this MCNP model to include the new model of the NBI ports. To this end all geometry cells (NBI ports, magnets, cryostat, void cells, etc.) that are found within the specified above parts 1-3 were removed from the input file. Those cells, that have cuts at the boundaries specified for parts 1-3, were modified respectively using newly introduced boundary surfaces. This assumes a huge number of manual modifications applied. At the end about 2800 geometry cells were deleted from the model and ~600 cells were manually corrected.

The cleaned MCNP A-lite model was then used for an integration of the newly produced MCNP NBI model. In the first step the voided MCNP model was developed for the testing of the adopted approach. To this end 3 voided MCNP models for each part were put together and arranged in the MCNP A-lite model as it shown in Fig. 5 (right).

Table 1: Number of the geometry cells in the new NBI ports MCNP model.

Part of the MCNP model	Material cells	Void cells	Total
Part 1	150	40	190
Part 2	2336	600	2936
Part 3	566	182	748
Total	3052	822	3874

Based on these material compositions the homogenized material mixtures given in Table 1 were prepared and final MCNP material descriptions using FENDL-2.1 [2] library were produced for material assignment in the NBI ports region of the MCNP model. The material assignment (MCNP material number and atomic density) was performed automatically during the McCad conversion process. The cut of the final MCNP model for NBI ports are shown in Fig. 6. After the McCad conversion 3874 new geometry cells, Table 1, for NBI ports were integrated in the ITER A-lite model. In spite of the model complexity the number of the void cells produced appeared to be quite small (822), that makes the new model very compact and logically consequent.

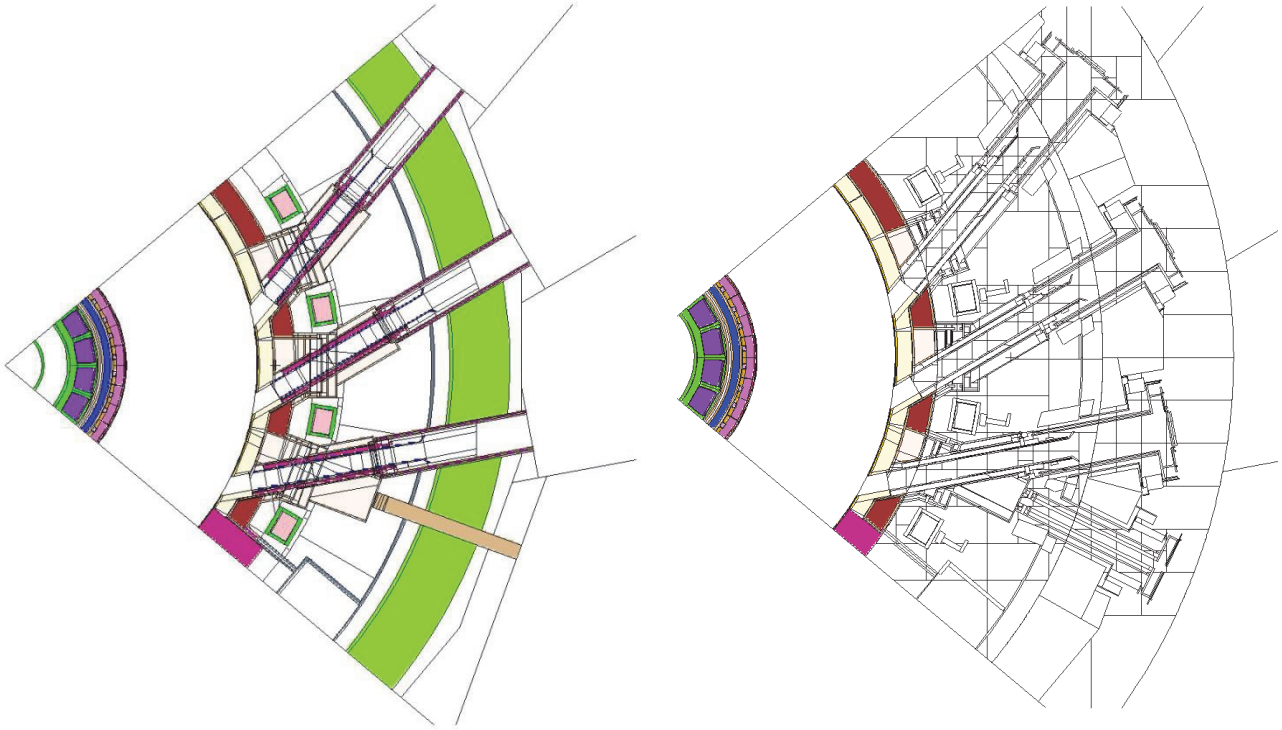

Fig. 5: The old MCNP NBI ports model (left) and the new voided model (right).

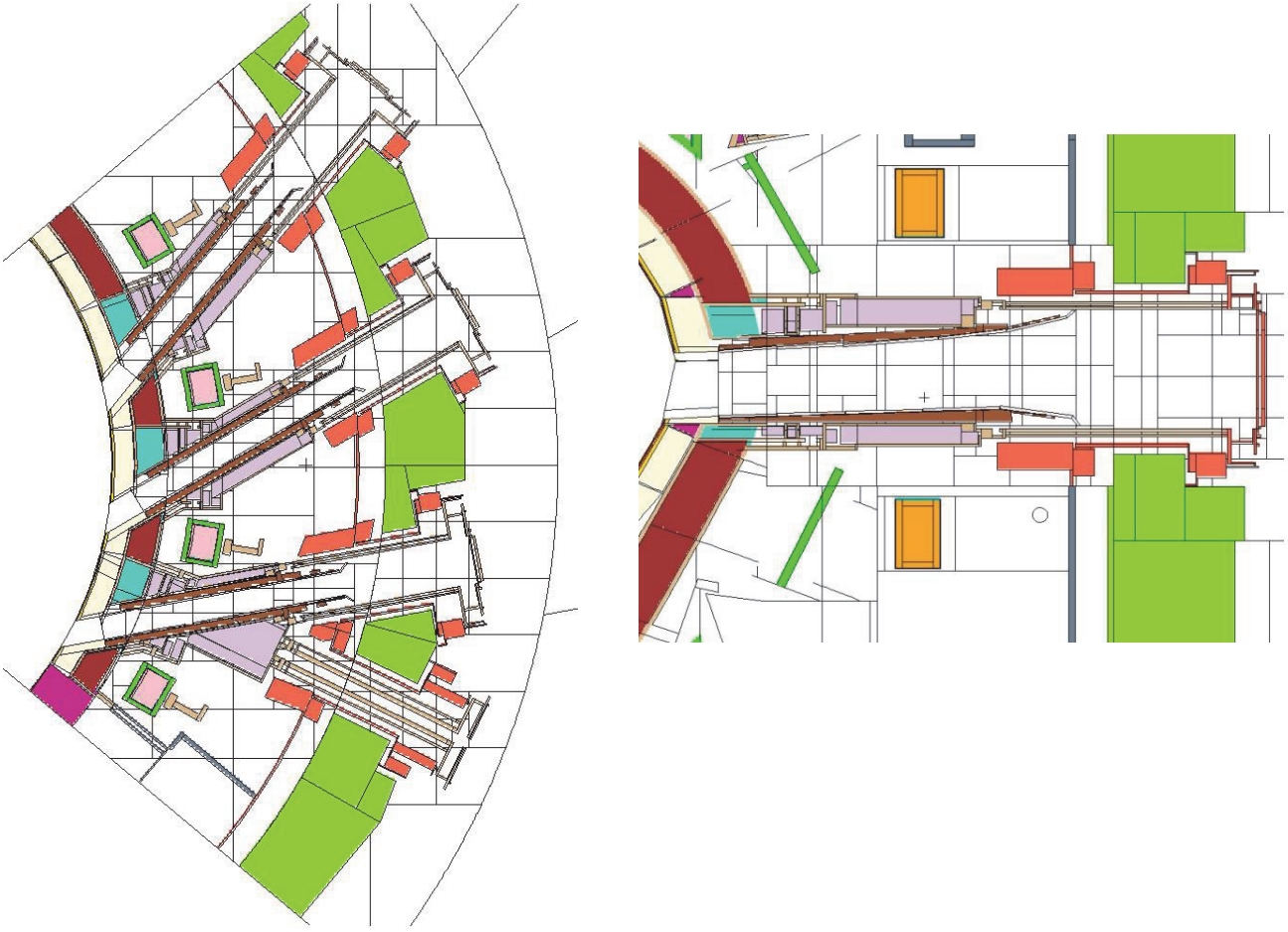

Fig. 6: Horizontal (left) and vertical (right) cuts of the MCNP NBI ports model.

Nuclear analysis

The calculations are being carried out making use of the geometry model discussed above and the MCNP5-1.6 [3] code with nuclear data from the FENDL-2.1 library. The neutron transport calculation in the space outside vacuum vessel (NBI ports region) is a heavy duty task for MCNP5 code. Due to a presence of steel-water blankets and vacuum vessel (~135 cm in total) the neutron flow to the space outside vacuum vessel is well shielded. To get accurate statistical results for requested nuclear responses in the NBI ports region is a challenge for the MCNP computer code based on a Monte Carlo technique. To reduce a statistical error of the MCNP results a variance reduction technique was applied.

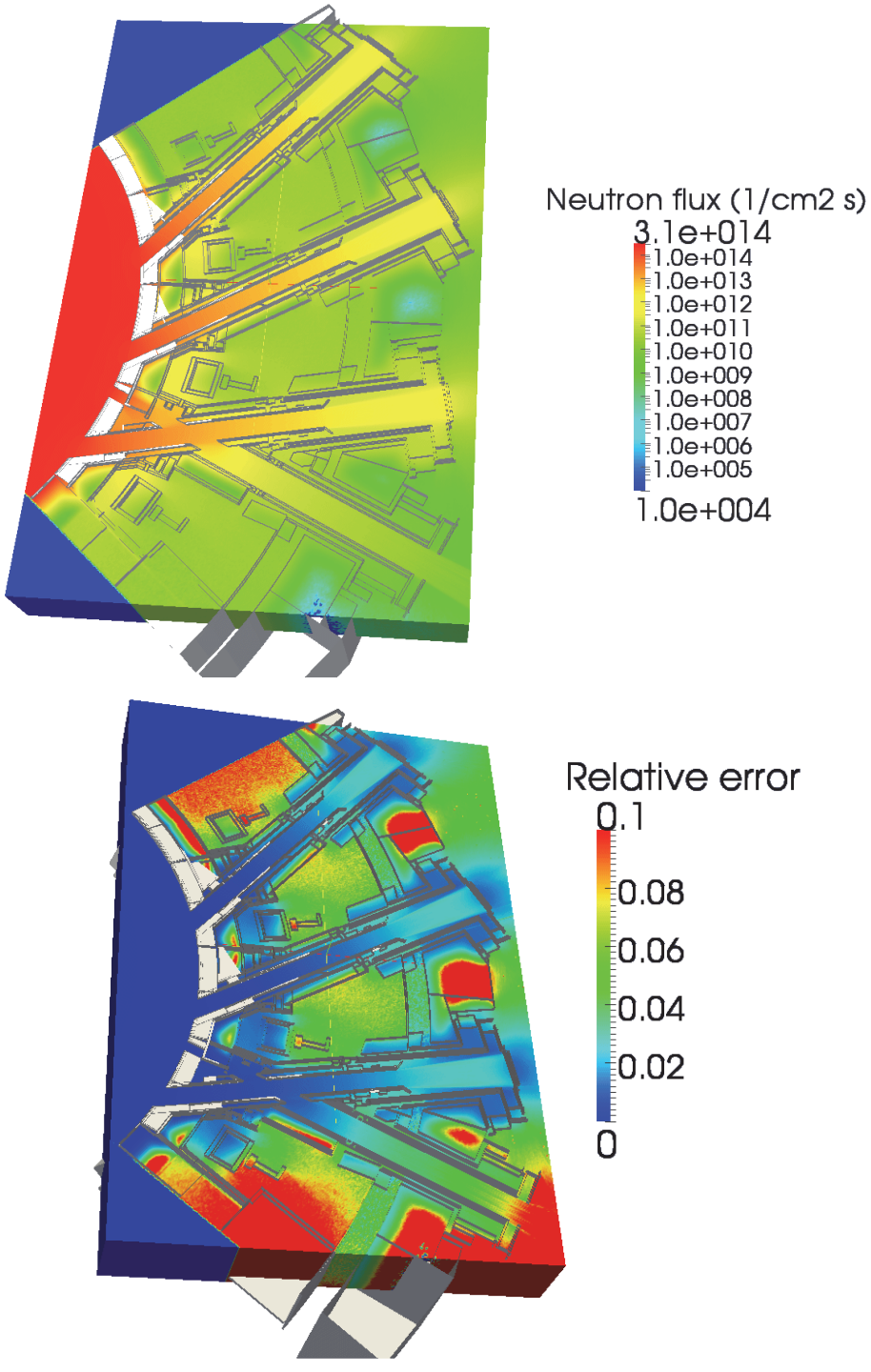

Fig. 7: Distribution of the neutron flux over the NBI ports region (top) and the corresponding statistical errors (bottom).

Preliminary estimates of the spatial neutron flux distribution and corresponding statistical errors over the NBI ports region is shown in Fig. 7. The results were obtained using superimposed mesh tally with the mesh size of 3x3x3 cm. Such mesh size is fine enough to get the neutron flux distribution with the high resolution. Because the NBI ports have openings directly to plasma the dominant neutron streaming appears to be along the axis of the NBI ports. The TFC magnets are subjected to the neutron irradiation with the flux of about 10^{12} n/cm^{2}s. These neutrons come mainly through the attachment of the NBI ports to the vacuum vessel. The neutron leakage from the NBI ports walls is less compared to the streaming through the NBI ports attachments. In the vacuum vessel the regions close to the blankets and NBI ports walls are subjected to the significant irradiation that can result in high nuclear responses at these positions.

For the calculations of the nuclear heating in the vacuum vessel the rectangular mesh superimposed over the geometry was used to get these nuclear responses. The mesh size was chosen to be 3x3x3 cm. This mesh size is comparable with an average neutron free path in the vacuum vessel. The nuclear power density in the vacuum vessel has maximum values in the wall faced to the plasma with the peaking value about 0.2 W/cm^3 and in the region close to the NBI ports walls with the peaking value about 1 W/cm^3, Fig. 8. The power density distribution shows a rise also in the region close to the NBI port attachment. The statistical errors do not exceed 10% for the peaking nuclear heating values, Fig. 8.

The calculations for nuclear damage responses (DPA and He-production) were calculated for the SS316L(N)-IG steel as a main component of the vacuum vessel mixture. For both cases one full reactor power year (FPY), 365 days, was taken for responses normalization. The He-production rate was calculated using full He-production cross sections MT=207 and MT=206 although the impact of the latter data is negligible for neutron energies below 14 MeV. The DPA cross section data for SS316L(N)-IG stainless steel are based on the NRT standard and they were prepared using FENDL-2.1 nuclear data library. The specially developed for this purpose data file in ACE format, suitable for direct MCNP tally multiplication, was included in MCNP data library. Both responses were calculated using superimposed mesh tally. The mesh size of 3x3x3 cm was chosen for neutron tally. The results for DPA damage production are shown in Fig. 9 (top). Because the FM card was applied for the whole tally mesh using the SS316L(N)-IG material card this approach does not distinguish the cells with vacuum and material inside. To make the results more suitable for classification the ITER geometry is presented as well. The results obtained show that the maximum DPA accumulation takes place in the shell of the vacuum vessel and the region closing to the NBI duct liner. The damage production for 1 FPY appeared to not exceed 0.1-0.2 DPA/year. The most loaded is the region between NBI ports.

Shown in Fig. 9 (bottom) are the results for He-production in the vacuum vessel. The same as for the DPA calculation the data were obtained using tally multiplication card FM using material card specification and MT number. Hence, the tally results for the whole mesh were converted into the He-production responses assuming that the whole mesh is filled with SS316L(N)-IG steel. The most loaded regions are the parts of the vacuum vessel close to NBI duct liner. Here the He-production can reach up to 1.0-2.0 appm/year.

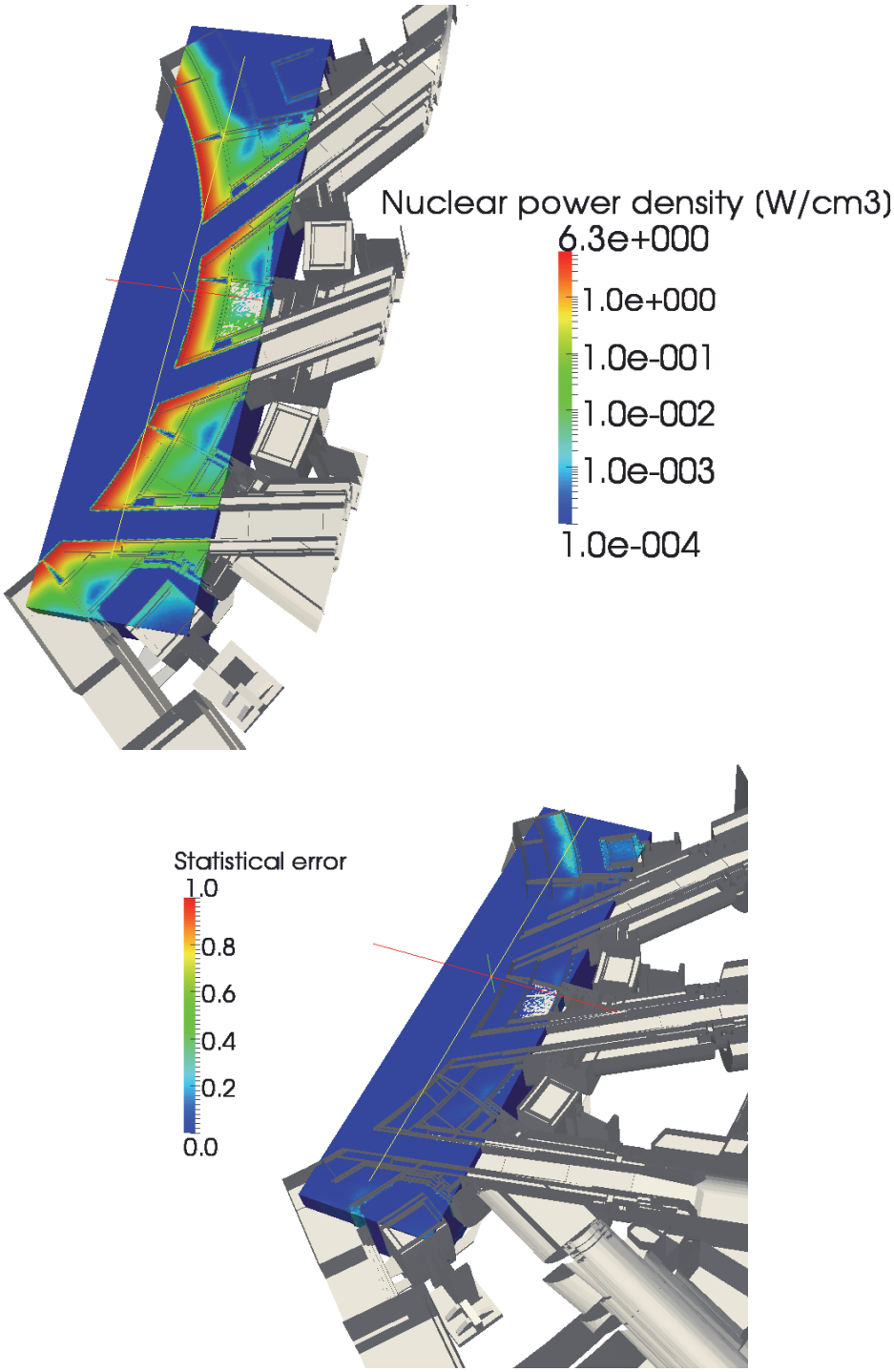

Fig. 8: Nuclear power density (top) and corresponding statistical errors (bottom) distribution in the vacuum vessel.

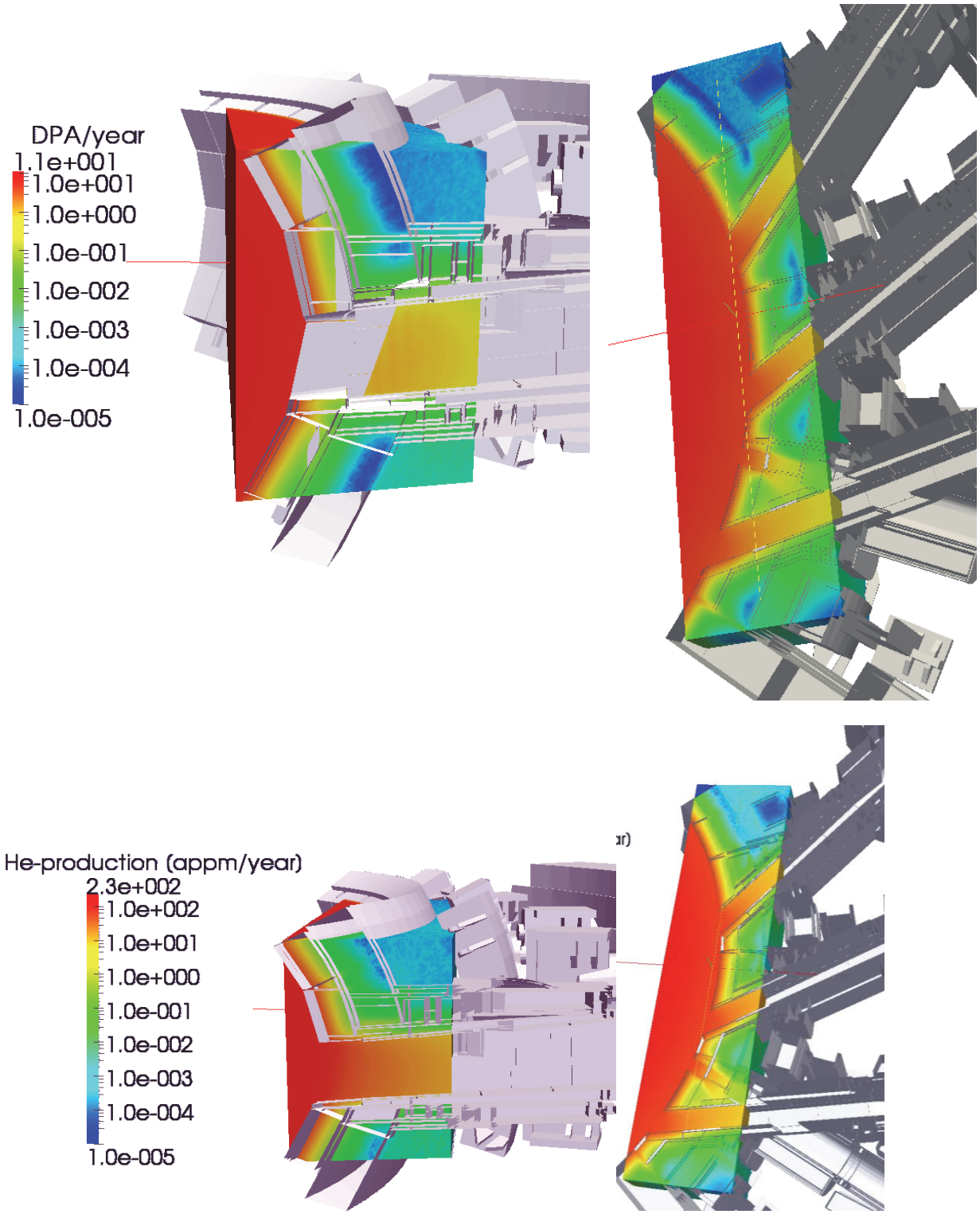

Fig. 9: Nuclear damage distribution in the vacuum vessel: DPA (top) and He-production (bottom).

The nuclear heating in all ducts were calculated invoking together neutron and photon transport simulations using superimposed mesh tally with the mesh size of 3x3x3 cm. Because for mesh tally only F4 tally (flux averaged over cell) is allowed two mesh results were obtained separately for neutron and photon responses. The both meshes were then processed and added together resulting in a total nuclear heating in all mesh cells. This approach enables to distinguish the mesh cells with and without materials that gives clear picture of the nuclear heating distribution over the NBI ports. Shown in the Fig. 10 are the results for the nuclear heating distribution in all ducts. The statistical errors do not exceed 12%

for the NBI ducts. The maximum nuclear power density was found in the walls of the NBI ducts close to ITER blankets. Here the power density can exceed 1 W/cm^3. The power density in the parts of the duct liner decreases with the distance from the blankets first walls and becomes about 10^{-3} W/cm^3 in the rear parts.

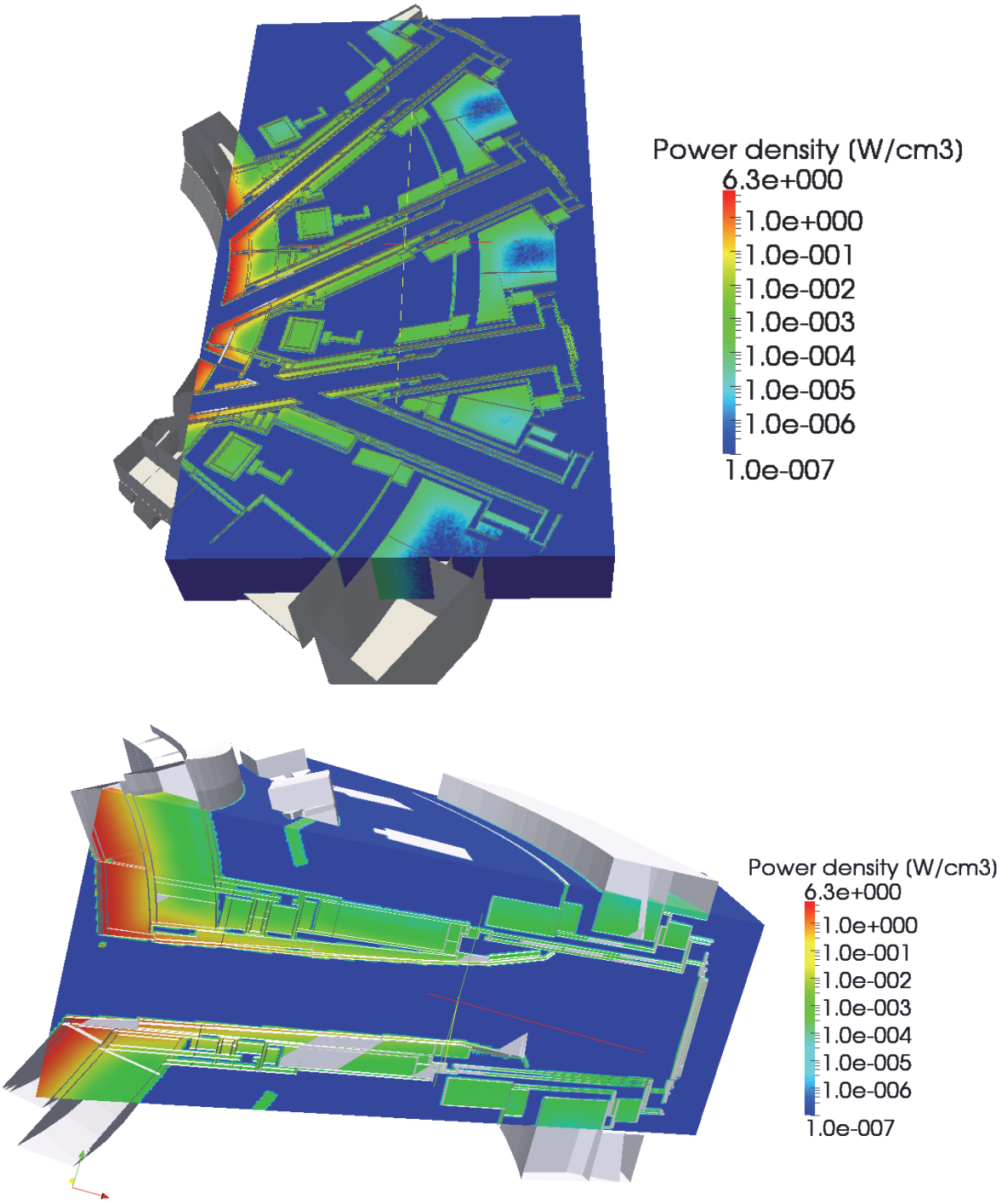

Fig. 10: Nuclear heating (W/cm3) in all ducts. Top is a horizontal cut and the bottom is a vertical cut through the NBI ports geometry.

The biological shutdown dose rates distributions in the NBI ports region can be determined by means of decay photon transport calculations making use of a time dependent decay gamma source. This can be realized within rigorous two step method (R2S). This approach includes as a first step a particle transport calculations to assess a 3D distribution of the neutron flux. The neutron spectra obtained on the first step and mapped over the NBI ports geometry are then used in the inventory activation calculations. This enables to quantify the

generation of the radioactive nuclides in different materials according to the chosen irradiation scenario. The calculated decay gamma spectra are used for the formation of the spatial decay gamma source that covers the whole geometry of the NBI ports. At the second step a transport calculation of the decay photons is performed to get the responses in all geometry cells and the biological dose rates respectively.

The neutron fluxes and corresponding neutron spectra obtained during the step 1 must be calculated with the high enough resolution. It is essential because flux attenuation can be significant due to the presence in the model of the steel and steel-water constructions. The current MCNP5 version enables calculations of the nuclear responses making use of the mesh superimposed over the geometry of interest. In this case the R2S method is applied for each cell of the spatial mesh used for the nuclear responses mapping. To facilitate this labor-intensive procedure an R2Smesh-2.1 was developed by KIT [4]. This interface actually takes care about proper preparation, execution and post processing of the huge amount of the activation calculations according to the mesh definition used on the first step.

The R2Smesh-2.1 interface is set of the computer codes aimed at the fast and efficient preparation of the final 3D decay gamma source. During the first step two neutron meshes with the same boundaries are tallied: so called fine mesh for neutron fluxes and coarse mesh for neutron spectra. Usually the size of the coarse mesh cell is a several times bigger compared to the fine mesh one. Therefore the neutron spectra can be resolved with high enough accuracy. It means that the same unit neutron spectrum is assigned for several fine mesh cells composing the same coarse mesh cell and the actual local neutron spectrum in the fine mesh cell is calculated as a product of the unit spectrum and the neutron flux intensity in it. This approximation increases the accuracy of the final results and decreases significantly the computer hardware requirements. The relation between the coarse and fine mesh cell size is a task dependent and usually does not exceed 3-5.

For the mesh based R2S method the sampling of all fine mesh cells is required to define the materials and their percentage in all these cells. Within R2Smesh-2.1 method this is done invoking the Monte Carlo sampling procedure. The highlight of the R2Smesh-2.1 interface is an inclusion of an additional subroutine performing this sampling in the MCNP5 executable. In fact the standard mesh output results include additionally detailed information about the fine mesh cell content. The activation calculations are performed using FISPACT [5] inventory code and EAF-2007 activation library [6]. The interface analyses all FISPACT results and prepares a collapsed decay gamma spectrum for each fine mesh using the material information obtained previously. In this way the 3D decay source is finally produced. This source is unique for each cooling step after the facility shutdown and it is intrinsically portable thanks to an inclusion automatically detected the fine mesh specification and the decay gamma spectrum for each cell. This source file contains information only for those cells having none zero decay photon intensity.

At the second step of the R2S mesh based approach a special source subroutine linked to MCNP5 samples uniformly over the fine mesh cells, containing decay photons, the Cartesian coordinates, energy and intensity of the emitted decay gamma quantum. The source subroutine is able to sample the decay gammas over the geometry of any complexity. In this approach the same input file, except problem and tally specifications, is used without changes at the 1st and 2nd steps for MCNP5 particle transport simulations.

For the fine mesh neutron flux calculations a mesh size of 3x3x3 cm was chosen. The statistical error of the neutron flux calculations for the cells having material content in the space outside vacuum vessel and inside cryostat is less than 2%. The coarse mesh cell size was chosen to be 15x15x15 cm. The neutron spectra are calculated using 175 VITAMIN-J group structure and the statistical uncertainty of the group spectra for the coarse mesh does not exceed 15%. The calculations were performed using 256 CPUs at the HELIOS supercomputer with $5 \cdot 10^9$ source particles. Such MCNP5 run takes usually about 20 hours of CPU time.

The FISPACT calculations were performed using R2Smesh-2.1 interface for all materials found in the coarse mesh cells. The specification of the materials involved in all FISPACT calculations is generated automatically by R2Smesh-2.1 interface. The interface reads all material cards used in the MCNP input file and prepares respectively the material compositions for activation calculations. If required the interface is able to pick up a very detailed material specification including fine impurities.

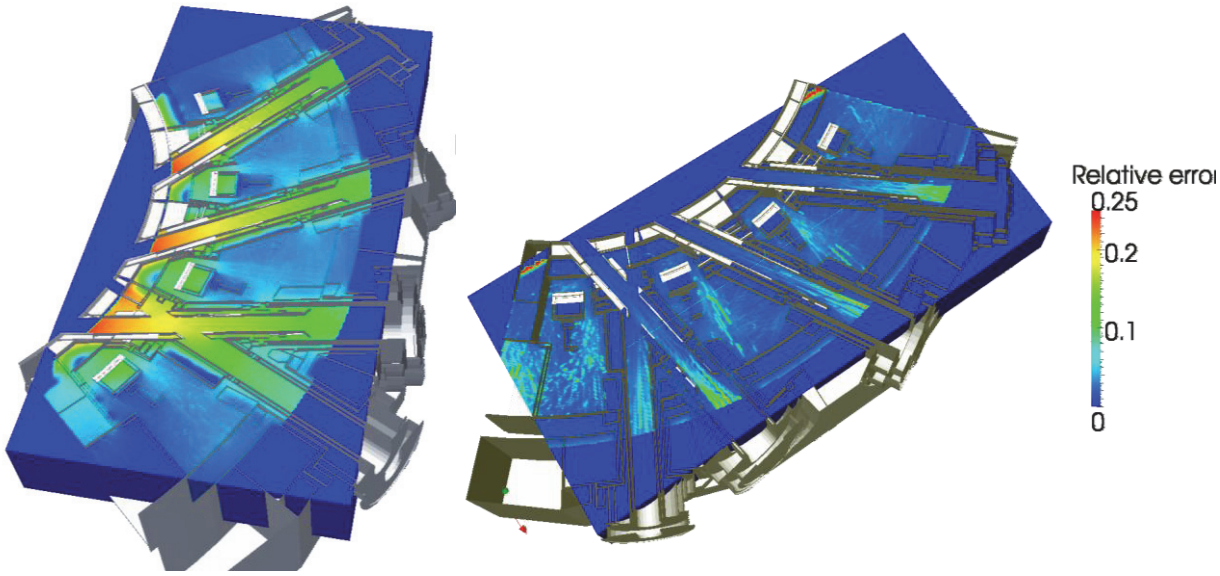

Fig. 11: Spatial dose rates distribution [Sv/h] around NBI ducts (left) and related statistical errors (right).

For the activation calculation a safety ITER irradiation scenario was assumed. A cooling time used for the analysis was agreed to be 10^6 seconds. It was found that the dominant nuclide for the dose rates is ^{60}Co that is produced mainly through ^{59}Co(n,γ)^{60}Co and ^{60}Ni(n,p)^{60}Co nuclear reactions.

As it is described above the decay gamma source for the space outside vacuum vessel and inside cryostat was prepared for the cooling time of 10^6s. This file contains information for ~8.5 million fine mesh cells that contain materials. The MCNP5 calculations were performed making use of the same input geometry file as it was used throughout all nuclear model calculations under this contract. The decay gamma transport simulations were done with the 10^{10} source particles. The superimposed mesh was used for the mapping of the dose rates in the space around NBI ducts. An example of the quality of results of the decay dose rates obtained are presented in Fig. 11(top) and the statistical errors for these results are shown in Fig. 11 (bottom).

Conclusions

The nuclear analysis in the NBI ports of ITER was performed making use of the consistent integral approach developed by KIT. This approach assumes generation of the geometry models for the nuclear analysis based on CAD designed models and their detailed automated conversion into the model suitable for the nuclear simulations. In this way the high quality, detailed geometry models satisfying quality assurance requirements are produced.

In this contract the engineering CAD geometry models of the NBI ports were first simplified on the basis of the CATIA platform to meet the requirements for the nuclear analysis. At this step the new material compositions for homogenized mixtures are calculated using CATIA intrinsic geometry functions. The simplified CAD models produced with the help of CATIA were then cleaned from small inconsistences found and some details were additionally segmented and simplified making use of SpaceClaim software. At the end the CAD models were converted into the STP format for further processing.

The geometry models of the NBI ports stored in STP format were divided into 3 geometry groups: 1) part of the model that must be arranged in the vacuum vessel, 2) the part that is integrated in the space between vacuum vessel and bio-shield and 3) the part in the bio-shield and outside it. This approach enables automated conversion of the CAD to MCNP geometry making use of the McCad conversion tool. The missing elements in the CAD NBI ports model such as TF coils were picked up from the available CAD ITER A-lite model and included in the STP files of the NBI ports. In this way 3 small separated MCNP geometry input files (including cell and geometry description parts) were generated. The material assignment was performed automatically with McCad interface.

The MCNP geometry ITER-NBI model is based on already available 80^o ITER A-lite model. To update this model the big horizontal layer was manually removed from the MCNP input file, the rest of the MCNP ITER A-lite model remaining unchanged. The cleaned MCNP model was carefully checked using several methods. The newly developed 3 MCNP models of the NBI ports for each geometry part were one by one integrated in the final MCNP NBI model. The material cards were developed using standard IO material specifications and included in the MCNP input file. This model was also checked using MCNP stochastic volume calculations.

The nuclear analysis was performed for several nuclear responses. The results obtained are based on the mesh tally superimposed over the geometry region of interest. The nuclear power density in the vacuum vessel has maximum values in the wall faced to the plasma and in the region close to the NBI ports walls. The peaking value exceeds 1 W/cm^3. The power density distribution shows a rise also in the region close to the NBI port attachment. The results obtained show that the maximum DPA accumulation takes place in the shell of the vacuum vessel and the region closing to the NBI duct liner. The damage production for 1 FPY appeared to not exceed 0.1-0.2 DPA/year. The most loaded is the region between NBI ports. The most loaded regions for He-production are the parts of the vacuum vessel close to NBI duct liner. Here the He-production can reach up to 1.0-2.0 appm/year.

The nuclear heating in all ducts was calculated using the mesh tally. The maximum nuclear power density was found in the walls of the NBI ducts close to ITER blankets. Here the power density can exceed 1 W/cm^3. The power density in the parts of the duct liner decreases with the distance from the blankets first walls and becomes about 10^{-3} W/cm^3 in the rear parts.

The nuclear loads in the insulator and magnet of the TF coils were calculated within the big layer including NBI ports. The TF coil between two NBI duct liners (2 and 3) was found to be the most loaded. Here the total dose to the insulator in the equatorial mid plane of the reactor exceeds 5 times the ITER limit (10^7 Gy) after 1 full power reactor year. The neutron flux in the magnet of the TF coil 3 has more than 65 % high energy neutron with the energy above 0.1 MeV. The total nuclear energy deposition in the magnet was calculated using the poloidal segmentation assumed in the MCNP A-lite model.

The activation and shutdown dose rates in the space between vacuum vessel and cryostat were calculated making use of the R2S method. The R2Smesh-2.1 interface developed by KIT was used for the calculations. This interface was developed to be user friendly and efficient in the calculations. The 3D decay gamma source produced is portable and can be used for further investigations

Staff:

U. Fischer
P. Pereslavtsev
Lei Lu
S. Vielhaber

Literature:

[1] L. Lu et al., Improved Algorithms and Advanced Features for the CAD to MC Conversion Tool McCad, Int. Symposium for Fusion Nuclear Technology, 16-20 September 2013, Barcelona, Spain

[2] D. L. Aldama, A.Trkov, FENDL-2.1: Update of an evaluated nuclear data library for fusion applications, Report INDC(NDS)-467, December 2004

[3] X-5 Monte Carlo Team, "MCNP—A general Monte Carlo N-particle Transport Code, Version 5, Los Alamos National Laboratory (Apr. 24, 2003).

[4] P. Pereslavtsev, U. Fischer, D. Leichtle, R. Villari, Novel approach for efficient mesh based Monte Carlo shutdown dose rate calculations, Fus. Eng. Design, Vol. 88, Iss. 9-10 (2013) 2719

[5] R. A. Forrest et al., "FISPACT 2007 user manual," UKAEA FUS 534 report (March 2007).

[6] R. A. Forrest, J. Kopecky, J-C. Sublet, The European Activation File: EAF-2007 Neutron-induced Cross Section Library, UKAEA FUS 535 report (2007).

Acknowledgement

This work was supported by ITER Organization under the service contract No. IT-ER/IO/12/4300000687. The views and opinions expressed herein reflect only the author's views. The ITER Organization is not liable for any use that may be made of the information contained therein.

Nuclear Analyses for Contact Dose on Transfer Cask and Dose outside Tokamak Building/Hot Cell Tunnel (ITER/CT/13/4300000763)

Objective

The objective of this work was to provide a reliable assessment of the biological dose rate fields around an automated ITER transfer cask loaded with activated in-vessel components. The dose rate maps were to be provided for an isolated transfer cask as well as for the transfer of a cask in the tunnel connecting the tokamak building and the hot cell building. These assessments were requested by the French nuclear safety authority.

Introduction

As part of the licensing process for ITER, the French nuclear safety authority requires to quantify the maximum biological dose rate around a transfer cask which is loaded with activated components that were removed from the ITER reactor. The knowledge of the dose rate levels will allow the authority to specify limits for the time period the work personnel is allowed to stay in the vicinity of a cask. To this end, it is required to provide a reliable assessment of the dose rate map around the transfer cask assuming it is loaded with different components that were irradiated in ITER.

Computational Approach

The R2Smesh (“Rigorous 2-step”) approach, developed by KIT for the determination of shutdown dose rate distributions on high resolution mesh grids [1], was utilized to provide the photon radiation dose fields around the transfer cask loaded with activated components. R2Smesh couples MCNP [2] transport calculations (neutron and decay gammas) and FISPACT [3] inventory calculations (decay gamma source) through suitable interfaces utilizing MCNP’s mesh tally capabilities. Neutron fluxes and the decay gamma sources are provided on high resolution mesh grids superimposed to the real geometry. Thus proper account is taken of the spatial variations of the flux and the decay gamma source distribution without the need to modify the MCNP geometry model. This feature enables to export the decay gamma source distribution from the irradiation site in the reactor to any external location for the determination of photon flux and dose rate distributions. The decay gamma source distribution, provided for a specified irradiation history of the considered ITER component, is then overlaid to the model of the component at the considered location.

Various in-vessel components including a divertor cassette (DIV), a blanket first wall module (BFWM), a generic diagnostic equipment port plug (GEPP) and a test blanket module (TBM) were assumed to be irradiated in ITER following the standard SA2 irradiation scenario. The activated components were then removed from the ITER torus sector model and integrated into a transfer cask model. The associated decay gamma source distributions were likewise transferred to the cask and overlaid to the geometry models of the activated components using the mentioned feature of the R2S approach. Spatial distributions of the resulting gamma flux and the biological dose rates were generated on detailed high-resolution maps in and around the transfer cask loaded with the different activated components.

A dedicated MCNP model was devised of the tunnel connecting the ITER tokamak building (TCB) and the hot cell facility building (HCFB) with a transfer cask integrated. For the tunnel dose analysis, the transfer cask was assumed to be loaded with an activated GEPP that was shown to provide the highest activation and dose rate levels.

Neutron transport and activation calculations for the In-vessel Components in ITER

In the first step, neutron transport calculations were performed with MCNP to provide the neutron flux distributions on a fine mesh overlaid to the considered in-vessel components in ITER. In the second step, activation calculations were performed with the FISPACT code to

provide the decay gamma source distribution for the activated components assuming the standard ITER SA2 irradiation scenario and a decay time of 21 days after irradiation. The following in-vessel components were considered: a divertor cassette (DIV), a blanket first wall module (BFWM), a generic diagnostic equipment port plug (GEPP), and a test blanket module (TBM). The B-lite and A-lite models of ITER were used for the calculation the decay gamma sources of the BFW, the GEPP, the DIV and the TBM, respectively.

FENDL2.1 [4] and EAF-2007 [5] cross section libraries were used for the transport and activation calculations, respectively. All calculations were performed on the HELIOS super computer cluster at Rokkasho, Japan [6], running MCNP in the parallel mode using mostly 16 nodes (256 cores).

As an example, Fig.1 shows the model used for the activation of the divertor in ITER. Fig 2 shows the resulting neutron flux distribution and the associated map of the statistical error.

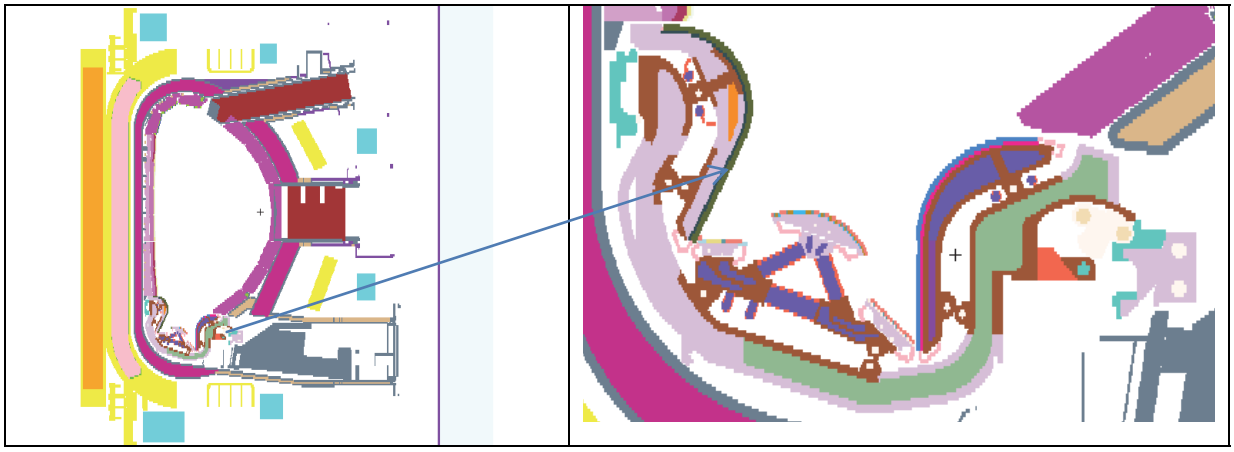

Fig. 1: MCNP model used for activation of the divertor (radial-poloidal cross section).

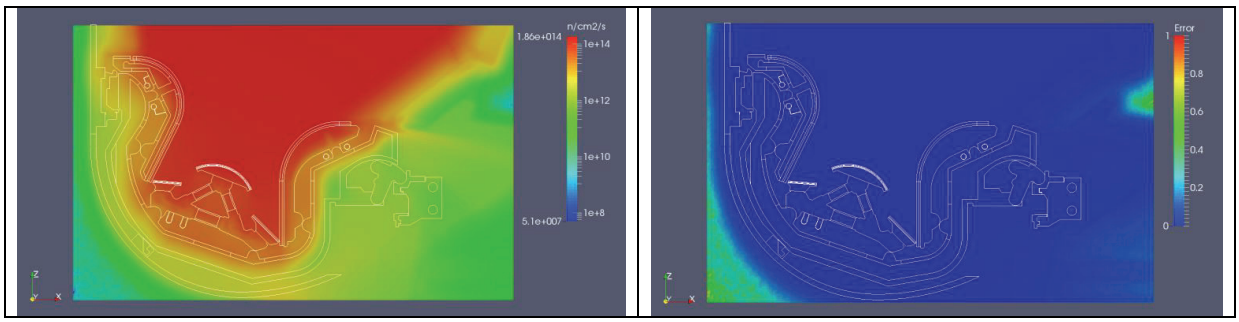

Fig. 2: Radial-poloidal distribution of the total neutron flux density in the divertor region (left) and associated statistical error (right).

Dose rate calculations for the isolated transfer cask

In the next step, dose rate calculations were performed for a transfer cask loaded with the activated divertor cassette, the BFWM of mid-plane blanket module #15 in B-lite, the GEPP of the equatorial port, and the European TBM system with HCLL and HCPB TBM sections. In the case of the BFWM, four first wall modules were placed into the transfer cask.

Figs. 3 – 6 show maps of the biological dose rates as calculated across the transfer cask (interior and exterior) and at the surface of the transfer cask. The maps include contour lines of the dose rates and also indicate the maximum dose level at the surface of the transfer cask. These amount to 56.6, 83.6, 18.5, and 54.2 Sv/h for the activated BFWM, GEPP, divertor and TBM, respectively.

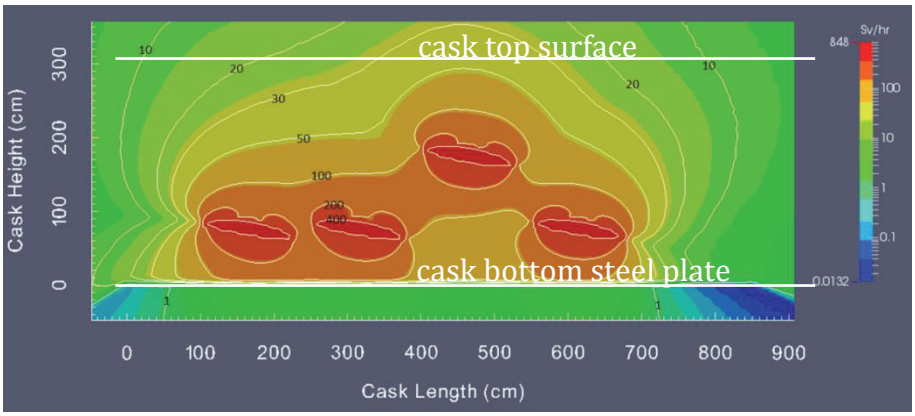

Fig. 3a: 2D map of biological dose rate around transfer cask loaded with four activated BFWM (vertical cut).

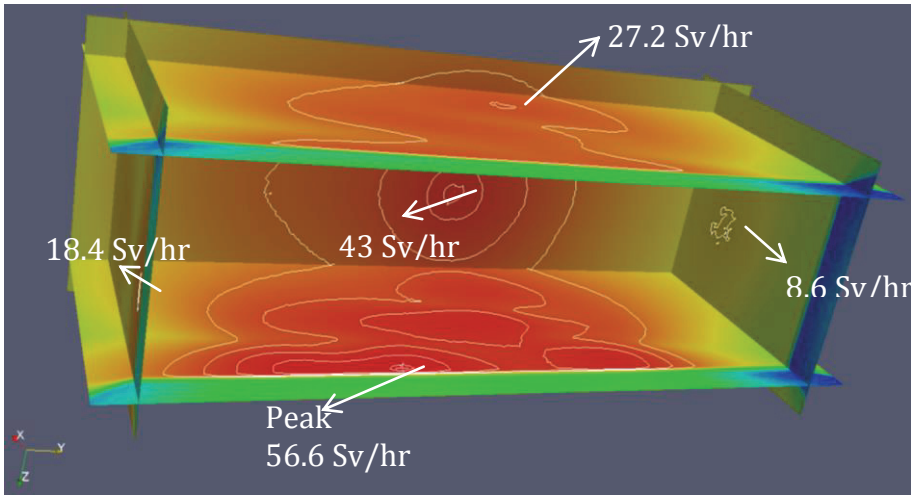

Fig. 3b: Isometric view of the biological dose rate at the surface of the transfer cask loaded with four activated BFWMs (view from the cask bottom).

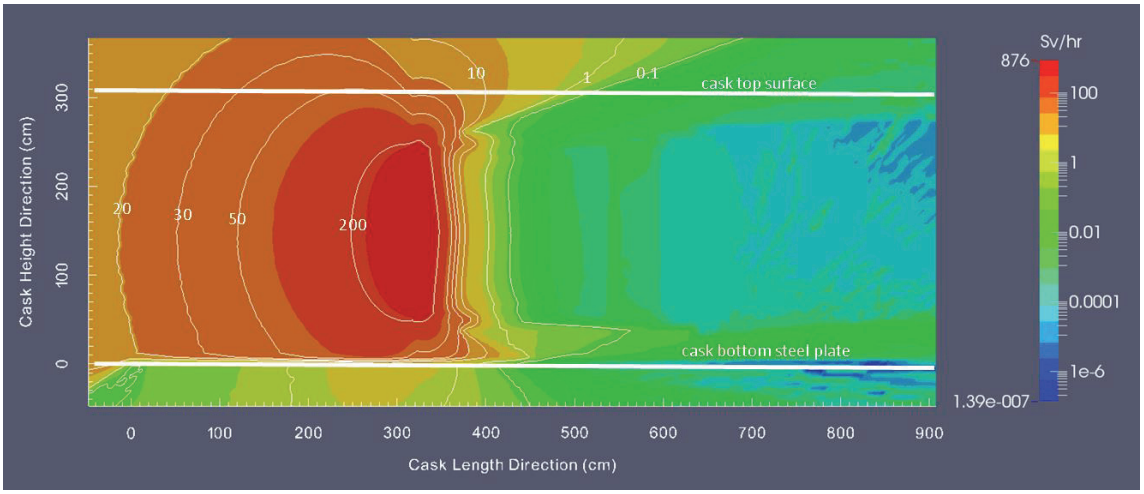

Fig. 4a: 2D map of biological dose rate around transfer cask loaded with the activated GEPP module (vertical cut).

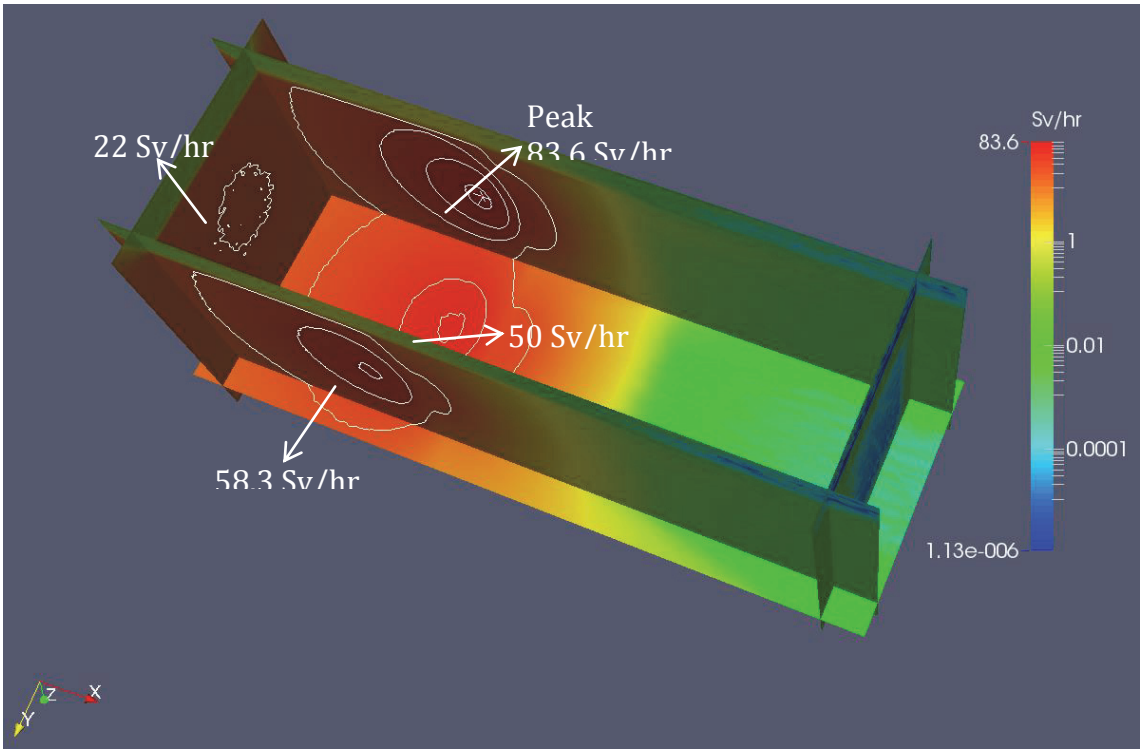

Fig. 4b: Isometric view of the biological dose rate at the surface of the transfer cask loaded with the activated GEPP module (view from the cask bottom).

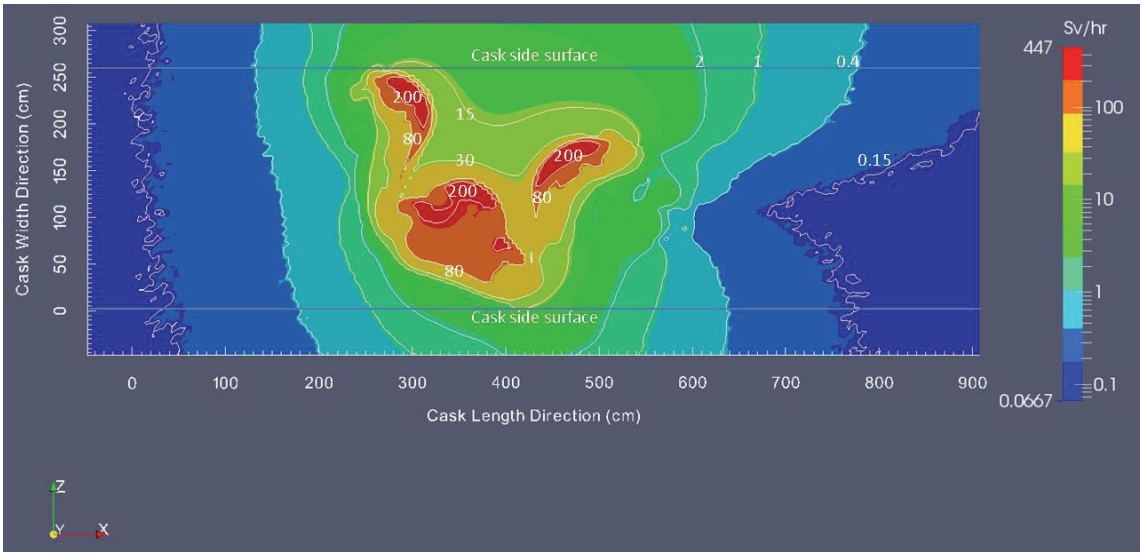

Fig. 5a: 2D map of biological dose rate around transfer cask loaded with the activated divertor cassette (horizontal cut).

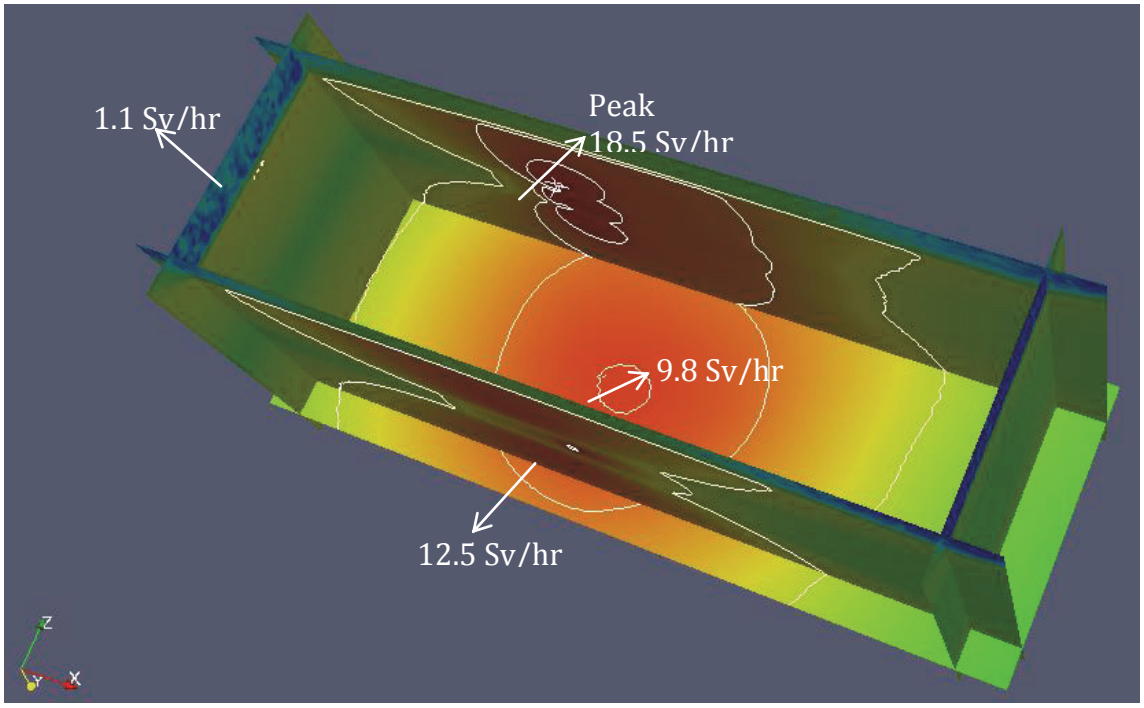

Fig. 5b: Isometric view of the biological dose rate at the surface of the transfer cask loade d with the activated divertor cassette (view from the cask bottom).

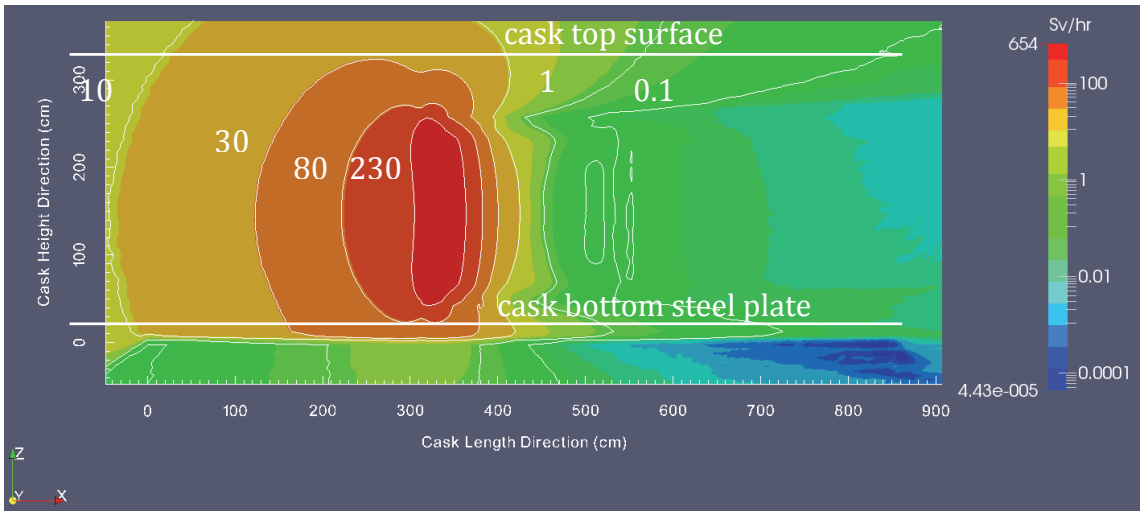

Fig. 6a: 2D map of biological dose rate around transfer cask loaded with the activated European TBM system (vertical cut).

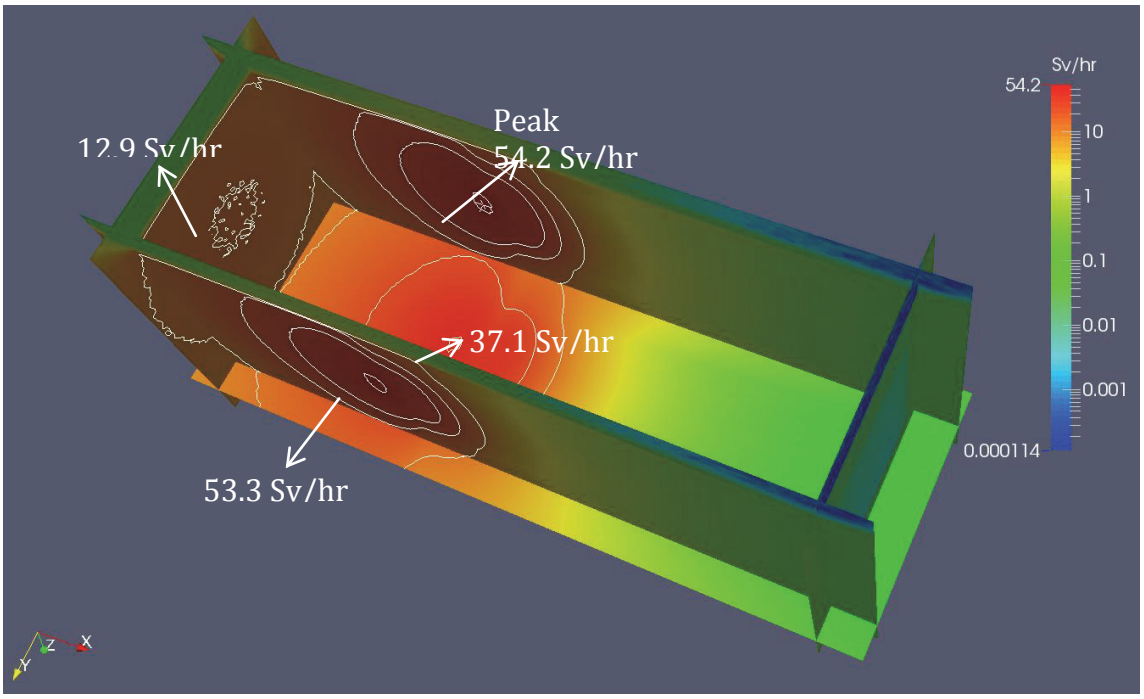

Fig. 6b: Isometric view of the biological dose rate at the surface of the transfer cask loaded with the activated European TBM system (view from the cask bottom).

The analysis showed that the activated GEPP module will produce the maximal biological radiation dose load around the transfer cask. The resulting maximal value on the surface of the cask is 83.6 Sv/hr. This is significantly lower than the limit of 430 Sv/h that was assumed by the French safety authorities.

Dose rate calculations for the Hot Cell Tunnel Exclusion Zone

The ITER Tokamak building and the hot cell building are connected by a tunnel through which the automated transfer casks travel. No exclusion area is foreseen outside the buildings while a transfer cask is passing through the tunnel. The objective of this work was to determine the dose-rate distribution outside the building while a transfer cask with the activated GEPP is present in the tunnel.

To accomplish this, an MCNP model of the tunnel connecting the Tokamak Complex Building (TCB) and the Hot Cell Facility Building (HCFB) was created. A model of the activated GEPP arranged within a transfer cask represented the radiation source for the determination of the dose rate distribution outside the tunnel. Fig. 7 shows a cross-section of the MCNP model with the transfer cask placed in the tunnel.

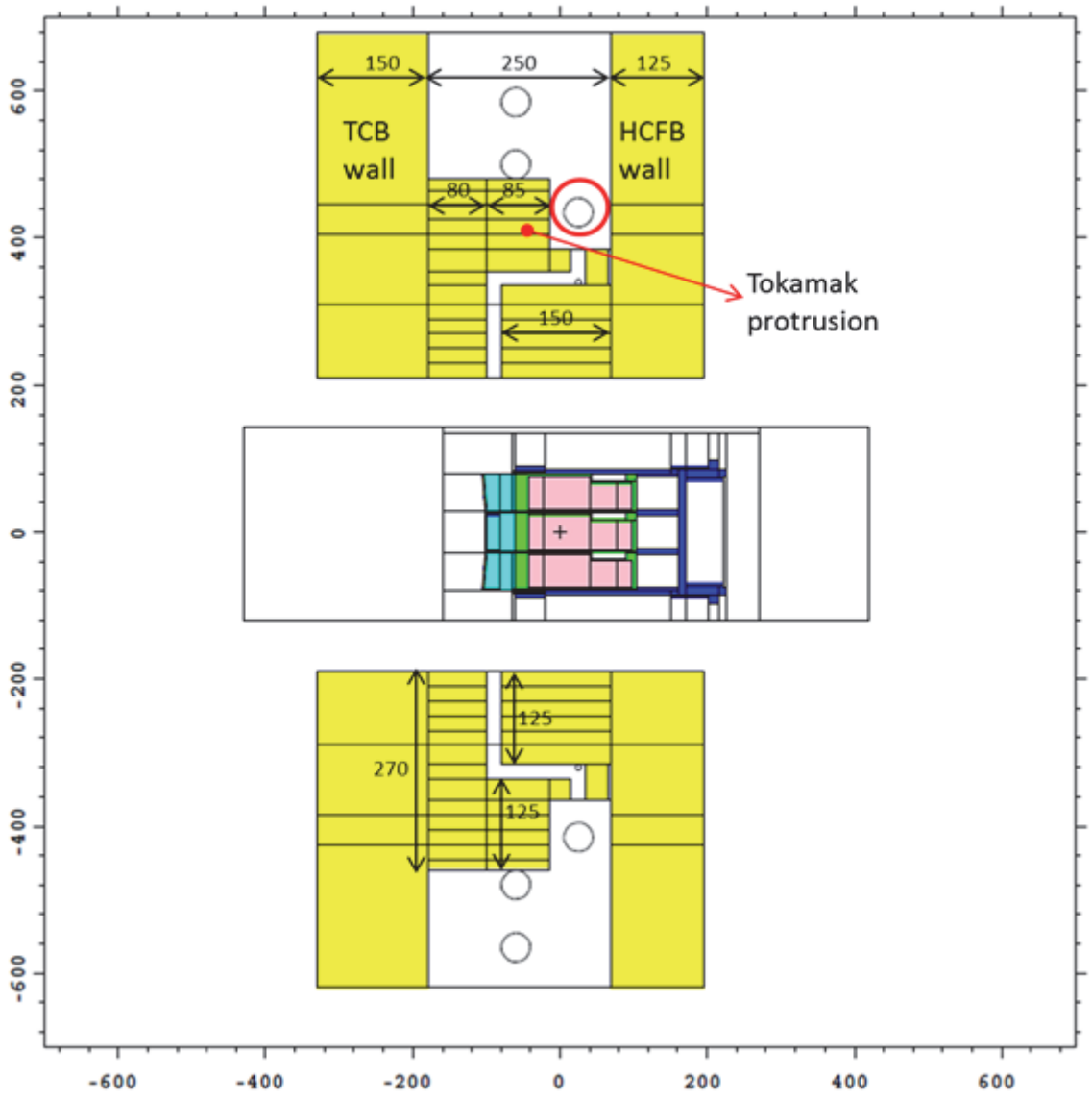

Fig. 7: Horizontal cross-section of the MCNP model of the tunnel connecting the Tokamak Complex Building (TCB) and the Hot Cell Facility Building (HCFB) with the transfer cask placed in the tunnel (dimensions and scale in cm). The red circle area designates the region of interest for the determination of the biological radiation dose loads.

The photon transport around the tunnel was calculated with the activated GEPP module as source in the transfer cask using the associated 3D decay gamma source distribution provided with the previous irradiation simulation in ITER. Fig. 8 shows the resulting distribution of the biological dose rate around the tunnel. The dose rate level in the nearest accessible location outside the tunnel is about 68.3 μSv/hr which is higher than the maximum steady dose rate limit of 0.5 μSv/hr for uncontrolled areas.

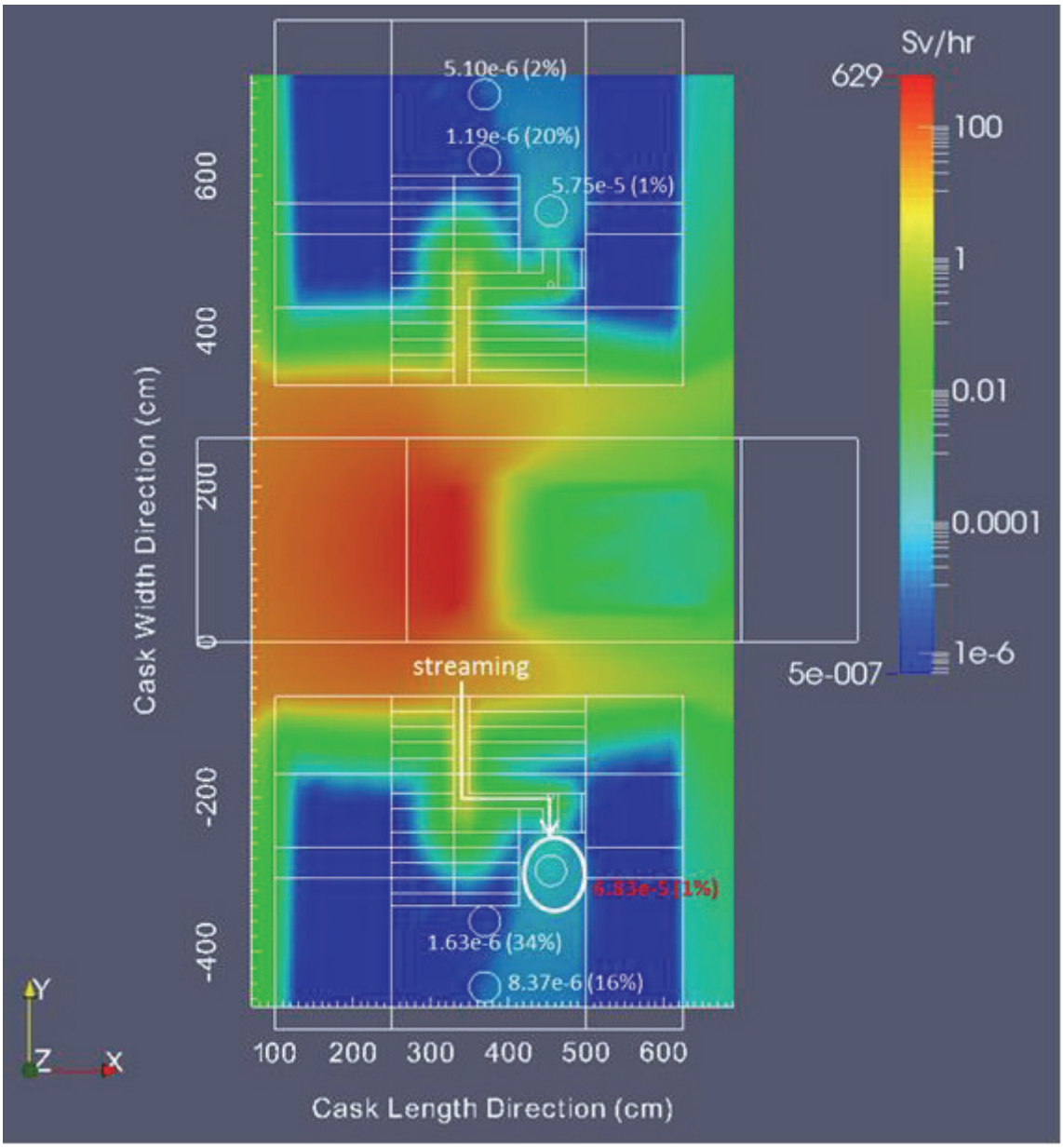

Fig. 8: 2D (horizontal) distribution of the biological dose rate around the tunnel with the transfer cask and the activated GEPP in the tunnel.

In order to reduce the dose rate at the nearest accessible location outside the tunnel, the TCB side protrusion (cf. Fig. 7) was extended to the HCFB side with only a 20 cm horizontal gap left. With the extended protrusion, the dose rate at the nearest accessible location outside the tunnel is still 9.31 μSv/hr. The normal protrusion design thus would create radiation risks outside the buildings during the transfer of casks with activated components such as the GEPP. Design optimization works such as the proposed extended protrusion contribute to the reduction of these risks. It was concluded that additional studies would be needed to check the doses at all the locations accessible to workers with such design optimization works.

Staff:

U. Fischer
H. Liu
P. Pereslavtsev
A. Serikov

Literature:

[1] M. Majerle, D. Leichtle, U. Fischer, A. Serikov, "Verification and validation of the R2Smesh approach for the calculation of high resolution shutdown dose rate distributions," *Fusion Engineering and Design* 87, 443-447 (2012).

[2] X-5 Monte Carlo Team, "MCNP—A general Monte Carlo N-particle Transport Code, Version 5, LA-UR-03-1987, Los Alamos Nat. Lab. (2003).

[3] R. A. Forrest et al., "FISPACT 2007 user manual," UKAEA FUS 534 report (March 2007).

[4] D. Lopez Aldama, A. Trkov, INDC(NDS)-467 (2004),: http://www-nds.iaea.org/fendl21.

[5] R. A. Forrest, J. Kopecky, J-C. Sublet, The European Activation File: EAF-2007 Neutron-induced Cross Section Library, UKAEA FUS 535 report (2007).

[6] Helios supercomputer at Computational Simulation Centre (CSC) of the International Fusion Energy Research Centre (IFERC): http://www.iferc.org

Acknowledgement

This work was supported by ITER Organization under the service contract No. IT-ER/CT/13/4300000763. The views and opinions expressed herein reflect only the author's views. The ITER Organization is not liable for any use that may be made of the information contained therein.

Nuclear Data Improvements and Development of Tools – Nuclear Data Evaluation (F4E-FPA-GRT-168.01)

Overall objective

The overall objective of the Framework Partnership Agreement F4E-FPA-168 on “Development of Nuclear Data Files“ between F4E and the “Consortium on Nuclear Data Development and Analysis“ is to contribute to the generation, maintenance and validation of nuclear data libraries relevant for ITER, IFMIF and DEMO. The Consortium, consisting of the research institutions of KIT (Germany), CCFE (UK), NRG (The Netherlands), JSI (Slovenia), TUW (Austria), CIEMAT (Spain) and IFIN-HH (Romania), combines available European expertise to provide the services requested by F4E to meet their objectives in the field of nuclear data development.

These services include nuclear data evaluations relevant to the various fusion applications encompassing neutron, proton and deuteron induced reactions, the generation of associated co-variance data for uncertainty assessments, the development of advanced nuclear models and codes, the processing and benchmarking of the evaluated data against integral experiments, as well as the development of suitable software tools for sensitivity and uncertainty analyses of fusion systems.

The first specific grant, F4E-FPA-GRT-168.01 on “Nuclear Data Improvements and Development of Tools - Nuclear Data Evaluation” started May 1, 2012, with activities on the evaluation of neutron induced reactions on ^{55}Mn, ^{63,65}Cu and ^{181}Ta, benchmark analyses for neutron (Fe, Pb) and deuteron (Cu, Al) induced reactions, the evaluation/generation of damage energy/displacement cross-section data, the evaluation of deuteron induced activation cross-section data, the development of optical model potentials for the emission of alpha-particles over a wide target nuclide mass range, the development of consistent TALYS model based activation/transmutation and transport neutron sub-libraries as well as the processing of photo-nuclear data libraries and thermal scattering data tables for Monte Carlo applications. Codes and software tools related activities are conducted on the further development of the stochastic and deterministic sensitivity/uncertainty approaches (MCSEN and SUSD3D codes), associated pre- and post-processing tools, and the MCUNED extension of MCNPX for the use of deuteron cross-section data in Monte Carlo transport calculations.

KIT is leading the Consortium and is co-ordinator of the FPA-168 and the associated grants. It contributes to the FPA-168.01 grant activities with the following tasks:

Task 1.2
Generation of genuine EFF/JEFF evaluated general purpose nuclear data files for n + ^{63,65}Cu including covariance data up to 150 MeV

Objective

Cu is an important heat sink material for fusion power reactors which is also used for diagnostics, microwave waveguides and mirrors in ITER. As there are no genuine JEFF data evaluations available for Cu, complete new evaluations of the cross-section data were to performed for n+ ^{63,65}Cu up to 150 MeV using consistent approaches for the cross-section evaluation and co-variance generation.

Computer Codes and Nuclear Models

Simulations of the n+63,65Cu interactions were performed making use of the TALYS code [1] in the energy range from 1 keV up to 200 MeV of the neutron incident energies. The analysis performed for the n+63,65Cu reactions revealed some deficiencies of the nuclear models included in latest version TALYS-1.4. In some cases the set of the experimental data could be fitted with TALYS-1.4 only by changing nuclear model parameters to unphysical

values. Improvements can be achieved by inclusion in TALYS of an additional model for the pre-equilibrium reactions description, namely the Geometry Dependent Hybrid model (GDH) [2]. The previous version TALYS-1.2 was already properly modified and well globally tested against experimental data for incident neutrons and protons. The modified TALYS-1.2 gives more accurate results for n+Cu reactions compared to TALYS-1.4. The GDH model was involved in calculations by making use of the new option of the keyword preeqmode 5. The nuclear level density was described with a phenomenological generalized superfluid model [3] (ldmodel 3).

The nuclear model calculations were done using TALYS built-in global Optical Model Potentials (OMPs) for neutrons and protons. The global OMPs for deuterons [4] and alphas [5] were used in the TALYS calculations. For tritons and helions, new OMPs were elaborated using a large experimental data base and available OMPs for some target nuclides [6]. The parameters of the global OMPs for d, t, 3He and alphas were separately calculated and used in TALYS calculations as external data files invoking optmod commands. All OMPs have the same valid incident energy range from keVs up to 200 MeV. Therefore the evaluated data are continuous and consistent in the full energy range of the incident neutrons. The results for total, elastic and inelastic scattering cross sections were obtained with the optical model making use of the local OMPs for both copper isotopes. All uncertainties arising during the evaluation process due to a possible adaptation of the reaction cross sections which do not come from nuclear model simulations (for example, already existing evaluated data) are accounted for in the elastic scattering cross section, keeping the total cross section unchanged.

Results of the nuclear model calculations

Resonance parameters

A complete resolved resonance parameter data set was evaluated for n+^{63}Cu and ^{65}Cu reactions at Oak Ridge National Laboratory (ORNL) using the SAMMY code [7]. This evaluation is based on the new low energy measurements performed at the Massachusetts Institute of Technology on ^{63}Cu and ^{65}Cu for the total cross sections and for the neutron transmission (energy range 0.01 eV- 0.1eV). Making use of the available experimental data for higher energies from EXFOR and the newly measured ones, new resonance parameters and their covariances were prepared for the stable copper isotopes. For both nuclei the resonance region was set from 10^{-5} eV to 300 keV. Results for the total and elastic scattering cross-sections are shown in Fig. 1.

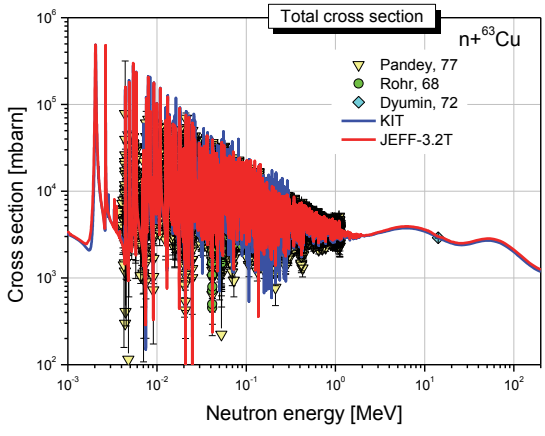

Fig. 1a: Evaluated total scattering cross section for n+63Cu.

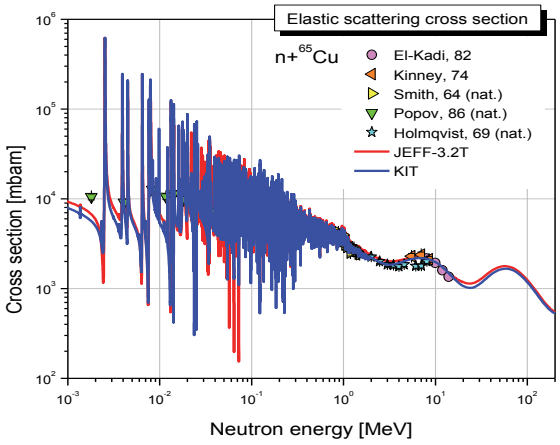

Fig. 1b: Evaluated elastic scattering cross-section for n + 65Cu.

Nuclide production cross sections

The nuclear data evaluation using the TALYS code was based on a sequential iteration procedure. Starting with default nuclear parameters, the results of the nuclear model simulations were consequently adjusted to the available experimental data by changing accordingly the parameters. Fig. 2 shows the newly evaluated cross sections compared to the measure-

ments and other evaluations from the JEFF-3.2T [8] and EAF-2010 [9] libraries. The presented results demonstrate evident improvements as compared to the JEFF-3.2T data.

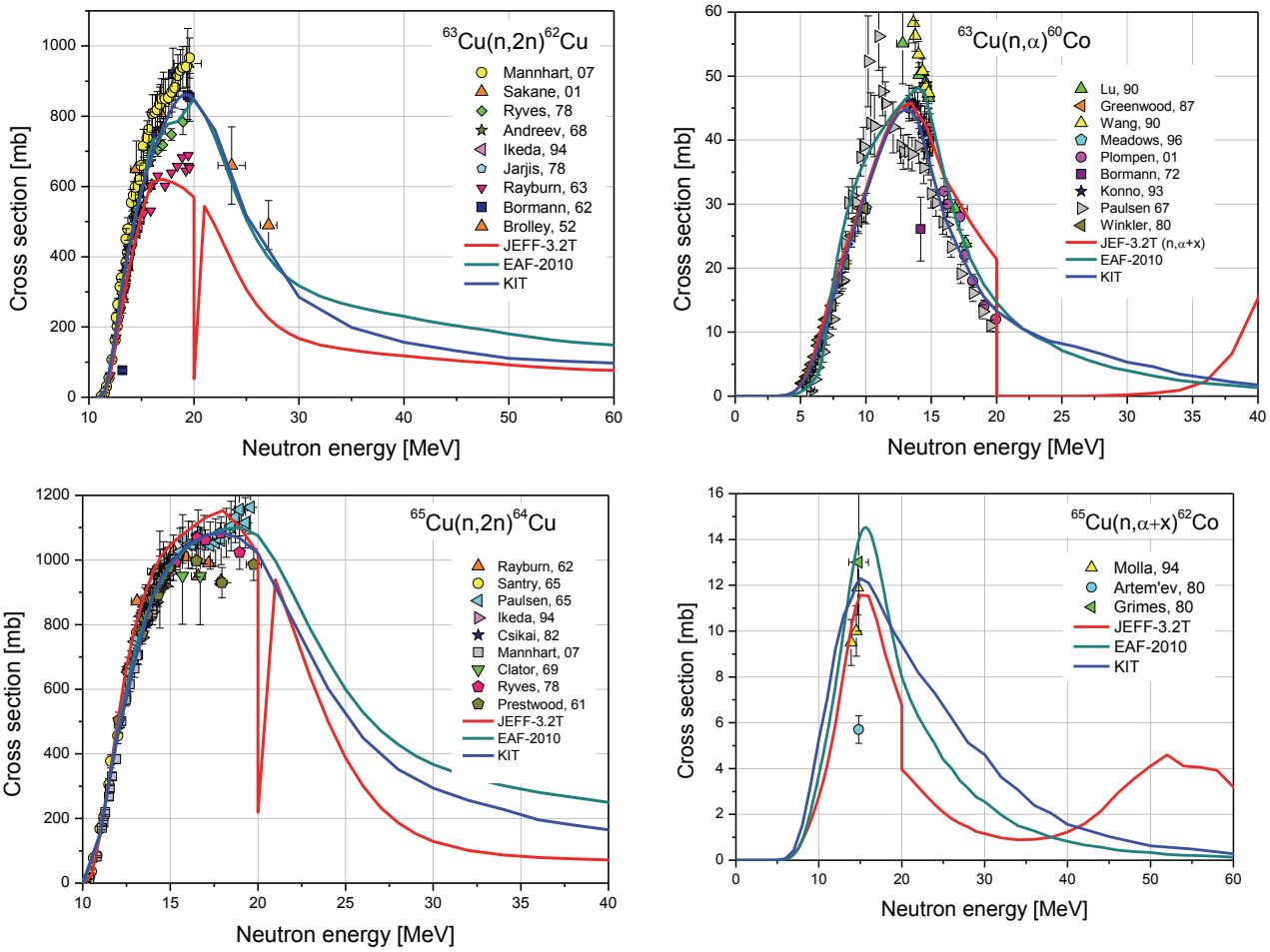

Fig. 2: Evaluated (n,2n) and (n,α) cross sections for ^{63}Cu (top) and ^{65}Cu (bottom).

Particle emission spectra

The equilibrium part of the particle emission spectra was calculated in TALYS in the framework of the multiple Hauser-Feshbach statistical model. The pre-equilibrium part of the particle spectra is described in the modified TALYS-1.2 code within the GDH model accounting for multiple pre-equilibrium processes.

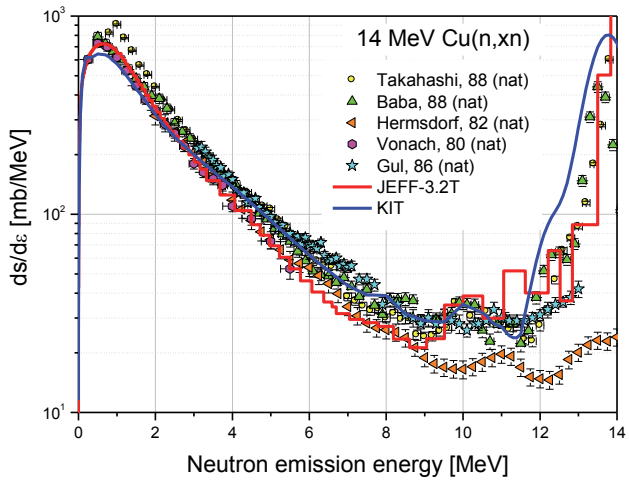

Fig. 3a: Evaluated neutron emission spectra for n+natCu at 14 MeV incident neutron energy.

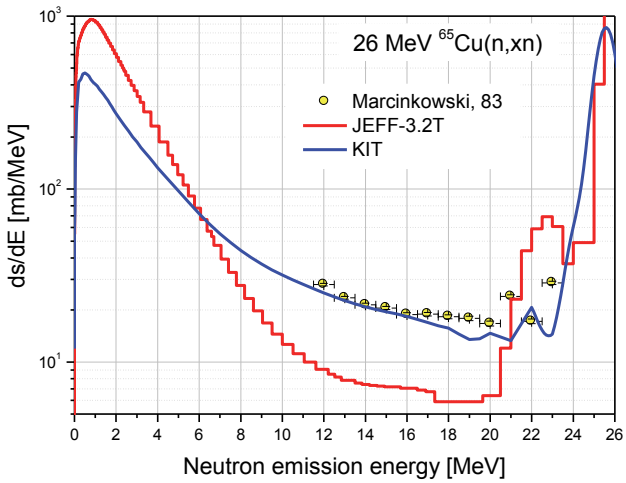

Fig. 3b: Evaluated neutron emission spectra for n+65Cu at 26 MeV incident neutron energy.

The results of the present evaluations for the neutron emission spectra are shown in Fig. 3 for natural copper at different energies. The new evaluated data fit the available experimental data much better compared to the JEFF-3.2T results.

Evaluations of covariance data

The cross-section evaluation procedure included the selection and analysis of experimental data, cross-section calculations using nuclear models, the computation of covariance matrices resulting from model calculations, the estimation of cross-sections and covariances using available experimental information and calculated cross-sections and covariance matrices.

In the present work, the co-variances were prepared making use of the BEKED [10] and the modified TALYS-1.2 codes. The BEKED code utilizes a Monte Carlo approach for calculations of the covariance matrices for the cross-sections. The principal steps of this method are as follows: set up of the uncertainties of the nuclear model parameters, preparation of the input files and execution of TALYS using the Monte Carlo technique for the model parameters sampling, finally calculations of the data covariances for the chosen reaction channels.

The BEKED code carries out the random sampling of the optical model parameters, deformation parameters for coupled channels calculations and nuclear level density parameters. With this method experimental uncertainties are also taken into account in the calculations of the final evaluated nuclear data covariances. The Monte Carlo samplings are performed until the deviation of the final results for two sequential runs becomes negligible. Reliable results can be obtained with several thousand TALYS runs for each copper isotope. Fig. 4 shows an example for the uncertainties of cross-sections obtained after the use of experimental data.

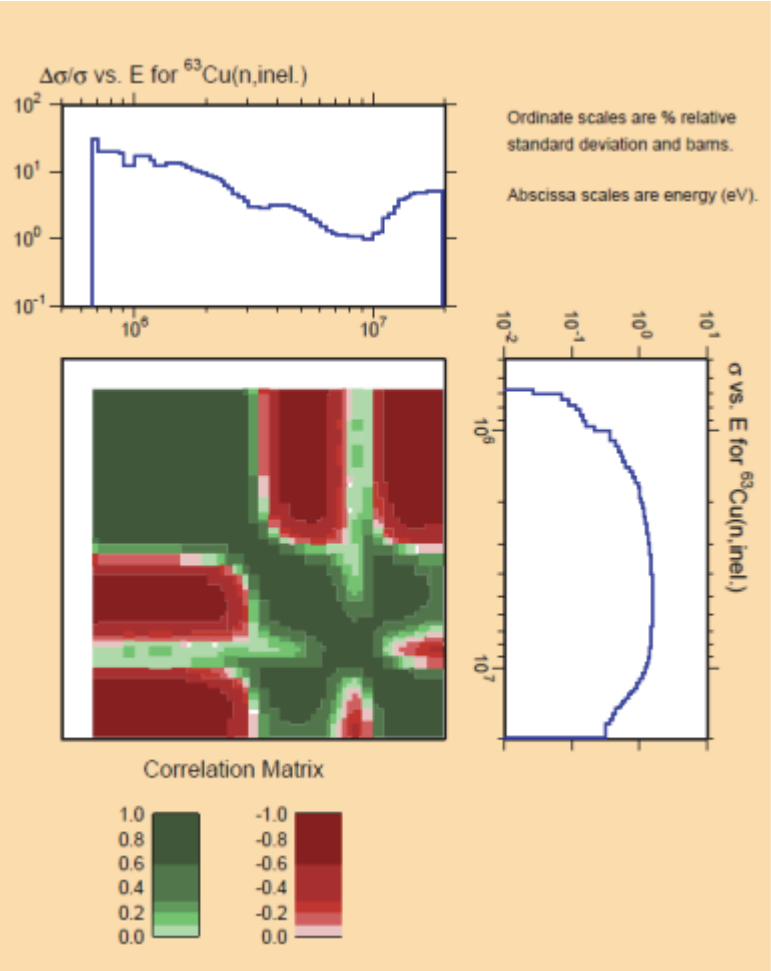

Fig. 4: Evaluated covariance matrix and related uncertainties for the ^{63}Cu(n,n')^{63}Cu inelastic reaction cross section.

Evaluated data files

The evaluated nuclear data files for n+63Cu and n+65Cu particle transport calculations were output in the standard ENDF-6 data format. The most severe problem for storing of the high energy data is the limitation of the ENDF-6 format for the number of the explicitly given reaction channels. In case of the n+Cu interactions the possible number of the open channels at 200 MeV can exceed several hundreds. The data file becomes extremely large and complicated for handling if such information like particle spectra is presented for each reaction channel. Furthermore, at high energies the experimentally measured cross sections are usually a sum of all possible channels leading to the formation of a particular nuclide. For the present evaluation, we adopted the following structure of the data files: below 20 MeV of the neutron incident energy we give the full detailed information for all open

reaction channels and above 20 MeV we present total particle emission spectra, total cross sections for the production of the residual nuclides and their recoil spectra. To this end, we use the MT5 section on the file above 20 MeV that is treated as a sum of all possible nuclear reactions except total and elastic scattering cross sections. The particle spectra and residual production cross sections can be restored using combination of the information for the section MT5 in the MF=6 and MF=3 files. The covariance data are presented in the evaluated data files in MF=32 for the resonance data, and MF=33 for all explicitly given reaction channels.

After checking and testing, the n+ 63,65Cu ENDF data files were provided to the NEA Data Bank, Paris, for inclusion in the new JEFF-3.2 data library, to be released in early 2014.

Staff:

U. Fischer
P. Pereslavtsev
A. Konobeev

Literature:

[1] A.J. Koning, S. Hilaire, M.C. Duijvestijn, Proceedings of the International Conference on Nuclear Data for Science and Technology (ND2007), April 22-27 2007 Nice France (2008).

[2] A.Yu. Konobeyev, U. Fischer, A.J. Koning, P.E. Pereslavtsev, M. Blann, Journal of the Korean Physical Society v. 59, No. 2, 935 (2011)

[3] A.V. Ignatyuk, R. Capote, Nu, IAEA-TECDOC-1506 (2006) p.85, http://www-nds.iaea.org/RIPL-2/handbook.html

[4] Haixia An, Chonghai Cai, *Phys. Rev*. C73, 054605 (2006)

[5] V. Avrigeanu, P.E. Hodgson, *Phys. Rev.* C49, 2136(1994).

[6] P.Pereslavtsev, U. Fischer, EFFDOC-974, NEA Data Bank, Paris, May 2006

[7] V. Sobes, B. Forget, L. Leal, K. Guber, et.al, this conference.

[8] A. Santamarina et. al, JEFF Report 22, NEA No. 6809, Nuclear Energy Agency, 2009

[9] L. Packer and J.-Ch.Sublet: The European Activation File: EAF-2010 decay data library, CCFE-R (10)02 (March 2010

[10] A.Yu. Konobeyev, U. Fischer, P.E. Pereslavtsev, Journal of the Korean Physical Society v. 59, No. 2, 923 (2011)

Task 2.1
Benchmark analyses of the general purpose data evaluations of Pb to assess their quality for design analyses of the HCLL breeder blanket concept

Objective

Pb is a material of highest importance for the European breeder blanket development programme which includes irradiation tests of Test Blanket Modules (TBM) in ITER and conceptual design studies for DEMO power reactors. The HCLL (Helium-Cooled Lithium-Lead) breeder blanket design utilizes Pb as neutron multiplier material. A neutronic experiment has been recently performed on a mock-up of the HCLL TBM to check and validate the capability of the neutronic tools and data to predict reliably the Tritium production and other nuclear responses of interest in the TBMs.

Benchmark analyses

The benchmark analyses performed on Pb under Task 2.1 of FPA-168-01 built on the results obtained in the analyses of this experiment and complemented them by analyses of benchmark experiments on pure material assemblies. The focus of the analyses was on the performance of the Pb data evaluations contained in the JEFF general purpose data library.

The following integral benchmark experiments on pure Pb assemblies using DT neutron sources were utilized for the present analysis:

1. TOF experiment on lead slabs (JAERI, 1985-1990)
   - Fusion Eng. Des. 18, pp. 287-291 (1991) (Ref.1)
   - Numerical data: JAERI-M 94-014 (Ref.2)

2. 45-cm slab in-situ experiment (JAEA, 2010)
   - Presented at the Nuclear Data conference 2010, Jeju Island, Korea
   - J. Korean Phys. Soc., 59, 2, pp. 1953-1956 (2011) (Ref.3)
   - Numerical data: unpublished

3. Leakage Gamma-ray spectrum measurement (Osaka University/JAERI, 2000)
   - Presented in at the Nuclear Data conference 2001, Mito, Japan
   - J. Nucl. Sci. Technol. Suppl. 2, pp. 955-958 (2002) (Ref.4, 5)
   - Numerical data: unpublished but available upon request

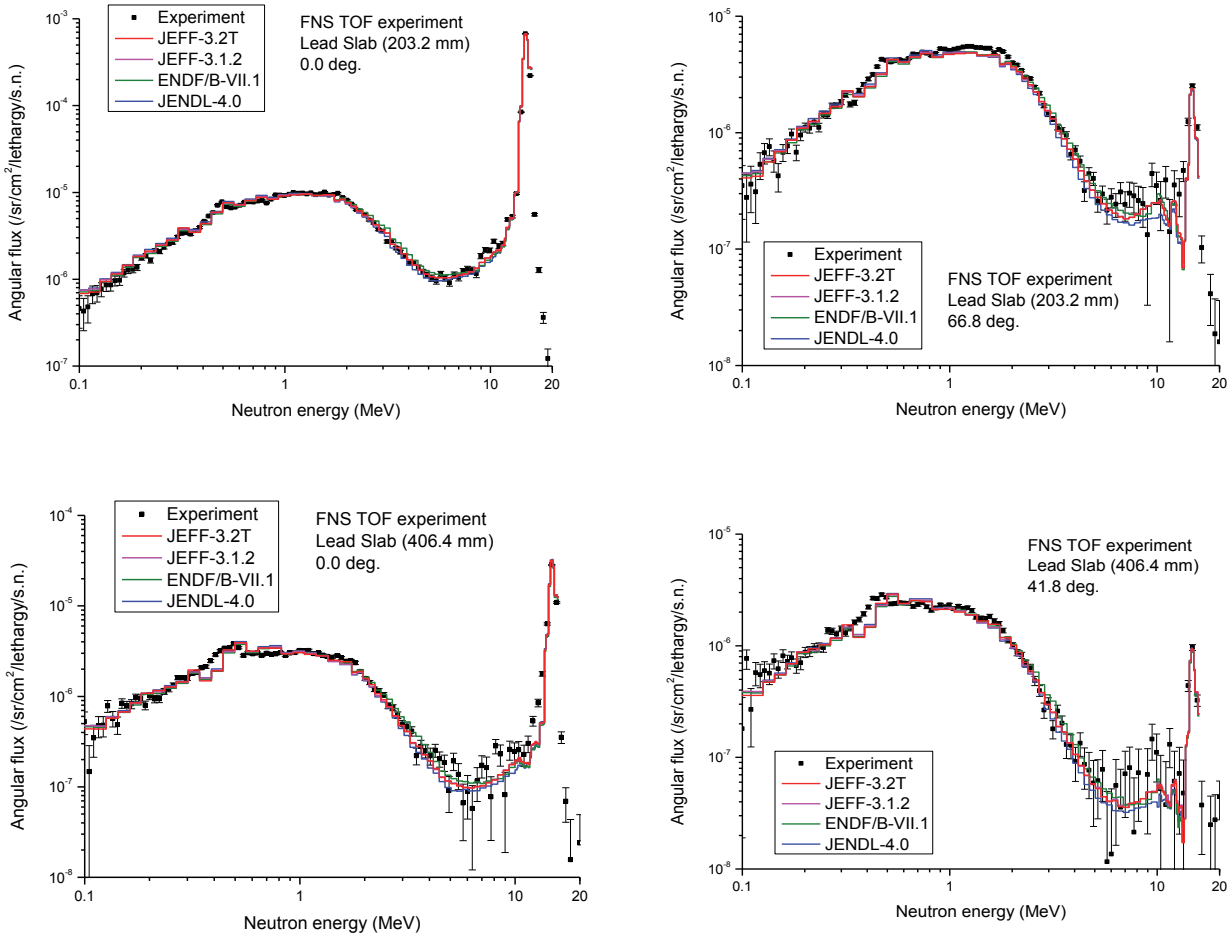

Fig. 5: TOF lead slab experiment: Comparison of measured and calculated angular neutron spectra for leads slabs of 20.32 cm (top) and 40.64 cm (bottom) thickness.

The benchmark experiments were analyzed with the JEFF-3.2T, JEFF-3.1.2, ENDF/B-VII.1 and JENDL-4.0 nuclear data evaluations. JEFF-3.2T/3.1.2 reproduced all the experimental data very well; it seems the best among all the libraries. Very small differences (up to 5% in the spectra only below 2-3 MeV and up to 3% in the reaction rates of Ni and In) were found between the results calculated with JEFF-3.2T and 3.1.2. Fig. 5 shows examples for the neutron flux spectra obtained for the TOF experiment on lead slabs.

The results of the analyses of the TOF experiment and the in-situ experiment were consistent each other. The tendency observed in the both experiments is that the neutron flux around 14 MeV was very well predicted but the neutron flux between 2 and 5 MeV was underestimated. The above result is also consistent with the HCLL mockup experiment. As a conclusion, the tritium production rate can be predicted accurately under the present HCLL blanket configuration, although there is slight discrepancy in neutron spectra.

It was concluded that there is no urgent need to update the present JEFF evaluation on Pb.

Staff:

U. Fischer
K. Kondo

Literature:

[11] H. Maekawa and Y. Oyama, Experiment on angular neutron flux spectra from lead slabs bombarded by D-T neutrons, Fusion Eng. Des. 18, pp. 287-291 (1991).

[12] (Ed.) Sub Working Group of Fusion Reactor Physics Subcommittee: Collection of Experimental Data for Fusion Neutronics Benchmark, JAERI-M 94-014, Japan Atomic Energy Agency (1994).

[13] K. Ochiai et al., DT Neutronics Benchmark Experiment on Lead at JAEA-FNS, J. Korean Phys. Soc., 59, 2, pp. 1953-1956 (2011).

[14] T. Nishio et al., Fusion Neutronics Benchmark Experiment on Structural and Advanced Blanket Materials - Leakage Gamma-ray Spectrum Measurement -, J. Nucl. Sci. Technol. Suppl. 2, pp. 955-958 (2002).

[15] I. Murata and A. Takahashi, Recent Measurements of Nuclear Data and Integral Tests for Fusion Reactor Application, J. Nucl. Sci. Technol. Suppl. 2, pp. 1112-1117 (2002).

Task 3.1
Upgrading of the MCSEN sensitivity software to comply with the current standard of the MCNP-5 Monte Carlo code

Objective:

The Monte Carlo sensitivity code MCSEN has been developed in the frame of previous EFDA tasks and the F4E Nuclear Data Grant F4E-2008-GRT-014 (ES-AC) as extension to the MCNP-4C code to enable the Monte Carlo based calculation of sensitivities and uncertainties of nuclear responses in arbitrary 3D geometry. In the frame of this task, the MCSEN software was to be upgraded to comply with the MCNP5 standard. This upgrading enables the user to apply MCSEN as software patch to the current state-of-the-art production Monte Carlo code MCNP-5 thus providing access to all of MCNP's latest features.

MCSEN5

MCSEN has several sensitivity capabilities beyond MCNP's own capabilities. Those are aiming at sensitivities due to perturbations of quantities like material density and isotopic composition or few energy groups. On the other hand, MCSEN was devised to efficiently calculate

sensitivities to many reactions and many energy groups at the same time. At the time of MCSEN's inception, in the 1990ies, the main reason for creating the MCSEN update was the need for sensitivity analysis of point-detector tallies. For this purpose, we developed the theory and algorithm based on the differential operator approach. Later, the code was upgraded to enable calculation of sensitivities to secondaries' angular distributions. The latest major upgrade of MCSEN was the capability to calculate efficiently sensitivities of track length estimators. This has been recognized as an important development step to apply MCSEN to typical MCNP tallies in fusion applications.

The MCSEN updates were written with the intention to be used in analyses of cross-section-induced uncertainties. These are typically performed by the "sandwich multiplication": Multiply the sensitivity matrix and the cross-section co-variance matrix and the transposed sensitivity matrix. Therefore, the MCSEN updates were designed to calculate efficiently in one run the sensitivities to many reactions of a specific "sensitivity" isotope, in many groups. The (sensitivity-) group structure is identical for all responses and all sensitivity-reactions, since it has to be in the same structure as the covariance matrix. The MCSEN patches were intentionally written for this specific scenario: Calculate efficiently sensitivities to many reactions with many sensitivity-energy bins that are identical for all reactions. Due to this strategy it is straightforward to add the specific input for sensitivity tallies and, even more, the calculation time is only slightly affected compared to a simple transport run. This is due to the fact, that sensitivity contributions are tallied along each particle history in the same way as the usual track-length and point-detector tallies.

MCSEN5 was created as an update of the MCNP5 code [16] so that the code will be able to perform all sensitivity capabilities of the 4C version of MCSEN, while retaining all MCNP5 capabilities. MCSEN5 is based on the 1.30 version of the MCNP5 code. The MCNP5 code was written to be compiled on various types of computers and compilers; also the MCSEN5 upgrade is in principle not computer- or compiler-specific. During the years, MCSEN has been run on various systems and compilers. The MCSEN5 version described here has been developed and tested on a 64-bit LINUX workstation with an INTEL ifort Fortran compiler.

Testing and verification

MCSEN5 is a local version of MCNP5 with extended capabilities. When running the MCNP5 standard test jobs with (unmodified) MCNP5 and with MCSEN5, we found that the resulting output files were not dependent on the code.

At various stages in its development, the sensitivity results of MCSEN were tested. Results of such tests appear in references [17-19] and were repeated with the upgraded MCSEN5 version. In the original article of 1996 [17], the sensitivities of assemblies similar to the Livermore pulsed spheres were analyzed. In that paper, sensitivities of pulsed aluminium spheres to the density of aluminium, of a pulsed carbon sphere to the first level inelastic scattering of carbon, and of a uranium-238 sphere to the fission cross section and the fission nubar were presented. When we run these jobs with the latest MCSEN5, the results obtained are very similar to the original graphs.

In 2003 we published the algorithm for estimating the sensitivity to secondaries' angular distributions, and its implementation [18]. These sensitivities were demonstrated by analysis of the sensitivity of the leakage from an iron shell with an anisotropic source in its center to the Legendre moments of the elastic scattering by Fe56.

We ran various jobs that are similar to the original test jobs with the latest version of (MCNP4C-based) MCSEN and with MCSEN5. In all instances the results obtained with the two codes were identical (with possible minute differences due to round-offs).

In 2003, the track-length estimator option was introduced [19]. When we calculated now MCSEN5 sensitivities of a C-2.9-mfp pulsed sphere with both approaches, point-detector and flux-in-cell track-length estimator, we found a very good agreement (within statistical uncertainty) between the sensitivities (and the leakage-responses) calculated by the two methods.

MCSEN5 code package

The MCSEN code was written over the years by successive editing of the MCNP code. Due to this approach and also forced by the licensing conditions of MCNP, the MCSEN code cannot be distributed as a stand-alone code, but as patch to MCNP. The distribution package for MCSEN5 was designed so that it can be installed by any user of MCNP5.

In order to install MCSEN5, the user needs the files for installing the MCNP5 code, with updates to version 1.30, and the file patch-MCNP5_RSICC_1.30_to_mcsen5. The installation of MCSEN5 is performed by following these instructions.

When upgrading MCSEN to MCSEN5, no change was introduced in the required input to the code. Therefore the instructions for specific input to MCSEN5 are equal to the instructions for MCSEN.

Since MCSEN is an update to MCNP, all MCNP input options continue to be relevant. In addition, there are specific input instructions for MCSEN. The MCSEN input makes use of these two standard MCNP input commands: IDUM (integer dummies) and FU (user tallies). Sensitivities can be calculated for track-length-estimator tally types (F4) or for point-detector tallies (F5). A general feature of the implementation is that the usual tally syntax applies.

MCSEN calculates the sensitivity to (many) reactions of a single given isotope. We define the following terms for convenience:

- Sensitivity isotope: nuclide for which the sensitivity has to be calculated
- Sensitivity reaction: cross section according to ENDF-nomenclature, defined by MT-numbers
- Coarse sensitivity reaction: a set of “fine” sensitivity reactions, i.e. sum of several individual reaction cross sections, each characterized by its MT-number.

The sensitivity is calculated to a given sensitivity cross section set of a given sensitivity isotope. If the MCNP input contains different cross section sets for the same isotope, only the chosen set will contribute to the sensitivity. This sensitivity isotope can be defined in three different ways.

- “Isotope in cell”: Calculate the sensitivities to a given isotope in a given cell. (Other occurrences of this isotope in other cells will not contribute to the sensitivity.)
- “Isotope in material”: Calculate the sensitivities to a given isotope in a given material. (All cells that have this material contribute to the sensitivity. Occurrences of the isotope in other materials will not contribute.)
- “Isotope all”: Calculate the sensitivities to all occurrences of a given isotope. (All cells and all materials that contain this isotope will contribute.)

When upgrading MCSEN to MCSEN5, no essential changes were introduced in the sensitivity-specific output of the code. The output of MCSEN is basically the output of MCNP, with some specific outputs. If the MCSEN sensitivity option is activated then MCSEN prints out the parameters of this sensitivity run: the identification of the isotope, its cross section file and the sensitivity MT-numbers. If the input contains an illegal MT-number, then MCSEN prints a list of legal MT-number for this specific isotope/cross-section-file. The sensitivity values are printed by the regular printing routines of MCNP.

The MCSEN5 patch to MCNP5 is planned to be provided to the international community through RSICC, Oak Ridge National Laboratory, USA; and the NEA Data Bank, Paris, France.

Staff:

U. Fischer
R. Perel (Hebrew University of Jerusalem)

Literature:

[16] X-5 Monte Carlo Team, MCNP - A General Monte Carlo N-Particle Transport Code, Version 5, LA-UR-03-1987, Los Alamos National Laboratory, Los Alamos, New Mexico, USA, (April 2003)

[17] R.L. Perel, J.J. Wagschal, Y. Yeivin, Monte Carlo Calculation of Point-Detector Sensitivities to Material Parameters, Nucl. Sci. Eng., 124 (1996) 197-209.

[18] R.L. Perel, "Monte Carlo Calculation of Sensitivities to Secondaries' Angular Distributions," Nucl. Sci. Eng. 143, 121-131 (2003).

[19] R.L. Perel, "Sensitivity Calculation of Monte-Carlo Track-Length Estimators for Cross-Section Sensitivity- and Uncertainty-Analyses", EFF-DOC-873, NEA, OECD, Paris (2003).

Task 3.3
Tools for pre- and post-processing of data for the S/U codes MCSEN and SUSD3D

Objective

The MCSEN and SUSD3D codes have been developed for Monte Carlo and deterministic sensitivity/uncertainty (S/U) calculations by KIT and JSI, respectively. The codes have been benchmarked against each other and qualified for fusion technology applications. This task aimed at unifying the data streams and processes for both approaches. To this end, suitable pre- and post-processing tools with visualisation capabilities were to be developed based on common standard data formats.

Pre- and post-processing tools:

Tools for sensitivity/uncertainty analyses with visualisation capabilities were developed jointly by JSI, Ljubljana, and KIT, based on common standard data formats. KIT developed modules for specific use of sensitivity data provided by MCSEN. JSI developed and implemented post processing tools suitable both for MC and deterministic S/U codes, such as MCSEN and SUSD3D. The tools are available for Unix and/or Windows platforms, their numerical output is given in user-readable format for easy transfer to graphical visualisation software.

The work performed by KIT consisted of the following activities:

- Definition of common standard data formats for covariance data and sensitivity profiles processing.
- Development of tools for covariance data processing and uncertainty calculations based on sensitivity profiles from MCSEN.
- Development of tools for processing of the results to interface with standard visualisation software, in agreement with JSI.
- Testing and validation of the tools.

In order to perform the uncertainty analysis based on MCSEN5, the following steps have to be executed:

1. The original standard covariances have to be transformed from the box-format to the cov-format by use of the code “box2cov”. This step can either be performed for each uncertainty analysis run, or, alternatively, it can be done once before the first time a certain covariance matrix is used. In that case, each further uncertainty analysis run accesses directly the cov-formatted covariance file, omitting this step number 1.
2. If one wishes to calculate the sensitivity of a certain response A to a certain isotope/reaction B, and if A is a reaction rate that depends explicitly on isotope/reaction B, then it is required to pre-process the sensitivity file (in mctal-format). This has to be done by application of the code “add_responseterm_mctal”. In all other cases, i.e. if the response is a flux/fluence, or if the response A does not explicitly depend on isotope/reaction B, this step number 2 can be omitted.
3. The actual uncertainty analysis is performed by application of the code “sandwich5”. The input data files are covariances in the cov-format (step 1) and sensitivities created by MCSEN5 (that were possibly modified - step 2).

The sandwich5 code is the main tool developed to perform the sensitivity- and uncertainty-analysis of systems based MCSEN5 calculations. This code calculates integrated sensitivities, uncertainties of the responses, and prepares data for plotting sensitivities with the PlotS software developed by JSI. The purpose of the box2cov code is to transform covariances from the box-format, which is the format of files created by the COVR module of NJOY and which is an international standard format for exchanging fixed-group covariances, to the local cov-format. The “add_responseterm_mctal” tool is required for responses which directly depend on a reaction cross-section.

These tools have been developed using common data formats agreed with JSI for the covariances and the sensitivity profiles. The tools have been tested in several application calculations. The tools are provided together with the MCSEN5 patch for MCNP5 based sensitivity/uncertainty analyses.

Staff:

U. Fischer
R. Perel (Hebrew University of Jerusalem)

Task 4.2
Evaluation of advanced damage energy and displacement cross-sections for the major EUROFER constituents based on an atomistic modelling approach

Objective

Reliable assessments of radiation induced damage in fusion reactor materials require the use of advanced simulation techniques for the underlying displacement damage mechanisms. The calculation of radiation damage rates (dpa per second) for the EUROFER reduced activation steel is, therefore, based on improved displacement cross-sections based on Molecular Dynamics (MD) and Binary Collision Approximation (BCA) simulation methods for the calculation of the number of lattice defects. This approach shows a better agreement with available experimental data of point-defect production in materials than the standard Norgett-Robinson-Torrens (NRT) approximation used e. g. by the NJOY code. Neutron induced damage energy and displacement cross-section were to be evaluated for the main EUROFER constituents (Fe, Cr, W, Ta) up to 150 MeV utilizing the advanced atomistic modelling approach.

Evaluation of displacement cross-sections for EUROFER

The calculations of the displacement cross-section σ_d were performed on the basis of recoil energy distributions processed from neutron data libraries and results of BCA-MD simula-

tions performed with the help of the IOTA code. For comparison, also, calculations of displacement cross-sections were carried out using the standard NRT dpa model. In all calculations, the value of the displacement energy E_d was taken equal to 40 eV.

The evaluation procedure included the removal of unphysical peculiarities in the σ_d values resulting from the use of $d\sigma/dT$ from neutron data libraries, especially at 20 MeV, the fitting to results of σ_d calculations using intra-nuclear cascade evaporation models above 150 MeV [1,2], and, as far as required, the combination of the different results below and above 20 MeV.

Fig. 6 show calculated and evaluated displacement cross-sections for the major EUROFER constituents taken into account in this work. Preference of the $d\sigma/dT$ data below 20 MeV neutron energy was given to JEFF-3.2T2 and to TENDL-2011 and TENDL-2012 above 20 MeV. An advantage of TENDL is the agreement of the corresponding σ_d values and results of calculations applying the intra-nuclear cascade evaporation models at primary particle energies above 150 MeV.

The final σ_d values for EUROFER were obtained by summing up the weighted displacement cross-sections of the main EUROFER constituents Fe, Cr, W, Mn, V, Ta, C, Si, and N. The values obtained with both the BCA-MD and the NRT model are shown in Fig. 7. For the NRT calculations, the σ_d values for EUROFER were calculated as weighted sum of the σ_d data of the individual materials (e. g. Fe in Fe, Cr in Cr, etc.) using the original version of the NJOY code.

Data files in ENDF and ACE format

The evaluated displacement cross-section data were processed in the ENDF format. Since the results of the BCA-MD model calculations give absolute numbers of stable displacements, the final values were recorded as cross-sections in units of barn. This data representation is different from the common representation of “damage energy production cross-sections” with MT=444 as used by the NJOY processing code. In the latter case, the displacement cross-section varies according to the E_d value, which is not reasonable for current results. The resulting cross-sections were stored on file MF = 3 in section MT = 900. This MT number was adopted to store such displacement damage cross-section data on the ENDF data file. The data file contains also the displacement damage cross-sections based on the NRT approximation. These cross-sections are stored on file section MT = 901.

The ENDF file was processed with NJOY to provide the data in the ACE format for MCNP. The resulting file was successfully tested with the MCNP code showing no inconsistencies in the data representation.

Staff:

U. Fischer
A. Konobeev

Literature:

[20] A.Yu. Konobeyev, C.H.M. Broeders, U. Fischer, Improved displacement cross sections for structural materials irradiated with intermediate and high energy protons, Proc. 8th International Topical Meeting on the Nuclear Applications of Accelerator Technology (AccApp'07), July 30 - August 2, 2007, Pocatello, Idaho, USA, p.241.

[21] A.Yu. Konobeyev, U. Fischer, L. Zanini, Advanced evaluations of displacement and gas production cross sections for chromium, iron, and nickel up to 3 GeV incident particle energy, Tenth International Topical Meeting on Nuclear Applications of Accelerators (AccApp’11), Knoxville, TN April 3-7, 2011.

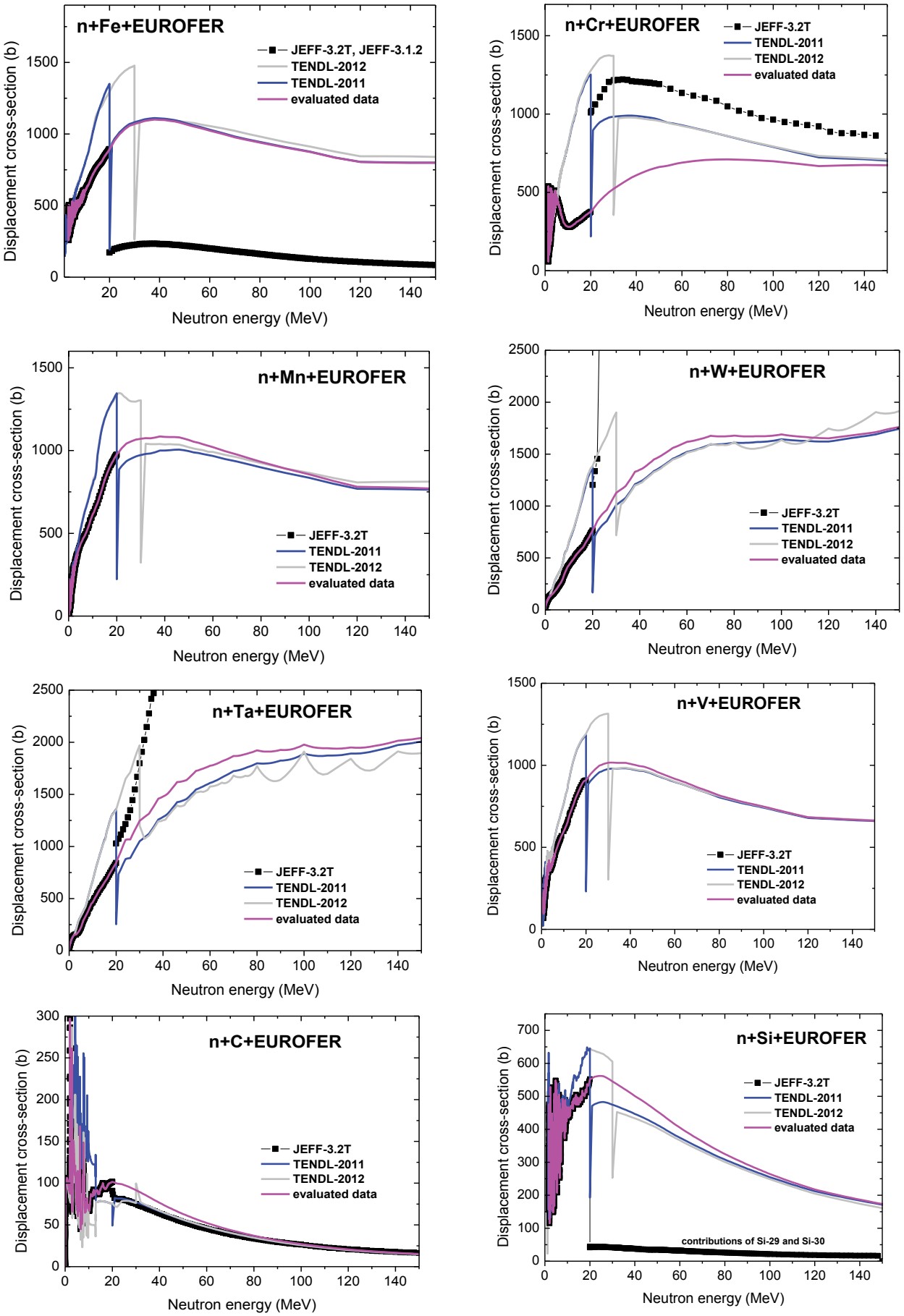

Fig. 6: Evaluated displacements cross-sections for Eurofer constituents in Eurofer.

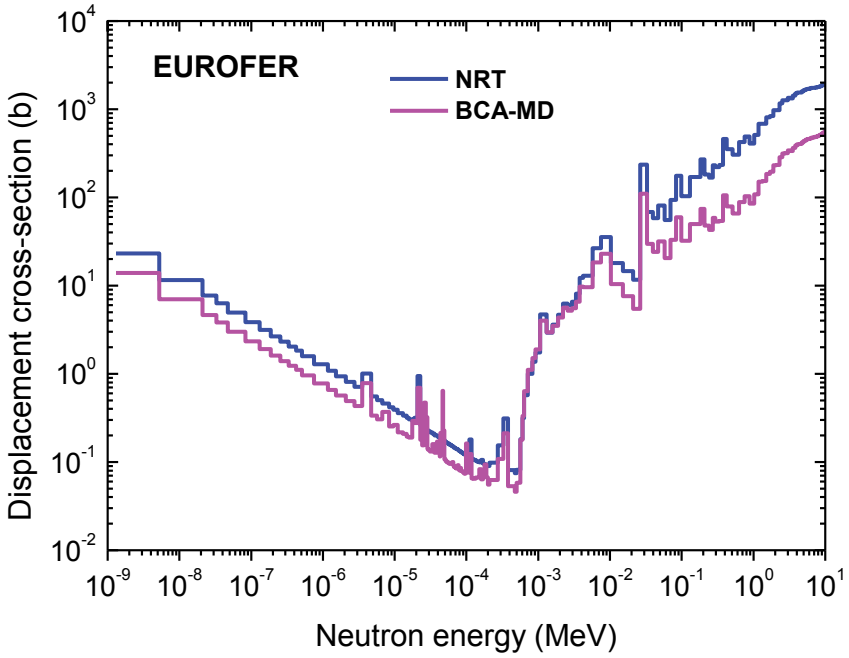

Fig. 7: Evaluated displacement cross-sections of EUROFER based on the BCA-MD approach and the NRT approximation.

Acknowledgement

This work was supported by Fusion for Energy under the Framework Partnership Agreement F4E-FPA-168.with collaboration by CCFE, UK; NRG, Netherlands; JSI, Slovenia; TUW, Austria; CIEMAT, Spain and IFIN-HH, Romania. The views and opinions expressed herein reflect only the author's views. Fusion for Energy is not liable for any use that may be made of the information contained therein.

Cu Experiment and TBM Nuclear Instrumentation (F4E-FPA-395-01)

Overall objective

This Specific Grant concerns the development of the experimental data base required for the validation of the nuclear data libraries and measurement techniques of nuclear responses relevant to ITER, the ITER Test Blanket Systems, IFMIF and DEMO. It covers the design, assembly, execution and measurements of an integral copper experiment in a 14-MeV neutron generator with dedicated pre- and post-analyses; assessment of integration issues for TBM nuclear instrumentation; development and testing of candidate sensors; and gas production measurements above 20 MeV. Activities are foreseen over 24 months from placement of the Specific Grant Agreement. The overall objective of the grant agreement was to provide the experimental data base required for the validation of the nuclear data libraries EFF and EAF developed in the frame of the EU Fusion Technology Program. The focus of the KIT tasks was on experimental validation activities of ITER and TBM design calculations and on development of detectors and measuring techniques.

Task 1
Design, assembly, execution and measurement of an integral Cu experiment relevant for determination of copper nuclear data under neutron irradiation at energies relevant for the fusion facilities (in collaboration with ENEA, AGH, JSI)

The task is concerned with the construction of an integral neutronics experiment on a copper assembly. KIT is involved in the design of the Cu assembly, the pre-analysis and the post analysis of the experiment and it will perform neutron and gamma ray spectra measurements with a NE-213 liquid scintillator spectrometer inside the Cu assembly under DT neutron irradiation at FNG.

The NE-213 scintillator has a diameter of 1.5“ and a height of 1.5”. It is coupled via a 60 cm long light guide to a photomultiplier. The scintillator’s response matrices for neutrons and gamma ray were calculated and experimentally verified [1]. The output signal will be processed with a CAEN 5720 digitizer. The digitizer has a resolution of 12 bit and a maximum sampling rate of 250 MS/s. Pulse shape discrimination to distinguish scintillator events from gamma-rays and neutrons is done on-the-fly with a special FPGA firmware.

Pre-analysis was performed with the MCNP Version 1.5 code [2] and a special source routine for the FNG neutron source. Neutron spectra were calculated for four experimental positions. The calculated neutron spectra and the measurement geometry (MCNP geometry plotter output) are shown in Figure 1. For the experiment, only two positions will be selected.

Staff:

A. Klix
M. Angelone (ENEA)

Literature:

[1] S. Guldbakke, H. Klein, A. Meister, J. Pulpan, U. Scheler, M. Tichy, S. Unholzer, „Response Matrices of NE213 Scintillation Detectors for Neutrons,“ Reactor Dosimetry, ASTM STP 1228, Harry Farrar IV, E. Parvin Lippincott, John G. Williams, and David W. Vehar, Eds., American Society for Testing and Materials, Philadelphia, 1994.

[2] “MCNP—A General Monte Carlo N-Particle Transport code”, Version 5, Report LA-UR-03-1987, Los Alamos, 2008

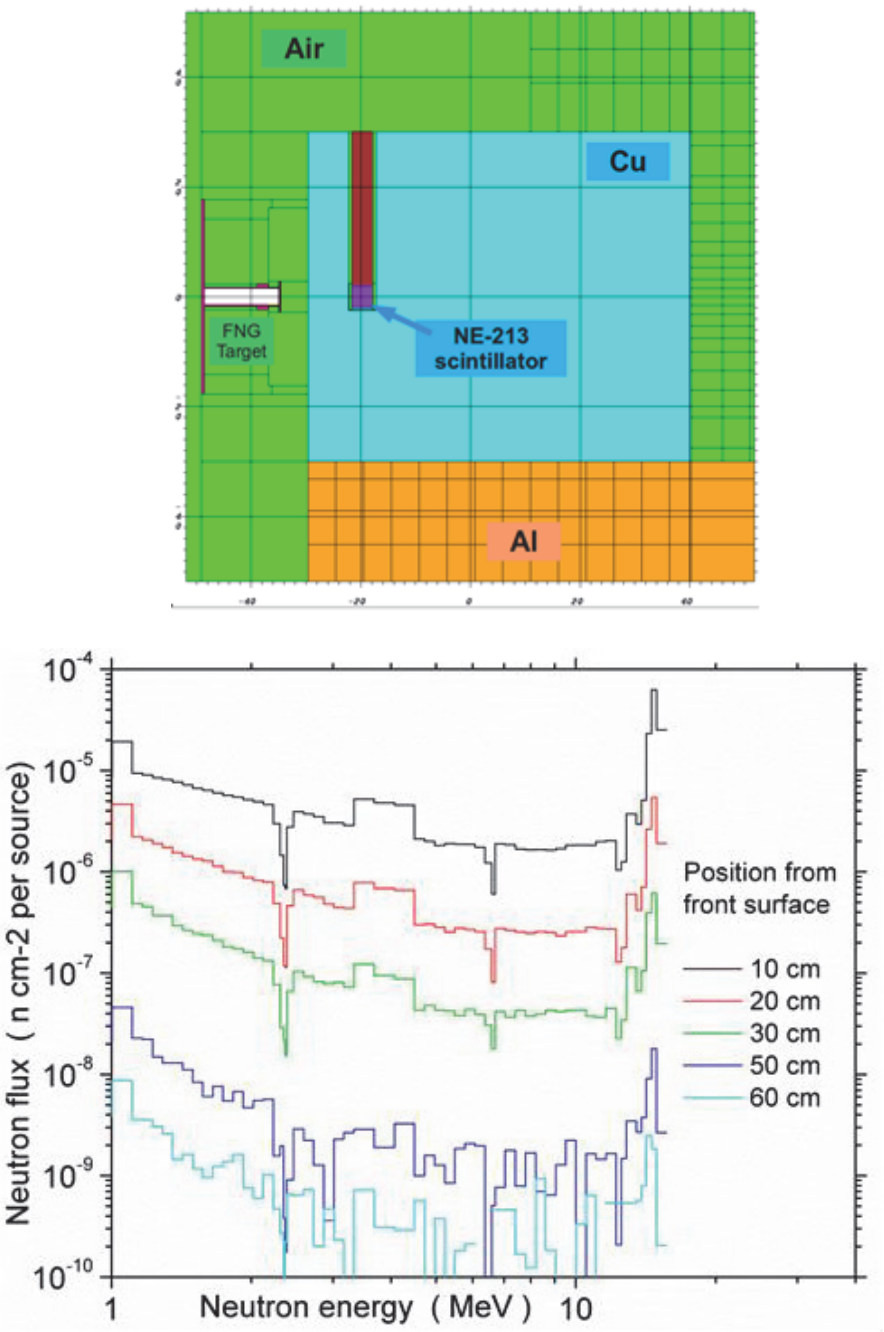

Fig. 1: MCNP geometry for the pre-analysis for measurement positions with the NE-213 (top) and calculated neutron spectra (bottom) in the Cu assembly.

Task 2.1
Pre-analysis of the copper benchmark experiment

The integral experiment on the Cu assembly will be conducted in the frame of Task 2 of FPA-395.01 with the objective to benchmark the available Cu nuclear data evaluation for fusion applications. The objective of Task 2.1 was to perform pre-analyses of the experiment in order to define suitable dimensions of the copper block and optimize the experimental set-up for the measurements. The pre-analyses included sensitivity/uncertainty assessments of the responses to be measured in the experiment. This was accomplished by means of cross-section sensitivity and uncertainty analyses using the deterministic SUSD3D code by JSI, Ljubljana, and the probabilistic MCSEN code by KIT.

In KIT's sensitivity analysis the recent MCSEN5 code has been used together with JEFF-3.1.1 nuclear cross-section data. The MCSEN5 sensitivity code has been developed in the frame of FPA-168.01 as extension to the MCNP5 Monte Carlo code for probabilistic sensitivity analysis. The executable for the present analysis was built on the basis of version MCNP5-1.40 together with the DT source subroutine for the Frascati Neutron Generator (FNG). The MCNP geometry model prepared by ENEA for the pre-analysis was used in the present calculation, though surface tallies were utilized, instead of the cell detectors defined in the original geometry, in order to improve the statistical convergence in the sensitivity analysis. The sensitivity was investigated for the responses to be measured in the experiment, i.e. reaction rates of several activation foils (Al, Ni, In, W and Au) and neutron and photon flux spectra. Integrated relative sensitivities and these energy profiles with respect to major reactions (elastic and inelastic scattering channels, (n,2n) reaction, and some gas-production reactions) were calculated for each reaction rate at each measuring points. The same quantities were estimated for the neutron/photon fluxes integrated in five energy intervals at several measuring points. The results show that the reaction rates of the threshold detectors (Al, Ni, and In) are sensitive to the inelastic scattering, ^{63,65}Cu (n,2n) and ^{63}Cu (n,n'p) cross sections. The Au and W (n,γ) reactions are mostly sensitive to the elastic scattering cross sections and the (n,γ) reaction cross sections in the low energy range. Other contributions are not significant. The results for the neutron fluxes are very consistent with to those for the activation foils. Fig. 2 shows, as an example, the radial sensitivity profiles for the total neutron flux density to the most important ^{63,65}Cu reaction cross-sections.

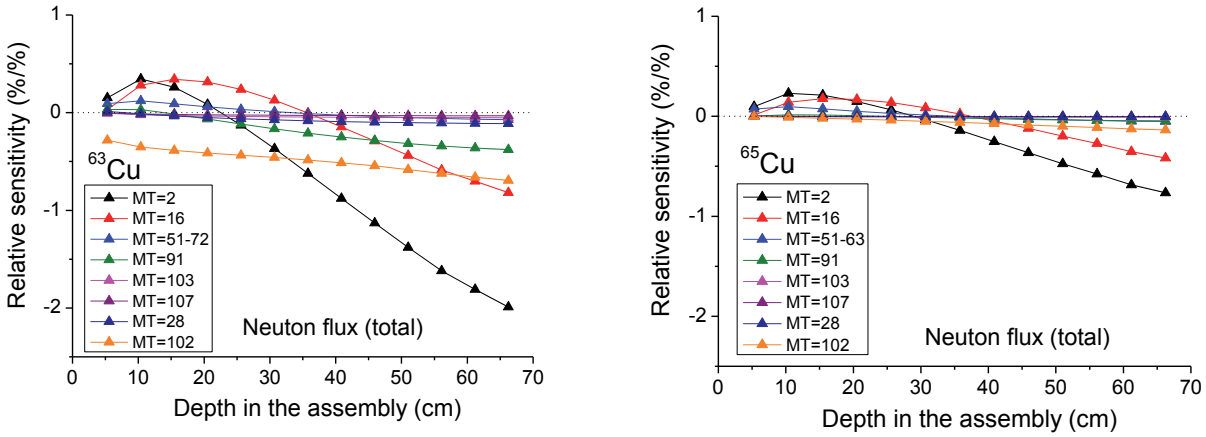

Fig. 2: Radial sensitivity profiles of the total neutron flux to the most important ^{63}Cu (left) and ^{65}Cu (right) reaction cross-sections in the copper assembly.

Staff:

U. Fischer
K. Kondo
I. Kodeli (JSI)

Task 3
Development of measurement techniques relevant to ITER, the ITER Test Blanket Systems, IFMIF and DEMO, including their qualification under system relevant conditions (temperature, magnetic field, chemical environment etc.; in collaboration with ENEA and CCFE)

Task 3.1
Assessment of TBM requirements for nuclear instrumentation, definition of related research plan and assessment of design integration feasibility

KIT has been involved in the development and qualification of nuclear instrumentation for the TBM for several years. The aim of this task is an assessment of the conditions in the TBM relevant for instrumentation as well as the state-of-the-art of neutron flux detectors which can be expected to qualify for TBM conditions if further R&D work is performed. The Task Deliverables are three reports:

In the first Interim Report a mapping of the environmental conditions for TBM was reported. This analysis was referring to both HCLL and HCPB TBM, however it is worth to mention that the installation of any nuclear sensor in the TBM must fulfil a number of conditions and constrains most of which are imposed by the environment surrounding the TBM itself. TBM is included in a larger environment called Tritium breeding system (TBS). This approach is usually referred to as *"integration"* of the instrumentation in the TBS.

The Second Interim Report of Task-3.1 focussed on a) Functional requirements and specifications of candidate sensors and b) Evaluation of current detector designs.

The final report focusses on *Needs for further development, estimated efforts, risks and potential; Proposal of a research plan up to integrated testing in JET DT experiment.* Another point discussed in the report is concerning the proposal for the number, type and position of nuclear detectors inside EU-TBM.

The candidate detectors considered in the reports are diamond and SiC detectors, self-powered neutron detectors and a neutron activation system. Micro fission chambers have not yet been considered in these reports since they are not under investigation in FPA-395-SG1.

Staff:

A. Klix
M. Angelone (ENEA)

Task 3.2
Self-powered Neutron Detectors (SPND)

Self-powered neutron detectors (SPND) were studied before within GRT-056 to see whether this type of detector can be proposed for further testing and qualification for neutron flux monitoring in an ITER-TBM. SPND have a number of interesting properties such as small dimensions, capability to operate in harsh environments, absence of external bias, simplicity etc. so they are attractive neutron monitors for TBM in ITER. However, several draw-backs must be considered, among them the most important is the fact that present available SPND are optimized for operation in a thermal nuclear reactor where the neutron spectrum is much softer than that expected in a TBM. This fact can limit the use of SPND in a TBM since the effective cross sections for the production of beta emitters are much lower in a fast neutron spectrum.

This task is concerned with further investigation of candidate emitter materials and their response to fast neutrons. A prototype SPND will be prepared for testing under a TBM-like radiation field. Additional testing under simultaneous representative EM fields and temperatures (up to 300°C) will be performed. In particular, EM tests are planned at ASDEX in Garching.

Staff:

A. Klix
M. Angelone (ENEA)

Task 3.4
Activation foils

An activation system is an attractive nuclear instrumentation for the TBM due to several advantages: no need for re-calibration, absolute neutron flux measurements with information on the neutron spectrum, could be used to monitor the performance of other nuclear instrumentation, only mechanical parts inside TBM so that it could survive all operational phases of ITER and the TBMs. A disadvantage is the high invasiveness and complicated integration into the TBS and ITER infrastructure.

Activation materials leading to short-living isotopes have been investigated within Grant 056 with the aim to develop a short cycle measurement method with coarse time resolution of the neutron flux measurement.

In this task, the proposed activation materials and the accuracy of the neutron flux measurement utilizing them will be further investigated in collaboration with CCFE. Some of the activation cross sections of interest will be experimentally checked at the ASP facility in Aldermaston (UK) and further tests of simultaneous activation measurements will be performed at TUD-NG in Dresden (Germany) with the pneumatic sample changing system constructed by KIT and TUD for this purpose.

Staff:

A. Klix
S. Lilley (CCFE)
D. Gehre (TUD)

Acknowledgement

This work was supported by Fusion for Energy under the Framework Partnership Agreement F4E-FPA-395-01 with collaboration by ENEA, Italy; AGH-UST, Poland; JSI, Slovenia; ASCR-NPI, Czech Republic and CCFE, UK. The views and opinions expressed herein reflect only the author's views. Fusion for Energy is not liable for any use that may be made of the information contained therein.

Monte Carlo Radiation Transport Calculations for Nuclear Fusion Facilities (HPC-FF-FSNMCFU)

Objective

The objective of the HPC-FF-FSNMCFU project was to provide computational neutronics support for the design development of ITER fusion reactor components utilizing the capabilities of the High Performance Computational supercomputer system for fusion applications (HPC-FF). The optimization and improvement of ITER radiation shielding parameters was achieved by the massive use of large-scale parallel Monte Carlo transport computations on HPC-FF.

Introduction

The computational simulations play important role in development of thermonuclear fusion devices. In that development, there is a great demand for computations in field of fusion neutronics. Only large, powerful multi-hundred CPU clusters, such as the HPC-FF system for fusion applications at Jülich Supercomputing Centre [1] could provide necessary resources for massive parallel Monte Carlo particle transport simulations for challenging tasks of shielding and activation analyses in ITER fusion reactor. It was demonstrated [2] that the parallel use of hundreds of the HPC-FF CPUs substantially accelerates the Monte Carlo calculations with the MCNP5 code [3]. Due to the available computational resources of the HPC-FF, it was possible to perform challenging radiation transport calculations in large and complicated toroidal geometry of ITER taking into account actual heterogeneous geometry directly converted from the underlying CAD models by using the McCad geometry conversion tool and related visualization capabilities [4].

Results

We have achieved substantial results in improvement of the radiation shielding performance of the ITER Upper Electron Cyclotron Heating (ECH) launcher and Diagnostics Equatorial and Upper Ports of ITER by applying high computational power of the HPC-FF supercomputer. To reach the ultimate goal of the radiation shielding for the ITER ports, we have conducted radiation transport computations with the Monte Carlo method using its inherent capability to track in parallel each particle individually on separate computer core of the HPC-FF. This method demonstrated strong scalability of the computation performance and speed-up by utilizing several hundreds of the HPC-FF cores. The parallel version of the Monte Carlo MCNP5 code has been compiled with the Intel Fortran and C/C++ compilers, and the MPI libraries. The MCNP5 parallel performance had been estimated approaching of a speed-up of 700 on 1600 cores of HPC-FF.

The challenging tasks of deep-penetration radiation transport for fusion neutronics in ITER were addressed successfully, e.g. nuclear heating and helium production rate have been calculated with high spatial resolution using the MCNP5 mesh tally capability. Long term experience of neutronics computational support for the design development of the ITER Upper Electron Cyclotron Heating (ECH) launcher [5] and ITER Diagnostics Ports [6] has shown that some tasks could be solved only on supercomputers. Among such tasks, the large-scale Shut-Down Dose Rates (SDDR) calculations are especially important to guarantee nuclear safety for the personnel along the maintenance access to the ITER ports. As result of the methodological work in solving the SDDR tasks, the R2Smesh interface [7] was developed to produce mesh-tally of shutdown dose rates superimposed over the MCNP5 model geometry. This interface allows exploring radiation pathways and pinpointing critical locations.

The recent achievements for the neutronics analysis of the ITER Upper ECH launcher are reported in works [8, 9]. The benefits of the use of the HPC-FF supercomputer resources in application for the neutronics analyses for the ITER Diagnostics Equatorial and Upper Ports [10-12] could be demonstrated with one brief excerpt from last investigation of the shielding

performance of the Upper Port Plug (UPP). In that UPP study neutron flux distributions and nuclear heating results were calculated in mesh tallies composed with 3D mesh-elements (voxels) with the MCNP5 code. The 3-D maps of total neutron fluxes (n-fluxes) are plotted in Figures 1 and 2. Mesh tally geometry was specified in the local coordinate system which was adjusted to the geometry of UPP. The potential capabilities of the radiation shielding of the ITER ports were studied by visualization of the neutron pathways around the UPP. As result, an excessive neutron streaming was revealed inside the gaps around the UPP shown in Figures 1 and 2. One can see that the total neutron flux is reduced drastically behind the UPP from 2e14 n/cm^2/s to 1e8 n/cm^2/s, indicating about strong radiation shielding. But inside the gaps neutrons can stream without any attenuation, causing activation of the structures behind the UPP where the personnel access is planned. Therefore, to solve this problem we have found several design solutions to mitigate this radiation streaming. These solutions are presented in details in works [2, 11-12]. The simplest one of them consists in filling the void space at the lateral and bottom side gaps with specially shaped blocks made of steel. The possibilities for ITER UPP shielding design improvements were thoroughly analysed in works [2, 12] with value of Shut-Down Dose Rate (SDDR) inside the interspace behind the UPP as a target nuclear response function of the UPP shielding optimization.

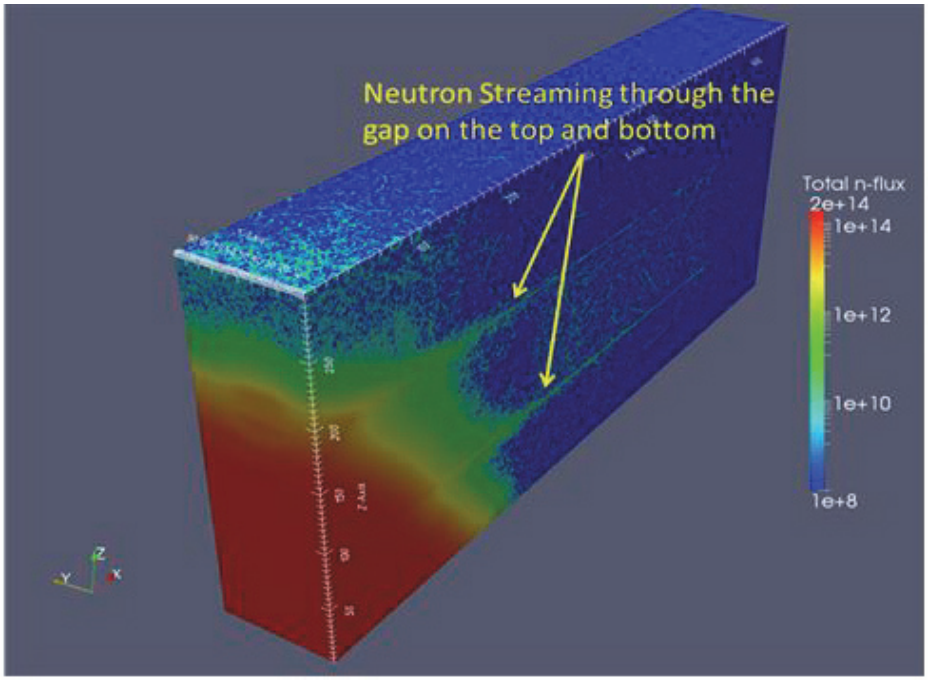

Fig.1: 3D map of total neutron flux distribution over the ITER Diagnostics Upper Port Plug (UPP) with revealing of the neutron streaming along the gaps on the top and bottom of UPP. Map is produced using the HPC-FF supercomputer for the FSNMCFU project.

The results obtained during the reporting period of 2013 were reported at several international conferences and published in peer-reviewed journals [2, 4, 8-12].

Staff:

U. Fischer
K. Kondo
A. Serikov
B. Weinhorst

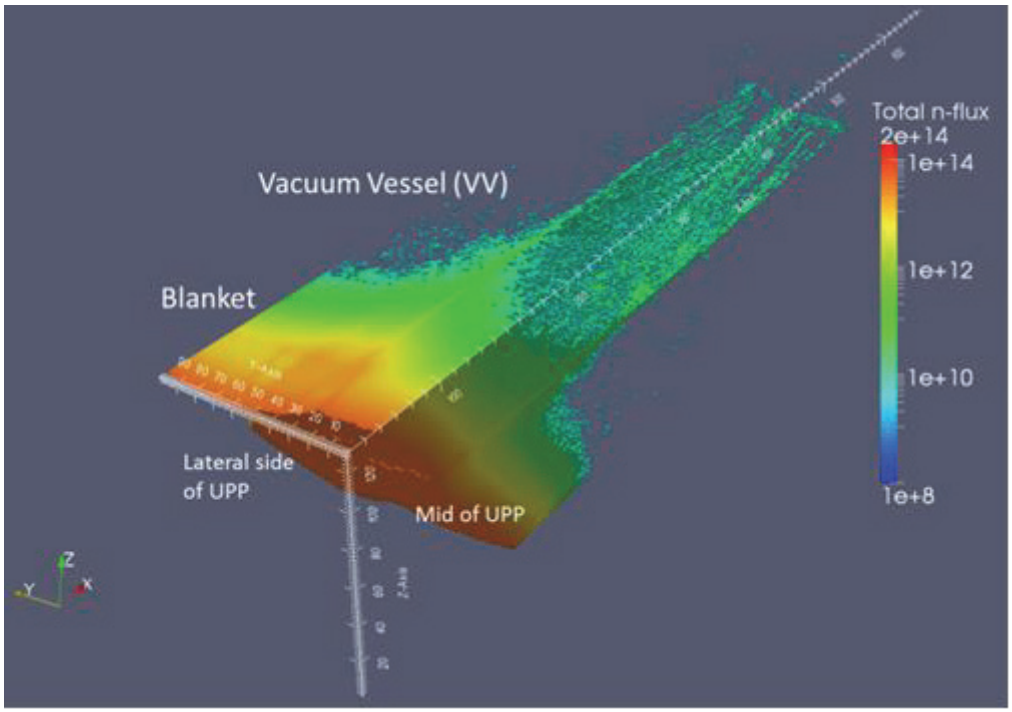

Fig. 2: Visualization of radiation transport with revealed pathways of excessive neutron streaming for the ITER Diagnostics Upper Port Plug (UPP) on its lateral side, obtained with massively parallel MCNP5 calculations on HPC-FF with the FSNMCFU project.

Literature:

[1] HPC-FF system: http://www.fz-juelich.de/ias/jsc/EN/Expertise/Supercomputers/JUROPA/JUROPA_node.html.

[2] A. Serikov, U. Fischer, C. S. Pitcher, A. Suarez, B. Weinhorst, "Computational Challenges of Fusion Neutronics for ITER Ports," Proceedings of Joint Int. Conference on Supercomputing in Nuclear Application and Monte Carlo (SNA+MC 2013), Paris, France, Oct. 27-31, 2013.

[3] X-5 Monte Carlo Team, "MCNP—A General Monte Carlo N-Particle Transport Code, Version 5, Volume I, MCNP Overview and Theory," LA-UR-03-1987, Los Alamos National Laboratory (Apr. 24, 2003; revised Oct. 3, 2005).

[4] D. Grosse, U. Fischer, K. Kondo, D. Leichtle, P. Pereslavtsev, A. Serikov, "Status of the McCad geometry conversion tool and related visualization capabilities for 3D fusion neutronics calculations," Fusion Engineering and Design, 88 (2013) 2210-2214, http://dx.doi.org/10.1016/j.fusengdes.2013.02.146.

[5] A. Serikov, U. Fischer, et al., "Evolution of shielding computations for the ITER Upper ECH Launcher," Nuclear Technology, 175 (1) (2011) 238–250.

[6] A. Serikov, U. Fischer, D. Leichtle, C.S. Pitcher, "Monte Carlo radiation shielding and activation analyses for the Diagnostic Equatorial Port Plug in ITER," Fusion Engineering and Design, 87 (2012) 690–694, http://dx.doi.org/10.1016/j.fusengdes.2012.02.003.

[7] M. Majerle, U. Fischer, D. Leichtle, A. Serikov, "Verification and validation of the R2Smesh approach for the calculation of high resolution shutdown dose rate distributions," Fusion Engineering and Design, 87 (2012) 443-447, http://dx.doi.org/10.1016/j.fusengdes.2011.12.010.

[8] B. Weinhorst, A. Serikov, U. Fischer, P. Spaeh, D. Strauss, "Neutronic Analyses for the ITER electron cyclotron-heating upper launcher," 11th Int. Symp. on Fusion Nuclear Technology (ISFNT-11), Barcelona, Sept. 16-20, 2013, to appear in Fusion Engineering and Design.

[9] B. Weinhorst, A. Serikov, U. Fischer and D. Grosse, "Status of the neutronic analyses for the electron cyclotron-heating upper launcher of ITER," Proceedings of the German Annual Meeting on Nuclear Technology (KTG-2013), Berlin, 14-16 May 2013.

[10] A. Serikov, U. Fischer, M. Henderson, D. Leichtle, C.S. Pitcher, P. Spaeh, “Neutronics for equatorial and upper ports in ITER,” Fusion Engineering and Design, 88 (2013) 1965–1968, http://dx.doi.org/10.1016/j.fusengdes.2013.03.037.

[11] A. Serikov, L. Bertalot, U. Fischer, S. Pak, A. Suarez, R. Villari, “Neutronic Challenges for the Estimation of Shut-Down Dose Rates in ITER Ports,” Transactions of the American Nuclear Society, 109 (2013) 1163-1166.

[12] A. Serikov, L. Bertalot, U. Fischer, C.S. Pitcher, A. Suarez, V.S. Udintsev, B. Weinhorst, “Shut-Down Dose Rate Analysis for the ITER Diagnostic Equatorial and Upper Ports,” 11th Int. Symposium on Fusion Nuclear Technology (ISFNT-11), Barcelona, Sept. 16-20, 2013, accepted in Fusion Engineering and Design, http://dx.doi.org/10.1016/j.fusengdes.2014.01.025.

Acknowledgement

This work, supported by the European Communities under the contract of Association between EURATOM and Karlsruhe Institute of Technology, was carried out within the framework of the European Fusion Development Agreement. The views and opinions expressed herein do not necessarily reflect those of the European Commission.

Monte Carlo Calculations of Covariances for Nuclear Reactions in Fusion Technology Applications (HCP-FF-FSNMCCO)

Objective

The objective of the FSNMCCO project was to utilize the capabilities of the HPC-FF parallel super computer for calculations of nuclear reaction cross-sections and their covariances using the Monte Carlo method as a part of uncertainty assessments in fusion neutronics applications.

Calculation of activation, gas production and displacement cross-sections for structural materials using the Monte Carlo method

In 2012-2013 the HPC-FF resources were used for calculations of activation, gas production and displacement cross-sections for a number of structural materials irradiated with protons of intermediate and high energies. The task comprised the calculation of covariance matrices combined with uncertainties of principal parameters responsible for simulations based on the intranuclear cascade evaporation model. The parameters describing nucleon-nucleon and pion-nucleon cross-sections, and nuclear level density parameters were involved in the procedure of the uncertainty assessment. The computations based on the Monte Carlo method were performed using the intranuclear cascade evaporation model implemented in the CASCADE (JINR, KIT) code. The final treatment of results was performed using the BEKED (KIT) code package. The obtained information was used for the evaluation of activation, gas production and displacement cross-sections for structural materials. Fig. 1 shows, as an example the displacement cross-section generated for ^{27}Al irradiated with protons.

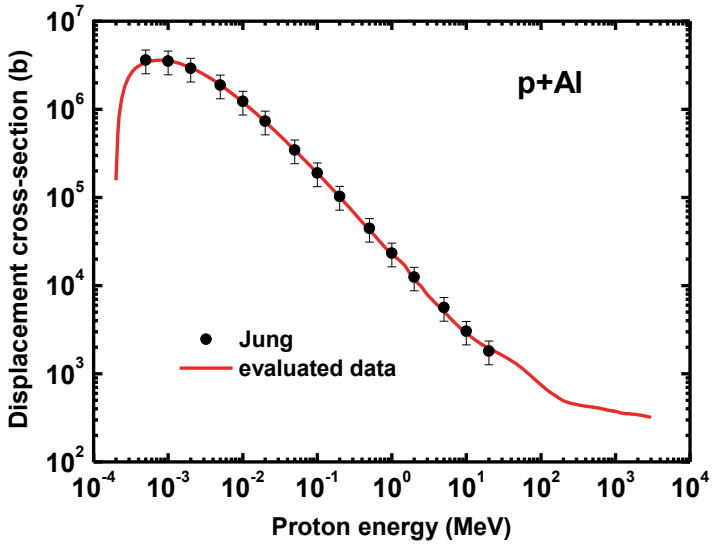

Fig. 1: Evaluated displacement cross-section for proton interactions with ^{27}Al.

Results of the calculations were reported at the JEFF Meetings, April 24-27 2012, NEA Data Bank, Paris, at the IAEA Technical Meeting on Primary Radiation Damage, October 1-4, 2012, and at the International Conference Nuclear data for Science and Technology, March 4-8 2013, New York.

Staff:

A. Konobeev
U. Fischer
P. Pereslavtsev

Literature:

[1] A. Yu. Konobeyev, U. Fischer, P. E. Pereslavtsev, D. Ene, Evaluated activation cross section data for proton induced nuclear reactions on W up to 3 GeV incidence energy, International Conference Nuclear data for Science and Technology, New York, March 4-8 2013.

Acknowledgement

This work, supported by the European Communities under the contract of Association between EURATOM and Karlsruhe Institute of Technology, was carried out within the framework of the European Fusion Development Agreement. The views and opinions expressed herein do not necessarily reflect those of the European Commission.

System Level Analysis - Neutronics (WP13-SYS-02)

Overall objective

The analyses on the system level of the EFDA PPPT Work Programme considered the interaction of several systems and included neutronic and electromagnetic (EM) analyses and plasma disruption simulations. The related results are major design driver for the tokamak architecture and most tokamak components, in particular the breeding blanket, the divertor, the shielding, the magnets, ports, remote handling tools, etc.

The objectives of the 2013 neutronics tasks have been (i) to develop a suitable DEMO MCNP model, (ii) to conduct critical neutronic design assessments e. g. of the tritium breeding performance, and (iii) to develop and improve neutronic analysis tools and their integration in the design and analysis process of tokamak components.

The WP13-SYS-02 neutronics activities were conducted in a joint effort of CCFE (UK), CEA (France), CIEMAT (Spain), ENEA (Italy), HAS (Hungary), IPPLM (Poland), JSI (Slovenia), and KIT (Germany). KIT co-ordinated the activities (Task T-01), conducted tasks on the “Development of a generic DEMO MCNP model” (Task T-05), on the “Tritium Breeding Ratio assessment of the HCPB DEMO” (Task T-06, D2), on the “Activation and rate map calculation of the HCPB DEMO” (Task T-08), the “Development of European Tool for the CAD import in MC code” (Task T-11) and contributed to Tasks 12 on “Development of a single European tool for coupled radiation transport and activation calculations”.

In the following summaries of the related task activities are given.

Task T01:
SYS-02 Neutronics task co-ordination

Objective

The objective of the task co-ordination was to guide and monitor the WP13-SYSY-02 neutronic activities to ensure the analyses and the development works are performed in a consistent manner and in agreement with the prescribed task specifications.

The following activities were performed, guided and monitored by the SYS-02 neutronic task coordinator:

Preparation of DEMO MCNP blanket concept-specific models, assessment of the shielding performance and the TBR

MCNP models were developed for the HCPB, HCLL, and WCLL blanket concept consistent with the updated DEMO tokamak design. The model development was carried out in two steps:

1. A generic MCNP model was prepared by KIT on the basis of the DEMO CAD model provided by EFDA. This model empty breeding blanket segment boxes.
2. Based on the generic model, three different MCNP models were developed for the HCPB, the HCLL, and the WCLL breeder blanket design variants by KIT, CIEMAT and ENEA, respectively, with the proper blanket module segmentation in each case. The breeder blanket modules were prepared on the basis of available CAD design models of the HCPB, HCLL and WCLL blankets.

Using these models tritium breeding assessment analyses have been performed. For the HCLL and WCLL blanket variants, it was also assessed by JSI how the first wall (FW) and armour affects the TBR. The impact of the loss of the blanket coverage area due to the integration of H&CD systems was assessed by HAS on the example of the HCLL blanket variant. The results are as follows:

- An ITER-like ECRH port plug with a (poloidal-toroidal) front area of 4 m^2 reduces the TBR by ~ 0.65% (HCLL blanket variant).
- Increasing the FW tungsten armour thickness from 2 to 3 mm reduces the TBR by ~0.2% (HCLL and WCLL blanket variants).

The TBR results for the currently assumed conceptual designs are very similar (TBR~1.03) and show the need to improve the breeding blanket design and configuration, e.g. by decreasing the number of blanket modules (i. e. larger module size) and minimizing the amount of steel structure in the breeding modules. (The currently assumed design of the breeding blankets is not optimized in this regard since it is based on the TBM design.)

The blanket concept specific neutron shielding calculations showed that the currently assumed radial build is sufficient to shield the TF coils provided that an efficient shielding material like WC can be used in the radiation shield. Otherwise the assumed radial dimensions need to be increased.

NB port integration assessment: neutron streaming in NB port

A Neutral Beam (NB) port neutron streaming assessment made by CCFE has shown that an ITER-like NB can be integrated in a 16 TF-coils DEMO. Integration seems possible up to ~18-20 TF coils. An MCNP model was built including an ITER-like NB port inclined for the neutral beam to be tangent on the inboard FW. The assumed shielding was found to be insufficient to meet the DEMO superconducting coil criteria for the power density. The unused available space between NB port and TF coils indicates that the same configuration could also be implemented in an 18 or 20-TF-coils DEMO.

In-vessel components activation calculation (KIT, CIEMAT, LEI)

Activation and decay heat calculations have been performed for the HCPB and the HCLL DEMO by KIT and UNED, respectively. Major contributor to the decay heat is the Eurofer steel which is employed as structural material for the HCPB and HCLL DEMO blankets. The decay heat is dominated by the Eurofer steel which in both DEMO variants is employed as structural material.. The decay heat both for short (a few days) and longer (more than a year) cooling times after shut-down is larger for the HCPB than for the HCLL DEMO. The differences are mainly caused by the different neutron spectra with a much softer spectrum for the HCPB blanket with beryllium used as neutron multiplier. For assessing the impact of potential alternative structural materials, comparison calculations were performed by LEI for a single outboard blanket module of the HCLL DEMO assuming High-Temperature Ferritic-Martensitic (HT-FTM) steel and SS-316 (LN) as structural material. The decay heat of Eurofer is highest until about 10 to 100 years after shut-down. The decay heat of HF-FTM steel is lower by one to two orders of magnitude while that of SS-316 is lower by one order of magnitude for cooling times less than 1 to 5 years and approaches the decay heat level of Eurofer afterwards.

Neutronic tool development: Benchmarking of alternative MC tools

The benchmarking of TRIPOLI, SERPENT, and FLUKA, identified in the frame of the WP12-DTM04 work as candidates for the further development of alternative Monte Carlo codes for DEMO nuclear analyses, was performed on the generic DEMO model with the associated neutron source. The TRIPOLI benchmarking was successful while the benchmarking of SERPENT and FLUKA could not be completed due to insufficient capabilities of the current versions of the codes in handling the DEMO model and performing the coupled neutron-photon transport simulations. In

- TRIPOLI: From the benchmark results provided by CEA it can be concluded that the TRIPOLI code would be fully capable to replace MCNP in transport calculations. Supporting tools such as the CAD import software McCad or the coupled radiation transport and activation scheme would need to be adapted to TRIPOLI.

- SERPENT: The benchmark model for SERPENT prepared by CCFE with a dedicated tool could not be completed due to some existing deficiencies of the code for handling the geometry and the source representation. In addition, coupled neutron-photon calculations cannot yet be done with the current SERPENT version. It was concluded that this work should be completed in the future. It is noted that the SERPENT development is an open-source project relying on voluntary contributions and organized by a single person (Jaakko Leppänen of VTT, Finland).
- FLUKA: A FLUKA benchmark model has been generated by IPPLM with some effort and some limitations using a yet unpublished version of the MCAM geometry conversion software of the FDS team, Hefei, China. It was not yet possible to perform a transport simulation calculation raising doubts on whether FLUKA could really be a candidate to replace MCNP in the near future for fusion neutronics calculations.

Neutronic tool development: CAD import in Monte-Carlo codes

The McCad software tool for the conversion of CAD geometry models for Monte Carlo particle transport simulation codes has been further developed. Its capabilities were extended, and its core algorithms were improved and re-designed for the implementation. The new McCad version 0.4.0 has already integrated new algorithms for the solid decomposition and the void generation. It also includes a new interface for the materials editing and assignment integrated to the GUI (Graphical User Interface). McCad 0.4.0, furthermore, has the new capability to convert CAD geometry models into the geometry representation of the TRIPOLI Monte Carlo code.

These improvements and new functions have been tested, verified and utilized with several DEMO and ITER applications. The applications, which involve very complex geometries, have demonstrated the efficiency and accuracy of the new conversion functions and showed a significantly improved performance of the CAD model conversion process. There are, however, still some remaining problems with the solid decomposition and the memory consumption which call for a further optimization of McCad's conversion algorithms.

The new MCad version, 0.4.0, is already available and will be provided to the external users for further testing and applications. It has been heavily used to generate the DEMO models for the MCNP calculations within the WP13-SYS-02 activities.

Neutronic tool development: Coupled radiation transport and activation calculations

The Rigorous-2-Step (R2S) methodology has been independently implemented by several European institutions, most notably R2SMesh (KIT), MCR2S (CCFE) and R2SUNED (UNED). The currently available R2S tools are based on neutron transport calculations with the MCNP code and activation calculations with FISPACT or ACAB codes coupled by several interfaces for the data exchange. The neutron flux spectra are provided on a superimposed mesh. The tools have been verified and validated against computational and experimental benchmarks. They are now applied in routine use for engineering design, operation and safety case of fusion technology.

There is, however, a general limitation in turnover and reliability of such calculations due to the intricate, non-standard nature of the coupling scheme and the underlying transport and activation codes, but also due to the stringent requirements on spatial and energy resolution for accurate results. Furthermore, the uncertainty of the final nuclear responses due to the propagation of uncertainties in all steps of the procedure is not yet accounted for. The task conducted in the frame of the WP13-SYS-02, led by D. Leichtle, F4E, aimed at specifying a common R2S scheme for DEMO shut-down dose rate analyses. This specification covered the areas of user requirements, functional requirements, architecture and quality assurance. As a major result, a common format for the decay gamma source representation was elaborated which will be implemented and tested in the follow-up programme within the Eurofusion project. In addition, a procedure was elaborated by UNED which enables to propagate the

uncertainties in the decay photon source of an activated system to the dose rate maps obtained by Monte Carlo photon transport simulations. The uncertainties due to both the gamma source input variables and those corresponding to the Monte Carlo transport simulation have been taken into account. The applicability of the methodology was assessed by performing a sample exercise which showed the uncertainty information provided by the method.

Staff:

U. Fischer
D.Leichtle (F4E)
L. Lu
P. Pereslavtsev

Task T05
Development of generic DEMO MCNP model

Objective

The objective was to develop a generic DEMO model which would serve as common basis for the integration of HCLL, HCPB or WCLL breeder blankets. This allows to perform nuclear analyses for the different DEMO variants and to compare the nuclear performance of the related blanket concepts for the same basic reactor configuration.

The generic model that serves as a common platform for the integration of the breeder blankets of different types was developed at EFDA on the basis of results of system code analyses, integration and maintenance considerations for the reactor components assuming that the DEMO will operate in a steady state. A sufficient blanket space is reserved in this model for the arrangement of the breeder blankets and manifolds. All other reactor components such as vacuum vessel, divertor, ports, magnet coils are the same in all reactor concepts. Table 1 shows the main parameters for the DEMO reactor as provided by PROCESS code results.

Table 1: Main parameters of the DEMO reactor.

Major radius, (m)	9.0
Minor radius, (m)	2.25
Plasma elongation	1.66
Plasma triangularity	0.33
Plasma peaking factor	1.7
Fusion power, (MW)	2119.
Net electric power, (MW)	500.0

On the basis of the generic CAD model of the DEMO reactor, developed by EFDA, a 22.5° torus sector model was created at KIT for numerical simulations, see Fig. 1. This model includes the plasma chamber, a banana-shaped space for the insertion of the breeder blankets and manifolds, divertor, vacuum vessel and ports, toroidal and poloidal magnetic field coils.

Structural elements inside the vacuum vessel are assumed to be manufactured from SS-316. The vacuum vessel has a radial thickness 56 cm including 5 cm thick steel walls at the front and the back. Its interior is filled with a homogenized mixture of 80% SS-316 and 20 % water. The toroidal magnetic field coils (TFC) are enclosed in a steel casing of 5 cm thickness. The divertor is modeled as a solid steel body except two layers facing the plasma. The first layer is a 5 mm thick tungsten armour followed by a second ~ 45 mm thick layer with a homogenized mixture of 12% W, 30% steel, 1% Cu and 57% void.

The generic MCNP model was generated by conversion of the CAD model with the McCad conversion tool. Prior to the conversion the CAD generic model was carefully checked for geometry errors such as gaps or overlaps and the presence of spline surfaces which were replaced by second order surfaces. The material assignment was performed on the McCad

platform using the corresponding feature implemented in McCad. A vertical cut of the MCNP generic model is shown in Fig. 2.

The McCad conversion of the CAD model resulted in 410 material and 204 void cells included in the MCNP geometry model. The MCNP generic model was verified by means of stochastic volume calculations. No lost particles were found for 10^8 source particles used for the tallying.

The generic MCMP model is available in the EFDA IDM at the following link: WP13-SYS02 - MCNP DEMO model with empty HCPB blanket modules .

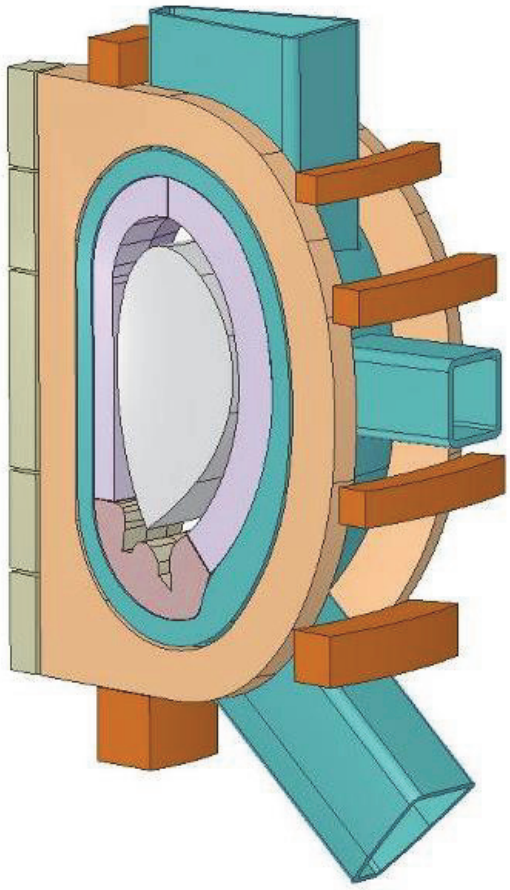

Fig. 1: Generic DEMO reactor model (22.5°torus sector, CAD model).

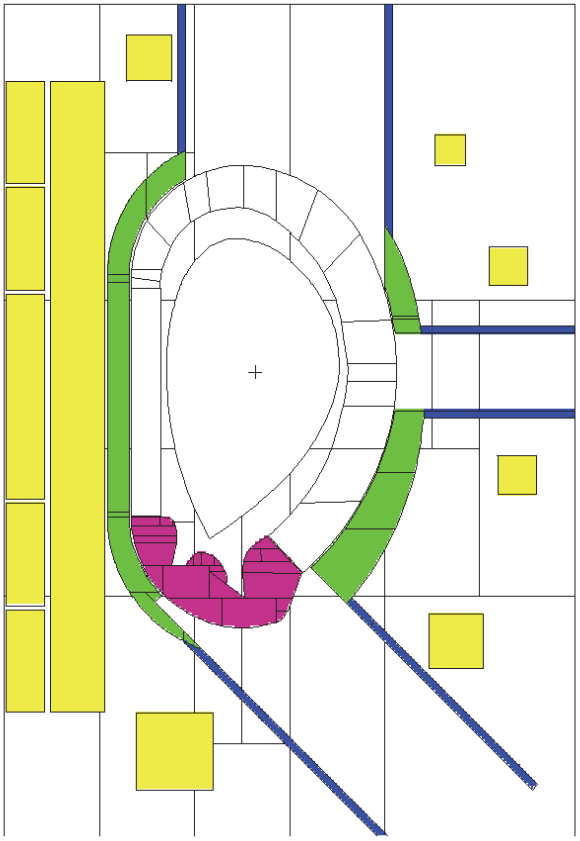

Fig. 2: Generic MCNP DEMO reactor model (22.5°torus sector, vertical cut).

Staff:

U. Fischer
P. Pereslavtsev
L. Lu

Task T06
Tritium Breeding Ratio Assessment for HCPB DEMO

Objective

The objective of this task was to perform an assessment of the tritium breeding and shielding performance of the HCPB DEMO using a dedicated MCNP model derived from the generic DEMO model by including HCPB blanket modules in the model.

The HCPB blanket concept is based on a multi-module segmentation scheme. Such an approach enables flexible installation, maintenance and disassembling of the plasma in-vessel components by means of remote access tools. Two HCPB DEMO blanket module were designed for the arrangement in the inboard and the outboard banana shaped blanket spaces of the generic DEMO model. 20 blanket modules are arranged around the plasma (10 inboard and 10 outboard). The size of an inboard blanket module is about 0.98 m x 1.35 m (poloidal x toroidal) and for an outboard module 1.17 m x 1.53 m. The blanket modules are welded on a massive back plate and attached to the blanket manifold block.

HCPB breeder blanket

The design of the HCPB DEMO module shown in Fig. 3, is based on the previous HCPB Test Blanket Module (TBM) design. The module is enclosed in a container made of Eurofer reduced activation steel. The cooling of the blanket is provided by high pressure He gas. The U-shape first wall (FW) of 30 mm thickness is attached and welded to a massive 35 mm thick back plate (BP) of the blanket. The FW is designed as U-shaped steel plate made of Eurofer steel. The plasma facing surface of the FW is coated with 2 mm tungsten layer. The helium gas distribution collector is formed by 5 steel plates of different thickness parallel to the blanket BP. The whole structure is stiffened with an internal rigid grid of radial-toroidal and radial-poloidal helium cooled steel plates which accommodates the breeder units (BU) of 20 cm x 20 cm (toroidal x poloidal) size.

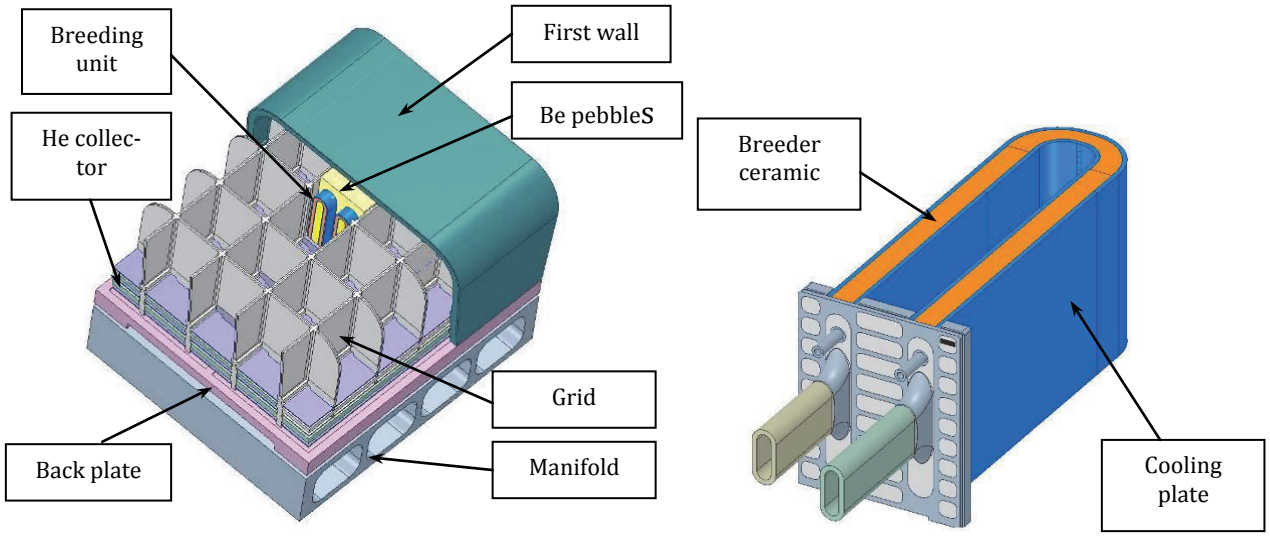

Fig. 3: Inboard HCPB breeder blanket module (left) and HCPB breeder unit (right).

The BU (Fig. 3) is designed for accommodating the breeder beds which provide both the nuclear power generation and the breeding of tritium. The breeder bed is formed by two separated bent U-shaped cooling plates with internal helium coolant channels. The U-shaped space between the cooling plates has a thickness of 10.5 mm and is supposed to be filled with Li_4SiO_4 pebbles. To enhance the tritium generation, the lithium of the Li_4SiO_4 is enriched up to 60 at% ^6Li. Each BU includes two such breeder beds. The remaining space of the BU around breeder beds is filled with Be pebbles which serve both for neutron moderation and

multiplication. The radial length of the breeder bed from the closing plate to the front is ~ 25 cm and ~44 cm, inboard and outboard, respectively.

The HCPB blanket is securely attached to the manifold of 20 cm thickness enclosing the inlet and outlet gas pipes. The gaps between blanket and manifold are 2 cm and 12 cm for inboard and outboard sides respectively. The inlet and outlet gas pipes are separated and surrounded in manifold with the steel matrix that takes up to ~44% of the manifold volume.

HCPB DEMO reactor model

A dedicated MCNP model of the HCPB DEMO was developed by integrating HCPB blanket modules into the generic DEMO model. The integration of the HCPB blanket modules was performed on the CATIA platform (Fig. 4). The inboard and outboard HCPB blankets were positioned inside the banana-shaped blanket container so that the FWs of the blankets follow as close as possible the contour of the FW in the generic model. In this way 10 inboard and 10 outboard HCPB blanket modules were arranged around the plasma chamber with 20 mm toroidal and poloidal gaps between the modules. Taking advantage of the symmetry of the DEMO reactor, a 11.25° torus sector was chosen for the model which includes, in toroidal direction, one full inboard and 1 and ½ outboard blankets. The interior structure of the blanket modules was not included in the CAD 11.25° model because a special technique was applied for modeling these parts with MCNP. Thus the final HCPB DEMO CAD model includes only casings of all blanket modules. This procedure enables the elaboration of a very compact neutronic geometry model.

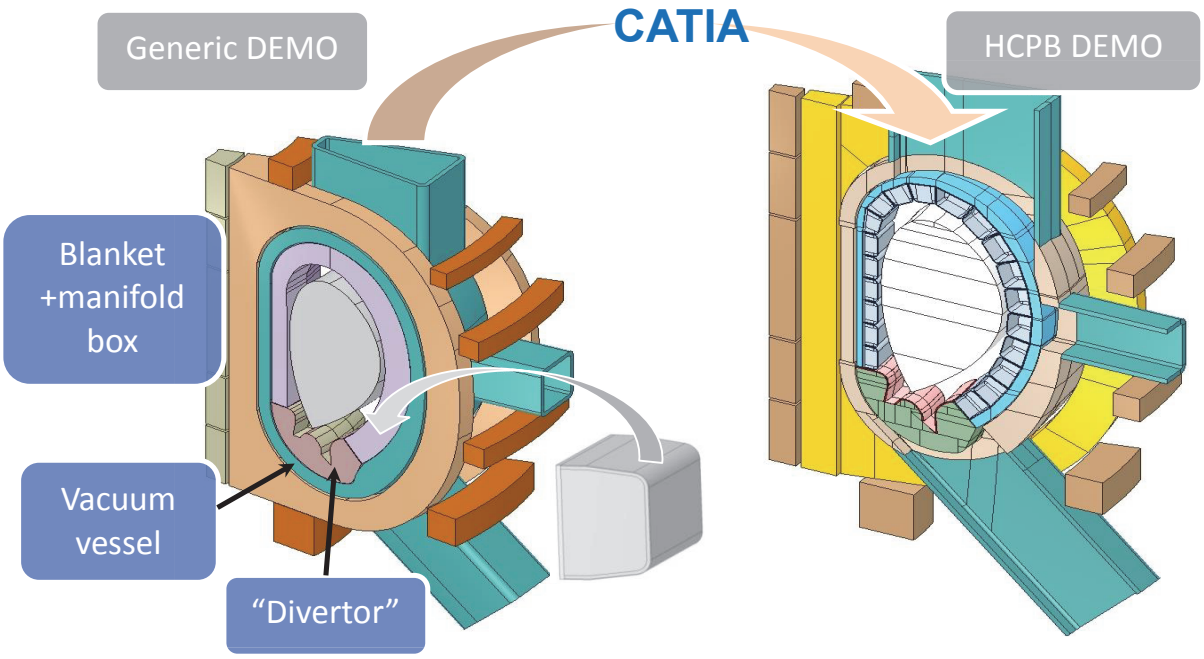

Fig. 4: Generation of the CAD model for the HCPB DEMO starting from the generic DEMO CAD model.

The 11.25° CAD model of the HCPB DEMO reactor was first adapted to the requirements for the neutronic applications. The CAD model was then converted with the McCad conversion tool into the MCNP geometry model as shown in Fig. 5 (left side). The interior structure of the blanket modules was not generated with McCad to avoid a too complicated MCNP model with many unnecessary repetitions. Instead the very efficient repeated structure technique available with MCNP was utilised to model the blanket interior structure. Actually, only two different MCNP blanket models were developed based on the CAD models for an inboard

and an outboard blanket module, respectively. No further simplifications were applied to the blanket interior structures. All blanket module boxes, inboard and outboard, were then filled with these blanket models using MCNP's repeated structure feature. The final MCNP HCPB DEMO model, shown in Fig. 5 (right side) includes 950 material and 280 void cells.

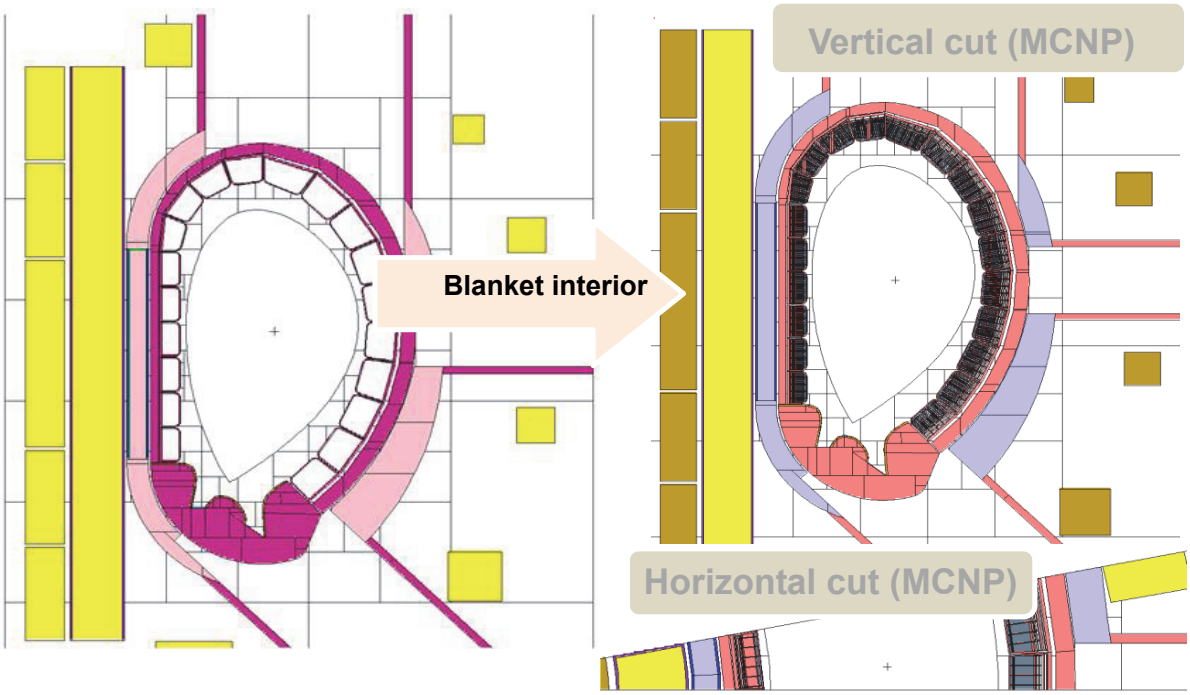

Fig. 5: Converted HCPB MCNP model with empty blanket module boxes (left side) and final MCNP model with blanket interior structures filled in (right side).

Nuclear Analysis of the HCPB DEMO

The neutronics analyses comprised the assessment of the nuclear performance of the newly developed HCPB DEMO reactor including the nuclear power generation, the tritium breeding capability and the shielding performance. The calculations were carried out making use of the geometry model discussed above and the MCNP5-1.60 code with nuclear data from the FENDL-2.1 library. The toroidal fusion neutron plasma source was simulated by making use of a specially developed source subroutine linked to the MCNP executable.

The tritium breeding capability of fusion power reactors based on the HCPB blanket has been proven in many previous studies. The present design suffers, however, from some deficiencies of the not yet optimized CAD design of the HCPB blanket modules including e. g. rather thick stiffening grid plates and a comparatively large number of blanket modules. This resulted in a rather high fraction of the blanket space around the plasma which is not available for the tritium breeding but consumed by the steel walls of the modules and the void gaps in between. With the present design and 20 blanket modules, a tritium breeding ratio of 1.04 can be achieved at a ^{6}Li enrichment of 60 at%. Further design optimization is required, however, to achieve a TBR in the range of 1.05 to 1.10 which would provide a sufficient safety margin to account for uncertainties and tritium losses.

The total power generation was calculated for the entire HCPB DEMO reactor assuming a fusion power of 2119 MW. The resulting nuclear power production is at 2216 MW with an energy multiplication factor of 1.31. About 85% of the total power is generated in the blanket modules and up to 70% of this amount is produced in the outboard modules. The divertor gives ~13% of the total power generation.

Nuclear power density radial profiles were calculated for the steel structure in the inboard torus mid-plane as shown in Fig. 6. With the present design assumptions the recommended limit for the power density in the TFC magnet of 50 W/m^3 is exceeded by approximately a factor of 5. This is due to the relatively small radial thickness of the vacuum vessel / shield of about 55 cm filled with a homogeneous steel-water mixture. A significantly better attenuation of the neutron radiation can be achieved by utilizing tungsten carbide (WC) as a more efficient shielding material. A typical mixture of WC (65%), Eurofer (10%) and water (25%) was introduced to this end in the 23 cm thick shield preceding the vacuum vessel. Fig. 6 compares the power density profiles for the considered cases employing a steel/water and a WC/steel/water mixture in the shield. It is noted that for the latter configuration the power density in the shield region decreases with a much steeper gradient. The resulting power density in TFC is only slightly higher than the recommended limit.

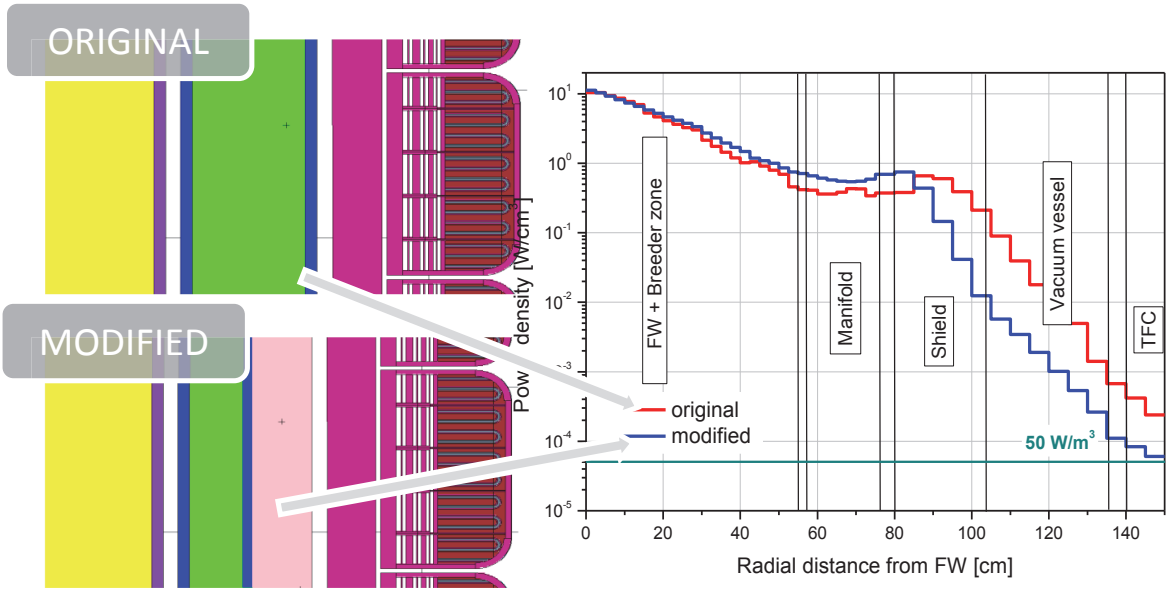

Fig. 6: Radial nuclear power density profile across the inboard torus mid-plane for the original and a modified layout of the vacuum vessel / shield.

Staff:

U. Fischer
P. Pereslavtsev
L. Lu

Task T11
Development of European software tool for the CAD import in MC codes

Objective

The objective of this task was to further improve and extend KIT's open source software McCad with the long-term goal to develop a mature and robust European software tool for the conversion of CAD geometry models for Monte Carlo particle transport simulations with MCNP and TRIPOLI.

Following this objective, the McCad software tool has been further developed in the frame of the WP13-SYS02-T11 task. Its capabilities were extended, its core algorithms were improved and re-designed for the implementation in McCad.

Improvements

The McCad conversion processing involves the decomposition of the original CAD geometry model and the void generation for the converted model. In order to improve the stability and efficiency, a detailed investigation was performed on the conversion algorithm, and most of the reasons for the occurrence of conversion errors were detected. To avoid or decrease the number of such errors, improvements of the applied algorithms were developed, including the optimisation of the solid decomposition strategy and the adoption of an entirely new void generation algorithm.

The new void generation algorithm no longer decomposes the solids with Boolean operations, but employs the collision detection technique to determine the geometric relations between the void box and the boundary surfaces. With this technique, each boundary surface of material solids is first discretized into a group of sample points. If one of them lies in the void box, the boundary surface is colliding with the box. The number of sample points is controlled by the sampling precision that determines the accuracy of the collision detection.

A new McCad version 0.4.0 was developed which has already integrated new algorithms for the solid decomposition and the void generation. It also includes a new interface for the materials editing and assignment integrated to the GUI (Graphical User Interface). McCad 0.4.0, furthermore, has the new the capability to convert CAD geometry models into the geometry representation of the TRIPOLI Monte Carlo code.

Testing and verification

The improvements and new functions have been tested, verified and utilized with several DEMO and ITER applications. The applications, which involve very complex geometries, have demonstrated the efficiency and accuracy of the new conversion functions and showed a significantly improved performance of the CAD model conversion process. There are, however, still some remaining problems with the solid decomposition and the memory consumption which call for a further optimization of McCad's conversion algorithms.

Fig. 7 shows an example of the improved decomposition algorithm applied to the divertor model of DEMO. Fig. 8 shows the CAD model of the HCPB TBM and the converted MCNP model employing the improved decomposition and void generation algorithms. Table 2 shows that both the efficiency of the conversion process in terms of the required computing time has been significantly improved and the complexity of the converted model in terms of the number of void cells generated has been greatly reduced.

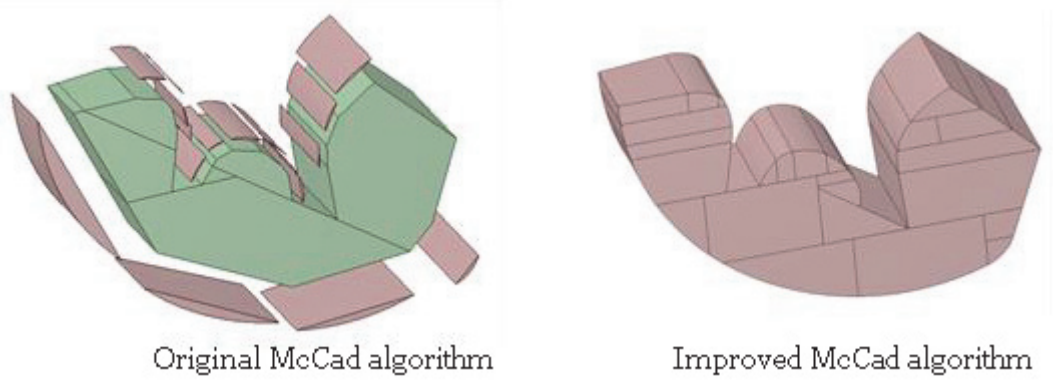

Fig. 7: Results of McCad's original and improved decomposition algorithms applied to the DEMO divertor model.

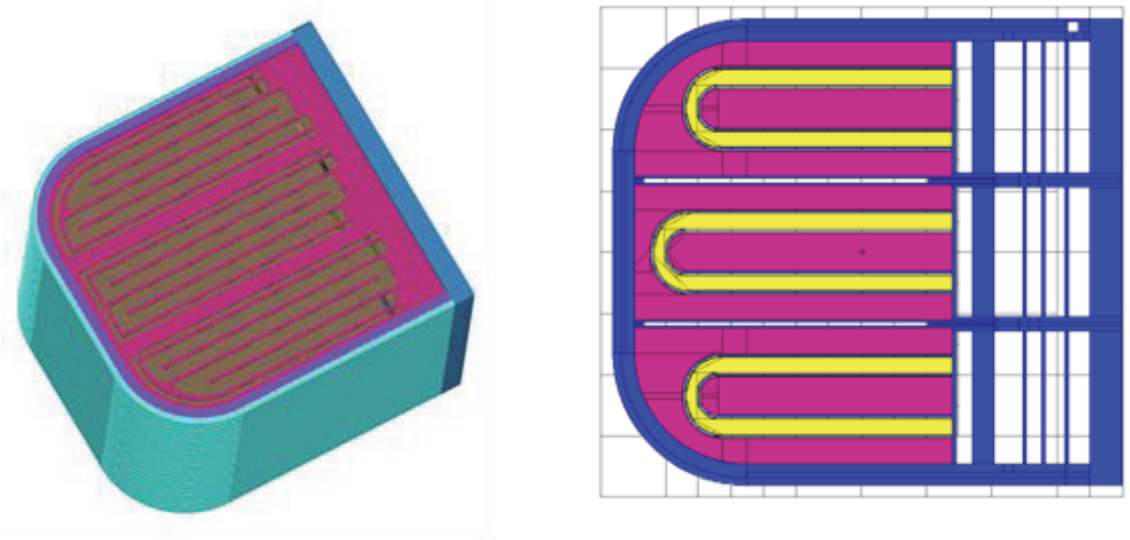

Fig. 8: CAD model of the HCPB TBM (left side) and converted MCNP model employing McCad's improved conversion algorithms.

Table 2: Results for the conversion of the HCPB TBM model employing McCad's original and improved conversion algorithms.

	Original algorithm	**New algorithm**
Number of material cells	5692	5627
Number of void cells generated	7549	1739
Number of surfaces	706	761
CPU time required for the conversion	7*24 hours	4 hours 10 min

The new MCad version, 0.4.0, is already available and will be provided to the external users for further testing and applications.

Staff:

U. Fischer
L. Lu
P. Pereslavtsev

Task T08
Activation and Radiation Dose Map Calculations

Objective

The objective of this task was to assess the activation inventory and the decay heat production for the HCLL and HCPB DEMO, and compare potential alternative structural materials to the low activation steel Eurofer.

Coupled particle transport and activation calculations for DEMO

Activation inventories, decay heat and shut-down radiation doses are important nuclear quantities which need to be assessed on a reliable basis for the safe operation of a fusion nuclear power reactor and its final decommissioning. Task WP13-SYS-02-T08 aimed at as-

sessing such radiological quantities for the HCPB and HCLL reactor models developed in the frame of the 2013 PPPT Work Programme for DEMO.

For the HCPB DEMO, the activation calculations were performed by KIT using the R2S system for coupled transport and activation calculations. The R2S system employs MCNP5 for the particle transport simulations and the FISPACT code for the inventory calculations. For the HCLL DEMO, the activation calculations were performed by UNED using the MC2ACAB system for coupled transport and activation calculations. This system employs MCNP5 for the particle transport simulations and the ACAB code for the inventory calculations. Both the HCPB and HCLL DEMO variants employ the RAFM steel Eurofer as structural material. For assessing the impact of potential alternative structural materials, activation calculations were performed by LEI for an outboard blanket module of the HCLL DEMO assuming High-Temperature Ferritic-Martensitic (HT-FTM) steel and SS-316 (LN) as structural material.

HCPB DEMO

The Rigorous 2-step approach, developed previously by KIT, was applied to calculate the activity inventory and decay heat of the HCPB DEMO. The EAF-2010 data library is used for the neutron activation cross section data and FENDL-2.1 for the cross-sections used in the particle transport simulations. Since the FISPACT code runs sequentially according to the number of cells, a FORTRAN routine is utilized to submit the job for each input file. Finally, data of interest, such as the activity of each material, decay heat generated by alpha, electron, and photo particles are extracted with a newly developed post-processing utility tool.

For the activation calculations, the HCPB blanket module was simplified into three parts: the blanket casing consisting of the first wall without armour and back plate, the 2 mm tungsten first wall armour, and a homogeneous mixture inside the casing representing the interior blanket structure. This mixture includes the stiffening grid, the cooling plates and the breeder units (BU). The He fraction in all steel components was accounted for in the homogeneous mixture. Thus the mixture includes 9.8% Eurofer steel, 43.596% beryllium, 9.702% breeder ceramic, and the rest is He/void. The manifold was not taken into account in this calculation. The activation analysis was performed for all 20 blankets arranged around the plasma (see Task T06 above) employing 374 material cells in total. The results were normalized to the DEMO fusion power of 2119 MW. The irradiation scenario assumed a DEMO operation over 5.2 years minus 10 days at 30% of the nominal fusion power. For the subsequent 10 days 48 pulses are assumed each lasting 4 hours at full power with 1 hour dwell time in between. After shutdown, the activity inventories were calculated at the cooling times of 1 hour, 1 day, 1 week, 1 month, 1 year, 10 years, 100 years, 1000 years.

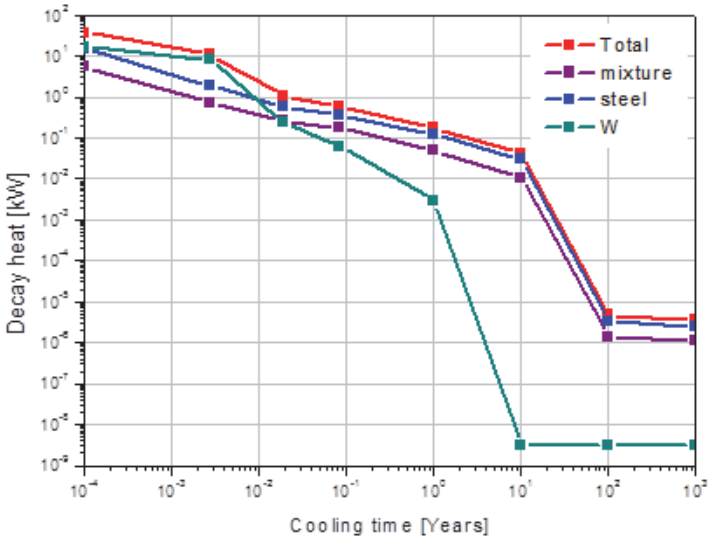

Fig. 9: Decay heat power of HCPB blanket module No. 16 (outboard mid-plane) as function of the cooling time after shutdown.

Fig. 9 shows, as an example, the total afterheat of blanket module No. 16 located at the torus mid-plane on the outboard side of DEMO and its break-down into the different materials/components. The temporal behaviour of the afterheat is similar to that of the activity inventory: The tungsten armour dominates over the first several days after shutdown, afterwards the breeder blanket mixture with the Eurofer structure is the major contributor to the afterheat of the blanket module.

HCLL DEMO

The activation analysis for the HCLL DEMO has been performed by UNED in a similar way as for the HCPB DEMO by KIT using the same generic MCNP DEMO model, however, with HCLL specific breeder blanket mixture filled in. The same irradiation history and the same normalization have been also employed. UNED applied, however, the MC2ACAB system with EAF-2010 activation cross-section data. Figure 10 shows a comparison of the resulting decay heat generation as calculated with the two approaches for the central outboard blanket modules, HCPB and HCLL DEMO, respectively. The decay heat is dominated by the Eurofer steel which in both DEMO variants is employed as structural material. The differences in the decay heat are thus mainly caused by the different neutron spectra and flux levels. It is revealed that the decay heat both for short (a few days) and longer (more than a year) cooling times after shut-down is large for the HCPB than for the HCLL DEMO. This is an effect of the softer neutron spectrum in the HCPB blanket, due to the presence of large amounts of the beryllium multiplier which also acts as moderator, and results in enhanced neutron capture reactions leading to radioactive products such as ^{187}W.

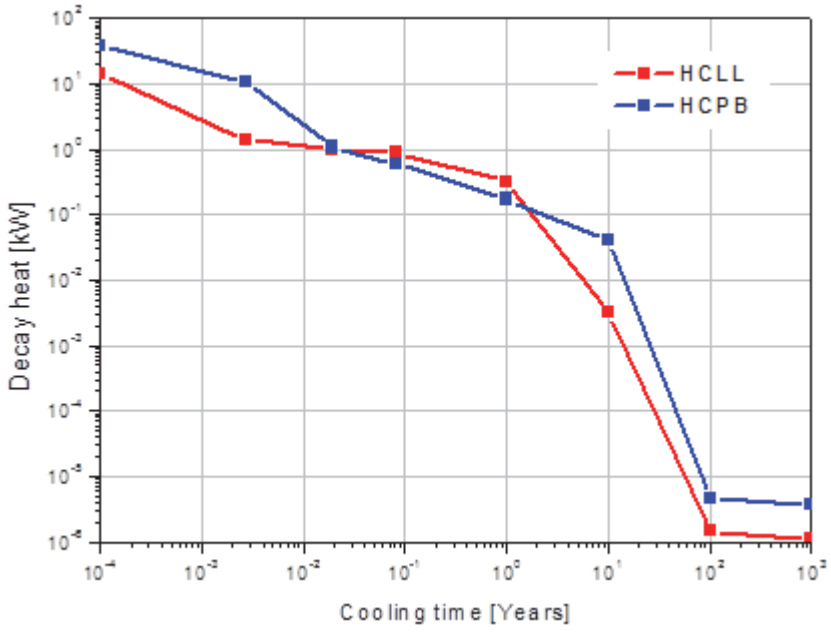

Fig. 10: Comparison of the decay heat power calculated for the central outboard blanket module No. 16 for the HCLL and HCLL DEMO variant.

Comparative analysis of SS-316L and HT F-M steels results

For assessing the impact of potential alternative structural materials, comparison calculations were performed by LEI for a single outboard blanket module of the HCLL DEMO assuming High-Temperature Ferritic-Martensitic (HT-FM) steel and SS-316 (LN) as structural material. The induced radioactivity is lowest for the SS-316 still until about 200 years after shut-down. Afterwards, the activity level of SS-316 steel is the highest. For these times, the activity of both Eurofer and the HT-FM steel is about one order of magnitude lower. Ni-63 and Mo-93 are the dominating radio-nuclides which are responsible for the higher activity level of SS-316 in this time period.

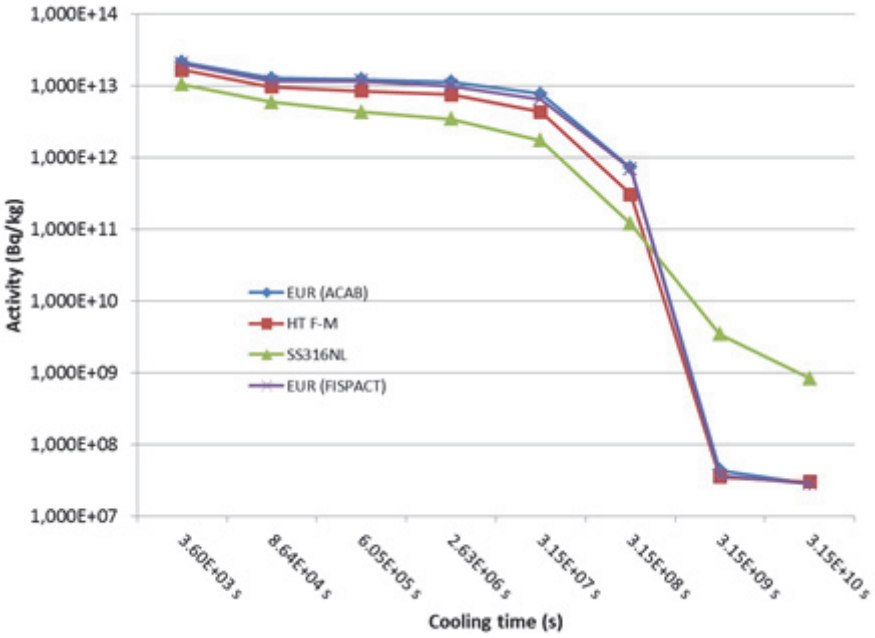

Fig. 11: Comparison of the specific activity of different steels used as structural material in the central outboard blanket module No. 16 of the HCLL DEMO.

Staff:

U. Fischer
P. Lu
P. Pereslavtsev

J.P. Catalán, UNED
R. García, UNED
F. Ogando, UNED
J. Sanz, UNED
G. Stankunas, LEI

Task T12
Development of a single European tool for coupled radiation transport and activation calculations

Objective

The objective of this task was to specify a general and flexible computation scheme for the later implementation in a single European R2S tool which is suitable for shut-down dose rate analyses of DEMO.

The Rigorous-2-Step (R2S) methodology has been independently implemented by several European institutions, most notably R2Smesh (KIT), MCR2S (CCFE) and R2SUNED (UNED). The currently available R2S tools are based on neutron transport calculations with the MCNP code and activation calculations with the FISPACT or ACAB codes coupled by several interfaces for the data exchange. They are applied in routine use for the engineering design, operation and safety case of fusion technology. There is, however, a general limitation in turnover and reliability of such calculations due to the intricate, non-standard nature of the coupling scheme and the underlying transport and activation codes, but also due to the stringent requirements on spatial and energy resolution for accurate results.

The task conducted in the frame of the WP13-SYS-02, Task T-12, aimed at specifying a common computation scheme for R2S based shut-down dose rate analyses of DEMO. This specification covered the areas of user requirements, functional requirements, architecture and quality assurance. A dedicated effort has been devoted to assess the requirements for a common decay gamma source format (CDGSF) and its associated sampling. As a major result, a suitable format for the decay gamma source representation was elaborated which will be implemented and tested in the follow-up programme within the Eurofusion project.

The Common Decay Gamma Source Format to be adopted for the common R2S tool is as follows:

- Header:
  - Descriptive data: Model name, date, reference number
  - Decay time [s]
  - Total source strength [gammas/s]
  - Gamma spectrum format: ID to select group/line data; number of groups/lines
  - Gamma group upper energies
- Mesh data:
  - Mesh geometry: ID to select structured/unstructured
  - Structured: ID to select rectangular/cylindrical; no. of mesh spacings in each dimension;
  - Structured: list of mesh spacings in each dimension
  - Unstructured: link to external mesh file
- Source data:
  - Mesh element information:
    - Element ID
    - Element total intensity [gammas/s]
    - Element volume [cm^3]
    - Number of cells under mesh element (1 for homogenous element)
  - Cell information (if required):
    - Cell ID
    - Cell volume fraction
    - Cell intensity [gammas/s]
    - Cell gamma spectrum: list of source strengths
    - Cell gamma spectrum uncertainties

Requirements for an efficient gamma source sampling scheme were also considered. Possible spatial sampling methods include:

- Sampling voxels with a probability proportional to the total source in a voxel (analogue sampling).
- Sampling voxels uniformly with weight adjusted based on the total source in a voxel (uniform).
- Sampling some voxels over others, according to some pre-determined importance map, with appropriately adjusted weight (biased).

Analogue sampling is usually inefficient, where a low probability region contributes the most to the result in the region of interest (for example, a whole port activation mesh, where dose rate is required in the interspace).

Uniform sampling enables the entire mesh to be sampled, and the weight is adjusted according to the intensity. This method has been shown recently to be problematic in the event of a small number of photon histories being able to stream from the high intensity region and contribute to the low source intensity region. Furthermore, the sampling method is not compatible with the use of weight windows maps applied for variance reduction purposes in MCNP calculations.

Sampling voxels according to a pre-determined importance map (i.e. biased sampling) would enable the user to quickly obtain dose rate results by preferentially sampling those regions which would be expected to dominate the dose rate contribution in the location of interest. Whilst not complex to implement, this method has the disadvantage of potentially undersampling important regions, if those regions are presumed to be unimportant but actually are not. In addition, the method of determining this important map is not clear, but would probably involve some type of adjoint calculation. There would be a potential benefit to having multiple schemes available in the source routine, from which the user could select.

Staff:

J. Catalan (UNED)
U. Fischer
D. Leichtle (F4E)
A. Turner (CCFE)
P. Sauvan (UNED)
P. Pereslavtsev
R. Villari (ENEA)

Acknowledgement

This work, supported by the European Communities under the contract of Association between EURATOM and Karlsruhe Institute of Technology, was carried out within the framework of the European Fusion Development Agreement. The views and opinions expressed herein do not necessarily reflect those of the European Commission.

Design Tools and Methodologies – Platform Independent Improvement Work (WP13-DTM-01-T03-01)

Background and objective

The design of nuclear components for fusion reactor systems relies on the neutronics, thermal and mechanical performance of the components, on the materials employed, their properties and behaviour under irradiation and at elevated temperatures and several other engineering issues. The design process thus involves several steps starting in general with scoping studies on the neutronic and thermal performance. Design optimisation is then achieved through an iterative process by performing a series of sequential neutronics, thermal hydraulics, and eventually structural mechanical calculations. All of these iterative steps require the exchange of geometry data and numerical results between the codes employed. In particular, it is required to provide the nuclear heating data, obtained as results of the neutronic simulation calculations, to the thermal hydraulic code for calculating the temperature distribution with the assumed boundary conditions.

The neutronic calculations in general are performed by Monte Carlo (MC) codes such as MCNP using a dedicated geometry representation which is well adapted to the engineering CAD models through the use of Boolean operations on solids or half-spaces. Thermal hydraulics calculations, on the other hand, are performed on structured or unstructured meshes adapted to the specific geometry of the component or system to be analysed. It is thus required to develop a suitable coupling scheme between the applied Monte Carlo and FE codes for the exchange of numerical results on meshes adapted to the problem geometry. Ideally, this coupling approach should be implemented on a simulation platform which integrates a CAD based geometry module for the generation of the Monte Carlo model, a module for the mesh generation, a module for data exchange, and a visualisation tool which is capable of visualising the neutronic and the thermal hydraulic results on the same mesh superimposed to the real geometry. The open-source computation platform SALOME is considered to be a very suitable candidate for the coupling approach implementation.

Task DTM-01-T03 of the EFDA 2013 work programme on Power Plant Physics & Technology (PPPT) aimed at developing a suitable approach for the data translation between MC codes and Computational Fluid Dynamics (CFD) codes. The approach was intended to be implemented and tested on the SALOME platform to enable the mesh generation, the data translation between the codes, as well as the results and geometry visualization as an entire computation cycle on one single platform.

Coupling approach design

The coupling approach was designed with the strategy to enable a good extensibility and adaptivity — free for coupling any MC and CFD codes, and suitable for various applications. It consists of a generic data translation kernel, and provides interfaces for data inflows and outflows. Meshes and data are stored inside the kernel using a universal format. Inflow/outflow data are converted to/from this internal data format. The kernel and interfaces are kept independent from each other, thus new interfaces can be integrated without influencing the kernel or other interfaces, or suffering from unnecessary constrains.

The coupling scheme is outlined in Fig. 1. Two functional modules form the data translation kernel. The mesh and data manipulation module provides mathematical operation and spatial transformation functionalities for ensuring consistence between the source meshes from MC codes and the target meshes from CFD codes. The physical conservative interpolation module performs flexible and high-fidelity data mapping among the structured/unstructured meshes. Inflow interfaces are utilized for post-processing meshes and reading the data from the MC code outputs. Outflow interfaces convert the translated data and write them in the specific interfacing files for the CFD codes. Currently the data inflow from MCNP5 and out-

flow to either CFX or the Fluent code are supported, however other MC codes and CFD codes are ready to be interfaced.

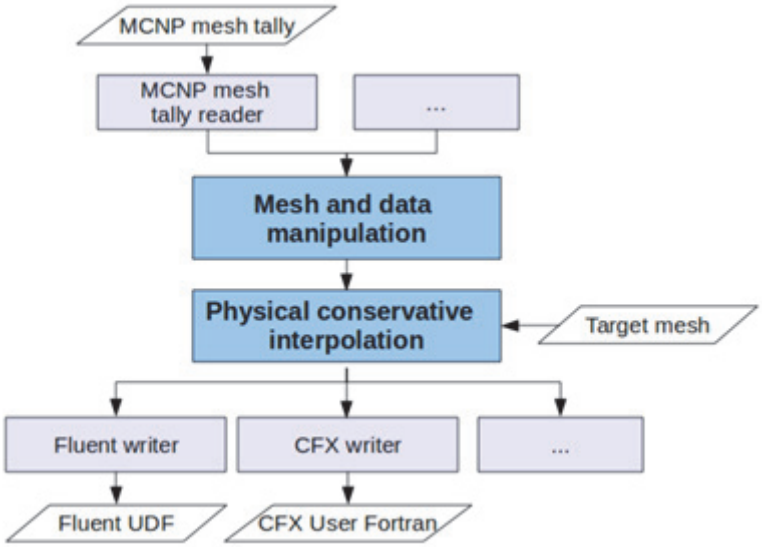

Fig. 1: Data flowchart for the coupling approach.

A key issue is to find a suitable solution for establishing the data translation kernel. Based on broad investigations and in-depth comparisons, the SALOME's MED format and its open-source library were selected. Meshes with most of the element types are supported by this format, and comprehensive mesh/data manipulation and interpolation functionalities are readily available with the library. The MED functionality is available in the open-source platform SALOME.

Code implementation

The SALOME software aims at providing a generic pre- and post-processing platform for external applications. It contains built-in modules such as GEOM for the CAD geometry modeling, SMESH for the mesh generation, ParaView for the data visualization, and MED for mesh and data management. The Common Object Request Broker Architecture (CORBA) is employed in SALOME to enable its data communication among modules, and also distributed calculations via CORBA interfaces. Each module is designed as a server and a client (the client is wrapped by the Graphic User Interface, GUI). The server is responsible for implementing core algorithms, and the GUI is responsible for user interactions.

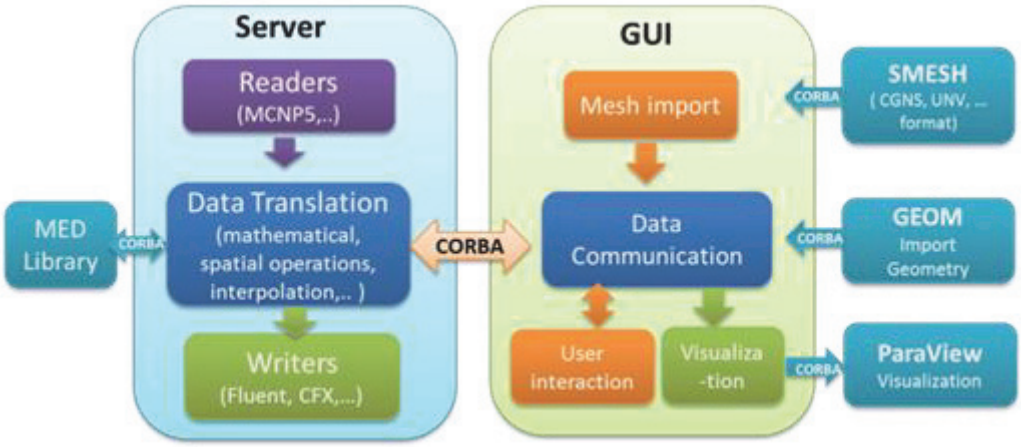

Fig. 2: McMeshTran consists of a server and a GUI and communicates data via CORBA interfaces.

The coupling approach is implemented and integrated into SALOME as a new module called McMeshTran (MC Mesh and data Transformation/Translation/Transfer). McMeshTran follows SALOME's guidelines in module architecting, as shown in Fig. 2. The mesh translation kernel and inflow/outflow interfaces are implemented in the McMeshTran server, which is supported by the MED library. The GUI is connected with the server, the SMESH, GEOM and ParaView modules via CORBA, to enable user interactions, mesh imports and mesh/data visualizations mapped on CAD geometry.

Test application and validation

For testing and verification purposes, a blanket test case model derived from the conceptual engineering design of the Helium Cooled Pebble Bed Test Blanket Module (HCPB TBM) was investigated. The model (Fig. 3) has the dimensions of 655 × 484 × 711 mm in poloidal, toroidal, radial directions, respectively. Comparing with the original HCPB TBM, the number of Breeder Units (BUs) has been reduced from 16 to 6 in the test case model. Flow channels were kept inside the First Wall (FW), the vertical/horizontal Stiffening Grids (v/hSGs), the lateral Caps, and also in the BU Cooling Plates (CPs). Simplifications have been done by removing of holes and fillets and combining flow channels inside the v/hSGs and Caps. The CAD model was then converted into MCNP descriptions using the geometry conversion tool McCad, and a MCNP model with around 13000 solid cells was obtained.

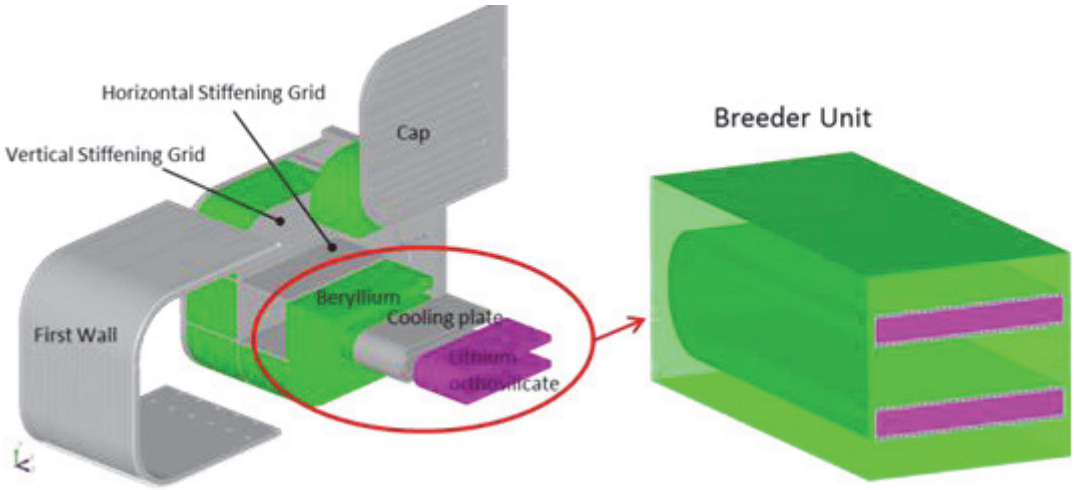

Fig. 3: Exploded view of the HCPB TBM test case model and its Breeder Unit (BU).

Although the conditions for the test case do not have to be identical with the HCPB TBM in ITER, the calculation was carried out for a typical ITER neutron radiation field. A surface source was assigned on the front surface of the boundary box. 14.07 MeV neutrons are emitted towards the FW with an ITER like angular distribution. An average neutron wall loading of 0.72 MW/m^2 was applied, which corresponds to an incident source intensity of 1.06×10^{17} n/s. Reflecting boundaries were assigned to the surfaces of the boundary box in poloidal and toroidal directions. The neutron and photon coupled transport calculation was performed with the MCNP5-1.60 code and FENDL-3.0 cross-section data.

Validation

In principle, the heating data provided for CFD calculations should agree with MCNP results. It is straightforward to check the integral heating value. However, comparing the heating data field is much more difficult due to the differences of meshes. In this work, a so-called Inversion Check approach was applied, and the BU high-lighted in Fig. 3 was checked via the following steps:

a. Tallying the neutron and photon (gamma) heating in the beryllium, CP, lithium orthosilicate (OSI), and mixed material respectively, with the same mesh configuration covering only this BU;

b. Summing the neutron and photon heating results in beryllium, CP and OSI, and interpolating them into target meshes of three subcomponents.

c. Merging the three meshes into one mesh, and re-interpolating the data on this mesh into the MC tally mesh;

d. Comparing with material-mixed heating mesh tally results.

A deliberate mesh tally configuration which fits well into geometry was assigned to the BU. It contains totally 4.24×10^6 cells. 7×10^8 source neutron histories were simulated in the MCNP transport calculation. Most of the mesh cells have statistical errors below 5%, which is a recommended criterion in neutronic simulations. The percentages of cells with >5% statistical errors are 0.002%, 0.167%, 3.647% and 0.118% for beryllium, CP, OSI and material-mixed mesh tallies, respectively. These cells are mostly located in the unimportant region. The three target meshes were generated for beryllium, CP and OSI using ANSYS Workbench, with totally 3.20×10^6, 1.14×10^6, 2.41×10^6 elements, respectively.

The total heating integrated over the interpolated meshes were compared with the values obtained with cell-based energy deposition tallies of MCNP (using the F6 card), as shown in Table 1. The statistical error for these cell-based tallies is negligible small. The difference was calculated with expression $abs(P_{MC} - P_{int})/ P_{MC}$, where P_{MC} is the MCNP tally results, P_{int} is the interpolated results. The differences are very small in the beryllium and OSI, and relatively larger in the CP due to the geometry complexity and higher statistical errors.

Table 1: Comparison of integral heating results.

Sub-component	MCNP tally result (W)	Integrated result (W)	Diff. (%)
Beryllium	1.55550×10^4	1.55970×10^4	0.270
CP	1.80361×10^3	1.84619×10^3	2.360
OSI	1.08624×10^4	1.08819×10^4	0.180

Next an Inversion Check was performed. Fig. 4 compares two cross-section views of the heating distributions at Z=100 mm, which look very similar. In order to check the data in more detail, differences of the heating value in each cell were calculated. Differences less than 5% are considered to be acceptable for engineering analyses. Fig. 5 categorizes the rest of cells into five ranges — (5%, 10%], (10%, 100%), [100%], (100%, ∞) and ∞, where the square brackets mean including the bound, and the parentheses not. The ratio of these cells is given in Table 2. The reasons for the high differences are discussed as follows:

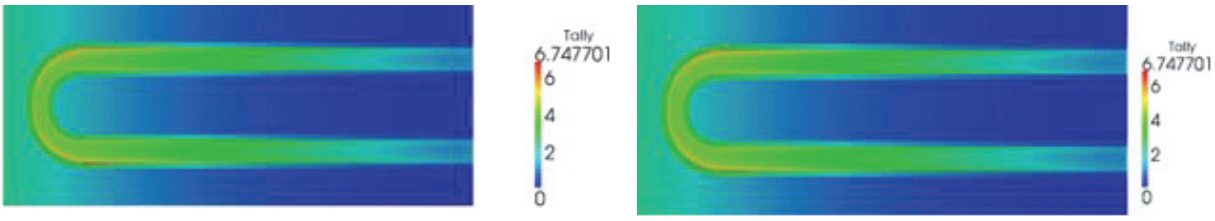

Fig. 4: Cross-section view of the MC material-mixed heating result (left) and the inverted heating field (right) (unit: MW/m^3).

Table 2: Range of differences and the ratio of cells.

Range of diff.	(5%, 0%]	(10%, 100%)	[100%]	(100%, ∞)	∞
Ratio(%)	0.49	0.44	0.01	0.06	2.85

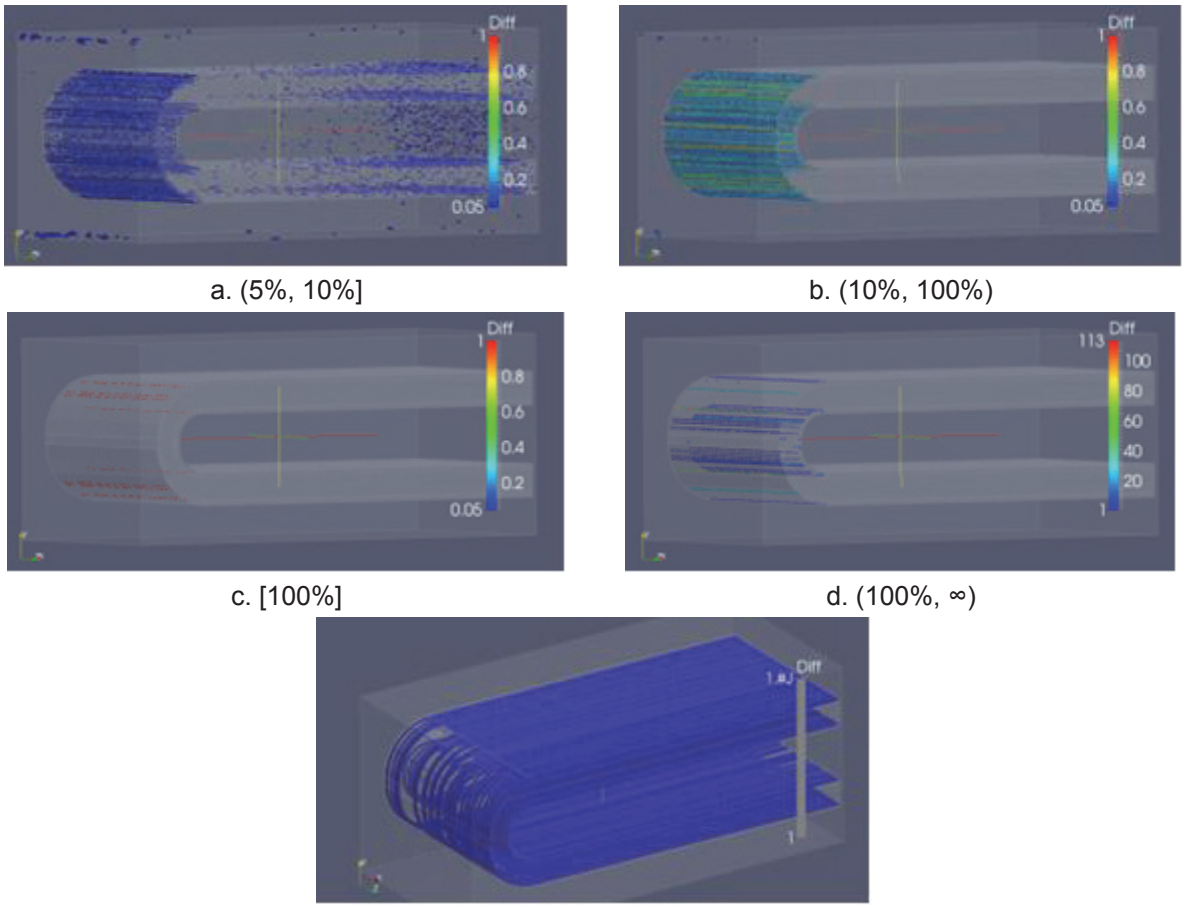

Fig. 5: Differences on each cell superimposed on the BU geometry.

a. (10%, 100%) and (100%, ∞): Fig. 5 indicates that most of the high-error cells are located in the bending portion of CP, and most of these cells contain both void and solid. The larger void fractions they have, the smaller heating values they get. Because the step *b* of the Inversion Check surely introduces some errors, it is clear that differences will become higher as heating values become smaller.

b. (5%, 10%]: the reason is similar as above. However, the effect of the statistical errors becomes dominant in this range.

c. [100%]: Because there are slight geometry differences between the CAD model and the target meshes (cylindrical surface become planar facets), the cells contain very tiny solid fractions in the MC model which might contain no solid fraction in the inverted mesh. This results in 100% differences.

d. ∞: void cells with zero heating value.

In case of a real analysis, mesh cells containing both void and solid would never appear in the target mesh. The differences of the interpolated field and the original field would be smaller than the result in Table 2 because the Inversion Check itself introduces some errors. In Table 2, there are only ~1% of cells which have differences larger than 5%. The reliability of McMeshTran mesh data translation scheme has thus been proven.

Verification with CFD calculations for the FW

In order to verify McMeshTran for its coupling capabilities, and also to conduct a cross-check on the interfaces for CFD codes, CFD calculations for the FW were carried out using both the CFX and Fluent codes. A 1/6 FW model was used for the analysis as shown in Fig. 6.

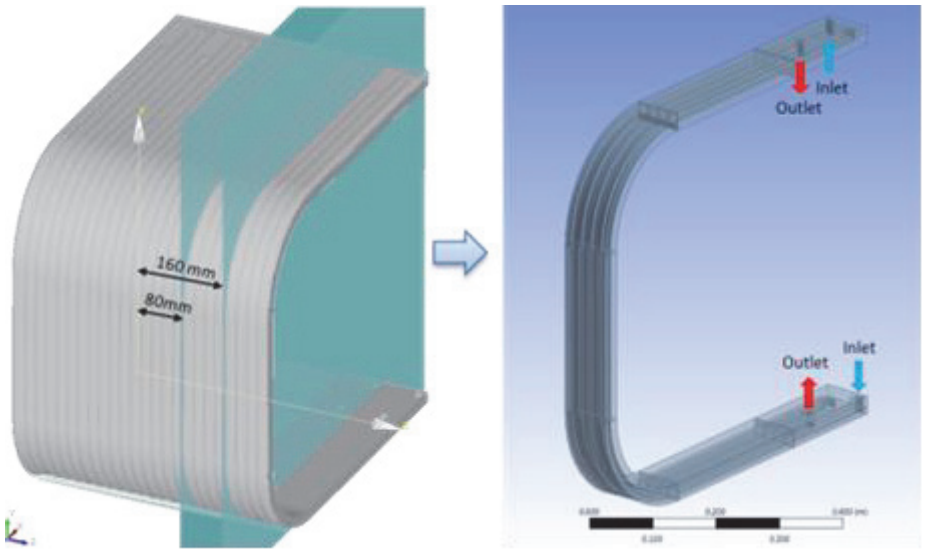

Fig. 6: The FW model for CFD calculations.

Unstructured meshes were generated using the ANSYS Workbench, with around 7.85×105 elements in the fluid domain and 7.88×105 elements in the solid domain. The volumetric heat source was calculated with 5×5×5 mm mesh tally cells, and was interpolated into the solid mesh using McMeshTran. The plasma-side surface of the FW was subjected to a 500 kW/m^2 heat flux in radial direction, and decrease to 0 kW/m^2 along the bending portion. The BU-side was assigned with a uniform heat flux of 83 kW/m^2. Based on the geometry feature, periodic boundary conditions were applied for the lateral surfaces of the model. The other outer surfaces were considered adiabatic thus no heat transfer was assumed toward the outside of the domain. The boundary conditions for one cooling channel are as follows: Inlet temperature 300 °C, pressure 80 bar, and mass flow rate 0.1 kg/s. The fluid helium was considered to be incompressible because of the low velocity of ~80 m/s.

As the temperature is of most concern in this comparison, the fluid and solid temperature distributions using the two codes were evaluated. From Fig. 7 it can be observed that the CFX and Fluent calculations agree well in the temperature ranges, temperature distribution pattern, and the locations of hotspots both for the fluid and the solid domains. The maximum temperature in the solid and fluid domains and the average outlet temperature results are listed in Table 3. The differences of 1-2 °C are considered to be negligibly small in CFD analyses.

In order to evaluate the contributions of the volumetric heat source, cases without loading the volumetric heat source were also calculated, and the temperature raises are also listed in Table 3. Very close temperature raises were obtained using both codes. These results show good evidence for the reliability of the two CFD interfaces.

Table 3: Maximum and outlet temperatures.

Temperature	CFX (°C)	Fluent (°C)	Diff. (°C)
Solid Max.	474.81	473.55	1.26
Fluid Max.	421.47	423.59	2.12
Outlet Avg.	335.45	334.94	0.51
Solid Max. raise	6.44	6.43	0.01
Fluid Max. raise	5.95	5.84	0.11
Outlet Avg. raise	4.93	4.53	0.40

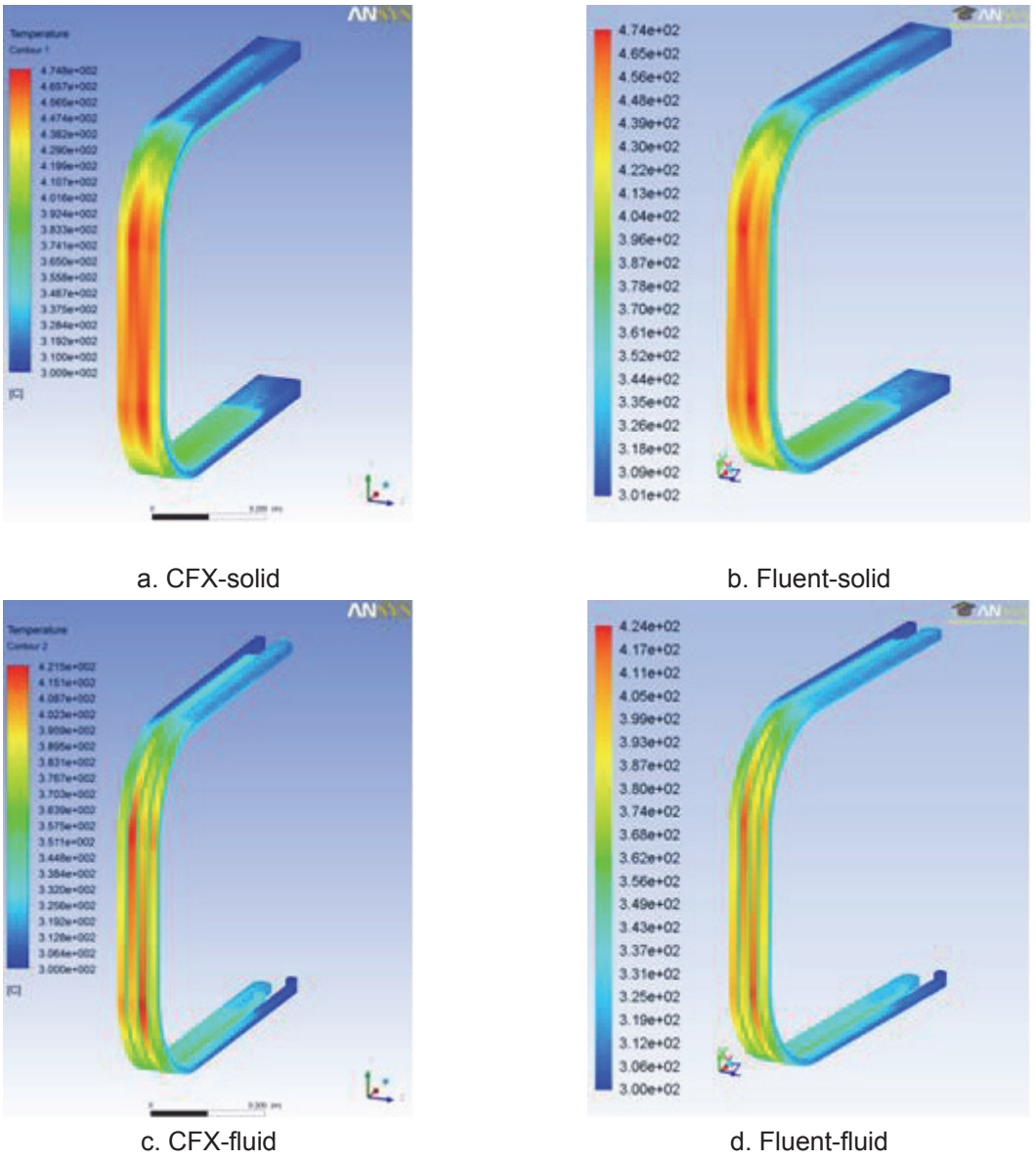

a. CFX-solid

b. Fluent-solid

c. CFX-fluid

d. Fluent-fluid

Fig. 7: Temperature distributions as calculated by CFX for the solid and the fluid of the 1/6 FW model (Units: °C).

Staff:

U. Fischer
Y. Qiu

Literature:

[1] X-5 Monte Carlo Team, MCNP – A General Monte Carlo N-Particle Transport Code Overview and Theory (Version 5, vol. I), Los Alamos National Laboratory, Report LA-UR-03-1987 (Revised 10/3/05), (24 April 2003).

[2] SALOME platform: http://www.salome-platform.org

Acknowledgement

This work, supported by the European Communities under the contract of Association between EURATOM and Karlsruhe Institute of Technology, was carried out within the framework of the European Fusion Development Agreement. The views and opinions expressed herein do not necessarily reflect those of the European Commission.

International Fusion Materials Irradiation Facility (IFMIF)

Broader-Approach Activity: IFMIF Test Cell and High Flux Test Module (BMBF Reference No. 03FUS0008)

Introduction

Scope of work

In the Engineering Validation and Engineering Design Activities (EVEDA) for the International Fusion Material Irradiation Facility IFMIF, which is an element of the Broader Approach activities launched jointly by several European countries and Japan, the German contribution includes engineering tasks for the IFMIF Test cell and the IFMIF irradiation experiments. This report covers tasks performed at the Institute for Neutron Physics and Reactor technology at the KIT attributed to the following procurement arrangements (PAs):

- PA TF-1 EU : Engineering design and Validation of the IFMIF High Flux Test Module
- PA TF-2: Irradiation in fission reactor (Responsible SCK-CEN, contribution by KIT)
- PA TF-4: Other irradiation modules (Responsible CIEMAT, contribution by KIT)
- PA ED-04: Test Cell, Access Cell, Test Module Handling Cell and Technology Rooms

In accordance to the planning for EVEDA, the engineering design tasks were completed in the timeframe up to 12/2013, while the validation tasks will be continued in 2014. In this report, the progress for the year 2013 is described.

System overview

The IFMIF facility is dedicated to fusion-relevant irradiation of structural and functional material specimens, with the objective to create an experimentally validated material properties database suitable for design and licensing of future fusion power plants. The facility is composed of several subsystems, namely the 40MeV 250mA deuteron accelerator facility (AF), the lithium target facility (LF) and the test facilities (TF). The target- and test cell (TTC) is part of the test facilities, containing the lithium target neutron source and the test modules. It has the primary function to shield the environment against the intense radiation generated by the target, and to safely contain all hazardous materials. Inside the TTC, the target and test modules are arranged, as shown in Figure 1.

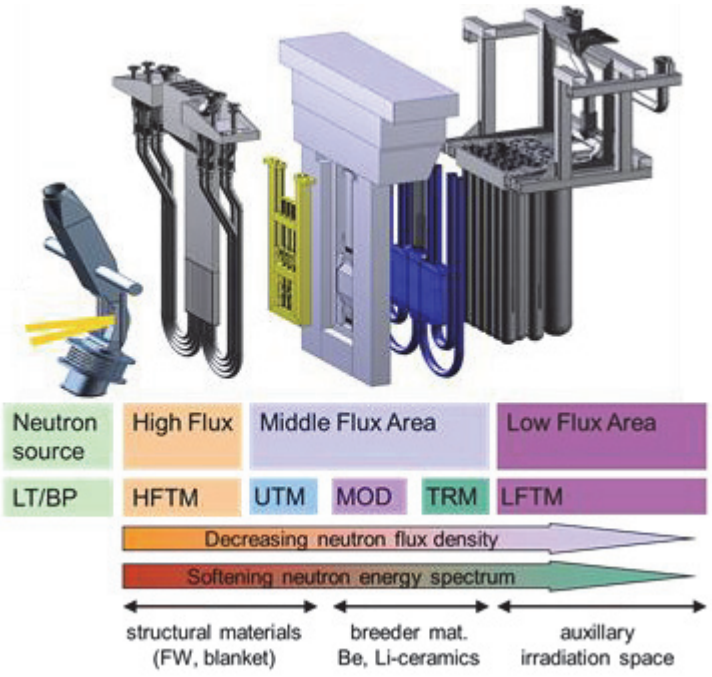

Fig. 1: Overview on the irradiation experiments inside the IFMIF Target- and Testcell (TTC).

The High Flux Test Module (HFTM) is the irradiation device for miniaturized SSTT samples of structural materials. The HFTM is positioned immediately behind the neutron source inside the TTC. The HFTM contains up to 24 irradiation rigs/capsules with approximately 80 SSTT

samples. It is possible to adjust individual temperatures for the specimens in each rig, in the range of 250 – 550°C.

The Tritium Release Test Module (TRM) is filled with specimen of tritium breeding materials, such as Li_2SiO_4, Beryllium, and others. The tritium release can be measured in situ during the irradiation, and the change in specimen structure (porosity etc.) can be examined after the irradiation.

Engineering Design and Validation of the HFTM and TRTM test modules

The design of the HFTM and TRTM was consolidated. Based on the latest CAD models and operation conditions, finalizing neutronic and thermal hydraulic (CFD) analyses were performed, and the derived design was documented in the TF01 and TF04 DDD-III design reports.

The written DDD-III reports define in detail the system functions, interfaces, requirements and design features. The design is characterized in terms of

- Component description including technical drawings, assembly (in hot cells) and quality control procedures
- Operation scenarios including control procedures and interfaces to the ancillary systems, as well as requirements on nuclear waste evacuation.
- Design analyses, describing nuclear thermal and mechanical results. Nuclear response include DPA and gas (He, H, T) production in the material specimens and the structures, as well as decay heat production. Thermal analyses prove that the required irradiation temperature distributions can be reached.

The validation activities progressed with single rig mockup tests and the construction of the HFTM prototype.

- A single rig was operated in the helium loop and proved that all required irradiation temperatures could be reached (Example run see Figure 2)

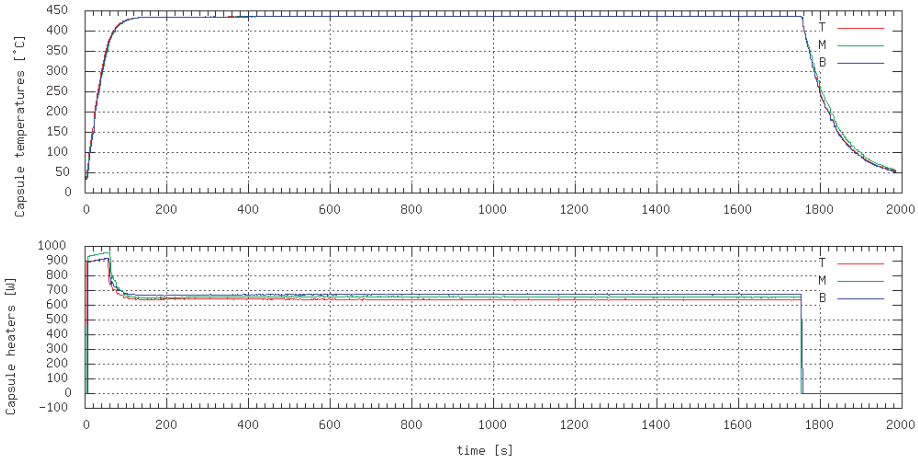

Fig. 2: Test run to operate the capsule at steady state temperature of 430°C.

- The HELOKA-LP test section port was finalized and tested.
- The HFTM-DC prototype manufacturing has been taken up, and the main body was machined.
- The handling of the small-scale specimens was practiced in a hot cell simulator, and estimates for the required maintenance times in IFMIF were derived (See Figure 3).
- Three capsules filled with specimens and NaK have been finalized, quality controlled and delivered to the BR2 reactor for irradiation tests in the scope of TF-02.

Fig. 3: Mounting of SSTT specimens into the assembly tray of an IFMIF capsule using a vacuum gripper operated by a standard manipulator in a hot cell simulator.

Engineering Design of the Target- and Test cell

The design of the test cell, adjacent handling cells and the ancillary systems was documented in the ED04 DDD-III document.

The written DDD-III report defines in detail the system functions, interfaces, requirements and design features. The design is characterized in terms of:

- Radiation protection analyses, dimensioning of shielding walls according to the calculated radiation loads
- Logistic flow of components during maintenance schemes, based on the plant requirements and optimizations using Event driven Process Chains. According physical layout was chosen and implemented in the global facility CAD model (See Figure 4)

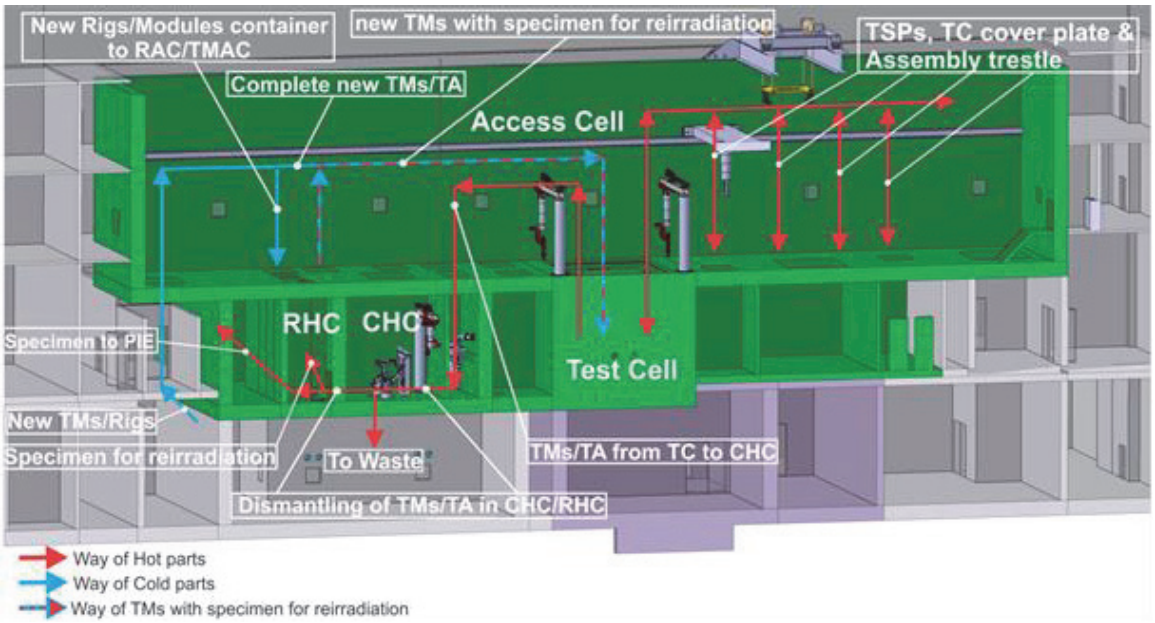

Fig. 4: Layout of handling cells around the test cell, showing major transportation paths and remote handling tools.

- Detail solutions for critical components, such as penetrations to the radiation protection areas, remote handled signal, energy and media connections, sealing, and cooling of nuclear heated components.

- Integration of requirements by client systems (i.e., test modules) in the definition of ancillary systems (helium or water cooling circuits, control units) and handling cells, basic dimensioning of the equipment and layout in the global facility CAD model.

Test Cell design and integration

- Design development and improvement of an assembly trestle (AST) to support and secure removal of the Test Modules (TMs) from the Test Cell (TC), respectively installation of new modules in the TC. With the help of the AST, the TMs are guided to their positions on the support structure, avoiding any danger of collision of the TMs with any part inside the TC during insertion / extraction of the TMs and guaranteeing accurate positioning. Additionally the design of the TC and TM Interface Heads (TMIH) was accordingly adapted for the use of the assembly trestle.
- Down-scaling and simplifying the TC CAD model in order to make a three-dimensional solid model of the Test Cell using a 3D printer.

Access Cell and Test Module Handling Cells

- Engineering design work on the access cell (AC) and test module handling cells (TMHCs) has been finished and successfully integrated in the IFMIF plant layout model.
- Updating and detailing specified and generic RH equipment of the TMHCs has been conducted
- The plant breakdown structure (pbs) has been updated
- Process description of maintenance activities on test modules and target assembly was detailed, based on information from parties.

Conclusions

The Engineering Design Activities for the IFMIF systems under responsibility of KIT have been successfully finished by preparation, review and approval of the according system design documents. The Validation activities for the High Flux Test Module, aiming at production and test of a prototype are ongoing, while results with single rigs already proved the fitness of the design.

Involvement of industrial partners

- Kraftanlagen Heidelberg GmbH: Construction of the HELOKA-LP low pressure helium cooling loop.
- Babcock Noell : Feasibility study of Test Cell concepts

Staff:

A. Abou-Sena	M. Kubaschewski
F. Arbeiter	C. Lang
T. Böttcher	V. Madzharov
Y. Chen	M. Mittwollen
B. Dolensky	A.-L. Muche
D. Eilert	G. Schlindwein
J. Freund	P. Schubert
T. Heupel	K. Tian
Ch. Klein	K. Zinn

Acknowledgement

This work was financially supported by the Ministry of Research and Education (BMBF) under the grant No. 03FUS0008. The views and opinions expressed herein do not reflect necessarily those of the BMBF or the European Commission.

Fuel Cycle –
Vacuum Pumping

High-performance Computation of Vacuum Flows in Fusion Reactors (HPC-FF-SIMVAC, IFERC-CSC-VACKIT)

Background and objectives

The prediction and calculation of vacuum gas flows is of key importance for the design and operation of fusion machines and the specific vacuum pumps used there. The gas flows in such systems vary from the free molecular regime to the hydrodynamic limit, with corresponding Knudsen numbers covering the whole range of rarefaction, and the corresponding simulation methods are different.

KIT has developed the ProVac3D (Profile of the Vacuum system of 3D complexities) software, which is a Test particle Monte Carlo simulation code for free molecular gas flow based on the time-of-flight accumulation method. After the parallelization, the powerful simulation capability of ProVac3D in the supercomputers of HPC-FF at JSC and Helios at IFERC-CSC makes it a versatile software to assist the design works of the vacuums systems of fusion reactors.

Simulation of a diffusion pump by ProVac3D

Within the EU activities in view of DEMO, an assessment of vacuum pump technology has been made and new concepts have been identified which promise to drastically reduce tritium inventories and processing times of the DEMO fuel cycle [1, 2]. Currently, a new program is underway to develop a mercury diffusion pump as an alternative for the cryopump used in present fusion devices because it is perfectly tritium compatible, much less demanding in operating complexity and cost, and has no need for regeneration.

Inside a diffusion pump, the molecules of the gas load to be pumped are deflected to the pump bottom because of the momentum transfer by collisions with the high speed vapour jets ejected in the nozzles of the diffusion pump. ProVac3D provides a modern molecular modeling technique to simulate a diffusion pump as follows. First, we calculate the background density of the mercury molecules established by the mercury jets. Secondly, the gas molecules of the gas load coming from the pump inlet will be simulated to check the influence from the pump geometry and properly consider the forepump influence. Finally, the collisions between the molecules of the gas load and the mercury molecules in the background will be considered.

As this stepwise approach is novel, ProVac3D has been modified accordingly and validated against experimental data of a large linear jet mercury pump built and tested in the Livermore Research Laboratory more than 50 years ago [3]. In longitudinal direction this pump featured two linear jet stages where the gas jet of the mercury molecules is ejected by a nozzle stock at a very high speed. The upper nozzle position of the pump was varied during the experiments, which allowed for a parametric study by ProVac3D for cross-check, see Fig. 1. The relative deviation of the ultimate pumping speed for the upper injection tube at the top positions was around 9%, which is good enough for such a big and complex pump which could never be modelled before, and which is also considered surprisingly good in view of the limited experimental accuracy that was available 50 years ago. This means that ProVac3D will be used as the development tool for the DEMO diffusion pump design [4]. The simulation results also showed that the pumping speed with the mercury jets has been enhanced by at least 10 times compared to the case without the mercury jet, and the pumping speed of the diffusion pump is not sensitive to the pumping speed of the forepump because the jets will prevent the backward movements of the gas molecules.

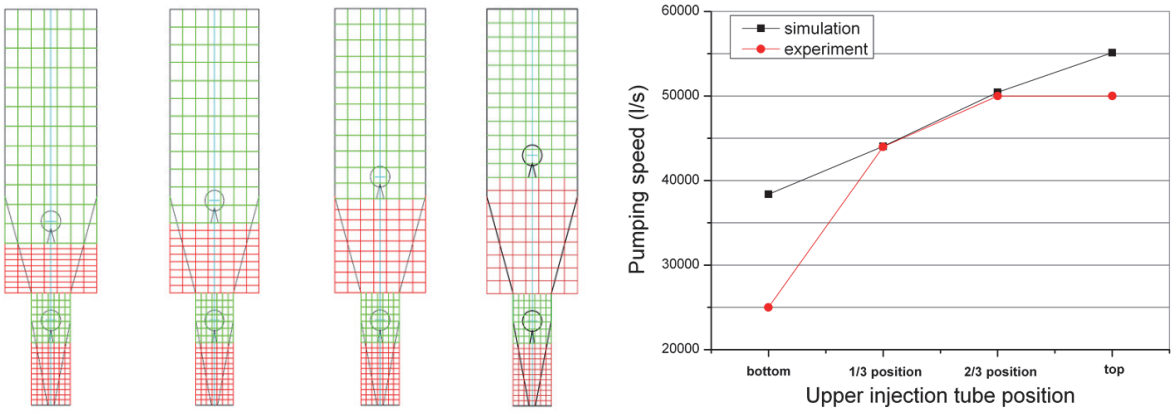

Fig. 1: Different upper injection tube positions and the corresponding simulation meshes (left), and the comparison between the simulation results and the experimental results.

Transmission probability studies of a cryopump baffle

For the present DEMO cryogenic pump design, the pumping effects come from the adsorption of the gas molecules on the pumping panels coated with activated charcoal, respectively. Generally speaking, the overall pumping speed of the cryopump depends on the pump geometry, such as the number of panels and their configuration, and obviously on the sticking coefficient of the gas molecules on the panel. In a new experiment in support of the DEMO cryopump development, we will use our TIMO facility to experimentally determine the sticking coefficient of different gas species on the cryogenic charcoal panel at different temperatures. Fig. 2 shows the experiment sketch.

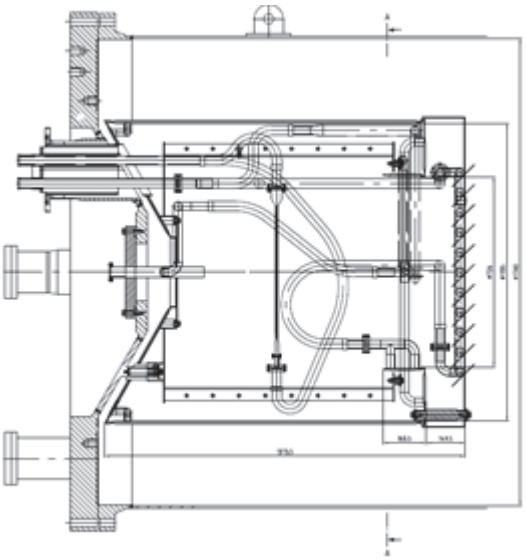

Fig. 2: Sketch of the experimental configuration with the pumping panel in the middle and the baffle in the front (right side).

The baffle in front of the vessel is used to protect the panel from the thermal radiation from the outside. However, it will reduce the transmission probability of the gas molecules. This effect has been assessed by ProVac3D simulations. In order to be precise, our simulation model has included not only the experimental vessel but also the total TIMO facility, as we calculated the pumping speed of the ITER model pump. As shown in Table 1, the transmission probability (w) has been simulated as a function of the number of the thermal shield fins (n), the tilted angle (a), and the shield width (d).

Table 1: Calculated transmission probabilities. The chosen case is highlighted in grey.

w(n=11,a=45,d=120)=0.30	w(n=11,a=45,d=120)=0.30
w(n=11,a=40,d=120)=0.33	w(n=11,a=40,d=132)=0.32
w(n=11,a=35,d=120)=0.35	w(n=11,a=35,d=148)=0.33
w(n=11,a=30,d=120)=0.37	w(n=11,a=30,d=170)=0.33
w(n=11,a=25,d=120)=0.39	w(n=11,a=25,d=201)=0.33
w(n=11,a=20,d=120)=0.41	w(n=11,a=20,d=248)=0.32
w(n=9,a=45,d=120)=0.34	w(n=9,a=45,d=150)=0.31
w(n=9,a=45,d=100)=0.36	

The optimum configuration in terms of manufacturability and performance was found with a transmission probability of 0.39 for a baffle structure with 11 baffle fins which have an angle to the horizontal axis of 25° and a length of 120 mm (shown also in Fig. 2).

Conclusions and outlook

The ProVac3D code has been used to simulate different vacuum systems. Our computation quota in the supercomputers of HPC-FF at JSC and Helios at IFERC-CSC provide us the capability to simulate also complicated systems. Further code development, validation and application are foreseen in the work plan of the next year.

Staff:

X. Luo

Literature:

[1] Chr. Day, Th. Giegerich, The direct internal recycling concept to simplify the fuel cycle of a fusion power plant, Fusion Engineering and Design 88 (2013) 616-620.

[2] Chr. Day, Th. Giegerich, Development of advanced exhaust pumping technology for a DT fusion power plant, IEEE Transactions on Plasma Science 42 (2014) 1058-1071.

[3] E. Lind, J. Steinhaus, Development of a large linear jet mercury diffusion pump, Report MTA-14, Livermore Research Laboratory, Livermore, CA, US, Jan. 1953.

[4] X. Luo, T. Giegerich, and C. Day, Monte Carlo simulation of a vapour diffusion pump, 19th Int. Vacuum Congress, Sept. 2013, Paris, France.

Acknowledgement

This work, supported by the European Communities under the contract of Association between EURATOM and Karlsruhe Institute of Technology, was carried out within the framework of the European Fusion Development Agreement. The views and opinions expressed herein do not necessarily reflect those of the European Commission.

Contribution to Neutral Beam Test Facility (F4E-FPA-NBTF + WP08-GOT-NIPEE)

Background and objectives

Within the Framework Partnership Agreement on the Neutral Beam Test Facility (NBTF) currently under construction in Padova, Italy, KIT is charged as Third Party to support Consorzio-RFX (the host of the experiment) in the area of thermohydraulic analyses of components installed in the MITICA vacuum chamber. The present reporting period is the second year of an eight year contract under which KIT is contributing. In 2013, the contributions were mainly aimed to support RFX on the design development of the Residual Ion Dump (RID), a main beam line component of the neutral beam injection system. An additional activity was the continuation of supporting RFX in the development of a Technical Specification for the cryogenic plant to be procured in 2014.

This work was also supported by the Goal Oriented Training Programme on Negative Ion Physics and Engineering Expertise (NIPEE) which was finalized in 2013.

In the following, the RID activities are described with three highlights: thermo-mechanical analyses of the system of cooling pipes of the component, a mechanical analysis of its support structure during a seismic event and the fluid-dynamical analysis of one cooling channel in great detail.

Thermo-mechanical verification analysis of the RID cooling pipework

The residual ion dump removes the remaining ion particles from the beam exiting the neutralizer. For this purpose, an electric field deflects the charged particles of the beam onto its panels. In order to dissipate the heat power, the RID (Fig. 1) consists basically of five water cooled vertical panels. This cooling pipework (Fig. 2) had to be analysed to verify the design regarding deformations and stresses occurring during operation. The major challenge results from the fact that the pipework is extraordinarily complex, with many different diameters and complicated mechanical constraints. The demanding thermal deformations to be checked are caused by the high temperature gradients between the cooling water in- and outlet sides and come from the enormous heat load to be handled by the RID.

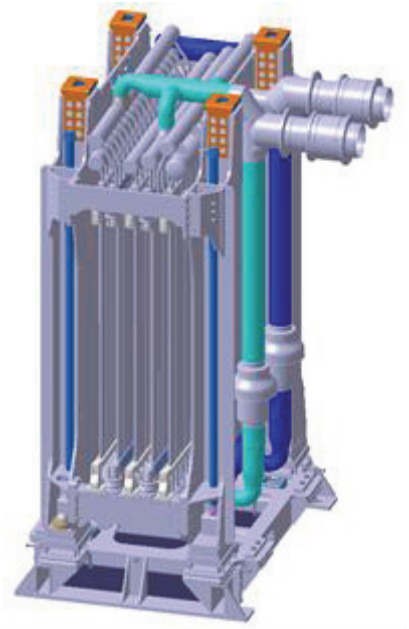

Fig. 1: Geometry of the RID, showing the five parallel plates inside which the not neutralized and still charged part of the beam is stopped.

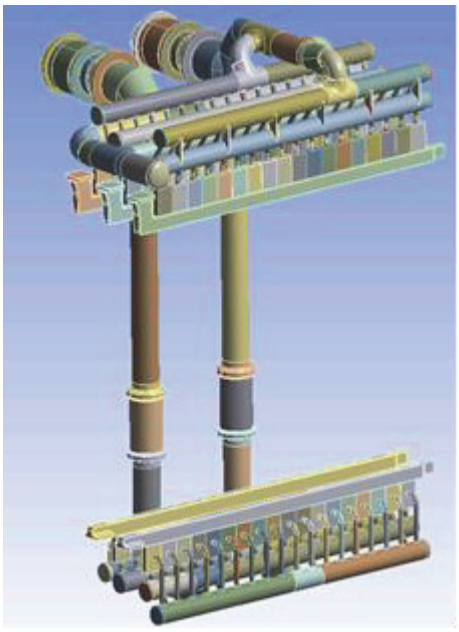

Fig. 2: Geometry of the cooling pipework with hidden plates.

While the mechanical results of the analyses was acceptable, the calculated thermal behaviour of the pipework (Fig. 3) was found to be not satisfactory and necessitated a significant design improvement, which is currently still being implemented at RFX. The basic idea behind is a strong reduction of deformation and stresses by bringing the horizontal manifold pipes along the component to a common level and increasing the length of the 180 individual supply pipes towards the beam stopper. This change will reduce the total deformations of the panels, improve therefore the precision for the beam optics and will additionally reduce the occurring stresses by an increased flexibility of the pipework.

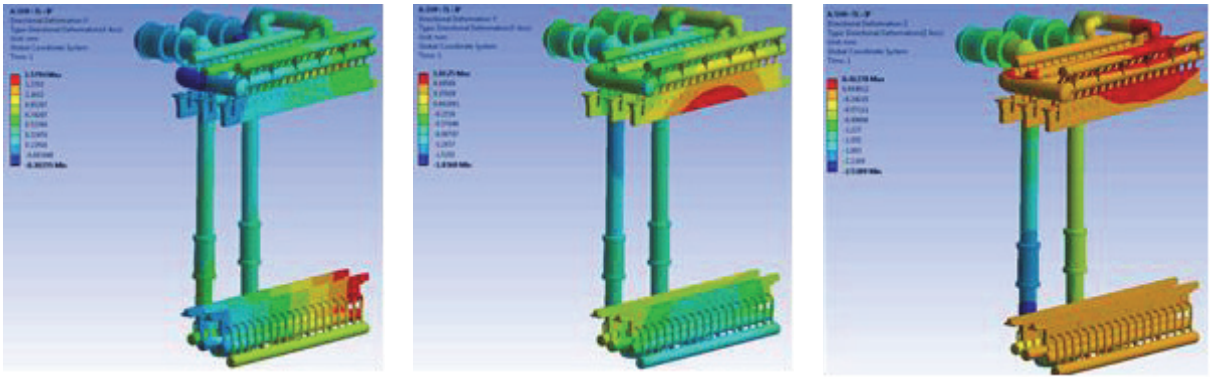

Fig. 3: The resulting displacements in the X,Y,Z direction of the original pipework; since they are not satisfactory for beam optics a re-design was decided and is ongoing.

Seismic analysis of the support structure of the RID

A further step taken in design verification was an appropriate investigation of the RID behaviour during a seismic event. This analysis started with the RID support structure which connects the entire RID directly to the Neutral Beam vessel. The analysis was required to be performed under the seismic spectrum of the ITER building which is more demanding as for the NBTF site. The treatment of the seismic response was applied to the structure via acceleration spectra. Such an approach consists of a static structural analysis to evaluate the prestress condition, a modal analysis and finally the response spectrum analysis.

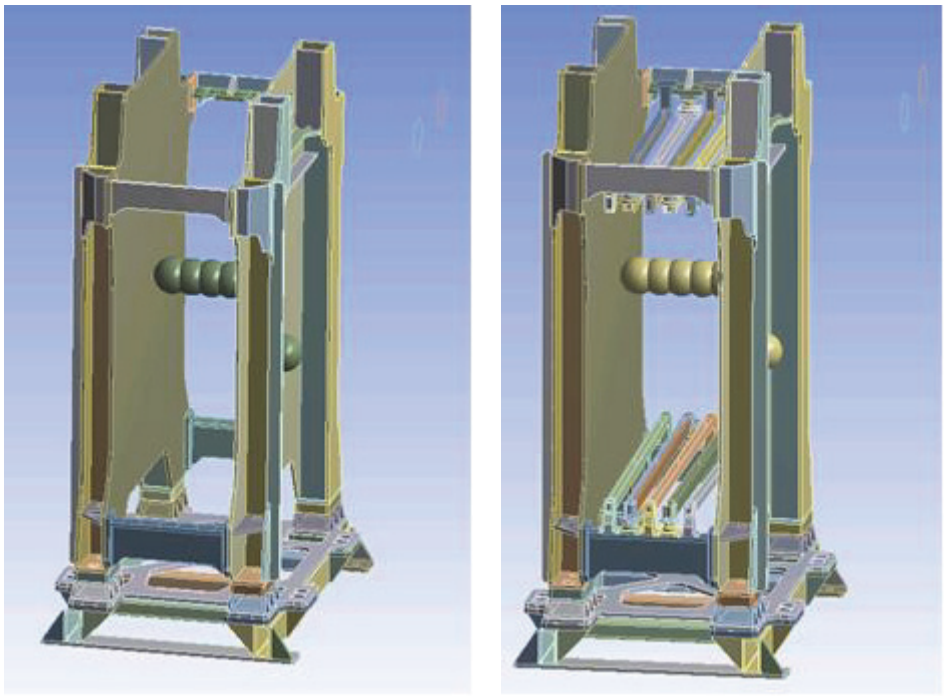

Fig. 4: Different simplifications of the RID structure.

To run such a comprehensive analysis, the model had to be simplified significantly to consider computational limitations. For this simplification, the panel masses have been replaced by lump masses while the mechanical behaviour and all real constraints of the component have to be kept (Fig. 4). The following modal analysis was then carried out until the number of calculated modes was sufficient to include a mass participation of at least 90% in each direction; Fig. 5 is showing an example result. Overall, a final design could be developed that fulfilled all seismic requirements.

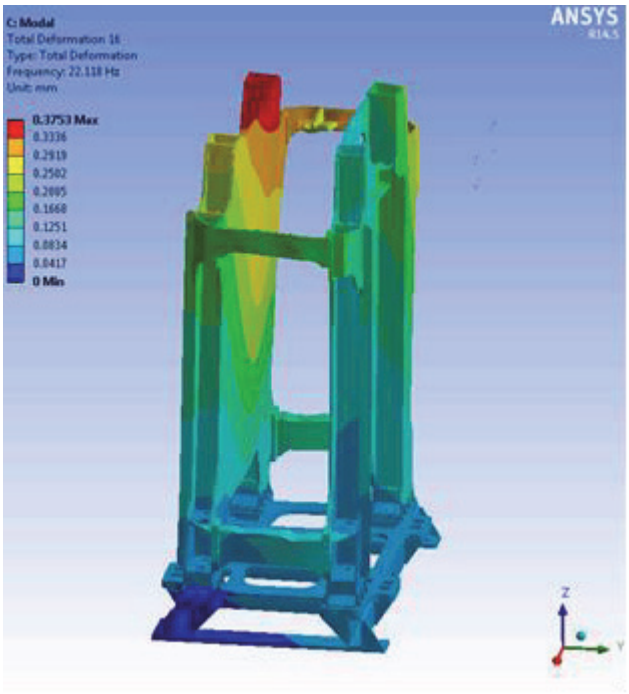

Fig. 5: Total deformation of the structure during a seismic event and for an individual mode – here for example under 22 Hz in Y- direction.

Fluid-dynamic detail analysis of a cooling channel

A substantial effort was made for the detailed fluid-dynamic analysis of the cooling channels inside the RID panels. This investigation was needed to optimize and verify the global cooling water supply scheme of the entire RID, of the cooling behaviour at the panel areas with the highest thermal load and of the detailed geometry inside those cooling channels to ensure optimum heat transfer.

Fig. 6: Schematic view of the inner structure of a BSE with parallel cooling channels (twisted tape for turbulence promotion not shown).

The RID contains five panels (see Fig. 1), each of these panels consists of 18 parallel segments, the beam stopping elements (BSE). Fig. 6 shows a schematic view of the internal cooling channel arrangement in each BSE.

During beam operation, the RID will be loaded thermally up to ~10 MW/m^2 locally and it is clearly needed to achieve best cooling efficiency to prevent the component from any damage. The design basis for optimal heat transfer is the implementation of twisted tape (TT) into the cooling channels leading to a strong turbulent flow inside and consequently an increased heat transport from the metal into the cooling water flow. Here, a manufacturing detail had to be implemented since it was of paramount importance: The cooling channels in the BSE have to be drilled from both ends, which leads to an unavoidable step in the middle of the channel which acts as a distortion of the water flow, influencing strongly the local behaviour and the total pressure loss. As a consequence to the step, also the tape has to be installed with two halves from both ends into the channel. The segmentation of the TT increases the local irregularity and had therefore to be investigated in a very detailed manner.

The performed analyses in general aimed to find an optimal balance between the strongly interlinked parameters tape thickness, resulting pressure loss along the channel and temperature rise in the cooling water bulk. Thereby, the investigation was done using a mixture of analytical calculations along the full channel length and a detailed CFX model in ANSYS of

a representative section of it. Fig. 7 shows a central cut out of the ANSYS model, visualizing the velocity distribution in the cooling water at the central step.

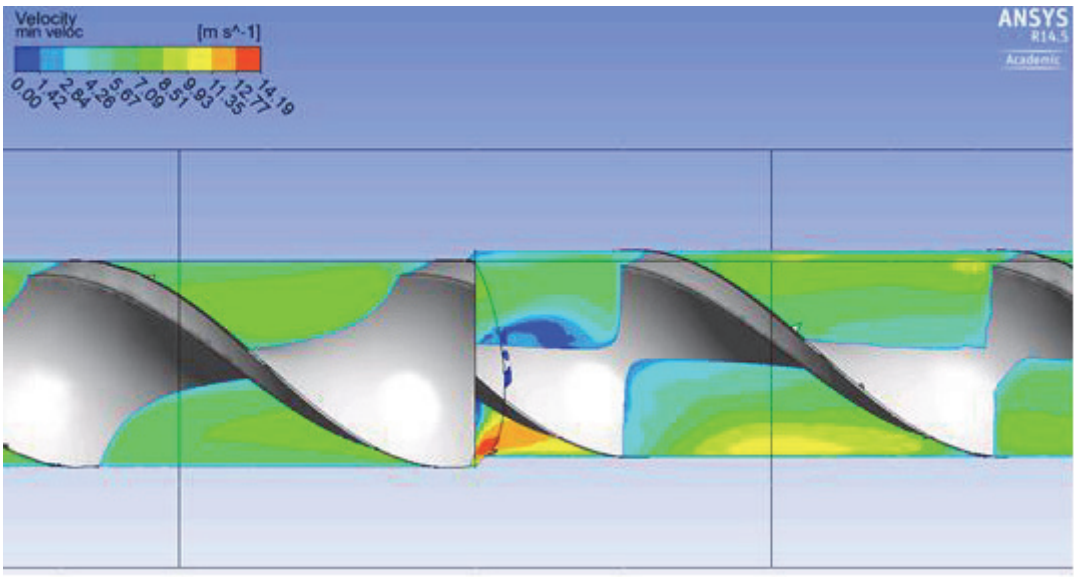

Fig. 7: Central section of the analysed channel showing the step in the drilling, the interruption of the twisted tape (grey) and the resulting effects on the cooling water velocity.

Since during the investigations several problems regarding supply scheme and insufficient mass flow have been found and solved, several iterative loops had to be performed. Thereby the global inlet temperatures of the cooling water were varied as well as the mass flow in the channel and the TT thickness. The final result that was achieved by these iterative investigations is now an adapted supply scheme for the whole RID and an accepted operation window which allows a higher inlet temperature of the water as it is foreseen in ITER. Moreover, a design was found which works with different TT thicknesses and therefore with different mass flows in the individual BSE to distribute the cooling potential according to the different local heating demands along the component.

Conclusions and future work

The thermo-mechanical analyses of the cooling pipework were completed successfully and resulted in some significant design improvements currently under implementation in the overall CAD model at RFX. The detailed and extensive investigations and optimizations on the fluid-dynamic behaviour of the cooling channels lead to an adaptation of the overall supply scheme of the RID, to a design change regarding the used types of TT and a detailed verification that these improved design and operation parameters will lead to a reliable operation under all expectable conditions. The successfully performed seismic analysis of the RID support structure will be continued within WP 2014 for the pipework system and the integrated model of the component, in order to support RFX preparing the upcoming final design review of several beam line components during 2014.

Additionally, it was already agreed to extend the seismic analyses from the RID to the NBTF beam source in 2014.

Staff:

S. Ochoa
St. Hanke
H. Strobel

Acknowledgement

This work was supported by Fusion for Energy under the Framework Partnership Agreement on the NBTF. The views and opinions expressed herein reflect only the authors' views. Fusion for Energy is not liable for any use that may be made of the information contained therein.

DEMO System Integration Study of Vacuum Pumping System (WP13-SYS-03-T04-01)

Background

KIT has developed the KALPUREX process [1] which is a new vacuum pumping concept for fusion power plants. The so-called Direct Internal Recycling (DIR) concept [2] is based on a short-cut around the tritium plant via short way separation of hydrogen isotopes from the torus exhaust gas stream and their mixing with enriched tritium or deuterium flows to be directly recycled into the reactor. Metal foil pumps separate the unburnt fuel into a pure fuel flow (that can be recycled directly back to the machine without being processed in the tritium plant) and a residual gas flow, that will be treated in the tritium plant. Both gas flows (pure fuel + impurity rich gas) downstream the metal foil pump have to be pumped by tritium compatible diffusion pumps, that use mercury as working fluid. As backing pumps for the diffusion pumps, liquid ring pumps – also with mercury as working fluid – are foreseen.

Scope of this report

Especially the primary vacuum pumping systems (i.e. the metal foil pumps and the diffusion pumps) must be located close to the torus which has a strong impact on the overall machine design. In this task, the integration of the primary pumps into the current DEMO design has been assessed. The most important integration issues investigated here were (i) the pump location, (ii) the space requirements and (iii) the maintenance requirements. Based on the findings of this assessment, the latest DEMO CAD model has been modified and delivered to EFDA.

Pump location and space requirements

The current DEMO design foresees an ITER-style divertor configuration. This means the pumps must be connected to the sub-divertor region to pump out the gas and the impurities that accumulate there, equatorial- or other ports cannot be used. The gas accumulation is based on physical processes and must be considered as input for the design of the pumping system. In addition, long distances between divertor and pumps (pumping ducts) must be avoided as this would immediately reduce the duct conductance: Long pumping ducts do directly result in a larger number of required pumps and ducts that have to be connected to several positions in the divertor region. This increases the complexity of the overall system and must be avoided as far as possible. KIT suggests a solution where extra pumping ducts are connected to the divertor maintenance ducts (Fig. 1).

The space required below the machine has been estimated to at least 3.5 m (2 m pump, 0.5 m boiler, 1 m piping), based on throughput, conductance and pressure values expected for DEMO. This number is slightly more than what is foreseen in the current DEMO CAD model and has to be considered in order to avoid complicated and expensive design changes in a later stage. In this task, it has been found that pumping ports have to be attached to almost every divertor maintenance port to fulfil the pumping requirements. Nevertheless, the number of required pumping ducts is given by throughput conditions, and is independent of the space required below the machine.

Infrastructure and maintenance

All pumps have to be connected to infrastructure systems (heating- and cooling circuits for the diffusion- and the metal foil pumps) [1] located below the machine (Fig. 1). This pipe network is fed by a pump supply facility located further away. Also the fore-vacuum lines are located below the machine and connect the primary pumps with the roughing pumps which are located in a distance of some ten meters to the machine. A list of requirements for the infrastructure system has been worked out during this task.

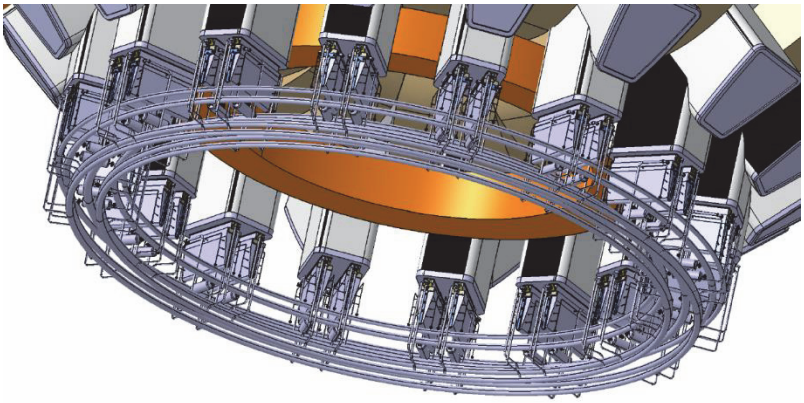

Fig. 1: Bottom view to the DEMO machine: Each segment is equipped with an additional pumping port (attached to the divertor maintenance port) that comprises two diffusion pumps. The pipe network needed to supply the pumps is also shown.

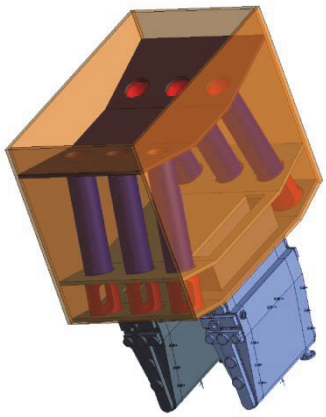

Fig. 2: The Metal Foil Pumps are located upstream the diffusion pumps inside the pumping ducts with access from below.

For remote maintenance, the metal foil pumps and the diffusion pumps have to be considered. Both pumps are installed between cryostat and bio-shield very close to the torus. This means that they will be exposed to strong neutronic radiation which will activate them to a certain extent. All pumps have to be optimized in a way that they do not need much maintenance. Whereas diffusion pumps have no movable components and thus are expected to be almost maintenance-free, for the metal foil pumps the situation could be different. It may also occur that one supply pipe becomes leaky. All systems must thus be installed in a way that they are accessible for remote maintenance. How this can be done e.g. in case of the metal foil pumps that have to be located upstream the diffusion pumps (and where, due to the machine cryostat, no access to the pumping duct from the side is possible), was investigated during this task. One possible result is shown in Fig. 2: The (cylindrical) metal foil pumps can be removed from below the machine.

Staff:

Th. Giegerich

Literature:

[1] Th. Giegerich, Chr. Day, The KALPUREX-Process - A new vacuum pumping process for exhaust gases in fusion power plants, ISFNT-2013, Sept. 2013, Barcelona, Spain, accepted for publication in Fusion Engineering and Design.

[2] Chr. Day, Th. Giegerich, The direct internal recycling concept to simplify the fuel cycle of a fusion power plant, Fusion Engineering and Design 88 (2013) 616-620.

Acknowledgement

This work, supported by the European Communities under the contract of Association between EURATOM and Karlsruhe Institute of Technology, was carried out within the framework of the European Fusion Development Agreement. The views and opinions expressed herein do not necessarily reflect those of the European Commission.

Activities in the EFDA ITER Physics Research Area A10 - Comprehensive Investigation of Fuelling and Pumping Operation Properties of Tokamaks (WP13-IPH-A10-P1)

Background and objectives

The EFDA ITER physics programme is divided in eleven research areas. The topic of research area 10 (project 1) is the inner fuel cycle modelling including pumping. In 2013, this area comprised five tasks from five different Associations (CCFE, DTU, FZJ, Hellenic Republic, and KIT). KIT was providing the project leadership co-ordinating the task and reporting to the responsible officer at EFDA.

The understanding of the complete inner fuel cycle including particle and impurity transport from/to plasma and the control of it with source and sink terms (gas puffing, pellets, vacuum pumping) is important for the operation of tokamaks. At normal operation, deuterium and tritium will be re-fuelled while helium and impurities should be removed from the core plasma via the divertor pumping system.

The operation of fuelling and pumping on fusion machines often relies on internal knowledge of the technical staff, gained by trial and error. This project aimed to set a validated knowledge base for the design and operation of the inner cycle of tokamaks and to identify the most prominent interdependencies between operational parameters as well as control and variability of system performance on one side and the relevant, most influential plasma parameters on the other side. Finally a predictive modelling of the complete fuel cycle was aimed for, with all its actuators in the four subsystems plasma chamber - divertor pumping – tritium plant.

In this reporting period, the subdivertor region (neutral gas side) was modelled by a most representative 3D Monte Carlo approach at physically sound boundary conditions, based on the preparation studies performed in WP12. This work was supported by an update of the two currently available lumped parameter code descriptions (kinetic database, ITERVAC) to reflect the recently revised, now frozen ITER divertor system design (change of the duct configuration, divertor cassette CAD design as received from ITER). The codes were upgraded accordingly. Plasma exhaust was simulated taking into account the X-point and MARFE formation, particularly under high density conditions. ITER-like pellet fuelling cases and different gas fuelling schemes were studied in order to reveal if there result any needs to modify the current understanding of flow rates involved. Finally, all information collected in this and the previous year was collected for integration, checked for consistency and finally a fuel cycle model being developed.

Co-ordination and monitoring of the whole project

In the first activity group, the development of a physics-based understanding of the ITER divertor neutral gas exhaust was continued and simulations of the neutral gas flow from divertor to the pumping systems were successfully performed. The input data were provided by B2/Eirene simulations showing one method of sharing results between different simulation programs. Further work is seen in the development of a 3D DSMC code for simulating the inner divertor flow and the finalisation of the network code developed in Hellenic Republic to handle large network models. The development of workflows that relate technical systems to physics parameters was found to be a very useful tool and it will be definitely further developed in the upcoming EUROFUSION programme.

In the subtask of plasma exhaust studies, simulations were performed as a sequence of steady-states with constant gas puffing rate. Similar to experiment, formation of a X-point MARFE is seen. Some quantities like the total flux incident can be calculated very well. Other quantities or changes of quantities, like the change of flux cannot be described. It is to be expected that better adjustment of the model to the conditions of particular experiments can

improve the agreement with measurements. Those adjustments include magnetic configuration, wall geometry, parameters of the pumping system, plasma content.

Experiments have been executed on MAST using pellet injection simultaneously with ELM mitigation with Resonant Magnetic Perturbations (RMP). The experiments show that the cloud surrounding the pellet is rather symmetric and has a diameter of about 5cm. The data are now carefully analysed with the aim to improve the physics models for plasmoids – which is critical for ITER fuelling. An analysis of post pellet transport properties continued using the linear GS2 code. It is clearly seen that the perturbation of density and temperature profiles due to fuelling pellets can change the microstability in the outer plasma region. The studies will continue in 2014 by analysing new data from MAST experiments, but also by performing dedicated experiments in AUG and JET. The aim is to validate a model which can be used to optimise the density and isotope control in ITER and DEMO.

In 2013, new experiments for developing the Collective Thomson scattering (CTS) were performed. A new set-up using two independent heterodyne receiver systems enables subtraction of the unknown part from the total spectrum, revealing the resulting CTS spectrum. After subtraction of the spurious signal from the spectra, good agreement was found between the measured CTS spectra and theoretical predictions. The present results demonstrate the promising use of this novel diagnostic, which is adding bulk ion rotation velocity and bulk ion temperature information on top of the fuel ion ratio measurements. These measurements with a microwave diagnostic have importance for ITER and future burning plasma experiments.

KIT contributions

Continued divertor neutral gas flow simulations with DSMC

In the EFDA working programme 2012 an approach was developed for how to provide a most representative 3D description of the subdivertor region. This is based on a promising combination of an efficient meshing tool and a powerful algorithm for solving the kinetic equation based on Direct Simulation Monte Carlo (DSMC) [1]. In the working programme 2013, this DSMC approach was then applied to the ITER divertor design (2008). It represents an expansion compared to the BGK model used in the neutral particle description involved in SOLPS/EIRENE. The calculations were done for some reference cases with the same assumptions and boundary conditions as done with SOLPS so that a comparison can directly reveal the influence of the DSMC collision kernel.

The numerical investigation of neutral helium/deuterium gas flow through the ITER 2008 divertor system was studied [2]. In Fig. 1 the bulk velocity contours for helium and deuterium are presented for two divertor gas reference pressures, namely 2.6 Pa and 9.9 Pa. In Fig. 1 it is seen that for both reference pressure cases, the gas flow located behind the inner vertical target (left-hand side of the divertor) travels towards the plasma chamber in all cases whereas for the duct behind the outer vertical target near to the pumping duct this does not always occur. It turns out that for helium gas only for the high-pressure case the particle flow reenters back into the plasma chamber through the gap of the outer duct (Fig. 1-top right). For the case of deuterium, the recirculation of neutral gas behind the targets and towards the plasma occurs for both studied divertor pressures.

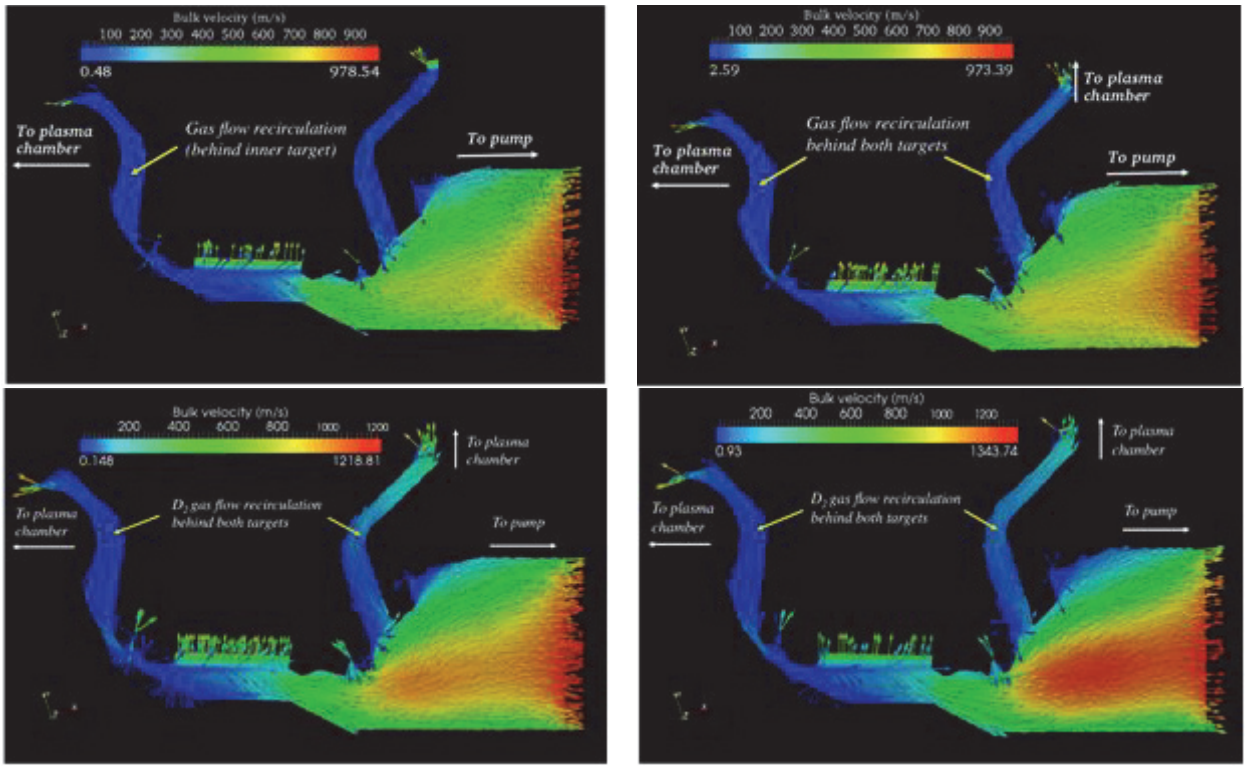

Fig. 1: Bulk velocity contour of helium (top) and deuterium (bottom) for two divertor reference gas pressures: 2.6 Pa (left) and 9.9 Pa (right).

Furthermore, the comparison between the corresponding DSMC modelling and ITERVAC results is presented. The study compares the local pressure values at specific locations of the sub-divertor geometry. 10 probe locations are defined and distributed along the sub-divertor geometry, see Fig. 2 (left). As seen in Fig. 2 (right), very good agreement was found for the probe locations below the dome and at all the probes located at the right-most part of the divertor geometry (outer arm and near the pump duct). Regardless the case study, the ITERVAC pressure values at the inner duct (probe 4 and 5) and nearby the inner slot (probe 3) differ by numerical factors between the values of (2, 3) when compared to those of the DSMC results. This probably suggests that toroidal effects, which are not taken into account in the present 2D-DSMC modelling, do play a role in the obtained flow pattern. The good agreement between DSMC and ITERVAC results was observed for the all the cases of gas helium and deuterium.

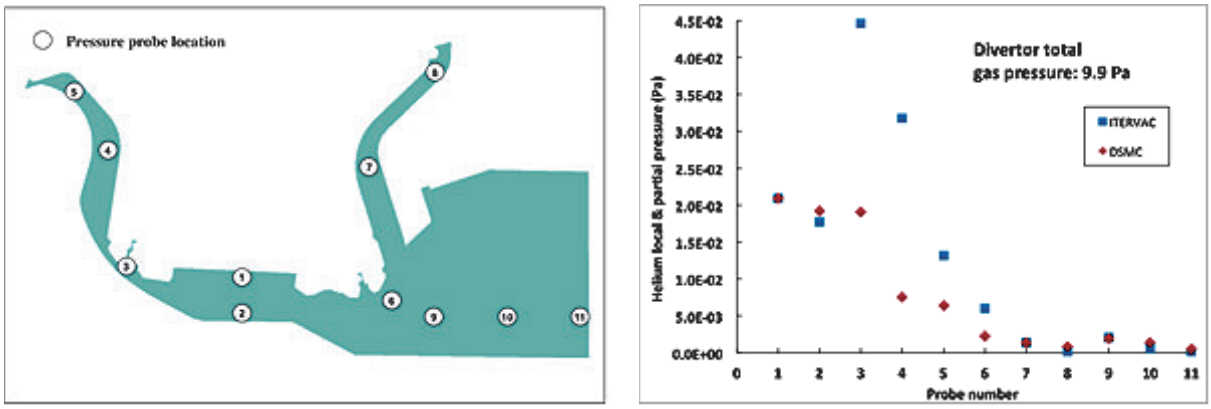

Fig. 2: A set of probe locations is distributed along the sub-divertor geometry (left). Comparison between DSMC and ITERVAC: local and partial pressure values at specific locations are compared in the sub-divertor region for helium gas (right).

The performance of the divertor pumping system under a massive gas injection event

The investigation of the role of the divertor cryopumps in the case of massive gas injection for disruption mitigation could be finalized in this reporting period. First some boundary conditions for massive gas injection events have been defined. Massive injections of deuterium, helium, neon, and argon have been studied. Then, gas flow calculations from the divertor dome towards the front of the cryopumps have been performed using ITERVAC, based on an upgraded divertor model. The calculated throughputs at the divertor just after a massive gas injection event are significantly larger than the maximum throughputs at the cryopumps, meaning that the cryopumps are overloaded, and resulting in a sudden pressure jump in front of the cryopumps.

The heat loads to the cryopump cryogenic circuits have been assessed and the large heat fluxes to the cryopumps result in a significant and rapid increase of the cryopumping surface temperatures normally cooled at 5 K. However, the consequences on the torus cryopumps operation depend on the gas species and quantities injected. The large quantities of deuterium and helium injected into the plasma cannot be fully processed by the torus cryopumps, leading to the spontaneous regeneration of the accumulated gases, while the pressure inside the torus remains high. As a consequence, additionally to the regeneration of the torus cryopumps, the large volume of the torus has to be pumped by the rough pumping system before the vacuum and thermal conditions for the start of the next plasma pulse are initiated again. On the other hand, the lower injected quantities of neon and argon required for plasma disruption mitigation can be efficiently pumped by the torus cryopumps, hence vacuum conditions in the torus are achieved again after a short time. Nevertheless, a regeneration of the accumulated neon and argon is recommended before starting a new pumping cycle. In these cases, the down-time of the torus pumping system is only limited to the regeneration time of the primary torus cryopumps. Moreover, the foreseen quantities of deuterium required for plasma disruption mitigation largely overpass the safety limit whereas neon and argon are not subject to any inventory safety limit.

Based on the primary torus cryopump operation after massive gas injection, the total amount of gas to be processed by the torus roughing and regeneration pumping system, the regeneration pressure and temperature of the torus cryopumps, and the pressure and temperature of the exceeding gas remaining in the torus have been estimated, opening a qualitative discussion on the turnover time of the torus vacuum system after a massive gas injection event.

Update and benchmark of the model for the ITER divertor pumping system

The whole divertor system is a complex arrangement of slots and ducts which provide intra-cassette and inter-cassette paths for gas flow. The divertor vacuum pumping system has to compete against the integral recycle flows towards the plasma. The conductance of this whole arrangement, which is, above all, operated in the transitional flow regime, represents a very complex geometry which is challenging for modelling. There are currently two approaches which are both based on treating the real case as a network of channels.

One of them, which is already well validated, is based on the KIT ITERVAC code, which is employing individual correlations for channel flows. There is already a model of the ITER divertor pumping system, but this is based on the ITER configuration of 2008 (with different divertor cassette designs, different ports, and different number of pumps). The other, recently developed in Hellenic Republic, is employing a database with solutions the kinetic equation. For this code, a model is currently being prepared based on the most recent ITER design.

The main work was therefore the update of the ITERVAC main model to the ITER divertor design released in 2012. Based on the main model the models for simulation of massive gas injection, a model of one single cassette and the model for comparison with the code developed by Hellenic Republic were generated. Several simulations were performed to support the other activities (massive gas injection, DSMC calculations) and a benchmarking of ITER-

VAC and the code developed by Hellenic Republic against each other. The simulations results show the large influence of the gaps between divertor cassettes at partly detached plasma operation.

Fuel Cycle system integration

The sizing of the inner fuel cycle of a fusion machine is defined by the machine gas throughput and composition, and the sub-divertor neutral pressure at which the exhaust gas has to be pumped. Hence, it is primarily given by plasma physics needs and plasma control aspects, so that an integrated design approach is needed, which has to combine physics and technology. Such an approach has been developed for the divertor pumping system for which it was shown how the technical design can be rigorously traced back to the physics of the plasma [4].

The detachment criterion defines very clearly operational limit points that can be translated into requirements on the gas throughput and the gas exhaust vacuum system. In order to illustrate this strong interrelation, a quantitative analysis has been made for the ITER like divertor and torus exhaust vacuum configuration (with cryopumps) in a DEMO reactor environment with argon as radiative seeding gas. The analysis provided the number of cryopumps required for steady-state operation under detached divertor conditions. The effective pumping speed at the full divertor ring could then be derived from a balance of the pumping speed of (all) the divertor vacuum pumps (connected via ducts and ports with the subdivertor region of some divertors; other divertors are linked to these via toroidal slots) and the plasma that is treated as a pump with black hole pumping speed via the openings with which divertor cassettes face the plasma (toroidally and poloidally). The dependence of the effective pumping speed per cryopump on divertor neutral density was approximated on the basis of literature values and complementary own simulations, the modelling of the transition from attached to detached states was done according the method outlined in [5]. To ensure the detachment onset, the particle flux to be exhausted can be calculated as a function of the divertor neutral density. The Figure 3 is illustrating the final result of the chosen example, namely the number of required cryopumps as a function of neutral density for different particle fluxes in the divertor.

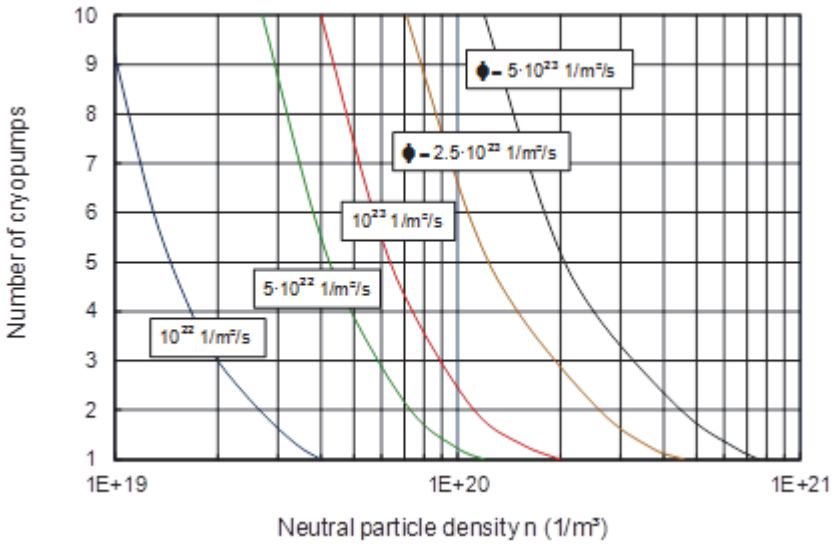

Fig. 3: Dependence of the required number of cryopumps on the neutral particle density at divertor.

Both the detachment analysis and the effective pumping speed evaluation are based on a 1D lumped approach. An alternative, much more consistent and physics-based approach is to simulate the sub-divertor neutral gas region by the Boltzmann equation for neutral gas movements using particle fluxes along the (simplified) divertor contour as boundary condi-

tions that have been consistently calculated in a separate step by a plasma physics code (SOLPS, SONIC). This approach will be studied in more detail in the future.

Current status and outlook

This 2-year project is now completed. Further understanding of the fuel cycle with a physics-based description of the interlinks between neutral gas and plasma will be developed in the EUROFUSION programme.

Staff:

Chr. Day
C. Gleason-Gonzalez
V. Hauer
M. Scannapiego
St. Varoutis

Literature:

[1] Cr. Gleason-Gonzalez, St. Varoutis, V. Hauer, Chr. Day, Divertor region gas kinetics – an engineering approach, Proc. 40th EPS Conference on Plasma Physics, Espoo, Finland, July 2013.

[2] Cr. Gleason-Gonzalez, St. Varoutis, V. Hauer, Chr. Day, Simulation of neutral gas flow in a tokamak divertor using the Direct Simulation Monte Carlo method, ISFNT-2013, Sept. 2013, Barcelona, Spain, accepted for publication in Fusion Engineering and Design.

[3] M. Scannapiego, Chr. Day, V. Hauer, Consequences of plasma disruption mitigation by massive gas injection on the ITER torus cryopumping system, ISFNT-2013, Sept. 2013, Barcelona, Spain, accepted for publication in Fusion Engineering and Design.

[4] Chr. Day et al., Towards a physics-integrated view of divertor pumping, ISFNT-2013, Sept. 2013, Barcelona, Spain, accepted for publication in Fusion Engineering and Design.

[5] Yu. Igitkhanov et al., Proc. 21st EPS Conference on Plasma Physics, Montpellier, France, June 1994.

Acknowledgement

This work, supported by the European Communities under the contract of Association between EURATOM and Karlsruhe Institute of Technology, was carried out within the framework of the European Fusion Development Agreement. The views and opinions expressed herein do not necessarily reflect those of the European Commission.

Investigation of Candidate Vacuum Pumping Systems for DEMO (WP13-DAS-05-T01-01)

Background

In 2011, in a task by the EFDA Power Plant Physics & Technology department, the fuel cycle requirements and different vacuum pumping systems for DEMO have been assessed. It was found that a simple up-scaling of the cryopump technology used at ITER to the DEMO throughput is critical, as it would lead to a very large tritium inventory in the whole pumping system and following from the batchwise operation mode of these pumps to a high cryogenic demand in a most complex operation mode. Instead of the discontinuous working solution adopted at ITER, KIT proposed a continuously working and non-cryogenic three stage pumping train for DEMO. It consists of a vapour diffusion pump as primary pump, backed up by a liquid ring pump. Both pumps are hermetically sealed and apply a liquid metal (mercury as initial candidate) as working fluid to make them tritium compatible.

Additional to these non-cryogenic pumps, a primary pump was proposed that provides a separating function for the pumped gas: The unburnt fuel (pure deuterium and tritium) is separated from other impurities (including helium) sharply and recycled directly to the machine [1, 2]. In consequence, only a small gas flow that is enriched with helium and other impurities must then be processed in the tritium plant, which could be appropriately downsized. This new concept has been introduced as an option for DEMO as Direct Internal Recycling (DIR) [3]. The development of this concept is the main objective of this task.

Scope of this work

The focus of the 2013 work was given to complete the experimental validation of this new pumping concept. The proof-of-principle testing of a small-scale mercury diffusion pump with integrated jet stage has already been successful in 2012 [4]. In this year, the proof-of-principle experiments of the liquid ring pump were done in the THESEUS facility, and the demonstration of the metal foil pump principle performed in a completely new facility, named HERMES (Hydrogen Experiment for Research of Metal foils and Superpermeability).

In parallel to the experimental work, modelling activities are ongoing to support the pump design activities of a diffusion pump and a metal foil pump in a DEMO relevant scale. These technical-scale pumps shall be manufactured and tested in THESEUS within the next years [5]. Also an infrastructure and space assessment for these pumps started as this gives important information for the preparation of the pump tests in THESEUS and even for the future DEMO design.

Metal foil proof-of-principle testing in HERMES

Primary aim of the HERMES experiment is the proof-of-principle of the superpermeability of metal foils and energetic hydrogen. Superpermeability describes the effect of a strong and hydrogen specific permeation through a metal foil against a pressure gradient, which occurs when a flux of energetic (atomic) hydrogen is applied to a metal foil. The experiment is designed in such a way that it is versatile enough to study superpermeability in a parametric way. It allows the measurement of the pumping speed and the compression ratio under variation of gas species, ion energy and foil material, temperature and thickness. It is expected to exploit the HERMES experiment intensively in the next years in order to generate a complete database which then can be used to support conceptual and detailed design activities of such a pump.

The experiment consists of two vacuum chambers, the up- and the downstream chamber, connected by a removable adapter in which the metal foil is installed; see Fig. 1 [6].

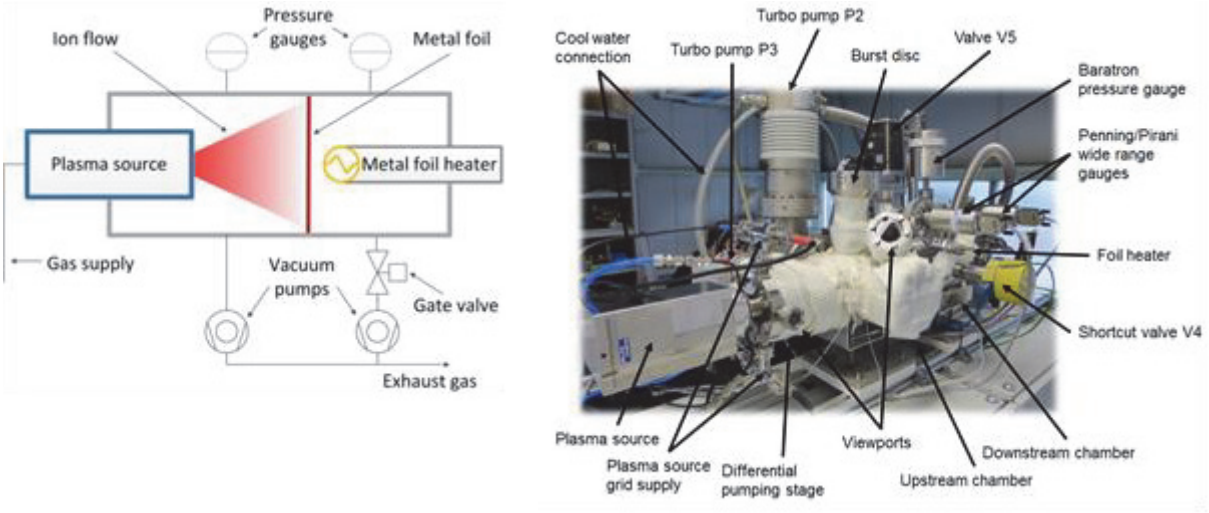

Fig. 1: The HERMES experiment. Schematic view (left) and Photo of the set-up.

When plasma is ignited in the upstream chamber to drive superpermeation, a pressure rise in the downstream chamber at the other side of the metal foil should be seen. Knowing the downstream chamber pressure and -volume, the particle flux through the metal foil and the compression can be calculated. These information is essential for the development of a proper design of a metal foil pump. As source of energetic hydrogen, a microwave excited plasma is used in HERMES. Fig. 2 illustrates the different light intensities of the hydrogen plasma at different pressures.

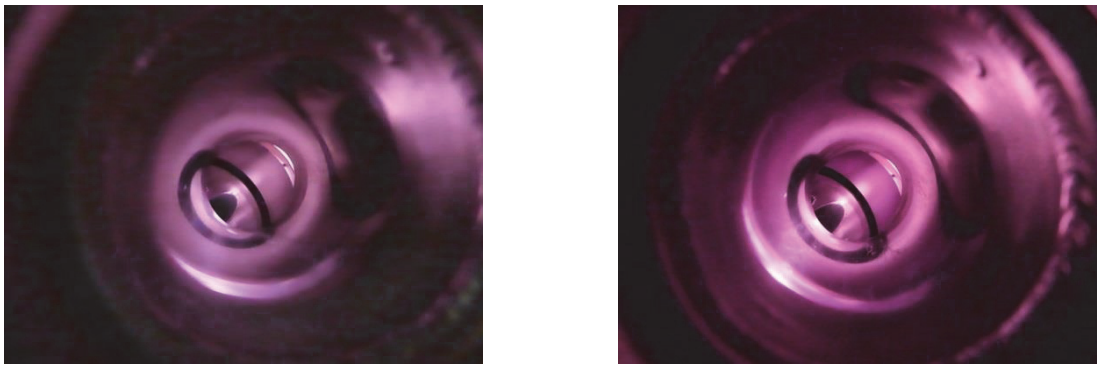

Fig. 2: Hydrogen plasmas in HERMES, at 0.8 (left) and 2 Pa (right).

Fig. 3 illustrates the successful proof-of-principle experiment. It was a measured with a vanadium foil, heated at 300 °C and shows the pressure rise in the downstream chamber only once plasma is generated in the upstream chamber.

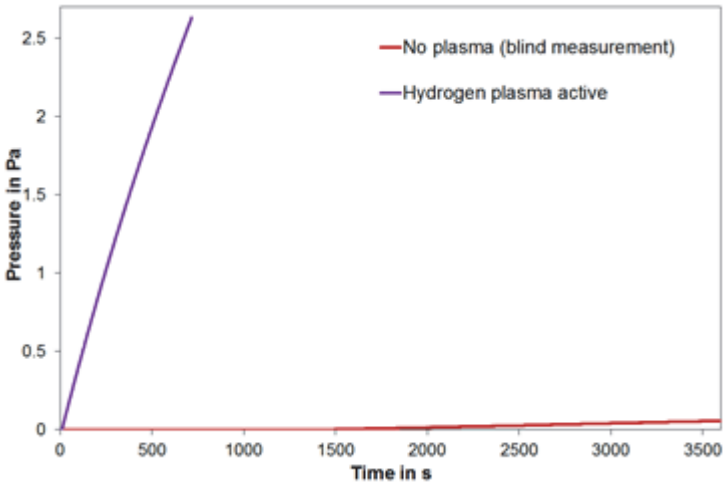

Fig. 3: Illustration of the superpermeability effect when the plasma is turned on.

Liquid ring pump proof-of-principle testing in THESEUS

The fact that liquid ring pumps are the most prominent pumps for chemical engineering and process industry was the motivation to start the development of this pump type in close consultation with industry. The tritium-compatible working fluid to be used is mercury, as for the vapour diffusion pump. Normally, the ultimate pressure is limited by the vapour pressure of the working fluid which is about 3 x 10^3 Pa for water. If a liquid is used whose vapour pressure is much lower, as is the case for mercury, an ultimate pressure of < 10 Pa could be reached theoretically. This has never been done in the past and it was one of the objectives in 2013 to identify the practical limits of that. Performance predictions have been tried, but it is felt to be difficult as the density of mercury is more than 13 times higher as the normally used water and also the vapour pressure is more than fourty times lower. So the prediction of ultimate pressure and pump performance as well as the validation of the mechanical design cannot be done without experiments in THESEUS. This facility (see Fig. 4, Fig. 5) will become the integrated test environment for the new vacuum pumps suggested for a fusion power plant [2, 5]. It shall demonstrate the applicability of the advanced pumping technologies and the DIR concept and build a rigorous understanding of how the pumps are working, and, by that, validate a predictive design code that will finally be used to elaborate the detailed design of a prototype in DEMO relevant, if not 1:1 scale.

The main properties of interest to measure in THESEUS are the ultimate pressure of the pumps, the pumping speed (defined as the ratio of throughput and inlet pressure) and compression at varied throughput. It is therefore mandatory to be able to test the pumps in a wide pressure range and for different gases. The throughput can be adjusted by mass flow controllers whereas the pressure can be measured by using capacitance diaphragm gauges. The pressure is measured in a dosing dome, to which all test pumps are connected.

Fig. 4: Gas dosing system, dosing dome and control room in THESEUS (upper level).

Fig. 5: Mercury vapour monitoring system and liquid ring pump housing in THESEUS (lower level).

The ring pump investigation has already started at KIT in 2012, when a pump design adapted to the high density working fluid mercury was developed and such a pump manufactured and procured. The 2013 work focused on the installation and the commissioning of the test pump in THESEUS. The pump has been commissioned by filling the mercury circuit with approx. 238 kg (18L) of liquid mercury. This amount of mercury accumulated mainly in the circuit (piping, flow meter, heat exchanger) and not only in the pump itself. Fig. 6 is showing a photo of the installed ring pump.

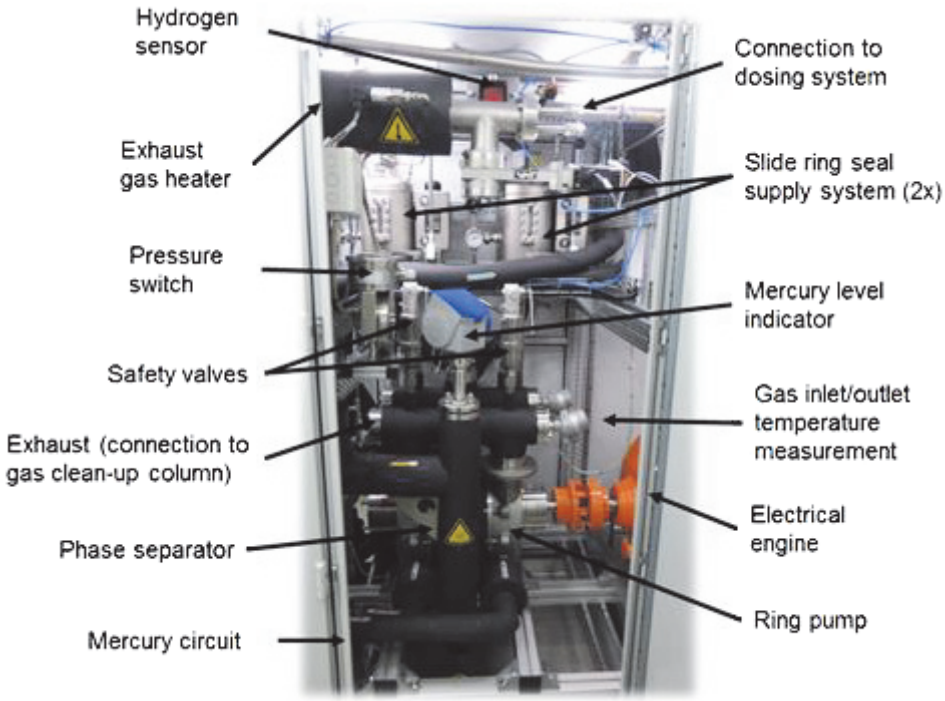

Fig. 6: The mercury filled liquid ring pump, as installed in THESEUS.

For commissioning, the pump was started by using the frequency transformer for a slow run-up. It was connected to the THESEUS dosing dome filled with nitrogen at ambient pressure and –temperature. The pump was turned until a rotor speed of 412 rpm was reached. At this speed, the single-stage pump reached a pumping speed of approx. 100 m³/h and an ultimate pressure of < 5 mbar (at compression against atmospheric pressure, see Fig. 7). This result was fully according expectation (water ring pumps do only achieve an ultimate pressure of 30 mbar) and therefore successfully demonstrates the working principle. Also a second pump stage could be simulated by lowering the exhaust pressure of the single-stage pump from ambient pressure to some mbar by means of a conventional backing pump. In this case, an ultimate pressure of 0.6 mbar could be achieved. In conclusion and as main result of this very first experimental campaign, it could be demonstrated that (i) mercury ring pumps work and (ii) that they can reach upstream pressures, low enough to use the pump as forepumps for the diffusion pumps foreseen for DEMO.

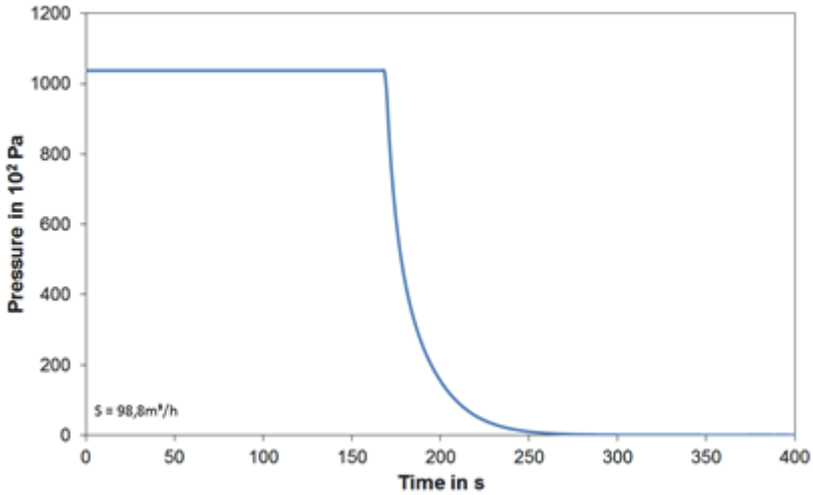

Fig. 7: Pump-down of the THESEUS dosing dome (0.45 m³) in THESEUS with the single-stage mercury ring pump.

Linear Diffusion Pump (LDP) development

A prototype pump for DEMO shall have a low working fluid inventory, be easy to scale and as compact as possible. To avoid any mercury vapour flowing back to the machine, baffles shall be integrated in the pump design. Linear diffusion pumps (LDPs) have been identified as most promising concept. In 2013, a design activity for the development of a LDP in a technical scale to be installed and tested in THESEUS has been started. For the test purposes, a high versatility in the pump design is needed, e.g. it must be possible to 'switch' different pumping stages on and off easily in order to study their effect on the overall performance. This increases the complexity of the pump and asks for additional, demountable components. Also, the installation of temperature and pressure sensors at different positions inside the pump must be possible. A conceptual design was elaborated as starting point for further calculations and simulations. The CAD drawing of this LDP designed by KIT for experimental investigations is shown in Fig. 8.

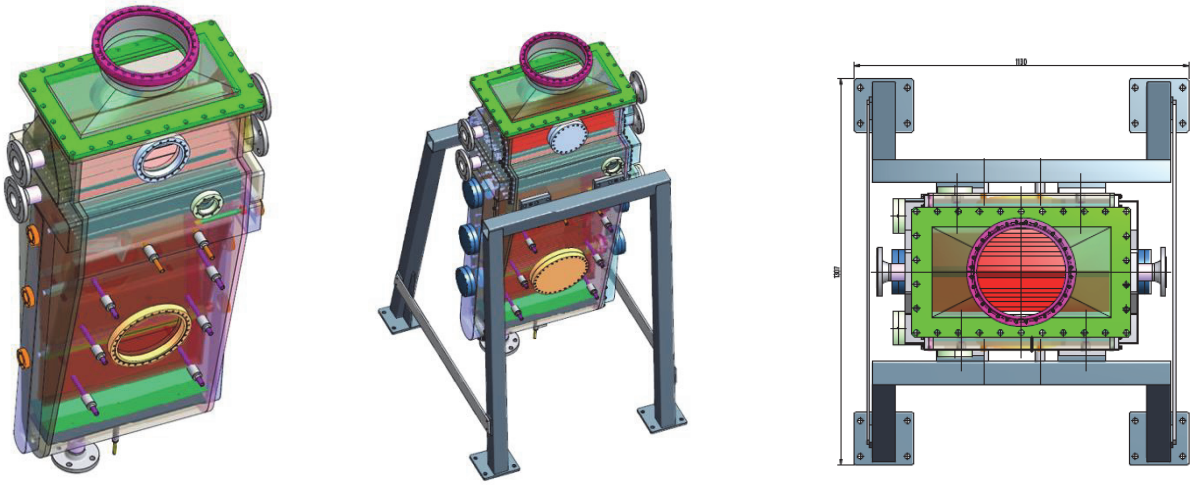

Fig. 8: Preliminary design of a linear mercury diffusion pump (left: top view).

The KIT in-house code ProVac3D was parallelized in 2012 and extended in 2013 to be able to simulate the interaction between the high speed mercury jet and the pumped gas. To benchmark this modified code, a test case was successfully carried through by comparison with literature data [7]. In general, the agreement between the simulation results and the experimental data was good. This means that ProVac3D will in the future be used as the development tool for the diffusion pump design.

The pressure inside the diffusion pump during operation varies from the foreline pressure provided by the liquid ring pumps as highest value down to the lowest pressure generated by the pump itself (i.e. the ultimate pressure). As the pump is located outside the cryostat with an ambient pressure of 1 bar(abs), the walls of the casing have to withstand a pressure difference of 1 bar during normal operation and without any buckling deformation. However, in case of a safety event, the pump has to withstand a much higher gauge pressure without damage. This safety event can be an internal explosion of an

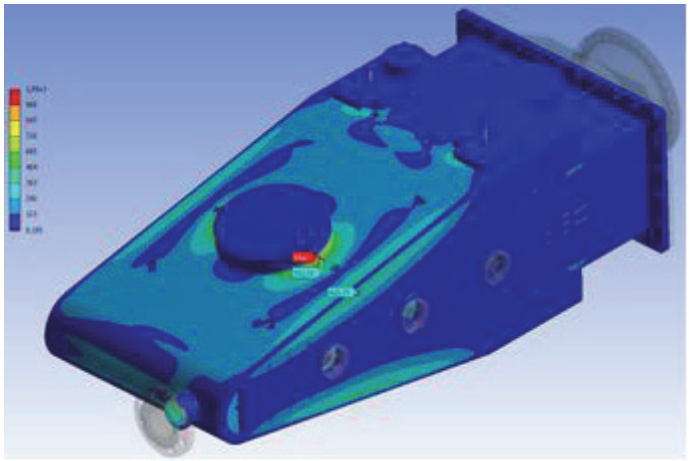

Fig. 9: Mechanical stress analysis of the pump casing if an internal pressure of 10 bar(g) is applied (The unities shown in the caption are MPa.)

oxygen/hydrogen mixture, if an air leak with ignition at ambient pressure is assumed as worst-case scenario. During such an event, a plastic deformation of the pump can be allowed, but a burst of the casing must be avoided in any case (shock pressure resistant design). Hence, the pump casing has to be designed for a pressure of 10 bar(g). This has to be considered in the pump design in an early stage as this defines the wall thickness of the pump and thus has a strong effect on the overall mechanical pump design. The forces and the stresses on each part of the pump housing have been analysed by using ANSYS. As input parameters, stainless steel 316L has been assumed. One result is plotted in Fig. 9, which illustrates that on some points the maximum allowed tensile strength is exceeded. As a next step in the pump simulation and development process, stiffening ribs will be introduced on the side walls. As soon as the mechanical optimization of the pump casing has been successful, all other internal components (cooling plates, baffles, cooling water feedthroughs etc.) will be included in the new model and also the thermal stresses (that have been neglected so far) will be considered in the final simulation.

The KALPUREX Process

Finally, a complete process has been developed that is the technical realization of the DIR concept with the pumps described above and the needed infrastructure [9]; it is called KALPUREX process (acronym for 'Karlsruhe liquid metal based pumping process for fusion reactor exhaust gases') and has been filed for patent. In the KALPUREX process, the tritium compatible pumping train in combination with the metal foil pump as described is used for pumping the reactor exhaust gases, see Fig. 10. In 2013, KALPUREX has been thoroughly studied from a process point of view [8].

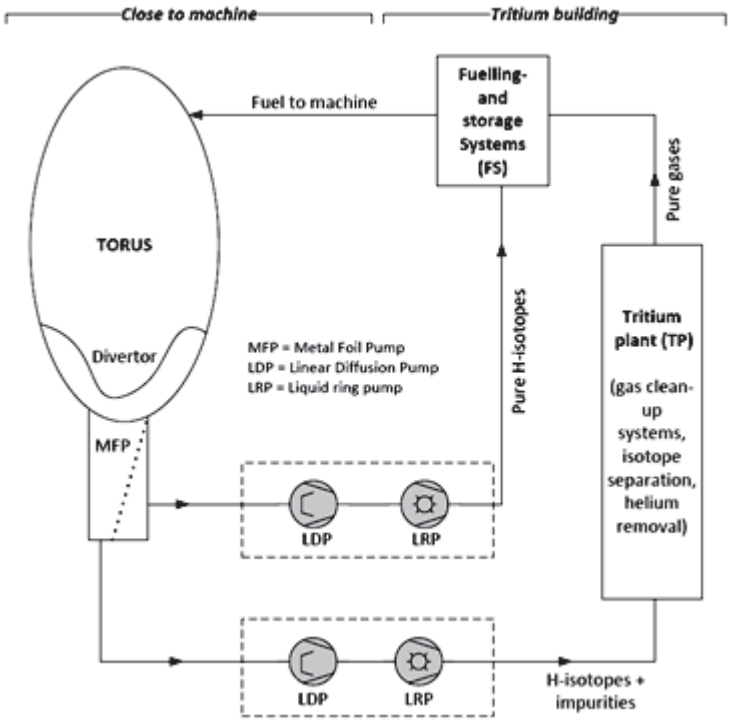

Fig. 10: Flow diagram of the KALPUREX process (without infrastructure parts).

As the gas separation of unburnt fuel (deuterium and tritium) shall take place as close as possible to the torus in order to minimize piping and conductance losses, the metal foil pump must be used as first pump, installed very close to the divertor. To ensure the vacuum conditions, two pump trains have to be used for further exhaust gas processing: one for pumping the permeate (the pure fuel that is separated and pumped by the metal foils) and one for the retentate (the residual gas that is not being pumped and enriched with impurities). The permeate is compressed by the diffusion pump and the liquid ring pump to a pressure that is

required for the fuelling system and recycled directly to the fuelling and storage systems (DIR). A second identical pumping train is used for compressing the retentate to the pressure required in the tritium plant, where the gas is cleaned up and further processed before it is also fed to the fuelling systems. If the performance of the metal foil pump and/or the fuelling systems allow for it (to be confirmed in the future R&D programme), the first pumping train (for the permeate) may even be omitted, what would lead to a further simplification of the whole pumping system.

Conclusions

The new DEMO vacuum pumping concept has been developed further on. The set-up and commissioning of the HERMES plasma experiment for the investigation of superpermeability and the successful proof-of-principle test of the mercury ring pump in THESEUS were important milestones. HERMES is now available for a detailed characterization of metal foils with hydrogen plasma, important for the design development of the metal foil pump. The THESEUS facility, which is the central test environment for all DEMO vacuum pumps, has been fully commissioned (but without hydrogen). Now, an extensive test programme will follow to characterize the mercury ring pump. The development of a linear mercury diffusion pump in DEMO-relevant scale, including the corresponding infrastructure systems, is proceeding well. Work has also been started to develop the infrastructure systems needed to operate the DEMO vacuum systems.

Staff:

Chr. Day
Th. Giegerich
Th. Johann
X. Luo
S. Ochoa
P. Pfeil
M. Scannapiego
H. Strobel
H. Stump
St. Varoutis
J. Weinhold

Literature:

[1] Chr. Day, Th. Giegerich, Exhaust pumping of DT fusion devices, Proc. 25th SOFE, June 2013, San, Francisco, CA, USA. June 2013.

[2] Chr. Day, Th. Giegerich, Development of advanced exhaust pumping technology for a DT fusion power plant, IEEE Transactions on Plasma Science 42 (2014) 1058-1071.

[3] Chr. Day, Th. Giegerich, The direct internal recycling concept to simplify the fuel cycle of a fusion power plant, Fusion Engineering and Design 88 (2013) 616-620.

[4] Th. Giegerich, Chr. Day, Conceptuation of a continuously working vacuum pump train for fusion power plants, Fusion Engineering and Design 88 (2013) 2206-2209.

[5] Th. Giegerich, Chr. Day, The THESEUS facility – A test environment for the torus exhaust vacuum pumping system of a fusion power plant, Proc. 25th SOFE, June 2013, San, Francisco, CA, USA. June 2013.

[6] Th. Giegerich, Chr. Day, Theoretical and experimental investigation of metal foil vacuum pumps for pumping and separating hydrogen, 19th Int. Vacuum Congress, Paris, France, Sept. 2013.

[7] E. Lind, J. Steinhaus, Development of a large linear jet mercury diffusion pump, Report MTA-14, Livermore Research Laboratory, Livermore, CA, US, Jan. 1953.

[8] Th. Giegerich, Chr. Day, The KALPUREX-Process - A new vacuum pumping process for exhaust gases in fusion power plants, ISFNT-2013, Sept. 2013, Barcelona, Spain, accepted for publication in Fusion Engineering and Design.

Acknowledgement

This work, supported by the European Communities under the contract of Association between EURATOM and Karlsruhe Institute of Technology, was carried out within the framework of the European Fusion Development Agreement. The views and opinions expressed herein do not necessarily reflect those of the European Commission.

Further Examination of Isotope Separation in a Cryopump (WP13-DAS-05-T02-01)

Background and objectives

KIT is charged with the development of the vacuum pumping systems for DEMO and a new pump concept with non-cryogenic and continuous pumps is under study and development, based on the idea to have a Direct Internal Recycling (DIR) of unburnt fuel [1-3]. However, as this completely new development is associated with certain risks that may become eminent only at a late stage, it has been decided to develop also the cryopump concept further so as to have a fall-back solution at a sufficient level of maturity, if needed. The cryogenic pump development path would be to install a separation function via design and operation in a way that hydrogenic separation becomes exploited in the course of the pumping + regeneration cycles. One design option towards such a pump is a three-stage cryopump that would provide separate pumping by its three stages: a blank metal shield at 80 K to condense all heavy species, a charcoal coated stage at 15-25 K (tbd) to pump the hydrogenic species and a charcoal coated stage at 5 K to pump the helium.

A molecular modelling effort has been conducted in WP12 to investigate potential designs of such a pump. This work revealed the sensitivity of the final result on the value employed for the sticking coefficient between the hydrogen isotopologues and the charcoal. The information is well known for the 5 K stage from the extensive R&D done for the ITER cryopumps which have only charcoal coated surfaces at 5 K. But the information is missing for the intermediate temperature stage and needed to confirm if this concept is working at all, and, if yes, to decide which temperature to choose. This is especially problematic because the sticking coefficient of the hydrogenic species is expected to vary significantly at this temperature. Moreover, the evolution of sticking with increasing sorbed amount is unknown, but of major importance to design the pump, such that pre-scribed inventory limitations are safely met. It is also known that these properties cannot be calculated ab initio.

It has therefore been decided to perform in the TIMO-2 test facility at KIT a dedicated fundamental experiment to characterise the gas-sorbent interaction in the temperature range of interest and, thus, to provide a database which can then be used for a confirmed Monte-Carlo based detail design of a ´real´ pump in a follow-up step.

New test rig and status of the work

To keep costs low, it was decided to realize this open panel test experiment by using parts from previous experiments. This includes an available test panel which was used in former tests as well as different parts of the ITER model pump, which is no longer in use and has been disassembled. The test panel is equipped with an electrical heating system which will simplify the test procedure and to set up the right temperature level. From the ITER model pump which was dismantled at the end of the final test campaign more than 5 years ago, the pump flange and the 80 K shielding can be used for the new test set up.

For the implementation of all the targets, planning and design activities as well as the workshop activities were necessary. The experiment itself shall be executed in the ITER cryopump test facility (TIMO-2 at KIT) to benefit from the existing and well calibrated vacuum and cryo-instrumentation and existing components. Before the manufacturing could start, it was important to define the conditions for the test setup correctly taking into account the experimental possibilities of the TIMO-2 test facility.

Finally, a rather simplified open panel test experiment was developed to characterise the gas-sorbent interaction in the temperature range of interest, with simple geometries to keep the costs down despite being cryogenic. The ultimate goal of this testing is to validate the staged cryopump concept and to create a database of sticking coefficients of the related

gases on charcoal surface in several temperatures, upon which the design of a real pump can be developed.

The design of the test installation was developed in two directions. On one hand, it was aimed to have a high capture coefficient in order to be able to extract the sticking coefficient information with good accuracy; on the other hand, the available possibilities at the TIMO-2 facility had to be taken into account. A comparison of the new test setup for the open panel test experiment inside the TIMO-2 test vessel compared with the model pump is shown in Fig. 1.

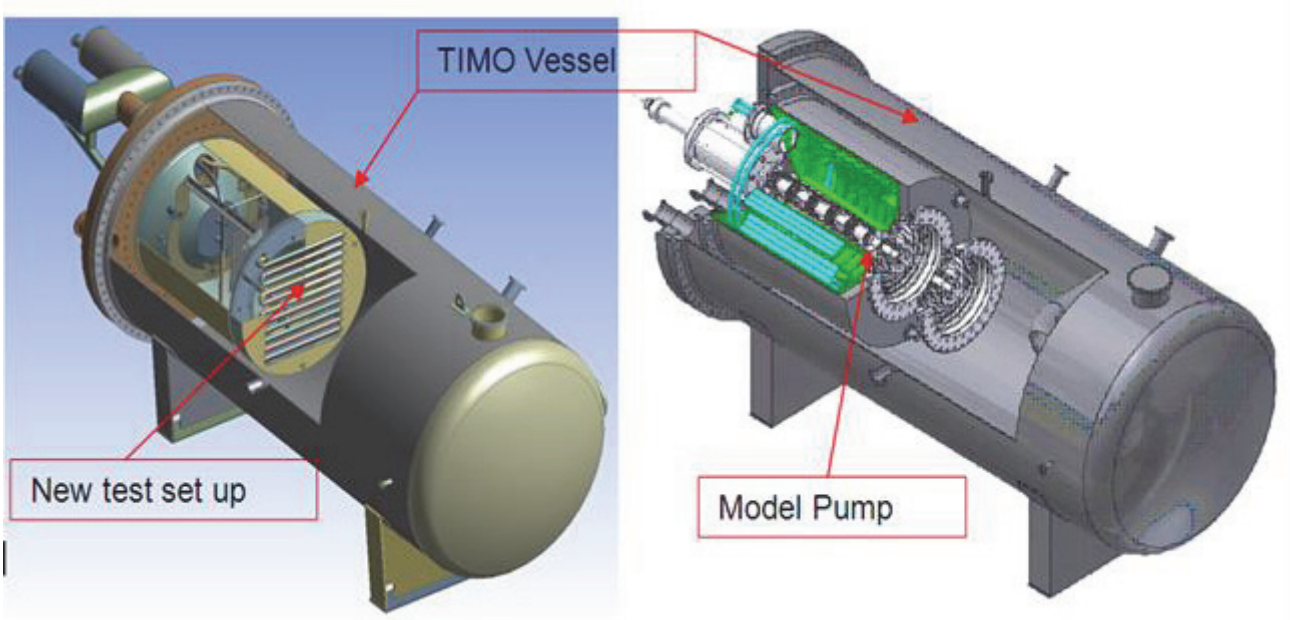

Fig. 1: Configuration of the new test set-up compared with the model pump configuration.

From the old model pump configuration the pump housing, the panel system and all parts of the inlet valve will be replaced. For the new test configuration, the main flange and parts of the 80 K shield system are re-used. The new test arrangement inside the TIMO-2 test vessel needs new supply lines for cryogen, a mounting frame for the test panel and a new baffle at the pump inlet. Instead of the rigid transfer line used with the ITER model pump, a new connection for the cryogenic supply is required.

For the open panel test experiment it was decided to use an available rectangular hydroformed cryopanel with the dimension 500x350 mm². This panel is already equipped with resistance heaters, on top of a matrix of a deposited copper layer on the outer surface. As a result of the hydroformed channel structure of this panel and the coated copper layer good temperature homogeneity is expected. The new charcoal coating on this panel is carried out in an area of ~80 % in which a very good temperature homogeneity is given. The rear side will not be coated. To minimize the influence on the pumping result, all blank 5 K surfaces will be protected.

The final design of the inlet baffle was found by detailed Monte Carlo studies. The optimum in terms of manufacturability and performance was found with a transmission probability of 0.39 for a baffle structure with 11 baffle fins which have an angle to the horizontal axis of 25° and a length of 120 mm, as shown in Figure 2.

The instrumentation of the open panel experiment includes temperature measurement on the test panel, a heating device to set up higher temperature level during the tests, pressure measurement inside the new test setup as well as in the TIMO-2 test vessel and the gas inlet flow.

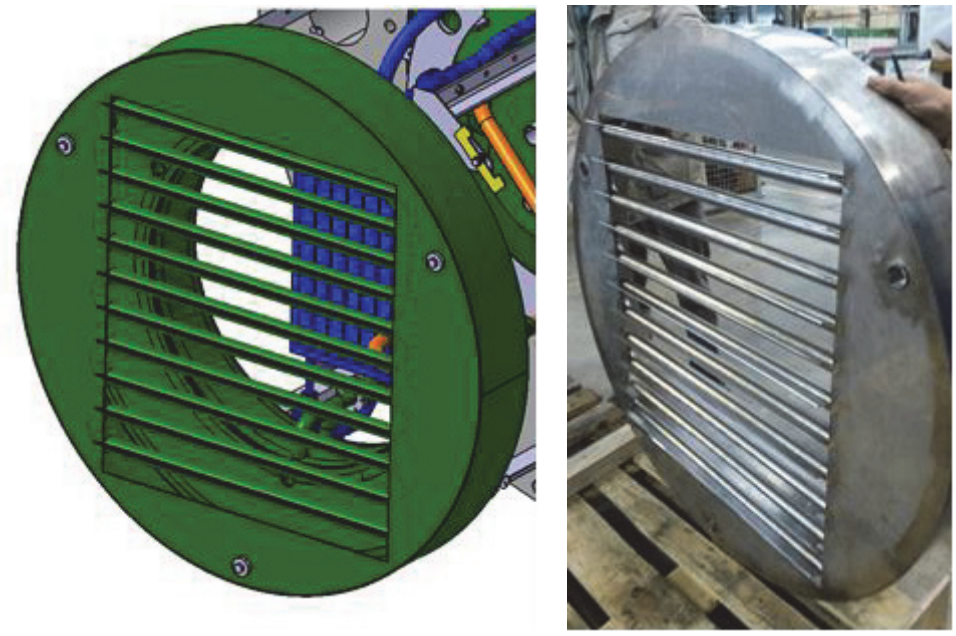

Fig. 2: New inlet baffle system of the panel test set up concept (left side the design drawing / right side the manufactured front shield).

Outlook

The preparation of the experiment in the KIT workshop as well as the preparation of the TIMO-2 facility (mainly control and data acquisition preparation) are on a good way and experimentation is expected to take place in mid 2014.

Staff:

H. Haas
Th. Johann
R. Simon
H. Strobel
J. Weinhold
X. Luo

Literature:

[1] Chr. Day, Th. Giegerich, The direct internal recycling concept to simplify the fuel cycle of a fusion power plant, Fusion Engineering and Design 88 (2013) 616-620.

[2] Chr. Day, Th. Giegerich, Development of advanced exhaust pumping technology for a DT fusion power plant, IEEE Transactions on Plasma Science 42 (2014) 1058-1071.

[3] Th. Giegerich, Chr. Day, The KALPUREX-Process - A new vacuum pumping process for exhaust gases in fusion power plants, ISFNT-2013, Sept. 2013, Barcelona, Spain, accepted for publication in Fusion Engineering and Design.

Acknowledgement

This work, supported by the European Communities under the contract of Association between EURATOM and Karlsruhe Institute of Technology, was carried out within the framework of the European Fusion Development Agreement. The views and opinions expressed herein do not necessarily reflect those of the European Commission.

Feasibility Study on the Exploitation of the JET DT-Campaign in View of DEMO Fuel Cycle Issues (JW13-FT-2.40)

Background

The JET machine has played an important role in the development of the physics basis for ITER and in demonstrating the application of different technologies to fusion research. In the period 2006 to 2011, significant investments have been made on JET, much of it already aimed to build up readiness for DT operation. For 2017 JET is preparing a new Deuterium Tritium Experiment (DTE2, following the first DT campaign in 1998 and the Trace Tritium Campaign in 2004). The timeline is shown in Fig. 1.

Fig. 1: Reference scenario for the JET DT-campaign.

The main motivation for DTE2 comes from the reduction of the risk of a longer than expected DT phase and so a delay in achieving the Q = 10 milestone in ITER. The operation of JET has several similarities with future ITER operation, especially when tritium is used. The contribution from JET in mitigating the risk for ITER in DT is in several areas, e.g. in gaining operational experience with tritium, isotope mixture control and tritium inventory control.

Scope of this task

Scope of this task was to find out how DTE2 can be used to support the fuel cycle development activities for DEMO. Therefore, the tritium processing plant in JET (the Active Gas Handling System, AGHS) had been studied in this task to find similarities and differences. Due to its impact, the fuel cycle area with strongest relevance to be checked under a DT experiment is the area of DEMO vacuum pumping for which a completely novel concept is under development (see the corresponding detail sections in this annual report).

Proposal for the JET DT campaign

The reference torus vacuum system concept of DEMO is based on novel, i.e. untested, technologies which allow for a direct internal recycling of unburnt fuel [1]. To fulfil this, a new vacuum pumping process is proposed for DEMO, the so-called KALPUREX process [2]. This process uses three different pumps (liquid ring pump, diffusion pump, metal foil pump), two of which are based on the use of liquid mercury as working fluid. In 2012 and 2013, proof-of-principle testing was done for all three pump types. Based on that, the liquid ring roughing pump is the one which is closest to an industrial manufacturing.

During discussions between AGHS and KIT, options for implementation of DEMO relevant components in the JET fuel cycle have been developed. In this exercise the proposal to test a DEMO relevant rough pump as part of the DT campaign in AGHS was further refined. KIT is thus recommending the installation of a pump train in AGHS, comprising a two-stage liquid ring pump with mercury as working fluid. If an additional pump would be integrated so as to achieve a lower ultimate pressure, this new pump train would have the potential to take over the pump duties as backing pump to the turbomolecular pumps. Efforts are under way at the moment to find a solution for that. This would allow a full characterization of the pump train without a risk for the JET DT campaign, as this pump would be installed in parallel to an existing pump. A preliminary design of the pump train installed in a safe containment is shown in Fig. 2.

If the implementation and characterization of this pumping system under tritium is successful, the liquid ring pump train will reach the highest possible technical readiness level (before operation on DEMO itself). Also valuable lessons will be learnt in handling of mercury as working fluid.

For the future EUROFUSION programme, it is intended to start a close collaboration between the JET-AGHS team and KIT for pump implementation and –operation. This gain of experience is a key issue of mutual benefit. The project will provide a very valuable output not only for designing and building pumping systems, but also for the operation and the design of the whole tritium processing systems. Also young people can be trained for further work and projects in the field of the fusion fuel cycle, which is one of the key components for fusion power plants.

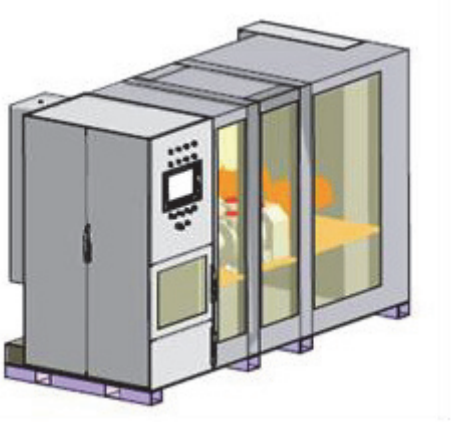

Fig. 2: Preliminary design of a 2-stage liquid ring pump train for JET AGHS. The housing is needed for a safe operation under tritium.

Staff:

Chr. Day
Th. Giegerich

Literature:

[1] Chr. Day, Th. Giegerich, The direct internal recycling concept to simplify the fuel cycle of a fusion power plant, Fusion Engineering and Design 88 (2013) 616-620.

[2] Th. Giegerich, Chr. Day, The KALPUREX-Process - A new vacuum pumping process for exhaust gases in fusion power plants, ISFNT-2013, Sept. 2013, Barcelona, Spain, accepted for publication in Fusion Engineering and Design.

Acknowledgement

This work, supported by the European Communities under the contract of Association between EURATOM and Karlsruhe Institute of Technology, was carried out within the framework of the European Fusion Development Agreement. The views and opinions expressed herein do not necessarily reflect those of the European Commission.

Goal Oriented Training Programme on Vacuum Technologies and Pumping (WP10-GOT-VACU-TEC (FU07-CT-2010-00065))

Background and objectives

The aim of the VACU-TEC training programme is to prepare five scientists for activities to support the ITER project and the long-term fusion programme in Europe in the area of vacuum technologies and pumping.

The European procurement for ITER in the area of vacuum technologies and pumping systems covers activities for the supply of cryopumps for torus, cryostat, heating and diagnostics neutral beam systems as well as the supply of cold valve boxes, instrumentation and the R&D needed to finalize the design of these components. All these requested areas are fully covered in the VACU-TEC goal oriented training programme (GOT) and each area is reflected by an individual work package (WP 1 to 5):

- Cryogenic Engineering: Cold turbo pump development (WP1 by CEA Grenoble)
- Instrumentation: Identification of total and high resolution partial pressure as well as outgassing measurements for ITER leak detection (WP2 by KIT)
- Leak Localization: Development of remote devices for ITER in-vessel leak localization (WP3 by CEA Cadarache)
- Mechanical Vacuum Engineering: Design of vacuum pumps for DEMO (WP4 by KIT)
- Physics: Vacuum gas dynamics and flow modelling (WP5 by the Hellenic Association, Volos)

The training programme for all trainees follows the same generic scheme with four main elements:

1. General education by participation in introductory as well as specialized courses, lectures and seminars all along the first year of the project
2. Practical education by being involved in the group activities related to the corresponding training topic
3. Secondments to other partners of the training programme at various stages of the project as project introduction, improvement or conclusive training
4. Participation in conferences, workshops and meetings

KIT is coordinating this network which started in 2011. So, the reporting year was the last full running year with all trainees. This report highlights the progress achieved in Work Package 2, whereas the activities under Work Package 4 were embedded in the EFDA-PPPT programme under WP13-DAS05-T01 and are reported separately.

VACU-TEC Work Package 2 (Instrumentation)

The main objective for Work Package 2 is to develop and characterize vacuum pressure instrumentation so as to improve the ITER leak detection system concept as well as to study the outgassing behaviour of candidate materials which will be employed in the ITER vacuum systems. The work in 2013 was mainly dedicated to further outgassing measurements and also partial pressure measurements for investigating the instrument capability to measure and resolve typical tokamak exhaust gases.

<u>Stainless steel measurements at the Outgassing Measurement Apparatus (OMA)</u>

The Outgassing Measurement Apparatus, which uses the difference method, had already been built in 2012 and first measurements of polymers had been performed. By changing the

conductances installed (0.1 - 2 l/s for N_2), it is possible to measure outgassing rates in the very wide range of 10^{-2} - 10^{-9} Pa m^3 s^{-1} m^{-2} at OMA.

In the first half of 2013, outgassing rate measurements of stainless steel 316L with different pre-treatments have been executed. Literature shows that the pre-treatment, like different manufacturing processes, surface treatments and pump-down histories, can have a large impact on the outgassing rate of a material exposed to vacuum [1]. Samples of the same batch of SS316L were used for the measurements, with an untreated (as received), gel-coated (with inorganic silica), and electropolished sample. Furthermore, two heat treated samples were investigated, namely after air-bake and after vacuum-bake, both carried out at 400 °C for 100 h. For all samples, measurements at room temperature (20 °C) as well as at 100 °C were conducted for 100 h in each case. Blank measurements were executed between the sample measurements, so that an influence of a different outgassing of the two vacuum chambers could be considered by a correction function. The outgassing rate per unit area of the sample is then calculated using the corrected pressure differences, the known conductances and the surface area of the sample.

The measured data were analysed and the outgassing results compared to theoretical curves considering diffusion limited outgassing. The results confirmed that the pre-treatment of the sample before measurement has a large impact on its outgassing rate (Fig. 1). By air- as well as vacuum-baking, the room temperature outgassing of the sample could be decreased by almost one order of magnitude in comparison to the untreated sample [2]. In all cases, the main outgassing component found was hydrogen.

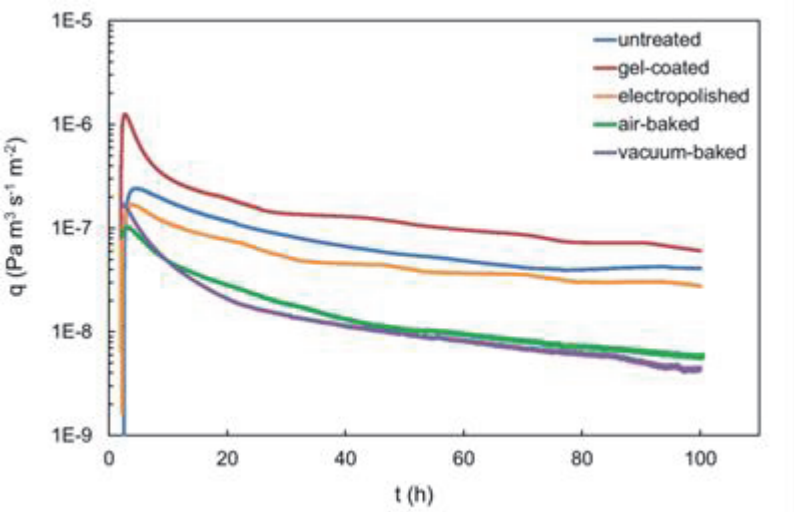

Fig. 1: Results of outgassing measurements at 20 °C of stainless steel 316L with different pre-treatments

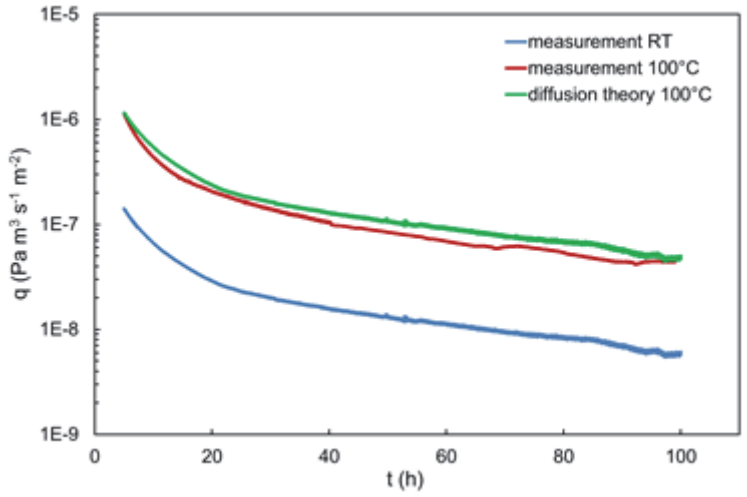

Fig. 2: Results of outgassing measurements of vacuum-baked stainless steel 316L at ambient temperature and 100 °C in comparison with the theoretical curve for 100 °C derived by assuming diffusion limited outgassing.

Fig. 2 shows the measured outgassing curves of vacuum-baked stainless steel at room temperature as well as at 100 °C in comparison with a theoretical curve for hydrogen diffusion from stainless steel at 100 °C, which showed a good agreement.

After the stainless steel measurements the Outgassing Measurement Apparatus was modified. Additional gauges like capacitive diaphragm gauges and spinning rotor gauges were added to extend the measurement range and decrease the uncertainties. Also the residual gas analyser and the conduct-

ance have been changed for future measurements with materials that potentially have higher outgassing rates.

Partial pressure measurements of tokamak exhaust gases

Another topic of the work package is partial pressure measurement for fusion applications, such as the use of mass spectrometers for leak detection or composition measurements of tokamak exhaust gases. Regarding the latter, devices with fast response times are needed as the plasma pulses can be short, but high resolution and a low detection limit have to be achieved simultaneously so that helium and deuterium can be separated at mass 4 and also small contents of impurities can be detected [3].

Therefore, to check the applicability of the devices, measurements with an already existing high-resolution quadrupole mass spectrometer (HR-QMS, Balzers GAM 400) and a new Auto-resonant Ion Trap Mass Spectrometer (ART-MS, Brooks 835 VQM) were performed. The results of the measurements were compared and it was found that both devices, GAM-400 and the ART-MS, can be used for measuring the gas composition of tokamak exhaust gases. However, the very fast scan time of the ART-MS leads to a clear decrease in accuracy, whereas with the HR-QMS He and D_2 can be separated and impurities in the ppm-range can be detected very well (Fig. 3).

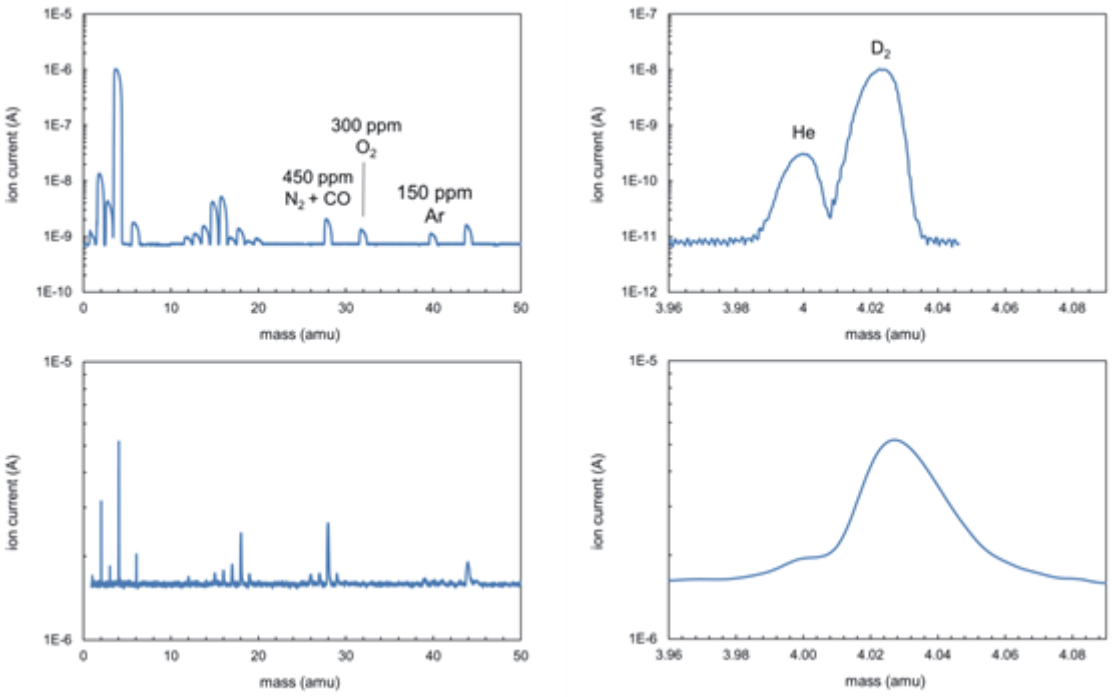

Fig. 3: Mass spectra of HR-QMS (top) and ART-MS (bottom) of gas mixture (D_2 96.1%; He 3.6%; impurities).

Conclusions

The EFDA GOT VACU-TEC training programme was continued in 2013. The involved trainees were able to develop their own network with other young fusion researchers, see Fig. 4. VACU-TEC demonstrated to be an excellent framework for young scientists to get a thorough education in fusion and be able to deliver own and self standing work for fusion research.

In December 2013, three of the five trainees have finalised their trainee contracts. The two CEA trainees have found a position in industry, whereas the Work Package 4 KIT trainee has been given a continuation contract at KIT under which he will take a leading role in the development of the DEMO vacuum pumping systems.

Fig. 4: 3rd network meeting of VACU-TEC, held in October 2013 at IPP Greifswald (top). VACU-TEC meeting with scientific colleagues at the ISFNT-Conference in Barcelona, Spain, Sept. 2013.

Staff:

K. Battes (trainee for WP2)
Chr. Day (for co-ordination)
A. Edinger
Th. Giegerich (trainee for WP4)
V. Hauer (mentor)
P. Pfeil
H. Stump
J. Weinhold

Literature:

[1] K. Battes, V. Hauer, Influence of the pre-treatment on outgassing, DPG Spring Meeting, Regensburg, Germany, March 2013.

[2] K. Battes, C. Day, V. Hauer, (Review and) measurement of outgassing rates of stainless steel and polymers, 19th Int. Vacuum Congress, Paris, France, Sept 2013.

[3] K. Battes, C. Day, V. Hauer, Tokamak exhaust gas composition measurement via different mass spectrometers, 11th ISFNT, Barcelona, Spain, Sept 2013.

Acknowledgement

This work, supported by the European Communities under the contract of Association between EURATOM and Karlsruhe Institute of Technology, was carried out within the framework of the European Fusion Development Agreement. The views and opinions expressed herein do not necessarily reflect those of the European Commission.

Fuel Cycle –
Tritium Processing

Finalization of the System Capacity, Enhancements Studies and Detailed Design of WDS Components including HAZOP Studies (F4E-2010-GRT-045 (PNS-VTP))

The test WDS facility TRENTA3 at the Tritium Laboratory Karlsruhe (TLK) was developed and installed to investigate an appropriate system to process tritiated water in a technical scale and to recover tritium from the waste water produced during the laboratory operation. The dedicated process selected for WDS operation is the CECE (Combined Electrolysis and Catalytic Exchange) process.

The experimental program of the TRENTA is focusing to identify the capability of the CECE process and its necessary system components under different operational conditions that shall be ITER relevant. One of these parameters of interest is the hydrogen isotope concentration in the process fluids. Since the deuterium concentration in the tritiated waste water is expected to be far above the natural content, the impact on the separation performances shall be detailed investigated and quantified. Therefore the activities have been focused on three main issues: developing of an experimental data base that is ITER relevant, calculation of the mass transfer coefficients of the chemical reaction involved in the process and the estimation of the size of the ITER Liquid Phase Catalytic Exchange (LPCE) column based on the calculated mass transfer coefficients.

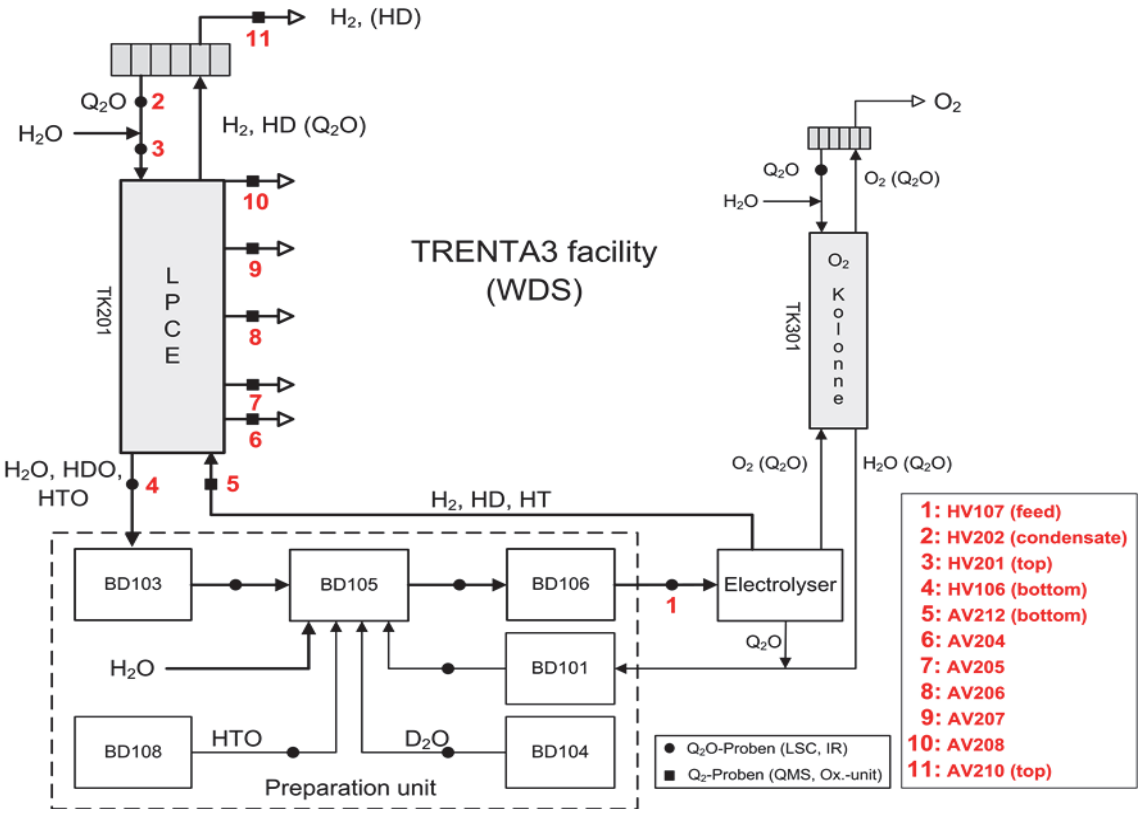

Fig. 1: The schematic configuration of the TRENTA3 facility.

The TRENTA3 facility consists of the following subsystems, which are relevant for the development of a CECE process:

- Electrolyser unit for the production of the tritiated hydrogen gas. The conversion of tritiated feed water into tritiated hydrogen is implemented by two electrolyser units. Each unit comprises a cell stack equipped with so called Solid Polymer Electrolyte (SPE) membranes as separation and also as electrolyte material;

- LPCE column which realize the catalytic hydrogen isotope exchange betweenand within the different phases of water and hydrogen. The LPCE column has an effective length of 8 m (diameter 55 mm) and is segmented in 4 sections, each of 2 m length. The total height of the packing/catalyst is of 8m and the packing and catalyst are in a homogeneous mixture.
- Preparation unit and controlling system that provide the storage, process and feed vessels, as well all other infrastructure components and the local control system. The preparation unit is located in the basement of the laboratory inside a dedicated caisson where all process vessels and pumps are located.

During the experimental runs of the TRENTA WDS gas and water samples have to be analyzed. Therefore, different analytical methods are integrated in the TRENTA3 facility. Besides the different phases of the sample, the isotope of interest plays an important role concerning the appropriate analytic technique.

The schematic configuration of the TRENTA3 facility showing the locations of the various sampling point is presented in Figure 1.

Several experimental campaigns have been conducted at TLK in order to evaluate the deuterium impact on the separation performances of the 8m LPCE column. After the first campaigns it was identified the necessity to improve the accuracy of the sampling procedure and also the gas oxidation in order to avoid the memory effects. Therefore, for each sampling location a dedicated oxidizer and collecting vessel was installed as shown in Figure 2.

Fig. 2: The oxidizer and collecting system of TRENTA 3 facility.

The tritium activity and the deuterium concentrations have been measured at the bottom, top of the LPCE column and at 1m, 2m, 4m and 6 m from the bottom of the LPCE column. A typical tritium distribution along the 8 m LPCE column is shown in Figure 3

Using the TRIMO++ software that was developed by TLK, the mass transfer coefficients of the reactions involved in the process both those related to deuterium separation and also tritium separation have been calculated. The results showed that there are not differences between the mass transfer coefficients calculated based on experimental data collected some years ago and those using the data measured during the campaigns carried out in 2013. This is a confirmation of the chemical and mechanical stability of the catalyst-packing mixture over the years. In Figure 4 is shown the agreement between the experimental data and the calculated data using TRIMO++ software. This very good agreement is relevant for the accuracy of the mass transfer calculations.

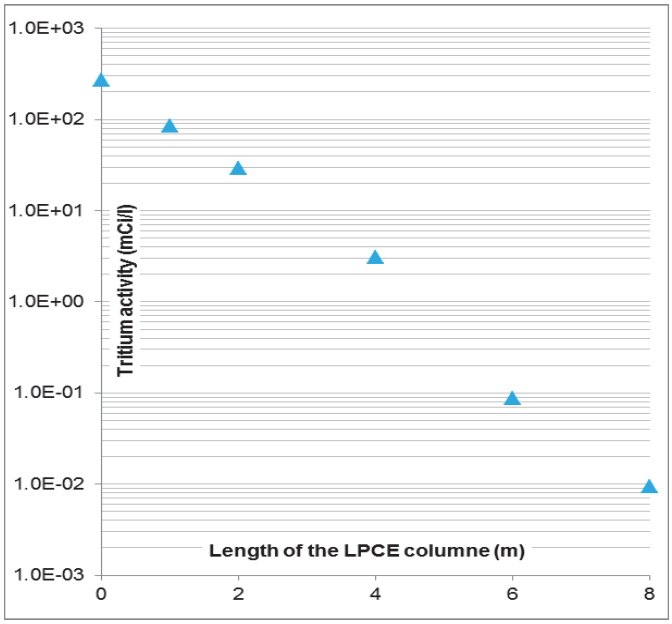

Fig. 3: Typical tritium distribution along the LPCE column.

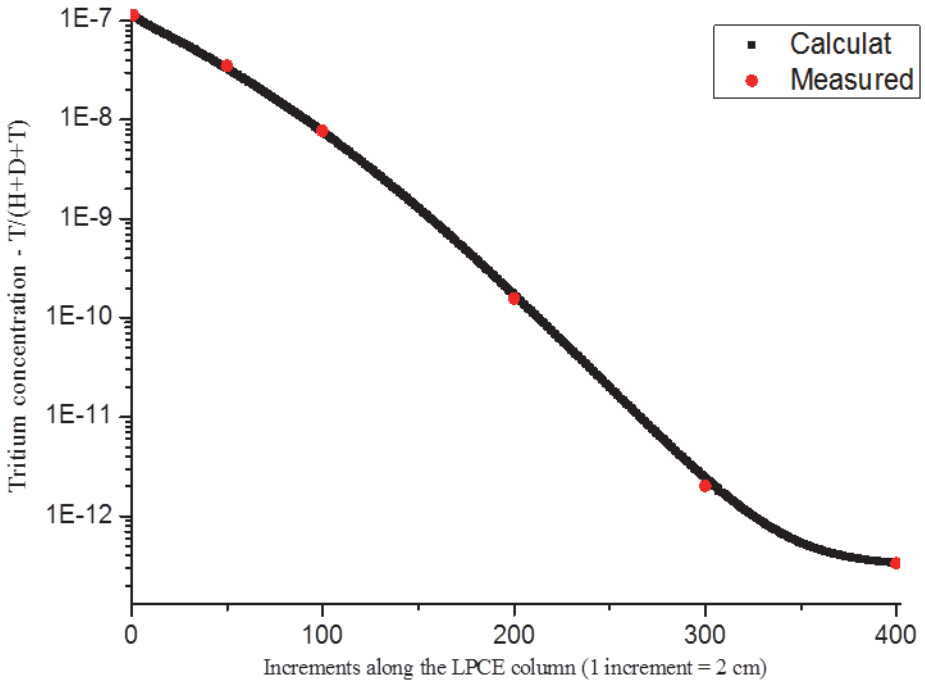

Fig. 4: Calculated tritium profile against the experimental data.

Conclusions

The decontamination factor along the LPCE columns is significantly influenced by the amount of deuterium in the feeding gas and by the ratio gas to liquid G/L along the column.

The accuracy in the calculations of the mass transfer coefficients also depends on the ratio gas to liquid and therefore it was necessary to implement several measures to improve the gas and liquid flow rate measurements and also the sampling procedure and the associated hardware such as oxidizers.

The calculated data based on TRIMO++ software have been found in very good accuracy with the experimental data.

At high deuterium concentration in the feeding gas, more than 35% and ratio G/L higher than 2 the LPCE column is not able to remove the entire deuterium and tritium fed at the bottom of the LPCE column. Therefore, most of the LPCE column will work with high deuterium concentrations and consequently the tritium decontamination is very poor due to the equilibrium constants of various chemical reactions.

The experimental data have showed that at tritium concentrations below 10^{-12} T/(H+D+T) the isotopic transfer is strongly slowed down and there are not sound experimental data for this range of very low tritium concentrations.

Staff:

I. Cristescu
N. Lohr
R. Michling
A. Niculescu - ICIT Romania
C. Petrutiu – ICIT Romania
S. Welte

Acknowledgement

This work was supported by Fusion for Energy under the grant contract No. F4E-2010-GRT-045 (PNS-VTP).with collaboration by ENEA Frascati, Italy; ICIT, Rm. Vâlcea, Romania and CEA Saclay, France. The views and opinions expressed herein reflect only the author's views. Fusion for Energy is not liable for any use that may be made of the information contained therein.

R&D on Capture and Exchange Method for Processing Highly Tritiated Water – Task 2: Laboratory Scale Tritium Testing with D2/DTO (ITER/IO/CT/10/4300000500)

Highly tritiated water (HTW) handling and processing is a severe concern for the safe operation of the ITER Tritium Plant. Small HTW amounts will be produced in the torus during nominal DT operation and could appear in case of acute tritium release in glove boxes. Among different process options, the Capture and Exchange (C&E) method has been identified as one of the most suitable in processing the HTW. It uses a platinum-molecular sieve bed (Pt-MSB) that can store the HTW, which can be afterwards detritiated in-situ via isotope swapping. This technique appears very attractive (simple and robust), but the lack of experimental data motivated experiments to be performed at TLK.

The Task 2 of this contract focused on small scale experiments with tritium. The CAPER facility of TLK has been especially upgraded (Figure 1) for this purpose integrating into the existing system a micro-channel catalytic reactor (µ-CCR) produced by the Institute for Micro Process Engineering (IMVT) of KIT. The µ-CCR produces the necessary HTW via the catalysed combustion of gaseous tritium (Q_2) with oxygen. Downstream of the µ-CCR, a small Pt-MSB hosting about 20 g of special Pt-zeolite material is operated at room temperature and collects up to 2 g of HTW. After having loaded the Pt-MSB with HTW, the second step of the experiment consists in HTW detritiation stage using fresh D_2 that liberates the tritium in the water via isotope exchange reaction. This tritium released in the molecular form (DT) is monitored on-line and in real-time with two complementary ionisation chambers (RX1002 and 847) of different sizes. The last step of the experiment consists in de-loading the Pt-MSB, collecting the detritiated HTW on a standard MSB that can be accommodated inside the most sensitive TLK calorimeter, thus enabling the residual activity in the detritiated HTW to be measured.

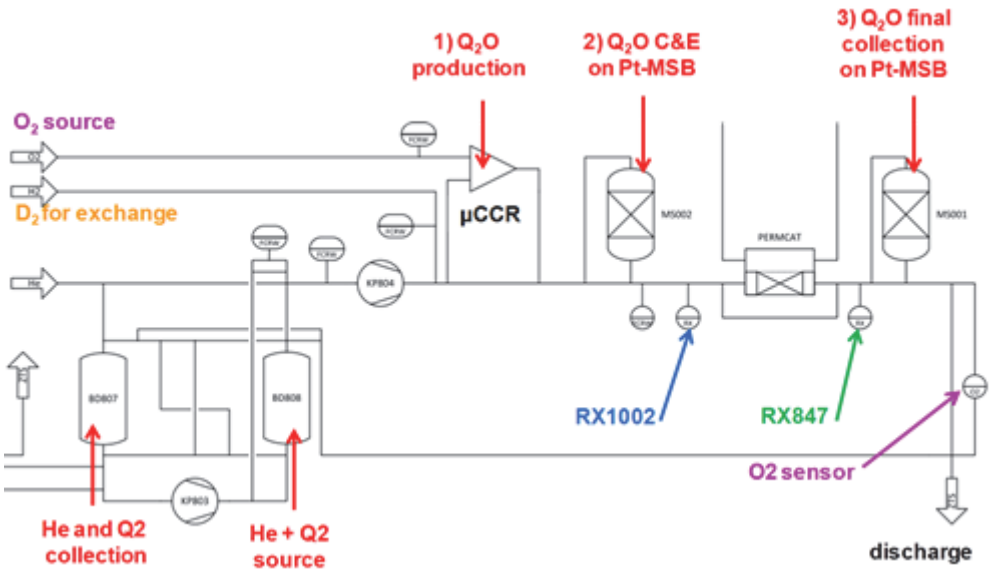

Fig. 1: New arrangement inside CAPER for HTW experiments using the Capture and Exchange (C&E) technique.

The detritiation step with C&E has been parametrically studied varying the exchange temperature and the D_2 purge mass flow rate. In total 9 runs were performed, each necessitating the full CAPER team for one week. During 3 months of CAPER full operation, more than 450 L of tritiated swamping gases containing 0.2 g of tritium were handled. The TLK infrastructure, and especially the isotope separation system, was heavily loaded to reprocess the tritiated gases (20 batches, one day each). More than 60 GC measurements were done to calibrate the real-time tritium measurement with ionisation chambers.

As main outcome from these experiments, the C&E process has been proven to be very robust and efficient for reaching moderately high decontamination factors up to 100; but residual tritium was always remaining in the water even after prolonged process as shown from the calorimetric measurements (Figure 2). Increasing the temperature during isotope exchange showed to be the most effective way for enhancing the detritiation performances.

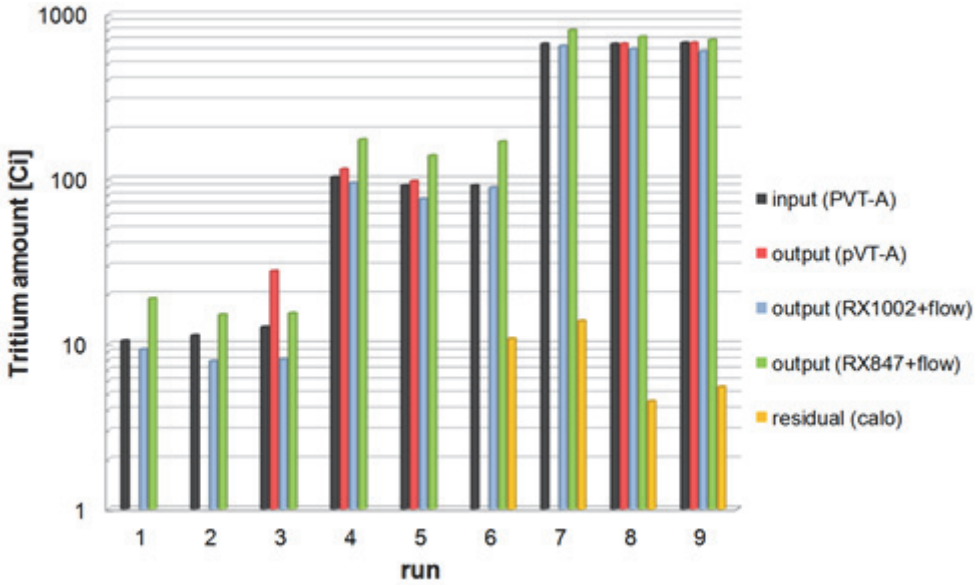

Fig. 2: Tritium balance for the 9 experiments on HTW in CAPER with C&E, showing good agreement between different measurements static with gas collection and GC measurement, and dynamic with mass flow rate and ionisation chambers, and some residual tritium in the water after detritiation.

Staff:

O. Borisevich
D. Demange
E. Fanghänel
N. Gramlich
T.L. Le
M. Schwarz
K.H. Simon
R. Wagner
S. Welte

Acknowledgement

This work was supported by ITER Organization under the service contract No. ITER/IO/CT/10/4300000500). The views and opinions expressed herein reflect only the author's views. The ITER Organization is not liable for any use that may be made of the information contained therein.

Breeding Blanket and Tritium Technology (TLK contribution)

The Breeding Blanket and Tritium Technology group of TLK contributed in design and experimental activities for both ITER and DEMO projects, coordinating at the European level several contracts. Hereafter are summarised the main achievements for 2013, with particular highlights on experiments for highly tritiated water processing, contributions to the ITER Test Blanket Modules, and conceptual studies of the tritium extraction systems for DEMO.

R&D Work for the ITER Test Blanket Modules and Systems (TBM & TBS)

a) Acceptance Tests and Criteria for ITER TBS

Provision of Services for the Definition of TBS Acceptance Criteria and of Required TBS Acceptance Tests (ITER/CT/13/4300000787)

One main objective of ITER is to operate at small scale several different breeding blanket concepts using Test Blanket Modules (TBM). Six different TBMs (two of them from Europe) shall be installed having on the one hand the TBM boxes accommodated inside the vacuum vessel directly facing the plasma, and on the other hand the ancillary circuits (TBS) dispatched along different building for extracting the tritium and cooling the boxes. The ancillary systems enabling the TBM operation mainly comprise the (Helium) Cooling Systems (HCS), the Coolant Purification Systems (CPS), the PbLi loops, and the Tritium Extraction Systems (TES). All these systems have to be designed and manufactured according to very high quality standards to meet the nuclear safety requirements and the high level operational targets. In particular, very high reliability of these systems has to be ensured so as not to jeopardise the overall ITER scientific programme.

The work performed in this contract consisted in developing and detailing the strategy for the overall acceptance scheme of all the TBMs and the serving ancillary systems. Starting from the information compiled in the Preliminary Safety Reports of the 6 TBMs, the first part of the work focused on listing all components, their operative conditions and the different classifications for safety, quality, (nuclear) pressurised equipment, tritium, etc. It turned out that these classifications were not adapted (at least not sufficiently) to build high level families with common acceptance tests and criteria. Families were built according to component types and operating conditions (mainly fluid type, pressure, and tritium).

In the TBMs, rather low amounts of tritium (max. 25 mg per day) shall be produced inside the TBMs during the later DT campaign, and tritium will be always much diluted. Despite of that, and following the ITER Tritium Manual guidelines, all the circuits handling tritium shall fall into the highest level of the tritium classification since they are considered as first confinement system using fixed installations, and acting as first static barrier.

As main outcome of this work, the strategy for acceptance tests and criteria has been fully developed, clearly defining and detailing the sequence of tests to be performed from the early manufacture at component level up to the final commissioning on ITER site at system level. The redundant character of key tests (surface cleanness, leak tightness, pressure tests) to be repeated at several time along the overall process (manufacture, installation and integration) has been considered as an issue, having potentially high impacting on costs and schedule for the inside the ITER machine.

Acknowledgement

This work was supported by ITER Organization under the service contract No. ITER/CT/13/4300000787. The views and opinions expressed herein reflect only the author's views. The ITER Organization is not liable for any use that may be made of the information contained therein.

b) Experiments and Design of the Ancillary Systems of the EU Test Blanket Modules

Design of TBM Ancillary Systems and Integration in ITER (F4E-OMF-331-02-01)

First R&D Experimental Activities in Support of the Conceptual and Preliminary Design of the European Test Blanket Systems (F4E-FPA-372-SG1)

Assessment of TBS Instrumentation Requirements (F4E-FPA-380 Action 2-SG1)

In view of the forthcoming conceptual design and preliminary design reviews of the European ITER Test Blanket Modules (TBM) and their associated ancillary systems (TBS), several contracts have been recently launched by F4E. They are strongly interconnected, and running in parallel over a 3-4 years period (Figure 1). The design and engineering work under OMF-331, with Lot-2 is the central activity is the focusing on the seven ancillary systems, stressing on integration in ITER buildings. In parallel, experimental campaigns shall be performed under Framework Partnership Agreements (FPA-372, FPA-380) to consolidate the technological choices, to demonstrate performances of the baseline technologies and support the engineering sizing of the different equipment.

In the frame of the design activities along OMF-331-Lot2-TO1, TLK has provided support to ENEA for reviewing and consolidating the technical baseline of the processes foreseen for the tritium extraction systems and coolant processing systems. In addition, the tritium classification of all the 7 sub-systems of the two EU TBS has been carefully checked and updated.

For experiments along FPA-372-SG1, tests at TLK using the last technical scale PERMCAT reactor have just been started. The major objectives are to gather experimental data at TBS relevant conditions, i.e. at rather high helium flow rate and very large tritium dilution. Complementary experiments at small scale with tritium are scheduled for 2014.

For experiments within FPA-380-A1, efforts have focused on preparing the first specific Grant in which TLK shall perform in 2014 R&D on getter beds using ZrCo to extract tritium from the Helium purge gas.

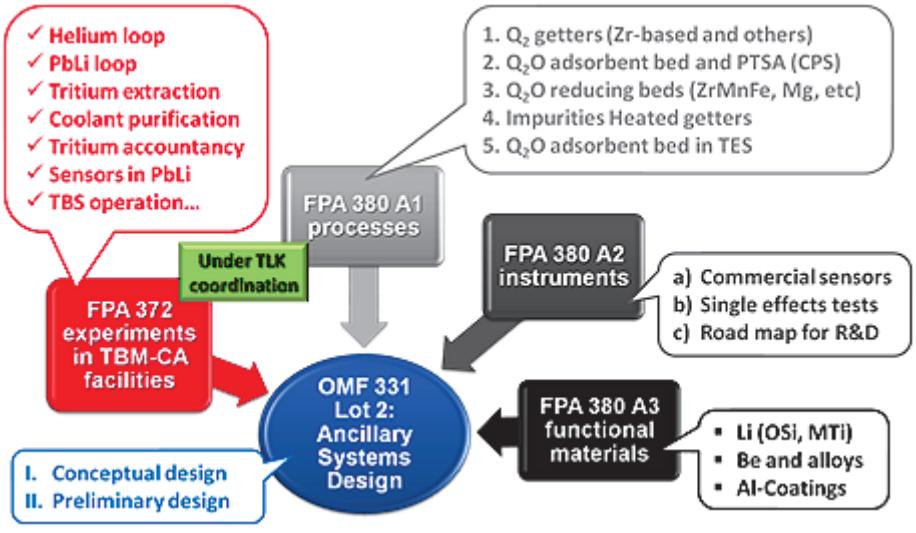

Fig. 1: Constellations of contracts launched by F4E with main and key contribution from the TBM Consortium of Associates (TBM-CA) with TLK acting as project leader for the execution of FPA-372 and FPA-380-A1.

Acknowledgement

This work was supported by Fusion for Energy under the Service Contract No. F4E-OMF-02-01 and the Framework Partnership Agreements No. F4E-FPA-372-SG1 and No. F4E-FPA-380 Action 2-SG1. The views and opinions expressed herein reflect only the author's views. Fusion for Energy is not liable for any use that may be made of the information contained therein.

R&D on Tritium Extraction Systems for DEMO

T Extraction and Permeation Analysis (WP13-DAS-06-T01-01)

Along the Design Assessment Studies for Tritium Systems of the EFDA-Power Plant Physics & Technology project, the work initiated in 2012 on the study for tritium extraction and permeation analysis has been pursued and extended. The main objective of this work is to consolidate the different strategies developed for managing the tritium in the breeding blanket and mitigating the issues with regards to its permeation and losses towards the environment.

For tritium permeation control requirements, KIT-INR upgraded the FUS-TPC (Fusion Tritium Permeation Code) implementing a new unified permeation model. It allows simulating the tritium permeation in a wide range of partial pressures, where the permeation regime can obey a transitional permeation scheme between the two limit cases of diffusion or surface limited regimes. In addition, pulsed operation scenario of the machine can now be simulated with this numerical tool. Further refinements considering temperature and tritium generation profiles in the breeding region will be the key parts of the future work.

For tritium permeation barriers, KIT-IAM produced a review on coating techniques for anti-permeation barriers considering the specific issues with respect to corrosion (compatibility with liquid breeding material PbLi) and irradiations. A roadmap for developing and qualifying this key technology for tritium control and mitigation of losses by permeation has been delivered as outcome.

For tritium extraction, KIT-TLK produced at the simplified block diagram level several different approaches for extracting and recovering the tritium from both the solid and liquid breeding blankets concepts. The technologies retained for ITER TBM relies on rather mature technological choices (this is actually the main selection criteria for use in TBMs) but advanced alternative technologies are being proposed for DEMO to simplify the tritium extraction and significantly improve the overall tritium management in the breeder blanket (Figure 2). A comprehensive list of criteria for process assessment has been established, covering all the key aspects with regards to tritium processes. The criteria have been arranged in main categories specific to safety & waste, design & integration, operation, and economics. These criteria will be used for processes selection, but only at a later stage. Indeed, during the next coming years, the ITER TBMs options will be matter of deep study supported by F4E contracts, whereas alternative options proposed for DEMO shall be consolidated along the Eurofusion project under establishment. In this new frame, the upcoming R&D activities shall put emphasis on experimental work to be performed both at small scale with tritium for proof of principle, and at larger scale without tritium for component testing.

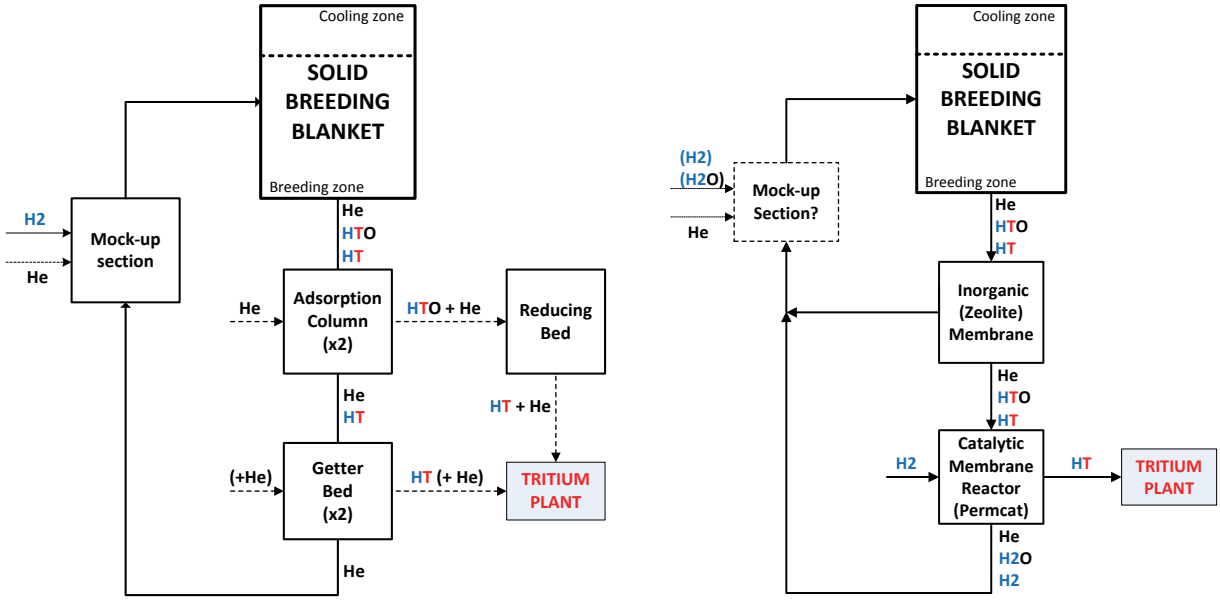

Fig. 2: Block diagrams view of the tritium extraction systems for solid breeder concept (HCPB) presently foreseen for the ITER TBM using conventional techniques (on the left) and TLK proposal for DEMO involving advanced technologies (on the right).

Acknowledgement

This work, supported by the European Communities under the contract of Association between EURATOM and Karlsruhe Institute of Technology, was carried out within the framework of the European Fusion Development Agreement. The views and opinions expressed herein do not necessarily reflect those of the European Commission.

Staff:

O. Borisevich
D. Demange
E. Fanghänel
N. Gramlich
T.L. Le
M. Schwarz
K.H. Simon
R. Wagner
S. Welte

Literature:

[1] M. Simplício, M.D. Afonso, O. Borisevich, X. Lefebvre, D. Demange “Permeation of single gases and binary mixtures of hydrogen and helium through a MFI zeolite hollow fibres membrane for application in nuclear fusion” *Separation and Purification Technology*, Vol. 122, pp. 199-205 (2014).

[2] B. Bornschein, C. Day, D. Demange, T. Pinna “Tritium management and safety issues in ITER and DEMO breeding blankets” *Fusion Engineering and Design*, Vol. 88 (6-8), pp. 466-471 (2013).

[3] D. Demange, O. Borisevich, N. Gramlich, R. Wagner, S. Welte “Zeolite membranes and palladium membrane reactor for tritium extraction from the breeder blankets of ITER and DEMO” *Fusion Engineering and Design*, Vol. 88 (9-10), pp. 2396-2399 (2013).

[4] F. Franza, L.V. Boccaccini, D. Demange, A. Ciampichetti, M. Zucchetti “Tritium permeation issues for helium-cooled breeding blankets” *Oral presented at SOFE 2013, paper submitted to IEEE Transactions on Plasma Science*.

[5] A. Santucci, A. Ciampichetti, D. Demange, F. Franza, S. Tosti “Impact of tritium solubility in liquid Pb-17Li on tritium migration in HCLL and WCLL blankets” *Oral presented at SOFE 2013, paper submitted to IEEE Transactions on Plasma Science*.

[6] D. Demange, L.V. Boccaccini, F. Franza, A. Santucci, S. Tosti, R. Wagner “Tritium management and anti-permeation strategies for three different PPP&T DEMO breeding blanket options“ *Poster presented at ISFNT 2013, paper accepted for publication in Fusion Engineering and Design.*

[7] D. Demange, I. Cristescu, E. Fanghänel, M. Glugla, N. Gramlich, T.L. Le, R. Michling, H. Moosmann, W.M. Shu b, K.H. Simon, R. Wagner, S. Welte, R.S Willms, “Integration of a Micro-Channel Catalytic Reactor in CAPER to study Highly Tritiated Water Handling and Processing” *Oral presented at Tritium 2013, paper accepted for publication in Fusion Science and Technology.*

[8] D. Demange, E. Fanghänel, S. Fischer, T.L. Le, F. Priester, M. Röllig, M. Schlösser, K.H. Simon “CAPER as central and crucial facility to support R&D with tritium at TLK” *Poster presented at Tritium 2013, paper submitted to Fusion Science and Technology.*

[9] O. Borisevich, D. Demange, M. Kind, X. Lefebvre “Zeolite membrane cascade for tritium extraction and recovery systems” *Poster presented at Tritium 2013, paper accepted for publication in Fusion Science and Technology.*

[10] R. Wagner, D. Demange, E. Fanghänel, T. L. Le, M. Schwarz, K.-H. Simon “Dismantling of the Petra glove box - tritium contamination and inventory assessment” presented at Tritium 2013, *Poster presented at Tritium 2013, paper submitted to Fusion Science and Technology.*

[11] W.M. Shu, I. Cristescu, R. Michling, D. Demange, R.S. Willms and M. Glugla "Highly tritiated water processing by isotopic exchange” *Oral presented at Tritium 2013, paper submitted to Fusion Science and Technology.*

[12] I. Ricapito, P. Calderoni, Y. Poitevin, A. Aiello, M. Utili, D. Demange "Tritium processing for the European tests blanket systems: current status of the design and development strategy” *Oral presented at Tritium 2013, paper submitted to Fusion Science and Technology.*

Fuel Cycle Simulator Development (WP13-DAS-06-T02)

The activities carried out address the simulation of DEMO fuel cycle using the simulation software DTRIMO++. The fuel cycle modelling is mandatory for the detailed understanding of the interaction between the different subsystems of the fuel cycle. The goal of the DTRIMO++ simulation software, at the present stage, is to use simple relations between central parameters like thermal power output, burn up fraction and tritium breeding ratio in combination with subsystem parameters like gas flow rate, inventory, and maximum pressure and gas composition in support of simulation of the fuel cycle of DEMO. In some cases, when it was possible to describe a sub component with simple equations, which could be solved analytically, the behavior of the related component was implemented accordingly. Nevertheless, this approach could not be used for the entire configuration of the DEMO fuel cycle.

The DTRIMO++ was developed to allow calculations and easy access to the main parameters such as tritium and deuterium inventory in subsystems and within the whole fuel cycle. Moreover, the influence of the volumes of buffer vessels to the stability of the plasma operation can be examined in detail, without having to take care about the precise physics in the plasma chamber. For assuring that the simulation delivers correct results, the single systems have been implemented in such a manner that they reproduce the behavior of the subsystem from easy defined parameters.

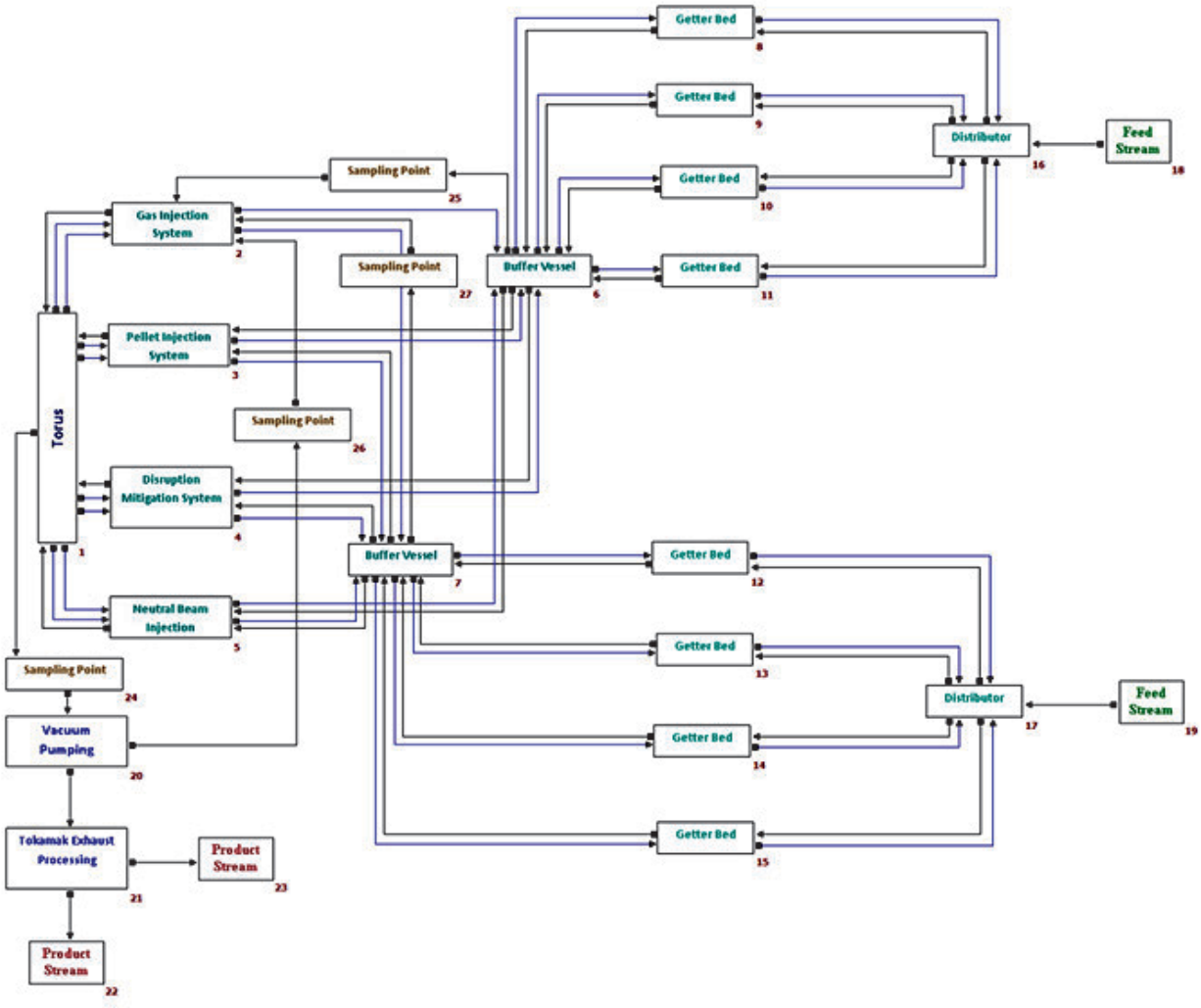

Fig. 1: Diagram of the simulated fuel cycle with TRIMO++.

Since the design of the DEMO fuel cycle design is at a very early stage it is mandatory for the simulation tool to be kept flexible in the sense that the combination of subsystems can be changed and also central parameters like fusion power, burn up fraction, etc. can be easily changed. Furthermore, all parameters describing single subsystems, like gas streams, volumes of various components need to be easy accessible. A graphic user interface has been developed in order to allow a wide variety of users, without programming experience, to simulate different fuel cycles. After setting up a fuel cycle, and inserting a wide variety of parameters specific to each scheme component, the whole scheme can be saved to an excel spreadsheet from where it can also be restored. After specifying the simulation time and the time steps for data saving, a simulation can be run by the user. The results for the simulation are independent of the time step chosen by the user; it only has an influence to the temporal resolution in data saving.

In this report, in order to demonstrate the functionality of DTRIMO++ a simplified fuel cycle scheme, shown in Figure 1, has been chosen. This shall enable the reader to easily see the increase in complexity of the behavior from the single components to the combined operation in a fuel cycle.

For demonstration of the working principle of DTRIMO++ a simplified fuel cycle scheme from Figure 1 was used. The complexity of such a system increases with every additional component. That's why the fuel cycle has not been closed to have a well-defined starting point, with constant feeding streams for deuterium and tritium. On the back end the exhaust streams are just sent to product streams. The user has the possibility of choosing between many more parameters like concentration, pressure and so on, to be shown by the simulation software.

The DTRIMO++ was used to calculate the tritium inventory on the various components of the configuration from Figure 1. In Figure 2 the time variation of the tritium inventory, on arbitrary scale, within the main components is shown. When the process starts, the getter bed 1 is filled with tritium. When it reaches the upper threshold it starts to send gas to the buffer vessel and then the second getter bed is filled and so on. After almost 0.8 hours, the buffer vessel reaches the exhaust pressure and starts to send gas to the fueling systems from where the gas is sent to the torus. So, the inventory of the torus starts to increase until the torus exhaust pressure is reached. From this point, the inventory of the torus is kept constant by adjusting the exhaust pumping speed to feeding speed.

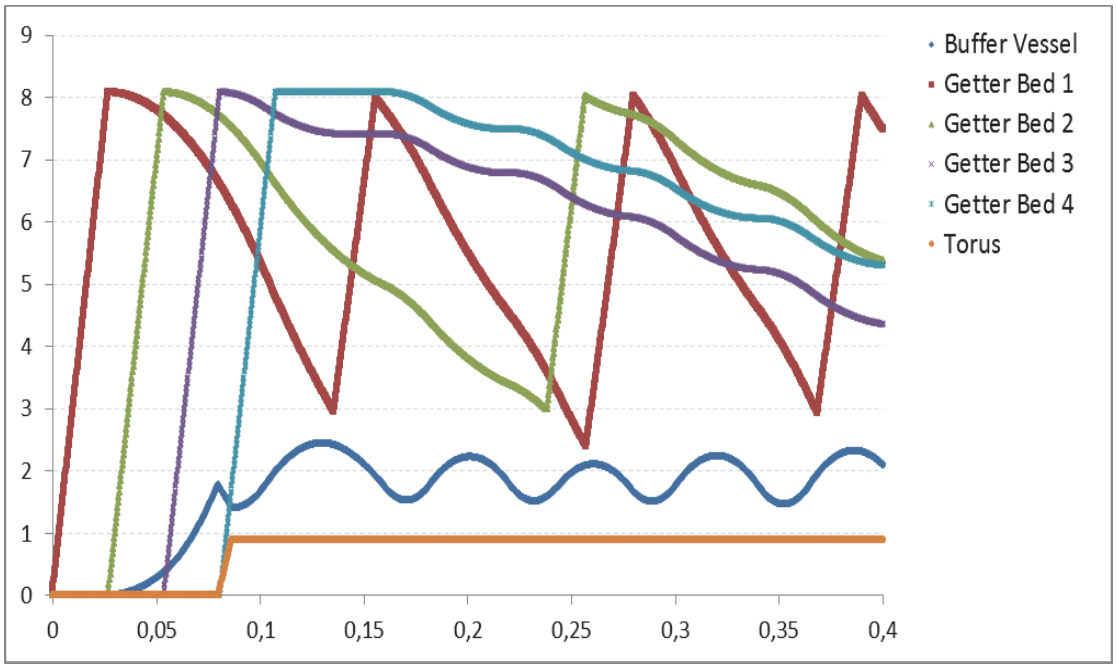

Fig. 2: Time behavior of tritium inventory (arbitrary scale) within the selected components of the reference configuration.

The simulation of this simplified fuel cycle configuration demonstrates that the simple logics of the subsystems produce a complex behavior of the whole system. Starting with a constant feeding stream, the getter beds have an oscillating inventory with different timescales. The buffer vessel also shows periodicity in its inventory but can always deliver a constant gas stream to the fueling systems resulting in a constant inventory of the torus. This tool can reveal secondary process values like the timescale on which getter beds shall be filled and emptied.

This example demonstrates very well the need and the working of DTRIMO++. This kind of non-static behavior would be very hard or impossible to be predicted with the analytical methods.

Staff:

I. Cristescu
R. Groessle
C. Petrutiu – ICIT Romania

Acknowledgement

This work, supported by the European Communities under the contract of Association between EURATOM and Karlsruhe Institute of Technology, was carried out within the framework of the European Fusion Development Agreement. The views and opinions expressed herein do not necessarily reflect those of the European Commission.

Safety

Identification of a Beryllium Substitute-small/medium Scale Experiments - Physics Models Validation (F4E-GRT-371)

The aim of this work is to continue the study on hydrogen/dust explosion hazards in case of a severe accident in ITER. Previous studies concerned graphite and tungsten dusts as candidates for the material of the ITER first wall. These studies have shown that both dusts could be exploded, however the required ignition energies were irrelevantly high for ITER accidental conditions. Another ignition source was shown to be more realistic in this case, namely, a local hydrogen explosion event. H_2-explosions can be triggered by a weak ignition source as an electric spark and are able to initiate a dust cloud explosion.

The aim is to study the scalability of the DUSTEX results and to extend the database of Al/H_2 explosion properties/regimes to medium scale. The database is used to support and validate a computer code (DET3D) under development in KIT-IKET to model pressure loads of severe accident scenarios in ITER.

Hybrid experiments in PROFLAM II were performed in July-November 2013. The material used to simulate beryllium was aluminum; Al dust of about 1 μm grain size was tested in DUSTEX experiments in 2012-13.

DUSTEX test results can be summarized as follows:

- Hybrid mixtures of 1 μm Al dust/hydrogen/air had been tested for five dust concentrations – 100, 200, 400, 800, and 1200 g/m^3 – each at 8 hydrogen concentrations stepping from 7 to 20 vol. %;
- At each dust concentration a reliable ignition occurred starting from 8 vol. % hydrogen;
- Explosion pressures ranged from 2.9 bar for the leanest mixture (8 vol. % H_2/100 g/m^3 Al dust) to 10.5 bar at 8 vol. % H_2/1200 g/m^3 Al dust;
- Pressure-rise rates ranged from 5 to 2200 bar/s (K_{st} from 1.4 m bar/s to 600 m bar/s);
- The lean H_2/Al dust mixtures reacted in two stages: first hydrogen exploded fast, then Al dust burnt out the remaining oxygen, the latter was usually slower than the former;
- The most 'severe' mixtures were with an Al dust concentration of 800 g/m^3; this value appeared to be the optimum dust concentration for pure dust/air mixtures.

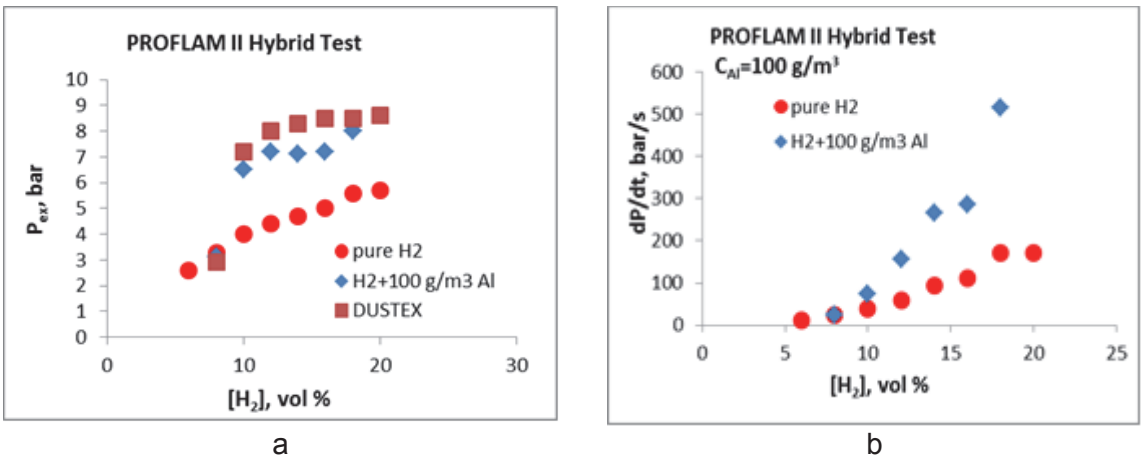

a b

Fig. 1: Explosion pressures (a) and pressure rise rates (b) in hybrid tests with 1 μm Al dust (100 g/m^3) in PROFLAM II. Explosion pressures measured in DUSTEX for the same mixtures are also shown for comparison.

Based on these results, the test matrix for PROFLAM II tests involved mixtures with 100, 400, 800, and 1000 g/m^3 Al-dust, each dust concentration to be tested at 8, 10, 12, 14, 16, 18, and possibly 20 vol. % hydrogen.

The PROFLAM test series was started with C_{dust} = 100 g/m^3. The test results are presented in Fig. 1a and 1b (explosion pressure and pressure rise rate). In addition to the hybrid test results, also the values measured in pure hydrogen tests in PROFLAM are presented. In general, the explosion behavior of these mixtures is quite similar to that observed in DUST-EX with similar mixtures (in the P_{ex} plot the data from DUSTEX are also shown).

Figure 2 shows the comparison of the DUSTEX and PROFLAM pressure rise rates in the normalized form of K_{st}. This value is used to compare the explosion 'speed' for vessels with different volumes V:

$$K_{st}=dP/dt\ V^{1/3}$$

which takes into account a natural reduction of the explosion speed in larger volumes. As can be seen, the explosions in DUSTEX are more 'severe' than those in PROFLAM. Explosion pressures are higher and the explosion processes develop faster in the smaller volume.

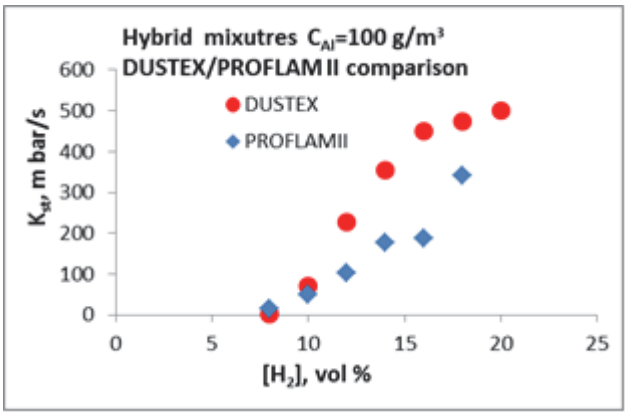

Fig.. 2: K_{st}-values for the tests in PROFLAM and DUSTEX with hydrogen/Al dust hybrid mixtures at C_{dust} = 100 g/m^3.

The PROFLAM II results with C_{dust} = 400 g/m^3 are presented in Fig. 3a and b. Explosion speeds in PROFLAM and DUSTEX are compared in Fig. 4. This test series was stopped at [H_2] = 13 vol. %. At this hydrogen concentration the explosion seemed to reach another regime: the explosion products and even flames emerged from the tube. The pressure rise rate in this case was enormously high – 1160 bar/s – which in K_{st} terms is 770 m bar/s. It has to be emphasized that this is 2.7 times higher than the value limiting the higher explosion Class 3 of 300 m bar/s, while the factor distinguishing Class 3 from Class 2 (200 m bar/s) is 1.5.

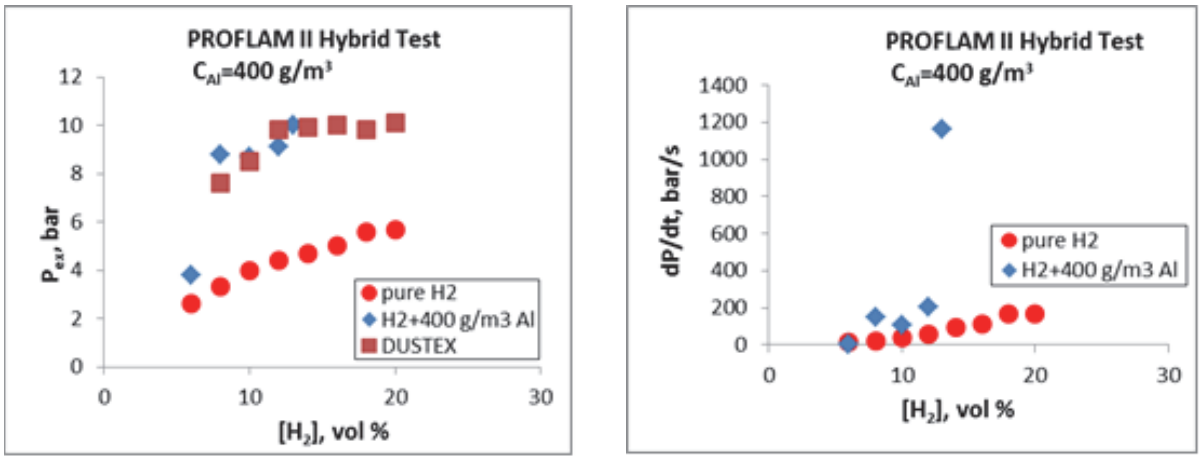

Fig. 3: Explosion pressures (a) and pressure rise rates (b) in hybrid tests with 1 μm Al dust (400 g/m^3) in PROFLAM II. Explosion pressures measured in DUSTEX for the same mixtures are also shown for comparison.

The comparison of the explosion speeds in DUSTEX and PROFLAM for C_{dust} = 400 g/m^3 is presented in Fig. 4. As can be seen, at [H_2] = 13 vol. % the explosions in a larger volume become more 'severe' than in a smaller one.

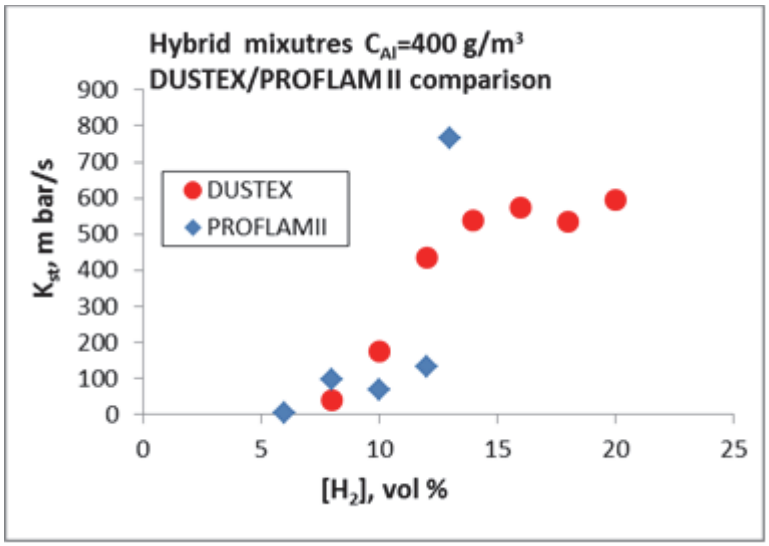

Fig. 4: K_{st}-values for the tests in PROFLAM and DUSTEX with hydrogen/Al dust hybrid mixtures at C_{dust} = 400 g/m³.

The test results are summarized in Figure 5.

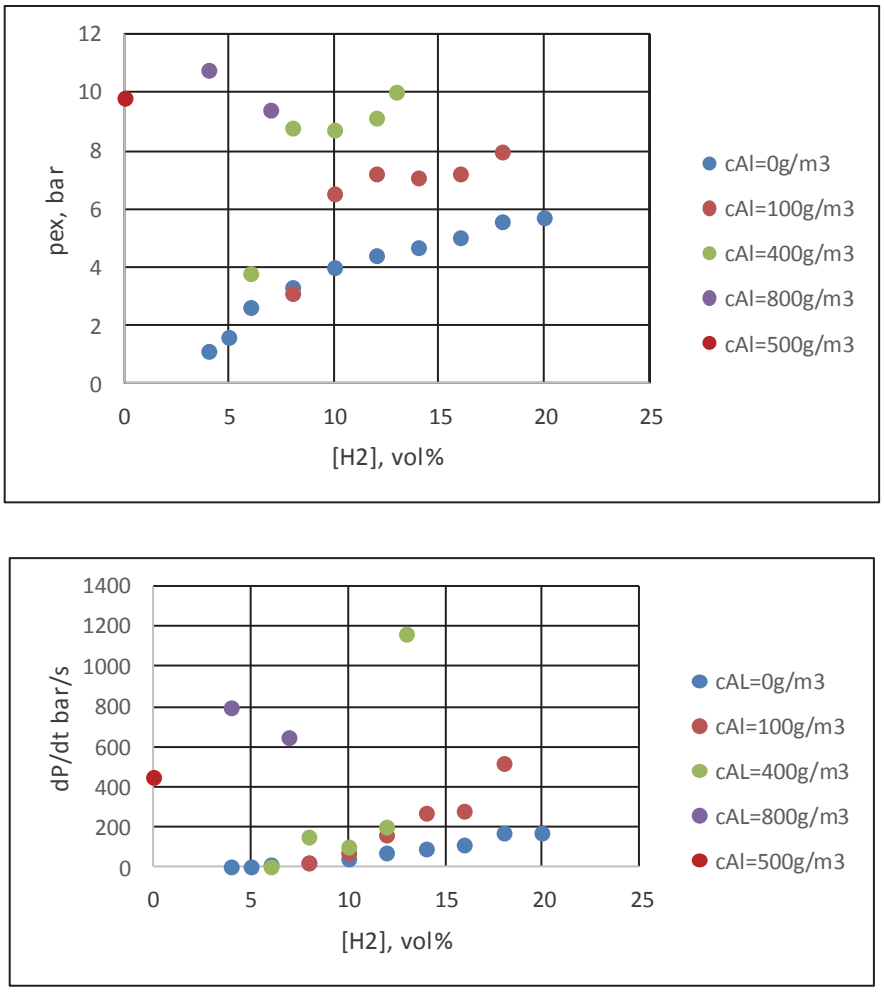

Fig. 5: Test results of hybrid explosions in PROFLAM II with 1 μm Al dust and hydrogen.

The data gained in the DUSTEX and PROFLAM facilities was used to validate the computer code DET3D. Modelling of the performed experiments was started and proceeded in parallel

with the tests. First results of the simulations with DET3D are shown in Fig. 6. Good agreement between experiment and calculations can be observed.

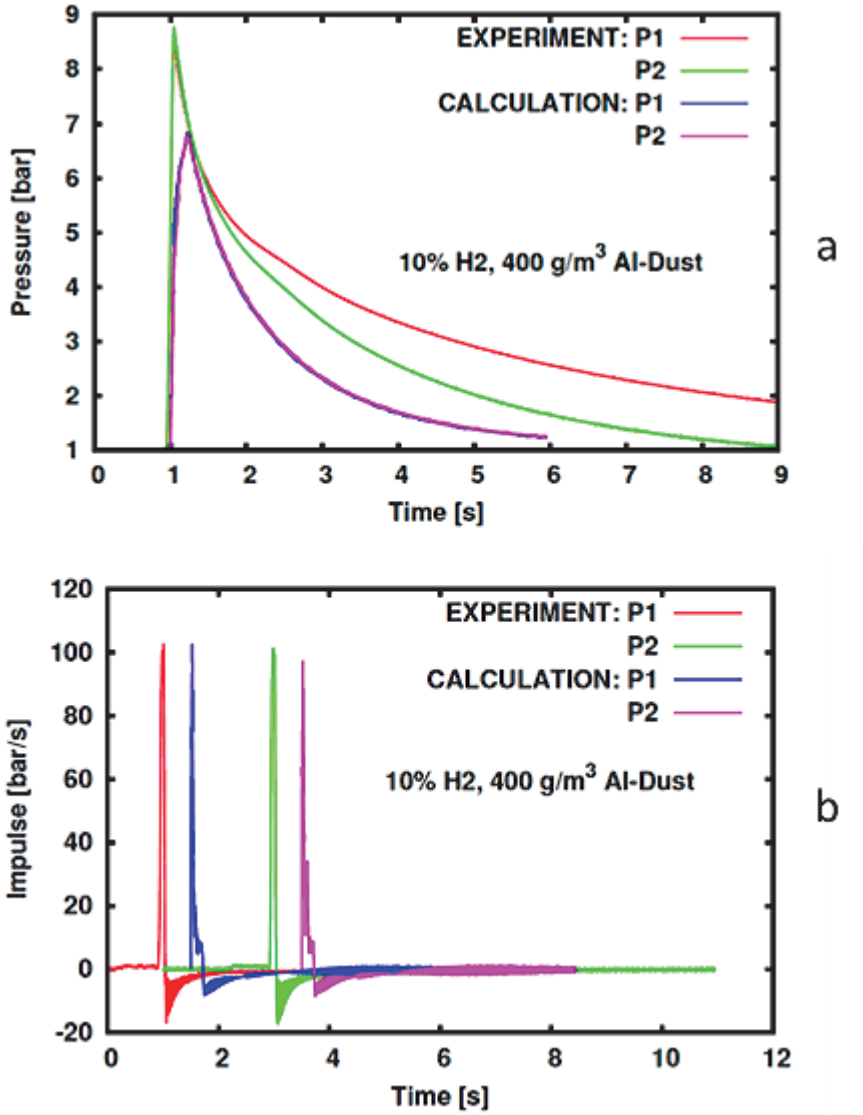

Fig. 6: Al-dust/H_2/Air combustions in the PROFLAM-II facility with 10% H_2 and 1 μm Al dust (400 g/m^3). Comparison of experimental data and DET3D-calculational results for: a) Pressure, and b) Pressure Rise Rate (shifted time scales).

Conclusions

Measurements of the explosion properties of the Be-substitute Al dust in mixtures with hydrogen have been performed. The results have shown that flames in hybrid Al/H_2 mixtures in closed geometries can accelerate to fast flame propagation regimes indicating that Be/H_2 hybrid mixtures can be much more dangerous than C or W/H_2 mixtures, resulting even in deflagration/ detonation regimes. Comparisons of the experimental data with calculations performed using the computer code DET3D show good agreement.

Outlook

Of special interest is the regime of the strong explosions observed at medium fuel concentrations in PROFLAM II, which can either be a Deflagration-to-Detonation Transition or a volumetric explosion. The distinguishing parameter is the speed of the flame front. Unfortunately it was impossible to measure the flame speed with the thermocouples installed to the facility, because they all started to react practically simultaneously shortly before they were burnt out. A suitable way to study fast flame propagation regimes with shock waves is an array of fast pressure transducers. Such a technique allows to retrieve the pressure wave pattern and to distinguish a detonation from a fast explosion.

Staff:

A. Denkevits
R. Redlinger
F. Prestel
A. Veser (Pro-Science GmbH)

Acknowledgement

This work was supported by Fusion for Energy under the grant contract No. F4E-GRT-371. The views and opinions expressed herein reflect only the author's views. Fusion for Energy is not liable for any use that may be made of the information contained therein

Supply of Documentation on Busbar Arcs Model Validation and Supporting Experiments (F4E-GRT-273)

Introduction

Experiences with tokamaks in operation indicate that electric arc accidents are not purely hypothetical [1]. Experience and calculations with the code system MAGS proved that the damage due to shorts and arcs inside coils is basically restricted to the coils themselves. Here no safety relevant consequences are expected; nevertheless the replacement of a damaged coil typically means a considerable effort. Things are less clear for the coil current leads (busbars). In case the protection systems fail, mobile electric arcs at the busbars of large fusion magnets may be able to penetrate the cryostat wall and threaten other safety relevant components in their neighbourhood. For ITER licensing this obviously requires an investigation of possible consequences of arcing. As full scale busbar arc experiments would be difficult, expensive and also of questionable significance due to the statistical behaviour of arcs, a numerical approach is advantageous. As however the real busbar arc behaviour is unknown and available models based on plasma equations ask for unknown input parameters, experimental investigation seemed crucial for the development and later validation of a successful, realistic model. Experimental practice could also be helpful if full scale experiments cannot be avoided.

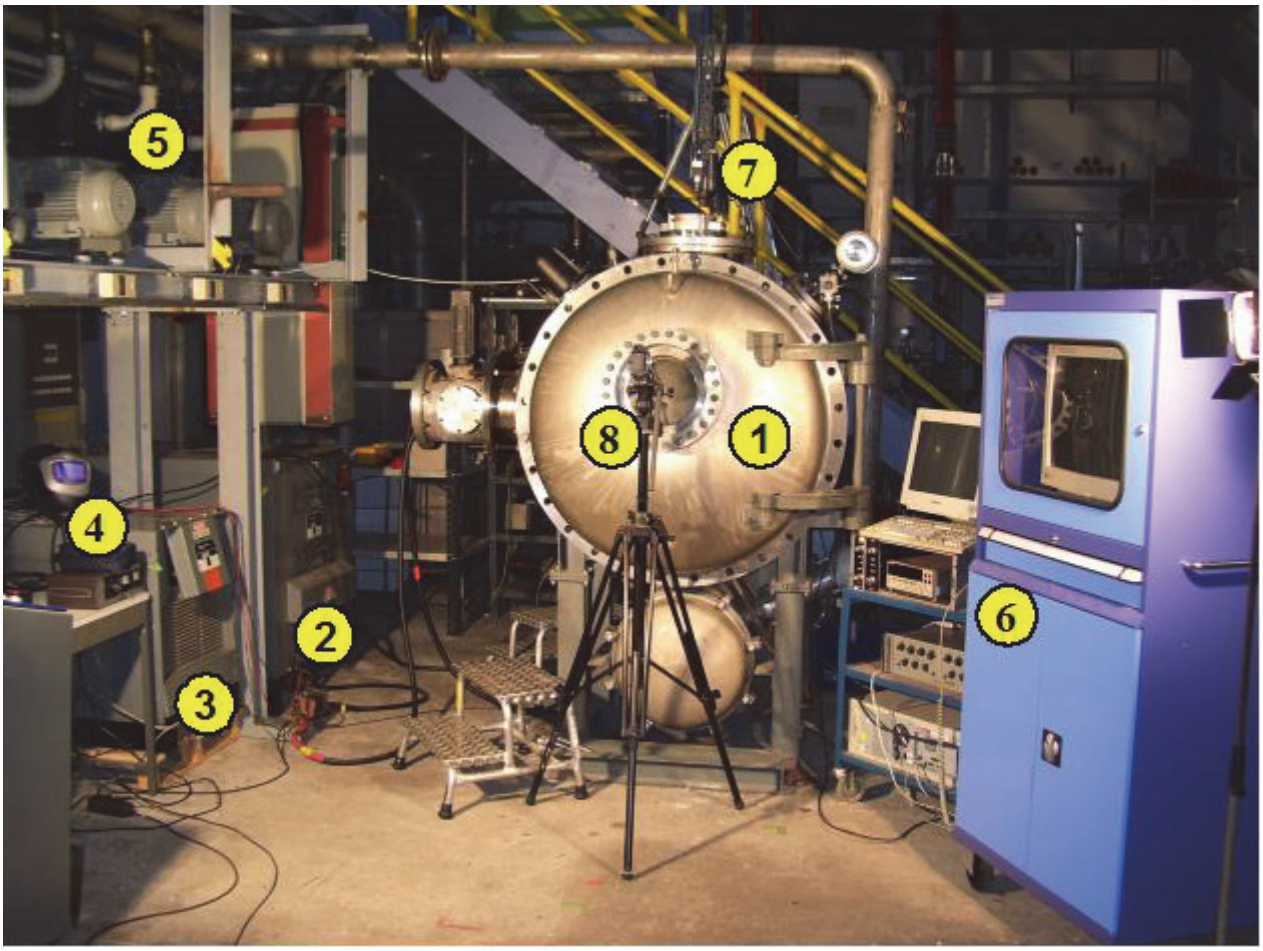

Fig. 1: VACARC device.
1) Vacuum vessel/arc chamber 2) large power converter 3) small power converter
4) Remote control for both power converters 5) Vacuum pumps 6) Data acquisition system
7) High speed camera 8) Canon camcorder.

The work in the frame of the task is basically documentation of work that has been done previously. For subtask 1, the results of the VACARC experiments (2006-2011) were summa-

rized and documented. The task of these small scale model experiments was to clarify basic destruction and propagation behaviour of busbar arcs. A very simplified setup was used to investigate the impact of different parameters as polarity, insulation thickness, conductor scale and pressure. Then the setup was successively brought more similar to a real ITER busbar feeder line. The most important finding with regard to ITER is that long arcs tend to split spontaneously in the presence of conducting structures into two arcs in series while the current is carried by the structure in between. This will exclude extreme busbar arcs, with lengths of several meters and powers of up to hundreds of megawatts in ITER. Another finding is that the ITER insulation is robust enough against arcing to avoid very fast arc propagation by cutting the insulation. The arc propagation speed is restricted to the burn down speed of the complete busbar metal and insulation cross section. It went also already clear that the inner ITER busbar feeder tube will not withstand a busbar arc. Moreover these experiments were performed to provide a database for the development and later validation of a numerical model which is subject of subtask 2.

In subtask 2, the present status of the BUSARC development was summarized. BUSARC is a numerical model to simulate propagating arcs at VACARC model conductors. Instead of developing a new code from scratch, BUSARC was developed based on the proven MAGS code system formalisms and physical models. BUSARC contains a new, additional MAGS module that requires no changes to the validated core MAGS code. This way the work concentrates on the arc description only. As available arc simulation codes typically suffer from unproven assumptions and unknown input parameters, BUSARC is developed as a phenomenological model following the results of the accompanying VACARC experiments. So far only the model conductor side is modelled, the structure side is only formally implemented. Present BUSARC results agreement with data is good within the experimental spread, although still several experiments cannot be described accurately. The experimental background for positive polarity of the model conductor is still weak and needs to be improved for a realistic assessment of the code results for this case. The present status of BUSARC development will be documented in the frame of F4E-GRT-273. As next steps BUSARC is to be completed and validated using own model experiment results at different scales and afterwards to be extrapolated to full ITER scale.

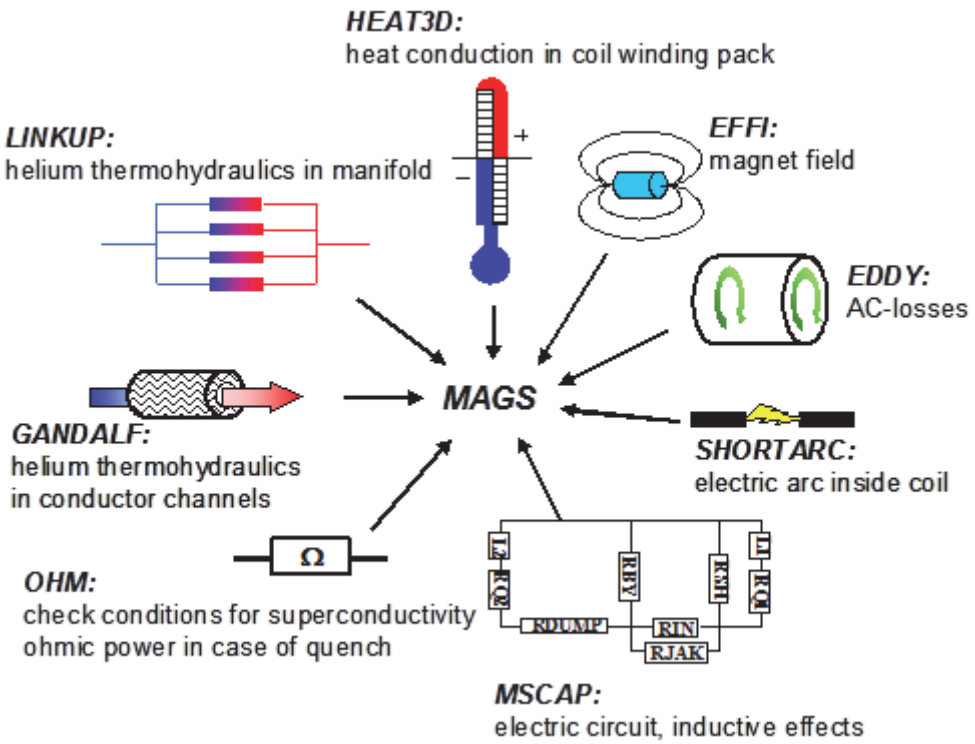

Fig. 2: Scheme of MAGS: main modules and capabilities.

Subtask 3 contains the advanced documentation of MAGS. While the MAGS code system is complete and works, the documentation still needs an upgrade to fulfill QA requirements that would allow using MAGS in ITER licensing. To do so, the MAGS documentation is to be revised using the INTRA documentation as a template. The documentation consists of the three volumes: (1) physical models, (2) user manual and (3) validation manual. These volumes are part of the deliverables of F4E-GRT-273 [2]. All deliverables had been completed in the frame of the foreseen time schedule of F4E-GRT-273 during 2013. The final acceptance data package was sent to F4E in August 2013 indicating the successful conclusion of this task.

Staff:

V. Pasler
D. Klimenko

Literature:

[1] D. Bruce Montgomery (MIT), review of fusion system magnet problems, proc. of 13th IEEE symp. on fus. eng., Knoxville, TN, USA, Oct. 1989.

[2] Volker Pasler, Final Report on Documentation of Physical Models used in the MAGS Code System, F4E-GRT-273-3D01, NUS-GEW-112731-RD-3D01-01, Nov. 2012;

[3] Volker Pasler, Final Report on User Manual of the MAGS Code System, F4E-GRT-273-3D02, NUS-GEW-112731-RD-3D02-01, Feb. 2013;

[4] Volker Pasler, Final Report on Validation of the MAGS Code System, F4E-GRT-273-3D03, NUS-GEW-112731-RD-3D03-01, Apr. 2013.

Acknowledgement

This work was supported by Fusion for Energy under the grant contract No. F4E-GRT-273. The views and opinions expressed herein reflect only the author's views. Fusion for Energy is not liable for any use that may be made of the information contained therein.

Survey Regarding Magnet Safety Studies for DEMO (WP13-SYS-04-T08-01)

Introduction

Recent experiences in ITER licensing indicated that magnet safety is taken serious by licensing authorities. Moreover this expressed in specific technical questions including deadlines beyond the work done for the ITER magnet safety documents so far and ITER had to launch a considerable effort on magnet safety under pressure of time. One should learn from this that DEMO should care for magnet safety adequately from the beginning on. The work in the frame of this task should contribute to a basis to a magnet safety concept for DEMO. The focus is on arcing, a distinction between in coil arcs and out of coil (busbar) arcs is done. Arc behaviour and damage potential is introduced, important accident scenarios are indicated. Related models from different associations are identified, described and discussed with regard to their usability for DEMO. On this basis, further R&D work for DEMO on this topic is to be identified. A proposal for recommended R&D work on magnet safety for DEMO based on the previous KIT work for ITER is provided and the problem of validation is discussed.

Arcing is no longer a topic of present research since several decades as plasma physics is basically understood and the equations are available [1]. Nevertheless the numerical modelling of arcs remains restricted to a quite narrow range of boundary conditions. Especially the behaviour of a free arc plasma column is still hard to predict. Here magnetic self forces tend to stabilize the arc column while other forces like even weak magnet fields, buoyancy or convection may bend and elongate the arc column. The key scenarios for magnet arcing are (i) arcing inside a coil winding pack and (ii) arcing at a coil busbar or at the outside of a coil. Whenever energy is sufficient and no measures are taken, an in coil arc will develop to a busbar or out of coil arc with time.

The modelling of arcs within the boundary conditions of fusion (tens of kA, burning times of tens of seconds, arc lengths in the order of metres) is difficult. Direct numerical modelling with a plasma code was very far from being realistic with the computers of early 2000's and probably is still not practicable. Models for in coil arcs are implemented in the MAGS code of KIT [2] and in the MAGARC code of INL [3]. Both models had been developed in the late 1990's and seem too simple with regard to the present requirements. For example the arc characteristics by Kronhardt [4] is gained at currents up to only 5kA and the different arc types, assumptions, threshold values and switching criteria (which differ significantly for MAGS and MAGARC) need to be reviewed in order to describe a realistic picture of an arc accident sequence. Here also experimental experiences from the small scale model experiments VACARC and LONGARC at KIT may be implemented. MAGS is the only code with a documentation at an acceptable status (represented by [2]). The ITER models used in the ITER safety documents turned out to be not available any more. Documentation to these models is unavailable, too.

For out of coil/busbar arcs, the important quantities to be modelled are arc propagation speed and arc power. Available models are the analytical model by V.V. Titkov [5] and numerical models by KIT and INL based on the in coil codes MAGS and MAGARC, respectively. The analytical model uses many questionable assumptions and unclear boundary conditions. There is also no validation, so this model results raise many questions. The KIT and INL models are operable in principle but are still incomplete. The MAGS code already is able to calculate small scale model experiments done with the KIT VACARC and the LONGARC devices. In both numerical codes, however, key correlations like a E(I) arc characteristic valid at the tens of kA range are still missing.

DEMO is expected to use a quite similar conductor concept like ITER, so no further basic code functionalities would be required. However adaptations to peculiarities like TF coils wound by two conductor types for the high and low field region will probably require minor code modifications to enable MAGS to do calculations for DEMO.

With regard to the future R&D work on magnet safety for DEMO, KIT may upgrade the MAGS code and complete and validate the busbar arc model. This also includes the review of model assumptions as well as properties data in the frame of arcing and arcing related failure behaviour. A key quantity required for in coil as well as out of coil arcs is the arc characteristics valid in the tens of kA range. Here due to improved computer performance, already direct numerical modelling with a plasma code might be an option to gain an acceptable E(I). Otherwise E(I) may be gained from collected existing high current experimental data as proposed by Raeder [6].

Code validation will be a key issue, however full scale validation experiments seem no a realistic option. This will mean the models have to be validated using simplified small scale model experiments like the KIT VACARC and LONGARC experiments and will have to be interpolated to full scale using a realistic E(I).

KIT submitted a corresponding work proposal on the open issues indicated above for the EFDA Power Plant Physics & Technology projects in the work programme 2014 and for the work plan 2014-2018.

Staff:

V. Pasler

Literature:

[1] Jürgen Raeder, On experiments simulating busbar arcs, EFDA_D_2L7NGL, 2008.

[2] Volker Pasler, Final Report on Documentation of Physical Models used in the MAGS Code System, F4E-GRT-273-3D01, NUS-GEW-112731-RD-3D01-01, Nov. 2012;

[3] Volker Pasler, Final Report on User Manual of the MAGS Code System, F4E-GRT-273-3D02, NUS-GEW-112731-RD-3D02-01, Feb. 2013;

[4] Volker Pasler, Final Report on Validation of the MAGS Code System, F4E-GRT-273-3D03, NUS-GEW-112731-RD-3D03-01, Apr. 2013.

[5] Brad J. Merrill, Final report on ITER Task Agreement 81-10, INL/EXT-09-1592, ITER IDM 2M4UQL_v1.0, January 2009.

[6] H. Kronhardt, Einfluß von Kurzschlüssen und Lichtbögen auf die Sicherheit von Magnetsystemen, Report Kernforschungszentrum Karlsruhe KfK 5096, May 1993 (in German).

[7] V.V. Titkov, Speed of Motion of a Short-Circuit Arc in an Insulated Conductor, Journal of Applied Mechanics and Technical Physics, Vol. 44, No. 1, p. 129-134, 2003.

[8] Jürgen Raeder, Electric arcs external to ITER magnet coils - synthesis of model voltage-current characteristics, annex 4e of ITER DDD 11 - 2.4 fault and safety, ITER IDM: G 83 MD5 02-10-14 W0.1, October 2002.

Acknowledgement

This work, supported by the European Communities under the contract of Association between EURATOM and Karlsruhe Institute of Technology, was carried out within the framework of the European Fusion Development Agreement. The views and opinions expressed herein do not necessarily reflect those of the European Commission.

Appendix I: KIT Departments Contributing to the Fusion Programme

KIT Department	KIT Institut/Abteilung	Director	Ext.
Institute for Applied Materials - Applied Materials Physics	Institut für Angewandte Materialien – Angewandte Werkstoffphysik (IAM-AWP)	Prof. Dr. H.J. Seifert Dr. A. Möslang (Acting Head)	23895 24029
Institute for Applied Materials - Materials and Biomechanics	Institut für Angewandte Materialien - Werkstoff- und Biomechanik (IAM-WBM)	Prof. Dr. O. Kraft	24815
Institute for Applied Materials - Material Processing Technology	Institut für Angewandte Materialien - Werkstoffprozesstechnik (IAM-WPT)	Dr. R. Knitter (Acting Head)	22518
Institute for Pulsed Power and Microwave Technology	Institut für Hochleistungsimpuls- und Mikrowellentechnik (IHM)	Prof. Dr. J. Jelonnek	22440
Institute for Nuclear and Energy Technology	Institut für Kern- und Energietechnik (IKET)	Prof. Dr. T. Schulenberg	23450
Institute for Neutron Physics and Reactor Technology	Institut für Neutronenphysik und Reaktortechnik (INR)	Dr. R. Stieglitz	22550
Institute for Technical Physics	Institut für Technische Physik (ITeP)	Prof. Dr. M. Noe	23500
- Tritium Laboratory Karlsruhe	- Tritiumlabor Karlsruhe (TLK)	Dr. B. Bornschein	23239
Institute for Data Processing and Electronics	Institut für Prozessdatenverarbeitung und Elektronik (IPE)	Prof. Dr. M. Weber	25612

Appendix II: Fusion Programme Management Staff

Head of the Research Unit	Dr. K. Hesch	ext. 25460 e-mail: klaus.hesch@kit.edu
Programme Assistant:	Ms. DP. A. Wagner	ext. 26461 e-mail: aleksandra.wagner@kit.edu
Secretary:	Ms. M. Spies	ext. 25461 e-mail: michelle.spies@kit.edu
Deputy Head; Program Budget, Administration, Reports, EU-Affairs	BW. M. Henn	ext. 25547 e-mail: michael.henn@kit.edu
	Ms. I. Pleli	ext. 28292 e-mail: ingrid.pleli@kit.edu
Blanket and Divertor Development, HELOKA, IFMIF, Materials Development, Fusion Materials Laboratory, CAD-Office, Public Relations	Dr. D. Radloff	ext. 28750 e-mail: dirk.radloff@kit.edu
Fuel Cycle, Superconducting Magnets, Plasma Heating Technology, Safety Studies, Neutronics, Summer School Fusion Technology	Ms. Dr. M. Ionescu-Bujor	ext. 28325 e-mail: mihaela.ionescu-bujor@kit.edu
Power Plant Integration, Gyrotron Development, Port and Plant Engineering	Dr. K. Hesch	ext. 25460 e-mail: klaus.hesch@kit.edu
Quality Management	Dr. J. Gafert	ext. 22923 e-mail: juergen.gafert@kit.edu
	Ms. Dr. M. Oron-Carl	ext. 25468 e-mail: matti.oron-carl@kit.edu
	Ms. DI. Ch. Schweier	ext. 28325 e-mail: christine.schweier@kit.edu

Address: **Karlsruhe Institute of Technology**
Nuclear Fusion Programme Management

Post Office Box 3640, D - 76021 Karlsruhe / Germany

Telephone No: **0721-608-Extensions .....**

Telefax No: **0721-608-25467**

world wide web: **http://www.fusion.kit.edu/**

Appendix III: Publications

Plasma Wall Interaction

[1] Bazylev, B.; Igitkhanov, Yu.; Saibene, G.
Erosion of DEMO FW W armor under RE impact.
14th Internat.Conf.on Plasma-Facing Materials and Components for Fusion Applications, Jülich, May 13-17, 2013, Book of Abstracts A122

[2] Bazylev, B.; Arnoux, G.; Brezinsek, S.; Igitkhanov, Yu.; Lehnen, M.; Riccardo, V.; Kiptily, V.; JET EFDA Contributors
Modeling of the Impact of runaway electrons on the ILW in JET.
Journal of Nuclear Materials, 438(2013) S.S237-S240, DOI:10.1016/j.jnucmat.2013.01.035

[3] Bazylev, B.; Coenen, J.W.
Modeling of tungsten melt layer erosion caused by JxB force at TEXTOR with the code MEMOS.
Problems of Atomic Science and Technology /
Voprosy Atomnoj Nauki i Techniki, 83(2013) Nr.1, S.3-6

[4] Igitkhanov, Y.; Bazylev, B.; Fetzer, R.; Boccaccini, L.
Design strategy for the PFC in DEMO reactor.
11th International Symposium on Fusion Nuclear Technology (ISFNT 2013), Barcelona, E, September 16-20, 2013

[5] Igitkhanov, Y.; Bazylev, B.; Landman, I.
Plasma facing materials lifetime in steady-state DEMO operation.
Fusion Science and Technology, 64(2013) S.245-249

[6] Igitkhanov, Yu.; Bazylev, B.; Landman, I.; Boccaccini, L.
Applicability of tungsten/EUROFER blanket module for the DEMO first wall.
Journal of Nuclear Materials, 438(2013) S.S440-S444, DOI:10.1016/j.jnucmat.2013.01.089

[7] Igitkhanov, Yu.; Bazylev, B.; Landman, I.; Fetzer, R.
Design strategy for the PFC in DEMO reactor.
KIT Scientific Reports, KIT-SR 7637 (Mai 2013)

[8] Igitkhanov, Yu.I.; Bazylev, B.N.
Energy and particle inpact on W surface for the case of repetitive ELMs and RE electrons in DEMO plasmas.
25th Symposium on Fusion Engineering (SOFE 2013), San Francisco, Calif., June 10-14, 2013

[9] Klimov, N.S.; Linke, J.; Pitts, R.A.; Zhitlukhin, A.M.; Kovalenko, D.V.; Podkovyrov, V.L.; Barsuk, V.A.; Thomser, C.; Pintsuk, G.; Bazylev, B.N.; Giniyatulin, R.N.; Budaev, V.P.; Khimchenko, L.N.
Stainless steel performance under ITER-relevant mitigated disruption photonic heat loads.
Journal of Nuclear Materials, 438(2013) Suppl., S.S241-S245, DOI:10.1016/j.jnucmat.2013.01.036

[10] Landman, I.; Bazylev, B.; Pitts, R.; Saibene, G.; Pestchanyi, S.; Putvinski, S.; Sugihara, M.
Radiation loads on the ITER first wall during massive gas injection.
Fusion Engineering and Design, 88(2013) S.1682-1685, DOI:10.1016/j.fusengdes.2013.01.052

[11] Landman, I.S.; Pestchanyi, S.E.; Igitkhanov, Y.; Pitts, R.
Modelling of massive gas injection for ITER disruption mitigation.
Journal of Nuclear Materials, 438(2013) S.S871-S874, DOI:10.1016/j.jnucmat.2013.01.188

[12] Makhlai, V.A.; Garkusha, I.E.; Aksenov, N.N.; Petrov, Yu.V.; Bazylev, B.; Landman, I.; Linke, J.; Wirtz, M.; Malykhin, S.V.; Pugachov, A.T.; Skladnik-Sadowska, E.; Sadowski, M.J.
Tungsten damage and melt losses under the plasma accelerators exposures in ITER ELM conditions.
14th Internat.Conf.on Plasma-Facing Materials and Components for Fusion Applications, Jülich, May 13-17, 2013, Book of Abstracts A043

[13] Makhlaj, V.A.; Garkusha, I.E.; Aksenov, N.N.; Chuvilo, A.A.; Chebotarev, V.V.; Landman, I.; Malykhin, S.V.; Pestchanyi, S.; Pugachov, A.T.
Dust generation mechanisms under powerful plasma impacts to the tungsten surfaces in ITER ELM simulation experiments.
Journal of Nuclear Materials, 438(2013) Suppl., S.S233-S236, DOI:10.1016/j.jnucmat.2013.01.034

[14] Pestchanyi, S.; Lehnen, M.; Huber, A.; Gerasimov, S.; Igitkhanov, Yu.; Landman, I. ; JET EFDA Contributers
Analysis of energy cross-transport during MGI: JET experiments and TOKES simulations.
Fusion Engineering and Design, 88(2013) S.1127-1131, DOI:10.1016/j.fusengdes.2013.01.052

[15] Pestchanyi, S.; Boboc, A.; Landman, I.; JET EFDA Contributors
Optimization of MGI in JET using TOKES code.
16th International Conference on Fusion Reactor Materials (ICFRM-16), Beijing, China, October 20-26, 2013

[16] Pestchanyi, S.; Landman, I.
Simulation of dust production from tungsten armour using PEGASUS-3D code.
11th International Symposium on Fusion Nuclear Technology (ISFNT 2013), Barcelona, E, September 16-20, 2013

[17] Pestchanyi, S.; Arkhipov, N.; Landman, I.; Poznyak, I.; Safronov, V.; Toporkov, D.
Simulation of tungsten plasma transport along magnetic field under ELM-like heat loads.
Journal of Nuclear Materials, 438(2013) S.S459-S462, DOI:10.1016/j.jnucmat.2013.01.093

[18] Pitts, R.A.; Carpentier, S.; Escourbiac, F.; Hirai, T.; Komarov, V.; Lisgo, S.; Kukushkin, A.S.; Loarte, A.; Merola, M.; Sashala Naik, A.; Mitteau, R.; Sugihara, M.; Bazylev, B.; Stangeby, P.C.
A full tungsten divertor for ITER: Physics issues and design status.
Journal of Nuclear Materials, 438(2013) Suppl., S.S48-S56, DOI:10.1016/j.jnucmat.2013.01.008

[19] Polosatkin, S.; Astrelin, V.; Bazylev, B.; Beklemishev, A.; Burdakov, A.; Gavrilenko, D.; Huber, A.; Ivanov, A.; Ivanov, I.; Kalinin, P.; Kandaurov, I.; Kreter, A.; Landman, I.; Postupaev, V.; Sinitsky, S.; Shoshin, A.; Trunev, Y.; Thumm, M.; Unterberg, B.
GDMT-T: Superconducting linear device for PMI studies.
Transactions of Fusion Science and Technology, 63(2013) Nr.1T, S.184-187

Part and Plant Engineering

[1] Aiello, G.; Vaccaro, A.; Meier, A.; Strauss, D.; Scherer, T.A.
Seismic analysis of the CVD diamond window unit.
25th Joint Russian-German Meeting on ECRH and Gyrotrons, Karlsruhe/Stuttgart/Garching, June 24-29, 2013

[2] Aiello, G.; Meier, A.; Scherer, T.; Strauss, D.; Vaccaro, A.
Seismic analysis of the CVD diamond window unit for the ITER EC H&CD upper launcher.
Workshop on RF Heating Technology of Fusion Plasmas, Speyer, September 9-11, 2013, Book of Abstracts T27

[3] Geßner, R.; Meier, A.; Scherer, T.A.
Qualification of CVD diamond window assemblies by computer tomographical inspection.
38th Internat.Conf.on Infrared, Millimeter and Terahertz Waves (IRMMW-RHz 2013), Mainz, September 1-6, 2013

[4] Gessner, R.; Aiello, G.; Grossetti, G.; Meier, A.; Ronden, D.; Spach, P.; Scherer, T.; Schreck, S.; Strauss, D.; Vaccaro, A.
The ITER EC H&CD upper launcher: design, analysis and testing of a bolted joint for the blanket shield module.
Fusion Engineering and Design, 88(2013) S.1881-1885, DOI:10.1016/j.fusengdes.2013.01.090

[5] Grossetti, G.; Harman, J.; Mittwollen, M.; Poli, E.; Scherer, T.; Späh, P.; Strauß, D.; Vaccaro, A.
DEMO: Heating and current drive system integration with blanket system.
Proceedings of the 25th Symposium on Fusion Engineering (SOFE 2013), San Francisco, Calif., June 10-14, 2013, Pisacataway, N.J. : IEEE, 2013, ISBN 978-1-4799-0169-2, DOI:10.1109/SOFE.2013.6635329

[6] Grossetti, G.; Aiello, G.; Chavan, R.; Geßner, R.; Goodman, T.; Heemskerk, C.; Meier, A.; Ronden, D.; Scherer, T.; Späh, P.; Schreck, S.; Strauß, D.; Vaccaro, A.; Van Oosterhout, J.
ITER EC H&D upper launcher: Design options and remote handling issues of the waveguide assembly.
11th International Symposium on Fusion Nuclear Technology (ISFNT 2013), Barcelona, E, September 16-20, 2013

[7] Grossetti, G.; Aiello, G.; Geßner, R.; Mazzochhi, F.; Meier, A.; Scherer, T.A.; Schreck, S.; Späh, P.; Strauß, D.; Vaccaro, A.
Overview of remote maintenance concepts for the ITER ECH&CD upper launcher.
25th Joint Russian-German Meeting on ECRH and Gyrotrons, Karlsruhe/Stuttgart/Garching, June 24-29, 2013

[8] Grossetti, G.; Aiello, G.; Heemskerk, C.; Elzendoorn, B.; Geßner, R.; Koning, J. ; Meier, A.; Ronden, D.; Späh, P.; Scherer, T.; Schreck, S.; Strauß, D.; Vaccaro, A.
The ITER EC H&CD upper launcher: Analysis of vertical remote handling applied to the BSM maintenance.
Fusion Engineering and Design, 88(2013) S.1929-1933, DOI:10.1016/j.fusengdes.2013.05.005

[9] Mittwollen, M.; Madzharov, V.; Kubaschewski, M.; Boccaccini, L.V.; Grossetti, G.
DEMO - initiation of remote maintenance requirements.
Proceedings of the 25th Symposium on Fusion Engineering (SOFE 2013), San Francisco, Calif., June 10-14, 2013, Pisacataway, N.J. : IEEE, 2013, ISBN 978-1-4799-0169-2, DOI:10.1109/SOFE.2013.6635472

[10] Rösch, M.J.; Mattiocco, F.; Scherer, T.A.; Siegel, M.; Schuster, K.F.
Modeling and measureing the optical coupling of lumped element kinetic inductance detectors at 120-180 GHz.
IEEE Transactions on Antennas and Propagation, 61(2013) S.1939-1946
DOI:10.1109/TAP.2012.2231933

[11] Ronden, D.M.S.; de Baar, M.; Chavan, R.; Elzendoorn, B.S.Q.; Grossetti, G.; Heemskerk, C.J.M.; Koning, J.F.; Landis, J.D.; Spaeh, P.; Strauss, D.
The ITER EC H&CD upper launcher: Maintenance concepts.
Fusion Engineering and Design, 88(2013) S.1982-1986

[12] Scherer, T.; Strauss, D.
Development of low loss dielectric CVD diamond window units for high power microwave transmission.
New Diamond and Nano Carbons Conference 2013 (NDNC 2013), Singapore, SGP, May 19-23, 2013

[13] Scherer, T.
Loss reduction of dielectrics: CVD diamond.
Frühjahrstagung DPG, Sektion Kondensierte Materie, Fachverband Dielektrische Festkörper, Regensburg, 10.-15. März 2013, Verhandlungen der Deutschen Physikalischen Gesellschaft, R.6, B.48(2013), DF 8.2

[14] Scherer, T.A.; Strauss, D.; Meier, A.; Aiello, G.; Gessner, R.
Recent developments in the design f the actual ITER CVD diamond torus window assembly.
25th Joint Russian-German Meeting on ECRH and Gyrotrons, Karlsruhe/Stuttgart/Garching, June 24-29, 2013

[15] Scherer, T.A.; Strauss, D.; Meier, A.; Aiello, G.; Gessner, R.
Recent developments in the design of the actual ITER CVD diamond torus window assembly.
Workshop on RF Heating Technology of Fusion Plasmas, Speyer, September 9-11, 2013
Book of Abstracts T22

[16] Späh, P.
Engineering principles for structural components of EC heating and current drive systems.
Workshop on RF Heating Technology of Fusion Plasmas, Speyer, September 9-11, 2013,
Book of Abstracts T29

[17] Spaeh, P.; Aiello, G.; Binni, A.; Gessner, R.; GOldman, A.; Grossetti, G.; Kroiss, A.; Meier, A.; Obermeier, C.; Scherer, T.; Strauss, D.; Vaccaro, A.
Prototyping of the blanket shield module for the ITER EC H&CD upper launcher.
11th International Symposium on Fusion Nuclear Technology (ISFNT 2013), Barcelona, E, September 16-20, 2013

[18] Spaeh, P.; Aiello, G.; Gessner, R.; Grossetti, G.; Meier, A.; Scherer, T.; Schreck, S.; Serikov, A.; Strauss, D.; Vaccaro, A.; Weinhorst, B.
The ITER EC H&CD upper launcher: structural system.
Fusion Engineering and Design, 88(2013) S.878-881, DOI:10.1016/j.fusengdes.2013.02.103

[19] Spaeh, P.; Aiello, G.; Bertizzolo, R.; Chavan, R.; Gessner, R.; Goodman, T.; Grossetti, G.; Henderson, M.; Krause, A.; Landis, J.D.; Meier, A.; Ronden, D.; Saibene, G.; Scherer, T.; Schreck, S.; Serikov, A.; Strauss, D.; Vaccaro, A.; Weinhorst, B.
The ITER ECH & CD upper launcher: Steps towards final design of the first confinement system.
Proceedings of the 25th Symposium on Fusion Engineering (SOFE 2013), San Francisco, Calif., June 10-14, 2013, Pisacataway, N.J. : IEEE, 2013, ISBN 978-1-4799-0169-2, DOI:10.1109/SOFE.2013.6635321

[20] Stober, J.; Wagner, D.; Leuterer, F.; Monaco, F.; Müller, S.; Münich, M.; Reich, M.; Schubert, M.; Schütz, H.; Treutterer, W.; Zohm, H.; Flamm, J.; Gantenbein, G.; Thumm, M.; Meier, A.; Scherer, T.; Strau, D.; Vaccaro, A.; Höhnle, H.; Kasparek, W.; Stroth, U.; Litvak, A.; Denisov, G.G.; Chirkov, A.V.; Tai, E.M.; Popov, L.G.; Nichiporenko, V.O.; Myasnikov, V.E.; Soluyanova, E.A.; Malygin, S.A.
The ECRH system for ASDEX upgrade. Status and plans.
25th Joint Russian-German Meeting on ECRH and Gyrotrons, Karlsruhe/Stuttgart/Garching, June 24-29, 2013

[21] Strauss, D.; Aiello, G.; Chavan, R.; Cirant, S.; deBaar, M.; Farina, D.; Gantenbein, G.; Goodman, T.; Henderson, M.A.; Kasparek, W.; Kleefeldt, K.; Landis, J.D.; Meier, A.; Moro, A.; Platania, P.; Plaum, B.; Poli, E.; Ramponi, G.; Ronden, D.; Saibene, G.; Sanchez, F.; Sauter, O.; Scherer, T.; Schreck, S.; Serikov, A.; Sozzi, C.; Spaeh, P.; Vaccaro, A.; Zohm, H.
Preliminary design of the ITER ECH upper launcher.
Fusion Engineering and Design, 88(2013) S.2761-2766, DOI:10.1016/j.fusengdes.2013.03.040

[22] Strauss, D.; Aiello, G.; Bruschi, A.; Chavan, R.; Farina, D.; Fgini, L.; Gagliardi, M.; Garcia, V.; Goodman, T.P.; Grossetti, G.; Heemskerk, C.; Henderson, M.A.; Kasparek, W.; Krause, A.; Landis, J.D.; Meier, A.; Moro, A.; Platania, P.; Plaum, B.; Poli, E.; Ronden, D.; Saibene, G.; Sanchez, F.; Sauter, O.; Scherer, T.; Schreck, S.; Serikov, A.; Sozzi, C.; Spaeh, P.; Vaccaro, A.; Weinhorst, B.
Progress of the ITER EC H&CD upper launcher.
11th International Symposium on Fusion Nuclear Technology (ISFNT 2013), Barcelona, E, September 16-20, 2013

[23] Strauß, D.; Aiello, G.; Grossetti, G.; Meier, A.; Scherer, T.; Schreck, S.; Spaeh, P.; Vaccaro, A.
The ITER ECRH upper launcher and an outlook beyond.
25th Joint Russian-German Meeting on ECRH and Gyrotrons, Karlsruhe/Stuttgart/Garching, June 24-29, 2013

[24] Strauss, D.; Aiello, G.; Brusci, A.; Chavan, R.; Farina, D.; Finigi, L.; Goodman, T.P.; Grossetti, G.; Henderson, M.A.; Kasparek, W.; Koning, J.; Landis, J.D.; Meier, A.; Moro, A.; Plaum, B.; Poli, E.; Ronden, D.; Saibene, G.; Sanchez, F.; Sautter, O.; Scherer, T.; Schreck, S.; Serikov, A.; Sozzi, C.; Spaeh, P.; Vaccaro, A.
The ITER ECRH upper launcher and an outlook to DEMO.
Workshop on RF Heating Technology of Fusion Plasmas, Speyer, September 9-11, 2013, Book of Abstracts T26

[25] Vaccaro, A.; Aiello, G.; Späh, P.; Scherer, T.A.; Strauss, D.
Definition of non constant heat loads in FEM analyses: nuclear heating on the BSM.
25th Joint Russian-German Meeting on ECRH and Gyrotrons, Karlsruhe/Stuttgart/Garching, June 24-29, 2013

[26] Vaccaro, A.; Aiello, G.; Scherer, T.; Spaeh, P.; Strauss, D.
FEM analyses of the blanket shield module with respect to surface and nuclear heat loads.
Workshop on RF Heating Technology of Fusion Plasmas, Speyer, September 9-11, 2013
Book of Abstracts T25

[27] Vaccaro, A.; Aiello, G.; Grossetti, G.; Meier, A.; Scherer, T.; Schreck, S.; Späh, P.; Strauß, D.; Serikov, A.; Weinhorst, B.
The ITER EC-H&CD upper launcher: FEM analysis of the blanket shield with respect to surface and nuclear heat loads.
Proceedings of the 25th Symposium on Fusion Engineering (SOFE 2013), San Francisco, Calif., June 10-14, 2013, Pisacataway, N.J. : IEEE, 2013, ISBN 978-1-4799-0169-2, DOI:10.1109/SOFE.2013.6635394

[28] Vaccaro, A.; Aiello, G.; Grossetti, G.; Meier, A.; Scherer, T.; Schreck, S.; Späh, P.; Strauß, D.; Saibene, G.; Cavinato, M.
The ITER EC H&CD upper launcher: EM disruption analysis.
Fusion Engineering and Design, 88(2013) S.1042-104, DOI:10.1016/j.fusengdes.2013.01.058

[29] Weinhorst, B.; Serikov, A.; Fischer, U.; Spaeh, P.; Strauss, D.
Neutronic analyses for the ITER electron cyclotron-heating upper launcher.
11th International Symposium on Fusion Nuclear Technology (ISFNT-11), Barcelona, E, September 16-20, 2013

[30] Weinhorst, B.; Serikov, A.; Fischer, U.; Große, D.
Status of the neutronic analyses for the electron cyclotron-heating upper launcher of ITER.
Jahrestagung Kerntechnik, Berlin, 14.-16. Mai 2013, Berlin : INFORUM GmbH, 2013, CD-ROM

Physics: Heating and Current Drive - ECRH

[1] Thumm, M.
State-of-the-art of high power gyro-devices and free electron masers: update 2012.
KIT Scientific Reports, KIT-SR 7641 (April 2013)

[2] Petelin, M.; Lubyako, L.; Zaitsev, N.; Pavelyev, V.; Dugin, N.; Erckmann, V.; Kasparek, V.; Kubo, S.; Thumm, M.; Van't Klooster, K.
Components for remote sensing of asteroids and dense plasmas.
25th Joint Russian-German Meeting on ECRH and Gyrotrons, Karlsruhe/Stuttgart/Garching, June 24-29, 2013

[3] Bin, W.; Bruschi, A.; Cirant, S.; Muzzini, V.; Simonetto, A.; Spnicchia, N.; Angella, G.; Dell'Era, F.; Gantenbein, G.; Leonhardt, W.; Nardone, A.; Samartsev, A.; Schmid, M.
Absorbing coatings for high power millimeter-wave devices and matched loads.
Fusion Engineering and Design, 88(2013) S.2510-2514, DOI:10.1016/j.fusengdes.2012.12.036

[4] Bosch, H.S.; [Hauptautor]; Gantenbein, G.; Jelonnek, J.; Thumm, M.; Hunger, H.; Samartsev, A.; Schmid, M.; [KIT-Autoren]; u.a.
Technical challenges in the construction of the steady-state stellarator Wendelstein 7-X.
Nuclear Fusion, 53(2013) S.126001/1-16, DOI:10.1088/0029-5515/53/12/126001

[5] Braune, H.; Erckmann, V.; Jonitz, L.; Kasparak, W.; Laqua, H.P.; Michel, G.; Noke, F.; Purps, F.; Schulz, T.; Uhren, P. ; W7-X ECRH Teams at IPP, IPF and KIT
Integrated commissioning of ECRH for W7-X.
38th Internat.Conf.on Infrared, Millimeter and Terahertz Waves (IRMMW-THz 2013), Mainz, September 1-6, 2013, Proceedings on USB-Stick

[6] Cordova, M.; Avramidis, K.; Illy, S.; Jelonnek, J.; Wu, C.
Thermo-mechanical study of the cavity deformation in the case of the 1 MW, 140 GHz CW gyrotron for W7-X.
Workshop on RF Heating Technology of Fusion Plasmas, Speyer, September 9-11, 2013

[7] Erckmann, V.; Braune, H.; Gantenbein, G.; Jelonnek, J.; Kasparek, W.; Laqua, H.P.; Lechte, C.; Marushchenko, N.B.; Michel, G.; Plaum, B.; Thumm, M.; Wolf, R.
ECRH and W7-X, an intriguing pair.
20th Topical Conference on Radio Frequency Power in Plasmas (RFPPC 2013), Sorrento, I, June 25-28, 2013

[8] Jelonnek, J.; Alberti, S.; Avramidis, K.A.; Erckmann, V.; Gantenbein, G.; Hesch, K.; Hogge, J.-P.; Illy, S.; Jin, J.; Kern, S.; Pagonakis, I.; Piosczyk, B.; Rzesnicki, T.; Samartsev, A.; Thumm, M.; W7-X Team; EGYC Team
Development of advanced gyrotrons in Europe.
Fusion Science and Technology, 64(2013) S.505-512

[9] Jelonnek, J.; Avramidis, K.A.; Franck, J.; Gantenbein, G.; Hesch, K.; Illy, S.; Pagonakis, I.; Rzesnicki, T.; Samartsev, A.; Scherer, T.; Schlaich, A.; Schmid, A.; Strauss, D.; Thumm, M.; Zhang, J.
Status, progress and future plans of EC RF source development at KIT.
Workshop on RF Heating Technology of Fusion Plasmas, Speyer, September 9-11, 2013

[10] Schlaich, A.; Jelonnek, J.; Thumm, M.
Millimeter-wave time-domain spectrum analysis system with unambiguous RF spectrum reconstruction.
2013 International Microwave Symposium (IMS 2013), Seattle, Wash., June 4-6, 2013, Proc.on USB-Stick, Piscataway, N.J. : IEEE, 2013, ISBN 978-1-4673-2141-9

[11] Schlaich, A.; Gantenbein, G.; Jelonnek, J.; Samartsev, A.; Thumm, M.
Time-dependent analysis of gyrotron RF output spectrum.
25th Joint Russian-German Meeting on ECRH and Gyrotrons, Karlsruhe/Stuttgart/Garching, June 24-29, 2013

[12] Schlaich, A.; Gantenbein, G.; Jelonnek, J.; Thumm, M.
Transient millimeter-wave signal analysis with unambiguous RF spectrum reconstruction.
IEEE Transactions on Microwave Theory and Techniques, 61(2013) S.4660-4666
DOI:10.1109/TMTT.2013.2283063

[13] Schmid, M.; Roy Choudhury, A.; Dammertz, G.; Erckmann, V.; Gantenbein, G.; Illy, S.; Jelonnek, J.; Kern, S.; Legrand, F.; Rzesnicki, T.; Samartsev, A.; Schlaich, A.; Thumm, M.
Recent achievements on tests of series gyrotrons for W7-X and planned extension at the KIT gyrotron test facility. Fusion Engineering and Design, 88(2013) S.945-949
DOI:10.1016/j.fusengdes.2013.01.041

[14] Thumm, M.; Avramidis, K.; Gantenbein, G.; Hesch, K.; Jelonnek, J.; Jin, J.; Pagonakis, I.; Piosczyk, B.; Rzesnicki, T.; Schmid, M.; Alberti, S.; Hogge, J.P. ; Tran, M.Q.; Erckmann, V.; Laqua, H.; Michel, G.; Benin, P.; Legrand, F.; Rozier, Y.; Vomvoridis, J.L.; Ioannidis, Z.C.; Latsas, G.P.; Tigelis, I.G.; Albajar, F.; Bonicelli, T.; Cismondi, F.
Series production of 1 MW, 140 GHz, CW gyrotrons for W7-X leading to EU-1 MW, 170 GHz, CW gyrotrons for ITER.
Workshop on Vacuum Electronic Devices and Applications (VEDA Kolleg 2013), Roorkee, IND, October 18-20, 2013

[15] Wolf, R.C.; Baldzuhn, J.; Bluhm, T.; Braune, H.; Cardella, A.; Endler, M.; Erckmann, V.; Gantenbein, G.; Hathiramani, D.; Heimann, P.; Hennig, C.; Hirsch, M.; Jelonnek, K.; Kasparek, W.; König, R.; Kornejew, P.; Kroiss, H.; Krom, J.G.; Kühner, G.; Laqua, H.; Laqua, H.P.; Lechte, C.; Lewerentz, M.; Maier, J.; Michel, G.; Riemann, H.; Schacht, J.; Spring, A.; Sunn Pedersen, T.; Thumm, M.; Turkin, Y.; Werner, A.; Zhang, D.; Zilker, M. ; Wendelstein 7-X Team
Preparation of steady-state operation of the Wendelstein 7-X stellarator.
Compilation of the EFDA-JET Papers Presented at the 24th IAEA Fusion Energy Conf., San Diego, Calif., October 8-13, 2012, CD-ROM Paper ITR/P1-23

[16] Braune, H.; Erckmann, V.; Jonitz, L.; Kasparek, W.; Laqua, H.P.; Michel, G.; Noke, F.; Purps, F.; Schulz, T.; Uhren, P. ; W7-X ECRH Teams at IPP, IPF and KIT
W7-X commissioning - Required enhancements of the ECRH control system.
25th Joint Russian-German Meeting on ECRH and Gyrotrons, Karlsruhe/Stuttgart/Garching, June 24-29, 2013

[17] Drotziger, S.; Buscher, K.-P.; Fietz, W.H.; Heiduk, M.; Heller, R.; Hollik, M.; Lange, C.; Lietzow, R.; Moennich, T.; Richter, T.; Rummel, T.
Overview of results from Wendelstein 7-X HTS current lead testing.
Fusion Engineering and Design, 88(2013) S.1585-1588, DOI:10.1016/j.fusengdes.2013.01.104

[18] Heller, R.; Buscher, K.P.; Drotziger, S.; Fietz, W.H.; Kienzler, A.; Lietzow, R. ; Mönnich, T.; Richter, T.; Rummel, T.; Urbach, E.
Status of series production and test of the HTS current leads for Wendelstein 7-X.
Fusion Engineering and Design, 88(2013) S.1482-1485, DOI:10.1016/j.fusengdes.2013.02.07

[19] Rizzo, E.; Bauer, R.; Heller, R.; Savoldi Richard, L.; Zanino, R.
1-D thermal-electrical analysis of the high temperature superconducting current leads for the ITER magnet system from 5 K to 300 K.
Fusion Engineering and Design, 88(2013) S.3125-3131, DOI:10.1016/j.fusengdes.2013.09.001

[20] Rizzo, E.; Heller, R.; Savoldi Richard, L.; Zanino, R.
CtFD-based correlations for the thermal-hydraulics of an HTS current lead meander-flow heat exchanger in turbulent flow. Cryogenics, 53(2013) S.51-60, DOI:10.1016/j.cryogenics.2012.06.001

[21] Rummel, T.; Moennich, T.; Buscher, K.-P.; Schauer, F.; Fietz, W.H.; Heller, R.
The current leads of the Wendelstein 7-X superconducting magnet system.
25th Symposium on Fusion Engineering (SOFE 2013), San Francisco, Calif., June 10-14, 2013

[22] Akhtar, M.J.; Thumm, M.
Measurement of complex permittivity of cylindrical objects in the E-plane of a rectangular waveguide.
IEEE Transactions on Geoscience and Remote Sensing, 51(2013) S.122-131 DOI:10.1109/TGRS.2012.2201259

[23] Arkhipov, A.; Dvoretskaya, N.; Gantenbein, G.; Kern, S.; Louksha, O.; Rzesnicki, T.; Samartsev, A.; Sominski, G.
Reconstruction of energy distributions in electron beams on the basis of Bremsstrahlung X-ray spectra.
IEEE Transactions on Plasma Science, 41(2013) S.2786-2789, DOI:10.1109/TPS.2013.2262379

[24] Arzhannikov, A.V.; Thumm, M.K.A.
Development of investigation of mm and sub-mm waves at LPIMTR of NSU.
9th All-Russian Seminar on Millimeter and Submillimeter Wavelength Radiophysics, Nizhny Novgorod, Russia, February 26 - March 1, 2013

[25] Arzhannikov, A.V.; Burdakov, A.V.; Burmasov, V.S.; Kalinin, P.V.; Kuznetsov, S.A.; Makarov, M.A.; Ivanov, I.A.; Mekler, K.I.; Popov, A.A.; Postupaev, V.V.; Rovenskikh, A.F.; Sinitsky, S.L.; Sklyarov, V.F.; Stepanov, V.D.; Timofeev, I.V. ; Thumm, M.K.A.; Vyacheslavov, L.N.
Experimental and theoretical investigations of high power sub-millimeter wave emission at two-stream instability of high-current REB.
Transactions of Fusion Science and Technology, 63(2013) Nr.1T, S.82-87

[26] Arzhannikov, A.V.; Ginzburg, N.S.; Zaslavsky, V.Yu.; Kalinin, P.V.; Peskov, N.Yu.; Sergeev, A.S.; Sinitsky, S.L.; Stepanov, V.D.; Thumm, M.
Generation of powerful narrow-band 75-GHz radiation in a free-electron maser with two-dimensional distributed feedback.
Technical Physics Letters, 39(2013) S.801-804, DOI:10.1134/S1063785013090149

[27] Arzhannikov, A.V.; Astrelin, V.T.; Burdakov, A.V.; Ivanov, I.A.; Kandaurov, I.V. ; Kurkuchekov, V.V.; Kuznetsov, S.A.; Makarov, M.A.; Mekler, K.I.; Polosatkin, S.V.; Popov, S.S.; Postupaev, V.V.; Rovenskikh, A.F.; Sinitsky, S.L.; Sklyarov, V.F.; Timofeev, I.V.; Trunev, Yu.A.; Thumm, K.K.A.; Vyacheslavov, L.N.
Sub-THz waves generation by magnetized plasma with strong turbulence driven by high-current REB.
38th Internat.Conf.on Infrared, Millimeter and Terahertz Waves (IRMMW-THz 2013), Mainz, September 1-6, 2013, Proceedings on USB-Stick

[28] Arzhannikov, A.V.; Kalinin, P.V.; Kuznetsov, S.A.; Sinitsky, S.L.; Stepanov, V.D.; Ginzburg, N.S.; Peskov, N.Yu.; Zaslavsky, V.Yu.; Thumm, M.K.A.
Synchronous generation of 4-mm radiation pulses in two-channel FEM.
9th All-Russian Seminar on Millimeter and Submillimeter Wavelength Radiophysics, Nizhny Novgorod, Russia, February 26 - March 1, 2013

[29] Avramidis, K.A.; Pagonakis, I.G.; Ioannidis, Z.C.; Tigelis, I.G.
Numerical investigations on the effects of electron beam misalignment on beam-wave interaction in a high-power coaxial gyrotron.
38th Internat.Conf.on Infrared, Millimeter and Terahertz Waves (IRMMW-THz 2013), Mainz, September 1-6, 2013, Proceedings on USB-Stick

[30] Avramidis, K.A.; Pagonakis, I.Gr.; Iatrou, C.T.; Vormvoridis, J.L.
The code-package EURIDICE for gyrotron interaction simulations and cavity design.
25th Joint Russian-German Meeting on ECRH and Gyrotrons, Karlsruhe/Stuttgart/Garching, June 24-29, 2013

[31] Beringer, M.H.; Kern, S.; Thumm, M.
Mode selection and coaxial cavity design for a 4-MW 170-GHz gyrotron, including thermal aspects.
IEEE Transactions on Plasma Science, 41(2013) S.853-861, DOI:10.1109/TPS.2013.2251870

[32] Betz, M.; Caspers, F.; Gasior, M.; Thumm, M.; Rieger, S.W.
First results of the CERN resonant weakly interacting sun-eV particle search (CROWS).
Physical Review D, 88(2013) S.075014/1-11, DOI:10.1103/PhysRevD.88.075014

[33] Burdakov, A.V.; Arzhannikov, A.V.; Burmasov, V.S.; Ivanov, I.A.; Ivantsivsky, M.V.; Kandaurov, I.V.; Kuznetsov, S.A.; Kurkuchekov, V.V.; Mekler, K.I.; Polosatkin, S.V.; Popov, S.S.; Postupaev, V.V.; Rovenskikh, A.F.; Sklyarov, V.F. ; Thumm, M.K.A.; Trunev, Y.A.; Vyacheslavov, L.N.
Microwave generation during 100 keV electron beam relaxation in GOL-3.
Transactions of Fusion Science and Technology, 63(2013) S.286-288

[34] Franck, J.; Avramidis, K.; Illy, S.
Mode selection for 240-300 GHz gyrotrons.
25th Joint Russian-German Meeting on ECRH and Gyrotrons, Karlsruhe/Stuttgart/Garching, June 24-29, 2013

[35] Gandini, F.; Chirkov, A.V.; Jawla, S.; Kalaria, P.; Oda, Y.; Rzesnicki, T.; Sharma, A.; Shapiro, M.; Denisov, G.; Gantenbein, G.; Keishi, S.; Rao, L.S.; Temkin, R.
Overview of a multi-code analysis of high power 170 GHz beams in terms of HEm, n modes.
Workshop on RF Heating Technology of Fusion Plasmas, Speyer, September 9-11, 2013

[36] Gandini, F.; Albajar, F.; Alberti, S.; Avramidis, K.; Baruah, U.; Bigelow, T.; Bonicelli, T.; Bruschi, A.; Chavan, R.; Cismondi, F.; Darbos, C.; Denisov, G.; Dumur, A.; Farina, D.; Gantenbein, G.; Gassman, T.; Goodman, T.P.; Hanson, G.; Hogge, J.P.; Jean, O.; Jelonnek, J.; Kajiwara, K.; Kasparek, W.; Kobayashi, N.; Kushwah, M.; Latsas, G.P.; Moro, A.; Nazare, C.; Oda, Y.; Omori, T.; Oustinov, A.; Pagonakis, I.; Piosczyk, B.; Popov, L.; Rao, S.L.; Rasmussen, D.; Ronden, D. ; Saibene, G.; Sakamoto, K.; Scherer, T.; Shapiro, M.; Singh, N.P.; Sozzi, C.; Spaeh, P.; Straus, D.; Sauter, O.; Takahashi, K.; Temkin, R.; Zohm, H.
Status of the ITER EC H&CD system.
Workshop on RF Heating Technology of Fusion Plasmas, Speyer, September 9-11, 2013

[37] Gantenbein, G.; Avramidis, K.; Franck, J.; Illy, S.; Jelonnek, J.; Jin, J.; Malygin, A.; Pagonakis, I.; Rzesnicki, T.; Samartsev, A.; Schlaich, A.; Thumm, M.; Zhang, J.
KIT gyrotron investigations and developments for W7-X, ITER and towards DEMO.
25th Joint Russian-German Meeting on ECRH and Gyrotrons, Karlsruhe/Stuttgart/Garching, June 24-29, 2013

[38] Geiger, J.; Wolf, R.C.; Beidler, C.; Cardella, A.; Chlechowitz, E.; Erckmann, V. ; Gantenbein, G.; Hathiramani, D.; Hirsch, M.; Kasparek, W.; Kißlinger, J.; König, R.; Kornejew, P.; Laqua, H.P.; Lechte, C.; Lre, J.; Lumsdaine, A.; Maaßberg, H.; Marushchenko, N.B.; Michel, G.; Otte, M.; Peacock, A.; Sunn Pedersen, T.; Thumm, M.; Turkin, Y.; Werner, A.; Zhang, D. ; W7-X Team
Aspects of steady-state operation of the Wendelstein 7-X stellarator.
Plasma Physics and Controlled Fusion, 55(2013) S.014006/1-6, DOI:10.1088/0741-3335/55/1/014006

[39] Illy, S.; Kern, S.; Pagonakis, I.; Vaccaro, A.
Collector loading of the 2-MW, 170-GHz gyrotron for ITER in case of power modulation.
IEEE Transactions on Plasma Science, 41(2013) S.2742-2747, DOI:10.1109/TPS.2013.2262607

[40] Illy, S.; Kahl, F.; Pagonakis, I.; Vaccaro, A.
Thermomechanical impact of gyrotron power modulation on the collector of a 2 MW, 170 GHz gyrotron.
25th Joint Russian-German Meeting on ECRH and Gyrotrons, Karlsruhe/Stuttgart/Garching, June 24-29, 2013

[41] Ivanov, I.A.; Arzhannikov, A.V.; Astrelin, V.T.; Burdakov, A.V.; Kandaurov, I.V. ; Kurkuchekov, V.V.; Kuznetsov, S.A.; Makarov, M.A.; Mekler, K.I.; Polosatkin, S.V.; Popov, S.S.; Postupaev, V.V.; Rovenskikh, A.F.; Sinitsky, S.L.; Sklyarov, V.F.; Trunev, Y.A.; Thumm, M.K.A.; Vyacheslavov, L.N.
High-power sub-THz waves generation during eletron beam transportation through magnetized plasmas.
IEEE Pulsed Power & Plasma Science Conference (PPPS 2013), San Francisco, Calif., June 16-21, 2013

[42] Jelonnek, J.; Avramidis, K.; Franck, J.; Gantenbein, G.; Hesch, K.; Illy, S.; Jin, J.; Malygin, A.; Pagonakis, I.; Rzesnicki, T.; Samartsev, A.; Scherer, T.; Schlaich, A.; Schmid, M.; Strauss, D.; Thumm, M.; Zhang, J.
KIT gyrotron development for future fusion applications.
38th Internat.Conf.on Infrared, Millimeter and Terahertz Waves (IRMMW-THz 2013), Mainz, September 1-6, 2013, Proceedings on USB-Stick

[43] Jelonnek, J.
Zukunft Fusion: Hochleistungsmikrowellentechnik im Brennpunkt der Plasmaphysik. (eingeladen)
Vortr.: VDE Hochschulgruppe, Karlsruhe, 14. Juni 2013

[44] Jin, J.; Flamm, J.; Jelonnek, J.; Kern, S.; Pagonakis, I.; Rzesnicki, T.; Thumm, M.
High-efficiency quasi-optical mode converter for a 1-MW TE32,9 mode gyrotron.
IEEE Transactions on Plasma Science, 41(2013) S.2748-2753, DOI:10.1109/TPS.2013.2261322

[45] Jin, J.; Jelonnek, J.; Pagonakis, I.; Rzesnicki, T.; Thumm, M.
Quasi-optical mode converter for TE32,9-mode gyrotron.
25th Joint Russian-German Meeting on ECRH and Gyrotrons, Karlsruhe/Stuttgart/Garching, June 24-29, 2013

[46] Kahl, F.; Illy, S.; Jelonnek, J.
Estimation of collector lifetime for the EU 1 MW, 170 GHz CW gyrotron for ITER using transient FE-analysis.
Workshop on RF Heating Technology of Fusion Plasmas, Speyer, September 9-11, 2013

[47] Kalaria, P.C.; Sharma, A.; Sawant, A.; Malik, J.; Rao, S.L.; Kartikeyan, M.V.; Thumm, M.
Mode purity estimation of the gyrotron RF beam.
38th Internat.Conf.on Infrared, Millimeter and Terahertz Waves (IRMMW-THz 2013), Mainz, September 1-6, 2013, Proceedings on USB-Stick

[48] Kuznetsov, S.A.; Astafyev, M.A.; Arzhannikov, A.V.; Thumm, M.K.A.
Microsstructured frequency selective quasi-optical components for subterahertz and terahertz applications.
38th Internat.Conf.on Infrared, Millimeter and Terahertz Waves (IRMMW-THz 2013), Mainz, September 1-6, 2013, Proceedings on USB-Stick

[49] Liu, J.; Jin, J.; Thumm, M.; Zhao, Q.; Li, H.
Design of adapted phase correcting mirrors for gyrotrons.
14th IEEE International Vacuum Electronics Conference (IVEC 2013), Paris, F, May 21-23, 2013
Proc.on USB-Stick, Piscataway, N.J. : IEEE, 2013, ISBN 978-1-4673-5977-1

[50] Liu, J.; Jin, J.; Thumm, M.; Jelonnek, J.; Li, H.; Zhao, Q.
Vector method for synthesis of adapted phase-correcting mirrors for gyrotron output couplers.
IEEE Transactions on Plasma Science, 41(2013) S.2489-2495, DOI:10.1109/TPS.2013.2276915

[51] Neudorfer, J.; Stock, A.; Stindl, T.; Schneider, R.; Roller, S.; Munz, C.D.; Auweter-Kurtz, M.
Efficient parallelization of a three-dimensional high-order particle-in-cell method applied to gyrotron resonator simulations.
Nagel, W. [Hrsg.]
High Performance Computing in Science and Engineering '12 : Transactions of the High Performance Computing Center, Stuttgart (HLRS) 2012, Berlin [u.a.] : Springer, 2013 S.583-596
ISBN 978-3-642-33373-6, DOI:10.1007/978-3-642-33374-3_42

[52] Pagonakis, I.; Illy, S.; Rzesnicki, T.; Piosczyk, B.; Avramidis, K.; Thumm, M.; Gantenbein, G.; Jelonnek, J.; Hogge, H.P.; Alberti, S.
A gun design criterion to limit the effects of the electron beam Halo in gyrotrons.
IEEE Pulsed Power & Plasma Science Conference (PPPS 2013), San Francisco, Calif., June 16-21, 2013

[53] Pagonakis, I.; Gantenbein, G.; Jelonnek, J.; Jin, J.; Illy, S.; Kern, S.; Pioscyk, B.; Rzesnicki, T.; Thumm, M.; Avramides, K.A.; Vomvoridis, J.L.; Dumbrajs, O.; Benin, P.; Rozier, Y.; Alberti, S.; Hogge, J.-P.; Schlatter, C.; Tran, M.-Q.; Bruschi, A.; Lontano, M.; Ioannidis, Z.C.; Latsas, G.P.; Tigelis, I.G.; Albajar, F.; Bonicelli, T.; Cismondi, F.
Design of the EU-1MW gyrotron for ITER.
14th IEEE International Vacuum Electronics Conference (IVEC 2013), Paris, F, May 21-23, 2013,
Proc.on USB-Stick, Piscataway, N.J. : IEEE, 2013, ISBN 978-1-4673-5977-1

[54] Pagonakis, I.G.; Avramidis, K.; Gantenbein, G.; Illy, S.; Jelonnek, J.; Jin, J.; Piosczyk, B.; Rzesnicki, T.; Thumm, M.
The 1 MW 170 GHz conventional cavity gyrotron for ITER.
25th Joint Russian-German Meeting on ECRH and Gyrotrons, Karlsruhe/Stuttgart/Garching, June 24-29, 2013

[55] Pagonakis, I.G.; Albajar, F.; Alberti, S.; Avramides, K.A.; Bonicelli, T.; Bruschi, A.; Cismondi, F.; Chelis, I.; Dumbrajs, O.; Gantenbein, G.; Hogge, J.-P.; Illy, S.; Ioannidis, Z.; Jelonnek, J.; Jin, J.; Latsas, G.; Lontano, M.; Piosczyk, B.; Rozier, Y.; Rzesnicki, T.; Thumm, M.; Tigelis, I.G.; Tran, M.-Q.; Vomvoridis, J.L.
The status of EU-1 MW gyrotron for ITER.
Workshop on RF Heating Technology of Fusion Plasmas, Speyer, September 9-11, 2013

[56] Roy Choudhury, A.; Thumm, M.
Investigations of dynamic after cavity interaction using uniform magnetc field and adiabatic approximation.
Workshop on Vacuum Electronic Devices and Applications (VEDA Kolleg 2013), Roorkee, IND, October 18-20, 2013

[57] Roy Choudhury, A.; D'Andrea, D.; Kern, S.; Thumm, M.
On the influence of B-field shape variations on gyrotron spurious oscillations.
Chancen der Energiewende.
Wissenschaftliche Beiträge des KIT zur 1.Jahrestagung des KIT-Zentrums Energie, 19.06.2012.
KIT Scientific Reports, KIT-SR 7640 (April 2013) S.175-180

[58] Rzesnicki, T.; Gantenbein, G.; Illy, S.; Jelonnek, J.; Jin, J.; Pagonakis, I.G.; Piosczyk, B.; Schlaich, A.; Thumm, M.
2 MW, 170 GHz coaxial-cavity short-pulse gyrotron - Investigations on electron beam instabilities and parasitic oscillations.
Workshop on RF Heating Technology of Fusion Plasmas, Speyer, September 9-11, 2013

[59] Rzesnicki, T.; Gantenbein, G.; Illy, S.; Jelonnek, J.; Jin, J.; Pagonakis, I.Gr. ; Piosczyk, B.; Schlaich, A.; Thumm, M.
2 MW, 170 GHz coaxial-cavity short-pulse gyrotron - Investigations on electron beam instabilities and parasitic oscillations.
38th Internat.Conf.on Infrared, Millimeter and Terahertz Waves (IRMMW-THz 2013), Mainz, September 1-6, 2013, Proceedings on USB-Stick

[60] Rzesnicki, T.; Piosczyk, B.; Gantenbein, G.; Illy, S.; Jelonnek, J.; Jin, J.; Pagonakis, I.Gr.; Samartsev, A.; Schlaich, A.; Thumm, M.
2MW, 170 GHz coaxial-cavity short-pulse gyrotron. Recent experimental results with the modified gyrotron setup.
25th Joint Russian-German Meeting on ECRH and Gyrotrons, Karlsruhe/Stuttgart/Garching, June 24-29, 2013

[61] Sadykov, V.; Usoltsev, V.; Yeremeev, N.; Mezentseva, N.; Pelipenko, V.; Krieger, T.; Belyaev, V.; Sadovskaya, E.; Muzykantov, V.; Fedorova, Y.; Lukashevich, A.; Ishchenko, A.; Salanov, A.; Okhlupin, Y.; Uvarov, N.; Smorygo, O.; Arzhannikov, A.; Korobeynikov, M.; Thumm, M.K.A.
Functional nanoceramics for intermediate temperature solid oxide fuel cells and oxygen separation membranes.
Journal of the European Ceramic Society, 33(2013) S.2241-2250,
DOI:10.1016/j.jeurceramsoc.2013.01.007

[62] Samartsev, C.A.; Dammertz, G.; Gantenbein, G.; Jelonnek, J.; Illy, S.; Thumm, M.
Experimental and numerical studies on eccentricity of annular electron beam in 1 MW gyrotron cavity.
Workshop on RF Heating Technology of Fusion Plasmas, Speyer, September 9-11, 2013

[63] Schlaich, A.; Gantenbein, G.; Jelonnek, J.; Samartsev, A.; Thumm, M.
Study of RF output window ARC event in a megawatt class 140 GHz gyrotron.
IEEE Pulsed Power & Plasma Science Conference (PPPS 2013), San Francisco, Calif., June 16-21, 2013

[64] Thumm, M.
Introduction to energy generation and heating in nuclear fusion plasmas.
Alexander-von-Humboldt-Colloquium, Indian Institute of Technology, Roorkee, IND,
October 17, 2013

[65] Thumm, M.
Lecture series on gyrotrons. 1: Principle of gyrotron. (eingeladen)
Vortr.: Institute of Electronics of the Chinese Academy of Sciences, Beijing, China,
December 2, 2013

[66] Thumm, M.
Lecture series on gyrotrons. 2: Electron gun, beam tunnel, magnets. (eingeladen)
Vortr.: Institute of Electronics of the Chinese Academy of Sciences, Beijing, China,
December 3, 2013

[67] Thumm, M.
Lecture series on gyrotrons. 3: Cavity, uptaper, Q.O.-mode converter, collector. (eingeladen)
Vortr.: Institute of Electronics of the Chinese Academy of Sciences, Beijing, China,
December 4, 2013

[68] Thumm, M.
Lecture series on gyrotrons. 4: RF window, state of the art of high power gyrotrons. (eingeladen)
Vortr.: Institute of Electronics of the Chinese Academy of Sciences, Beijing, China,
December 4, 2013

[69] Thumm, M.
Lecture series on gyrotrons. 5: W7-X gyrotron, HV power supply. (eingeladen)
Vortr.: Institute of Electronics of the Chinese Academy of Sciences, Beijing, China,
December 5, 2013

[70] Thumm, M.
Lecture Series on Gyrotrons. 6: Coaxial cavity gyrotrons. (eingeladen)
Vortr.: Institute of Electronics of the Chinese Academy of Sciences, Beijing, China,
December 6, 2013

[71] Thumm, M.
Lecture series on gyrotrons. 7: Frequency tunable gyrotrons, technology gyrotrons. (eingeladen)
Vortr.: Institute of Electronics of the Chinese Academy of Sciences, Beijing, China,
December 6, 2013

[72] Thumm, M.
Lecture series on gyrotrons. 8: Gyrotrons for spectroscopy, gyro-amplifiers. (eingeladen)
Vortr.: Institute of Electronics of the Chinese Academy of Sciences, Beijing, China,
December 9, 2013

[73] Thumm, M.
Lecture series on high-power MM-wave transmission. 1: Mode conversion in overmoded waveguides. (eingeladen)
Vortr.: Institute of Electronics of the Chinese Academy of Sciences, Beijing, China,
December 10, 2013

[74] Thumm, M.
Lecture series on high-power MM-wave transmission. 2: HE11 mode, beam waveguides. (eingeladen)
Vortr.: Institute of Electronics of the Chinese Academy of Sciences, Beijing, China,
December 11, 2013

[75] Thumm, M.
Lecture series on high-power MM-wave transmission. 3: Quasi-optical mode converters. (eingeladen)
Vortr.: Institute of Electronics of the Chinese Academy of Sciences, Beijing, China,
December 12, 2013

[76] Thumm, M.
Lecture series on high-power MM-wave transmission. 4: W7-X ECRH System. (eingeladen)
Vortr.: Institute of Electronics of the Chinese Academy of Sciences, Beijing, China,
December 13, 2013

[77] Thumm, M.; Wagner, D.; De Rijk, E.; Bongers, W.; Kasparek, W.; Leuterer, F.; Macor, A.; Monaco, F.; Münich, M.; Schütz, M.; Stober, J.; van den Brand, H.; Bieren, A.von
Multi-frequency notch filters and corrugated 500 to 750 Ghz waveguide components manufactured by stacked ring technology.
4th Shenzhen International Conference on Advanced Science and Technology (SICAST 2013), Shenzhen, China, November 3-9, 2013

[78] Thumm, M.; Wagner, D.; De Rijk, E.; Bongers, W.; Kasparek, W.; Leuterer, F.; Macor, A.; Ansermet, J.Ph.; Monaco, F.; Münich, M.; Schütz, M.; Stober, J.; van den Brand, H.; Bieren, A.von
Multi-frequency notch filters and corrugated 200 to 400 Ghz waveguide components manufactured by stacked ring technology.
Terahertz Science and Technology, 6(2013) S.212-222

[79] Thumm, M.; Jelonnek, J.; Gantenbein, G.; Dammertz, G.; Illy, S.; Jin, J.; Leonhardt, W.; Pagonakis, I.; Piosczyk, B.; Roy-Choudhury, A.; Rzesnicki, T.; Samartsev, A.; Schlaich, A.; Schmid, M.
Status of high-power fusion gyrotron development at KIT.
Internat.Symp.on Development of Terahertz Gyrotrons and Applications, Fukui, J,
March 14-15, 2013

[80] Thumm, M.
Worldwide state-of-the-art of high power gyrotrons for ECH&CD in thermonuclear fusion experiments.
International Advisory Committee Inaugural Conference of the Cooperative Innovation Centre of THz Science, Chengdu, China, November 3, 2013

[81] van 't Klooster, K.; Petelin, M.; Thumm, M.; Aloisio, M.
Ka-band groundstation antenna aspects for deep space telecommunication and radar.
Proceedings of the 7th European Conference on Antennas and Propagation (EuCAP), Göteborg, S, April 8-12, 2013, Piscataway, N.J. : IEEE, 2013 S.242-246
ISBN 978-1-4673-2187-7

[82] Zagubisalo, P.S.; Paulish, A.G.; Kuznetsov, S.A.; Arzhannikov, A.V.; Thumm, M.K.A.
Simulation of the thermophysical processes in the subterahertz imager based on a thin-film metamaterial converter.
Radiophysics and Quantum Electronics, 56(2013) Nr.1, S.20-35
DOI:10.1007/s11141-013-9413-5

[83] Zhang, J.; Illy, S.; Pagonakis, I.Gr.; Jelonnek, J.; Dammertz, G.
Effect of emitter surface roughness in gyrotron.
25th Joint Russian-German Meeting on ECRH and Gyrotrons, Karlsruhe/Stuttgart/Garching, June 24-29, 2013

[84] Zhang, J.; Illy, S.; Pagonakis, I.G.; Jelonnek, J.
Preliminary study on the effects of emitter surface roughness on gyrotron electron beam quality.
38th Internat.Conf.on Infrared, Millimeter and Terahertz Waves (IRMMW-THz 2013), Mainz, September 1-6, 2013, Proceedings on USB-Stick

[85] Bagryansky, P.A.; Demin, S.P.; Gospodchikov, E.D.; Kovalenko, Y.V.; Malygin, V.I.; Murakhtin, S.V.; Savkin, V.Y.; Shalashov, A.G.; Smolyakova, O.B.; Solomakhin, A.L.; Thumm, M.; Yakovlev, D.V.
ECR heating system for the gas dynamic trap.
Transactions of Fusion Science and Technology, 63(2013) S. 40-45

[86] Gantenbein, G.; Dammertz, G.; Jelonnek, J.; Losert, M.; Samartsev, A.; Schlaich, A.; Scherer, T.; Strauss, D.; Thumm, M.; Wagner, D.
Operation of a step-frequency tunable gyrotron with a diamond brewster angle output window.
14th IEEE International Vacuum Electronics Conference (IVEC 2013), Paris, F, May 21-23, 2013
Proc.on USB-Stick, Piscataway, N.J. : IEEE, 2013, ISBN 978-1-4673-5977-1

[87] Ivanov, I.A.; Arzhannikov, A.V.; Burdakov, A.V.; Burmasov, V.S.; Ivantsivsky, M.V.; Kuznetsov, S.A.; Mekler, K.I.; Popov, S.S.; Polosatkin, S.V.; Postupaev, V.V.; Rovenskikh, A.F.; Sinitsky, S.L.; Sklyarov, V.F.; Thumm, M.K.A.
Generation of terahertz radiation in beam-plasma interaction experiments at the GOL-3 facility.
9th All-Russian Seminar on Millimeter and Submillimeter Wavelength Radiophysics,
Nizhny Novgorod, Russia, February 26 - March 1, 2013

[88] Ives, R.L.; Read, M.; Marsden, D.; Collins, G.; Falce, L.; Busbaher, D.; Effgen, M.; Schwartzkopf, S.; Malygin, A.; Borchard, P.
Advanced CPR cathode research.
14th IEEE International Vacuum Electronics Conference (IVEC 2013), Paris, F, May 21-23, 2013
Proc.on USB-Stick, Piscataway, N.J. : IEEE, 2013, ISBN 978-1-4673-5977-1

[89] Jelonnek, J.; Gantenbein, G.; Hesch, K.; Jin, J.; Pagonakis, I.; Piosczyk, B.; Rzesnicki, T.; Thumm, M.; Alberti, S.; Hogge, H.P.; Tran, M.Q.; Erckmann, V.; Laqua, H.; Michel, G.; Benin, P.; Legrand, F.; Rozier, Y.; Avramidis, K.; Vomvoridis, J.L.; Ioannidis, Z.C.; Latsas, G.P.; Tigelis, I.G.; Albajar, F.; Bonicelli, T.; Cismondi, F.
From series production of gyrotrons for W7-X towards EU-1 MW gyrotrons for ITER.
IEEE Pulsed Power & Plasma Science Conference (PPPS 2013), San Francisco, Calif.,
June 16-21, 2013

[90] Jelonnek, J.
Introduction to gyrotrons and related research at IHM (part 1).
Vortr.: NUDT, Changsha, China, May 6-12, 2013

[91] Jelonnek, J.
Introduction to gyrotrons and related research at IHM (part 2).
Vortr.: NUDT, Changsha, China, May 6-12, 2013

[92] Jelonnek, J.
Overview on IHM research topics and plans (plenary introduction).
Vortr.: NUDT, Changsha, China, May 6-12, 2013

[93] Jelonnek, J.
Research in pulsed power and microwave technology at IHM.
Vortr.: Institute of Electronics, Chinese Academy of Sciences, Beijing, China,
May 2013

[94] Kartikeyan, M.V.; Jelonnek, J.; Thumm, M.
A 1.0-1.3 MW CW, 238 GHz conventional cavity gyrotron.
38th Internat.Conf.on Infrared, Millimeter and Terahertz Waves (IRMMW-THz 2013), Mainz,
September 1-6, 2013, Proceedings on USB-Stick

[95] Losert, M.; Jin, J.; Rzesnicki, T.
RF beam parameter measurements of quasi-optical mode converters in the mW range.
IEEE Transactions on Plasma Science, 41(2013) S.628-632, DOI:10.1109/TPS.2012.2232942

[96] Malygin, A.; Illy, S.; Pagonakis, I.G.; Avramides, K.; Thumm, M.; Jelonnek, J.; D'Andrea, D.; Ives, R.L.; Munz, C.-D.
Analysis of mode competition in 10kW/28GHz gyrotron.
14th IEEE International Vacuum Electronics Conference (IVEC 2013), Paris, F, May 21-23, 2013

[97] Malygin, A.; Illy, S.; Pagonakis, I.Gr.; Avramidis, K.; Thumm, M.; Jelonnek, J.; Balk, M.; Ives, R.L.
Analysis of mode competition in 10kW/28GHz gyrotron.
25th Joint Russian-German Meeting on ECRH and Gyrotrons, Karlsruhe/Stuttgart/Garching,
June 24-29, 2013

[98] Malygin, A.; Illy, S.; Pagonakis, I.G.; Avramides, K.; Thumm, M.; Jelonnek, J.; D'Andrea, D.; Ives, R.L.; Munz, C.-D.
Analysis of mode competition in 10kW/28GHz gyrotron.
14th IEEE International Vacuum Electronics Conference (IVEC 2013), Paris, F, May 21-23, 2013
Proc.on USB-Stick, Piscataway, N.J. : IEEE, 2013, ISBN 978-1-4673-5977-1

[99] Malygin, A.; Illy, S.; Pagonakis, I.; Piosczyk, B.; Kern, S.; Weggen, J.; Thumm, M.; Jelonnek, J.; Avramides, K.; Ives, L.; Marsden, D.; Vollins, G.
Design and 3-D simulations of a 10-kW/28-GHz gyrotron with a segmented emitter based on controlled-porosity reservoir cathodes.
IEEE Transactions on Plasma Science, 41(2013) S.2717-2723, DOI:10.1109/TPS.2013.2255069

[100] Samartsev, A.; Dammertz, G.; Gantenbein, G.; Jelonnek, J.; Schlaich, A.; Thumm, M.
First operation of a D-band megawatt gyrotron with elliptically brazed diamond window.
25th Joint Russian-German Meeting on ECRH and Gyrotrons, Karlsruhe/Stuttgart/Garching, June 24-29, 2013

[101] Samartsev, A.; Dammertz, G.; Gantenbein, G.; Jelonnek, J.; Schlaich, A.; Thumm, M.
First operation of a D-band megawatt gyrotron with elliptically brazed diamond window.
38th Internat.Conf.on Infrared, Millimeter and Terahertz Waves (IRMMW-THz 2013), Mainz, September 1-6, 2013, Proceedings on USB-Stick

[102] Samartsev, A.; Dammertz, G.; Gantenbein, G.; Jelonnek, J.; Illy, S.; Thumm, M.
Influence of annular beam displacement on the performance of a high-power gyrotron.
IEEE Transactions on Plasma Science, 41(2013) S.872-878, DOI:10.1109/TPS.2013.2248385

[103] Samartsev, A.; Dammertz, G.; Gantenbein, G.; Jelonnek, J.; Thumm, M.; Jin, J.; Piosczyk, B.
Numerical and experimental study of electron beam axial misalignment on the performance of 1 MW step-tunablegyrotron.
25th Joint Russian-German Meeting on ECRH and Gyrotrons, Karlsruhe/Stuttgart/Garching, June 24-29, 2013

[104] Schlaich, A.; Gantenbein, G.; Jelonnek, J.; Kern, S.; Thumm, M.
Neuartige Millimeterwellen-Spektraldiagnostik am IHM. Chancen der Energiewende.
Wissenschaftliche Beiträge des KIT zur 1.Jahrestagung des KIT-Zentrums Energie, 19.06.2012.
KIT Scientific Reports, KIT-SR 7640 (April 2013) S.169-174

[105] Schlaich, A.; Gantenbein, G.; Jelonnek, J.; Thumm, M.
Simulations of high power gyrotron operation during window arc.
38th Internat.Conf.on Infrared, Millimeter and Terahertz Waves (IRMMW-THz 2013), Mainz, September 1-6, 2013, Proceedings on USB-Stick

[106] Stober, J.; Wagner, D.; Leuterer, F.; Monaco, F.; Müller, S.; Münich, M.; Reich, M.; Schubert, M.; Schütz, H.; Treutterer, W.; Zohm, H.; ASDEX Upgrade Team; Flamm, J.; Gantenbein, G.; Thumm, M.; Meier, A.; Scherer, Th.; Strauß, D.; Vaccaro, A.; Höhnle, H.; Kasparek, W.; Stroth, U.; Litvak, A.; Denisov, G.G.; Chirkov, A.V.; Tai, E.M.; Popov, L.G.; Nichiporenko, V.O.; Myasnikov, V.E.; Soluyanova, E.A.; Malygin, S.A.
The ECRH system for ASDEX upgrade - Status and plans.
25th Joint Russian-German Meeting on ECRH and Gyrotrons, Karlsruhe/Stuttgart/Garching, June 24-29, 2013

[107] Thumm, M.
Attenuation and mode conversion in overmoded waveguides.
Vortr.: NUDT, Changsha, China, May 6-12, 2013

[108] Thumm, M.
Diagnostics and adiabatic mode converters in overmoded waveguides.
Vortr.: NUDT, Changsha, China, May 6-12, 2013

[109] Thumm, M.
High-power millimeter wave quasi-optical components and mode converters.
Vortr.: NUDT, Changsha, China, May 6-12, 2013

[110] Thumm, M.
Lecture series on gyrotrons. 1: Principle of gyrotron.
Vortr.: Electrotechnology Research Institute, Changwon, Korea, 16. April 2013

[111] Thumm, M.
Lecture series on gyrotrons. 2: Electron gun, beam tunnel, magnets.
Vortr.: Electrotechnology Research Institute, Changwon, Korea, 16. April 2013

[112] Thumm, M.
Lecture series on gyrotrons. 3: Cavity, uptaper, Q.O.-mode converter, collector.
Vortr.: Electrotechnology Research Institute, Changwon, Korea, 16. April 2013

[113] Thumm, M.
Lecture series on gyrotrons. 4: RF window, state of the art of high power gyrotrons.
Vortr.: Electrotechnology Research Institute, Changwon, Korea, 16. April 2013

[114] Thumm, M.
Lecture series on gyrotrons. 5: W7-X gyrotron, HV power supply.
Vortr.: Electrotechnology Research Institute, Changwon, Korea, 17. April 2013

[115] Thumm, M.
Lecture Series on Gyrotrons. 6: Coaxial cavity gyrotrons.
Vortr.: Electrotechnology Research Institute, Changwon, Korea, 17. April 2013

[116] Thumm, M.
Lecture series on gyrotrons. 7: Frequency tunable gyrotrons, technology gyrotrons.
Vortr.: Electrotechnology Research Institute, Changwon, Korea, 17. April 2013

[117] Thumm, M.
Lecture series on gyrotrons. 8: Gyrotrons for spectroscopy, gyro-amplifiers.
Vortr.: Electrotechnology Research Institute, Changwon, Korea, 17. April 2013

[118] Thumm, M.
Mode converters and components in overmoded waveguides I.
Vortr.: NUDT, Changsha, China, May 6-12, 2013

[119] Thumm, M.
Mode converters and components in overmoded waveguides II.
Vortr.: NUDT, Changsha, China, May 6-12, 2013

[120] Thumm, M.
Recent advances in the gyrotron development activities worldwide.
25th Symposium on Fusion Engineering (SOFE 2013), San Francisco, Calif., June 10-14, 2013

[121] Thumm, M.
Recent advances in the worldwide development of gyrotrons for fusion plasma research.
Vortr.: Central Electronics Engineering Research Institute, Pilani, IND, 23.Oktober 2013

[122] Thumm, M.; Kasparek, W.; Wagner, D.; Wien, A.
Reflection f TE0n modes at open-ended oversized circular waveguide.
IEEE Transactions on Antennas and Propagation, 61(2013) S.2449-2456
DOI:10.1109/TAP.2013.2243098

[123] Thumm, M.K.A.
Millimeter-wave gyro-amplifier RADAR systems.
Vortr.: IEEE-MTT Student Chapter of Indian Institute of Technology, Roorkee,
IND, 21.Oktober 2013

[124] van 't Klooster, K.; Petelin, M.; Thumm, M.
Deep space telecom and radar in a Ka-band ground station antenna.
Proceedings of the 23rd International Crimean Conference 'Microwave and Telecommunication Technology (CriMiCo'2013), Sevastopol, UA, September 9-13, 2013
Piscataway, N.J. : IEEE, 2013 S.1109-1111, ISBN 978-966-335-395-1

[125] Wagner, D.; Bongers, W.; Kasparek, W.; Leuterer, F.; Monaco, F.; Münich, M.; Schütz, H.; Stober, J.; Thumm, M.; van den Brand, H.
Multifrequency notch filter for sub-THz applications based on Photonic bandgaps in corrugated circular waveguides.
38th Internat.Conf.on Infrared, Millimeter and Terahertz Waves (IRMMW-THz 2013), Mainz, September 1-6, 2013, Proceedings on USB-Stick

[126] Wagner, D.; Bongers, W.; Kasparek, W.; Leuterer, F.; Monaco, F.; Münich, M.; Schütz, H.; Stober, J.; Thumm, M.; van den Brand, H.
Progress in the development of multifrequency notch filters.
25th Joint Russian-German Meeting on ECRH and Gyrotrons, Karlsruhe/Stuttgart/Garching, June 24-29, 2013

[127] Wagner, D.; Stober, J.; Leuterer, F.; Monaco, F.; Müller, S.; Münich, M.; Schubert, M.; Schütz, H.; Zohm, H.; Jelonnek, J.; Thumm, M.; Scherer, T.; Strauss, D.; Gantenbein, G.; Kasparek, W.; Plaum, B.; Lechte, C.; Litvak, A.G.; Denisov, G.G.; Chirkov, A.; Popov, L.G.; Nichiporenko, V.O.; Myasnikov, V.E.; Tai, E.M.; Solyanova, E.A.; Malygin, S.A.
The ASDEX upgrade multi-frequency ECRH system status and plans.
Workshop on RF Heating Technology of Fusion Plasmas, Speyer, September 9-11, 2013

Magnets and Affiliated Components

[1] Bagrets, N.; Barth, C.; Weiss, K.-P.
Low temperature thermal and thermo-mechanical properties of soft solders for superconducting applications.
International Conference on Magnet Technology (MT 2013), Boston, Mass., July 14-19, 2013

[2] Bagrets, N.; Barth, C.; Weiss, K.-P.
Low temperature thermal and thermo-mechanical properties of soft solders for superconducting applications.
IEEE Transactions on Applied Superconductivity, 24(2014) pp.7800203/1-3
DOI:10.1109/TASC.2013.2283869

[3] Bagrets, N.; Fischer, E.; Sugita, K.; Walter, W.; Weiss, K.-P.
Mechanical properties of carbon wires at low temperatures.
Cryogenic Engineering Conf.and Internat.Cryogenic Materials Conf. (CEC-ICMC), Anchorage, Alaska, June 17-21, 2013

[4] Bagrets, N.; Bayer, C.; Weiss, K.-P.
Thermal and thermo-mechanical properties of soft solders for superconducting applications.
7th Mechanical and Electromagnetic Effects in Superconductors Workshop (MEM 2013), Aix-en-Provence, France, March 12-14, 2013

[5] Bagrets, N.; Goldacker, W.; Jung, A.; Weiss, K.P.
Thermal properties of REBCO copper stabilized superconducting tapes.
IEEE Transactions on Applied Superconductivity, 23(2013) S.6600303/1-3
DOI:10.1109/TASC.2012.2233268

[6] Barth, C.; Bagrets, N.; Weiss, K.-P.; Bayer, C.M.; Bast, T.
Degradation free epoxy impregnation of REBCO coils and cables.
Superconductor Science and Technology, 26(2013) S. 055007/1-10
DOI:10.1088/0953-2048/26/5/055007

[7] Barth, C.; Weiss, K.-P.; Vojenciak, M.; Schlachter, S.
Electro-mechanical analysis of Roebel cables with different geometries.
Superconductor Science and Technology, 25(2013) S. 025007/1-9
DOI:10.1088/0953-2048/25/2/025007

[8] Bayer, C.; Barth, C.; Gade, P.V.; Heller, R.; Weiss, K.-P.
FBI - Measurement facility for high temperature superconducting cable designs.
International Conference on Magnet Technology (MT 2013), Boston, Mass., July 14-19, 2013

[9] Bayer, C.; Bagrets, N.; Barth, C.; Goldacker, W.; Weiss, K.-P.
Low resistive soldering joints for HTS tapes.
7th Mechanical and Electromagnetic Effects in Superconductors Workshop (MEM 2013), Aix-en-Provence, France, March 12-14, 2013

[10] Fietz, W.H.; Fink, S.; Kraft, G.; Scheller, H.; Weiss, E.; Zwecker, V.
High voltage testing of ITER prototype axial breaks.
IEEE Transactions on Applied Superconductivity, 23(2013) S.4200604/1-4
DOI:10.1109/TASC.2012.2234177

[11] Fietz, W.H.; Fink, S.; Fuhrmann, U.; Müller, R.; Urbach, E.; Zwecker, V.; Brummer, A.; Oberstarr, R.; Wildner, C.; Wimmer, F.; Woelfl, K.
Pluggable 56 kV instrumentation feedthrough prototypes for ITER magnets.
International Conference on Magnet Technology (MT 2013), Boston, Mass., July 14-19, 2013

[12] Fietz, W.H.; Barth, C.; Drotziger, S.; Goldacker, W.; Heller, R.; Schlachter, S.I.; Weiss, K.P.
Prospects of high temperature superconductors for fusion magnets and power applications.
Fusion Engineering and Design, 88(2013) S.440-445, DOI:10.1016/j.fusengdes.2013.03.059

[13] Fink, S.; Fietz, W.H.; Kraft, G.; Scheller, H.; Urbach, E.; Zwecker, V.
Paschen testing of ITER prototype cryogenic axial breaks.
Fusion Engineering and Design, 88(2013) S.1475-1477, DOI:10.1016/j.fusengdes.2012.11.028

[14] Gade, P.V.; Bayer, C.; Franza, F.; Heller, R.; Weiss, K.-P.
Conceptual design of a toroidal field coil for a fusion power plant using high temperature superconductors.
23nd International Conference on Magnet Technology (MT 2013), Boston, Mass., July 14-19, 2013

[15] Heller, R.
Representative device builder points of view - current leads.
European Conference on Applied Superconductivity (EUCAS 2013), Genova, I, September 15-19, 2013

[16] Hollik, M.; Fietz, W.H.; Fink, S.; Gehrlein, M.; Heller, R.; Lange, C.; Möhring, T.
Design of electronic measurement and quench detection equipment for the current lead test facility Karlsruhe (CuLTKa).
Fusion Engineering and Design, 88(2013) S.1445-1448, DOI:10.1016/j.fusengdes.2013.02.082

[17] Kuffner, B.; Richter, T.; Lietzow, R.
Cryogenic control valves - Measurements of characteristic curves at cryogenic conditions.
Cryogenic Engineering Conf.and Internat.Cryogenic Materials Conf. (CEC-ICMC), Anchorage, Alaska, June 17-21, 2013

[18] Lange, C.; Fietz, W.H.; Gröner, F.
Influence of contact surface quality and contact material on the contact resistance of high current connections.
Fusion Engineering and Design, 88(2013) S.1581-1584, DOI:10.1016/j.fusengdes.2013.01.049

[19] Qin, J.; Wu, Y.; Yu, M.; Liu, B.; Liu, H.; Weiss, K.P.; Li, L.; Li, H.; Niu, E.; Bruzzone, P.
Manufacture of ITER feeder sample conductors.
Fusion Engineering and Design, 88(2013) S.1461-1464, DOI:10.1016/j.fusengdes.2013.01.008

[20] Qin, J.; Weiss, K.P.; Wu, Y.; Liao, G.; Wu, Z.; Li, L.; Li, H.; Niu, E.
Mechanical test on the ITER CC and Feeder jacket.
Fusion Engineering and Design, 88(2013) S.151-155, DOI:10.1016/j.fusengdes.2013.01.089

[21] Richter, T.; Lietzow, R.
Cryogenic experiences during W7-X HTS-current lead tests.
Cryogenic Engineering Conf.and Internat.Cryogenic Materials Conf. (CEC-ICMC), Anchorage, Alaska, June 17-21, 2013

[22] Urbach, E.; Bagrets, N.; Weiss, K.P.
Implementation of a quality management system at the PHOENIX facility (CryoMaK).
Fusion Engineering and Design, 88(2013) S.2631-2635, DOI:10.1016/j.fusengdes.2013.04.052

[23] Vostner, A.; Pong, I.; Bessette, D.; Devred, A.; Sgobba, S.; Jung, A.; Weiss, K.-P.; Jewell, M.C.; Liu, S.; Yu, W.; Boutboul, T.; Hamada, K.; Park, S.-H.; Tronza, V.; Walsh, R.P.
Benchmarking of mechanical test facilities related to ITER CICC steel jackets.
IEEE Transactions on Applied Superconductivity, 23(2013) S.9500705/1-5
DOI:10.1109/TASC.2013.2243895

[24] Weiss, K.P.; Bayer, Ch.; Barth, Ch.
High temperature superconduction current leads: A necessary tool for superconducting applications.
Annual Meeting of the Deutscher Kaelte und Klimatechnischer Verein 2012 / Deutsche Kaelte-Klima-Tagung 2012, Würzburg, November 21-23, 2012, Proc.Vol.1 S.204, Red Hook, N.Y. : Curran Associates, 2013, ISBN 978-1-62748-271-4

[25] Weiss, K.-P.; Westenfelder, S.; Purr, B.; Boyer, C.; Foussat, A.
Mechanical fatigue testing of a TF-He-inlet prototype at cryogenic temperature.
International Conference on Magnet Technology (MT 2013), Boston, Mass., July 14-19, 2013

[26] Weiss, K.-P.; Bayer, C.; Bagrets, N.
Mechanical properties of superconductor cable jacket and casing material for cryogenic magnet application.
Cryogenic Engineering Conf.and Internat.Cryogenic Materials Conf. (CEC-ICMC), Anchorage, Alaska, June 17-21, 2013

[27] Kamada, Y.; Barabaschi, P.; Ishida, S.
Progress of the JT-60SA project.
Nuclear Fusion, 53(2013) S.104010/1-17, DOI:10.1088/0029-5515/53/10/104010

[28] Yoshida, K.; Murakami, H.; Tsuchiya, K.; Kizu, K.; Kamiya, K.; Koide, Y.; Philips, G.; Zani, L.; Wanner, M.; Barabaschi, P.; Decool, P.; Cucchiaro, A.; Fietz, W.H.; Heller, R.; Michel, F.
Mass production of the superconducting magnet system for the JT-60SA.
International Conference on Magnet Technology (MT 2013), Boston, Mass., July 14-19, 2013

[29] Vojenciak, M.; Grilli, F.; Stenvall, A.; Kling, A.; Goldacker, W.
Influence of the voltage taps position on the self-field DC and AC transport characterization of HTS superconducting tapes., Cryogenics, 57(2013) S.189-194,
DOI:10.1016/j.cryogenics.2013.08.001

[30] Weiss, K.-P.; Urbach, E.; Kraft, G.; Scheller, H.
Cryogenic mechanical testing of ITER prototype axial breaks.
Fusion Engineering and Design, 88(2013) S.1533-1536, DOI:10.1016/j.fusengdes.2013.02.046

Blanket Breeding

[1] Abou-Sena, A.; Arbeiter, F.; Boccaccini, L.V.; Rey, J.; Schlindwein, G.
Experimental study and analysis of the purge gas pressure drop across the pebble beds for the fusion HCPB blanket.
Fusion Engineering and Design, 88(2013) S.243-247, DOI:10.1016/j.fusengdes.2013.02.122

[2] Abou-Sena, A.; Arbeiter, F.; Boccaccini, L.V.; Schlindwein, G.
Measurements of the purge helium pressure drop across pebble beds packed with lithium orthosilicate and glass pebbles.
11th International Symposium on Fusion Nuclear Technology (ISFNT 2013), Barcelona, E, September 16-20, 2013

[3] Boccaccini, L.V.
Blanket development for fusion reactors.
2013 Seminar Series, Universita di Pisa, I, July 12, 2013

[4] Boccaccini, L.V.
Tritium production and blankets design: Issues and solutions.
14th Course 'Neutronics of Fusion Reactors: Design, Technology and Diagnostics', Erice, I, May 6-13, 2013

[5] Hernandez, F.; Kolb, M.; Ilic, M.; Kunze, A.; Nemeth, J.; von der Weth, A.
Set-up of a pre-test mock-up experiment in preparation for the HCPB breeder unit mock-up experimental campaign.
Fusion Engineering annd Design, 88(2013) S.2378-2383, DOI:10.1016/j.fusengdes.2013.02.107

[6] Kecskes, Sz.; Porempovics, G.; Ghidersa, B.E.
Experimental layout and thermo-mechanical studies on a thermo-mechanical cycle mock up (TCM) plate.
Fusion Engineering and Design, 88(2013) S.1823-1826, DOI:10.1016/j.fusengdes.2013.05.079

[7] Neuberger, H.; Franza, F.; Maione, I.A.; Kecskes, S.; Boccaccini, L.V.
Design integrated system for power plant development.
Proceedings of the 25th Symposium on Fusion Engineering (SOFE 2013), San Francisco, Calif., June 10-14, 2013, Pisacataway, N.J. : IEEE, 2013, ISBN 978-1-4799-0169-2, DOI:10.1109/SOFE.2013.6635478

[8] Neuberger, H.; Rey, J.; Materna-Morris, E.; Bolich, D.; Handl, T.; Milker, T.
Progress in the KIT approach for development of the HCPB TBM stiffening plate feasibility mock up fabrication.
Fusion Engineering and Design, 88(2013) S.265-270, DOI:10.1016/j.fusengdes.2012.12.037

[9] Rey, J.; Rieth, M.; von der Weth, A.; Boccaccini, L.V.; Krüger, F.
FUSION-helium cooled pebble bed test blanket modul für ITER: First Wall Produktionsstrategien.
Fachmesse Werkzeug und Formenbau (WFB 2013), Gießen, 19.-20. Juni 2013

[10] Annabattula, R.K.; Kolb, M.; Rolli, R.; Gan, Y.; Kamlah, M.
Size dependent crush analysis of lithium othosilicate pebbles for fusion reactors.
16th International Conference on Fusion Reactor Materials (ICFRM-16), Beijing, China, October 20-26, 2013

[11] Arlt, T.; Chowdhury, V.; Bühler, L.; Mistrangelo, C.
Influence of contact resistance on MHD liquid metal flows in rectangular ducts.
549th Wilhelm und Else Heraeus-Seminar 'Liquid Metal MHD', Bad Honnef, October 15-18, 2013

[12] Basuki, W.W.; Knaak, S.; Aktaa, J.
Thermo-mechanical analysis of diffusion bonded W/EUROFER97 with V-interlayer.
16th International Conference on Fusion Reactor Materials (ICFRM-16), Beijing, China, October 20-26, 2013

[13] Boccaccini, L.V.; Fischer, U.
Relevance of TBM programme to DEMO power and tritium extraction. (eingeladener Vortrag)
25th Symposium on Fusion Engineering (SOFE 2013), San Francisco, Calif., June 10-14, 2013

[14] Bühler, C.; Mistrangelo, C.
Liquid-metal MHD experiments in a scaled mock-up of a fusion test blanket module. (eingeladen)
Symposium Simulation von Strömungsprozessen in der Metallurgie (SymSim 2013), Oberhof, 17.-20. Juni 2013

[15] Bühler, L.; Mistrangelo, C.; Konys, J.; Bhattacharyay, R.; Huang, Q.; Obukhov, D.; Smolentsev, S.; Utili, M.
Facilities, testing program and modeling needs for studying liquid metal magnetohydrodynamic flows in fusion blankets. (eingeladen)
11th International Symposium on Fusion Nuclear Technology (ISFNT 2013), Barcelona, E, September 16-20, 2013

[16] Bühler, L.; Mistrangelo, C.
Influence of non-insulted gaps between flow channel inserts in ducts of DCLL blankets.
25th Symposium on Fusion Engineering (SOFE 2013), San Francisco, Calif., June 10-14, 2013
Proceedings on CD-ROM Paper 1351, Piscataway, N.J. : IEEE, 2013, ISBN 978-1-4799-0169-2

[17] Bühler, L.
Liquid metal magnetohydrodynamics in strong magnetic fields. (eingeladen)
RTG Summer School 'Lorentz Force Velocimetry and Lorentz Force Eddy Current Testing', Karlsruhe, September 30, 2013

[18] Bühler, L.; Mistrangelo, C.
Magnetohydrodynamic flows for fusion applications: modeling and experiments. (eingeladen)
549th Wilhelm und Else Heraeus-Seminar 'Liquid Metal MHD', Bad Honnef, October 15-18, 2013

[19] Bühler, L.; Mistrangelo, C.
Magnetohydrodynamic flows in breeder units of a HCLL blanket with spatially varying magnetic fields.
Fusion Engineering and Design, 88(2013) S.2314-2318, DOI:10.1016/j.fusengdes.2013.03.009

[20] Bühler, L.; Brinkmann, H.-J.
MEKKA facility for DCLL blanket MHD experiments.
1st EU-US DCLL Workshop, Karlsruhe, April 23-24, 2013

[21] Bühler, L.
MHD flows in WCLL blankets: similarities with other designs and concept- specific problems.
WCLL Blanket Workshop, Paris, F, October 7-8, 2013

[22] Bühler, L.
MHD pressure drop at bare welding positions in pipes of DCLL blankets.
KIT Scientific Reports, KIT-SR 7636 (Januar 2013)

[23] Chakin, V.; Rolli, R.; Moeslang, A.; Vladimirov, P.; Kurinskiy, P.; van Til, S.; Magielsen, A.J.; Zmitko, M.
Characterization of constrained beryllium pebble beds after neutron irradiation at HFR at high temperatures up to helium production of 3000 appm.
Fusion Engineering and Design, 88(2013) S.2309-2313, DOI:10.1016/j.fusengdes.2013.04.034

[24] Chowdhury, V.; Bühler, L.
Experimental investigations of magnetically induced instabilities (Project A3).
LIMTECH Summer School, Dresden, May 27-29, 2013

[25] Ehrhard, S.; Buehler, L.
Influence of magnetic field deformation by ferromagnetic wall materials on MHD flows in pipes and ducts of fusion blankets.
11th International Symposium on Fusion Nuclear Technology (ISFNT 2013), Barcelona, E, September 16-20, 2013

[26] Ehrhard, S.; Bühler, L.
Numerical analysis of magnetohydrodynamic flows in ferromagnetic channels.
LIMTECH Summer School, Dresden, May 27-29, 2013

[27] Ehrhard, S.
Simulation of MHD flows in ferromagnetic channels.
Symposium für Strömungsprozesse (SymSim 2013), Ilmenau, 17.-20. Juni 2013

[28] Franza, F.; Ciampichetti, A.; Ricapito, I.; Zucchetti, M.
Sensitivity study for tritium permeation in helium-cooled lead-lithium DEMO blanket with the FUS-TPC code.
Fusion Science and Technology, 64(2013) S.631-635

[29] Franza, F.; Boccaccini, L.V.; Ciampichetti, A.; Demange, D.; Zucchetti, M.
Tritium permeation issues for helium-cooled breeding blankets.
25th Symposium on Fusion Engineering (SOFE 2013), San Francisco, Calif., June 10-14, 2013

[30] Franza, F.
Tritium transport analysis in HCPB DEMO blanket with the FUS-TPC code.
KIT Scientific Reports, KIT-SR 7642 (Mai 2013)

[31] Franza, F.; Baccaccini, L.V.; Ciampichetti, A.; Zucchetti, M.
Tritium transport analysis in HCPB DEMO blanket with teh FUS-TPC code.
Fusion Engineering and Design, 88(2013) S.2444-2447, DOI:10.1016/j.fusengdes.2013.05.045

[32] Gan, Y.; Hernandez, F.; Annabattula, R.K.; Pereslavtsev, P.; Kamlah, M.
A thermal discrete element analysis of EU solid breeder blanket subjected to neutron irradiation.
16th International Conference on Fusion Reactor Materials (ICFRM-16), Beijing, China, October 20-26, 2013

[33] Guzman, F.; Aktaa, J.
Modeling the interface reactions during diffusion bonding of tungsten and EUROFER97 using a vanadium interlayer.
2nd International Conference on Materials for Energy (EnMat 2013), Karlsruhe, 12.-16. Mai 2013

[34] Hernandez, F.; Kolb, M.; Annabattula, R.; Bitz, O.; Haefner, U.; Ilic, M.; Schmidt, R.; von der Weth, A.
Construction of PREMUX and preliminary experimental results, as preparation for the HCPB breeder unit mock-up testing.
11th International Symposium on Fusion Nuclear Technology (ISFNT 2013), Barcelona, E, September 16-20, 2013

[35] Kecskes, S.; Carloni, D.; Kang, Q.; Ilic, M.; Bitz, O.
Status of the new DEMO HCPB blanket design in the European DEMO studies.
11th International Symposium on Fusion Nuclear Technology (ISFNT 2013), Barcelona, E, September 16-20, 2013

[36] Knitter, R.; Kolb, M.H.H.; Leys, O.
Ba DEMO R&D activities on advanced tritium breeders in EU.
Jahrestagung Kerntechnik, Berlin, 14.-16. Mai 2013, Berlin : INFORUM GmbH, 2013, CD-ROM

[37] Knitter, R.; Kolb, M.H.H.; Kaufmann, U.; Goraieb, A.A.
Fabrication of modified lithium orthosilicate pebbles by addition of titania.
Journal of Nuclear Materials, 442(2013) Suppl.1, S.S433-S436, DOI:10.1016/j.jnucmat.2012.10.034

[38] Knitter, R.; Chaudhuri, P.; Feng, Y.J.; Hoshino, T.; Yu, I.K.
Recent developments of solid breeder fabrication.
Journal of Nuclear Materials, 442(2013) Suppl.1, S.S420-S424,DOI:10.1016/j.jnucmat.2013.02.060

[39] Koehly, C.; Wang, X.R.; Tillack, M.S.; Najmabadi, F.
Alternative design options for a dual-cooled liquid metal blanket for ARIES-ACT2.
La Jolla, Calif. : University of California, Center for Energy Research UCSD-CER-13-02 (August 2013) http://aries.ucsd.edu/LIB/REPORT/ARIES-ACT/UCSD-CER-13-02.pdf

[40] Koehly, C.; Tillack, M.S.; Wang, X.R.; Najmabadi, F.; Malang, S.; ARIES Team
Flow distribution systems for liquid metal cooled blankets.
25th Symposium on Fusion Engineering (SOFE 2013), San Francisco, Calif., June 10-14, 2013
Proceedings on CD-ROM Paper 1173, Piscataway, N.J. : IEEE, 2013, ISBN 978-1-4799-0169-2

[41] Kolb, M.; Leys, O.; Odemer, C.; Frey, C.; Knitter, R.
Behavior of advanced ceramic breeder pebbles in long-term heat treatment.
17th International Workshop on the Ceramic Breeder Blanket Interactions (CBBI-17), Barcelona, E, September 12-14, 2013

[42] Kolb, M.H.H.; Leys, O.H.J.B.; Knitter, R.
Long-term annealing of lithium orthosilicate based ceramic breeder pebbles.
11th International Symposium on Fusion Nuclear Technology (ISFNT 2013), Barcelona, E, September 16-20, 2013

[43] Kolb, M.H.H.
Tritium breeder materials. (eingeladen)
7th Karlsruhe International School on Fusion Technologies, Karlsruhe, September 2-13, 2013

[44] Kurinskiy, P.; Vladiirov, P.; Moeslang, A.; Rolli, R.; Zmitko, M.
Characteristics of microstructure and tritium release properties of different kinds of beryllium pebbles for application in tritium breeding modules.
Jahrestagung Kerntechnik, Berlin, 14.-16. Mai 2013, Berlin : INFORUM GmbH, 2013, CD-ROM

[45] Kurinskiy, P.; Moeslang, A.; Chakin, V.; Klimenko, M.; Rolli, R.; van Til, S.; Goraieb, A.A.
Characteristics of microstructure, swelling and mechanical behaviour of titanium beryllide samples after high-dose neutron irradiation at 740 and 873 K.
Fusion Engineering and Design, 88(2013) S.2198-2201, DOI:10.1016/j.fusengdes.2013.05.084

[46] Leys, O.; Odemer, C.; Maciejewski, U.; Kolb, M.H.H.; Knitter, R.
Microstructure analysis of melt-based lithium orthosilicate/metatitanate pebbles.
Mikrostrukturanalyse von schmelzprozessierten Lithiumorthosilikat-/Lithiummetatitanat-Kugeln.
Praktische Metallographie - Practical Metallography, 50(2013) S.196-203

[47] Leys, O.; Kolb, M.; Goraieb, A.; Knitter, R.
Recent developments of the melt-based production of lithium orthosilicate pebbles.
17th International Workshop on the Ceramic Breeder Blanket Interactions (CBBI-17), Barcelona, E, September 12-14, 2013

[48] Li-Puma, A.; Boccaccini, L.V.; Bachmann, C.; Norajitra, P.; Mistrangelo, C.; Aiello, G.; Aubert, J.; Carloni, D.; Kecskes, S.; Kang, Q.L.; Morin, A.; Sardain, P.
Design and development of DEMO blanket concepts in Europe.
11th International Symposium on Fusion Nuclear Technology (ISFNT 2013), Barcelona, E, September 16-20, 2013

[49] Maione, I.A.; Vaccaro, A.
Analysis of electromagnetic loads on EU-DEMO inboard and outboard blanket vertical segments.
11th International Symposium on Fusion Nuclear Technology (ISFNT 2013), Barcelona, E, September 16-20, 2013

[50] Maione, I.A.; Vaccaro, A.
Parametric analysis of EM loads acting on DEMO vertical segments with respect to module's dimension.
25th Symposium on Fusion Engineering (SOFE 2013), San Francisco, Calif., June 10-14, 2013

[51] Maione, I.A.; Marracci, M.; Tellini, B.
Study on remanent magnetizaiton of Fe-9Cr steel and it s effect on in-vessel remote handling for future fusion reactors.
Fusion Engineering and Design, 88(2013) S.2092-2095, DOI:10.1016/j.fusengdes.2013.02.037

[52] Martin, T.
Hydraulische und mechanische Tests am HFTM Single-Rig Exeriment.
Bachelorarbeit, Hochschule Karlsruhe Technik und Wirtschaft 2012

[53] Mistrangelo, C.; Bühler, L.
Buoyancy-driven magnetohydrodynamic (MHD) flows. (eingeladen)
Symposium Simulation von Strömungsprozessen in der Metallurgie (SymSim 2013), Oberhof, 17.-20. Juni 2013

[54] Mistrangelo, C.; Bühler, L.
Influence of variable heat source on magneto-convective flows in HCLL blankets.
25th Symposium on Fusion Engineering (SOFE 2013), San Francisco, Calif., June 10-14, 2013
Proceedings on CD-ROM Paper 1355, Piscataway, N.J. : IEEE, 2013, ISBN 978-1-4799-0169-2

[55] Mistrangelo, C.; Bühler, L.
Liquid metal magnetohydrodynamic flows in manifolds of dual coolant lead lithium blankets.
11th International Symposium on Fusion Nuclear Technology (ISFNT 2013), Barcelona, E, September 16-20, 2013

[56] Mistrangelo, C.; Bühler, L.
Magneto-convective flows in electrically and thermally coupled channels.
Fusion Engineering and Design, 88(2013) S.2323-2327, DOI:10.1016/j.fusengdes.2013.03.063

[57] Mistrangelo, C.; Bühler, L.
Numerical and asymptotic modeling of MHD flows for liquid metal blankets.
Liquid Breeder Blanket Subtask Collaboration Workshop, Barcelona, E, September 20-21, 2013

[58] Mistrangelo, C.; Bühler, L.
Numerical modeling of MHD flows in DCLL blankets, KIT activites.
1st EU-US DCLL Workshop, Karlsruhe, April 23-24, 2013

[59] Mukai, K.; Yasumoto, M.; Terai, T.; Hoshino, T.; Kolb, M.; Knitter, R.; Suzuki, A.
Vaporization proeprty of lithium metatitanate and orthosilicate pebbles by high temperature mass spectrometry.
17th International Workshop on the Ceramic Breeder Blanket Interactions (CBBI-17), Barcelona, E, September 12-14, 2013

[60] Munakata, K.; Wada, K.; Nakamura, A.; Kim, J.H.; Nakamichi, M.; Knitter, R.
Basic studies on new neutron multiplier and breeder materials.
17th International Workshop on the Ceramic Breeder Blanket Interactions (CBBI-17), Barcelona, E, September 12-14, 2013

[61] Neuberger, H.; Franza, F.; Maione, I.A.; Kecskes, S.; Boccaccini, L.V.
Design integrated system for power plant development.
25th Symposium on Fusion Engineering (SOFE 2013), San Francisco, Calif., June 10-14, 2013

[62] Reimann, J.; Beres, O.; Colle, J.Y.; Dorn, C.; Harsch, H.; Koenigs, R.; Kurinsky, P.
First measurments of beryllide vapor pressures.
Proceedings of the 10th IEA International Workshop on Beryllium Technology
KIT Scientific Reports, KIT-SR 7650 (September 2013) S.258-262

[63] Reimann, J.; Abou-Sena, A.; Brun, E.; Fretz, B.
Packing experiments of Beryllium pebble beds for the fusion reactor HCPB blanket.
11th IEA International Workshop on Beryllium Technology (BeWS 2013), Barcelona, E, September 12-13, 2013

[64] Reimann, J.; Abou-Sena, A.; Nippen, R.; Tafforeau, P.
Pebble bed packing in prismatic containers.
Fusion Engineering and Design, 88(2013) S.2343-2347; DOI:10.1016/j.fusengdes.2013.05.100

[65] Reimann, J.; Abou-Sena, A.; Nippen, R.; Ferrero, C.
Pebble bed packing in square cavities.
KIT Scientific Reports, KIT-SR 7631 (Januar 2013)

[66] Rolli, R.; Chakin, V.; Möslang, A.; Schneider, H.C.; Dorn, C.
Tritium release properties of beryllium grades of Materion Corporation production after loading by tritium/hydrogen gas mixture.
11th IEA International Workshop on Beryllium Technology, Barcelona, E, September 12-13, 2013

[67] Vladimirov, P.; Reimann, J.; [Hrsg.]
Proceedings of the 10th IEA international workshop on beryllium technology.
KIT Scientific Reports, KIT-SR 7650 (September 2013)

[68] Zarins, A.; Kizane, G.; Knitter, R.; Supe, A.
Influence of chemisorption products of carbon dioxide on radiolysis of tritium breeding ceramic.
11th International Symposium on Fusion Nuclear Technology (ISFNT 2013), Barcelona, E, September 16-20, 2013

[69] Zhao, S.; Gan, Y.; Kamlah, M.
Failure initiation and propagation of Li4SiO4 pebbles in fusion blankets.
Fusion Engineering and Design, 88(2013) S.8-16, DOI:10.1016/j.fusengdes.2012.09.008

[70] Zhao, S.; Gan, Y.; Kamlah, M.; Kennerknecht, T.; Rolli, R.
Influence of plate material on the contact strength of Li4SiO4 pebbles in crush tests and evaluation of the contact strength in pebble-pebble contact.
Engineering Fracture Mechanics, 100(2013) S.28-37, DOI:10.1016/j.engfracmech.2012.05.011

[71] Zmitko, M.; Poitevin, Y.; Knitter, R.; Magielsen, L.; van Til, S.
Development and qualification of ceramic breeder materials for the EU test blanket module: strategy and R&D achievements.
17th International Workshop on the Ceramic Breeder Blanket Interactions (CBBI-17), Barcelona, E, September 12-14, 2013

[72] Ghidersa, B.E.; Jin, X.; Rieth, M.; Ionescu-Bujor, M.
KATHELO: A new high heat flux component testing facility.
Fusion Engineering and Design, 88(2013) S.854-857; DOI:10.1016/j.fusengdes.2013.02.065

[73] Jin, X.; Chen, Y.; Ghidersa, B.E.
Conceptual design of a helium heater for high temperature applications.
11th International Symposium on Fusion Nuclear Technology (ISFNT 2013), Barcelona, E, September 16-20, 2013

[74] Hesch, K.
The German DEMO working group. Perspectives of a fusion power plant.
ATW - International Journal for Nuclear Power, 58(2013) S.486-490

Divertor

[1] Koncar, B.; Draksler, M.; Norajitra, P.
Design and cooling of the edge segments of the DEMO divertor.
Fusion Engineering and Design, 88(2013) S.1831-1835, DOI:10.1016/j.fusengdes.2013.05.112

[2] Lang, P.; Day, Ch.; Lehnen, M.; Pautasso, G.
Plasma control aspects of fuelling - pumping - disruption mitigation.
2nd IAEA DEMO Programme Workshop, Wien, A, December 17-20, 2013

[3] Norajitra, P.; Basuki, W.; Spatafora, L.
Deep drawing W thimble.
MAT-HHFM Monitoring Meeting, Garching, February 21-22, 2013

[4] Norajitra, P.; Basuki, W.W.; Spatafora, L.; Stegmaier, U.
He-cooled divertor for Demo: Technological study on joining tungsten components with titanium interlayer.
16th International Conference on Fusion Reactor Materials (ICFRM-16), Beijing, China, October 20-26, 2013

[5] Norajitra, P.; Basuki, W.; Koncar, B.; Spatafora, L.
He-cooled divertor: study on low-temperature design using Ta alloy as thimble material.
Proceedings of the 25th Symposium on Fusion Engineering (SOFE 2013), San Francisco, Calif., June 10-14, 2013, Piscataway, N.J. : IEEE, 2013, ISBN 978-1-4799-0171-5
DOI:10.1109/SOFE.2013.6635453

[6] Norajitra, P.; Basuki, W.; Spatafora, L.
Joining of W components with Ti interlayer.
MAT-HHFM Monitoring Meeting, Garching, February 21-22, 2013

[7] Norajitra, P.; Basuki, W.; Giniyatulin, R.; Koncar, B.; Kuznetsov, V.; Mazul, I.; Richou, M.; Spatafora, L.
Status and prospects of the EU development of the He-cooled divertor for DEMO power plant.
11th International Symposium on Fusion Nuclear Technology (ISFNT 2013), Barcelona, E, September 16-20, 2013

[8] Norajitra, P.; Spatafora, L.; Koncar, B.; Basuki, W.; Dahm, R.
WP13-DAS02-T12 helium cooled divertor.
Final Meeting WP13-DAS02-T12 Helium Cooled Divertor, Garching, 10.Dezember 2013

[9] Richou, M.; Missirlian, M.; Vignal, N.; Cantone, V.; Hernandez, C.; Norajitra, P.; Spatafora, L.
Non-destructive examination of the bonding interface in DEMO divertor fingers.
Fusion Engineering and Design, 88(2013) S.1753-1757, DOI:10.1016/j.fusengdes.2013.05.071

Structural Materials

[1] Aktaa, J.
Application of viscoplasticity for modeling the inelastic deformation behavior of irradiated RAFM steels.
16th International Conference on Fusion Reactor Materials (ICFRM-16), Beijing, China, October 20-26, 2013

[2] Aktaa, J.; Boccaccini, L.V.; Bachmann, C.
Impact of pulsed operation on lifetime of DEMO blanket.
Proceedings of the 25th Symposium on Fusion Engineering (SOFE 2013), San Francisco, Calif., June 10-14, 2013, Pisacataway, N.J. : IEEE, 2013., ISBN 978-1-4799-0169-2
DOI:10.1109/SOFE.2013.6635460

[3] Aktaa, J.; Basuki, W.; Weber, T.; Norajitra, P.; Krauss, W.; Konys, J.
Manufacturing and joining technologies for helium cooled divertors. (eingeladen)
11th International Symposium on Fusion Nuclear Technology (ISFNT 2013), Barcelona, E, September 16-20, 2013

[4] Aktaa, J.; Kecskes, S.; Pereslavtsev, P.; Fischer, U.; Boccaccini, L.V.
Non-linear failure analysis of HCPB blanket for DEMO taking into account high dose irradiation.
11th International Symposium on Fusion Nuclear Technology (ISFNT 2013), Barcelona, E, September 16-20, 2013

[5] Albinski, B.; Schneider, H.C.; Sacksteder, I.; Kraft, O.
A new high-temperature indentaion device for characterization of materials for fusion applications.
Journal of Nuclear Materials, 442(2013) Suppl.1, S.S865-S868,
DOI:10.1016/j.jnucmat.2013.04.064

[6] Antusch, S.; Commin, L.; Heneka, J.; Müller, M.; Rieth, M.; Walter, H.; Weingärtner, T.
2Component-powder injection molding (2C-PIM).
Final Meeting WP13-DAS02-T12 Helium Cooled Divertor, Garching, 10.Dezember 2013

[7] Antusch, S.; Commin, L.; Heneka, J.; Piotter, V.; Plewa, K.; Walter, H.
A new fully automatic PIM tool to replicate two component tungsten DEMO divertor parts.
Fusion Engineering and Design, 88(2013) S.2461-2465, DOI:10.1016/j.fusengdes.2013.04.037

[8] Antusch, S.; Commin, L.; Denker, N.; Hoffmann, J.; Holzer, P.; Klein, A.; Knabl, W.; Reiser, J.; Rieth, M.; Walter, H.
Fabrication and optimization of different armour materials by PIM.
MAT-HHFM Monitoring Meeting, Bucuresti, R, July 1-2, 2013

[9] Antusch, S.; Armstrong, D.; Commin, L.; Dudarev, S.; Gibson, J.; Hoffmann, J.; Knabl, W.; Müller, M.; Rieth, M.; Roberts, S.; Walter, H.
Fabrication of different armour prototype materials by PIM.
Final Meeting WP13-DAS02-T12 Helium Cooled Divertor, Garching, 10.Dezember 2013

[10] Antusch, S.; Piotter, V.
Fully automatic PIM multicomponent tool kit enables the replication and joining of parts without brazing for nuclear fusion power plants.
Powder Injection Moulding International, 7(2013) Nr.1, S.28-29

[11] Antusch, S.; Hanemann, T.; Piotter, V.; Rieth, M.
Mass production of components for future fusion power plants via one- and two component PIM.
2nd International Conference on Materials for Energy (EnMat 2013), Karlsruhe, 12.-16. Mai 2013

[12] Antusch, S.; Armstrong, D.E.J.; Britton, T.B.; Commin, L.; Gibson, J.S.K.L.; Greuner, H.; Hoffmann, J.; Knabl, W.; Müller, M.; Pintsuk, G.; Piotter, V.; Reiser, J.; Rieth, M.; Roberts, S.G.; Weingaertner, T.
Multicomponent powder injection molding as method for mass production, joining, and material development for tungsten armour materials.
16th International Conference on Fusion Reactor Materials (ICFRM-16), Beijing, China, October 20-26, 2013

[13] Antusch, S.; Armstrong, D.E.J.; Gibson, J.S.K.L.; Knabl, W.; Rieth, M.; Roberts, S.G.; Weingärtner, T.
Processing of complex shaped tungsten parts by PIM.
Workshop on Tungsten for Nuclear Applications, Oxford, GB, September 23-25, 2013

[14] Antusch, S.; Barrett, T.; Commin, L.; Denker, N.; Hoffmann, J.; Holzer, P.; Klein, A.; Knabl, W.; Reiser, J.; Rieth, M.; Walter, H.
Production of real-size parts consisting of different W materials using PIM as an alternative joining process.
MAT-HHFM Monitoring Meeting, Bucuresti, R, July 1-2, 2013

[15] Armstrong, D.; Hoffmann, A.; Knabl, W.; Schulmeyer, W.; Traxler, H.; Antusch, S. ; Commin, L.; Krauss, W.; Nemeth, A.; Reiser, J.
Tungsten - an overview on production , basic properties, processing and applications.
Workshop on Tungsten for Nuclear Applications, Oxford, GB, September 23-25, 2013

[16] Basuki, W.W.; Qu, D.; Vassen, R.; Aktaa, J.
Functionally graded Tungsten/EUROFER coatings manufactured by VPS for application in fusion power plants.
16th International Conference on Fusion Reactor Materials (ICFRM-16), Beijing, China, October 20-26, 2013

[17] Bohnert, C.; Schmitt, N.J.; Weygand, S.M.; Kraft, O.
A finite element analysis of the fracture behavior of tungsten at the micro scale.
Frühjahrstagung DPG, Sektion Kondensierte Materie, Fachverband Metall- und Materialphysik, Regensburg, 10.-15. März 2013
Verhandlungen der Deutschen Physikalischen Gesellschaft, R.6, B.48(2013), MM 30.4

[18] Chakin, V.; Rolli, R.; Moeslang, A.; Klimenkov, M.; Kolb, M.; Vladimirov, P.; Kurinskiy, P.; Schneider, H.C.; van Til, S.; Magielsen, A.J.; Zmitko, M.
Tritium release retention properties of highly neutron-irradiated beryllium pebbles from HIDOBE-01 experiment.
Journal of Nuclear Materials, 442(2013) Suppl.1, S.S483-S489, DOI:10.1016/j.jnucmat.2013.03.032

[19] Commin, L.; Rieth, M.; Dafferner, B.; Zimmermann, H.; Bolich, D.; Baumgärtner, S.; Ziegler, R.; Dichiser, S.; Fabry, T.; Fischer, S.; Hildebrand, W.; Palussek, O.; Ritz, H.; Sponda, A.
A fail-safe and cost effective fabrication route for blanket first walls.
Journal of Nuclear Materials, 442(2013) S.538-541, DOI:10.1016/j.jnucmat.2013.07.043

[20] Commin, L.; Antusch, S.; Baumgärtner, S.; Goldacker, W.; Lukits, P.; Rieth, M.; Bolich, D.; Hoffmann, M.
Assessment of copper based materials fr the water-cooled divertor concept of the DEMO European fusion reactor.
Proceedings of the 25th Symposium on Fusion Engineering (SOFE 2013), San Francisco, Calif., June 10-14, 2013, Piscataway, N.J. : IEEE, 2013 ThPO-15, ISBN 978-1-4799-0171-5
DOI:10.1109/SOFE.2013.6635275

[21] Commin, L.; Rieth, M.; Widak, V.; Dafferner, B.; Heger, S.; Zimmermann, H.; Materna-Morris, E.; Lindau, R.
Characterization of ODS (Oxide Dispersion Strengthened)Eurofer/Eurofer dissimilar electron beam welds.
Journal of Nuclear Materials, 442(2013) Suppl.1, S.S552-S556,
DOI:10.1016/j.jnucmat.2012.11.019

[22] Commin, L.; Baumgärtner, S.; Dafferner, B.; Heger, S.; Rieth, M.; Möslang, A.
Creep-fatigue interaction in Eurofer 3 electron beam welds.
16th International Conference on Fusion Reactor Materials (ICFRM-16), Beijing, China, October 20-26, 2013

[23] Commin, L.
Work package No.1: Irradiation damage - advanced characterization and modeling, FabriCharMe.
GOT Program Progress Meeting, Warszawa, PL, July 15, 2013

[24] Dethloff, C.; Gaganidze, E.; Aktaa, J.
Quantitative TEM analysis of precipitation and grain boundary aegregation after neutron irradiation.
16th International Conference on Fusion Reactor Materials (ICFRM-16), Beijing, China, October 20-26, 2013

[25] Dethloff, C.; Gaganidze, E.
Quantitative TEM investigation of neutron irradiated EUROFER97 from WTZ and ARBOR1.
EFDA MAT-IREMEV Monitoring Meeting, Bucaresti, R, June 26-28, 2013

[26] Gaganidze, E.; Aktaa, J.
Assessment of neutron irradiation effects on RAFM steels.
Fusion Engineering and Design, 88(2013) S.118-128, DOI:10.1016/j.fusengdes.2012.11.020

[27] Gaganidze, E.; Aktaa, J.
EUROFER behaviour under neutron irradiation.
Water Cooled Lithium Lead Workshop, Paris, F, October 7-8, 2013

[28] Gaganidze, E.; Rupp, D.; Aktaa, J.
Fracture behaviour of polycrystalline tungsten.
16th International Conference on Fusion Reactor Materials (ICFRM-16), Beijing, China, October 20-26, 2013

[29] Gaganidze, E.
Fracture-mechanical characterization of W-alloys.
MAT-HHFM Monitoring Meeting, Garching, February 21-22, 2013

[30] Gaganidze, E.; Kohnle, S.; Litvinov, D.
Fracture-mechanical characterization of W-alloys.
MAT-HHFM Monitoring Meeting, Bucuresti, R, July 1-2, 2013

[31] Gaganidze, E.
Main objectives and status of radiation effects in RAFM steels: Experiments & modelling (RadEff) - WP01.
Monitoring Meeting of the GOT-4 programs RIMES and RadEff, Madrid, E, December 2-3, 2013

[32] Gaganidze, E.
Needs of fission reactor irradiation programmes on RAFM steels.
Kick-Off Meeting 'Material Database Status and Needs for DEMO Conceptual Design Activities', Garching, May 14, 2013

[33] Gaganidze, E.
Radiation effects in RAFM steels: Experiments & modelling (RadEff).
Technical Meeting of the EFDA-GOT4 Programme RadEff, Saclay, F, June 5, 2013

[34] Gaganidze, E.
Status of the work WP13-MAT-02-02-01/KIT.
Progress Meeting 'MAT-02 : Material Database Status and Needs for DEMO Conceptual Design Activities', Petten, NL, October 2-3, 2013

[35] Greuner, H.; Maier, H.; Balden, M.; Linsmeier, Ch.; Böswirth, B.; Lindig, S.; Norajitra, P.; Antusch, S.; Rieth, M.
Investigation of European tungsten materials exposed to high heat flux H/He neutral beams.
Journal of Nuclear Materials, 442(2013) Suppl.1, S.S256-S260, DOI:10.1016/j.jnucmat.2013.04.044

[36] He, P.; Klimenkov, M.; Möslang, A.; Lindau, R.
Fatigue-structure correlation of 13.5%Cr ODS steels at 5500C for fusion application.
16th International Conference on Fusion Reactor Materials (ICFRM-16), Beijing, China, October 20-26, 2013

[37] He, P.; Liu, T.; Moeslang, A.; Nikitenko, S.
Systematic XAFS investigations of the structural evolution of ytrrium-enriched oxides in ODS ferritic steels by advanced synchrotron source at ESRF.
GETMAT International Workshop, Berlin, September 17-19, 2013

[38] He, P.; Lindau, R.; Möeslang, A.; Sandim, H.R.Z.
The influence of thermomechanical processing on the microstructure and mechanical properties of 13.5Cr ODS steels.
Fusion Engineering and Design, 88(2013) S.2448-2452, DOI:10.1016/j.fusengdes.2013.04.005

[39] Heneka, J.; Guttmann, M.; Plewa, K.; Hanemann, T.; Saile, V.
Cost-effective mass production of single polymeric micro parts due to micro injection molding and X-Ray LIGA mold inserts.
8th Internat.Conf.on MicroManufacturing, Victoria, CDN, March 25-28, 2013

[40] Hoffmann, J.; Antusch, S.; Dafferner, B.; Commin, L.; Jäntsch, U.; Rieth, M.; Ziegler, R.
Basic studies on processing of a large scale ODS batch.
International Workshop on Structural Materials for Innovative Nuclear Systems, Idaho Falls, Idaho, October 7-10, 2013

[41] Hoffmann, J.; Möslang, A.; He, P.; Rieth, M.
Validation of the production of ODS alloys by extended x-ray absorption fine structure (EXAFS).
16th International Conference on Fusion Reactor Materials (ICFRM-16), Beijing, China, October 20-26, 2013

[42] Klimenkov, M.
Microstructural characterization of neutron irradiated EUROFER97.
5th Workshop on Nuclear Fe Alloys, Roma, I, November 28-29, 2013

[43] Klimenkov, M.; Möslang, A.; Matern-Morris, E.
New method for detection of Li inside He bubbles formed in B10-alloyed steel after neutron irradiation.
Micron, 46(2013) S.51-56, DOI:10.1016/j.micron.2012.12.005

[44] Klimenkov, M.; Materna-Morris, E.; Möslang, A.
Study of the spatial distribution of Li and He inside steel using low energy loss spectroscopy.
Enhanced Data Generated by Electrons (EDGE 2013) : Internat.EELS Workshop, St.Maxime, F, May 26-31, 2013,Book of Abstracts S.35

[45] Klimenkov, M.; Möslang, A.; Lindau, R.; Coppola, R.
TEM characterizaion of neutron irradiated defects in EUROFERS97.
16th International Conference on Fusion Reactor Materials (ICFRM-16), Beijing, China, October 20-26, 2013, Abstract on USB-Stick

[46] Klimenkov, M.; Chakin, V.; Möslang, A.; Rolli, R.
TEM characterization of beryllium pebbles after neutron-irradiation up to 3000 appm of helium production (HIDOBE-01).
11th IEA International Workshop on Beryllium Technology (BeWS 2013), Barcelona, E, September 12-13, 2013

[47] Klimenkov, M.; Chakin, V.; Möslang, A.; Rolli, R.
TEM study of beryllium pebbles after neutron irradiation up to 3000 appm helium production.
Journal of Nuclear Materials, 443(2013) S.409-416, DOI:10.1016/j.jnucmat.2013.07.050

[48] Klimenkov, M.; Chakin, V.; Möslang, A.; Rolli, R.
TEM study of neutron irradiated beryllium pebbles.
16th International Conference on Fusion Reactor Materials (ICFRM-16), Beijing, China, October 20-26, 2013

[49] Konys, J.
Advanced processes for T-permeation and corrosion barriers for the DCLLmod. concept.
1st EU-US DCLL Workshop, Karlsruhe, April 23-24, 2013

[50] Konys, J.; Krauss, W.; Zhu, Z.; Huang, Q.
Comparison of corrosion behavior of EUROFER and CLAM steels in flowing Pb-15.7Li.
16th International Conference on Fusion Reactor Materials (ICFRM-16), Beijing, China, October 20-26, 2013

[51] Konys, J.; Krauss, W.
Corrosion and precipitation effects in a forced-convection Pb-15.7Li loop.
Journal of Nuclear Materials, 442(2013) Suppl.1, S.S576-S579, DOI:10.1016/j.jnucmat.2013.04.016

[52] Konys, J.
Flowing PbLi corrosion of RAFM steels.
1st EU-US DCLL Workshop, Karlsruhe, April 23-24, 2013

[53] Krauss, W.; Konys, J.; Wulf, S.E.
Corrosion barriers processed by Al-electroplating and their resistance against flowing Pb-15.7Li.
16th International Conference on Fusion Reactor Materials (ICFRM-16), Beijing, China, October 20-26, 2013

[54] Krauss, W.; Lorenz, J.; Konys, J.
Joining HHF components applying electroplating technology.
11th International Symposium on Fusion Nuclear Technology (ISFNT 2013), Barcelona, E, September 16-20, 2013

[55] Krauss, W.; Lorenz, J.; Konys, J.
Performance of electroplated and joined components for divertor applications.
Fusion Engineering and Design, 88(2013) S.1704-1708, DOI:10.1016/j.fusengdes.2013.04.049

[56] Krsjak, V.; Wei, S.H.; Antusch, S.; Dai, Y.
Mechanical properties of tungsten in the transition temperature range.
16th International Conference on Fusion Reactor Materials (ICFRM-16), Beijing, China, October 20-26, 2013

[57] Materna-Morris, E.; Klimenkov, M.; Möslang, A.
The influence of boron on structural properties of martensitic 8-10% Cr-steels.
Pinto, A.M. [Hrsg.]
Advanced Materials Forum IV : Proc.of 6th Internat.Materials Symp., Guimaraes, P, April 18-20, 2011
Durnten-Zürich : Trans Tech Publ., 2013 S.877-882, (Materials Science Forum ; 730-732), DOI:10.4028/www.scientific.net/MSF.730-732.877

[58] Möslang, A.; Diegele, E.; Ibarra, A.
Candidate materials for DEMO - Uncertainties and strategies to close knowledge gaps.
11th International Symposium on Fusion Nuclear Technology (ISFNT 2013), Barcelona, E, September 16-20, 2013

[59] Möslang, A.
ODS steels and their behavior under neutron irradiation. (eingeladen)
Monaco International Fusion Energy Days (MIFED 2013), Monaco, MC, December 2-4, 2013

[60] Reiser, J.; Rieth, M.; Möslang, A.; Hoffmann, A.
Advances in technologies for power exhaust solutions.
21st Congress 'Materials, Interfaces, Processes: New Challenges for Future Applications', Catania, I, May 15-17, 2013

[61] Reiser, J.; Rieth, M.; Dafferner, B.; Hoffmann, A.
Charpy impact properties of pure tungsten plate material in as-received and recrystallized condition (1 h at 20000C (2273 K)).
Journal of Nuclear Materials, 442(2013) Suppl.1, S.S204-S207, DOI:10.1016/j.jnucmat.2012.10.037

[62] Reiser, J.; Rieth, M.; Dafferner, B.; Hoffmann, A.
Ductilisation of W: Synthesis, analyses and characterization of W-laminates made of W-foils.
18th Plansee Seminar, Reutte, A, June 3-7, 2013, Paper on USB-Stick

[63] Reiser, J.; Rieth, M.; Möslang, A.; Dafferner, B.; Hoffmann, A.; Yi, X.; Armstrong, D.E.J.
Tungsten foil laminate for structural divertor applications. Tensile test properties of tungsten foil.
Journal of Nuclear Materials, 434(2013) S.357-368, DOI:10.1016/j.jnucmat.2012.12.003

[64] Reiser, J.; Rieth, M.; Möslang, A.; Dafferner, B.; Hoffmann, J.; Mrotzek, T.; Hoffmann, A.; Armstrong, D.E.J.; Yi, X.
Tungsten foil laminate for structural divertor applications. Joining of tungsten foils.
Journal of Nuclear Materials, 436(2013) S.47-55, DOI:10.1016/j.jnucmat.2013.01.295

[65] Reiser, J.; Rieth, M.; Möslang, A.; Hoffmann, J.; Franke, P.; Klimenkov, M.; Knabl, W.; Hoffmann, A.; Mrotzek, T.; Roberts, S.; Armstrong, D.E.J.; Yi, X.; Pippan, R.; Wurster, S.
Tungsten (W) foil laminate materials. Advances for innovative high temperature energy conversion systems?
Fraunhofer Seminar, Freiburg, 8.November 2013

[66] Reiser, J.; Rieth, M.; Dafferner, B.; Hoffmann, J.; Baumgärtner, S.; Jäntsch, U. ; Klimenkov, M.; Ziegler, R.; Bohlich, D.; Hoffmann, M.; Leiste, H.; Weingärtner, T.; Nemeth, A.; Scherbarth, J.; Möslang, A.; Franke, P.; Antusch, S.; Armstrong, D.E.J.; Yi, X.; Mrotzek, T.; Hoffmann, A.
Wolfram-Laminatwerkstoffe.
Wanner, A. [Hrsg.]
19.Symposium Verbundwerkstoffe und Werkstoffverbunde, Karlsruhe, 3.-5.Juli 2013
Tagungsband, ISBN 978-3-00-042309-3

[67] Reiser, J.; Rieth, M.; Dafferner, B.; Widak, V.; Hoffmann, A.
Wolframlaminate für die Energiewende.
Chancen der Energiewende. Wissenschaftliche Beiträge des KIT zur 1.Jahrestagung des KIT-Zentrums Energie, 19.06.2012. KIT Scientific Reports, KIT-SR 7640 (April 2013) S.181-186

[68] Rieth, M.; Dudarev, S.L.; Gonzalez de Vicente, S.M.; Aktaa, J.; Ahlgren, T.; Antusch, S.; Armstrong, D.E.J.; Balden, M.; Baluc, N.; Barthe, M.F.; Basuki, W.W.; Battabyal, M.; Becquart, C.S.; Blagoeva, D.; Boldyryeva, H.; Brinkmann, J. ; Celino, M.; Ciupinski, L.; Correia, J.B.; De Backer, A.; Domain, C.; Gaganidze, E.; Garcia-Rosales, C.; Gibson, J.; Gilbert, MR.; Giusepponi, S.; Gludovatz, B.; Greuner, H.; Heinola, K.; Höschen, T.; Hoffmann, A.; Holstein, N. ; Koch, F.; Krauss, W.; Li, H.; Lindig, S.; Linke, J.; Linsmeier, Ch.; Lopez-Ruiz, P.; Maier, H.; Matejicek, J.; Mishra, T.P.; Muhammed, M.; Munoz, A.; Muzyk, M.; Nordlund, K.; Nguyen-Manh, D.; Opschoor, J.; Ordas, N.; Palacios, T.; Pintsuk, G.; Pippan, R.; Reiser, J.; Riesch, J.; Roberts, S.G.; Romaner, L.; Rosinski, M.; Sanchez, M.; Schulmeyer, W.; Traxler, H.; Urena, A.; van der Laan, J.G.; Veleva, L.; Wahlberg, S.; Walter, M.; Weber, T.; Weitkamp, T.; Wurster, S.; Yar, M.A.; You, J.H.; Zivelonghi, A.
A brief summary of the progress on the EFDA tungsten materials.
Journal of Nuclear Materials, 442(2013) Suppl.1, S.S173-S180
DOI:10.1016/j.jnucmat.2013.03.062

[69] Rieth, M.; Commin, L.; Hoffmann, J.; Antusch, S.
Development of a reduced activation (austenitic) stainless steel (RASS).
Fusion Materials Topical Group Monitoring Meeting, Garching, February 21-22, 2013

[70] Rieth,M.
Divertor design and Materials.
Doctoral Training Network Course 'Materials in Fusion', Oxford, November 11-15, 2013

[71] Rieth, M.; Möslang, A.; Jäntsch, U.
High-alloyed steels. Structure, phases, properties, and applications.
Bereichsseminar 'Plasmarand und Wand', IPP Garching, 10.April 2013

[72] Rieth, M.; Commin, L.; Hoffmann, J.; Dafferner, B.; Heger, S.; Baumgärtner, S.
On the use of W-Cu laminate pipes as a heat sink.
Fusion Materials Topical Group Monitoring Meeting, Bucuresti, R, July 1-2, 2013

[73] Rieth, M.; Reiser, J.; Hoffmann, A.; Knabi, W.; Schulmmeyer, W.; Commin, L.; Antusch, S.
Possibel applications of tungsten materials in power production and future large-scale projects.
18th Plansee Seminar, Reutte, A, June 3-7, 2013

[74] Rieth, M.
Power plant divertor. Design options and materials.
NFRI/KIT Cooperation Meeting, Karlsruhe, February 14-15, 2013

[75] Rieth, M.; Dudarev, S.L.; Gonzalez de Vicente, S.M.; Aktaa, J.; Ahlgren, T.; Antusch, S.; Armstrong, D.E.J.; Balden, M.; Baluc, N.; Barthe, M.F.; Basuki, W.W.; Battabyal, M.; Becquart, C.S.; Blagoeva, D.; Boldyryeva, H.; Brinkmann, J. ; Celino, M.; Ciupinski, L.; Correia, J.B.; De Backer, A.; Domain, C.; Gaganidze, E.; Garcia-Rosales, C.; Gibson, J.; Gilbert, M.R.; Giusepponi, S.; Gludovatz, B.; Greuner, H.; Heinola, K.; Höschen, T.; Hoffmann, A.; Holstein, N.; Koch, F.; Krauss, W.; Li, H.; Lindig, S.; Linke, J.; Linsmeier, Ch.; Lopez-Ruiz, P.; Maier, H.; Matejicek, J.; Mishra, T.P.; Muhammed, M.; Munoz, A.; Muzyk, M.; Nordlund, K.; Nguyen-Manh, D.; Opschoor, J.; Ordas, N.; Palacios, T.; Pintsuk, G.; Pippan, R.; Reiser, J.; Riesch, J.; Roberts, S.G.; Romaner, L.; Rosinski, M.; Sanchez, M.; Schulmeyer, W.; Traxler, H.; Urena, A.; van der Laan, J.G.; Veleva, L.; Wahlberg, S.; Walter, M.; Weber, T.; Weitkamp, T.; Wurster, S.; Yar, M.A.; You, J.H.; Zivelonghi, A.
Recent progress in research on tungsten materials for nuclear fusion applications in Europe.
Journal of Nuclear Materials, 432(2013) S.482-500, DOI:10.1016/j.jnucmat.2012.08.018

[76] Rieth, M.; Commin, L.; Dafferner, B.; Heger, S.; Baumgärtner, S.; Ziegler, R.
W-laminates for structural divertor applications: W-Ti laminates.
Fusion Materials Topical Group Monitoring Meeting, Bucuresti, R, July 1-2, 2013

[77] Sacksteder, I.; Hostettler, S.; Charbonneau, G.; Albinski, B.; Schneider, H.C.
Requirements for investigating the temperature-dependent fracture behavior of irradiated materials by indentation.
Fusion Engineering and Design, 88(2013) S.2577-2580, DOI:10.1016/j.fusengdes.2013.04.033

[78] Schneider, H.-C.; Albinski, B.; Sacksteder, I.
Determining mechanical properties by instrumented high-temperature indentation.
Zwick Academia Day, Manchester, GB, April 17, 2013

[79] Svetukhin, V.; L'vov, P.; Tikhonchev, M.; Gaganidze, E.; Krestina, N.
Modeling of chromium nanocluster growth under neutron irradiation.
Journal of Nuclear Materials, 442(2013) S.S624-S627, DOI:10.1016/j.jnucmat.2013.03.030

[80] Tikhonchev, M.; Svetukhin, V.; Gaganidze, E.
MD simulation of atomic displacement cascades near chromium-rich clusters in FeCr alloy.
Journal of Nuclear Materials, 442(2013) S.S618-S623, DOI:10.1016/j.jnucmat.2012.11.058

[81] Tröber, O.
Needs of dual-beam irradiation experiments.
Technical Meeting of the EFDA-GOT4 Programme RadEff, Saclay, F, June 5, 2013

[82] Weber, T.; Härtelt, M.; Aktaa, J.
Considering brittleness of tungsten in failure analysis of helium-cooled divertor components with functionally graded tungsten/EUROFER97 joints.
Engineering Fracture Mechanics, 100(2013) S.63-75, DOI:10.1016/j.engfracmech.2012.07.024

[83] Wulf, S.E.; Krauss, W.; Konys, J.
Comparison of coating processes in the development of aluminum-based barriers for blanket applications.
11th International Symposium on Fusion Nuclear Technology (ISFNT 2013), Barcelona, E, September 16-20, 2013

[84] Wulf, S.E.; Holstein, N.; Krauss, W.; Konys, J.
Influence of deposition conditions on the microstructure of Al-based coatings for applications as corrosion and anti-permeation barrier.
Fusion Engineering and Design, 88(2013) S.2530-2534, DOI:10.1016/j.fusengdes.2013.05.060

[85] Zinkle, S.J.; Möslang, A.
Evaluation of irradiation facility options for fusion materials research and development.
Fusion Engineering and Design, 88(2013) S.472-482, DOI:10.1016/j.fusengdes.2013.02.081

[86] Zinkle, S.J.; Möslang, A.; Muroga, T.; Tanigawa, H.
Multimodal options for materials research to advance the basis for fusion energy in the ITER era.
Nuclear Fusion, 53(2013) S.104024/1-13, DOI:10.1088/0029-5515/53/10/104024

Nuclear Data

[1] Fischer, U.; Leichtle, D.; Serikov, A.; Pereslavtsev, P.; Villari, R.
Review and validation of shutdown dose rate estimation techniques for application to ITER.
Fusion Science and Technology, 64(2013) S.563-570

[2] Pitcher, C.S.; Barnsley, R.; Bertalot, L.; Encheva, A.; Feder, R.; Friconneau, J.P.; Hu, Q.; Levesy, B.; Loesser, G.D.; Lyublin, B.; Macklin, B.; Martins, J.P. ; Padasalagi, S.; Pak, S.; Reichle, R.; Sato, K.; Serikov, A.; Seyvet, F.; Suarez, A.; Udintsev, V.; Vayakis, G.; Veshchev, E.; Walker, C.; Walsh, M.; Watts, C.; Zhai, Y.
Port-based plasma diagnostic infrastructure on ITER.
Fusion Science and Technology, 64(2013) S.118-125

[3] Serikov, A.; Fischer, U.; Pitcher, C.S.; Suarez, A.; Weinhorst, B.
Computational challenges of fusion neutronics for ITER ports.
International Conference on Supercomputing in Nuclear Applications and Monte Carlo (SNA & MC 2013), Paris, F, October 27-31, 2013

[4] Serikov, A.; Bertalot, L.; Fischer, U.; Pak, S.; Suarez, A.; Villari, R.
Neutronic challenges for the estimation of shut-down dose rates in ITER ports.
ANS Winter Meeting and Nuclear Technology Expo, Washington, D.C., November 10-14, 2013

[5] Serikov, A.; Fischer, U.; Henderson, M.; Leichtle, D.; Pitcher, C.S.; Spaeh, P.; Strauss, D.; Suarez, A.; Weinhorst, B.
Neutronics for equatorial and upper ports in ITER.
Fusion Engineering and Design, 88(2013) S.1965-1968, DOI:10.1016/j.fusengdes.2013.03.037

[6] Serikov, A.; Bertalot, L.; Fischer, U.; Pitcher, C.S.; Suarez, A.; Udintsev, V.S.; Weinhorst, B.
Shut-down dose rate analysis for ITER diagnostic equatorial and upper ports.
11th International Symposium on Fusion Nuclear Technology (ISFNT 2013), Barcelona, E, September 16-20, 2013

[7] Fischer, U.; Grosse, D.; Lu, L.; Kondo, K.; Pereslavtsev, P.; Serikov, A.; Vielhaber, S.
Applications of the McCad geometry conversion tool in fusion technology - ITER, IFMIF and DEMO.
Transactions of the American Nuclear Society, 109(2013) S.729-732

[8] Fischer, U.; Angelone, M.; Batistoni, P.; Bohm, T.; Kondo, K.; Konno, C.; Sawan, M.; Villari, R.; Walker, B.
Benchmarking of the FENDL-3 neutron cross-section data starter library for fusion applications.
International Conference on Nuclear Data for Science & Technology, New York, N.Y., March 4-8, 2013

[9] Fischer, U.
Fusion neutronics principles: Methods, data & nuclear design applications.
14th Course 'Neutronics of Fusion Reactors: Design, Technology and Diagnostics', Erice, I, May 6-13, 2013 (eingeladener Vortrag)

[10] Fischer, U.; Bachmann, C.; Catalan, J.P.; Lengar, I.; Szieberth, M.; Pampin, R.; Porton, M.; Pereslavtsev, P.; Ogando, F.; Tracz, G.; Villari, R.
Neutronic analyses and tools development efforts in the European DEMO programme.
11th International Symposium on Fusion Nuclear Technology (ISFNT 2013), Barcelona, E, September 16-20, 2013

[11] Fischer, U.
Nuclear data needs for fusion - ITER, IFMIF, DEMO.
JEFF-NEEDS Workshop on Nuclear Data Measurements, Paris, F, November 25-26, 2013

[12] Fischer, U.; Avrigeanu, M.; Kodeli, I.; Leeb, H.; Rochman, D.; Sauvan, P.; Sublet, J.-C.; Dupont, E.; Izquierdo, J.
The activities of the European consortium on nuclear data development and analysis for fusion.
International Conference on Nuclear Data for Science & Technology, New York, N.Y., March 4-8, 2013

[13] Große, D.; Fischer, U.; Kondo, K.; Leichtle, D.; Pereslavtsev, P.; Serikov, A.
Status of the McCad geometry conversion tool and related visualisation capabilities for 3D fusion neutronics calculations.
Fusion Engineering annd Design, 88(2013) S.2210-2214, DOI:10.1016/j.fusengdes.2013.02.146

[14] Klix, A.; Fischer, U.; Gehre, D.; Kleizer, G.; Rovni, I.; Ruecker, T.
Experimental neutronics tests for a neutron activation system for the European ITER TBM.
International Conference on Fusion Reactor Diagnostics, Varenna, I, September 9-13, 2013

[15] Klix, A.; Angelone, M.; Domula, A.; Fischer, U.; Gehre, D.; Kleizer, G.; Lyoussi, A.; Ruecker, T.; Rovni, I.; Szalkai, D.
Neutronics instrumentation for the European ITER TBM.
25th Symposium on Fusion Engineering (SOFE 2013), San Francisco, Calif., June 10-14, 2013

[16] Klix, A.; Domula, A.; Fischer, U.; Gehre, D.; Kleizer, G.; Rovni, I.
Preliminary experimental test of activation foil materials with short half-lives for neutron spectrum measurements in the ITER TBM.
Fusion Science and Technology, 64(2013) S.604-612

[17] Kondo, K.; Fischer, U.
Analyses of TIARA shielding benchmark experiments using the FENDL-3 library.
American Nuclear Society Winter Meeting 2013, Washington, D.C., November 10-14, 2013

[18] Kondo, K.; Fischer, U.
Analyses of TIARA shielding benchmark experiments using the FENDL-3 library.
Transactions of the American Nuclear Society, 109(2013) S.1256-1259

[19] Kondo, K.; Arbeiter, F.; Fischer, U.; Große, D.; Heinzel, V.; Kix, A.; Lu, L.; Mittwollen, M.; Serikov, A.; Tian, K.; Weber, V.
Neutronic analysis for the IFMIF EVEDA reference test cell and test facility.
11th International Symposium on Fusion Nuclear Technology (ISFNT 2013), Barcelona, E, September 16-20, 2013

[20] Kondo, K.; Abou-Sena, A.; Arbeiter, F.; Brand, J.; Fischer, U.; Große, D.; Klix, A.; Lu, L.; Serikov, A.
Neutronic analysis of the IFMIF tritium release test module based on the EVEDA design.
16th International Conference on Fusion Reactor Materials (ICFRM-16), Beijing, China, October 20-26, 2013

[21] Kondo, K.; Fischer, U.; Klix, A.; Pereslavtsev, P.; Serikov, A.
Re-analysis of fusion relevant benchmark experiments using recent nuclear data libraries.
International Conference on Nuclear Data for Science & Technology, New York, N.Y., March 4-8, 2013

[22] Kondo, K.; Arbeiter, F.; Fischer, U.; Große, D.; Heinzel, V.; Klix, A.; Serikov, A.; Tian, K.; Weber, V.
Re-evaluation of the irridation conditions in the IFMIF test cell based on the EVEDA phase design.
Fusion Engineering and Design, 88(2013) S.2589-2593, DOI:10.1016/j.fusengdes.2013.05.029

[23] Kondo, K.; Fischer, U.; Serikov, A.
Shielding analysis of the high flux test module activated in IFMIF.
American Nuclear Society Winter Meeting 2013, Washington, D.C., November 10-14, 2013

[24] Kondo, K.; Fischer, U.; Serikov, A.
Shielding analysis of the high flux test module activated in IFMIF.
Transactions of the American Nuclear Society, 109(2013) S.1171-1173

[25] Kondo, K.; Fischer, U.; Heinzel, V.; Leichtle, D.; Serikov, A.
The application of 'Helios' supercomputer in radiation safety studies for the IFMIF.
Joint International Conference on Supercomputing in Nuclear Applications and Monte Carlo 2013, Paris, F, October 27-31, 2013

[26] Konobeev, A.Y.; Fischer, U.; Pereslavtsev, P.E.; Blann, M.
Improved simulation of the pre-equilibrium triton emission in nuclear reactions induced by nucleons.
International Conference on Nuclear Data for Science & Technology, New York, N.Y., March 4-8, 2013

[27] Lu, L.; Fischer, U.; Pereslavtsev, P.
Improved algorithm and advanced features for the CAD to MC conversion tool McCad.
11th International Symposium on Fusion Nuclear Technology (ISFNT 2013), Barcelona, E, September 16-20, 2013

[28] Pereslavtsev, P.; Fischer, U.; Lu, L.
Neutronic analyses of the HCPB DEMO reactor using a consistent integral approach.
11th International Symposium on Fusion Nuclear Technology (ISFNT 2013), Barcelona, E, September 16-20, 2013

[29] Pereslavtsev, P.; Konobeyev, A.; Fischer, U.; Sobes, V.; Leal, L.
New evaluation of n+Cu-63,65 nuclear cross section data up to 200 MeV neutron energy.
International Conference on Nuclear Data for Science & Technology, New York, N.Y., March 4-8, 2013

[30] Qiu, Y.; Lu, P.; Fischer, U.; Pereslavtsev, P.; Kecskes, S.
A generic date translation scheme for the coupling of high-fidelity fusion neutronics and CFD calculations.
11th International Symposium on Fusion Nuclear Technology (ISFNT 2013), Barcelona, E, September 16-20, 2013

[31] Rücker, T.; Kleizer, G.; Klix, A.; Domula, A.; Gehre, D.
Neutronenspektrometer basierend auf Aktivierungsfolien mit kurzen Halbwertszeiten für die Europäischen ITER-Testblanketmodule.
Jahrestagung Kerntechnik, Berlin, 14.-16. Mai 2013, Berlin : INFORUM GmbH, 2013, CD-ROM

International Fusion Materials Irradiation Facility (IFMIF)

[1] Abou-Sena, A.; Arbeiter, F.
Development of the IFMIF tritium release test module in the EVEDA phase.
Fusion Engineering and Design, 88(2013) S.818-823, DOI:10.1016/j.fusengdes.2013.02.041

[2] Arbeiter, F.; Abou-Sena, A.; Chen, Y.; Freund, J.; Klix, A.; Kondo, K.; Vladimirov, P.
Preliminary dimensioning of the IFMIF tritium release test module.
Fusion Engineering and Design, 88(2013) S.2585-2588, DOI:10.1016/j.fusengdes.2013.05.076

[3] Chen, Y.; Klein, C.; Arbeiter, F.; Ibaceta, G.
Numerical simulation and experiments on gaseous flow and heat transfer in multiple narrow channels in transition region.
21th International Conference on Nuclear Engineering (ICONE21), Chengdu, China, July 29 - August 2, 2013, Proc.on DVD Paper ICONE21-16172, New York, N.Y. : ASME, 2013

[4] Chen, Y.; Arbeiter, F.
Numerical simulation on gaseous flow and heat transfer in multiple narrow channels of IFMIF high flux test module.
Fusion Engineering and Design, 88(2013) S.2814-2824, DOI:10.1016/j.fusengdes.2013.04.038

[5] Chen, Y.; Arbeiter, F.; Heinzel, V.; Kondo, K.; Mittwollen, M.; Tian, K.
Numerical simulations on natural convective heat transfer and active cooling of IFMIF test cell.
11th International Symposium on Fusion Nuclear Technology (ISFNT 2013), Barcelona, E, September 16-20, 2013

[6] Jin, X.Z.; Schlindwein, G.; Schlenker, M.; Ghidersa, B.-E.; Chen, Y.; Arbeiter, F.
Thermal-hydraulic system study of the HELOKA-LP helium loop using RELAP5-3D code.
Fusion Engineering and Design, 88(2013) S.2560-2564, DOI:10.1016/j.fusengdes.2013.05.035

Taubmann, P.
Inbetriebnahme und Kalibrierung einer Drei-Draht-Sonde.
Diplomarbeit, Hochschule Karlsruhe - Technik und Wirtschaft 2012

[7] Tian, K.; Arbeiter, F.; Heinzel, V.; Kubaschewski, M.; Madzarov, V.; Mittwollen, M.
Current status of the major cells design of IFMIF test facility and arrangement of the cells.
21th International Conference on Nuclear Engineering (ICONE21), Chengdu, China, July 29 - August 2, 2013, Proc.on DVD Paper ICONE21-15991, New York, N.Y. : ASME, 2013

[8] Tian, K.; Arbeiter, F.; Chen, Y.; Heinzel, V.; Kondo, K.; Mittwollen, M.
Engineering design of the IFMIF EVEDA reference test cell and key components.
11th International Symposium on Fusion Nuclear Technology (ISFNT 2013), Barcelona, E, September 16-20, 2013

[9] Tian, K.; Arbeiter, F.; Heinzel, V.; Heupel, T.; Kondo, K.; Mittwollen, M.
IFMIF test cell design: Current status and key components.
Fusion Engineering and Design, 88(2013) S.635-639, DOI:10.1016/j.fusengdes.2013.03.055

Fuel Cycle – Vacuum Pumping

[1] Battes, K.; Hauer, V.
Influence of the pre-treatment on outgassing.
Frühjahrstagung DPG, Sektion Kondensierte Materie, Fachverband Vakuumphysik und Vakuumtechnik, Regensburg, 10.-15. März 2013
Verhandlungen der Deutschen Physikalischen Gesellschaft, R.6, B.48(2013), VA 3.1

[2] Battes, K.; Day, C.; Hauer, V.
Review and measurement of outgassing rates of stainless steel and polymers.
19th Internat.Vacuum Congress (IVC-19), Paris, F, September 9-13, 2013

[3] Battes, K.; Day, C.; Hauer, V.
Tokamak exhaust gas composition measurement via different mass spectrometers.
11th International Symposium on Fusion Nuclear Technology (ISFNT 2013), Barcelona, E, September 16-20, 2013

[4] Day, C.; Haas, H.; Hanke, S.; Hauer, V.; Luo, X.; Scannapiego, M.; Varoutis, S.
20 years experience in designing and testing customized cryopumps - A review.
Cryogenic Engineering Conf.and Internat.Cryogenic Materials Conf. (CEC-ICMC), Anchorage, Alaska, June 17-21, 2013

[5] Day, C.
20 years of customized cryopumps in fusion research.
24th National Symposium on Cryogenics (NSC 2013), Ahmedabad, IND, January 21-24, 2013

[6] Day, C.
A two-lecture shourt course on cryopumps.
24th National Symposium on Cryogenics (NSC 2013), Ahmedabad, IND, January 21-24, 2013

[7] Day, C.
ITER - Der Weg zu einem Fusionskraftwerk.
Bad Honnefer Industriegespräche, Bad Honnef, 17. Juli 2013

[8] Day, C.
Kryovakuumtechnik und Kryopumpen.
Kryotechnik : Grundlagen und Arbeitstechniken, Entwicklungsstand, -tendenzen, Anwendungen ; VDI-Wissensforum, Karlsruhe, 27.Februar - 1.März 2013

[9] Day, C.; Hauer, V.; Igitkhanov, J.; Kalupin, D.; Valovic, M.; Varoutis, S.
Towards a physics-integrated view of the fusion fuel cycle.
11th International Symposium on Fusion Nuclear Technology (ISFNT 2013), Barcelona, E, September 16-20, 2013

[10] Day, Chr.
Kryotechnik und Kryopumpen.
Jousten, K. [Hrsg.]
Wutz Handbuch Vakuumtechnik, Wiesbaden : Springer Vieweg, 2013 S.523-577
ISBN 978-3-8348-1745-7

[11] Dremel, M.; Pearce, R.; Strobel, H.; Hauer, V.; Day, C.; Wikus, P.; Papastergiou, S.
The new build to print design of the ITER torus cryopump.
Fusion Engineering and Design, 88(2013) S.760-763, DOI:10.1016/j.fusengdes.2013.02.026

[12] Gleason-Gonzalez, C.; Varoutis, S.; Day, C.
Divertor region gas kinetics: an engineering approach.
40th European Physical Society Conference on Plasma Physics (EPS 2013), Espoo, SF, July 1-5, 2013

[13] Gleason-Gonzalez, C.; Varoutis, S.; Day, C.
Simulation of neutral gas flow in a tokamak divertor using direct simulation Monte Carlo method.
11th International Symposium on Fusion Nuclear Technology (ISFNT 2013), Barcelona, E, September 16-20, 2013

[14] Luo, X.; Hauer, V.; Ochoa, S.; Day, Chr.
Simulation of the thermal radiation heat load of a large-scale customized cryopump with the Monte Carlo ray trace method.
Funaki, K. [Hrsg.]
Proc.of the 24th Internat.Cryogenic Engineering Conf., Internat.Cryogenic Materials Conference 2012, Fukuoka, J, May 14-18, 2012, Tokyo : Cryogenics and Superconducting Society of Japan, 2013 S.111-114, ISBN 978-4-9906959-0-3

[15] Luo, X.; Giegerich, T.; Day, C.
Transient gas flow studied by a test particle Monte Carlo approach with ProVac3D.
Mareschal, M. [Hrsg.]
28th Internat.Symp.on Rarefied Gas Dynamics (RDG 28), Zaragoza, E, July 9-13, 2012
Vol.1 S.857-863, Melville, N.Y. : American Institute of Physics, 2012, (AIP Conference Proceedings ; 1501), ISBN 978-0-7354-1116-6

[16] Ochoa Guaman, S.; Hanke, S.; Day, C.
Heat transfer enhancemenbt of NBI vacuum pump cryopanels.
Fusion Engineering and Design, 88(2013) S.882-886, DOI:10.1016/j.fusengdes.2013.02.111

[17] Scannapiego, M.; Day, C.; Hauer, V.
Consequences of plasma disruption mitigation by massive gas injection on the ITER torus cryopumping system.
11th International Symposium on Fusion Nuclear Technology (ISFNT 2013), Barcelona, E, September 16-20, 2013

[18] Scannapiego, M.; Day, Chr.
R&D design for the cryogenic vacuum pumps of ITER.
IUVSTA Workshop on UHV Techniques for Large Volume Devices, Gandhinagar, IND, March 19-22, 2013

[19] Varoutis, S.; Saglietti, C.; Luo, X.; Day, C.; Zanino, R.
Experimental and computational investigation of rarefied gas flows through bellows and very short tubes.
19th International Vacuum Congress (IVC 2013), Paris, France, September 9-13, 2013

[20] Varoutis, S.; Day, C.
Transient rarefied gas flow through short channels at arbitrary pressure ratios.
Frühjahrstagung DPG, Sektion Kondensierte Materie, Fachverband Vakuumphysik und Vakuumtechnik, Regensburg, 10.-15. März 2013
Verhandlungen der Deutschen Physikalischen Gesellschaft, R.6, B.48(2013), VA 2.1

[21] Yang, Y.; Marujama, S.; Kiss, G.; Ciattaglia, S.; Putvinski, S.; Yoshino, R.; Li, W.; Jiang, T.; Li, B.; Varoutis, S.; Day, C.
Concept desing of fusion power shutdown system for ITER.
Fusion Engineering and Design, 88(2013) S.824-826, DOI:10.1016/j.fusengdes.2013.01.055

[22] Bornschein, B.; Day, Chr.; Demange, D.; Pinna, T.
Tritium management and safety issues in ITER and DEMO breeding blankets.
Fusion Engineering and Design, 88(2013) S.466-471, DOI:10.1016/j.fusengdes.2013.03.032

[23] Day, C.; Giegerich, Th.
Exhaust pumping of DT fusion devices - Current state-of-the-art and a potential roadmap to a power plant.
Proceedings of the 25th Symposium on Fusion Engineering (SOFE 2013), San Francisco, Calif., June 10-14, 2013, Pisacataway, N.J. : IEEE, 2013, ISBN 978-1-4799-0169-2
DOI:10.1109/SOFE.2013.6635297

[24] Day, C.; Giegerich, T.
Non-cryogenic pumps for DEMO. (eingeladen)
21st Congress 'Materials, Interfaces, Processes: New Challenges for Future Applications', Catania, I, May 15-17, 2013

[25] Day, C.; Giegerich, T.
The direct internal recycling concept to simplify the fuel cycle of a fusion power plant.
Fusion Engineering and Design, 88(2013) S.616-620, DOI:10.1016/j.fusengdes.2013.05.026

[26] Giegerich, T.; Day, C.
A metal foil vacuum pump for the fuel cycle of fusion power plants.
Frühjahrstagung DPG, Sektion Kondensierte Materie, Fachverband Vakuumphysik und Vakuumtechnik, Regensburg, 10.-15. März 2013
Verhandlungen der Deutschen Physikalischen Gesellschaft, R.6, B.48(2013), VA 1.2

[27] Giegerich, T.; Day, C.
Conceptuation of a continuosly working vacuum pump train for fusion power plants.
Fusion Engineering and Design, 88(2013) S.2206-2209, DOI:10.1016/j.fusengdes.2013.05.019

[28] Giegerich, T.; Day, C.
The KALPUTREX-Process - A new vacuum pumping process for exhaust gases in fusion power plants.
11th International Symposium on Fusion Nuclear Technology (ISFNT 2013), Barcelona, E, September 16-20, 2013

[29] Giegerich, T.; Day, C.
The THESEUS facility - A test environment for the torus exhaust vacuum pumping system of a fusion power plant.
Proceedings of the 25th Symposium on Fusion Engineering (SOFE 2013), San Francisco, Calif., June 10-14, 2013, Pisacataway, N.J. : IEEE, 2013, ISBN 978-1-4799-0169-2
DOI:10.1109/SOFE.2013.6635290

[30] Giegerich, T.; Day, C.
Theoretical and experimental investigation of metal foil vacuum pumps for pumping and separating hydrogen.
19th International Vacuum Congress (IVC 2013), Paris, France, September 9-13, 2013

[31] Luo, X.; Giegerich, T.; Day, C.
Monte Carlo simulation of a vapour diffusion pump.
19th Internat. Vacuum Congress (IVC-19), Paris, F, September 9-13, 2013

Fuel Cycle – Tritium Processing

[1] Beck, A.; Grössle, R.
First calibration of TApIR (tritium absorption IR-spectroscopy).
Frühjahrstagung DPG, Sektion AMOP, Fachverband Molekülphysik, Hannover, 18.-22. März 2013
Verhandlungen der Deutschen Physikalischen Gesellschaft, R.6, B.48(2013), MO 11.5

[2] Beck, A.; Grössle, R.
First measurements with TApIR (tritium absorption IR-spectroscopy).
Frühjahrstagung DPG, Sektion AMOP, Fachverband Molekülphysik, Hannover, 18.-22. März 2013
Verhandlungen der Deutschen Physikalischen Gesellschaft, R.6, B.48(2013), MO 11.6

[3] Bekris, N.
Surface analysis techniques for the study of plasma wall interactions.
3rd EIROforum School of Instrumentation (ESI 2013), Geneve, CH, May 27-31, 2013

[4] Demange, D.
Advanced tritium extraction process for HCPB breeding blanke t.
17th International Workshop on the Ceramic Breeder Blanket Interactions (CBBI-17), Barcelona, E, September 12-14, 2013

[5] Demange, D.; Fanghänel, E.; Fischer, S.; Le, T.L.; Priester, F.; Röllig, M.; Schlösser, M.; Simon, K.H.
CAPER as central and crucial facility to support R&D with tritium at TLK.
10th International Conference on Tritium Science and Technology (TRITIUM 2013), Nice, F, October 21-25, 2013

[6] Demange, D.; Fanghänel, E.; Gramlich, N.; Le, T.L.; Moosmann, H.; Simon, K.H.; Wagner, R.; Welte, S.
Integration of a micro-channel catalytic reactor in CAPER to study highly tritiated water handling and processing.
10th International Conference on Tritium Science and Technology (TRITIUM 2013), Nice, F, October 21-25, 2013

[7] Fischer, S.; Schönung, K.; Rolli, R.; Schäfer, V.; Sturm, M.
Investigation of durability of optical coatings in high purity tritium gas.
10th International Conference on Tritium Science and Technology (TRITIUM 2013), Nice, F, October 21-25, 2013

[8] Größle, R.; Beck, A.; Bornschein, B.; Fischer, S.; Kraus, A.; Rupp, S.
First calibration measurements of an IR absorption spectroscopy system for liquid hydrogen isotopologues.
10th International Conference on Tritium Science and Technology (TRITIUM 2013), Nice, F, October 21-25, 2013

[9] Klein, M.
Funktionsnachweis eines Messsystems zur Bestimmung der Tritiumkonzentration in Wasser mittels Verstärkerfolie und Photodioden.
77. Jahrestagung der DPG und DPG-Frühjahrstagung, Fachverband Physik der Hadronen und Kerne, Dresden, 4.-8.März 2013
Verhandlungen der Deutschen Physikalischen Gesellschaft, R.6, B.48(2013), HK 75.6

[10] Michling, R.; Bekris, N.; Cristescu, I.; Lohr, N.; Plusczyk, C.; Welte, S.; Wendel, J.
Water detritation processing of JET purified waste water using the TRENTA facility at tritium laboratory Karlsruhe.
Fusion Engineering and Design, 88(2013) S. 2361-2365

[11] Niemes, S.
Tritium measurement in water using bremsstrahlung X-rays and a silicon drift detector.
77. Jahrestagung der DPG und DPG-Frühjahrstagung, Fachverband Physik der Hadronen und Kerne, Dresden, 4.-8.März 2013
Verhandlungen der Deutschen Physikalischen Gesellschaft, R.6, B.48(2013), HK 75.7

[12] Plusczyk, C.; Bekris, N.; Cristescu, I.; Lohr, N.; Michling, R.; Moosmann, H.; Welte, S.
Experimental assessment of a catalytic hydrogen oxidation system for the off-gas processing of the ITER WDS.
Fusion Engineering and Design, 88(2013) S.2332-2335, DOI:10.1016/j.fusengdes.2013.05.104

[13] Priester, F.; Röllig, M.
Post service examination of TMP after stress testing with kg-scale tritium throughput.
10th International Conference on Tritium Science and Technology (TRITIUM 2013), Nice, F, October 21-25, 2013

[14] Röllig, M.; Priester, F.; Babutzka, M.; Bonn, J.; Bornschein, B.; Drexlin, G.; Ebenhöch, S.; Otten, E.W.; Steidl, M.; Sturm, M.
Activity monitoring of a gaseous tritium source by beta induced X-ray spectrometry.
Fusion Engineering and Design, 88(2013) S.1263-1266, DOI:10.1016/j.fusengdes.2012.11.001

[15] Schlösser, M.; Bornschein, B.; Fischer, S.; James, T.M.; Kassel, F.; Rupp, S.; Sturm, M.; Telle, H.H.
Raman spectroscopy at the Tritium Laboratory Karlsruhe.
10th International Conference on Tritium Science and Technology (TRITIUM 2013), Nice, F, ctober 21-25, 2013

[16] Shu, W.M.; Cristescu, I.; Michling, R.; Demange, D.; Willms, R.S.; Glugla, M.
Highly tritiated water processing by isotope swapping.
10th International Conference on Tritium Science and Technology (TRITIUM 2013), Nice, F, October 21-25, 2013

[17] Sturm, M.; Niemes, S.; Michling, R.; Bornschein, B.
Determination of tritium concentration in water using beta induced x-ray spectrometry with a silicon drift detector.
10th International Conference on Tritium Science and Technology (TRITIUM 2013), Nice, F, October 21-25, 2013

[18] Wagner, R.; Demange, D.; Fanghänel, E.; Le, T.L.; Schwarz, M.; Simon, K.-H.
Decommissioning of the PETRA experiment - Status and progress.
10th International Conference on Tritium Science and Technology (TRITIUM 2013), Nice, F, October 21-25, 2013

[19] Welte, S.; Cristescu, I.; Dittrich, H.; Lohr, N.; Melzer, R.; Michling, R.; Plusczyk, C.; Schäfer, P.
Setup and commissioning of a combined waer detritiation and isotope separation experiment at the Tritium Laboratory Karlsruhe.
DOI:10.1016/j.fusengdes.2013.03.061

[20] Welte, S.; Besserer, U.; Osenberg, D.; Wendel, J.
Tritium laboratory Karlsruhe (TLK): Administrative and technical framework for isotope laboratory operation.
10th International Conference on Tritium Science and Technology (TRITIUM 2013), Nice, F, October 21-25, 2013

[21] Borisevich, O.; Demange, D.; Kind, M.
Zeolite membrane cascade for tritium extraction and recovery systems.
10th International Conference on Tritium Science and Technology (TRITIUM 2013), Nice, F, October 21-25, 2013

[22] Demange, D.; Borisevich, O.; Gramlich, N.; Wagner, R.; Welte, S.
Zeolite membranes and palladium membrane reactor for tritium extraction from the breeder blankets of ITER and DEMO.
Fusion Engineering and Design, 88(2013) S.2396-2399, DOI:10.1016/j.fusengdes.2013.05.102

[23] Ricapito, I.; Calderoni, P.; Poitevin, Y.; Aiello, A.; Utili, M.; Demange, D.
Tritium processing for the European tests blanket systems: current status of the design and development strategy.
10th International Conference on Tritium Science and Technology (TRITIUM 2013), Nice, F, October 21-25, 2013

[24] Santucci, A.; Ciampichetti, A.; Demange, D.; Franza, F.; Tosti, S.
Impact of tritium solubility in liquid Pb-Li on tritium migration in HCLL and WCLL blankets.
25th Symposium on Fusion Engineering (SOFE 2013), San Francisco, Calif., June 10-14, 2013

[25] Schlösser, M.; Rupp, S.; Mirz, S.; Fischer, S.
How can Raman-inactive helium Be made visible in Raman spectra of tritium/helium gas mixtures?
10th International Conference on Tritium Science and Technology (TRITIUM 2013), Nice, F, October 21-25, 2013

Safety

[1] Akkerman, V.; Bychkov, V.; Kuznetsov, M.; Law, C.K.; Valiev, D.; Wu, M.H.
Fast flame acceleration and deflagration-to-detonation transition in smooth and obstructed tubes, channels and slits.
Proceedings of the 8th National Combustion Meeting, Park City, Utah May 19-22, 2013
Vol.2 S.970-978, Red Hook, N.Y. : Curran Associates, 2013, ISBN 978-1-62748-842-6

[2] Kuznetsov, M.
Flame acceleration and DDT in linear and circular geometries.
International Workshop on Detonation for Propulsion (IWDP 2013), Tainan, Taiwan,
July 26-28, 2013

[3] Klimenko, D.; Pasler, V.
Busbar arcs at large fusion magnets: conductor to feeder tube arcing model experiments with the LONGARC devce.
11th International Symposium on Fusion Nuclear Technology (ISFNT 2013), Barcelona, E,
September 16-20, 2013

Appendix IV: Glossary

2C-PIM	2Component-Powder Injection Molding
AC	Alternating Current
ACE	A Compact ENDF Data Format for MCNP
ACI	After-Cavity Interaction
ACP	Activated Corrosion Product
AES	Auger Electron Spectroscopy
AEUL	University of Latvia
AGHS	Active Gas Handling System
AMF	Active Maintenance Facility
Appm	Atomic parts per million
ARB	Accumulative Roll Bonding
ART-MS	Auto-Resonant Ion Trap Mass Spectrometer
ASDEX	Tokamak Research Reactor in Garching
ASP	Neutron Generator located at Aldermaston (UK)
ASTM	American Society for Testing and Materials
AUG	ASDEX Upgrade
BA	“Broader Approach” project
BA DEMO	Broader Approach DEMO
BCA	Binary Collision Approximation
BDT	Brittle-to-Ductile Transition
BDTT	Brittle to Ductile Transition Temperature
BEKED	Nuclear Data Evaluation Code System developed by KIT
BF	Bright Field
BFWM	Blanket First Wall Module
B-lite	Monte-Carlo MCNP general model of ITER in 3D geometry
BM	Base Material
BO	Basal Octahedral Interstitial Position
BoP	Balance of Plant
BP	Back Plate
BSE	Beam Stopping Element
BSM	Blanket Shield Module

BSS	Back Supporting Structure
BT	Basal Tetrahedral Interstitial Position
BU	Breeder Unit
BUSARC	Subroutine of MAGS for the simulation of mobile arcs at coil external current leads (busbars)
BZ	Breeding Zone
C&E	Capture and Exchange
CAD	Computer Aided Design
CARM	Cyclotron Auto Resonance Maser
CASCADE	Code for the simulation of nucleon and nuclei interaction with targets using the intranuclear cascade evaporation model
CBED	Convergent Beam Electron Diffraction
CBN	Cubic Boron Nitride
CCFE	Culham Centre for Fusion Energy, UK
CCRC	Coated Conductor Rutherford Cable
CEA	Commissariat à l'Énergie Atomique, Saclay (France)
CECE	Combined Electrolysis and Catalytic Exchange
CFD	Computational Fluid Dynamics
CFN	Center of Functional Nanostructures (KIT)
CFX	ANSYS Module for Fluid-dynamics Analysis
CHC	Component Handling Cell, radiation protection cell for large scale components
CIEMAT	Centro de Investigaciones Energeticas Medioambientales y Tecnologicas
CNR	Consiglio Nazionale delle Ricerche, Milano, Italy
COBRA	Common Object Request Broker Architecture used in SALOME for data communications between modules
COD	Crack Opening Displacement
COVR	Module of the NJOY Code for Processing Co-Varnance Data
CP	Cooling Plate
CPS	Coolant Purification System
CPU	Central Processing Unit
C-R	Circumferential Orientation
CRPP	Centre de Recherces en Physique des Plasmas, Lausanne, Switzerland
CS	Central Solenoid
CTS	Collective Thomson Scattering
Cu	Copper
CuLTKa	Current Lead Test Facility Karlsruhe
CVD	Chemical Vapour Deposition
CW	Continuous Wave
CWS	Coolant Water System

D1S	Direct 1-Step (method for shutdown dose rate calculations)
DA	Either Domestic Agency or ITER Member TBM Team
DBH	Dispersed Barrier Hardening
DBTT	Ductile-to-Brittle Transition Temperature
DCLL	Dual Coolant Lead Lithium
DD	Double Disk
DDD	Design Description Document
DEMO	Demonstration Fusion Power Plant
DFW	Diagnostics First Wall panel of the port plug
DIFFER	Dutch Institute for Fundamental Energy Research, Netherland
DIR	Direct Internal Recycling Concept
DOF	Degree of Freedom
Dpa	Displacement per atom
DSM	Diagnostics Shielding Module of the port plug
DSMC	Direct Simulation Monte Carlo
DT	Deuterium – Tritium (fusion reaction)
DTE	JET Deuterium Tritium Experiment
DWMF	Double Wall Main Frame
EAF	European Activation File
EB	Electron Beam Welding
EBSD	Electron Backscatter Diffraction
EC	Electron Cyclotron or European Commission
ECAP	Equal Channel Angular Pressing
ECCD	Electron Cyclotron Current Drive
ECH	Electron Cyclotron Heating
ECM	Electron Cyclotron Maser
ECRH	Electron Cyclotron Resonance Heating
EDIPO	European Dipole
EDM	Electro Discharge Machining
EDX	Energy Dispersive X-ray Spectroscopy
EELS	Electron Energy Loss Spectroscopy
EFDA	European Fusion Development Agreement
EFF	Êuropean Fusion File
EFTEM	Energy Filtered Transmission Electron Microscopy
ELM	Edge Localized Model of plasma to be controlled in ITER
EM	Electromagnetic

ENDEP	Name of Code
ENDP	Evaluated Nuclear Data File (USA)
ENEA	Italian National Agency for New Technologies, Energy and Sustainable Economy Development
EOS	Equation of state
EPP	Equatorial Port Plug of ITER
ESR	Early Stage Researcher (= Trainee)
EU	European Union
EUROFER	European reduced activation ferritic-martensitic steel
EV	Expansion Volume
EVEDA	Engineering Validation and Engineering Design Activities
EXFOR	Exchange Format for Experimental Data
F	Compression force (N)
F4E	Fusion for Energy
FabriCharMe	Fabrication and Characterization of Materials
FCI	Flow Channel Insert
FCS	First Confinement System
FDS	Fusion Design Study / Fusion Digital Simulation (Hefei, China)
FE	Finite Element
FEA	Finite Element Analysis
FEG	Field Emission Gun
FEM	Finite Element Method
FEM	Free Electron Maser
FENDL	Fusion Evaluated Nuclear Data Library
FFMEA	Functional Failure Modes and Effects Analysis
FIB	Focused Ion Beam Microscope
FISPACT	Activation Inventory Code CCFE, UK
FLF	Flux Limit Factor
Fluent	CFD Code
FLUKA	Particle Physics Monte Carlo simulation code system
FM	Fracture-Mechanical
FML	Fusion Materials Laboratory (KIT, Germany)
FNG	Frascati Neutron Generator
FPP	Fusion Power Plant
FPY	Full Power Year
FSSS	Fisher Sub-Sieve Size

FT	Fracture Thoughness
FW	First Wall
FW-BK	First Wall - Blanket
FZJ	Forschungszentrum Jülich
FZK	Forschungszentrum Karlsruhe (now KIT)
GDH	Geometry Dependent Hybrid Nuclear Model
GEOM	SALOME Module for geometry modelling
GEPP	Generic Equatorial Port Plug
GOT	Goal Oriented Training Programme
GUI	Graphical User Interface
GUPP	Generic Upper Port Plug of ITER
H&CD	Heating and Current Drive
H_2	Hydrogen
HAADF	High Angle Annular Dark Field
HAD	Hot-dip Aluminizing Process
HAS	Hungarian Academy of Sciences
HAZ	Heat Affected Zone
HCBB	Helium Cooled Breeding Blanket
HCF	Hot Cell Facility
HCFB	Hot Cell Facility Building
HCLL	Helium Cooled Lead Lithium
HCPB	Helium Cooled Pebble Bed
HCS	Helium Coolant System
HELIOS	Supercomputer at International Fusion Energy Research Centre (IFERC) – Computational Simulation Centre (CSC) in Rokkasho, Japan
HELOKA-HP	Helium Loop Karlsruhe – High Pressure
HELOKA-LP	Helium Loop Karlsruhe – Low Pressure (experimental facility at KIT)
HEMJ	Helium Modular Jet-cooling
HERMES	Test Facility for Metal Foil Vacuum pumps
Hf	Hafnium
HFR	High Flux Reactor (Petten)
HFTM	High Flux Test Module, irradiation experiment containing small scale specimens
HHF	High Heat Flux
HHFM	High Heat Flux Materials
HIP	Hot Isostatic Pressing
HP	High Pressure

HPC-FF	High Performance Computer for Fusion, Jülich
HPT	High Pressure Torsion
HRP	Hot Radial Pressing
HR-QMS	High Resolution Quadrupole Mass Spectrometer
HTHE	High Temperature Helium Embrittlement
HTS	High Temperature Superconductor
HTW	Highly Tritiated Water
HVAC	Heating Ventilating Air Conditioning System
HVPS	High Voltage Power Supply
IAEA	International Atomic Energy Agency
IAM	Institute for Applied Materials
IAP	Institute of Applied Physics
IB	Inboard
I_c	Critical Current
ICRP	International Commission on Radiological Protection
IDM	ITER Document Management
IFMIF	International Fusion Material Irradiation Facility
IHM	Institute for Pulsed Power and Microwave Technology
ILF	Immediate Local Fracture
INTRA	In-Vessel Transient Analyses Code by Studsvik
IO	ITER Organization
IPF	Institut für Plasmaforschung
IPFL	Immediate Plastic Flow Localization
IPP	Max Planck Institut für Plasmaphysik, Garching,/Greifswald, Germany
IPPLM-WUT	Institute of Plasma Physics and Laser Microfusion – Warsaw University of Technology, PL
ITEP	Institute for Technical Physics
ITER	International Thermonuclear Experimental Reactor
ITERVAC	Network Code for Vacuum Flows
JAEA	Japan Atomic Energy Agency
JEFF	Joint Evaluated Fission and Fusion File (EU nuclear data library)
JENDL	Japanese Evaluated Nuclear Data Library
JET	Joint European Torus
J_{IC}	Critical value of J-integral at the onset of stable crack growth
JINR	Joint Institute for Nuclear Research, Dubna, Russia
JSC	Jülich Supercomputing Centre

JSC “SSC RIAR”	Joint Stock Company “State Scientific Centre Research Institute of Atomic Reactors”
JSI	Johan Stefan Institute, Ljubljana, Slovenia
KALOS	Karlsruhe Lithium Orthosilicate
KALPUREX	Karlsruhe Liquid Metal Based Pumping Process for Fusion Reactor Exhaust Gases
K_{IC}	Critical Stress Intensity Factor for Model I Loading
KIT	Karlsruhe Institute of Technology
KLST	Smallest available type of charpy specimen shape
KTH	Royal Institute of Technology, Stockholm, Sweden
L and H-mode	The low and high confinement modes of operations in tokamak
LCF	Low Cycle Fatigue
LDP	Linear Diffusion Pump
LF	Low Frequency
LHT	Launcher Handling Test Facility at KIT
LOCA	Loss of Coolant Accident
LOFA	Loss Of Flow
LOM	Light Optical Microscope / Microscopy
LONGARC	Improved experimental device for small scale model arc experiments
LP	Low Pressure
LPCE	Liquid Phase Catalytic Exchange
L-R	Longitudinal orientation; expected crack propagation direction is radial
LTA	Long-term Annealing
LTS	Low Temperature Shield
MA	Mechanical Alloying
MAGARC	INL magnet safety code
MAGS	KIT Magnet Safety Code System (MAGnet System)
MARFE	Multifaceted Asymmetric Radiation From the Edge
MC	Monte Carlo
McCAD	Software tool for CAD to MC geometry conversion (by KIT)
McMeshTran	MC Mesh and Data Transformation/Translation/Transfer Interface
MCNP	Monte Carlo Code for Multi Particle Transport Simulations
MCSEN	Monte Carlo Sensitivity Code based on MCNP
MD	Molecular Dynamics
MD	Major Disruption
MED	Data Exchange Format used
MEMOS	Name of Code

Mf	Multi-frequency
MHD	Magnetohydrodynamic
MIG	Massive Gas Injection
ML	Monolayer (measure of hydrogen surface coverage defined as a function of adsorption sites occupied with H atoms)
MMS	Multi-Module Segment (Blanket)
MPI	Message Passing Interface
NAS	Neutron Activation System of ITER Diagnostics
NBI	Neutral Beam Injector
NBTF	Neutral Beam Test Facility
NDS	Normal Detritiation System
NE213	Liquid scintillator with capability to discriminate between gamma-ray and neutron interaction
NEA	Nuclear Energy Agency, Paris, France
NEB	Nudged Elastic Band (a method for calculation migration barriers)
Ni	Nickel
NJOY	Code for the Processing of Nuclear Data
NRG	Nuclear Research and Consultancy Group, National Nuclear Research Institute of the Netherlands, located in Petten
NRT	Norgett-Robinson-Torrens displacement damage approximation
NWL	Neutron Wall Loading
O	Octahedral Interstitial Position
OB	Outboard
ODS	Oxygen Dispersion Strengthened
ODSFS	Oxide Dispersion Strengthened Ferritic Steel
OMA	Outgassing Measurement Apparatus
OMP	Optical Model Potential
OSI	Lithium Ortho Silicate
PA	Procurement Arrangement
ParaView	Open Source Software for Data Visualisation
PBC	Plant Breakdown Structure
PbLi	Eutectic lead-lithium alloy (actually containing 15.8 at.% Li)
PCDP	Personal Career Development Plan
PCS	Pressure Control System
Pd	Paladium
PF	Poliodal Field
PFC	Poloidal Field Coil
PFC	Plasma Facing Component

PHTS	Primary Heat Transfer System
PIC	Particle-in-cell
PIE	Post Irradiation Examination
PIM	Powder Injection Moulding
PM	Project Management
PPCS	Power Plant Conceptual Study
PPPT	Power Plant Physics and Technology
PPS	Pulse Plasma Sintering
PROCESS	Code for system analyses (by CCFE, Culham)
ProVac3D	KIT Code for Vacuum Flow Calculations
PWHT	Post Weld Heat Treatment
PWR	Pressurized Water Reactor
QA	Quality Assurance
QDS	Quick Disconnect Systems
R2Smesh	Rigorous 2-Step mesh method for shutdown-dose rate calculations
RAC	Rig Assembly Cell: radiation protected cell to allow integration of irradiation rigs
RadEff	Radiation Effects in RAFM Steels ¨Experiments & Modelling”
RAFM	Reduced Activation Ferritic Martensitic (Steel)
RAMI	Reliability, Availability, Maintainability, Inspectability
RE	Runaway Electrons
RF	Radio Frequency
RFX	Consorzio RFX, Padova, Italy
RH	Remote Handling
RHE	Remote Handling Equipment
RID	Residual Ion Dump
RMP	Resonant Magnetic Perturbations
RSICC	Radiation Safety Information Computational Centre
RT	Room Temperature
S/U	Sensitivity/Uncertainty
SALOME	Computation Platform
SCK-CEN	Studiecentrum Voor Kernenergie – Centre d‘Etude de L’Energie Nucleare
SDC	Single-Stage Depressed Collector
SDDR	Shut-Down Dose Rate

SDR	Shutdown Dose Rate
SDS	Stand-by Detritiation System
SEM	Scanning Electron Microscopy
SERPENT	Monte Carlo reactor physics burn-up code (by VTT, Finland)
SF	Stiffening Finger
SF	Snow Flake Magnetic Configuration in the Vicinity to x-point
SG	Stiffening Grid
SiC_f/SiC	Silicon Carbide Composite
SMESH	SALOME Module for generation
SOL	Scrape-off L ayer
SPD	Severe Plastic Deformation
SPE	Solid Polymer Electrolyte
SPND	Self-Powered Neutron Detector
SRS	Strain Rate Sensitivity
SSTT	Small Specimen Testing Technology
St	Steel
STEM	Scanning Transmission Electron Microscopy
SUSD3D	Deterministic Sensitivity/uncertainly Code, developed by JSI
SWCS	Secondary Water Cooling System
T-111	Tantalum-base alloy (Ta-8wt%W-2wt%Hf)
TA	Target Assembly, the liquid lithium target with attachment structures
Ta-10W	Tantalum-base alloy (Ta-10wt%W)
TALYS	Nuclear Model Code (NRG)
TBC	To Be Confirmed
TBD	To Be Defined
TBM	Test Blanket Module
TBR	Tritium Breeding Ratio
TBS	Test Blanket System
TC	Test Cell: radiation protected cell containing the IFMIF neutron source
TCWS	Tokamak Coolant Water System
TD	Theoretical Density
TED	Thales Electron Devices at Velizy, France
TEKES	Finnish Funding Agency for Technology and Innovation
TEM	Transmission Electron Microscope / Microscopy

TENDL	TALYS based Evaluated Nuclear Data Library
TES	Tritium Extraction System
TF	Toroidal Field
TFC	Toroidal Field Coli
THESEUS	Test Facility for DEMO Vacuum Pumps
Ti	Titanium
TIG	Tungsten Inert Gas Welding
TIMO	Test Facility for ITER Model Pump
TLK	Tritium Laboratory Karlsruhe
Tm	Melting Point (K)
TMAC	Test Module Assembly Cell
TMFS	Transverse Magnetic Field Sweeping
TOKES	Integrated code, describing the steady state and transient processes in tokamak plasmas
TOSKA	Torusspulen Testanordnung Karlsruhe
TQ	Thermal/current Quench
TRIPOLI	Monte Carlo particle transport code (by CEA, France)
TRM	Tritium Release Test Module, irradiation experiment for tritium breeding
TS	Thermal Shield
TT	Twisted Tape
TU Berlin	Technical University of Berlin
TUD-NG	Neutron Generator located at Technical University Dresden
UFG	Ultra-fine Grained
UNED	Universidad de Educación a Distancia, Madrid, Spain
UPP	Upper Port Plug (UPP) of ITER
VACARC	Experimental device for small scale model arc experiments /VACuum ARC)
VDE	Vertical Displacement Event (disruption)
VMFS	Vertical Magnetic Field Sweeping
VNC	Vertical Neutron Camera of ITER Diagnostics
VUV	Vacuum Ultra-Violet spectrometer of ITER Diagnostics
VV	Vacuum Vessel
VVPSS	VV Pressure Suppression System
W	Tungsten
WBS	Work Breakdown Structure
WCLL	Walter Cooled Lead Lithium

WDS	Water Detritiation System
WL10	Tungsten with 10 % of La2O3
WP	Work Programme
WTZ	Wissenschaftlich-Technische Zusammenarbeit 01/577
XRD	X-Ray Diffraction Analysis